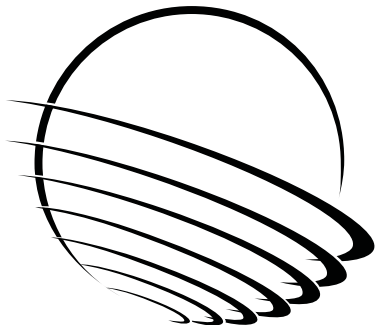


NASA/CP—2018-219887



44th Aerospace Mechanisms Symposium

*Edward A. Boesiger, Compiler
Lockheed Martin Space Systems Company, Sunnyvale, California*



NASA STI Program . . . in Profile

Since its founding, NASA has been dedicated to the advancement of aeronautics and space science. The NASA Scientific and Technical Information (STI) Program plays a key part in helping NASA maintain this important role.

The NASA STI Program operates under the auspices of the Agency Chief Information Officer. It collects, organizes, provides for archiving, and disseminates NASA's STI. The NASA STI Program provides access to the NASA Technical Report Server—Registered (NTRS Reg) and NASA Technical Report Server—Public (NTRS) thus providing one of the largest collections of aeronautical and space science STI in the world. Results are published in both non-NASA channels and by NASA in the NASA STI Report Series, which includes the following report types:

- **TECHNICAL PUBLICATION.** Reports of completed research or a major significant phase of research that present the results of NASA programs and include extensive data or theoretical analysis. Includes compilations of significant scientific and technical data and information deemed to be of continuing reference value. NASA counter-part of peer-reviewed formal professional papers, but has less stringent limitations on manuscript length and extent of graphic presentations.
- **TECHNICAL MEMORANDUM.** Scientific and technical findings that are preliminary or of specialized interest, e.g., "quick-release" reports, working papers, and bibliographies that contain minimal annotation. Does not contain extensive analysis.
- **CONTRACTOR REPORT.** Scientific and technical findings by NASA-sponsored contractors and grantees.
- **CONFERENCE PUBLICATION.** Collected papers from scientific and technical conferences, symposia, seminars, or other meetings sponsored or co-sponsored by NASA.
- **SPECIAL PUBLICATION.** Scientific, technical, or historical information from NASA programs, projects, and missions, often concerned with subjects having substantial public interest.
- **TECHNICAL TRANSLATION.** English-language translations of foreign scientific and technical material pertinent to NASA's mission.

For more information about the NASA STI program, see the following:

- Access the NASA STI program home page at <http://www.sti.nasa.gov>
- E-mail your question to help@sti.nasa.gov
- Fax your question to the NASA STI Information Desk at 757-864-6500
- Telephone the NASA STI Information Desk at 757-864-9658
- Write to:
NASA STI Program
Mail Stop 148
NASA Langley Research Center
Hampton, VA 23681-2199

NASA/CP—2018-219887



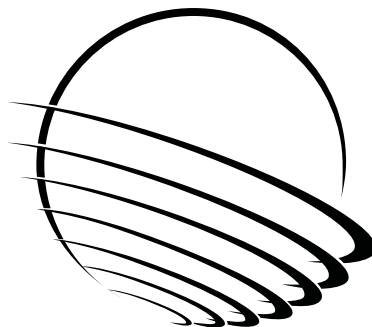
44th Aerospace Mechanisms Symposium

*Edward A. Boesiger, Compiler
Lockheed Martin Space Systems Company, Sunnyvale, California*

Proceedings of a conference held at Hilton Cleveland Downtown
Hosted by NASA Glenn Research Center and Lockheed Martin Space Systems Company
Sponsored and organized by Mechanisms Education Association
Cleveland, Ohio
May 16–18, 2018

National Aeronautics and
Space Administration

Glenn Research Center
Cleveland, Ohio 44135



Trade names and trademarks are used in this report for identification only. Their usage does not constitute an official endorsement, either expressed or implied, by the National Aeronautics and Space Administration.

Level of Review: This material has been technically reviewed by technical management.

Available from

NASA STI Program
Mail Stop 148
NASA Langley Research Center
Hampton, VA 23681-2199

National Technical Information Service
5285 Port Royal Road
Springfield, VA 22161
703-605-6000

This report is available in electronic form at <http://www.sti.nasa.gov/> and <http://ntrs.nasa.gov/>

PREFACE

The Aerospace Mechanisms Symposium (AMS) provides a unique forum for those active in the design, production, and use of aerospace mechanisms. A major focus is the reporting of problems and solutions associated with the development and flight certification of new mechanisms. Sponsored and organized by the Mechanisms Education Association, responsibility for hosting the AMS is shared by the National Aeronautics and Space Administration and Lockheed Martin Space. Now in its 44th symposium, the AMS continues to be well attended, attracting participants from both the United States and abroad.

The 44th AMS was held in Cleveland, Ohio, from May 16 to 18, 2018. During these 3 days, 45 papers were presented. Topics included payload and positioning mechanisms, components such as hinges and motors, CubeSats, tribology, docking systems, and mechanism testing. Hardware displays during the supplier exhibit gave attendees an opportunity to meet with developers of current and future mechanism components.

The high quality of this symposium is a result of the work of many people, and their efforts are gratefully acknowledged. This extends to the voluntary members of the symposium organizing committee representing the eight NASA field centers, Lockheed Martin Space, and the European Space Agency. Appreciation is also extended to the session chairs, the authors, and particularly the personnel at Glenn Research Center responsible for the symposium arrangements and the publication of these proceedings. A sincere thank you also goes to the symposium executive committee who is responsible for the year-to-year management of the AMS, including paper processing and preparation of the program.

The use of trade names of manufacturers in this publication does not constitute an official endorsement of such products or manufacturers, either expressed or implied, by the National Aeronautics and Space Administration.

CONTENTS

Symposium Schedule	xi
Symposium Organizing and Advisory Committees.....	xv
Scroll Compressor for Mars Atmospheric Acquisition.....	1
John Wilson, Bryce Shaffer & Ted Iskenderian	
The Regolith and Ice Drill for Exploration of New Terrains (TRIDENT); a One-Meter Drill for the Lunar Resource Prospector Mission.....	13
Gale Paulsen, Zachary Mank, Alexander Wang, Paul Chow, Cody Hyman, Thomas Thomas, Allen Lee, Kris Zacny, James Smith, Jacqueline Quinn, Erik Mumm & Ron Hayes	
KaRIn Alignment Mechanism Design, Development and Testing.....	27
John Luke Wolff	
Environmental Chamber Testing of a Rock Sampling Drill for Venus Exploration	41
Fredrik Rehnmark, Evan Cloninger, Cody Hyman, Jameil Bailey, Nick Traeden, Kris Zacny, Kristopher Kriechbaum, Joseph Melko, Brian Wilcox, Jeffery Hall & Kristopher Sherrill	
A Discussion of Friction Anomaly Signatures in Response to Electrical Discharge in Ball Bearings.....	55
William Bialke	
Efficacy of Lead Naphthenate for Wear Protection in Mixed Lubrication Regime	69
Jason T. Galary	
Dynamic Behavior of Ball Bearings under Axial Vibration	83
Virgil Hinque & René Seiler	
The Design & Development of the Ocean Color Instrument Precision Superduplex Hybrid Bearing Cartridge.....	97
Joseph Schepis, Timothy Woodard, Claef Hakun, Konrad Bergandy, Joseph Church, Peter Ward, Michael Lee, Alfred Conti & Jeffrey Guzek	
Evaluation of Friction Characteristics and Low Friction Mechanism of Tungsten Disulfide for Space Solid Lubricant at Elevated Temperature in a Vacuum	113
Ayaka Takahashi, Josaphat Tetuko S S & Keizo Hashimoto	
Performance of MoS ₂ Coated Gears Exposed to Humid Air during Storage	127
Timothy Krantz, Claef Hakun, Zachary Cameron, Iqbal Shareef & Michael Dube	
An Improved Solid Lubricant for Bearings Operating in Space and Terrestrial Environments	141
Arindam Paul, Harpal Singh, Kalyan C. Mutyala & G.L. Doll	
Hybrid Lubrication of PFPE Fluids and Sputtered MoS ₂	151
Michael Buttery, Anthony Kent, Dave Forster & Achilleas Vortselas	
Solving a Performance Limiting Resonance Frequency Problem of the SOFIA Secondary Mirror Mechanism by Structural Modifications	165
Yannick Lammen, Andreas Reinacher & Alfred Krabbe	

Enhanced Vibration Isolation Using a Magnetic Linear Gear for Highly Demanding Aerospace Applications.....	177
José Luis Perez-Diaz, Ignacio Valiente-Blanco, Juan Sanchez García-Casarrubios, Cristian Cristache, Fernando Rodriguez-Celis, Judit Esnoz-Larraya, Efrén Diez-Jimenez & José Luis Perez-Alamo	
A Mechanisms Perspective on Microvibration – Good Practices and Lessons Learned	191
Geert Smet & Sandro Patti	
Investigation of Bolt Preload Relaxation for JWST Thermal Heat Strap Assembly Joints with Aluminum-1100 and Indium Gaskets	205
Andrew Bartoszyk, Thomas Walsh, Jody Davis, Jason Krom, Patrick Williams, Jason Hylan & Edgar Hemminger	
Validation and Test Results of the 2.5D Technology for Pancake Slip Rings	211
Mélanie Henry & Sandro Liberatoscioli	
Quantifying Threaded Fastener Locking.....	217
Daniel P. Hess & Christopher DellaCorte	
Reliability Calculation Methodologies for Mechanisms and Actuators	223
Tanner Horne & Evan Harrington	
Development of the NEA Mini for Low Load Applications	233
John Sudick & Geoff Kaczynski	
Compliant Mechanisms Re-Design based on Additive Manufacturing and Topology Optimization.....	239
Lionel Kiener, Hervé Saudan, Gérald Perruchoud & Johan Kruis	
Non-Pyrotechnic Multi-Point Release Mechanisms for Spacecraft Release	247
Ambrosio Mejia, John Sudick & Geoff Kaczynski	
Validation of a Novel High Performance Magnetic Gearbox for Space.....	255
Ignacio Valiente-Blanco, Judit Esnoz-Larraya, Efrén Diez-Jimenez, Juan Sanchez García-Casarrubios, Cristian Cristache, Fernando Rodriguez-Celis & José Luis Perez-Diaz	
Qualification of a Networked Pyrotechnic Initiation System for the CST-100 Starliner Spacecraft.....	263
David Novotney, Craig Boucher, Joseph Smith, Robert Morlath & Hervens Beauge	
Use and Advantages of Direct-Drive Brushless DC Actuators for Precision Instrument Pointing of the Total and Spectral Solar Irradiance Sensor.....	269
Patrick Brown, Andrew Engelmann & Ryan Lewis	
Testing and Maturing a Mass Translating Mechanism for a Deep Space CubeSat.....	283
Alex Few, Tiffany Lockett, Richard Wilson, David Boling & Erik Loper	
Solar Array Drive Assembly Qualification Lessons Learned	293
Jonathan Wood & Timothy Pargett	
Determining Root Causes of Mysterious Hardware Failures using High Resolution CT Scanning.....	307
Michael R. Johnson	

Testing and Development of the NEA Scout Solar Sail Deployer Mechanism.....	323
Alex Few, Tiffany Lockett, Richard Wilson & David Boling	
Mechanism Design & Flight Build of Furled High Strain Composite Antenna for CubeSats	337
Bruce Davis, Ryan VanHalle, Kevin Cox & Will Francis	
Failure of the Ball-Lock Mechanism on the NanoRacks CubeSat Deployer	351
Michael Lewis & Conor Brown	
Lessons Learned from a Deployment Mechanism for a Ka-band Deployable Antenna for CubeSats.....	361
Jonathan Sauder, Nacer Chahat, Richard Hodges, Eva Peral, Yahya Rahmat-Samii & Mark Thomson	
Design and Development of CubeSat Solar Array Deployment Mechanisms Using Shape Memory Alloys	375
Allen Guzik & Othmane Benafan	
Lessons Learned in the Flight Qualification of the S-NPP and NOAA-20 Solar Array Mechanisms....	389
Daniel Helfrich & Adam Sexton	
Spacecraft Common Deployable Boom Hinge Deploy and Latching Mechanisms	403
Paul Lytal & Marcel Renson	
Precision High-Strain Composite Hinges for Deployable Space Telescopes.....	417
Mark Silver & Michael Echter	
The Synchronization Mechanism for Solar Array with a Three-Stage Deployment.....	431
Zehong Yan, Hongjun Shang, Guowei Zhao, Qiaolong Yang, Jingya Ma & Jianjun Wang	
Mechanisms and New Space	443
Bill Purdy	
Development of the Multi-Purpose Transportation System for the Space Launch System Core Stage Flight Article	459
Sarah Sandridge, Hue Lien, Ronald Hunt, Ayana Reese & Christopher Doktor	
NASA Docking System Block 1: NASA's New Direct Electric Docking System Supporting ISS and Future Human Space Exploration.....	471
Justin McFatter, Karl Keiser & Timothy Rupp	
Capture Latch Assembly for the NASA Docking System.....	485
Brandon Dick, Nathan Mauch & Timothy Rupp	
High Speed Bearing Wear Rate Measurements for Spacecraft Active Thermal Control Fluid Pumps with a Novel Pin on Disk Apparatus.....	499
Robert J. Bruckner & Richard A. Manco II	
Accelerated Testing of Tribological Components - Uncertainties and Solutions	513
Simon Lewis, Mike Buttery, Oliver Poyntz-Wright, Anthony Kent & Achilleas Vortsellas	

Developmental Bearing and Bushing Testing for Mars Gearboxes.....	529
David Suffern & Jonathan Parker	
Experimental Method for Determining Ball Bearing Lubricant Quantity Factor	543
Yoshimi R. Takeuchi, Peter P. Frantz and Tim P. Woodard	

SYMPOSIUM SCHEDULE

WEDNESDAY, 16 MAY 2018

7:00 **Wednesday Presenters' Breakfast** – Veterans Room B

7:00 **CHECK-IN AND REFRESHMENTS** – 5th Floor Lobby

8:15 **INTRODUCTORY REMARKS** – Superior Ballroom, Section A

Damon Delap, Host Chairman, NASA Glenn Research Center, Cleveland, OH
Edward Boesiger, General Chairman, Lockheed Martin Space, Sunnyvale, CA
Marla E. Pérez-Davis, Deputy Director, NASA Glenn Research Center, Cleveland, OH

8:30 SESSION I – INSTRUMENTS

Session Chair: Rius Billing, MDA US Systems, Pasadena, CA

- Scroll Compressor for Mars Atmospheric Acquisition
John Wilson & Bryce Shaffer, Air Squared, Inc., Broomfield, CO; Ted Iskenderian, Jet Propulsion Laboratory, Pasadena, CA
- The Regolith and Ice Drill for Exploration of New Terrains (TRIDENT); a One-Meter Drill for the Lunar Resource Prospector Mission
Gale Paulsen et al., Honeybee Robotics Spacecraft Mechanisms Corp, Pasadena, CA/Longmont, CO;
James Smith & Jacqueline Quinn, NASA Kennedy Space Center, FL
- KaRIn Alignment Mechanism Design, Development and Testing
John Wolff, Jet Propulsion Laboratory, Pasadena, CA
- Environmental Chamber Testing of a Rock Sampling Drill for Venus Exploration
Fredrik Rehnmark et al., Honeybee Robotics Spacecraft Mechanisms Corp, Pasadena, CA; Kristopher Kriechbaum et al., Jet Propulsion Laboratory, Pasadena, CA

10:10 SESSION II – BEARINGS & LUBRICATION

Session Chair: Merritt Webb, Harris Corporation, Fort Wayne, IN

- A Discussion of Friction Anomaly Signatures in Response to Electrical Discharge in Ball Bearings
William Bialke, Lochridge Farm LLC, Trumansburg, NY
- Efficacy of Lead Naphthenate for Wear Protection in Mixed Lubrication Regime
Jason Galary, NYE Lubricants Inc, Fairhaven, MA
- Dynamic Behavior of Ball Bearings under Axial Vibration
Virgil Hinque & René Seiler, European Space Agency/ESTEC, Noordwijk, The Netherlands
- The Design & Development of the Ocean Color Instrument Precision Superduplex Hybrid Bearing Cartridge
Joseph Schepis et al., NASA Goddard Space Flight Center, Greenbelt, MD; Timothy Woodard, Peter Ward & Michael Lee, The Aerospace Corporation, El Segundo, CA; Alfred Conti, The Barden Corporation, Danbury, CT; Jeffrey Guzek, Design Interface, Columbia, MD

11:50 LUNCH

Lunch for AMS Attendees in the Superior Ballroom, Section D

12:50 SESSION III – SOLID LUBRICATION

Session Chair: Brian Gore, The Aerospace Corporation, El Segundo, CA

- Evaluation of Friction Characteristics and Low Friction Mechanism of Tungsten Disulfide for Space Solid Lubricant at Elevated Temperature in a Vacuum
Ayaka Takahashi & Josaphat Tetuko S S, Chiba University, Chiba, Japan; Keizo Hashimoto, Teikyo University, Tokyo, Japan
- Performance of MoS₂ Coated Gears Exposed to Humid Air During Storage
Tim Krantz & Zachary Cameron, NASA Glenn Research Center, Cleveland, OH; Claef Hakun, NASA Goddard Space Flight Center, Greenbelt, MD; Iqbal Shareef, Bradley University, Peoria, IL; Michael Dube, NASA Langley Research Center, Hampton, VA
- An Improved Solid Lubricant for Bearings Operating in Space and Terrestrial Environments
Arindam Paul et al., University of Akron, Akron, OH
- Hybrid Lubrication of PFPE Fluids and Sputtered MoS₂
Michael Butterly et al., European Space Tribology Laboratory, ESR Technology Ltd., Warrington, United Kingdom

2:30 BREAK

2:45 SESSION IV - “OH THE NOISE! NOISE! NOISE!”

Session Chair: John Beasley, BEI Precision Systems & Space Division, Maumelle, AR

- Solving a Performance Limiting Resonance Frequency Problem of the SOFIA Secondary Mirror Mechanism by Structural Modifications
Yannick Lammen, Andreas Reinacher & Alfred Krabbe, Deutsches SOFIA Institut, University of Stuttgart, Stuttgart, Germany
- Enhanced Vibration Isolation Using a Magnetic Linear Gear for Highly Demanding Aerospace Applications
Jose Luis Perez-Diaz & Efrén Diez-Jimenez, Universidad de Alcalá, Alcalá de Henares, Spain ; Ignacio Valiente-Blanco et al., MAG SOAR S.L, Valdemoro, Spain
- A Mechanisms Perspective on Microvibration – Good Practices and Lessons Learned
Geert Smet & Sandro Patti, European Space Agency, Noordwijk, The Netherlands

4:00 SESSION V – POTPOURRI OF POSTERS

Session Chair: Joseph Pellicciotti, NASA HQ, Washington, D. C.

- Investigation of Bolt Preload Relaxation for JWST Thermal Heat Strap Assembly Joints with Aluminum-1100 and Indium Gaskets
Andrew Bartoszyk et al., NASA Goddard Space Flight Center, Greenbelt, MD; Thomas Walsh, Stinger Ghaffarian Technologies, Greenbelt, MD; Jason Krom, Sigma Space Corporation, Lanham, MD; Edgar Hemminger, Ares Corporation, Greenbelt, MD
- Validation and Test Results of the 2.5D Technology for Pancake Slip Rings
Mélanie Henry & Sandro Liberatoscioli, RUAG Schweiz AG, Nyon, Switzerland
- Quantifying Threaded Fastener Locking
Daniel Hess, University of South Florida, Tampa, FL; Christopher DellaCorte, NASA Glenn Research Center, Cleveland, OH

- Reliability Calculation Methodologies for Mechanisms and Actuators
Tanner Horne & Evan Harrington, Avior Control Technologies, Inc, Longmont, CO
- Development of the NEA Mini for Low Load Applications
John Sudick & Geoff Kaczynski, NEA Electronics, Inc., Moorpark, CA
- Compliant Mechanisms Re-Design based on Additive Manufacturing and Topology Optimization
Lionel Kiener et al., Centre Suisse d'Electronique et de Microtechnique S.A., Neuchatel, Switzerland
- Non-Pyrotechnic Multi-Point Release Mechanisms for Spacecraft Release
Ambrosio Mejia, John Sudick & Geoffrey Kaczynski, Ensign Bickford Aerospace NEA Electronics, Inc., Moorpark, CA
- Validation of a Novel High Performance Magnetic Gearbox for Space
Ignacio Valiente-Blanco et al., MAG SOAR SL., Valdemoro, Spain; Efrén Diez-Jimenez & José Luis Perez-Díaz, Universidad de Alcalá, Alcalá de Henares, Spain
- Qualification of a Networked Pyrotechnic Initiation System for the CST-100 Starliner Spacecraft
David Novotney et al., Ensign Bickford Aerospace, Simsbury, CT

6:00 -10:00 **RECEPTION** – Hilton Cleveland Downtown

Invited component suppliers display current products and provide tutorials along with FIRST Robotics Team demonstrations and a light buffet meal.

THURSDAY, 17 MAY 2018

7:00 Thursday Presenters' Breakfast – Veterans Room B

8:00 SESSION VI – ACTUATORS

Session Chair: Boz Sharif, Cobham Motion Control Solutions, Hauppauge, NY

- Use and Advantages of Direct-Drive Brushless DC Actuators for Precision Instrument Pointing of the Total and Spectral Solar Irradiance Sensor
Patrick Brown, Andrew Engemann & Ryan Lewis, University of Colorado, Boulder, CO
- Testing and Maturing a Mass Translating Mechanism for a Deep Space CubeSat
Alex Few, Tiffany Lockett & Erik Loper, NASA Marshall Space Flight Center, Huntsville, AL; Richard Wilson & David Boling, Jacobs Technologies, Huntsville, AL
- Solar Array Drive Assembly Qualification Lessons Learned
Jonathan Wood, Lockheed Martin Space, Sunnyvale, CA; Timothy Pargett, Moog Space and Defense Group, Mountain View, CA
- Determining Root Causes of Mysterious Hardware Failures using High Resolution CT Scanning
Michael Johnson, Jet Propulsion Laboratory, Pasadena, CA

9:40 BREAK

9:55 SESSION VII – CUBESATS

Session Chair: Henk Cruijssen, Airbus Defence & Space, Leiden, The Netherlands

- Testing and Development of the NEA Scout Solar Sail Deployer Mechanism
Alex Few & Tiffany Lockett, NASA Marshall Space Flight Center, Huntsville, AL; Richard Wilson & David Boling, Jacobs Engineering, Huntsville, AL
- Mechanism Design & Flight Build of Furled High Strain Composite Antenna for CubeSats
Bruce Davis et al., Roccor, Longmont, CO
- Failure of the Ball-Lock Mechanism on the NanoRacks Cubesat Deployer
Michael Lewis & Conor Brown, NanoRacks, LLC, Webster, TX
- Lessons Learned from a Deployment Mechanism for a Ka-band Deployable Antenna for CubeSats
Jonathan Sauder et al., Jet Propulsion Laboratory, Pasadena, CA; Yahya Rahmat-Samii, University of California Los Angeles, Los Angeles, CA; Mark Thomson, Northrop Grumman Astro Aerospace, Carpenteria, CA
- Design and Development of CubeSat Solar Array Deployment Mechanisms Using Shape Memory Alloys
Allen Guzik & Othmane Benafan, NASA Glenn Research Center, Cleveland, OH

12:00 LUNCH

Lunch for AMS Attendees in the Superior Ballroom, Section D

1:00: SPECIAL PRESENTATION: Restore-L: Enabling a New Era

Hsiao Smith: Acting Deputy Division Director, Satellite Servicing Projects Division NASA Goddard Space Flight Center

Hear about the mission to robotically refuel Landsat 7 in low earth orbit. Learn about the novel robotic hardware being developed to grab and refuel this satellite that was never designed to be refueled.

2:05 SESSION VIII – DEPLOY AND SOMETHING NEW

Session Chair: David Rohweller, Northrop Grumman Astro Aerospace, Carpinteria, CA

- Lessons Learned in the Flight Qualification of the S-NPP and NOAA-20 Solar Array Mechanisms,
Dan Helfrich, NASA Goddard Space Flight Center, Greenbelt, MD; Adam Sexton, Ball Aerospace Corporation, Boulder, CO
- Spacecraft Common Deployable Boom Hinge Deploy and Latching Mechanisms
Paul Lytal, NASA Jet Propulsion Laboratory, Pasadena, CA; Marcel Renson, D.E.B. Manufacturing Inc., Lakewood, NJ
- Precision High-Strain Composite Hinges for Deployable Space Telescopes
Mark Silver & Michael Echter, MIT Lincoln Laboratory, Lexington, MA
- The Synchronization Mechanism for Solar Array with a Three-Stage Deployment
Zehong Yan et al., Beijing Institute of Spacecraft System Engineering, Beijing, China; Guowei Zhao, Beihang University, Beijing, China
- Mechanisms and New Space
Bill Purdy, Purdy Engineering, Poolesville, MD

4:05 BREAK

4:20 INVITED PRESENTATION –Doug Wheelock, Aerospace Engineer and Astronaut

Doug has been launched into space via the Space Shuttle Discovery and Soyuz TMA-19, and spent more than 5 months in space aboard the Space Station. He has made multiple spacewalks to repair equipment and will have stories to tell.

7:00-11:00 BANQUET – Rock and Roll Hall of Fame
Dinner, entertainment and exhibits celebrating music history.

FRIDAY, 18 MAY 2018

7:00 **Friday Presenters' Breakfast** – Veterans Room B

8:00 SESSION IX – TRANSPORTATION & DOCKING

Session Chair: Brandon Robertson, NASA Johnson Space Center, Houston, TX

- Development of the Multi-Purpose Transportation System for the Space Launch System Core Stage Flight Article
Sarah Sandridge, NASA Marshall Space Flight Center, Huntsville, AL; Hue Lien et al., Jacobs Space Exploration Group, Huntsville, AL
- NASA Docking System Block 1: NASA's New Direct Electric Docking System Supporting ISS and Future Human Space Exploration,
Justin McFatter, The Boeing Company, Houston, TX; Karl Keiser, The Boeing Company, Huntsville, AL; Timothy Rupp, NASA Johnson Space Center, Houston, TX
- Capture Latch Assembly for the NASA Docking System
Brandon Dick & Nathan Mauch, The Boeing Company, Huntsville, AL; Timothy Rupp, NASA Johnson Space Center, Houston, Texas

9:15 BREAK**9:30 SESSION X – TESTING**

Session Chair: Peter Stromberg, Sandia National Laboratories, Albuquerque, NM

- High Speed Bearing Wear Rate Measurements for Spacecraft Active Thermal Control Fluid Pumps with a Novel Pin on Disk Apparatus
Robert Bruckner, NASA Glenn Research Center, Cleveland, OH; Richard Manco II, HX5 Sierra, Cleveland, OH
- Accelerated Testing of Tribological Components - Uncertainties and Solutions
Simon Lewis et al., European Space Tribology Laboratory, ESR Technology Ltd., Warrington, United Kingdom
- Developmental Bearing and Bushing Testing for Mars Gearboxes
Dave Suffern & Jonathan Parker, Sierra Nevada Corp, Durham, NC
- Experimental Method for Determining Ball Bearing Lubricant Quantity Factor
Yoshimi Takeuchi, Peter Frantz & Tim Woodard, The Aerospace Corporation, El Segundo, CA

11:10 SPECIAL PRESENTATION ON NASA GLENN RESEARCH CENTER**11:40 TECHNICAL SESSIONS CONCLUSION**

Stu Loewenthal, Deputy Chairman, Lockheed Martin Space, Sunnyvale, CA

11:55 LUNCH

Lunch for AMS Attendees in the Superior Ballroom, Section D

1:00 – 5:00 TOURS

Attendees may go on a special tour of either NASA Glenn Research Center or NASA Plum Brook Station.

SYMPOSIUM ORGANIZING COMMITTEE

Host Chair - Damon C. Delap, NASA GRC
Co-Host Chair - Steven W. Bauman, NASA GRC

General Chairman - Edward A. Boesiger, Lockheed Martin Space
Deputy Chairman - Stuart H. Loewenthal, Lockheed Martin Space

William Caldwell, NASA ARC
Jared A. Dervan, NASA MSFC
Adam G. Dokos, NASA KSC
Michael J. Dube, NASA NESCC
Barry J. Dunn, NASA LaRC
Carlton L. Foster, NASA MSFC (retired)
Lionel Gaillard, ESA/ESTeC
Clae F. Hakun, NASA GSFC
Christopher P. Hansen, NASA JSC
Louise Jandura, JPL
Alan C. Littlefield, NASA KSC (retired)
Ronald E. Mancini, NASA ARC (retired)
Fred G. Martwick, NASA ARC
Donald H. McQueen, Jr., NASA MSFC
Robert P. Mueller, NASA KSC
Joseph W. Pellicciotti, NASA HQ
Minh Phan, NASA GSFC
Brandan Robertson, NASA JSC
Joseph P. Schepis, NASA GSFC
Donald R. Sevilla, JPL
James E. Wells, NASA LaRC
Jonathan P. Wood, Lockheed Martin Space

Scroll Compressor for Mars Atmospheric Acquisition

John Wilson*, Bryce Shaffer* and Ted Iskenderian**

Abstract

The Mars In Situ Resource Utilization Experiment (MOXIE) will be an experiment onboard the M2020 mission to Mars. The goal of this project is to develop and demonstrate flight hardware which can ingest Martian atmosphere and convert it to O₂ and CO through solid oxide electrolysis. Air Squared, Inc was tasked with designing a scroll compressor to capture the Martian atmosphere and compress the gas to a specific pressure required to pass through the solid oxide electrolysis (SOXE) stack, converting the CO₂ into O₂ and CO.

Introduction

In Situ Resource Utilization (ISRU) technologies are critical to the advancement of human missions to extraterrestrial bodies. For example, in a Design Reference Architecture mission study from 2009, it is estimated that ISRU technology for generating oxygen will reduce the landed dry mass requirement from 100 to 70 metric tons. ISRU processes are achieved by collecting, separating, pressurizing or processing materials found in the environment of extraterrestrial bodies.

In the MOXIE experiment aboard the M2020 mission to Mars, gasses from the Mars atmosphere are collected and compressed for reaction in a Solid Oxide Electrolysis (SOXE) stack. The goal of this project is to develop and demonstrate flight hardware which can ingest Martian atmosphere and convert it to O₂ and CO through solid oxide electrolysis. The oxygen can be used to for breathable air for astronauts and potentially to generate fuel for any return mission.

Air Squared has been working with JPL and NASA on developing flight-ready hardware for MOXIE. Air Squared's contribution to this system is a compressor that compresses CO₂ from 5 torr up to at least 540 torr. The mechanism that feeds the MOXIE experiment with Martian atmosphere comprises an electronically commutated direct current motor coupled to a "scroll pack" gas compressor. There is one compressor assembly (motor plus scroll pack) in the MOXIE experiment. The compressor is of the scroll type, with a moving (orbiting) scroll orbiting a stationary (fixed) scroll. The motion of the orbiting scroll is controlled by ball-bearing mounted idler shafts. A brushless DC motor provides the rotational power. Figure 1 shows an overview of the scroll compressor assembly.

* Air Squared, Inc., Broomfield, CO

** Jet Propulsion Laboratory, Pasadena, CA

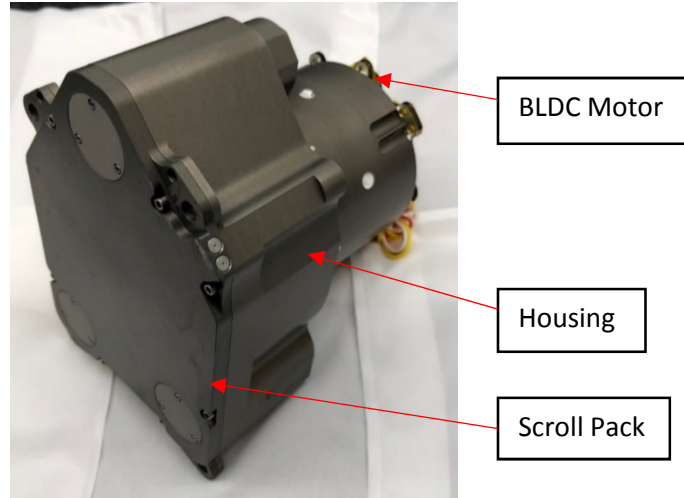


Figure 1. P09H026A-A01 Scroll Compressor Assembly

Scroll Compressor Major Components

Scrolls

The scroll involutes are the heart of the scroll compressor. The involutes are sized for each application depending on the operating pressures, flows and operating fluid, among other variables. There are two scrolls for this application, one is called the fixed scroll and the other is called the orbiting scroll.

The orbiting scroll operating principle can be seen Figure 2. The fixed scroll is represented by the white involute, which is stationary during operation. The orbiting scroll, shown in blue, orbits in a circular motion about the fixed scroll involute. The scrolls capture pockets of gas (Orbiting-1) in the two outside chambers and compress that gas radially inward until the pocket discharges out the center of the scrolls (Orbiting -3). The two outside chambers (Orbiting-1) are called the suction volume or displacement of the compressor. The scroll compressor displacement is how much volume is captured and moved through the involutes per revolution of the orbiting scroll. The process continues to expel gas at the center, while a new cycle of compression begins with fresh pockets of gas at the outer diameter (Orbiting-4).

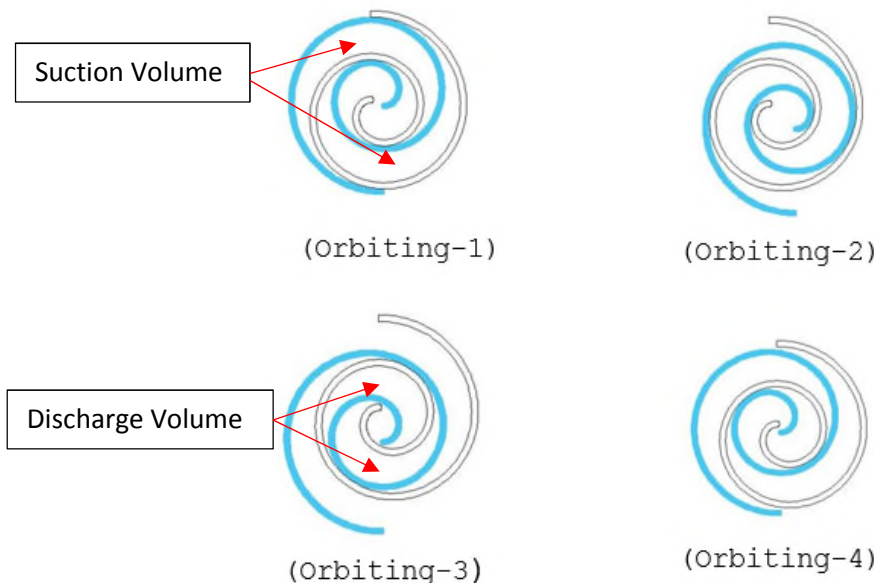


Figure 2. Orbiting Scroll Operating Cycle

The volume ratio of the compressor is defined as the ratio of the suction volume (Orbiting-1) to the discharge volume (Orbiting-3). The built-in volume ratio of a scroll compressor directly impacts the compression efficiency of the compressor, or how close the actual compression process is to an ideal compression process. In general, a large imposed pressure ratio over the machine will result in the selection of a large volume ratio. Selection of the ideal volume ratio for an application is a complex optimization problem, involving the compressor envelope, operating conditions, manufacturing considerations, as well as the cost considerations.

Idler Shafts

There are many benefits to scroll technology, specifically for this application. This scroll compressor is what Air Squared calls an oil-free design, which does not utilize any oil in the operating fluid for sealing.

Typically, oil is used in a scroll compressor to allow it to be a compliant design, which means that the orbiting scroll involute directly contacts the fixed scroll involute. It is important for this application to not utilize oil in the operating fluid due to the sensitivity to contamination of the downstream system.

Instead of utilizing an Oldham ring, which many oil lubricated refrigeration compressors use, the scrolls are phased with one another using three idler shafts shown in Figure 3. The idler shafts not only control the phasing of one scroll relative to the other, they also control the radial and axial gaps between the two scrolls. The idler shafts have an offset shaft on a precisely toleranced “eccentric”. It is critical that the idler shaft prevent the scrolls from touching for an oil-free design. Significant radial contact of the involutes could result in a failure of either the scroll compressor or the downstream system from contamination.

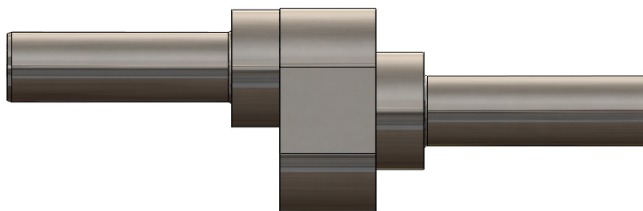


Figure 3. Scroll Compressor Idler Shaft

MOXIE Requirements

On the M2020 science rover, resources such as mass and power are constrained when compared to what would be required for oxygen production on a human-scale mission. The volume available to the compressor was severely limited in two dimensions due to the small packaging requirement for the MOXIE experiment. Restrictions on all these resources drove design choices and compromises in compressor size, operating speed, and performance.

Table 1. Compressor Requirements

Compressor Mechanical Requirements	
Dimensions [mm]	150 x 96 x 175
Mass [kg]	1.96
Compressor Performance Requirements	
Gas Inlet Pressure Range [Torr]	4 to 7
Gas Inlet Temperature Range [°C]	-45 to +55
Gas Outlet Pressure [Torr]	760
Mass Flow Rate Minimum [g/hr]	60
Life [hr]	60

The specific inlet conditions for the compressor had to be narrowed down to a single point for sizing and testing purposes. The specific design condition was for a nominal inlet condition of 20°C and 7.0 torr gas, comprising ~95% carbon dioxide, 3% nitrogen and 2% argon. The compressor had to be able to handle a gas inlet temperature range of -45°C to +55°C. Since the original requirements document was created, the inlet conditions have since changed to more accurately reflect the landing site of the rover. Instead of the inlet pressure being 7 torr, it will more likely be around 5 torr for the inlet pressure.

The original outlet conditions required were to compress the gas up to 760 torr, but further testing of the SOXE system showed that lower outlet pressures were permissible without degradation to health of the system.

Development Plan

Prototype

For the MOXIE operating conditions, an ideal volume ratio of 44.26 is required, which is not practical for any scroll machine, let alone in the footprint requirement imposed by JPL. Just for reference, if the design utilized a volume ratio of 44.26, it would require approximately 29 scroll wraps and the footprint would increase by 465 millimeters. Instead of using a 44.26 volume ratio, the design again fit the largest volume ratio within the given 95-mm footprint.

The 5.82 volume ratio results in a pressure-volume (P-V) curve as shown in Figure 4. The purple curve is the ideal P-V curve for the operating pressures required. The compression process starts at the far right of the curve, when the scrolls seal off the suction volume pockets. As the scroll rotates, the volume of the gas pocket decreases, traveling right to left along the purple line. If the compressor were to have a volume ratio of 44.26, the process would follow along the purple line all the way to the upper left corner of the curve until it reached its desired outlet pressure of 760 torr, when the scroll pockets open. Instead, the volume ratio was decreased to 5.8 and the compression process jumps from the ideal compression process around 0.18 on the x-axis.

The scroll compressor then relies on a downstream orifice to continue the compression process and reach the desired outlet pressure. The additional work required to do the compression downstream is represented by the pink area in the P-V curve in Figure 4. The total compression power for the MOXIE scroll compressor is the purple area and the pink area of the P-V curve added together.

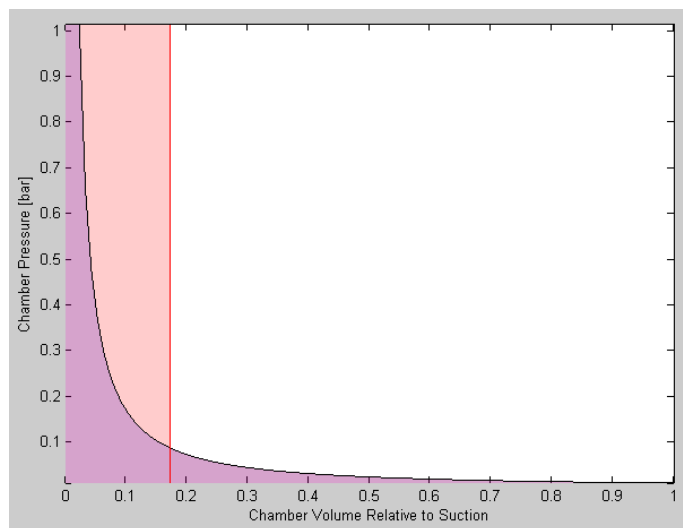


Figure 4. MOXIE Compressor P-V Curve

Air Squared first provided a prototype compressor to JPL to permit demonstration of proof of concept. This prototype design was based on previous Air Squared vacuum pumps, which also required a high built-in volume ratio. The volume ratio settled on (5.84) was the largest volume ratio that could fit into the given 105-mm width. Air Squared used its patented delayed porting design to get this high of a volume ratio in such a small footprint. Delayed porting (Figure 5) is a small radius towards the end of the scroll involute which delays when the compression pocket opens by 180°. This additional 180° of rotation significantly increases the compression ratio of the compressor, which improves the performance for this application.

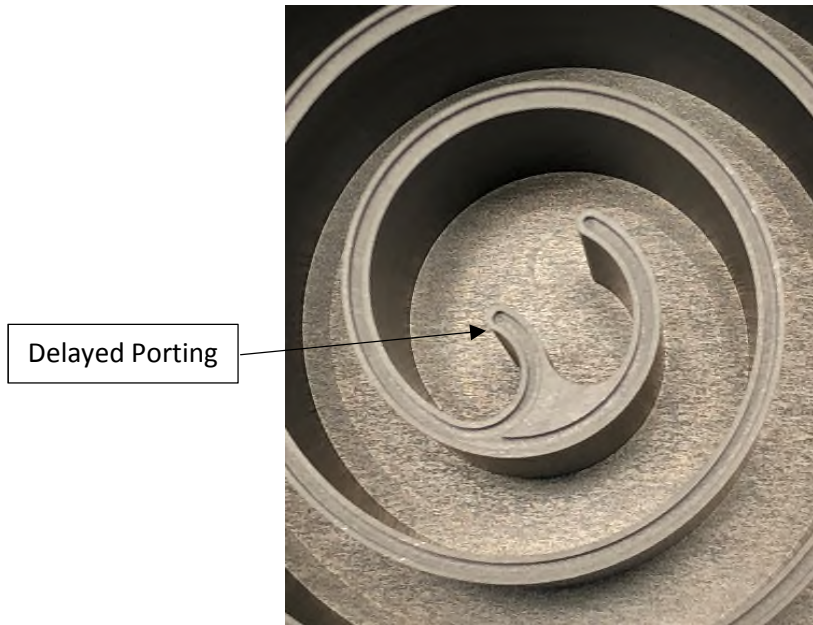


Figure 5. Delayed Porting

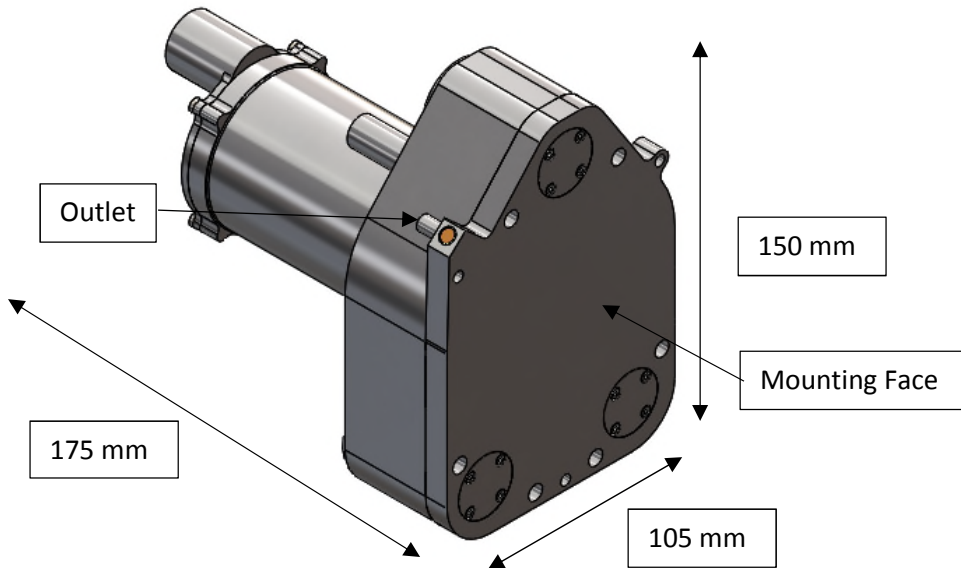


Figure 6. Prototype Scroll Compressor (P11H024A-A01)

Another unique design feature that the prototype scroll compressor utilized was a flat fixed scroll plate with the outlet routed through the base and pointing backwards towards the motor. The reason for this design feature was primarily due to the mounting requirements given by JPL and the location of the MOXIE experiment on the rover. The compressor will be mounted face down on the bottom of the MOXIE baseplate, which will be acting as the heat sink for the compressor. It wasn't possible to route plumbing through the baseplate of the MOXIE system, so instead the fixed scroll routes the outlet flow towards the back of the unit.

One discovery during testing of the prototype at JPL was the pressure oscillations that naturally occur in a scroll compressor. It was feared that these may be detrimental to the SOXE, as it had never been tested with a pulsating input flow. To reduce these pressure oscillations, a check valve and viscous flow control device were inserted downstream of the compressor. These additional components not only decreased the pressure pulsations, they also help prevent backflow through the compressor.

Another potential issue discovered with the prototype scroll compressor was that the bearing grease seemed to be pulled through the bearing shields during pressure cycles, as shown in Figure 7. If bearing grease were to enter the operating fluid flow, it could be detrimental to the SOXE stack. The thermal decomposition of the grease would deactivate the catalytic active sites on the cathode. It has been estimated that approximately 100 micrograms of halogenated compounds would destroy the stack, although the number has a lot of uncertainty. Certain design changes would be implemented on the flight unit to try and prevent this from becoming a major issue.

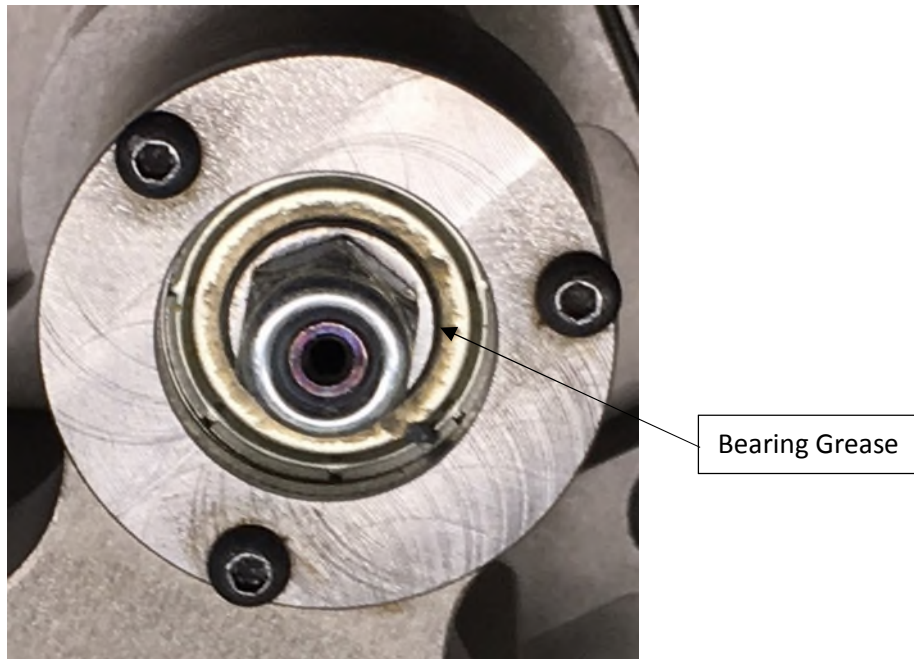


Figure 7. Prototype Idler Bearing Grease Loss

The prototype was inserted into the MOXIE testbed at JPL, where it was able to meet the flow and pressure requirements desired by JPL. Successful testing of the prototype unit led to a flight unit development agreement between JPL and Air Squared.

Flight Design and Development

Scroll Geometry

With the validity of the MOXIE architecture firmly established, flight design proceeded with tighter restriction on the compressor's footprint, mass, and power. With 10 millimeters less to work with on the width of the compressor (95 mm), the involute needed to be resized from the prototype (105-mm width).

The decreased width of the compressor footprint drove the design to utilize a smaller involute pitch, which decreased the suction volume of the compressor. Instead of keeping the same ratio of involute height to involute spacing as the prototype, the height of the unit was increased to provide more margin on the minimum mass flow rate requirement. The increased height added risk to the machining of the scrolls, but after the first machining iteration, it was found not to be a concern.

Figure 8 shows the mass flow rate estimate for the flight compressor which was done at the start of the design process. It shows that the major consequence to the performance was a lower overall mass flow rate, which was reduced from 114 g/hr in the prototype to 84 g/hr for the flight unit for the 7 torr, 20°C inlet condition.

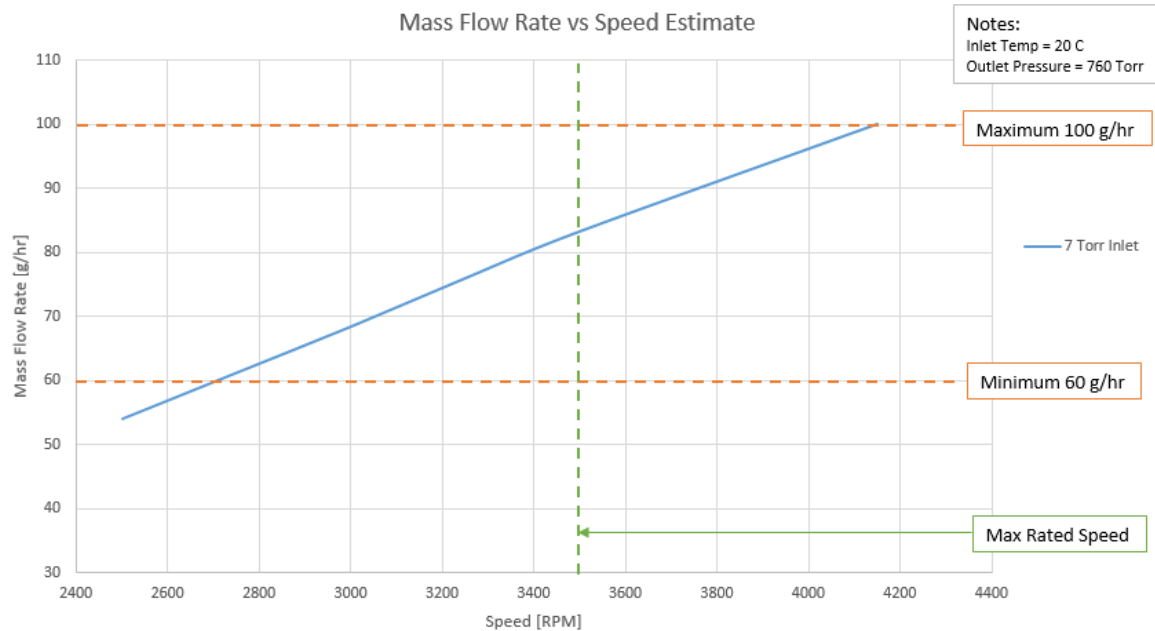


Figure 8. MOXIE Compressor Sizing

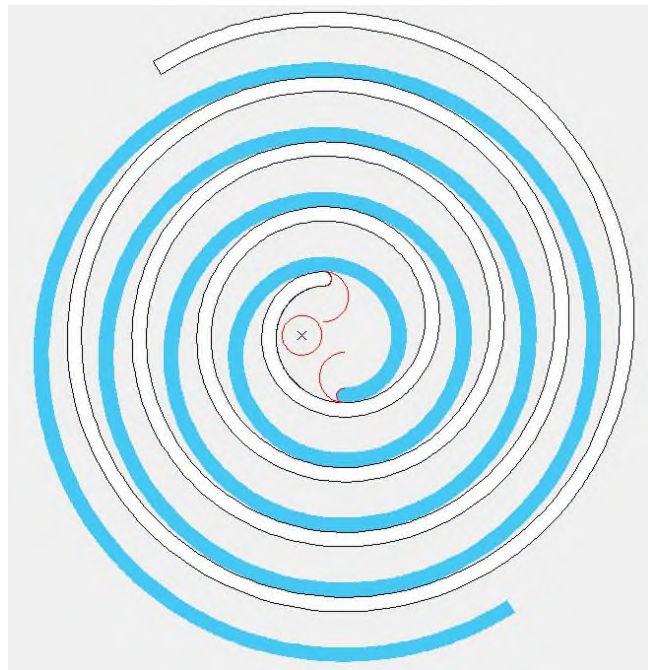


Figure 9. P09H026A-A01 Scroll Geometry

Bearing Configuration

The bearing configuration for the flight scroll compressor varied slightly from the prototype compressor. The flight compressor now had to be designed for launch loads as well as normal operational loads, which means that the bearings needed to be preloaded for launch. To accomplish this, the bearings used were a ground, matched pair bearing set. The spacers used for ventilation, as shown in Figure 10, had to be matched as well to ensure the preload on the bearings did not change. The spacers had cross holes put in them as well as a groove machined in the outside to allow air trapped between the bearings to vent through the side holes instead of pulling out bearing grease, which was an issue on the prototype.

The bearing grease used switched from a Krytox to a Braycote 600 Micronic EF, which is a better grease for the specified operating conditions. Another important study conducted at the beginning of the flight unit testing was a power draw study over the operating temperature of the compressor. It was found the lower grease fill of 10% gave the most torque margin for startup torque at when the compressor is at -55°C.

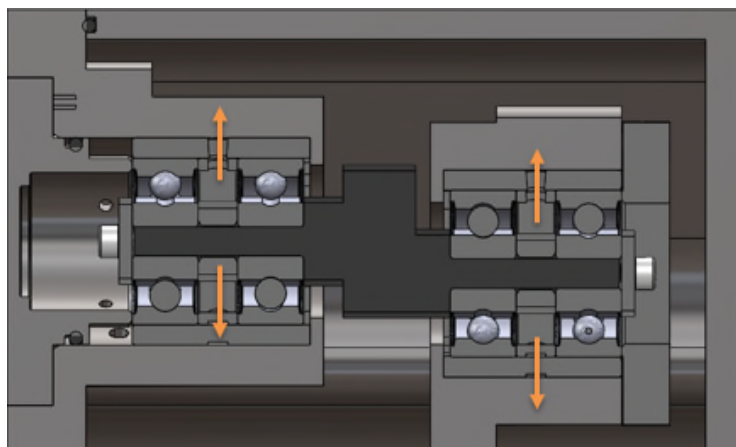


Figure 10. Flight Compressor Idler Bearing Venting Configuration

Motor and Thermal Performance

Another major change between the prototype compressor and flight compressor is the motor. The compressor still uses a BLDC motor, but it is a housed motor design instead of a frameless motor which was used in the prototype. The primary reason for the motor change was to use a motor vendor that has flight heritage, which the prototype motor did not have. The major concerns with the new motor design are heat transfer from the motor, increased motor mass, and additional tolerance stack-up with the motor shaft alignment to the scroll pack.

The change to a flight motor came with many tradeoffs and design changes to accommodate the motor. First, the motor was much heavier than the prototype motor, partly due to the torque margin required, but also due to the stainless steel housing. The stainless steel housing was used to better match up the CTE of the motor winding and bearings to the motor housing, which helps prevents losing the fit on the stator and the bearings. Due to the heavier mass of the motor, additional weight needed to be removed from the compressor and housing to get closer to the mass spec. The majority of the mass was removed from the fixed scroll base, which needed to be thicker for the cross hole to be drilled through the base.

An important design factor of these compressors is the mounting interface, which were designed to be mounted on the flat fixed scroll face. This is beneficial when it comes to removing the heat of compression from the fixed scroll, but it is far from optimal for removing heat from the hall sensors, which are located at the back of the motor. With the de-rated maximum temperature of the hall sensors set to 105°C, getting the heat out of the motor through the housing and fixed scroll into the heat sink became a challenge. It was discovered during the testing phase that only mounting the motor to the housing and having a small interface to transfer heat out of the motor would not result in acceptable temperatures at the hall sensor locations. The worst case operating condition, which is a 70°C fixed scroll, resulted in a hall sensor temperature of approximately 135°C. Figure 11 shows a correlated thermal model of the original scroll compressor, without a motor sleeve, which has a temperature differential across the motor alone of 37.2°C. This is greater than the allowable temperature differential across the entire compressor, which led to the housing-motor-sleeve design.

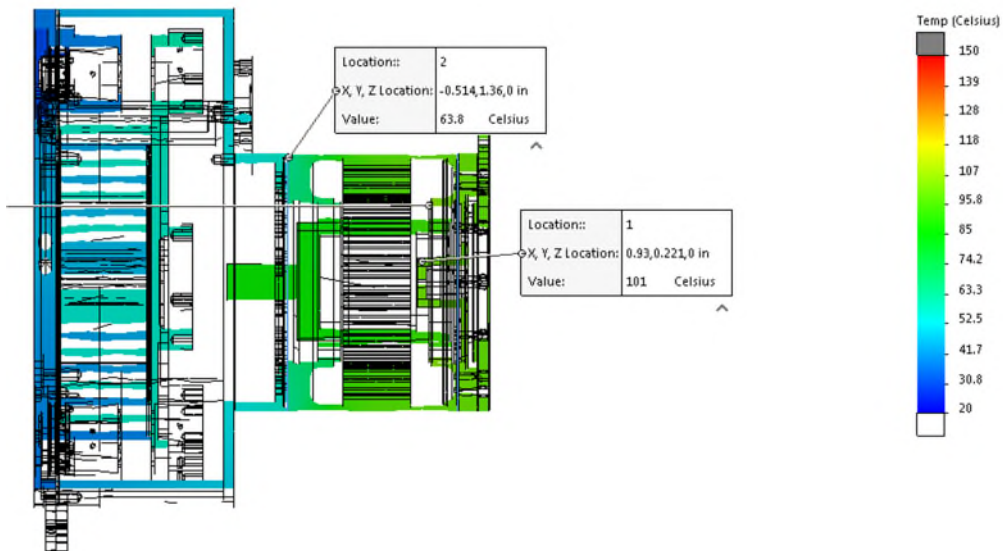


Figure 11. MOXIE Compressor Thermal Model

The heat transfer concern is being mitigated by changing the housing design to use an aluminum thermal sleeve, shown in Figure 12, which is bonded to both the motor housing using Nusil. This sleeve improved the thermal path for the hottest part of the system, the stator, and better conducts it down through the housing to the fixed scroll. The steady state temperature gradient across the compressor for the hot operating condition (70°C) was ~35°C, or a decrease of 30°C from the non-sleeved motor.

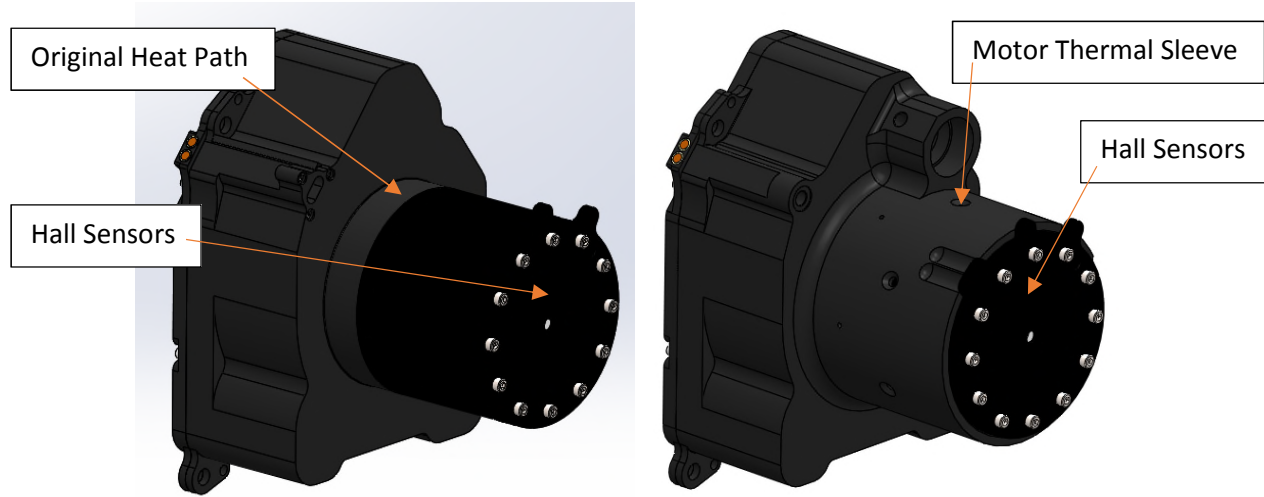


Figure 12. Motor Thermal Sleeve (Original on Left, Updated on Right)

Compressor Performance

The scroll compressor was still tested at the original 7-torr design condition and the results are shown in Figure 13. The prototype performance very clearly informed the performance estimates of the flight unit (shown in blue) and even though the flight unit was scaled down, the efficiency estimates from the prototype were still accurate, as the actual performance shows in yellow.

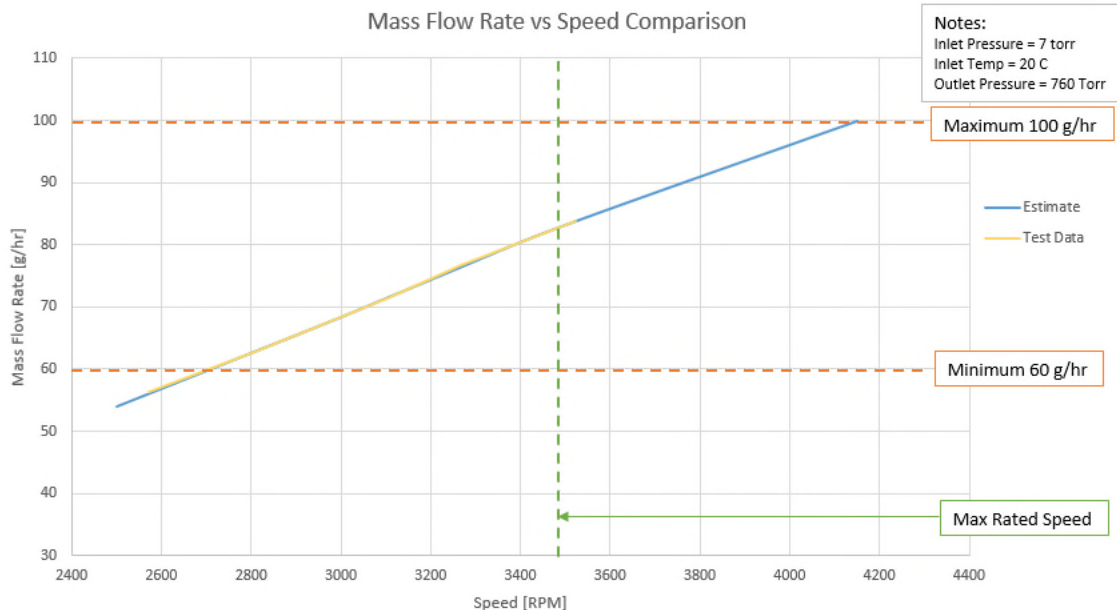


Figure 13. Performance Estimate vs Actual

As the compressor design matured, so did the proposed landing sites for the rover. The landing site has been narrowed down and there is now a better understanding of the inlet conditions the compressor will see. A more likely inlet pressure for the compressor is now 5 torr, instead of the original 7-torr inlet pressure that Air Squared designed around. This clearly will influence the mass flow rate of the unit, since the density of the inlet fluid has been reduced by ~28%.

The compressor is still capable of reaching the minimum requirement of 60 g/hr, even with the 5-torr inlet pressure. A complete flow curve can be seen in Figure 14 for the 5-torr inlet condition. At 3500 RPM, the nominal speed for the compressor, it can produce ~63 g/hr of CO₂ flow at a discharge pressure of ~660 torr.

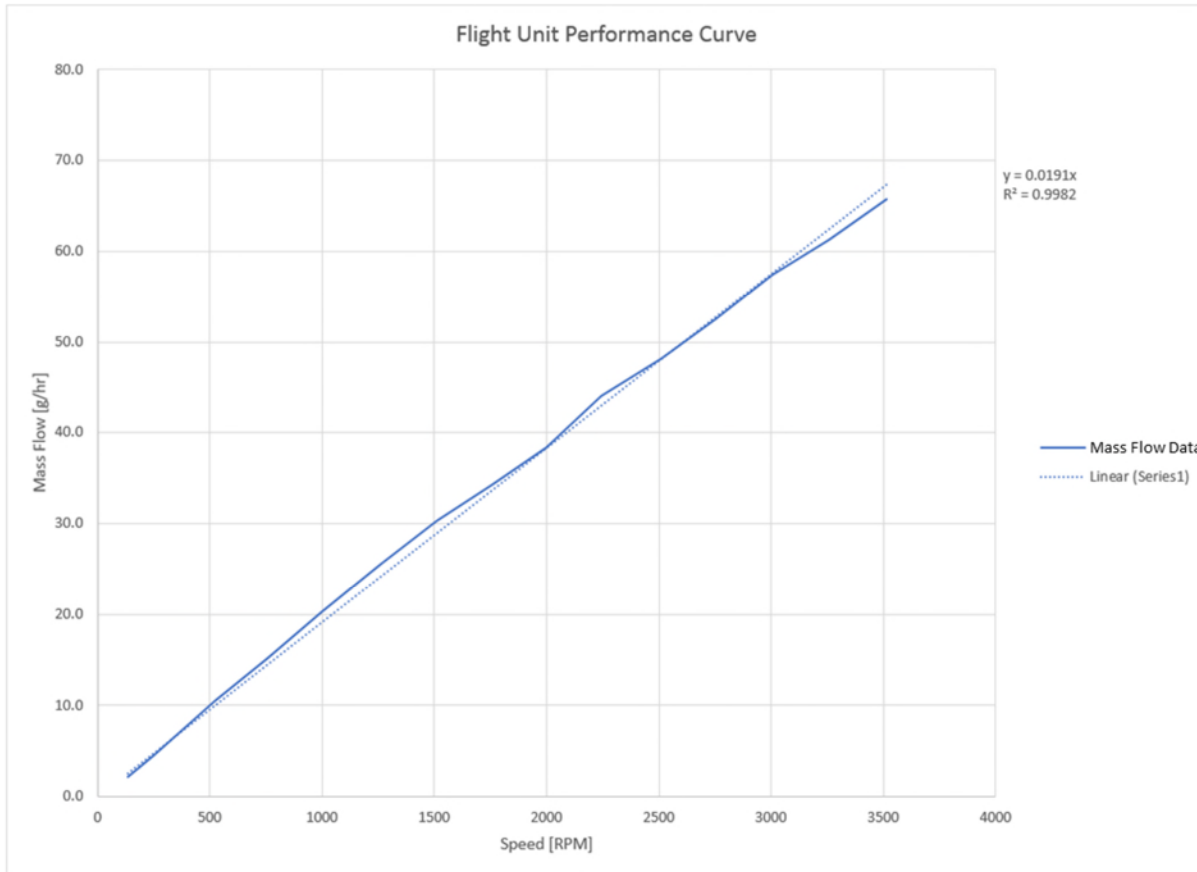


Figure 14. Flight Unit Performance Curve - 5 Torr Inlet

Conclusion

The major challenges that arose during the design and testing process was the heat removal and grease retention. The heat removal from the motor was improved by ~30°C by adding an extension to the aluminum compressor housing to increase the conductance from the motor housing to the MOXIE baseplate, or heat sink. The grease loss concern was mitigated, and no significant grease has been detected on the compressor outlet by providing vent holes for all trapped air pockets between bearings to vent during pressure cycles.

The flight compressors have survived shock, random vibration, thermal cycling and a qualification unit survived an 18-hour life test. The flight units will soon be delivered to JPL for integration into the MOXIE system, which has an estimated launch of summer 2020.

The Regolith and Ice Drill for Exploration of New Terrains (TRIDENT); a One-Meter Drill for the Lunar Resource Prospector Mission

Gale Paulsen*, Zachary Mank*, Alexander Wang*, Paul Chow*, Cody Hyman*, Thomas Thomas*, Allen Lee*, Kris Zacny*, James Smith**, Jacqueline Quinn**, Erik Mumm*** and Ron Hayes***

Abstract

A desire to prospect for resources on the Moon, namely water, has led to the development of The Regolith and Ice Drill for Exploration of New Terrains (TRIDENT) drilling system. TRIDENT is a 16-kg rotary percussive drill and deployment system that was designed to be deployed from a roving platform and drill to a depth of 1 meter. Designs and testing supported by the Resource Prospector (RP) mission have enabled the TRIDENT system to reach a NASA TRL of 6. Through the development of this system, many lessons were learned. These include lessons learned for cable/pulley and capstan mechanisms, custom slip-ring designs, instrumentation of temperature sensors for measuring subsurface temperatures, sample transfer mechanisms, brazing tungsten carbide to titanium, and the replacement of the drill's cable harness with flexible printed circuits. This summary highlights some of the major lessons learned along with recommended designs and tests to improve the design of the TRIDENT.

Introduction

In 2014, Honeybee Robotics was selected to help the NASA Resource Prospector (RP) mission [1] meet its goals of advancing the technology readiness level (TRL) of the Resource Prospector system by increasing the TRL of the drilling subsystem. The primary goal of the RP mission is to explore the Lunar South Pole Aitken Basin in search of water ice and other volatiles. Instruments on board the RP rover are designed to help locate and quantify the concentration of volatiles (with emphasis on water). This mission is to provide ground truth data in support of previous water detection missions (i.e. LCROSS [2] and other surveying spacecraft). The Lunar environment that the RP mission will experience include hard vacuum, cryogenic temperatures (down to 40K), radiation, and low gravity ($1/6^{\text{th}}$ g).

Hurley et. al. [3] state that the desiccated layer on the Moon is on the order of 10's of cm. This would suggest that to find ice on the Moon would require penetrating the surface beyond a few centimeters. The mission requirement, derived from the current remote sensing data, is to have the ability to drill to a depth of 1 meter below the Lunar surface. However, penetrating the surface is only one of the functions of the drilling system. Other functions include sample delivery to a surface directed Near Infrared Volatile Spectrometer Subsystem (NIRVSS), delivering sample to an onboard Oxygen & Volatile Extraction Node (OVEN) and Lunar Advanced Volatile Analysis (LAVA) subsystem, and to measure the subsurface temperature and strength of the regolith.

This paper describes the development of The Regolith and Ice Drill for Exploration of New Terrain (TRIDENT) subsystem for the Resource Prospector mission (Figure 1). Over the course of this development there have been a few important lessons learned on the drill mechanism design and on using this particular mechanism for sensing. These lessons include:

* Honeybee Robotics Spacecraft Mechanisms Corp., a division of Ensign Bickford Industries, Pasadena, CA

** NASA Kennedy Space Center, FL

*** Honeybee Robotics Spacecraft Mechanisms Corp., a division of Ensign Bickford Industries, Longmont, CO

- Lessons learned with using a Capstan Mechanism as a driving mechanism for linear feed and deployment stages.
- Proper isolation of temperature sensors to improve the measurement response of sensors embedded in the mechanism.
- Simplified Slip-ring design to help reduce production time and cost.
- Materials selection and design of a passive brush system to assist with sample transfer of regolith.
- Manufacturing approach for brazing Tungsten Carbide (WC) to Titanium (Ti).
- Replacement of the drill's cable harnesses with three unique Flexible Printed Circuits (FPC) to reduce system mass and increase reliability.

Capstan Mechanism

A capstan mechanism uses a driven spool and a cable pulley system with two independent cables. In the case of the TRIDENT linear feed mechanism, one of the cables routes to the top side of a carriage on a guide rail system and the other cable routes to the bottom side of this carriage. This allows the capstan mechanism to apply force to the carriage in both directions. For instance, when the spool rotates clockwise, the cable attached to the bottom of the carriage will be in tension and pull on the carriage. In this case, the bottom cable gets wound on the spool while the top cable is being unwound. When the spool rotates in the counter-clockwise direction, the opposite is true. In this case, the cable attached to the top of the carriage is in tension and this cable becomes wound on the spool while the bottom cable is unwound.

In space flight applications, such as a drill, where a relatively long linear feed stage is required, the capstan feed approach offers some key benefits over other drive mechanisms such as screws and belt drives. The primary benefit is significant mass savings.

When compared to screw mechanisms, the cable pulley type mechanism is also much more robust to dusty environments; can more easily accommodate coefficient of thermal expansion mismatches between the rail and the driving mechanism (i.e. screw or cable); and because the mechanism is not as stiff, the capstan mechanism attenuates more of the vibrations from the percussive drill that are traveling back towards the rover. When compared to belt systems, the capstan offers better material options for cryogenic and vacuum environments and because there are two cables fixed at both ends (one to the carriage and one to the spool), cable slippage is not a possible failure.

The TRIDENT Engineering Test Unit (ETU) is a third generation one-meter class drill that utilizes the capstan for driving linear feed and/or deployment stages. Previous drill designs (IceBreaker [4] and LITA Drill [5]) used a stainless-steel wire rope cable to drive the carriages. These mechanisms worked quite well

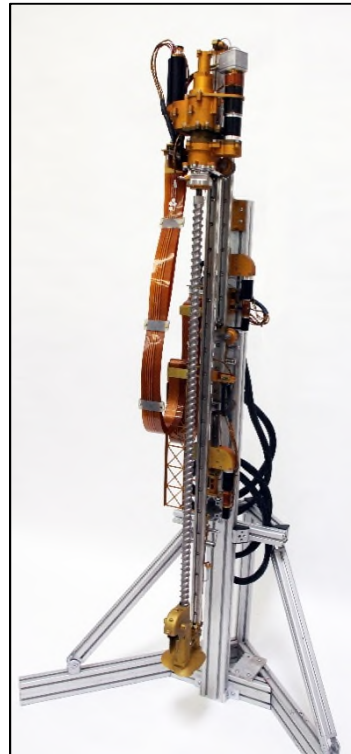


Figure 1. TRIDENT Drill and Deployment System.

for both of these drilling systems. On the LITA Drill, there were some fatigue issues with the initial cable selection as the bend radius of the pulleys in the drive system were too small for the cable. However, switching to a more flexible wire arrangement (7 x 19 cable) eliminated any further failures due to fatigue. For the TRIDENT ETU, however, a new challenge existed: selecting a drive cable that could survive not only the vacuum environment, but also the cryogenic environment that can get as low as 40K. After a preliminary study, Technora – a para-aramid fiber cable produced by Teijin Aramid - was selected as the drive cable. This material offered great tensile strength properties and a broad operating temperature range. A PTFE coating on this cable is used to provide some protection against UV degradation.

On paper, the Technora 600 cable appeared to be an excellent choice to replace the stainless-steel wire rope: a 2-mm-diameter cable was rated to 2667 N (600 lbf) of static tension compared to the 2001 N (450 lbf) rating of the wire rope, and both had comparable allowable bend radii. In testing, however, there were some subtle issues that made this type of cable a relatively poor choice for the capstan mechanism. A “finger trap” loop splice at the ends of the cable (Figure 1) created slight diametrical growth and increased fatigue susceptibility within the last 10 cm of the cable. This region is still nearly as flexible as the rest of the cable and was originally designed to pass over the end pulleys to minimize the length of the deployment structures (z-axes). However, this resulted in an early-life cable failure at the end of the spliced area. Instead, this region of each cable should be treated as a “dead zone” (length at the end of a cable that cannot be passed over a pulley), and in fact this length is much larger for Technora than that created by crimped terminations used for wire rope. Fraying and diametrical growth are also observed in all cable areas subjected to fatigue or abrasion: the spool, the pulleys, and the tensioner mechanisms in particular (Figure 2).

For the cables to wind neatly onto the capstan spool, it works well to use a single row and let the cables route side by side. When using steel cables at low rotational speeds, this is not a problem because of the relative hardness of the wire rope. With the Technora cable (and other fibrous cables) this is far from ideal, however, as the rubbing friction between two cables in contact increases the rate of fraying. The Teijin manufacturer data sheet reports that Technora can abrade up to 219% faster when moving in contact with itself than it does when moving over a metal surface [6]. Once fraying begins, the damage to the cable is amplified as the fibers that fray can get trapped under the wrap on the spool that is adjacent to the frayed portion of the cable. When the cable is being spooled out, these trapped fibers are pulled on with the full force of cable tension. This type of behavior significantly reduces the life of the cable.



Figure 1. Technora cable termination and spool.

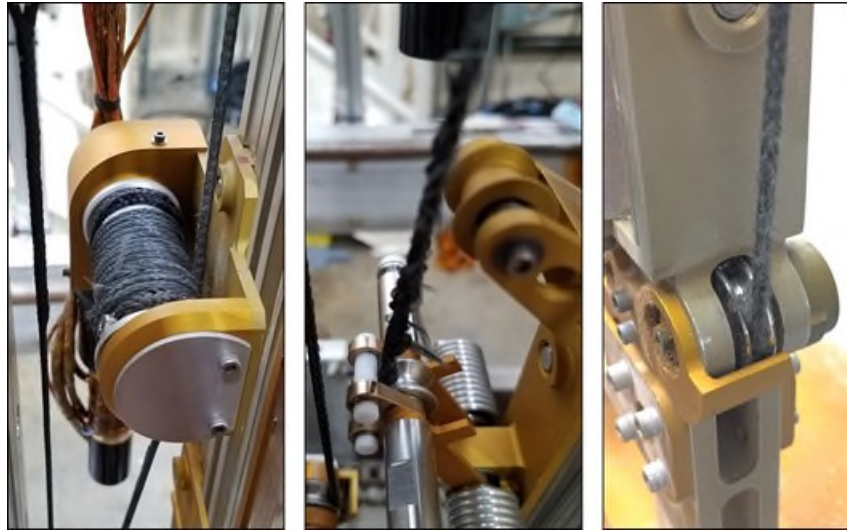


Figure 2. Fraying observed at various cable bend locations throughout the capstan mechanism (left – spool; center – tensioner; right – pulley).

In-house testing was conducted to better characterize the expected bending fatigue degradation of the cables. With a minimum mission operational life of eight holes to a depth of one meter each (and an expected “bite” size of 10 cm), the absolute minimum capstan system life is 80 up-and-down Z-stage moves, excluding any factor of safety. A representative load test put different small sections of cable under maximum expected tension (310 N, or 11.6% of the Technora static load rating) and cycled that section up and down over a single 90° pulley bend. When the section tested included part of the loop end termination, cables were found to only survive around 110 cycles and always failed at the end of the splice. When tested in an otherwise featureless middle section, cables could survive more than 250 cycles. No testing was conducted to characterize the wear rate on the spool, but it was believed to have a worse cycle life expectancy than the cable middle segments on the pulleys due to the increased Technora-on-Technora abrasion consideration.

With the failure of the Technora cable, an additional study on rope or cable options was conducted. Again, the most important first consideration is that the cable maintains flexibility in cryogenic environments. Though more tests are required, the cable down selection process thus far has indicated that the titanium wire rope cable is the frontrunner for replacement. The titanium wire rope provides similar fatigue performance characteristics as the stainless-steel wire rope but maintains its ductility properties better at cryogenic temperatures.

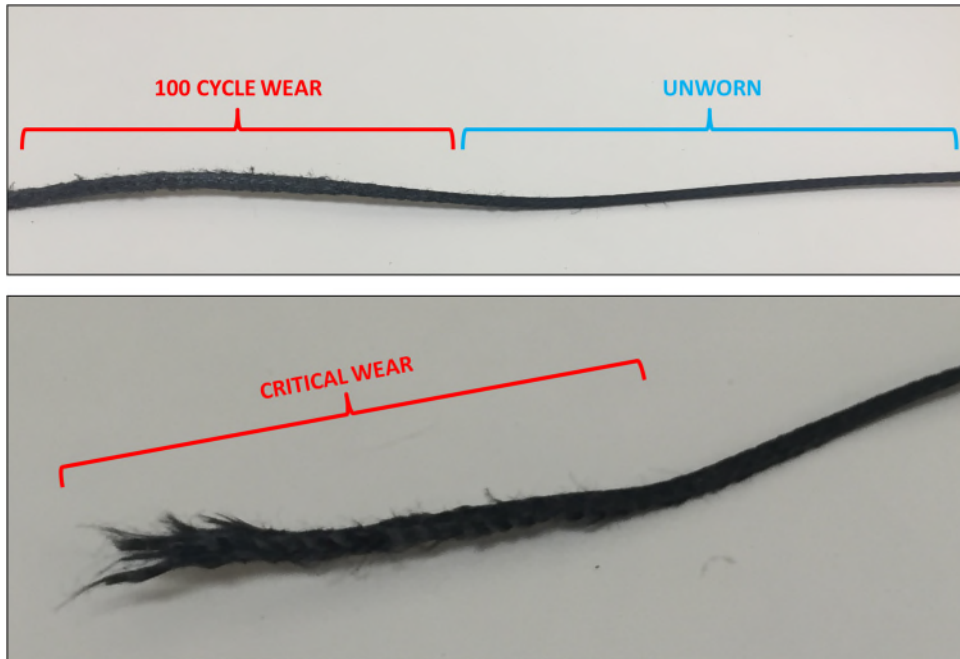


Figure 3. Cable fatigue characterization test results (top – Technora 600 cable with a featureless middle section cycled up and down 100 times over a 90° pulley bend; bottom – the same cable after continued testing to failure).

Using the TRIDENT Drill for Temperature Measurements

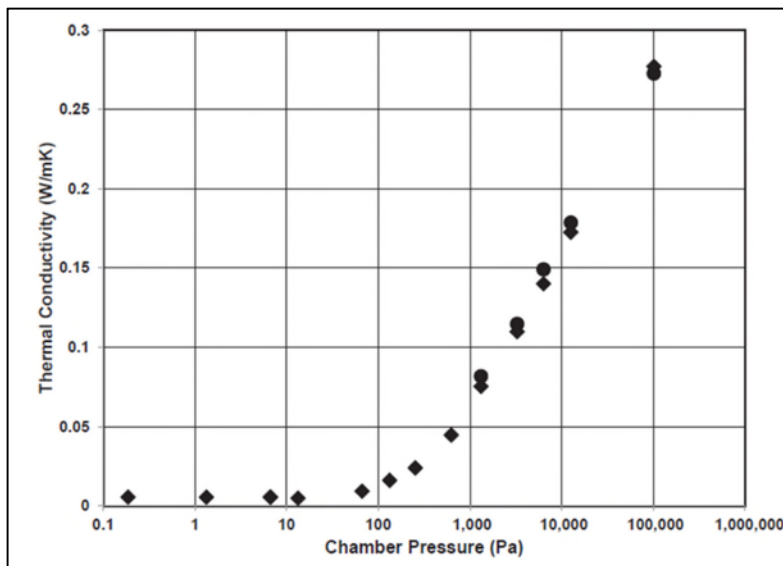


Figure 4. Thermal Conductivity of JSC-1A vs. Atmospheric pressure [7].

This makes the task of measuring the subsurface lunar temperature even more challenging. Two design concepts have been tested that involve embedding a Resistive Temperature Detector (RTD) in the drill string. The first concept had the RTD embedded in the center of the drill bit (near the tungsten carbide cutter - Figure 5, top). The RTD was thermally bonded to the metal structure (in this case 17-4 Stainless

Obtaining subsurface regolith measurements on the Moon is difficult because of the low thermal conductivity of the regolith. The thermal conductivity of the lunar regolith (~0.01 W/mK) (Figure 4) is expected to be a few orders of magnitude lower than thermal conductivity of a titanium drill auger (~6.7 W/mK). Of course, variables such as relative water / ice concentrations in the regolith, among other things (particle size, concentration, density) can affect the thermal conductivity of the regolith. Relatively speaking, the baseline concept of drilling operations only allows for a short time duration for temperature measurement, as the drill string is only ever in contact with regolith at depth for a few minutes at a time.

Steel) using a thermally conductive epoxy. The second concept attempted to expose the RTD directly to the lunar regolith and thermally isolate the sensor from the rest of the drill string (Figure 5, bottom).

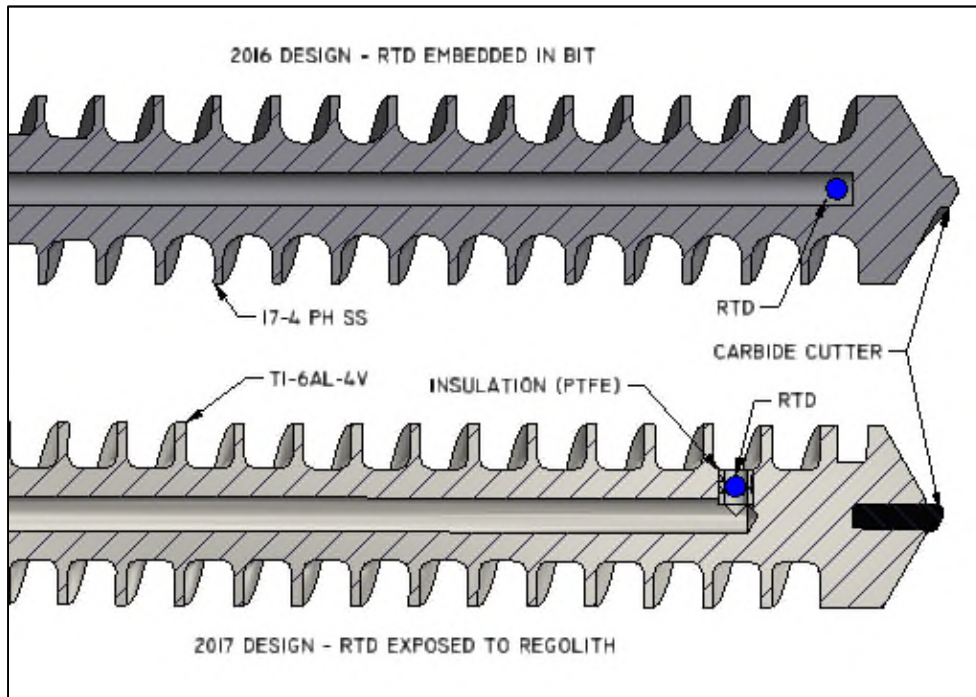


Figure 5. RTD placement within the TRIDENT drill string (top – 2016 design; bottom – 2017 design).

There was a noticeable improvement in response time for the second concept, but the assembly of this option is more complex. The increased assembly complexity for the second concept is because the assembly requires bonding a thermal isolator to the base metal using a thermally insulating epoxy and then bonding the RTD to the insulation using a thermally conductive epoxy. The goal here is ultimately to minimize the mass or thermal inertia of the temperature sensor (including the epoxy used to bond and protect the sensor). Though improvements to the design / assembly can still be made, the initial results show great promise. When comparing the two concepts over a similar operational scenario, it is apparent that the rate of change measured with the RTD is much faster in the 2017 tests ($\sim 8^\circ\text{C} / \text{min}$) compared to the 2016 tests ($\sim 2^\circ\text{C} / \text{min}$) (Figure 6).

In tests performed in 2016 and 2017, the average regolith temperature was $< -100^\circ\text{C}$ with the ambient chamber temperature being $< -50^\circ\text{C}$ and atmospheric pressure $< 10^{-5}$ Torr. In both cases, the NU-LHT 3M lunar regolith had 5% weight water added to simulate expected values from LCROSS data. Similar drilling profiles were performed for these tests though the Rate of Penetration (ROP) during the 2017 tests were a little faster than in the 2016 tests. This means that the 2016 tests were putting more energy into the regolith per cm of regolith displaced. During both tests shown here, the power required to displace the regolith was comparable and on average only a few Watts. It is unlikely that the additional energy used during the 2016 test would have account for the large differences in measured temperatures between the two tests. The 2017 test actually started with the drill bit approximately 20°C warmer than in the 2016 test, but was more than 15°C colder by the time a 40-cm depth was reached. Another interesting observation is that the 2016 test never measured a temperature colder than the initial starting temperature of approximately -65°C whereas the sensor in the 2017 test ended up measuring temperatures less than -105°C shortly after reaching a 75-cm depth.

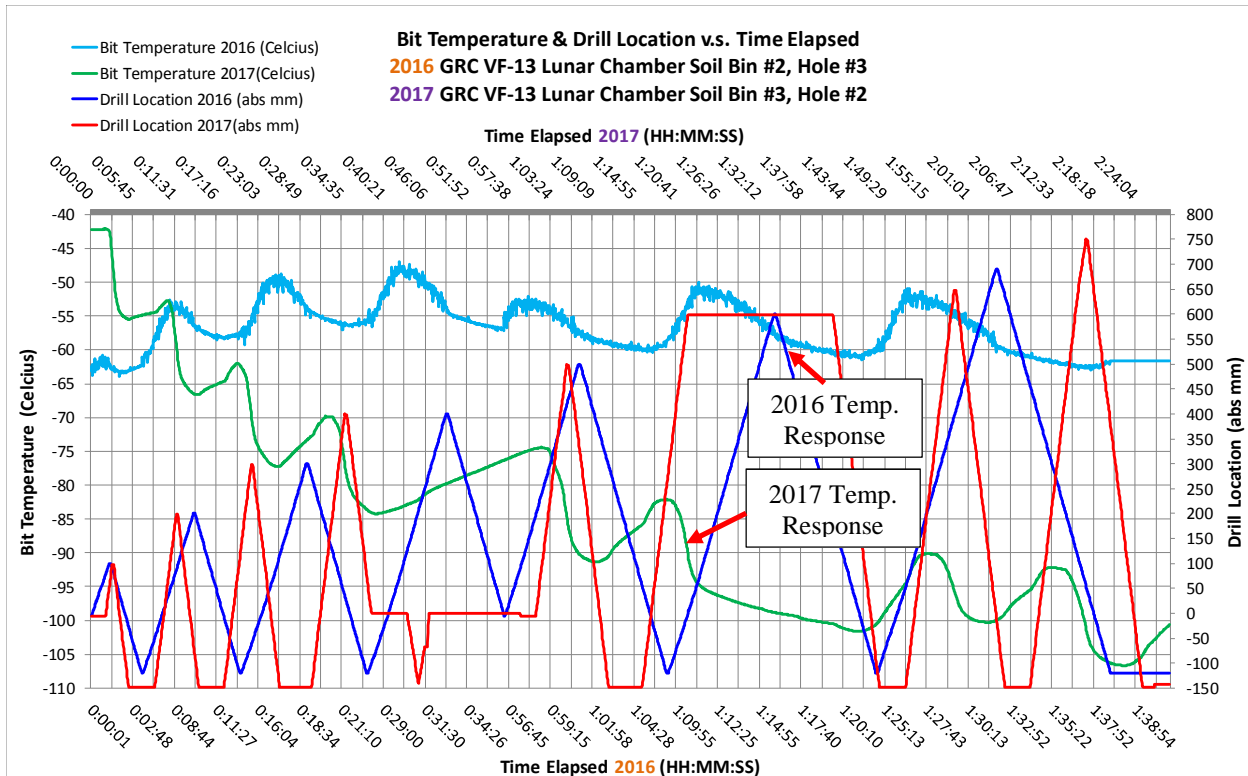


Figure 6. Drill Bit Temperature vs. Depth (2016 & 2017- Original & Modified Design).

There are ongoing analyses being performed to help predict steady state temperatures from the response of the temperature sensors over a relatively short time duration. Vetted models to predict temperatures are required as extrapolation is almost certainly necessary to estimate the actual temperature of the lunar regolith at various depths. Currently the time required for the sensor to reach a steady state temperature measurement is on the order of several hours. Improvements to the sensitivity of the temperature sensor in the form of improved thermal isolation from the drill bit, reduced mass, and reduced thermal resistance between the sensor and the regolith will result in better estimations of the regolith temperature.

Slip-Ring Design

To enable the use of an embedded temperature sensor in the drill bit, it's necessary to use an electrical slip-ring to convey the electrical signal through the rotating auger joint. The drill design preceding TRIDENT was originally designed and built under a different NASA program targeting more terrestrial field testing [4]. In the early stages of the RP program, the drill, then named RP15, underwent random vibration testing to qualification levels. The drill mechanisms all survived and continued to function nominally, except for the slip ring. During the Z axis vibration test (in-axis with the drill bit), the off-the-shelf slip-ring experienced separation between the rotor and the stator at a bonded interface, as shown in Figure 7. Certainly, this commercial-off-the-shelf (COTS) slip-ring was not designed for this environment and definitely not the large response observed at ~110 Hz (Figure 8). Though the COTS slip-ring did survive several hours of testing on the rotary percussive drill system up to this point, the random vibration environment proved to be more than the bonded joint could handle. Given this failure, it was apparent that for the TRIDENT drill design, slip-ring design and/or selection was going to require a more concerted effort.

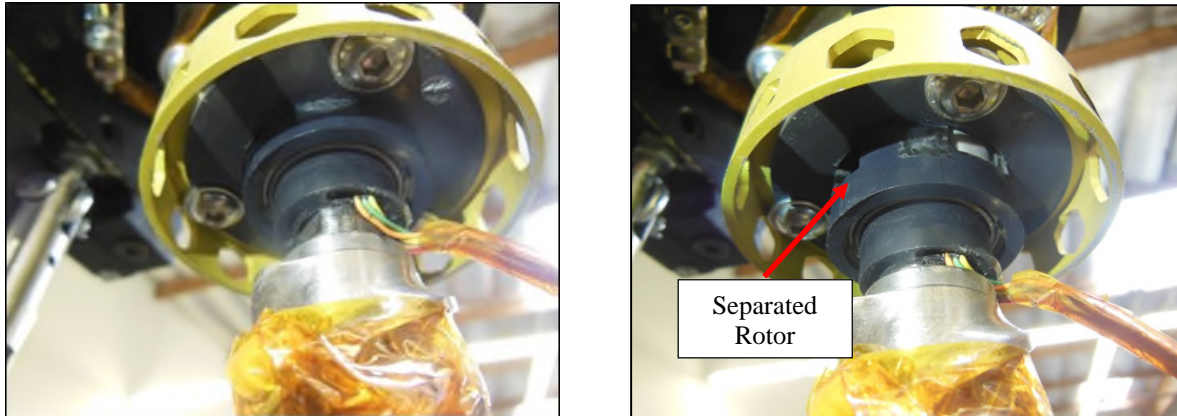


Figure 7. Slip-ring damage from system random vibration test (left – undamaged Slip-ring before test; right – damaged Slip-ring after test).

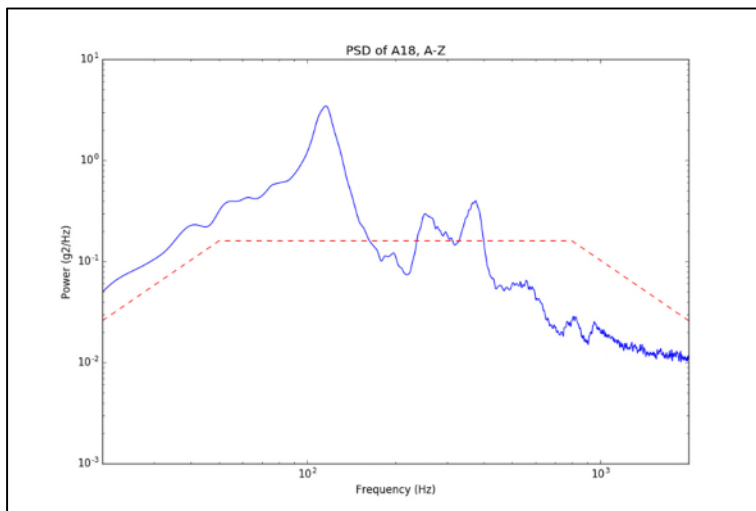


Figure 8. Response of Drill Head Accelerometer during Z-axis Random Vibe.

After researching availability of slip-rings that would meet the form, fit, and function for the TRIDENT drill, it became evident that a custom solution was going to be necessary. To help save on time and costs, the solution for TRIDENT was to design and build the slip-ring using in-house expertise. Fortunately, there existed a heritage design that closely fit the size and signal requirements for TRIDENT. This was a significant benefit to reduce the time required for materials selection, coatings, sizing, etc. However, the heritage process used for space-flight applications to build up the rotor, secure the internal rings in place, and isolate the rings (or channels) from each other is highly involved and quite expensive. The more traditional process was not a financially viable option given the budget available to produce and test the TRIDENT Engineering Test Unit (ETU). Fortunately, this problem had a relatively simple solution which was to use Vespel spacers to isolate and constrain the conductive rings (Figure 9).

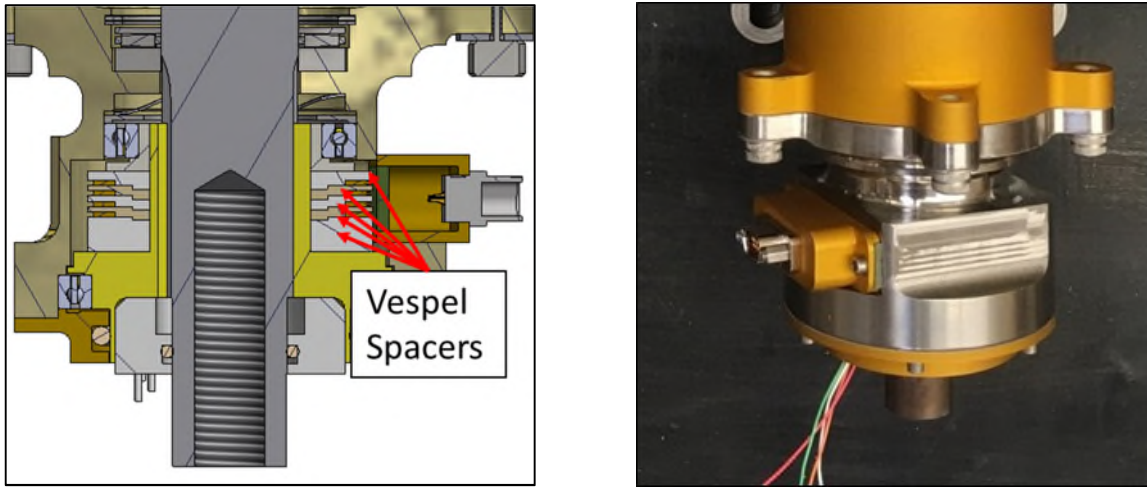


Figure 9. Slip-ring assembly overview (left – assembly cross section showing Vespel spacers; right – final assembly).

Once this solution was realized, the design and fabrication of the hardware was completed. The slip-ring assembly was then assembled and integrated into the TRIDENT ETU. To date, the TRIDENT slip-ring continues to perform as designed (the 2017 temperature response from Figure 6 is evidence of its functionality). This mechanism, along with the rest of the TRIDENT drill, went through the same vibrational test procedure as the RP 15 drill. However, improved designs for launch lock concepts greatly reduced the response at the drill head (Figure 10). It's conceivable that the COTS slip-ring may have survived the significantly reduced loading experienced at the drill head during this test. However, other environmental factors (temperature, atmospheric pressure, etc.) also dictate the necessity of a custom slip-ring for this application.

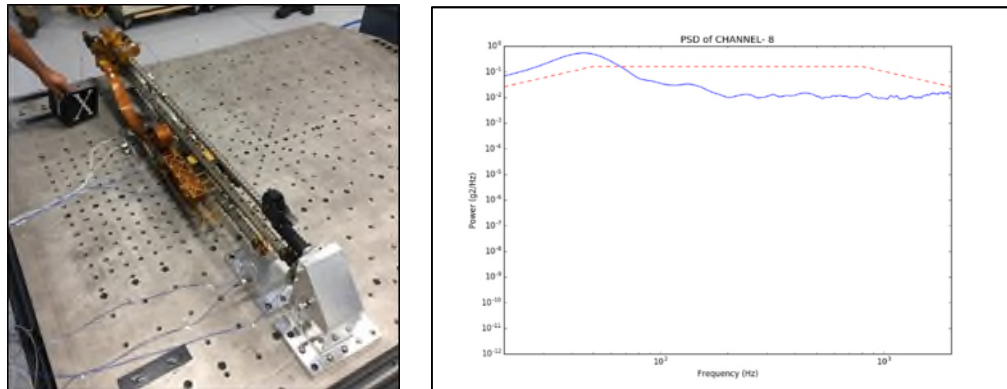


Figure 10. Improved fixtures / launch lock concepts for the TRIDENT drill in random vibration testing (left – drill on vibration table; right – significantly reduced response at the drill head).

Passive Brush for Sample Transfer

One of the key systems in ensuring enough sample is delivered to the OVEN subsystems is a passive brushing system designed to help remove regolith from the drill auger and direct it to a chute leading to the OVEN crucible. The RP environmental requirements have greatly reduced the trade space for materials that can be used in the passive brush. To protect against electrostatic charge build up, the brush material had to be conductive while also remaining flexible at cryogenic temperatures. The effectiveness of the brush at removing regolith from the auger is dependent on a number of factors which include: cohesiveness of regolith, size of brush bristles, length of brush bristles, stiffness of material used for the brush bristles, wear rate of the bristle material, and position of the brush with respect to the auger.



Figure 11. Keyed scraper for IceBreaker (a TRIDENT predecessor drill) [5].

The trade space studied included brass brushes of various bristle and brush diameters, Tampico, Thunderon, and conductive Nylon 66 (Table 1). Regolith used for the testing included JSC 1A and NULHT 2M Lunar regolith. Criteria used to evaluate the various brush materials included electrical conductivity; brush life expectancy, and effectiveness of cleaning debris from the drill string. Observations from the testing were:

- Bronze offered excellent electrical conductivity & was the most effective cleaner, but experienced significant wear after only a single hole which has a significant effect on the ability to clean the drill string for subsequent drilled holes.
- Thunderon fibers were too small to be an effective cleaner.
- Tampico cleaned sufficiently well, had sufficient life expectancy, but because it is a natural fiber, it will have more variance in conductivity.
- Conductive Nylon 66 cleaned sufficiently well, had sufficient life expectancy, and excellent conductivity.

Table 1. Brush materials and physical dimensions.

Material	Bristle Diameter mm (in)	Outside Diameter mm (in)	Brush Thickness mm (in)
Bronze	0.152 (0.006)	63.5 (2.5)	9.53 (0.375)
Bronze	0.356 (0.014)	63.5 (2.5)	9.53 (0.375)
Bronze	0.356 (0.014)	76.2 (3.0)	15.88 (0.625)
Tampico	0.203 (0.008)	63.5 (2.5)	9.53 (0.375)
Tampico	0.203 (0.008)	76.2 (3.0)	9.53 (0.375)
Thunderon	0.051 (0.002)	63.5 (2.5)	9.53 (0.375)
Conductive Nylon 66	0.203 (0.008)	76.2 (3.0)	9.53 (0.375)

Though test results thus far have been instructive in selecting the appropriate brush parameters, there is still much that can be improved. Other items to investigate are: alternative brush materials (other than what has already been tested - i.e. titanium) and alternative brush mounting configurations. The end goal driving the selection is ultimately based on the volume of material that the brush helps deliver to the instruments and the consistency of the volume delivered.

Traditional brushes were not the only thing considered to remove material from the auger flutes. A spring-loaded and rotating scraper design was also considered (Figure 11). This design was used on a preceding drill design and was largely more effective at removing more cohesive cuttings than traditional brushes. A prototype design was built and tested for the RP drill (Figure 12). One challenge in this case was designing the rotating scraper to interact with both fine pitch and coarse pitch flutes on the auger. For the TRIDENT drill, this variable pitch combination is necessary to help retain cuttings / regolith near the bit (fine pitch) for delivery to other instruments and more efficiently transfer cuttings / regolith through the remaining auger length (coarse pitch). Though the concept would work well while operating in either section of the auger (fine or coarse pitch), the transition point between the fine and coarse pitch flutes was a failure point for this mechanism. The primary reason causing the failure is that the coarse pitch flute requires the scraper to rotate twice as fast as the fine pitch flute because the pitch of the coarse flute is twice that of the fine pitch flute. This discrepancy could not be easily reconciled for this sample transfer approach.

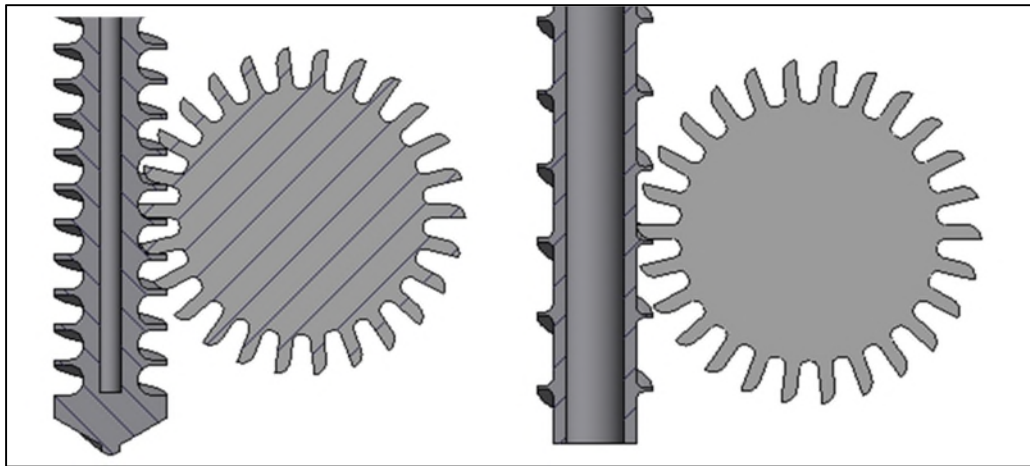


Figure 12. Single Rotating Scraper design (left – scraper interacting with fine pitch flutes; right – scraper interacting with coarse pitch flutes).

Although the brush has an obvious direct impact in the performance of the sample cleaning system, the mechanism supporting the brush is equally important. For both the 2016 and 2017 tests, the same conductive nylon brush design was used. However, there were significant performance differences. In 2016, a single brush lasted the entire test phase with minimal wear. In 2017, it was apparent that the brush stopped rotating as significant wear on only one part of the brush was observed after only a few tests (after which the brush had to be replaced). Two factors likely led to this change: one was an offset on the axis of the brush in the 2017 test to bias the brush towards one side of the auger; the other factor was a design modification in the 2017 design to help better protect the brush bearings by adding a seal between the brush housing cavity and the bearings for each bearing (Figure 13).

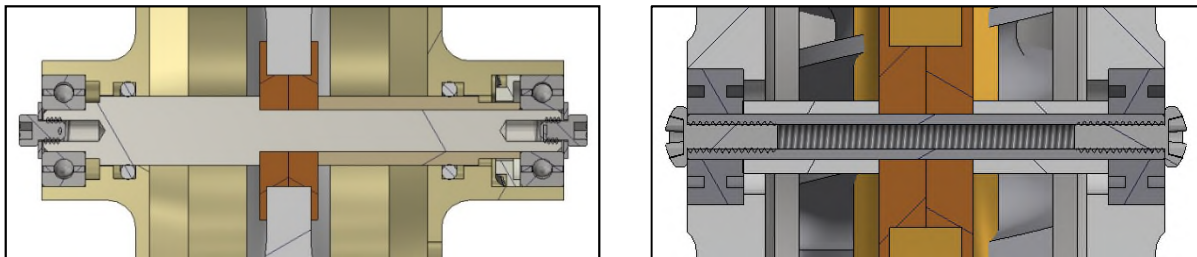


Figure 13. TRIDENT brush mechanism cross-sections (left - 2017 TRIDENT brush mechanism; right – 2016 RP15 brush mechanism).

Adding the axial offset in the brush was originally intended to help improve removal of cuttings / regolith from the drill string. However, this offset led to periodic pinching of bristles between the auger and auger tube which would ultimately pull out or shear bristles in the brush. If this happens enough in one section of the brush, there is no longer enough bristle engagement with the auger to cause the brush to rotate. Of course, this also reduces the ability of the brush to clean the auger.

Using seals to better protect the bearings also had a negative impact on the brush. For the 2016 configuration, the design was more simplistic and only relied on bearing shields to protect the bearings. Though this wasn't ideal, given the proximity of the bearings to regolith dust, these bearings had never failed – low speeds, cycles, and loads minimized the chances of failure in the bearings. The seals added in the 2017 design were entirely precautionary, but the increased drag from the seals made brush rotation more difficult and contributed to a reduction in the life of the brush

Design improvements around the brush and brush support are both necessary to help improve sample transfer efficiency. One design that can be leveraged to support the brush may be the design built to support the Atacama Rover Astrobiology Drilling Studies (ARADS) project [8]. This particular design (Figure 14) utilizes a rotating scraper (the ARADS drill has a constant auger pitch) that is supported on a cantilevered arm. The scraper could be replaced with a brush and the mechanism can be simplified due to the more compliant nature of a brush compared to the more rigid scraper (i.e. spring loaded arm is not required).



Figure 14. Alternative Support to use for brush (scraper shown here).

Brazing Tungsten Carbide (WC) to Titanium

To help reduce the overall system mass for the TRIDENT ETU, a titanium drill string was used instead of a stainless-steel drill string (as was used on RP15). This change introduced a new challenge of bonding the tungsten carbide (WC) cutter to the titanium drill string. Given the properties of titanium, a vacuum brazing approach is required. Also non-traditional brazing materials must be utilized. Because this is not a common process, there are not many vendors that have the capabilities or knowledge to perform this properly. In this case, a third-party vendor (Titanium-Brazing) was used to perform this work.



Figure 15. Assembled drill bits with deposited brazing paste in graphite support.

A standard titanium-based filler metal TiBraze200 (AWS BTi-5) reinforced by 20% of niobium particles was used for brazing. Melting temperature of the filler metal TiBraze200 is 863°C, melting temperature of niobium is 2477°C. Therefore, niobium powder is not melted together with the matrix TiBraze200 but is reinforcing it to improve strength of brazed joints. Also, the un-melted niobium powder increases viscosity of the melt to fill out uncontrolled, non-capillary gaps that may appear after assembling carbide tips with titanium drill bodies.

Brazing paste was deposited inside the slot in the drill body, then the carbide tip was inserted into the slot and compressed. A simple graphite fixture was manufactured to support assembled parts and fix them in the vertical position during heating and cooling in the vacuum furnace. Assembled drill bits with the deposited brazing paste are shown in Figure 15. The graphite support with parts to be brazed were positioned in the vacuum furnace. An alumina ceramic plate loaded by the "dead weight" ~250 g (0.5 lb) was placed on top of carbide tips in order to compress them after melting the brazing filler metal.

Overall, the brazing process was successful at bonding the WC cutters to the Titanium auger. No voids were found in the brazed joints, but there were rolls of excessive filler metal on the surface of the titanium bodies. The rolls were formed because brazing paste had to be deposited outside of the gap to provide enough filler metal. Also, a few of the WC bits were bonded noticeably off-center as they shifted during the brazing process. Recommendations to improve this process would be to add holes or grooves to the WC insert to provide more volume for the filler metal to reside between the insert and the Titanium auger. Also, an improved fixture design is necessary to help keep the insert on center with the auger axis during the brazing process.

Flexible Printed Circuit Cable Harness

TRIDENT ETU's cable harnessing system consists of three unique flexible printed circuits (FPCs). The first circuit carries motor power signals, the second circuit carries motor feedback signals, and the third carries heater and RTD signals. Each circuit is around 65 in (1.65 m) in length, 2 in (5 cm) in width and less than 0.015 in (1.3 mm) in thickness. The three circuits are stacked and joined together via twelve thru-hole right angled MIL-DT-83513 Micro-D connectors, which in turn translates to 148 discrete wires with a current carrying capacity of 3 ampere on each pin.

The FPC assembly approach offers numerous advantages over a discrete wire harness assembly. The motor power and motor feedback FPCs each have its own integrated crossed-hatched copper shields to

protect the drill and other subsystems from Electromagnetic Interference (EMI) and reduce signal cross-talk. The mass of the cable harnesses was also reduced by 85% (from 7 lb to 0.5 lb (3 kg to 0.2 kg)) in comparison to the RP15 Drill (Figure 16 and Figure 17).

The FPC assembly has proven to be extremely robust since the base dielectric and overlay material of are all made from Polyimide (e.g. Kapton). Not only does this perform well in cryogenic application, it also provides excellent electrical insulation and low outgassing profile in the vacuum environment.

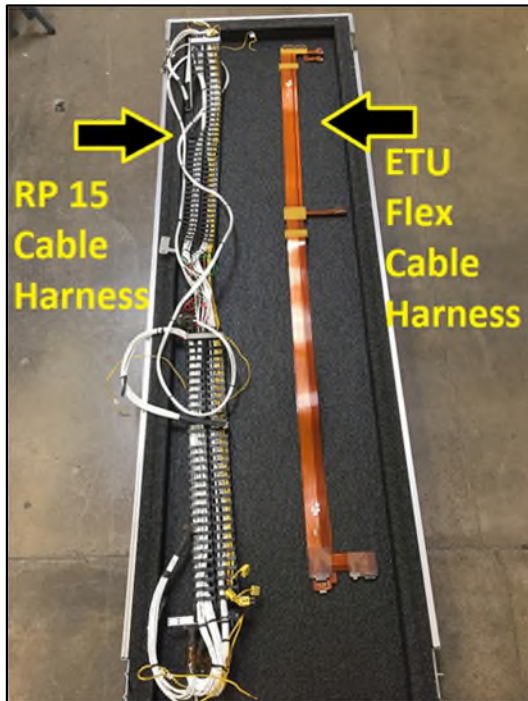


Figure 16. Side by side comparison of RP15 cable harness with TRIDENT ETU flex cable harness.



Figure 17. Reduced bulkiness and mass from RP15 (left) to TRIDENT (right).

References

1. D. Andrews, et al. "Introducing the Resource Prospector (RP) Mission", AIAA SPACE 2014 Conference and Exposition, AIAA SPACE Forum, (AIAA 2014-4378)
2. A. Colaprete, et al. "Detection of Water in the LCROSS Ejecta Plume", Science. 330 (6003): 463–468.
3. D. Hurley, et al "Lunar Polar Volatiles: Assessment of Existing Observations for Exploration." https://ssed.gsfc.nasa.gov/dream/docs/PolarVolatiles_HEOMD_Hurley.pdf. Accessed October 4, 2017.
4. K. Zacny, et al. "Life in the Atacama: The Drill and Sample Delivery System." 44th Lunar and Planetary Science Conference (2013).
5. Paulsen et al., "Testing of a 1 meter Mars IceBreaker Drill in a 3.5 meter Vacuum Chamber and in an Antarctic Mars Analog Site." AIAA Space 2011.
6. Teijin Aramid, "Technora Catalog," Technora datasheet. https://www.teijin.com/products/advanced_fibers/aramid/contents/aramid/technora/pdf_1/Technora_catalog%28E%29.pdf. Accessed February 2, 2018.
7. S. Nagihara, et al. "Improved Data Reduction Algorithm for the Needle Probe Method Applied to In-Situ Thermal Conductivity Measurements of Lunar and Planetary Regoliths." Planetary and Space Science, Volume 92, p. 49-56.
8. D. Waller. "Mars rover tests driving, drilling and detecting life in Chile's high desert." <https://phys.org/news/2017-03-mars-rover-drilling-life-chile.html>. Accessed January 31, 2018.

KaRIn Alignment Mechanism Design, Development and Testing

John Luke Wolff*

Abstract

The **Ka**-Band **R**adar **I**nterferometric System (KaRIn) will characterize the ocean mesoscale/sub-mesoscale circulation and provide a global inventory of all lakes, reservoirs, wetlands, and major rivers. There are two identical Alignment Mechanisms (AM) mirrored on the instrument to correct KaRIn Azimuth radar pointing errors. Each AM is a one-degree-of-freedom precision mechanism. The mechanism must meet challenging thermoelastic distortion requirements over a wide temperature range. The flight design was qualified in less than two years, and the flight hardware is currently in acceptance testing. Discussed are key design details along with supporting development and qualification test results.

Introduction

The KaRIn instrument uses radar interferometry to perform science measurements, which dictates tight alignments between the respective radar elements. The instrument requires a series of deployments, as shown in Figure 1. The AM enables the KaRIn instrument to correct residual post-deployment antenna pointing errors. The choice to maintain pointing passively imposed challenging thermoelastic distortion requirements on the AM. To simplify the mechanism overall complexity, launch locks are not used. Each AM consists of a Mechanism Strut Assembly (MSA) and Rotation Flexure Assembly, shown in Figure 2. The Rotation Flexure Assembly contains a hexfoil rotary flexure, which acts as the mechanism pivot axis for the one-degree-of-freedom commanded motion. The mechanism pivot axis is configured such that rotations about the pivot axis are linearly proportional to KaRIn Azimuth angle. The MSA consists of single-blade and coaxial double-blade flexures to create a kinematic five-bar linkage configuration, with the diagonal strut element containing a Linear Actuator Assembly (LAA). The LAA can lengthen or shorten via a geared stepper motor with an ACME leadscrew output. This linear length change in the diagonal strut causes a parallelogram effect in the MSA. The parallelogram effect results in primarily a rotation about the mechanism pivot axis. The small extraneous angular motion in the orthogonal axis is acceptable. The key design requirements are summarized in Table 1.

Table 1. Summary of Key Design Requirements

Mechanical Environments	0.0 kHz to 0.1 kHz: Sine Input, Peak 38G, All 3-Axes 0.1 kHz to 2.0 kHz: Random Input, 6.8 G _{rms} , All 3-Axes Note: Structurally support additional mass (NTE 4.6 kg)
Thermal Environments	Non-Operation: -95°C to +100°C Operation: -35°C to +100°C Note: Operation limit includes motor self-heating
Thermoelastic Distortions	Relative Azimuth: 2 mdeg (1-sigma) Note: Based on on-orbit temperature predictions
Commanded Motion	Accuracy: <6% of commanded motion Resolution: 0.6 mdeg Range of Motion: 150 mdeg to 250 mdeg Note: Step rate chosen to be 10 Hz based on electronics

* Jet Propulsion Laboratory, California Institute of Technology, Pasadena, CA

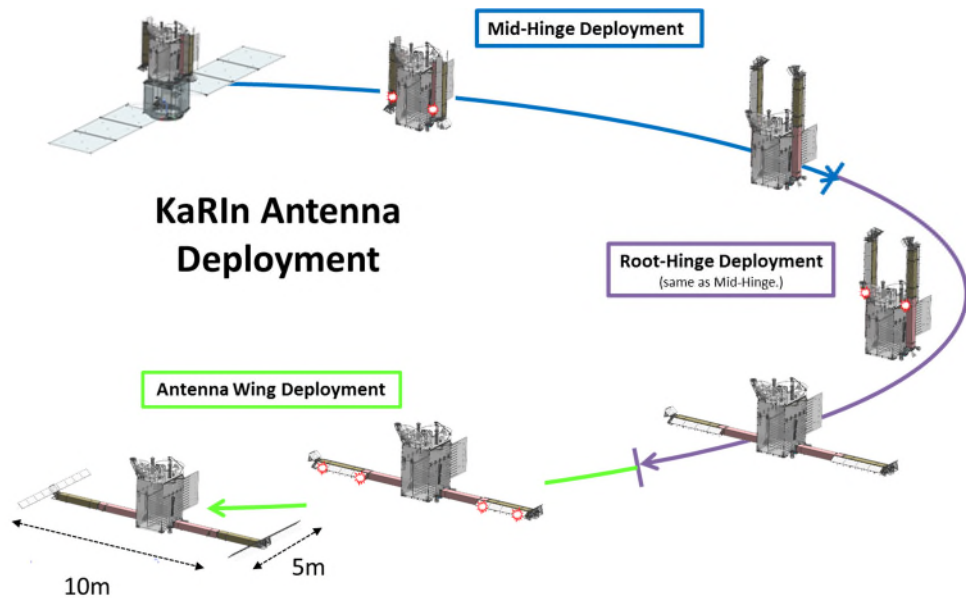


Figure 1. KaRIn Antenna Deployment

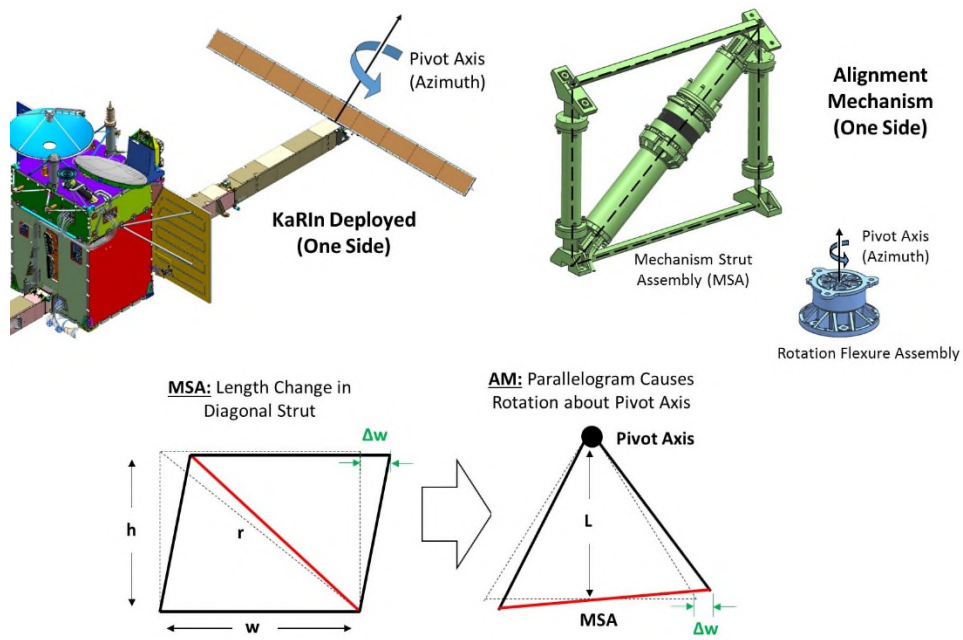


Figure 2. Alignment Mechanism Configuration

Design Overview for Thermoelastic Distortions

KaRIn Azimuth thermoelastic distortions, caused by the MSA, are the primary concern due to the instrument's strong sensitivity to this parameter. Therefore, this paper focuses solely on those thermoelastic distortions. The MSA 1D-thermoelastic distortion model, see Eq. 1, has been validated by FEM (Finite Element Model) and by testing, which is discussed later in this paper. Eq. 2 is the uncertainty in the model. For each key term, the partials are shown in Figure 3. Summarized in Table 2 are the model uncertainties and associated mitigation approaches. The dominant error sources are the coefficient of thermal expansion (CTE) uncertainty¹ and 3D thermoelastic distortions due to bolt slip.

¹ Includes hysteresis between thermal cycles, measurement error, and unit-unit variability.

Coefficient of Thermal Expansion (CTE)

To use reference sources ([1], [2]) for instantaneous CTE over temperature, the thermoelastic distortion model would need to incorporate unacceptably high CTE uncertainties. To mitigate this risk, all flight piece parts, except the LAA, were fabricated from controlled slabs of material whose CTE was characterized per ASTM E289². To build confidence in the CTE over temperature for the LAA, a flight-like LAA was built, with the CTE measured per ASTM E289. Due to difficulties controlling all of the materials in the LAA, the team continued to assume a large CTE uncertainty for the LAA until the flight LAAs were each measured. In Figure 5, the measured instantaneous CTE over temperature is compared to several reference sources. All CTE uncertainties used in the model are summarized in Table 3.

Thermoelastic Distortion due to Bolt Slip

As the temperature is changed for CTE mismatched materials bolted together, radial strain increases until joint friction due to bolt preload is overcome, whereby radial strain projects into axial distortion errors. Where possible, this error source was eliminated by adding radial flexures to one side of the bolted joint to eliminate radial coupling at the bolted joint. At all other bolted joint locations, a low friction surface coating was applied to improve our confidence in the design and the repeatability. At these bolted joints, thermoelastic distortion uncertainty was empirically estimated by varying in the FEM the radial stiffness at each bolted joint location for a 10°C bulk soak case. Then, the FEM results were linearly scaled based on closed form solutions estimating the maximum temperature change required for each bolted joint to slip.

$$\delta\theta = 1/L \left[(r/w)\delta r - (h/w)\delta h - \delta w \right] \quad (1)$$

$$\partial(\delta\theta) = 1/L \sqrt{[(r/w)(\partial\{\delta r\})]^2 + [(h/w)(\partial\{\delta h\})]^2 + [\partial\{\delta w\}]^2} \quad (2)$$

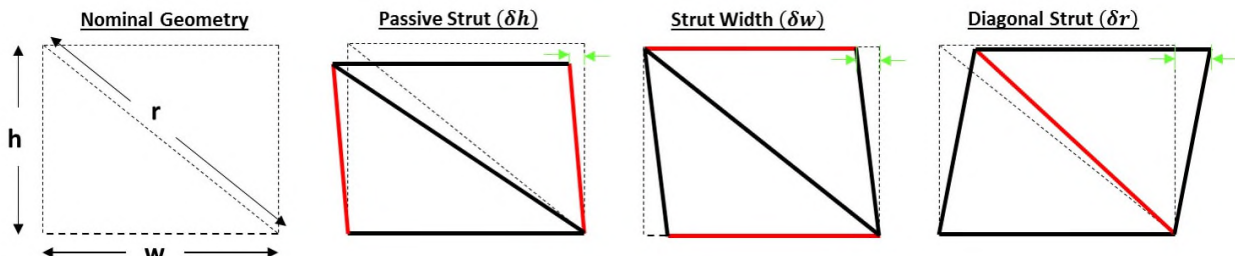


Figure 3. Mechanism Strut Assembly Thermoelastic Distortions Key Terms

Table 2. Thermoelastic Distortion Uncertainty Error Sources

Uncertainty Sources	Mitigation – Design Intent	Development Test (Prior to Mechanism Level Test)
Temperature (Gradient)	Top-to-bottom and left-to-right, materials chosen are nearly symmetric. Minimize CTE by utilizing High Purity (HP) Invar36 ³ where possible. See Figure 4.	None
Temperature (Bulk)		
Coefficient of Thermal Expansion	Metallic hardware and bolted joints to improve confidence in incorporating test results to model predicts.	Characterize CTE for flight material and prototype LAA. Final verification, characterize CTE for each flight LAA.
3D Effect (due to bolt slip)	Radial flexures where configuration allows OR low friction surface coating (SF-2).	None
Linear Lengths	Control fabrication/assembly tolerances.	Inspect part/assembly tolerances.

² Five coupons machined from each slab of material, with three thermal cycles measured per coupon.

³ HP Invar36 exhibits very good dimensional stability properties. While not discussed further in this paper, HP Invar36 is critical to the mechanism temporal stability performance [4].

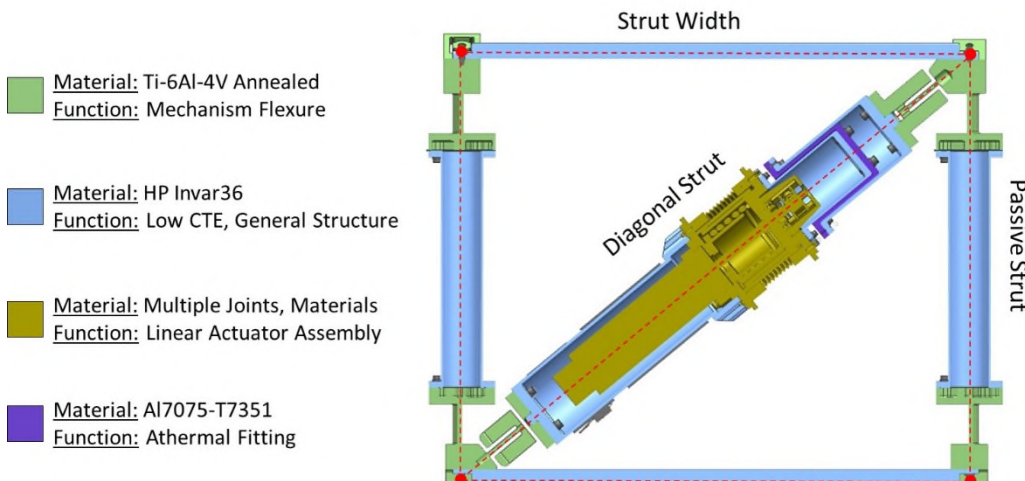


Figure 4. Mechanism Strut Assembly Configuration

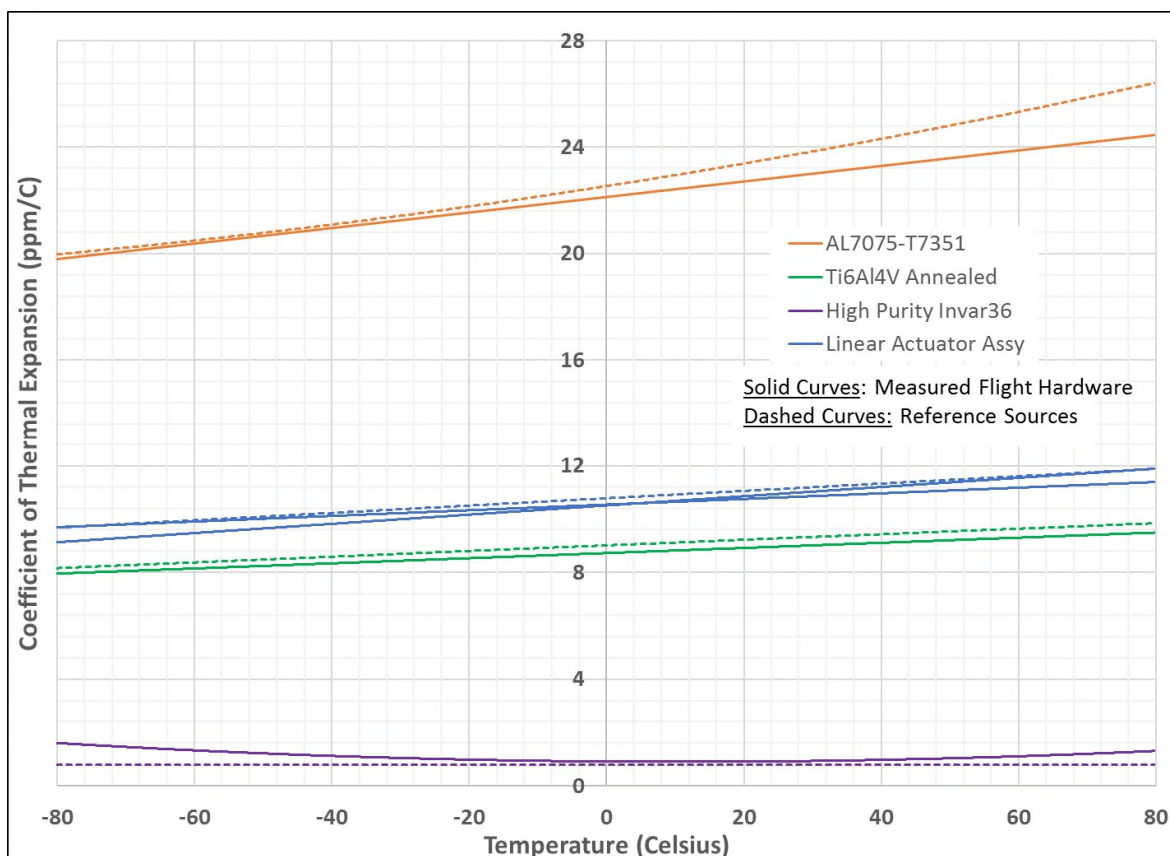


Figure 5. Instantaneous CTE over Temperature

Table 3. CTE Uncertainty

	Ti6Al4V Annealed	Al7075-T7351	HP Invar36	LAA 1	LAA 2
Reference Value (% of Mean CTE)	---	---	---	0.40 ppm/C (3.7%)	
Measured Flight (% of Mean CTE)	0.11 ppm/C (1.3%)	0.13 ppm/C (0.6%)	0.06 ppm/C (8.2%)	0.20 ppm/C (1.9%)	0.32 ppm/C (3.0%)

Key Design Features

Illustrated in Figure 6 are the mechanism key design features. The bolt spacers increase the bolt length and thereby limit thermally induced bending stresses in the respective bolts. The single blade flexures, coaxial double blade flexures, and the rotation flexure provide the necessary boundary conditions to achieve a quasi-kinematic structure. KaRIn thermoelastic distortions are verified by analytically combining subsystem test data into the instrument level Structural Thermal Optical model. Therefore, it is critical to limit interface distortions, as they are not captured in the respective tests. The thermoelastic distortions due to the MSA interfaces are removed by the presence of the strut interface bar in conjunction with the respective radial flexures. The mechanism is nominally athermalized via an athermal fitting, illustrated in Figure 4. The remaining radial flexures remove thermoelastic distortion uncertainty.

Flexure Design

All flexures were fabricated by electrical discharge machining (EDM), with the titanium flexures requiring chemical etching post-machining to remove the beta-alpha recast layer. Trade studies were completed to balance the competing design considerations, summarized in Table 4. To determine the appropriate FEM mesh density for stress analysis, it is recommended to have at least two nodes across the fillet region and the flexure thickness. To limit the FEM file size, the FEM mesh density was not sufficient to assess the radial flexures stresses. The radial flexure stresses were analyzed using beam shear, beam axial, and beam bending free body equations for the respective load cases, illustrated in Figure 7. The flexure fillet radii were selected to limit the stress concentration factor to 1.5 [3]. The flexure margins were analyzed at the worst-case manufacturing geometry tolerances. The bolt install torque is critical to include in the radial flexure stress margins. Where appropriate, flexure stress margins also need to include imposed deflections due to mechanism motion.

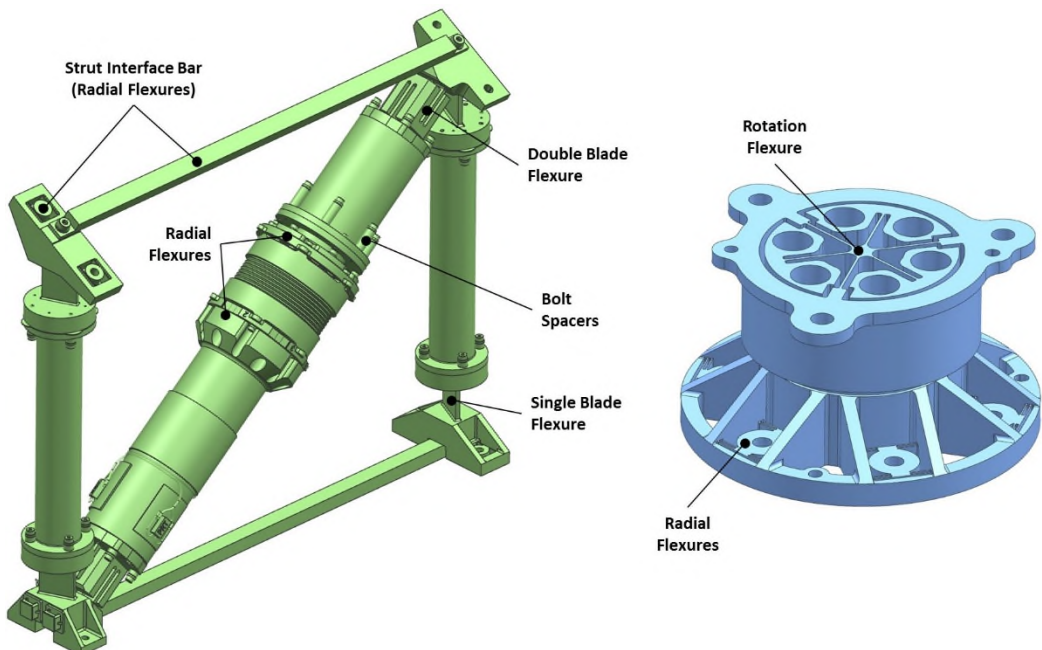


Figure 6. Key Design Features in Alignment Mechanism

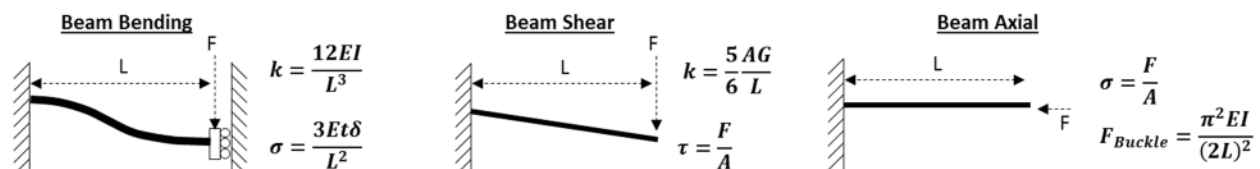


Figure 7. Radial Flexure Free Body Diagrams

Table 4. Flexure Design Considerations

Location	Flexure Function	Flexure Design Driver: Stiffness	Flexure Design Driver: Stress
Single Blade Flexure (Thick:2.00 \pm 0.05 mm)	Kinematic B.C. (5-Bar Linkage)	1) <u>Bending</u> : LAA force required for mechanism motion 2) <u>Axial</u> : KaRIn Deployed 1 st mode	Mechanism range of motion
Double Blade Flexure (Thick:1.75 \pm 0.05 mm)		1) <u>Bending</u> : Assembly 2) <u>Axial</u> : KaRIn Deployed 1 st mode	Mechanical environments (and diagonal strut mass)
Hexfoil Rotary Flexure (Thick:0.60 \pm 0.05 mm)	Mechanism Pivot Axis	1) <u>Torsion</u> : LAA force required for mechanism motion 2) KaRIn Deployed 1 st mode	Mechanical environments (and supported mass)
Radial Flexures (Thick:0.30 \pm 0.05 mm)	Thermoelastic Distortion	1) <u>Radial</u> : Thermoelastic model prediction accuracy/repeatability 2) <u>Axial</u> : KaRIn Deployed 1 st mode	1) Thermal environments 2) Mechanical environments with bolt install torque added

Linear Actuator Assembly Design

Key LAA design features are illustrated in Figure 8. The LAA converts commanded rotational steps from the actuator into linear steps required by the mechanism. As the LAA is part of the primary load path, it must react large axial, lateral, and bending loads as well as contribute to the MSA thermoelastic distortion. To gain confidence in the design, a prototype LAA was built early in the design phase. The main objectives with the prototype LAA were to characterize the linear step size and the effective axial instantaneous CTE over temperature. Summarized in Figure 9 is the LAA test setup along with annotated test data graphs. The LAA key performance metrics are summarized in Table 5.

The actuator consists of a 3-phase stepper motor, 2-stage planetary gearhead, thrust module with a hard-shimmed leadscrew, and hall sensor assembly for confirming step integrity (not motor commutation). Except for the thrust module, the actuator consists of entirely flight heritage components, which allowed for a short procurement and development timeline. The thrust module relies on a pair of needle roller thrust bearings to improve the axial load capability and axial stiffness within a small packaging volume. As the LAA was only preloaded for mechanism operations, the actuator gaps in the axial direction during launch and vibration testing. The dynamic axial stiffness was estimated as being one-half the static axial stiffness.

The telescoping cylindrical plain bearing housings provided high bending stiffness during high bending load events, like launch or vibration testing. To estimate the bending stiffness, a non-linear contact FEM was required. The Inner Bearing Housing was greased plated C63200 (Aluminum-Bronze). The Outer Bearing Housing and the Leadscrew were fabricated from CRES 15-5PH condition H1025. The plain bearing housings had tight diameter tolerances and used a 1.0 length to diameter ratio, thereby ensuring minimal dynamic effects and minimal bending loads transferred through the actuator⁴. When assessing the concentricity of the bearing housings to the leadscrew, it is advantageous to include the ACME radial play.

Table 5. Linear Actuator Assembly (LAA) Key Characteristics

Characteristic	Value	Notes
Total Mass	270 grams	As built, includes harnessing
Interface Loads (Approximate)	Axial: 1800 N Shear: 700 N Moment: 400 N*m	Quasi-static equivalent. Dynamic analysis used to verify margins and make test predicts.
Dynamic Stiffness (Approximate)	Axial: 32,000 N/mm Moment: 14,000 N*m/rad	Torsional stiffness is high due to bellows.
Range of Motion	600 μ m to 1000 μ m	As built shown. Mechanism capable of 2160+ μ m.
Nominal Step Size	0.5 μ m \pm 6%	Characterize mechanism step size over ROM

⁴ Leadscrew has a reduced diameter between ACME thread interface and actuator, thereby further limiting the lateral and bending loads transferred through the actuator.

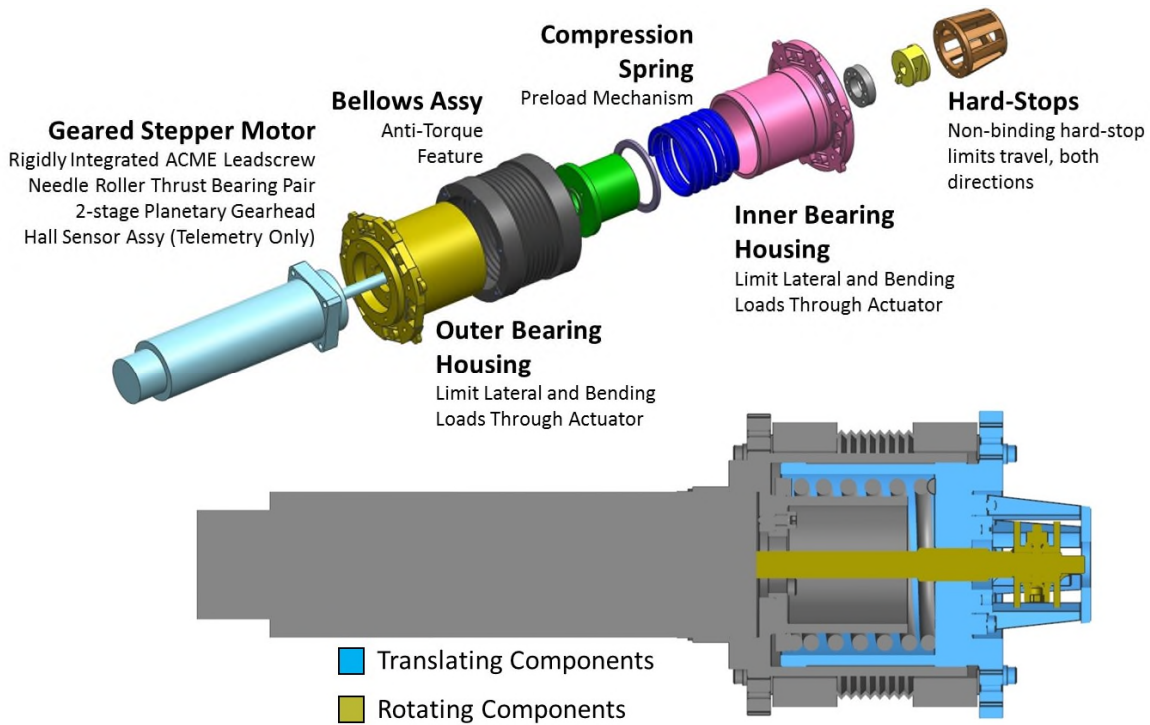


Figure 8. Linear Actuator Assembly Key Design Features

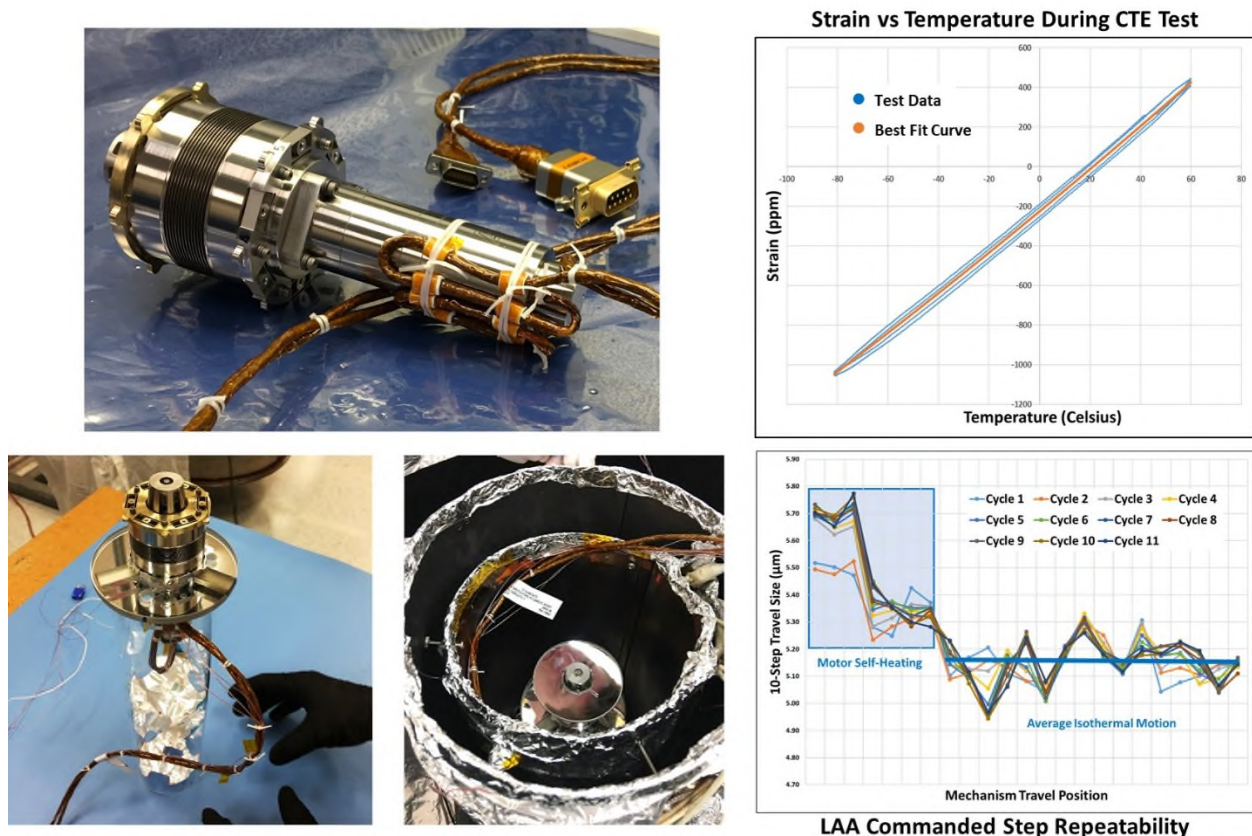


Figure 9. Prototype Linear Actuator Assembly Testing (Setup and Key Test Data Graphs)

Commanded Motion Functional Testing

Before and after vibration testing, an auto-collimator coarsely measured the mechanism motion, where the objective was to verify mechanism step repeatability. The hall sensors provide feedback on the motor step integrity. While the mechanism is integrated with the vibration GSE hardware, a mirror is attached near the top of the rotation flexure. See Figure 10, the mechanism motion was repeatable in both directions, and the hall sensors measured no missed or skipped motor steps. A nearly perfect quadratic best-fit curve matches both sets of data to better than 2%, which is better than expected when considering the crude test setup. When the mechanism changes stepping direction or runs into either mechanical hard stop, there will be a dead band zone. The test setup illustrated in Figure 15 will be used to create the calibration curves at temperature limits for the mechanism motion, as well as measure the dead band zones and extraneous motion about other axes; this test is planned for late January 2018.

By substituting Equation 3 into Equation 1, where δh and δw equal zero, the mechanism motion could be estimated. However, this produced an over-estimate when compared to the motion actually measured, with the difference being roughly 20%. Some variance due to the ACME lead, flexure geometry, or mechanism geometry is expected, but not to this magnitude. The auto-collimator appeared clocked at a 20° , which would cause a trigonometric projection error. Since we were borrowing the auto-collimator from another team, the author did not tinker with their hardware. In addition, thermoelastic distortions due to motor self-heating would cause a similar effect seen in Figure 10. During LAA commanded step repeatability testing, summarized in Figure 9, a quasi-isothermal environment was achieved, whereas this functional test did not. While not important for this functional test, this oddity merits some further investigation if it is observed during later characterization testing of the mechanism isothermal motion.

$$\delta r = n \frac{\gamma N}{2\pi} \quad (3)$$

N: Commanded Steps, γ : Geared Motor Output Angle (rad), n: ACME Lead

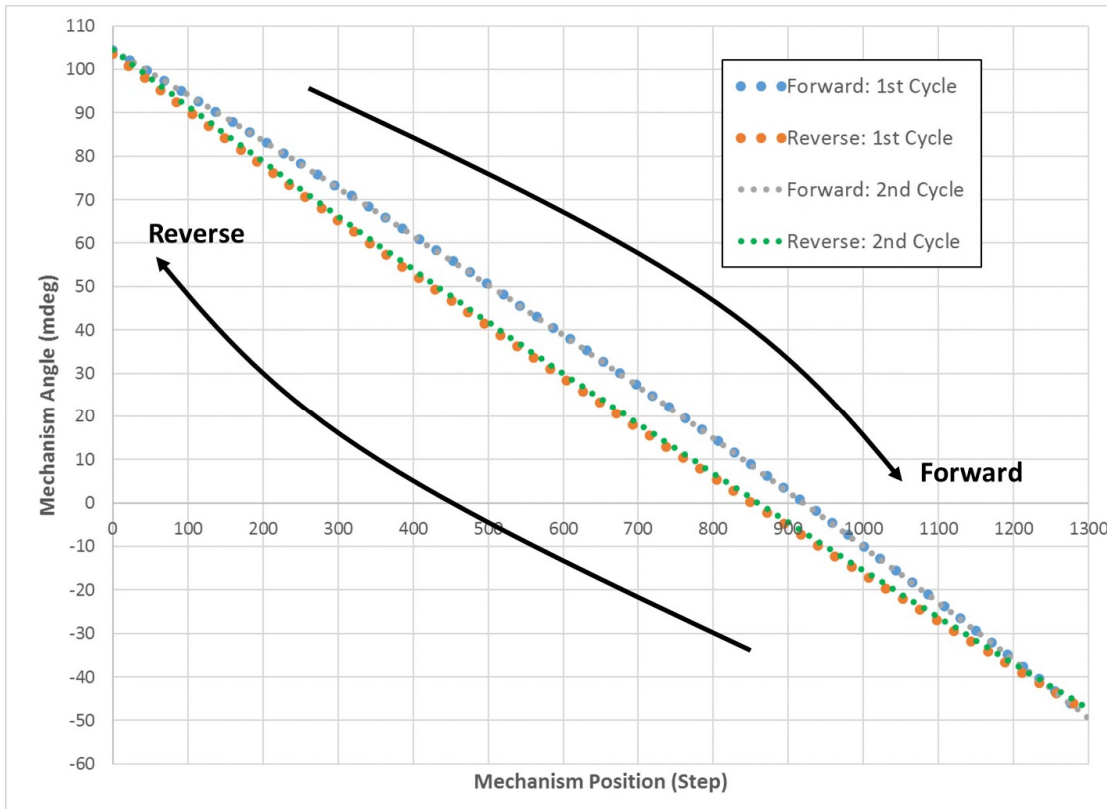


Figure 10. Mechanism Functional Test (Pre & Post Vibration Testing)

Vibration Testing

Figure 11 illustrates the test configuration and the test instrumentation, with the environments previously summarized in Table 1. The diagonal strut first bending mode (Y-Axis Input, Sine) and the first global mode of the mechanism (X-Axis Input, Random) drive the mechanism design minimum stress margins. The four single-axis accelerometers mounted on the LAA in 45° increments measure the responses of the diagonal strut first bending mode. The force transducers at the base of the mechanism measure the mechanism global mode responses and they are used to force limit during random vibration testing.

The mass simulator was designed to be a rigid body, which simulates the mass properties of hardware mounted to the AM in the flight configuration during launch. All test predicts used a coarse mesh density for the mass simulator FEM. As mechanical environments evolve late in the project, the coarse mesh density allowed the team to complete the dynamic pre-test analysis in a timelier manner. Table 6 illustrates the modal mass comparison between the two FEMs. In general, the mode frequencies are higher with the finer meshed GSE FEM, supported by the test results in Figure 12. As input decreases at higher frequencies, typically higher stiffness results in lower stresses. For Random-X, force (RMS) was measured 15% higher than predicts, which is acceptable based on the stress margins of safety.

As previously discussed, the LAA initially transfers small bending loads through the leadscrew and then, as the loads are further increased, transitions to the cylindrical bearing housings being the primary bending load path. For X-axis and Y-axis inputs, the transition from soft to stiff bending load path appears clearly in the single-axis accelerometer responses around 45 Hz, see Figure 13. Above 80 Hz, the response appears to deviate from the predicts for the Y-Axis Sine input, which seems at least partially due to the input not ramping down entirely. Figure 14 shows the diagonal strut first bending mode frequency came close to predicts. Interestingly, the diagonal strut first rigid bending mode does not appear for the Z-axis input, which is likely due to the input levels being insufficient to engage the cylindrical bearing housing load path.

The AM vibration test envelopes the stresses within the AM flight hardware during all higher level of assembly vibration testing. During vibration testing, the hall sensors monitored the motor rotor position, which verified the motor did not back-drive. While the mechanism does still move during vibration testing due to ACME thread resettling and 0.2% plastic deformation, the motion is small relative to the mechanism range of motion (ROM). Random vibration signature runs pre- and post- 0dB level test runs verify no change greater than 5%. As a mechanism functional health check, the mechanism stepped through its ROM after each test axis, with the hall sensor data used to verify the step integrity. After all vibration testing, an auto-collimator measures the mechanism stepping through its ROM, with the results previously discussed.

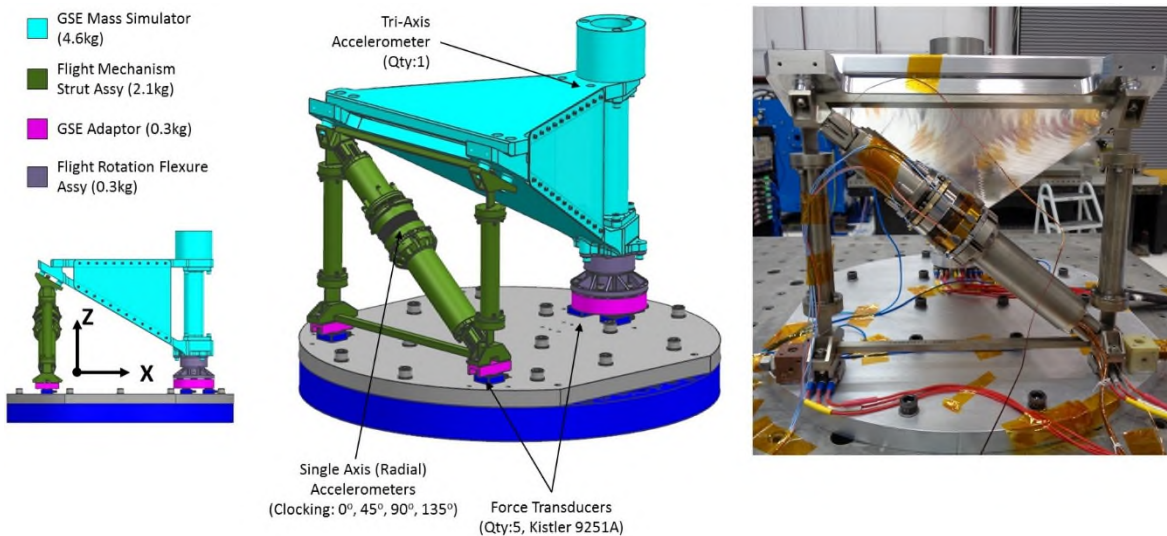


Figure 11. Alignment Mechanism Vibration Test Configuration

Table 6. GSE FEM Mesh Density Modal Comparison

(a) Coarse Mesh, GSE FEM					(b) Fine Mesh, GSE FEM				
Mode	Frequency	X-Input	Y-Input	Z-Input	Mode	Frequency	X-Input	Y-Input	Z-Input
2	111 Hz	0%	14%	10%	2	115 Hz	0%	16%	10%
3	119 Hz	29%	0%	0%	3	123 Hz	25%	0%	0%
4	183 Hz	11%	51%	1%	4	181 Hz	1%	59%	1%
5	191 Hz	44%	12%	0%	5	213 Hz	49%	3%	1%
9	321 Hz	1%	0%	47%	9	354 Hz	1%	0%	0%
10	360 Hz	1%	0%	1%	10	422 Hz	3%	0%	60%

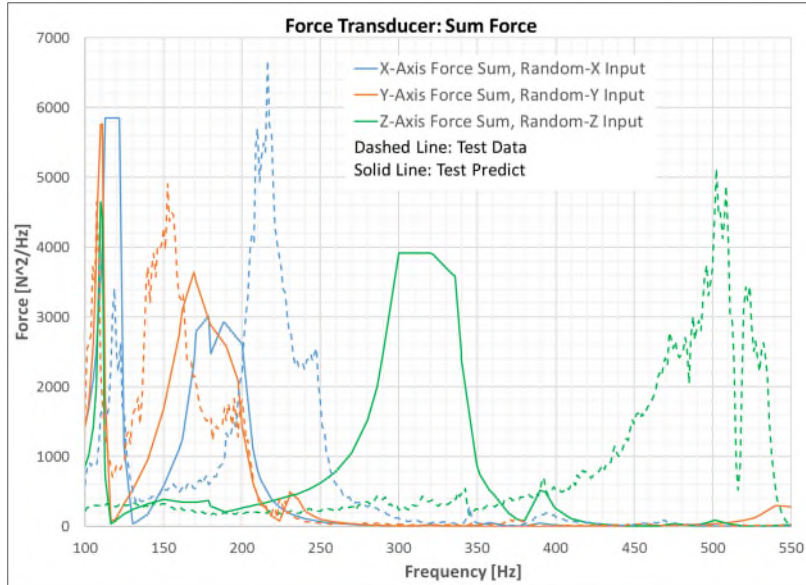


Figure 12: Random Vibration Test, Mechanism 1st Global Mode ⁵

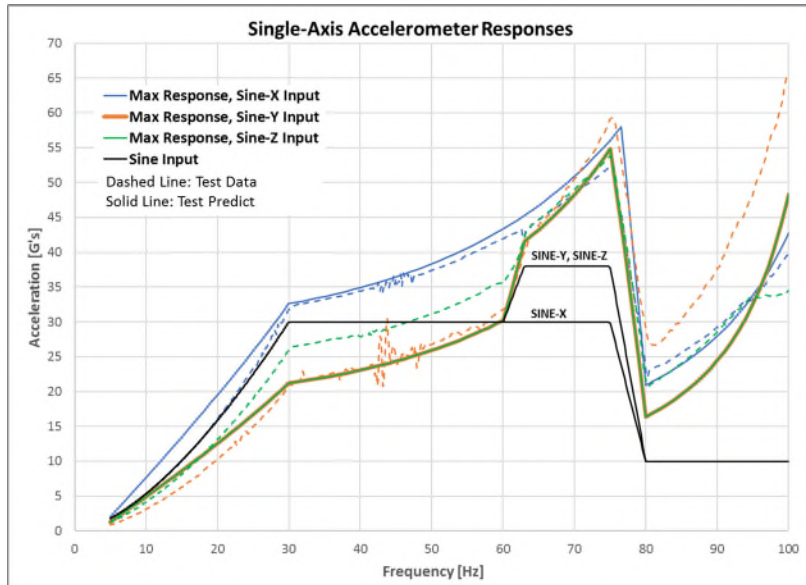


Figure 13. Sine Vibration Test, Single-Axis Accelerometer Responses

⁵ To identify mode frequency, responses are normalized by force-limited inputs. When normalized, X/Y results align well with predicts. Z result is higher than predict, likely due to GSE mesh density too small.

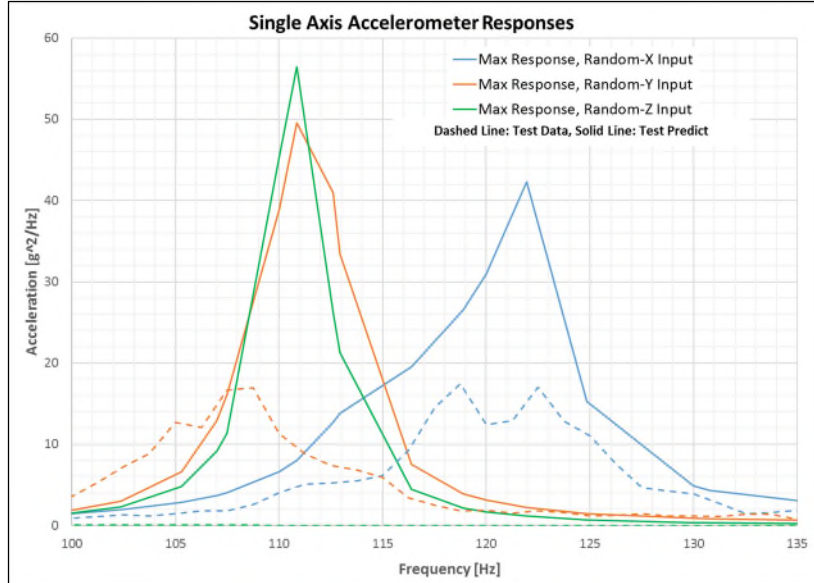


Figure 14. Random Vibration Test, Diagonal Strut 1st Bending Mode

Thermoelastic Distortion Testing

Figure 15 illustrates the test configuration, which is done at Precision Measurement and Instrumentation Corp (PMIC). The test setup measures accurately the flight mechanism angular thermoelastic distortions about the mechanism pivot axis. When gradients are kept small (less than 5°C), the GSE is designed to not contribute to the thermoelastic distortion of concern. The 32-thermocouple-sensors are calibrated together with 4-silicone-diode-sensors (Lakeshore DT-670-SD-70H) providing reference absolute temperature measurements, with an accuracy better than 50 mK. A PMIC proprietary setup measures the optical length between the laser and the detector. The base plate mounted mirror measures the bulk bias of the test setup. The mirror mounted near the top of the rotation flexure is the primary data point, with the mirrors mounted near the MSA intended as redundant measurements. The reduced chamber pressure is backfilled with helium to balance thermal conduction with optical measurement needs. Quartz rods support the test hardware with a quasi-kinematic interface. The quartz rods are mounted to a water-cooled plate.

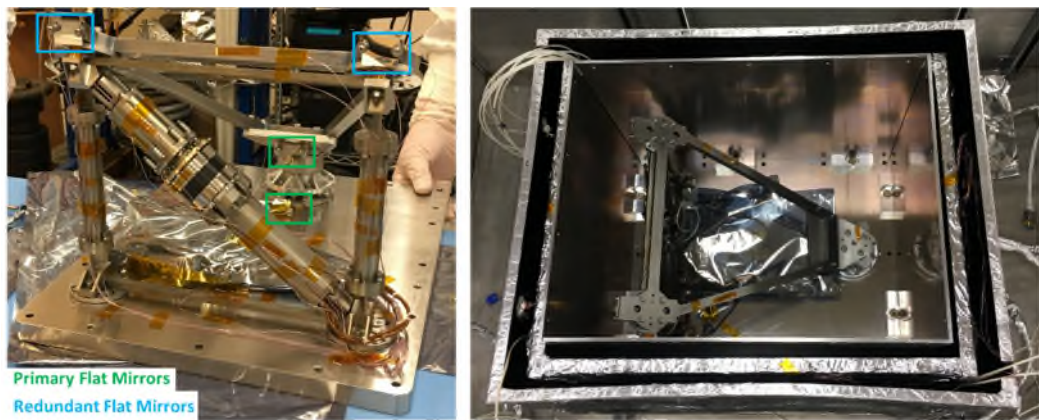


Figure 15. Thermoelastic Distortion Test Configuration

The GSE interfacing directly with flight hardware was titanium, which is the flight configuration, to ensure the radial flexures are not overstressed. The large GSE pieces on top and bottom are both Invar36 to minimize overall thermoelastic distortions. To eliminate thermoelastic distortion uncertainty between CTE-mismatched GSE hardware bolted together, radial flexures are implemented (26 flexures in the GSE). There are 24 temperature sensors mounted on the JPL hardware, where each segment illustrated in Figure

16 has temperature directly measured during the test⁶. To predict the thermoelastic distortion based on measured temperatures, substitute Eq. 4-6 into Eq. 1. To estimate the prediction uncertainty, substitute Eq. 7-9 into Eq. 2, where length uncertainty (∂L) and temperature uncertainty (∂T) is negligible.

$$\delta r(T_i) = \sum_{i=1}^7 \{[\alpha_i][L_i][\Delta T_i]\} + \sum_{i=1}^4 \Delta x_i \quad (4)$$

$$\delta h(T_i) = \sum_{i=8}^{13} \{[\alpha_i][L_i][\Delta T_i]\} + \sum_{i=5}^6 \Delta x_i \quad (5)$$

$$\delta w(T_i) = \sum_{i=14}^{15} \{[\alpha_i][L_i][\Delta T_i]\} \quad (6)$$

$$\partial[\delta r] = \sqrt{\sum_{i=1}^7 \{[\partial\alpha_i][L_i][\Delta T_i]\}^2 + \sum_{i=1}^4 [\partial\Delta x_i]^2} \quad (7)$$

$$\partial[\delta h] = \sqrt{\sum_{i=8}^{13} \{[\partial\alpha_i][L_i][\Delta T_i]\}^2 + \sum_{i=5}^6 [\partial\Delta x_i]^2} \quad (8)$$

$$\partial[\delta w] = \sqrt{\sum_{i=14}^{15} \{[\partial\alpha_i][L_i][\Delta T_i]\}^2} \quad (9)$$

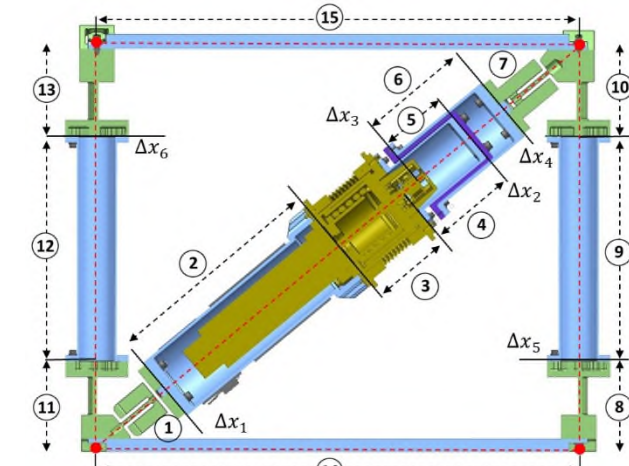


Figure 16. MSA Thermoelastic Distortion Variables

Test Anomaly: MSA Mirror Locations

Shortly after beginning the test, the two detectors pointed at the mirrors mounted near the MSA started measuring unexplained and unrepeatable angles. In addition, there was a large settling in the mirror mounted near the upper right in Figure 15 (passive strut only side), which became apparent when the test returned to room temperature. While the test only needs the two mirrors illustrated in Figure 15, the team is still investigating the anomaly with the two other locations. The team believes the prime culprit has to do with the instrumentation outside the chamber. To summarize what is going on, it is important to understand the laser measurements. The laser goes through beam steering optics and a single beam splitter optic before entering the chamber. The laser, detector, and optical levers are all mounted on different locations of the optical bench outside the chamber. However, the MSA mirror instrumentation is mostly grouped together, whereas the rotation flexure and base-plate mirror instrumentation are mostly grouped in another location. The team believes that the MSA mirror instrumentation is not properly attached to the respective mounts. However, to avoid disrupting the test, the investigation is on-hold until after the first mechanism completes the thermoelastic distortion testing in early January 2018. Therefore, only the two primary flat mirror locations illustrated in Figure 15 are discussed in this paper.

Test Results

While the test data processing is still on going for the first (of two) flight AM, the thermoelastic distortion model represented by Equation 1 appears to be validated by the test results. In Figure 17 and 18, the first cycle cooling-down from -40°C to -80°C is illustrated. The sample rate of the angular and temperature measurements was 0.2 Hz. Per the pre-test calibration of the angular measurement, the angular measurement accuracy is better than 0.1 mdeg. In addition, there is roughly 0.25-mdeg noise in the angular measurement. PMIC takes extreme measures to minimize noise in the system, but a crude low pass filter is still required. While a more extensive analysis could identify the correct frequency(s), a 12-point (1-minute) moving average best-fit curve seems appropriate to this author. The temperature measurement during the test is very stable. Based on thermocouple and silicon-diode calibration data, the temperature accuracy is better than ±0.2°C. At thermal steady state, the temperature measurements align to within about 0.5°C, see Figure 18⁷. Summarized in Table 7, the last 12-point (1-minute) test data average is compared to the predictions, with the measured data being within the 1-sigma prediction envelope.

⁶ The LAA bulk temperature was calculated as a linear average of several temperature measurements.

⁷ Although thermocouples are uniquely calibrated/serialized, PMIC only uses standard curve to simplify implementation; PMIC controls shroud temperatures. In Figure 18, author incorporates calibration data.

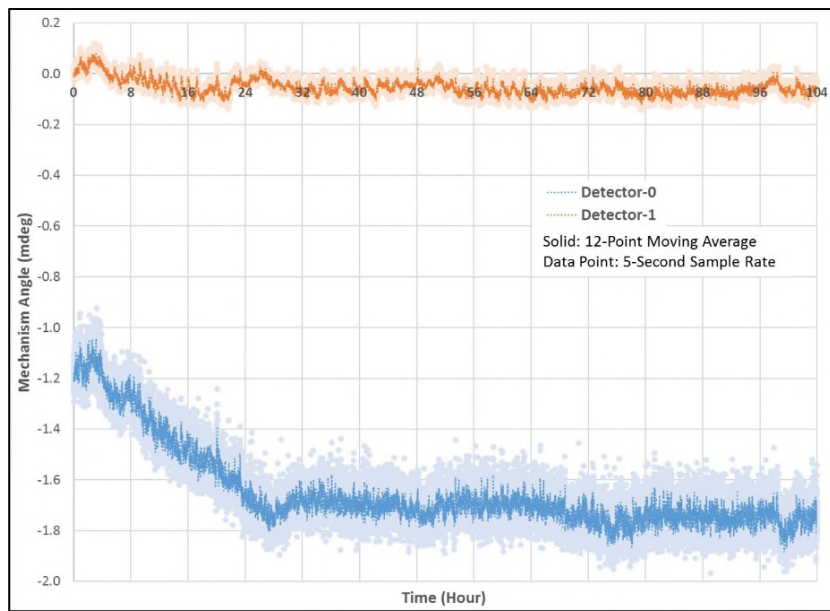


Figure 17. MSA Thermoelastic Distortion Angular Measurement

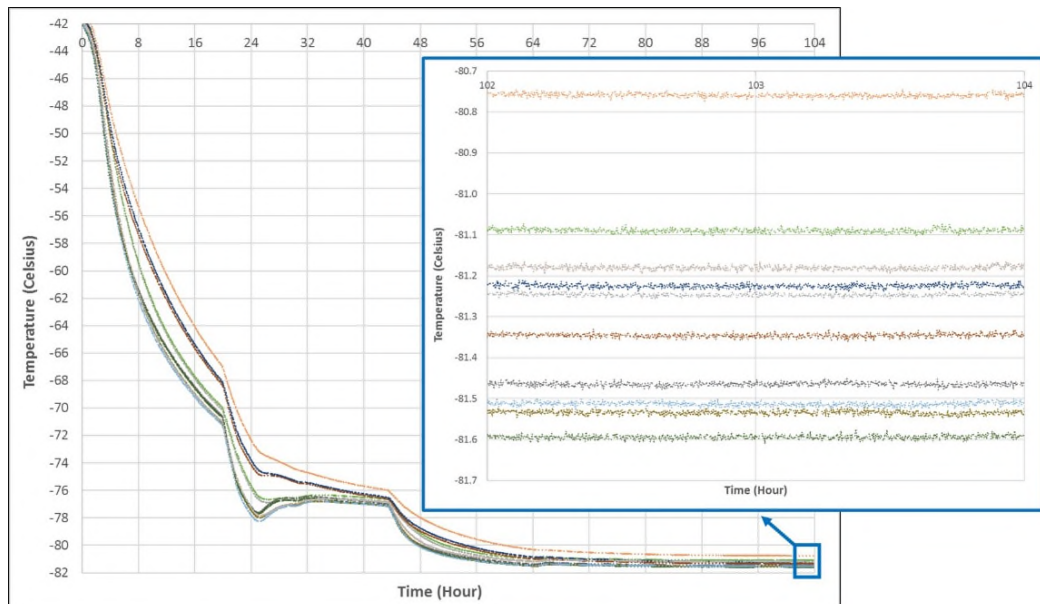


Figure 18. MSA Temperature Measurements

Table 7. MSA Thermoelastic Distortion Test Data Summary⁸

Approximate Bulk Temperature	Warming-Up		Cooling-Down	
	Data (mdeg)	Predict (mdeg)	Data (mdeg)	Predict (mdeg)
+80 Celsius	-0.70	-0.95 \pm 0.45	-1.16	-1.02 \pm 0.45
+20 Celsius	-0.20	+0.00 \pm 0.35	-0.10	-0.05 \pm 0.35
-40 Celsius	+0.90	+0.49 \pm 0.45	+0.88	+0.46 \pm 0.45
-80 Celsius	+1.11	+1.22 \pm 0.50	+1.39	+1.12 \pm 0.50

⁸ Initial measurement bias was subtracted from test data results summarized in Table 7.

Lessons Learned

The Nedox SF-2 low-friction coating caused significant issues. Some of the issues encountered include: lost all part serialization, baked out to wrong temperature (per industry/vendor specifications), and rough handling (deep marks visible in titanium). While process inspection and/or quality control points help prevent issues, post-machining activities can fall through the cracks due to their perceived low technical or programmatic risk. Therefore, it is important to consider a part's complexity (e.g. lead-time, cost) when deciding on the proper oversight at a vendor facility. The design team should carefully consider whether each post-machining activity is required, especially when requiring a third-party vendor. If the activity is still required, the design team should strive to minimize masking and carefully manage the activity.

To limit the tunnel vision syndrome, this author actively engaged a broad set of senior personnel for constructive criticism of the design throughout the design cycle (not just at design reviews). While providing the obvious benefit of pointing out design shortcoming(s) along with potential solutions(s), they can also help provide cover from the continual battle of micromanagement by "others". Ultimately, final design decision should always remain with the mechanism team, but the team should make design decisions with eyes open to the associated compromises. This was a large contributor to the team's success.

Conclusion

The mechanism has demonstrated by test the capability to survive the mechanical and thermal environments specified. Based on both FEM and test validation, the mechanism thermoelastic distortion has inherent hysteresis and uncertainty, but the characteristic over temperature is enveloped by a few simple 1-D equations. While the commanded motion has been demonstrated by test to be repeatable to better than the 6% requirement over the entire range of motion, the mechanism might not have a linear relationship between step size and angular motion. To achieve the thermoelastic distortion stability and the commanded motion performance required, understanding sub-micron motion is required, which drives the test setup requirements. While having limited resources (personnel, schedule, money), two high-performance space mechanisms can be delivered in a short period (roughly two years).

Key Future Work

- After the mechanism life cycle test program is complete, the mechanism will be disassembled. Of particular interest, the gapping/sliding surfaces will be inspected for unacceptable damage or wear.
- Commanded motion performance tests will measure isothermal mechanism motion for each flight AM, using an identical test setup discussed for thermoelastic distortion testing.

Acknowledgements:

Mike Johnson, Don Sevilla, Kim Aaron, Gary Wang, Andy Kissil, and Kerry Klein for being a constant source of independent and constructive feedback from the concept design through flight hardware testing. The entire mechanism team: Brandon Metz (Electronics), ATA structural analysis support, Eddie Ketsiri (Drawing), Robert Demerjian (Manufacturing), Don Lewis (Materials). Last but not least, PMIC staff for working long shifts through the holidays! The research was carried out at the Jet Propulsion Laboratory, California Institute of Technology, under a contract with the National Aeronautics and Space Administration

References

1. MIL-HDBK-5J-1. (2003). *Metallic Materials and Elements for Aerospace Vehicle Structures*. Department of Defense.
2. Touloukian, Y., Kirby, R., Taylor, R., & Desai, P. (1975). *Thermal Expansion: Metallic Elements and Alloys (Volume 12)*. New York: Purdue Research Foundation.
3. Walter D. Pilkey, D. F. (2008). *Peterson's Stress Concentration Factors*. John Wiley & Sons.
4. Witold M. Sokolowski, S. F. (1993). Dimensional Stability of High-Purity Invar 36. *International Symposium on Optics, Imaging, and Instrumentation*. San Diego.

Environmental Chamber Testing of a Rock Sampling Drill for Venus Exploration

Fredrik Rehnmark*, Evan Cloninger*, Cody Hyman*, Jameil Bailey*, Nick Traeden*, Kris Zacny*, Kristopher Kriechbaum**, Joseph Melko**, Brian Wilcox**, Jeffery Hall** and Kristopher Sherrill**

Abstract

Honeybee Robotics has developed a rotary-percussive rock sampling drill and high temperature (HT) electromagnetic actuator for a proposed mission to Venus known as VISAGE (Venus In Situ Atmospheric and Geochemical Explorer). The drill is powered by two brushless DC motors that have been characterized in dynamometer tests run at both room temperature and Venus surface temperature of ~462°C. Dynamometer test results are compared with performance estimates obtained using ANSYS Maxwell analysis software, demonstrating that losses at high temperature can be predicted with reasonable accuracy. Drilling trials conducted in JPL's Venus Material Test Facility (VMTF) have demonstrated the feasibility of sampling threshold strength Venus analog material within a time window compatible with the proposed VISAGE mission concept of operations.

Introduction

The surface of Venus presents a harsh environment for robotic exploration. Many of the critical subsystems comprising a Venus lander would be housed inside an insulated pressure vessel protecting them from the extremely hot and dense atmosphere (95% CO₂ at 462°C and >90 bar pressure). Under these conditions, conventional thermal management methods can provide only a few hours of mission life before the lander interior overheats. The surface sampling subsystem, on the other hand, must be mounted externally to interact directly with rocks and soil at the landing site. Environmentally "hardened" robotic mechanisms and high temperature (HT) sensors and actuators are needed to deploy to the ground, drill into rock and transport samples into the lander.

A logical first step in designing a mechanism for an extreme and unfamiliar environment like Venus is to build and test a high-fidelity prototype. In order to survive Venus conditions and yield useful performance data in a realistic test, albeit a very short one, the prototype should be built using high TRL (i.e., flight-like) materials, components and fabrication techniques. Per the proposed VISAGE (Venus In Situ Atmospheric and Geochemical Explorer) mission concept, the rock sampling drill breaks up surface rock into fine powder that can be pneumatically transported via an airlock into the cool interior of a lander, where science instruments can analyze the sample to determine elemental composition and other properties. Due to the short mission life, the drill should nominally penetrate to a 5-cm depth in threshold strength Venus analog material (Saddleback Basalt ~130 MPa) in 10 minutes. This desired penetration rate drives the drilling power which, in turn, drives the actuator sizing.

Honeybee Robotics has developed a rotary-percussive rock sampling drill and high temperature (HT) electromagnetic actuator (motor, sensor and gearbox) for Venus [1]. The motors have been characterized in dynamometer tests and simulations to study the effects of the high temperature environment. Drilling trials have been conducted in a CO₂ gas atmosphere at full Venus temperature and pressure (VTP) in JPL's Venus Materials Test Facility (VMTF). These tests have demonstrated the feasibility of collecting surface samples in threshold strength Venus analog material within the time window allocated for sampling. The paper will present a comparison of predicted and measured motor performance at room temperature and

* Honeybee Robotics, Pasadena, CA

** Jet Propulsion Laboratory, California Institute of Technology, Pasadena, CA

Venus temperature and the resulting drill performance in each case. The work described herein represents the first pass through the design-build-test cycle that would eventually culminate in a flight drill.

Honeybee's HT Motor and Sensor Technology

Electric motors offer many advantages for actuation of robotic systems deployed to Solar System destinations. They are versatile, simple to control and a variety of materials are available to suit different environments. With support from NASA's SBIR program beginning in 2005, Honeybee Robotics has built and tested a number of different HT sensor and actuator technologies including a Switched Reluctance Motor (SRM), a Brushless DC (BLDC) motor, a resolver, and a variable reluctance commutation sensor known as PIPS (Pulse Injection Position Sensor) [2]. Based on this work, the BLDC motor was selected for further development because it can produce more torque than the SRM, although the BLDC motor operating temperature is limited by the Permanent Magnets (PMs) installed in the rotor. The PIPS sensor was selected instead of the resolver to provide rotor position feedback for commutation and speed control due to ease of fabrication, although the resolver can provide better resolution than PIPS.

Under a recent two-year SBIR project ending in 2017, Honeybee designed and built a new HT actuator consisting of a BLDC motor, PIPS sensor and custom planetary gearbox to power a prototype rock sampling drill for Venus. This actuator, shown in Figure 1, has been successfully dynamometer tested at both room temperature and Venus temperature in a 1-atmosphere oven [3][4]. Remote PIPS interface electronics located outside the oven provide Hall sensor signals compatible with commercial servo motor controllers.

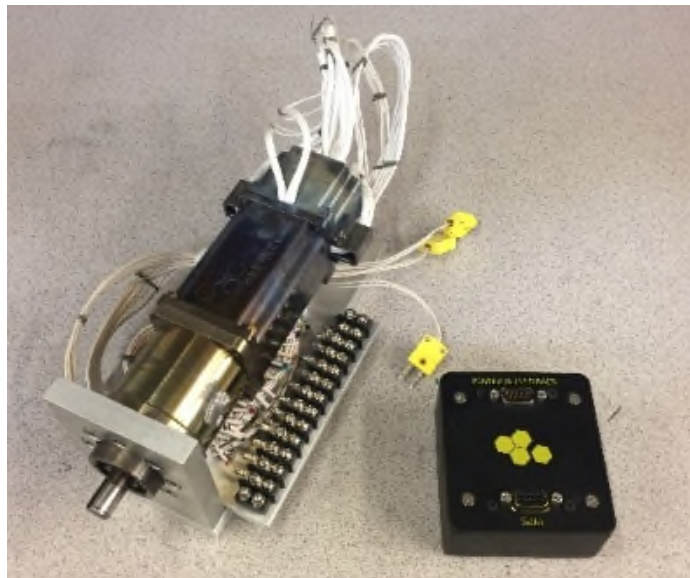


Figure 1. Honeybee HT actuator with remote (i.e., room temperature) interface electronics

In the following sections the measured motor performance will be compared with theory and estimates obtained using ANSYS Maxwell analysis software, demonstrating that losses at high temperature can be predicted with reasonable accuracy.

Temperature Effects on Electric Motor Performance

Actuator sizing for operation in high-temperature environments must account not only for variability in the driven load but also for reduced torque and efficiency available from the motor. The reduced performance at elevated temperature is due to two important temperature dependencies that must be accounted for when designing for operation across a wide temperature range. The first is the increase in electrical resistance R of the motor coils at elevated temperature, which both increases i^2R losses (self-heating) in

the motor and decreases the theoretical stall current (and, therefore, stall torque) of the motor for a given supply voltage. It can be calculated using the temperature coefficient of the magnet wire α_R . The second is the decrease in magnetic flux density B_g in the air gap between the rotor and stator, which can be calculated using the Reversible Temperature Coefficient (RTC) of the PMs. This decreases the motor torque constant K_t , which, in turn, reduces the stall torque even further. The motor speed constant K_e is decreased by the same amount, thereby increasing the no-load speed. The overall effect is a reduction in motor maximum power output.

The equations used to calculate theoretical motor stall torque and maximum power output and their dependency on temperature are collected here [5][6]:

$$\text{Stall Torque} = \tau_{st} = K_t I_{st} \quad (1)$$

$$\text{Max Power} = P_{max} = \frac{\omega_{nl}\tau_{st}}{4} = \frac{V_s I_{st}}{4} = \frac{V_s^2}{4R} \quad (2)$$

$$K_t = 2NB_g L_{st} R_{ro} \quad (N, L_{st}, R_{ro} \text{ fixed by motor geometry}^1 \rightarrow K_t \propto B_g) \quad (3)$$

$$I_{st} = \frac{V_s}{R} \quad (4)$$

$$R = R_{ref} [1 + \alpha_R (T - T_{ref})] \quad (5)$$

$$B_g = B_{g,ref} [1 + RTC (T - T_{ref})] \quad (6)$$

For the temperature range of interest (i.e., room temperature to 500°C), the temperature coefficients for the Ni-plated Cu magnet wire and Sm₂Co₁₇ PMs used in the Honeybee motor are, respectively:

$$\alpha_R = .0038/\text{°C}$$

$$RTC = -.060\%/\text{°C}$$

Competing motor designs may be compared on the basis of how efficiently they produce torque. For a given design, this performance characteristic can be quantified by calculating the motor constant K_m , defined in Eq. 7.

$$K_m = \frac{T}{\sqrt{I^2 R}} = \frac{K_t}{\sqrt{R}} \text{ in units of } \left[\frac{\text{Nm}}{\sqrt{\text{W}}} \right] \quad (7)$$

In Eq. 7, T is the torque output of the motor when supplied with current I and R is the resistance of the motor windings. In general, motors with a higher K_m can produce more torque and they can operate for longer periods of time before overheating. Larger motors have a clear advantage in this regard. A given motor's K_m will be reduced at high temperature, however. Table 1 presents a comparison between theoretical performance of Honeybee's HT motor at room temperature and high temperature. The calculations predict a reduction of 72% in stall torque and a reduction of 62% in maximum power output at high temperature. Actual test results will vary due to the simplifying assumptions made in these calculations.

¹ N = number of turns of wire in motor coil, L_{st} = axial length of motor, R_{ro} = air gap radius

Table 1. Comparison of theoretical motor performance at RT and Venus temperature

Parameter	Symbol	Room Temp. 20 °C	High Temp. 482 °C	Units	Ratio HT/RT
Supply Voltage	V_s	48	48	V	
Coil Resistance	R	1.05	2.74	ohms	2.61
Stall Current	I_{st}	46	18	A	0.38
Torque Constant	K_t	0.115	0.083	Nm/A	0.72
Speed Constant	K_e	12.04	8.70	V/krpm	0.72
Stall Torque	T_{st}	5.26	1.46	Nm	0.28
Max Power	P_{max}	549	210	W	0.38
Motor Constant	K_m	0.112	0.050	NmW ^{-0.5}	0.45

Motor Model Validation and Simulation Results

Like ordinary electric motors, custom HT BLDC motors can be designed to meet mission requirements using conventional modeling and simulation tools. If the temperature dependency of winding resistance and magnetic flux density are known, motor performance at any temperature can readily be simulated. Other temperature-dependent properties, such as magnetic permeability of the magnet steel used in the rotor and stator, can be modelled as well if data are available. Prior to detailed modeling, rough estimates of motor torque and efficiency can be obtained from simplified scaling calculations.

A 2-dimensional finite-element model of Honeybee's HT motor was built using ANSYS Maxwell (Figure 2). The motor is a 3-phase brushless DC motor with 6 slots and 4 poles. The PMs are housed in the rotor and the coils are mounted on the stator.

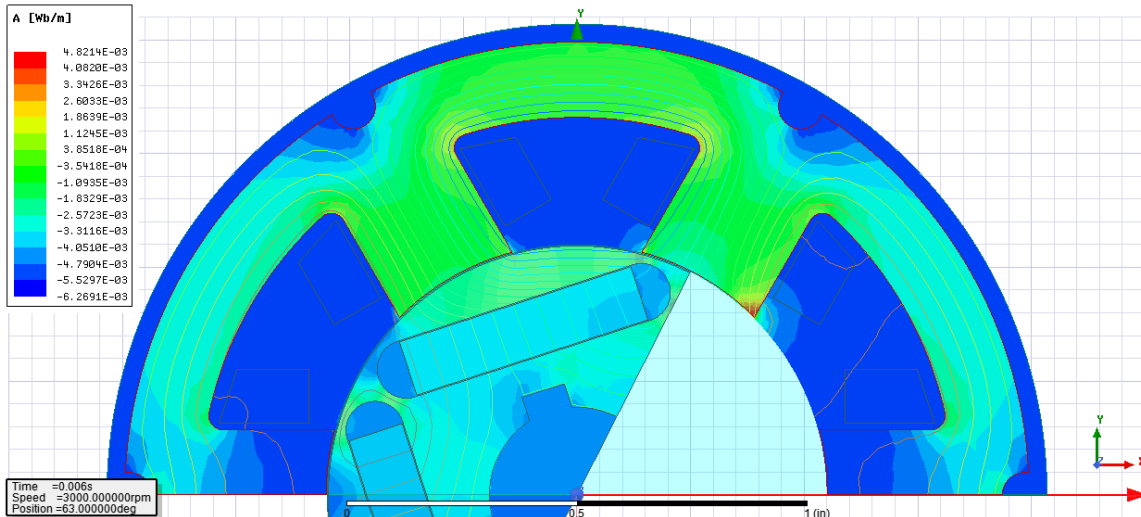


Figure 2. Finite-element model of Honeybee's HT motor

Motor Back-EMF (Test vs. Simulation)

To check the accuracy of the model, the simulated back-EMF waveforms of the unloaded motor were compared with actual motor data captured at RT and 500°C at two different speeds. The back-emf measurement is passive and the test equipment does not introduce any significant additional losses or dynamics, making it especially useful in validating the motor model. To collect the waveforms, the HT motor was placed in a 1-atmosphere oven and all three motor phases were connected to an oscilloscope. A second conventional brushed DC motor was then used to rotate the motor armature at the desired speed

by means of a feed-through in the oven door. The results indicate excellent agreement between the model and the test data at both operating temperatures, as shown in Table 2. The measured and simulated waveform plots at 3000 rpm are included in the Appendix.

Table 2. Unloaded motor back-EMF Vrms per phase at RT and 500°C (measured and simulated)

Motor Shaft Speed	Test			Simulation		
	RT (20C)	HT (500C)	HT/RT	RT (25C)	HT (500C)	HT/RT
1500 rpm	5.34 Vrms	3.65 Vrms	0.68	5.28 Vrms	3.35 Vrms	0.63
3000 rpm	10.68 Vrms	7.26 Vrms	0.68	10.6 Vrms	6.74 Vrms	0.64
Calculated Motor Phase Back-EMF Constant						
K _e per phase	3.56 V/krpm	2.41 V/krpm	0.68	3.53 V/krpm	2.25 V/krpm	0.64

Motor Performance Under Load (Test vs. Simulation)

The motor model was further validated by comparing simulated performance under load against actual dynamometer test results at RT and 482°C. These simulations, however, require modelling of additional components, including the commutation feedback sensor, motor controller and power supply, to generate the motor excitation signal (see schematic in Figure 3). Because they are idealized representations, these models introduce error and uncertainty that should be considered when evaluating simulation results. For example, an ideal DC power supply can generate a steady output at 100% of the nominal voltage, regardless of the current demand. However, the ideal model overlooks potentially significant inefficiencies that could impact motor performance in a control system, resulting in a simulation that may overpredict motor performance. If possible, these inefficiencies should be measured and included in the model to improve its fidelity. Clearly, validating the standalone motor model using back-emf measurements helps build confidence in the integrated control system model, as well.

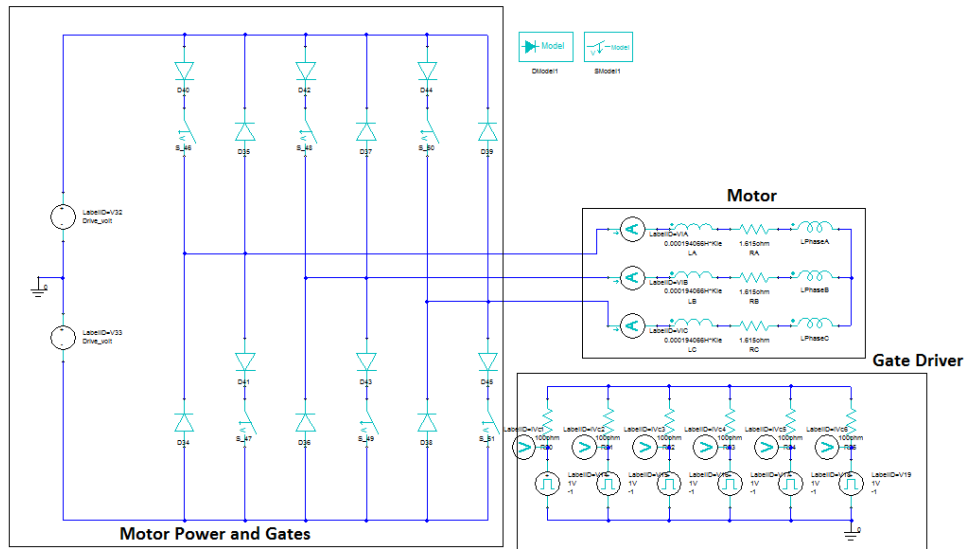


Figure 3. Schematic of modelled components required to generate motor excitation signal

The plots shown in Figure 4 through Figure 7 demonstrate excellent agreement between simulated and measured performance at RT (where confidence in material properties is high) and reasonable agreement at 482°C (where material properties are extrapolated).

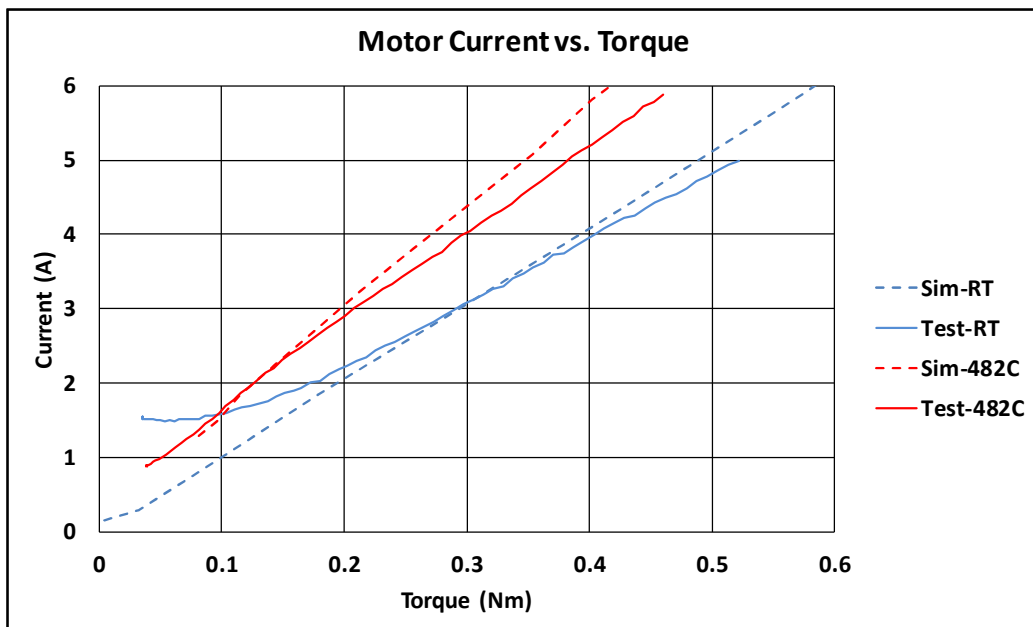


Figure 4. Motor current vs. torque plots at RT & 482°C (measured and simulated)

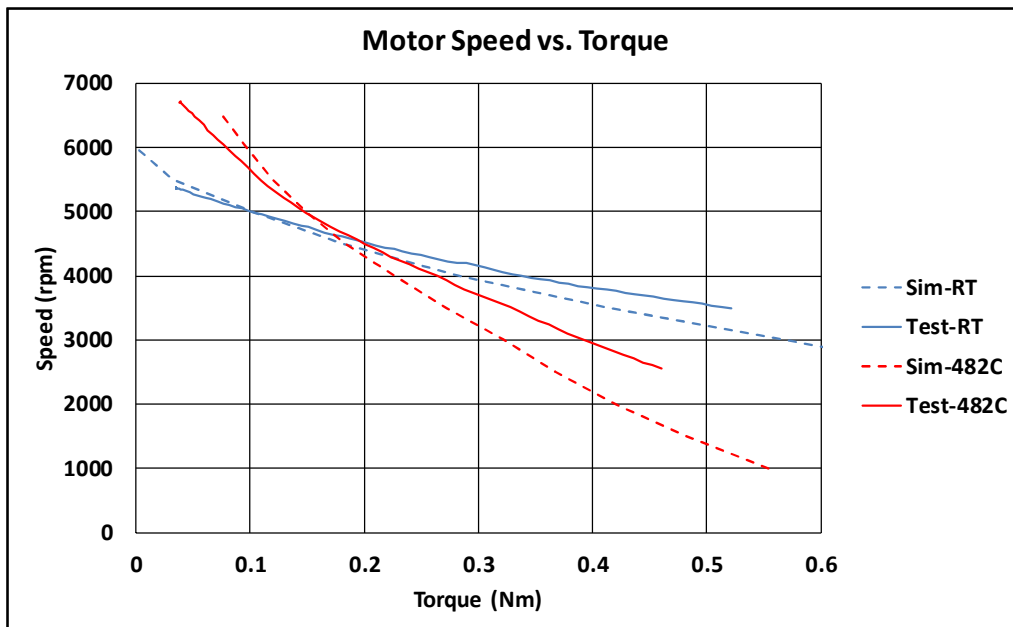


Figure 5. Motor speed vs. torque plots at RT & 482°C (measured and simulated)

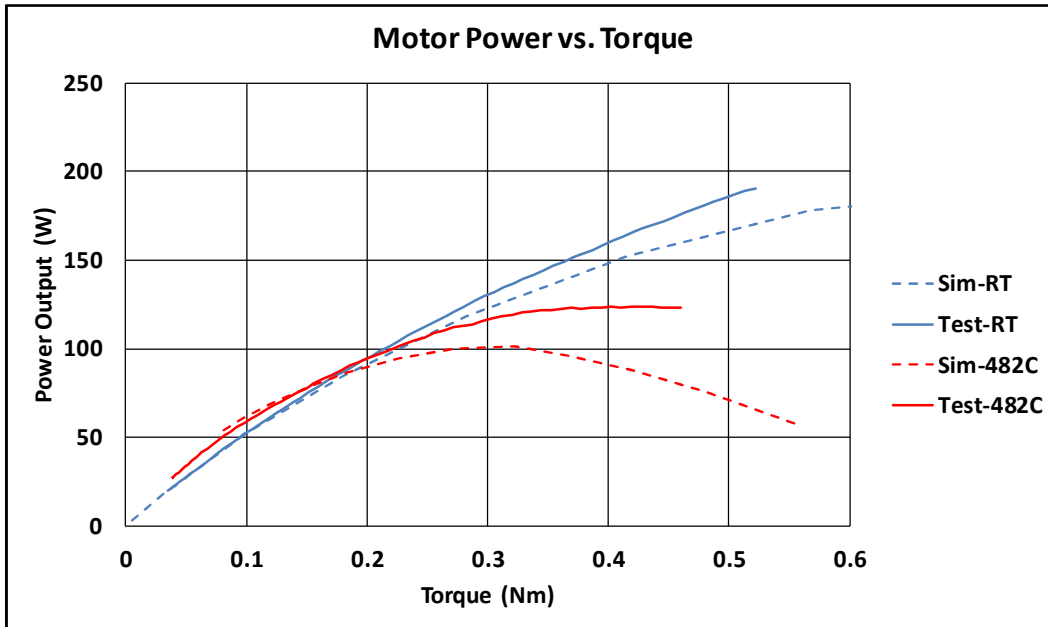


Figure 6. Motor power output vs. torque plots at RT & 482°C (measured and simulated)

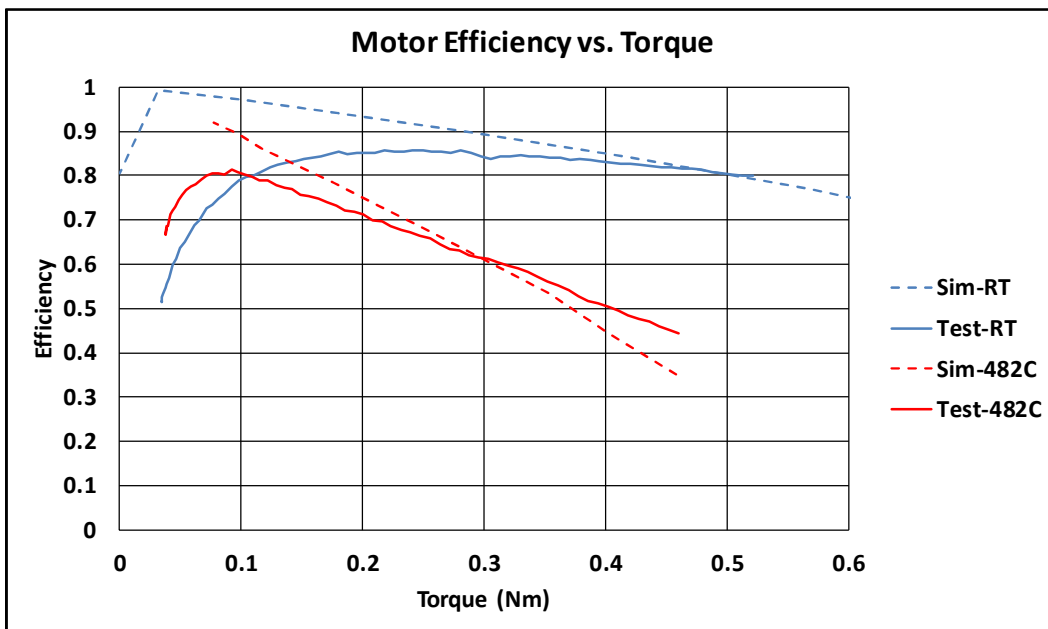


Figure 7. Motor efficiency vs. torque plots at RT & 482°C (measured and simulated)

Table 3 compares the measured and simulated motor torque constant K_t calculated at RT and HT (482°C for the test and 500°C for the simulation). The ratio of K_t at HT to RT matches the theoretical result in Table 1 almost exactly.

Table 3. Motor torque constant K_t at RT and HT (measured and simulated)

Test			Simulation		
RT (20C)	HT (482C)	HT/RT	RT (25C)	HT (500C)	HT/RT
0.12 Nm/A	0.08 Nm/A	0.73	0.10 Nm/A	0.07 Nm/A	0.73

These comparisons validate the HT motor model and support the use of a similar model to aid in the design of the flight motor for the Venus drill. The effects of high temperature on motor performance can be estimated with reasonable confidence and, therefore, the motor design can be optimized for power output vs. mass and volume.

The Venus Drill

Drilling Power

Drilling tools have been successfully deployed on the Moon, Mars and Venus to sample surface rock. In these applications, drill rate of penetration (ROP) depends on several variables including the strength of the rock (Unconfined Compressive Strength or UCS, expressed in MPa), weight on bit, drilling power, and whether percussion is used or not [7]. For a given rock type, specific energy (SE) can be defined as the amount of energy required to break up a unit volume of rock into fine particles that can be transported out of the borehole. Since the efficiencies of different drilling heads, bits and feed mechanisms can vary widely, specific energy (expressed in Whr/cc or J/mm³) provides a convenient measure to compare the performance of different drilling systems.

Applied to a single drilling system, specific energy can be used to compare performance at different environmental conditions, such as temperature and pressure. It can be calculated from the results of a drilling trial by measuring the average rate of penetration (v_{ROP}) achieved when drilling with a bit of diameter d_b while controlling drilling parameters such that the average drilling power (P_{ave} = motor power output) remains approximately constant.

$$SE = \frac{4P_{ave}}{\pi d_b^2 v_{ROP}} \quad (8)$$

Rearranging the equation slightly, drilling power is seen to be proportional to specific energy, rate of penetration, and the square of the bit diameter.

$$P_{ave} = SE \left(\frac{\pi d_b^2}{4} \right) v_{ROP} \quad (9)$$

Before the actuators for the Venus drill can be properly sized to deliver this power, the specific energy for drilling at Venus conditions must be determined by conducting drilling trials at VTP, underscoring the need for a high-fidelity prototype drill. A discussion of the design and fabrication of the prototype drill can be found in [3] and [8]. The prototype is a HT version of a proven Honeybee design that has previously demonstrated the desired drilling performance [9]. The selected drill design parameters are listed in Table 4.

Table 4. Venus drill design parameters

Bit Diameter	2 cm
Weight on Bit	105 N
Spindle Speed	120 rpm
Spindle Torque	1.1 Nm
Net Spindle Power	13.7 W
Percussive Energy	2.0 J/blow
Percussive Frequency	980 blows/min
Net Percussive Power	33 W
Target Penetration Rate	0.5 cm/min

Test Configuration Used in Drilling Trials

Following performance characterization on the dynamometer, two HT motors were integrated with the prototype drill and a series of drilling trials were conducted at Venus temperature and pressure in JPL's VMTF environmental chamber. The VMTF is a heated-wall pressure chamber with an electrical feedthrough mounted in the lid. The test article is suspended from the lid so that it hangs down inside the chamber when the lid is installed (see Fig. 8). The high temperature environment in the VMTF severely restricts the choice of materials that can be used for both the test article (i.e., the drill) and test instrumentation, in particular materials suitable for electrical insulation and termination. Details of the material selection for the drill and actuators are reported in [8].

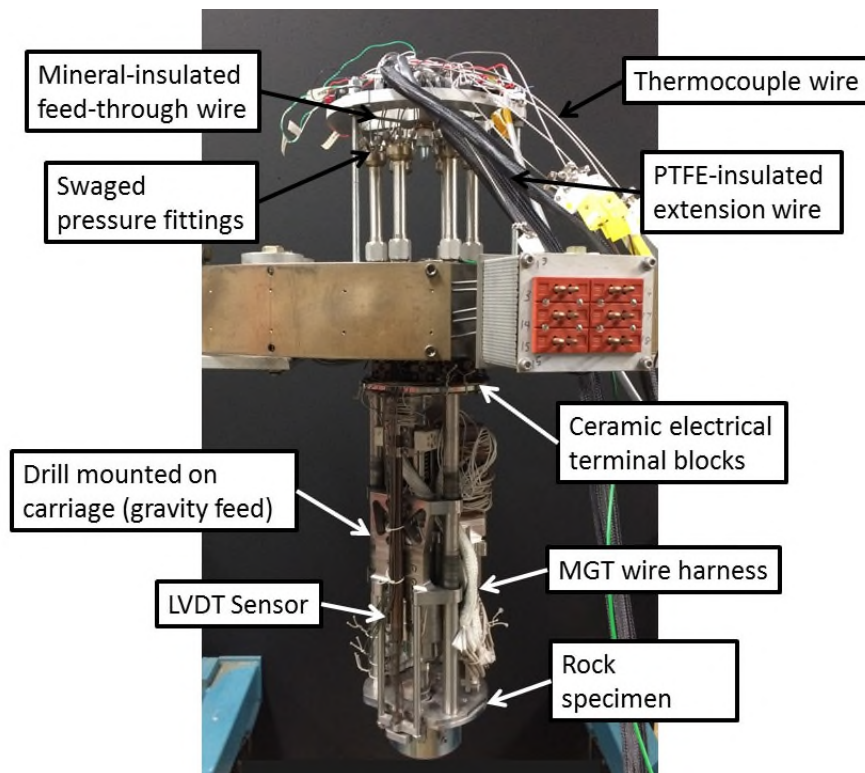


Figure 8. VMTF lid with Venus drill installed

Drilling Test Results

Table 5 shows the average motor torque and speed for each of the two mechanisms comprising the Venus drill under different test conditions. Average torque was calculated by taking the average motor current over the entire drilling time and multiplying by the motor torque constant K_t . Peak torque was measured directly

by driving the percussor cam through the second stage of the spur gear with a torque watch and then dividing the maximum reading by the first stage spur gear ratio.

Table 5. Venus drill motor torque and speed under various test conditions

Drilling Test RT = Room Temp VTP = Venus Temp & Press	Motor	Motor Peak Torque* (Nm)	Motor Current, Ave. (A)	Kt (Nm/A)	Motor Cont. Torque, Ave. (Nm)	Motor Velocity, Ave. (RPM)	Power Output, Ave. (W)
Bench (Flat Basalt, RT Spring)	Auger		1.561	0.115	0.180	2945	55
	Percussor	0.57	2.816	0.115	0.324	3217	109
RT3 (Sloped Basalt, HT Spring)	Auger		1.362	0.115	0.157	2900	48
	Percussor	0.68	3.469	0.115	0.399	3521	147
VTP3 (Flat Basalt, HT Spring)	Auger		1.217	0.084	0.102	2931	31
	Percussor	0.57	3.874	0.084	0.325	2867	98

* estimates based on measurement with a torque watch

Whereas it has been shown that surface sliding friction at the bit to rock interface increases with temperature under both Earth and Mars atmospheric pressures [10], the results of the VMTF drilling trials with the Venus drill (see Table 6) suggest that temperature would not significantly impact specific drilling energy at Venus conditions, at least for rotary-percussive machines. On the other hand, the rate of penetration at high temperature is expected to be slower because the stiffness of the percussive spring (and, therefore, the percussive energy per blow) is reduced. Furthermore, increased electrical (i^2R) losses are expected at high temperature because the resistance of the motor coils is increased. However, it should be noted that specific energy, as defined herein, reflects mechanical performance only and does not include electrical losses. Accordingly, SE is calculated using Total Power Output in Table 6, which is the combined mechanical power output from both motors, rather than Estimated Power Consumption, which applies efficiencies read from dynamometer test results in Figure 7.

Table 6. Specific energy for drilling measured at room temperature and high temperature

Drilling Test RT = Room Temp VTP = Venus Temp & Press	Total Power Output, Ave. (W)	Est. Power Consumption (W)	Drilling Depth (cm)	Drilling Time (sec)	ROP (mm/min)	Specific Energy (Whr/cc)
Bench (Flat Basalt, RT Spring)	164	261	4.81	568	5.08	1.67
RT3 (Sloped Basalt, HT Spring)	195	358	4.19	429	5.86	1.71
VTP3 (Flat Basalt, HT Spring)	129	202	2.36	373	3.79	1.75

Motor Torque Margin and Thermal Considerations

Per spaceflight mechanism design requirements in AIAA S-114-2005 Moving Mechanical Assemblies, the flight drill would need actuators capable of providing at least twice the nominal torque (both peak and continuous) needed to operate the drill in worst-case environmental conditions. This margin allows for modelling uncertainty, such as the detrimental effects of operating in the Venus atmosphere, and unexpected failures that could cause additional drag on the mechanism, such as a seized bearing.

Like conventional DC motors, the continuous output torque of the HT motors is limited by their ability to dissipate waste heat generated in the coils. The motors could be operated intermittently at higher torques if they were periodically turned off and allowed to cool down but such operational constraints would not be compatible with the unusually short life (only a few hours!) of a Venus surface mission. The motor peak torque, on the other hand, may be limited by either the demagnetization potential of the PMs, which can be determined from the characteristic B-H curve of the magnetic material, or the magnetic permeability of the magnet steel used in the motor stator and rotor. The continuous and peak current capacity of the motor controller and power supply should not be overlooked, either, though they are remotely located and not affected by the test chamber environment.

Since the $\text{Sm}_2\text{Co}_{17}$ PMs mounted in the rotor should be kept below a temperature of 525°C to minimize the risk of demagnetization, the allowable temperature rise over the 10-minute drilling duration specified in the proposed VISAGE mission timeline is 63°C (starting at an ambient temperature of 462°C). The difference between the continuous average torque needed to drill to the target depth of 5 cm in 10 minutes and the controlled constant torque load at which the motors reach their maximum allowable operating temperature in the same period of time is the motor continuous torque margin. This margin can be accurately determined using a dynamometer.

Figure 9 presents drill depth and motor thermocouple data from a successful drilling trial performed at VTP. In this test, the drill reached a depth of 5 cm in 13.5 minutes and the drill motors reached steady-state temperature with a 25°C temperature margin left on the percussor motor. If thermal constraints were removed, however, a quick inspection of the high temperature torque vs. speed curve in Fig. 5 shows an available torque of 0.4 Nm at 3000 rpm, or a margin of 23% over the average torque required to drive the percussor from Table 5.

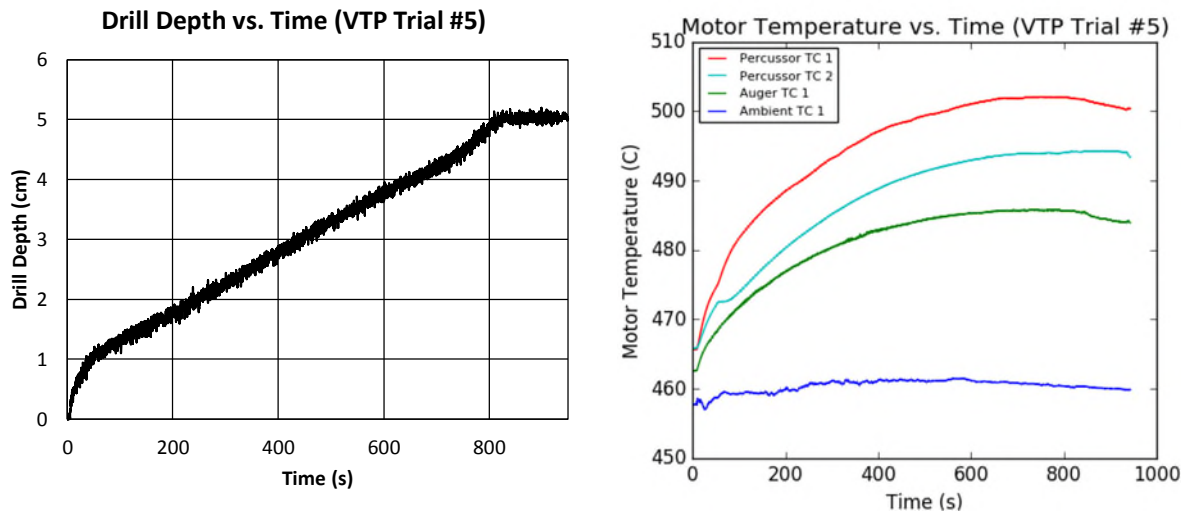


Figure 9. Drill depth and motor thermocouple data from a drilling test performed at full Venus conditions

These results highlight the need for better thermal modelling of the motor, since the thermal coupling between the stator, where the heat is generated in the coils, and the rotor, where the temperature-sensitive PMs are mounted, has not been characterized. If it can be demonstrated that the rotor stays significantly cooler than the stator while the motor is operating, the maximum allowable operating temperature of the motor could be increased. In addition, passive heat sinks (e.g., fins, etc.) could be added to the motor housing to improve heat dissipation to the ambient environment. After these thermal effects have been accounted for and the motor torque margins have been accurately measured, the flight drill motors can be correctly sized to achieve the desired drilling performance.

Summary

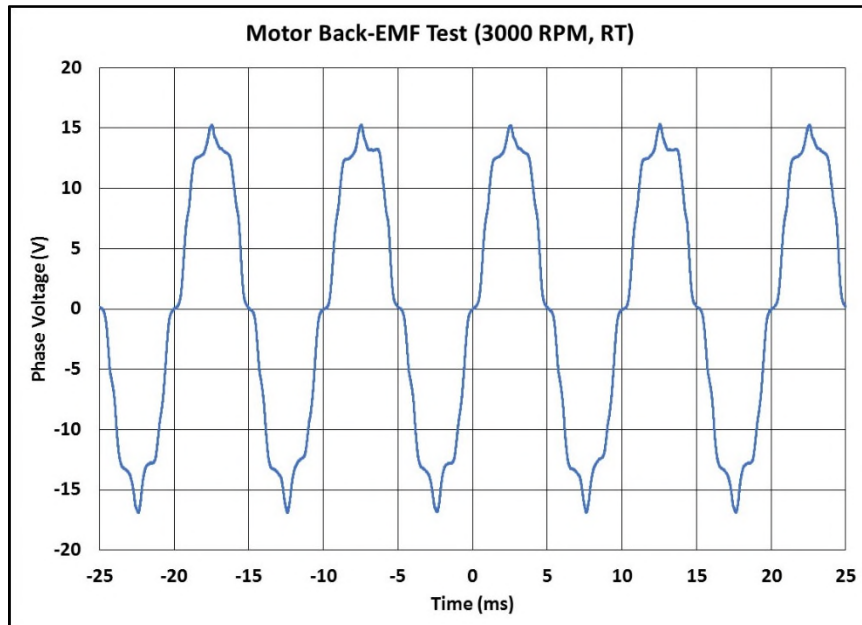
The HT motor model has been validated with test data, confirming that conventional methods can be used to size these motors and account for losses at high temperature. The VMTF drilling trials have confirmed the feasibility of drilling into rock at Venus temperature and pressure to generate fines suitable for pneumatic transport per the proposed VISAGE mission concept of operations. They have also produced drilling performance and average power consumption benchmarks useful for mission resource planning. The motor torque margins are limited by the maximum operating temperature of the PMs. However, these margins can be improved by accurate thermal modelling of the motor and the addition of passive heat sinks.

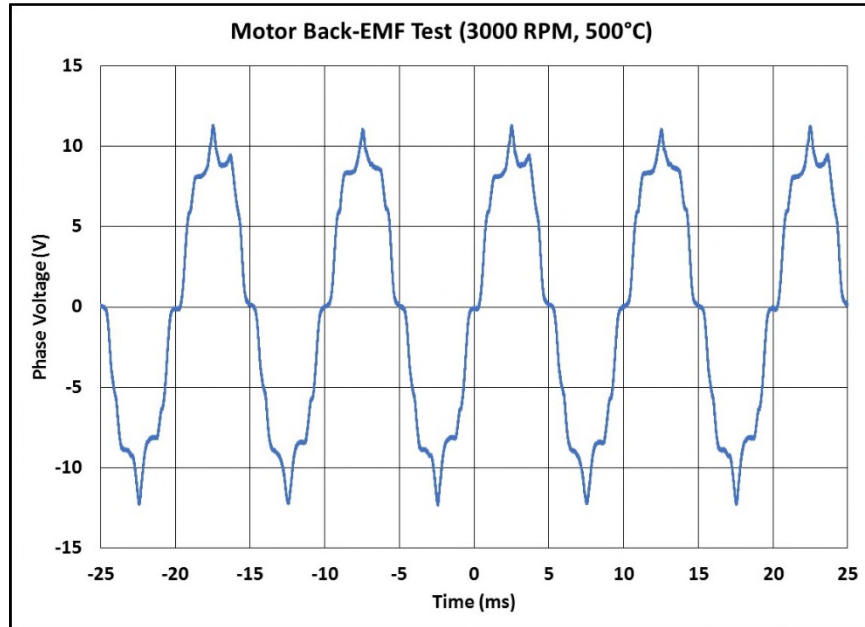
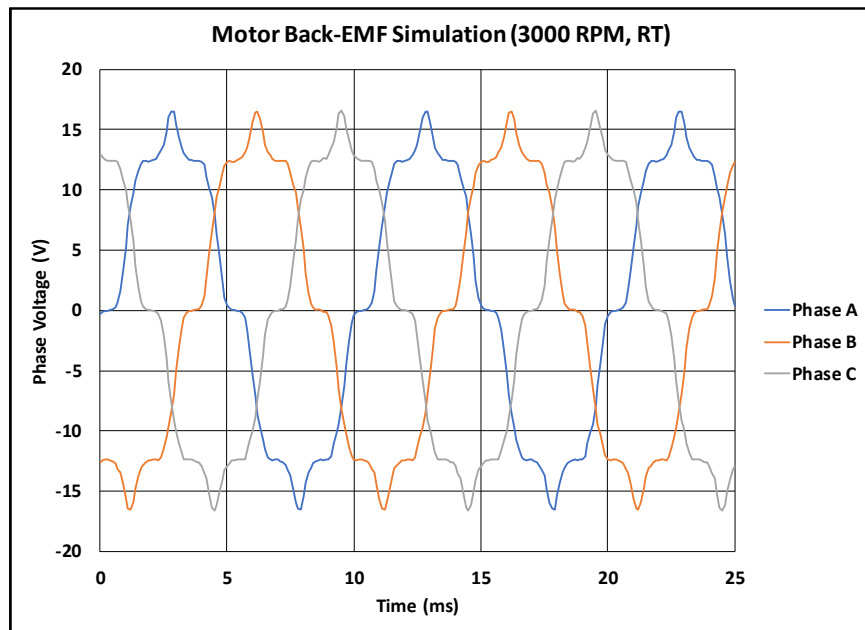
Acknowledgements

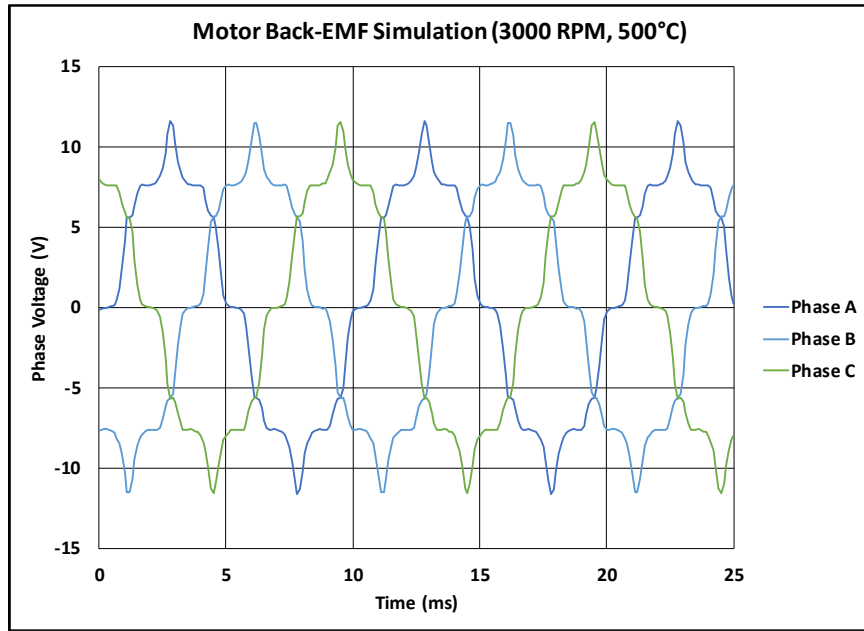
This work was funded by NASA's HOT (High Operating Temperature) Technology Program. We owe our sincere thanks and appreciation to Program Officer Dr. Quang-Viet Nguyen and Technology Coordinator Dr. Gary Hunter. Part of this research was carried out at the Jet Propulsion Laboratory, California Institute of Technology, under a contract with the National Aeronautics and Space Administration.

Appendix

Measured and simulated back-EMF waveform plots at 3000 rpm and two different operating temperatures are included here for reference.







References

1. Rehnmark, F. et al. (2017). VISAGE Rock Sampling Drill, Venus Modeling Workshop, May 2017, Cleveland, Ohio.
2. Kumar, N. (2014). High-Temperature Motors. In High Temperature Materials and Mechanisms (Ed. Y. Bar-Cohen), CRC Press, Boca Raton, Florida, 281-295.
3. Zacny, K. et al. (2017). Development of Venus Drill, Proc. of IEEE Aerospace Conf., Big Sky, Montana.
4. Rehnmark, F. et al. (2017). Performance Characterization of HT Actuator for Venus. VEXAG 2017, Laurel, Maryland.
5. Montone, D. Temperature Effects on DC Motor Performance, downloaded from <http://www.pittman-motors.com/Resources.aspx>
6. Hanselman, D. (2006) Brushless Permanent Magnet Design, Magna Physics Publishing, 206-209.
7. Paulsen, G. et al. (2010). Rotary-Percussive Deep Drill for Planetary Applications, Proc. of ASCE Earth and Space 2010, Honolulu, Hawaii.
8. Rehnmark, F. et al. (2017). High Temperature Electromagnetic Actuator and Sampling Drill for Venus Exploration, Proc. of ESMATS 2017, Hatfield, UK.
9. Zacny, K. et al. (2013). Reaching 1 m Deep on Mars: The Icebreaker Drill. Astrobiology 13(12), 1166-1198.
10. Zacny, K. A., and G. A. Cooper (2007). Friction of drill bits under Martian pressure, J. Geophys. Res., 112, E03003, doi:10.1029/2005JE002538.

A Discussion of Friction Anomaly Signatures in Response to Electrical Discharge in Ball Bearings

William Bialke *

Abstract

Friction anomalies and failures in spaceflight ball bearings have commonly been attributed to lubricant dynamics, but can also be a result of electrical discharge. Plausible scenarios of the root cause of various bearing friction signatures in response to microscopic changes in bearing surface finishes resulting from electrical discharge are discussed, along with supporting anecdotes, test results and observations in the laboratory and in space. The objective of the discussion is to inform and possibly shed a new light on previously unexplained or unverified bearing anomalies and failures.

Introduction

Electrical Discharge in bearings is a well established source of bearing degradation and failures in terrestrial applications as discussed in Reference 1, resulting in the growing practice of grounding shafts or using ceramic balls in many industrial motors. Only recently has electrical discharge been associated with spaceflight bearing anomalies and failures as discussed in Reference 2, which concluded that there is a remarkable correlation between on-orbit Reaction Wheel Assembly (RWA) bearing friction events and large geomagnetic storms, strongly supporting electrical discharge as a likely root cause.

Conventional lore has frequently resulted in assigning blame for friction anomalies to the Goldilocks syndrome: either too much lubricant or lubricant starvation. We examine the possible connection of a variety of sources of electrical discharge with examples of ball bearing friction signatures specifically observed in RWAs. Mysterious friction anomalies discussed herein occurred frequently over a lifetime of trending on-orbit reaction wheel friction and testing hundreds of reaction wheels. The signatures made the most logical sense to the author when electrical discharge was recently considered as a variable.

The scope of this paper is not to present scientifically proven models or conclusions, but only to open the discussion of anomalous friction signatures to include the effects of electrical discharge and introduce this possible root cause into the paradigms of aerospace mechanism bearings and tribology.

Background

RWA bearing friction anomalies and failures have plagued many missions since the dawn of the space age. The ITHACO RWA product line, purchased by United Technologies Corporation as part of the acquisition of Goodrich in 2012, had failures on a number of spacecraft over the years, starting with two RWAs on the Far Ultraviolet Spectroscopic Explorer (FUSE) Spacecraft in November of 2001, and eventually the failure of all four of the RWAs on that spacecraft. A series of failure investigations performed for over a decade ultimately failed to successfully determine root cause of the bearing failures. United Technologies, after their acquisition of Goodrich Corporation, which included the ITHACO RWA product line, embarked on a Relentless Root Cause Analysis (RRCA) to resolve the RWA failures and anomalies. A rigorous test program accompanied detailed modeling and analysis of every aspect of the RWA design. A very large number of initially credible items were positively eliminated from the fault tree by test, inspection or analysis, including many previously eliminated items, which were revisited and exonerated with fresh objective evidence.

* Reaction Wheel Consultant, Lochridge Farm LLC, Trumansburg, NY

Ten dedicated RWAs were built and utilized in over 75 controlled tests. The key scenarios investigated were bearing alignment, preload, contamination, and anomalous raceway wear observed during the bearing run-in process. These initially credible scenarios were completely eliminated by the results of the testing, with the exception of bearing wear observed during the run-in process. This initiated a series of controlled tests to determine the variables that could affect the anomalous wear. Test bearings were lubricated with a controlled amount of free oil supplemented by a charge of grease. With the standard lubrication process, the bearing inner race wear depth was consistently 0.3 to 0.4 microns, regardless of how the grease was initially distributed. When identical tests were run with only oil, the bearings showed an increase in wear depth when marginally lubricated with oil and when completely flooded with oil. These contradicting results led to a conclusion that the rheological lubricant properties were not affecting the wear, since the oil is significantly more mobile than any oil/grease mixture and should tend to reduce any lubricant starvation effects. This quandary led to brainstorming which resulted in the introduction of electrical discharge as a new branch of the fault tree.

The next significant breakthrough of the RRCA was when a strong correlation was made between RWA bearing failures/anomalies and space weather, specifically coronal mass ejections from the Sun and the resulting geomagnetic storms. In addition, there were a number of failures or anomalies on different spacecraft, which occurred during the same geomagnetic storm. While the correlation is strong on all reviewed failures and anomalies, the statistical arguments herein only take into account the failures and anomalies on the FUSE spacecraft, since the author is not at liberty to discuss much of the data that exists.

Failures of all four of the RWAs on FUSE were preceded by dry friction anomalies, which recovered to normal levels after operating at high speed (2000 rpm or more) for a period of days or hours. The date of the initiation of the friction increase was derived from the trending data. A list of the prominent FUSE anomalies and failures is presented in Table 1, with the magnitude and date of the friction increase, and the ranking of any geomagnetic storm within the 3 days leading up to the observed friction increase. The torque authority of the motor in the FUSE RWAs was 40 mN-m. Any friction increase beyond that value is deemed a failed RWA.

The failure of FUSE RW-X on November 25, 2001 occurred on the same day that a dry friction increase was observed on RW-Y, which remained in the elevated friction state until it failed 15 days later. These simultaneous friction increases on two RWAs occurred during the 20th largest geomagnetic storm since 1994. Of the 12 prominent friction events observed, 4 occurred shortly after or during geomagnetic storms ranked in the top 20 of severity since 1994. The rarity of these events results in a Probability of Correlation of 99.9998% as computed in Reference 2, or nearly a 1 in a million chance of occurring randomly.

*Table 1.
FUSE Friction Increase Dates*

Friction Increase	Friction Initiation Date	Geomagnetic Storm Ranking since 1994
RW-X		
5 mN-m	13 Feb 2001	Not ranked
700 mN-m	25 Nov 2001	20th
RW-Y		
3 mN-m	15 July 2000	5th
2 mN-m	27 July 2000	Not ranked
5 mN-m	3 July 2000	Not ranked
4 mN-m	5 Oct 2000	16th
1.2 mN-m	25 Nov 2001	20th
1400 mN-m	10 Dec 2001	Fail after operating at low speed for 15 days in elevated friction state.
RW-Z		
5 mN-m	12 Sept 2002	Not ranked
>40 mN-m	Dec 2004	N/A
RW Skew		
7 mN-m	30 April 2007	Not ranked
>40 mN-m	12 July 2007	Not ranked

Testing in the lab successfully duplicated the changes in friction signatures observed on orbit by simply applying a modest voltage across RWA bearings, supporting the theory that bearing friction can be increased by electrical discharge across the bearing. This unexpected result led to a retrospective review of other unexplained RWA friction anomalies, which are included in this discussion.

Scenario for Electrical Discharge Induced Bearing Failures

Figure 1 shows the sequence of events in which electrical discharge can lead to a bearing failure. This figure is meant to provide the reader an overview of the entire process. Each of the elements of the figure will be explained in greater detail throughout the paper.

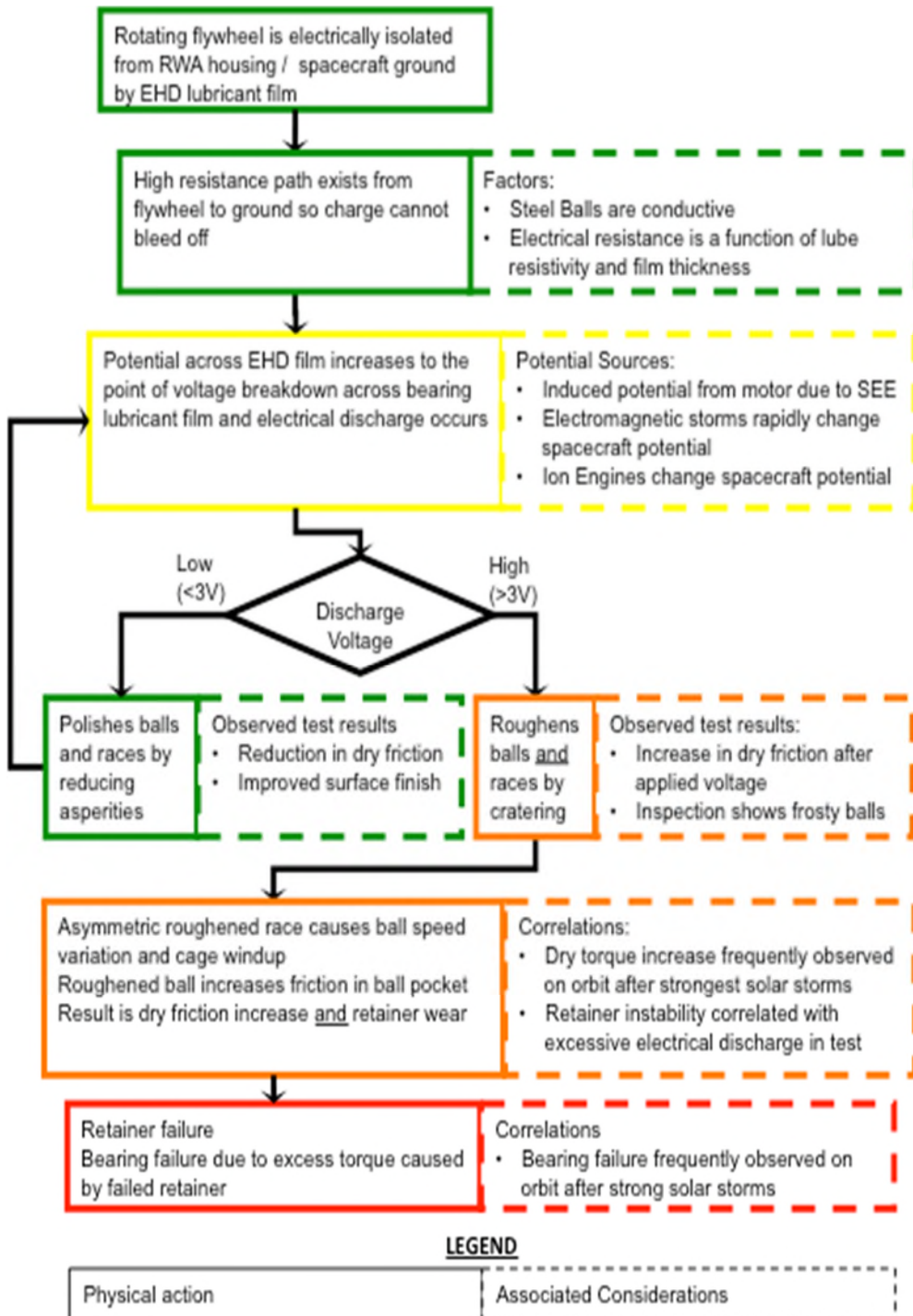


Figure 1. Scenario for bearing failure due to electrical discharge

Electrical Discharge Mechanism

The problem starts with increasing surface roughness of the balls and races. The mechanism for increasing surface roughness of the ball and races in a bearing is due to electrical discharge across the ball to race interface. Friction increase has been observed in bearings at potentials as low as 6 V as discussed in Reference 2. Increased coefficient of friction is the key ingredient necessary for the discussion of anomalous friction signatures and plausible causes. The most significant variables with electrical discharge in bearings are the Elasto-Hydro-Dynamic (EHD) film thickness (electrode gap), the lubricant electrical properties (resistance and breakdown voltage), and the characteristics of the differential voltage across the bearing, as depicted in Figure 2.

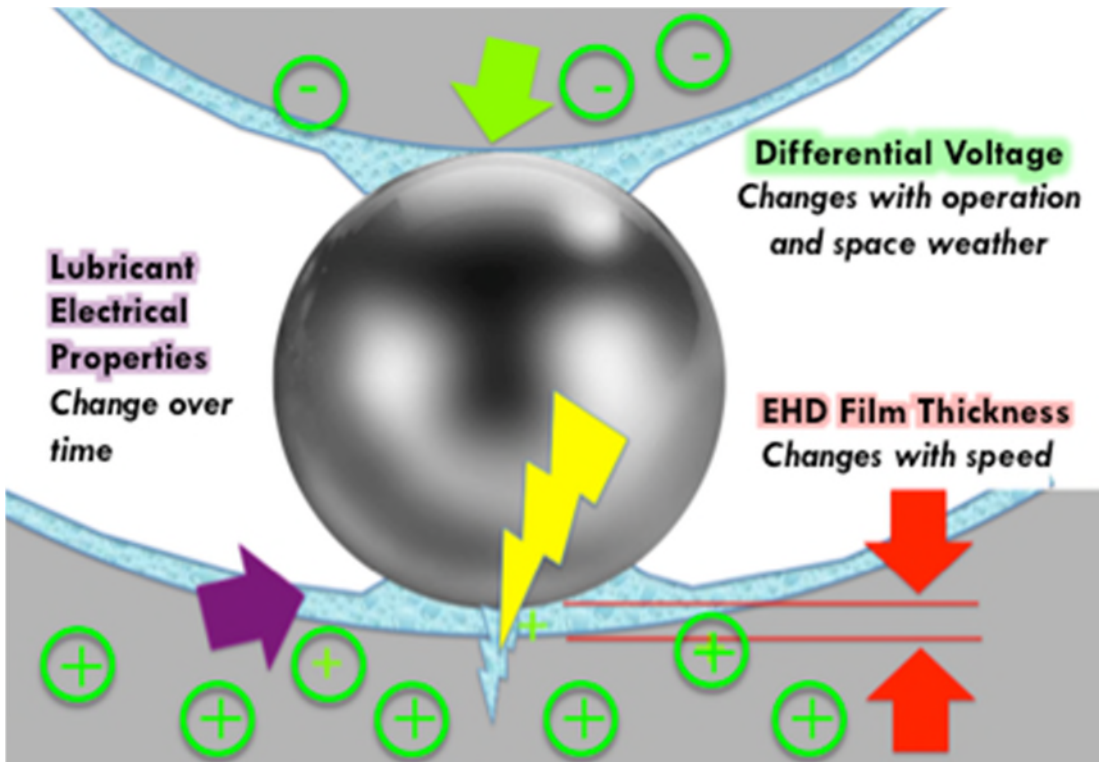


Figure 2. Electrical Discharge variables in an oil lubricated ball bearing

These variables are constantly changing. The EHD film thickness is highly dependent on the bearing rotation rate, and goes to zero at zero speed. Therefore, at rest, the resistance across the bearings is shorted and no electrical discharge can occur. The lubricant electrical properties are the most important variable since a high electrical resistance is necessary to avoid bleeding off any charge developed across the lubricant film. Synthetic lubricants, or highly refined lubricants, are especially susceptible to electrical discharge due to their high electrical resistivity.

The differential voltage across the bearing has been measured to be +/- 1 to 2 volts during normal operation in some reaction wheels, which are induced by the quiescent motor current. It is assumed that higher voltage differentials are present during space weather events, when friction events have been observed. The cause of higher voltage differentials is not yet understood, but could be induced by single event electrical effects and transients in the motor driver during periods of spacecraft charging.

It is important to note that the effects of electrical discharge are microscopic due to the scale of the EHD film thickness (~0.1 micron), which is a key variable. It is also important to note that the electrical discharge damage mechanism is not a single event, but likely a series of discharge events happening at high frequency. The induced voltage waveform measured in a reaction wheel revealed voltages induced at many kHz, so discharges can occur thousands of times per second for significant periods of time.

Electrical discharge across the bearing lubricant film at sufficiently high voltages results in crater formation. An example of the results of a discharge across a lubricant film is shown in Figure 3, which also presents the inevitable hardness increase of the rim of the formed crater since the molten race material will be instantly oil quenched by the lubricant in the bearing, resulting in formation of untempered Martensite has a hardness as high as Rockwell C65, compared to the tempered hardness of C58 and C60 for the race and ball, respectively. The height of the rim of the crater increases the roughness and the higher hardness increases the abrasive properties of the roughened bearing surfaces.

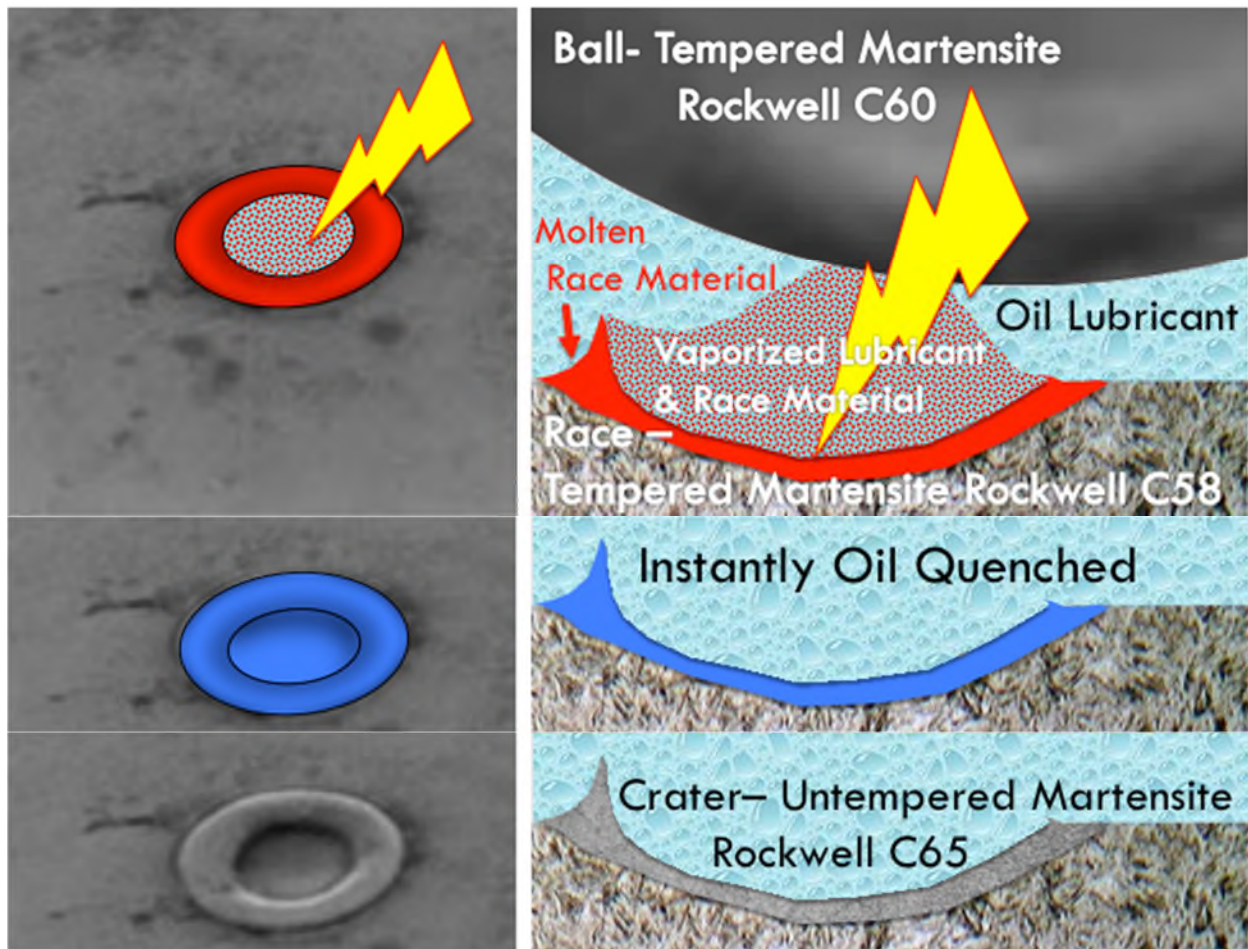


Figure 3. Electrical Discharge crater formation resulting in increased roughness

The electrical discharge mechanism is also capable of improving the surface finish of bearings with low voltage discharges less than 3 volts. The cases of friction recovery from an elevated state are believed to be the result of electrical discharge while operating at high speeds when the EHD film thickness increases, and large asperities formed by higher voltage electrical discharge events are the path of discharge for the lower voltage differential induced by the motor. The result is the erosion of the asperities, similar to the routine manufacturing process of electro-polishing of metal surfaces as shown in Figure 4.

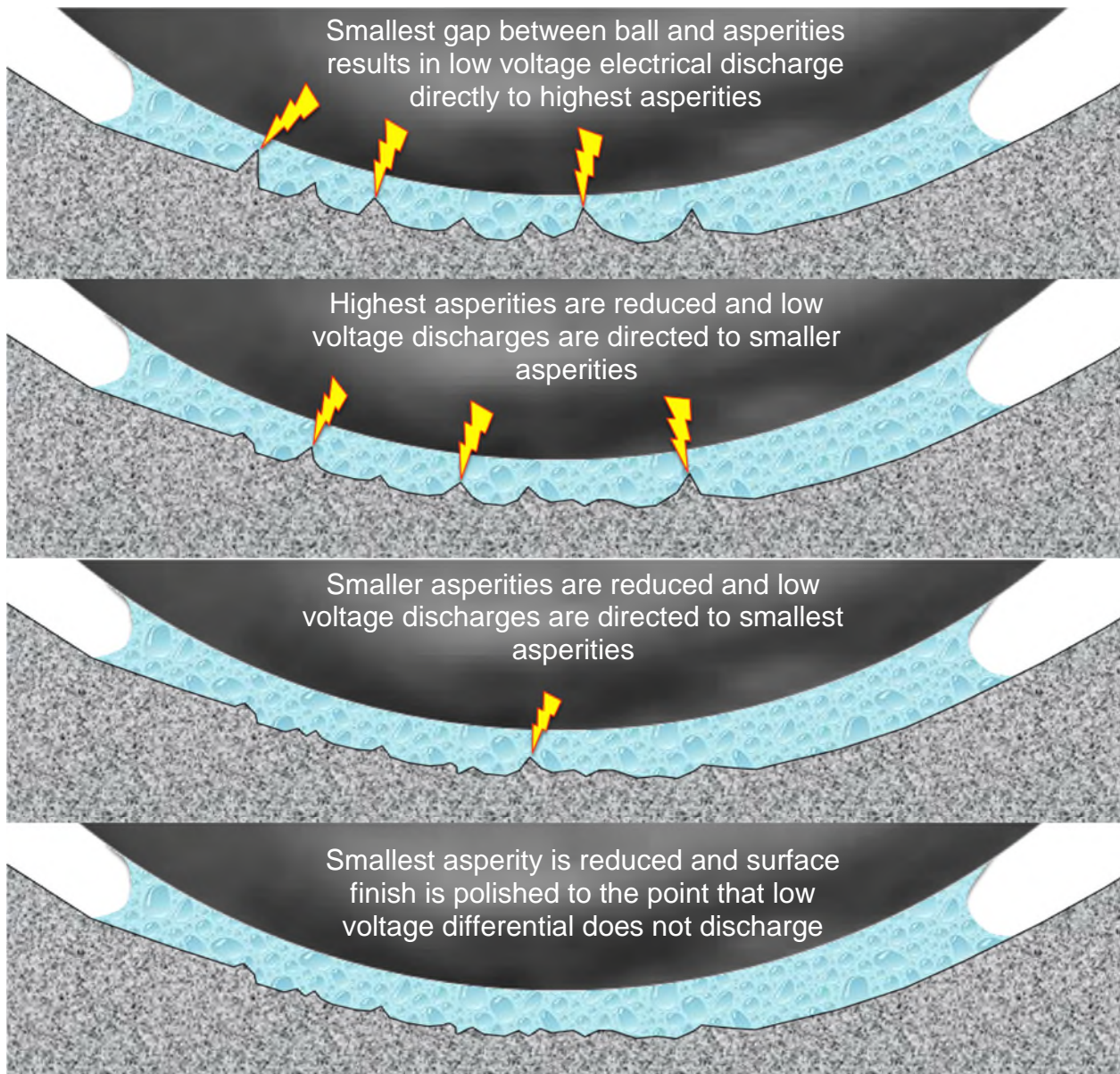


Figure 4. Low Voltage Electrical Discharge electro-polishing resulting in improved surface finish

If the composite roughness has degraded to the point that it exceeds the film thickness even at the high speed, the asperities continuously short circuit the lubricant film and the bearing can never go into electrical isolation. In this condition, the re-polishing mechanism is ineffective and the bearing may continue to degrade until the retainer is weakened by wear and fractures.

The in-situ bearing polishing mechanism is documented in more detail in a United Technologies Corporation patent application listed as Reference 3.

Sources of Differential Voltage Across Bearings

The rotating flywheel is nominally electrically floating relative to the reaction wheel housing when the wheel is spinning fast enough to develop a full EHD film. The only electrical path from housing to flywheel is through the ball bearings and this path must flow through the lubricant film. High frequency switching of motor currents has been shown to induce a voltage of 1-2 volts to a reaction wheel rotor relative to ground when it is operating on an EHD lubricant film. This is a well-established and confirmed source of differential across the bearings, which has been measured directly. Since the 1-2 volt electrical discharge typically results in a smoother surface finish, the source of higher voltage transients is more important for explaining friction anomalies associated with electrical discharge.

Motor-Induced Voltage

The 1-2 volts motor-induced voltage measured on a typical RWA was during steady state operation. A higher voltage could be present when applying full torque, or with larger motors. One example of anomalous friction occurred after a spacecraft went out of control and tumbled for a day or two. While tumbling, the attitude control system went unstable and commanded an RWA motor to full torque in alternate directions at a frequency of several cycles per second. When control of the spacecraft was regained, the dry friction torque of the RWA had clearly increased. At the time, there was no known connection between the motor and the bearings. The wheel spent some time near zero speed while tumbling, but it had spent years of operation near zero speed with no detrimental effects. In hindsight, the repeated high current oscillation in the motor likely resulted in higher than normal voltage electrical discharge, which likely affected the bearing surface finish.

Ion Engine Charging

Ion engines can quickly change the ground potential of a spacecraft during on/off cycling and affect the local plasma and charging environment. Out of 7 interstellar spacecraft using ITHACO reaction wheels, only two had reaction wheel failures, specifically NASA's DAWN and JAXA's Hayabusa, and both experienced multiple reaction wheel failures. When it is considered that only these two spacecraft had ion engine propulsion, a Probability of Correlation of 99.8% between the ion engine and reaction wheel failure results. While the mechanism for coupling of the ion engine operations into a voltage differential across the bearings is not understood, the statistics cannot be ignored, and ion engine use should therefore be considered as a potential cause of electrical discharge.

Space Charging

Space charging as a source of electrical discharge is supported in Reference 2 by a rock-solid correlation of reaction wheel friction events with major geomagnetic storms. The failures and anomalies of the RWAs on NASA's Far Ultraviolet Spectroscopic Explorer (FUSE) spacecraft have a probability of correlation greater than 99.999% to geomagnetic storms ranked in the top 20 since 1994. It is therefore nearly only a one in a million chance that the events and the geomagnetic storms are only related randomly, or nearly 100% certainty that they there is a correlation. This strong correlation has also been confirmed in larger data sets of RWA friction anomalies and failures, and a significant number of additional simultaneous anomalies on different spacecraft have also been observed.

It is important to note that correlation does not prove causation. In the case of the space plasma environment and mechanisms there are no known parallel or related potential causes other than the potential effects of space charging or charged particle radiation. We therefore still regard space charging as a likely source of differential voltage, and have used the correlations only to conclude that the root cause of friction anomalies is related to the space environment, which could also include effects of charged particle radiation upsets in the motor driver electronics producing a differential across the bearings.

Anomalous Friction Signatures

Most observed friction anomalies can be segregated into dry friction (Coulomb kinetic friction) or wet friction (Newtonian viscous friction). The magnitude of a dry friction increase is independent of rotational speed and therefore remains present while crossing zero speed. This is a characteristic of rubbing friction between two surfaces under load. Viscous friction increase is proportional to rotational speed, with no change exhibited at zero speed, which is typically a response to Newtonian shearing of a fluid between two surfaces moving relative to each other. The characteristic signatures of both of these types of friction anomalies are represented graphically in Figure 5. It is typical in a reaction wheel application for a dry friction increase to occur gradually over a period of a few days and then stabilize at the elevated friction level, while the viscous friction increase is instantaneous.

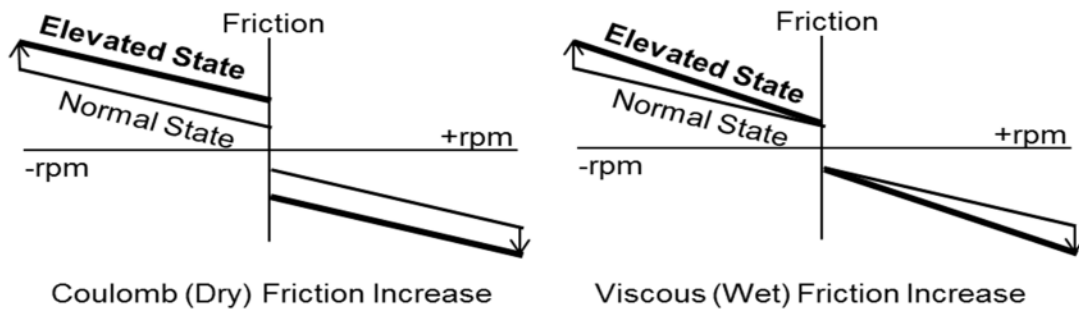


Figure 5. Dry and Wet Friction Increase Signatures

Coulomb (Dry) Friction Increase

Dry friction in reaction wheel applications is typically characterized by a 1-2 mN-m increase in friction, which is independent of speed. A perfect example of this type of friction increase is Case 1 from Reference 4, shown in Figure 6, which clearly shows this type of friction increase occurring starting after Day 39 from launch.

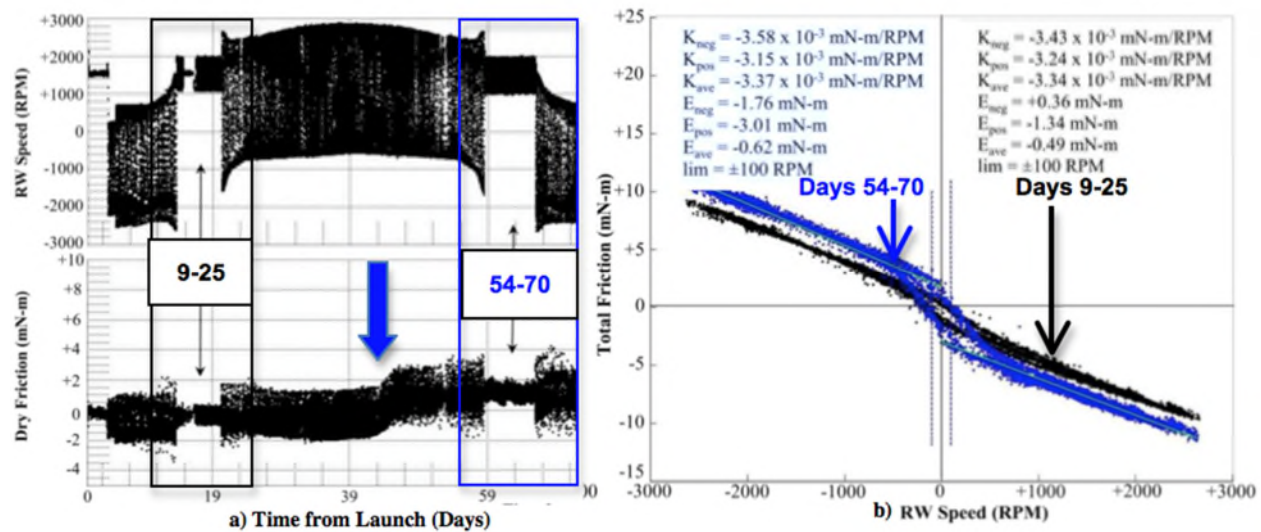


Figure 6. Example of dry friction increase in time domain (a) and relative to wheel speed (b). The solid blue arrow identifies the inception of the friction anomaly, showing a gradual increase over a few days.

The most likely mechanism for this signature is retainer windup combined with a roughened surface finish on the balls. Retainer windup occurs when sufficient asymmetry is present in the bearing raceway to result in ball speed variation displacement exceeding the ball pocket clearance. This results in binding of the retainer and rubbing in the ball pockets and between the retainer pilot diameter and outer race guiding land, as shown in Figure 7. It is believed that the asymmetry is caused by an asymmetric increase in surface roughness of the race due to electrical discharge. In laboratory tests, the increased friction signature could not be duplicated by severe retainer windup alone, which supports the claim that increased roughness of the balls rubbing in the ball pockets is also necessary for the friction to increase.

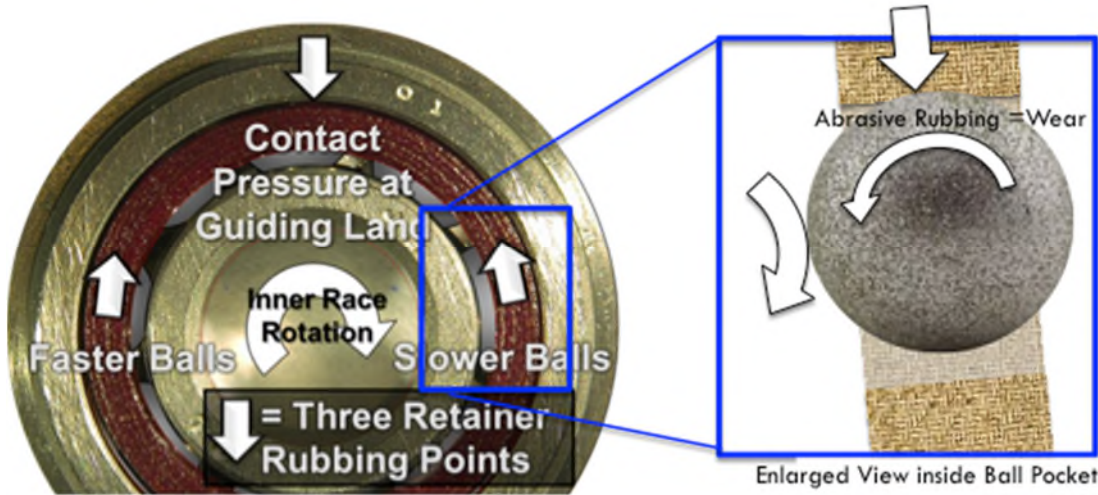


Figure 7. Retainer Windup Rubbing Points due to excessive ball speed variation.

Viscous (Wet) Friction Increase

Viscous friction increases are a less common friction event for reaction wheels and are characterized by an instantaneous increase in viscous friction, which is speed dependent. A perfect example of this type of friction increase is Case 2 from Reference 4, shown in Figure 8, which clearly shows this type of friction increase occurring instantaneously while operating at a constant speed of 1400 rpm on Day 45 from launch. Subsequent on-orbit testing varied the wheel speed to characterize the friction signature, which proved that the change is clearly speed dependent.

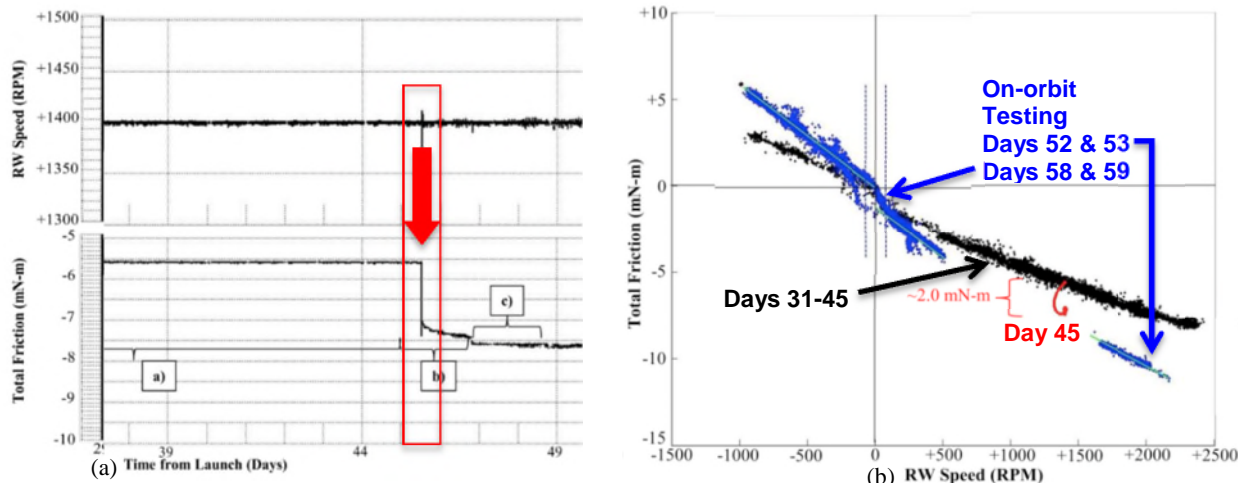


Figure 8. Example of viscous friction increase in time domain (a) and relative to wheel speed (b). The solid red arrow identifies the inception of the friction anomaly, showing an instantaneous increase which is dependent on speed, decreasing to no change at zero RPM

This friction change signature is believed to be due to a change in ball control from inner race spin control to outer race spin control. The balls in an angular contact ball bearing have a spin component, and in a stable bearing, the controlling race will have pure rolling at the contact and the other race will have a slight amount of spin at the contact. Which race is the controlling race is determined by the values of resisting spin torque at each contact ellipse, with the higher resisting torque becoming the controlling race. Since the load on each ellipse is the same, the resisting torque will be primarily a function of the contact ellipse major axis dimension 'a' and the coefficient of friction. Most bearings have a larger contact 'a' dimension on the inner race, which results in inner race control for a normal bearing. If an electrical discharge event occurs which quickly increases the roughness of the outer race, thereby increasing the coefficient of friction, the spin control could quickly change to the outer race causing the inner race to take the spin component as shown in Figure 9.

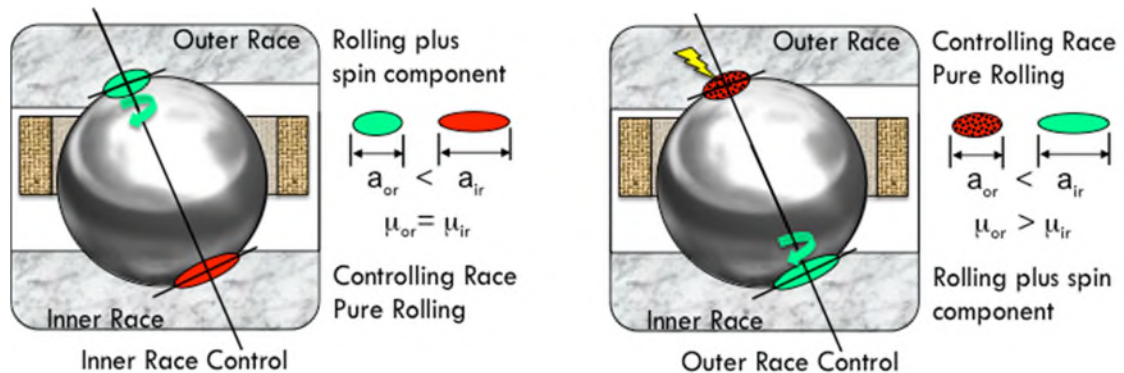


Figure 9. Inner race control changing to outer race control due to the increase in friction coefficient of the outer race resulting from an electrical discharge

The result of the change in ball control is a change in the viscous friction torque in the EHD film at the non-controlled contact ellipse due to ball spin. The spin of the ball on the thin EHD film will result in Newtonian shear, which can be imagined as the friction torque resulting from a disk spinning on a plate separated by an extremely thin viscous fluid. The larger 'a' dimension from the ball spin on the inner race instead of the smaller value on the outer race would result in an increase in the viscous friction value.

An interesting anecdote supporting this model occurred during a long-term reaction wheel test when a torque change with a signature nearly identical to the on-orbit example in Figure 6 occurred. The new friction level was stable and the wheel was operated for a considerable period of time following the friction change. At the end of the test, the bearings were removed and inspected and it was observed that a ball had two circumferential ball wear bands with two different widths, one the approximate width of the inner race ball track and one the approximate width of the outer race ball track, as sketched in Figure 10. This is what would be expected if the spin control shifted from inner race to outer race and spent considerable operating time in each state.

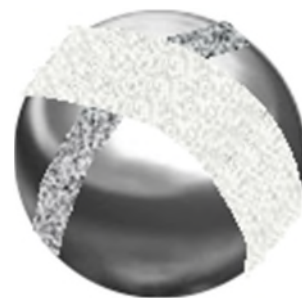


Figure 10. Artist sketch of ball inspected after viscous friction change

The viscous friction anomaly has not been known to result in a reduction in lifetime, which is also consistent with the model. There is no progressive wear encountered, no binding or windup of the cage, merely an increase in surface roughness on one race, which changes the balance of forces and torques within the bearing.

Oil Jog

Viscous friction spikes in some applications have been attributed to ‘oil jogs’. Tests have shown that these “oil jog” torque signatures can be a result of electrical discharge; a theory for the phenomena will be presented. “Oil jogs” are characterized by an abrupt increase in friction, usually while operating at a constant speed, followed by a decay lasting seconds, minutes or hours, as approximated in Figure 10. They have been frequently attributed to a sudden migration of lubricant into an area of the bearing where viscous churning results in a temporary increase in torque, and which decays as the lubricant is redistributed. These instantaneous jogs were duplicated in tests by merely applying a small voltage across the bearings, with both positive jogs and negative jogs, as depicted in Figure 11, which does not strongly support the common hypothesis that they are the result of lubricant dynamics. While it is hard to imagine a mechanism for the sudden burst of lubricant migrating into a bearing, it is even harder to imagine a mechanism for a sudden migration of bulk lubricant out of a bearing.

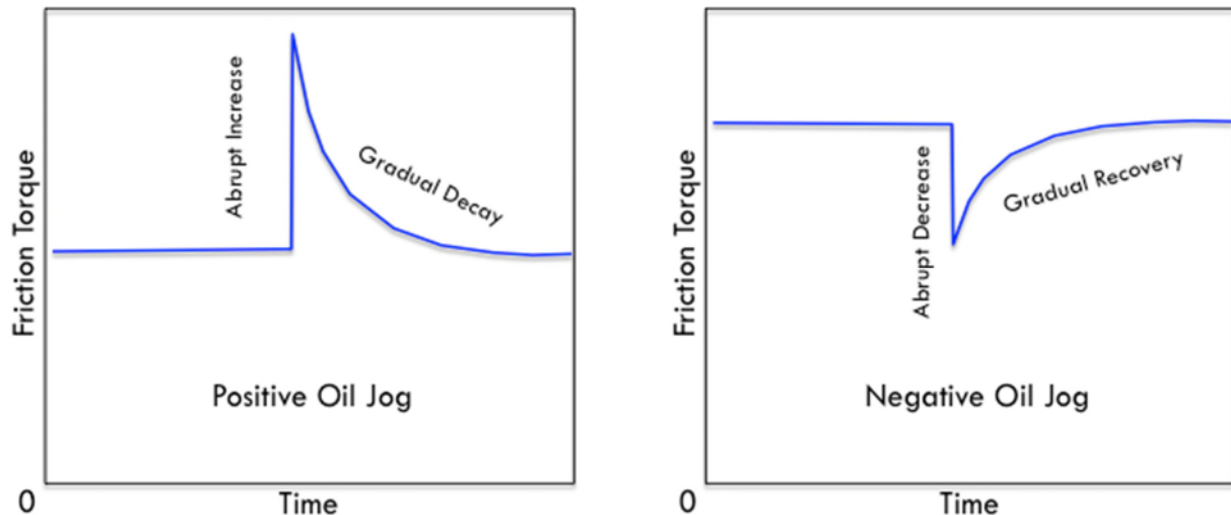


Figure 11. Positive and Negative Oil Jog Signatures

An alternative scenario of the mechanism generating these events is the result of electrical discharge. The same mechanism described in the previous section for the viscous friction increase may apply to this transient event. The abrupt increase can be due to an electrical discharge event increasing the coefficient of friction on the outer race, which transfers ball control to the outer race, and the gradual recovery to inner race control occurs as the low voltage electrical discharge from the motor re-polishes the outer race, as depicted in Figure 12. This scenario can apply to a negative oil jog as well, where the bearing is in a stable outer race control condition, and an electrical discharge event increases the coefficient of friction on the inner race, resulting in an abrupt decrease in viscous friction and similar gradual recovery.

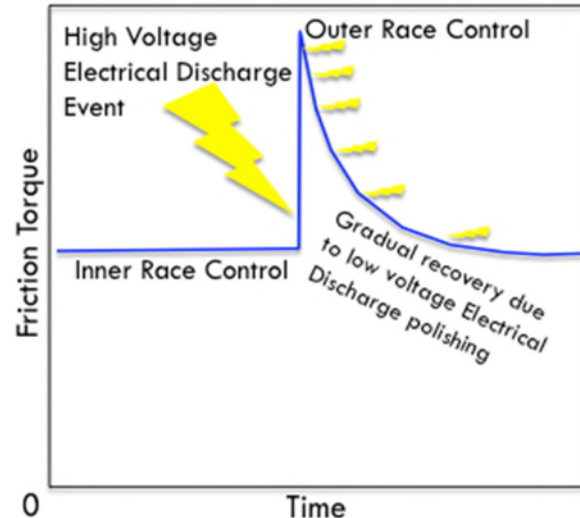


Figure 12. Electrical discharge scenario for Oil Jog Signature

Retainer (Cage) Instability

Retainer instability is a severe type of bearing friction anomaly, which can ultimately lead to bearing failure if the retainer fractures. It is characterized by an almost instantaneous increase in friction and audible noise, which periodically comes and goes, and is universally attributed to the chaotic motion of the retainer in unstable energetic modes resulting from increased coefficient of friction between the retainer and the other bearing parts. Reference 5 concluded that ball pocket friction is more critical to stability than retainer land friction for the bearing investigated. The increase in ball pocket friction has been widely attributed to lubricant starvation, despite the trend that occurrences do not necessarily seem to increase with accumulated operating time, and the contradictory evidence that it is sometimes observed in conjunction with 'oil jogs' which would tend to suggest ample, or even excessive, lubricant supply. However, electrical discharge can be an obvious source of increased ball pocket friction by increasing the surface roughness of the balls, rather than the more popular theory of starving the surfaces of the retainer of lubrication. Therefore, it is suggested that electrical discharge increasing the surface roughness of balls may be a plausible path to the initiation of cage instability, in the lab due to electrical currents, and in space due to space charging.

In Reference 6, this author cited an example of "Vibration-Induced" retainer instability in the lab with brand new well-lubricated bearings, in which the retainer instability could literally be turned on and off with an electrical switch that changed the motor from delta to wye. Figure 13 shows a waterfall chart from an accelerometer during a run-up from 0 rpm to 3600 rpm, with data sampled every 200 rpm. A 36x per revolution disturbance dominates the plot. The retainer instability is clearly visible in the 1-kHz range above 3000 rpm. The source of the 36x disturbance was the prototype motor used to drive the reaction wheel. Circulating currents in the delta-configured motor were caused by excessive amplitude modulation of the magnetic flux density in the motor gap. To prove this, the motor was rewired to a wye configuration, which eliminated potential circulating current loops and the waterfall measurement was immediately retaken. The results are shown in Figure 14, which clearly shows elimination of the 36x per revolution disturbance and no signs of retainer instability. The modified motor winding was the only change to the reaction wheel between the data taken in Figures 13 and 14. At the time Reference 6 was written, the observed retainer instability was assumed to be due to micro-vibrations from the circulating currents in the motor, since no other connection with the circulating currents could be imagined. In hindsight, it is more likely that the large circulating currents were resulting in high voltage electrical discharge across the bearings above 3000 rpm, which would tend to roughen the balls and increase the friction coefficient between the ball and ball pocket, and which increased the potential for retainer instability.

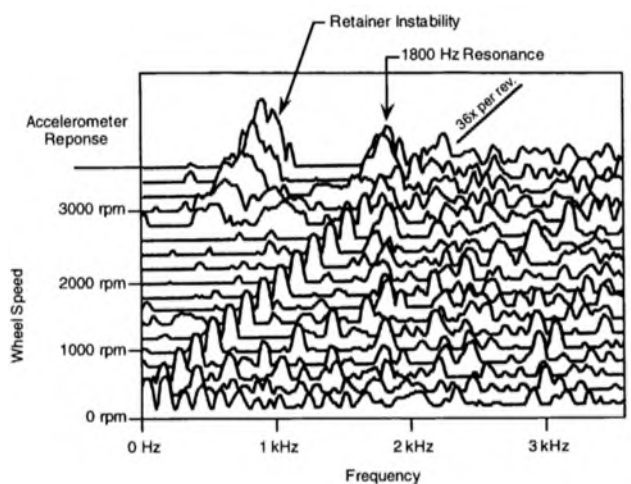


Figure 13. Run-up with large circulating motor currents at a frequency of 36X per revolution and resulting cage instability

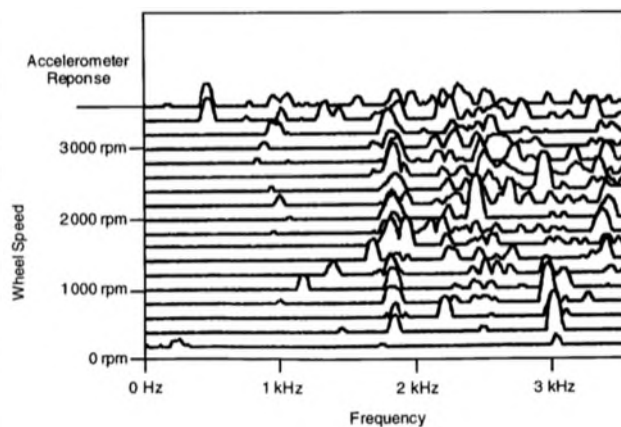


Figure 14. Run-up without circulating motor currents – no cage instability

During recent verification testing of the electrical discharge hypothesis, just 28 minutes after applying ± 6 volts across a bearing, one RWA bearing exhibited a 20 mN-m friction spike and produced a rare audible rumbling sound. This large friction increase (10x the normal bearing friction) at the same time as the noise is characteristic of severe retainer instability. The author had never observed cage instability in that size RWA bearing prior to that event. This test result implies the correlation between electrical discharge and retainer instability.

Another point regarding the possible connection between electrical discharge and retainer instability is that in addition to roughening the balls, electrical discharge can also result in instantaneous local raised defects, which could also result in a cyclical radial excitation of the retainer at the ball rotation frequency, as depicted in Figure 15. This vibration excitation would seem to be more destabilizing than static increases in frictional coefficients.

The intent here is not to try to oversimplify something as complex as cage instability, but to include electrical discharge as a variable which should be considered as a possible factor during investigation of retainer instability.

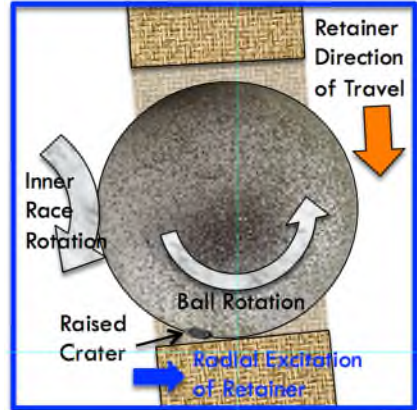


Figure 15. Top View, ball pocket depiction of effect of raised crater on cyclical radial excitation of bearing retainer

Stiction (Breakaway Torque) Increase

Breakaway torque and rolling friction are two performance parameters typically measured on RWAs during acceptance testing. Breakaway torque is the minimum amount of torque required to start the wheel from rest, and rolling friction is the minimum amount of torque required to keep the wheel turning. They are intended to be indicative of the health of the bearing, and their magnitudes can affect spacecraft attitude control during zero crossings if they are excessive.

Anomalies of breakaway torque occurred for a new high torque RWA design. Previous RWAs with the same bearings and lubricant had expected values of breakaway torque. When a change to a heritage design was made to significantly increase the current in the motor, breakaway torque values skyrocketed during the initial phases of acceptance testing. A root cause analysis initially concluded that it was due to a variable in the bearing lubrication process, but corrective actions based on this hypothesis were ineffective. The breakaway torque improved to acceptable limits with accumulated operating time, but the mystery of why the torque went up compared to the heritage product was not resolved. Increase of the motor torque capability inevitably increases the quiescent motor-induced voltage across the bearings. In retrospect, it is believed that the motor torque increase affected the properties of motor-induced electrical discharge during extended low speed operation encountered just prior to the breakaway torque test.

Preventative Measures

The likelihood of electrical discharge can be reduced using bearing design features intended to prevent the chain of events presented. The use of ceramic balls blocks the electrical discharge through the bearings via the isolation provided by ceramics. It is noted in Reference 2 that 72 ITHACO RWAs with hybrid ceramic bearings have been flown with no known anomalous friction events. However, once the electrical path from reaction wheel housing to flywheel through the bearings has been eliminated, another means for providing the flywheel an electrical path must be provided. It must be considered that if the flywheel were perfectly isolated, very large potentials could develop possibly leading to very large discharges, which could damage spacecraft electronics. Alternately, with steel bearings, a grounding brush can be used to bleed off any charge across the lubricant film, or conductive lubricant additives can reduce the resistance across the bearing. All of these measures are used routinely in terrestrial applications to mitigate electrical discharge in bearings.

Lessons Learned

When analyzing root cause of friction anomalies in rotating mechanisms, it is important to consider the possible effects of electrical discharge. The following recommendations are presented to facilitate this, based on recent experiences in reaction wheel applications:

1. If the friction anomaly occurs in space, review the timing of the initiation of the friction anomaly against the local space weather. Coronal mass ejections, geomagnetic storms, and specifically the direct observation of aurora may indicate a correlation with space charging events.
2. If the friction anomaly occurs in the lab, review the timing of the anomaly relative to motor current changes, or specifically test equipment failures or grounding circuit changes or transients.
3. Measure the shaft voltage and bearing electrical resistance during various operating conditions. This can be easily done with a brush applied to the shaft. Several companies offer pickups specifically designed to measure rotating shaft voltage to detect electrical discharge.
4. Measure the electrical properties of the lubricant and consider how they may evolve over time. Resistivity greater than $2.5 \text{ G}\Omega\text{-m}$ (conductivity less than 400 pS/m) has been considered to be a possible danger zone for electrical discharge. This is more likely with synthetic or refined lubricants.
5. Directly test the sensitivity of a sample mechanism to electrical discharge by applying an alternating voltage directly across the bearing. This can be done with a brush used to measure shaft voltage. The rate of change of the voltage is an important variable, as slow voltage changes will bleed off.
6. When inspecting bearings that may have been affected by electrical discharge, look for the following physical features which may be associated with electrical discharge:
 - a. Pitting or small craters from electrical discharge, usually between 5 to 10 microns.
 - b. Countless microscopic pits on the balls or races known as "frosting" of the surfaces.
 - c. Wear grooves, with depths ranging up to 1 micron or more.
 - d. Blackened or discolored lubricant and staining of the retainers at the expected rubbing points.
 - e. Repetitive micro-denting of the ball track on the race, which may be a result of a hard electrical discharge crater formed on a ball.

Conclusions

Analysis of anomalous friction in ball bearings in laboratory and space environments should include electrical discharge as a possible cause. Potential sources of electrical discharge, plausible explanations for response of various friction signatures to electrical discharge and supporting observations from the author's experience have been presented for consideration.

References

1. Busse, D., J. Erdman, et. al. (1996) System Electrical Parameters and Their Effects on Bearing Currents, *IEEE Transactions on Industry Applications*, Volume 32, Issue 6, p 71-85.
2. Bialke, W. and Hansell, E. (2017), A Newly Discovered Branch of the Fault Tree Explaining Systemic Reaction Wheel Failures and Anomalies, *17th European Space Mechanisms and Tribology Symposium*
3. Bialke, W. and Hansell, E. Inventors (2017), USPTO Patent Applications 15668663 titled *Bearing Assemblies with Electrodynamically Matched Races* and 15668669 titled *Electrodynamically Finished Plain Bearings*. United Technologies Corporation, Owner.
4. Hacker, J.M., J. Ying, P Lai (2015) Reaction Wheel Friction Data Processing Methodology and On-Orbit Experience, *Journal of Astronautical Science*, 62:254
5. Boesiger, E.A. and Warner M.H. (1991) Spin Bearing Retainer Design Optimization, *NASA/ CP-3113, 25th Aerospace Mechanisms Symposium*
6. Bialke, W. (1998) Experiences with Differentiating Ball Bearing Retainer Instabilities, *NASA/CP-1998-207191, 32nd Aerospace Mechanisms Symposium*

Efficacy of Lead Naphthenate for Wear Protection in Mixed Lubrication Regime

Jason T. Galary^{*†}

This research investigated the efficacy of lead naphthenate as a wear additive in multi alkylated cyclopentane (MAC) fluid. The use of lead naphthenate in MAC lubricants has a history of more than thirty years with spaceflight heritage. However, despite its history of use in a variety of rolling and sliding applications, there is still a lack of understanding about this additive's wear protection mechanism and its performance. This paper will illustrate the efficacy of lead naphthenate to protect a lubricated contact against wear in a variety of conditions including atmospheric, vacuum, and mixed film lubrication. The effects of varying levels of lead naphthenate, different compositions of steel (52100 and 440C), and varying temperatures was investigated.

This research investigates the performance of this additive in simulated contact testing using an SRV as well as a Mini Traction Machine (MTM). The SRV testing of the lead naphthenate will be in boundary and mixed film contact under vacuum and atmospheric conditions to better understand how the additive functions on a lubricated 52100 and 440C contact. The MTM will be utilized for scuffing/galling wear tests which will be performed in a mixed film and boundary lubrication conditions in a counter-rotation rolling/sliding contact. Through use of counter-rotation, the entrainment speed can be decoupled so that the scuffing/galling properties of the lubricant can be determined in boundary and mixed film conditions over a range of sliding speeds. This also allows for the rolling friction and sliding friction to be decoupled and measured separately.

Introduction and Background

Lead naphthenate has been used heavily as an anti-wear and extreme pressure additive in multi alkylated cyclopentane lubricants for high-vacuum space mechanisms. The additive consists of a centralized lead ion that is bonded with the oxygen atoms of two carboxylate groups each attached to naphthenate aromatic rings. The naphthenate aromatic hydrocarbon rings provide the solubility of the lead naphthenate in different hydrocarbon oils but the way the additive reacts with steel and protects against wear in various lubrication regimes is still not fully understood.

The historical use of lead naphthenate originates from industrial gears and bearings where it was used as an extreme pressure additive over fifty years ago. Over the last thirty years, it has gained a lot of spaceflight history although there are still many questions regarding its efficacy, primarily how does it function in various lubrication regimes, the effects of different metallurgy, and how does the environmental pressure effect its performance.

With the increasing number of space mechanisms being developed and launched as well as the increasing length of mission time required, it is critical to have a robust design with high reliability. To improve the reliability, it is necessary to have long lives for all of the components in the design. This will require that the lubricants used for space mechanism environments must also improve. The use of lead naphthenate additive in multi alkylated cyclopentane fluids is a proven additive package with spaceflight history but in order to develop and advance the lubrication technology for high vacuum space mechanisms, additional understanding of its tribological performance is needed.

^{*} Applied Science and Tribology, Nye Lubricants, Inc, Fairhaven, MA

[†] Department of Mechanical Engineering, University of Massachusetts Dartmouth

While there are a wide variety of atmospheric tribology tests, there are far fewer that operate under high vacuum conditions. The three most important of these vacuum tribology tests are the 4-ball, SRV, and the SOT, all of which have their particular tradeoffs.

The use of a 4-ball wear test under vacuum provides good comparison to a large amount of published data as this test has been used for decades in various lubricants. However, this test has a high Hertzian contact stress that operates in a pure sliding mode typically within the mixed lubrication regime. Because of the high speeds this test is typically operated at, the sliding motion, and operating in a single rotational direction, strong films are created which prevent this test from being able to properly evaluate anti-wear or extreme pressure additives. The SRV, while similar to the 4-ball wear, offers more flexibility and operates in an oscillating motion which allows for better evaluation of lubricant additives. The SRV also provides a variety of contact geometries, loads, and speeds to help simulate a tribological contact. The SOT is in a class by itself as it was purposely designed to simulate angular contact bearings in a vacuum environment and has a rolling/pivoting motion.

When considering how to research the efficacy of lead naphthenate and how it functions as a tribofilm, it is important to look at various methodologies to characterize its performance. In the beginning stages, this is easiest performed by using simulated contact testing. In this respect, an SRV makes the best choice as it is very flexible in regards to the contact mechanics and environmental conditions. The availability of SOT testing is somewhat limited but a Mini Traction Machine (MTM) can be used in a manner to simulate the same type of application conditions with a ball running in an orbital pattern on a disc with a mixture of rolling/sliding. While the MTM cannot currently run in a vacuum condition, it can be used to understand the complexities of lead naphthenate operating in a rolling/sliding mixed application. When this is combined with the vacuum/atmospheric testing on the SRV, the performance of the lead naphthenate can be made clearer.

To understand the functionality of lead naphthenate as an anti-wear additive, it is important to understand the genesis of wear in order to be able to reduce or control it. There are many forms of wear including adhesive, abrasive, and fretting, however they all have a starting point where the first damage to the surface occurs and an ending point which is either a seizure or contact fatigue. Recent work had been done to illustrate how scuffing wear is believed to be the point where this wear starts [1] [13].

Scuffing wear has been described by many ways over the years. It can be used in cases synonymously with galling or scoring, all of which to some degree are different stages of the same wear phenomenon. When a contact is supported by a lubricating film whether it is in Boundary, Mixed, or an EHD lubrication regime, both the additives and fluid are performing different roles to prevent wear in the contact. The scuffing point or genesis of wear, which I will define as instantaneous breakdown of the fluid film supporting the contact, marks the time when wear will begin to occur, and the severity is then related to the strength of the tribofilm. The breakdown of the fluid film can be caused by several methods including, increased contact stress, entrainment speed, or degradation.

Over the last 100 years there has been considerable work done to develop the knowledge surrounding scuffing wear and contact fatigue. In the 30's and 40's, Blok did a lot of research to study the scuffing properties of lubricants with respect to their viscosity [2]. He was also the first to research and publish work on how counter-rotation works to decouple the sliding and entrainment speeds. This will eliminate torque effects and separate the different frictional elements.

Over the years, the research into scuffing has led to the creation of many different test methods or equipment. Some of these include the 4-Ball Wear test which has been used for scuffing and contact fatigue testing. The FZG gear test is one of the more well-known scuffing tests but has limitations due to its cost, reproducibility, and being able to investigate the scuffing before catastrophic damage to the gear occurs [3] [4].

More recently several researchers have started investigating this wear mechanism and different methods to evaluate it. Some work has been done by Galary to study scuffing on an SRV [5] as well as to simulate the FZG test [6]. In the more recent work by Galary, he investigates a method to simulate the FZG scuffing test on an SRV using custom specimens and fixtures. This new method used the same type of gear steel and contact pressures as the FZG test, was much less expensive, showed great repeatability, and had a strong correlation to the FZG test. It also had expanded load stages beyond the standard FZG test, but its main limitation was that it remained a pure sliding test.

Wedeven has been one of the pioneers in using a rolling/sliding tribometer for scuffing analysis and he has promoted the value of separating the sliding speed from the entrainment velocity to better understand the tribological contact [7]. This is accomplished through counter-rotation and is critical in understanding the wear regime and what is happening in the contact. The approach of Wedeven is different than in this paper as he approaches the problem by variation of the contact angle between mating bodies as opposed to the counter-rotation method used in this work.

Experiments

Two different tribological test methods were used in this research. One of the methods is run in pure sliding under both atmospheric and vacuum conditions (5×10^{-5} Torr min) while the second testing is a mixed rolling/sliding contact in atmospheric conditions only. The friction/traction properties along with the wear rates were measured for two multiply alkylated cyclopentane (MAC) hydrocarbon oils formulated with 3% and 5% lead naphthenate (2001-3PB and 2001-5PB) along with unformulated MAC oil (2001A). The lead naphthenate used in these samples was vacuum treated prior to formulation to improve vacuum outgassing characteristics and make it suitable for a space mechanism lubricant.

For the sliding testing, an SRV tribometer was used in a ball on disc configuration. The SRV has a fixed lower specimen allowing the upper ball to be oscillated at various frequencies while the frictional force is measured. The contact area is coated with 5 ml of lubricant for the testing that will be run at temperatures of 20°C and 75°C (controlled during test). For this research, AISI 52100 steel balls and discs were used that had a Young's Modulus of 210 GPa and a Poisson ration of 0.30. The balls had a 10-mm diameter with a roughness (R_a) of 25 nm and a Rockwell hardness of 62 HRC. The 24-mm discs are vacuum arc remelted and had a hardness of 58 HRC with a lapped surface that has a roughness (R_z) of 500 nm. The 440C steel balls and discs that were used had a Young's Modulus of 210 GPa and a Poisson ration of 0.30. The balls had a 10-mm diameter with a roughness (R_a) of 25 nm and a Rockwell hardness of 62 HRC. The 24-mm discs had a hardness of 58 HRC with a lapped surface that has a roughness (R_z) of 500 nm. All the tests were run in duplicate and with a maximum Hertzian contact stress of 2.12 GPa and a sliding speed of 300 mm/s.

The experimental testing methodology is as follows. Test specimens are ultrasonically cleaned in heptane followed by acetone. The testing apparatus is then assembled, and oil is applied for the experiment. The lower specimen is then heated to the testing temperature with no force applied to the contact and no oscillation. Once the testing temperature is reached, the force is applied to the specimens and oscillatory motion starts. The test continues for two hours or until the coefficient of friction exceeds the test limits or seizure occurs.

The mixed rolling/sliding testing was performed using a mini-traction machine (MTM) with a ball on-disc configuration which is shown in Figure 1. In the MTM, the ball and disc are driven independently which allows any combination of rolling and sliding. The measurement of frictional force is done through a load cell that is attached to the bearing housing of the ball motor shaft. The lower testing specimen (disc) and the contact area is completely immersed in oil for testing which is kept at a controlled temperature of 50°C and 150°C for this testing.

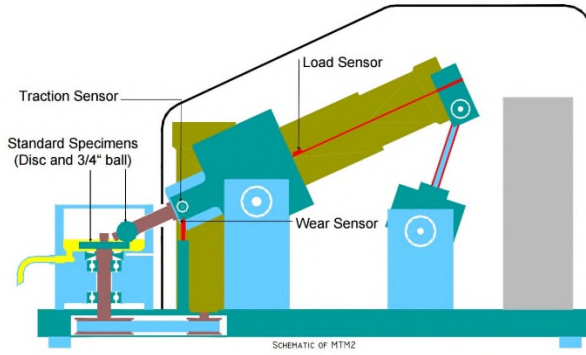


Figure 1. Schematic of Mini Traction Machine

The sliding speed is defined as

$$U_s = |u_1 - u_2| \quad (1)$$

where u_1 and u_2 are the speeds of the two surfaces in respect to each other. The entrainment (rolling) speed or velocity is then

$$U = \left(\frac{u_1 - u_2}{2} \right) \quad (2)$$

With the slide to roll ratio (SRR) being the ratio of the sliding speed to the rolling speed of a contact.

$$SRR = \left(\frac{u_1 - u_2}{U} \right) \quad (3)$$

When the slide-roll ratio is between 0 and 2, the ball and disc will rotate in the same direction relative to the contact. At SRR of 0, the contact sees pure rolling while at 2 it is in pure sliding with the ball held stationary relative to the disc. While in this range of SRRs, any increase in the sliding speed causes a proportional increase to the entrainment speed U . This increase in the sliding speed also creates a thicker film separating the surfaces which will lead to less contact and a stronger EHD film [8].

For this research, in order to keep the tribological contact in a mixed film condition, the use of counter-rotation will be employed. Counter-rotation drives the ball and disc in opposite directions independently. Through operation of the MTM in opposite directions relative to the contact, the rolling/sliding speeds can become large while the entrainment speed stays fixed. This allows for very high sliding speeds with an entrainment speed at the contact that can theoretically be 0. The advantage to performing tests in this manner is to eliminate the effect of an EFD film creation and allows for additives and surface chemistry to be tested in either boundary or mixed film lubrication regimes.

The film thickness for Mixed Film Lubrication was calculated as follows.

$$h \approx 1900\eta U \quad (4)$$

where η is the Dynamic Viscosity and U is the Entrainment Velocity.

In previous work by the author and when considering other scuffing tests, it was noticed that most simulations use a load stage progression. This can be seen in the FZG, 4-Ball EP, SRV, OK Load Test, and Timken tests. The testing in this work will be done using progressive speed as opposed to a load stage test. Part of the reason for this is because the higher sliding speeds will allow for a more aggressive wear rate to help differentiate the efficacy of the additives. Another reason that may be more important is the fact

that in a test where the contact stress increases at every stage, the contact patch will also increase at every stage. This leads to fresh nascent metal being exposed at every stage. This new area of contact does not have a tribofilm on it and so it is more likely to have aggressive wear. This is why tests run in a progressive load methodology will typically have failures at the step increase and have lower repeatability.

For this research, AISI 52100 steel balls and discs were used that had a Young's Modulus of 210 GPa and a Poisson ration of 0.30. The balls had a 19.05-mm diameter with a roughness (R_q) of 10 nm and a Rockwell hardness of 62.5. The discs had a hardness of 60.5 and a roughness (R_q) of 11 nm. All the tests were run in duplicate and with a maximum Hertzian contact stress of 1.25 GPa.

The experimental testing methodology is as follows. Test specimens are ultrasonically cleaned in heptane followed by acetone. The testing apparatus is then assembled and filled with oil for the experiment. The temperature of the oil is then heated to 150°C while the ball and disc are rotated at a slow speed while not in contact. This continues for 30 minutes to allow for any chemical absorption of the additives on the surfaces. After this, there is a 10-minute run-in period with a Hertzian contact stress of 1.25 GPa and an SRR of 1. Once the run-in has completed, a progressive speed test starts with running stages for 1 minute and rest stages for 30 seconds. The SRR is varied at each stage in order to maintain the entrainment speed for each stage but increase the sliding speed at the contact. The test continues until either all stages (51) are completed (maximum speed for MTM) or scuffing wear and seizure occurs.

Results and Discussion

SRV (Sliding in Atmospheric and Vacuum Conditions)

The results in Tables 1-3 and Figure 2 are from the experiment on the MAC with 0%, 3%, and 5% lead naphthenate when tested in a mixed film regime, at 20°C on the SRV under both atmospheric and vacuum conditions. These plots illustrate the wear rate of each material which is determined by the total wear volume (μm^3) per millimeter traveled in the test. The wear volumes were measured using an Ametek 3D Optical Profilometer.

Table 1. Wear Performance for MAC fluid with 0% Lead at 20°C

Material	Temp (°C)	Environment	Specimen	Avg Wear Scar (mm ²)	Disc Wear Volume (μm ³)	Wear Rate (μm ³ /mm)
0% Lead	20	Atmosphere	440C	1.939	599,972	0.28
0% Lead	20	Vacuum	440C	1.924	518,400	0.24
0% Lead	20	Atmosphere	52100	2.260	481,018	0.22
0% Lead	20	Vacuum	52100	2.265	410,400	0.19

Table 2. Wear Performance for MAC fluid with 3% Lead at 20°C

Material	Temp (°C)	Environment	Specimen	Avg Wear Scar (mm ²)	Disc Wear Volume (μm ³)	Wear Rate (μm ³ /mm)
3% Lead	20	Atmosphere	440C	1.966	410,400	0.19
3% Lead	20	Vacuum	440C	1.945	216,000	0.10
3% Lead	20	Atmosphere	52100	2.278	342,356	0.16
3% Lead	20	Vacuum	52100	2.251	259,200	0.12

Table 3. Wear Performance for MAC fluid with 5% Lead at 20°C

Material	Temp (°C)	Environment	Specimen	Avg Wear Scar (mm ²)	Disc Wear Volume (μm ³)	Wear Rate (μm ³ /mm)
5% Lead	20	Atmosphere	440C	2.129	291,600	0.14
5% Lead	20	Vacuum	440C	1.879	172,800	0.08
5% Lead	20	Atmosphere	52100	2.742	263,520	0.12
5% Lead	20	Vacuum	52100	2.242	216,000	0.10

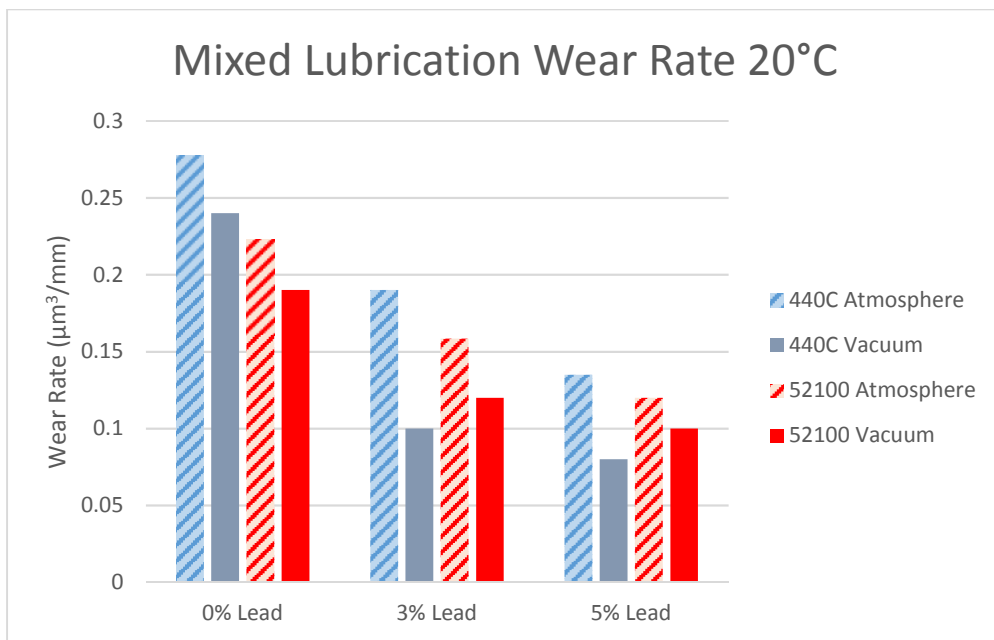


Figure 2. Mixed Film Lubrication Wear Rate at 20°C

In atmospheric conditions, the wear rates for 52100 steel was consistently lower than the 440C. Under vacuum conditions, this still holds true for the sample with 0% lead but the samples with 3% and 5% lead produced lower wear rates with 440C than 52100. Interestingly enough, when looking at the average wear scar there is no correlation to the disc wear volume of the wear rate. Until recently, most published papers used the average wear scar to compare efficacy of wear additives and performance in testing. Using this measurement simply gives you a dimension of the worn area with no indication of how much material was removed. The results from this study as well as those presented by St. Pierre [9] have illustrated that two-dimensional wear measurements cannot be relied on to understand what is going on in a mechanism or tribological contact. By using 3D profilometry, a deeper understanding of what is going on can be attained.

The results in Tables 4-6 and Figure 3 are for the multiply alkylated cyclopentane with 0%, 3%, and 5% lead naphthenate when tested in a mixed film regime, at 75°C on the SRV under both atmospheric and vacuum conditions.

Table 4. Wear Performance for MAC fluid with 0% Lead at 75°C

Material	Temp (°C)	Environment	Specimen	Avg Wear Scar (mm^2)	Disc Wear Volume (μm^3)	Wear Rate ($\mu\text{m}^3/\text{mm}$)
0% Lead	75	Atmosphere	440C	1.949	1,080,000	0.50
0% Lead	75	Vacuum	440C	2.286	962,688	0.45
0% Lead	75	Atmosphere	52100	1.978	263,796	0.12
0% Lead	75	Vacuum	52100	2.426	276,480	0.13

Table 5. Wear Performance for MAC fluid with 3% Lead at 75°C

Material	Temp (°C)	Environment	Specimen	Avg Wear Scar (mm^2)	Disc Wear Volume (μm^3)	Wear Rate ($\mu\text{m}^3/\text{mm}$)
3% Lead	75	Atmosphere	440C	2.380	977,730	0.45
3% Lead	75	Vacuum	440C	2.853	691,200	0.32
3% Lead	75	Atmosphere	52100	3.987	622,811	0.29
3% Lead	75	Vacuum	52100	2.216	259,200	0.12

Table 6. Wear Performance for MAC fluid with 5% Lead at 75°C

Material	Temp (°C)	Environment	Specimen	Avg Wear Scar (mm ²)	Disc Wear Volume (μm ³)	Wear Rate (μm ³ /mm)
5% Lead	75	Atmosphere	440C	3.003	756,000	0.35
5% Lead	75	Vacuum	440C	1.874	388,800	0.18
5% Lead	75	Atmosphere	52100	3.335	612,415	0.28
5% Lead	75	Vacuum	52100	1.842	162,000	0.08

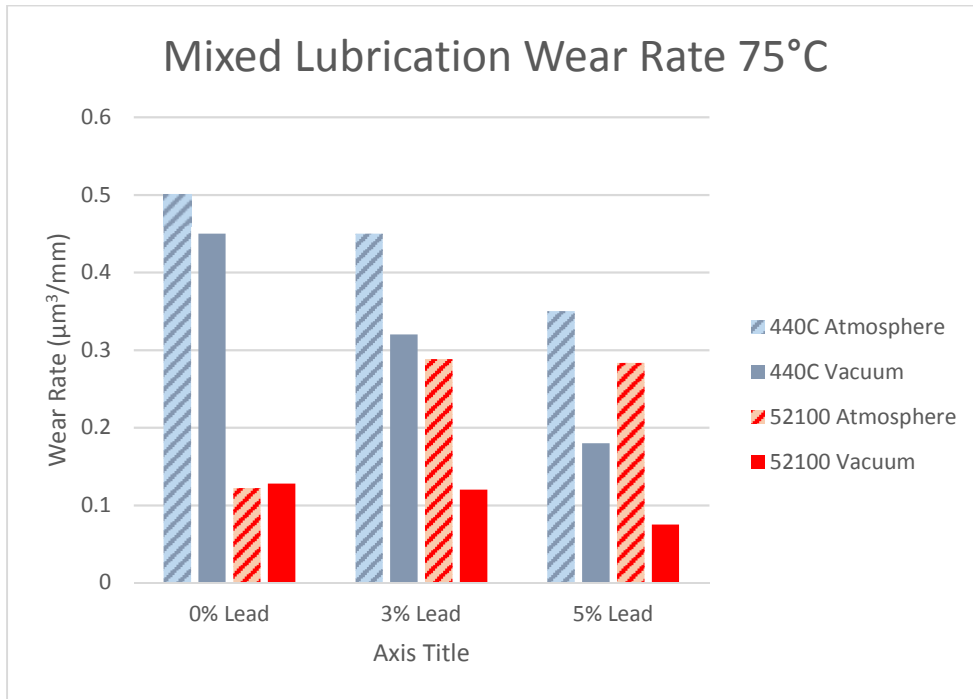


Figure 3. Mixed Film Lubrication Wear Rate at 75°C

In atmospheric conditions, the wear rate for 52100 steel was consistently lower than the 440C although they trended in opposite directions with the increase in lead content. Under vacuum conditions, the effect for the sample with 0% lead was minimal but the samples with 3% and 5% lead produced considerably lower wear rates for both 440C and 52100. This opposite trend between the 52100 and 440C is believed to be related to the way lead naphthenate interacts with the chemical composition of the steel [10]. With 52100, the lead naphthenate reacts with the iron oxide present at the surface layer and creates wear debris. When under vacuum there is less iron oxide formation which allows the lead naphthenate to provide more wear protection. Regarding the 440C, the lead naphthenate will chemisorb into the chromium layers of the stainless and provide better wear protection as the concentration increases and the environment goes from atmospheric to vacuum.

Comparing the wear performance between 20°C and 75°C, all samples had a higher wear rate (2-3X) on 440C at 75°C. As this SRV testing is a pure sliding test, the lower wear resistance for the 440C at 75°C across all concentrations is tied to the more complex layered structure of the metal. The structure of the 440C would require both chemisorption and physical absorption for the best performance. On the 52100 specimens, the samples with 0% lead had half the wear at 75°C, approximately the same level of wear at a 3% loading of lead, and at 5% lead the wear rate was higher for samples tested in atmospheric conditions while the wear under vacuum was slightly lower.

MTM (Rolling/Sliding Contra-Rotation)

The results in Figures 4-6 are for the MAC cyclopentane with 0%, 3%, and 5% lead naphthenate when tested in a mixed film regime rolling/sliding configuration on the MTM at 50°C and at 150°C. These plots in Figures 4 and 5 illustrate the traction coefficient over time during a mixed film scuffing wear test. In Figure 6, the wear rate of each material is shown. This wear rate was determined by the total wear volume (μm^3) per millimeter traveled in the test. In Figure 5, a benchmark sample is added to illustrate a material that was developed for a non-vacuum application that illustrates exceptional anti-scuffing performance. This is a target to work towards for anti-wear performance improvement of the MAC lubricants for space mechanisms.

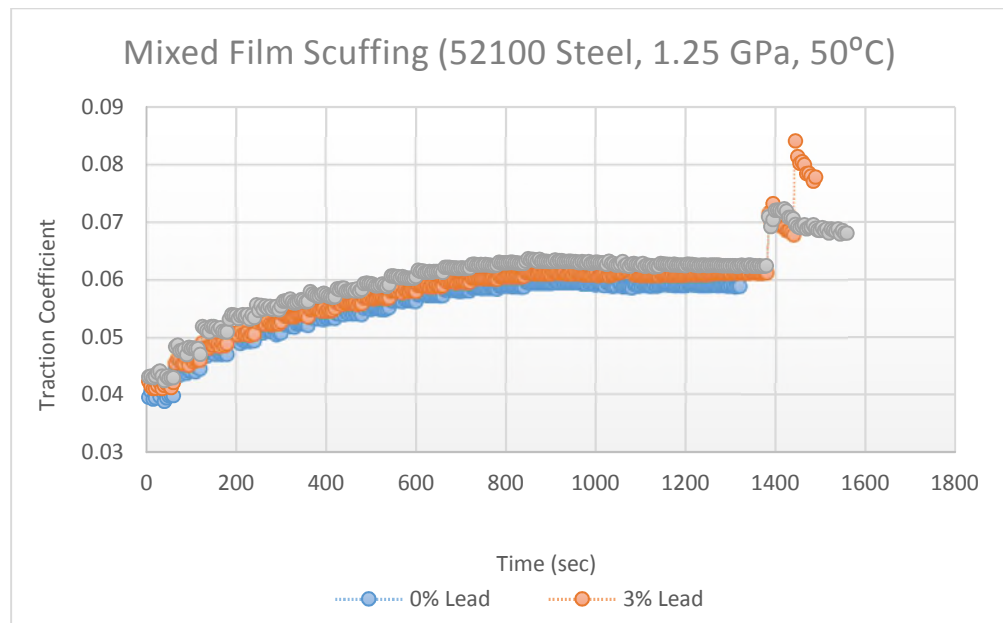


Figure 4. Mixed Film Progressive Speed Scuffing Test at 50°C

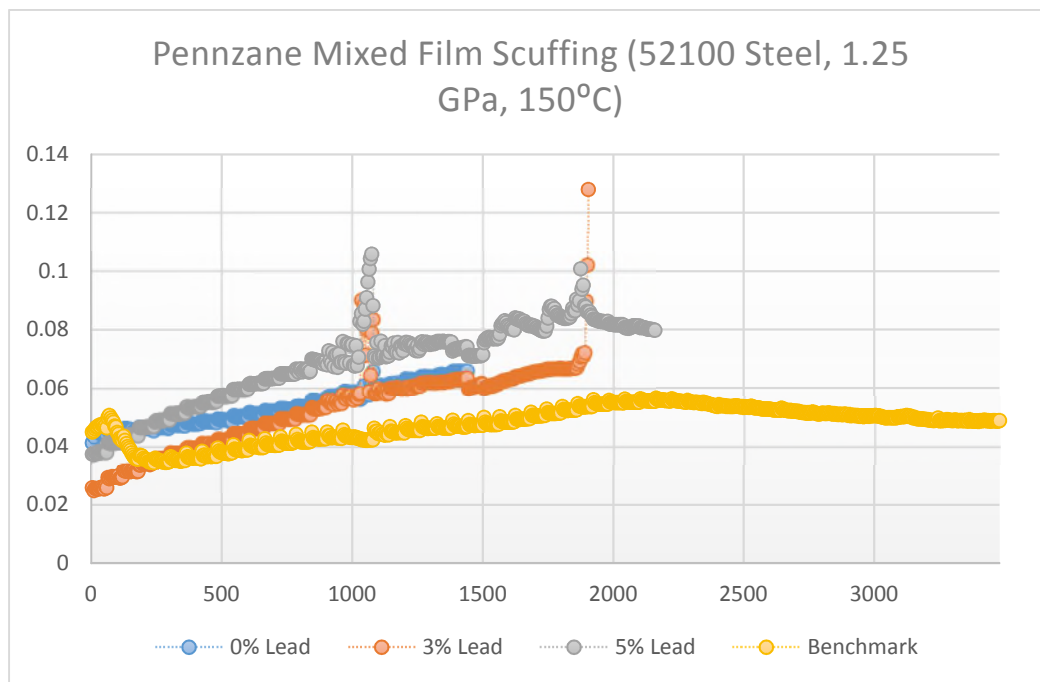


Figure 5. Mixed Film Progressive Speed Scuffing Test at 150°C

In general, anti-wear and EP additives are thought to reduce friction in a lubricated contact however in these scuffing wear tests, the friction for all the samples with lead naphthenate are generally higher in friction. Although the friction was higher, this did not create larger wear rates. The higher friction in the contact is caused by the formation of a lead tribofilm on the ball and disc. This tribofilm of lead formed on the disc surface while protecting the contact also increases the friction against the contact and tribofilm on the ball. This should not be considered a negative effect but instead illustrates the importance of run-in to allow lead naphthenate to chemisorb and physisorb on a metal surface.

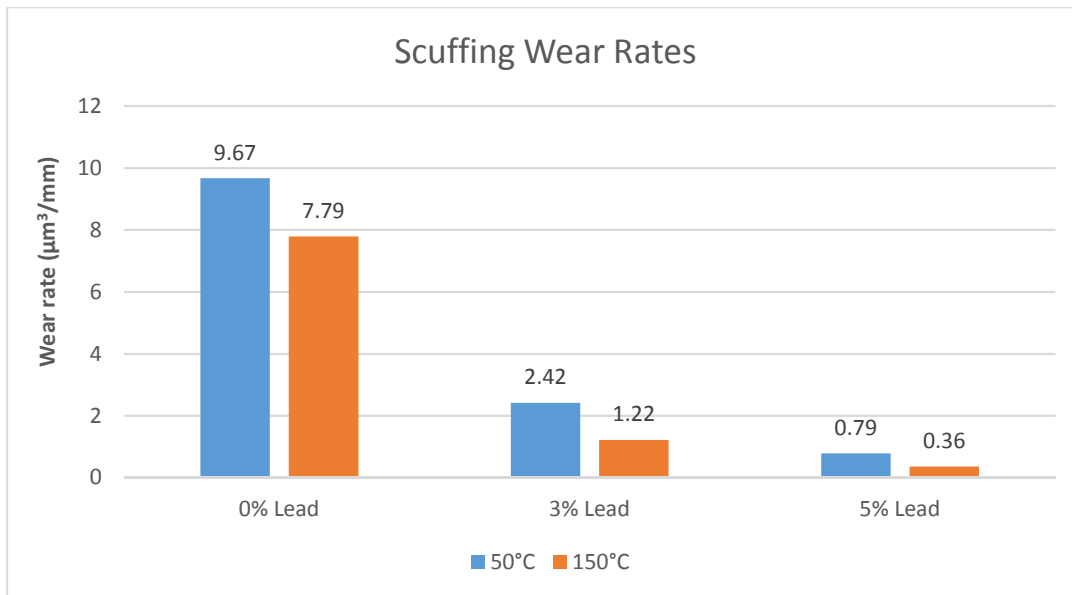


Figure 6. Mixed Film Scuffing Wear Rate Comparison

In Figures 7-9, the wear profiles for the 0%, 3%, and 5% lead are shown from one section of the tested disc. The wear pattern of the experiment using the 0% lead is a typical rough worn groove with indications of adhesive wear along the contact area. The 3% lead experiment shows a much shallower wear depth and overall a smoother wear pattern. The 5% lead experiment is the most interesting as there was almost no wear below the steel surface. In this experiment, it can be seen from the profile analysis that a 2 to 4- μm layer has been created on the surface of the steel. It is this surface that was then wearing away during the experiment. Upon further investigation using X-ray Spectroscopy, it was determined that this tribofilm that had been created on the surface of the steel was primarily composed of lead.

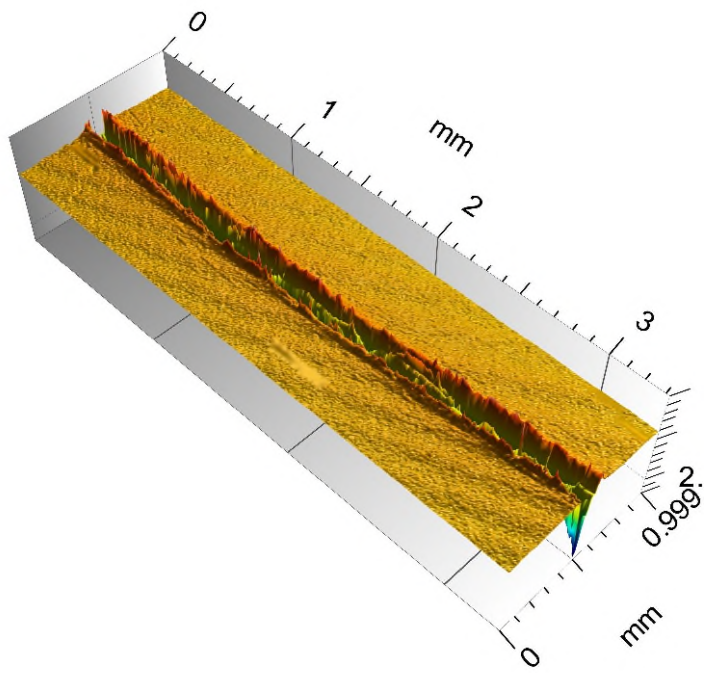


Figure 7. MTM Wear Profile of 0% Lead Naphthenate

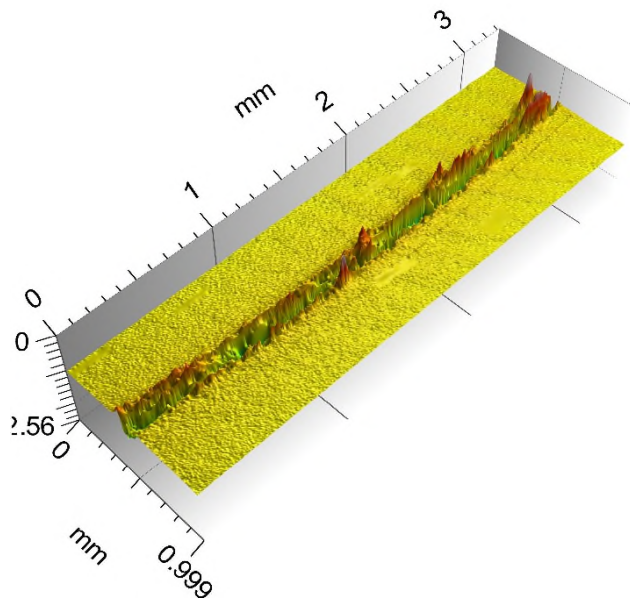


Figure 8. MTM Wear Profile of 3% Lead Naphthenate

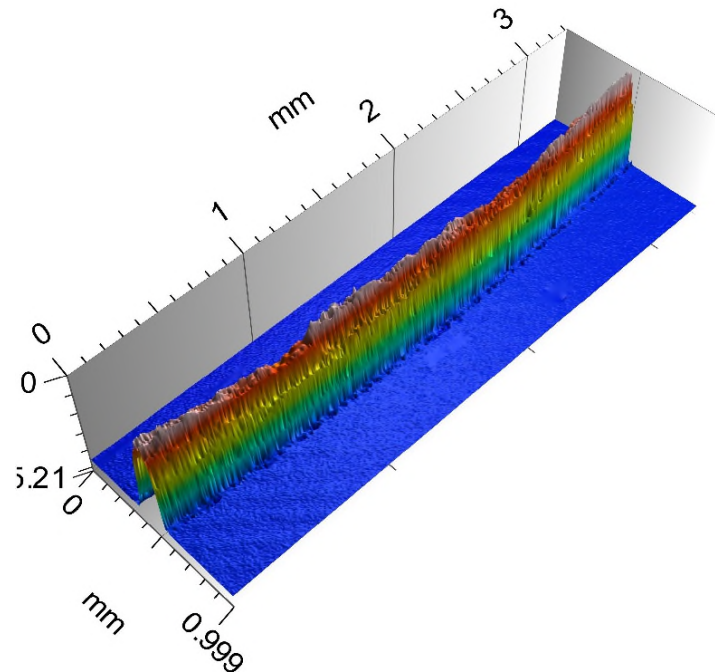


Figure 9. MTM Wear Profile of 5% Lead Naphthenate

From these results, we can see that there is a transition point in the concentration of lead in these MAC fluids and how it reacts with the surface metal to form an anti-wear tribofilm. It should be noted, that this phenomenon was not seen in the SRV testing. It is believed that the aggressive sliding in the SRV test creates an entirely separate wear mechanism that prevents the lead naphthenate from reacting with the surface and building a strong tribofilm. In the MTM testing, there is a mixed rolling/sliding which will promote a tribofilm to be created in a fashion much more similar to bearings and gears. This agrees and confirms work done by Carre et al [11] where it was found in ball bearing test data that lead naphthenate reacts with metal wear particles to create lead-containing surface coatings.

Conclusions

In previous studies done on lead naphthenate using the SRV and other sliding tribometers, results have typically been inconclusive regarding the efficacy of this additive to protect a lubricated contact. The standard SRV testing includes conditions that could be inappropriate for evaluating many anti-wear additives including lead naphthenate. This includes the sliding speed which would create a thicker film preventing the additive function from being studied. The contact stress is also much higher in standard ASTM tests which will influence how the tribofilms are created and in the case of lead naphthenate, the higher contact stresses will create additional wear which will react and consume available lead naphthenate making it unavailable to create a protective tribofilm. From this research, the following conclusions were found.

SRV Oscillatory sliding experiments

- At 20°C in pure oscillatory sliding testing, it was shown that samples with lead naphthenate used as an anti-wear additive outperformed neat MAC samples in all experiments. Under vacuum conditions, the samples with lead naphthenate offered twice the wear protection with 440C performing the best.
- At 75°C in pure oscillatory sliding testing on 52100 steel, samples with lead naphthenate in an atmospheric environment performed worse as the concentration of lead increased. However, when in a vacuum environment, as the concentration increased the wear rate decreased.
- At 75°C in pure oscillatory sliding testing on 440C, samples with lead offered up to twice the wear protection over the neat samples in a vacuum environment.
- Lead Naphthenate had better anti-wear performance at lower temperatures and increasing the amount of lead directly reduced the wear rate. At higher temperatures the wear rate was almost double for the highest lead loading across all tests.

MTM mixed rolling/sliding experiments

- At 50°C in the counter-rotation wear test, lead naphthenate offered three times the wear protection when in a 3% concentration and eleven times the protection for 5% lead compared to the neat MAC fluid.
- At 150°C in the counter-rotation wear test, lead naphthenate offered five times the wear protection when in a 3% concentration and twenty times the protection for 5% lead compared to the neat MAC fluid.
- There appears to be a transition point between 3% and 5% lead naphthenate where the available lead can react with both the surface and worn metal to create a strong lead anti-wear tribofilm. This tribofilm that is created is between 2-4 µm thick and while it will cause an overall increase in friction at the surface, the wear of the contact is greatly reduced.
- Lead Naphthenate had better anti-wear performance at high temperatures and increasing the amount of lead directly reduced the wear rate.

Lessons Learned

- The additive function of lead naphthenate is a combination of physical absorption through rubbing or pressure and chemisorption.
- Depending on the mechanics in the contact (sliding versus rolling), the effect of temperature had a significant effect. This appears to indicate that higher concentrations of lead would be required for more severe applications involving pure sliding and/or high temperatures as the lead is consumed faster through reaction with surface layer steel oxides and sublayers.
- In rolling and mixed contacts, lead naphthenate creates a strong tribofilm on the steel surface that aids in protecting from wear but at the same time will increase the friction in the contact.
- The formation and durability of lead naphthenate tribofilm is dependent on the environment with higher performance coming under vacuum conditions. It is also believed the lack of oxygen promotes this life due to the lack of oxide formation on the steel and degradation of the lead naphthenate.
- In general, an increase in lead content will decrease the wear rate.

Acknowledgements

I would like to thank the team at Nye Lubricants specifically Craig Deschenes for providing the samples of the lead based Pennzane, Allison McGlynn for the MTM testing and profilometry, and Paul Moses for running the SRV testing and profilometry.

References

- [1] Jason Galary. Rolling Wear and Fatigue in Lubricated Contacts. PhD thesis, University of Massachusetts at Dartmouth, 2018.
- [2] H Blok. Gear wear as related to viscosity of oil. JT Burwell, Jr., American Society of Metals, Ohio, pages 199-277, 1950.
- [3] HC Mougey and JO Almen. Extreme pressure lubricants. Proc. API, Refining Div, pages 76-94, 1931.
- [4] FF Musgrave. The development and lubrication of the automotive hypoid gear. J. Inst. Pet, 32:32-44, 1946.
- [5] Jason T Galary. Synthetic gear lubricants go green. Gear Solutions, 8(84):24 31, 2010.
- [6] Jason Galary. Study of wear properties of environmentally friendly lubricants for gearing applications as a function of film thickness transition. In Environmentally Considerate Lubricants. ASTM International, 2014.
- [7] LD Wedeven. Traction and film thickness measurements under starved elastohydrodynamic conditions. JOURNAL OF LUBRICATION TECHNOLOGY, TRANS. ASME, Series F, 97:321-329, 1975.
- [8] Bernard J Hamrock and Duncan Dowson. Ball bearing lubrication: the elastohydrodynamics of elliptical contacts. 1981.
- [9] St. Pierre, Nicole. "Use of 3D Optical Profilometry to Differentiate Between Additive Chemistry" STLE Annual Meeting, 2017
- [10] Didziulis, Stephen V., and Paul D. Fleischauer. "Chemistry of the extreme-pressure lubricant additive lead naphthenate on steel surfaces." Langmuir 7.12 (1991): 2981-2990.
- [11] Carre, D. J., P. A. Bertrand, and J. R. Lince. *Lead naphthenate additive tribochemistry in hydrocarbon oils*. No. TR-2002 (8565)-2. AEROSPACE CORP EL SEGUNDO CA LAB OPERATIONS, 2001.
- [12] Peterangelo, Stephen C., et al. "Improved additives for multiply alkylated cyclopentane-based lubricants." Lubrication Science 25.1 (2008): 31-41.
- [13] Marc Ingram, Clive Hamer, and Hugh Spikes. A new scuffing test using contra-rotation. Wear, 328:229 240, 2015.

Dynamic Behavior of Ball Bearings under Axial Vibration

Virgil Hinque * and René Seiler *

Abstract

The paper addresses the dynamics of ball bearings when exposed to vibration loads along their axis of rotation. Following common practice in space mechanisms design, the bearings are mounted in either hard preloaded or soft preloaded pairs. A computer-based model has been developed for the analysis and prediction of the load-deflection characteristics in bearing systems. Furthermore, the model may be used to quantify the maximum loads applied on the bearings and the resulting stresses during a vibration test or a spacecraft launch.

In parallel to the model development, an experimental test program has been carried out in order to get sufficient data for model correlation. In this context, the paper also elaborates on the post-processing of the acquired test signals and discusses specific effects, for instance nonlinearities due to the use of snubbers, in the time domain as well as in the frequency domain.

Introduction

Many space mechanisms use ball bearings for rotation functions. Therefore, assessing the bearing performance for the relevant environmental conditions is one of the typical challenges faced during the equipment design process. In this frame, it is common engineering practice to reduce the effect of a sine and random vibration environment to quasi-static equivalent loads and stresses. The relevant ball bearing systems often comprise two identical deep-groove or angular-contact bearings in an axially preloaded configuration. Several studies on the influence of the preload and other parameters on the structural behavior of such bearing assemblies have been done by the European Space Tribology Laboratory (ESTL). In a recent investigation, 25 ball bearing cartridges (“test units” or “bearing housings”) with different preload and snubber configurations were submitted to a series of sine and random vibration tests. The discussion of findings was mainly based on the analysis of frequency-domain data and bearing damage assessment via visual inspection [1].

The ESTL investigation inspired a number of ideas for continuation of the research, among others the development of a computer-based model that would be able to simulate the behavior of the bearing cartridges, especially those showing nonlinear features in their response. An adequate model should be able to predict the load transmission across the bearings in static and dynamic load situations. As the main sizing criterion for ball bearings is based on the allowable peak Hertzian contact pressure between the balls and the races [2], accurate knowledge of the maximum bearing loads is a key aspect for successful bearing selection and implementation in a space mechanism.

During the current investigation at the European Space Research and Technology Centre (ESTEC), a model was built using MATLAB®/Simulink®, with only the axial degree of freedom in a bearing taken into consideration. Because model correlation with real test results is of importance, a test program complementary to that reported in [1] has been conducted, with specific focus on the acquisition and interpretation of time-domain data. The following chapters describe the computer-based model, the design of the test units, as well as the details of the test campaign and corresponding results. The last part of the paper is dedicated to the comparison between the model output and the experimental test data.

* European Space Agency (ESA/ESTEC), Noordwijk, The Netherlands

Proceedings of the 44th Aerospace Mechanisms Symposium, NASA Glenn Research Center, May 16-18, 2018

Motivation and Background

Ball bearing systems in space mechanisms are usually composed of two angular contact or deep-groove bearings, which are preloaded along their axial direction in order to ensure a sufficiently high stiffness, the required precision of rotation, and a stable friction torque (within acceptable limits). The bearing preload can be applied using two different basic methods: hard or soft preload. In the hard preload method, a deflection is forced on the bearing pair by rigid mounting parts, corresponding to the desired preload magnitude (knowing the load-deflection characteristic of the bearings). The soft preload method relies on a compliant element, typically some spring-type component, to apply an axial force on the bearing pair corresponding to the controlled deflection of the compliant element (i.e., knowing its load-deflection curve). Both methods have their pros and cons [3] that will not be further detailed here for brevity. In fact, both methods are used in space mechanisms, and they imply different approaches for modelling and simulation. A schematic overview of both methods is given in Figure 1.

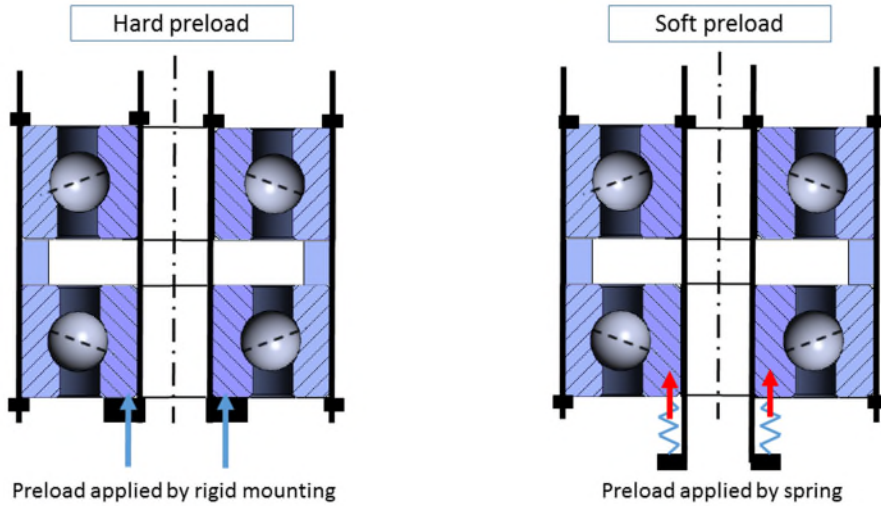


Figure 1. Hard and soft preload methods in ball bearing systems [3]

When an axial load is applied on a bearing pair (during launch or normal operation), it is generally shared between the two bearings, increasing the total load on one of them and gradually off-loading the other bearing. When a bearing gets completely off-loaded, the balls lose the controlled contact with the races, a phenomenon commonly known as gapping. This effect does not happen in the same way for the two different preload methods.

Hard preloaded bearings are pressed together with a displacement $\delta_{preload}$ corresponding to the preload magnitude on the load-deflection curve of an individual bearing. For reaching the onset of gapping in a bearing, it must be displaced by the same amount in the opposite direction, causing an axial load corresponding to $2 \cdot \delta_{preload}$ in the other bearing. Assuming a relationship between axial bearing load and deflection according to Equation 1 (see e.g. [4]) and knowing that the entire load will then be carried by the remaining bearing, the off-loading or gapping force may be estimated with:

$$F_{gapping} = k \cdot (2 \cdot \delta_{preload})^{\frac{3}{2}} = 2^{\frac{3}{2}} \cdot k \cdot \delta_{preload}^{\frac{3}{2}} = 2\sqrt{2} F_{preload} \approx 2.83 F_{preload} \quad (1)$$

where k is a bearing specific stiffness coefficient. The static behavior of a hard-preloaded bearing pair can be visualized according to Figure 2. When gapping has occurred in either direction, the load-deflection curve follows that of an individual bearing. Both characteristics sum up in the operating range without gapping. Therefore, the linearized stiffness around the preload point (origin in Figure 2) can be approximated by twice the stiffness of a single bearing at the preload magnitude.

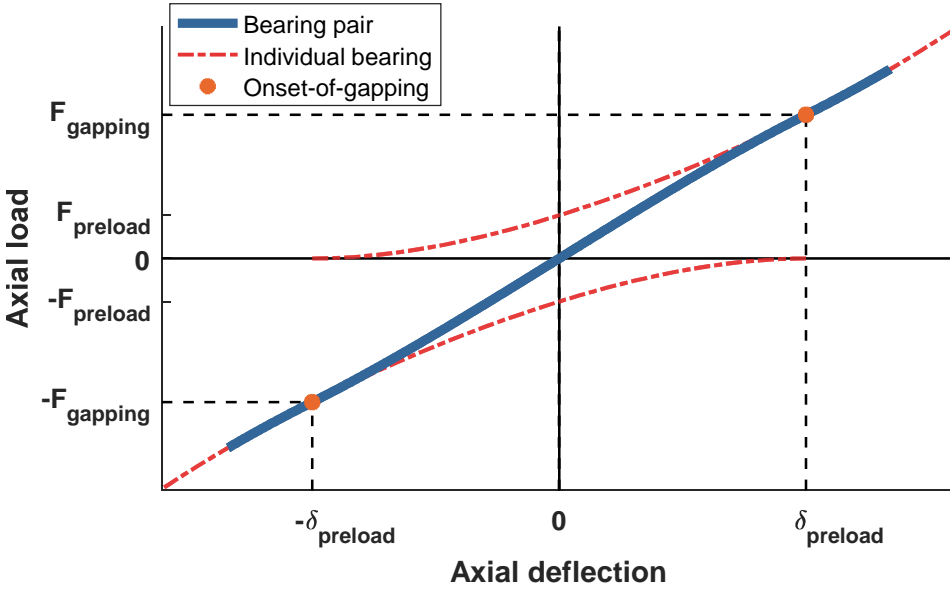


Figure 2. Axial load-deflection characteristic and gapping points for hard preloaded bearings

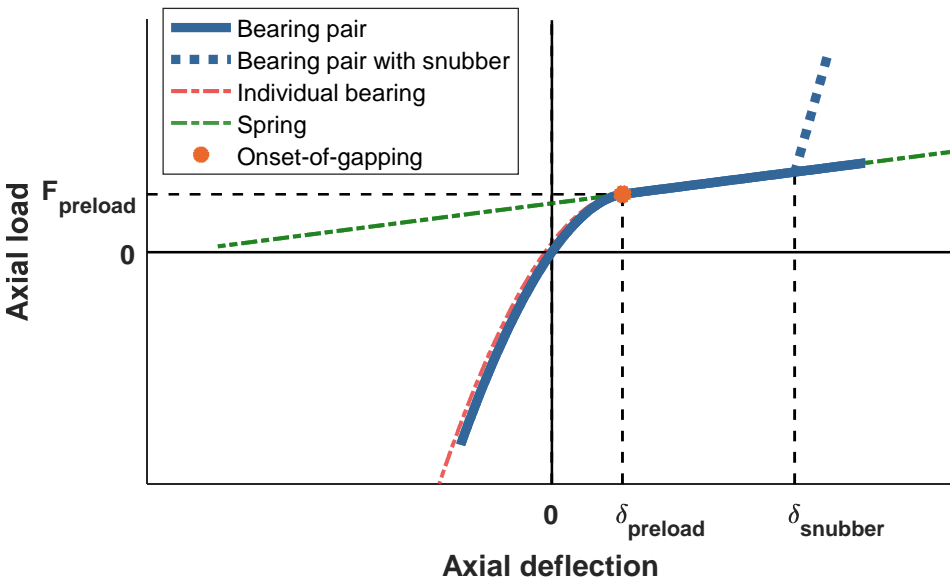


Figure 3. Axial load-deflection characteristic and gapping points for soft preloaded bearings

Soft preloaded bearing pairs have a static and dynamic behavior very different from that of hard preloaded pairs. Their fundamental difference in stiffness for the two loading directions causes an asymmetric load-deflection characteristic. Furthermore, off-loaded races may experience considerable axial travel, independent from the rest of the bearing. Therefore, their motion should be taken into account as additional mass bodies in a dynamic model. In order to remain concise, the related equations of motion and further model details are not presented here. As a key effect, when a force equivalent to the preload magnitude is applied on the preload spring via the adjacent bearing, gapping occurs in the opposite bearing. If the force keeps increasing, the spring stiffness will dominate the load-deflection characteristic of the bearing system. Without gapping, the stiffness of the bearing opposite to the spring is dominating. Therefore, the linearized stiffness of the bearing system can be approximated by the stiffness of a single bearing at the preload magnitude. The load deflection curve of a soft preloaded bearing pair is presented in Figure 3. Hence, soft

preloaded bearing pairs tend to be more compliant in general, and gapping occurs at load points lower than with equivalent bearing pairs under hard preload. Sometimes, snubbers are added to limit the stroke in the gapping range by adding a mechanical end-stop. The snubber effect can also be seen in Figure 3.

Modelling and Simulation Approach

In general, ball bearings have nonlinear load-deflection characteristics, with substantial asymmetries and possibly additional dynamic effects, e.g. due to snubbers, in the soft preloaded case. Therefore, predicting their dynamic behavior may be rather challenging. This has been the main reason to create a computer-based model for the investigation. The widely used software package MATLAB®/Simulink® was selected for modelling and simulation. At this stage of the research, the dynamic model only takes the axial degree of freedom of the bearings into account. In this context, a numerical solver integrates the equations of motion for the bearing system and generates results in the time domain. The load-deflection characteristics of the bearings are modelled on the basis of the bearing geometry, mounting and preload configuration as well as material parameters, referring to established bearing analysis, see for instance in [5]. Under quasi-static assumptions, they are pre-computed by an iterative numerical solver (based on the same algorithm as used in the ball bearing software tool CABARET [6]) before running a dynamic simulation, and they form the “backbone” of the model. Furthermore, other relevant phenomena, e.g. gapping and snubber contact, have been added to the dynamic model.

As part of the modelling and simulation process (see overall structure in Figure 4), the user can input any time-domain profile for housing acceleration (base excitation), equivalent to a shaker test. Alternatively, a force profile may be applied on the shaft, simulating a static tension/compression test. On this basis, the dynamic behavior of the individual bodies is computed, including the bearing loads. A separate post-processing module has been developed to extract additional values of interest like contact stresses or gapping distances.

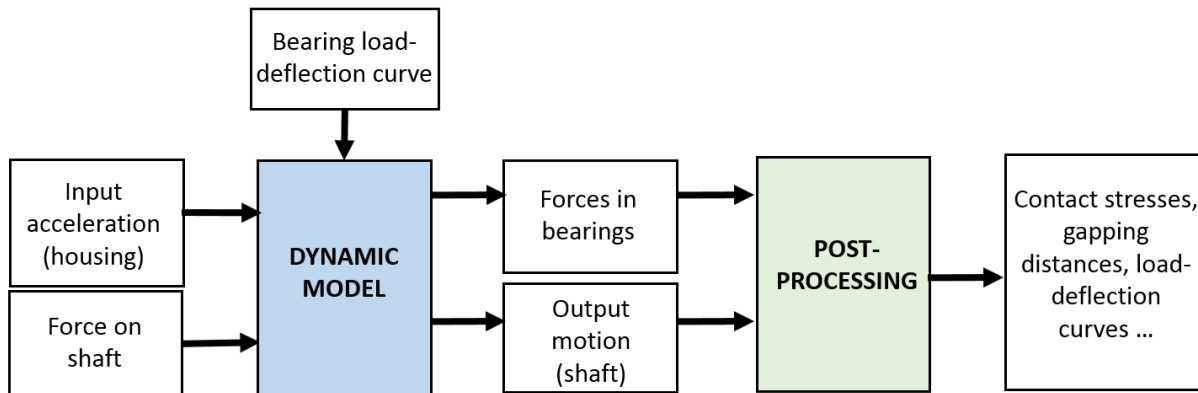


Figure 4. Overall structure of the modelling and simulation approach

Experimental Test Set-up

In order to correlate the model results with real experimental data, a vibration test program has been carried out. Three different bearing cartridges have been used as test units. In fact, the same test articles had been used before in a related investigation led by ESTL [1]. All of them comprise two bearings preloaded in a back-to-back configuration. Their design is shown in Figure 5. On the top of the shaft, a dummy mass of 1.25 kg has been attached, with the option of increasing the total mass by an additional 0.625 kg. For the soft preloaded bearing cartridges, a set of Belleville washers (conical disc springs) at the bottom end of the shaft pushes on the inner ring of the lower bearing. The inner ring has a clearance fit, i.e. is allowed to slide along the shaft. Moreover, a snubber is added at the top of the bearing assembly. When touching a shoulder

on the shaft, it prevents excessive displacements during gapping. The three test units differ from each other in terms of their preload characteristics, summarized in Table 1.

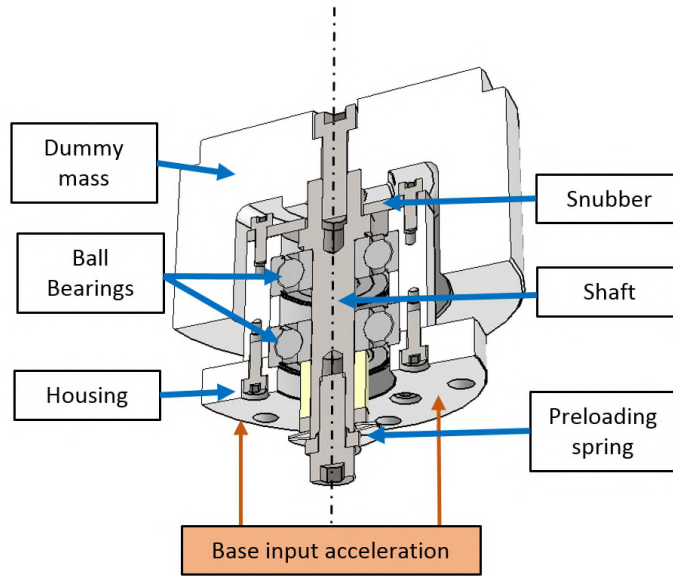


Figure 5. Cross section of the bearing cartridges (test units)

During the test program, the bearing cartridges were mounted on two different shakers, the first one for low amplitudes and the second for higher-level vibrations. The test units were only excited along the axial direction. One accelerometer (two for the stronger shaker) was used for input acceleration control and monitoring. Another accelerometer was placed on the dummy mass. Furthermore, three load cells were mounted in the adapter placed between the shaker and the test unit. Their purpose was to monitor the shaker input force by direct measurement. The phase of the force signals was also used to identify the direction of the structural modes observed, and to discriminate any non-axial modes. The test set-ups are depicted in Figure 6. In the left picture, a test unit with standard dummy mass is mounted on the small shaker. In the right picture, a test unit with additional dummy mass sits on the stronger shaker.

Table 1. Test unit preload parameters

Test ID	Preload type	Preload magnitude	Preload stiffness
3	Soft	20 N	250 N/mm
6	Soft	20 N	900 N/mm
22	Hard	160 N	(not applicable)

The test units have been exposed to a number of vibration tests: sine sweep, constant frequency sine with different amplitudes and random vibration.

Summary of Test Results

For all the tests, the time-domain signals of all sensors were recorded. The sine sweeps were carried out from 20 Hz to 2 kHz, with an input amplitude varying from 0.1 g to 1 g for the soft preload test units and from 1 g to 9 g for that with hard preload. The random tests ranged from 0.1 g_{rms} to 9 g_{rms} for all units. The constant frequency sines were applied at 5 different frequencies around the first main resonance of the test units (two below, one at the resonance frequency and two above). The amplitude ranged from 0.2 g to 5 g for the soft preload units and from 1 g to 58 g for the hard preload unit. Most of the tests were repeated using the additional dummy mass. A comparison of the low-level sine sweeps before and after the high-level runs confirmed that the dynamic response of the bearing cartridges was not affected by the tests.

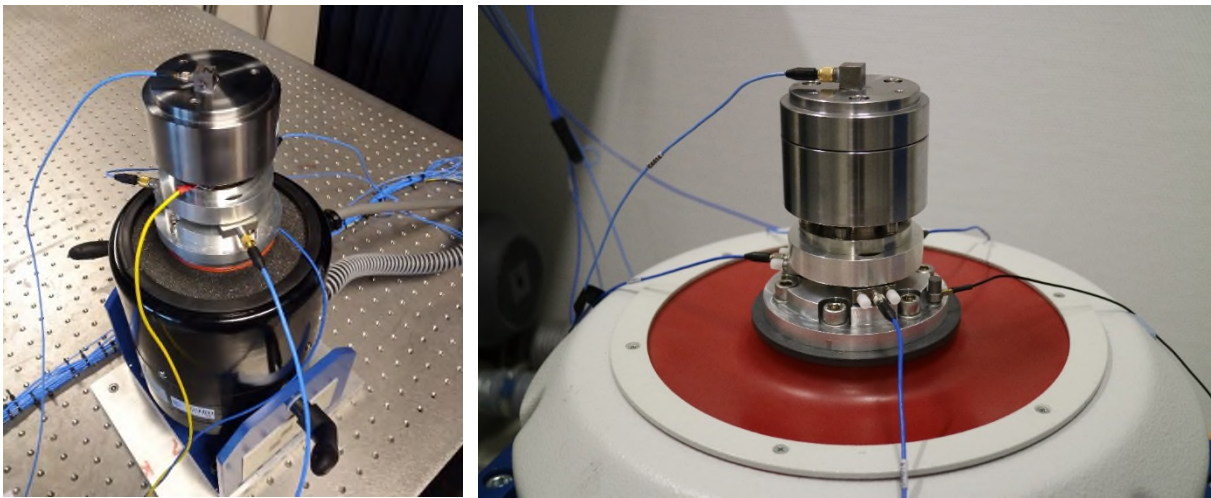


Figure 6. Test units mounted on the small and stronger shaker, including instrumentation

Discussion of Test Results

Frequency Domain

A first overview of the results can be obtained by inspecting the estimated Power Spectral Densities (PSDs) of the output (response) acceleration, for random excitation (see Figure 7). For the hard preload test unit, the resonance frequency decreases slightly with increasing excitation magnitude. Some other features have been found in the PSD plots, but a closer analysis of the load cell phases indicated that those features resulted from a cross-coupling between a radial mode and the axial excitation. For the soft preload cases, it is found that the resonance frequency (and, hence, the apparent stiffness of the bearing system) starts decreasing with an increasing excitation magnitude. However, when the excitation becomes high enough to reach snubber contact, then the resonance frequency of the system starts rising again. Moreover, higher frequency content is introduced due to contact with the snubber.

Moreover, Figure 8 underlines that the quality factor and the resonance frequency are linked, as functions of the excitation level. Overall, the observations have confirmed the findings by ESTL derived from the previous test campaign [1].

Time Domain (for constant frequency sine vibration input)

In the runs with constant frequency sine excitation, the increasing input levels were maintained over sufficiently long periods of time in order to reach steady state. Thanks to this, the measurement noise and other random components could be reduced by coherent averaging of the response signals. The averaged responses are shown for the hard preload case and one soft preload case (#3) in Figure 9. While the hard preload test unit behaves symmetrically, the acceleration asymmetry is clearly visible for the soft preload test unit.

At resonance, housing acceleration (input) and dummy mass and shaft acceleration (output) are shifted in phase. Therefore, the bearings undergo higher deflections. Double integration of input and output accelerations and subsequent evaluation of their difference allows to estimate the relative displacement between housing and dummy mass and shaft. Consequently, multiplying the dummy mass acceleration by the total moving mass (dummy mass plus shaft) results in a good estimate of the dynamic force applied on the shaft. This allows for a comparison with the theoretical (quasi-static) load-deflection curve presented in Figure 2. However, it should be kept in mind that the complete equation of motion comprises:

$$m_{shaft}\ddot{z}_{shaft} = K\{z_{shaft}, z_{housing}\} - L\{\dot{z}_{shaft}, \dot{z}_{housing}, z_{shaft}, z_{housing}, \dots\} \quad (2)$$

where \mathbf{K} is a generalized stiffness term considering the nonlinear load-deflection characteristic of a bearing system as described in Figure 2 and Figure 3, and \mathbf{L} is a generalized loss term catering for viscous damping, contact interface friction and other dissipative effects. Thus, the loss term manifests itself in the form of hysteresis between the load-deflection curves for the two motion directions.

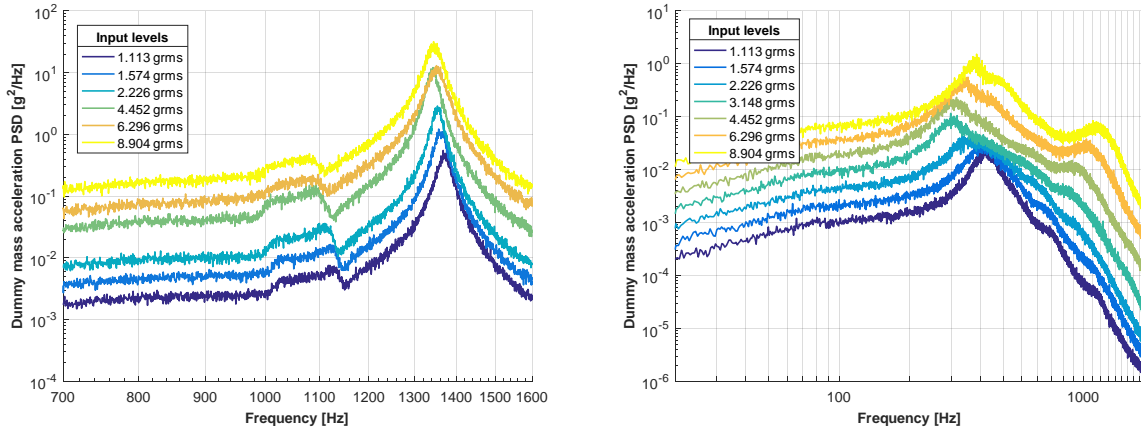


Figure 7. Output acceleration PSD for the hard preload unit (left) and soft preload unit #3 (right)

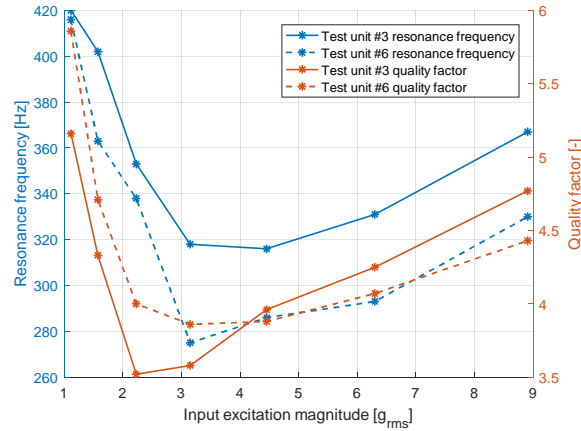


Figure 8. Quality factor and resonance frequency vs. excitation magnitude

The corresponding results are presented in Figure 10, including the modelled load-deflection curves. The hard preload unit reacts in an almost perfectly linearly form (also acknowledging the rather high preload). The hysteresis and, hence, the corresponding loss term is very small. The dummy mass and shaft load reaches ~1200 N, which is about 7.5 times the bearing preload. Therefore, considerable gapping is occurring in the bearings, however the transition to and from the gapping state appears entirely smooth.

Only one of the soft preload units (#3) is presented for brevity. As the main difference compared to the hard preload case, the load (and, hence, the stiffness) evolves in a much more nonlinear way over the entire deflection range, as expected. The bearing system enters the gapping state (= “compliant range” in spring compression direction) at approximately 50 N, which is around 2.5 times the preload. However, in the spring relaxation direction, the gapping state is left at around 20 N, i.e. at the preload. Such discrepancy may be explained by a combination of elastic spring force and viscous damping and interface friction forces at the Belleville washers. Evidently, a considerable amount of energy is dissipated in the gapping process and the interaction with the preload spring.

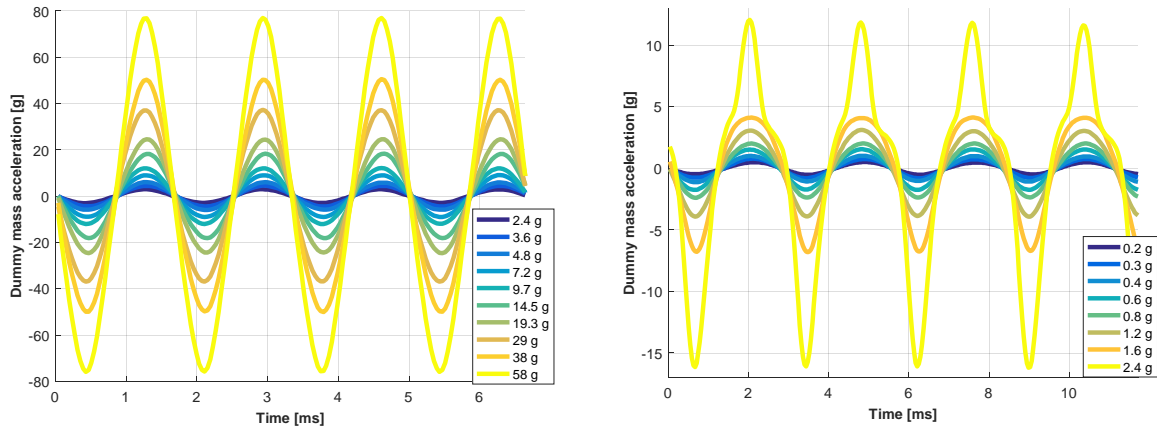


Figure 9. Steady-state response of the hard preload unit (left) and soft preload unit #3 (right), constant frequency excitation with increasing amplitude

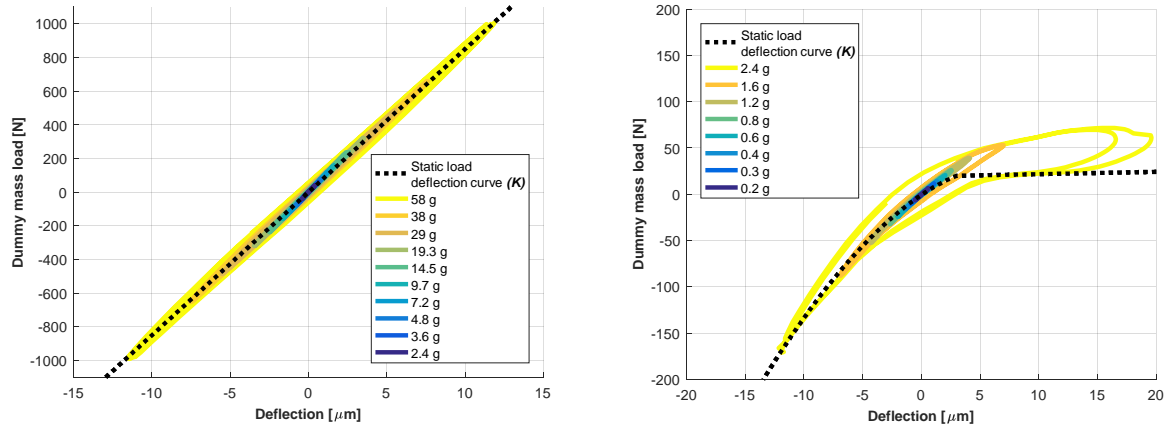


Figure 10. Quasi-static force vs. deflection for hard preload (left) and soft preload (#3, right)

Time Domain (for random vibration input)

For the random vibration tests, the histograms of the input and output accelerations have been analyzed to infer on the underlying statistics. Figure 11 shows the histograms for the hard preload unit and increasing levels of excitation. The hard preload unit maintains a normally distributed output (no skewness) across all excitation levels applied, even when high peak amplitudes (and therefore gapping) are reached. The red curve represents a best-fit analytical model of a normal distribution.

Figure 12 shows the histograms for one of the soft preload test units. For low levels of excitation, any distortions (as identified via skewness) remain small. However, the response gets more and more skewed (asymmetric) with increasing input power. In this context, the left side of the histogram corresponds to the gapping state. For high-level excitation (see right histogram), two modes become evident as spiky features. They correspond to the compression and relaxation processes of the preload spring. Furthermore, when the shaft hits the snubber, the load increases rapidly, which may be noticed as the elevated left-side tail of the histogram. The right-side tail of the distribution corresponds to the stiff range of bearing compression. In fact, the highest bearing loads are reached in that region.

A common practice to approximate the response RMS level can be found with the Miles formula [7]. Using the resulting RMS value (standard deviation), a 3σ value can be calculated and used to size the bearings. Table 2 summarizes the number of dummy mass acceleration samples (and indirectly, the bearing forces)

that are greater than the related 3σ value. For this purpose, the natural frequencies and quality factors for small levels of excitation have been applied in Miles formula. Because the 3σ rule is based on the fact that only 0.27% of the samples will be higher (normally distributed samples), it becomes evident that this rule is only valid for the hard preload unit, for the specific cases investigated.

The dummy mass acceleration can be related to the dummy mass load and, hence, to the bearing loads. On this basis, using the bearing design parameters, the model can deliver the Hertzian contact stress in the ball-race contacts (equal load distribution among all balls in axial direction). The maximum Hertzian contact pressure reached during in the tests (estimated via the maximum output acceleration) are compared to those obtained via the predicted 3σ values in Table 3. It can be seen that the extreme value events are significantly higher than what would be predicted with the Miles formula (even for the hard preload unit, although the predictions are closer).

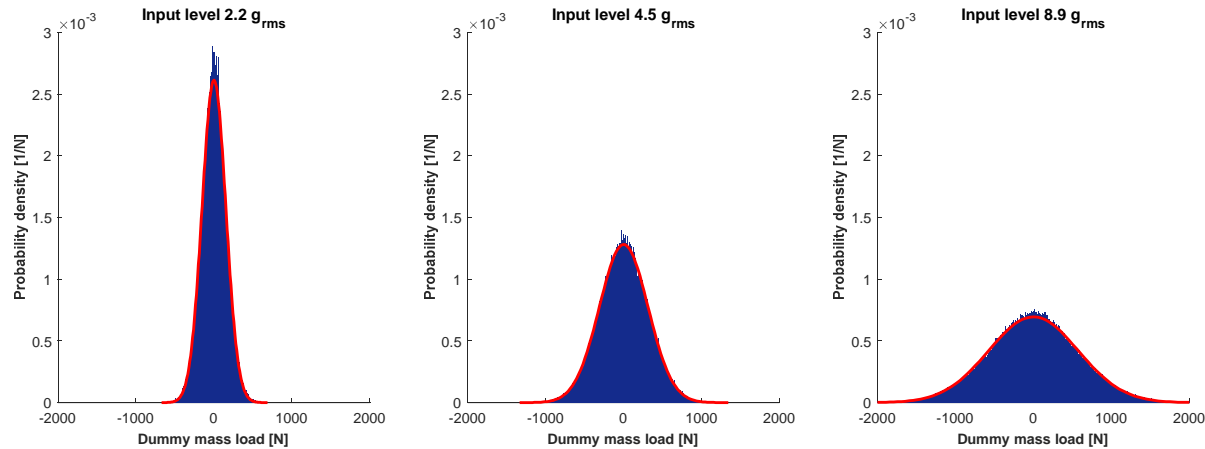


Figure 11. Histograms of the output acceleration for random excitation 2.2, 4.5 and 8.9 g_{rms} (hard preload unit)

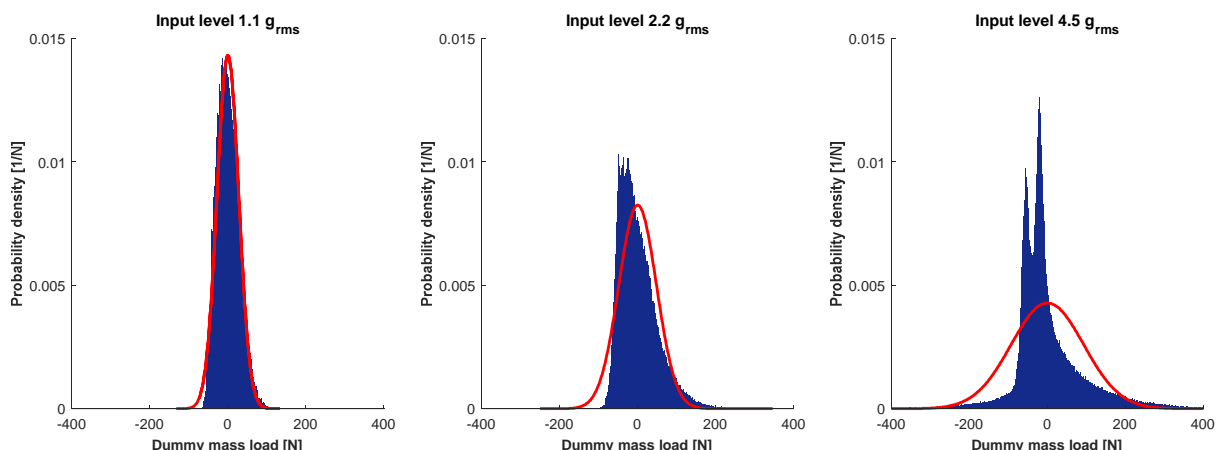


Figure 12. Histograms of the output acceleration for random excitation 1.1, 2.2 and 4.5 g_{rms} (soft preload unit #3)

Table 2. Percentage of output acceleration samples exceeding the related 3σ value

Test unit ID	1.1 g _{rms}	1.6 g _{rms}	2.2 g _{rms}	4.5 g _{rms}	6.3 g _{rms}	8.9 g _{rms}
#3 (soft)	1.04%	0.62%	0.78%	1.54%	3.07%	5.51%
#6 (soft)	1.41%	1.92%	1.21%	1.70%	2.88%	2.64%
#22 (hard)	0.37%	0.37%	0.57%	0.26%	0.15%	0.29%

Table 3. Comparison of maximum contact pressures with 3σ equivalent values

Test unit ID	Max. Hertzian Pressure [MPa]	1.1 g _{rms}	1.6 g _{rms}	2.2 g _{rms}	4.5 g _{rms}	6.3 g _{rms}	8.9 g _{rms}
#3 (soft)	3 σ	940	1120	1188	1569	1693	1830
	peak	1382	1486	1772	2240	2478	2595
#6 (soft)	3 σ	975	1102	1299	1386	1605	1739
	peak	1534	1661	1902	2049	2171	2563
#22 (hard)	3 σ	1300	1483	1651	2104	2308	2543
	peak	1541	1762	1949	2457	2613	2899

Model Correlation

Ball Bearing Stiffness

Around the preload point and for low levels of vibration, the stiffness of the bearing cartridges can be linearized. This “tangential” or “differential” stiffness (slope of the load-deflection curve around the origin) relates to the resonance frequency.

The load-deflection curves of a single bearing, as predicted using the model equations in [5] and derived from the test results, are compared in Figure 13 for the soft preload units (left) and for the hard preload unit (right). Several geometry parameters are used to compute the load-deflection characteristics. The one with the highest uncertainty (and the strongest effect on the stiffness) is the contact angle, linked to the radial clearance in deep groove bearings. A range from 5 to 20 degrees is indicated in Figure 13. As stated before, single bearings of the soft preload units can be represented and compared directly, just by plotting the non-gapping range and shifting it by the preload magnitude. Indeed, the stiffness of the single bearing dominates that range. The stiffness of a single bearing in a hard preload configuration is more difficult to extract from the test results. Nevertheless, a linearized approximation may be obtained by dividing the stiffness by two and shifting it by the preload magnitude and corresponding deflection.

Via above approach, the free contact angle of test unit #3 and #6 is estimated with approximately 13 degrees. The stiffness of the hard preload test unit is higher than expected with such free contact angle. At this stage of the investigation, two potential reasons are considered: The free contact angle might actually be higher than 13 degrees, or the preload magnitude might be higher than expected, keeping in mind that a hard preload is set by a small deflection with high precision, which is more sensitive to errors. Another interesting observation comprises the load-deflection characteristic for the soft preload cases: It can be fit with a function $F = k \cdot \delta^x$, where the exponent $x \approx 2.1$, which is higher than the 1.5 used to derive the rule of $F_{gapping} \approx 2.83 \cdot F_{preload}$. In order to correlate the hard preload results with the model, another bearing model using a different contact angle and preload magnitude was assumed. Its characteristic corresponds to a model function with an exponent of 1.79, closer to 1.5.

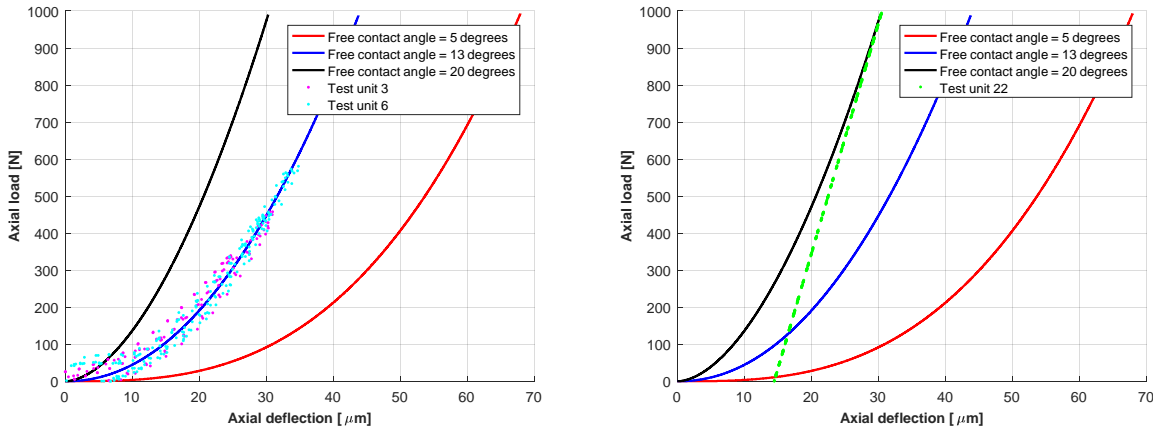


Figure 13. Load-deflection characteristics of the test bearings vs. model output
(left: hard preload unit, right: soft preload units)

Sine Sweeps Results

A comparison between the Simulink® model output and the test results is made using the output of the sine sweeps runs. **Figure 14** shows the resulting peak acceleration vs. excitation frequency. The peak amplitude is presented for both motion directions acknowledging the strong asymmetry in the soft preload cases.

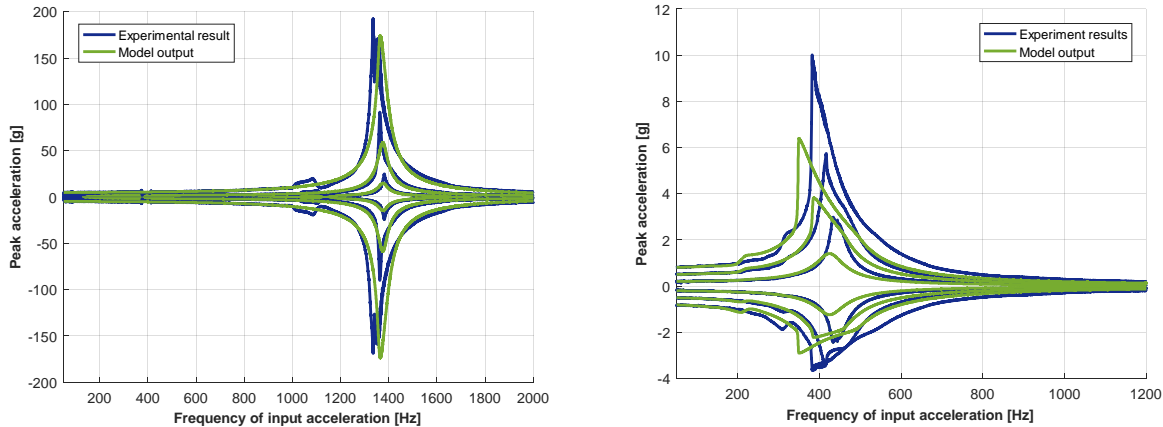


Figure 14. Output acceleration magnitude vs. excitation frequency
(left: hard preload unit, right: soft preload unit #3)

For both test units, the largest difference is found with the higher quality factor derived from the test data. This may be due to the fact that the input acceleration was somewhat disturbed during the test runs because the shaker controller had some problems to keep the input level steady (possibly a sign of shaker saturation). For the hard preload unit, the system acts in a fairly linear way (left plot in Figure 14). Also for the soft preload unit, the overall evolution of the response is broadly similar. However, the nearly vertical rise at about 380 Hz and the pronounced asymmetry around the resonance for the highest excitation level (right plot in Figure 14) is typical of a non-linear transition in a vibrating system. In this particular case, it happens when the dummy mass acceleration is high enough to create gapping and to reach the spring compression range in the load-deflection characteristic.

In Figure 15, the deflection is plotted against the force on the shaft for the sine sweep with the highest amplitude. In the test results, the gapping range appears stiffer than predicted by the model. This was already found in Figure 10, and is probably caused by friction and other effects in the spring assembly. As

a major element of the continued investigation, it will be attempted to measure the static load-deflection characteristic of the bearing cartridges with higher precision, for a more comprehensive model validation.

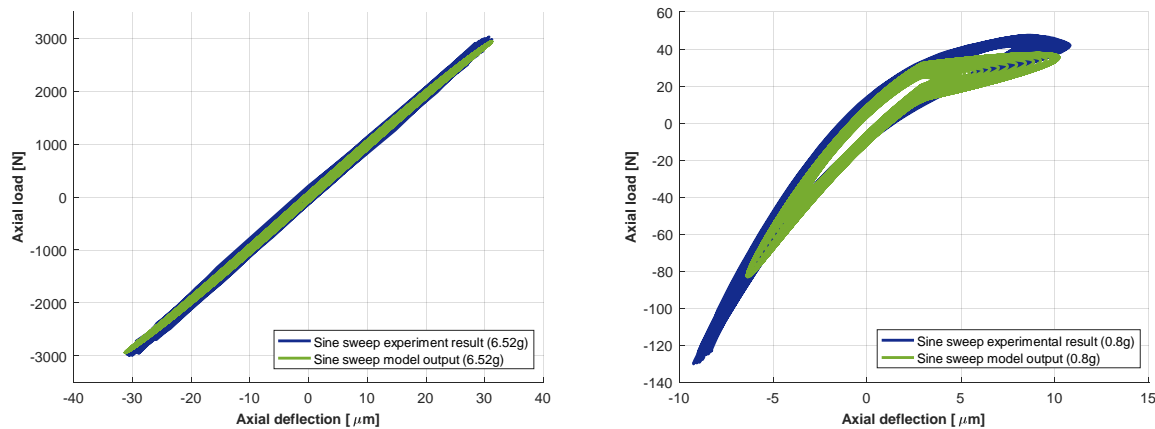


Figure 15. Load-deflection characteristics of the test units for the highest amplitude sine sweeps (left: hard preload unit; right: soft preload unit #3)

Constant Frequency Sine Vibration Input and Snubber Interaction

In some of the constant frequency sine runs with the soft preload units, the deflection in the gapping range was large enough to hit the snubber. This interaction is also represented in the Simulink® model. Figure 16 shows the model output compared to the experimental results for test units #3 and #6.

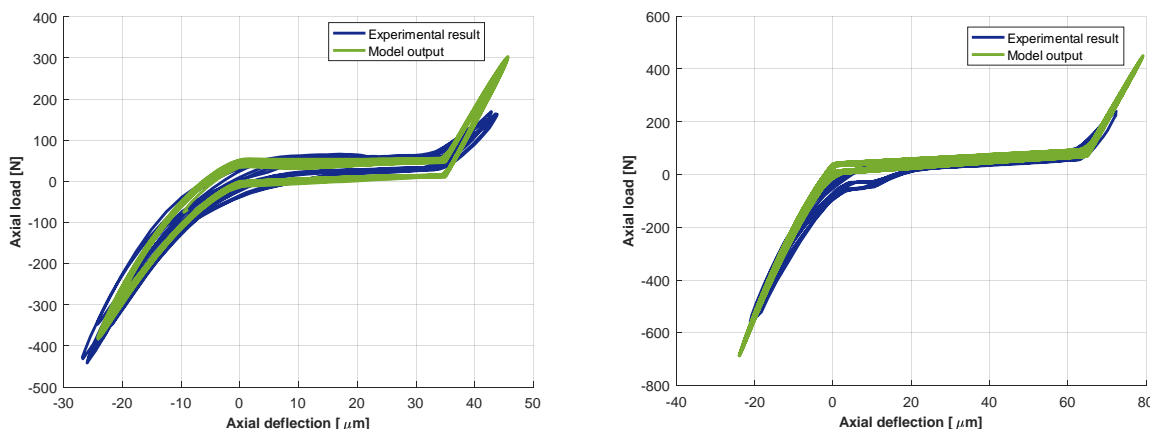


Figure 16. Snubber interaction for the soft preload units (left: #3, right: #6)

The blue lines represent the model output while the green lines are the experimental results. Within the long and nearly horizontal stroke, it can be seen that the predicted stiffness of the spring matches the test data rather well. At the right end of the stroke, the snubber interaction is evident. However, the stiffness transition and evolution in the vibrations test results appears smoother than in the simulated output, an area for future model refinement.

In general, it can be noticed that the behavior of the bearing system is more complex when the snubber is hit. Concerning the maximum load reached for re-contact after gapping (left end of the graphs), the model shows good correlation. However, the load and stroke reached when hitting the snubber is not well predicted yet (right end of the graphs).

Random Vibration Results

Since the model will also accept a random time series as input, the signal acquired from the input accelerometer (on the shaker interface) can be directly used as model excitation for comparison of the results. This avoids any differences in the input due to shaker control, etc. The histograms of the resulting loads on the dummy mass are presented in Figure 17 and Figure 18.

For the hard preload case, the random vibration response of the model matches the test data rather closely, see Figure 17. Due to the skewness and relatively complex shape of the histograms for soft preload (Figure 18) a statistical interpretation tends to be more difficult than for the hard preload case. Nevertheless, the overall shapes of the model response histograms follow those for the test response. For the highest excitation (right plot in Figure 18), the two statistical modes, i.e. the two clearly separated spikes, are represented by only a single peak in the model response. This is explained by the fact that the hysteresis of the spring preload system is not fully represented in the model yet.

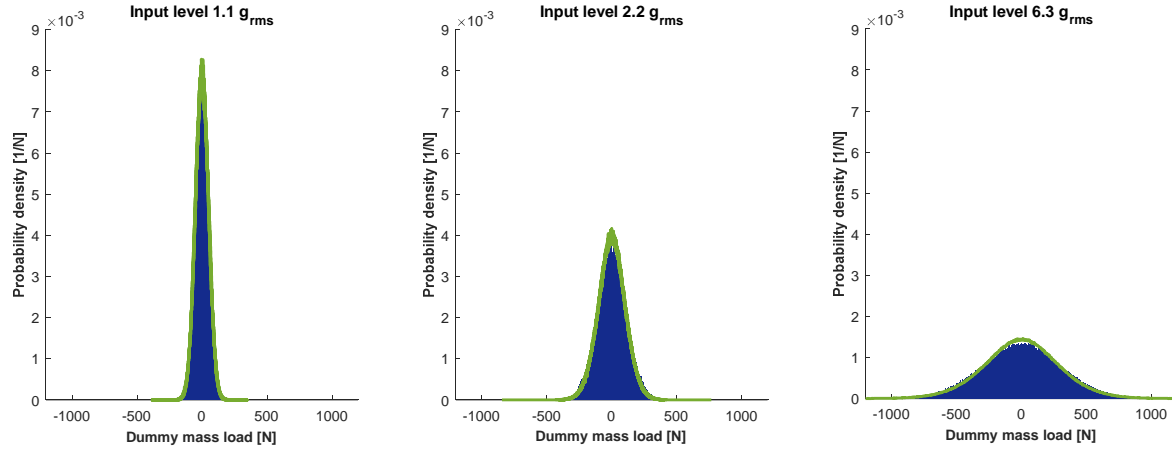


*Figure 17. Histograms of the dummy mass loads for the hard preload unit
(blue: derived from vibration test data, green: model output)*

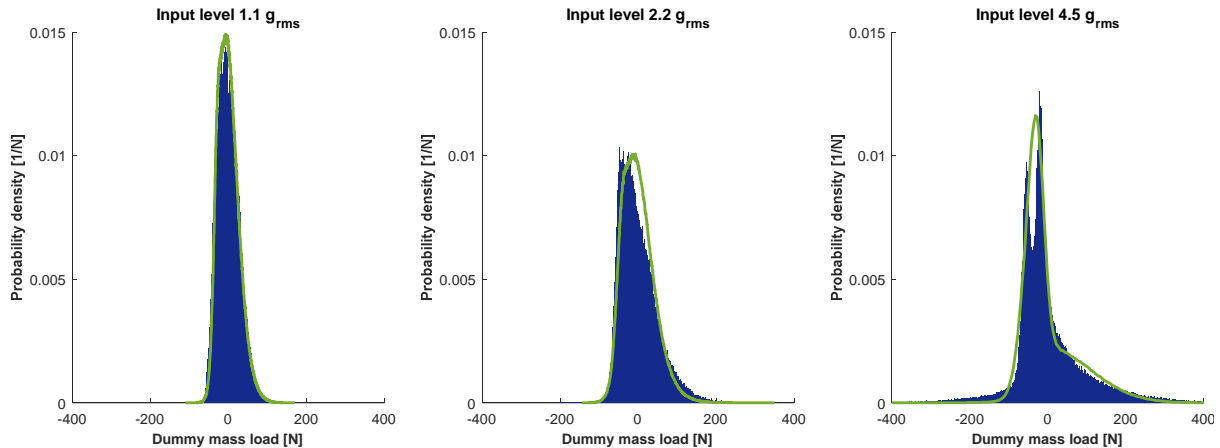


*Figure 18. Histograms of the dummy mass loads for the soft preload unit #3
(blue: derived from vibration test data, green: model output)*

Conclusions

Relying on earlier work regarding the vibration response of preloaded ball bearings, the investigation has focused on the dynamic behavior of simplified bearing systems. In this conjunction, a dynamic model for the axial degree of freedom has been developed in MATLAB®/Simulink®. As a key capacity beyond predicting the load-deflection characteristics of bearing systems, it produces a numerical solution to the dynamic problem. On top of this, a series of vibration tests has been performed on three sample bearing cartridges. For validation of the computer-based model, special attention has been given to the post-processing of the test results in the frequency domain as well as in the time domain.

The main findings of the investigation encompass the following aspects:

- In general, the behavior of hard preloaded bearings appears more linear and predictable with higher confidence than that of soft preloaded bearings. Snubber interactions in conjunction with gapping and hysteresis in soft preload systems are challenging details, which require further work.
- The model-based prediction of load-deflection characteristics relies on an accurate knowledge of the most relevant bearing design parameters (like the free contact angle), which appears difficult to obtain for individual bearing samples without dedicated measurements (among others, because of production tolerances).
- Performing static load tests to infer on the load-deflection characteristics of bearing systems may be helpful, however getting reliable results from static tests appears more difficult than expected (potential problems with test rig stiffness, sensor precision and parasitic effects).

Acknowledgments

In the frame of the ongoing research project, the authors gratefully acknowledge the cooperation and support by Grant Munro and Simon Lewis of the European Space Tribology Laboratory (ESTL, ESR Technology). Furthermore, the authors would like to thank Ronan Le Letty and Lionel Gaillard (ESTEC Mechanisms Section) for their encouragement and help, specifically regarding the in-house tests and analysis work.

References

1. Munro, G., Checkley, M., Forshaw, T., Seiler, R. "Preloaded Bearing Characteristics under Axial Vibration." *Proceedings of the 15th European Space Mechanisms and Tribology Symposium (ESMATS 2013)*, September 2013.
2. European Cooperation of Space Standardization (ECSS) "Space Engineering: Mechanisms." ECSS-E-ST-33-01C, Rev. 1, ESA, February 2017.
3. Videira, E., Lebreton, C., Gaillard, L., Lewis, S.D., "Guidelines for space mechanism ball bearing design assembly and preloading operations." *ADR, ESA and ESTL*, September 2013.
4. Guay, P., Frikha, A. "Ball Bearing Stiffness. A New Approach Offering Analytical Expressions." *Proceedings of the 16th European Space Mechanisms and Tribology Symposium (ESMATS 2015)*, September 2015.
5. Harris, T. A. "Rolling Bearing Analysis." Second edition, John Wiley and Sons, 1984.
6. Lewis, S. D. "Advanced bearing technology - Analysis and modelling report." ESTL/TM/119, European Space Tribology Laboratory, March 1991.
7. Sarafin, T. P. "Spacecraft Structures and Mechanisms." Springer, 1995.

The Design & Development of the Ocean Color Instrument Precision Superduplex Hybrid Bearing Cartridge

Joseph Schepis*, Timothy Woodard**, Claef Hakun*, Konrad Bergandy*, Joseph Church*, Peter Ward**, Michael Lee**, Alfred Conti+ and Jeffrey Guzek⁺⁺

Abstract

A high-precision, high-resolution Ocean Color Imaging (OCI) instrument is under development for the Plankton, Aerosol, Cloud, ocean Ecosystem (PACE) mission which requires a pair of medium-speed mechanisms to scan the ocean surface continuously. The design of the rotating telescope (RT) mechanism operating at 360 RPM and the half-angle mirror (HAM) mechanism synchronized at 180 RPM was concern for maintaining pointing precision over the required life and continuous operations. An effort was undertaken with the manufacturer to design and analyze a special bearing configuration to minimize axial and radial runout, minimize torque, and maintain nominal contact stresses and stiffness over the operating temperature range and to maximize life. The bearing design, analysis, development and testing along with the design-specific technical challenges imposed upon mechanism engineers will be discussed. Bearing performance, runout as achieved and verified during encoder installation, and operating torque will be described.

Introduction

PACE will extend the high-quality ocean ecological, ocean biogeochemical, cloud, and aerosol particle data records begun by NASA in the 1990s, building on the heritage of the Sea-Viewing Wide Field-of-View Sensor (SeaWiFS), the Moderate Resolution Imaging Spectroradiometer (MODIS), the Multi-angle Imaging SpectroRadiometer (MISR), and the Visible Infrared Imaging Radiometer Suite (VIIRS). The mission will be capable of collecting radiometric and polarimetric measurements of the ocean and atmosphere, from which biological, biogeochemical, and physical properties will be determined.

The PACE observatory is comprised of two instruments, an Ocean Color Instrument (OCI), Figure 1, and a Multi-Angle Polarimeter. The OCI is the primary instrument on the observatory and is being developed at GSFC. The OCI is a hyper-spectral scanning radiometer designed to measure spectral radiances from the ultraviolet to shortwave infrared to enable advanced ocean color and heritage cloud and aerosol particle science. OCI accomplishes its mission objectives by implementing an RT mechanism, rotating at 360 RPM, and phase locked to the HAM mechanism rotating at half the RT speed. These synchronized mechanisms scan ocean surfaces with 1000-m resolution and 20-m track-to-track overlap. The PACE satellite is planned to be launched in 2022-2023. [1, 2]

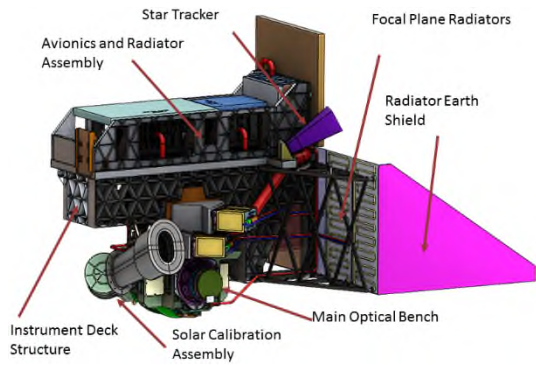


Figure 1. OCI Configuration

* NASA Goddard Space Flight Center, Greenbelt, MD

** The Aerospace Corp, El Segundo, CA

+ The Barden Corp, Danbury, CT

⁺⁺ Design Interface, Columbia, MD

Mechanism Operating Requirements

The RT and HAM are precision mechanisms spinning synchronously to scan the ocean surface and place the optical image through the OCI slit. The requirements considered for these mechanism designs include:

- Speed: 360 & 180 RPM
- Position: 40 arc-sec knowledge and 10 arc-sec maximum error (2^{15} bits), sampling at 50 kHz
- Life: ground testing + 3 months in-orbit commissioning + 3 years continuous on-orbit operations
- Torque: minimize mechanical power to minimize thermal conditions at the bearing and for minimizing control electronics overhead
- Mechanical Loads
 - Structural: worst-case launch vehicle mass acceleration curve (MAC), 42g, for mechanisms; sine vibration 10g from 5-100 Hz
 - Thermal: 10°C to 30°C qualification range, including self-generated heat

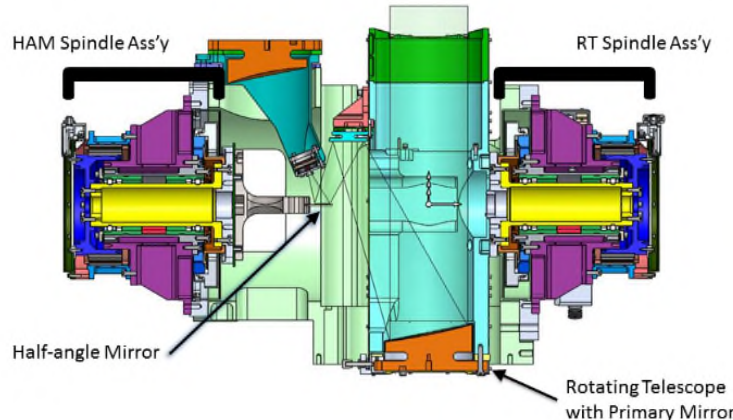


Figure 2. RT and HAM Mounted on Main Optical Bench

Runout: Challenges to Meet Requirements

Minimizing the axial and radial runouts were primarily driven by the optical system sensitivity estimates and the need to meet challenging pointing requirements. Both synchronous runout and asynchronous runout had to be minimized to keep the bearing cartridge runouts within the requirements. The RT and HAM, with precision optical encoders mounted to the shaft flange end, runout requirements were most challenging while the motor and encoder supported by the aft end have slightly relaxed requirements. The cartridge total indicator runout (TIR) requirements are given in Table 1. As these were very challenging requirements, the bearing vendor was taking all reasonable steps necessary within their capabilities to achieve these values while operating in a “best effort” mode.

Table 1. TIR Runout Requirements

	Shaft Flange End	Aft End	Outer Races (ea.)
Radial Runout	2.54 µm (100 µ-in)	2.54 µm (100 µ-in)	0.51 µm (20 µ-in)
Axial Runout	1.27 µm (50 µ-in)	5.08 µm (200 µ-in)	NA

These challenging requirements meant that the best geometrical precision in bearing races, ball roundness and their potential lobing was required. Additionally, the number of mating surfaces with their inherent errors due to tolerance buildup had to be minimized. For these reasons, the mechanism designers decided not to use commercial off-the-shelf bearing designs but rather to start with no preconception and design a system that maximized the likelihood of success. The cartridge design demanded complete customization that led to inner races ground on the same grinder setup. There were no shaft fit or concentricity errors because

there was no shaft. The outer rings also required very high tolerances that resulted in a hybrid superduplex configuration.

Cartridge Design: To Flange or Not to Flange?

The preliminary design of the RT and HAM were based on a simplified loads assessment of standard 108H angular contact bearings, preloaded as a duplex back-to-back (DB) pair with a 10.16-cm (4.00-in) row separation. By working with the bearing manufacturer to minimize radial and axial runout, a new cartridge design configuration was developed. The OCI bearing cartridge concept is similar to x-ray bearing cartridges, wherein the inner raceways are ground directly into a shaft and the preload is provided by fitting a spacer between wide outer rings. The spacer is essentially in a "C" shape to facilitate assembly. This entire preloaded cartridge can be fitted into a housing structure and clamped into position. The bearing manufacturer has experience building this type of bearing cartridge.

The detailed design included selection of contact angle, material, and fits. Material selection was dominated by the launch load demands and other qualitative considerations. Two contact angles were considered: 15° and 25°. The 25° contact angle offered lower contact stress due to preload and better axial capability with a slight decrease in radial capability and no truncation issues. Though a tighter raceway curvature could be used to decrease operating contact stress and increase the load capacity, a looser raceway curvature provides a lower running torque given the smaller contact area.

The initial target preloads evaluated were 111 N (25 lbf), 267 N (60 lbf), and 445 N (100 lbf). The 267-N preload offered the best balance between protection during launch and operating contact stress. The as-built bearing cartridge is shown in Figure 3.

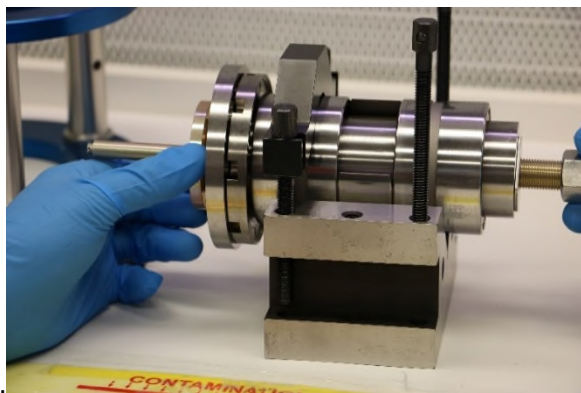


Figure 3. Bearing Cartridge Showing Captured Titanium Mounting Collar (Floating)

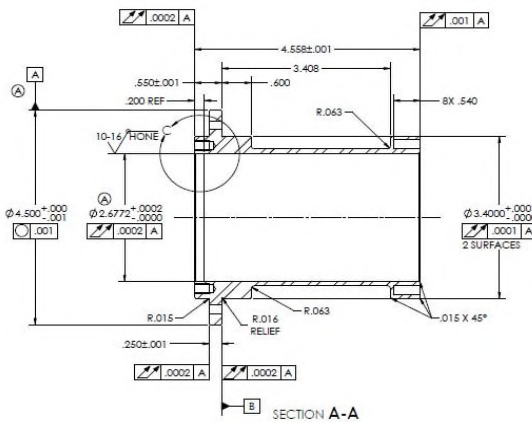


Figure 4. Flanged Sleeve

While material selection will be discussed next, that selection process did indeed have a direct effect on the design. Disregarding material concerns for the moment, the original design concept was to implement a mounting flange on the forward (shaft flanged end) outer ring. The original material consideration of M62 brought with it a concern and a reality of limited supply stock size options. That reason, combined with requiring different designs for the two outer rings (and the increased cost of such), drove the design away from a flanged cartridge. This required the use of the sleeve to mount the cartridge into the mechanism housing. When the material choice later led to 440C, this decision was not revisited. The result of the flange question was for the mechanism team to implement "sleeving". The sleeve provides a method for mounting the cartridge into the aluminum mechanism housing, which also provides structural support for the encoder read heads and motor stator. In order for the sleeve to provide maximum performance enhancement for the RT and HAM assemblies, it must: 1) be a relatively close coefficient of thermal expansion (CTE) match;

2) be relatively easy to thermally control; 3) have precision interfaces (fits) to the cartridge and the housing; and 4) must completely capture the cartridge.

The cartridge basic outer diameter and sleeve bore are 67.75 mm (2.6772 in). The sleeve bore runout is specified as 5.08 µm (0.0002 in). Cartridge to sleeve fit up design values are given in Table 2. Fit ups for the sleeve to housing were similar.

Table 2. Cartridge to Sleeve Fit Up

	Diametric Tolerance	Total Clearance
Cartridge	+0.00 µm (+0.0000 in) -2.54 µm (-0.00001 in)	Line-to-line, min 7.62 µm (0.0003 in), max
	+5.08 µm (+0.0002 in) -0.00 µm (-0.0000 in)	

Thermal control of the cartridge is accomplished by mounting a flexible, wrap-around Kapton® heating element on the exterior mid-section of the sleeve. Test thermocouples and flight thermistors were also installed for heater control and telemetry. The sleeve is shown in cross-section in Figure 4. Capturing the cartridge in the sleeve was completed with a customer-supplied titanium mounting collar that was “captured” between the rotating shafts and fixed outer forward outer races during clean assembly. At the aft end of the sleeve, a tabbed collar was mounted such that there was axial compression providing a nominal 3.89-kN (875-lbf) clamping force. Sleeve material selection for CTE and machinability will be described in the next section.

Material Choices

Materials considered for the bearing rings included M62 tool steel and 440C stainless steel. The M62 tool steel has a higher allowable contact stress than 440C (Table 3), which potentially allows the use of a smaller bearing. A smaller bearing would lower the running torque, weight, and stiffness. For the same geometry and load, the M62 bearing would operate at a higher contact stress with a correspondingly smaller contact area. The 440C stainless steel is more available and is a common bearing steel, which lowers risks associated with supply and specialized processing. Ultimately, the 440C was able to provide adequate load capacity with the initially determined bearing size and M62 was not used. This choice assured material availability and reduced risks associated with specialized material processing at the cost of reduced stiffness and lower load capacity.

Table 3. Bearing Component Material Properties

	M62	440C	Si3N4
Allowable Max Contact Stress	3790 MPa (550 ksi)	2310 MPa (335 ksi)	n/a
Modulus	235 GPa (34.1e6 psi)	205 GPa (29.7e6 psi)	320 GPa (46.4e6 psi)
Poisson's Ratio	0.29	0.283	0.26
Density / Specific Gravity	8.17 g/cc (0.295 lbm/in ³)	7.8 g/cc (0.282 lbm/in ³)	3.16 g/cc (0.114 lbm/in ³)
Thermal Expansion Coefficient	10.66e-6 1/C	10.2e-6 1/C	2.9e-6 1/C
Type	Tool Steel	Stainless Steel	Ceramic
Expected Hardness	RC 65	RC 61	HV 1550

The ball materials considered were 440C stainless steel or silicon nitride ceramic (Si₃N₄). The silicon nitride ball offers several benefits of enhanced lubricant life, lighter weight, and higher stiffness at the expense of significantly different coefficient of thermal expansion compared to the steel rings [3, 4, 5, 6]. The additional

change in preload over temperature due to a difference in material thermal expansion coefficients was determined by analysis to be an acceptable detriment, given the other benefits of silicon nitride.

The sleeve material of 440C stainless steel was used in order to minimize thermal expansion coefficient differences between bearing rings and the sleeve (Table 4). The sleeved cartridge fits into an aluminum housing, which provides the structural connection to the instrument optical bench. With precision fits, the separation and support provided by the stainless steel sleeve minimizes the effect of the thermal expansion coefficient differences between the steel bearing and aluminum housing.

Table 4. Structural Component Material Properties

	Al 6061-T6	440C	Ti-6Al-4V
Modulus	69 GPa	205 GPa	114 GPa
Poisson's Ratio	0.33	0.283	0.33
Density/Specific Gravity	2.7 g/cc (0.098 lbm/in ³)	7.8 g/cc (0.282 lbm/in ³)	4.43 g/cc (0.16 lbm/in ³)
Thermal Expansion Coefficient	23.6e-6 1/C	10.2e-6 1/C	8.6e-6 1/C
Type	Aluminum	Stainless Steel	Titanium

The ball retainer material is machined phenolic, MIL-I-24768, Type FBE, often used in many space applications due to its light weight and ability to be properly impregnated with the lubricating oil, acts as an oil reserve. To provide additional lubrication reservoirs, Nysorb® rings, also impregnated with oil, were designed to fit into outer race inner grooves.

Analysis Approach

A bearing analysis was conducted to ensure that the assembled and integrated bearing cartridge would meet design and performance requirements. This analysis was performed concurrently with detailed design of the cartridge to aid final design decisions, such as material selection and fits. The analysis ensured that two primary requirements were met: the maximum mean contact stress in the bearing must be within allowable limits during launch and the final preload range during operation was suitable for the rotating telescope. The goal was to have an appropriate preload range over the expected operating temperatures and the given manufacturing tolerances of the piece parts. A higher preload means a shorter fatigue life and higher drag torque, while a lower preload might compromise the stiffness of the system. An example preload goal range might be between 44.5 N (10 lbf) and 445 N (100 lbf) preload. The analysis also ensured no truncation of the contact ellipse on the land, as well as provided estimates for running torque and stiffness.

Key parameters that affect the analysis results include:

- Material properties (Young's modulus, Poisson's ratio, coefficient of thermal expansion)
- Bearing geometry (bearing size, raceway curvature, contact angle, straddle)
- Mounting (clamping force, interference fits, initial preload)
- Operating parameters (temperatures, speed, launch loads, preload)

With the materials, geometry, and operating parameters fixed, the final design decisions were related to the mounting of the bearing into the sleeve and housing. Therefore, this bearing concept described above leads to a number of issues that must be accounted for in the detailed design and mounting analysis:

- Clamping effect on preload
- C-spacer effect on raceway parallelism
- Sleeve fitting effect on preload
- Sleeve/housing fit

Clamping effect on preload

The bearing integration concept calls for the bearing cartridge, which consists of the outer rings preloaded with the C-spacer and shaft, to be clamped into the bearing sleeve. The clamping rings squeeze the outer rings together, compressing the outer rings and the C-spacer. Since the outer rings are being compressed, the outer raceways move closer together which lowers the preload. The compression also increases the diameter of the raceways due to Poisson's effect. This axial displacement of the raceway and increase in diameter of the rings are included in the bearing mechanical analysis via a change in the initial preload and change in fit.

C-Spacer effect on raceway parallelism

The circumferential gap in the C-spacer caused an uneven distribution of the preload on the inner face of the outer rings. Although the clamping ring was contacting the entire face of the outer ring, the C-spacer only supported a section of the outer ring; this caused a variation in axial displacement of the outer raceway. The concern was a loss of parallelism between the outer raceways. Finite Element Analysis (FEA) was used to evaluate raceway parallelism affected by the C-spacer as shown in Figure 5. The worst-case difference in axial displacement due to clamping of any point on the raceway was predicted by the FEA to be around 525 μm (0.000021 in).

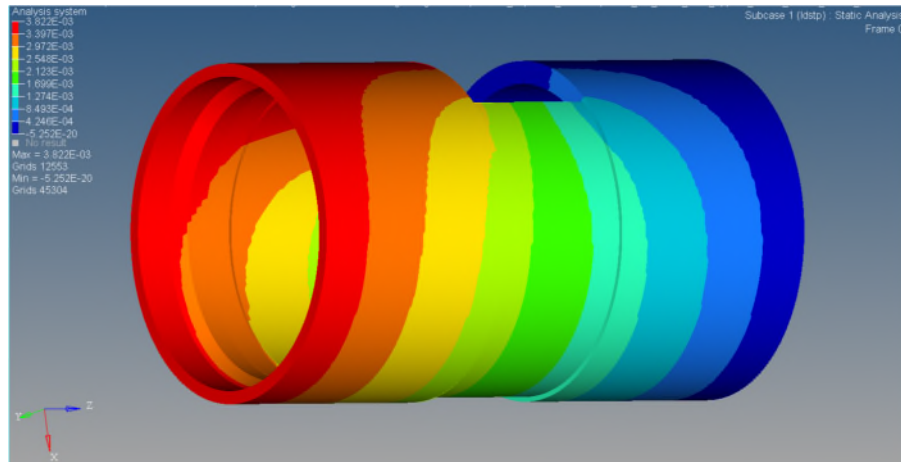


Figure 5. FEA Results Showing Deformation of the Outer Rings Due to Clamping Load

Sleeve fitting effect on preload

As it is well known in the bearing field, an interference fit of the outer rings in the sleeve increases preload by compressing the rings and decreasing the radial play. This decrease in radial play is seen by the preloaded bearing as a change in preload and contact angle.

Mechanism housing fit effect on sleeve fit

The interference fit of the sleeve into the mechanism housing affects the sleeve diameter in turn also affects the bearing/sleeve fit.

Analysis process

The BRGS10C software was used for the bearing internal mechanical analysis and Python for scripting and cartridge mounting mechanical analysis. The process had to take into account the effects mentioned above. The bearing mechanical analysis software BRGS10C was originally created for analyzing directly adjacent preloaded pairs with conventional housings, shafts, and clamping. BRSG10C cannot on its own properly analyze the complex mounting of a cartridge such as the OCI concept. The Python scripting was able to account for the unique mounting concept as well as provide a means of iterating through the entire design space quickly. The ability to iterate through all design configurations allowed a better understanding of each parameter's effect on the final configuration. The adopted analysis process includes the following steps:

1. Apply a temperature
 - *Survival cold, cold, room temp, hot, survival hot*
 - *Calculate new part geometries*
2. Apply a sleeve clamping load (based on allowable C-spacer deformation)
 - *3.34, 3.89 & 4.45 kN (750, 875, & 1000 lbf)*
 - *Find axial displacement of raceway due to compression (at temperature)*
 - *Find Poisson's effect on outer diameter (at temperature)*
3. Apply housing-sleeve fit
 - *0.0000 to 5.08 µm (0.0002 in) interference*
 - *Calculate change in fit between sleeve & bearing*
4. Apply sleeve-bearing interference fit
 - *-7.62 µm (-0.0003 in) to 0.0000 clearance*
 - *Adjust fit due to Poisson's effect from clamping & housing fit*
5. Adjust preload due to clamping compression (based on axial stiffness)
6. Run BRGS10C with adjusted preload & sleeve-bearing fit
7. Report results:
 - *Final preload*
 - *Maximum mean stress*
 - *Stiffness / Displacement*
 - *Truncation*

This process was followed for each combination of design parameters to determine their effect on final preload, contact stress, and stiffness. The information was plotted in order to examine the entire design space, as well as to determine each parameter's effect on the result. In this way, the best decision could be made regarding the final fit, clamping load, and initial preload.

Analysis results

The analysis process provided results for each combination of detailed parameters. Figure 6 shows maximum mean contact stress results for the worst-case fits and clamping configuration given a combination of axial and radial loads.

Figure 7 shows the final preload variation for all temperature, sleeve fit, housing fit, and clamping combinations considered. At colder temperatures, the shrinking sleeve and housing fits, along with the silicon nitride ball, cause a rise in preload. Figure 8 shows the maximum mean contact stress for launch and operational cases. Though a lower operating contact stress is desirable, the changes seen given the mounting parameters considered are no cause for significant alarm.

In order to allow a better understanding of each parameter's effect on the results, series of cases were run where certain parameters were held constant, and only one varied. The effect of the varied parameter can then be directly determined by examining the obtained result. Figure 9 shows the effect of housing fit on final mounted preload given a loose sleeve fit and 3.89-kN (875-lbf) clamping force. Only at colder temperatures does the housing fit affect preload.

Figure 10 shows the change in preload due to varying sleeve fit over temperature given a nominal housing fit. As the figure shows, the sleeve fit has a greater influence on the final preload than the housing fit. This made sense because the sleeve is closer to the raceways and is made of a stiffer material.

Figure 11 shows the effect of clamping on the final preload. The effect is fairly consistent over the temperature range and is a smaller effect than the sleeve or housing fits.

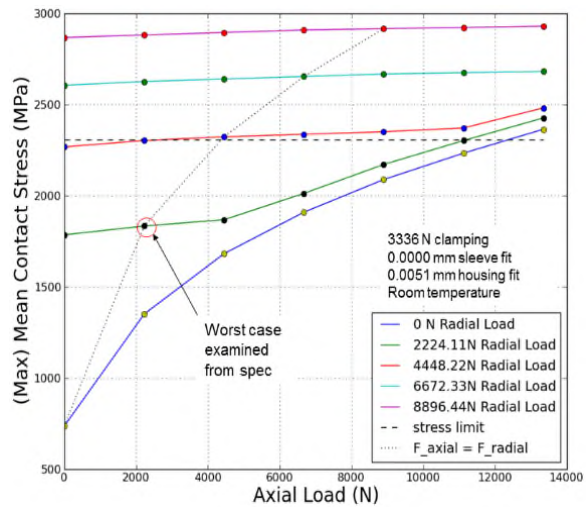


Figure 6. Contact Stress Capability vs. Radial and Axial Load Cases

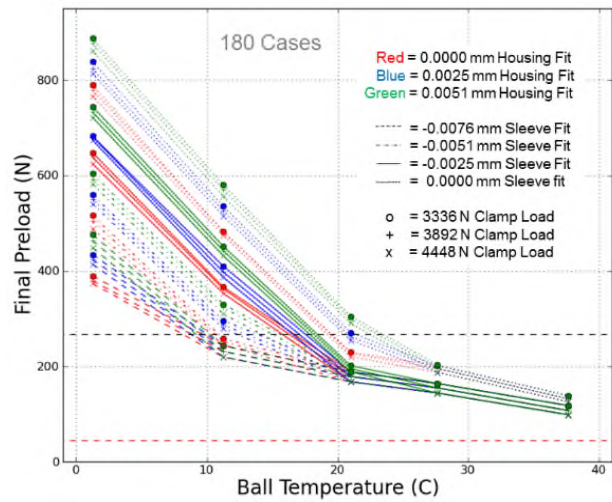


Figure 7. Final Mounted Preload Variation

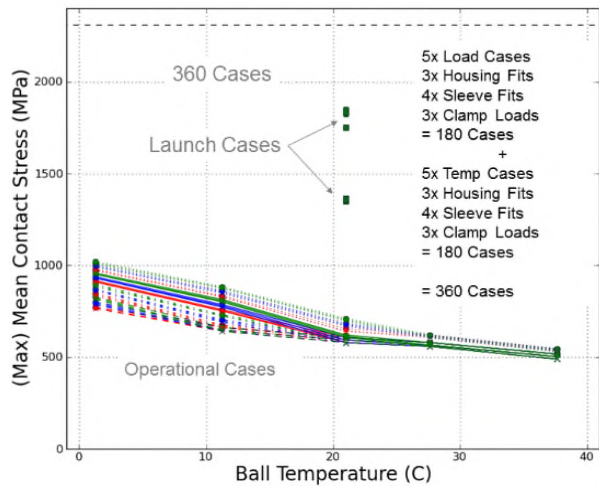


Figure 8. Maximum Mean Stress for Launch and Operational Case

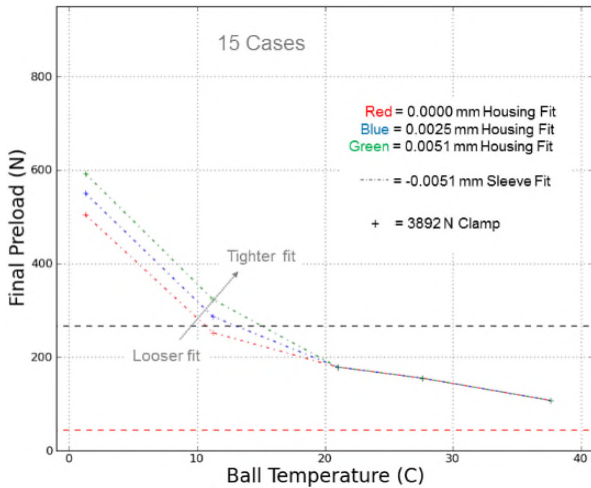


Figure 9. Effect of Housing Fit on Final Preload

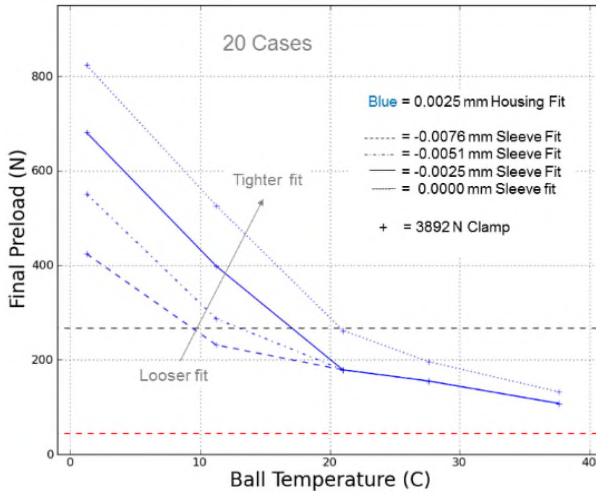


Figure 10. Change in Final Preload Due to Sleeve Fit, Given a Loose Housing Fit

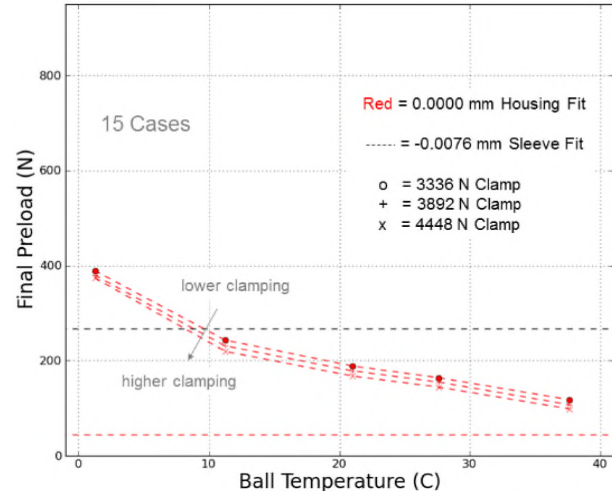


Figure 11. Change in Final Preload Due to Outer Ring Clamping

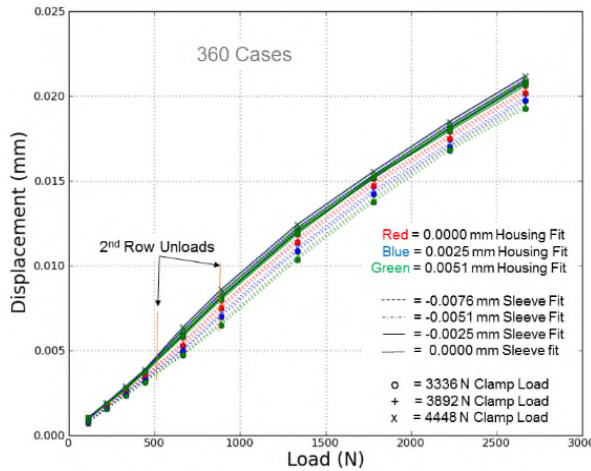


Figure 12. Axial Load Displacement

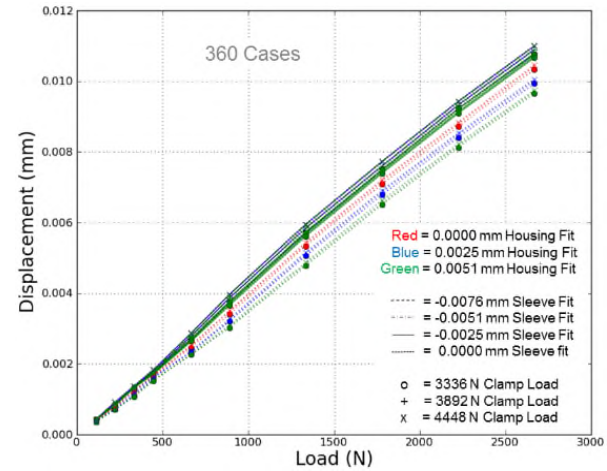


Figure 13. Radial Load Displacement

Figure 12 and Figure 13 show the load-displacement relationship for axial and radial loads, respectively. The change in the shape of the curve clearly shows where the front row unloads for the axial load case.

Given the numerous design parameters and the likelihood of achieving such close tolerances on each of those parameters, the ability to create permutations through each range, and evaluate the effect of each tolerance gave increased confidence in the performance of the fully assembled bearing.

Lubrication

The bearing cartridge is assembled after being lightly lubricated with Nye Lubricants 2001 synthetic oil. Nye 2001 has proven itself to be a reliable space lubricant as long as enough lubricant is available to the bearing. NyeBar®-P oil barrier films are added to each end of the cartridge to reduce oil migration from the bearing. A Nyesorb™ lubricant reservoir in each outer ring ensures lubricant is available throughout the lifetime of the mechanism. Cages and reservoirs are vacuum impregnated with lubricant and weighed prior to assembly to ensure oil take-up. A life test will be conducted to ensure adequate lubricant life for the OCI design and operating conditions.

It should be noted that the use of the silicon nitride balls and its material dissimilarity to its friction couple, steel, has shown remarkable lubrication life extensions in other applications and has for years allowed the luxury of using just oil in critical applications that require extreme torque quietness over extended periods of time. The oil is not damaged as fast as with all-steel bearings and therefore extra grease or grease dams for life extension are not needed. The lubricant life tests, discussed in a later section, should bear this conclusion out and provide more real data for the aerospace mechanism community.

Cartridge Runout Verification

To measure and document the axial and radial runout requirements given in Table 1, the bearing vendor developed new test hardware to verify cartridge performance. A non-contacting, capacitive picometer sensor was mounted in adaptable setups to determine synchronous and asynchronous TIR at the four specified interfaces and at both 360 and 180 RPM. Initial setups indicated that external electrical and mechanical noise, structural modes, and sensor surface squareness, generally in that order of effect, were all contributors to significant measurement error. By diligent effort, all error sources were eliminated.

Electrical noise was addressed by establishing a thorough grounding scheme, as well as by establishing an electrically “quiet” facility location and controlling local equipment usage. Structural noise was addressed by redesigning to a very stiff sensor mounting block and a stiff structural loop between the sensor and cartridge mounts. The motor drive signature was isolated using a pulley with an O-ring driving a jack shaft supported by Rulon bearings then coupled to the cartridge with Tygon tubing. By attention to sensor positioning, it was noted that the surface squareness of the sensor relative to the cartridge could be altered by indexing (i.e., rotating on axis) the transducer body by 90° to 270°. The sensor output was sent to a dual-trace spectrum analyzer to display the displacement in time and frequency components. After corrective actions, by taking a time trace reading with no shaft motion, static sensor readings in all four locations indicated approximately 0.0127- μ m (0.5- μ in) noise. During high-speed shaft rotations, sensor displacement vs. time gave us a total runout (synchronous and asynchronous) and the frequency trace served to distinguish between synchronous and asynchronous runout. The result was that virtually all runout was synchronous (that is, on the orders of rotations).

Cartridge Performance Predictions and Verifications

Performance predictions

During the superduplex cartridge fabrication, an effort was begun to predict starting and running torque at 360 RPM for inclusion in the drive electronics design capability. To that end, analysis and tests were used to predict performance. Generally, bearing torque consists of a load torque caused by sliding and rolling friction between components in the bearing, and a viscous torque, due to the plowing and squeezing of the lubricant. The load torque is largely dependent on loading, and weakly dependent on speed, while the viscous torque is largely dependent on speed, and weakly dependent on load. Both BRSG10 and ORBIS bearing analysis codes provide similar estimations of load torque at zero speed, as show in Table 5, given the same assumption of coefficient of friction.

Table 5. Load and Speed Torque Predictions

	BRGS10	ORBIS	units
Load Torque Est. μ = 0.08, P = 60 [lb]	6.9 (0.974)	6.8 (0.96)	mN-m (in-oz)
Viscous Torque Est. 350 cSt, LQF = 0.3	39.5 (5.6)	25.4 (3.6)	mN-m (in-oz)
Viscous Torque Est. 240 cSt, LQF = 0.3	30.1 (4.35)	19.9 (2.82)	mN-m (in-oz)

The viscous torque is affected by the lubricant viscosity and quantity of lubricant in the bearing. The lubricant viscosity is affected by temperature while the quantity of lubricant and its effect on torque is dependent on the size of the bearing, type of lubricant, and other miscellaneous factors. This leads to an empirical factor, called lubricant quantity factor (LQF) used in viscous torque estimation and the need for testing to anchor

the analysis. The viscous torque estimates can be found in Table 5, for BRSG10 and ORBIS. The ORBIS values are lower because of its use of dynamic rather than kinematic viscosity, and because of BRGS10's addition of a ball factor, which is the number of balls divided by 10. When corrected for these differences, the estimation differs by less than 2 percent.

In addition, a pair of off-the-shelf 108H bearings were disassembled and cleaned, then reassembled with Nye 2001A oil-impregnated phenolic retainers and ceramic balls. These bearings were then preloaded in a back-to-back configuration and verified with an in-situ load cell. Here, the lubricant condition was duplicated to what was to be the actual cartridge condition. The oil meniscus between ball and race in this test was visually identical to final assembled cartridges. Once assembled into a torque test rig, starting and running torque were measured as a function of preload.

The 108H bearings were subjected to Coulomb (starting) torque measurements at various preloading values, as shown in Figure 14, with the slope and y-intercept identified. Notice that if the negligible y-intercept value is ignored, the starting torque is the slope of the curve multiplied by the preload force. As such, the slope is an alternative form for the friction coefficient, in this case, $\mu = 0.0152$.

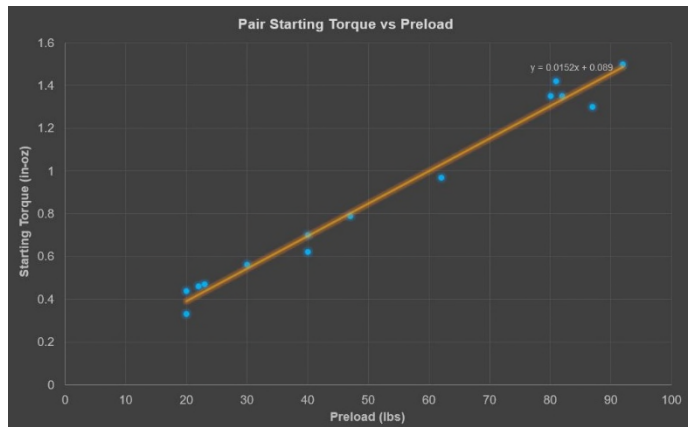


Figure 14. 108 Pair Starting Torque vs Preload (Note: units are in lb and oz•in)

Running torque as a function of time can be seen in Figure 15. This data shows that the viscous torque is clearly associated with speed, as shown in the data where the speed was changed and the torque changed respectively. Here the effect of run in can be dramatically seen; after 47 minutes of running the torque reduced from 56 mN•m (8 oz•in) to 39 mN•m (5.5 oz•in). This data also shows that the viscous torque is only weakly associated with preload, as shown with the changes in preload but only minor changes in torque given the same speed.

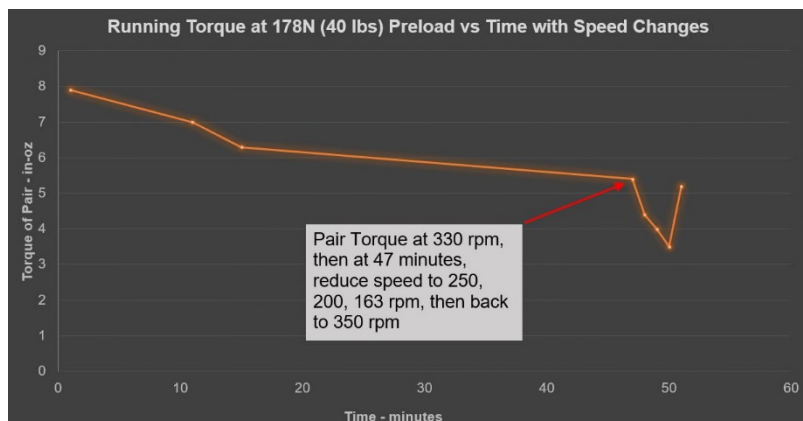


Figure 15. Torque vs. Time Test Results (Note: units are oz•in)

As-Built Cartridge Torque Performance

Prior to shipping from the manufacturer, the bearings were torque tested on a Vibrac machine. Torque data is typically captured during 0.5 RPM to 2 RPM rotations. Example results can be seen in Figure 16 and summarized in Table 6. This data shows that the low-speed torque for the cartridge is about 50 percent higher than expected from analysis or off-the-shelf testing. This means that 1) the preload is higher than expected, 2) the coefficient of friction is higher than expected, or 3) the viscous contribution at low speed is higher than expected. Torque testing is necessary to ground / anchor the torque estimation given the many empirical factors included in torque estimation methods.

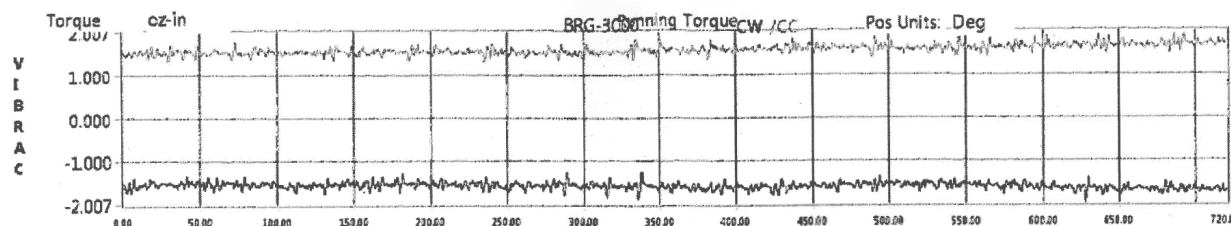


Figure 16. VIBRAC Running Torque Test on SN 006, Typical (Note: units are oz•in)

Table 6. SN 006 Torque Test Summary

	CW	CCW	Units
Peak Torque	-14.17 (-2.007)	13.76 (1.949)	mN•m (oz•in)
Average Running Torque	-11.21 (-1.588)	11.21 (1.588)	mN•m (oz•in)
Maximum Hash Width	4.44 (0.629)	2.75 (0.389)	mN•m (oz•in)
Average Hash Width	2.27 (0.322)	0.71 (0.101)	mN•m (oz•in)

Spindle Assembly and Thermal Conditioning

Spindle assembly appeared simpler “on paper” but was more difficult in the practice due to the tight tolerances. Pre-assembly steps included precision cleaning of the sleeve, housing and flexible clamp as well as installation of the thermal control hardware onto the sleeve. The sleeve bore was carefully inspected for internal surface abnormalities. The sleeve bore was lubricated with a light film of Nye 2001 oil with a clean swab and then the heater leads were connected to a 30-V power supply to expand the sleeve for installation. Since the assembly was taking place in the swift moving, cool air of a flow bench (ISO 14644-1 Class 5), the sleeve in its support stand was covered to reduce convection losses. During the heating process, the exterior of the bearing cartridge was also coated with a thin film of Nye oil and placed in a

flange-up orientation to allow any excess oil to pool on the lead in edges of the cartridge. Once the sleeve temperature, as measured by a thermistor at the flange end, reached 50-55°C the cartridge was manually suspended over the sleeve at the lead in and dropped in. Being that the cartridge and sleeve are the same material (and CTE) and have a very tight tolerance, binding was always a concern. While the first of five assemblies resulted in a cartridge seizing with only a small fraction of the cartridge passed the lead in, the remaining four cartridges dropped in flawlessly, guided by the expert hands of our assembly technicians. The partially installed cartridge was bagged along with the sleeve and support stand and pressed into position on a tension testing machine with approximately 534-N (120-lbf) load. The collar fasteners were installed and torqued to fully seat the cartridge. After that, the flex clamp was installed and torqued. Figure 17 shows the thermal control hardware mounted to the sleeve prior to assembly and the cartridge installed and fully seated in the sleeve.

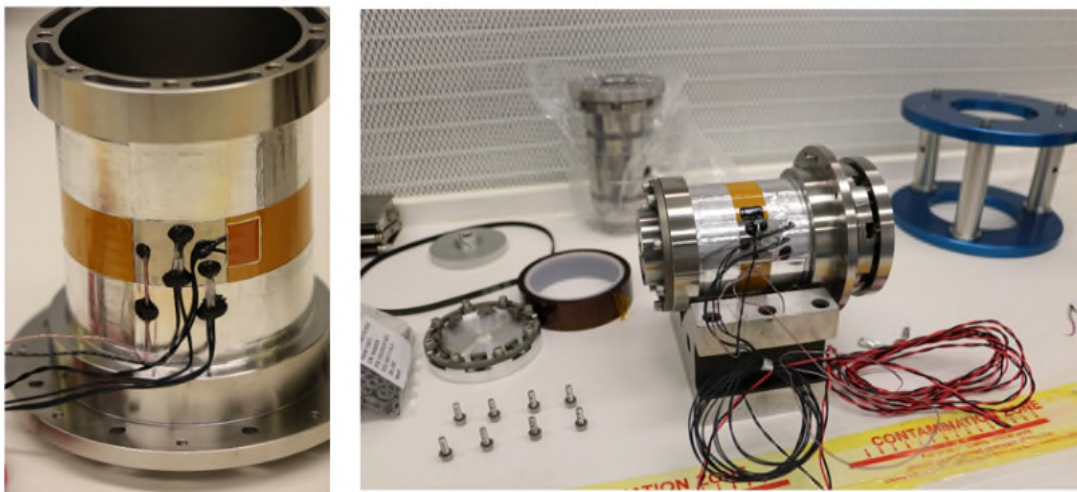


Figure 17. Flanged sleeve with and without bearing cartridge

Upon completion of the sleeve installation, the housing bore was inspected and lightly lubricated with Nye oil. It was then placed on a ceramic electric heating element until a thermistor registered 65-70°C. During heating, the sleeve external lands were similarly lubricated with Nye oil. The sleeve was dropped into the aluminum housing and registered with its alignment pin without any difficulty. The completed housing assembly is shown being installed in its support stand in Figure 18.

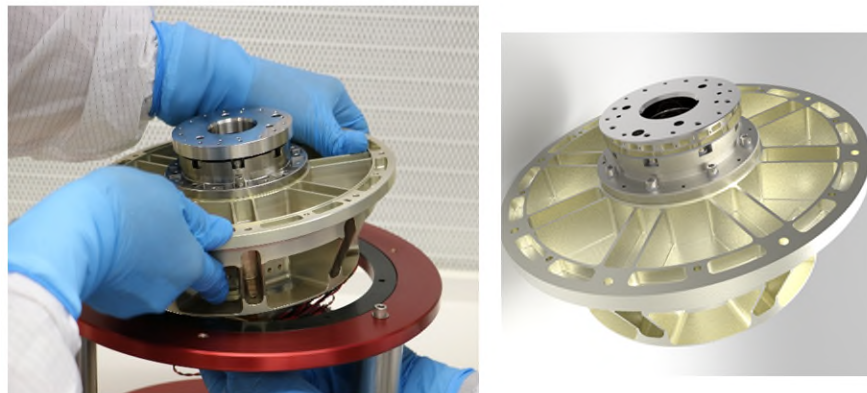


Figure 18. Assembled spindle (hardware and CAD model)

In order to hold repeatable relative position of the encoder code disk and read head, the completed spindles were exposed to thermal conditioning prior to shipment for installing the encoder components.

The spindles were exposed to 12 ½ thermal cycles at ambient pressure over the survival temperature range of 0°C to 40°C. The cycles assure that there is no residual assembly shear stress present due to differential offsets from the shrink fits.

Spindle Performance

Upon thermal settling cycles, spindle performance testing was undertaken to assure that the assembly mounting had not adversely affected the preload, starting torque, running torque or runout. Drive electronics to be used for spindle testing and the basis for life testing electronics were developed. The mechanism drive electronics (MDE) is capable of commutating a zero-cogging torque motor mounted to the flanged end of the spindle based on a 23,600-line optical encoder also mounted on the flanged end. The MDE can accelerate to 360 RPM with the same preliminary profile as is expected for flight. It then runs for a fixed time in order to capture any torque decrease/change as a function of running in and then similarly decelerate. The MDE can operate in low-speed dynamometer mode to measure Coulomb friction at 0.5 to 2 RPM.

Figure 19 shows typical low-speed torque data for a 5-minute test. The red and blue traces represent motor current captured at 10 Hz and 500-point median filtered data via a MATLAB script. Figure 20 shows the entire torque test results using red and blue traces as described. The data shows a decrease in running torque at 360 RPM from 47.67 mN•m (6.75 oz•in) to 26.83 mN•m (3.8 oz•in) after 1 hour of ambient laboratory operation.

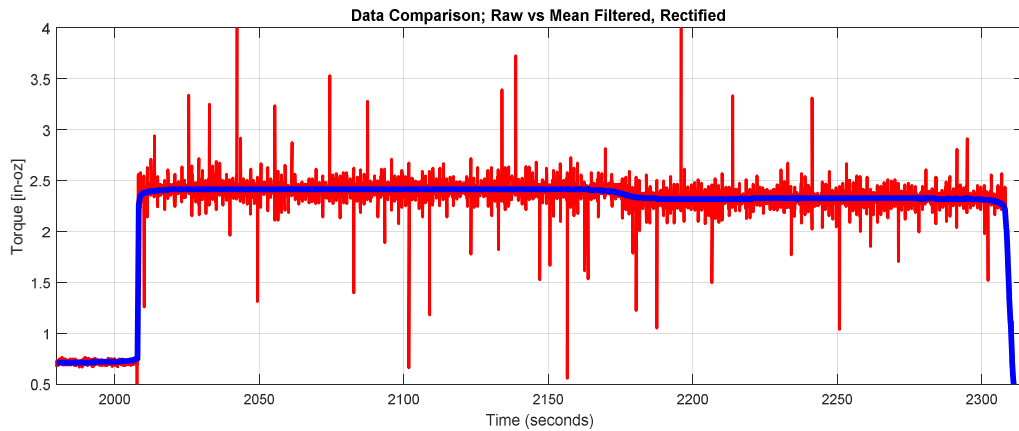


Figure 19. Spindle Coulomb friction measurement (16.7 mN•m [2.36 oz•in], average; units are oz•in)

Two spindle assemblies were delivered to BEI Precision for high-resolution encoder installation. Their installation process usually requires the grinding of the flange mounting interface to the encoder disk to minimize runout and achieve the required accuracy. In this case, BEI responded with confirmation of $0.38\text{-}0.51\cdot10^{-6}$ m ($15\text{-}20\cdot10^{-6}$ inch) runout, axial, including the flange surface finish. When coupled to their accuracy tester, $0.33\text{-}0.53\cdot10^{-6}$ m ($13\text{-}21\cdot10^{-6}$ inch) runout, axial, and $0.84\cdot10^{-6}$ m ($33\cdot10^{-6}$ inch), radial, and do not include surface finish. The cartridge performance was “without question, the best bearing assemblies we’ve ever seen” and therefore required no pre-installation grinding.

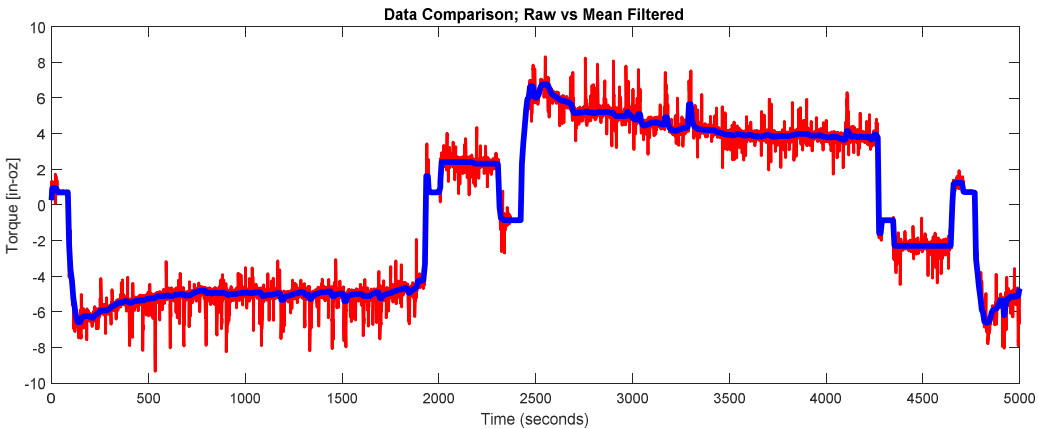


Figure 20. Spindle torque measurement, ± 360 RPM running, ± 2 RPM Coulomb (units are oz•in)

Life Testing Plan

A plan has been created to document details of the life testing. The testing will be in two parts to address separate life-related risks. The first tests will be of bearings only, abbreviated BOLT (for bearings only life test) and will address the risk of lubricant life and potential degradation. For this test, 6 bearing cartridges have been selected as representative of the lot. They will be installed into 440C sleeves with an appropriate fit, representing flight unit fits, and then installed into stove pipe fixturing representing the mechanism housing, again, with an appropriate fit. Heaters and thermistors will be applied as in the flight configuration allowing us to control the bearings' bulk temperatures within OCI's operational range. A life test with multiple units under test (UUTs) allows us to gain the same confidence with fewer cycles than with only one UUT. The UUTs will be fitted with a mass simulator prior to random vibration and sine sweep testing. The mass simulators will be removed and the UUTs will then be installed in pairs into three thermal vacuum (TVAC) chambers sharing a vacuum pump and chiller. The vast majority of testing will consist of operation at 360 RPM as torque is "self-sensed" using the current to a cogless brushless motor. Occasional spin downs to 180 RPM and 2 RPM for Coulomb friction measurements will be performed over the course of the non-accelerated testing. Spin down time testing may also be used to estimate any changes in friction over time.

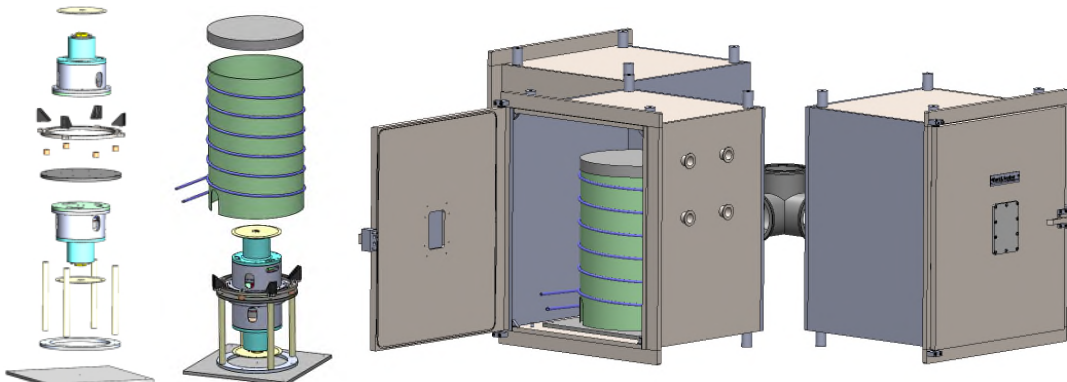


Figure 21. BOLT Test Configuration

The second test will be of the RT and HAM mechanisms working in synchronization and will address the risk that changes over time will affect the ability of the control electronics to synchronize the relative RT and HAM position and velocity such that the image passes through the instrument optical slit and illuminates the detectors with the required accuracy. These two mechanisms will be configured with an engineering test unit telescope and half-angle mirror and installed on a surrogate optical bench. The UUTs will be

subjected to random vibration and sine sweep testing prior to testing in TVAC. This non-accelerated testing is expected to begin in late summer of 2018.

Preparations are underway to assemble the BOLT at the time of writing this paper.

Summary

Some obvious and some not so obvious conclusions can be taken away from the OCI-specific bearing cartridge application design effort. Several key points are summarized as follows:

- Interference fits and their change over temperature have a larger impact on resulting (as installed) preload than outer ring clamping force.
- Ball material CTE mismatch with respect to the rings affects preload change over temperature at least as much as sleeve material choice.
- Sleeve fit dominates preload variation compared to housing fit within the temperature range.
- Ball CTE dominates preload change at the hot extreme as the sleeve and housing fits loosen and no longer radially squeeze the outer rings.
- Silicon nitride provides benefits such as increased lubricant life, lower weight, and higher stiffness with the detriment of a significantly different CTE and corresponding change of preload with temperature.
- 25-degree contact angle provides lower operating contact stress with minimal loss of launch load capability (compared to 15-degree contact angle).
- Parametric exploration of the design space allows a better understanding of the effects and significance of each parameter.
- For critical or ultra-precision applications, do not immediately assume that commercial off-the-shelf components are the ideal solution. Fully investigate the design space for available alternatives. While there may be more time and expense invested in the initial design activity, savings will be forthcoming once mechanism integration and test phases have begun.

Acknowledgements

The authors would like to thank the production, verification and quality team at Barden, especially Douglas Stange, for their dedication to producing world-class bearings for OCI and engineers at BEI Precision for their expertise at measuring and evaluating precision spindle assemblies. We also acknowledge the OCI team that supported the effort as we worked through the lessons learned, as described in this paper and others. We finally acknowledge Nick Kwiatkowski and Tom Huber for their outstanding efforts during assembly.

References

- [1] NASA Goddard Space Flight Center (2017). PACE. Retrieved from <https://pace.gsfc.nasa.gov/>
- [2] "Keeping the PACE", *The Critical Path*, Volume 25, Number 3, NASA Goddard Space Flight Center. Retrieved from https://fpd.gsfc.nasa.gov/critical_path/critical_path_17winter.pdf
- [3] Tang, C., et al, "A Study on the Effects of Ball Defects on the Fatigue Life in Hybrid Ball Bearings", Proceedings from the 42nd Aerospace Mechanisms Symposium, May 2014, Baltimore, MD.
- [4] Park, W., et al, "Rolling Contact Fatigue and Load Capacity Tests of M62 Bearing Steel", Proceedings from the 32nd Aerospace Mechanisms Symposium, May 1998, Cocoa Beach, FL.
- [5] Leveille, A. and Ward, P., "Wear Potential due to Low EHD Films during Elevated Temperatures", Proceedings from the 42nd Aerospace Mechanisms Symposium, May 2014, Baltimore, MD.
- [6] Smith, D., et al, "REX 20/Si3N4 Control Moment Gyroscope Bearing Development", Proceedings from the 32nd Aerospace Mechanisms Symposium, May 1998, Cocoa Beach, FL.

Evaluation of Friction Characteristics and Low Friction Mechanism of Tungsten Disulfide for Space Solid Lubricant at Elevated Temperature in a Vacuum

Ayaka Takahashi*, Josaphat Tetuko S S* and Keizo Hashimoto**

Abstract

A development for a synthetic aperture radar for exploration of another planet is planned. A synthetic aperture radar satellite needs a deployment system for a large antenna for both telecommunication and observation of the planet. The spacecraft will be required to withstand harsh environments without maintenance during the mission. One option is to use a solid lubricant in the sliding portions. Tungsten disulfide (WS_2) for use as a solid lubricant at elevated temperatures in space has been examined. In order to simulate the friction during deployment, measurements for the friction coefficient at room temperature and high temperature in a vacuum using three types of WS_2 coating films on a metal disk have been conducted. The first WS_2 bonded film was compared to molybdenum disulfide (MoS_2) bonded film with the same coating condition and using the same equipment. MoS_2 has been mainly utilized in current spacecraft and it has similar crystal structure as that of WS_2 . The wear life of WS_2 bonded film shows longer life than MoS_2 bonded film at 500°C under vacuum. Sputtered films and shot peening films were also examined. The friction coefficient of WS_2 shot peening films are extremely low at room temperature and high temperatures. Furthermore, an effort was made to confirm the low friction mechanism from the result of analysis after the friction tests. The friction mechanism of these materials is attributed to weakly bonding of the (0002) plane. It was shown that a specimen having strong texture on the (0002) plane has a low friction coefficient.

Introduction

Spacecraft mechanisms cannot be maintained or inspected after launch. The extreme environments of interplanetary space present a more challenging wear environment, introducing failure modes not seen in terrestrial environments. Therefore, any satellite components subjected to sliding wear must be sufficiently lubricated to survive mission requirements. Recent exploration programs subject spacecraft to more extreme environments than seen in the earth orbital environment. One option to provide lubrication for interplanetary missions is solid lubrication.^[1, 2].

There is evidence in the literature by NASA in 1969^[3] that WS_2 has demonstrated a great potential for a high-temperature solid lubricant for space. MoS_2 has been utilized successfully as a solid lubricant for space equipment. Recently, nanoscale multilayers of MoS_2/WS_2 ^[4] and nanocomposite films^[5-8] have been studied for their tribological properties using X-ray diffraction (XRD) and Transmission Electron Microscopy. Although the friction coefficient of WS_2 was very low at elevated temperatures, studies of WS_2 have not been as extensive as that of MoS_2 which has the same crystal structure. The crystallographic structure of WS_2 is shown in Figure 1. The friction characteristics of WS_2 are attributed to the crystal structure, which is composed of hexagonal close-packed tungsten atomic layers sandwiched between two hexagonal close-packed sulfur atomic layers. Therefore, two adjacent sulfur layers held by Van der Waals force are weakly bonded and slide easily on the (0002) sulfur basal planes.

To simulate the deployment and driving friction, pin-on-disk reciprocating tribometer and rotary tribometer experiments have been conducted under vacuum at ambient and elevated temperatures with WS_2 on the metal disk.

* Center for Environmental Remote Sensing National University Corporation, Chiba University, Japan

** Department of Aerospace Engineering, Teikyo University, Japan

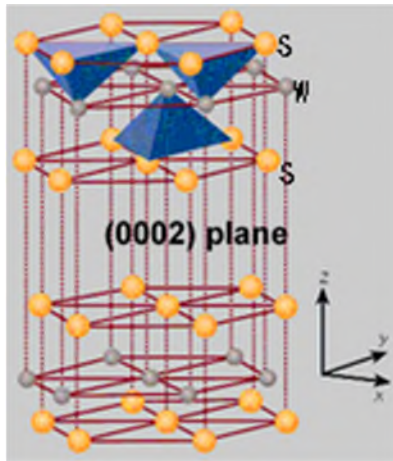


*Figure 1. Crystal structure of WS_2 Hexagonal $P6_3/mmc$ [5 - 9]
 $(0.3154 \times 0.3154 \times 1.236 nm^3)$*

The purpose of this research is to evaluate three fabrication techniques of WS_2 coating films for an application at high temperature in a vacuum environment: bonded films with an inorganic binder, sputtered films with titanium intermediate layer, and shot peening films of WS_2 powder.

Experimental Procedure

Two types of friction testing equipment were utilized: a pin-on-disk type reciprocating tribometer and a pin-on-disk type rotary tribometer, each in a vacuum chamber. After the friction tests, the surfaces of both disk and ball were observed by an optical microscope and the surface profile at the wear tracks was measured by a contact profilometer. The structural and chemical properties were analyzed with a scanning electron microscope (SEM) and energy dispersive X-ray spectrometry (EDS). Crystallographic structures of the wear and the non-wear regions were examined by imaging plate X-ray diffraction (IPXRD).

Pin-on-disk type reciprocating tribometer

Pin-on-disk type friction tests were carried out using a reciprocating tribometer to investigate the friction characteristics of various types of lubricant coatings in air and in vacuum. The test conditions are listed in Table 1. Figure 2 shows a schematic diagram of the reciprocating tribometer, which can evaluate friction under a constant applied load and sliding speed. The tribometer was installed inside a vacuum chamber to allow tests to be carried out in air and under vacuum. A pin slides repeatedly against a disk coated with lubricant, with a load of 10 N applied by a weight located outside the vacuum chamber. The speed of the sliding is controlled by the reciprocating motion of the disk.

The sliding speed and the stroke were 10 mm/s and 10 mm, respectively. For tests under vacuum conditions, the chamber was evacuated by a turbo molecular pump to a pressure on the order of 10^{-4} - 10^{-6} Pa. The friction test was interrupted when the friction became high or it was suspected that the wear had reached the substrate of the disk.

Table 1. Tested condition of the reciprocating tribometer

Load [N]	10
Contact Pressure [GPa]	0.35
Speed [mm/s]	10
Friction Distance [mm]	10
Atmosphere [Pa]	Vacuum (under 10^{-5})
Temperature [$^{\circ}\text{C}$]	22–24

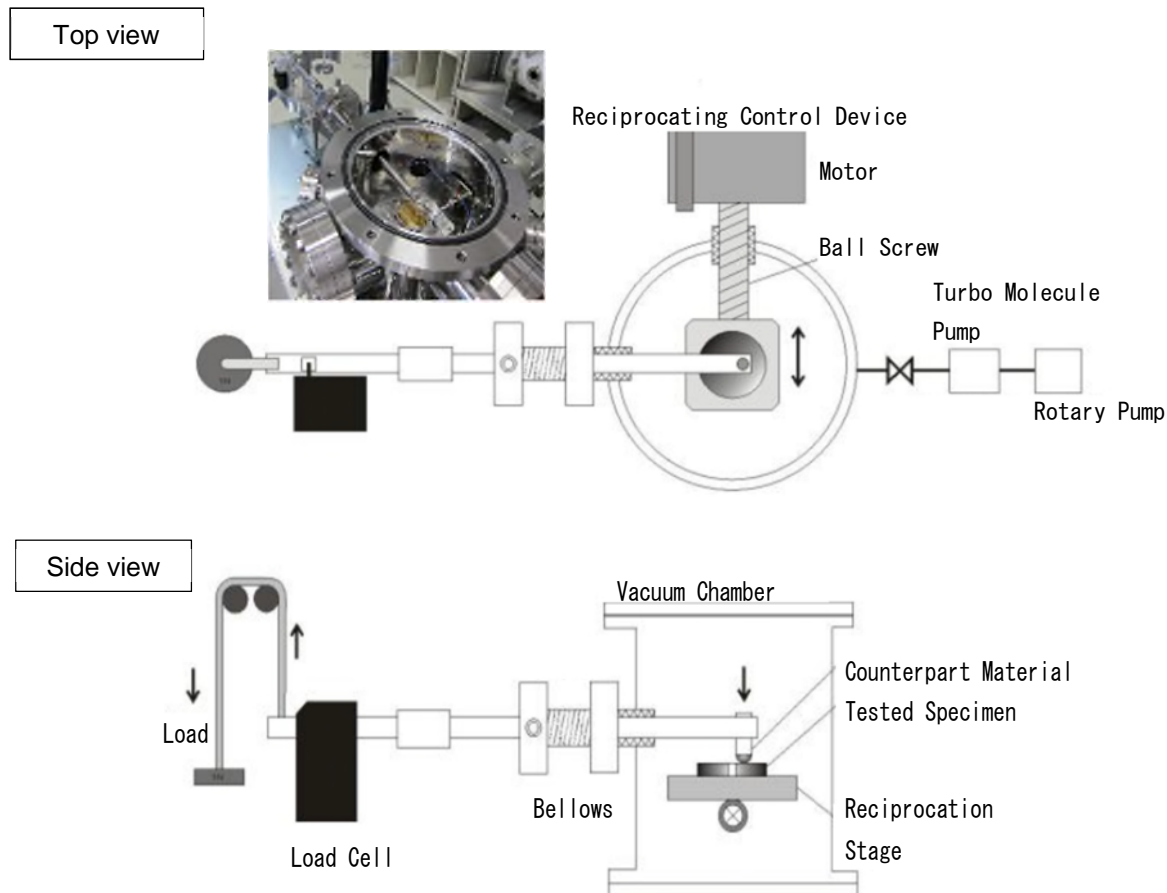


Figure 2. Overview of reciprocating tribological test

Pin-on-disk type rotary tribometer

The friction characteristics of many types of WS₂ and MoS₂ coatings were investigated at elevated temperatures under vacuum using a pin-on-disk rotary tribometer. The test conditions are listed in Table 2. Figure 3 shows a schematic drawing of the test apparatus. The vacuum chamber was evacuated by a turbo molecular pump to a pressure on the order of 10⁻⁵ Pa, and the temperature of the specimen was controlled by a molybdenum heater and a thermocouple welded on the specimen. The temperature relationship between the test specimen and the outer cover was monitored using thermocouples.

Table 2. Test conditions of the rotary tribometer

Load [N]	10, 30
Speed [m/s]	0.1, 0.5 (inspection) 40π (47.7)
Friction Distance [mm] (rotational speed [rpm])	36π (53.0) 32π (59.7) 28π (68.2)
Atmosphere [Pa]	Vacuum ($<10^{-5}$)
Temperature [°C]	20, 100, 200, 300, 400, 500

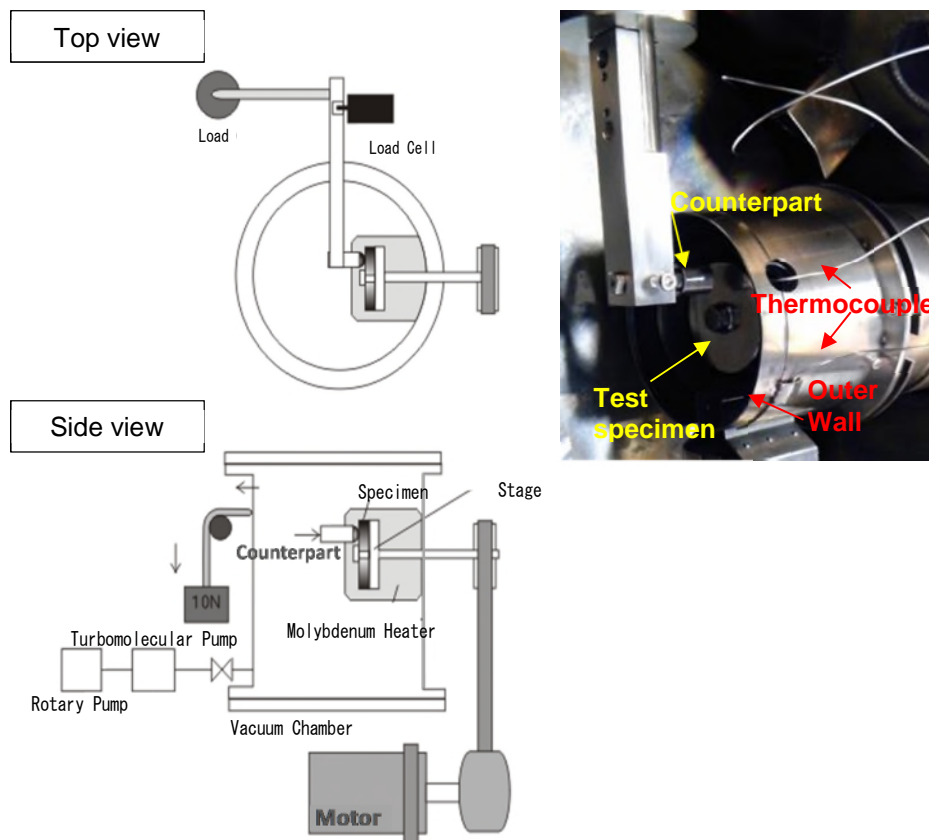


Figure 3. Diagrams of the rotary tribological test apparatus

X-Ray Diffraction Analysis

The crystallographic structure of wear and non-wear regions were examined by IPXRD. The wavelength of the X-ray was 0.1542 nm and it was collimated to a spot size of 0.3 mm, which was small enough to distinguish between a worn or non-worn area of the coating. A high-magnification CCD camera was used to align the X-ray spot on the specimen. In order to capture a diffraction image of the surface film layer of the coating, the X-ray was introduced at a low angle relative to the face of specimen. The incident angle of the X-ray, and the specimen rotation angle were set to 45° as shown in Figure 4. 360° Debye-ring pattern can be used to quantify the textured crystal structure, because the development of preferred orientation was expected due to the wear. A beta diffraction peak can be obtained from one rotation of the specimen (360 degrees). XRD patterns were quantified by measurements of the imaging plate.

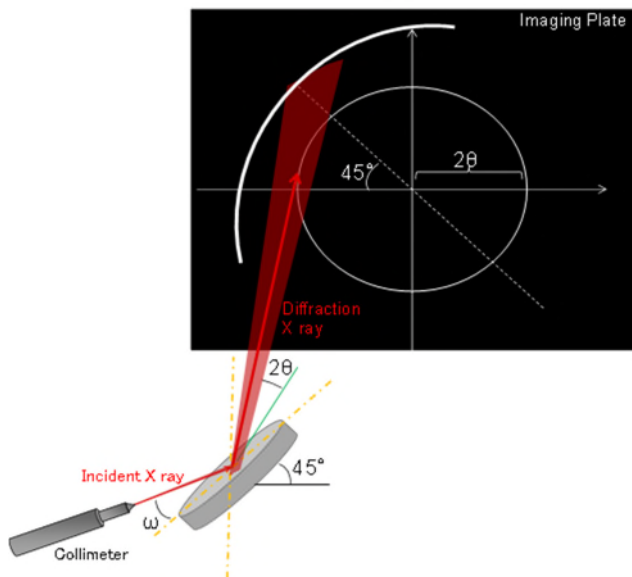


Figure 4. Geometry between incident X-ray beam angle and the sample stage in IPXRD equipment.

Materials

Three kinds of coatings on the SUS316L stainless steel disk ($\Phi 40\text{ mm} \times 8\text{ mm}$), which has relatively good creep strength at high temperature, were fabricated. Counterpart material was a SUS316 ball (7.93-mm diameter).

Bonded Film

MoS_2 is known as a high performance solid lubricant in a vacuum environment [10-13] from numerous research results and applications on spacecraft mechanisms. Two bonded films were fabricated using WS_2 and MoS_2 lubricant powder by one vendor in order to compare tribological characteristics in vacuum at elevated temperatures under the same conditions. Table 3 lists the fabricating conditions for the lubricant powder quality, quantity, and binder material, etc. The coating is fabricated by an annealing treatment for 60 minutes at 200°C using a furnace, then drying in an air environment for 20-30 minutes. This coating method is necessary to form a chemical inorganic binder with better elevated-temperature performance in vacuum than organic binders [14]. Thickness of all coatings were controlled to 10 μm .

Table 3. Coating condition of the bonded films

	MoS_2	WS_2
Grain size(μm)	0.94	0.94
Degree of crystallization (%)	80	-
Powder morphology circularity(%)	0.7~1	0.7~1
Inorganic specimen Vol (%)	40	40
Binder material	Na_2SiO_3	Na_2SiO_3
Thickness	10 μm	10 μm

Sputtered Film

A sputtering technique is suitable for applying a high purity coating with only WS₂ on the top surface of the SUS316L stainless steel disk. As a result of preliminary testing, which showed that the film did not have good adhesion with the interlayer on the mirror-polished surface, a titanium interlayer was applied between the base material and the WS₂ coating. Furthermore, the surface roughness of the SUS316L substrate was varied to improve adhesion. Roughness treatments were carried out using a shot blast method after the mirror surface treatment. Three levels of surface roughness were evaluated; Ra: 0.013 (this is the mirror treatment), Ra: 0.4, and Ra: 0.7.

Table 4. Coating condition of the sputtered film

Surface Roughness of Base Materials [μm]	Ra: 0.013, 0.4, 0.7
Target Material	Ti (Inter layer), WS ₂ (Top layer)
Pre-Sputtered Pressure [Pa]	4×10 ⁻³
Ar Injection Pressure [Pa]	3.2×10 ⁻¹
Output [W]	100
Ar Flow [ccm]	7.5
Ar Etching Time [h]	Ti : 0.5, WS ₂ : 0.5
Sputtered Time [h]	Ti : 1, WS ₂ : 4 - 5
Film Thickness [μm]	1.5~1.8

Shot Peening Film

The WS₂ shot peening coatings on the SUS316L stainless steel disk were applied using WS₂ powder of 2-μm and 0.5-μm particle size with a coating pressure of 8.0 MPa in open air. The average thickness of the WS₂ coating was less than 0.5 μm. This coating method is also available to coat only WS₂ on an outermost surface without an interlayer and/or binder. Furthermore, this coating does not have a part size limit and can be fabricated without special chambers or furnaces. The lack of a size limit for the shot-peening film is an important point, especially for spacecraft with large wearing parts.

Quantitative surface condition measurements of the coatings were made by EDS analysis. Figure 5 shows the EDS detection results of tungsten and sulfur across the surface of the disk. Vertical axis shows the ratio of the counts of tungsten (W) and sulfur (S) normalized by the peak intensity of the steel (Fe) in the specimen for each measurement. Horizontal axis is the location of the measurement across the disc from 0 mm to 45 mm. The thickness of coating film has a gradient since the W and S atomic counts were found to increase across the width of the disk.

Figure 6 shows the measured friction coefficient data versus position. Friction coefficient data was measured by a rotary tribometer with a load of 10 N in the air of room temperature and sliding speed of 0.5 m/s, data accumulation rate is 1000 points per second. Vertical axis is friction coefficient and horizontal axis is measurement location. Accordingly, the friction coefficient is inconsistent across the coating. Friction coefficient was decreased at locations showing high atomic counts via EDS. Thus improvement is necessary, however this coating method was included in the study since it has useful characteristics such as ease of application.

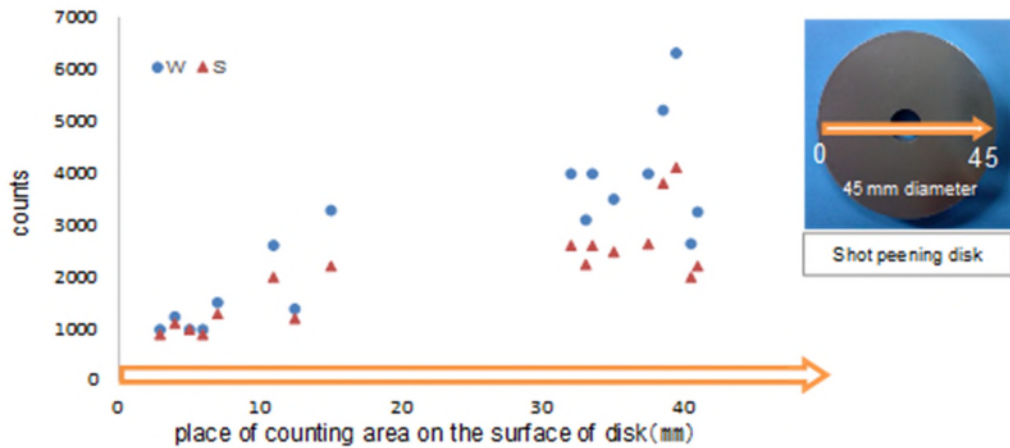


Figure 5. Detection result of tungsten and sulfur atomic from top surface by EDS

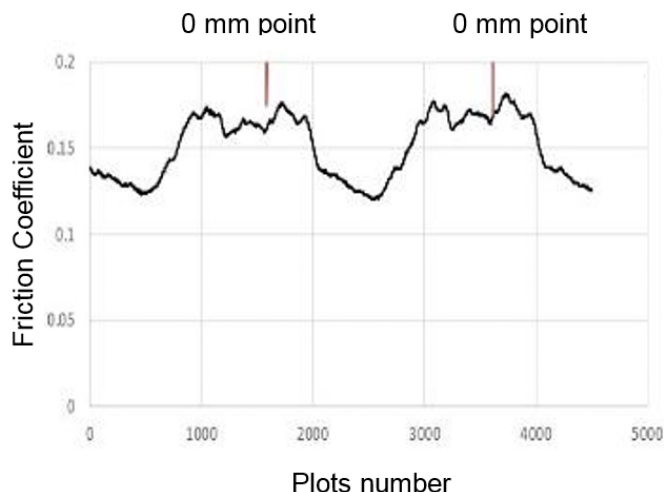


Figure 6. Measured friction coefficient versus position

Results and discussions

Results of the Reciprocating Tribo Tests

The friction test was continued for 100,000 cycles with a load of 10 N under vacuum (10^{-5} Pa) at ambient temperature. The test was conducted using two substrates with different bonded films, one with MoS_2 and the other with WS_2 . Both bonded films were fabricated using the same inorganic binder. Results of the friction test with each bonded film are shown in Figure 7. Both coefficients of friction have similar trends that increased with number of wear cycles. Maximum friction coefficient and/or when friction test finished were 0.04 for MoS_2 and 0.06 for WS_2 . Figure 8 shows optical microscope photos, measured surface wear roughness, SEM observation and EDS analysis of each specimen after the friction tests. A transfer film was observed on the surface of the ball (counterpart material), verified by optical microscope and EDS analysis from both tests. Furthermore, neither substrate was exposed due to wear after completion of 100,000 cycles.

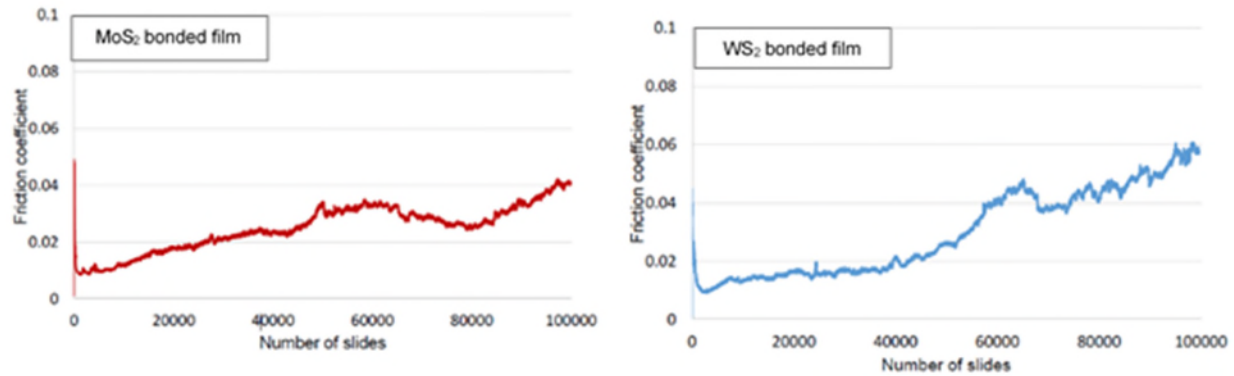


Figure 7. Friction coefficients as a function of time for WS₂ bonded film and MoS₂ bonded film by reciprocating tribometer in the vacuum at room temperature^[13]

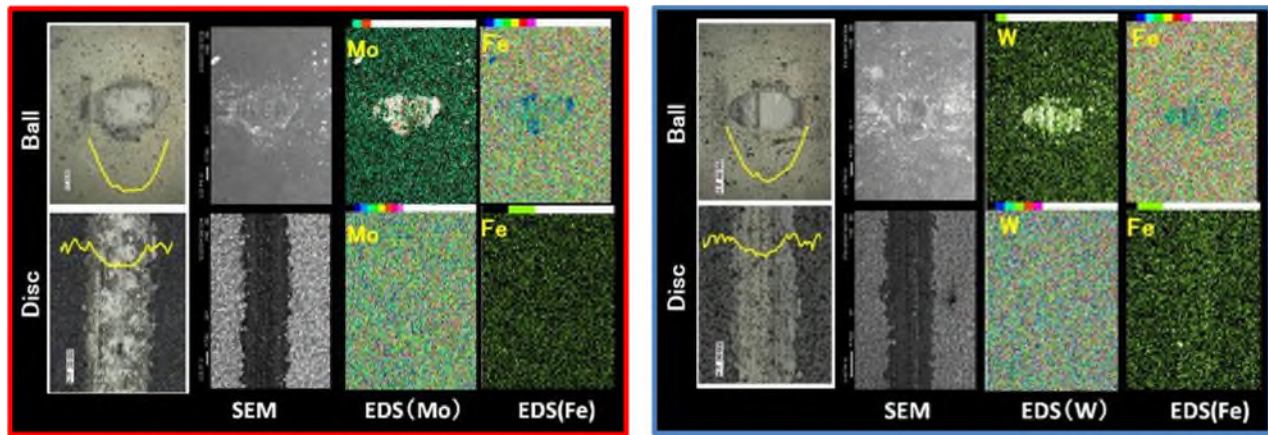


Figure 8. Optical microscope observation, SEM micrographs and EDS mappings of the surface of each bonded film after reciprocating friction test^[9]

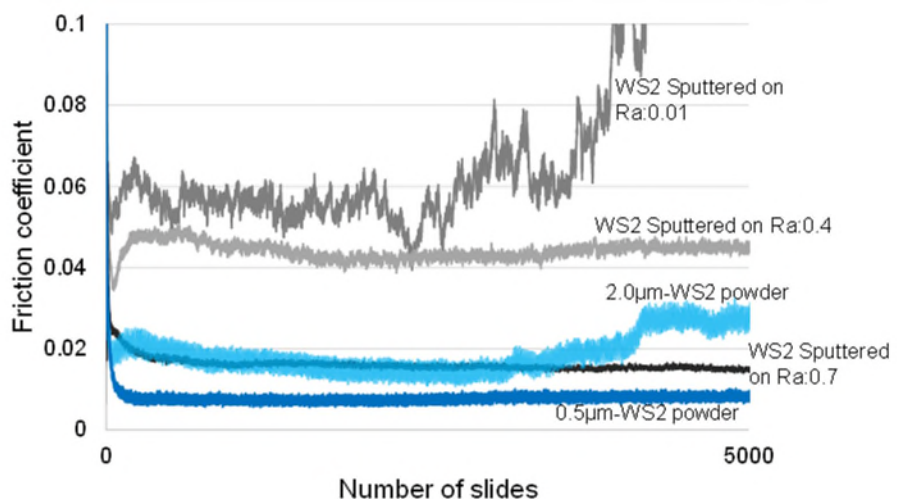


Figure 9. Friction coefficient of WS₂ sputtering and WS₂ shot peening coating by reciprocating tribometer in vacuum at room temperature

Figure 9 shows the results of friction measurements taken using the reciprocating tribometer over 5000 wear cycles under a normal load of 10 N, under vacuum at ambient temperature with a variety of coupons. Sputtered films with a Titanium interlayer applied over substrates with different surface roughness levels, and shot-peened films with different WS₂ particle sizes were tested. Both of these coating methods are capable of creating a pure WS₂ outer surface. With the sputtering films, the friction coefficient of the Ra: 0.01 specimen increased before 5000 cycles and the Ra: 0.4 mm and Ra: 0.7 mm coupons were stable throughout the test. The Ra: 0.7 mm specimen produced a lower friction coefficient than the Ra: 0.4 mm specimen. With the shot peening films, 0.5-μm WS₂ shot peening produced the lowest and most stable friction coefficient.

Results of the rotary tribo tests

Figure 10 shows the temperature dependence of friction coefficient for two types of WS₂ shot peening measured by rotary tribometer with a load of 10 N and speed of 0.1 m/s in a 10⁻⁵ Pa vacuum condition at several temperatures. These friction tests were continued for a nominal 1000 cycles, or the test was interrupted when the frictional force became high.

Friction coefficients of 0.5-μm WS₂ shot peening and 2-μm WS₂ shot peening increase almost linearly with increasing test temperatures. Friction coefficient of 0.5-μm WS₂ was lower than that of 2-μm WS₂ at all temperatures. Testing of the 2-μm WS₂ was terminated before reaching 500°C due to wear-through of the WS₂ layer. The 0.5-μm WS₂ shot peening coupon did not reach 1000 cycles at 300°C for the same reason. Although 2-μm WS₂ shot peening did not produce the lowest friction coefficient, it did maintain friction coefficients below 0.1 at 400°C in the vacuum. We propose that 2-μm WS₂ shot peening has potential for continued research for high-temperature spacecraft applications.

Since spacecraft generally receive no maintenance after launch, the durability of the coating and wear life in the intended environment are considered. Figure 11 shows the comparison between WS₂ bonded films and MoS₂ bonded films by rotary tribometer with a load of 30 N and sliding speed of 0.5 m/s in a 10⁻⁵ Pa vacuum condition at high temperatures. These films were made by the same coating method using the same inorganic binder. The endurance life of WS₂ was longer than that of MoS₂ at all temperatures tested under vacuum [14].

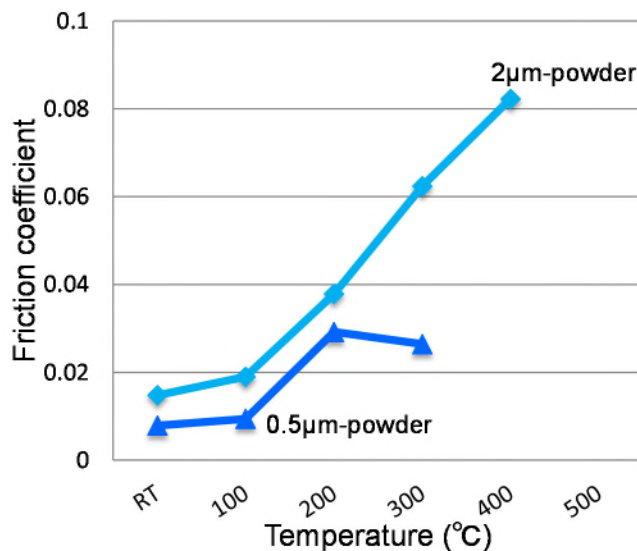


Figure 10. Behavior of friction coefficient of 2-μm powder WS₂ and 0.5-μm powder WS₂ with increasing temperature by Rotary tribometer in vacuum

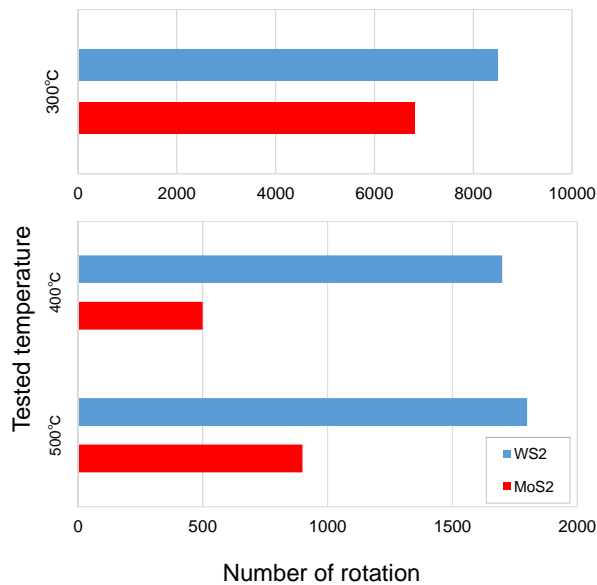


Figure 11. Comparison of endurance life between WS₂ bonded film and MoS₂ bonded film by Rotary tribometer in vacuum at elevated temperature (300°C, 400°C, 500°C).

IPXRD observations

For each specimen, a two-dimensional diffraction image was used to capture the diffraction pattern in worn and non-worn areas, as shown in Figure 12. The (0002) plane is formed and the (0004) plane overlaps a layer. The (0002) plane consists of the two hexagonally closed-packed sulfur atom layers which form the slip-plane. All specimens were fixed at an angle of 45 degrees for measurement conditions of the (0002) plane. Existence of the (0002) plane is established from X-ray Debye ring patterns. An area detector is used to obtain a 360° Debye-ring pattern and to quantify the textured structure because the development of preferred orientation was expected during the friction test.

No clear (0002) plane Debye-ring pattern was detected from the bonded films in the non-wear points. This is likely due to the fact that the WS₂ particles are distributed randomly in a binder so the (0002) planes do not align. WS₂ sputtering film did not show the (0002) planes on the non-wear point. Consistent (0002) plane Debye-ring patterns were detected from the wear points on all coupons. Only WS₂ shot peening film showed (0002) Debye-ring patterns before friction. Since there is no doubt that the existence of the (0002) plane is the friction mechanism for tungsten disulfide^[15], the presence of the (0002) plane before wear is an important point. The relationship between friction coefficient and X-ray diffraction results is shown in Table 5. All WS₂ coating films showed extraordinary low measured friction coefficients at room temperature. The friction coefficient was lowest in the specimens having only pure WS₂ coatings.

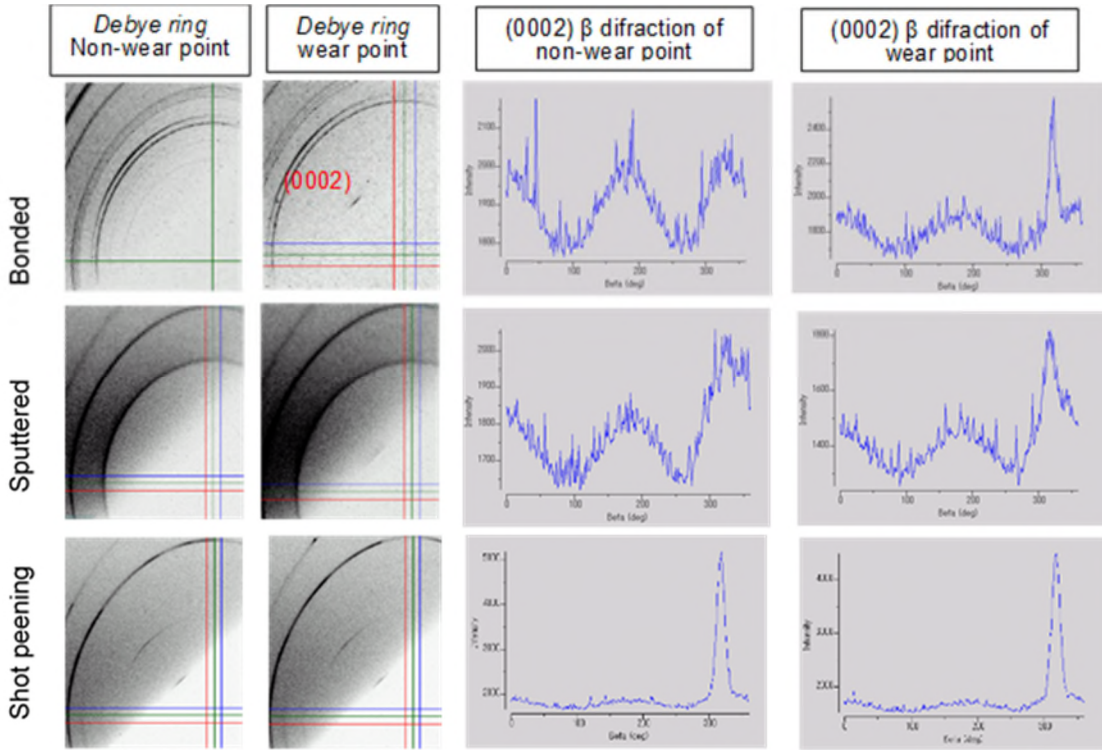


Figure 12. X-ray Debye ring patterns and Intensity profile against β angle of (0002) plane on the wear point and non-wear point of WS_2 specimen surface.

Table 5. Results of friction test and X-ray diffractions

Coating Method	Bonded	Sputtered	Shot Peening
Lubricant	WS_2		
Film Thickness [μm]	10	1.5~1.8	0.1~0.5
Friction Coefficient at Room temperature	0.01~0.06	0.016~0.028	0.01~0.02
Endurance life at Room temperature	Not less than 100,000	Not less than 10,000	Less than 10,000
Friction Coefficient at 400°C	0.05~0.23	-	0.06~0.1
Friction Coefficient at 500°C	0.05~0.15	-	Doesn't work
(0002) Plane in Non-Wear Region	Δ	✗	○
(0002) Plane in Wear Region	○	○	○

○: Exist, ✗: Not Exist, Δ: Partially Exist

Figure 14 demonstrates the temperature dependence of the half width of (0002) peaks in Figure 13. The half width of (0002) peaks decreased with increasing test temperature from room temperature to 200°C, however, the half width jumps to a high value at 300°C. Data of half width at 300°C are scattered widely, since different areas were examined. The half width of the X-ray peak is directly related to both grain size and elastic strain of the WS_2 crystal. As severe deformation occurs during friction, materials can undergo recovery and recrystallization at elevated temperature. WS_2 could be recrystallized to form finer grains at temperatures above 300°C. The abrupt increase of the half width can be explained by a recrystallization process of the WS_2 film.

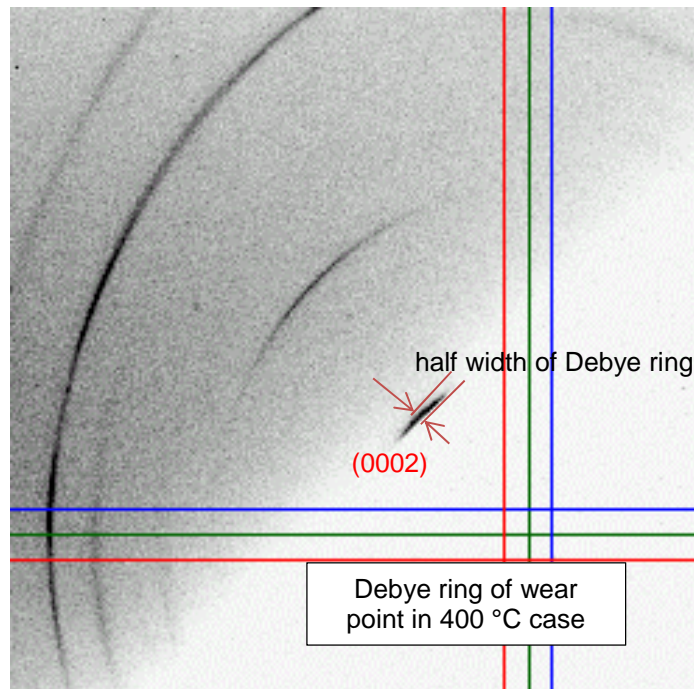


Figure 13. Measurement half width of (0002) peaks by X-ray Debye ring patterns

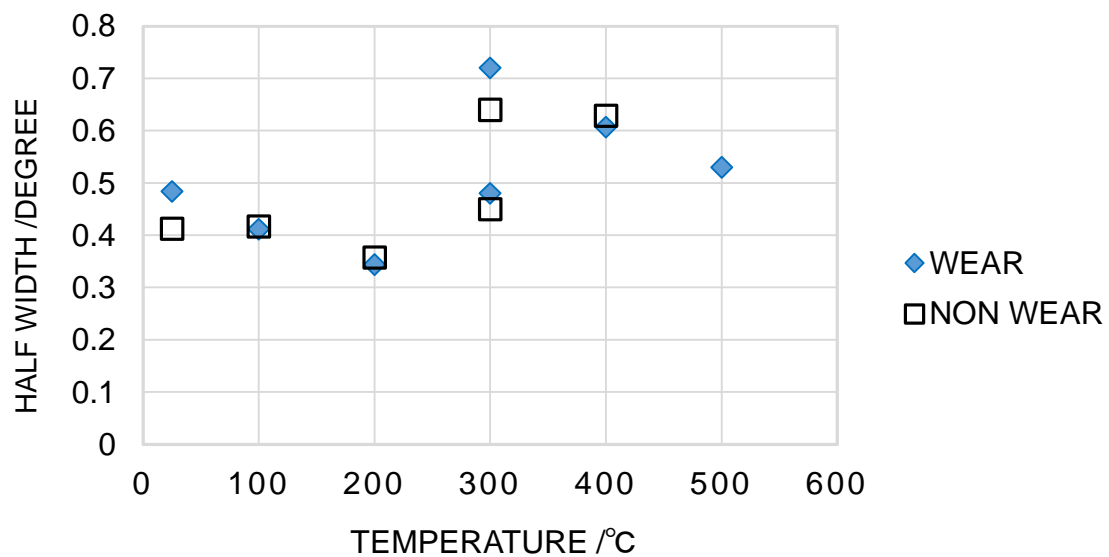


Figure 14. Effects of test temperatures on half width of (0002) peaks on 2- μm WS_2 shot peening

Concluding Remarks

It is necessary to understand the detailed characteristics of a lubricant for use in space since maintenance can almost never be performed after launch. Therefore, the mission-unique environments must be considered when selecting a lubricant. WS₂ was considered as an option for lubrication in high-temperature space environments. The test results presented confirm the possibility of WS₂ as a solid lubricant for elevated temperature space applications.

Three types of WS₂ lubricant films were prepared: bonded film with inorganic binder, sputtered film with titanium interlayer and shot peening film. The results of this study show that all WS₂ coatings tested produced very low measured friction coefficients.

This study had two purposes. The first was to evaluate WS₂ solid lubricants for elevated temperature in vacuum using current technology. One approach was to compare the tribological properties of the WS₂ coatings to MoS₂ coatings since MoS₂ and WS₂ share similar crystal structures. Furthermore, MoS₂ has many previous studies showing it to be an excellent solid lubricant in a vacuum environment. The other approach was to compare the performance of pure WS₂ coatings produced with different methods of application. The second purpose was to verify the low friction mechanism of WS₂ Sputtering films which can be applied without binder and with high purity. Shot peening WS₂ is able to apply the coating without binder or interlayer. These test methods are better to investigate the friction properties of WS₂ than only from analytical results.

The friction coefficients of WS₂ shot peening films are extremely low at room temperature and also at elevated temperatures. This lubricant film showed increasing friction coefficient with an increase in test temperature, however friction coefficient at 400°C is still under 0.1. The low friction mechanism has been confirmed based by the result of XRD analysis after the friction tests. All the WS₂ shot peening specimens show a preferred orientation of (0002) basal plane aligning parallel on the disc surface. It is therefore concluded that the friction coefficient values of WS₂ strongly depend on the (0002) crystal structure and lattice defects in the crystal. These results suggest that behaviors of the lattice defect play an important role on the low friction mechanism of WS₂ that relies on sliding of the (0002) plane.

Endurance life of WS₂ bonded films were longer than the other coatings. However, friction coefficient increased over life. It is proposed from results of shot peening XRD analysis that the orientation (0002) plane aligning parallel on top surface is one of reason for increasing of friction coefficient.

The testing performed showed WS₂ to have good performance and endurance life at elevated temperatures. Based on a comparison of the test results between WS₂ and MoS₂ bonded film, it can be concluded that WS₂ is a promising solid lubricant candidate at elevated temperature.

Acknowledgments

The authors wish to thank Drs. M. Suzuki, K. Matsumoto and H. Shiomi of Japan Aerospace Exploration Agency (JAXA) for their technical assistances and helpful discussion. A measurement of friction coefficient was carried out at JAXA. Stainless steel base material was fabricated by Uchiyama and Uetake of Teikyo University. The bonded films of WS₂ and MoS₂ were supplied from Kawamura Corporation laboratory. WS₂ sputtering film produced with Prof. Koike, Associate Prof. Sutou and Mr. Toyoda of Tohoku University in Japan. The shot peening WS₂ substrate were made by Japan Lubricant LTD. They cooperated for this research. I would like to say sincere thanks to all of the people who supported this research.

References

1. Robert L. Fusaro. "Lubricant of Space System." *NASA/TM-1994-106392*, (1994).
2. Peter M. Magie. "A review if the properties and potentials of the new heavy metal derivative solid lubricant." *Lub. Eng.*, (Jul.1966).
3. William A. Brainard. "NASA Technical note." *NASA TN D-5141*, (10. Apr. 1969).
4. S Watanabe, J Noshiro, S Miyake: Friction properties of WS₂/MoS₂ multilayer films under vacuum environment, *Surface and Coatings Technology* Vol. 188–189, pp 644–648, (2004).
5. Somuri Prasad and Jeffrey Zabinski. " Hollow nanoparticles of WS₂ as potential solid-state lubricants", *Nature* 387, 761-763, (19 June 1997).
6. L. Rapoport, V. Leshchinsky, M. Lvovsky, I. Lapsketr, Yu. Volovik, Y. Feldman, R. Popovitz-Biro, R. Tenne. " Superior tribological properties of powder materials with solid lubricant nanoparticles", *Wear* 255, pp.794-800, (2003).
7. Fredrik G., Fredrik S., Ulf B., Staffan J. " Nanoparticle based and sputtered WS₂ low-friction coating – Differences and similarities with respect to friction mechanisms and tribofilm formation", *Surface & Coating Technology*, 232, pp.616, (2013).
8. Monica Ratoi, Vlad Bogdan Niste, Jhon Walker, Jurgita Zekonyte. "Mechanism of Action of WS₂ Lubricant Nanoadditives in High-Pressure Contacts", *Tribol. Lett.* DOI 10.1007/s11249-013-0195-x, (21 August 2013).
9. V. L Kalikhman: *Izv. Akad. Nauk SSSR, Neorg. Mater.* 19, 1060, (1983).
10. Farr, J.P.G., "Molybdenum Disulfide as a Lubricant: A Review of the Fundamental Knowledge", *Wear*, 10, 442-452, (1967).
11. Spalvins, T., "Deposition of MoS₂ Films by Physical Sputtering and Their Lubrication Properties in Vacuum," *ASLETrans.*, Volume 12, pp.36-43, (1969).
12. Johnson, R. L., "A Review of the Early Use of Molybdenum Disulfide as a Lubricant," *NASA TMX 52343*, (1967).
13. K. Matsumoto, H. Shiomi, S. Kawamoto, Y. Ohkawa, K. Iki, and A. Takahashi, "Mechanisms and lubrication of electrodynamic tether system for debris removal", *15th European Space Mechanisms & Tribology Symposium*, (25–27 September 2013).
14. K. Matsumoto, M. Suzuki, T. Nogi, Y. Aoki, M. Kawamura, "Tribological characteristics of several bonded MoS₂ films under various conditions." *JAXA-RM-07-020*, (31. March.2008).
15. A. Takahashi, and K. Hashimoto, "Evaluation of Frictional Properties of Tungsten Disulfide Bonded Films at High Temperature in Vacuum Environments." *J. Japan Inst. Met. Mater.* Vol. 80, No. 4, pp. 289-296, (11. March. 2016).

Performance of MoS₂ Coated Gears Exposed to Humid Air During Storage

Timothy Krantz*, Claef Hakun**, Zachary Cameron*, Iqbal Shareef+ and Michael Dube++

Abstract

The purpose of this work was to study the effect of exposure to humid air on the durability of a molybdenum disulfide (MoS₂) dry film lubricant on spur gears operated in vacuum. This study was motivated by the James Webb Space Telescope (JWST) Mission. Some mechanisms of the JWST using MoS₂ dry film lubricants have been exposed to humid air during storage as a subassembly and after integration into a higher-level assembly. In this study MoS₂ dry film lubricant was applied to steel spur test gears and subsequently tested in vacuum environment. One-half of the gears had essentially zero time exposure to humid air prior to testing, and the other half were exposed to humid air of 57 percent relative humidity up to 77 days prior to testing. All tests were completed at constant torque and speed. On average the film durability was shorter for gears exposed to humid air compared to those with zero exposure. For the unexposed gears, the durability ranged from 53,300 to 190,300 pinion revolutions with an average value of 100,200 and a median value of 83,500 revolutions. For the exposed gears, the durability ranged from 21,000 to 84,700 pinion revolutions with an average value of 64,900 and a median value of 68,800 revolutions. Using the unexposed gears as a baseline, the exposure reduced the average durability by 35 percent and the median value of durability by 18 percent. Red-brown coloration was noted on some of the gear teeth that had been exposed to humid air. The colored regions appeared as soon as 17 days after exposure to humid air. SEM inspections showed that at least some of these colored areas included material raised above the surrounding MoS₂ film.

Introduction

The purpose of this work was to study the effect of exposure to humid air on the durability of a molybdenum disulfide (MoS₂) dry film lubricant on spur gears operated in vacuum.

This study was motivated by the James Webb Space Telescope (JWST) Mission, and the study is one part of a NASA Engineering Safety Center effort to evaluate potential risks and performance effects to JWST instrument mechanisms and components lubricated with sputtered MoS₂ coatings. The coatings are exposed to humid air environments during integration, ground operations, and storage prior to launch. The mechanism configurations included in the scope of the study are the fine guidance sensor (FGS) coarse focus mechanism, the FGS fine focus mechanism, the FGS dual-wheel mechanism, and the near-infrared camera focus adjust mechanism. Some details about the design, life testing, and engineering enhancements of these mechanisms have been reported [1-3]. The mentioned mechanisms have sputtered MoS₂ dry film lubricants on gears and other components. The practical effects of exposure to humidity on the performance of MoS₂ are not fully understood, and to our knowledge a dedicated study of such effects has not been conducted for MoS₂ films lubricating gear teeth. The focus of this study was the durability of a MoS₂ dry film lubricant on spur test gears that have been exposed to humid air up to 77 days.

* NASA Glenn Research Center, Cleveland, OH

** NASA Goddard Space Flight Center, Greenbelt MD

+ Bradley University, Peoria, IL

++ NASA Langley Research Center (NESC), Hampton, VA

Lince, Loewenthal, and Clark provide a recent and thorough discussion of previous studies regarding MoS₂ aging and oxidation. They comment that long-term storage life test data for sputter-deposited MoS₂ coatings are uncommon [4]. They also completed and reported a study, motivated by the JWST observatory, on the degradation of three nanocomposite MoS₂ coatings during storage in air. The tests used to evaluate endurance were pin-on-disk tests, and storage times were up to 2.3 years. They found that exposure to air could degrade the endurance of the coatings by up to 55 percent. The severity of degradation depended on both the exposure duration and coating composition.

Experimental Equipment

Test Gears

Readily available stock gears with appropriate center distance were selected and customized for use in this study. The customizations of the stock gear design were the bore diameters, sized for a commercial off-the-shelf keyless shaft-locking device, and custom face widths. The pinions and gears were 3-mm module spur gears with standard tooth proportions. The pinions had 26 teeth and a 13-mm face width. The gears had 48 teeth and 10-mm face width. There were six pairs of pinions and gears. The material was S45C steel (equivalent to AISI 1045). The teeth were induction hardened to surface hardness of HRc 50-60 and ground.

The test gears were coated with MoS₂ by sputtering. While certain mechanisms of the JWST use nanocomposite MoS₂ coatings [4], the mechanisms of interest for this work have a pure MoS₂ coating, and so the test gears were provided with such a composition. The chamber capacity required two coating runs. Witness coupons were in the chamber during sputtering. The thickness of the coating on the witness coupons were reported by the vendor to be 37,000 angstroms for one run and 30,000 angstroms for the second run. After coating the test gears were sealed in bags using a dry inert cover gas by the coating vendor. Gears to be tested as unexposed remained in the sealed bags until the start of the installation procedure. The time from the opening of the bag until the gears were in a vacuum condition in the gear test rig was minimized to all practical extent.

The tooth surface roughness was measured along the involute profile direction of a randomly selected pinion tooth using a stylus profilometer prior to sputtering. Another tooth was inspected after sputtering and subsequent exposure to humid air prior to testing. The data were filtered using an ISO standard Gaussian filter with 0.8-mm cutoff and 300:1 bandwidth. The resulting calculated roughness average value, 0.42 micrometer Ra, was the same prior to and after sputtering. The peak-to-valley range of the roughness-filtered data was approximately the same as the measured thickness of the coating on witness samples that were in the sputtering chamber with the gears. The roughness topography features were the same prior to and after sputtering (Fig. 1).

One half of the available tooth surfaces were exposed to humid air prior to testing. The exposure was done in a closed chamber with the gears placed on a perforated plate. Beneath the plate was a saturated solution of water and sodium bromide. The saturated salt solution provided a relative humidity of approximately 57 percent, this value being near the upper limit 60 percent relative humidity of certain storage conditions for the mechanisms of interest.

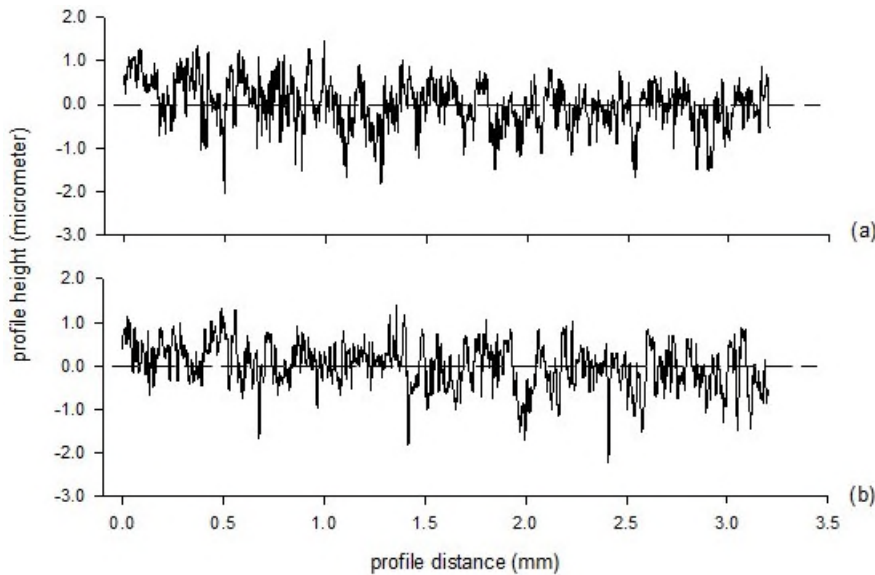


*Figure 1. Roughness profiles of pinion teeth, measurement along the involute direction.
(a) Prior to sputtering. (b) After sputtering and then exposure to humid air.*

Gear Test Rig

To accomplish gear testing in vacuum, a test rig previously used for testing of rollers [5-7] was adapted for gear testing. To adapt the rig, the spacing from the input to the output shaft was increased from 36 mm used for roller testing to 112 mm for gear testing. Otherwise, the rig setup was the same as had been used for roller testing.

The vacuum gear rig is depicted in schematic form in Figure 2. The pinion motion is provided by a variable speed electric motor. A magnetic-particle brake attached to the output shaft imposes torque on the gear. A pressurized air cylinder controls the pinion position. The air cylinder acts through a pivot axis to rotate the drive motor plate that mounts the driving shaft and drive motor. The rotation of the drive motor plate moves the pinion toward the gear in an arc motion to bring the teeth into mesh. The pressure to the cylinder, and thereby shaft center distance, is adjusted by a hand-operated valve. A linear variable displacement transducer (LVDT) measures the position of the drive motor plate, and this sensor output was used to establish the proper operating center distance. The rig features a turntable that is used to impose controlled misalignment of shafts for roller experiments. For gear testing, the turntable was adjusted to provide for an aligned shaft condition. A turbomolecular pump assisted by a scroll pump provides vacuum in the test chamber. Ferrofluid seals maintain the vacuum at the shaft-chamber interfaces. The typical condition in the test chamber is a pressure of 3×10^{-7} Torr. The most prevalent remaining constituent in the chamber during testing is water vapor as was determined using a residual gas analyzer [8].

The torque on the output shaft is measured by a strain-gage type torquemeter of 22 N-m (200 in-lb) torque capacity. Calibration was done in place using deadweights acting on a torque arm of known length attached at the test gear position and reacting the output shaft to ground.

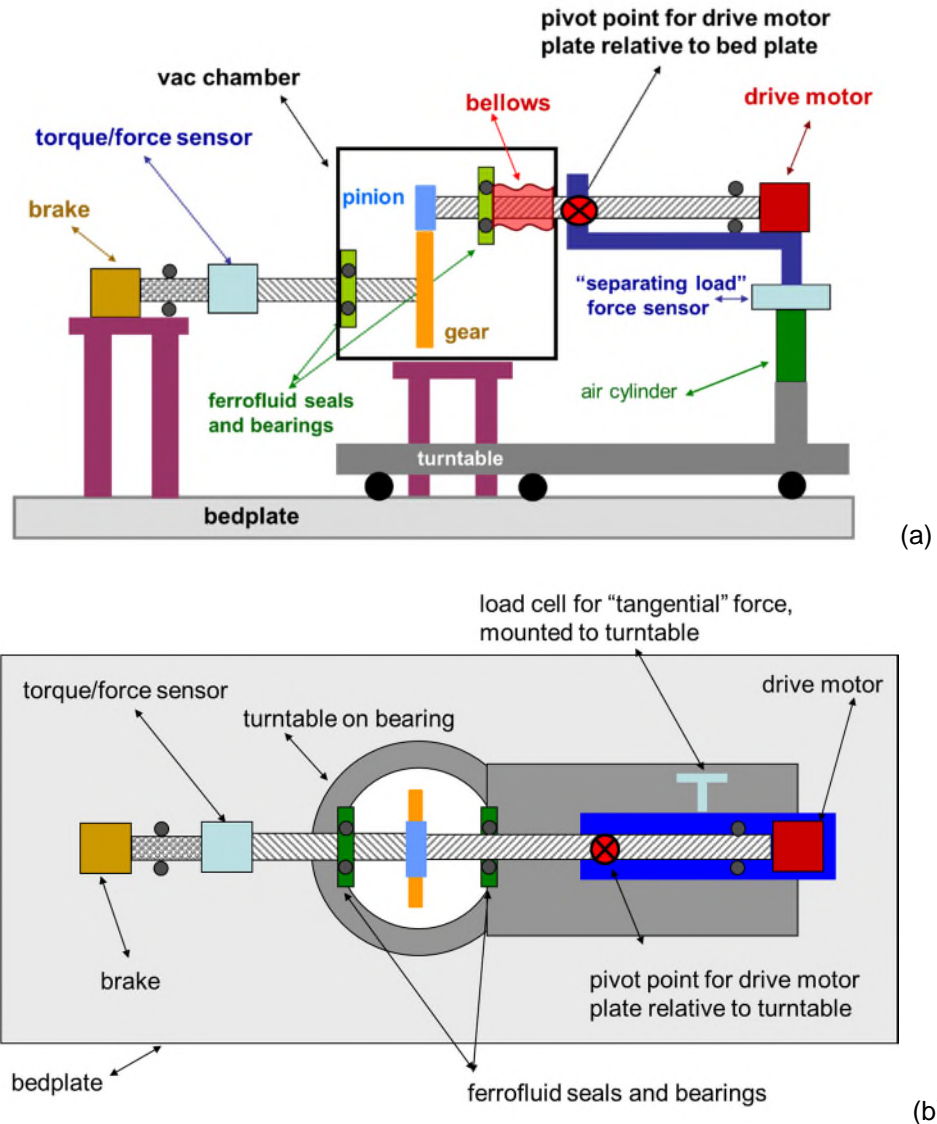


Figure 2. Schematic representation of vacuum gear rig. (a) Side view. (b) Overhead view.

The force created by the meshing gear teeth can be described as three orthogonal forces. Each of these force components influences a sensor as will be described with the aid of Figure 2. The tooth force component directed tangent to the pitch circle is termed the tangential force. The torque on the gear is a product of the tangential force and the operating pitch radius. The gear tooth tangential force attempts to rotate the drive motor plate about a pivot axis, but the table is constrained to the turntable through a load sensor termed as the “tangential” force sensor. The tooth force component directed along the line joining the gear centers, the separating force, acts through a pivot axis and thereby attempts to tilt the drive motor table, but the table motion is constrained by the air cylinder through a sensor termed the “separating load” force sensor. Because the drive motor plate is not balanced about the pivot point, the force measured on this “separating force” sensor is a combination of the gear separating force action and the unbalanced overhung weight of the motor and plate. The third component of gear tooth force acts along the direction of the gear shaft, the gearing thrust force. Although spur gears create, theoretically, zero thrust forces, in practice a thrust force is indeed created because of inevitable manufacturing tolerances and small mounting misalignments. The magnitude of the resulting thrust force depends in part

on the friction between the mating gear teeth. The action of spur gears creating a thrust force is analogous to the friction-dependent thrust forces created by misaligned rollers (Ref. 5).

Shaft speeds and total number of shaft revolutions were measured using encoders on each shaft. The encoder pulses were counted and recorded via a digital pulse counter. The encoders provide 6000 pulses for each shaft revolution.

A linear variable differential transformer (LVDT) measures the tilting position of the drive motor plate. The tilting of the plate changes the pinion-to-gear center distance, and so the LVDT output thereby measures the operating center distance. As the gears operate, the operating center distance changes slightly because of the gearing action. As the tooth contact position on the pinion moves from the dedendum, through the pitch point, and to the addendum region, the friction force changes direction. This changing friction force causes slight changes in the instantaneous center distance, because of elastic deflections, and thereby the friction force affects the output of the LVDT.

The gear teeth surface conditions were photographed at regular intervals during testing through a viewport. The images were captured digitally using a single-lens reflex camera with a 150-mm micro lens and a 12-million effective pixel image sensor.

Experiment Method

The experimental approach was to conduct an equal number of tests using unexposed and exposed surfaces. The test matrix of Table 1 was selected for the study. The pinions and gears were assigned randomly as 6 test pairings per Table 1. With the ability to test both front (side "A") and back (side "B") of each tooth, 12 tests were possible. Test article pairings 1 through 4 were assigned to have side "A" tested with zero exposure to humid air. There was some minimal exposure time to air during installation procedure into the rig, but in this report such minimal exposure is considered as zero exposure. For test article pairings 1 through 4, once "side A" of the teeth were tested, the pair was placed into the humidity exposure chamber to begin the exposure time for the tooth sides "B". For gear pair 5, there was zero exposure and sides "A" of the teeth were tested. Then the test chamber was opened long enough to remove the gears from the shafts and remount immediately for testing of teeth sides "B" as also unexposed. For test article pair 6, the pinion and gear were placed into the exposure chamber at the beginning of the test program to obtain a long exposure time while testing the other gears. Both sides "A" and "B" of pair 6 were tested after an exposure time of 77 days. The exposure times for other test were less than 77 days as was dictated by the testing pace and sequence.

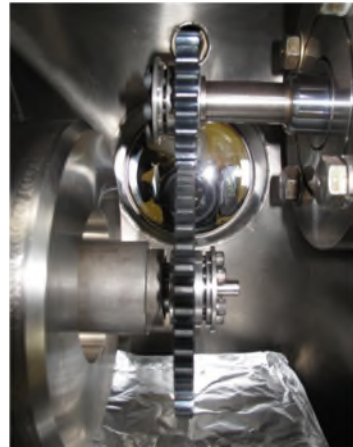
As the test sequence progressed, it was decided that photo documentation of the conditions of the teeth prior to test may prove insightful. Beginning with the fifth test in the testing order sequence (test MoS₂ 4-A, per Table 1) the first step of the testing sequence was to document the visual condition of each gear by digital photographs. Next, the gear pair was then mounted onto the test shafts, the vacuum chamber closed, and then the chamber vacuum condition was established over several hours, and typically overnight, prior to applying torque and motion. The chamber pressure was 7×10^{-7} Torr or less at the beginning of each test. Figure 3 shows a pair of the MoS₂ coated test gears out of sealed bags just prior to test and in the test chamber just prior to closing the vacuum chamber door.

Table 1. Test matrix.

Test Name	Test Article Pairing	Pinion Serial Number	Gear Serial Number	Tooth Side Loaded	Exposed	Total Exposure Time (days)	Testing Order Sequence
MOS2 1-A	1	P4	G1	A	No	-	1
MOS2 1-B				B	Yes	10	3
MOS2 2-A	2	P6	G6	A	No	-	2
MOS2 2-B				B	Yes	28	6
MOS2 3-A	3	P2	G2	A	No	-	4
MOS2 3-B				B	Yes	17	9
MOS2 4-A	4	P1	G3	A	No	-	5
MOS2 4-B				B	Yes	17	10
MOS2 5-A	5	P3	G5	A	No	-	7
MOS2 5-B				B	No	-	8
MOS2 6-A	6	P5	G4	A	Yes	77	11
MOS2 6-B				B	Yes	77	12



(a)



(b)

*Figure 3. Test gears. (a) Just prior to testing.
(b) Installed in rig just prior to closing test chamber.*

Testing was done at a constant brake torque and motor speed. The torque was 6.8 Nm for the gear as was applied by the brake and measured by torque sensor. The test speed was 80 rpm for the pinion (and consequently 43.3 rpm for the gear). The power transmitted was 31 watts. The torque was selected to provide a tooth load intensity (force per unit face width) similar to the tooth load intensity for the mechanisms of interest. The speed was selected as the maximum speed that did not induce any significant rig dynamic loading or vibrations as had been determined by previous testing of similar test gears. Testing for endurance of the coatings typically required durations longer than a working day, and unattended testing was not attempted. The testing was paused overnight, as needed, with the test chamber vacuum maintained by continuous operation of the turbopump, and then testing was resumed the following day.

The test progression was monitored by visual inspection of the tooth surfaces through a viewport, aided at times by a strobe light to “freeze” the motion. The visual condition was also recorded by digital photographs illuminated by a short duration flash through a second viewport that provided a view of the gear teeth (but not of pinion teeth). The test progression was monitored by displays of the sensor data

plotted as functions of pinion revolutions. Some previous development test revealed that as wear severity and friction increase, sensor outputs became more erratic even though their mean value remain constant. For example, when friction on the gear teeth increases, the range of the separation force increases even though the mean may still be constant. This phenomenon is the result of the tooth friction force reversing direction as the tooth contact passes through the pitch point. Thereby, the friction force first adds to, and then subtracts from, the magnitude of the separating force during the tooth mesh cycle. With higher tooth friction the excursions from the mean become larger. These observations and experience in health monitoring of geared machines led to the definition and use of “condition indicators” as a means to monitor the overall capability of the MoS₂ films to provide low friction. Condition indicators were defined as follows. Data records were collected for 1 second at 1-kHz sampling rate. For each data record, the standard deviation was calculated as the “condition indicator”, stored, and plotted as a function of accumulated pinion revolutions. Such condition indicators were reliable indicators of a change in the MoS₂ performance. Figure 4(a) provides a trend plot from test MOS2 1B of the condition indicator for the LVDT sensor that measures gear center distance changes. Marked on the plot is the indication where the MoS₂ functioning compromise has started. Also marked are three regions: Region I being the smooth running regime, Region II being near the start of MoS₂ compromise, and Region III being a significant friction regime. An example of a data record from which a “condition indicator” was calculated is shown in Figure 4(b), for the thrust force sensor, during operation in Region III. In plot of 4(b) there was relatively high tooth friction during the last 400 samples of this particular data record causing a varying thrust force.

Film durability was determined using the condition indicator trend plots. The film durability was defined as the number of pinion revolutions until the film compromise started, such as indicated on Figure 4. The film compromise was defined as the very beginning of a steady degradation of the film’s performance regarding friction. A mechanism may continue to perform its intended function for some time after such film degradation begins. The intent was to assess a relative measure of the film durability, with and without exposure to humid air.

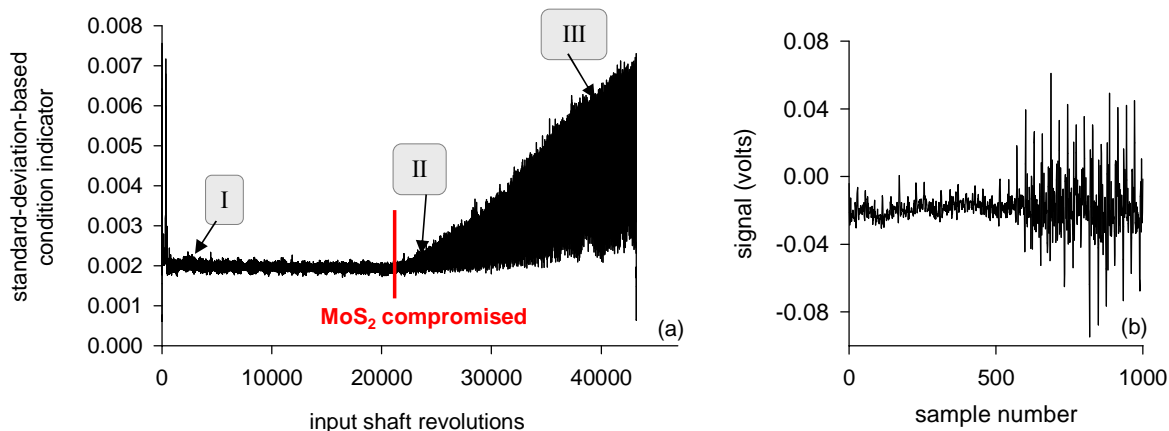


Figure 4. Typical trend and features of a condition indicator of MoS₂ film function. (a) Trend of condition indicator for the center distance (LVDT sensor), for test 1B. (b) Typical data record for calculation of standard-deviation-based condition indicator.

Experiment Results

First will be discussed the results of quantitative measures of film durability. As was described in the previous section, “condition indicators” were calculated from sensor data. A set of condition indicators were calculated every second. Figure 4(a) is an example condition indicator data trend plot from test 1B. The number of pinion revolutions corresponding to the start of film compromise, as marked on Figure 4, was determined for each test by visual inspection of such trend plots. This film durability measure was determined from each of three sensors, the gear center distance, the gear thrust force, and the gear

tangent force sensors. For each test, the average film durability was calculated as the average of the values from each sensor. The results are collected in Table 2. On average the film durability was shorter for gears exposed to humid air compared to gears with zero exposure. The film durability for gears with zero exposure ranged from 190,300 to 53,300 pinion revolutions with an average value of 100,200 and a median value of 83,500 revolutions. The film durability for gears exposed to humid air ranged from 84,700 to 21,000 pinion revolutions with an average value of 64,900 and a median value of 68,800 revolutions. Using the unexposed-gear film durability as a baseline, the exposure reduced the film durability by 35 percent based on average values or 18 percent based on median values. These reductions in film durability are similar magnitude compared to the 55 percent to 20 percent range of reductions reported by Lince, Loewenthal, and Clark [4].

Table 2. Test Results of Film Durability

Test Name	Exposure (days)	Film Durability (pinion revolutions)			
		Center Distance	Thrust Force	Tangent Force	Average Value *
MOS2 1-A	0	52,000	52,000	56,000	53,333
MOS2 2-A	0	59,000	61,000	65,000	61,667
MOS2 3-A	0	207,000	184,000	180,000	190,333
MOS2 4-A	0	86,000	69,000	94,000	83,000
MOS2 5-A	0	125,000	125,000	136,000	128,667
MOS2 5-B	0	83,000	80,000	89,000	84,000
MOS2 1-B	10	21,000	20,000	22,000	21,000
MOS2 2-B	28	69,000	55,000	74,000	66,000
MOS2 3-B	17	59,000	65,000	66,000	63,333
MOS2 4-B	17	81,000	78,000	95,000	84,667
MOS2 6-A	77	84,000	76,000	88,000	82,667
MOS2 6-B	77	70,000	71,000	74,000	71,667

* average value is the average of the 3 columns to the left

unexposed group	average = 100,200	median = 83,500
exposed group	average = 64,900	median = 68,800
percent reduction	35%	18%

The film durability values, from the “Average Value” column of Table 2, are plotted as a function of the duration of exposure to humid air in Figure 5. The plot shows that while as a group the durability was longest for zero days of exposure, there is no clear trend of rate of reduction with exposure time. The range of scatter for the film durability for six tests at zero time of exposure is greater than is the difference between average durability of exposed and unexposed gears.

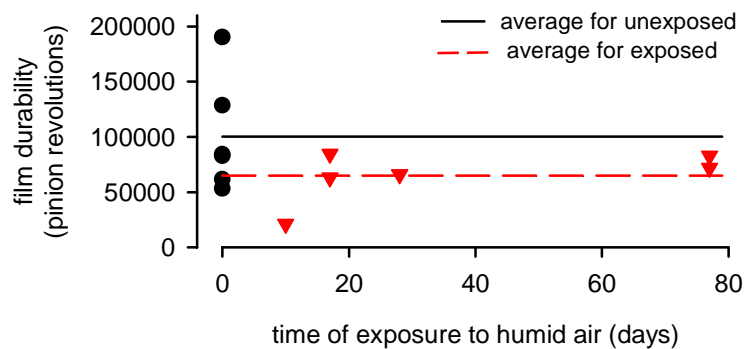


Figure 5. Film durability as function of time of exposure to humid air.

The behaviors of the films were also evaluated by studying photographs, profilometry, and scanning electron microscope inspections. During initial running of each gear pair, it was noted that the tooth surface running-in required very few tooth contact cycles. In other words, the tooth surface appearance changed dramatically, becoming more glossy and reflective in appearance, after only a few revolutions, and subsequent further visual changes to the tooth surfaces occurred at a very slow and steady rate. Figure 6 illustrates typical results of how the surface visual appearance changed for the gear teeth during a test. The first two images from left to right show the teeth prior to any running and then again after only 1 percent of the total running time. The other two images of Fig. 6 show the teeth after 50 percent and 99 percent of the test duration. The last two images show that with further running the visual condition changes less dramatically over the final 98 percent of running as compared to the first 1 percent of running durations.

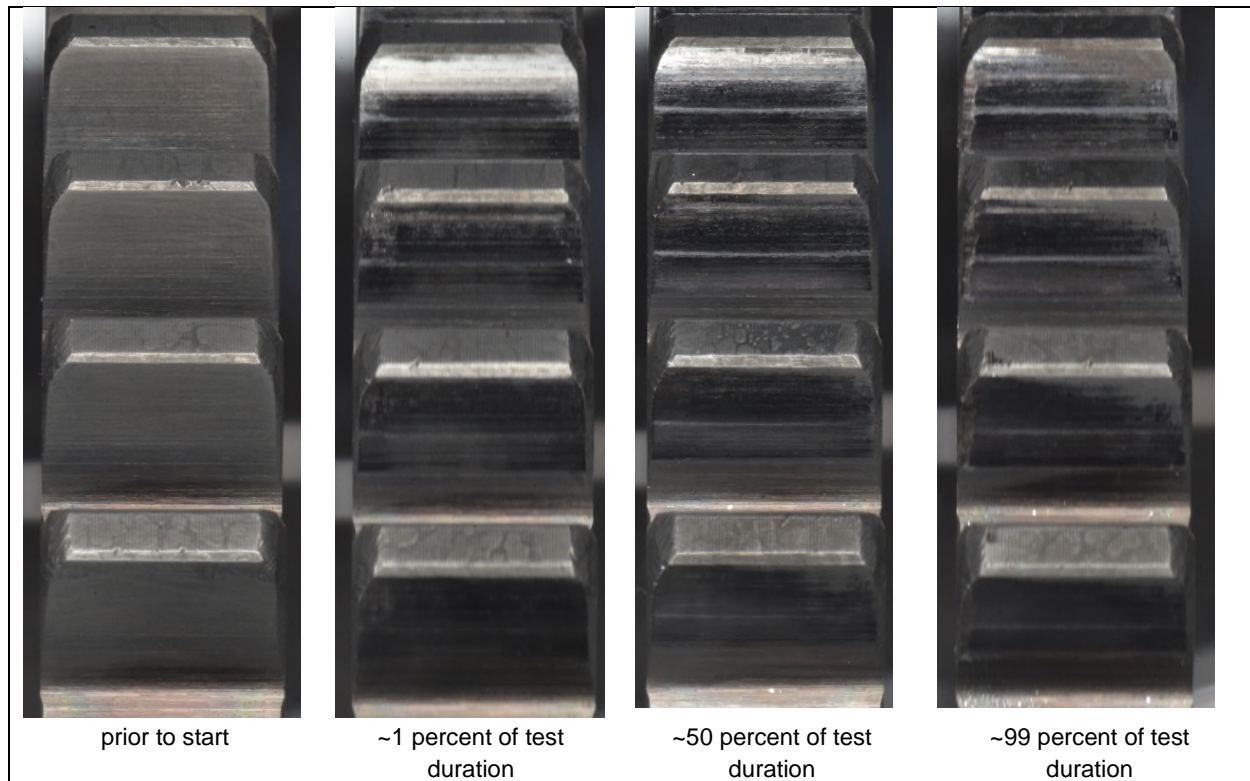
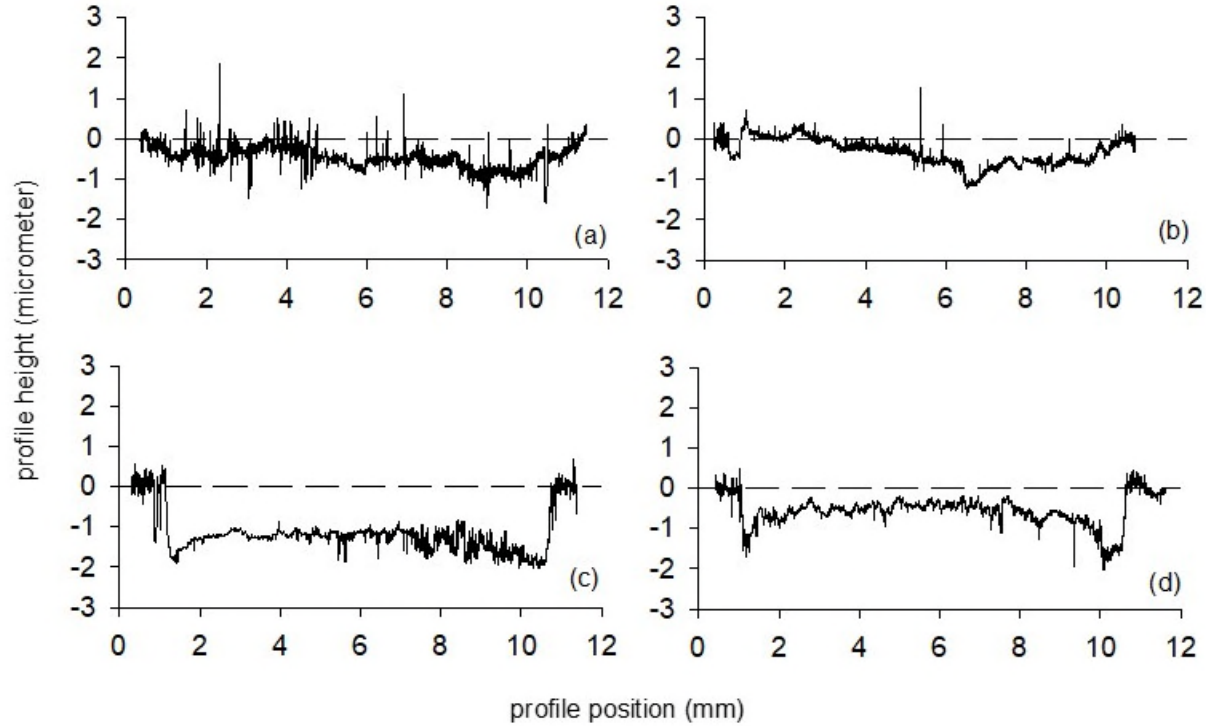


Figure 6. Gear teeth surface appearance for different durations of testing

Wear and running-in of pinion teeth were assessed using a stylus profilometer. The teeth were inspected moving the stylus with a 2-micrometer radius conisphere tip across the face width. Because the mating gear tooth face width was slightly less than that of the pinion, there were regions of the pinion tooth near each edge that did not experience contact with the gear. The data were processed to remove a least-squares linear form, using only the small regions from each edge of the trace that did not experience contact for the form removal. Traces of teeth prior to test were collected and processed in the same manner. Typical results of the inspections are provided in Figure 7. The data plots of Figs. 7(a-b) are for teeth prior to test. The surfaces show some waviness and some peak and valley features, with peak to valley distances on order of 3 micrometer, similar distance as the requested film thickness. The data plots of Figs. 7(c-d) are for tested teeth, and there is an overall wear depth of about 2 micrometers. Certain worn regions are very smooth.

After 77 days of exposure to humid air, small areas of reddish-brown coloration were noted on some teeth. Figure 8 is an example of the noted colorations. Close study of digital photographs of the pinions

and gears recorded prior to testing revealed that some coloration appeared as early as 17 days after exposure to humidity. However, not all teeth had such colored spots. For the pinion and gear pair exposed for 77 days, there was more coloration on the gear than there was on the pinion. Teeth with colorations were inspected using a scanning electron microscope (SEM). SEM images from a region having coloration, at three increasing levels of magnification, are provided in Figure 9. The image orientation has the face width direction in the vertical direction. The vertical lines are topography resulting from grinding of the teeth. This region inspected by SEM revealed that the colored areas included raised material above the surrounding surface. The highest magnification image reveals details suggesting a “growth” pushing aside and/or through the film. Figure 10(a) provides another SEM image of a similar structure as that of Fig. 9(c), from a slightly different viewpoint. During this inspection, energy-dispersive spectroscopy (EDS) was done at the four locations as marked on Fig. 10(a). The resulting spectrum of Fig. 10(b) is typical of all four inspections. The two prominent peaks of the spectrum are associated with Mo (molybdenum), S (Sulphur), and Fe (iron). It is speculated that iron oxidation was occurring at the MoS_2 film-substrate interface and progressed to eventually become evident at the surface.



*Figure 7. Profilometer inspections of pinion teeth with traces along the face width direction.
(a-b) Prior to test (c-d) After test.*



Figure 8. Red-brown coloration noted after 77 days exposure to humid air

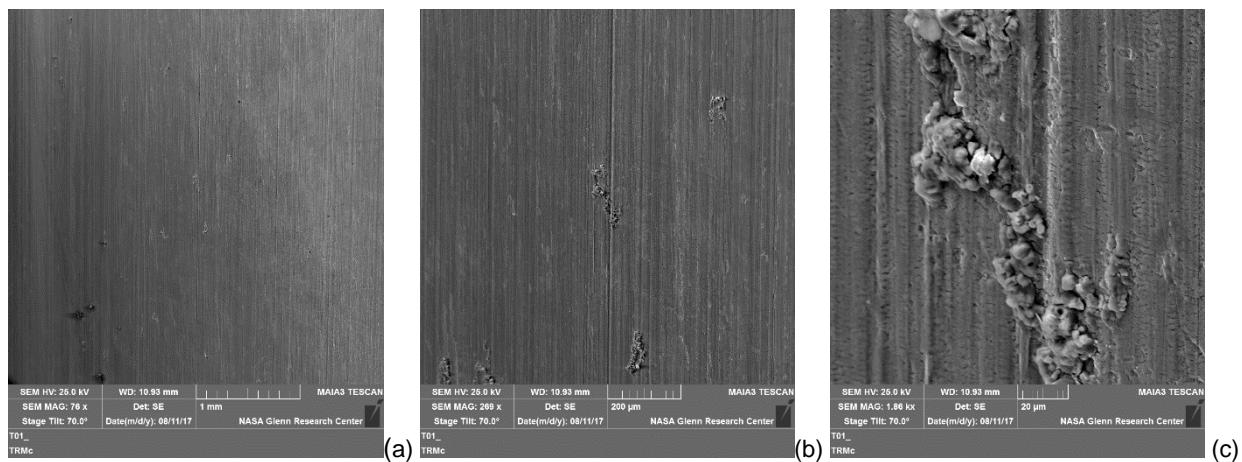


Figure 9. Scanning electron microscope inspections of a region having red-brown coloration at three increasing levels of magnification. The vertical direction is the face width direction.

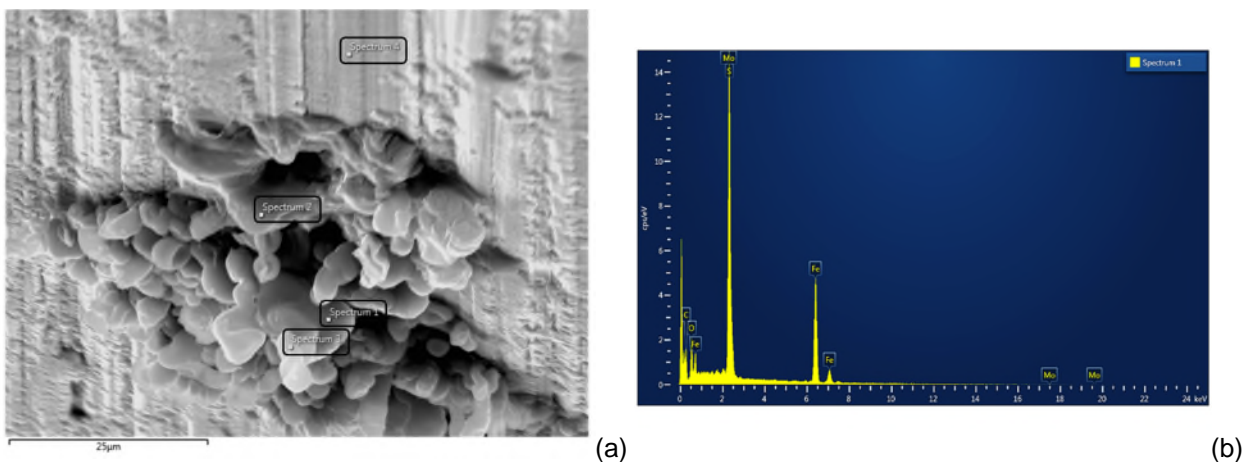


Figure 10. Scanning electron microscope inspection using energy-dispersive spectroscopy. (a) Regions inspected, per markings. (b) Spectrum for region 1, typical of all four inspections.

Study of plots of profilometry inspections of teeth prior to test revealed one inspection with an interesting topography that suggests a fortuitous tracing over a region such as revealed in the SEM images of Figs. 9(c) and 10(b). The profilometry data of this inspection, plotted using three different aspect ratios, are provided in Figure 11. The inspection was of pinon P5, in the face width direction, tooth side "B" that later was subjected to test MOS2 6B per Table 1. Fig. 11(a) reveals a localized valley feature of about 1.5-micrometer depth but having a prominent peak feature rising above, out of the valley, by about 6 micrometers. Figure 11(b) plotted using aspect-ratio 20:1 shows some details of the shape of the feature, while Fig. 11(c) illustrates the shape with true aspect ratio. The breadth of this feature is about 1.5 mm.

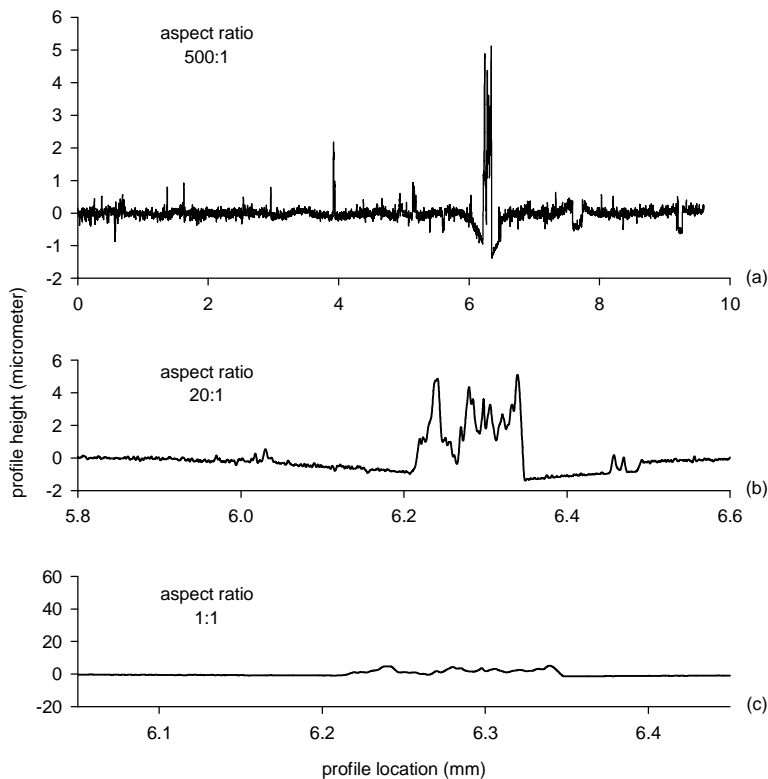


Figure 11. Profilometer inspection of a tooth after exposure to humidity for 77 days, prior to test. The same data are plotted using three aspect ratios (500:1, 20:1 and 1:1).

SEM inspection of a tooth of the pinion, after test MOS2 2A per Table 1, revealed a wide variety of features on the worn tooth surface. An inspection summary is provided in Figure 12. Figs. 12(a) and (b) can be used to locate the features of Fig. 12(c) showing highly smoothed MoS₂, blistering, and a region of loss of film thickness that thereby revealed the underlying grinding-line striation topography. The elongated blister features are aligned with the direction of rolling and sliding. Although the "delaminated" region of Fig 12(c) might suggest exposure of the steel substrate, the higher magnified image of 12(d) has appearance of material flowing in the direction of rolling and sliding. EDS inspection near the center of this region resulted in a spectrum associated with Mo (molybdenum), S (Sulphur), and Fe (iron) showing that the region did not experience complete loss of all MoS₂ thickness through this region.

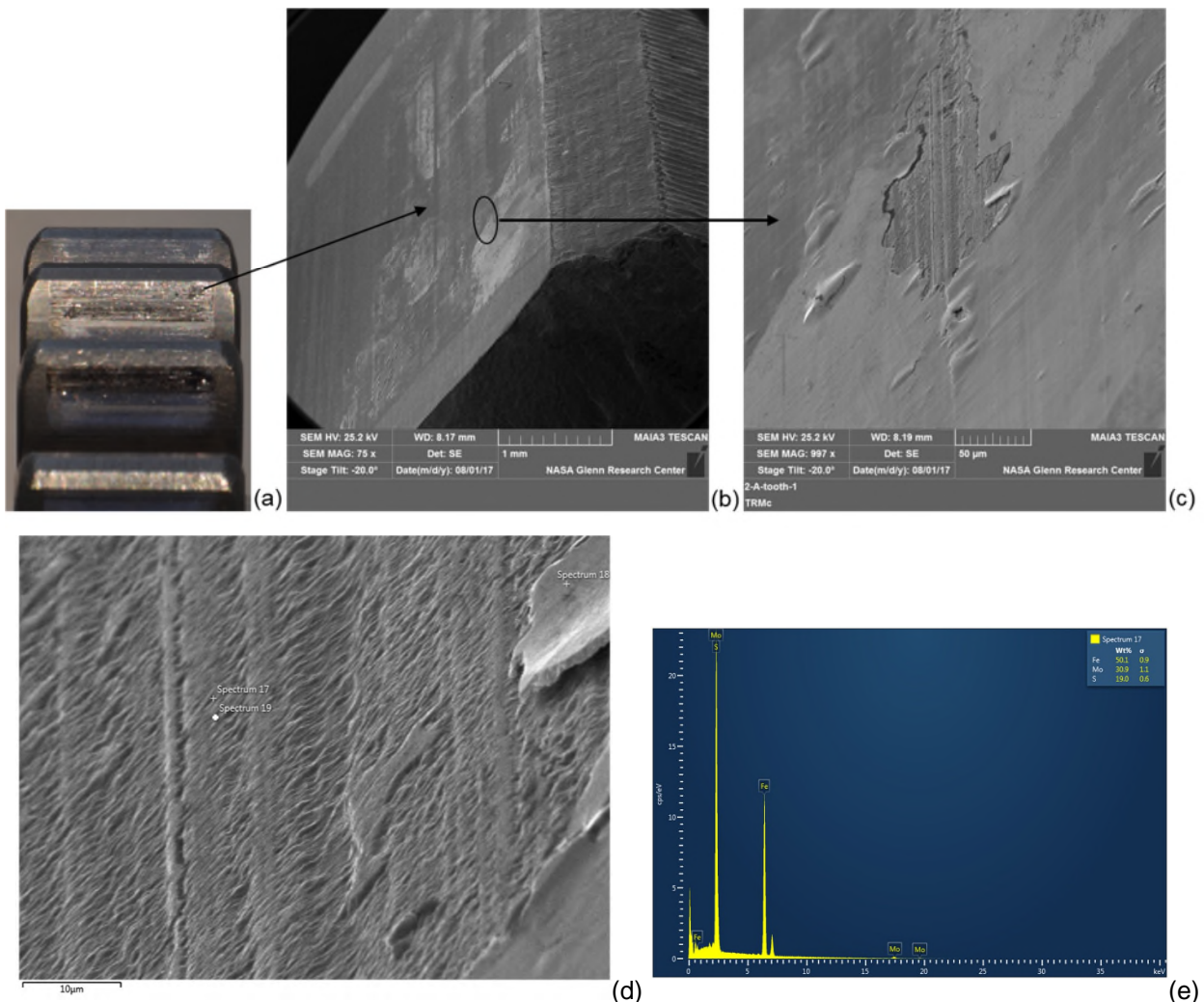


Figure 12. Scanning electron microscope inspection summary of a pinion tooth after test 2A, no exposure to humidity prior to testing. (a) Optical image showing location of SEM inspection. (b) SEM image near tooth tip. (c) SEM image of blistering and delamination of the film. (d) Close up of delaminated region. (e) EDS spectrum taken from the center of the image immediately to left.

Summary

The purpose of this work was to study the effect of exposure to humid air on the durability of a molybdenum disulfide (MoS_2) dry film lubricant applied to spur test gears and subsequently tested in vacuum environment. MoS_2 was applied by sputtering onto gears made from induction hardened and ground S45C steel. Twelve gear tests were completed in a vacuum gear rig at constant speed and torque. For this study, film durability was defined as the initiation of compromise of the MoS_2 's ability to provide low friction. Test durations were long enough to initiate this compromise. One-half of the gears tested had zero time exposure to humid air prior to testing. The other half of the gears were exposed to air of 57 percent relative humidity for exposure durations up to 77 days prior to testing.

On average the film durability was shorter for gears exposed to humid air compared to gears with zero exposure. The film durability for gears with zero exposure ranged from 190,300 to 53,300 pinion revolutions with an average value of 100,200 and a median value of 83,500 revolutions. The film

durability for gears exposed to humid air ranged from 84,700 to 21,000 pinion revolutions with an average value of 64,900 and a median value of 68,800 revolutions. Using the unexposed-gear film durability as a baseline, the exposure reduced the film durability by 35 percent based on average values or 18 percent based on median values. These reductions in film durability are similar magnitude compared to the 55 percent to 20 percent range of reductions reported by Lince, Loewenthal, and Clark [4].

The gear teeth had a very glossy appearance after very few revolutions of the gears. After this initial running-in, further change in the appearance of the teeth was a slow, steady process. Profilometry revealed that the wear depth at test completion was on the order of the specified MoS₂ film thickness.

Red-brown coloration was noted on some of the teeth that had been exposed to humid air. The colored regions appeared as soon as 17 days after exposure to humid air. SEM inspections showed that at least some of these colored areas included material raised above the surrounding MoS₂ film.

Acknowledgements

This research was supported by the NASA Engineering Safety Center (NESC). The experimental work was done with assistance from Tysen Mulder, NASA Pathways Intern. Dr. Iqbal Shareef was supported by the NASA GRC Summer Faculty Fellowship Program.

References

1. Gibson, A., et al, "Overview of Design and Validation of the Fine Guidance Sensor Mechanism for JWST", 15th European Space Mechanisms and Tribology Symposium, vol. 718. 2013
2. Gibson, A. et al, "Life-test Investigation and Status of the NIRISS Dual Wheel Cryogenic Mechanism for JWST." 15th European Space Mechanisms and Tribology Symposium, vol. 718. 2013
3. Aldridge, D, et al, "Cryogenic Motor Enhancement for the NIRISS Instrument on the James Webb Space Telescope." ESA Special Publication, vol. 737. 2015.
4. Lince, J., Loewenthal, S. and Clark, C. "Degradation of Sputter-Deposited Nanocomposite MoS₂ Coatings for NIRCam during Storage in Air", Proceedings of the 43rd Aerospace Mechanisms Symposium, (May, 2016) pp. 221-234, NASA/CP-2016-219090.
5. Krantz, Timothy, DellaCorte, C. and Dube, M., "Experimental Investigation of Forces Produced by Misaligned Steel Rollers." Proceedings of the 40th Aerospace Mechanisms Symposium, NASA/CP-2010-216272.
6. Krantz, T., and Shareef, I., "Wear of Steel and Ti6Al4V Rollers in Vacuum." Proceedings of the 41st Aerospace Mechanisms Symposium, NASA/CP-2012-21763.
7. Dellacorte, C., Krantz, T., and Dube, M., "ISS Solar Array Rotary Joint (SARJ) Bearing Failure and Recovery: Technical and Project Management Lessons Learned", NASA/TP-2011-217116.
8. Pepper, S., "Research Note-Characterization of the Test Environment of JWST Roller Wear Evaluation at NASA-GRC", Aug. 1, 2011.

An Improved Solid Lubricant for Bearings Operating in Space and Terrestrial Environments

Arindam Paul*, Harpal Singh*†, Kalyan C. Mutyala*‡ and G.L. Doll*

Abstract

The lubricity and durability of molybdenum disulfide (MoS_2) is controlled by the interfilm sliding and intrafilm flow. The primary reason for its ability to reduce friction is attributed to its crystal structure, which allows easy shearing of MoS_2 layers. Effective lubrication has been achieved under vacuum and dry conditions by employing MoS_2 as a solid lubricant. However, under humid conditions, the tribological performance of MoS_2 deteriorates. The deterioration can be offset through the incorporation of certain elements in MoS_2 , which can also improve its tribological and mechanical properties. Demands on robustness and reliability provide motivations for improvements to broaden the application range of MoS_2 coatings in mechanical systems. Although Ti- MoS_2 coatings have been shown to perform extremely well in rolling contact, it is instructive to compare the tribological performance of this coating to MoS_2 and MoS_2 doped with Sb_2O_3 and Au, in sliding contact applications. Results of this investigation indicate that the Ti- MoS_2 coating outperforms MoS_2 and MoS_2 doped with Sb_2O_3 and Au in reciprocating sliding contact experiments performed in laboratory air at 30°C and 100°C.

Introduction

Solid lubricants are materials that can reduce friction between two surfaces sliding against each other without the use of a liquid media. Solid lubricants such as MoS_2 have been successfully utilized to reduce friction and wear in vacuum applications where liquid lubricants cannot be employed. MoS_2 -based coatings are used as solid lubricants in various applications on earth and space such as cutting tools, gears, bearings, actuators and slip rings, among many others [1-3]. The tendency of MoS_2 to re-orient, from an initially random orientation, to a state where the {002} basal planes orient parallel to the surface is believed to be the major reason for its success as a solid lubricant [4, 5]. MoS_2 has a hexagonal crystal structure ($D_{4h}^6 - P6_3/mmc$) with a low friction coefficient due to the ease of its basal plane shearing. Basal planes have strong covalent bonds between S-Mo-S and weak van der Waals bonds between the planes. However, MoS_2 is susceptible to humid environments due to reactive edge sites that inhibit basal plane shearing and thereby increase its friction coefficient in the presence of oxygen and moisture [6]. Various elements (such as Ti, Cr, Zr, Au, Pb and Ni) and oxides (SbOx , PbO) have been incorporated into MoS_2 coatings to improve their tribological performance [7–12]. The addition of metals or oxides greatly affects the tribological, mechanical and structural properties of MoS_2 composite coatings [13,14].

Ti and $\text{Sb}_2\text{O}_3/\text{Au}$ doped MoS_2 coatings have found their way into several aerospace applications. The hardness and Young's modulus of doped MoS_2 is much higher than sputter-deposited MoS_2 . The improvement in mechanical properties, load bearing capacity, and wear resistance over pure MoS_2 has also been attributed to the dopant content [1]. Recently, a Ti- MoS_2 coating was developed for rolling contact applications [4]. Although this particular coating was found to perform excellently as a solid lubricant material for rolling element bearings operating in laboratory air and vacuum testing, it was also found to greatly enhance fatigue life of rolling contact applications that operate in lubricated conditions [12]. Although the friction and wear of these coatings have been extensively studied using unidirectional and reciprocating sliding, it is beneficial to compare the tribological performances of several varieties of MoS_2 coatings that are deposited similarly. In this study, Ti-containing, $\text{Sb}_2\text{O}_3/\text{Au}$ -containing, and pure MoS_2 coatings were

* Timken Engineered Surfaces Laboratory, University of Akron, Akron, OH

† Currently at Sentient Science, West Lafayette, IN

‡ Currently at Argonne National Laboratory, Lemont, IL

sputter-deposited on steel test coupons and their tribological performance was studied in humid air at two temperatures. The objective of this study was to determine the wear rates of the coatings and the wear rates of the uncoated, steel counter-faces.

Experimental Procedure

Deposition

Coatings were deposited onto AISI 52100 steel specimens in a high-vacuum, magnetron sputtering system. Ti and Sb₂O₃/Au targets were co-sputtered with MoS₂, a description of which can be found elsewhere [4], [6]. Singh et al. [4] described the deposition procedure and parameters in detail for the Ti-MoS₂ coating. All three coating depositions followed the same basic procedure. After ultrasonically cleaning the substrates in isopropyl alcohol, the substrates for the Ti-MoS₂ and MoS₂ coatings were placed onto a stationary fixture that faced two 50-mm-diameter magnetrons. First, the substrates were sputter etched with Ar ions for about 30 minutes. This removed surface contaminants and some of the native oxide from the steel specimens. Next, about 100 nm of Ti was deposited onto the substrates to form metallurgical bonds to the steel as well as to the functional coating. Different combinations of target materials were used in the deposition of the functional top layers of the three coating architectures. Only MoS₂ targets were sputtered to form the functional top layer of the undoped MoS₂ coating specimens, while both Ti and MoS₂ targets were sputtered simultaneously to form the functional top layer of the Ti-doped MoS₂ coating specimens. The functional top layer of the Sb₂O₃/Au-doped MoS₂ coating was deposited by simultaneously sputtering MoS₂ and Sb₂O₃/Au targets.

Characterizations

All three coatings were determined to be $1.1 \pm 0.2 \mu\text{m}$ thick by means of the calotest procedure. Adhesion strengths of the coatings to their substrates were qualitatively determined to be excellent according to the standard Rockwell C indentation tests (DIN CEN/TS 1071-18). Whereas the Ti-MoS₂ and Sb₂O₃/Au-MoS₂ functional top layers have been determined previously to be amorphous by transmission electron microscopy, the undoped MoS₂ functional top layer was found to comprise randomly oriented, micro-crystallites of MoS₂. Compositional measurements performed by x-ray photoelectron spectroscopy indicated that all three functional top layers were slightly sub-stoichiometric in sulfur, and the dopant concentrations were about 18% and 15% for the Ti-MoS₂ and Sb₂O₃/Au-MoS₂ top layers, respectively.

Surface roughness measurements of the coatings were performed by 3D optical interferometry. The rms roughness values for the MoS₂, Sb₂O₃/Au-MoS₂, and Ti-MoS₂ coatings were determined to be $9 \pm 1 \text{ nm}$, $7 \pm 2 \text{ nm}$, and $8 \pm 2 \text{ nm}$, respectively. The average rms roughness values of the uncoated AISI 52100 balls was $598 \pm 19 \text{ nm}$.

Tribological Test Parameters

Dry reciprocating sliding contact experiments were performed on a ball on disk tribometer at a contact stress of 660 MPa (96 ksi). These tests were conducted with a sliding amplitude of 1 mm, a frequency of 20 Hz, and a normal load of 1 N. Tests were conducted in laboratory air (17% RH) and at 30°C and 100°C. Coefficients of friction were determined in situ, and at least 3 different durations (sliding distances) were performed for each temperature. Subsequent to each test, wear scars in the coatings and on the uncoated balls were measured using 3D optical profilometry. Wear volumes for the steel balls and coated disks were determined as a function of dissipated energy (E_d), where E_d is the product of the frictional force and the sliding distance. Although wear volumes of the coating were determined directly using 3D optical interferometry, wear volumes of the balls were calculated from a measurement of the radius of the wear scar

$$V_{ball} = \frac{\pi h}{6} (h^2 + 3r^2) \quad (1)$$

where

$$h = R_b - \sqrt{R_b^2 - r^2} \quad , \quad (2)$$

R_b is the radius of the ball [μm], and r is the radius of the wear scar [μm].

Results

MoS₂

Average friction coefficients (μ_{avg}) with standard deviations measured for the three coatings at 30°C and at 100°C are displayed in Figure 1. The three values of μ_{avg} at 30°C for steel paired with MoS₂, Sb₂O₃/Au-MoS₂ and Ti-MoS₂ are 0.19 ± 0.03 , 0.21 ± 0.04 , and 0.20 ± 0.01 , respectively and are statistically equivalent. Average friction coefficients for the 100°C tests are 0.09 ± 0.01 , 0.04 ± 0.00 , and 0.09 ± 0.03 for steel paired with MoS₂, Sb₂O₃/Au-MoS₂ and Ti-MoS₂, respectively. Notably, μ_{avg} corresponding to the Sb₂O₃/Au-MoS₂ pairing is about 50% less than the values obtained for the Ti-MoS₂ and MoS₂ pairings. The low value of μ_{avg} for the Sb₂O₃/Au-MoS₂ coating has been attributed to thermally driven Ostwald ripening of the Ag and subsequent diffusion of agglomerated Ag to the Sb₂O₃/Au-MoS₂ surface [6].

Wear volumes (V) for the MoS₂ coating and mated steel ball obtained from tests performed at 30°C are displayed and plotted against E_d in Figure 2 along with optical images of the wear scars generated after 17,000 cycles. Lines in the figures are least square fits of

$$V = \alpha E_d + V_0 \quad (3)$$

where α is the wear coefficient $\mu\text{m}^3/\text{J}$, E_d is the dissipated energy J, and V_0 is the offset μm^3 . The values of R^2 close to unity indicate the goodness of the fits. The wear coefficients for the ball and the MoS₂ coating were determined to be $772 \pm 26 \mu\text{m}^3/\text{J}$ and $3282 \pm 10 \mu\text{m}^3/\text{J}$, respectively.

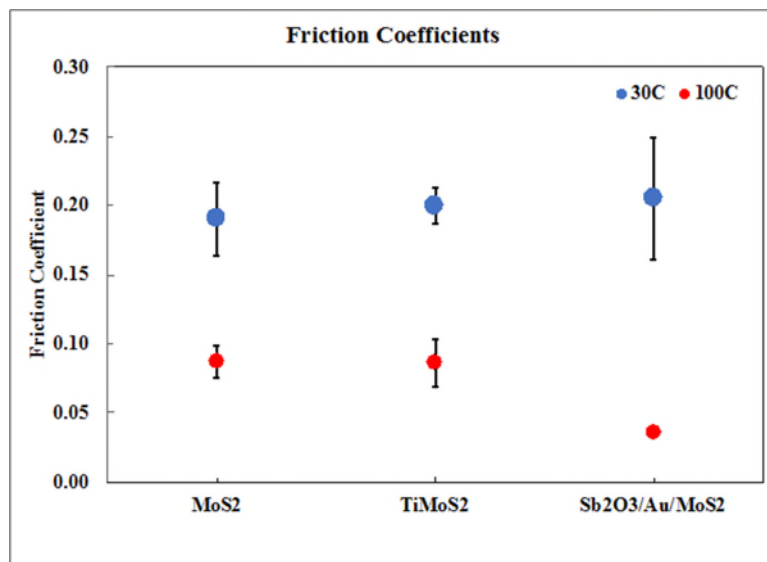


Figure 1. Average friction coefficients and standard deviations for the three coatings at 30°C and 100°C obtained in reciprocating sliding contact with a sliding amplitude of 1 mm, a frequency of 20 Hz, and a contact stress of 660 MPa.

Wear volumes for the MoS₂ coating and mated steel balls obtained from tests performed at 100°C are displayed and plotted against E_d in Figure 3 along with optical images of the wear scars generated after 17,000 cycles. The wear coefficients for the ball and the MoS₂ coating for tests performed at 100°C were determined to be $719 \pm 56 \mu\text{m}^3/\text{J}$ and $12,832 \pm 747 \mu\text{m}^3/\text{J}$, respectively. The 100°C wear coefficient of the MoS₂ is about four times that associated with the 30°C results.

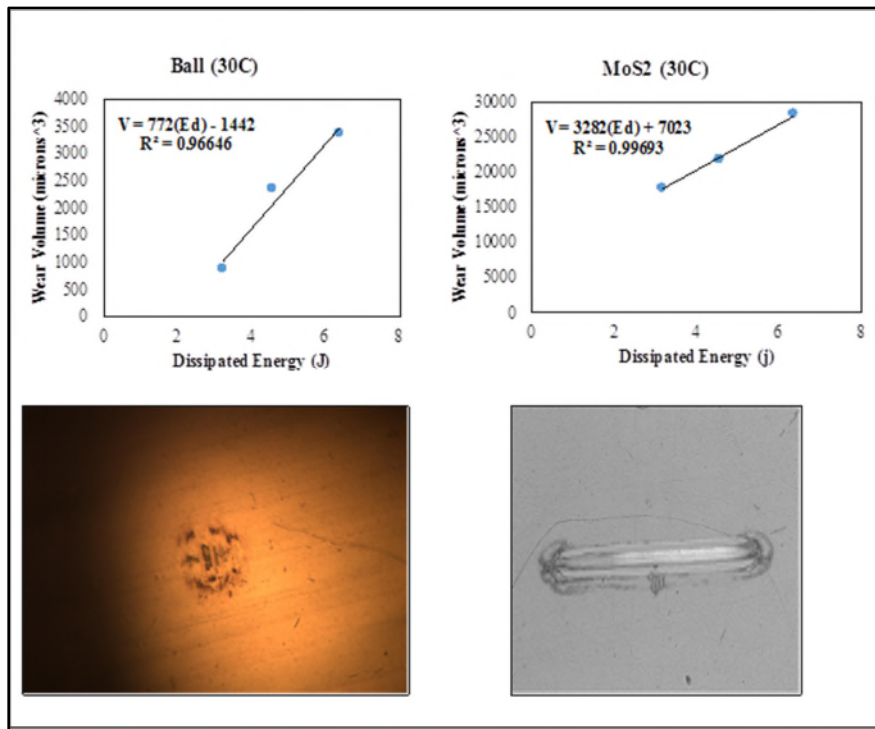


Figure 2. Wear volumes (V) for the MoS_2 coating and mated steel ball obtained from tests performed at 30°C are plotted against E_d along with optical images of the wear scars on the ball and coating generated after 17,000 cycles. Lines in the figures are least square fits of Eq. 3 to the data.

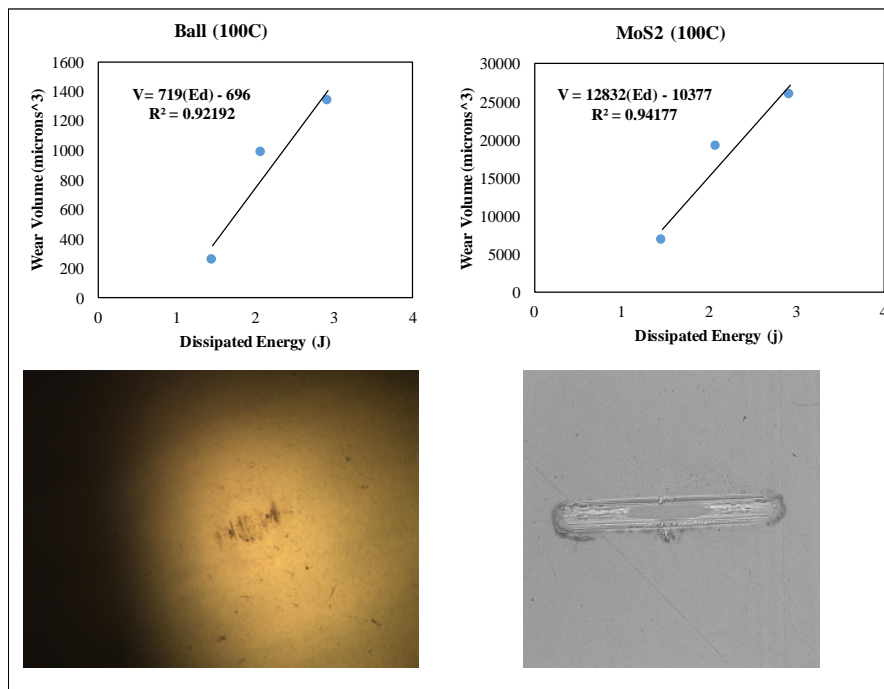


Figure 3. Wear volumes (V) for the MoS_2 coating and mated steel ball obtained from tests performed at 100°C are plotted against E_d along with optical images of the wear scars on the ball and coating generated after 17,000 cycles. Lines in the figures are least square fits of Eq. 3 to the data.

Inspection of the optical images of the ball and MoS₂ in Figure 3 provides support for the wear results. That is, the very small wear scar on the ball contains less transferred material than the ball wear scar in Figure 2, and the wear scar on the MoS₂ coating in Figure 3 is deeper than that in Figure 2. In fact, the image of the MoS₂ wear scar may show an elliptical patch of the substrate or the Ti interlayer in the center of the scar.

Sb₂O₃/Au-MoS₂

Wear volumes (V) for the Sb₂O₃/Au-MoS₂ coating and mated steel ball obtained from tests performed at 30°C are displayed and plotted against E_d in Figure 4 along with optical images of the wear scars generated after 17,000 cycles. The wear coefficients for the ball and the Sb₂O₃/Au-MoS₂ coating for tests performed at 30°C were determined to be $17,000 \pm 3,000 \mu\text{m}^3/\text{J}$ and $4,233 \pm 194 \mu\text{m}^3/\text{J}$, respectively. The optical image of the ball shows an extremely large wear scar with isolated islands of transferred material, which is consistent with the large value of the wear coefficient. On the other hand, the wear scar produced on the Sb₂O₃/Au-MoS₂ coating is relatively shallow.

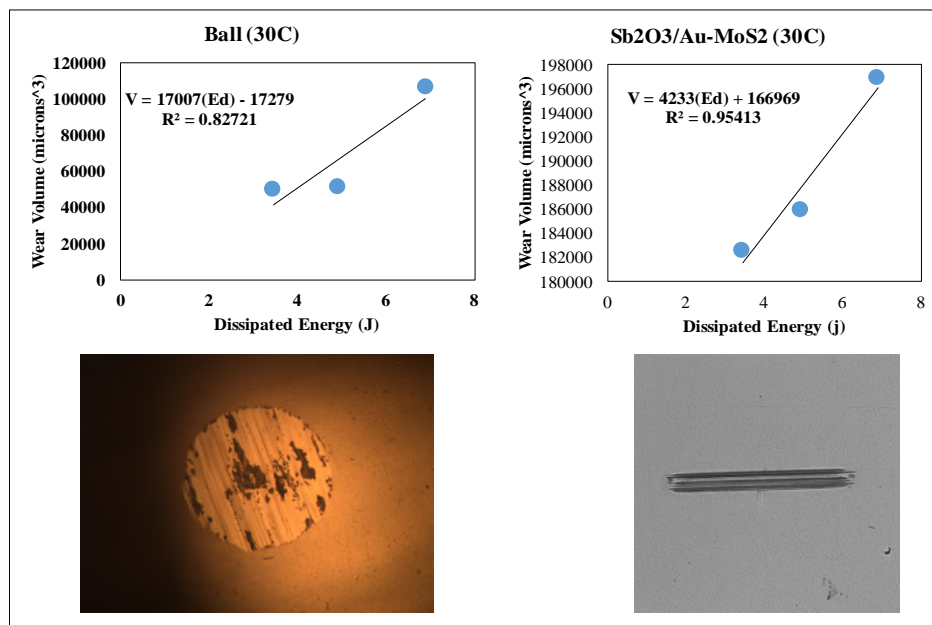


Figure 4. Wear volumes (V) for the Sb₂O₃/Au-MoS₂ coating and mated steel ball obtained from tests performed at 30°C are plotted against E_d along with optical images of the wear scars on the ball and coating generated after 17,000 cycles. Lines in the figures are least square fits of Eq. 3 to the data.

Figure 5 displays the wear volumes for the Sb₂O₃/Au-MoS₂ coating and mated steel ball obtained from tests performed at 100°C. The wear coefficients for the ball and the Sb₂O₃/Au-MoS₂ coating were determined to be $2187 \pm 6 \mu\text{m}^3/\text{J}$ and $5,032 \pm 386 \mu\text{m}^3/\text{J}$, respectively. The image of the wear scar on the Sb₂O₃/Au-MoS₂ coating displays a very shallow depth without a debris field surrounding the scar. The ball wear scar radius is very small and the scar is well-covered by a transfer film. The absence of a debris field suggests that the majority of the coating that was worn in the test, became a transfer film on the ball. This is an indication that the Sb₂O₃/Au-MoS₂ coating formed an effective VAL during the 100°C test.

Ti-MoS₂

Wear volumes for the Ti-MoS₂ coating and mated steel ball obtained from tests performed at 30°C are displayed and plotted against E_d in Figure 6 along with optical images of the wear scars generated after 17,000 cycles. The wear coefficients for the ball and the Ti-MoS₂ coating for tests performed at 30°C were determined to be $290 \pm 89 \mu\text{m}^3/\text{J}$ and $10,816 \pm 894 \mu\text{m}^3/\text{J}$, respectively. The optical image of the ball shows a moderate wear scar with an almost complete coverage of transferred material, which is consistent with the small value of the wear coefficient. The wear scar produced on the Ti-MoS₂ coating is relatively shallow and does not exhibit a large debris field. This indicates that the majority of the coating that was worn in the

test wound up as a transfer film on the ball. This is an indication that the Ti-MoS₂ coating formed an effective VAL during the 30°C test.

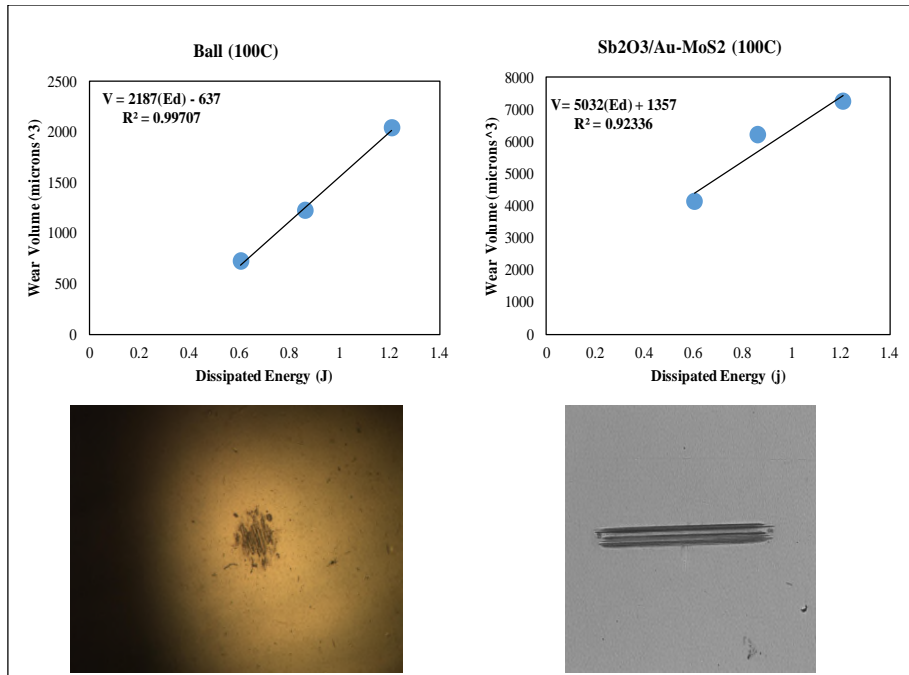


Figure 5, Wear volumes (V) for the $Sb_2O_3/Au-MoS_2$ coating and mated steel ball obtained from tests performed at 100°C are plotted against E_d along with optical images of the wear scars on the ball and coating generated after 17,000 cycles. Lines in the figures are least square fits of Eq. 3 to the data.

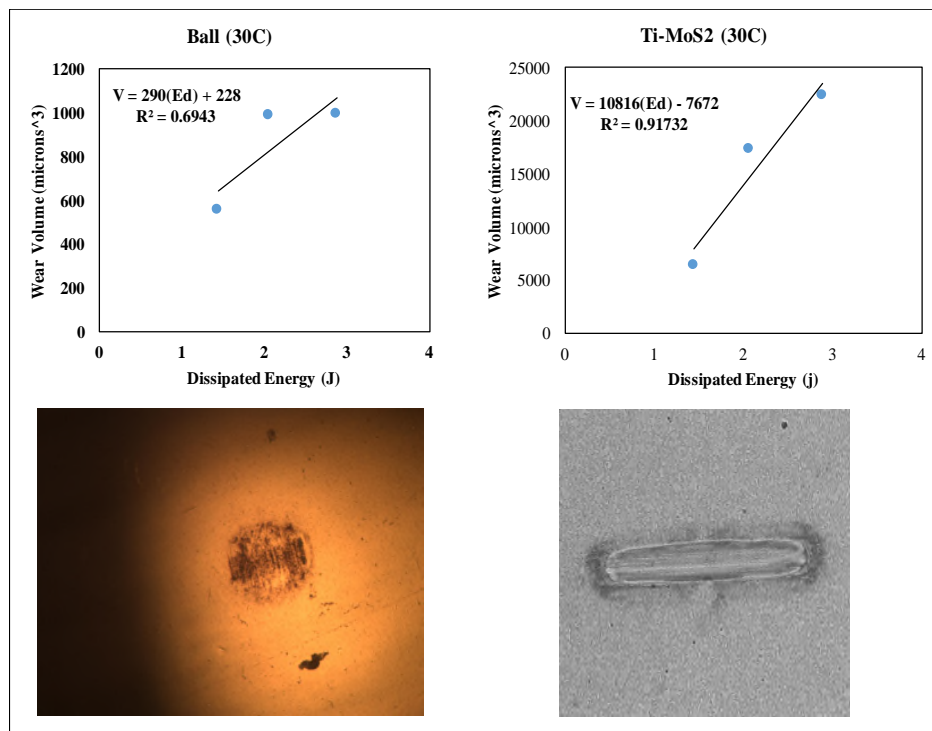


Figure 6, Wear volumes (V) for the Ti-MoS₂ coating and mated steel ball obtained from tests performed at 30°C are plotted against E_d along with optical images of the wear scars on the ball and coating generated after 17,000 cycles. Lines in the figures are least square fits of Eq. 3 to the data.

Figure 7 displays the wear volumes for the Ti-MoS₂ coating and mated steel ball obtained from tests performed at 100°C. The wear coefficients for the ball and the Ti-MoS₂ coating were determined to be $1,438 \pm 16 \text{ mm}^3/\text{J}$ and $7,941 \pm 222 \text{ mm}^3/\text{J}$, respectively. The optical image of the ball shows a moderate wear scar radius with complete coverage of transferred material, which is consistent with the small value of the wear coefficient. The wear scar produced on the Ti-MoS₂ coating is relatively shallow and does not exhibit a large debris field. This indicates that the majority of the coating that was worn in the test wound up as a transfer film on the ball, and an indication that the Ti-MoS₂ coating also formed an effective VAL during the 100°C test.

Discussion

Ball and coating wear coefficients determined from analysis of the 30°C and 100°C data are gathered in Table 1. It is convenient to assign wear regimes as low ($\alpha_L < 1000 \text{ } \mu\text{m}^3/\text{J}$), moderate ($1000 \text{ } \mu\text{m}^3/\text{J} < \alpha_M < 10,000 \text{ } \mu\text{m}^3/\text{J}$), and high ($\alpha_H > 10,000 \text{ } \mu\text{m}^3/\text{J}$). According to this convention, low ball wear rates were obtained for the 30°C measurements from the Ti-MoS₂ and MoS₂ coatings, with the lowest ball wear rate produced by the Ti-MoS₂ coating. An extraordinarily high ball wear rate was produced by the Sb₂O₃/Au-MoS₂ coating during the 30°C test. Whereas the 30°C measurements generated moderate wear rates on the Sb₂O₃/Au-MoS₂ and MoS₂ coatings, the wear rate of the Ti-MoS₂ just falls in the high wear category. The MoS₂ coating had the lowest wear rate at 30°C.

The MoS₂ coating produced the lowest ball wear rate of the 100°C tests, while the Ti-MoS₂ and the Sb₂O₃/Au-MoS₂ coatings generated moderate ball wear rates. Of the coating wear rates at 100°C, the Ti-MoS₂ and the Sb₂O₃/Au-MoS₂ coatings had moderate wear rates while the MoS₂ coating had a high wear rate.

The Sb₂O₃/Au-MoS₂ coating exhibited a high degree of abrasiveness to the steel ball. Incorporation of the Sb₂O₃ in the MoS₂ is believed to disrupt the ability of the material to achieve long range crystallographic order, making the coating less susceptible to degradation from moisture [10]. The proposed mechanism through which this coating can achieve a sustainable VAL is by the thermally driven diffusion of Ag to the surface of the coating [6]. It is proposed that the average friction coefficient of $\mu_{avg} = 0.2$ measured in the 30°C experiments was insufficient to generate enough local heating of the coating to initiate Ag diffusion. Furthermore, it is also proposed that the Sb₂O₃ content in the coating was responsible for the abrasiveness exhibited during the 30°C testing. On the other hand, the coating was much less abrasive in the 100°C tests and the pairing with the steel ball yielded a very small friction coefficient of $\mu_{avg} = 0.04$. This appears to indicate that the elevated temperature of 100°C was sufficient to establish a beneficial VAL between the steel and this coating.

An effective VAL is one that inhibits high amounts of wear of the coating and the counterface over the temperature range and relative motion experienced by a specific application. Although Ti-MoS₂ has been previously shown to perform exceptionally well in rolling contact [4,9,12], based upon the results of these measurements, it can be concluded that the Ti-MoS₂ coating would meet the VAL requirements better than the tested MoS₂ and Sb₂O₃/Au-MoS₂ coatings when in contact with reciprocating sliding steel counterfaces over a temperature range of 30°C to 100°C.

It is important to point out that although the experiments were performed in laboratory air, the environment had a very low humidity (17% RH) during the testing. Although it is expected that the wear rates of all three coatings will increase with increasing relative humidity, undoped MoS₂ tends to experience the greatest increase [3].

Table 1: Wear rates in [mm³/J] determined for the mated ball and coatings tested at 30°C and 100°C.

Coating	30°C		100°C	
	Ball Wear [μm ³ /J]	Coating Wear [μm ³ /J]	Ball Wear [μm ³ /J]	Coating Wear [μm ³ /J]
MoS ₂	772 ± 326	3,282 ± 10	719 ± 56	12,832 ± 747
Sb ₂ O ₃ /Au-MoS ₂	17,007 ± 2,939	4,233 ± 194	2,187 ± 6	5,032 ± 386
Ti-MoS ₂	290 ± 89	10,816 ± 894	1,438 ± 16	7,941 ± 222

Conclusions

Some aerospace applications such as rolling element bearings and gears have utilized MoS₂ and Sb₂O₃/Au-MoS₂ solid lubricant coatings in demanding environments where conventional oils or greases are unsuitable. Results of this study combined with the results of previous studies [4,9,12], strongly indicate that Ti-MoS₂ merits consideration as a solid lubricant coating for rolling element bearing and gearing applications. Important findings of this study include:

- Whereas the MoS₂ coating performed well at 30°C, it experienced a high wear rate at 100°C and failed to form a VAL in the contact with a steel counterpart.
- The Sb₂O₃/Au-MoS₂ coating required an elevated temperature of 100°C to form a VAL, and was extremely abrasive to the steel counterpart at 30°C.
- The Ti-MoS₂ coating formed effective VALs at 30°C and 100°C.

Acknowledgements

The authors are thankful to The Timken Company for providing financial support and guidance for this project. The authors appreciate the help of Dr. Barbara Fowler of Timken Engineered Surface Laboratories for her help in tribological testing and characterization analysis, and Haifeng Qin (UA Chemical and Biomolecular Engineering) and Zhencheng Ren (UA Mechanical Engineering) for their assistance with the deposition system. The authors also thank Dr. Ryan Evans from The Timken Company, Dr. Hamidreza Mohseni (now at Bosch) and Prof. Thomas Scharf at the University of North Texas for past contributions.

References

1. Teer, D. G. "New solid lubricant coatings." *Wear* 251.1-12 (2001): 1068-1074.
2. Hilton, Michael R., et al. "Structural and tribological studies of MoS₂ solid lubricant films having tailored metal-multilayer nanostructures." *Surface and Coatings Technology* 53.1 (1992): 13-23.
3. Sliney, Harold E. "Solid lubricant materials for high temperatures—a review." *Tribology International* 15.5 (1982): 303-315.
4. Singh, H., et al. "Tribological performance and coating characteristics of sputter-Deposited Ti-Doped MoS₂ in rolling and sliding contact." *Tribology Transactions* 58.5 (2015): 767-777.
5. Singer, I. L., et al. "Role of third bodies in friction and wear of protective coatings." *Journal of Vacuum Science & Technology A: Vacuum, Surfaces, and Films* 21.5 (2003): S232-S240.
6. Scharf, T. W., P. G. Kotula, and S. V. Prasad. "Friction and wear mechanisms in MoS₂/Sb₂O₃/Au nanocomposite coatings." *Acta Materialia* 58.12 (2010): 4100-4109.

7. Singh, H., et al. "An investigation of material and tribological properties of Sb₂O₃/Au-doped MoS₂ solid lubricant films under sliding and rolling contact in different environments." *Surface and Coatings Technology* 284 (2015): 281-289.
8. Stupp, Bernard C. "Synergistic effects of metals co-sputtered with MoS₂." *Thin solid films* 84.3 (1981): 257-266.
9. Singh, H., et al. "Tribological performance and coating characteristics of sputter-Deposited Ti-Doped MoS₂ in rolling and sliding contact." *Tribology Transactions* 58.5 (2015): 767-777.
10. Singh, Harpal, et al. "An atom probe tomography investigation of Ti–MoS₂ and MoS₂–Sb₂O₃–Au films." *Journal of Materials Research* 32.9 (2017): 1710-1717.
11. Pope, L. E., and J. K. G. Panitz. "The effects of hertzian stress and test atmosphere on the friction coefficients of MoS₂ coatings." *Surface and Coatings Technology* 36.1-2 (1988): 341-350.
12. Mutyala, Kalyan C., et al. "Deposition, characterization, and performance of tribological coatings on spherical rolling elements." *Surface and Coatings Technology* 284 (2015): 302-309.
13. Stoyanov, Pantcho, et al. "Microtribological performance of Au–MoS₂ and Ti–MoS₂ coatings with varying contact pressure." *Tribology letters* 40.1 (2010): 199-211.
14. Windom, Bret C., W. G. Sawyer, and David W. Hahn. "A Raman spectroscopic study of MoS₂ and MoO₃: applications to tribological systems." *Tribology Letters* 42.3 (2011): 301-310.
15. Berthier, Y., M. Godet, and M. Brendle. "Velocity accommodation in friction." *Tribology Transactions* 32.4 (1989): 490-496.
16. Godet, Maurice. "Third-bodies in tribology." *Wear* 136.1 (1990): 29-45.

Hybrid Lubrication of PFPE Fluids and Sputtered MoS₂

Michael Butterly*, Anthony Kent*, Dave Forster* and Achilleas Vortselas*

Abstract

We present an overview of the recent activities performed by the European Space Tribology Laboratory (ESTL) into the potential of hybrid lubrication of PFPE fluids (Fomblin Z25 & Braycote 601EF) and sputtered MoS₂. Test campaigns were performed using a spiral orbit tribometer (SOT), pin-on-disc tribometer (PoD), and at spur-gear level.

Results demonstrated mixed behavior of hybrid lubrication. In the best case the lifetime is extended beyond that predicted by the individual constituent lubricants, with no elevation in friction coefficient. In the worst case the application of a grease to the sputtered MoS₂ appears to inhibit the favorable tribological behavior of the solid lubricant film, reducing the lifetime and elevating the friction/torque.

The degree of success of hybrid lubrication appears to be related to the physical properties of the applied fluid lubricant (film thickness, viscosity), rather than the tribo-chemical lifetime. A model is proposed by which this behavior occurs.

We gratefully acknowledge that this work was funded by the European Space Agency.

Introduction

For a mechanism engineer lubricant selection often comes down to a trade-off between solid and fluid lubrication, with merits and disadvantages to both solutions. Solid lubricants are typically chosen in situations where temperature restraints preclude the use of fluid lubricants (due to evaporative losses or viscous torque increases), as well as applications for which contamination is a major consideration (e.g. involving optics). Fluid lubrication is typically selected for applications operating at high speeds over medium-to-long periods (high duty). Fluid lubricants also typically display lower torque noise and higher thermal conductance.

Solid Lubrication – Sputtered molybdenum disulphide

Molybdenum disulphide (MoS₂), deposited as a thin film via physical vapor deposition (PVD), is commonly used as a solid lubricant within high vacuum and spacecraft mechanism applications. Such films yield very low friction and relatively long lives when operated under high vacuum conditions [1]. These tribological properties are maintained over a wide range of temperatures [2, 3]. As such, MoS₂ coatings are used routinely to lubricate spacecraft mechanisms. However, when operated in moist air the coatings adsorb water molecules and this affects their shear properties which in turn causes the friction to increase (by up to an order of magnitude) [1].

Furthermore, the coating oxidizes and, as a result, wears at a much more rapid pace than would be the case in vacuum. Thus, operation in moist air severely reduces the subsequent in-vacuum life of the coatings [4, 5]. This reduction in life is shown to be dependent upon running duration in-air, with even short running periods producing dramatic reductions in subsequent in-vacuum life (Figure 1).

Following operation in air, friction coefficient values can return to their low vacuum-running values, but often only after a period of high friction. The magnitude and duration of this increased friction upon

* ESTL (European Space Tribology Laboratory), ESR Technology Ltd., Warrington, U.K.

subsequent vacuum running has been shown to be related to the in-air dwell period and the extent of moist air running (Figure 2) [6], and is more severe if the sputtered MoS₂ is exposed to in-air heating [7].

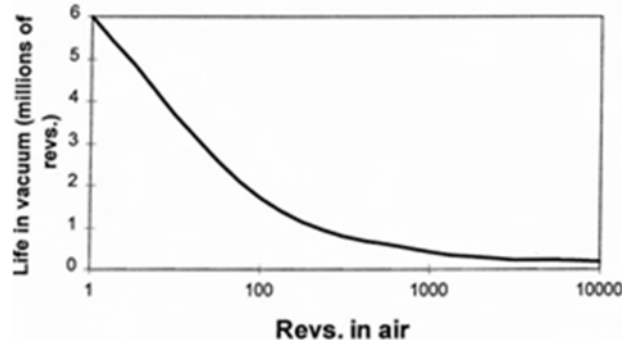


Figure 1. Low-torque life of MoS₂ lubricated ED20 bearings in vacuum as a function of in-air operation prior to vacuum testing [4]

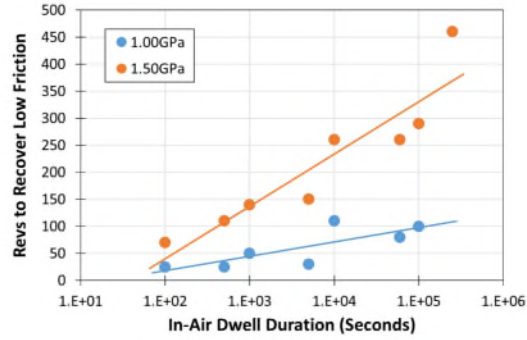


Figure 2. PoD revs required to achieve low friction performance of sputtered MoS₂ under vacuum following moist air dwell period [6]

This deleterious effect on subsequent lifetime under vacuum is of concern for space mechanisms applications, where demonstration of a successful deployment on ground is often demanded as part of the qualification program. Whilst the use of a protective dry nitrogen environment can theoretically be employed to protect the sputtered MoS₂ lubricated components during ‘on ground’ operation, this may have practical limitations especially at spacecraft level.

Numerous attempts have been made to improve the lubricating performance of sputtered MoS₂ films in moist air, including doped variants. However, this paper concentrates only on improving the performance of the existing film.

Fluid Lubrication – PFPE oils

Perfluoropolyether (PFPE) type fluids are well suited for applications in space due to their low vapor pressures, low pour points, resistance to radiation and atomic oxygen, good tribological properties, and being highly chemically inert [8]. Z-type PFPEs (such as Fomblin Z25, Brayco 815Z, and greases based upon these oils such as Braycote 601EF) are constructed from linear polymer chains and have been employed extensively as lubricants in spacecraft mechanisms for many decades [9]. However, under boundary conditions such lubricants are susceptible to chemical degradation, resulting in increased friction coefficients, material wear, and eventually component failure [10, 11]. This tribo-chemical degradation occurs primarily through the reaction between the polymer chains and chemically active sites in the substrate steel [12]. Nevertheless Z-type PFPE fluids are commonly used in spacecraft mechanisms.

PFPE fluid lubricants also offer the advantage that their tribological performance in vacuum is not compromised by prior operation in moist air, as displayed by sputtered MoS₂. In fact, lifetimes of PFPE fluids (and multiply alkylated cyclopentanes) are shown to be extended in moist air in comparison to vacuum [13, 14].

Hybrid Lubrication

The suggestion is occasionally made within the space mechanisms community that a form of hybrid lubrication may circumvent the restriction on in-air operation of MoS₂, through the application of a controlled quantity of PFPE fluid lubricant to a component lubricated in the conventional way with sputtered MoS₂, thus ‘protecting’ the MoS₂ from the moist environment. The suggestion states that the fluid lubricant will provide low friction during operation in moist air and will subsequently be lost (either through evaporation or tribo-chemical degradation depending upon the fluid) under vacuum, allowing the

(hopefully) uncompromised MoS₂ film to provide low friction and long life for the remainder of operation under vacuum.

The potential advantage of synergistic behavior between the fluid and solid lubricating constituents also exists, where performance of the whole lubrication solution is greater than the sum of its parts. Essentially this occurs where the presence of one lubricant constituent prolongs the operational performance of the other, and vice-versa. This behavior may occur on a physical and/or chemical level.

This paper details the recent testing campaigns at ESTL to understand and characterize the potential of hybrid lubrication of PFPE fluids and sputtered MoS₂ with respect to the advantages stated above, performed at both tribometer and component level. These testing campaigns shall be discussed individually.

Spiral Orbit Tribometer Experimental Campaign

SOT Phase One – Feasibility Study

A feasibility demonstration of hybrid lubrication was performed using a Spiral Orbit Tribometer (SOT). The SOT is essentially a rolling tribometer, where a solid or low volume of fluid lubricant can be assessed under representative conditions of an angular contact bearing operating within the boundary regime. Details of the SOT are described elsewhere [15].

SOT test balls of 52100 steel were first lubricated with sputtered MoS₂. These same test balls were then lubricated with ~50 µg of PFPE oil Fomblin Z25 via solvent plating, providing hybrid Z25/MoS₂ lubrication. Hybrid lubricated balls were inserted into the SOT test chamber and rotated in moist air for a defined duration and subsequently under high vacuum to failure. Test conditions were 2.25-GPa peak contact stress, 100-RPM rotation speed, and 23°C. Failure of the hybrid lubricant was defined as an increase in friction coefficient to ≥ 0.28.

Initial feasibility results demonstrated encouraging behavior, with indications that a small volume of fluid lubricant acts to protect the sputtered MoS₂ from elevated wear rates in moist air, and some degree of extension in life is observed under vacuum. In addition, the friction coefficient of the hybrid lubrication was found as 0.02 (Figure 3), identical to the value for MoS₂ alone in vacuum [16]. Given that Z25 provides a friction coefficient of 0.1 under vacuum on the SOT, we can say with some confidence that the MoS₂ was providing lubrication at this time. A more detailed account of this initial feasibility study is provided elsewhere [17].

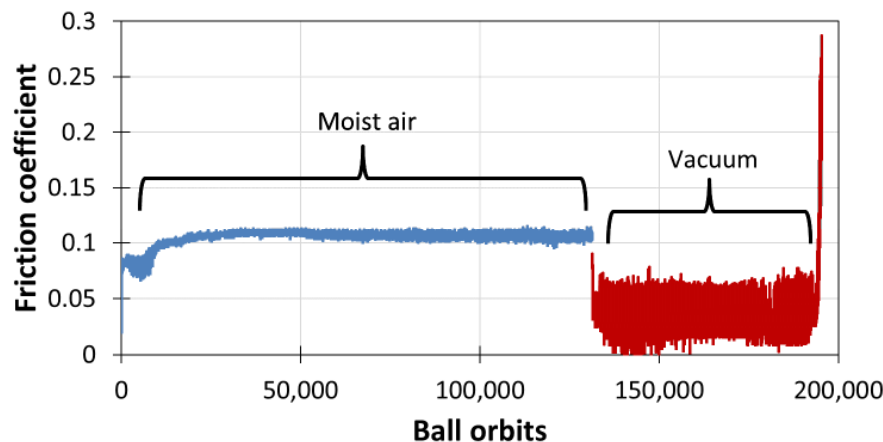


Figure 3. Hybrid Z25/MoS₂ rolling in air (blue) and vacuum (red). Elevated frictional noise during vacuum running is an artifact introduced by the analysis software and is not real

Given the encouraging performance of the hybrid Z25/MoS₂ lubrication, additional SOT tests were performed to further investigate this behavior.

SOT Phase Two – Detailed SOT Study

Phase Two of SOT testing was performed in an equivalent manner to Phase One, with the following alterations.

- Tests performed at three contact stresses (3.00 GPa, 2.25 GPa & 1.50 GPa peak).
- Tests performed with varying durations of in-air running prior to vacuum.
- In-air running durations defined as percentages of in-vacuum MoS₂ life.

Prior to hybrid lubrication testing, the lifetimes of MoS₂ under vacuum at the above contact stress was assessed. From these lifetimes the in-air durations required for the Phase Two hybrid testing can be calculated. The required in-air running durations are given in Table 1, with L_x being the in-vacuum MoS₂ life at a given contact stress S_x.

Table 1. Required in-air running for SOT Phase One

Peak stress	S ₁ (3.00 GPa)	S ₂ (2.25 GPa)	S ₃ (1.50 GPa)
Required in-air operation	0.0005 L ₁	0.0005 L ₂	0.0005 L ₃
	0.005 L ₁	0.005 L ₂	0.005 L ₃
	0.05 L ₁	0.05 L ₂	0.05 L ₃
	0.5 L ₁	0.5 L ₂	0.5 L ₃

Results of Phase Two SOT testing on hybrid lubrication are presented in Table 2.

Except for S1-D, all tests passed the in-air duration of running without displaying evidence of lubricant failure, with S1-D displaying failure after operating for 98% of the required orbits. These results allow us to state that the application of ~50 µg of Fomblin Z25 oil can allow balls lubricated with sputtered MoS₂ to run in-air for 50% of their in-vacuum lifetime without displaying evidence of failure.

Following in-air testing each sample was run until failure under vacuum conditions. Vacuum lifetimes show that in almost all cases vacuum lifetimes were extended in comparison to sputtered MoS₂ alone.

Table 2. Moist-air and subsequent normalized vacuum lifetimes of hybrid Z25/MoS₂ lubricated SOT tests

ID	Peak Stress (GPa)	Required in-air operation	In-air Pass/Fail	Subsequent vacuum life / MoS ₂ only life	Total life / predicted vacuum life
S1-A	3.00	0.0005 L ₁	Pass	2.199 L ₁	2.176
S1-B	3.00	0.005 L ₁	Pass	1.501 L ₁	1.484
S1-C	3.00	0.05 L ₁	Pass	2.106 L ₁	2.130
S1-D	3.00	0.5 L ₁	Fail (98%)	0.000 L ₁	0.486
S2-A	2.25	0.0005 L ₂	Pass	1.521 L ₂	1.463
S2-B	2.25	0.005 L ₂	Pass	3.644 L ₂	3.550
S2-C	2.25	0.05 L ₂	Pass	2.456 L ₂	2.399
S2-D	2.25	0.5 L ₂	Pass	0.002 L ₂	0.482
S3-A	1.50	0.0005 L ₃	Pass	1.210 L ₃	1.103
S3-B	1.50	0.005 L ₃	Pass	4.686 L ₃	4.291
S3-C	1.50	0.05 L ₃	Pass	2.976 L ₃	2.833
S3-D	1.50	0.5 L ₃	Pass	2.392 L ₃	2.648

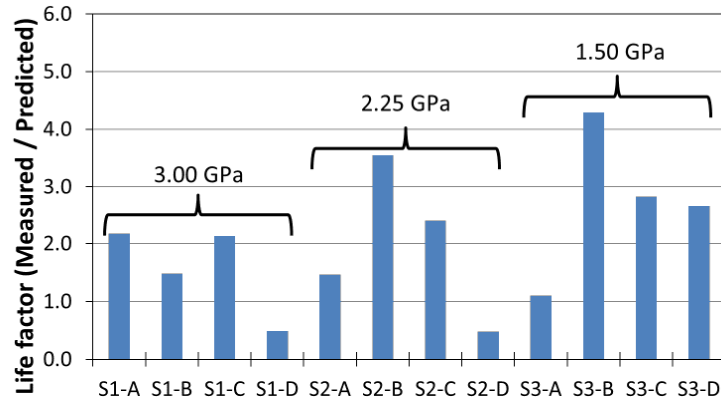


Figure 4. Measured lifetimes of hybrid Z25/MoS₂ lubrication as factor of predicted life

Using the predictions of fluid lifetimes taken from [16], we can calculate the individual contributions from the fluid and solid components of these tests under vacuum (assuming no prior in-air running). Such calculations demonstrate that for all Phase Two SOT tests (except for S1-D and S2-D), the total hybrid lubrication lifetime is longer than that of the individual lubricant constituents (Figure 4). That is to say there is a synergistic lubrication effect.

$$\text{Life of PFPE/MoS}_2 \text{ lubrication} > \text{Life of PFPE lubrication} + \text{Life of MoS}_2 \text{ lubrication}$$

In addition, the steady state friction coefficient in during the vacuum stage of testing was significantly below 0.1 in all cases. This suggests that the MoS₂ was providing the lubrication during the in-vacuo stage of all hybrid tests throughout the extended life.

Post-test inspections of the test pieces showed mixed regions of MoS₂ debris captured within the degraded PFPE oil, displaced to the edges of the ball tracks. No dusting of loose MoS₂ debris was observed, in contrast to the typical post-test observations of MoS₂ alone on the SOT.

Pin-on-Disc Tribometer Experimental Campaign

PoD Phase One – High volume fluid lubrication

To assess the potential for hybrid lubrication in a pure sliding environment a series of Pin-on-Disc (PoD) tests were performed under the following test conditions.

- Discs lubricated with Braycote 601EF grease only.
- Discs lubricated with sputtered MoS₂ only.
- Disc lubricated with both sputtered MoS₂ and Braycote 601EF. Where possible the same test disc was used as for the MoS₂-only test.

Grease lubricant was applied following standard ESTL procedure recommending 10 mg/cm² to a disc of surface area 4.4 cm², amounting to 44 mg onto the surface of each test disc. The grease was applied by syringe and then distributed using a ISO class-5 wipe to the necessary volume of grease, measured using a microbalance.

All tests were performed under vacuum, 0.6 ms⁻¹ sliding speed, on standard 52100 steel PoD test pieces. Contact stress and temperature was varied as detailed below. Failure of the lubricant was defined as an increase in friction coefficient to ≥ 0.3 . Friction and lifetime results are provided in Table 3.

Table 3. Tribological behaviors of PoD test campaign of hybrid Braycote 601EF/MoS₂ lubrication. Lifetimes are normalized to behavior of MoS₂-only, RT, 1500 MPa

Test ID	Lubricant	Peak stress (MPa)	Temp	Normalized Lifetime	Friction coefficient
PoD.A1	Braycote 601EF	850	23	0.001	0.20
PoD.B1	MoS ₂	850	23	8.591	0.03
PoD.C1	Braycote 601EF/MoS ₂	850	23	0.253	0.06
PoD.A2	Braycote 601EF	1500	23	0.005	0.15
PoD.B2	MoS ₂	1500	23	1.000	0.02
PoD.C2	Braycote 601EF/MoS ₂	1500	23	0.272	0.04
PoD.A3	Braycote 601EF	2000	23	0.000	0.17
PoD.B3	MoS ₂	2000	23	0.060	0.06
PoD.C3	Braycote 601EF/MoS ₂	2000	23	0.070	0.04
PoD.A4	Braycote 601EF	850	120	0.004	0.26
PoD.B4	MoS ₂	850	120	1.867	0.10
PoD.C4	Braycote 601EF/MoS ₂	850	120	0.413	0.15
PoD.A5	Braycote 601EF	1500	120	0.012	0.26
PoD.B5	MoS ₂	1500	120	0.194	0.06
PoD.C5	Braycote 601EF/MoS ₂	1500	120	0.008	0.16
PoD.A6	Braycote 601EF	2000	120	0.014	0.26
PoD.B6	MoS ₂	2000	120	0.007	0.06
PoD.C6	Braycote 601EF/MoS ₂	2000	120	0.039	0.04

Considering hybrid lubrication, the Braycote 601EF/MoS₂ tests are disappointing in comparison to the SOT testing campaign, with the following conclusions drawn (demonstrated in Figure 5).

- The addition of MoS₂ to a grease lubricated surfaces will increase the lifetime significantly.
- The addition of grease to MoS₂ lubricated surfaces will not increase the lifetime significantly.

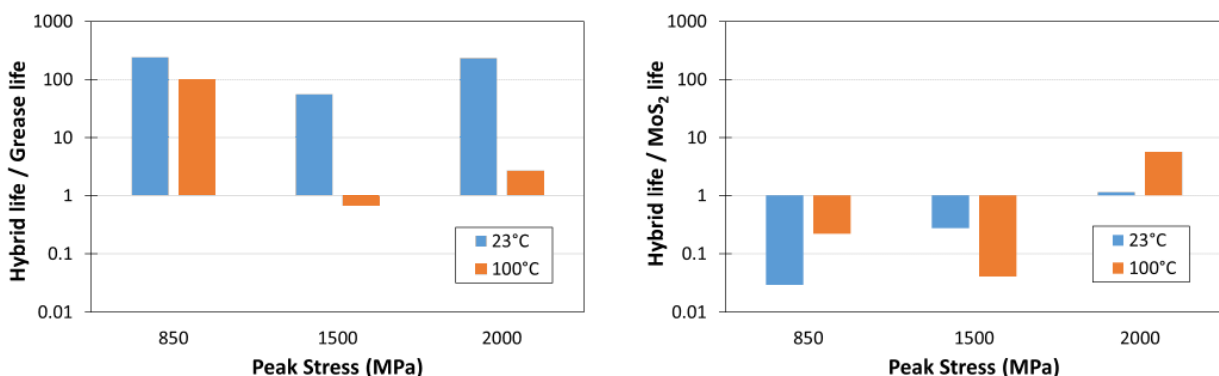


Figure 5. Hybrid Braycote 601EF/MoS₂ lifetimes as a factor of Braycote 601EF-only (left) and sputtered MoS₂ only (right) lifetimes

In addition, the friction coefficient of the Braycote 601EF/MoS₂ tests is, in most cases, elevated in comparison to MoS₂. Other observations are made from the test data above.

- The test results demonstrate that under vacuum conditions the lifetime of MoS₂ decreases with increasing temperature and contact stress. This is in line with previous data and expectations.

- As a general guide the lifetime of grease lubrication under vacuum increases with increasing temperature. This is seemingly counter-intuitive and not in line with our expectations given the known dependence of PFPE lubricant degradation and tribological lifetime upon temperature [11].

It is clear that the grease lifetimes in these PoD tests are dictated by some physical limitations of the lubricant, rather than tribo-chemical degradation. This can be conclusively demonstrated using a RGA system, where no evidence of residual gas by-products of the PFPE degradation were observed in any of the above tests, including those with hybrid Braycote 601EF/MoS₂ lubrication. Failure of the grease is therefore likely caused by the physical displacement of the fluid lubricant away from the contact zone, in contrast to the SOT tests, which may also contribute the poor hybrid performance during these PoD tests.

The improved performance of the grease at 200°C also leads to the suggestion that lower viscosity of the fluid selected may be helpful for the hybrid effect, due to an improved rate of lubricant flow into the contact zones. This can be demonstrated through repeating of a small selection of tests detailed in Table 3, utilizing the PFPE oil Fomblin Z25 as a replacement to Braycote 601EF. All other test conditions including the application method were held identical.

Results demonstrated that the Fomblin Z25 oil performed significantly better at PoD level than Braycote 601EF, with RGA data showing shear-induced tribo-chemical degradation of the lubricant under test. Hybrid Z25/MoS₂ tests were also improved in comparison to Braycote 601EF/MoS₂ (Table 4) but showed elevated test variability.

*Table 4. Performance of hybrid Z25/MoS₂ under vacuum on PoD.
Tests performed at RT, 1500 MPa*

Normalized lifetime		
Fomblin Z25	MoS ₂	Hybrid Z25/MoS ₂
2.723	1.000	0.365

Whilst Fomblin Z25 performs better than Braycote 601EF as a hybrid lubricant, it is clear that the highly encouraging performance observed at SOT is not replicated in the sliding environment of the PoD. This is potentially due to the significantly lower fluid volumes, and/or fluid film thicknesses, of the SOT testing campaign in comparison to the PoD tests (for context, the volume of fluid in a typical SOT test is three orders of magnitude less than the PoD). To explore this possibility, a second phase of PoD testing was performed utilizing a reduced lubricant volume, applied following the solvent-plating technique employed on the SOT onto MoS₂-lubricated discs.

PoD Phase Two – Low volume fluid lubrication

Three levels of Fomblin Z25 lubrication were achieved for low volume fluid lubrication tests.

- Discs lubricated with sputtered MoS₂ exposed to a PFPE solvent bath – To confirm that the solvent used for the oil plating technique (PF5060) does not adversely influence the tribological performance of the solid lubricant.
- Discs lubricated with sputtered MoS₂ and low mass of Fomblin Z25 (~40 µg).
- Discs lubricated with sputtered MoS₂ and high mass of Fomblin Z25 (~400 µg). It should be made clear that this ‘higher’ mass is still two orders of magnitude less than the recommended amount for a fluid lubricated component.

All tests were performed under vacuum, 0.6 ms⁻¹ sliding speed, 900-MPa peak contact stress, on standard 52100 steel test components. Multiple repeat tests were performed under each condition. Failure of the lubricant was defined as an increase in friction coefficient to ≥ 0.3. Mean friction and normalized lifetime results are presented in Table 5.

Table 5. Performance of varying levels of hybrid Z25/MoS₂ lubrication under vacuum on PoD. Tests performed at 900 MPa, 23°C. Lifetimes normalized to MoS₂-only life at room temperature

Lubricant	Life / MoS ₂ life (RT)	Friction coefficient
MoS ₂ only	1.000	0.03
MoS ₂ with solvent bath	0.998	0.03
MoS ₂ with Z25 (~40 µg)	1.271	0.03
MoS ₂ with Z25 (~400 µg)	1.848	0.03

Results demonstrate no tribological influence from the solvent bath, demonstrating that a PF5060 solvent immersion does not influence the lifetime of the sputtered MoS₂ film in a measurable manner.

Hybrid lubricated tests show an increase in sliding lifetime in comparison to MoS₂, with the higher mass of the applied fluid lubricant increasing the success of the hybrid lubrication (Figure 6). In addition, the friction coefficient was not compromised by the addition of the oil onto the sputtered MoS₂.

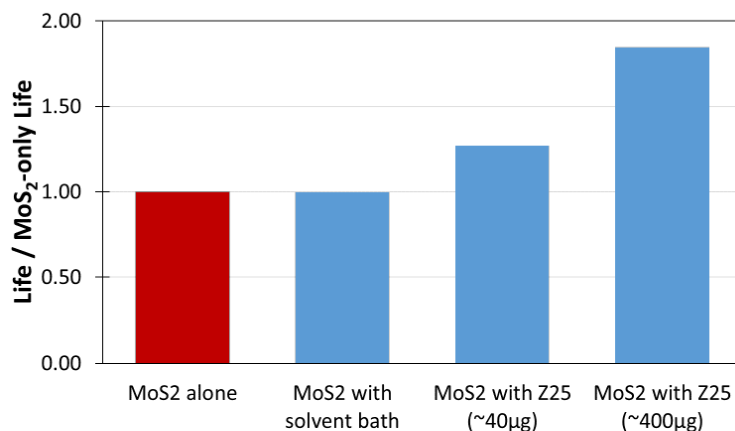


Figure 6. Normalized performance of Z25/MoS₂ lubrication under vacuum

The above tests were then repeated under vacuum at elevated temperature (200°C), displaying greater sliding lifetimes than those achieved at room temperature, again with no increase in friction coefficient (see Table 6). This is a surprising observation given that the degradation lifetimes of both the sputtered MoS₂ films and Fomblin Z25 oil are known to dependent upon operating temperature.

Table 6. Comparison of hybrid Z25/MoS₂ lubrication at room temperature and 200°C under vacuum

Lubricant	Temp (°C)	Life / MoS ₂ -only life (RT)	Friction coefficient
MoS ₂ with Z25 (~400 µg)	23	1.848	0.03
MoS ₂ with Z25 (~400 µg)	200	2.261	0.03

Using data from the Phase One PoD testing (Table 3) we observe that the sliding lifetime of sputtered MoS₂ films under vacuum at 120°C is reduced to ~10 – 20% of the lifetime achieved at room temperature. Although the nature of this reduction in life is not fully known (i.e. to what level the increased reaction between oxygen/moisture with the MoS₂ film, and the softening of the substrate steel factor into this reduction), and the dataset is not sufficient enough to produce a confident life vs. temperature relationship, it is clear that the sliding life of MoS₂ at 200°C is predicted to be <10 – 20% of the room temperature lifetime for a given contact stress.

A similar relationship exists for Fomblin Z25, where the rolling lifetime of the fluid lubricant at 100°C is reduced to ~30 – 50% of the lifetime achieved at room temperature on the SOT, due to an increase in the

degradation rate of the PFPE [11]. It is also known that, when not experiencing shearing, spontaneous degradation of Fomblin Z25 occurs between 190 – 250°C [11]. Together these indicate that the lifetime of the oil should be severely reduced when operating at 200°C (assuming the lifetime is dictated by the chemical degradation of the fluid).

It is therefore suggested that the increased lifetime of the hybrid Z25/MoS₂ at elevated temperature is again a result of temperature-related viscosity changes within the fluid lubricant, allowing ‘reflow’ of fluid into the running track to occur more easily. This is highly surprising given the low volumes of lubricant employed during these low fluid volume PoD tests, the fact that the low coefficient of friction suggests that the lubrication between the contacts is still predominantly provided by the MoS₂ film, and the extent of the predicted MoS₂ lifetime reduction. By whatever mechanism hybrid lubrication occurs (see below), it is clearly influenced by operating temperature.

Spur Gear Experimental Campaign

In parallel to the SOT and PoD test programs, a small series of spur gear tests was performed to determine if the hybrid lubrication effect could be reproduced at component level. These gear tests form part of an ongoing campaign to evaluate and characterize the performance of solid, fluid, and hybrid lubricated gears under vacuum and are reported in detail elsewhere [18].

Selected gears were BS4582 class B (DIN867 Q7) (hobbed) precision, manufactured in 17-4PH steel (Condition A) without further surface treatment. Gears were 0.5 modulus, the pinion having 40 teeth (face width 5 mm) and the wheel 120 teeth (face width 2.5 mm). It should be noted that the gears do not have a “hunting tooth” ratio, such that the same teeth contact repeatedly in each revolution.

Whilst the 17-4PH material was selected for similarity with known applications, its relatively low hardness was chosen to permit both a comparison with earlier work on non-hardened steels and a subsequent evaluation of the beneficial impact of more typically hard surface treatments (Condition A results in a minimum hardness of 35 HRC (~333 Hv)). The relatively low gear precision class and surface finish (hobbed rather than ground gears) were selected for reasons of similarity with earlier test campaigns, and to permit these production factors to become a variable in the wider context of the larger test campaign. A unique gear set was employed for each test.

Spur gear tests were performed under vacuum at 23°C, with a preload of 7.5 Nm, equivalent to a peak stress of 1000 MPa. Sputtered MoS₂, Braycote 601EF grease, and hybrid Braycote 601EF/MoS₂ provided the lubrication, with the recommended 10-mg/cm² volume of grease applied directly to the gear teeth. Rotation speed was 100 RPM for the fluid and hybrid lubricated gears, 50 RPM for the MoS₂ lubricated gears. Failure of each test was defined as an increase of the long-term torque measurement to 1.25x the steady-state value. The steady-state torque was determined by averaging the torque after an initial running-in period.

Given these selected conditions and ratio we might expect these results to provide a demanding (even perhaps a kind of “worst”) test case for the lubricants used.

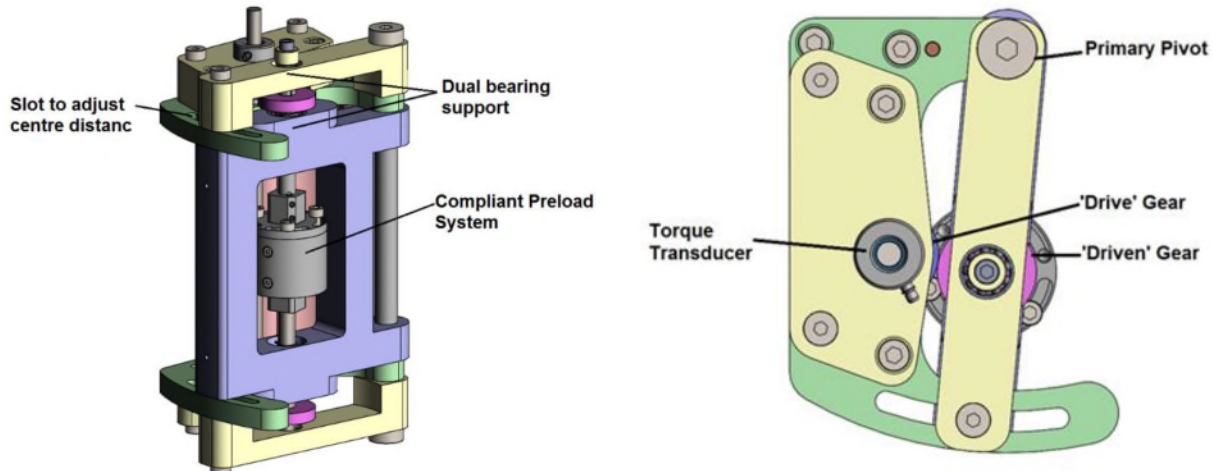


Figure 7. Conventional gear test setup for ESTL's miniature gear/pinion testing rig

Tests were performed using ESTL's miniature gear/pinion testing rig, utilizing the 4-square principle with compliant gear preloading (Figure 7). The test gears are supported on both sides by rolling element bearings to avoid any misalignment/stiffness issues. The compliant preload system maintains axial alignment between the gear shafts by supporting the shafts with plain bushings and locating the two shafts with a recess and boss. The torque was assessed via a transducer.

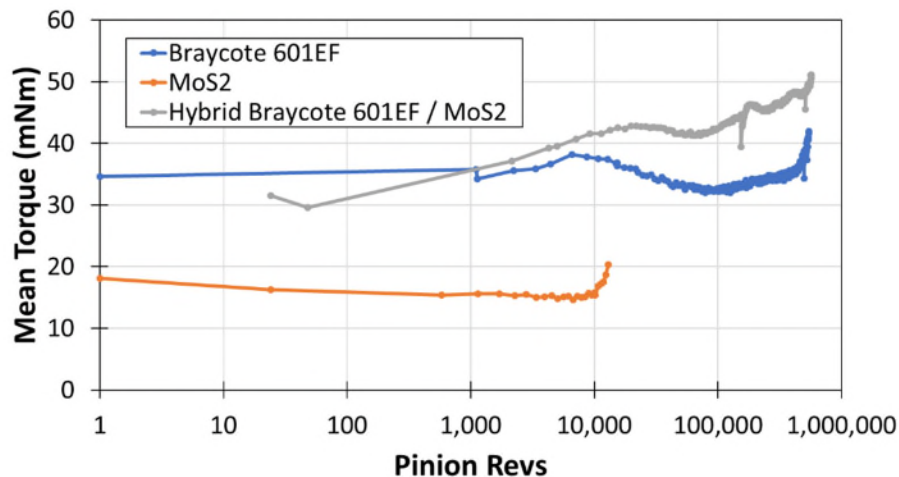


Figure 8. Mean torque behavior of spur gear tests (parasitic torques removed)

Results from the gear testing was unfortunately inconclusive. Whilst true that the hybrid lubricated test lasted longer than the sum of the lifetimes for the solid and fluid lubricated gears individually, this lifetime extension is extremely minimal and likely falls within the margin of error. The elevated torque value is also disappointing, suggesting that for the hybrid lubricated gears the lubrication was predominantly being provided by the fluid, and not the MoS₂.

Table 7. Summary of spur gear test behavior

Lubricant	Lifetime (revs)	Steady-state torque (mNm)	End-of-life torque (mNm)
Braycote 601EF	545,545	33.4	41.8
MoS ₂	12,525	15.2	19.0
Braycote 601EF / MoS ₂	567,490	42.3	52.9

Post-test inspection of gears showed clear evidence of lubricant failure, with varying degrees of scuffing and pitting of the teeth leading to metallic wear.

It is recognized that despite the similar fluid lubricant volumes employed, significant differences exist between the gear and tribometer testing which may influence the lubricant behavior, and hence the success of hybrid lubrication. The PoD tribometer is an assessment of the lubricant behavior in a pure sliding regime only, whilst the motion on the SOT is predominantly rolling. In contrast, the spur gears experience a combination of rolling motion during gear meshing at the pitch point, combined with sliding as the mesh moves from the pitch point. This meshing action of the gears can act to redistribute the fluid lubricant in the contact, bringing about an extension in life for the fluid lubricated gears, and also potentially altering the behavior in the hybrid lubricated case in a way not comparable to the PoD (or SOT).

Discussion of Results and Theory of Hybrid Lubrication

From these experimental test results the commonality can be drawn that the key factor in the success of hybrid PFPE/MoS₂ lubrication appears to be the mass and/or viscosity of the fluid layer applied to the sputtered MoS₂. This observation shall now be discussed in the context of three proposed models for the hybrid lubricating behavior.

It has been shown that hybrid lubrication has the potential for two attractive tribological behaviors.

- Hybrid lubrication can act to protect the sputtered MoS₂ film from elevated degradation/wear/oxidation when operating in moist air.
- Hybrid lubrication provides a vacuum lifetime greater than the vacuum lifetime of its constituent parts (i.e. it is synergistic), with no subsequent increase in friction/torque.

The mechanism by which these behaviors arise is not clear, but three general models are proposed.

- **Model 1) Protection of PFPE fluid from degradation** – It is known that the lifetime of a PFPE lubricant can be extended through physical protection of the fluid from reaction with the substrate steel, in this instance provided by an MoS₂ film. However, if this model were to dominate we would expect to observe a higher friction coefficient, more akin to fluid lubrication than MoS₂, when observing an extension in life. This is not the case during SOT and PoD testing.
- **Model 2) Protection of sputtered MoS₂ film from degradation** – An alternative model has been proposed whereby the layer of PFPE fluid upon the surface of the MoS₂ film acts to protect the solid lubricant from reacting with the environment, prolonging the wear life of the MoS₂. This model is attractive to explain the protection seen by the MoS₂ film when rolling in moist air but is less applicable to explain the extension of life under vacuum, where the presence of moisture/oxygen is severely reduced.
- **Model 3) MoS₂ transfer film establishment** – It is understood that the production of a 3rd-body transfer film is vital for successful lubrication of MoS₂ [19]. Given that this 3rd-body transfer film is produced from what is essentially ‘wear debris’ of the MoS₂, it is proposed that the physical presence of a viscous fluid within and around the contact zone helps to retain this MoS₂ debris, and is advantageous to the formation/protection of a 3rd-body layer.

It is clear that the success of hybrid lubrication is sensitive to the film thickness of the applied oil (or ratio of fluid film thickness to MoS₂ film thickness). If we assume an equal distribution of oil, the fluid film thickness achieved during the Phase Two PoD tests ranged from 0.05 to 0.55 μm, applied onto a ~1-μm sputtered MoS₂ film. SOT tests described above employed a similar fluid film thickness of ~0.17 μm over

a 0.5- μm MoS₂ film, assuming fluid distribution over the ball only. These test cases demonstrate an extension in life provided by the hybrid lubrication, where the fluid film thickness is 5-50% of the originally deposited MoS₂ film.

In instances where a significantly larger mass of fluid lubricant is applied to a sputtered MoS₂ film, typical of the mass applied to a grease-only lubricated component (e.g. Phase One PoD tests and spur gear tests), the fluid film thickness is closer to 50 μm , and the positive effect of hybrid lubrication is essentially lost. This demonstrates that a threshold may exist above which the application of additional fluid lubricant onto the surface of the sputtered MoS₂ film is detrimental to the performance, rather than an improvement.

Figures 9 and 10 suggests a mechanism by which this process may occurs, whereby a thicker fluid film is proposed to dislodge the lightly adhered MoS₂ transfer film from the contact via viscous drag effects (assuming Model 3). This threshold for fluid lubricant volume would appear to exist at a significantly lower volume than the amount prescribed by the standard grease lubrication procedure.

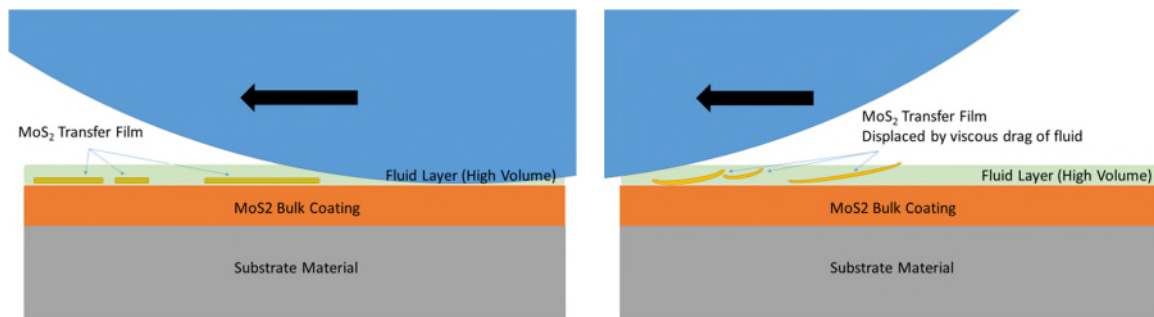


Figure 9. MoS₂ transfer film formation (3rd body) of high fluid volume hybrid lubrication

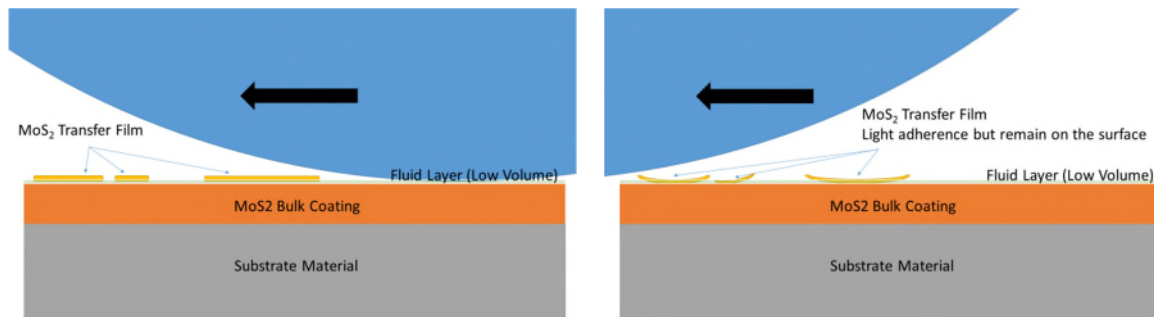


Figure 10. MoS₂ transfer film formation (3rd body) of low fluid volume hybrid lubrication

The improved performance of hybrid lubrication at elevated temperatures suggests that the viscosity of fluid also is a factor in determining the success of hybrid lubrication, with the reduced viscosity of the Fomblin Z25 at 200°C potentially allowing for greater re-flow of the lubricant within the contact zones, producing longer life. It is known that the physical lifetime of Fomblin Z25 is longer than the more viscous grease Braycote 601EF when assessed on a PoD tribometer, despite their tribo-chemical degradation lives behaviors identical [16], due to reflow effects. Given the above it is likely that a relationship exists whereby the success of hybrid lubrication is governed by the lubricant film thickness, and the physical properties (i.e. viscosity) of the fluid itself (as well, potentially, as the surface roughness of the substrate).

The true mechanism of hybrid lubrication of PFPE/MoS₂ is likely to be a combination of these above models.

Non-PFPE fluids in Hybrid Lubrication

The above hypothesis states that the success of hybrid lubrication depends primarily upon the ability of the fluid constituent to retain the 3rd-body MoS₂ transfer film within the contact zone, a phenomenon related to film thickness (or ratio of film thickness to MoS₂ thickness) and viscosity of the fluid. If this is the case, the tribological properties of the fluid itself may be second order effects compared to the physical properties of the fluid (vapor pressure, viscosity), potentially allowing for the selection of more favorable fluids to achieve hybrid lubrication.

For instance, the lower viscosity offered by the MAC fluid Nye 2001a may prove advantageous in a hybrid regime. However, this fluid is characterized by a relatively higher vapor pressure, and so potentially is not so attractive for elevated temperature operations. In such cases the ultra-low vapor pressure fluid Fomblin Z60 may be a viable candidate, despite its poorer tribo-chemical lifetime [16].

Table 8. Vapor pressures and viscosities for potential candidate fluids for hybrid lubrication

	Fomblin Z25	Nye 2001a	Fomblin Z60
Vapor pressure (mbar)			
20°C	2.13 x 10 ⁻¹³	1.53 x 10 ⁻¹¹	1.47 x 10 ⁻¹⁶
38°C	4.13 x 10 ⁻¹²	1.34 x 10 ⁻¹⁰	7.33 x 10 ⁻¹⁵
100°C	3.73 x 10 ⁻⁰⁹	4.74 x 10 ⁻⁰⁸	5.47 x 10 ⁻¹¹
Kinematic viscosity (cSt)			
20°C	263	297	600
40°C	157	108	355
100°C	49	14.6	98
Viscosity index	358	137	360

An SOT testing campaign to explore the potential of other fluids in a hybrid lubrication regime is planned to take place at ESTL in 2018.

Conclusions

The work presented here (and elsewhere by ESTL) demonstrates the potential for hybrid lubrication, but also the limitations. Under the right conditions the lifetime of a sputtered MoS₂ film can be significantly extended under vacuum and protected from a reasonable degree of moist-air operation, with no consequential increase in friction coefficient. In other cases, however, attempts at hybrid lubrication have resulted only in the loss of the good tribological properties of the sputtered MoS₂, resulting in shorter operational lifetimes.

These results would suggest that the physical properties of the applied fluid lubricant are potentially more important to the success of hybrid lubrication than their tribo-chemical properties (which more dictate their performance alone). For successful hybrid lubrication a layer of fluid lubricant of sufficient volume is required to protect the MoS₂, but this layer must be sufficiently thin, mobile and/or fluid to ensure it does not disrupt the formation of the MoS₂ transfer film or provide a fully fluid lubrication regime over the MoS₂ (i.e. the friction/torque retains the characteristic of solid lubrication).

Component and tribometer level testing activities are continuing at ESTL to verify this hypothesis, and to demonstrate the potential of hybrid lubrication at angular contact bearing level.

References

1. Roberts, E. W. "Towards an Optimised Sputtered MoS₂ Lubricant Film" *Proc. 20th Aerospace Mechanisms Symposium*, NASA CP-2423 (1986)
2. Hampson, M. et al. "Towards the Effective Solid Lubrication of Ball Bearings Operating at High Temperature" *Proc. 12th ESMATS*, ESA SP-653 (2007)
3. Hampson, M. & Roberts, E. "Cryogenic-Vacuum Assessment of Bearings Fitted with PGM cages and Lubricated with MoS₂ or Dicronite" *ESA-ESTL-TM-0055 01-* (2008)
4. Cunningham, J. "Effects of Ground Testing on the Torque Performance of MoS₂ Lubricated Ball Bearings Fitted with Duriod Cages" *ESA-TM-193* (1998)
5. Butterly, M. & Roberts E. "Impact of Environment on MoS₂" *ESA-ESTL-TM-0118 01-* (2014)
6. Butterly, M. & Cropper, M. "Effect of Air Exposure and In-Vacuo Dwell on Lubricant Coatings of Molybdenum Disulphide and Lead" *ESA-ESTL-TM-0071 01-* (2010)
7. Butterly, M. "Effect of Curing Temperature on Solid Lubricant Films" *ESA-ESTL-TM-0081 01-* (2011)
8. Jones Jr, W. "The Properties of Perfluoropolyether Used for Space Applications" *NASA TM-106275* (1993)
9. Conley, P. & Bohner, J. "Experience with synthetic fluorinated fluid lubricants" *Proc. 24th Aerospace Mechanisms Symposium*, NASA CP-3062 (1990)
10. Mori, S. & Morales, W. "Tribological Reactions of Perfluoroalkyl Polyether Oils with Stainless Steel Under Ultrahigh Vacuum Conditions at Room Temperature" *Wear* 132(1), pp. 111 (1989)
11. Butterly, M. "Fomblin Z25: A New Method for its Degradation Assessment & Proposal for Safe Operation in Space" *Proc. 15th ESMATS* (2013)
12. Carre, D. "Perfluoropolyalkylether Oil Degradation: Inference of FeF₃ Formation on Steel Surfaces under Boundary Conditions" *SLE Transactions*, 29(2), pp. 121 (1986)
13. Pepper, S. "Effect of Test Environment on Lifetime of Two Vacuum Lubricants Determined by Spiral Orbit Tribometry" *Proc. 38th Aerospace Mechanisms Symposium*, (2006)
14. Kent, A. "Life of Space Greases in Air" *ESA-ESTL-TM-0190 01-*, (2016)
15. Pepper, S. & Kingsbury, E. "Spiral Orbit Tribometry – Part I: Description of the Tribometer" *Pepperl.JanTT03*, (2002)
16. Butterly, M. "An Evaluation of Liquid, Solid and Grease Lubricants for Space Mechanisms Using a Spiral Orbit Tribometer" *Proc. 40th Aerospace Mechanisms Symposium*, (2010)
17. Butterly, M. "Hybrid Lubrication" *ESA-ESTL-TM-0110 01-* (2012)
18. Vortselas, A. "Preliminary Evaluation of Solid, Fluid and Hybrid Lubricated Gears" *ESA-ESTL-TM-0202 01-* (2018 in prep)
19. Colas, G. et. al. "Dry Lubrication Efficiency: From Ground to Space" *Proc. 15th ESMATS*, (2013)

Solving a Performance Limiting Resonance Frequency Problem of the SOFIA Secondary Mirror Mechanism by Structural Modifications

Yannick Lammen^{*},[†], Andreas Reinacher^{*},[†] and Alfred Krabbe^{*}

Abstract

The Stratospheric Observatory for Infrared Astronomy (SOFIA) is a 2.7-m infrared telescope built into a Boeing 747 SP. It reached its full operational capability in 2014 and takes off about three to four times a week to explore the infrared sky from stratospheric altitudes above most of the atmosphere's water vapor content. Since its installation in 2002, the active Secondary Mirror Mechanism (SMM) has proven to be a reliable part of the telescope assembly. However, its performance is limited by a strong structural resonance at a frequency of about 300 Hz. Solving this resonance on the hardware level would lead to a wider actuation bandwidth and therefore a faster transition time for infrared chopping and pointing corrections. Based on finite element simulations, a ring-shaped reaction mass made of aluminum has been identified as the main cause of this mode. Concepts have been developed to eliminate the resonance by changing the mass distribution along the ring shape and by implementing a parallel kinematic suspension. An end-to-end simulation including the mechanical finite element model and a model of the control algorithm was used to predict the final system performance of the developed concepts. Based on the simulation results, a prototype of the new reaction mass was designed and manufactured. An extreme mass redistribution along the ring shape by combining tungsten and AlSiC ring-segments shows the best results. The new ring was integrated and thoroughly tested on a mockup of the SMM confirming the predicted performance improvement. The closed-loop actuation bandwidth is improved by 80%. Based on this prototype, two flight units will be manufactured for future SOFIA science missions.

Introduction

After reaching its full operational capability in 2014, the Stratospheric Observatory For Infrared Astronomy (SOFIA) takes off several times a week to explore the universe. This, today's largest airborne observatory, consists of a 2.7-m-diameter infrared telescope mounted in the aft fuselage of a modified Boeing 747SP aircraft. Maximizing the scientific output requires successive optimizations of the telescope performance while not interfering with science.

One of the most complex systems of the observatory is the Secondary Mirror Mechanism (SMM) providing fast mirror steering capability for image stabilization and infrared square wave chopping. The SMM is mounted 446 mm before the focus of the primary mirror, close to the cavity opening and exposed to harsh environmental conditions (see Figure 1). After more than 10 years of use and 400 flights, this mechanism, designed and manufactured by CSEM in Switzerland, proves to be a reliable part of the observatory. However, since its integration in 2002 the performance of the SMM is limited by a strong structural resonance at a frequency of 300 Hz. For more information about SOFIA and the SMM refer to [1], [2] and [6].

^{*} Deutsches SOFIA Institut, University of Stuttgart, Stuttgart, Germany

[†] SOFIA Airborne Systems Operations Center, NASA Armstrong Flight Research Center, Edwards CA

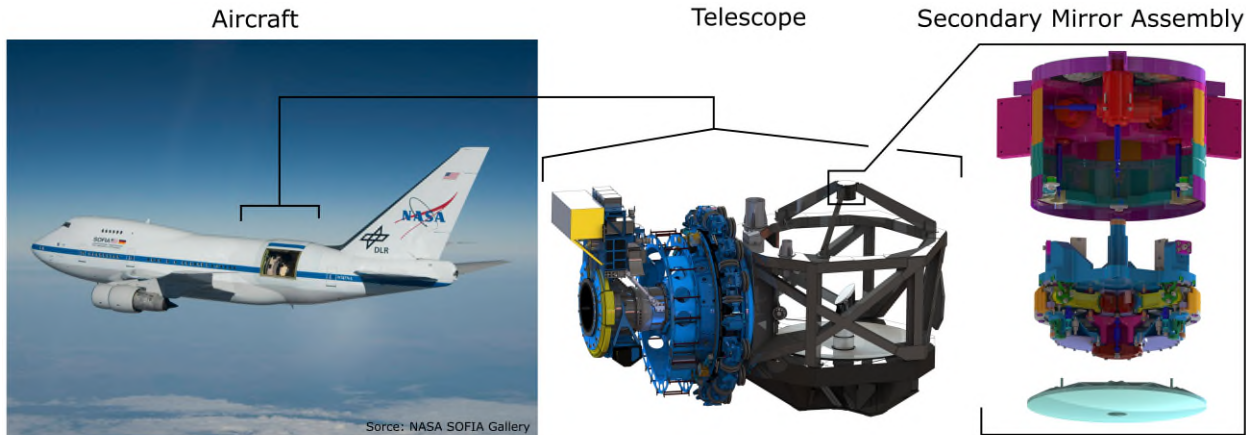


Figure 1. Location of the Secondary Mirror Assembly on the SOFIA observatory. The SMA is mounted between three spider arms positioning the secondary mirror below the focus of the primary mirror, close to the cavity opening exposed to harsh environmental conditions.

The Secondary Mirror Assembly

The Secondary Mirror Assembly (SMA) is a three-stage system that enables mirror movements in seven degrees of freedom. The design can be separated into three subsystems, the light weight silicon carbide mirror, the Tilt Chopping Mechanism (TCM), and the Focus Center Mechanism (FCM). The FCM is a hexapod platform, attached to the spider arms of the telescope structure and enables mirror movements in two rotational degrees of freedom (DoF) (tip-tilt) and three translational DoF to setup the M2 collimation and focus position. The TCM is mounted on top of the FCM and enables high-frequency tip-tilt M2 motions for infrared chopping and pointing corrections. When chopping (1125 arcsec max), the mirror is alternating the field of view by following a square wave pattern up to 20 Hz at a settling time of about 10 ms. Stationed in the Mojave Desert and flying in stratospheric altitudes, the typical mission temperature range is between -60°C and 30°C.

Figure 2 shows a schematic 120-deg section cut through the TCM presenting the main moving components and all flexure elements of the mechanism. The system is driven by three moving magnet linear actuators. The lever arm assembly amplifies the actuator force and reduces the stroke to allow high precision positioning. Three pivot rods are transferring the actuator load to the mirror holder. A set of force sensors is measuring the induced load. The mirror cell is suspended by a combination of a central pivot rod and a membrane that allows the holder to rotate in the tip and tilt domain. The rod provides stiffness and prevents motion in the focal direction. The membrane prevents side movements of the mirror holder and locks the rotational degree of freedom around the focal axis. The silicon carbide mirror is mounted to the aluminum mirror cell by three bipods to prevent stress due to thermal expansion.

A set of three eddy current sensors is used to measure the mirror position indirectly by tracking the motion of the mirror cell. To eliminate any load induction to the telescope structure when chopping, the lever arm assembly is tilting a ring-shaped reaction mass, the ‘compensation ring’, in the mirror’s opposite direction. This ring is mounted to the three lever arms by a set of flexures. All moving components of the TCM are suspended in their center of mass to prevent any excitation due to external loads.

The main structural mode of the SMA is the chop motion of the TCM at about 32 Hz. The first dominant unwanted resonance that results in mirror jitter is at 300 Hz. So far, this resonance is addressed by the controller, reducing the unwanted mirror motion at the expense of mirror steering performance (refer to [3], [4] and [5] for further information). Constraining this resonance on the hardware level would not only lead to a wider actuation bandwidth and therefore a faster transition between the two chop positions but also reduce the image jitter introduced by external disturbances acting on the active mechanism itself. From

experimental modal analysis and finite element simulations, the compensation ring was identified as the main cause of the 300-Hz mode, from here on referred to as CBEND. The mode shape presented in Figure 3 shows a deformation of the ring geometry and lateral shift of the ring on its soft serial-kinematic suspension. Mirror motion results from this coupled mode.

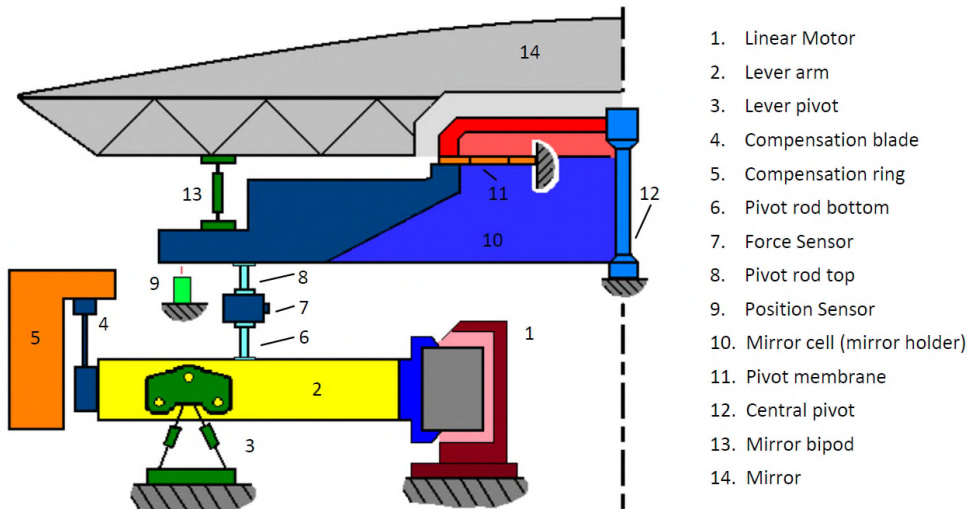


Figure 2. Schematic 120-degree section cut of the Tilt Chopping Mechanism showing the main moving components. Flexure elements are used throughout the whole system to reduce friction, backlash, and wear out.

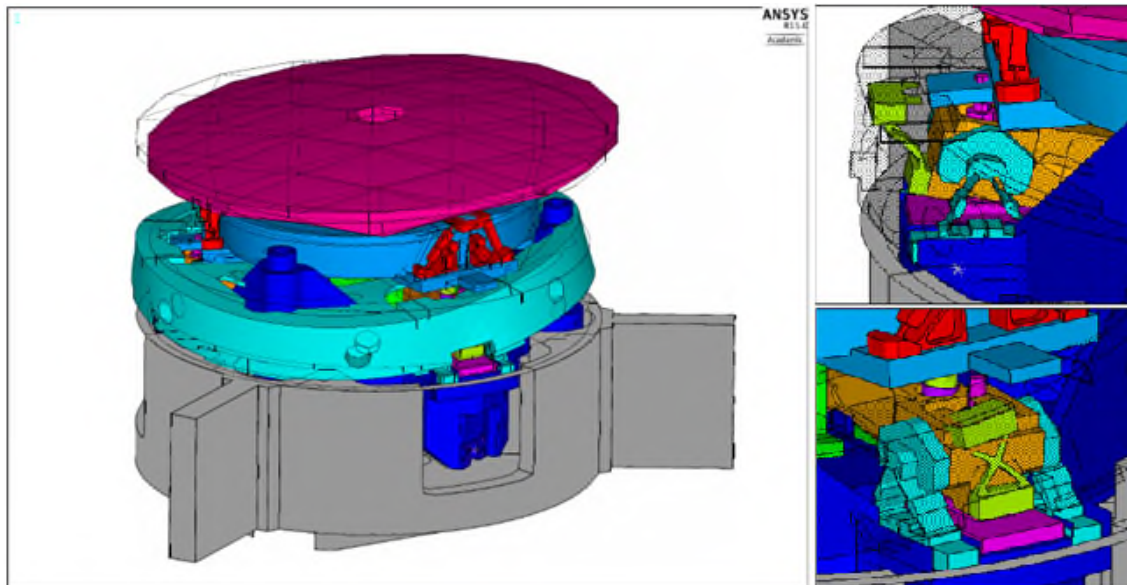


Figure 3. Mode Shape of the 300-Hz resonance (CBEND).

Left: Deformation of the compensation ring (cyan) and the coupled tip-tilt motion of the mirror (magenta). Right: A lateral shift of the compensation ring is the result of the soft serial-kinematic mount and the soft compensation ring. The compensation blade flexure (green) and the lever pivots (cyan) show deformations.

Solving the 300-Hz Resonance Problem

Concepts have been developed to constrain the 300-Hz resonance. The goal is to find a minimal invasive solution providing maximal performance gain to not interfere with the ongoing science campaigns. One approach that has been followed is the implementation of a parallel kinematic suspension to stiffen the non-operational degrees of freedom of the compensation ring as shown in Figure 4 (left). The original ring is supported by a serial kinematic suspension as shown in Figure 3. Here the loads are transferred from the ring over the compensation blades, the lever arm, and the lever pivots to the FCM interface. Serial kinematic suspensions are to be avoided when seeking high stiffness since the flexibility and positioning error of each element adds up. The other approach is to stiffen the compensation ring itself and to concentrate mass at the suspension points (nodes of mode shape). Taking strain energy out of the mode will reduce its magnitude. Please note that the inertia tensor of the ring has to remain unchanged to retain its original functionality.

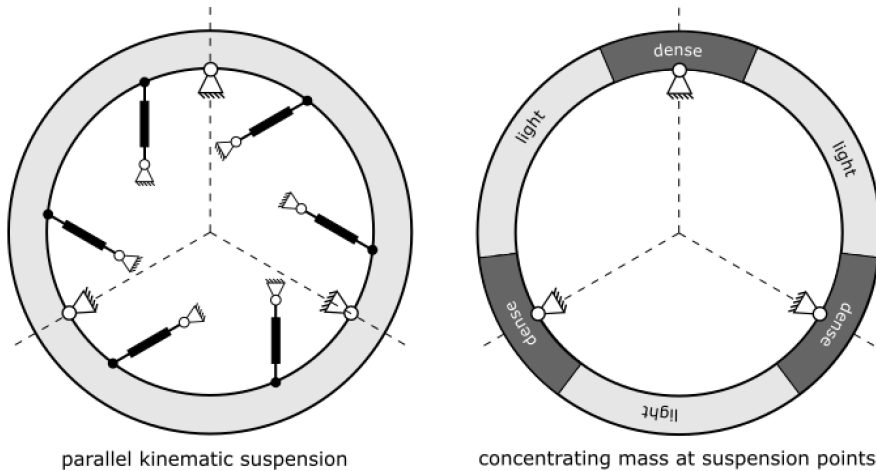


Figure 4. Two design concepts to eliminate the 300-Hz structural resonance. Left: Parallel kinematic suspension to constrain in plane deformations of the compensation ring as well as in plane translational motion of the ring on top of the suspension. Right: Concentrating mass at the suspension points (nodes of mode shape) will take strain energy out of the mode. Selecting stiffer materials will additionally push the resonance to higher frequencies.

Both concepts, the new suspension architecture and the compensation ring with optimized mass distribution (material combination) have been analyzed in a finite element model to predict the new system response. The results are shown in Figure 5 where the system response is plotted over the frequency range of interest.

The dominant resonance (CBEND) is clearly visible for the original configuration. Another structural resonance is present at about 430 Hz (SWAY), a sideways motion of the mirror coupled with a deformation of the compensation ring. Different material combinations are shown combined with the serial kinematic suspension (SKS) and the parallel kinematic suspension (PKS). A clear improvement is visible for both concepts. The CBEND magnitude is decreasing and the mode is pushed to higher frequencies. Applying the parallel kinematic suspension while keeping the original aluminum ring results in a magnitude drop of about 35%. Applying an extreme mass concentration at the suspension points using a material combination of tungsten and aluminum while keeping the SKS results in a CBEND magnitude drop of about 90%.

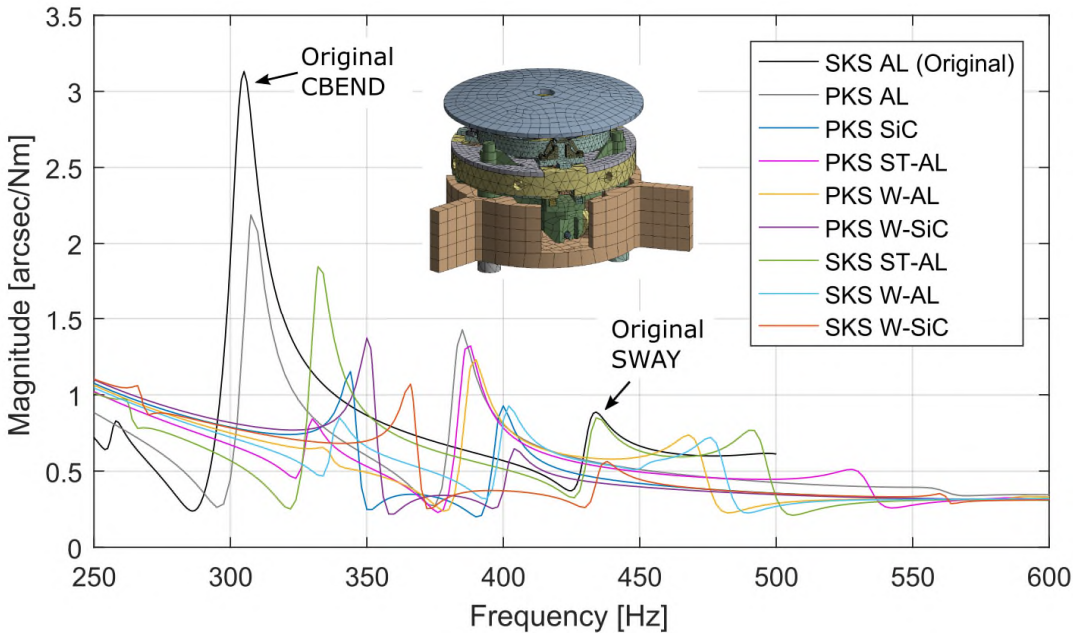


Figure 5. Open Loop frequency response for different compensation ring designs named by the suspension type (SKS = Serial Kinematic Suspension, PKS = Parallel Kinematic Suspension) and the material combination. The parallel kinematic suspension shows a reduced CBEND amplitude compared to the original configuration. However, the improvement by concentrating mass at the suspension points (diverse material combination) is dominant and leads to a reduced amplitude and a frequency shift toward higher values.

Combining both concepts can basically result in an elimination of the CBEND mode but promotes the SWAY resonance as shown for PKS W-AL. Using stiffer material combinations (less damping) results in a moderate reduction of the CBEND mode without amplifying SWAY (see PKS W-SiC and SKS W-SiC). In general, it can be observed that the more strain energy is taken out of the ring by concentrating mass at the suspension points, the lower the positive effect of the parallel kinematic mount becomes.

Even though a general improvement for most configurations is visible, predicting the new system performance from the open-loop frequency response is not trivial. Does a reduced magnitude or a displaced resonance frequency result in a larger actuation bandwidth? Therefore, these transfer functions were implemented in a control simulation developed in [3] and [4]. It was determined that the parallel kinematic suspensions in combination with an extreme mass redistribution (PKS W-SiC and PKS W-AL) show the largest performance improvement of about 95%. Silicon carbide benefits from its high specific stiffness while aluminum benefits from its good damping behavior. When combining the extreme mass redistribution with the original serial kinematic suspension (SKS W-SiC and SKS W-AL), there is still an improvement of around 80%. Considering the hardware changes required to implement the parallel kinematic suspension to the extra 15% performance gain, the decision was made to retain the original suspension. A detailed description of the end-to-end simulation used to predict the new closed-loop mechanism performance is covered in [7].

Manufacturing of a Prototype

Even if the combination of tungsten and silicon carbide showed a slightly better performance, the SKS W-AL is selected for manufacturing a prototype. Making a complex structure from pure silicon carbide is very challenging and expensive. Furthermore, once installed to the aircraft, the compensation ring is inaccessible for periodic inspections so very fragile materials should be avoided.

Nevertheless, joining two very divergent materials such as tungsten and aluminum can be challenging as well. Due to their diverse material properties, classical brazing or welding is not an option. Consequently, a mechanical joint has to be designed that is stiff and able to compensate the divergent thermal expansions. Figure 6 shows an approach of using flexure elements for the thermal expansion compensation. The heavy tungsten compensation mass (material at the node location) and the lightweight aluminum bridge element (material at the anti-node location) are bolted at the lower joint. A tempered steel flexure connects the two bodies on the upper joint allowing vertical thermal expansion. All other degrees of freedom are blocked keeping a high stiffness of the compensation ring assembly.

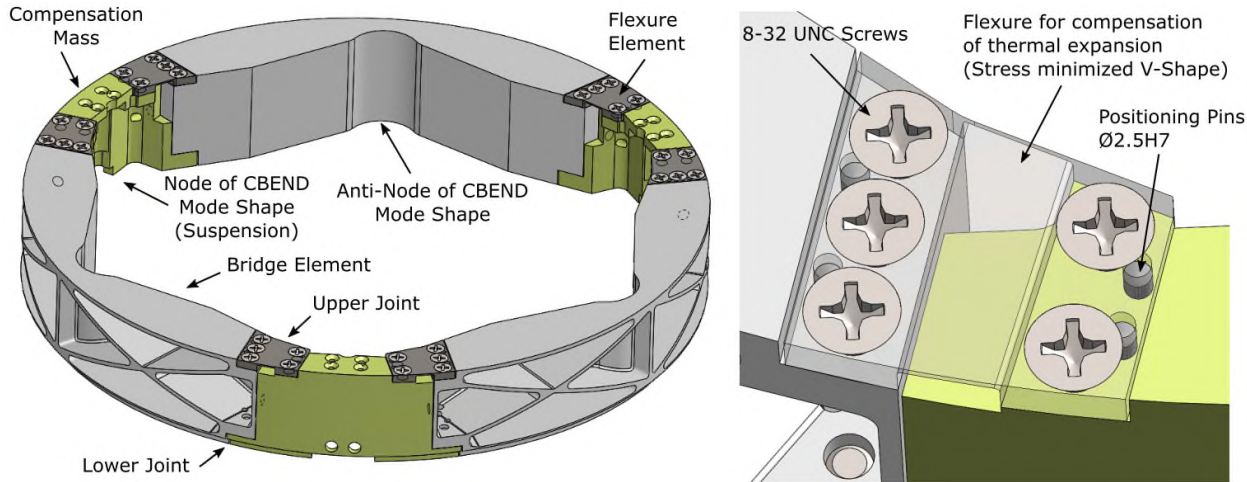


Figure 6. CAD model of the new compensation ring showing the segmentation. To compensate the vertical thermal expansion, the bridge element and the compensation mass are connected by a flexure joint shown on the right.

A heavy tungsten alloy (97%W, 2.1%Ni, 0.9%Fe) is used for the compensation masses shown in Figure 7a. Along with its high density (18.5 g/cm^3) this tungsten alloy comes with a very high Young's modulus (365 GPa) providing stiffness at three of the weak cross sections of the ring. Solid carbide tools with polychrome coating were used to machine this tough material. A dynamic trochoidal milling approach was applied to reduce the tool wear and machining loads. To reach a very precise planarity and parallelism of the contact surfaces, they have been precision ground.

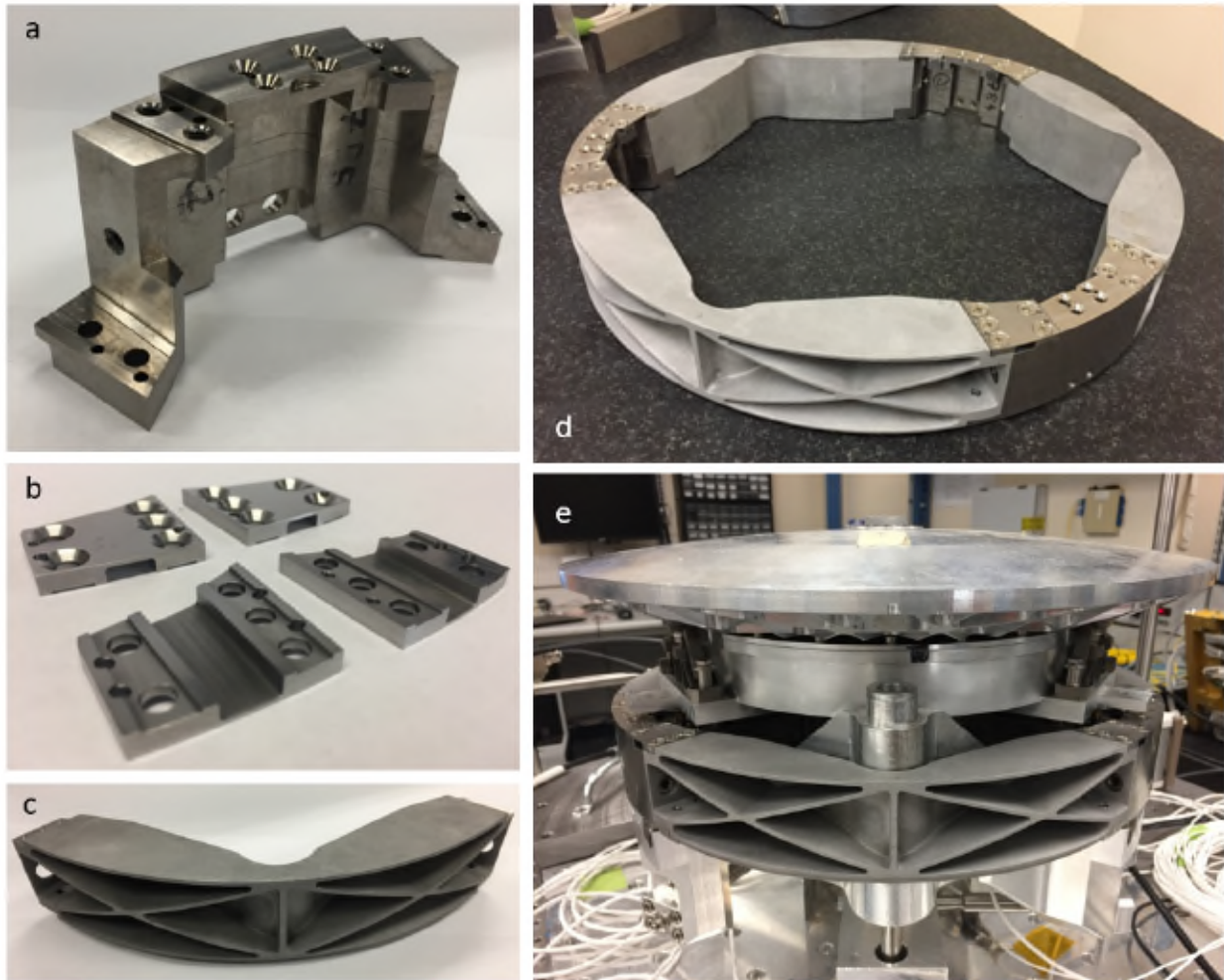


Figure 7. Compensation Ring Assembly. a: Heavy tungsten compensation mass. b: Steel flexure for thermal expansion compensation. c: Lightweight MMC bridge element. d: Assembled compensation ring. e: Compensation ring integrated into the SMA test bench.

To maintain a high stiffness but at a low density in between the tungsten parts, the light weighted bridge elements (Figure 7c) are made from an aluminum-based metal matrix composite (MMC Al70-SiC30). This material has a low density of 2.9 g/cm^3 and provides a high stiffness of about 120 GPa. It combines the advantages of aluminum (fracture toughness, damping behavior, density) and silicon carbide (stiffness, density) at a manageable machinability. To reduce secondary machining, the main geometry has been cast. A prototype casting approach was selected based on the thin wall geometry, the deep pockets, and the small quantity ordered (10 pieces). A wax model was 3D printed and invested into a ceramic mold (see Figure 8a-c). After burning out the wax, liquid AISiC is poured into the resultant cavity forming the final part (Figure 8d). Hot Isostatic Pressing is used to reduce the porosity of the cast as well as to improve the chemical and mechanical bonding of the SiC phase in the metal matrix. This leads to improved material properties and prevents the harder SiC from breaking off during machining and use. Due to the high ceramic content of the material, post machining of the joints has been performed using diamond-coated tools (Figure 8e). Complex fixtures were prepared to enable a steady and defined positioning of the cast part on the milling machine.

To compensate the thermal expansion in the operational temperature range between -60°C to 30°C , flexure elements made of high strength steel are used, shown in Figure 7b. The flexure geometry is optimized in a

way to minimize local stress concentrations during cool down. The assembled compensation ring is shown in Figure 7d.

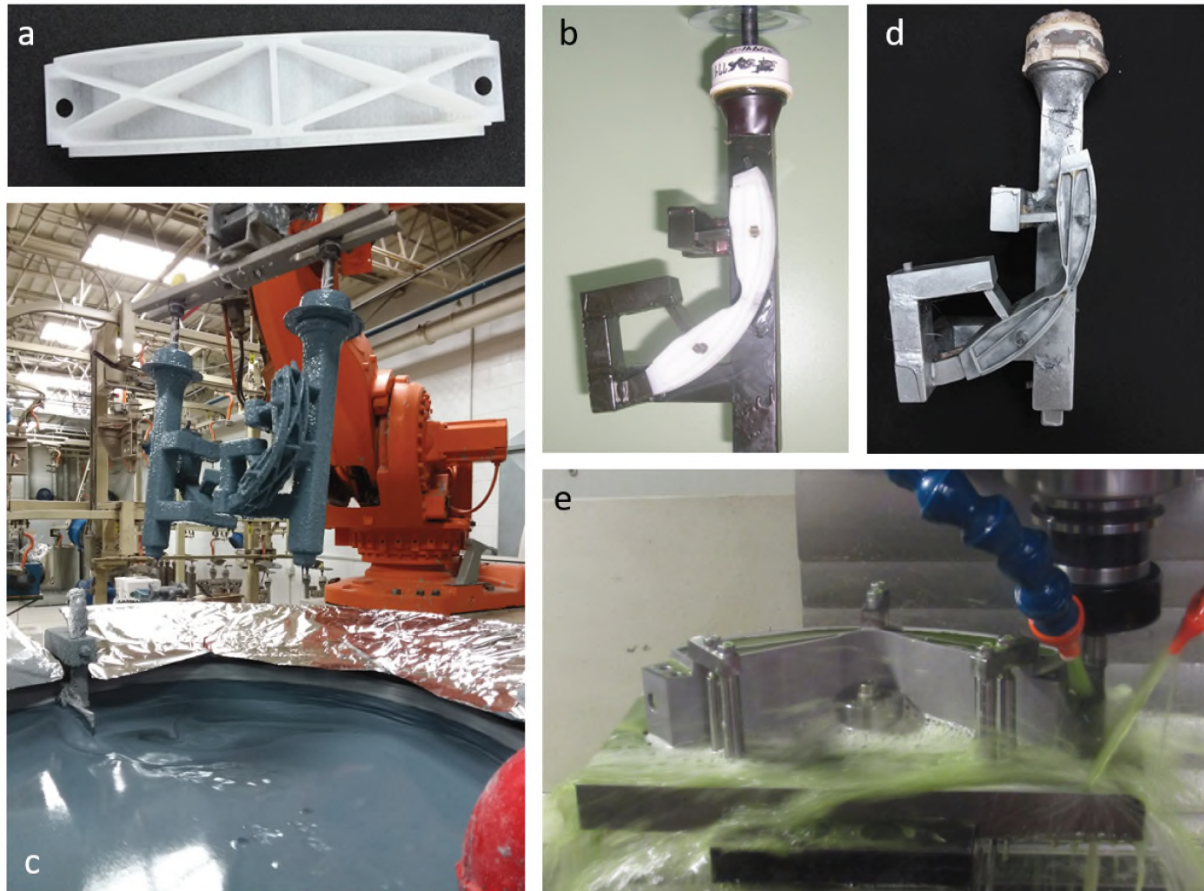


Figure 8. Manufacturing process of the MMC parts. a: 3D printed wax model. b: Additional wax features are added to the printed wax model forming the spruing, riser and pouring cup of the mold. c: Mold building. d: Casting part after removing the mold. e: Post machining of the critical surfaces, threads and pin holes.

Performance Testing

To prove the new design concept and to verify the resulting in-flight performance, extensive testing has been performed on a mockup of the Secondary Mirror Assembly (test bench) (Figure 7e). The test bench is a true scale rebuild of the TCM plus FCM suspension mounted on a heavy optical table. Flight electronics (controller boards, amplifier) were used to operate the test bench for better comparison with the actual SMA. For more information on the test bench please refer to [7]. Figure 9 shows the open-loop system response of the original and the new compensation ring tested on the testbench. The system was driven by applying a white noise excitation to the voice coil actuators while measuring the mirror movements with the eddy current sensors.

Compared to the original aluminum ring, a significant improvement is visible. The CBEND amplitude dropped by approximately 80% while the frequency increased by about 33 Hz. As predicted by the finite element simulations, the frequency of the SWAY mode drops. Fortunately, an increase in SWAY amplitude is absent, which can be credited to the SiC phase in the MMC bridge element when comparing to the SKS W-AL and SKS W-SiC curve in Figure 5. Please note that due to the stiff suspension of the test bench

(mounted on an optical table), the resonance of higher frequency modes (CBEND, SWAY) is amplified compared to the spider arm suspended system of the flight hardware (applied in FE simulations).

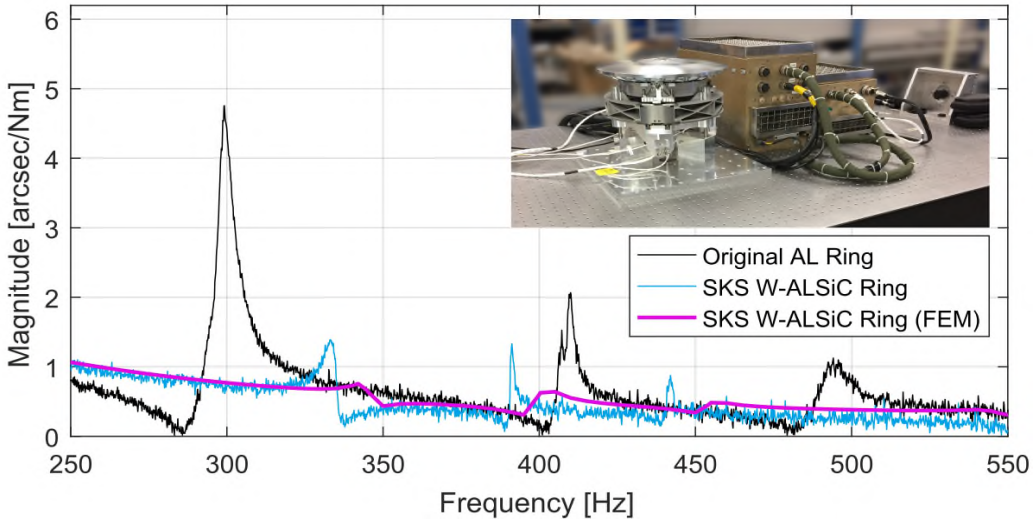


Figure 9. Open-loop frequency response of the original and the new compensation ring mounted on the test bench. A noticeable deviation between the new hardware and the simulation result is visible, which is mainly caused by the stiffer suspension of test bench (optical table vs. spider arms of the telescope) and by simplifications of the contact stiffness in the FE model.

Adjusting the controller to the new open-loop system response leads to the closed-loop response shown in Figure 10. Again, the system was driven by a white noise actuator input while measuring the mirror position. The controller gains are changed in a way to adjust the controller to its new stability limit. Based on the -90° cutoff frequency, the actuation bandwidth was improved by 80% (from 50 Hz to 90 Hz). Figure 10 additionally shows a closed-loop simulation result from [8] using the material properties of Al70-SiC30 for the bridge elements. Here a closed-loop bandwidth of about 95 Hz (90%) is predicted. The deviation of 5 Hz can be explained by simplifications in the finite element model such as assuming a rigid behavior of the frictional contacts. Also the stiff suspension of the test bench (optical table) as described above is expected to have an influence on the closed-loop bandwidth.

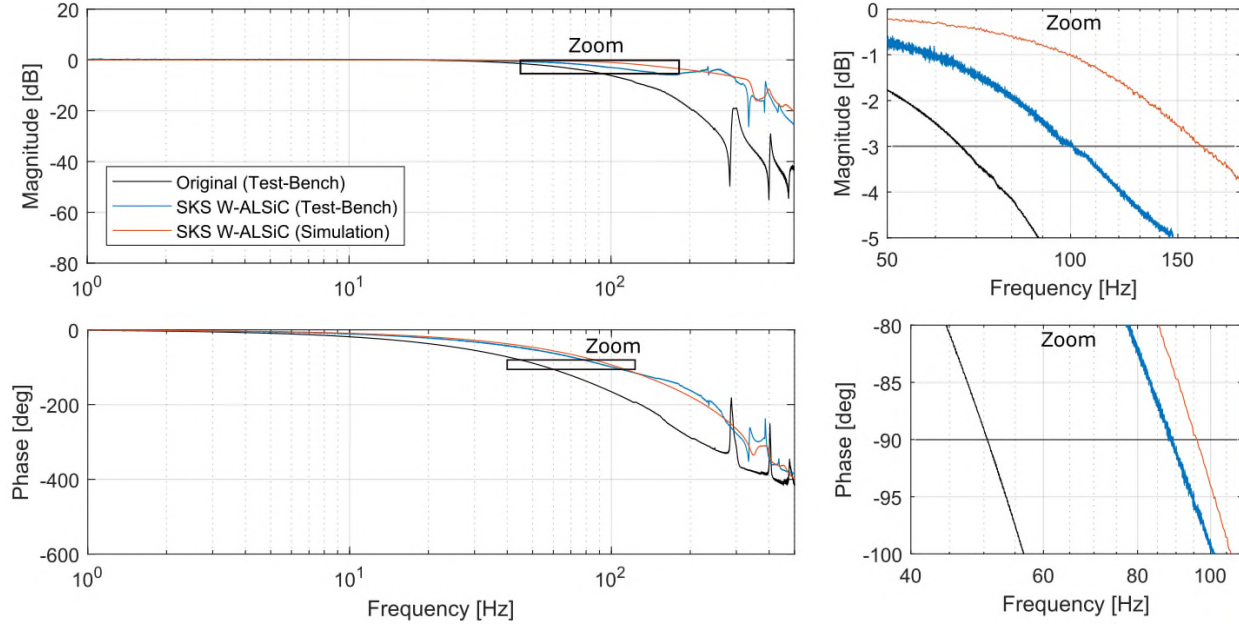


Figure 10. Closed-loop frequency response of the original and the new compensation ring mounted on the test bench. Zoom of magnitude and phase plot presenting the bandwidth improvement based on the -3 dB and the -90° cutoff frequency.

Conclusion

As a conclusion, the 300-Hz structural resonance of the SOFIA secondary mirror mechanism has been solved by redesigning the ring-shaped compensation mass in a way that its mass is concentrated at the suspension points while keeping the same inertia tensor. Tungsten and AlSiC ring segments are combined to achieve the extreme mass redistribution. The high elastic modulus of the tungsten and the SiC phase of the metal matrix composite additionally provide an improved overall stiffness. Eliminating the resonance enables a more aggressive controller design. Adjusting the control gains to the new stability limit, a significant improvement in actuation bandwidth of 80% was determined from testing the prototype on a full-scale system mockup. Based on this prototype design, two flight units will be manufactured for future SOFIA missions. The improved actuation bandwidth will provide faster mirror steering capability for image stabilization and infrared square wave chopping.

References

1. L. Zago, P. M. Genequand, and J. Moerschell, "Extremely compact secondary mirror unit for the SOFIA telescope capable of 6-degree-of-freedom alignment plus chopping," in Advanced Technology Optical IR Telescopes VI, L. M. Stepp, ed., Proc. SPIE 3352, pp. 666–674, 1998.
2. Alfred Krabbe, "SOFIA telescope", Proc. SPIE 4014, Airborne Telescope Systems, (20 June 2000); doi: 10.1117/12.389103
3. Andreas Reinacher, "Inflight Commissioning and Performance Improvement of the SOFIA Secondary Mirror Mechanism" *Dissertation*, 1 (2014), University of Stuttgart.
4. Andreas Reinacher and Hans-Peter Roeser, "Modeling of the SOFIA secondary mirror controller," Proc. SPIE 8336, 83360S-83360S-10 (2011).
5. Andreas Reinacher, Yannick Lammen and Hans-Peter Roeser, "SOFIA's Secondary Mirror Assembly: In-Flight Performance and Control Approach", (2016) Proc. SPIE 9908, doi: 10.1117/12.2232851
6. Yannick Lammen, Andreas Reinacher, Ivar Kjelberg, Serge Droz, Holger Jakob, Friederike Graf, Michael Lachenmann, Alfred Krabbe, "SOFIA secondary mirror mechanism heavy maintenance and improvements", Proc. SPIE 9906, Ground-based and Airborne Telescopes VI, 99061R (27 July 2016); doi: 10.1117/12.2231352
7. Yannick Lammen, Andreas Reinacher, Rick Brewster, Benjamin Greiner, Friederike Graf, Alfred Krabbe, "A new test environment for the SOFIA secondary mirror assembly to reduce the required time for in-flight testing", Proc. SPIE 9906, Ground-based and Airborne Telescopes VI, 99064T (27 July 2016); doi: 10.1117/12.2232152
8. Yannick Lammen, Andreas Reinacher, Alfred Krabbe, "Bandwidth increase of SOFIA's tilt chop mechanism by hardware modifications and subsequent controller adjustments to achieve better image quality and improve observation efficiency" (2018), Proc. SPIE, (in preparation)

SOFIA, the "Stratospheric Observatory For Infrared Astronomy" is a joint project of the Deutsches Zentrum fuer Luft- und Raumfahrt e.V. (DLR; German Aerospace Centre, grant: 50OK0901) and the National Aeronautics and Space Administration (NASA). It is funded on behalf of DLR by the Federal Ministry of Economics and Technology based on legislation by the German Parliament, the state of Baden-Wuerttemberg and the Universität Stuttgart. Scientific operation for Germany is coordinated by the German SOFIA-Institute (DSI) of the Universität Stuttgart, in the USA by the Universities Space Research Association (USRA).

Enhanced Vibration Isolation Using a Magnetic Linear Gear for Highly Demanding Aerospace Applications

José Luis Perez-Díaz **, Ignacio Valiente-Blanco*, Juan Sanchez García-Casarrubios*, Cristian Cristache*, Fernando Rodriguez-Celis*, Judit Esnoz-Larraya*, Efrén Diez-Jimenez**
and José Luis Perez-Alamo*

Abstract

Z-Damper is a new technology for vibration isolation in aerospace structures and equipment that takes advantage of impedance matching inside a magnetic linear gear to optimize vibration isolation performance and, at the same time, reduce weight and space requirements. Since there is no contact between moving parts except from the supporting linear bearings, it is suitable for long-life operation in space environmental conditions without wear or debris generation.

A theoretical model describing the dynamic behavior of the Z-Damper is presented in this paper. Additionally, two demonstrators have been designed, manufactured and tested for the FP7 Clean Sky Z-Damper project. One breadboard model is an empowered eddy current damper (Z-Damper) for operation at high temperatures and the other prototype is a reduced mass tuned vibration absorber (Z-TVA). The Z-Damper demonstrated a viscous damping coefficient up to 35 Ns/mm at 200°C. The Z-TVA was designed with a resonant frequency of 18 Hz. With a mass of only 9.6 kg, it demonstrated similar performance to a classic tuned vibration absorber of 150 kg.

Introduction and State of the Art

High performance vibration isolation solutions with small mass and envelope are needed for applications such as micro-vibration isolation [1], damping of launch loads [2], suppression of spacecraft-borne disturbances [3], or dampers for deploy mechanisms and structures [4].

Magnetic mechanisms such as bearings [5], gears [6] or dampers [7] are drawing increasing attention due to their convenient properties for their use in space environment: lubrication is no longer required, wear and debris generation are eliminated and they are able to operate in a wide temperature range. Finally they present no backlash, which makes them good candidates for precision positioning without contact [8] [9]. Magnetic dampers based on hysteresis or eddy current energy dissipation are frequently used in space systems because of their high temperature range, their absence of damping fluids, their vacuum compatibility, and their long space heritage. However, the performance of any eddy current damper is limited by the fact that the damping constant is proportional to the vibration speed. Therefore, for low frequency vibrations or short strokes, the capacity of the dampers is highly limited.

Another frequent solution for vibration isolation of structures excited at a known frequency are tuned vibration absorbers (TVA) [10]. TVA working principle is based on storing the vibration energy into a properly tuned resonant mass attached to the main vibrating body. Their effectiveness is directly related to the total mass of the absorber. Therefore, the required envelope and the costs induced by maintenance and installation are also main factors to be considered in many application cases.

In this paper, a new technology is presented for vibration isolation that takes advantage of the impedance matching inside a linear magnetic gear to enhance the performance of any damping system proportionally

* MAG SOAR S.L, Valdemoro, Spain

** Universidad de Alcalá, Alcalá de Henares, Spain

to the square of the multiplication ratio of the gear (n^2) [11]. Theoretical principles are discussed, and two demonstrators of the technology were designed, manufactured and tested. An overview of the tests results of the demonstration of a high-temperature integrated eddy current damper (Z-Damper) able to operate up to 200°C and a mass reduced tuned vibration absorber (Z-TVA) are presented in this paper.

Operational Principle Description

The basic principle behind the Z-Damper technology is simple: a linear magnetic gear is used to multiply the input vibration displacement amplitude, speed and acceleration. The magnetic gear is composed of three stages: a stator (1), an input or slow stage (2) and an output or fast-moving stage (3) as shown in Fig. 1.

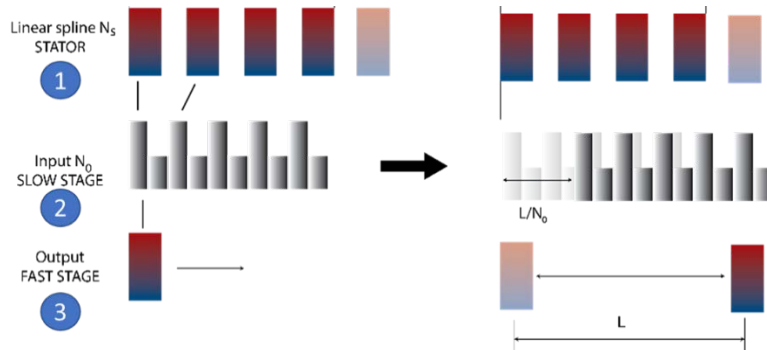


Figure 1. Working principle of a linear magnetic gear.

The gear ratio is defined by the number of magnetic elements involved in the gear unit as [11]:

$$n = \frac{N_o - N_s}{N_o} \quad (1)$$

where

N_o is the number of soft magnetic teeth per gear unit (Input stage)

N_s is the number of stator magnets per gear unit

For an ideal gear, the gear ratio can be defined as shown in Eq. 2:

$$n = \frac{F_{input}}{F_{fast}} = \frac{V_{fast}}{V_{input}} \quad (2)$$

where

F_{input} and F_{fast} are the input and fast-moving stage forces respectively

and V_{input} and V_{fast} are the input and fast stage speed.

The impedance matching between Stages 2 and 3 can then be described as:

$$\frac{Z_{input}}{Z_{fast}} = \frac{F_{input} \cdot V_{fast}}{F_{fast} \cdot V_{input}} \quad (3)$$

Therefore, by combining both Equations 2 and 3 into Equation 4:

$$\frac{Z_{input}}{Z_{fast}} = n^2 \quad (4)$$

However, when dynamic effects of the internal masses and damping forces are considered, a more complex model is required [12] to define the vibration isolation performance of the Z-Damper. Fig.2 shows an internal diagram of the Z-damper and the diagram of the Z-Damper connected to a vibrating mass.

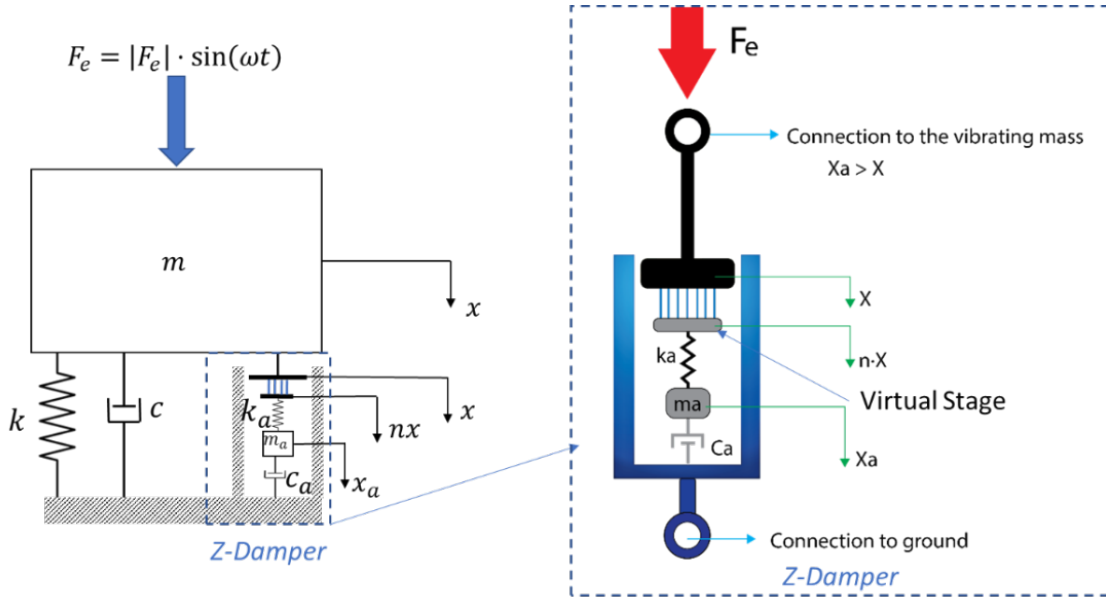


Figure 2. Internal diagram of the Z-Damper (right) and diagram of the Z-Damper when connected to a vibrating mass (left).

The black body represented in Fig.2 (right) is the input or slow-moving stage of the magnetic gear, which is rigidly connected to the vibrating mass. The blue body represents the stator of the Z-Damper, rigidly connected to the ground. A virtual intermediate stage is defined inside the gearbox to assist the theoretical description of the device and the interpretation of the proposed model. This “virtual stage” presents a perfect displacement multiplication with regard to the input stage displacement ($n \cdot x$). An inertial mass (ma) is magnetically coupled to the “virtual stage” by an equivalent spring of stiffness (ka). The magnetic equivalent stiffness will be only acting when a relative displacement from the virtual stage and the inertial mass is induced by internal inertial or damping forces.

The main contribution to damping will be generated by eddy current dissipation inside the device. An equivalent viscous damping coefficient (ca) can be defined related to the speed of the inertial mass with regard to the stator of the device.

It has to be noted that those couplings or connection between stages inside the Z-Damper are based on contactless magnetic interactions and the representation of ka and ca are only intended to assist the interpretation of the phenomena. No physical contact is required between the moving stages.

Based on the previous model, the motion equation for the inertial mass of the Z-Damper (ma) can be defined as:

$$-m_a \ddot{x}_a - k_a(x_a - nx) - c_a \dot{x}_a = 0 \quad (5)$$

The displacement (x_a) can be related to the input displacement (x) by the equation:

$$x_a = nx \cdot \frac{k_a}{(k_a - m_a \omega^2) + jc_a \omega} = nx \cdot \frac{1}{(1 - \Omega^2) + 2\xi_a \Omega} \quad (6)$$

where

Ω is the frequency ratio between excitation and natural frequencies $\Omega = \frac{w}{w_n}$,

ξ_a is the damping ratio $\xi_a = \frac{c_a}{2\sqrt{k_a m_a}}$

It can be useful to define a normalized displacement as a relationship between the fast moving and the input stage displacements:

$$ND = \frac{x_a}{x} = n \frac{1}{(1 - \Omega^2) + 2\xi_a \Omega} \quad (7)$$

The magnetic forces acting on the fast mass (m_a) will depend on the relative displacements between the “virtual intermediate stage” and the inertial mass

$$F_{fast} = -k_a(X_a - nX) = nk_a X \cdot \frac{m_a \omega^2 - jC_a \omega}{(k_a - m_a \omega^2) + jC_a \omega} \quad (8)$$

By hypothesis of the magnetic linear gearbox, the input reactive force exerted by the device when connected to the main system mass (m) is multiplied by the gearbox ratio:

$$F_{input} = -n \cdot F_{fast} \quad (9)$$

Therefore, combining Eq.7 and Eq.8 and including a friction damping component to represent the friction in the linear bearings observed during tests.

$$F_{input} = -n^2 k_a X \left[\frac{m_a \omega^2 - jC_a \omega}{(k_a - m_a \omega^2) + jC_a \omega} \right] + jF_c \cdot sign(X) \quad (10)$$

where

F_c is the Coulomb equivalent force,

$sign(X)$ represents the sign of the input displacement vector.

Two potential advantages can be derived from previous equation. One is that the enhancement of the input force of the Z-Damper is proportional to the square of the gear ratio and the other is the maximization of the input force at the resonance of the Z-Damper.

When connected to a vibrating mass, the overall system can be described as a two-mass system with a motion equation of the shape:

$$\begin{bmatrix} m & 0 \\ 0 & m_a \end{bmatrix} \cdot \begin{bmatrix} \ddot{x} \\ \ddot{x}_a \end{bmatrix} + \begin{bmatrix} c + c_a & -c_a \\ -c_a & c_a \end{bmatrix} \cdot \begin{bmatrix} \dot{x} \\ \dot{x}_a \end{bmatrix} + \begin{bmatrix} k + nk_a & -nk_a \\ -nk_a & k_a \end{bmatrix} \cdot \begin{bmatrix} x \\ x_a \end{bmatrix} = \begin{bmatrix} \vec{F_e} \\ 0 \end{bmatrix} \quad (11)$$

In order to represent the effectiveness of the vibration isolation performance, the normalized displacement amplitude of the vibrating mass ($ND = \left| \frac{xk}{F_e} \right|$) is frequently used:

$$\left| \frac{xk}{F_e} \right| = \sqrt{\frac{\left(1 - \frac{\Omega^2}{\beta^2} \right)^2 + \left(2\xi_a \frac{\Omega}{\beta} \right)^2}{\left(\frac{\Omega^4}{\beta^2} - \left(\frac{4\xi_a \xi_p}{\beta} + \frac{1}{\beta^2} + (n^2 \mu + 1) \right) \Omega^2 + 1 \right)^2 + 4 \left(\Omega \left(\frac{\xi_a}{\beta} + \xi_p \right) - \frac{\Omega^3}{\beta} \left(\xi_a (n^2 \mu + 1) + \frac{\xi_p}{\beta} \right) \right)^2}} \quad (12)$$

where

n is the multiplication ratio of the linear magnetic gearbox in the Z-TVA,

Ω is the frequency ratio between excitation and natural frequencies $\Omega = \frac{w}{w_n}$,

β is the ratio between the natural frequencies of the Z-Damper and the main mass $\beta = \frac{w_a}{w_p}$,

The internal natural frequencies of the Z-Damper and main system natural frequencies can be defined as

$$\omega_a = \sqrt{\frac{k_a}{m_a}} \quad \text{and} \quad \omega_p = \sqrt{\frac{k}{m}}$$

respectively.

ξ_a and ξ_p are the TVA and the structural damping ratios $\xi_a = \frac{c_a}{2\sqrt{k_a \cdot m_a}}$ and $\xi_p = \frac{c}{2\sqrt{k \cdot m}}$

Devices Description

Two passive prototypes are designed, manufactured and tested in a relevant environment to demonstrate the impedance matching principle. First, a prototype of a high-temperature enhanced eddy current damper (Z-Damper) able to operate at nominal temperatures up to 200°C and second, a mass reduced tuned vibration absorber (Z-TVA). Fig. 3 shows both prototypes installed in the test bench and ready to be tested.

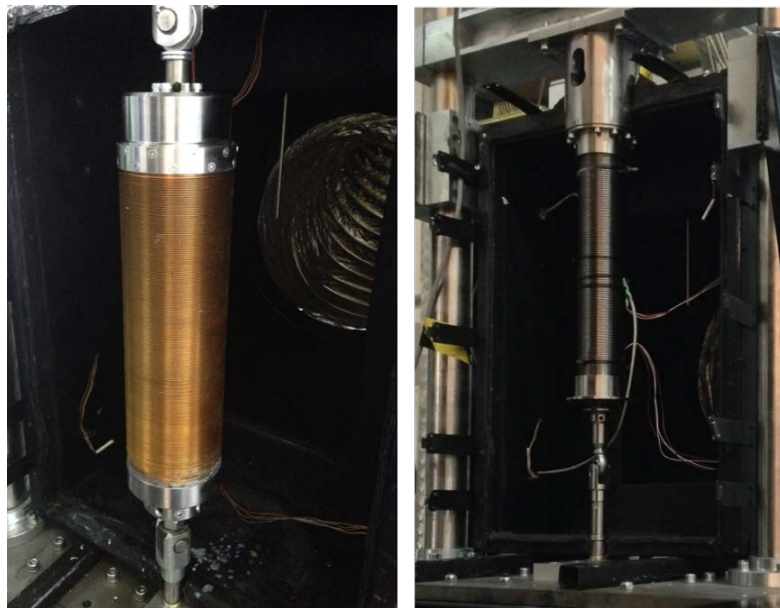


Figure 3. Z-Damper prototype (left) and Z-TVA prototype (right)

The philosophy of the Z-Damper prototype is to maximize damping at a desired frequency determined by design specifications. Operation at 200°C was required. The philosophy of the Z-TVA was to demonstrate a single degree of freedom tuned vibration absorber with a highly reduced internal mass (m_a) but similar performance to a classic tuned vibration absorber. A design resonant frequency of 18 Hz was fixed by design for the TVA. A summary of performance and figures of both prototypes is given in Table 1.

Table 1. Z-Damper and Z-TVA prototypes main characteristics

	Z-TVA	Z-Damper	
Gear Ratio	7:1	7:1	-
Diameter	82	105	mm
Length	493	491	mm
Total Weight	9.6	19.6	kg
TVA weight	3.6	NA	kg
Maximum input displacement	>±5	>±5	mm
Max. Input Force (25°C)	4670	6500	N
Temperature sensitivity	-2.9	-1.8	N/°C
Operational Temperature Range (validated by tests)	[RT,95]	[-50 to 200]	°C
Survival Temperature Range (validated by tests)	[-70,95]	[-70,270]	°C
Internal Resonant Frequency	18	12	Hz
Internal mass (ma)	3.6	8.5	kg
Input maximum stiffness (k)	2081	2548	N/mm
Fast-stage stiffness (ka)	42	52	N/mm
Max. Equivalent viscous damping coefficient at 12 Hz (200°C)	NA	35	Ns/mm

Z-Damper description

The Z-Damper prototype has been designed with a gear ratio of 7:1. Fast-moving stage and stator are mainly composed of ring shaped permanent magnets made of SmCo 32H with a high temperature resistance to demagnetization. The input stage is mainly composed of FeCo alloy laminated rings. FeCo rings were heat treated for an optimum magnetic and mechanical performance. Ti grade-5 ring spacers are used to control the gap between the different elements in the gearbox. Most structural elements of the device (shafts, flanges, rods...) are made also of Ti grade 5 due to its excellent mechanical strength and relatively low density. Self-lubricated PTFE bearings are used in order to allow relative motion between the different stages of the device. The materials used in the Z-Damper allow operation of the device at very high temperatures, theoretically up to 300 °C.

Finally, the outermost layer of the Z-Damper is composed of an electrolytic copper finned shell. Eddy currents are generated in the shell by motion of the fast stage permanent magnets (PMs), and then the generated heat is dissipated to the environment by forced convection. Fig.4 shows a real picture of the Z-Damper and a schematic representation:

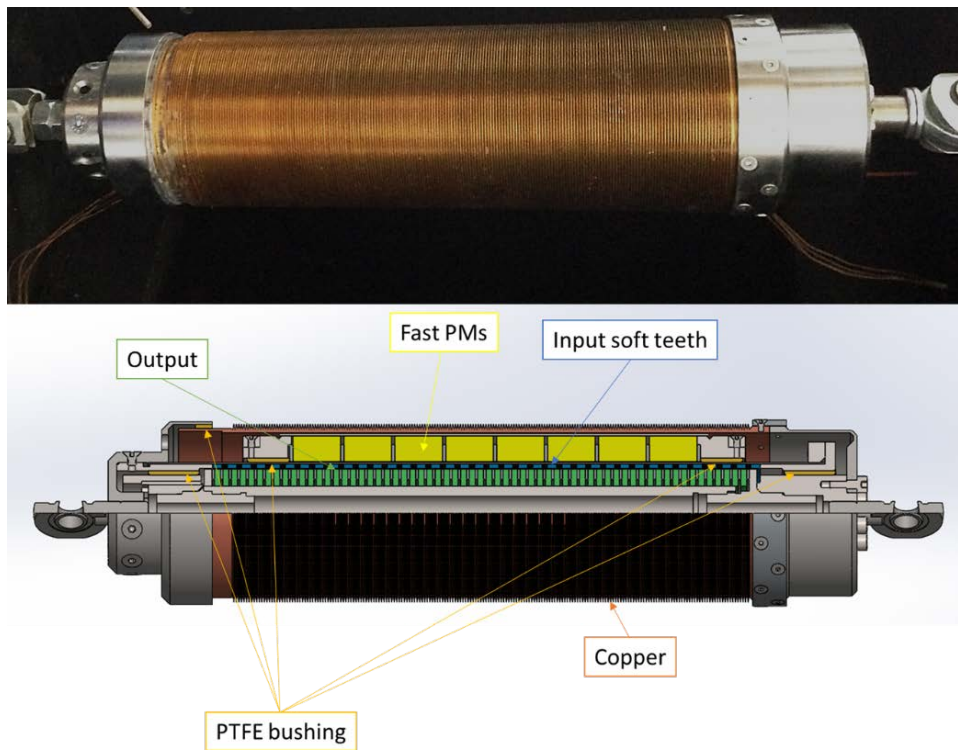


Figure 4. Z-Damper prototype (top) and diagram of the internal elements of the Z-Damper (bottom)

Z-TVA description

The Z-TVA prototype has been designed with a gear ratio of 7:1. The stator and the fast-moving stage are mainly composed of NdFe N48H ring permanent magnets, axially magnetized. Permanent magnets are placed with facing opposing polarities and kept in position using epoxy adhesives and mechanical fixtures. The input stage is mainly composed of low carbon steel AISI 1010 laminated soft magnetic teeth that are assembled inside a Ti grade 5 seamless tube. Non-magnetic titanium spacers are used for a proper disposition of the soft magnetic teeth in the magnetic gearbox.

Linear ball bearings, grease lubricated, are used to allow relative motion between the fast-moving stage and the input, and grease-lubricated bushings are used between the stator and the input stage. Most of the structural components of the device are manufactured using Ti grade 5 due to its high yield strength and low density. Fig. 5 shows a real picture and a partial cross section of the device.

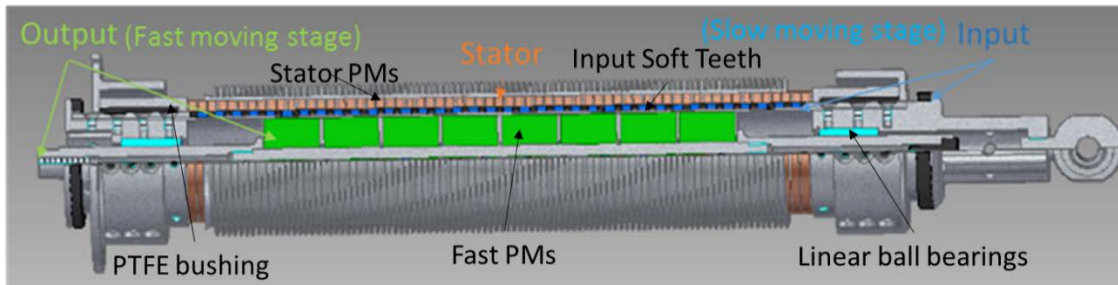


Figure 5. Z-TVA prototype (top) and diagram of the internal elements of the Z-TVA (bottom)

Test Bench and Set Up

Both the Z-Damper and the Z-TVA were tested at a component level. A dedicated test bench (Fig. 6) has been designed, manufactured and set up to demonstrate the Z-Damper concept. The test bench is mainly composed of a bench structure (1) and a supporting structure (2), a 15.7-kN hydraulic actuator with hydrodynamic seals for high-frequency actuation from Moog (3). The actuator is feed with ISO grade 32 oil pumped by the hydraulic group equipped with a 15 CV electric motor (4). A climatic chamber is used to control the prototype temperature (5), a 3-kW high-temperature-resistant centrifugal fan (6) and a PID-controlled 12-kW heat resistor (7) are used to control the ventilation flow and the climatic chamber temperature. The test bench is controlled from a fixed PC station (8). Finally, flexible high temperature resistant ducts are used for recirculation of the ventilation air (9).

Input position is measured by a LVDT sensor with 0.01-mm accuracy. Input force is measured by a HBM U10M traction-compression load cell with a measurement range up to 25 kN and 0.02 precision class. The position of the fast-moving stage is measured by a Micro-Epsilon optoNCDT ILD-1402 laser triangulator with 5- μm resolution. Several PT-100 temperature sensors in a 4-wire configuration are used to characterize the temperature of the flowing air and the prototype temperature. The data acquisition system is composed of NI9217, NI9203 and NI9263 acquisition cards from National Instruments installed in a NI 9188 rack.

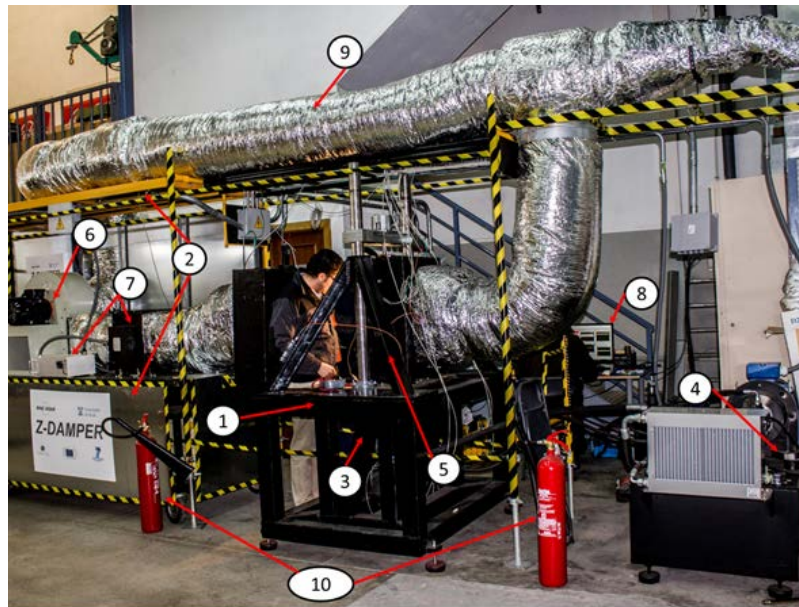


Figure 6. Test bench

Test Results

Z-Damper tests results

Fig.7 shows the input and fast stage displacement of the Z-Damper at room temperature when no copper dissipater is installed. An input sinusoidal excitation of about 1-mm amplitude is forced at different excitation frequencies from 1 to 60 Hz. Displacement multiplication ($n=7$) induced by the magnetic gear is observed even at low frequencies.

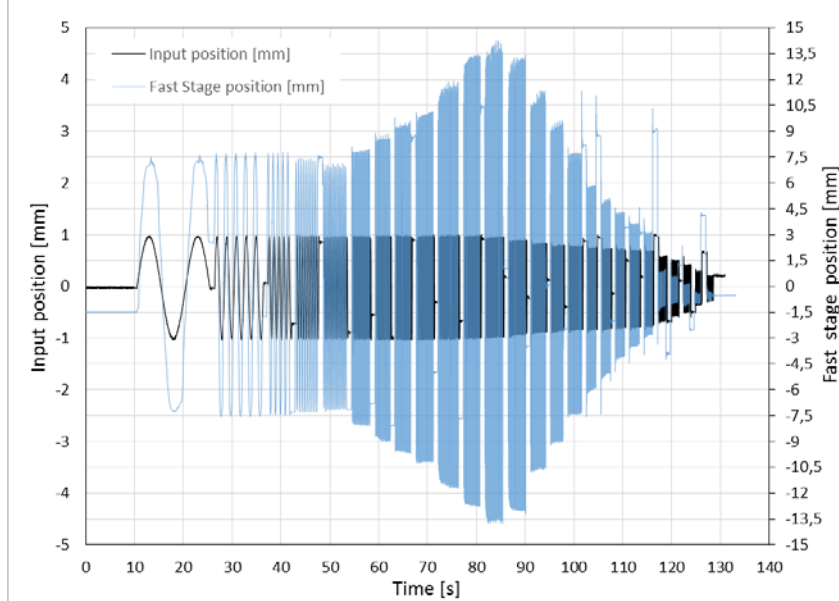


Figure 7. Input and fast stage position vs. time for different sinusoidal harmonic excitation frequencies

Fig. 8 shows the theoretical prediction and the experimental results of the internal normalized displacement, as described in Eq. 7, of the Z-Damper fast stage as a function of the excitation frequency. Results including the outermost copper dissipater (blue data) and not including it (black data) are provided. The increase in damping is evident when the copper dissipater is installed.

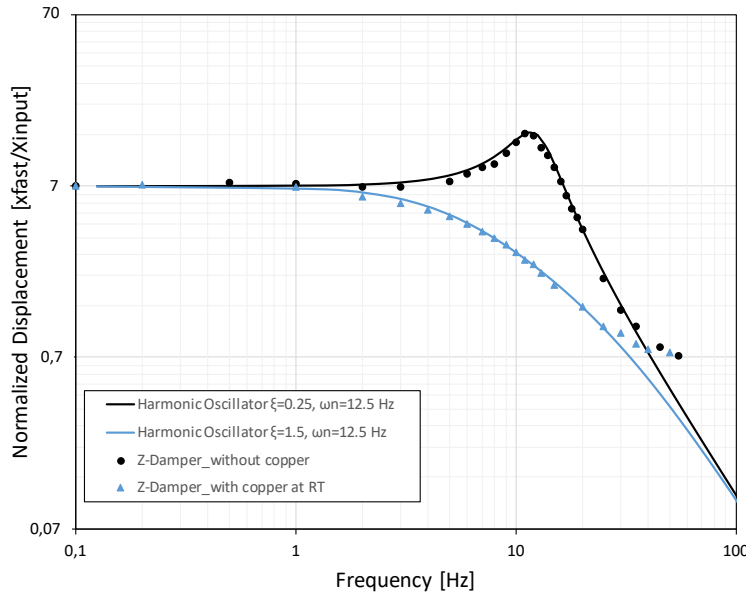


Figure 8. Normalized displacement of the Z-Damper with copper dissipater (blue) and without copper dissipater (black) for different excitation frequencies.

Fig. 9 shows the experimental input force of the Z-Damper when subjected to sinusoidal harmonic excitations of 2-mm amplitude and at a temperature of 200°C. Good agreement with theoretical predictions of Eq. 10 is observed. It can also be observed how the damping input force is maximized at the desired resonant frequency.

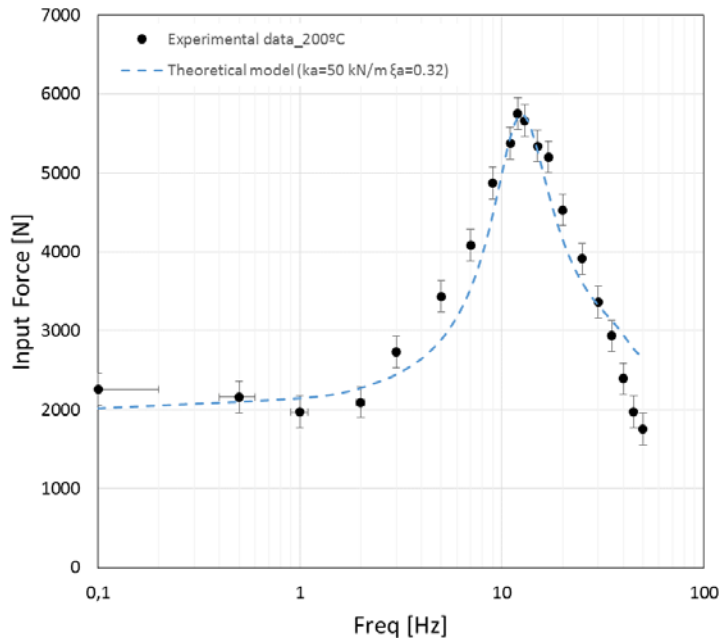


Figure 9. Theoretical prediction (blue) and experimental data (black) of the Z-Damper input force for different excitation frequencies.

Finally, Fig. 10 shows the hysteresis loops of the Z-Damper at various temperatures. Maximization of the dissipated energy is obtained at the operational temperature of 200°C. From damping curves at 200°C, a maximum viscous damping coefficient of 35 Ns/mm has been calculated.

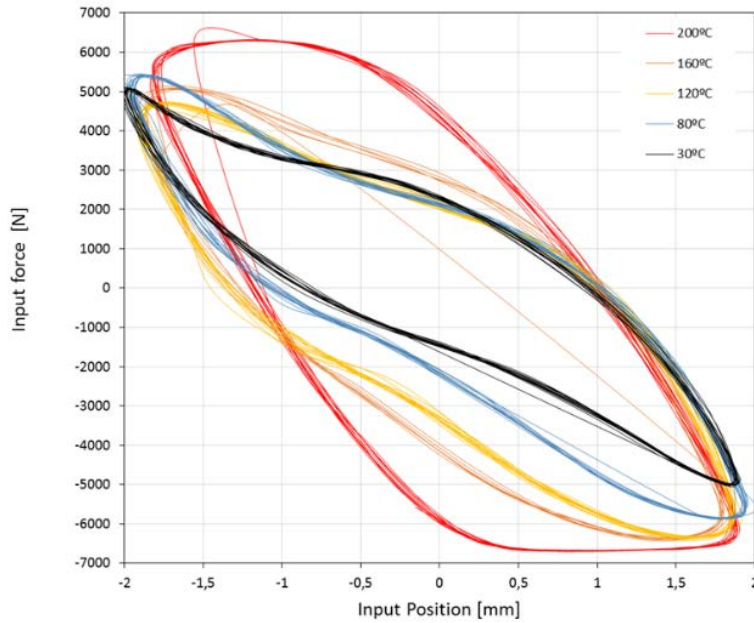


Figure 10. Input forces vs. input position for a 2-mm input sinusoidal vibration of 12 Hz at different temperatures from room temperature to 200°C.

Z-TVA Test Results

Fig.11 shows the normalized displacement of the inertial mass of the Z-TVA. Very good agreement is reached with theoretical predictions from Eq. 7.

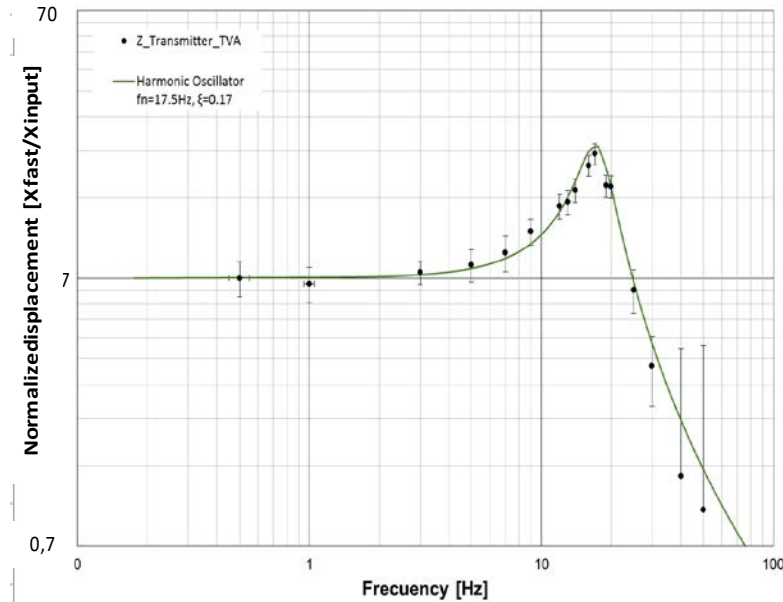


Figure 4. Normalized displacement of the Z-TVA fast moving stage for various sinusoidal harmonic excitation frequencies.

Input force of the Z-TVA has been also measured at different excitation frequencies. Despite that good agreement has been found between the experimental data and the theoretical predictions from Eq.10 at the resonance region, minor discrepancies have been found at lower frequencies. The reasons for that are not very well understood and further investigation is still required.

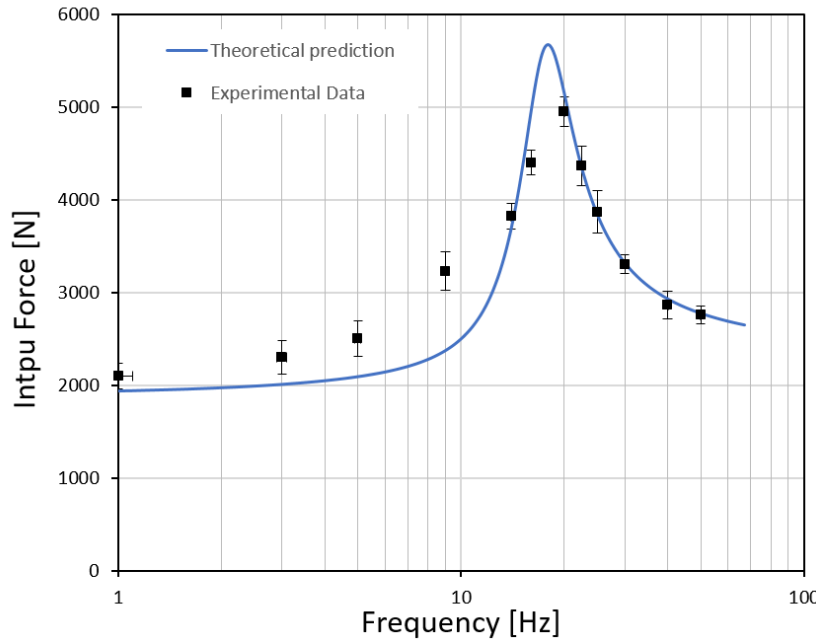


Figure 5. Input force vs. excitation frequency of the Z-TVA.
Theoretical Performance Evaluation

Since the conducted tests did not include a vibrating mass system as the one described in Fig.2, an evaluation was conducted of the performance as a tuned vibration absorber of the Z-TVA based on the experimentally validated model described in Eq.12. Fig.12 shows the expected normalized displacement of three different systems:

- A 5000-kg vibrating mass and a typical system stiffness of $4.8 \cdot 10^7$ N/m with a natural frequency of 18 Hz, with no tuned vibration isolation device but typical structural damping ($\xi=0.01$)
- System with structural damping ($\xi=0.01$) and a 150-kg optimal TVA.
($\mu = 0.03, \xi_a = 0.105, \beta = 0.97$)
- System with structural damping ($\xi=0.01$) and a 9.6 kg Z-TVA device.
($\mu = 0.00073, \xi_a = 0.113, \beta = 0.97$)

Fig. 13 shows the vibration isolation performance obtained with the three different isolation methods. Perfect overlapping of the curve of the transmissibility of the Z-TVA and a classic TVA is observed. However, it is very remarkable that the weight of the TVA system is more than one order of magnitude larger than the proposed Z-TVA solution.

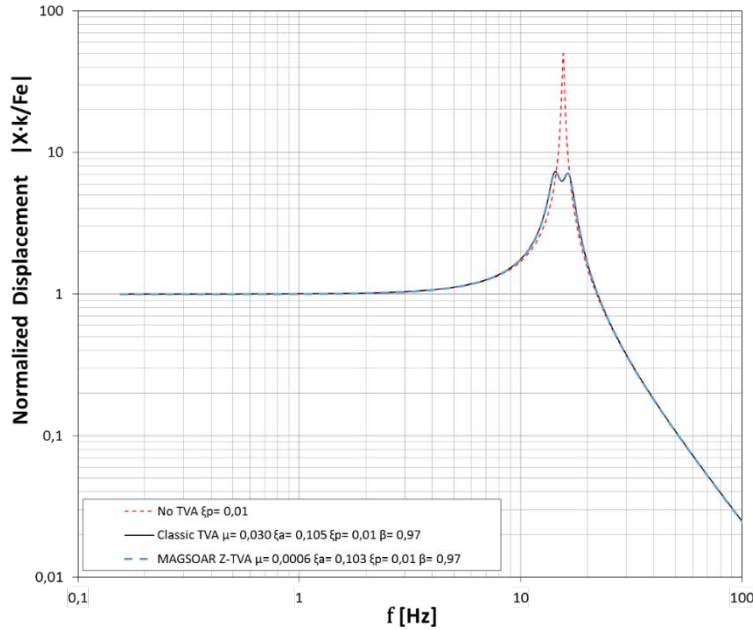


Figure 6. Normalized displacement of the vibrating mass vs. excitation frequency when no damping system (red dashed line), a classic optimized TVA with 150 kg (black line) and a Z-TVA of 9.6 kg attached to the vibrating structure.

Conclusions and Lessons Learned

Z-Damper is a new technology for vibration isolation in aerospace structures and equipment. It takes advantage of impedance matching in a magnetic linear gear to optimize vibration isolation performance. At the same time, it reduces the weight and space requirements of the solution. Since there is no contact between moving parts except from the supporting linear bearings, it is suitable for long-life operation in space environmental conditions without wear or debris generation.

In this paper the theoretical dynamics of Z-Damper is presented and experimentally validated. Two prototypes of the technology were designed, manufactured and tested: a prototype of an enhanced eddy current damper (Z-Damper) able to operate at temperatures up to 200°C and a prototype of an extra-light tuned vibration absorber (Z-TVA). The Z-TVA was designed with a resonant frequency of 18 Hz. With only 9.6-kg mass, it showed a similar performance to a classic tuned vibration absorber of 150 kg, demonstrating the potential of the technology for significant weight-saving and tight space requirements.

Some lessons learned during the project are:

- A Z-Damper high temperature eddy current damper can achieve high damping ratios (up to 35 Ns/mm) at operational temperatures up to 200°C even for low input displacement amplitudes.
- The use of a magnetic linear gear allows a high reduction of the inertial mass of a tuned vibration absorber. The Z-TVA demonstrated a similar performance to a classic TVA more than 10 times heavier.

Acknowledgements and Previous Publication Record

This work has been partially funded by the Seventh Framework Clean Sky Program of the EU Commission, under grant JTI-CS-2013-02-SFWA-03-013.

References

- [1] C. Liu et al., "Recent advances in micro-vibration isolation," *Mechanical Systems and Signal Processing*, vol. 56–57, (May 2015) pp. 55–80,.
- [2] C. D. Johnson, P. S. Wilke, and S. C. Pendleton, "SoftRide Vibration and Shock Isolation Systems that Protect Spacecraft from Launch Dynamic Environments," *Proceedings of the 38th Aerospace Mechanisms Symposia*, (May 2006), pp. 89-102.
- [3] R. G. Cobb, J. M. Sullivan, A. Das, L. P. Davis, T. T. Hyde, T. Davis, Z. H. Rahman, and J. T. Spanos, "Vibration isolation and suppression system for precision payloads in space," *Smart Materials and Structures*, vol. 8, no. 6, (December. 1999), pp. 798–812.
- [4] S.C. Burgess and P.J. Clarkson, "The development of a novel rotary damping mechanism for aerospace deployment systems," *Materials & Design*, vol. 18, no. 1,(February 1997) pp. 17–24.
- [5] I. Valiente-Blanco, E. Diez-Jimenez, C. Cristache, M. A. Alvarez-Valenzuela, and J. L. Perez-Diaz, "Characterization and Improvement of Axial and Radial Stiffness of Contactless Thrust Superconducting Magnetic Bearings," *Tribology Letters*, vol. 54, no. 3, (June 2014), pp. 213–220.
- [6] J. Perez-Diaz, E. Diez-Jimenez, I. Valiente-Blanco, C. Cristache, M.-A. Alvarez-Valenzuela, J. Sanchez-Garcia-Casarrubios, C. Ferdeghini, F. Canepa, W. Hornig, G. Carbone, J. Plechacek, A. Amorim, T. Frederico, P. Gordo, J. Abreu, V. Sanz, E.-M. Ruiz-Navas, and J.-A. Martinez-Rojas, "Performance of Magnetic-Superconductor Non-Contact Harmonic Drive for Cryogenic Space Applications," *Machines*, vol. 3, no. 3, (July 2015), pp. 138–156,.
- [7] Q. Pan, T. He, D. Xiao, X. Liu, Q. Pan, T. He, D. Xiao, and X. Liu, "Design and Damping Analysis of a New Eddy Current Damper for Aerospace Applications," *Latin American Journal of Solids and Structures*, vol. 13, no. 11, (November 2016), pp. 1997–2011.
- [8] J. Serrano-tellez, F. Romera-juarez, D. González-de-maría, M. Lamensans, J. L. Perez-Diaz, J. Sanchez-Casarrubios, E. Diez-Jimenez, and I. Valiente Blanco, "Experience on a cryogenic linear mechanism based on superconducting levitation," *Proceedings of SPIE Modern Technologies in Space- and Ground-based Telescopes and Instrumentation II*, vol. 8450, (August 2012).
- [9] J. L. Perez-Diaz, I. Valiente-Blanco, E. Diez-Jimenez, and J. Sanchez-Garcia-Casarrubios, "Superconducting noncontact device for precision positioning in cryogenic environments," *IEEE/ASME Transactions on Mechatronics*, vol. 19, no. 2, (April 2014), pp. 598-605.
- [10] J. Q. Sun, M. R. Jolly, and M. A. Norris, "Passive, Adaptive and Active Tuned Vibration Absorbers—A Survey," *Journal of Mechanical Design*, vol. 117, no. B, (June. 1995), pp. 234-242.
- [11] J. Pérez-Díaz, I. Valiente-Blanco, and C. Cristache, "Z-Damper: A New Paradigm for Attenuation of Vibrations," *Machines*, vol. 4, no. 2, (June 2016), pp. 1-11.
- [12] I. Valiente-Blanco, C. Cristache, J. Sanchez-Garcia-Casarrubios, F. Rodriguez-Celis, and J.-L. Perez-Diaz, "Mechanical Impedance Matching Using a Magnetic Linear Gear," *Shock and Vibration*, vol. 2017, (August 2017).

A Mechanisms Perspective on Microvibration – Good Practices and Lessons Learned

Geert Smet* and Sandro Patti*

Abstract

In September 2017, the ESA Mechanisms Section organized the first Advanced Mechanisms Design Course. The course focused on how to anticipate and avoid the most common problems encountered in several different fields of space mechanisms design. One of the topics addressed was ‘A Mechanisms Perspective on Microvibration’. This tutorial paper draws from the content of this well-received training, focusing on practical tips and good practices, complemented by lessons learned from operational missions and their on-orbit performance.

Introduction

The purpose of this paper is to make mechanisms engineers aware of the microvibration problem and offer practical knowledge and tools on how to deal with it. This paper will cover:

- What microvibration is
- What causes microvibration in mechanisms
- How microvibration is typically handled at the system level
- What a microvibration requirement for a mechanism looks like
- Which verification methodologies are appropriate in which circumstances
- How verification approaches can be used most effectively and which pitfalls to avoid
- Which approach can be used to minimize microvibration

This paper does not cover recovery actions to be undertaken in case a microvibration problem manifests on orbit. If possible, changing operational parameters of the mechanisms generating the noise is recommended. In certain cases, post-processing the data from the payload may be used to offset the effects of microvibration.

Microvibration and Mechanisms

What is microvibration?

Microvibration can be defined as a structure-borne vibration generated from equipment in the spacecraft that causes motion of the payload or other sensitive equipment that could cause degradation in performance. It is important to note that several terms are typically used interchangeably to discuss one phenomenon: microvibration, micro-vibration, microdisturbances, jitter or even simply noise. Microvibration disturbances are usually in the range of micro-g's (μg) typically occurring at frequencies from as low as 0.1 Hz up to 1000 Hz. Mechanisms such as Reaction Wheels (RW), Control Moment Gyros, Antenna Pointing Mechanisms (APM), Cryocoolers, Solar Array Drive Mechanisms (SADM), scanners, and optical mechanisms are typically the main sources of mechanical noise on a spacecraft.

Microvibration is a significant technical challenge for the current generation of space missions due to the stringent stability requirements of the payloads. The current state of the art is $\sim 0.1 \mu\text{rad}$ Line of Sight stability. This equates to motions in the order of only a few nanometres in payloads. A further order of magnitude improvement is required for future missions. Microvibration is a system-level problem and involves several disciplines, such as systems, mechanisms, mechanical systems & analysis, optical, attitude & orbital control systems, and spacecraft ops. This further complicates the mechanisms designer's task.

* European Space Agency, Noordwijk, The Netherlands

What causes microvibration in mechanisms?

Physical causes of microvibration can be anything generating forces in the mechanism. A non-exhaustive list of causes is rotor imbalance, mechanical bearing irregularity, bearing friction and imperfections, motor cogging, stepper motors, and gear meshing and contact. Knowledge and understanding of these causes is key to optimize a mechanism for low microvibration.

Several aspects complicate dealing with mechanisms as noise sources:

- Noise is generated in six degrees of freedom (DOF). Measurement or analysis of the mechanism needs to assess all six DOF, and not remain limited to the DOF most directly related to the mechanism motion, e.g. the rotation axis for a SADM.
- The phase of the six DOF of noise may be important but is often lost when multiple noise source data is combined for analysis. This is particularly relevant at spacecraft level, but could be of note to a mechanism designer in charge of delivering multiple mechanisms.
- The dynamic coupling of the noise source to the spacecraft affects the noise injected into the spacecraft. This aspect is typically handled at system level.
- Noise generation depends on operational parameters (for example APM noise is dependent on axis position as well as rotational speed). For mechanisms with multiple degrees of freedom, this could lead to a cumbersome verification campaign. From a design point of view, the modal design of mechanisms is typically aimed at surviving the launch. Structural modes of the mechanism will amplify noise generated internally to the mechanism. These modes can differ significantly for different configurations of the mechanism and may lead to additional design constraints.
- Some noise sources have varying noise performance over time. Mechanical wear of certain components can worsen the performance. In addition, some mechanisms may show intermittent periods of generating higher noise, for example if bearing cage instability occurs.
- There is unavoidable inherent variability between individual seemingly identical noise sources. Figure 1 shows how 8 identical RWs may vary in noise up to one order of magnitude in Power Spectral Density (PSD).
- The noise performance may be affected by vacuum, temperature, gravity effects, exposure to vibration and shock, and changes over life. Figure 1 shows how the noise of these RWs increases after vibration test. Figure 2 shows how different levels of pressure impact the modal behavior of another RW. This RW is evacuated. Removing the ambient pressure changes the shape of the thin walled pressure vessel, which in turn stiffens the main lateral mode.

These aspects have an impact on how the microvibration requirements are derived and need to be verified.

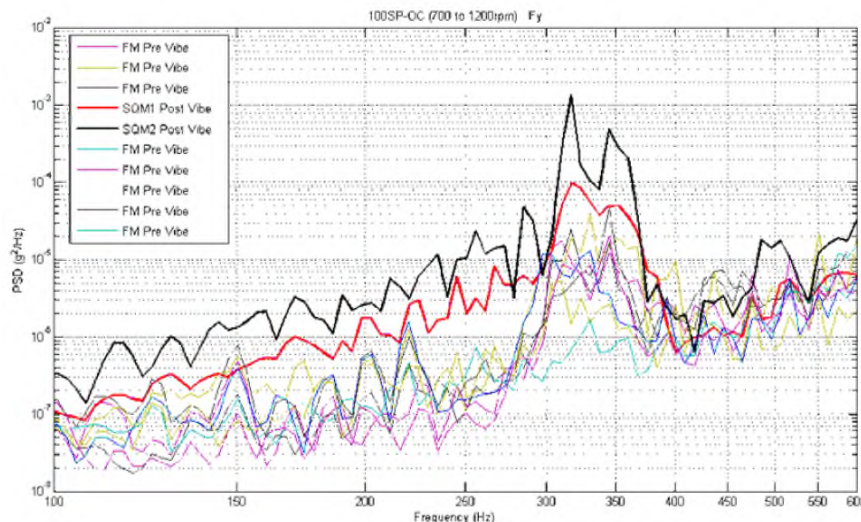


Figure 1. RW noise for several identical units and impact of vibration tests. Image courtesy of SSTL.

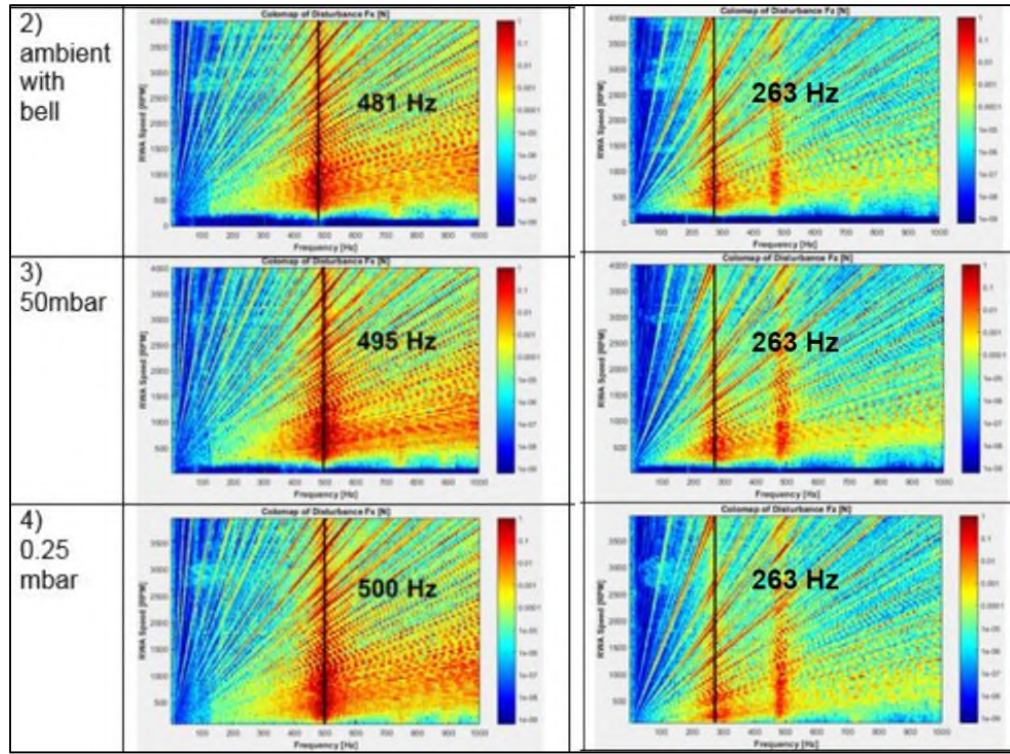


Figure 2. Reaction wheel noise at different pressure. Images courtesy of Bradford Engineering [2]. The structural modes are excited by the internally generated noise and strong amplification can be seen across the speed range. One of these modes is sensitive to the surrounding pressure and changes.

Case study: On ground versus on orbit noise behavior for a dry RW

For a European Space Agency (ESA) R&D study, Surrey Satellite Technology Ltd (SSTL) performed in-orbit microvibration measurements using an in-situ microvibration monitoring system [1]. Several different noise sources were measured, but the most surprising results appear on two reaction wheels that are identical except for the lubricant used. One wheel uses a synthetic oil, whereas the other uses dry lubricant in the form of a sacrificial bearing cage.

Figure 3 shows how the dry-lubricated RW becomes significantly noisier on orbit. In comparison, its oil-lubricated counterpart behaves the same in orbit as it did during on ground tests, as shown in Figure 4. The explanation put forward by SSTL theorizes particles generated by the sacrificial bearing cage are kept out of the bearing raceway on ground due to gravity effects but may impact the noise signature of the RW in absence of gravity. This example demonstrates how assessing microvibration generated by a mechanism can be significantly impacted by the conditions on ground.

Measurements for these reaction wheels and other noise sources were taken over a time period of 18 months. In that time, no clear degradation of the microvibration performance was recorded. However, in case there is a real concern regarding microvibration degradation performance for a specific mechanism, a monitor such as the one flown by SSTL can be used for in situ health monitoring. Early warning of changing performance gives the spacecraft operator the opportunity to take the necessary corrective action where possible.

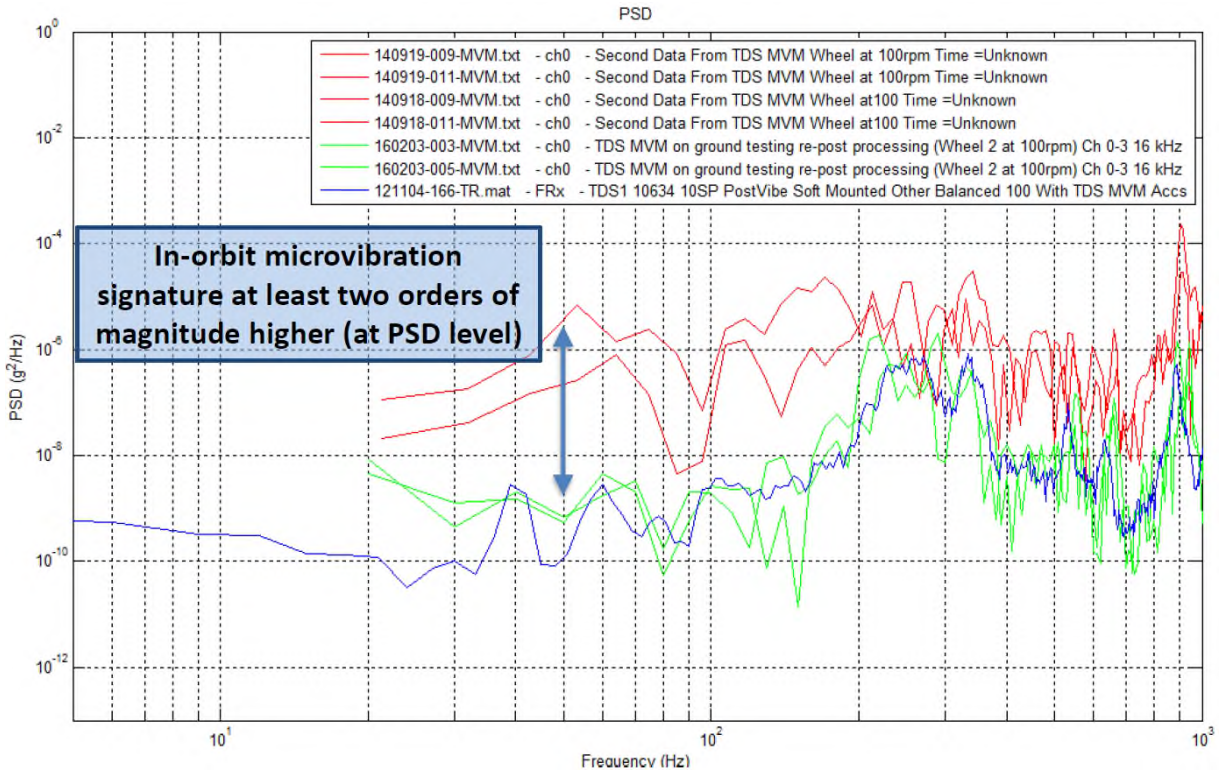


Figure 3. Noise signature for the dry lubricated RW: in-orbit data (red), on-ground spacecraft data (green) and Kistler data (blue). Image courtesy of SSTL [1].

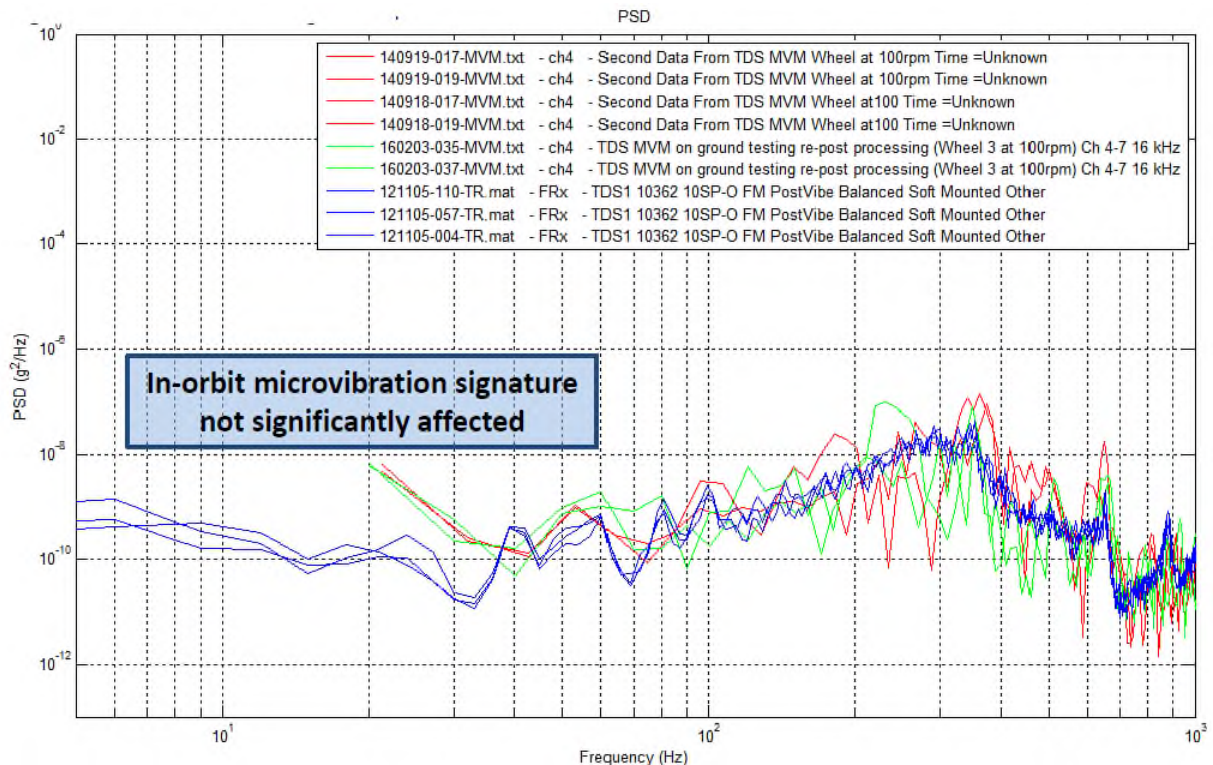


Figure 4. Noise signature for the oil lubricated RW: in-orbit data (red), on-ground spacecraft data (green) and Kistler data (blue). Image courtesy of SSTL [1].

System-Level Aspects and Microvibration Requirements

How is microvibration handled at system level?

System-level microvibration assessments investigate the transmission of very low vibrations by the spacecraft structure from the disturbance source to the receiver location which might be a sensitive instrument or payload and, where necessary, to find adequate methods to attenuate the vibrations along the transmission path. The system-level responsible engineer needs to identify whether the performance requirements for the instrument or payload are fulfilled under the influence of the relevant disturbance sources.

System-level microvibration verification is not straightforward. Directly measuring microvibration susceptibility is difficult. The performances cannot be validated on ground in a representative on-orbit environment (e.g. zero gravity, in-vacuum, perfectly unconstrained “free-free” condition). In addition, the background noise, mechanical and/or electrical, may be too high to measure the actual performance. Therefore, the verification of the microvibration performances is usually based on a combination of analytical predictions and hardware tests to validate models. Different analysis methods, such as Finite Element Modeling (FEM), Stochastic Energy Analysis, or a combination, may be appropriate. Microvibration generally occurs in the mid-frequency range where FEM is inaccurate. Therefore, several ESA R&D studies have been performed over the last years to further develop these methodologies [3] [4] [5]. For one of these methodologies, the on-orbit performance of the mission has later been reported [7].

Several challenges occur at system level that can have an influence on the mechanism development. For example, microvibration emissivity and susceptibility requirements need to be defined at an early stage in the project while the system-level modelling is still at an immature stage. Microvibration budgeting is notoriously difficult and over specification can drive the system-level design. In addition, contractual interfaces can lead to over specification. It is up to the system-level authority to manage these requirements between all parties as the design matures. However, as mechanism designers it is imperative to be critical towards the initial requirements and highlight its impact on the design in case it is a driving requirement as there may be scope for flexibility.

Another difficulty at system level is to appropriately combine the microvibration generated by different noise sources simultaneously. Generally, a satellite has different sources of microvibration. They all generate noise in 6 DOF and have varying modes of operation, which can lead to a large number of cases to simulate. Alternatively, enveloping cases can be devised, although they can in turn lead to additional, potentially unwanted, conservatism.

Lastly, coupling noise sources to the flexible spacecraft structure changes the dynamic behavior of both source and structure. This is notable, as microvibration requirements are typically defined on a clamped interface. Depending on the methodology used at system level, additional requirements can be imposed on the mechanism designer to accurately model this coupling, such as an accurate model of the mechanism or a dynamic mass measurement to obtain the accelerance matrix of the mechanism [3].

What does a mechanisms microvibration requirement look like?

Microvibration requirements will either be in force and torque (or PSD) versus frequency, or as a maximum instantaneous disturbance versus time.

Figure 5 shows an example of a force versus frequency requirement. It is important to note this requirement is applicable over the entire performance range of the mechanism, for example speed and position range, as well as for the entire set of potential environments. This requirement is specified for a clamped boundary condition. This particular requirement is challenging and may not be realistic, as it is specified over a very large frequency range. Verification of this requirement may be problematic, especially at the low and high end of the frequency range. The mechanism designer is encouraged to be critical of such a requirement, and of its prescribed verification approach, as either one may not be appropriate. This will be illustrated later in this paper when the verification approaches are discussed.

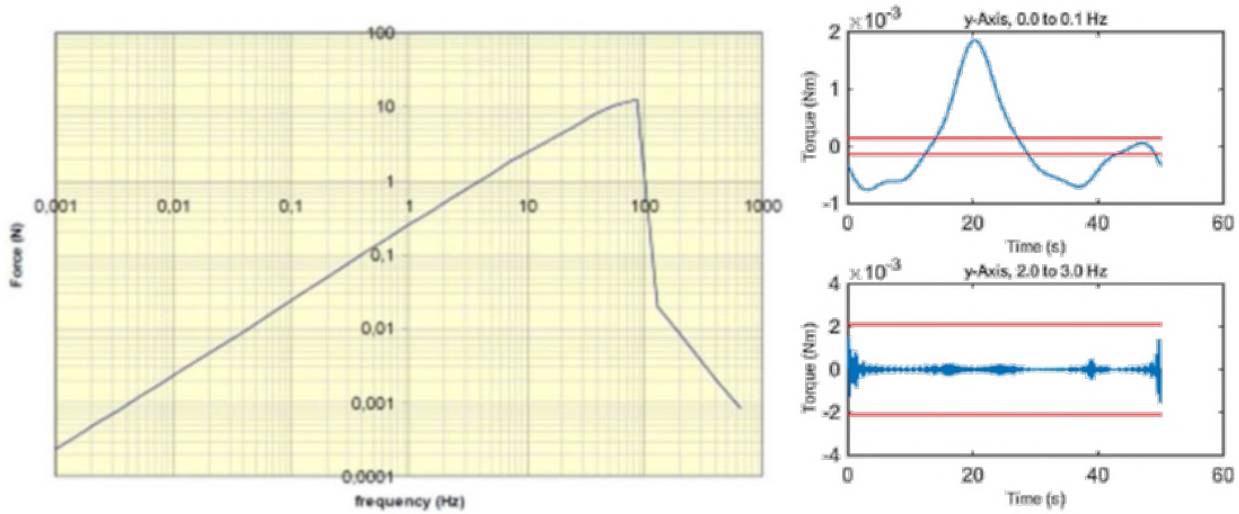


Figure 5. Left: Example of a force vs frequency requirement. Right: Example of two frequency bands of a maximum instantaneous torque versus time requirement.

Figure 5 also shows a maximum instantaneous disturbance versus time requirement. This type of requirement is more appropriate for (but not limited to) mechanisms with short or intermittent duty cycle. The type of requirement used is often dictated by instrument needs. In order to verify this requirement, the time history signal (from analysis or test) needs to be split into different frequency contributions and to be compared to the requirements in each frequency band, as illustrated in Figure 5.

Microvibration Verification

Which verification methodologies are appropriate?

Verification by test and analysis or a combination of both approaches may be more suitable in different circumstances.

Verification by analysis can be very useful in the early stages of the design when there is no hardware available yet. In addition, in some cases performing a test on the complete system is not feasible. For example, assessing the induced microvibration by the coupled system of a solar array and a SADM is not possible by test. In this case, analysis or a combination with test data at SADM level is more appropriate. Lastly, verification by analysis may be required if no suitable test facility is available due to the required sensitivity, frequency range or physical size of the test subject.

Verification by test is advisable when representative hardware is available, as well as a suitable test facility. It can validate (part of) the analysis model. Testing is particularly useful to assess the impact of environmental tests or different environmental conditions on the microvibration performance of the mechanism.

How to perform verification by analysis?

Microvibration verification by analysis is typically performed in a two-step approach:

- mechanism level (source of disturbance)
- system level

The objective of the mechanism-level analysis is to estimate the expected exported torque/force between the mechanism and a hard-mounted interface during operation, represented by F_{EXPORTED} in the diagram (Figure 6). F_{IN} represents internal mechanism forces/torques such as electric motor torque.

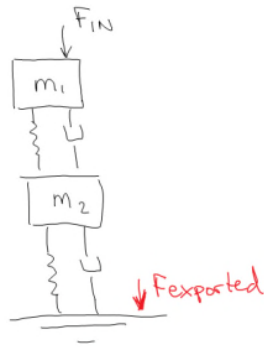


Figure 6. Mechanism-level exported microvibration model

The objective of the system-level analysis is to estimate the expected performance of the disturbance-affected equipment (e.g. pointing performance of optical equipment) when input mechanism disturbance is applied at the relevant mechanism to spacecraft interface point. For such an analysis, either a blocked force approach or coupled mechanism-spacecraft model can be used to simulate the input disturbance (Figure 7).

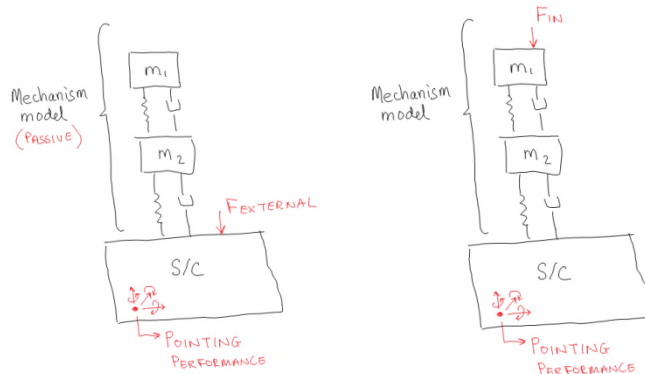


Figure 7. System-level model. Right: Coupled mechanism & S/C model. Left: Blocked force model.

An example model developed in MATLAB/Simulink is shown in Figure 8. The standard building blocks of such a microvibration model may consist in:

- Motor drive electronics
 - Current control
 - Position control
 - Output voltage to be applied on motor
- Electric motor model
 - Stepper, Voice coil, brushless DC etc.
 - Coil dynamics (R, L, back-EMF, detent, eddy current losses)
 - Rotor dynamics
- Mechanism components
 - Gearbox (transmission error, backlash, friction)
 - Other non-linear force contributors: Slip-ring, Cable wrap
- Structural parts
 - Structural parts with significant modes in frequencies of interest represented as state space matrix of flexible body exported from FEM tool
 - Typical parts modeled as FEM: Doors, Solar array, Scanner etc.

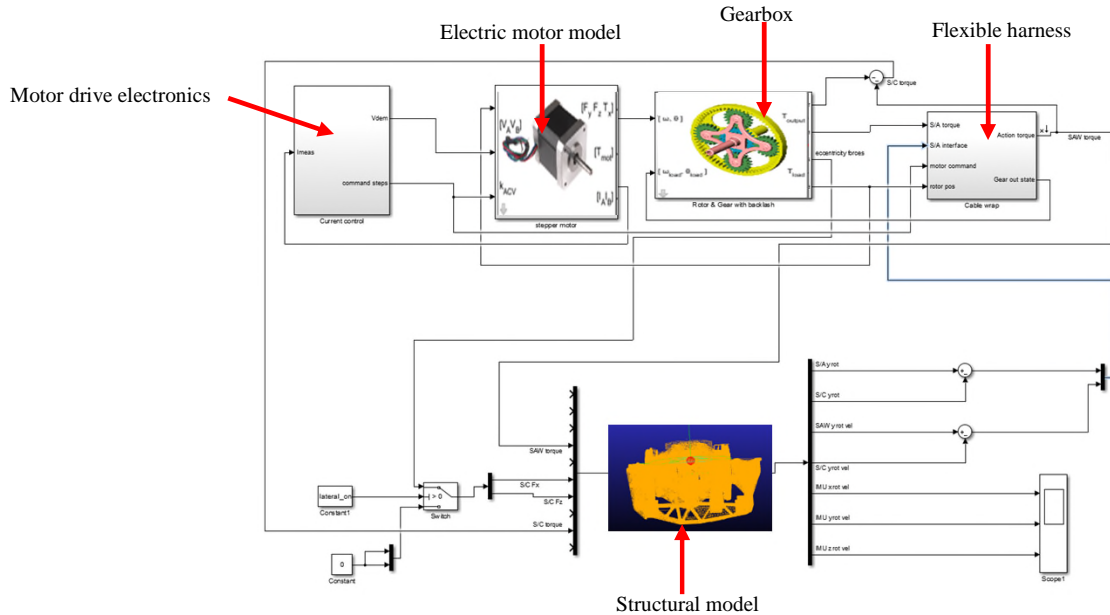


Figure 8. Example of a microvibration model in MATLAB/Simulink

Verification by analysis is an integral part of the overall verification process at unit level and especially important at system level, due to the complexity of performing system-level performance testing under gravity conditions. As such, an effective way to accurately assess system-level microvibration performance can be to perform simplified system-level tests, correlate the results with the simulation and perform the detailed performance assessment using the correlated analytical model.

This process can provide an extremely accurate prediction of in-flight performance, as shown by the example in Figure 9 of in-flight spacecraft jitter data versus analytical prediction performed during initial commissioning of a spacecraft.

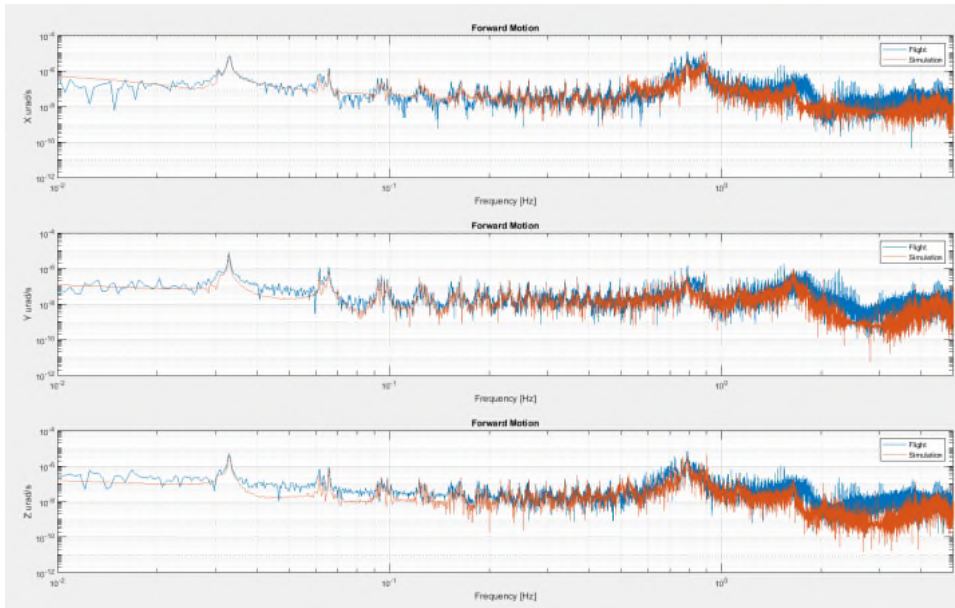


Figure 9. Comparison of inflight S/C jitter vs analytical estimate (Plotted as FFT)

How to perform verification by test?

Verification by test at mechanism level is typically performed on a dynamometer, often referred to as Kistler table (after the brand name of the predominant supplier). To illustrate the capabilities and limitations of this type of equipment, two facilities are discussed here: the Reaction Wheel Characterisation Facility (RCF) (Figure 10) and the 6-DOF microvibration test facility (6dMVMS) (Figure 11). Even though the RCF is named after RWs, it can be and has regularly been used for other mechanisms as well. Figure 12 shows the specification of both facilities. Test results using the relatively new 6dMVMS have already been reported elsewhere [10].

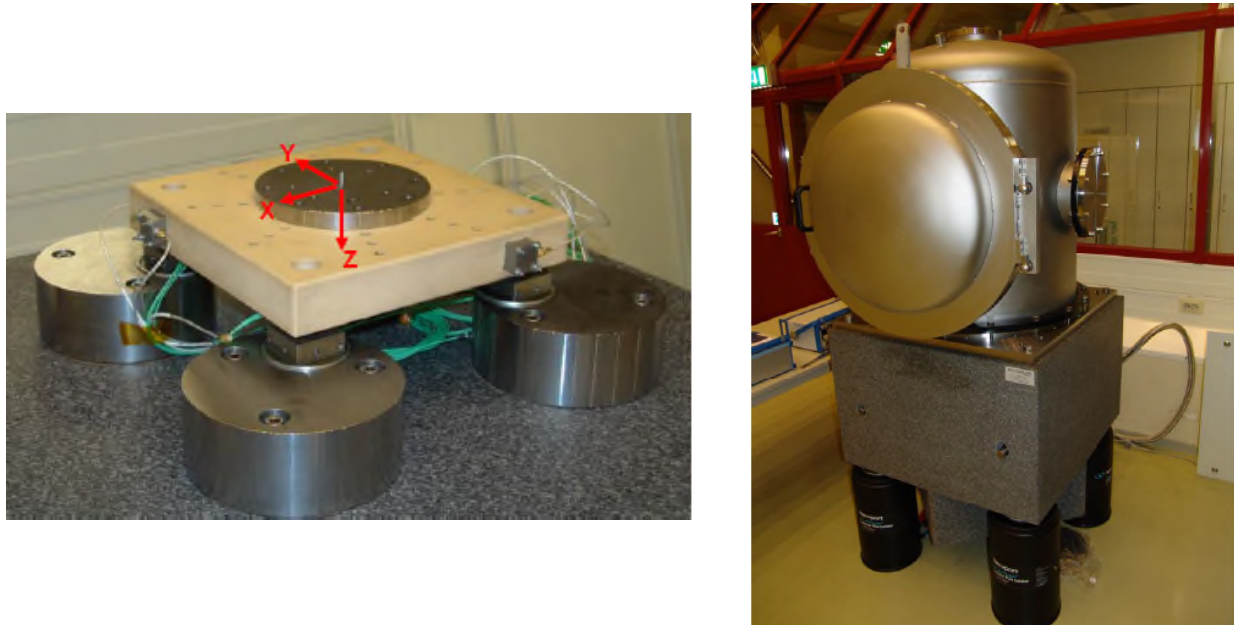


Figure 10. The RCF facility at ESA [8]

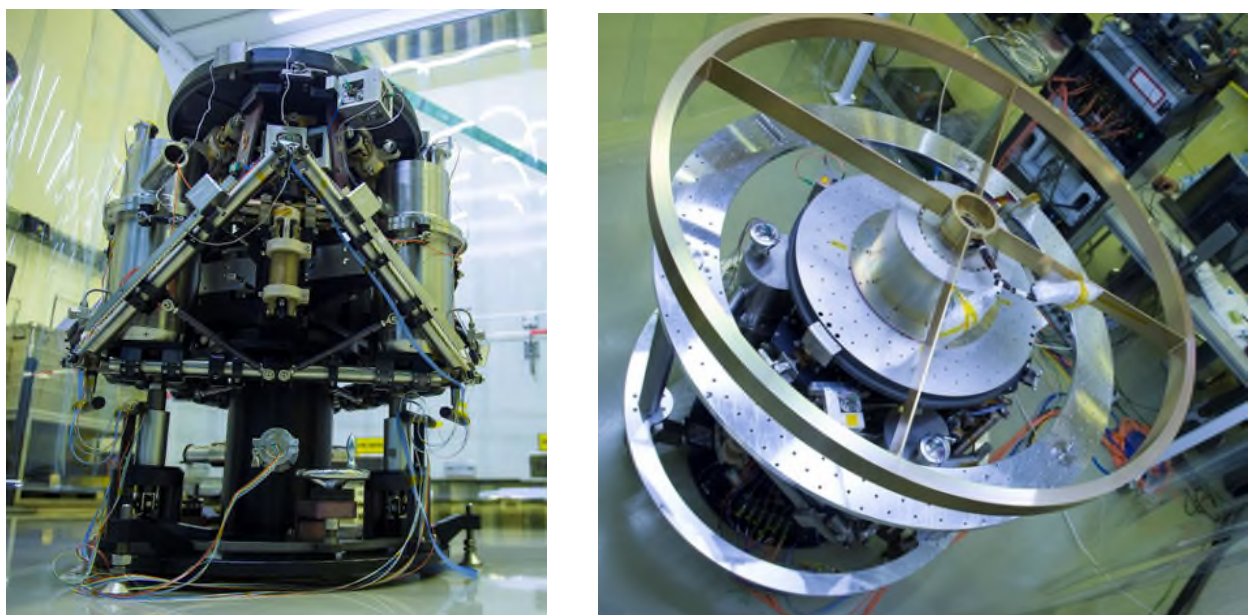


Figure 11. The 6dMVMS facility at ESA [9]

Description	Value
Payload mass [kg]	20 (max)
Achievable vacuum level [mbar]	0.25
Test table dimensions [mm]	320 x 320
<i>Measurement range</i>	
Lateral Forces Fx, Fy [N]	0.020 - 200
Vertical Forces Fz [N]	0.040 - 200
Moments Mx, My [Nm]	0.002 - 20
Torques Mz [Nm]	0.006 - 25
Frequency bandwidth [Hz]	2 - 1000
Measurement resolution *) [mN]	< 20
Linearity [%]	< 1.5
Cross-talk [%]	< 1.6
Background noise level *) [N]	< 5 * 10-5
<i>Empty table eigenfrequencies</i>	
fx [Hz]	> 1200
> 1200	
fz [Hz]	> 1750
*) Depending on full scale range.	

Description	Value
Dimensions and mass	
Overall diameter [mm]	1050
Height [mm]	1100
Total mass empty [kg]	394
<i>Payload range</i>	
Mass [kg]	0 - 50
<i>Excitation mode</i>	
Accelerations [ms^{-2}]	$10^{-5} - 10^{-3}$
angular accelerations [rads^{-2}]	$10^{-5} - 10^{-2}$
Frequency range [Hz]	$30 \cdot 10^{-3} - 50$
<i>Measurement mode</i>	
Measure force [μN]	$10 \cdot 10^6$
Measure torque [μNm]	$< 10 \cdot 10^6$
Frequency range [Hz]	$30 \cdot 10^{-3} - 10^1$

¹ Please note that the actual measurement range is strongly dependent on the payload and software parameters frequencies

Figure 12. Test facility specifications. Left: RCF specifications. Right: 6dMVMS specifications [8] [9]

The RCF system is composed of the following subsystems [8]:

- Instrumentation of the facility and interconnection to the data handling system
- Test table providing a rigid interface between the specimen and the instrumentation
- Marble block acting as seismic reaction mass and hosting the test facility
- Pneumatic isolation system to decouple from disturbing environmental ground vibrations
- Vacuum bell equipped with a dry pumping system and a vacuum gauge
- Signal conditioning, data acquisition and processing system

The microvibration measurement system is composed of two platforms [9]:

- a measurement and excitation platform (lower platform)
- a vibration isolation platform (top platform)

Each platform is formed from a Minus-K passive isolation system and an array of sensors and actuators which provide 6 DOF control and measurement. The measurement platform is a bespoke design, and has two modes:

- measurement, where the platform measures the 6 DOF force/torque exerted on the platform;
- excitation, where the platform subjects a specimen to a controlled 6 DOF microvibration environment.

The platform is designed to allow measurements and excitation at low frequencies (< 0.03 Hz) and very low amplitudes (μN).

The facilities both have unique capabilities missing in the other facility. The RCF can be equipped with its vacuum bell to perform measurements in vacuum if required. The 6dMVMS can excite equipment and is therefore uniquely capable of verifying microvibration susceptibility requirements by test. The frequency range of both facilities is complementary, with only relatively small overlap, although an extension of the frequency range for the 6dMVMS is currently under investigation.

There are several good practices to take into account when verifying microvibration requirements by test:

- Modes of the test set-up can influence the data. This usually limits the frequency range and mass of the unit under test. For the RCF, the modes of the empty table are higher than 1250 Hz. With a payload, the unit under test and its MGSE, of 10 kg this drops to ~1000 Hz and even lower for

heavier payloads. This means the usable frequency range depends on the payload and varies on a case by case basis. The upper value of the usable frequency range is lower still than the natural frequency of the table with payload, as the upslope of this mode will skew results. For the RCF, it means the usable frequency range will be typically up to 900 Hz.

- Inappropriate modal design of mechanical ground support equipment (MGSE) can compromise data. The MGSE should be designed so its main modes are outside the measurement range of interest where possible. This may be challenging in certain cases as microvibration facilities have a limited mass capability. The combined mass of stiff MGSE and the unit under test may have an impact on the modes of the test facility itself as discussed above.
- Gravity offloading equipment may impact the microvibration measurement. For example, microvibration isolation systems can be designed to be very compliant. Therefore, they may require gravity offload systems to operate. These offloading devices themselves are usually also designed to be very compliant. Care needs to be taken not to influence the performance of the isolation system with the offload system. A second example of impact by gravity offload systems will be discussed in the case study below.
- Electrical ground support equipment (EGSE) can create electrical noise affecting the data. The EGSE used for the test facility itself are usually designed to avoid these effects, but the EGSE needed to run the mechanism may cause interference. If it is not possible to take this into account in the design stage of the EGSE, care should be taken when interpreting the results. It is common to see spikes at 50 Hz (in Europe) and its higher harmonics related to mains electrical noise.
- Careful selection of test durations and post-processing methods is required. Specifically, obtaining valid low frequency data leads to long test durations.
- Appropriate run-in of mechanisms may be required in order to measure stable performance, rather than start-up performance. For example, fluid lubricated mechanisms may require some time to clear out excess oil from the bearing races after a period of standstill and to reach a stable temperature which impacts the viscosity of the lubricant. On the other hand, mechanisms which are used intermittently may actually require testing after a long stand still.
- Plan for microvibration tests throughout the qualification campaign and after the life test prior to mechanism strip-down for sensitive applications. Where possible, it is even recommended to test in between different mechanical tests (sine vibration, random vibration, shock). In case a significant performance degradation is measured, it will be easier to trace it back to a specific test environment and potentially negotiate a relaxation of this requirement or design in specific protection for the mechanism.
- Assess other environmental impacts such as temperature and vacuum where possible. Often the impact is smaller than the impact of mechanical environmental tests. However, it is recommended to assess these effects on at least one unit.
- Test ALL units. Small build to build variability can lead to significant microvibration performance changes, as demonstrated in Figure 1.

Case study: Verification by test for a large rotating scanner

In order to demonstrate some of the issues with verification by test, one specific case study is discussed here. The force versus frequency requirement shown in Figure 5 is actually applicable on a large rotating scanning instrument. Verification by test is specified for this requirement. The scanner mass is 200-300 kg, with a rotating mass of more than half of the total mass. The scanner is designed to rotate at a constant speed of <1 Hz.

When comparing the requirement to the specification of state of the art test facilities (Figure 12), several observations can be made. Firstly, the instrument is too large for the entire instrument to be tested. A larger facility may need to be developed in order to test the complete instrument. However, the scan mechanism in the instrument is compatible with these two facilities.

Comparing the frequency range of the requirement to the test facility specifications shows that both facilities would be required to cover the entire range. Even then, the 6dMVMS can measure as low as 0.03 Hz, whereas the requirement goes lower than 0.001 Hz.

The sensitivity and measurement range of both facilities are also relevant. It seems the sensitivity and range of the RCF is only compatible with the requirement up to 150 Hz. At higher frequencies the requirement is below the sensitivity of the facility. The 6dMVMS can actually measure forces lower than the minimum force specified of 1 mN. However, it can only measure up to 1 N. For an instrument this large, rotating at <1 Hz, the exported force is unlikely to be as low as 1 N at the main rotating frequency.

The instrument requires gravity offloading to operate under a 1g environment, although it can also be operated for short periods of time without gravity offloading. However, a measurement in both of these configurations impacts the data in a different way. The offloading MGSE itself includes bearings as it needs to allow for the rotation. These can generate additional noise. Furthermore, the MGSE changes the inertia and the modal behavior of the instrument. On the other hand, operating without offloading significantly changes the preload of the bearings in the scan mechanism. This may in turn have a significant impact on the microvibration performance. Both potential test configurations have clear drawbacks.

Lastly, the scanner is not axisymmetric and has a large cut-out on one side. As a consequence, there are significant additional unbalance forces due to windage losses when operating in air. In order to make meaningful measurements, the test would need to take place in vacuum.

It is clear for this particular case that the specified requirement along with the specified verification method is very challenging to achieve. As mechanism designer, discussing these issues early during the development with the customer is strongly advised in order to avoid unnecessarily ambitious design constraints and to come up with a feasible verification approach.

Which Approach can be Used to Minimize Microvibration?

There are several potential approaches on how to minimize the microvibration generated by mechanisms. This includes potential design improvement methodologies, minimizing the impact of assembly, integration and test (AIT) on the microvibration performance as well as solutions external to the mechanism in case design optimization and other measures prove to be insufficient.

A mechanism designer can attempt to optimize a mechanism for low noise performance during the design phase. The following tactics can be used:

- Reduction of the amplitude of the noise generated by carefully selecting components, materials, surface finishes and lubricants. It is recommended to try out different options at breadboard stage for especially demanding applications.
- Screening of components and subassemblies during the manufacturing stage. As shown in the example in Figure 1, identical mechanisms can still differ significantly. Performance of key components or subassemblies can be screened prior to integration in the mechanism to minimize the spread of the noise performance and reduce it as much as possible. This approach is generally taken in case larger numbers of identical mechanisms need to be made, as setting up the screening process requires quite some effort.
- Improve the modal design. The main structural modes of the mechanism are likely to be excited by internally generated noise and therefore amplify the exported microvibration. This can be seen very clearly in Figure 2. Designing the mechanism structural modes in frequency ranges where higher microvibration is allowed by the specification will reduce the impact of these modes getting excited. The requirement in Figure 5 shows a clear frequency range allowing higher amplitudes of exported microvibration. If compatible with the structural requirements of the mechanism or instrument, this would be an obvious target area in terms of modal design.

- Control electronics can significantly impact performance. This is specifically the case for closed-loop controlled mechanisms. It is important to test these mechanisms with the real control electronics in order to assess this effect, or to include it in the microvibration model.
- Tune the operational parameters, e.g. restrict/tune the speed range. If certain speeds excite structural modes of the mechanism and it is possible to avoid these speeds without impacting the operations, this could be a valid approach to minimize the exported microvibration.
- More innovative design solutions, such as magnetic bearings or flexures instead of tribological contacts could be envisaged.

Noise source optimization does not necessarily end at the design stage, but can continue during AIT. Reducing the environmental loads on mechanisms generally reduces the final microvibration performance. If it is clear which (mechanical) environment has the largest impact on the performance, local reductions could potentially be negotiated. Alternatively, the mechanism can be protected using vibration isolation systems. In addition, the selected model philosophy can also have an impact. For protoflight/protoqual models, the higher qualification mechanical loads can lead to higher exported microvibration. Choosing a full qualification model (QM) means the flight models will only be exposed to the lower acceptance-level vibration environment.

Noise source isolation can be an effective approach to attenuate the exported microvibration. It may be more efficient and cost effective to isolate particular mechanisms than to design a low-noise mechanism. For certain very demanding requirements, a combination of both may be required [11]. Dedicated isolation systems can be used to reduce the exported microvibration, but it may even be possible to design isolation into the mechanism itself. Passive isolation systems based on visco-elastic isolators are used most often, although other, more performant/complex systems exist as well. Interestingly, isolation systems can be designed with a dual function to reduce the environmental loads on the mechanism, thereby protecting the mechanism and improving its performance, as well as reducing the exported microvibration.

Conclusion

Microvibration can be a design driver for mechanisms. This paper has collected a number of good practices and lessons learned on how to deal with microvibration when designing a mechanism. Appropriately understanding the impact of microvibration requirements and taking them into account in the early stages of a mechanism development can avoid many problems later during the project. A clear and feasible verification approach needs to be devised at the same time.

Further improvements in this area are key for future missions, both in terms of mechanism design and verification approaches which avoid unnecessary conservatism.

References

1. Cabon, B., Seabrook, T. and Richardson G. "TDS-1 In-orbit microvibration experiment." *Mechanisms Final Presentation Days*, 15-17 June 2016.
2. Ferreira, R. A. "Reaction Wheel Technology Consolidation Final Report." *ESA Contract No. 4000116154/15/NL/PS*, 3 November 2017.
3. Richardson G., Aglietti, G., Remedia, M., Seabrook T. "Methodology for Analysis of Structure-borne Microvibration – Final Presentation." *ESA Contract No. 4000101914/0/0/0*, 26 June 2014.
4. Soula, L. "METhodology for Analysis of structure-borne MICro-vibrations (METAMIC)." *ESA Contract No.4000101886/10/NL/RA*, 18 February 2012.
5. Steier, F., Runte, T. "MicroMap – Microvibration Management Approach – Final Presentation." *Mechanisms Final Presentation Days*, 15-17 June 2016.
6. Gupta, Pradeep K. *Advanced Dynamics of Rolling Elements*. Berlin: Springer-Verlag, ©1984.

7. Richardson, G., Seabrook, T. "Ground and on orbit microvibration verification of the triplesat 1m resolution earth imaging spacecraft constellation." *ECSSMET 27-30 September 2016*.
8. Wagner, M., Selle, J. "Reaction wheel characterisation facility – Facility description." 24 October 2013.
9. Wagner, M., Selle, J. "6 degree of freedom micro-vibration test facility – Facility description." February 2017.
10. Wagner, M., Selle, J. "First real-life results of novel micro vibration measurement facility." *ESMATS*, 20-22 September 2017.
11. Smet, G., Richardson G., McLaren S., Haslehurst, A. "Managing reaction wheel microvibration on a high resolution EO small spacecraft." *ESMATS*, 25-27 September 2013.

Investigation of Bolt Preload Relaxation for JWST Thermal Heat Strap Assembly Joints with Aluminum-1100 and Indium Gaskets

Andrew Bartoszyk*, Thomas Walsh**, Jody Davis*, Jason Krom+, Patrick Williams**, Jason Hylan* and Edgar Hemminger++

Abstract

Accurately predicting fastener preload relaxation in the James Webb Space Telescope (JWST) heat strap assemblies is essential to insure adequate thermal performance during its mission lifecycle. The mechanisms for preload relaxation in the strap joints include Al-1100 material creep, indium gasket flow-out, and embedment of the joint faying surfaces. This report documents the results from a bolted joint relaxation test, including analysis and curve fitting of the test data for predicting preloads five years after initial torque application. The report also includes the derivation of a preload uncertainty factor enveloping both torque/preload application scatter and expected preload relaxation at the end of mission life.

Introduction

The JWST thermal control system includes Al-1100 heat straps for controlling heat flow to and from temperature critical instruments in order to meet instrument performance requirements and optimize observatory science capability. Critical to heat strap performance is preload maintenance at the bolted joint interfaces over mission lifetime. To improve thermal conduction through the bolted interfaces, Al-1100 and indium gaskets are integral in many of the joints. Although these materials are common for improving thermal conduction in aerospace bolted joints, Al-1100 creeps under load at room temperature and indium gaskets can gradually flow out. Creep and flow-out will relax joint preload and therefore degrade joint thermal conductance over time. Many of the heat strap joints also include threaded inserts in Al-1100, resulting in high stresses in the parent material around the insert and exacerbating Al-1100 creep. Figure 1 illustrates a representative flight joint for the JWST heat strap assemblies.

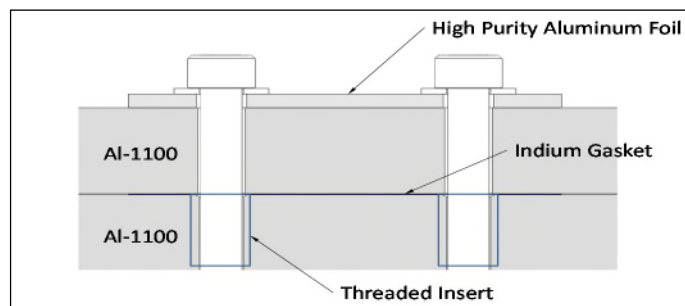


Figure 1. Representative Heat Strap Bolted Joint Interface

Because Al-1100 is relatively low in strength, compression of Al-1100 under washers and threaded insert pull-out limit the design space for the initial bolt preload. This limited design space necessitates a rigorous approach for predicting joint preloads in the heat straps throughout the joint life cycle.

* NASA Goddard Space Flight Center, Greenbelt, MD

** Stinger Ghaffarian Technologies, Greenbelt, MD

+ Sigma Space Corporation, Lanham, MD

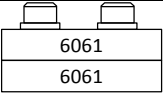
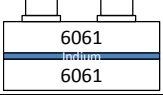
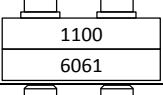
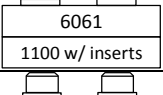
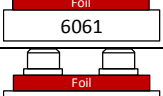
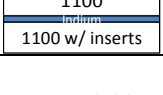
++ Ares Corporation, Greenbelt, MD

In order to quantify preload loss over time, a comprehensive joint relaxation test was completed. The test includes a set of representative flight-like joints, a control set, and various joint configurations in order to compare preload loss between different drivers for joint relaxation. The different joint coupons were torqued to the same nominal preload and the preload relaxation was measured over a period of eight months. The test data was then processed in an Excel spreadsheet for future preload loss predictions. Uncertainty factors were also derived for calculating max and min expected preloads, accounting for both scatter in initial preload application and joint relaxation over time.

Test Description

Table 1 lists the joint configurations tested. For each group, with the exception of the control group, a set of 3 coupons were tested with the bolts re-torqued 24 hours after the initial torque-up and a set of 3 coupons were not re-torqued. For the control group, only 3 coupons were tested without any re-torqueing of the bolts. The coupons included #10-32 A-286 fasteners, phosphor-bronze threaded inserts (2D length), and lubrication of external/internal threads with Braycote. All coupons were torqued to a nominal preload of 1550 N (350 lbf).

Table 1. Coupon Test Configurations

Configuration	Description	
Control	Al-6061 top plate compressed against an Al-6061 bottom plate	
Indium	0.005-in (0.13-mm) thick Indium foil between Al-6061 plates	
1100C	Al-1100 plate compressed against an Al-6061 bottom plate	
1100T	Al-6061 plate bolted into an Al-1100 plate, putting threads in tension	
Foil	Multiple layers of 0.002-in (0.05-mm) thick high-purity aluminum (99.999% Al) in direct compression against an Al-6061 bottom plate	
Flight	Combines multi-layer aluminum foil in compression, 1100 plate in compression, Indium in compression, 1100 in tension	

All test coupons included a FUTEK piezo-electric load cell for preload monitoring. The data acquisition system included the SENSIT Test and Measurement Software. The program was set to sample load cell outputs every 0.1 second during initial torque-up for each joint. After initial torque-up, the load cells were sampled every 10 minutes. Test data was downloaded on a daily basis for monitoring and analysis. A separate load cell was put under a known weight and monitored for several months to confirm that the load cell read-out did not drift over time.

Joint Relaxation Test Data Analysis

The physical mechanisms driving preload loss in a thermally conductive bolted joint with Al-1100 and an indium gasket are varied and complicated, making it difficult to derive a simple mathematical model for predicting joint relaxation. An alternative approach is to curve fit data from a joint relaxation test and extrapolate the empirical model for predicting future preload loss. After curve fitting the test data with several candidate functions, the natural logarithm function proved to be the most accurate for fitting the data across the various coupon test configurations.

Using the method of least squares, the data was processed in Excel and the software's Solver Tool was applied for minimizing the sum of the chi square values (the square of the difference between the real data and the predicted data). Since the data acquisition system sampled preload every 10 minutes for 32 joint coupons and the test duration was more than 8 months, the spreadsheet was set up to sample the test data every 24 hours. This minimized the processing time for each Solver Tool run and kept the spreadsheet at a manageable size. A number of curve fits were also processed with higher analysis sampling rates in order to check the nominal analytical sampling rate. Additionally, the coefficient of determination (R^2) was calculated for each curve fit to quantify how well the test data fit the curve. Figure 2 is a plot of the test data and curve fit for the Flight-1 coupon.

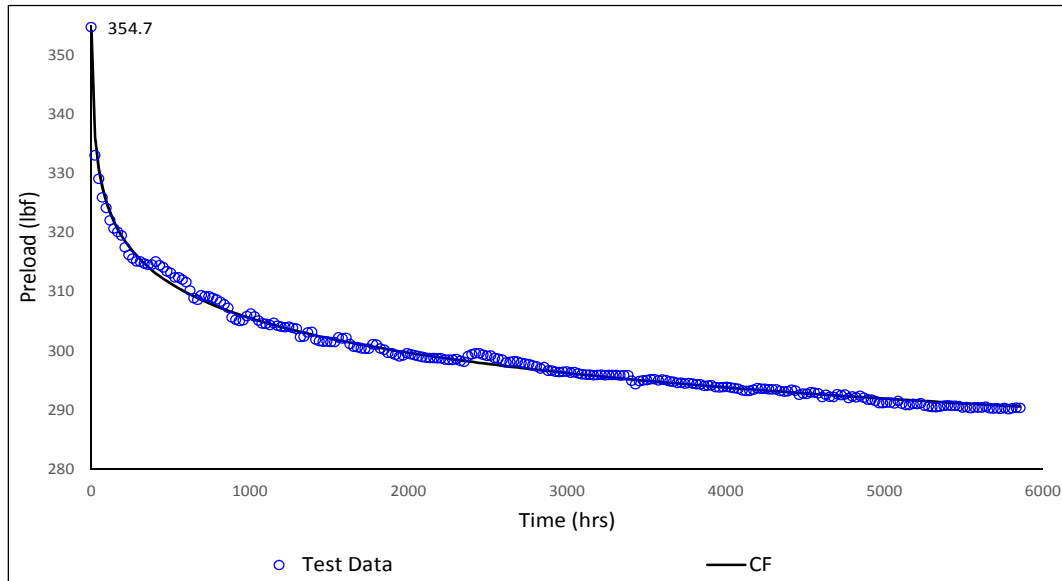


Figure 2. Test Data and Curve Fit for Flight-1 Coupon

Joint Relaxation Test Results

Figure 3 plots the average preload predictions after 5 years, with 2-sigma error bars calculated from the test data. The results from this test are specific to the joint configurations tested (materials, thicknesses, configurations, initial nominal preload, etc.) and apply only to these specific configurations. Caution should therefore be exercised when extrapolating the results to design deviations from the specific configurations tested. As can readily be seen in Figure 3, the flight configuration (with 1 re-torque), is predicted to lose ~25% of its initial preload (average + 2-sigma). Without the re-torque, the preload loss is >40%. For comparison, the control configuration, a typical joint for structural applications in flight and ground support hardware, is predicted to lose ~5% of its initial preload after 5 years. The test results also show that the biggest drivers for joint relaxation are the Al-1100 in tension (inserts embedded in Al-1100) and the high-purity aluminum foil in compression. Joint relaxation from indium flow-out appears to benefit the most from a single re-torqueing of the bolts (from ~25% to <10%).

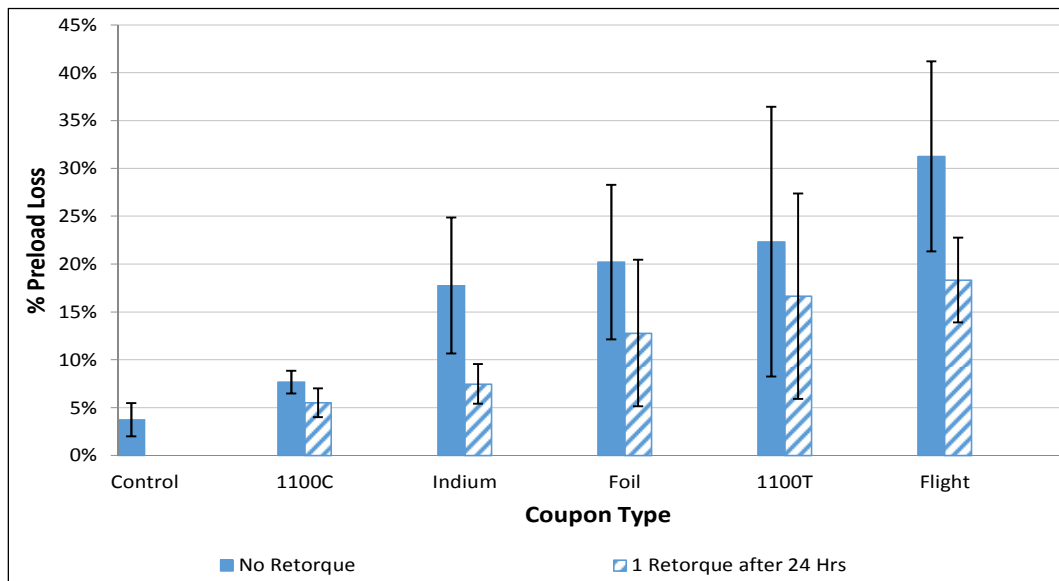


Figure 3. Joint Relaxation Preload Loss Predictions (5 years out)

The plot in Figure 4 compares the curve fits for the different configurations. The plots only include the coupons that were re-torqued, with the exception of the control coupons. Figure 4 shows the curve fits for preload loss after approximately 6000 hours of testing (~8.3 months), the flight coupons were losing ~0.25 lbf (1.1 N) of preload per week and the control group was losing <0.1 lbf (0.4 N) of preload per week.

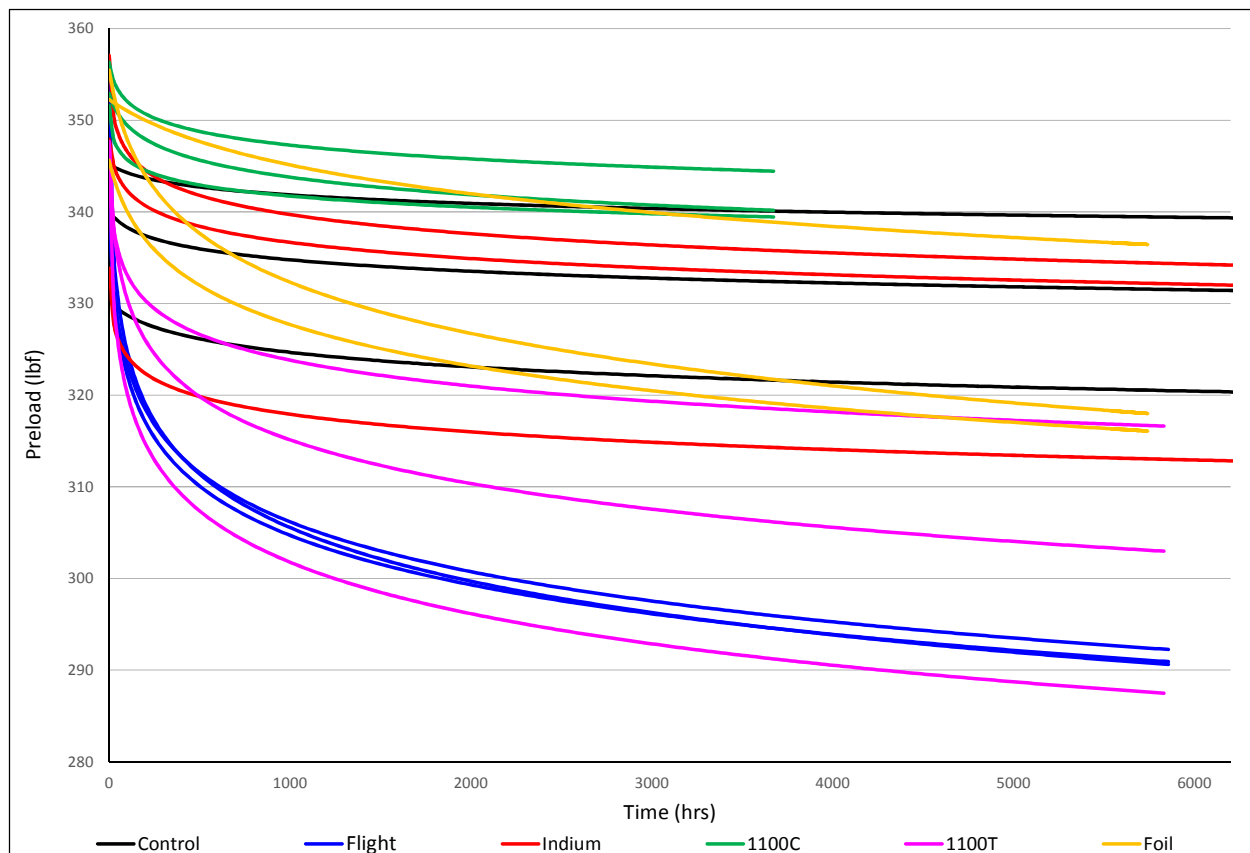


Figure 4. Curve Fits for Preload Loss Over Time

Preload Uncertainty Factor

A torque/preload uncertainty factor (UF) is typically included in bolted joint analysis for calculating the expected maximum and minimum preloads after torque application to a design nominal preload. The UF for a given joint configuration can be recovered from torque/preload test data with the assumption that the preload probability distribution function (PDF) is Gaussian. NASA-STD-5020 [1] recommends the recovery and use of a B-basis (90% of population with 95% confidence) UF for bolted joint analysis.

In addition to the torque/preload UF, the calculated max/min preload must also account for preload loss over time, especially when preload is critical for joint performance. A total UF, accounting for the scatter in preload from both the initial torque-up of a bolt and relaxation over time, is derived in order to simplify the final bolted joint analysis and retain the use of existing in-house analysis programs. Preload changes due to temperature effects are not included in the UF since it is calculated separately.

In order to easily combine the preload scatter for the nominal installation preload and joint relaxation, the PDF for preload loss from joint relaxation is assumed Gaussian and independent from the initial torque-up preload PDF. This is a reasonable assumption if the torque/preload UF is low. The average relaxed preload after torque-up and preload loss is simply the nominal initial preload minus the average predicted preload loss across all coupons for a given configuration.

$$\text{Preload}_{\text{relax_average}} = \text{Preload}_{\text{nom}}(1 - \%Loss_{\text{average}}) \quad (1)$$

Since the initial preload and preload loss are uncorrelated random variables and their PDFs are Gaussian, the B-basis UF for the relaxed preload PDF is simply the RSS (root sum square) of the UF values for the initial preload PDF and preload loss PDF.

$$UF_{\text{relax}} = \sqrt{UF_{\text{initial}}^2 + UF_{\text{loss}}^2} \quad (2)$$

A total UF⁻ can then be derived for the minimum expected preload.

$$\text{Preload}_{\text{min}} = \text{Preload}_{\text{nom}}(1 - \%Loss_{\text{average}})(1 - UF_{\text{relax}}) \quad (3)$$

$$\text{Preload}_{\text{min}} = \text{Preload}_{\text{nom}}(1 - \%Loss_{\text{average}} - UF_{\text{relax}} + \%Loss_{\text{average}}UF_{\text{relax}}) \quad (4)$$

$$\text{Preload}_{\text{min}} = \text{Preload}_{\text{nom}}(1 - UF^-) \quad (5)$$

$$UF^- = \%Loss_{\text{average}} + UF_{\text{relax}} - \%Loss_{\text{average}}UF_{\text{relax}} \quad (6)$$

Figure 5 illustrates the relationships between UF⁻ and the nominal preload.

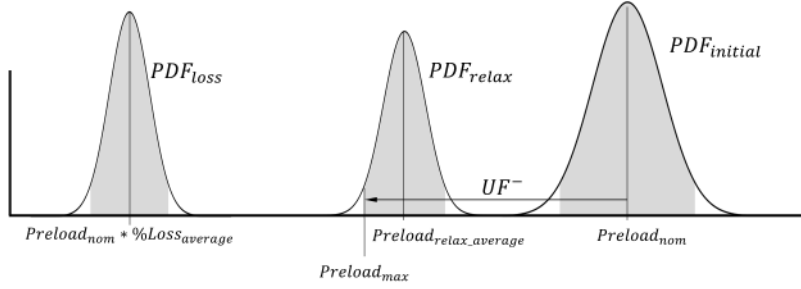


Figure 5. UF⁻ and Nominal Preload

UF⁺ is simply equal to the torque/preload UF, since the max preload for any given time is before joint relaxation progresses.

$$\text{Preload}_{\text{max}} = \text{Preload}_{\text{nom}}(1 + UF^+) \quad (7)$$

$$UF^+ = UF_{\text{initial}} \quad (8)$$

Table 2 summarizes the calculation for the total UF to be applied to the nominal preload loss at room temperature for the heat strap flight joints at specified intervals after re-torque. It is noted that re-torque decreases UF- from 0.69 to 0.52 for the expected minimum preload after 5 years. Calculations are based on a torque/preload UF of 0.36, which was determined from a separate nut factor test for this bolt/insert flight configuration.

Table 2. Total Preload UF for Flight Joints After Re-torque

Coupon	Retorque	Max Preload (lbf)	% Preload Loss from CF		
			after 24 hrs	after 5 years	after 13 years
Flight-1	Y	354.7	4.9%	22.9%	25.1%
Flight-2	Y	344.5	3.1%	20.1%	22.3%
Flight-3	Y	341.4	1.6%	19.1%	21.3%
		Average	3.2%	20.7%	22.9%
		Sigma	1.7%	2.0%	2.0%
		B-basis Preload UF (Torque/Preload)	0.36	0.36	0.36
		B-basis Preload UF (Loss)	0.14	0.14	0.16
		Preload UF (Relax)	0.39	0.40	0.40
		UF(+)	0.36	0.36	0.36
		UF(-)	0.41	0.52	0.54

Conclusion

A joint relaxation test was completed, specific to the JWST heat strap attachment joints. The flight joints include threaded inserts embedded in Al-1100, washers bearing directly on high purity aluminum foils, and indium gaskets. Al-1100 is known to creep under load at room temperature and indium gaskets can gradually flow out of a bolted interface. The results of the test and post-test processing of the data show that the flight joints can lose ~ 25% of its initial preload (average+2-sigma) in 5 years after initial torque application. A relative high torque/preload UF of 0.36 was also determined based on a separate test for bolts with threaded inserts in Al-1100. Combining the results from the joint relaxation test and a separate torque/preload test, a total uncertainty factor of 0.52 was calculated for the minimum expected preload in a flight joint five years after initial torque-up. In other words, the minimum expected preload five years after initial torque application is 52% of the nominal installation preload. The test and data analysis results presented in this report has been applied to the JWST heat strap attachment joint analysis for predicting preloads and checking thermal performance requirements.

Several observations are noted from the test results and curve fits. The largest relaxation drivers in the heat strap joints are (1) threaded inserts embedded in Al-1100 and (2) washers bearing directly on high purity aluminum foils. Also, pull-out strengths for inserts in Al-1100 are low due to the very low shear strength of the parent material which further reduces the design space for the attachment joints. It is recommended that threaded inserts in Al-1100 are avoided if possible in future joint designs. Alternate options for joints requiring Al-1100 members for thermal performance could include nuts or nut plates. The test results also demonstrate the benefit of re-torqueing bolts in joints that include indium gaskets. For the indium and flight joint coupons, re-torque after initial torque-up reduced the total preload loss (5 years out) by ~50%.

Caution must be exercised when applying the results from this test to joint configurations that deviate from the JWST heat strap joint designs (material, initial torque, indium gasket, bolt size, etc.). It is recommended that the results in this report are not directly applied to other joints configurations, but may be used for guidance and insight when designing joints with similar configuration.

References

- NASA, "Requirements for Threaded Fastening Systems in Spaceflight Hardware", NASA-STD-5020

Validation and Test Results of the 2.5D Technology for Pancake Slip Rings

Mélanie Henry* and Sandro Liberatoscioli*

Abstract

A slip ring assembly project has been performed to demonstrate that in future space mechanisms a slip ring assembly based on 2.5D printed circuit board (PCB) technology can replace the currently used risky and costly design. Four units with 2.5D technology have been manufactured, assembled and tested for an ESA ARTES 5.2 project to validate this technology at a level of TRL5.

The 2.5D PCB technology slip rings have undergone all the mechanical and environmental tests without showing any degradation. During the TVAC test, some lines have shown high dynamic resistance performance. After investigation, it was confirmed that this degradation (noise) was linked to a contamination problem.

The same level (even better) of performance is achieved with this type of technology compared to the standard one.

2.5D Slip Ring Definition and Validation

The data and power transfer within space mechanisms, such as a Solar Array Drive Mechanism (SADM), is in principle ensured by a contact technology. These components known as slip rings are of two types: cylindrical and pancake. The pancake slip ring concept is the one discussed in this paper. The pancake solution is made of electrical conducting tracks arranged on a flat disk as concentric rings centered on the rotating shaft (Fig. 1). The planetary configuration allows optimization of weight, volume and electrical features of the circuits.

The 2.5D PCB slip ring is a planetary slip ring composed of two sub-assemblies:

- The stator assembly, the fixed part of the slip ring.
- The rotor assembly, the rotating part of the slip ring.

The contact between the stator and rotor is ensured by wire brushes, soldered on the stator side on a PCB and preloaded to be in contact with the track during the whole life time.

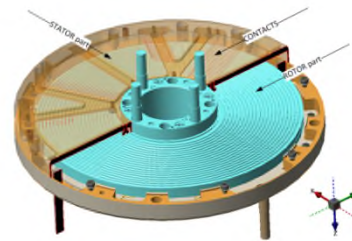


Figure 1. 2.5D slip ring overview

The main challenge of the project was to manufacture the rotor sub-assembly in only one part (PCB technology) to remove all the operations of gluing, machining, potting and soldering that increases the manufacturing activities. Therefore, the novelties of this innovative technology are:

- To apply a thickness layer of pure copper up to 500 µm based on PCB technology, this in order to manufacture a groove for brush guidance.
- To apply a hard gold plating on the tracks (according to a space-qualified RUAG process)
- To obtain the insulation barriers between tracks during PCB manufacturing operations
- To create a guidance groove in each track during PCB manufacturing operations
- To have a thermal drain inside the PCB to dissipate as much as possible the heat at the interface
- To choose the better candidate between different possibilities for the insulating barrier material

* RUAG Schweiz AG, Nyon, Switzerland

In addition, special attention was focused on the stator sub-assembly to simplify the integration phase. A dedicated stator PCB was designed to improve the thermal dissipation of the slip ring and reduce the variation of current distribution into the wire brushes. The main modifications are showed in Figure 2 and Figure 3.

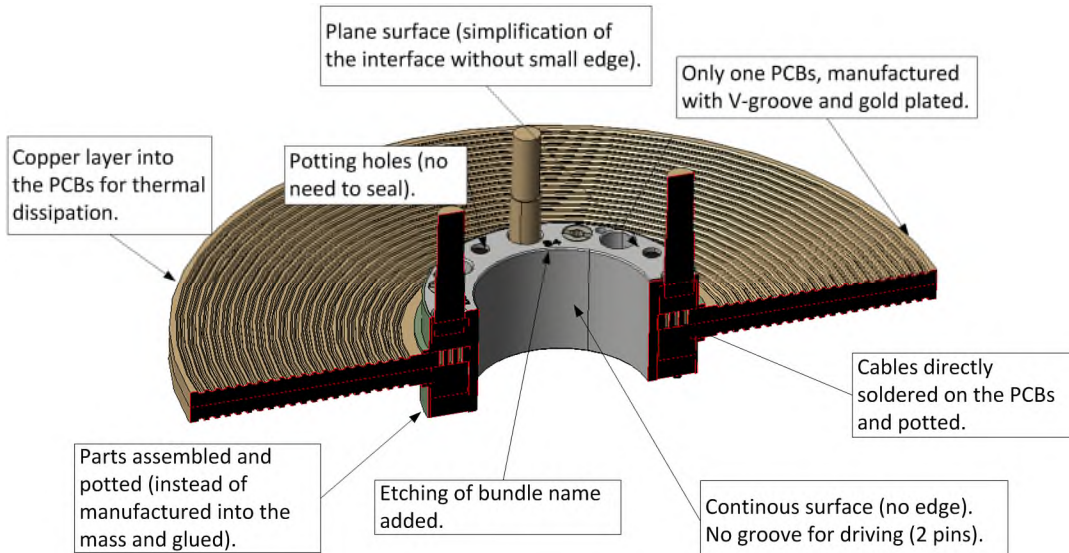


Figure 2. Rotor sub-assembly improvement

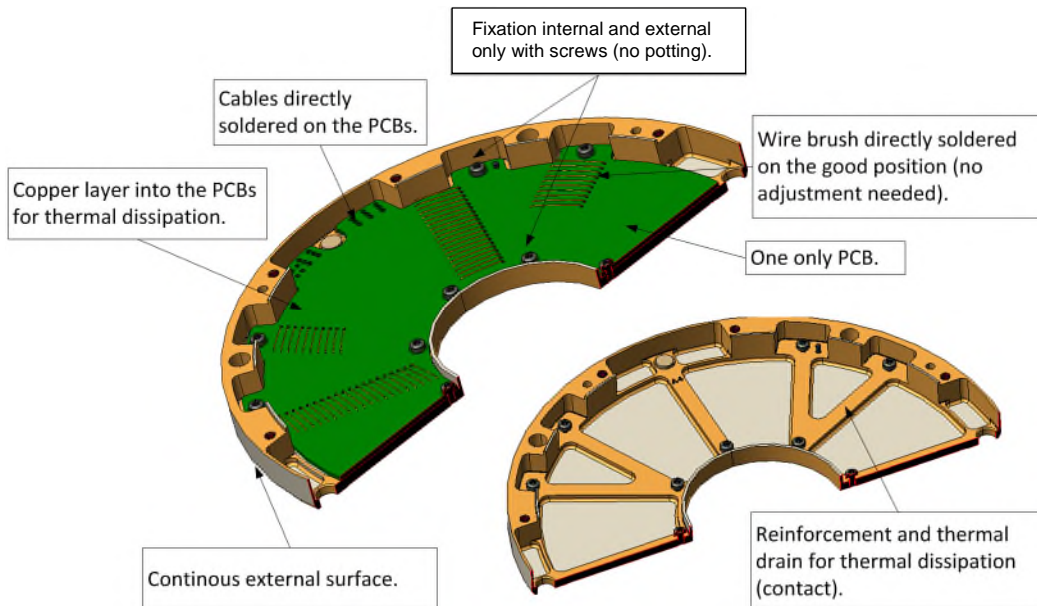


Figure 3. Stator sub-assembly improvement

The main benefits due to these improvements are:

- Reduction of manufacturing process time (no gluing, no adjustment of wire brushes, direct soldering) by about 50%
- Better reliability (controlled processes)
- High thermal dissipation on both sides (rotor and stator)
- Better current repartition into the wire brush (decrease of creep effect)
- Possibility to be modular

The electrical configuration of one module of a 2.5D slip ring consists of 20 power lines designed for 5.4 A and 20 signal lines designed for 1.1 A. This allows transfer of a total current of about 130 A (forward and return). For two modules in parallel, the transferred current can be doubled.

All steps performed during assembly have been verified and the process was validated. The final sub-assembly and assembly pictures are shown in Figure 4.

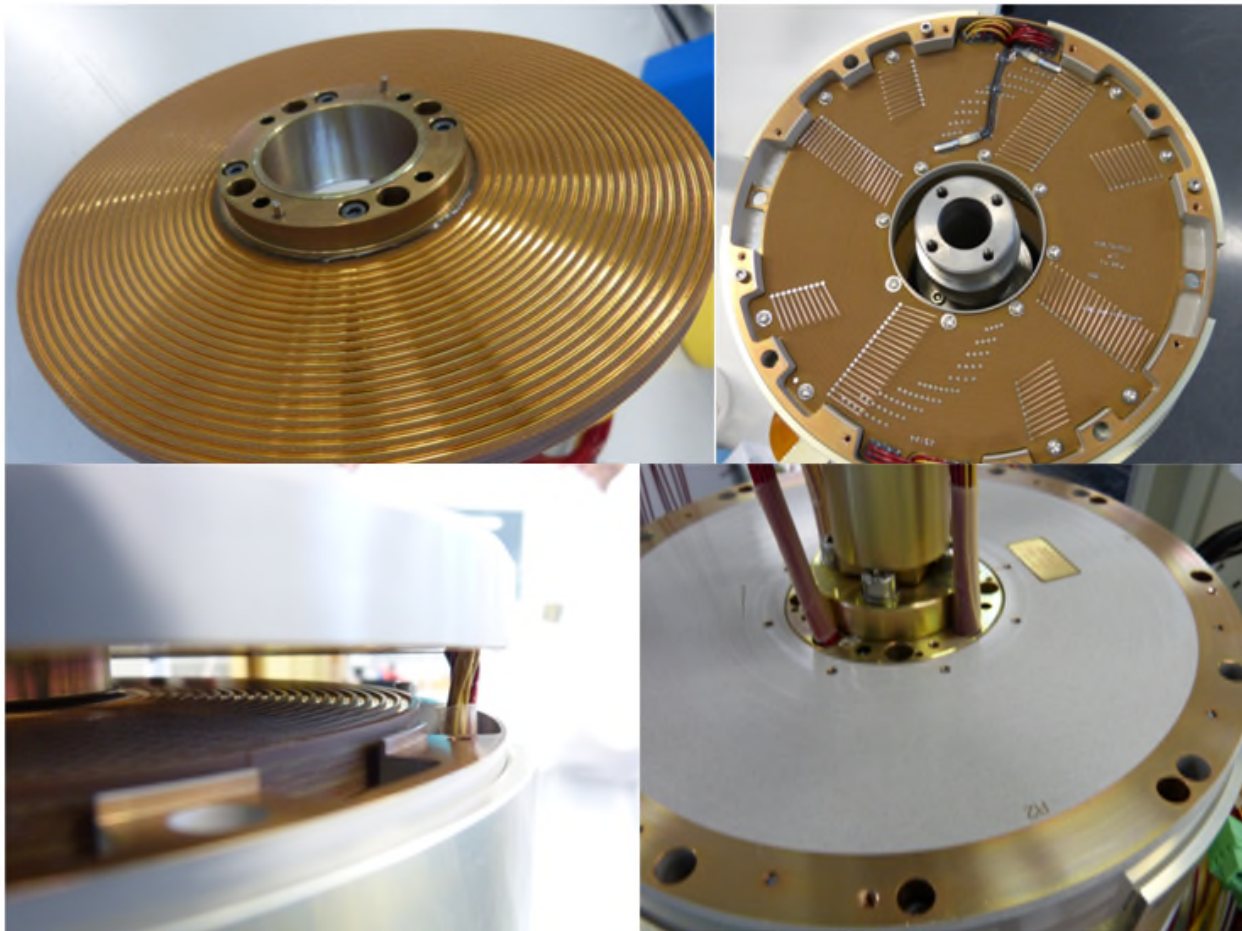


Figure 4. Sub-assembly and assembly pictures

Four units have then been tested according to the test sequence shown in Figure 5.

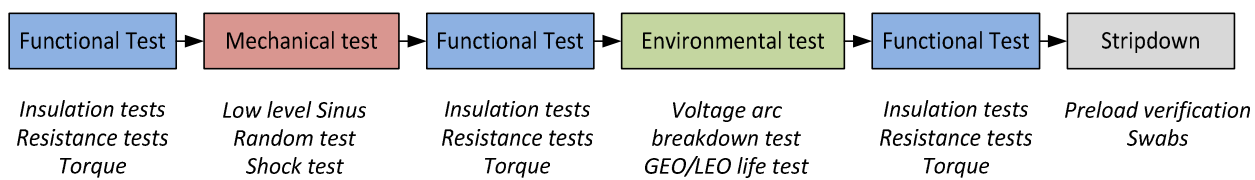


Figure 5. Qualification test sequence

The 2.5D slip rings performed all the mechanical and environmental tests without showing any degradation. Some lines were detected out of specification in terms of dynamic resistance performance during the environmental tests. After an investigation, it was confirmed that the identified noise was linked

to contamination during integration. It has been assessed that a potential contamination occurred onto the slip rings rotors while cycling them into the oven. (Rotors were positioned into the oven as described in Figure 6).

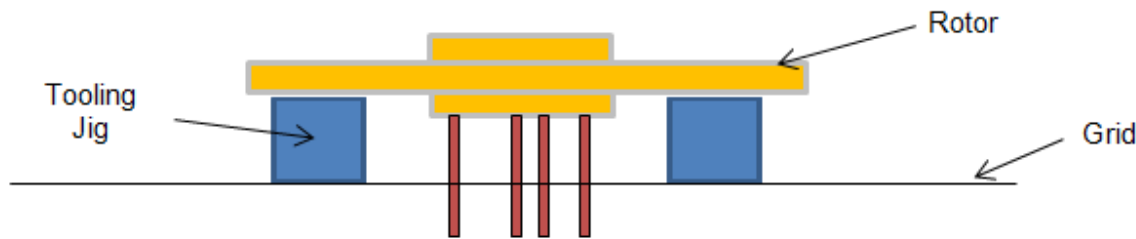


Figure 6. Rotor sketch assembly into the oven

The investigation showed that the tooling jigs the rotor rests onto into the oven have the exact same shape as the one observed on the rotor. Some Kapton® tape residue was present on the jigs and the assumption is made that contamination occurred at this stage. Kapton® tape glue has evaporated onto the rotor track during the temperature cycling. The rotor clearly exhibits a discoloration as depicted in Figure 7.

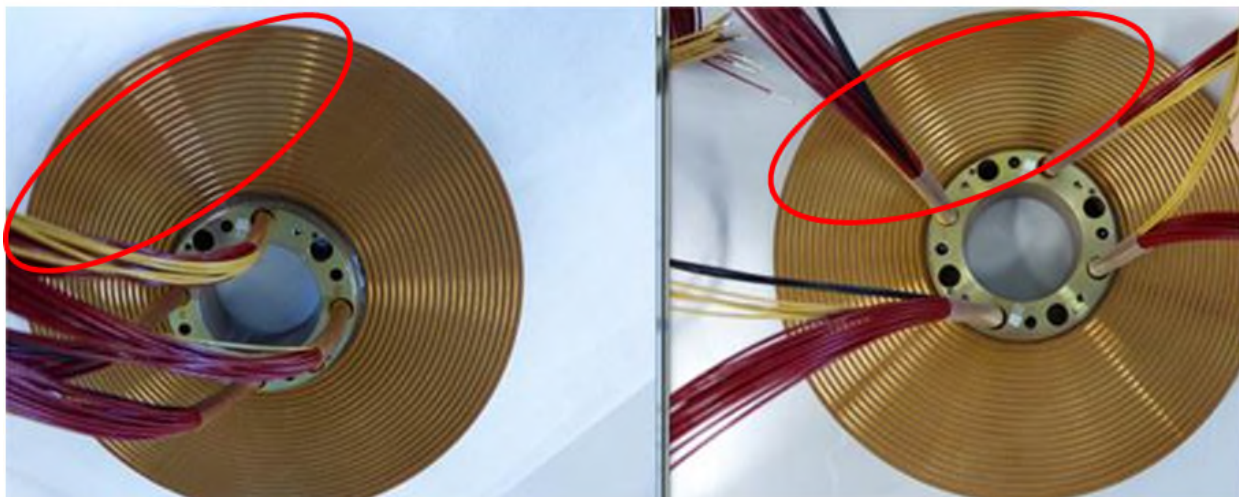


Figure 7. Discoloration on rotor track

Right after the tear down activity, a deep cleaning of the rotor was performed to verify any effect this could have on the resistance final results. Slip ring was re-assembled and tested after the cleaning and the new dynamic resistance test passed. The difference between the results at the end of the test sequence and after cleaning is shown in Figure 8 (resistance over one complete revolution on one track).

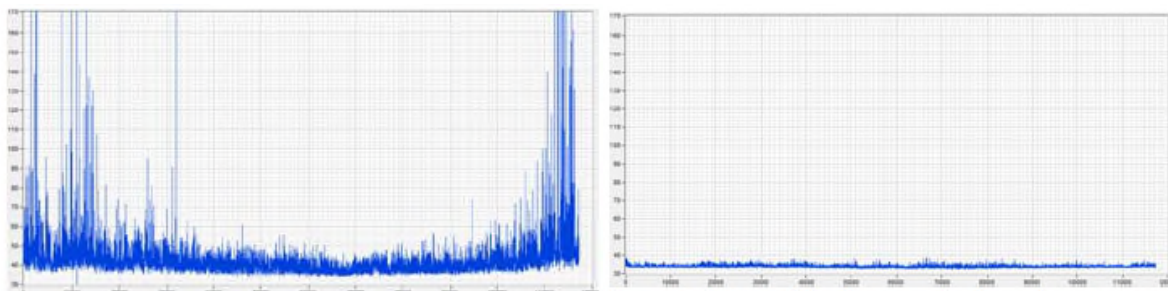


Figure 8. Noise before cleaning (left) and after (right)

The conclusion has been made that Kapton® glue on the track is the root cause of the deviation we found. Such contamination can generate noise and resistance test deviations.

The new rotor technology implemented in the 2.5D slip ring has demonstrated its performance in terms of:

- Insulation properties
- Resistance properties
- Mechanical properties
- Thermal behavior
- Wear (GEO and LEO applications)

In addition, this design has demonstrated its robustness with regards to the current capacity, by working without any damage with a current of 6.2 A on all the power lines during 24 hours at hot temperature.

The same level of performance is achieved with this type of technology compared to the standard one, see Figure 9.

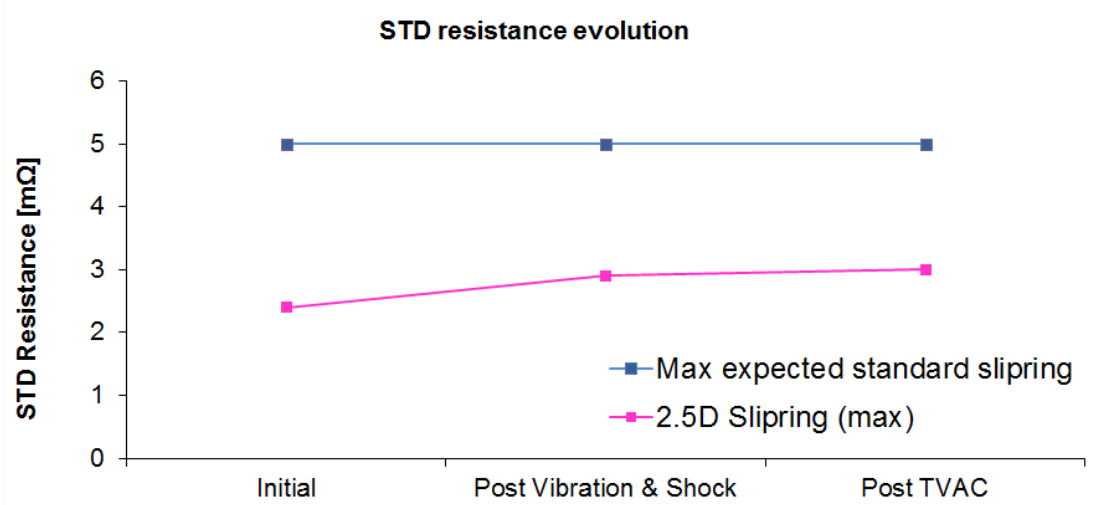


Figure 9. Standard deviation evolution

At the end of the validation test campaign, a tear down was performed on two units: SN001 that performed the GEO life test, and SN004 that performed the LEO life test (Fig. 10). The tear down confirmed that the wear present in the slip ring is nominal and that there is still enough gold on the track after the GEO and LEO life test.

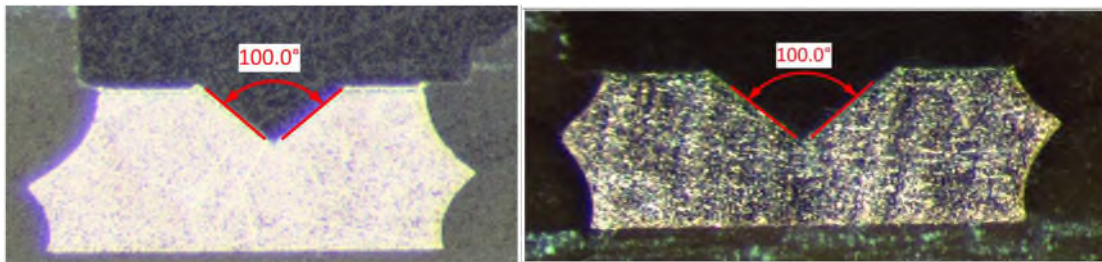


Figure 10. GEO life test (left), LEO life test (right)

In addition, the wear on the wire brushes is as usual and the wire brush preload verification has demonstrated that 99% of the wire brushes were in the expected range of preload at the end of the life test.

Conclusion

In conclusion, the 2.5D technology can be used to replace the standard costly and risky concept.

The perspective for further technical evolution is quite large. A great benefit with this kind of design is the modularity. The number of tracks, the electrical configuration, as well as the number of wire brushes can be modified to be in line with the customer specification.

Today, there are two technical limitations of this system:

- The stacking of only two modules
- The thermal aspect

For the stacking, some change in the design can be foreseen to have the possibility to stack an infinity of modules. The main change will be the output of the wires that shall go out on the external side of the stator, respectively on the internal side of the rotor.

For the thermal aspect, the result of additional tests has demonstrated that the system can survive additional current and power, but in a limited range. The temperature at a soldering location is only 10°C under the allowable temperature. This margin shall be kept for other applications.

From a commercial perspective, the 2.5D PCB technology activity is fully in-line with the development of new SADM and instrument applications and provides a competitive and technological advantage to our company. The optimization with an industrialization process is an undisputable advantage against other space slip ring manufacturers worldwide.

This innovative technology will not only improve the product reliability, the performance and the repeatability, but will also drastically decrease the procurement lead time. Indeed, with today's technology several uncompressible processes are needed leading to a final delivery time of twelve months for the two first modules. With the 2.5D PCB technology, the lead time will be reduced by at least a factor of two.

Furthermore, the competitiveness at a SADM level being more and more difficult worldwide, the cost of a slip ring is becoming one of the drivers in the SADM price. With the new 2.5D PCB technology, the final price of the product would be also reduced.

Finally, an important lesson learned was Kapton® tape with Kapton® glue shall not be used during the manufacturing, assembly, integration and test of a slip ring.

Quantifying Threaded Fastener Locking

Daniel P. Hess* and Christopher DellaCorte**

Abstract

A mechanism for loosening of threaded fasteners is explained and defined in terms of the self-loosening moment inherent to threaded fasteners and an external load induced loosening moment. Equations for these loosening moments are defined. The locking moment needed to prevent loosening due to the self-loosening moment and an external load loosening moment in threaded fastener joints is quantified. This together with secondary locking moment data provide a basis for specifying secondary locking in threaded fasteners to prevent loosening. An example is presented for an aerospace fastener.

Introduction and Background

Assembly of a bolted joint generally involves application of a tightening torque to threaded fasteners with resulting relative angular motion and stretch defined by the thread helix. After assembly, this stretch and associated potential energy is often held by the inherent friction at the thread and bearing interfaces. This friction is the primary locking mechanism or feature in preloaded threaded fasteners and is proportional to preload.

In many cases, a secondary locking feature is added to a threaded fastener [1]. These include mechanical locking (e.g., cotter pin or safety wire), prevailing torque locking (e.g., deformed thread or polymer patch), adhesive locking (e.g., anaerobic adhesive), and free spinning locking (e.g., serrated bearing surface or lock washer).

Use of a secondary locking feature may be required as in some aerospace applications [2] to provide redundancy and to counter possible loosening and failure in the event of unexpected loads. Often it is added to correct an observed or documented fastener loosening problem. In cases of fasteners without preload, it provides the only form of locking in fasteners.

Despite the widespread availability and use of secondary locking features, very little quantitative design guidelines exist. This paper aims to quantify locking and to help answer the question “What moment does a secondary locking feature need to provide to prevent loosening?”

Self-Loosening Moment

Threaded fasteners exhibit an inherent self-loosening moment. This self-loosening moment is evident from the torque equation for a bolted joint. The tightening torque for a threaded fastener in a bolted joint is generally [3-5] defined as shown in Eq. 1.

$$T_t = F_p \left(\frac{P}{2\pi} + \frac{\mu_t r_t}{\cos \beta} + \mu_n r_n \right) \quad (1)$$

Here T_t is the tightening torque, F_p is the preload, P is the thread pitch, μ_t is the thread interface friction coefficient, r_t is the nominal thread interface radius, μ_n is the nut interface friction coefficient, and r_n is the

* University of South Florida, Tampa, FL

** NASA Glenn Research Center, Cleveland, OH

nominal nut interface radius. The first term in Eq. 1 is the torque required to stretch the bolt and the remaining two terms are the torque required to overcome thread and nut friction.

The removal torque is shown in Eq. 2.

$$T_r = F_p \left(-\frac{p}{2\pi} + \frac{\mu_t r_t}{\cos \beta} + \mu_n r_n \right) \quad (2)$$

This removal torque is the torque required to overcome thread and nut friction minus the torque from bolt stretch. This negative term (Eq. 3) defines the self-loosening moment.

$$M_{self-l} = \frac{F_p p}{2\pi} \quad (3)$$

This results from the bolt stretch torque and associated potential energy in the bolt. It is inherent to the threaded fastener and is proportional to preload and thread pitch.

Loosening Moment from External Loads

In addition to the inherent self-loosening moment in fasteners due to bolt stretch, external loads introduce loosening moments. An external transverse load on a bolted joint is illustrated in Figure 1.

Since threaded fasteners are made with lateral clearance for assembly, the nut can be moved sideways by an amount equal to this lateral clearance. Consider the cross section of a bolted joint as shown in Figure 1 with a force applied to the front of the nut. Since the right side will move with greater difficulty, it acts as a pivot point about which the nut slips and turns loose. When a force is applied to the back of the nut as shown in Figure 2, the left side becomes the pivot point about which the nut slips and rotates loose. The net effect of a dynamic or cyclic transverse force is a ratcheting loosening motion, and the amount of slip and resulting loosening increases with lateral thread clearance.

Taking the pivot points on the thread pitch diameter and the external transverse load applied at the center of the fastener, the moment arm is the thread pitch radius r_t and the loosening moment from front and back external transverse loads is shown in Eq. 4.

$$M_{ext-l} = F_{front} r_t = F_{back} r_t \quad (4)$$

Similar loosening moments can result from other external loads such as axial loads, bending loads, and combined loads.

Primary locking

The friction terms in the tightening and removal torque (Equations (1) and (2)) define the primary locking moment in a bolted joint as shown in Eq. 5.

$$M_{primary \ locking} = F_p \left(\frac{\mu_t r_t}{\cos \beta} + \mu_n r_n \right) \quad (5)$$

This primary locking moment is dependent on preload and friction. Unfortunately, if sustained cyclic slip occurs in a bolted joint, this primary locking moment is ineffective and locking must be provided by a secondary locking feature.

Secondary Locking Moment

In a joint subjected to only an external transverse load, the total loosening moment is shown in Eq. 6.

$$M_l = M_{self-l} + M_{ext-l} = \frac{F_p P}{2\pi} + F_{ext-trans} r_t \quad (6)$$

In cases with sustained cyclic slip where thread and nut friction are ineffective, this total loosening moment from combined self-loosening moment and external load loosening moment defines the needed locking moment from a secondary locking feature. Specifically, the needed secondary locking feature locking moment is shown in Eq. 7.

$$M_{locking} \geq M_l = M_{self-l} + M_{ext-l} \quad (7)$$

Prevailing Torque Locking

The tightening torque equation with secondary locking prevailing torque feature added is shown in Eq. 8.

$$T_t = F_p \left(\frac{P}{2\pi} + \frac{\mu_t r_t}{\cos \beta} + \mu_n r_n \right) + T_{pv} \quad (8)$$

Here T_{pv} is the prevailing torque. It is independent of preload F_p .

The removal torque equation with secondary locking prevailing torque feature added is shown in Eq. 9.

$$T_r = F_p \left(-\frac{P}{2\pi} + \frac{\mu_t r_t}{\cos \beta} + \mu_n r_n \right) + T_{pv} \quad (9)$$

Even without friction and preload, a locking moment equal to the prevailing torque T_{pv} remains. Prevailing torque locking features provide locking even with complete loss of preload. As a result, prevailing torque locking is often used in applications where complete disassembly and loss of components must not occur.

Well-defined standards exist for fasteners with prevailing torque locking [6-11]. These provide allowable minimum and maximum prevailing torque for a given thread size.

Secondary Locking Measurement

The locking moment provided by a secondary locking feature can be measured with a torque wrench or sensor on test specimens or actual hardware. This measurement should be taken as a separate test with the fastener in a state of zero preload. This is routinely performed in practice for prevailing torque locknuts, but can also be performed for adhesives, safety lock wire, cotter pins in castle nuts, and other secondary locking features.

Aerospace Fastener Example

As an example, consider an NAS1004 0.25-28 UNJF (approx. M6x1) thread fastener in a joint with a 2400-lb (10.7-kN) preload. The thread pitch is 1/28 inch. The self-loosening moment is shown in Eq. 10.

$$M_{self-l} = \frac{F_p P}{2\pi} = \frac{2,400}{2\pi(28)} = 13.6 \text{ in-lb (1.54 N-m)} \quad (10)$$

For a 0.25-28 UNJF thread fastener, the prevailing torque locking standards [6-11] list an allowable 3.5 in-lb (0.40 N-m) minimum and 30 in-lb (3.4 N-m) maximum prevailing torque. Since the self-loosening moment for the thread is 13.6 in-lb (1.54 N-m), meeting the minimum 3.5 in-lb (0.40 N-m) is not enough to counter the self-loosening moment.

If a prevailing torque locking feature is used with a measured prevailing torque of 20 in-lb (2.3 N-m), then the locking moment is 20 in-lb (2.3 N-m) which is in excess the self-loosening moment.

Data [12] exists from dynamic transverse load tests with NAS1004 0.25-28 UNJF threaded fasteners. Minimum and maximum pitch diameter are 0.2243 (5.697 mm) and 0.2268 inch (5.761 mm) for an average of 0.2256 inch (5.730 mm). The dynamic transverse force is 200 lb (890 N) and the preload is 2400 lb (10.7 kN). Therefore, the loosening moment from this external transverse load is shown in Eq. 11.

$$M_{ext-l} = F_{front} r_t = F_{back} r = (200)(0.1128) = 22.6 \text{ in-lb (2.55 N-m)} \quad (11)$$

This 200-lb (890-N) external transverse force is the amount that acts on the fastener. The dynamic transverse test machine [12] used is designed with bearings between the clamped components of the joint. This intentionally puts the applied external transverse force on the fastener which makes the test severe. In practice with a typical joint, additional friction between the clamped components of the joint would counter the external transverse load. This joint friction force would need to be subtracted from the external load to determine the transverse force on the fastener that is used in the previous equation. An estimate of this joint friction force is the product of clamping force and coefficient of friction at the joint interface.

At a preload of 2400 lb (10.7 kN), the test fasteners were subjected to a dynamic external transverse load of 200 lb (890 N), and a total loosening moment shown in Eq. 12.

$$M_l = M_{self-l} + M_{ext-l} = 13.6 + 22.6 = 36.2 \text{ in-lb (4.09 N-m)} \quad (12)$$

A set of tests [13] for a variety of secondary locking features provide measured locking moment data for 0.25-28 UNJF (similar to M6) thread fasteners. Specifically, the following locking moment data was obtained: 16-23 in-lb (1.8-2.6 N-m) for metal and nonmetal prevailing torque locknuts, 15-18 in-lb (1.7-2.0 N-m) for medium strength Loctite, 55-65 in-lb (6.2-7.3 N-m) for high strength Loctite, 50-60 in-lb (5.6-6.8 N-m) for cotter pins with castle nuts, and 36-42 in-lb (4.0-4.7 N-m) for 0.032-inch (0.813-mm) Inconel safety lock wire through bolt heads. This data indicates only high-strength Loctite, cotter pins, and safety lock wire provide sufficient locking to overcome the loosening moment due to combined self-loosening and the severe external transverse loading. However, in the absence of the external load, all of the locking features tested provide locking moments in excess of the self-loosening moment.

Conclusions

This paper provides some guidance for specifying secondary locking features in threaded fasteners to provide sufficient locking and prevent loosening.

A mechanism for loosening of threaded fasteners is provided and defined in terms of a self-loosening moment inherent to threaded fasteners and an external load loosening moment.

Equations for loosening moments are defined. Secondary locking feature moments are quantified in terms of these loosening moments.

An example is provided. Some sample data for measured locking moments is given for one thread size.

References

1. Hess, D, "Threaded fastener secondary locking requirements," *Journal of Failure Analysis and Prevention Joints* 17 (2017) 724-730.
2. NASA-STD-5020, Requirements for threaded fastening systems in spaceflight hardware, 2012.
3. Bickford, J, *An Introduction to the Design and Behavior of Bolted Joints*, CRC Press (1995) 140-142.
4. VDI 2230, *Systematic Calculation of High Duty Bolted Joints – Joints with One Cylindrical Bolt*, Verein Deutscher Ingenieure, 2003.
5. Oberg, E, Jones, F, Horton, H, Ryffel, H, *Machinery's Handbook 25th Edition*, Industrial Press, 1996.
6. NASM25027, Nut, self-locking, 250°F, 450°F and 800°F, National Aerospace Standard, 1999.
7. NASM8846, Inserts, screw-thread, helical coil, National Aerospace Standard, 1998.
8. MIL-I-45914A, Insert, screw thread – locked in, key locked, Department of Defense Military Specification, 1991.
9. MIL-I-45932/1C, Insert, screw thread – thin wall, locked in, Department of Defense Military Specification, 1994.
10. NAS3350, Nuts, self-locking, 450°F and 800°F, high quality, National Aerospace Standard, 2006.
11. MIL-DTL-18240F, Fastener element, self-locking, threaded fastener - 250°F maximum, Department of Defense Detail Specification, 1997.
12. Cheatham, C, Acosta, C, Hess, D, "Tests and analysis of secondary locking features in threaded inserts," *Engineering Failure Analysis* 16 (2009) 39-57.
13. Hess, D, "Secondary locking feature locking moment measurements," to appear.

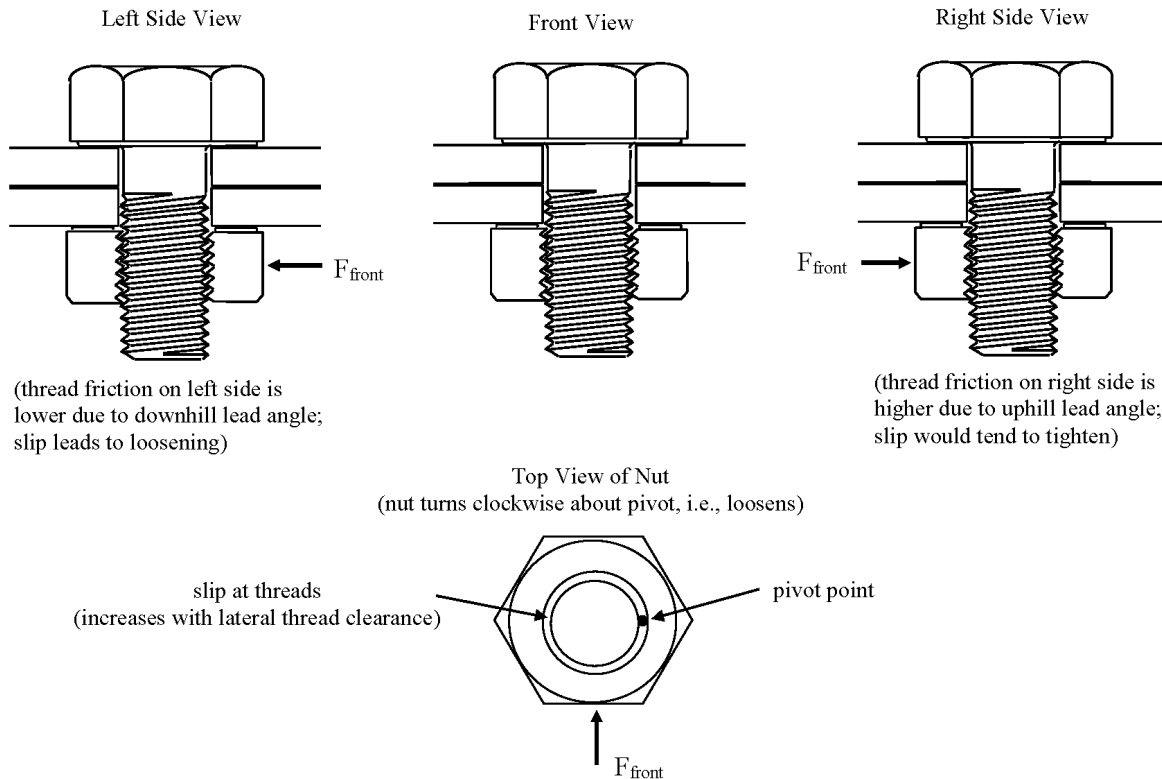


Figure 1. Bolted joint with force applied to nut from front.

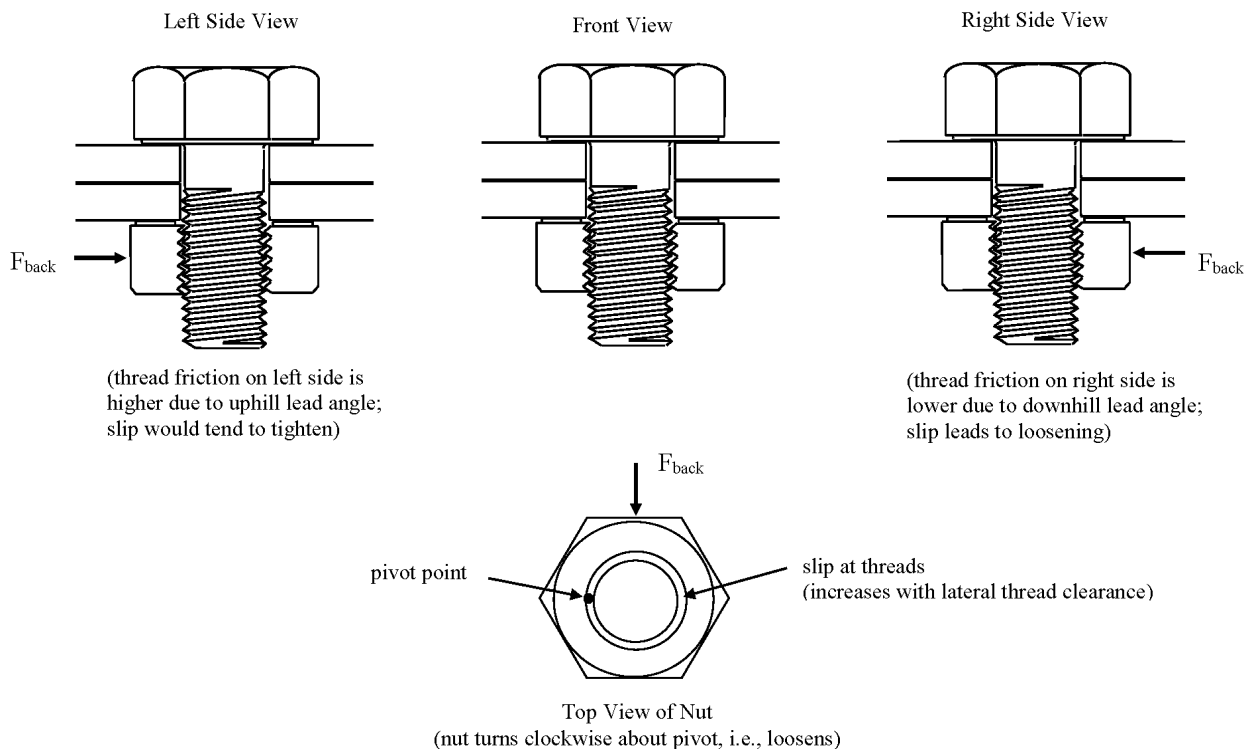


Figure 2. Bolted joint with force applied to nut from back.

Reliability Calculation Methodologies for Mechanisms and Actuators

Tanner Horne* and Evan Harrington*

Abstract

MIL-HDBK-217 and similar reliability calculation methodologies inadequately assess the reliability of complex electro-mechanical components and mechanisms. This paper utilizes accepted reliability methodology techniques to achieve realistic and technically justifiable approaches for MTBF and reliability ratings. Additionally, this paper will address the historically overlooked effects of radiation on the accelerated degradation of insulation systems, such as those used in motors and other wound components.

Introduction

The challenging overall system requirements for aerospace mechanisms and gearboxes have led to several innovative and unique solutions for the application. One of the most demanding of system requirements is the reliability and number of steps. Even when the load friction is minimal, there is considerable transmitted torque through the gearbox to accelerate the load inertia. We will assess the methodologies used in determination of transmitted torques, as well as several other key requirements.

Analysis of Transmitted Torques

Calculation of Load Acceleration Torques

An often-overlooked implication of high torque margin in driving inertial loads is the acceleration torques at each step of the stepper motor. These torque pulses can be significant and must be considered in the mechanical structural and life analysis. For an example application, assume the load inertia is coupled directly to the output shaft, supported by a separate bearing system. Also, assuming the load friction is extremely low, and the driven load inertia is relatively high, each step of the stepper motor will accelerate the load and this will translate a reaction torque throughout the actuator. If the motor current is limited to maintain a maximum holding output torque this translates to a torque at low pulse rate (T_{PPS-0}) of at the motor. Using the torque at low pulse rate for these calculations will provide the *mean acceleration* and torque during each step. The Peak Torque and acceleration will be 41% higher than the mean calculated values.

For applications that do not implement current limiting, nominal and maximum motor torque calculations should be analyzed. That is, nominal voltage, resistance and temperature for the nominal case, and minimum temperature and resistance as well as maximum torque constant and voltage for the maximum case. The engineer needs to make sure that they have structural and endurance margin at maximum conditions, but it is also of value to assess the nominal conditions to gage how conservative the analysis is. Since torque margin requirements are calculated at the minimum conditional values, the maximum conditions may result in surprising results.

The mean acceleration at the load (α_L) is calculated in Eq. 1. The mathematical proof of this equation is available by contacting the authors.

$$\alpha_L = \frac{(T_{PPS-0} - F_M)(N \cdot \eta_G) - F_L}{J_L + (J_M \cdot N^2 \cdot \eta_G)} \quad (1)$$

* Avior Control Technologies, Inc, Longmont CO

where (Application Values)

- α_L = Mean Acceleration of the Load
- T_{PPS-0} = Torque at Low Pulse Rate at Motor
- F_M = Detent Plus Friction at the Motor
- N = Gear Ratio
- F_L = Load Friction
- J_L = Load Inertia
- J_M = Motor Rotor Inertia
- η_G = Gearbox Efficiency

The Torque to Accelerate the Load ($T_{\alpha L}$) is calculated by Eq. 2:

$$T_{\alpha L} = J_L \cdot \alpha_L \quad (2)$$

This torque is actually transmitted through the gearbox at every pulse of the system. As a note, since the gearbox efficiency attenuates the acceleration at the output, it is most conservative to use 100% gearbox efficiency.

Calculation of Loaded Time and Mean Loaded Velocity

Now that we have determined the peak-transmitted torque to the load, we must determine the *time* the unit is under load. Stepper motors do not transmit torque between step pulses when the shaft is settled. As long as the inertia factor is reasonable (under 3.0) the overshoot and stabilization torque are also insignificant. Therefore, we are primarily interested in the *time* it takes to accelerate the load at each pulse ($t_{\alpha L}$). Which is estimated in Eq. 3.

$$t_{\alpha L} = \sqrt{\frac{2 \cdot \Delta \Theta_L}{\alpha_L}} + \tau_e \quad (3)$$

where (Application Values)

- $t_{\alpha L}$ = Time to Accelerate Load
- $\Delta \Theta_L$ = Step Size at Load
- α_L = Acceleration at Load
- τ_e = Motor Electrical Time Constant

This results in a time to accelerate the load at each pulse of in a period of seconds. Given the life requirement of a number of steps a Loaded-Lifetime requirement of can be calculated. There are several offsetting secondary and tertiary components that affect the actual load characteristics and step kinematics, however, this analysis is considered conservative and appropriate. System drive electronics, internal damping characteristics as well as backlash will have minor effects on the step kinematics. These system variables can be difficult to predict or quantify, and their affects are much less significant compared to the primary variables defined in Eqs. 1-3.

Now that the torque and time components are established, we must determine the mean velocity when the mechanical energy is transferred. This calculation is presented in Eq. 4.

$$\omega_{L_Loaded} = \frac{\Delta \Theta_L}{t_{\alpha L}} \quad (4)$$

where (Application Values)

- ω_{L_Loaded} = Mean Loaded Velocity

This analysis results in a Mean Loaded Velocity in Radians per second. The analyzed load acceleration torques ($T_{\alpha L}$), Mean Loaded Velocities, and Loaded Lifetime must be used in the gearbox and bearing

endurance and analysis. The most important factor that we are communicating here is that *the torque and velocity that is transmitted through stepper motor actuators are typically significantly higher than the load friction and step-rate velocity requirements. Increasing torque motorization margin will necessarily increase the torque transmitted through the gearbox, regardless of the magnitude of the load frictional components.*

Another key take-away, the Loaded Lifetime can be orders of magnitude less than the operational time, since stepper motor actuators are not transmitting torque during idle and settled times between steps. Additionally, if you run through the numbers, you will see that lower gear ratios will reduce T_{aL} at the actuator output. Doing this will increase your inertia factor and increase the probability of unstable step performance, as described in Ref. [1].

Reliability Analysis

There are many statistical approaches to calculate the failure rates of components and systems. Many of which do not adequately assess the failure rates of electro-mechanical systems such as a mechanical. It is also impractical to manufacture a statistically significant number of units to determine failure rates and probabilities. The authors believe the approach presented herein is much more appropriate and statistically valid for mechanisms and components manufactured for the space industry.

Reliability Block Diagram

The example in Fig. 1 breaks down the components of an actuator in a Reliability Block Diagram. The motor may be driven through either the primary or redundant motor winding. Single-string gearbox components are typical for the industry, as differential gearing adds significant cost, mass and complexity. The output position may be measured by either the primary or redundant sensor windings. Reliability Block Diagrams may seem trivial, but it provides a graphic representation of the system configuration and aides in the determination of potential failure modes and their effects. Also of note in the example that the mechanism is still functional even with the loss of both resolvers. Step counting or optical performance data may be used to determine load position.

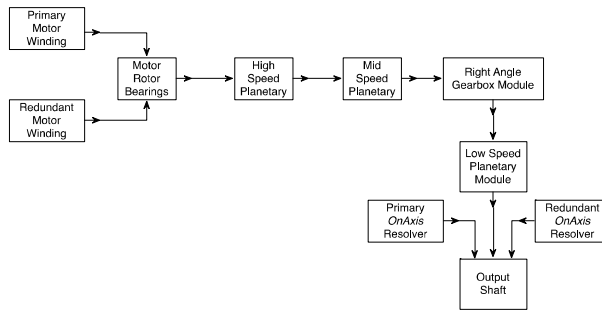


Figure 1. Reliability Block Diagram

Reliability Analysis of Each Component

The methodologies of the reliability of the components are presented in the 3.3.1 of this paper. The detail summaries are shown in Appendix A herein. This methodology uses a combination of estimated L_2 life analysis, combined with classical Weibull reliability statistical analysis. We must first determine the L_2 of the Mechanical and Electrical components of the actuator. Note: Avior uses L_2 for most space flight hardware analysis, although mathematically, you will achieve the similar reliability figures for Characteristic Life and MTBF if you use L_{10} values.

Gears and Bearings

Structural bending fatigue analysis is conducted on all gears, per AGMA 2001. The analysis is conducted to determine how many cycles and hours of operation at the mean torque and velocities described in section 3 herein may be achieved. We calculate the L_2 life each of the mechanical gearing elements in the gearbox,

using the AGMA equations. This calculated value tabulated in the Appendix A table. The authors conservatively use one million hours of L_2 life for each module if the calculated value is greater than one million hours.

Bearings are similarly calculated for a factored L_2 life using classical tools and software. In the right-angle gearbox, the bearings see thrust, tangential, and radial loads due to the bevel gear mesh. If there are pure-torque modules in the actuator, conservative estimates of radial loads are provided, due to imperfect gear meshing and load sharing in the planetary gearboxes. Typically, 10 to 50 Newtons of radial force at the extreme of the gear mesh is assumed for the supporting bearing loads. Planet gear bearings see radial loads through the transmitted torque at each stage of gearing.

Brancato Method of Motor Winding Life

Winding life estimates are analyzed using methods described in the Brancato Method, Ref. [3]. Avior's Class H220 Insulation system is rated at 20,000 hours minimum regression life at +220° C. The Percentage of Life at a conservatively estimated Hot Spot Temperature of +120° C is as follows:

$$L_w = 100 \cdot 2^{\frac{T_R - T_{HS_M}}{10}} \quad (5)$$

where

- L_w = Percentage of Life (To Be Calculated)
- T_R = Rated Insulation System (+220° C)
- T_{HS_M} = Motor Winding Hot-Spot Temperature (+120° C)

This equates to a lifetime of **102,400 percent greater** than a typical minimum regression rating of 20,000 hours. This translates to 2.05 E+07 Hours of life for the winding insulation system. In this application, Avior generally uses an attenuation factor of for motor and sensor windings used in Geosynchronous and Deep-Space (high radiation) applications. In the next section, we will introduce a more appropriate de-rating strategy. When exposed to gamma ray and ultraviolet radiation, there are insulation aging degradations that are similar in effects to thermal radiation aging. Due to ultraviolet radiation having low penetration it can be neglected. The following section introduces alternate methods for dealing with the effect of ionizing radiation aging of electrical components.

Radiation De-rating of Winding Assemblies

As denoted above, and for the purpose of derating, it is assumed that geosynchronous radiation similarly degrades electrical components as thermal radiation. Two methods based on similar principles were developed to handle the effects of ionizing radiation aging. The first method (ψ) accounts for both the amount of radiation absorbed and the rate at which the radiation is absorbed. The second (γ) incorporates the amount of radiation absorbed.

The first method is to calculate an effective temperature from the incident radiation and ambient temperature, with the components approximated as a black body. Thermal radiation is taken into account with T_a .

$$T_{eff} = \sqrt[4]{T_a^4 + \psi * \zeta} \quad (6)$$

where

- T_a = ambient or operating temperature (K)
- ζ = incident space radiation / σ_B (space radiation is about 7 W/m²)
- σ_B = Stefan-Boltzmann constant 5.67E-08
- ψ = Harrington Psi Life Function (proposed), de-rates electrical and insulation components

$$\psi(\delta) = a * \delta^b \quad (7)$$

where

- δ = Total ionizing dose of space radiation during the mission (rad)
- a = proposed constant, for Teflon insulation applications, $a = 1.176$

- b = proposed constant, for Teflon insulation applications, $b = 0.144$

The constant in Eq. 7 arises from the success of the chosen insulation system. The equation is used to add an additional margin of safety to the degradation of electrical components. Introducing ε the exposure ratio,

$$\varepsilon = \frac{L_o}{L_M} \quad (8)$$

where

- L_o = Electrical Operating Time in Hours
- L_M = Mission Life in Hours

Finally, combining the results into the Brancato Method:

$$L_w = 100 * (\varepsilon * 2^{\frac{T_R - T_{effo}}{10}} 10 + (1 - \varepsilon) * 2^{\frac{T_R - T_{effi}}{10}}) \quad (9)$$

where

- L_w and T_R can be found following Eqn. 5

One alternative to energy methods for calculating insulation life due to radiation is to assume that the insulation follows the reliability equation. Instead, we propose time be replaced with total ionizing dose (rads)

$$R = e^{-\left(\frac{\delta}{\eta}\right)^{1.2}} \quad (10)$$

where

- δ = Total ionizing dose of space radiation during the mission (rad), assumed to be 10000 rads for 5-year mission at geosynchronous orbit
- $\eta = 4.25E7$ rads, proposed constant for insulation reliability, see appendix C

Reliability Analysis Toolkit

Using the on-line tools of the Reliability Analysis Toolkit, Ref. [2], we are able to predict the reliability failure rate of an actuator. The methods used in this approach are derived from the NSWC Handbook of Reliability Prediction Procedures for Mechanical Equipment. The online tools, using the equations described in 3.3.2 applicable Weibull distribution functions for different components.

Reliability Equations

Using the L_2 to MTBF Conversion, the equations represent a three-parameter Weibull distribution, with δ shown in the equations; however, for purposes of this tool this parameter (sometimes called "failure free life") is assumed to be zero, and eliminated from these equations. Note, the variables and symbols used in this section are consistent with those used in Ref. [2].

$$\text{Reliability Function } R(t): \quad R(t) = e^{-\left(\frac{t}{\eta}\right)^\beta} \quad (11)$$

$$\text{Probability Density Function } f(t): \quad f(t) = \frac{\beta(t)^\beta - 1}{\eta^\beta} e^{-\left(\frac{t}{\eta}\right)^\beta} \quad (12)$$

Probability Density Function $f(t)$:

$$\text{h(t), instantaneous failure rate:} \quad h(t) = \frac{f(t)}{R(t)} \quad (13)$$

The average failure rate is calculated using the Eq. 14:

$$\lambda_{Average} = \frac{1 - R(T)}{\int_0^T R(t) dt} \quad (14)$$

System Input Parameters:

1. Shape parameter (β): Weibull shape “Beta” factors. From Ref. [2]. Usages of Typical or High-End factors are provided. A Beta factor of 1.2 is used for windings, 1.3 for Ball Bearings and 2.0 for Gearboxes. Higher complexity assemblies utilize higher β factors.

2. Characteristic Life (η) is the 63.2% failure point for a mechanical system. The Characteristic Life is determined by the L_2 life and the β factor. For instance, for a β of 1.3, as for a bearing, the Characteristic Life is about 20x the L_2 life. For a β factor of 2.0, the multiplication factor is about 7x the L_2 life. η can be calculated exactly by using Eq. 15.

$$\eta = L_n \left(-\ln \left(1 - \frac{n}{100} \right) \right)^{-1/\beta} \quad (15)$$

3. Maintenance interval for item renewal (T): No maintenance of this product is required or assumed. A value of 100 years is used in the on-line tool equations.

MTBF with the Reliability Toolkit

The on-line Reliability Toolkit was used to generate a MTBF, from the β function and the L_2 predicted life. The same equations used in the on-line tool are available in this paper. The lifetime estimations of the bearings and gears are based on conservative de-ratings of fatigue and wear-out considerations, with margin, the failure rate of these estimations will be proportional to the required life over the predicted life. This method has been used in reliability analysis presented to, and accepted by many other programs and subject matter experts in the industry. The justification for this analysis methodology is the additional manufacturing precision, workmanship testing and quality inspections that take place for space flight hardware to eliminate infant mortality and other workmanship issues that affect commercial hardware.

MTBF can be calculated using Eq. 16

$$MTBF = \frac{\frac{\eta}{\beta} \gamma\left(\frac{1}{\beta}, \frac{T}{\eta}\right)}{1 - e^{-\left(\frac{T}{\eta}\right)^{\beta}}} \quad (16)$$

where, $\gamma(a,x)$ is the lower incomplete gamma function.

Equation 11 can be ‘altered’ by setting $MTBF = T$. By doing so, a ‘Maintenance Free’ interval is achieved i.e. the part on average would fail at the maintenance interval. The equation reduces to $\eta/\beta * \Gamma(1/\beta)$ for ‘No Maintenance’. See Appendix C for the method and code.

Redundancy Factor for Windings

Since there is selectable redundancy for the motor and resolver windings, we may use the Redundancy Factor described in the Reliability Toolkit. We use the Effective Failure Rate on One Standby Offline Unit with One Active On-line Unit Required for Success (without repair), See Eq. 20.

Reliability Number

We essentially have two separate life analyses to consider, the mechanical reliability and the electrical reliability. The windings and the electrical insulation system are exposed to radiation the entire time in orbit, so regardless of powered-on time we assume the time on orbit degrades the insulation system. For a five-year orbital mission for a high-radiation, geosynchronous application, we have an electrical life requirement

(t_E) of 44,000 hours of operation and $2E+04$ Rads Total Ionizing Dose (TID) of radiation during mission life. Refer to Appendix A for a table of analysis parameters.

To calculate the Mechanical Reliability for the operational profile from the MTBF, Eq. 17 is used.

$$R_{tM} = e^{\left[\frac{-t_M}{MTBF_M} \right]} \quad (17)$$

where

- R_{tM} = Mechanical Reliability
- t_M = Time of loaded operation (Hours)
- $MTBF_M$ = Mechanical Mean Time Between Failures ($1.20E+05$)

This results in an $R_{tM} = 0.99736$

Similarly, the Electrical Reliability is calculated by:

$$R_{tE} = e^{\left[\frac{-t_E}{MTBF_E} \right]} \quad (18)$$

where

- R_{tE} = Electrical Reliability
- t_E = Time of exposure, in Hours (44,000)
- $MTBF_E$ = Electrical Mean Time Between Failures using ($8.95E+12$) calculated using γ de-rated Averaged Brancato method.

Which results in an $R_{tE} = 0.99999$

The insulation reliability is calculated in equation (19)

$$R_i = e^{\left[\frac{-\delta}{MTBF} \right]} \quad (19)$$

where

- R_{tM} = Insulation Reliability
- δ = Total Ionizing Dose (10000 rads)
- $MTBF$ = Insulation Mean Time Between Failures ($4E+7$)

Which results in an $R_i = .99975$.

And the overall reliability (R_o) is calculated by:

$$R_o = R_M \cdot R_E \cdot R_i \quad (20)$$

Therefore, the overall reliability $R_o = 0.99701$ is achieved.

The MTBF for n redundant units, 1 spare with no repair interval:

$$MTBF_R = MTBF * n * (P + 1) \quad (21)$$

where

- n = number of active units
- P the probability that the spare will work

The probability of the spare working can be treated as that units' reliability. Using these equations for both cases of the electrical components results in $R_o = .99736$ for the ψ factored electrical decay. See Appendices A and B for more information on reliability values. If we needed to increase the resultant overall reliability, we would address the two lowest MTBF components. In this case, the Mid-Speed Carrier

Bearings that see the radial and thrust loads from the bevel mesh and the low-speed planetary module are the reliability-driving components. Possible methods to increase reliability in these components is to increase the gearbox and bearing size, or possibly change materials to increase the L₂ ratings.

Conclusion

Requirements for torque margin may have structural and endurance implications for transmitted torque through the mechanism that must be considered. Non-current limited applications may also have significant torque consequences at extreme conditions that are often not analysed. The paper also details a methodology for calculating reliability using approved analysis techniques and methodologies. We also introduce two types of analysis for de-rating life estimates for motor insulation systems, due to insulation aging effects due to prolonged exposure to radiation.

References

1. "Primer – Stepper Motor Nomenclature, Definition, Performance and Recommended Test Methods" Starin et al. Proceedings of the 42nd Aerospace Mechanisms Symposium, NASA Goddard Space Flight Center, May 14-16, 2014
2. <http://reliabilityanalyticstoolkit.appspot.com/>
3. "Estimation of Lifetime Expectations of Motors" Emanuel L Brancato, iEEE Electrical Insulation Magazine, May/June 1992-Vol. 8 No.3
4. "Analyze of Reliability of Gears" Dr. N. Ungureanu et al
5. "How to Determine the MTBF of Gearboxes" Dr. Gerhard G. Antony Neugart, Paper for 2007 AGMA FTM
6. NSWC Handbook of Reliability Prediction Procedures for Mechanical Equipment, May 2011.
7. "Nuclear and Space Radiation Effects on Materials", NASA, July 1970.
8. "Design and Development Implication of High Inertia Earth-Science Mechanism Actuator", ESMATS 2017

Appendix A – MTBF and Reliability Table - Mechanical						
A	B	C	D	E	F	G
Subsystem Module or Component	Beta (Weibull Shape Parameter)	L ₂ Life (Hours)	Characteristic Life (Hours)	MTBF (Hours)	Average Failure Rate (Hours)	Reliability
N/A	β	See 5.2	η	Ref. [2]	λ	Eq. 5
Motor Rotor Bearing	1.3	4.50E+05	9.05E+06	9.57E+06	1.05E-07	0.99997
High Speed Planetary Module	2	1.00E+06	7.04E+06	7.79E+06	1.28E-07	0.99996
High Speed Planet Gear Bearings	1.3	1.00E+05	2.01E+06	2.13E+06	4.70E-07	0.99985
High Speed Carrier Bearings	1.3	5.27E+05	1.06E+07	1.12E+07	8.93E-08	0.99997
Mid Speed Planetary Module	2	1.00E+06	7.07E+06	7.79E+06	1.28E-07	0.99996
Mid Speed Planet Gear Bearings	1.3	8.75E+05	1.76E+07	1.86E+07	5.38E-08	0.99998
Mid Speed Carrier Bearing	1.3	2.94E+04	5.91E+06	6.25E+05	1.60E-06	0.99949
Right Angle Bevel Gears	2	1.00E+06	7.04E+06	7.79E+06	1.28E-07	0.99996
Right Angle Carrier Bearing	1.3	3.17E+07	6.38E+08	6.74E+08	1.48E-09	0.99999
Right Angle Support Bearing	1.3	5.40E+06	1.09E+08	1.15E+08	8.71E-09	0.99999
Low Speed Planetary Gearing	2	2.50E+04	1.76E+05	1.95E+05	5.14E-06	0.99837
Low Speed Planet Gear Bearings	1.3	1.03E+05	2.07E+06	2.19E+06	4.57E-07	0.99985
Low Speed Carrier Bearings	1.3	2.34E+06	4.71E+07	4.97E+07	2.01E-08	0.99999
			Total	1.20E+05	8.33E-06	0.99736

Appendix B – MTBF and Reliability Table - Electrical							
A	B	C	D	E	G	H	I
Subsystem Module or Component	Beta (Weibull Shape Parameter)	L ₂ Life (Hours)	Characteristic Life (Hours)	MTBF (Hours)	Reliability	R _o	Redundant R _o
.1 Avior standard* at te=44000	1.2	2048000	5.29E+07	2.76E+07	0.99841	0.99577	0.99656
.1 Averaged Brancato at te=44000	1.2	2.60E+09	2.69E+10	1.40E+10	0.99999	0.99736	0.99736
ψ at te=44000	1.2	1.47E+11	3.80E+12	1.98E+12	0.99999	0.99736	0.99736
γ Averaged Brancato at te=44000	1.2	6.63E+11	1.13E+13	8.95E+12	0.99999	0.99736	0.99736

Calculations of reliability and MTBF include both the On-Axis Resolver and Motor Windings

*The Avior “old” standard is the Brancato L₂ life at 120°C multiplied by .1

The averaged Brancato method can be found in Eq. 9 and in Appendix D

A value of -30°C was used for the cold or non-powered state of electrical components

A value of +120°C was used for the hotspot temperature of electrical components

Appendix C

The following code was written in Anaconda Spyder to calculate η, MTBF, λ, and no maintenance interval (T)

denotes code comment

from scipy.special import gammaincc, gamma

from math import *

from math import exp as e

B = β #beta shape parameter

L2 = L₂ #L₂ life

n = L2*(-log(.98))**(-1/B) #η, characteristic life for L2

le = 5*365*24 #mission life for electrical components (Hours)

lm = 318 #usage life requirement for

T = 50 #initial guess in hours of no maintenance interval

R = e(-(T/n)**B) #reliability function

MTBF = (n/B*gamma(1/B)*gammainc(1/B,(T/n)**B))/(1-R) #see (◊)

err = abs(T-MTBF)/MTBF*100 #percent error

ep = .1 #final percent error

while err>ep: # subroutine solves T for conditions stated after Eq. 11 by simply convergence

 T = MTBF # Iterated map on T

 R = e(-(T/n)**B)

 MTBF = (n/B*gamma(1/B)*gammainc(1/B,(T/n)**B))/(1-R)

 err = abs(T-MTBF)/MTBF*100

print(n,MTBF,1/MTBF,e (-lm/MTBF)) #reports results η, MTBF, λ, and reliability R_o

print(T/365/24,"Years") #no maintenance life in years

◊scipy gammaintc is normalized, so it has to be multiplied by gamma

from scipy.special import gamma

B = β #beta shape parameter

L2 = L₂ #L₂ life

n = L2*(-log(.98))**(-1/B) #η, characteristic life for L2

R = e(-(T/n)**B) #reliability function

MTBF = n/B*gamma(1/B)

Appendix D

Graph of ψ implemented Life decay, implementing Eq. 9

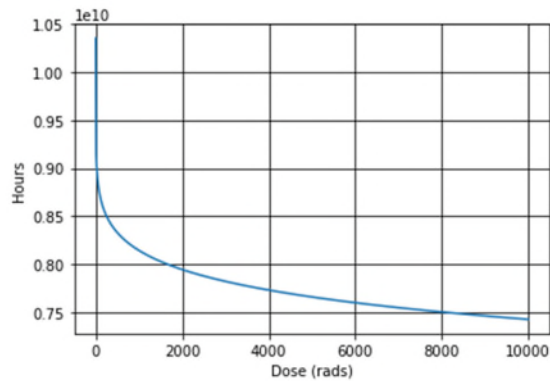
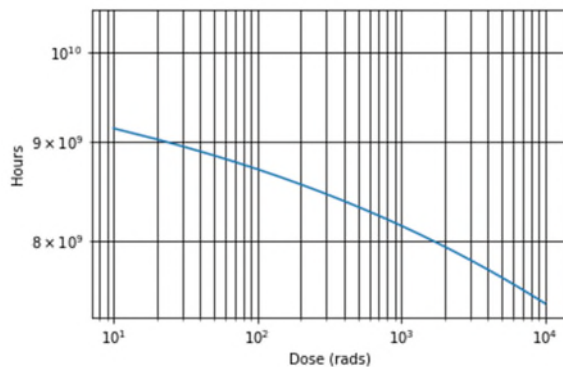
Averaged Broncato Equation (Generalized Equation 9),

$$L_w = 100 * \sum_i \varepsilon_i * 2^{\frac{T_R - T_i}{10}}$$

where

$$\sum_i \varepsilon_i = 1$$

- T_i = some temperature
- ε_i = percent exposure to T



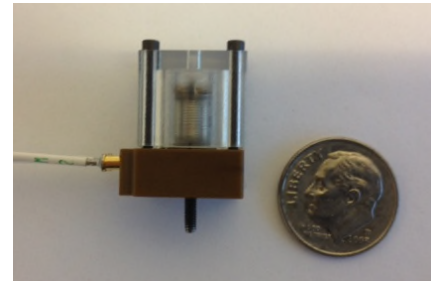
Development of the NEA Mini for Low Load Applications

John Sudick* and Geoff Kaczynski*

Abstract

Small satellites require simple, reliable and low-cost release devices. Nichrome burn wire solutions have been embraced by the Small Satellite community because they require low power, are inexpensive and readily available. Industry feedback gathered over the past 7 years at the Small Satellite Symposium in Logan, Utah, suggests that the failure rate of Nichrome wire is too high and a more reliable solution is needed. Based upon this industry feedback, NEA started working to see if we could adapt our GEO NEA battery bypass switch into a release mechanism for small sat applications.

Looking across our stable of qualified release products, NEA determined that the release mechanism utilized in our battery bypass switches are small, light, low power, low shock, and have high reliability. Our goal for this paper was to perform a series of load and shock output test to determine if the release mechanism in our bypass switch could be modified for used in standard release mechanism applications.



Introduction

The small satellite market has expanded quickly over the last 5 years. With affordable access to space becoming a reality, the need for a 50 - 200 lbf (89 – 890 N) class, low cost, low power, low shock, high reliability release mechanism has become a reality. Customers are now looking for ways to increase their mission success rates without breaking the bank. NEA's goal was to determine if we could leverage the volume of our battery bypass mechanism product line to offer a low cost high reliability release mechanism. The development team's charter stipulated that they had to utilize off-the-shelf common stock parts that are utilized in our bypass switch release mechanism. The stock parts could be modified for the application, but no new parts were allowed. This paper walks through the initial test data and lessons learned during the development of the NEA Mini 9300 release mechanism.

* NEA Electronics Inc., Moorpark, CA

Basic Design

The development of the NEA Mini centered on being able to utilize the common release mechanism from our battery bypass switches. The release mechanism in the bypass switch (Figure 1) is similar in operation to our standard release mechanisms and utilizes the same patented fuse wire technology.

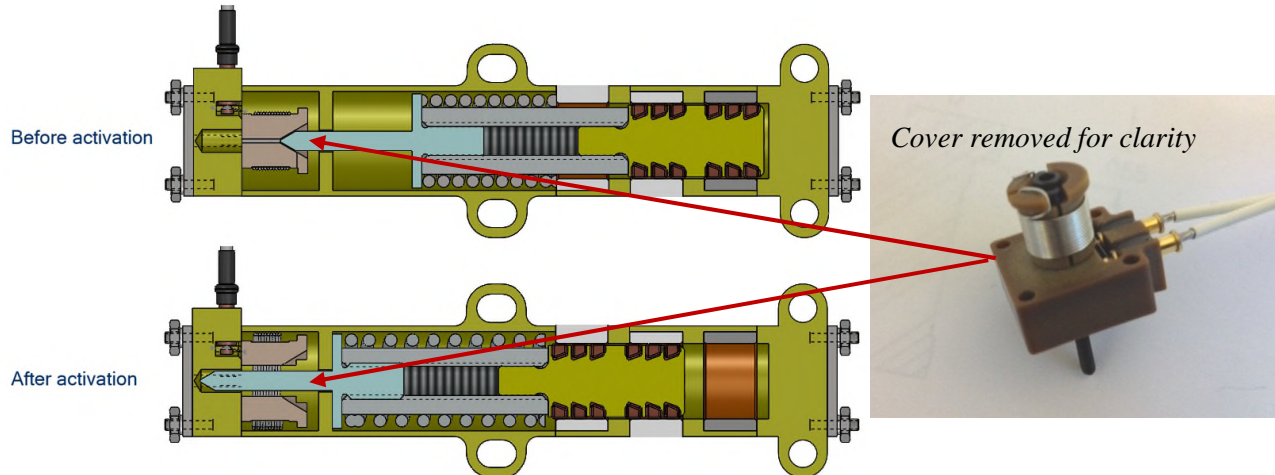


Figure 1. Battery bypass switch

For switch activation, an electrical pulse of 1.2 amps or greater is sent to the mechanism. The fuse wire breaks and releases the restraining wire that holds two spool halves together. A preloaded spring assembly pulls a plunger forward once the spools are released. The shock is minimized by releasing the stored strain energy over a longer period of time. The electrical characteristics for the fuse wire assembly are time and current dependent as shown in Figure 2:

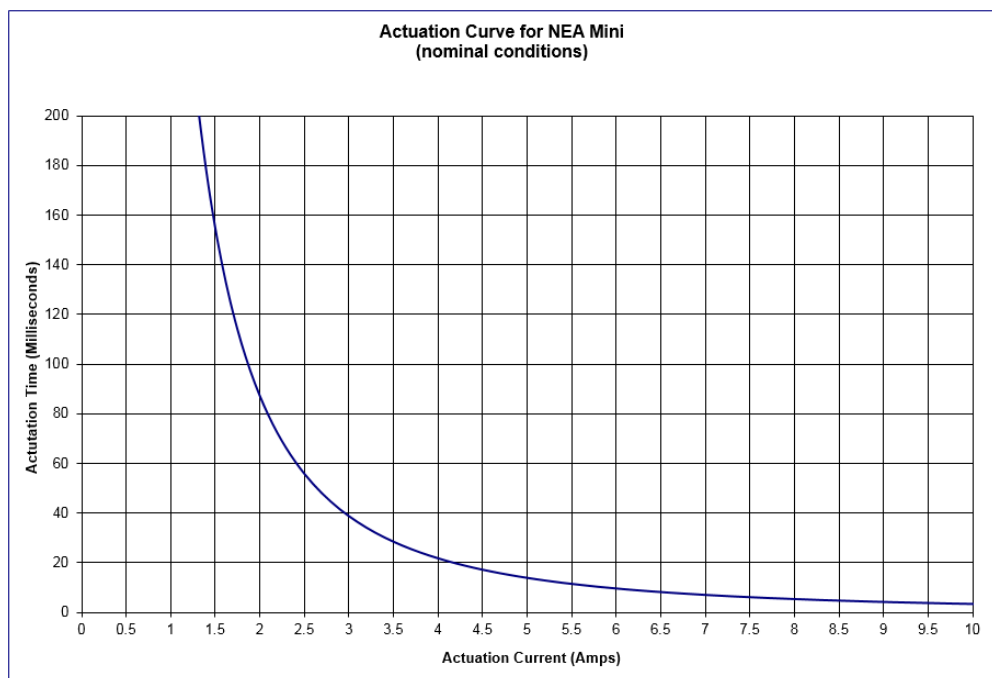


Figure 2. NEA Mechanism Actuation Curve

Based on qualification, NEA's largest bypass switch spring imparts a load of 65 lbf (289 N) on the spools of the release mechanism, so the team knew that the release part of the device could hold at least 65 lbf (289 N) of load. The next questions to be answered were, how high of a load could it handle and what were the limiting factors in the load capability of the mechanism? Was the limiting design factor the Spool Material, Restraining Wire, Fuse Wire, or Release Rod? NEA started by load testing the bypass switch release mechanism to determine its maximum load capability. The team designed tooling to push on spools until the unit failed. The load released at approximately 750 lbf (3300 N) with the restraining wire breaking first (Figure 3).

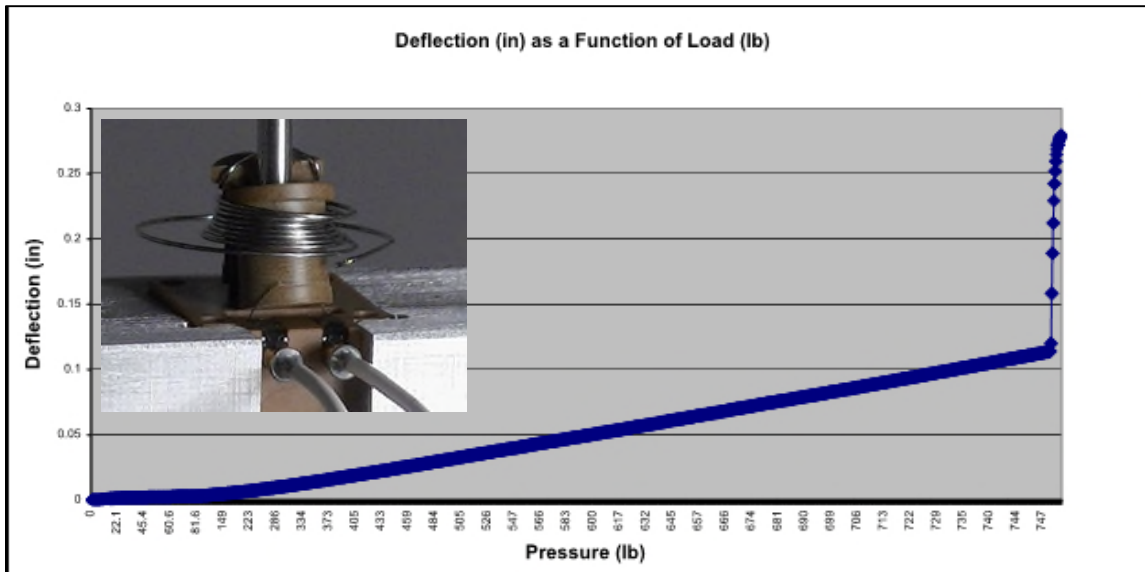


Figure 3. NEA Ultimate Load Test

Now that we knew the ultimate load of the bypass switch release mechanism, we next turned our attention to the design of the release rod. As discussed above, to hit our cost targets, the team was only allowed to alter stock bypass release mechanism parts. They reviewed the piece part detailed drawings to determine our design constraint for the size of release rod. It was determined that the size of the hole that could be drilled between the guide pins that restrain the spools was the limiting factor. This is shown in Figure 5. Our calculations showed that we could install a hole in the assembly that would support the release of a #1 fastener (release rod) and that this rod would have the structural capability to hold 450 lbf (2000 N).

We then looked at the contact pressure at the conical interface between the release rod and the spools. As it turned out, this was the limiting factor relative to the maximum load capability of the device. The spools are machined from a high-strength engineered plastic that has a maximum compressive strength of 28,900 psi (199 MPa).

$RRod_{Dia_minor} := .0560 \cdot in$	$Spool_{Contact_Area} := .01063 \cdot in^2$
$RRod_{Tensile_Area} := \frac{\pi}{4} \cdot (RRod_{Dia_minor})^2 = 0.0025 \text{ in}^2$	$Spool_{Comp_Strength} := 28900 \cdot psi$
$RRod_{UTS} := 180000 \text{ psi}$	
$RRod_{Strength} := RRod_{Tensile_Area} \cdot RRod_{UTS} = 443.3 \text{ lbf}$	
$Spool_{Comp_max} := Spool_{Comp_Strength} \cdot Spool_{Contact_Area} = 307.2 \text{ lbf}$	

Figure 4. Release Rod Load Calculations

The design team armed with the ultimate load data and release rod load data set off to do our first prototype test. We modified a bypass release mechanism and machined the release rod in our rapid development lab. The release rod was made by modifying a commercial #1 socket head cap screw.

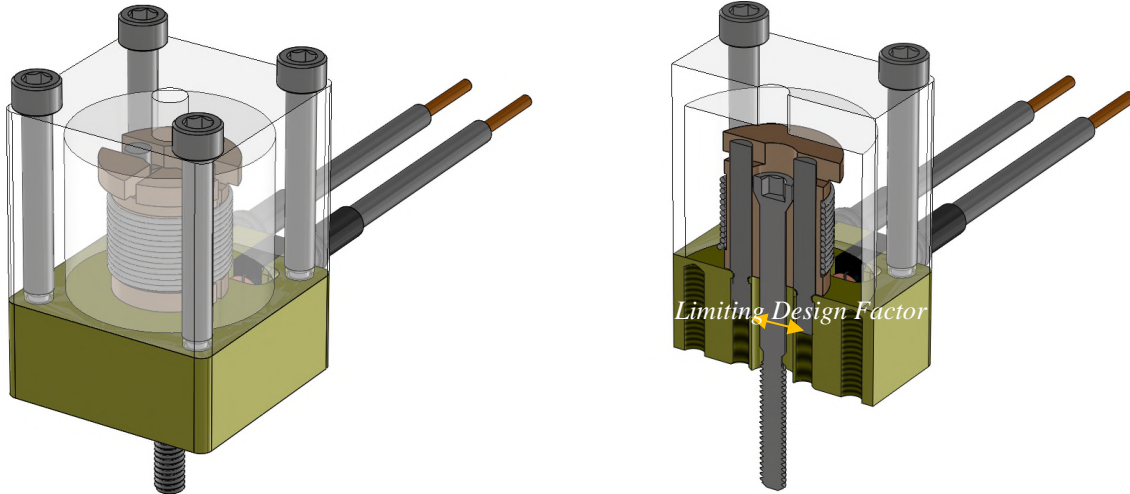


Figure 5. Release Rod and Release Mechanism Modified

At this point we had our first lessons learned. Our first experiment (Ultimate Load) along with the release rod load calculations theorized that the load capability of the mechanism should be near 450 lbf (2000 N). The first test of the mechanism produced contrary results. The initial load test done with the bypass switch mechanism was performed by pushing on the spools (using an Instron test apparatus) with a constant load rate; hence, load creep or loss was not measured. In reality, the plastic spools of the baseline mechanism deflect radially outward at applied loads greater than 150 lbf (660 N). While this test was considered acceptable because the load was within the desired 50 to 200 lbf (89 – 890 N) load range, the team felt they could improve the results.

A detailed finite element analysis confirmed that the spools were deflecting only in the area above the restraining wire; that is, in the area unsupported by the restraining wire. Based on this analysis, the team elected to modify the spools by lowering the conical section deeper within the spool, assuring that the radial load generated by the conical area was fully supported by the restraining wire. This deviated from the charter of the project because parts needed be altered such that stock parts could not be used. The results of the second test were much more favorable and improved the load capability of the mechanism to more than 300 lbf (1330 N).

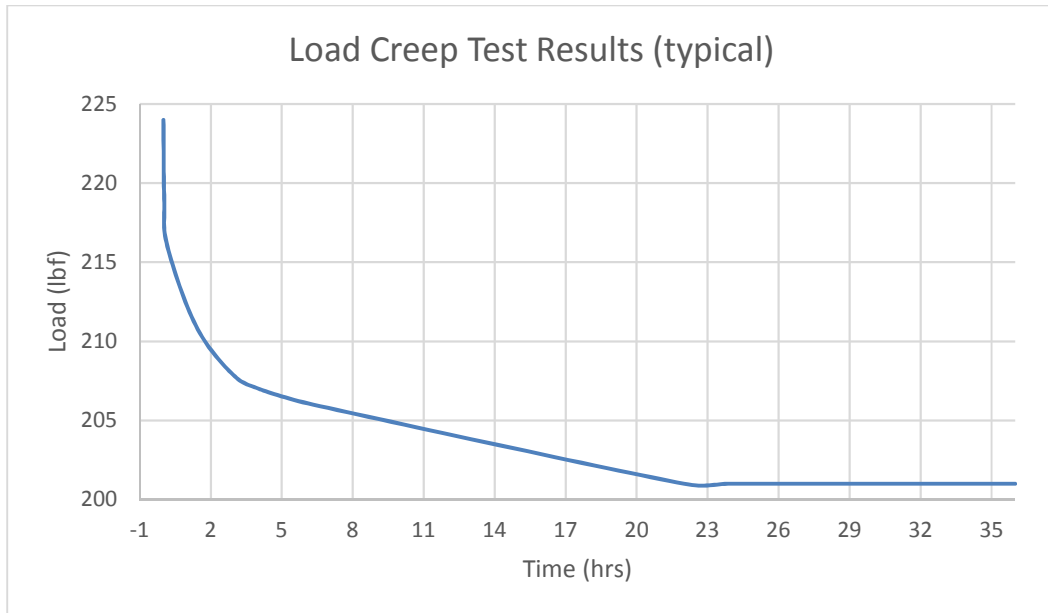


Figure 6. Load Creep Test Results

Now that load characterization was complete, the team moved on to capture shock output data. Given the small size of the device, a modest 12 inch by 12 inch (30 cm by 30 cm) aluminum plate (1/8-inch (3-mm) thick) was used for shock output testing. The test set up is shown in Figure 6.

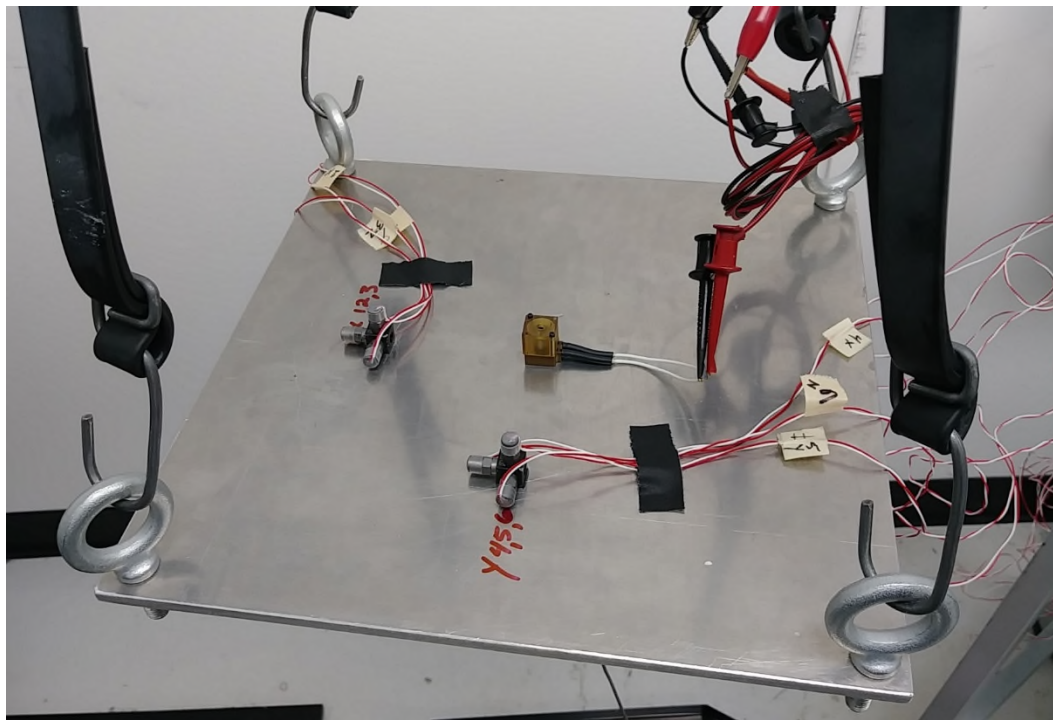


Figure 7. Shock Test Setup

NEA built and tested 5 (five) units for the shock output test. The units were loaded to 250 lbf (1100 N) and then actuated with 4.5 amps of current. The results of the output test are shown in Figure 8.

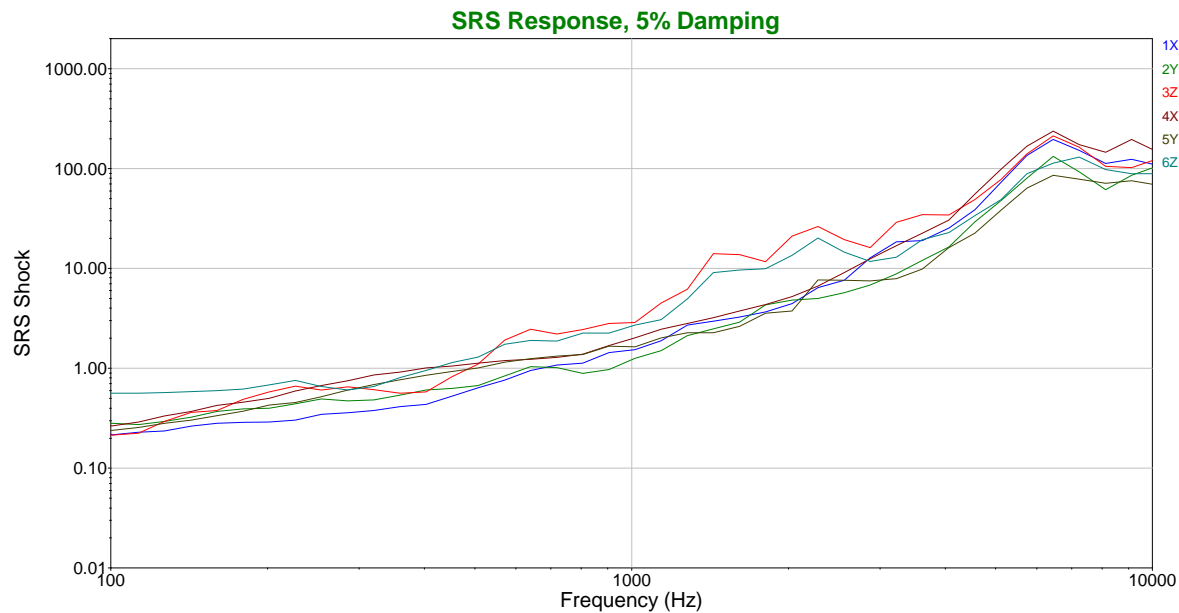


Figure 8. Shock Output Test Results

Conclusions and Lessons Learned

1. NEA produced a 100-lbf (440-N) release mechanism using common parts with our production bypass switch mechanism.
2. Much higher loads (>250 lbf (1100 N)) are achievable with slight design modifications to common parts.
3. By changing from plastic spools to metal spools, loads of 450 lbf (2000 N) can be achieved, but at a higher cost.
4. The shock output of the mechanism is well below expectations and industry standards.
5. More attention to the rod to spool interface could have saved a design iteration.

Compliant Mechanisms Re-Design based on Additive Manufacturing and Topology Optimization

Lionel Kiener*, Hervé Saudan*, Gérald Perruchoud* and Johan Kruis*

Abstract

The use of Additive Manufacturing (AM) processes for cutting-edge applications is a constantly growing topic of interest in various sectors such as space, astrophysics, medical and watchmaking industries. While the largest part of the research presently reported is focused on developing and optimizing designs of what could be described as “structural or massive parts”, little work has been published up to now to determine the limits related to the manufacturing of thin, flexible structures used in compliant mechanisms [1].

While the common thinking is that everything can be done by AM - which is only partially true - it can be added that it cannot be done haphazardly. The Additive Manufacturing process needs to be well mastered as it introduces several new challenges which need to be taken into account in the design phase. In parallel, reproducing by Additive Manufacturing the same parts that are currently produced by traditional methods such as machining is usually of no interest. To ensure the highest added value, the entire device - and not only the individual parts - need to be reconsidered under a process-oriented design perspective, the whole being driven according to a system engineering mindset. CSEM is investigating the new capabilities of AM with the aim to help industries to redesign their products according to this holistic approach.

This paper exposes the status of the Research & Development activities carried out at CSEM with the aim to produce novel designs of mechanisms, including compliant structures based on AM. The general development strategy is presented, followed by material & process characterization and testing results. The re-design, including topology optimization of space products and compliant mechanisms are presented as well.

Introduction

CSEM is active in the design and development of very high performance flexural elements and mechanisms for more than 30 years. Notable examples for space applications are the HAFHA flexural pivot and the Corner Cube Mechanism which is currently operated in the IASI instrument on board MetOp satellites, to date with more than 800 million cycles (linear stroke of ± 15 mm) achieved in 10 years. Other mechanisms (e.g. Slit Mask, tip-tilt and chopper) have been developed and produced for ground-based telescopes as well as for the airborne SOFIA telescope.

In the same philosophy, the elaboration of new products made by additive manufacturing has been investigated at CSEM over several years targeting the general goals of assessing the benefits and weaknesses of the AM fabrication process for compliant mechanisms and getting a sufficient level of expertise on AM-produced compliant mechanisms for future projects.

Development Strategy

For future development projects, CSEM tackled the challenge of producing compliant structures by Selective Laser Melting (SLM). The first chapter of this endeavour started in 2014 with the development

* CSEM SA, Neuchâtel, Switzerland

Proceedings of the 44th Aerospace Mechanisms Symposium, NASA Glenn Research Center, May 16-18, 2018

of a 2-DoF linear stage demonstrator and continued with a second chapter consisting in the development of an end-to-end production strategy addressing the optimization of the material properties. The main conclusions derived from the characterization of these samples were that - in their optimized version - their tensile properties were similar to those of the commercial grade alloy, while their alternate bending fatigue lifetime was greater than 15 million cycles under cyclic loads near to 50% of their Yield Strength. Based on these encouraging results, a third chapter was opened in 2017 with the aim to design, produce and test several topologically optimized parts and mechanisms.

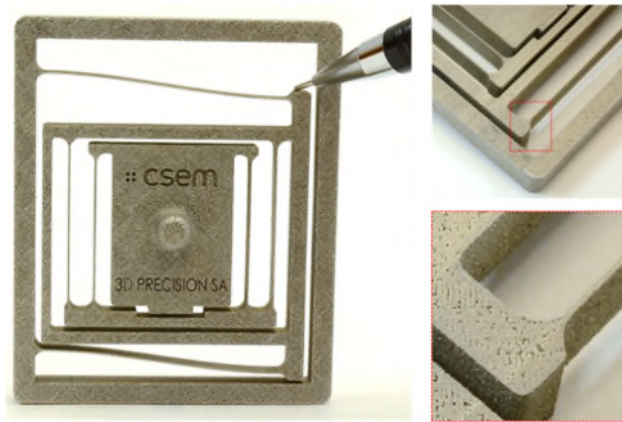


Figure 1. AM-SLM produced 316L stainless steel 2-DoF linear stage. Flexures thickness = 300 μm , aspect ratio respectively 80 and 123 for the blades of the double and simple parallelograms

Materials Selection, Development and Validation

The material choice was oriented toward high-strength stainless steel alloys available in powder form, with the aim of approaching the exceptional mechanical properties and stress corrosion cracking (SCC) resistance of MARVAL X12, the material usually chosen by CSEM for demanding applications. This high-strength precipitation-hardened stainless steel offers both high SCC resistance [2] and high fatigue resistance when it is submitted to alternate bending deformation, a parameter which was experimentally verified through several internal fatigue test campaigns. The alloy chosen – Concept Laser's CL92PH – is an equivalent of the widely used and studied 17-4PH martensitic precipitation-hardening stainless steel [3, 4]. Recently, the AM process for titanium alloy has been optimized following the same procedure. Other prototypes have been made of aluminium AlSi10Mg and copper by SLM.

SLM Process Optimization

The optimization of the SLM parameters was performed in an iterative manner with the aim to minimize porosity and surface roughness, whilst seeking to optimize micro-structure for high mechanical performances.

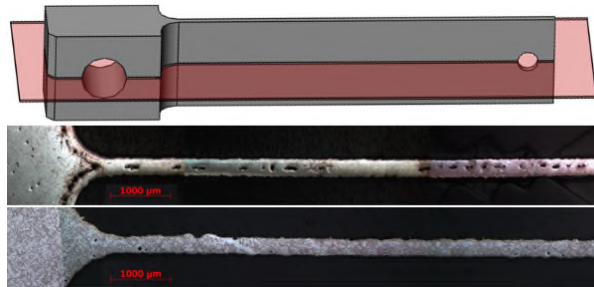


Figure 2. Fatigue sample cross-sections before and after SLM parameters optimization. The thickness of the blade is 350 μm .

Among the process parameters evaluated, such as layer thickness, laser beam power, focus point or scan speed, the laser pattern was confirmed to be the key parameter leading to homogenous material quality on both massive and thin geometries, as shown in Figure 2.

The impact of the manufacturing direction was also investigated. The only notable differences were found on the transverse cut where Y samples showed a finer micro-structure compared to X. These visual differences were all suppressed after the Hot Isostatic Pressing (HIP) treatment, which removed all porosity and improved the micro-structure, such that X and Y could no longer be distinguished (see Figure 3). The analysis confirmed that the HIP treatment permits the removal of the residual porosity and the improvement of the microstructure in terms of homogeneity and grain size.

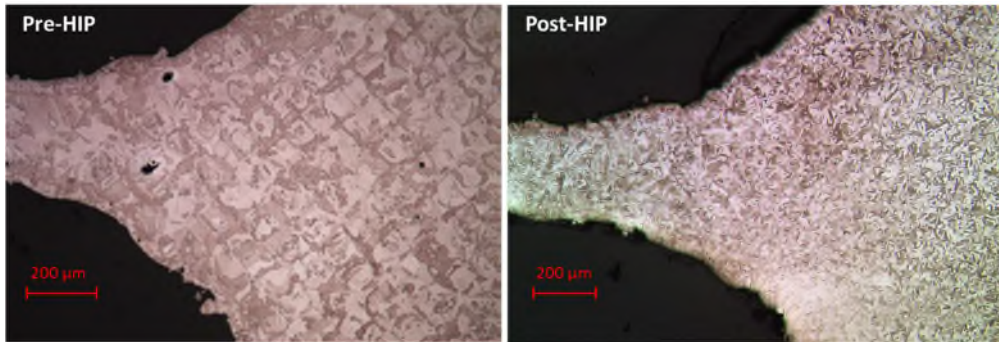


Figure 3. Sample cross-sections before and after HIP processing.

Tensile Test Results

The tensile tests were conducted for two groups of samples representing two plausible final heat conditions for mechanical parts of a compliant mechanism. The samples were produced according to the three manufacturing directions, X-Y-Z, to highlight potential anisotropies in the final heat condition states. The second objective was to quantify the difference expected between HIP and non-HIP material. The tensile test samples were designed according to the ASTM E8/E8M – 15a standard. Raw rods were produced and submitted to the heat treatment sequences. Finally, the rods were machined to their final geometry and tested.

The results show that for both heat treatment conditions, the SLM produced samples show similar or higher R_m and R_p 0.2 compared to the commercial grade 17-4PH. The elongation at break for non-HIP samples tend to show a fragile behavior which is confirmed by the fracture inspection. The tensile tests revealed minor anisotropy according to the manufacturing directions, X showing the highest R_m & R_p 0.2, followed by Z and Y. The overall relative variations of R_m & R_p 0.2 versus the manufacturing directions are below 5% for the HIP samples and 10% for non-HIP samples, which tends to show a slight improvement on anisotropy induced by the HIP treatment.

Fatigue Test Campaign

The graph of Figure 4 compares the approximated S-N curves and fatigue limit estimations S_f of each fatigue test sample (FTS) group. As expected, the group C whose FTS were manufactured from commercial grade 17-4PH and machined according to the best WEDM-based protocol shows the highest fatigue performance with S_{fc} estimated at 680 MPa. This group is to be compared with group B, where FTS were machined according to the same WEDM-based protocol, but from additively manufactured and HIP raw material. The subsequent loss in fatigue performance is around 25% with S_{fb} estimated at 510 MPa.

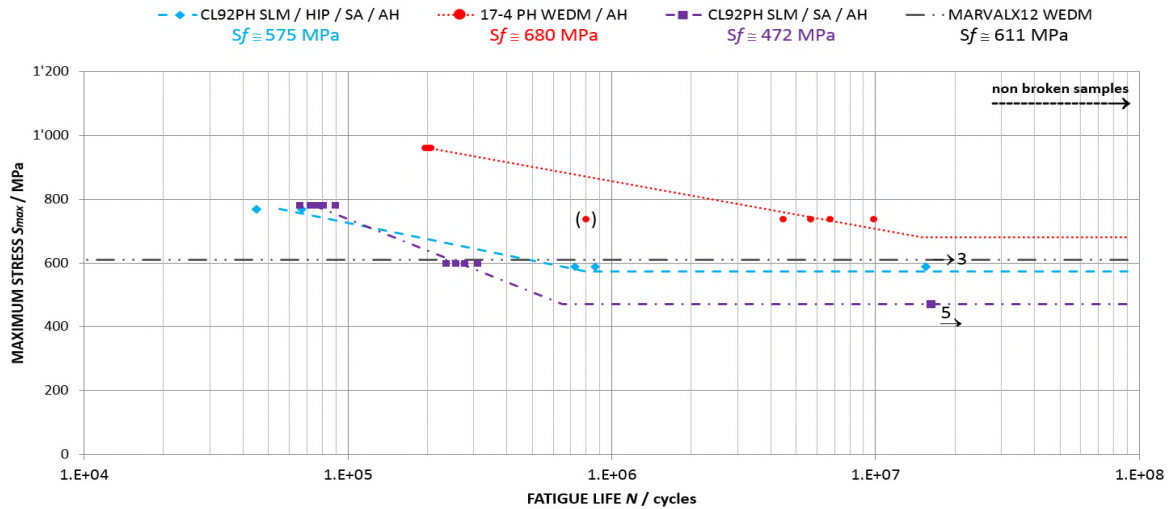


Figure 4. S-N curves estimates for SLM (CL92PH) and WEDM (17-4PH) samples. The fatigue limit of MARVALX12 was determined experimentally during the MTG-CCM test campaign.

Design for Additive Manufacturing

Using AM technologies to reproduce a part whose design was driven by a conventional manufacturing strategy such as turning and milling is often not pertinent, since it does not take into account most of the advantages given by AM. For example, the complexity of the assembly can be reduced by designing a monolithic mechanism or by decreasing the number of parts and combining functions.

To ensure an optimized redesign for AM, a system engineering vision will allow understanding all parameters pertaining to the mechanism and therefore being aware of all key requirements to be considered during the design phase. On the other hand, the design constraints associated with AM are to be well understood.

A major limitation of the current AM technologies (e.g. SLM) is the need of support structures when the part comprises overhanging areas with an angle of usually less than 45 degrees with respect to the horizontal plane. Therefore, keeping in mind the following strategies during the redesign will contribute to obtain better results and will ease the removal of the part from the baseplate:

- redesign with overhanging angles greater than 45 degrees from horizontal
- changing the part orientation to minimize support structures
- allowing support material in dedicated areas

Examples of parts and compliant structures redesigned for Additive Manufacturing

A successful product redesign for AM is the rotor of a slipring performed in partnership with RUAG Space Switzerland Nyon, where the support material could be avoided. The production of complex geometries by AM-SLM allowed us to integrate the electrical conductors within the rotor structure leading to a drastic reduction in the number of parts – from 36 to 1 for a 12-track rotor – and therefore a significant reduction of the manufacturing and assembly time.



Figure 5. Slipring rotor made by Additive Manufacturing

For compliant mechanisms, the redesign is more challenging since the design guidelines of most of the AM processes recommend avoiding thin structures and abrupt thickness variations, which are characteristic of flexible structures. CSEM's approach is therefore to work on several aspects of AM in parallel, such as redesign, thin structures manufacturing and testing, mechanical and thermal post-processes, Finite Element Modelling (FEM) and topology/parametric optimization.

Topology Optimization is actually the most efficient approach to improve various properties of structural parts designed for AM, such as mass reduction, eigen-frequency tuning, thermal transfer, thin-wall thickness optimization, etc. Unfortunately, the use of commercial software is currently limited to the optimization of structural geometries, since the algorithms are not able to handle flexible structures. Due to their own nature, the algorithms try to *decrease* the compliance of the structure (see example in Figure 6), which is the opposite of what is requested for flexible structures. To optimize those, we need to determine where and how to locally increase the compliance in order to provide the requested movement. Since commercial software solutions were not able to fulfil this need, some particular tools have been developed internally to be able to generate the geometry for compliant mechanisms.

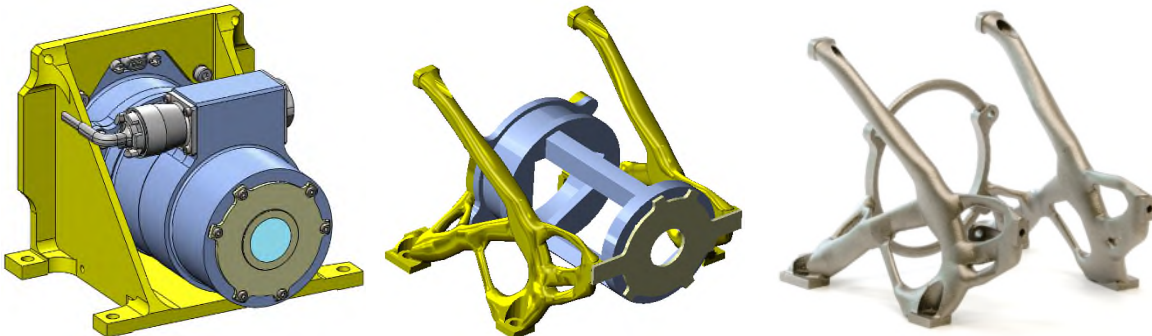


Figure 6. Example of CLUPI (EXO MARS Mission) bracket redesigned with topology optimization. Left: classical bracket, middle: geometry optimized to maximize the stiffness with a given mass diminution, right: part additively manufactured in titanium alloy.

An intermediate approach currently under investigation at CSEM is to improve the rigid parts of the mechanism, keeping conventional flexure geometries as they have been used successfully up to now. This concept is currently under investigation at CSEM with the redesign of first, the HAFHA pivot alone, before integrating the result in a more complex scanning mechanism using two such pivots. Some pictures of the preliminary concepts are shown in Figure 7 and 8.

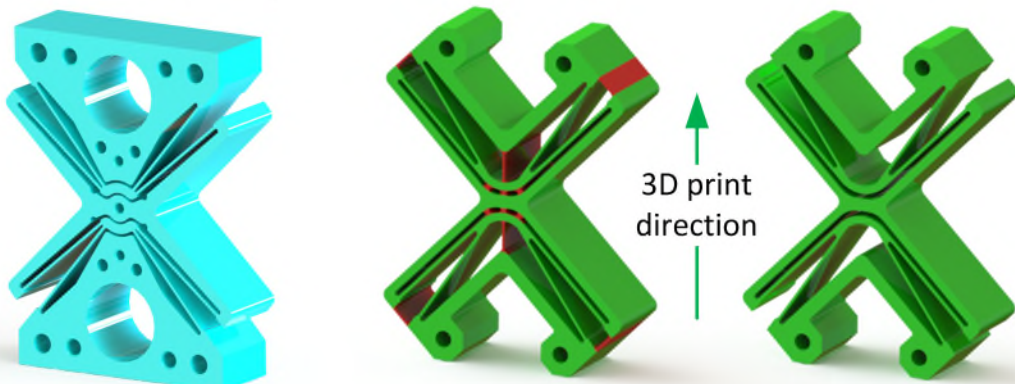


Figure 7. Example of HAFHA pivot redesigned for monolithic AM with a given print direction. Left: classical pivot, middle: optimized for AM with support bridges in red, right: AM pivot after bridge removal.

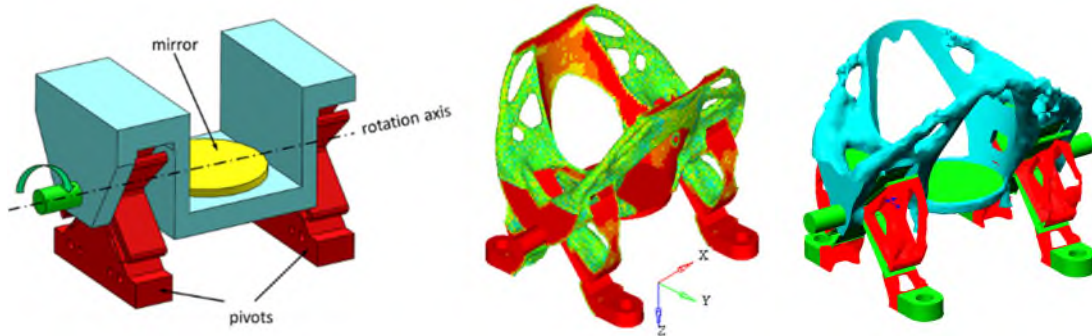


Figure 8. Example of scanning compliant mechanism designed and optimized for monolithic additive manufacturing. Left: architecture overview, middle: first results without support material considerations, right: raw result with constrained parameters to avoid overhanging structure of less than 45° from horizontal plane.

Conclusions

After showing in 2014 the feasibility of manufacturing an elementary compliant structure made of stainless steel with AM-SLM, CSEM successfully developed – jointly with the company 3D PRECISION – a comprehensive end-to-end SLM-based manufacturing and post-processing production method for a high-strength precipitation-hardened stainless steel comparable to the widely known and used 17-4PH.

The tensile properties of the material were tested for the three manufacturing directions and for two thermal post-processing conditions, highlighting the tremendous improvement of the performances after HIP treatment, with the conclusion that the SLM manufacturing of CL92PH powder material can lead to tensile performance similar to a commercial grade 17-4 PH stainless steel, provided the appropriate post-processing strategy is applied. The positive influence of the HIP treatment was also investigated at a microscopic scale through detailed metallographic analysis which revealed the successful suppression of macro porosity and the improvement of the microstructure for both structural and flexural segments.

The fatigue performance of the flexural segments was investigated in detail through a comprehensive alternate bending fatigue test campaign covering four different sample groups. The collected fatigue test data helped to highlight the contribution of the key material and surface defects on the final fatigue performance. The beneficial effect of the HIP treatment on fatigue performance was demonstrated, with further investigations to be carried out on the impact of the geometry of the parts versus HIP and subsequent thermal post-processing efficiency and side effects. The percent replication of the fatigue data collected allows us to affirm that from a lifetime point of view, SLM-manufactured compliant structures have the potential to be eligible for demanding applications. Despite the loss in fatigue performance, it is possible to design – provided a well-adapted sizing – a compliant structure offering lifetime above 15 million cycles.

Similarly, the AM process for a titanium alloy has been recently optimized following the same procedure. From the mechanical design point of view, SLM manufacturing is acknowledged to have the potential to enable new design strategies, leading to high mass/stiffness optimized parts and simplified assemblies. The present study demonstrates that even thin structures can offer sufficient fatigue performance and geometrical accuracy to be foreseen for space applications. Nevertheless, it must be stressed that SLM also brings some challenges which need to be addressed. The use of material support and the subsequent need for material removal is foreseen to be the main source of design restrictions and needs some additional creativity.

Another critical issue encountered during this study is the accumulation of internal mechanical stresses during the SLM process and the necessity for annealing post-processing which avoids the emergence of macroscopic warpage during the delicate step of separating the part from its manufacturing substrate.

From the design point of view, new generation design tools such as topology optimization software could lead to interesting results. With their capacity to minimize or control the effects associated with the thermal history of the parts, the emergence of AM process simulation tools should also contribute to improve the design of the parts. But all these software tools are only complementary to the understanding of the designer which needs to be aware of the possibilities and limitations offered by Additive Manufacturing.

The present study demonstrates how the most critical steps related to Additive Manufacturing of high-precision and compliant mechanisms were addressed, starting from the specific mechanical design, followed by the definition of the Additive Manufacturing and post-processing strategies and concluded with the validation strategy. This approach has led to the successful redesign of a space slingshot rotor and will continue with other products.

The near future work is to design and build more demonstrators integrating all the developments achieved over these last few years, especially in the frame of a development project for the European Space Agency.

References

1. Merriam, Ezekiel G., Stiffness Reduction Strategies for Additively Manufactured Compliant Mechanisms, All Theses and Dissertations. Paper 5873, 2016.
2. ECSS, *Material selection for controlling stress-corrosion cracking*, ECSS-Q-ST-70-36C, 2009.
3. The Boeing Company – Vertol Division, *Fatigue Properties of 17-4 PH and 15-5 PH Steel in the H-900 and H-1050 Condition*, Report D8-1038, 1969.
4. US Department of Defence, *Metallic Materials and Elements for Aerospace Vehicle Structures*, MIL-HDBK-5H, 1998.

Non-Pyrotechnic Multi-Point Release Mechanisms for Spacecraft Release

Ambrosio Mejia*, John Sudick* and Geoff Kaczynski*

Abstract

The Non-Explosive Actuator (NEA) is an electrically initiated Hold-Down Release Mechanism (HDRM) that has the ability to carry a very high tensile preload until commanded to release, with the additional advantage of very low output shock. The NEA has been used for many different spacecraft hold-down applications over the years, but has had limited use as a payload release mechanism due to the limited data regarding its simultaneity capability. The objective of this paper is to expand on this simultaneity database by describing and summarizing Phase I of the NEA Multi-Point Separation Testing that shows that the variation in NEA actuation time can meet certain simultaneity requirements necessary for spacecraft payload separation. The data collected shows NEA's can meet simultaneity requirements of less than 5 ms.

Introduction

NEA Electronics manufactures both pyrotechnic and non-pyrotechnic release mechanisms. NEA Electronics was recently involved in several opportunities that required the release of multiple spacecraft using the multi-point hold down method. All the opportunities pursued elected to use our pyrotechnic separation nuts instead of our low-shock Non-Explosive Actuator (NEA). At the time, the reason stated by potential users for selecting the pyrotechnic device technology over the NEA centered on concerns with the lack of simultaneity data between multiple NEA's used in a time-critical application.

Pyrotechnic devices have been widely used for payload separation in the past, but with the increased need for low-shock mechanisms, especially with smaller constellation payloads, this simultaneity data for NEA release mechanisms will prove very useful to the aerospace mechanism community for alternative low-shock design solutions. This paper is an expansion of the data collected and presented in a poster presentation for ESMATS 2017.

Background

Before diving into the testing, it is best to understand the basics of the NEA design, as well as the details of what constitutes NEA actuation time, including the primary factors that affect the actuation time.

The NEA HDRM is an electrically initiated, one-shot release mechanism that has the ability to carry a very high tensile preload until commanded to release. The preload is applied through a release rod held in place by two separable spool halves which are in turn held together by a tightly wound restraining wire. The restraint wire is held in place by redundant electrical fuse wires; actuation of either circuit allows release, assuring maximum reliability. When sufficient electrical current is applied, the restraint wire unwinds allowing the spool halves to separate, releasing the release rod and the associated preload.

The NEA actuation time is the time from application of current to the start of the release rod exiting from the NEA (i.e., preload drop to zero). This actuation time can be split into two (2) independent segments per Figure 1.

* NEA Electronics, Moorpark, CA (subsidiary of Ensign-Bickford Aerospace and Defense)

- 1) Fuse Wire Burnout time (FWBO): This is the time from application of current to fuse wire burnout. This time is primarily dependent on input current – the higher the input current, the faster the fuse wire burn time.
- 2) Preload Drop time: Time from fuse wire burnout to when the restraining wire uncoils sufficiently to drop the system preload to zero and allow the release rod to start exiting the NEA.

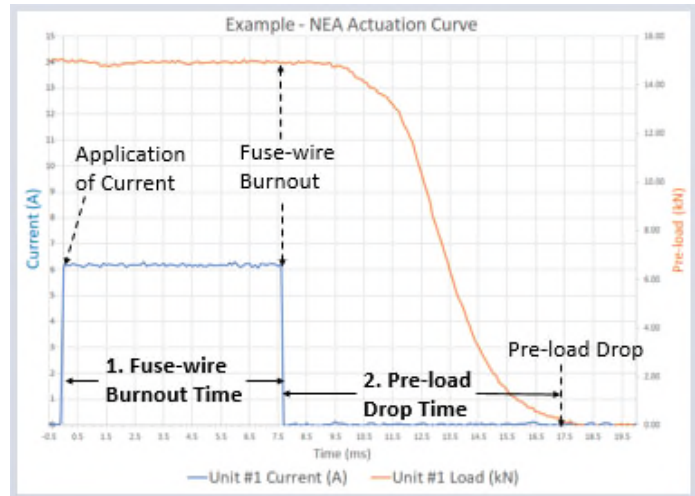


Figure 1. Example of Typical NEA Actuation Time Curve

There were two distinct series of testing performed as part of Phase 1 of the NEA Multi-point Separation Testing. Series I consisted of testing with a 4-point release test plate using a break-link to measure actuation time. Series II consisted of testing performed with units actuated individually using a load cell to measure actuation time.

Series I – Four-Point Release Testing

Series I - Test Setup and Plan

Series I testing consisted of two sub-series of tests where preload and firing current were adjusted. Each sub-series test consists of data from each of the 4 NEA's actuated during that test, for a total of 28 data points (see Table 1)

Table 1. Series I Test Plan

		Firing Current	Target Preload
Sub-Series I.1	Test I.1.1	3.0 Amps	11.6 kN (2,600 lbf)
	Test I.1.2	4.5 Amps	11.6 kN (2,600 lbf)
	Test I.1.3	4.5 Amps	11.6 kN (2,600 lbf)
	Test I.1.4	7.0 Amps	11.6 kN (2,600 lbf)
Sub-Series I.2	Test I.2.1	7.0 Amps	17.8 kN (4,000 lbf)
	Test I.2.2	7.0 Amps	17.8 kN (4,000 lbf)
	Test I.2.3	7.0 Amps	17.8 kN (4,000 lbf)

4 actuation data points are collected for each test

This initial series of tests were conducted using an NEA model SSD9102J, an M6-sized HDRM with an integral 60-degree cup/cone interface and retraction spring. Four NEA's were affixed to the corners of two 610-mm (24-inch) square aluminum plates; each plate being 19-mm (0.75-inch) thick and weighing

approximately 177 N (40 lbf). The aluminum plates were suspended in a frame so that the plates were parallel to the ground. Application of the actuation current activates the NEA's and allows the bottom plate to fall and separate from the top plate with gravity providing the separation force (see Figure 2).

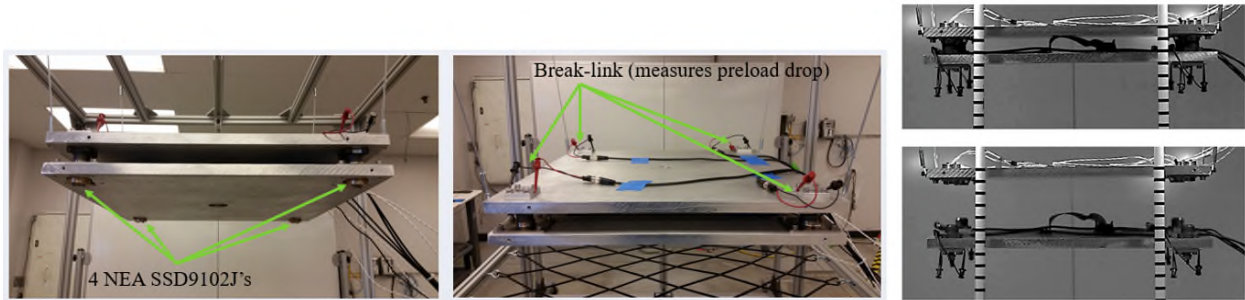


Figure 2. Test Setup

A multi-channel Synergy Data Acquisition System was used to capture Fuse Wire Burnout time and Preload Drop Time. Because load cells could not be installed directly into the NEA assembly for this configuration, a “break link” was used to estimate the Preload Drop Time. This break link consists of a piece of lead fixed in proximity to the release rod exit path – once the preload dropped and the release rod begins to move, it breaks the “break link” and a signal is shown on the data acquisition system.

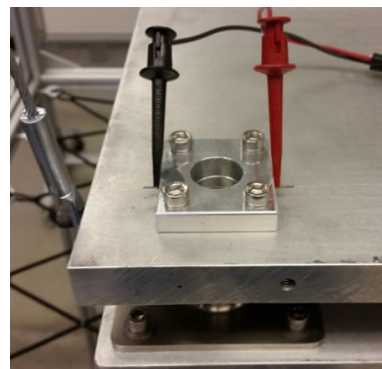


Figure 3. Break Link Setup

Series I - Test Results

Figure 4 and Figure 5 shows that overall actuation time is primarily influenced by the input firing current. As the current increases, the actuation time decreases significantly (Figure 4). It also reveals that preload does not significantly influence actuation time as shown with the significant overlap in individual actuation time data points (Figure 5).

Figure 6 shows that the reason input current is the primary influence on Actuation Time is because of its effect on Fuse Wire Burnout Time – higher input current reduces the magnitude and variation in Fuse Wire Burnout Time. Figure 6 also shows Preload Drop Time is independent of input current.

Figure 7 summarizes the effects of input current to the Simultaneity Range of each test - the range of actuation time for each test between the 4 NEA's was determined and sorted by input current. This data shows the simultaneity between 4 NEA actuated together improves significantly with increasing input current, with a max simultaneity range of 5.1 ms.

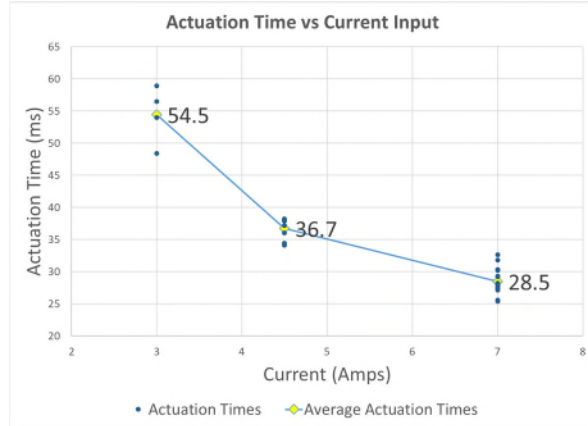


Figure 4. Actuation Time vs Current

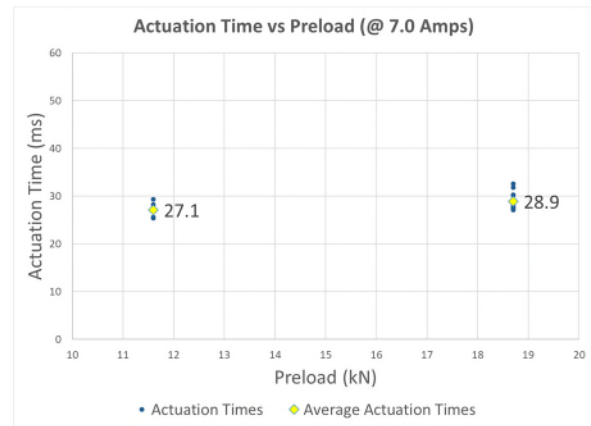


Figure 5. Actuation Time vs Preload

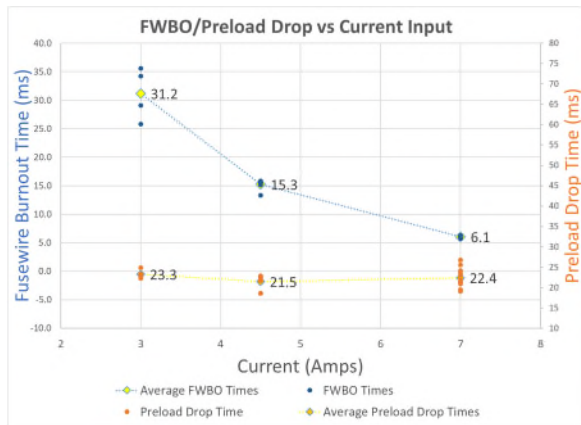


Figure 6. FWBO/Preload Drop vs Current

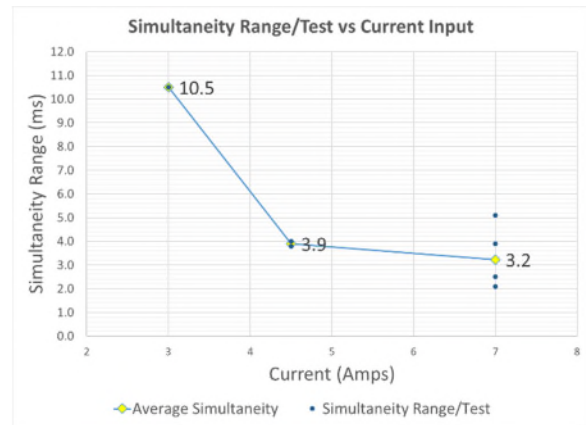


Figure 7. Simultaneity Range/Test vs Current

Series I testing was an excellent start to better understanding the simultaneous capability of our mechanism, but the lack of direct preload data and concern that some of the variance could be caused by the test setup led our team to the next series of testing.

Series II – Individual Release Testing

Series II – Test Setup and Plan

Similar actuation testing parameters were used as in Series I, but the units were tested individually and with a load cell in-line. This allowed us to understand the true preload drop time of the NEA, compare it to the break-link data above, and isolate the internal NEA dynamics from the effects of the 4-point test plate setup. The team also decided to add some additional factors to understand if the units behaved consistently across different assembly operators and over several build lots. Table 2 summarizes the test plan for Series II. Figure 8 provides a schematic of the test setup used.

Table 2. Series II Test Plan

	Firing Current	Preload	Assembly Technician (A or B)
Test II.1	7.0 Amps	11.6 kN (2,600 lbf)	A
Test II.2	7.0 Amps	17.8 kN (4,000 lbf)	A
Test II.3	7.0 Amps	17.8 kN (4,000 lbf)	A
Test II.4	7.0 Amps	17.8 kN (4,000 lbf)	B

Each test series represents a different build lot

8 actuation data points are collected for each test series above

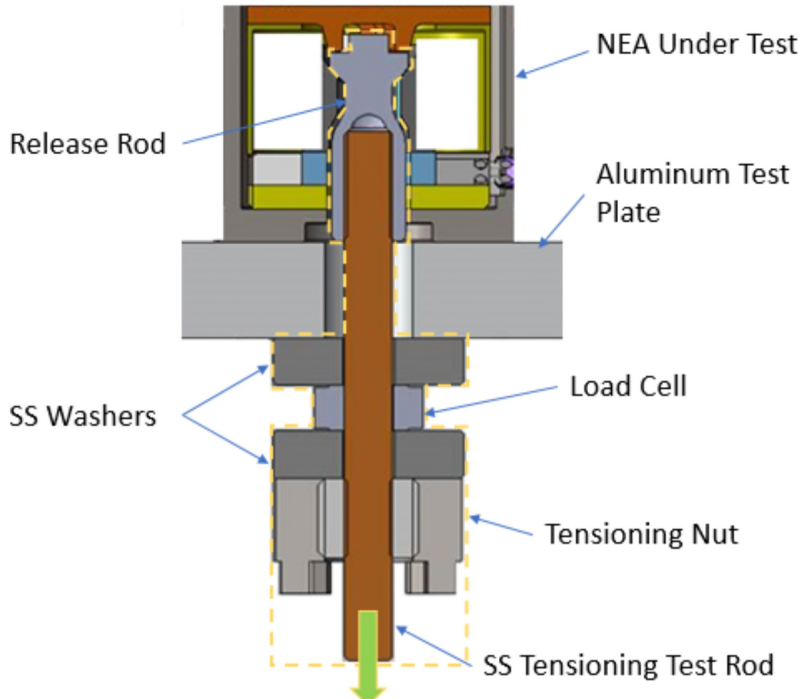


Figure 8 - Series II Test Setup Schematic

1. Tensioning Nut creates a tensile preload thru the test rod and into the NEA, compressing the Test Plate and Load Cell between the NEA and washers.
2. After actuation, the NEA releases the preload in the Test Rod, allowing the highlighted components to release, using gravity as the separation force.

Series II - Test Results

All testing under Series II used the same input current since the factors affected by the input current were already understood from Series I testing. Figure 9 shows that the actuation time is still primarily unaffected by the preload, similar to Series I testing.

Comparing the Series I and Series II data, there are a few key insights to highlight. The first is the difference between the break-link signal (Series I) and the preload drop time (Series II) – see Figure 10. On average, the preload drop time was 9.8 ms faster than the break-link signal. This is expected since sufficient movement of the release rod after preload release is required to fracture the break-link assembly. This extra movement, and the act of breaking the lead, adds variation which leads to the second key difference in the data.

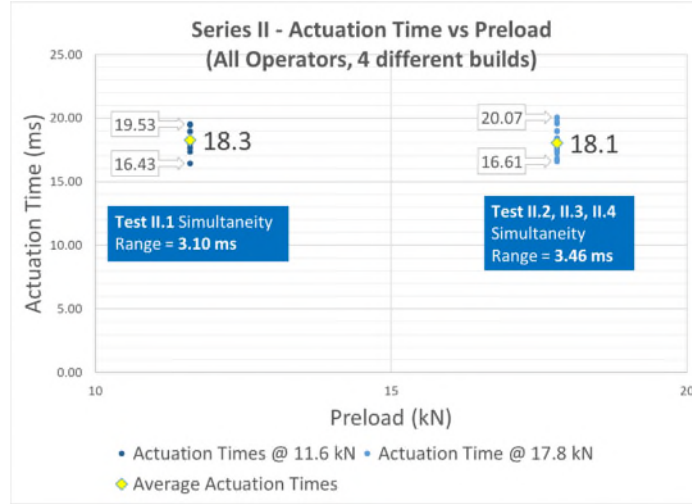


Figure 9. Series II Actuation Time vs Preload

The second significant difference between Series I and II, is the reduction in actuation time variation of 37%, from 5.50 ms to 3.46 ms (Figure 11 shows all data compared at 17.8 kN). This reduction in variation can be attributed to the elimination of variables in the test setup. The test setup in Series II is much more simplified, focusing primarily on the NEA capability itself. Now that the NEA variance in actuation time is understood – which has shown that it can meet a 5-ms simultaneity requirement – the next phase of testing can be centered around building a more flight-like test setup to validate the system.

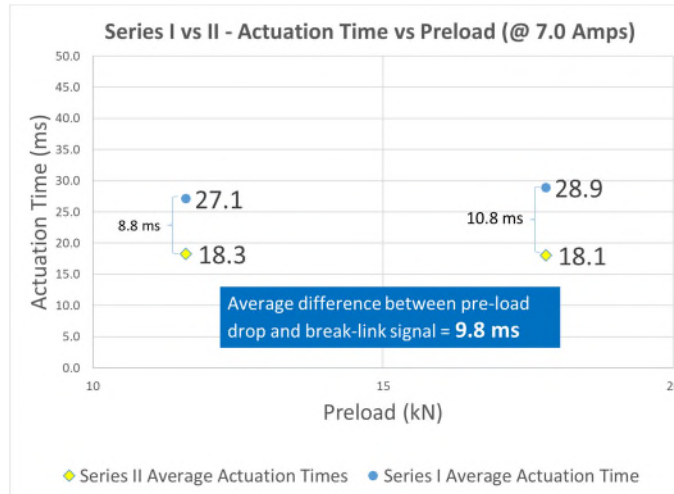


Figure 10. Series I (break-link) vs Series II (load cell) Actuation Time

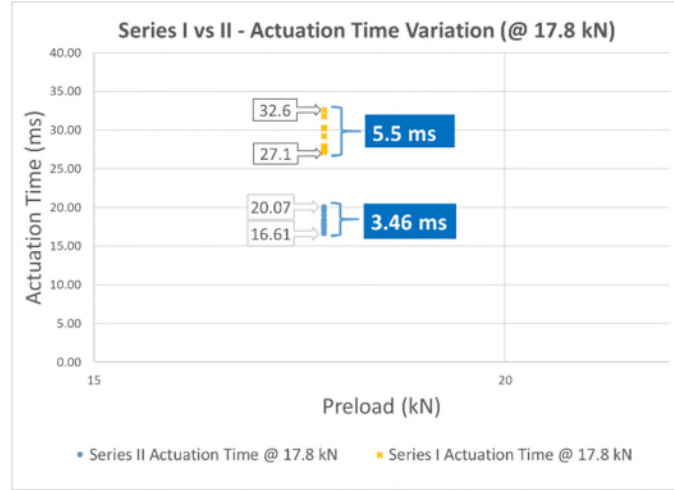


Figure 11. Series I (break-link) vs Series II (load cell) Actuation Time Variation

Conclusions & Lessons Learned

Phase 1 of the NEA Multi-point Separation Testing completed shows the NEA's actuation time capability can meet a simultaneity requirement of 5 ms or less, even across different build lots and different assembly technicians.

Although several lessons were learned during the scope of this testing, the ones of most interest and importance is the dependence of input current on actuation time simultaneity (higher current improves the simultaneity behavior because of reduced fuse wire burn-time variation) and conversely, the independence of preload on simultaneity.

NEA Multi-point Separation Testing Phase 2 has also begun. During this phase, NEA plans to incorporate a more flight-like setup thru cooperation with potential customers, and create a reliable analytical model predicting spacecraft trajectory and tip-off using this empirical data. This data will be ready later this year.

Validation of a Novel High Performance Magnetic Gearbox for Space

Ignacio Valiente-Blanco*, Judit Esnoz-Larraya*, Efrén Diez-Jimenez**, Juan Sanchez García-Casarrubios*, Cristian Cristache*, Fernando Rodriguez-Celis* and José Luis Perez-Díaz*

Abstract

In this paper, experimental validation of a novel high-performance magnetic gearbox for space applications, developed within the ESA ITI program is presented. This lubricant-free gearbox is manufactured using SmCo magnets, with a well known space heritage [1] and provides an unprecedented torque density for this sort of device (92.3 kNm/m^3 , 15.4 Nm/kg). A high efficiency in an extended temperature range (up to 92% at -40°C and 500 rpm) has also been demonstrated, showing a potential advantage of the technology for application in cryogenic environments [2]. Accuracy, zero backlash performance, and magnetic contamination are also investigated.

Introduction and State of the Art

The working principle of a magnetic gear (MG) is similar to a mechanical gearbox. However, teeth are replaced by permanent magnets so torque and speed conversion are produced by a modulated magnetic field [3]. Power is transmitted without contact, therefore, lubrication is not needed; the lack of contact eliminates wear and debris generation and potentially increases lifetime. They are also able to operate in a wider temperature range temperature range from -200°C to 300°C . Finally there is no backlash, which represents a potential advantage for accuracy applications [4] [5]. Additionally, MGs provide vibration isolation between the motor and the payload and its inherent overload protection mechanism prevents against potential catastrophic failures [6].

Despite all these advantages, up to now the technology has shown a low level of maturity and the developed demonstrators are frequently heavy, present low torque capability, reduction ratios typically below 6, and sometimes poor efficiency [7]. Magnetic pollution levels of previous breadboard models are significantly high and not compliant with ECSS space standards [8]. In addition, MGs are usually manufactured using NdFe magnets which are known to present several drawbacks for their use in space environments [9]. Figure 1 shows a summary of the state-of-art of this technology dividing between SmCo and NdFe magnetic gearboxes. Model D57r10 is the gearbox described in this paper.

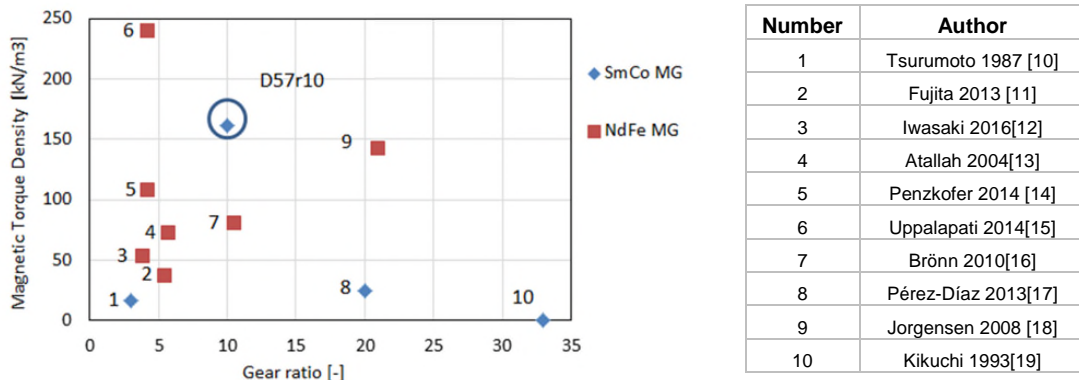


Figure 1. Summary of the state of the art of Magnetic Gearboxes

* MAG SOAR SL. Valdemoro, Spain

** Universidad de Alcalá, Alcalá de Henares, Spain

The Innovation

In this paper, experimental validation of magnetic gear in a controlled laboratory environment is provided. The MG is made of SmCo magnets with known space heritage. A high torque capability, a reduction ratio of 1:10 and low magnetic pollution levels according to ECSS standards were demonstrated. A high efficiency up to 92% at 500 rpm and -40°C is one of the strongest points of the technology. The elimination of contact allows the optimization of power transmission in terms of efficiency. This provides the opportunity of high weight savings in motor-gear assemblies at low temperatures where the use of solid lubrication highly limits the efficiency and torque capacity of the systems. The performance demonstrated by this MG is far superior to the current state of the art of the technology and opens the window for several potential applications in space.

Model Description

The magnetic gearbox presented in this paper is composed of three main elements: an input rotor (1), an output rotor (2) and a stator (3) as shown in Figure 2. Input rotor and stator are mainly composed of SmCo XYG 32 permanent magnets while the output rotor is mainly composed of laminated soft magnetic alloy teeth. Magnets in the stator are arranged in a Halbach configuration to maximize magnetic flux density inside the gearbox. 72 magnets are used in the stator, with 18 soft magnetic teeth and 4 input magnets. According to the reduction ratio calculation formula [20], the reduction ratio of the gearbox presented in this paper is equal to 10.

Four ball bearings are used to support the radial loads (theoretically spurious) during operation and to allow relative motion between the moving parts and the stator of the device. The selected bearings were lubricated with low-temperature grease. Titanium grade 2 alloy has been used as structural material for the housing, flanges and internal parts of the gearbox to obtain a good structural performance with a reduced mass penalty. The relatively high electric resistivity of titanium also contributes to an improvement of the efficiency of the gearbox at high speeds. Standard mechanical interface flanges have been designed. Fig. 2 shows the magnetic gearbox after assembly and the summary of the main physical properties and performance specifications:

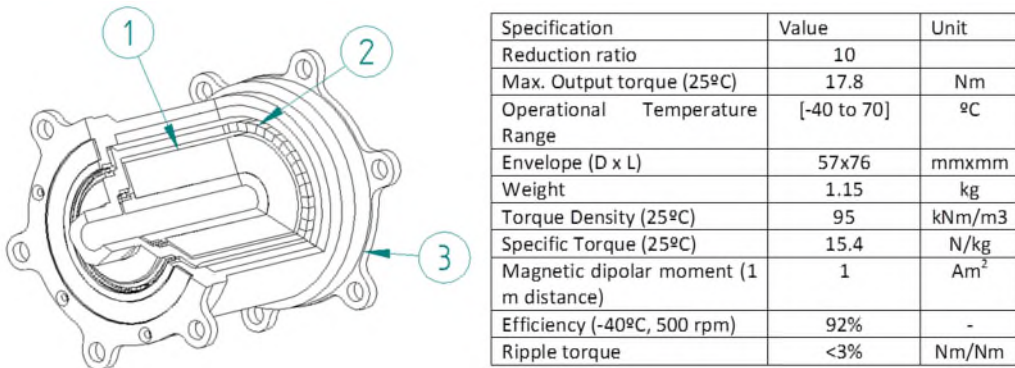


Figure 2. Assembled gearbox and summary characteristics

Test Set Up and Results

A dedicated test bench was set up to accurately characterize the breadboard model under different temperature conditions from -40°C to 70°C, speeds and load conditions from 0 to 100% output load (lock situation). Functional characterization tests were conducted, including static and dynamic performance, temperature influence, gear ratio, transmission error, backlash, and efficiency and magnetic field contamination.

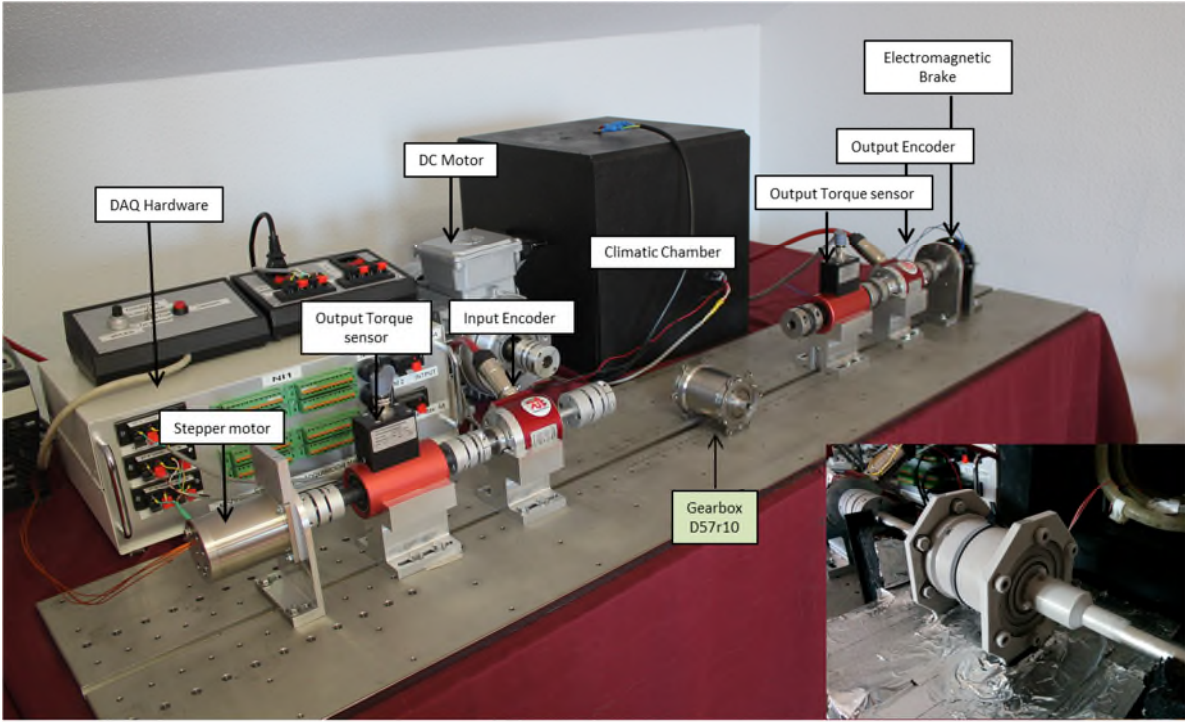


Figure 3. Dedicated test bench and a view of frozen model after -40°C test

Maximum Output Torque vs. Temperature

To evaluate the maximum output torque capacity of the gearbox, an infinite impedance is set at the output shaft (braking torque significantly higher than the maximum expected torque in the gearbox). Then, the input shaft is rotated slowly until slip occurs. The process is repeated 10 times in CW and CCW directions to have a statistical characterization. The maximum output torque measured at different operational temperature is depicted in Fig. 4 and compared to magneto-static FEM calculations. Results are in good agreement with the simulation models.

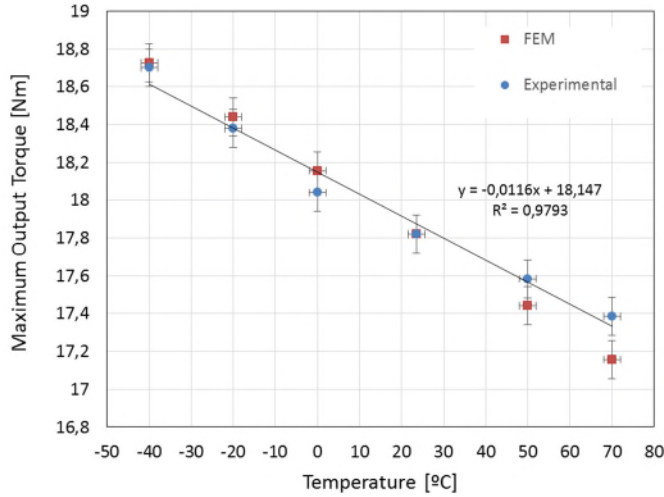


Figure 4. Maximum output torque vs temperature characterization

Maximum output torque at 25°C is 17.8 ± 0.1 Nm. It is clear that the maximum output torque increases at low temperatures. A temperature sensitivity about -0.012 Nm/deg has been calculated. The measured value of maximum output torque provides an actual torque density of 92.3 kNm/m³ and actual specific torque 15.4 Nm/kg at room temperature. The actual torque density is different from active torque density.

Meanwhile the active torque density considers only the magnetic parts, the actual torque density considers the whole volume of the device (bearings, shields, etc). Taking into account the material used (SmCo), the gear ratio and the active torque density obtained, these results provide a significant improvement of the previous state of the art [21].

Reduction Ratio

Kinematic reduction ratio is evaluated in dynamic conditions for various operational speeds between 50 and 1000 rpm, different load conditions and temperatures. Figure 5 shows a typical speed profile for the kinematic reduction ratio characterization test.

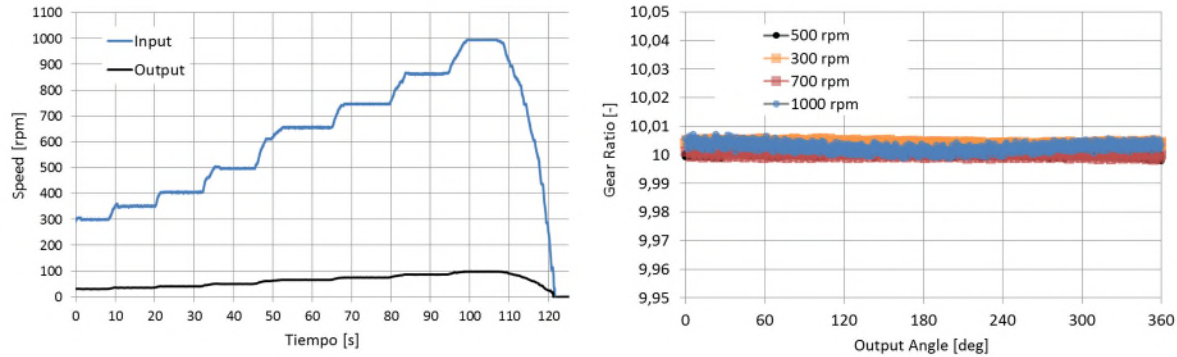


Figure 5. Test bench and three breadboard models

The overall reduction ratio has been calculated at about 10 ± 0.01 with no significant dependency on the operational speed, load condition, or temperature.

Transmission Error

Transmission error of a gearbox is defined as:

$$TE = \theta_{output} - \frac{\theta_{input}}{r}$$

where

θ_{output} is the angle measured in the output shaft.

θ_{input} is the angle measured in the input shaft.

r is the theoretical gearbox reduction ratio, r=10.

The transmission error has been calculated at different speeds, load conditions and temperatures. Fig. 6 shows, as an example, the transmission error measured at 5 rpm, zero load condition, and room temperature. Two main contributions to the transmission error have been found at about 2 and 9.2 output degrees. Average RMS values of the transmission error under different load and temperature conditions are calculated at about 290 arcsec. The same value was obtained under different temperatures and operational conditions. The fact that the contribution to the transmission error can be deterministically defined opens new opportunities to highly improve the accuracy of the gearbox by motor active control.

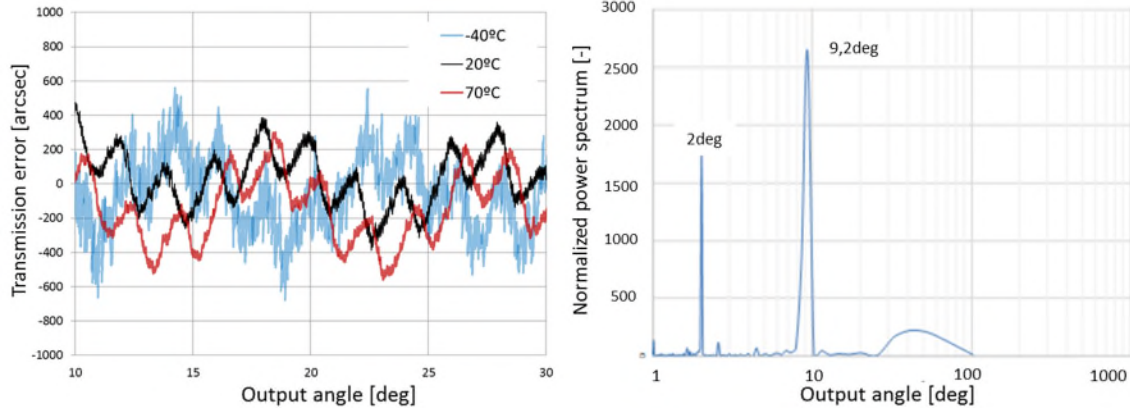


Figure 6. Transmission error and FFT amplitude

Backlash

Backlash was also characterized for the magnetic gearbox. Reciprocating quasi-static motion of low amplitude (from 1 to 10 deg) is induced in the input shaft. Then, the output rotation is observed and backlash characterized. The experiment was repeated at various temperature conditions and different input relative positions. The backlash observed was always below the DAQ system resolution (<20 arcsec).

Efficiency

The efficiency of the magnetic gearbox has been characterized at different operational conditions. In this paper, results at different speeds and temperature for an output load of 50% of the maximum output load are presented. Fig. 7 shows the efficiency measured at different temperatures and compared with FEM results. Both values are in relatively good agreement. Efficiency obtained from experimental data presents error bars up to 10% at low speeds due to test set up limitations. To improve the readability of the data, error bars were not plotted on graph. Efficiency seems to remain higher than 90% even at low temperature; this is one of the main strengths of the technology. On the contrary, mechanical gearboxes are highly affected by cold temperatures, with efficiency of solid lubricated gears rapidly reduced to 10% at -25°C [22].

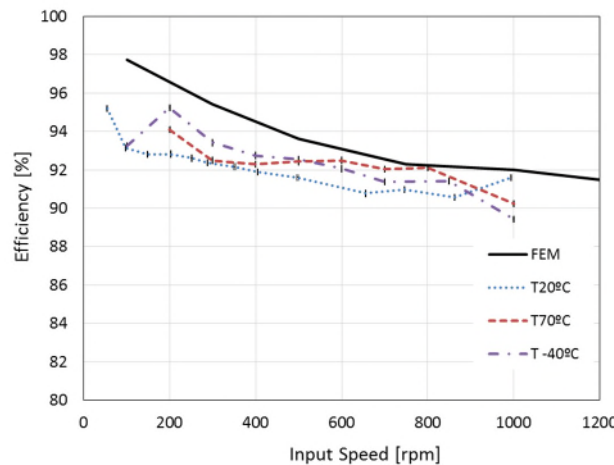


Figure 7. Efficiency test results at different temperatures

Magnetic Pollution

A critical parameter for instruments used in space is the magnetic contamination induced in the surroundings. Frequently, scientific missions and on-board instruments require very low magnetic contamination to assure that there is no interference with the satellite instruments. Scant attention has been

paid to this critical issue in the past regarding magnetic gearboxes. Space standards establish that an acceptable limit for magnetic contamination is a value of $0.2 \mu\text{T}$ at 1-meter distance from the device.

Fig. 8 shows the magnetic field contamination in the most unfavorable direction (radial) from the gearbox vs. distance to the gearbox. A very good agreement with FEM results is observed. The measured magnetic flux density at 1-meter distance is extrapolated from the FEM model of the gearbox. The value obtained is equal to $0.15 \mu\text{T}$, below ECSS limits. The equivalent dipolar moment calculated at 1-meter distance is about $1 \pm 0.2 \text{ A/m}^2$.

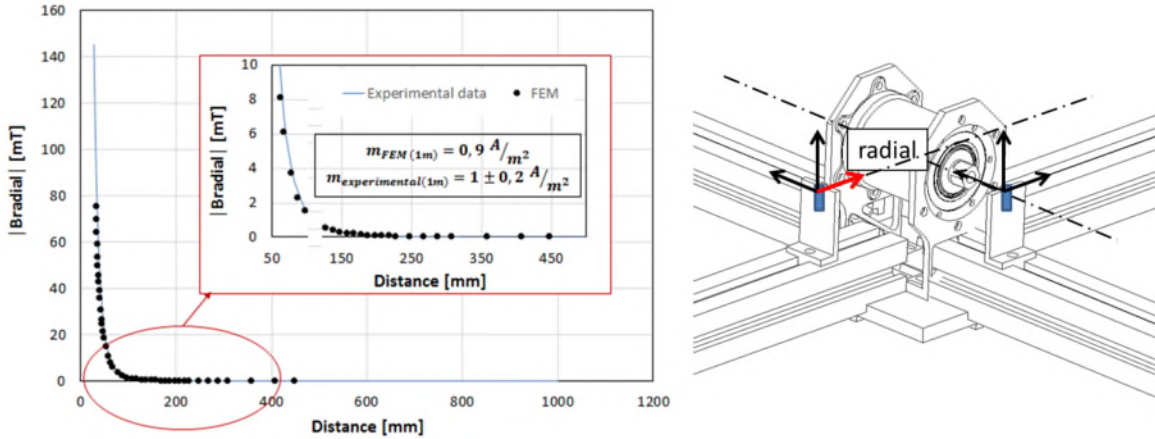


Figure 8. Efficiency and magnetic pollution test results

Conclusions and Lessons Learned

A high-performance breadboard model of a magnetic gearbox has been designed for space applications, manufactured and tested. The breadboard model demonstrated a reduction ratio of 10, with an unprecedented actual torque density (92 kNm/m^3 , 15.4 Nm/kg), high efficiency for operation even at low temperatures (92% at -40°C and 500 rpm), and magnetic pollution levels compliant with ECSS requirement specifications. The results obtained showed a significant improvement in term of torque density and gear ratio compared to previous developments and prove that MGs are competitive against mechanical gearboxes.

During the project, the lessons learned are:

- High efficiency can be achieved for operation even at low temperatures by common techniques such as soft magnetic material lamination or selection of low conductivity materials.
- Efficiency and torque capacity are little affected by the environment temperature
- Sources of inaccuracy can be well predicted by FEM models. The deterministic nature of these errors allows multiple strategies to improve the accuracy and reduce the ripple.
- Magnetic pollution level is below ECSS standard requirements.

Acknowledgements and Previous Publication Record

This project was founded by ESA, under the contract number N° 4000113972/15/NLCBi/GM ITI activity. A general view of the three breadboard models developed under this activity was summarized in ESMATS proceedings 2017 [9]. This paper present original information and tests results never published before

References

1. E. W. Blackmore, "Radiation Effects of Protons on Samarium-Cobalt Permanent Magnets," *IEEE Trans. Nucl. Sci.*, vol. 32, no. 5, (October 1985) pp. 3669–3671.
2. J. Perez-Diaz, E. Diez-Jimenez, I. Valiente-Blanco, C. Cristache, M.-A. Alvarez-Valenzuela, J. Sanchez-Garcia-Casarrubios, C. Ferdeghini, F. Canepa, W. Hornig, G. Carbone, J. Plechacek, A. Amorim, T. Frederico, P. Gordo, J. Abreu, V. Sanz, E.-M. Ruiz-Navas, and J.-A. Martinez-Rojas, "Performance of Magnetic-Superconductor Non-Contact Harmonic Drive for Cryogenic Space Applications," *Machines*, vol. 3, no. 3, (July 2015) pp. 138–156.
3. N. Niguchi, K. Hirata, M. Muramatsu, and Y. Hayakawa, "Transmission torque characteristics in a magnetic gear," in *The XIX International Conference on Electrical Machines - ICEM 2010*, (september 2010) pp. 1–6.
4. J. L. Perez-Diaz, I. Valiente-Blanco, E. Diez-Jimenez, and J. Sanchez-Garcia-Casarrubios, "Superconducting noncontact device for precision positioning in cryogenic environments," *IEEE/ASME Trans. Mechatronics*, vol. 19, no. 2, (March 2014)pp 598-605
5. H. Komiyama and Y. Uchimura, "Contactless magnetic gear for robot control application," *Electr. Eng. Japan*, vol. 184, no. 4, (September 2013) pp. 32–41.
6. C. Cristache, E. Diez-jimenez, I. Valiente-blanco, J. Sanchez-Garcia-Casarrubios, and J. L. Perez-Diaz, "Aeronautical Magnetic Torque Limiter for Passive Protection against Overloads," *Machines*, vol. 4, nº. 17, 2016.
7. D. Painter, "A Comparative Study of the Performance Capabilities of Magnetic Gears," Portland, OR, January 2016.
8. ESA-ESTEC, "ECSS-E-ST-20-07C-Rev1 Space Engineering, Electromagnetic compatibility," 2012.
9. C. L. Bowman, "Design Issues for Using Magnetic Materials in Radiation Environments at Elevated Temperature," *Proc. Nucl. Emerg. Technol. Sp.* ,(February 2013) p. 6801.
10. K.Tsurumoto and S.Kikuchi, "A new magnetic gear using permanent magnet," *IEEE Trans. Magn.*, vol. 23, no. 5, (September 1987) pp. 3622–3624.
11. T. Fujita, Y. Ando, K. Nagaya, M. Oka, and T. Todaka, "Surface Magnet Gears with a New Magnet Arrangement and Optimal Shape of Stationary Pole Pieces," vol. 5 nº 6, (June 2013) pp. 243–249.
12. N. Iwasaki, M. Kitamura, and Y. Enomoto, "Optimal Design of Permanent Magnet Motor with Magnetic Gear and Prototype Verification," *Electr. Eng. Japan*, vol. 194, no. 1, (January 2016) pp. 60-69.
13. K. Atallah, S. D. Calverley, and D. Howe, "Design, analysis and realisation of a high-performance magnetic gear," *IEE Proc. - Electr. Power Appl.*, vol. 151, no. 2, (March 2004) pp. 135–143.
14. A. Penzkofer and K. Atallah, "Magnetic Gears for High Torque Applications," *IEEE Trans. Magn.*, vol. 50, no. 11, (December 2014) pp. 1–4.
15. K. Uppalapati, J. Z. Bird, J. Wright, J. Pitchard, M. Calvin, and W. Williams, "A magnetic gearbox with an active region torque density of 239Nm/L," in *IEEE Energy Conversion Congress and Exposition (ECCE)*, (September 2014), p. 1422–1428.
16. L. Brönn, R.-J. Wang, and M. J. Kamper, "Development of a shutter type magnetic gear," in *Proceedings of the 19th Southern African Universities Power Engineering Conference SAUPEC 2010, University of the Witwatersrand, Johannesburg*, January 2010.
17. J. L. Perez-Diaz, E. Diez-jimenez, C. Cristache, I. Valiente-blanco, M. A. Alvarez-Valenzuela, J. Sanchez-Garcia-Casarrubios, V. Castro, E. M. Ruiz-Navas, C. Ferdeghini, F. Canepa, H. W., G. Carbone, J. Plechacek, A. Amorin, J. Serrano, and V. Sanz, "Magnetic Non-Contact Harmonic Drive," *ASME Proc.*, November 2013.
18. F. T. Jorgensen, T. O. Andersen, and P. O. Rasmussen, "The Cycloid Permanent Magnetic Gear," *IEEE Trans. Ind. Appl.*, vol. 44, no. 6, (Nov-December 2008)pp. 1659–1665.
19. S. Kikuchi and K. Tsurumoto, "Design and characteristics of a new magnetic worm gear using permanent magnet," *IEEE Trans. Magn.*, vol. 29, no. 6, (November 1993), pp. 2923–2925.
20. R. Montague, C. Bingham, and K. Atallah, "Servo Control of Magnetic Gears," *IEEE/ASME Trans. Mechatronics*, vol. 17, no. 2, (April 2012) pp. 269–278.
21. J. Esnoz-Larraya, I. Valiente-Blanco, C. Cristache, J. Sanchez-Garcia-Casarrubios, F. Rodriguez-Celis, E. Diez-Jimenez, and J. L. Perez-Diaz, "Optimagdrive: High-Performance Magnetic Gears Development for Space Applications," *Proccedings of the ESMATS*, 2017.

22. E. W. Roberts, P. Bridgeman, M. Jansson, M. Schulke, and A. Tvaruzka, "The Performance and Life of Fluid-Lubricated Harmonic Drive® Gears," *Proceedings of the ESMATS*, 2015.

Qualification of a Networked Pyrotechnic Initiation System for the CST-100 Starliner Spacecraft

David Novotney*, Craig Boucher*, Joseph Smith*, Robert Morlath* and Hervens Beauge*

Abstract

Ensign-Bickford Aerospace & Defense (EBAD) Company has more than 60 years of continuous innovation in the field of space components and subsystems. While EBAD first developed linear explosive technologies such as Linear Shaped Charge for separation events on missile and manned space platforms, we have added newer technologies such as Non-Explosively Actuated (NEA) mechanisms made by our NEA Electronics and TiNi Aerospace subsidiaries for separation events on spacecraft launched in the last 15 years. The traditional method of pyrotechnic initiation on manned and Mars exploration platforms involve large batteries supplying high current pulses (greater than 5 amps) via heavy gauge wires to NASA or ESA Standard Initiators for U.S. and European-based platforms. EBAD developed a smart, networked initiation system several years ago as a means to simplify the complexity and lower the weight of the pyrotechnic initiation system. We recently completed qualification of this initiation system for Boeing's CST-100 Starliner spacecraft developed for NASA's Commercial Crew Development program and believe this technology has benefit to newer space platforms.

Introduction

Satellite and spacecraft platforms employ many "one-shot" devices and mechanisms for payload, communication, propulsion, and power systems. These mechanisms are used for solar array and antenna deployment, separation events, propulsion and instrument boom deployment, propulsion isolation valve actuation, and battery cell isolation switch activation. Critical timing of these events are magnified on manned and exploration platforms, where fast-acting pyrotechnic events are employed to assure achievement of millisecond timing and simultaneity of multiple events, especially during events for safe landing on Earth, Mars, or other space bodies.

The number of "one shot" events on manned and exploration platforms can range from more than fifty to greater than one hundred. This is also the case for many large geosynchronous satellite platforms and satellite constellation dispensing systems, where the number of "one shot" mechanisms can easily be greater than fifty. The tax on the power systems and weight / complexity of cable harnessing consume valuable resources that could be used for additional payload capability.

EBAD developed a smart networked initiation system several years ago as a means to simplify the complexity and lower the weight of the pyrotechnic initiation system. We recently completed qualification of this initiation system for Boeing's CST-100 Starliner spacecraft developed for NASA's Commercial Crew Development program. This system saved significant mass from the mission by simplifying the one-shot cable harnesses, and by lowering the peak power load required during pyrotechnic initiation. This paper discusses the networked initiation technology, the qualification effort for CST-100, and application for future satellite and spacecraft platforms, including future use with many non-pyrotechnic actuated devices.



* Ensign-Bickford Aerospace & Defense Company, Simsbury, CT

Smart Initiation System Background

EBAD's Smart Initiation architecture moves the ordnance initiation electronics typically found in a centralized firing controller to a within the initiator metallic housing. This creates a more efficient architecture as the firing circuitry is less than 25 mm (1 inch) away from the bridge element and one-shot events are commanded to actuate via a data bus rather than using point-to-point wiring. The initiation architecture consists of a small Initiation Controller (IC) capable of controlling more than 120 Smart Initiators (SI); the system elements are shown in Figure 1. Implementation of an architecture like this has resulted in a dramatic reduction in the size, weight, and power needed for firing of ordnance events on a missile and space platforms. EBAD also has a Smart Detonator (SD) configuration for applications where a detonation input is required.



*Figure 1. Smart Initiation System Elements.
Left to Right: Initiation Controller (IC) & Cable Harness, Smart Initiators (SI)*

Initiation Controller (IC) Functional Characteristics

The Initiation Controller (IC) provides the interface between the host vehicles' electrical/data interfaces and provides digital commands to Smart Initiators (SI) to perform arming, firing, and Built-In-Test functions. Commands are based on signals from the ground system or host vehicle and execute discrete commands and/or trigger a predetermined sequence of events. The IC does not change based on the number of SIs but rather on the mission profile and mission needs. The IC is a low-power electronics unit drawing less than 100 mA of quiescent current.

Smart Initiator (SI) Functional Characteristics

The Smart Initiator (SI) contains the arming and firing functions that are typically contained in a centralized firing controller. Each SI contains a unique address and is commanded to arm and fire by receiving digital commands over a data bus from the Initiation Controller (IC); it contains electronic safety interlocks that preclude inadvertent firing, provides Arming and Firing functions when commanded, and has extensive Built-In-Test capability. Initiator functional and safety characteristics are accomplished by having the proper physical, electrical, pyrotechnic, and software/firmware features in the SI. The SI provides a NASA Standard Initiator equivalent pyrotechnic (pressure-time/caloric) output.¹

Key Technologies for Size and Power Reduction

Two technological advances enabled the successful development and fielding of a smart initiation system. The first is the availability of small, low cost, reliable microelectronics that allows the integration of SI circuitry into a very small package. The second is the availability of a low-energy Semiconductor Bridge (SCB) element for initiation of pyrotechnic materials. The primary advantage of a SCB firing element is that it requires 1/100th the firing energy over conventional Hot Bridgewire (HBW) elements, enabling use of a small, capacitive discharge firing circuit. The SI trickle charges its firing capacitor during arming, drawing less than 10 mA during arming/firing versus a typical 5-A current draw for a NASA Standard Initiator or equivalent initiator. This is particularly important for systems where multiple events are required to be actuated simultaneously.

SCB Initiation Element Characteristics

Our SI design utilizes a Semiconductor Bridge (SCB) firing element manufactured by our SCB Technologies division in Albuquerque, NM. SCB technology was originally developed by Sandia National Labs in the mid-1980s as a low-energy replacement for HBW and Exploding Bridgewire devices. EBAD manufactures more than 10,000 SCB based initiation devices each year used in aerospace and industrial initiation applications.

SCB firing elements offer a significant reduction in the all-fire energy over conventional HBW devices, while meeting 1.0 A/1.0 W no-fire performance. The low-energy all-fire level of an SCB device is a direct result of the much smaller mass of a semiconductor bridge as compared to a typical HBW initiator. The all-fire energy for a typical SCB device is 200 microjoules, whereas the corresponding all-fire energy of an HBW initiator is greater than 25 millijoules. While the all-fire energy is low, the application of a short-duration, high-current pulse allows a SCB element to rapidly change from solid to plasma state in tens of microseconds, providing a convective heat transfer into the surrounding pyrotechnic material.²

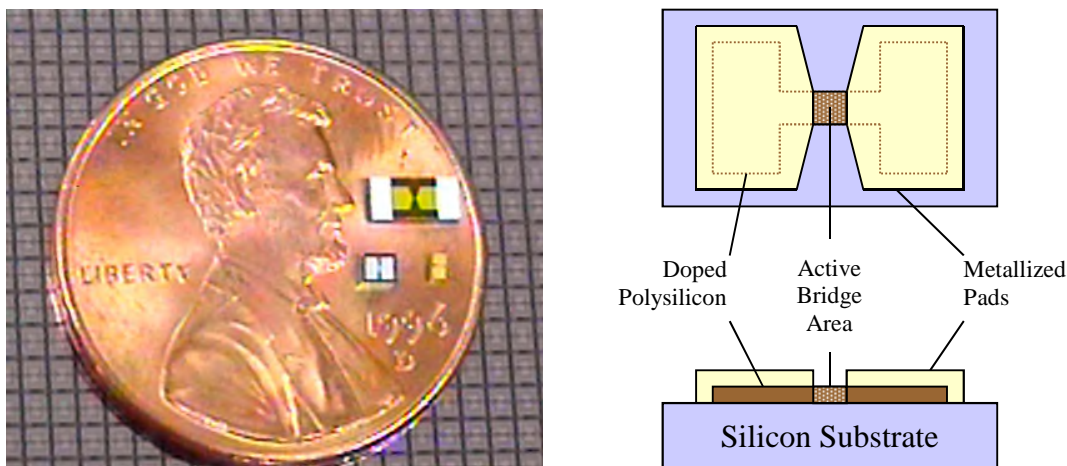


Figure 2. Semiconductor Bridge Construction

Smart Initiator Environmental Testing

Prior to application on the CST-100 program, EBAD successfully tested our SI to the following environments. This provided confidence that our SI could hold up to the rigors demanded by a manned spacecraft environmental qualification test program.

- Thermal Cycling: -54°C to 71°C
- Random Vibration: 111 grms, 180 sec/axis
- Pyrotechnic Shock: 14,000g peak
- EMI: CE102, CS101, CS106, CS116, RE102, RS103, TT101
- Ionizing Radiation: To 8.00E+7 Protons/cm²-sec flux, 5.39 kRadSi total dose

Prior Applications

Prior to CST-100, EBAD had significant test and fielding experience of our smart initiation system, having produced nearly 6000 smart initiators. Most of the applications were for tactical systems, so our SI had a Technology Readiness Level of 7 for manned space environments prior to our CST-100 qualification effort. Prior papers described our technology being applied to derivative systems: an RF safe Mobility Unit³ and a tactical missile divert and attitude control system⁴. Both applications demonstrated the technology could be configured to the custom application needs of divergent systems, and could be readily scaled up to relatively high production volumes.

Application to CST-100 Starliner

EBAD's Smart Initiation System was adopted for use on the CST-100 Starliner spacecraft for NASA's Commercial Crew Program. The benefit to the spacecraft was estimated savings of several hundred pounds in cabling, firing electronics, and pyrotechnic batteries over a traditional initiation system using heritage manned space HBW initiators. Our experience is that there are very few options on manned and exploration spacecraft that can offer mass savings of this magnitude.

Radiation Environments

Prior to selection for the CST-100 platform, our Smart Initiator (SI) electronics were subjected to radiation equivalent of 10X the estimated maximum mission life and worked flawlessly. Subsequently, EBAD has implemented a Radiation Lot Acceptance Test (RLAT) screening process on EEE parts used in our design to assure proper parts operation during radiation environments. Our design architecture has inherent immunity to Single Event Upset since initiators remain in a powered-off configuration until immediately prior to actuation when they enter a rapid Arm-Fire sequence. This sequence take place in less than several seconds, so probability to upset is minimized.

Devices Initiated

Our Smart Initiators (SI) and Smart Detonators (SD) were used to initiate many unique devices used on the CST-100 platform including separation nuts and bolts, cutters, frangible joints, and many other devices. While the photographs shown in Figure 3 are not necessarily the exact devices, they offer a good representation of the devices actuated on CST-100. EBAD provides the majority of the initiators, detonators, and pyrotechnically actuated devices used on CST-100 and other current manned platforms in the U.S.



*Figure 3. Types of Devices Initiated by Smart Initiators
Left to Right: Separation Nuts, Separation Bolts, Cutters, Frangible Joints*

Environmental Validation and Qualification

EBAD successfully completed an extensive validation and qualification test program for the CST-100 platform. Testing was first done at the SI and SD level, and subsequently at the device level, joining the SI and SDs to end effectors such as separation nuts. The total validation and qualification effort involved more than 700 Smart Initiators and Detonators. The environments were roughly within prior test levels. Some issues arose from self-induced shock, where there were high shock levels observed during actuation of the various devices used on the spacecraft to redundant initiators. While there were a few bumps during the test program, EBAD was able to fix these issues and successfully completed its qualification effort in 2017.

Application to Future Platforms

With the successful qualification for the CST-100 platform, this technology is being adopted on other platforms within the space community. One of the applications is coupling this technology with a non-explosive Split Spool Release Device (SSRD) offered by our NEA Electronics subsidiary. NEA SSRDs are widely used in the space industry for solar array, antenna reflector, payload release, and spacecraft separation and are well known for high preload capability while offering low shock separation. The weight and mass benefits can be similar for systems that use various one-shot technologies, although they were very pronounced for the CST-100 application due to the large number of pyrotechnic devices employed during the launch and subsequent re-entry events.



Figure 4. Example of an NEA SSRD Device

References

1. Boucher, C., and Novotney, D. B., "Performance Evaluation of an Addressable Integrated Ordnance System," AIAA 2001-3636, *37th AIAA/ASME/SAE/ASEE Joint Propulsion Conference and Exhibit*, Salt Lake City, UT, July 8-11, 2001.
2. Boucher, C., and Novotney, D. B., "Next Generation Semiconductor Bridge Initiators," AIAA 2000-3731, *36th AIAA/ASME/SAE/ASEE Joint Propulsion Conference and Exhibit*, Huntsville, AL, July 16-19, 2000.
3. Barglowski, M, and Boucher, C., "Advanced Ordnance Initiation System Development for a Unique Set of Requirements," AIAA 2002-4333, *38th AIAA/ASME/SAE/ASEE Joint Propulsion Conference and Exhibit*, Indianapolis, IN, July 7-10, 2002.
4. Novotney, D. B., and Kochanek, A., "Intelligent Initiation Systems for Divert and Attitude Control Applications," AIAA 2005-4502, *41st AIAA/ASME/SAE/ASEE Joint Propulsion Conference and Exhibit*, Tucson, AZ, July 10-13, 2005.

Use and Advantages of Direct-Drive Brushless DC Actuators for Precision Instrument Pointing of the Total and Spectral Solar Irradiance Sensor

Patrick Brown*, Andrew Engelmann* and Ryan Lewis*

Abstract

This paper describes the use of direct-drive brushless direct current (BLDC) actuators for precision solar pointing of the Total and Spectral Solar Irradiance Sensor (TSIS) instrument that is currently flying on the International Space Station (ISS). Advantages of direct-drive BLDC actuators compared to stepper-based actuators are described with an emphasis on the ability to provide excellent disturbance attenuation to base motion jitter. Lessons learned from incorporating direct-drive BLDC actuators into the TSIS system are presented to provide a context of the challenges that are associated with this technology. Finally, measured results from ground testing and on-orbit solar tracking are presented that demonstrate superior pointing performance compared to stepper-based actuators with solar tracking errors of less than 4 arcseconds 1σ per axis.

TSIS Instrument

TSIS is a NASA instrument designed, built, and operated by the Laboratory for Atmospheric and Space Physics (LASP) at the University of Colorado that continues the 39-year-long record of total solar irradiance (TSI) and 14-year-long record of spectral solar irradiance (SSI) [1]. Both TSI and SSI are critical to long-term climate monitoring. TSI is measured by the Total Irradiance Monitor (TIM), and SSI is measured by the Spectral Irradiance Monitor (SIM). These two sensors comprise the TSIS instrument along with the pointing system that will be discussed in this paper.

TSIS was launched to the International Space Station (ISS) on December 15, 2017 aboard a SpaceX Falcon 9 rocket in the Dragon trunk. It was then installed on the zenith side of the ISS at Site 5 of Express Logistics Carrier (ELC) 3 as shown in Figure 1. After robotic arm installation, the TSIS deployment system rotated the gimbaled instrument suite into its operational position above the ELC. TSIS's operational position above the ELC allows for a hemispherical view of the sky and solar viewing every orbit during its 5-year mission.

In order to perform solar measurements, TSIS must be pointed directly at the sun with less than 0.017 deg (60 arcseconds) 1σ precision while subject to movement by the nadir-pointed ISS. To decouple the TSIS instruments from ISS motion, the Thermal Pointing System (TPS) was developed. The TPS provides both thermal and pointing control for the TSIS scientific sensors; however, this paper is only concerned with the pointing aspects of the TPS.

* Laboratory for Atmospheric and Space Physics, University of Colorado, Boulder, CO

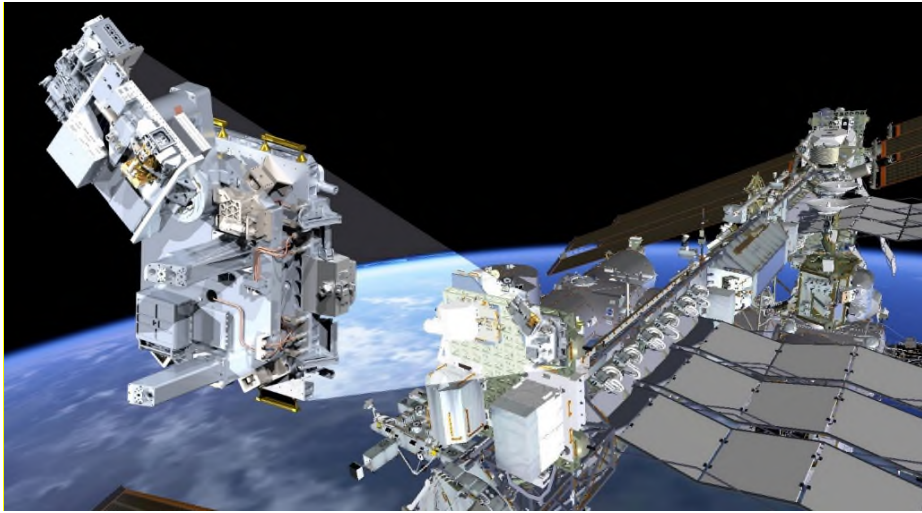


Figure 1. TSIS Instrument Shown at ELC-3 Mounting Location on ISS

TPS Hardware Configuration

The heart of the TPS is a two-axis, elevation over azimuth gimbal that points the instrument optical bench (including the SIM and TIM sensors) relative to the TSIS base plate as shown in Figure 2. The optical bench dimensions are 1.0-m wide by 0.9-m deep by 0.38-m tall with a moving mass of 83 kg and a rotational inertia of $10.2 \text{ kg}\cdot\text{m}^2$ about the azimuth axis and $3.8 \text{ kg}\cdot\text{m}^2$ about the elevation axis. BLDC actuators are used for both rotational axes and consist of the following key components: BLDC direct-drive motors, 2-speed (1x,16x) resolvers, brakes, twist capsules for signal/power feed-thru, and output duplex pair bearings. The TPS has a dedicated control electronics box that includes the drive electronics, a flight computer, power handling, and interfaces to the various TPS actuators and sensors. For closed-loop pointing control with respect to the sun, the TPS has redundant High-rate Fine Sun Sensors (HFSS) that are mounted on the optical bench near the TIM and SIM sensors. Finally, as already mentioned, the TPS includes a deployment system that rotates the optical bench to its operational position and holds it rigidly in place. Incidentally, the primary deployment actuator was derived directly from the NICER DAPS actuator that is also flying on the ISS [2].

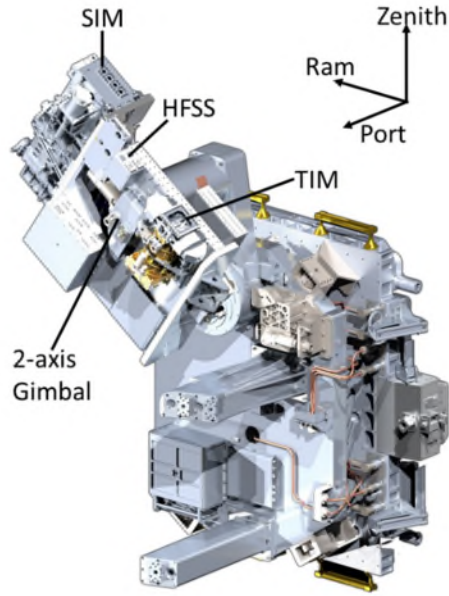


Figure 2. TSIS Instrument Components

Gimbal Motion Profile

TSIS follows approximately the same motion profile every orbit as shown by the example flight data in Figure 3. The azimuth axis provides the primary motion of the gimbal over the course of the orbit as it tracks the sun overhead from sunrise to sunset from +110 to -110 deg at a rate of approximately 4 deg/min. The elevation axis accounts primarily for variations in the solar beta angle that varies periodically every 60 days with annual maxima/minima of ± 75 deg. Additionally, both axes account for motion due to static and dynamic offsets of the ISS flight attitude relative to the Local Vertical-Local Horizontal reference frame. Also, the TPS points to zenith during every eclipse to support dark space measurements.

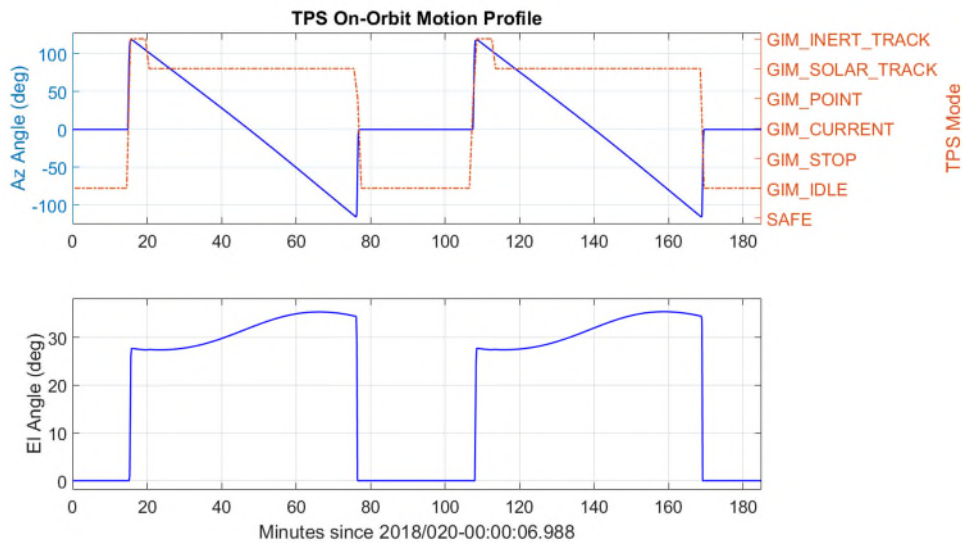


Figure 3. TPS Gimbal Motion Profile

ISS Jitter Environment

When TSIS was directed in 2014 to fly on the ISS, the ISS disturbance environment was poorly understood from a pointing perspective, which led to significant uncertainty in the effect that base motion-induced jitter

would have on TSIS pointing. In particular, very little information was available about ISS jitter and most of it focused on ISS vibration as it related to structural safety at non-ELC locations and not to pointing performance for external payloads on ELCs. The few payload studies that did exist attempted to apply translational acceleration measurements across the ISS structure in order to estimate angular jitter on the ELCs, and these estimates were near or close to the TSIS maximum allowable jitter. Additionally, due to the large physical scale and dynamic configuration of payloads, modules, and visiting vehicles, past predictions and measurements may differ or change spatially depending on mounting location and temporally as the station configuration evolves. Finally, it became clear that no procedural mechanism existed (or will exist) to manage ISS jitter, so instrument payloads (e.g., TSIS) must design their instruments to be robust to ISS jitter based on their own performance requirements and risk posture.

As an aside and a sign of progress, in the past year several ELC-mounted payloads, including OPALS [3], SAGE III, and now TSIS, have been able to successfully measure the jitter environment at their specific ELC mounting locations. It is anticipated that these new measurements will reduce the uncertainty in the ISS jitter environment for future payloads.

Actuator Selection

Faced with the uncertain jitter environment and other design accommodations specific to ISS, the LASP engineering team performed a detailed comparison between stepper-based actuators used on similar LASP pointing systems, including the TIM Pointing System for the Glory mission and a previous iteration of TSIS for the NPOESS mission, and direct-drive BLDC actuators. The next section will describe many of the differences in these actuators along with some of the key advantages BLDC motors can offer for precision pointing applications.

For context, it is worth mentioning that stepper-based actuators are usually intended for coarse pointing applications such as solar array drive mechanisms and antenna pointing mechanisms with typical pointing accuracies around 1 degree. By contrast, TSIS requires precision solar pointing with less than 60 arcseconds 1σ of jitter that is only marginally compatible with a common cardinal step size of \sim 30 arcseconds.

BLDC Advantages Compared to Stepper-Based Actuators

This section provides a qualitative description of many of the advantages that direct-drive BLDC actuators provide compared to stepper-based actuators in the hopes that it may be helpful to others trying to select an appropriate actuator type for precision pointing applications. For this comparison of space-borne actuators, it is assumed that the stepper motors are mated to harmonic drive based gear train to increase torque output and reduce step size. It is also assumed that the reader is familiar with both technologies, but expertise at the first-principals mathematical level is not required.

Continuous Torque Command Authority

A distinct advantage to stepper motors is their functional simplicity. The controller requests that the motor moves a number of steps (angle) and the motor responds by moving that amount. For simple applications where the step size is small relative to required angular precision, this open-loop approach is ideal for its set-it-and-forget-it simplicity.

However, for more precise applications, these benefits can become a liability. At an abstracted level, the stepper motor operates in a discrete manner as governed by the cardinal step size of the motor in combination with any additional gearing in the actuator. This is accomplished by applying a step change in power to the motor windings that results in a corresponding change in torque to the rotor. This torque moves the rotor along with the load to the next angular position with associated dynamic overshoot. If the desired angle is smaller than the step size, the controller is unable to reduce the angular error. This effect can be reduced somewhat through microstepping, but it comes at a cost of increased complexity and reduced holding torque while still subject to most of the limitations of stepper motors.

Alternatively, BLDC actuators can achieve much finer angular resolution due to the way they operate. Instead of commanding a number of steps (discrete torque step commands), the controller asks the motor to apply a continuously-variable current that translates directly to torque that results in corresponding continuous angular motion. Closed-loop control is then applied to achieve the desired angle with much finer resolution than could be achieved via the stepping approach.

Minimal Self-induced Jitter

Because of the step changes in torque application that are described above, stepper motors generate self-induced torque disturbances that result in oscillatory pointing jitter and associated torque disturbances reflected back to the spacecraft. This self-induced jitter is not directly controllable due to the fact that it is a byproduct of the system mechanics, but it can potentially be reduced by several means during the design phase (e.g., microstepping). Because these effects are fixed thereafter, they must be accounted for through appropriate, detailed analysis that demonstrates compatibility with the overall system design requirements. Doing so requires accurate analytic models of the stepper motor dynamics and the control excitation approach. However, these models include inherent nonlinearities (step commands) that complicate standard linear controls analysis. In past LASP programs, significant effort and time was spent modeling, predicting, and communicating the stepper motor disturbances produced by the solar array drives and the instrument pointing system to ensure mutual compatibility with each other and the spacecraft's attitude control system.

By contrast, because BLDC motors apply torque in a continuous rather than discrete manner, they do not produce oscillatory self-induced jitter like steppers do. This results in greatly reduced angular jitter and torque disturbances reflected back to the spacecraft, both of which are highly desirable goals. And because the torque application is applied continuously, the actuator dynamics of the BLDC motors can be accurately and simply modeled as linear systems that support standard linear controls analysis.

Increased Active Control Bandwidth

Stepper motor control circuits typically limit the maximum commanded step rate in order to avoid loss of motor synchronization, and this rate limiting in combination with the discrete step size has the associated effect of limiting the control bandwidth. While this limitation may be acceptable for coarse pointing applications, it can be a hindrance for more precise pointing applications where improved tracking and disturbance attenuation capabilities are needed.

In contrast, BLDC actuators behave linearly and are not rate limited in the same manner, so increased active control bandwidth can be achieved that allows for improved tracking of dynamic inputs and for increased active disturbance attenuation.

Structural Separation

A direct consequence of the harmonic drive-based gear train arrangement is that the actuator input and output are structurally coupled about the rotational axis with the coupling primarily determined by the stiffness and damping of the harmonic drive.

By comparison, direct-drive BLDC actuators have very little structural coupling between the input and output about the rotational axes, and the small couplings that do exist are primarily due to bearing friction, back EMF, and harness routing (e.g., twist capsules). Because the pointing goal of TSIS is to point at the sun, which is approximately fixed in inertial space compared to the rotational motion of the underlying spacecraft (ISS), structural separation is an important advantage that will be further expanded upon in the following paragraph.

Significant Increase in Base Disturbance Attenuation

When TSIS was comparing direct-drive BLDC to stepper-based actuators for the TPS on ISS, simulations were performed using representative actuator dynamics and load inertias to compare the output pointing responses of both actuator types to base motion disturbances. For an inertially pointed instrument such as TSIS, the objective is for the output motion (i.e., SIM and TIM sensors) to be as insensitive to input base

motion as possible (i.e., ISS jitter). These simulations were performed by exciting the base of a 1 degree of freedom actuator with a range of sinusoidal frequencies at fixed amplitude and comparing the output motion of the load when operating in both open-loop and closed-loop cases.

The stepper-based actuator results are shown in Figure 4 for open- and closed-loop cases. The y-axis shows the transmissibility, which is defined as the absolute value of the output magnitude to the input magnitude expressed in decibels. The x-axis shows the base excitation frequency in hertz on a log scale.

Examining the open-loop response, three regimes are present in different frequency ranges that are characteristic of a spring-mass-damper system subjected to base excitation. For low frequencies (< 5 Hz), the output motion tracks the input motion identically (0 dB) as a rigid body, which implies that any base motions are replicated exactly in the output. For mid-frequencies near the natural frequency (~11 Hz) of the load/actuator system, the output motion is amplified compared to the input motion by up to 14 dB (5x amplification). And finally, for higher frequencies above the natural frequency, the output motion is less than the input motion, which represents attenuation that is also referred to as seismic isolation. It is worth mentioning that for this characteristic, the larger the output inertia, the lower the natural frequency and the larger the frequency range of passive seismic (inertial) attenuation.

The closed-loop response assumes a control bandwidth that is much lower than the fundamental frequency, which is a reasonable assumption given the need to avoid active excitation of the fundamental mode. The response is nearly identical to the open-loop response, except that the closed-loop control is able to actively attenuate low-frequency base motion. This is an intuitive result given the successful implementation of solar arrays steppers to track the sun in the presence of slowly varying spacecraft base motion.

The key take-away of this plot is that a range of frequencies exist that can pose a risk to precise pointing where base motion jitter is either passed to the output in a rigid body manner or, even worse, amplified to magnitudes larger than the input frequency. If the base motion jitter is well understood and the predicted output is within allowable levels, this uncompensated jitter regime might be acceptable. But in the case of the poorly understood ISS jitter environment and with little margin in the pointing budget, this stepper motor characteristic posed a significant risk to the TSIS TPS jitter performance.

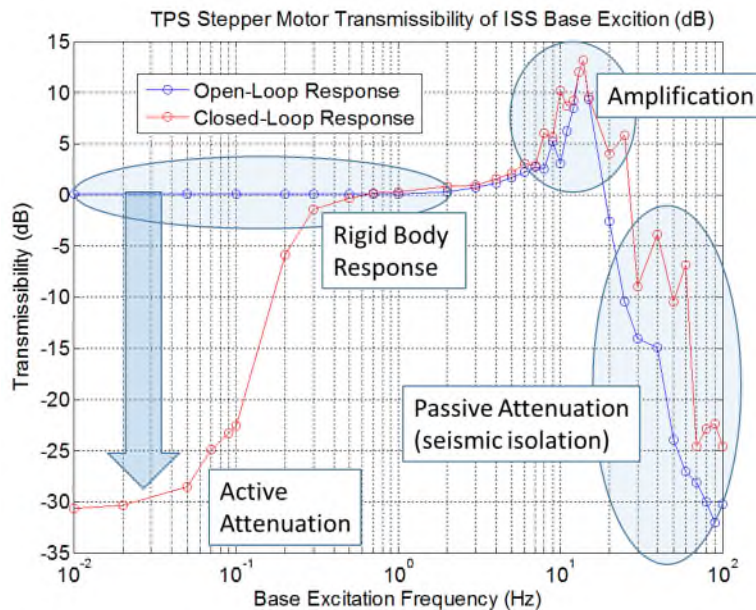


Figure 4. Stepper Frequency Regimes in Response to Base Excitation

Next, open-loop responses are compared between the stepper-based actuators that were just discussed and direct-drive BLDC actuators as shown in Figure 5. Because of the direct-drive aspect of the BLDC actuators that were described earlier as structural separation, the BLDC response has no significant resonance and the rigid body coupling is only present at low frequencies (< 1 Hz). In the same manner as the stepper-based actuators, seismic (inertial) isolation/attenuation is present but at a much lower frequency of ~1 Hz compared to ~15 Hz. This is a significant difference between the two actuator types that is capable of providing significant additional passive attenuation to base motion that increases with increasing load inertia.

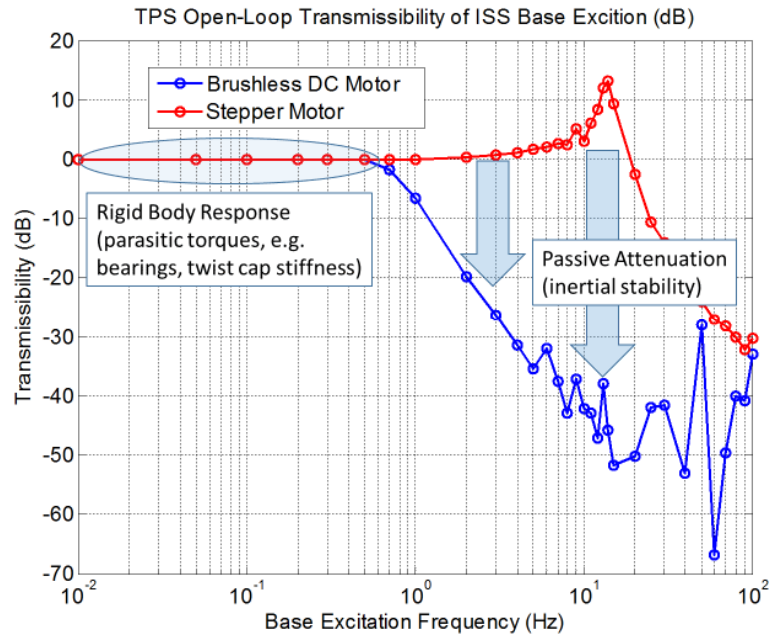


Figure 5. Comparison of BLDC to Stepper Open-Loop Responses

Finally, closed-loop responses are compared between the stepper-based actuators and direct-drive BLDC actuators as shown in Figure 6. The increased active control bandwidth of the BLDC actuator is able to complement the passive attenuation to produce the robust, broadband jitter attenuation that is shown in the plot. The BLDC actuator clearly provides increased attenuation across all frequencies compared to the stepper-based actuator with none of the significant rigid body and resonant susceptibility. For this reason, BLDC actuators were selected to provide a robust pointing solution for TSIS in the presence of the uncertain ISS jitter environment.

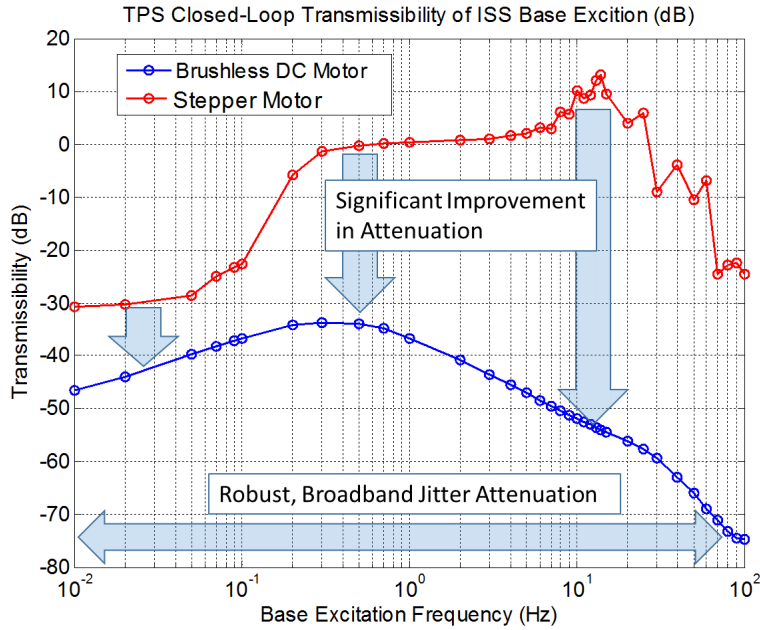


Figure 6. Comparison of BLDC to Stepper Closed-Loop Transmissibility Responses

Lessons Learned

Although direct-drive BLDC actuators can provide superior pointing performance compared to stepper-based actuators for precision pointing applications, there are associated challenges that were learned first-hand during TSIS development and will be shared here.

Control Electronics Complexity

Stepper control electronics are well understood and relatively easily matched to actuators for most applications. A prime reason is that the electronics operate open-loop with respect to the actuator motion. On the other hand, BLDC actuators require closed-loop control in order to function properly for pointing applications. Properly developing the closed-loop system that consists of the actuator, the feedback sensors, the drive electronics, and the control law is much more complicated than open-loop stepper electronics.

In particular, for TSIS, the electronics and motors were developed concurrently which often resulted in a case of the “chicken or the egg” for development decisions. In order to minimize this effect, prototype versions of the actuators and control electronics were developed and tested together to ensure mutual compatibility. This prototype approach is highly recommended.

Additionally, BLDC pointing performance is directly correlated to the feedback sensor performance, so the feedback sensor electronics are much more critical than they are for stepper-based actuators. Finally, having a configurable control law in software is much more complex and performance critical than most stepper commanding approaches. For all of these reasons, it is critical that sufficient resources are allocated for development of control/feedback sensor electronics and associated software if BLDC actuators are used.

Performance Dependent on Tuning

As originally mentioned, steppers use a simple set-it-and-forget-it control approach that does not require any tuning after they are built. BLDC actuators, on the other hand, require precise and frequent tuning in order to operate properly and meet requirements.

For TSIS, tuning was performed via direct frequency response measurements that applied sinusoidal command signals to the hardware and then measured the system response. Performing these measurements was quite time consuming and also had problems associated with the test hardware that further increased measurement time. On the other hand, the ability to take direct measurements of the system dynamics was enormously beneficial in the ability to tune the system, correlate models, and improve confidence in the system performance.

Tuning was performed quite frequently throughout the integration and test (I&T) program in order to match controller tuning to the specific hardware configuration (mechanical and electrical) that evolved and changed numerous times (10+) during I&T. Taken together with the duration of each measurement, tuning added significant, yet important, time to the program schedule. In the future, a software-based tuning approach may be developed that could reduce the measurement time for each of these tuning activities.

Center of Gravity Sensitivity

Because the BLDC actuators are directly coupled, they are particularly sensitive to offsets in the center of gravity (CG) of the instrument payload mass relative to the intersection of the rotational axes in two main ways. First, on-orbit translation disturbances couple into rotational disturbances via the offset CG. Second, ground testing may require offload/balancing ground support equipment (GSE) to account for gravity-induced torques. Additionally, the configuration change associated with any balancing GSE may necessitate separate controller tuning. For these reasons, it is highly desirable to locate the CG of the moving mass as close to the rotational axes intersection as is reasonably possible.

Bearing Friction Sensitivity

Bearing friction is a dominant dynamic that affects BLDC motor control and the limits of performance. In general, the friction should be as small as possible and as linear as possible. Of course, this is challenging to achieve given other constraints on the system. In particular, bearings that carry significant launch loads need to be appropriately large and with sufficiently high preload, both of which increase bearing friction.

Although suggested methods exist to select proper preload and Hertzian contact stress, a perfect approach does not exist that is as good as experience with actual hardware. For this reason, early testing and measurements are particularly valuable to understanding and compensating for bearing friction.

Unpowered Free Motion

An obvious direct consequence of a direct-drive system with low friction is that it will experience free motion when not powered. This was accounted for by including brakes in the actuator design that operate in the unpowered state. But as an additional mechanism, the brakes added their own complexities to the system design and operation that would have been easily accounted for by detent torque in a stepper-based actuator. Nonetheless, the brakes did function properly and prevent free motion when TSIS is unpowered on-orbit.

Structural Coupling

Even though the primary structural mode associated with the stepper-based harmonic drive was eliminated by selecting direct-drive BLDC actuators, structural dynamics still had to be accounted for to ensure successful actuator operation. In particular, it is important to provide frequency separation between the controller bandwidth and the structural modes in order to avoid resonant excitation of those modes. This was accomplished through frequent mechanical design iteration and communication between the mechanical engineers and the controls engineers. Additionally, to reduce risk, modal testing of the TPS structure was performed that was able to identify the structural modes and damping. The measured modes were actually closer to the controller bandwidth than was desired, but frequency response measurements of actuator control loops showed acceptable bending margins without any excitation of the structural modes. This was attributed to higher than originally predicted structural damping, which was attributed to the specific mechanical architecture of the TSIS system. One important lesson learned was that structural damping can be extremely beneficial to ensuring compatibility between the structural and control design,

and that there is no substitute for direct measurements because they may differ dramatically compared to predictions.

End-to-End Testing

Appropriate end-to-end testing is invaluable for any space-borne system, and it definitely holds true for BLDC-based systems because of all the lessons that were previously described. In addition to the prototype testing, frequency response measurements, and modal testing, TSIS performed a rigorous end-to-end test program that exercised every pointing mode in a flight-like manner that even included physical simulations of the rotating ISS with an inertially fixed sun as shown in Figure 7. As the following section will attest, all of this testing contributed positively to the successful operation and performance of the TSIS TPS when it reached orbit.

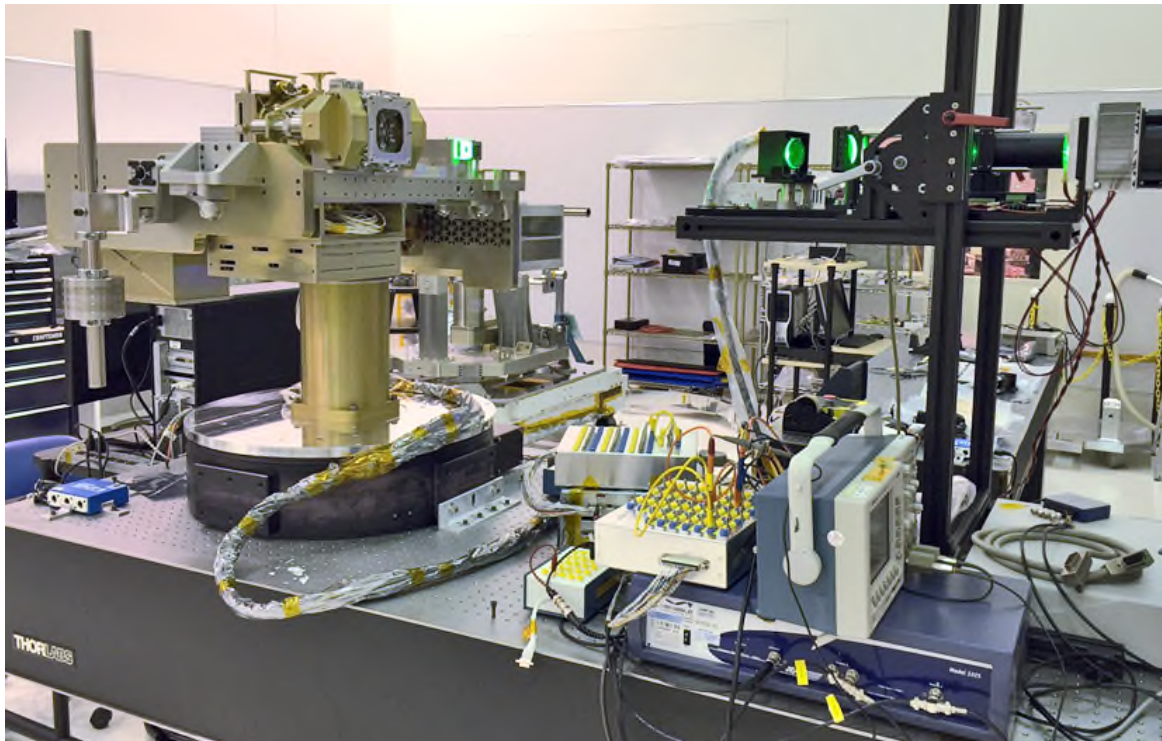


Figure 7. TSIS TPS Test Configuration During Subsystem Characterization

Results

In spite of the challenges that were associated with using direct-drive BLDC actuators, excellent results were achieved during the test program and during early on-orbit operations that confirmed the many benefits of BLDC actuators for precision pointing. A small sampling of results is shown in this section.

Stepper Performance Baseline

For comparison, correlated simulation results from an earlier, NPOESS-era of the TSIS TPS design are presented in Figure 8. These results show the residual azimuth axis error of 33 arcseconds 1σ when solar tracking at ~ 3.6 deg/min without any additional structural error (10 arcseconds 1σ) or spacecraft base motion (41 arcseconds 1σ). This residual motion profile was a consequence of commanding steps at ~ 8

steps/s which repeatedly excited the first mode (~11 Hz). When considering all of these error sources, the 60 arcseconds 1σ requirement was only marginally satisfied.

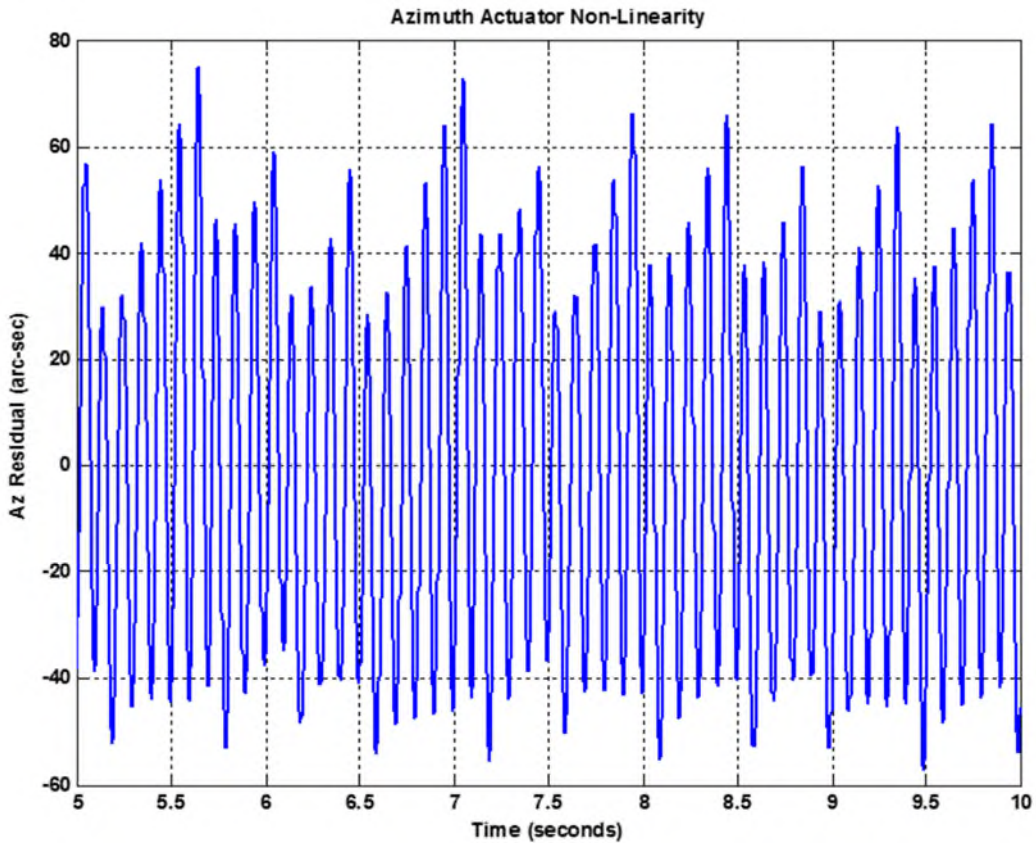


Figure 8. TPS Residual Jitter Motion for NPOESS-era Design

Disturbance Transfer Function Measurements

As previously described, frequency response measurements of the BLDC actuators were performed frequently throughout the test program, and these measurements included different transfer functions including the transfer function shown in Figure 9. This plot shows the modeled and measured “input” disturbance transfer function that is an indication of how well the closed-loop BLDC actuator is at attenuating torque disturbances. This disturbance transfer function was selected because it can be readily measured in the lab, whereas the previously discussed BLDC closed-loop transmissibility transfer function in Figure 6 would require a shaker-table approach for direct measurement that was beyond the scope of the TSIS program. The as-built system agrees extremely well with the modeled dynamics and shows robust, broadband disturbance attenuation that far exceeds a stepper/harmonic drive-based actuator and serves as the best measurement of robust disturbance attenuation for this system.

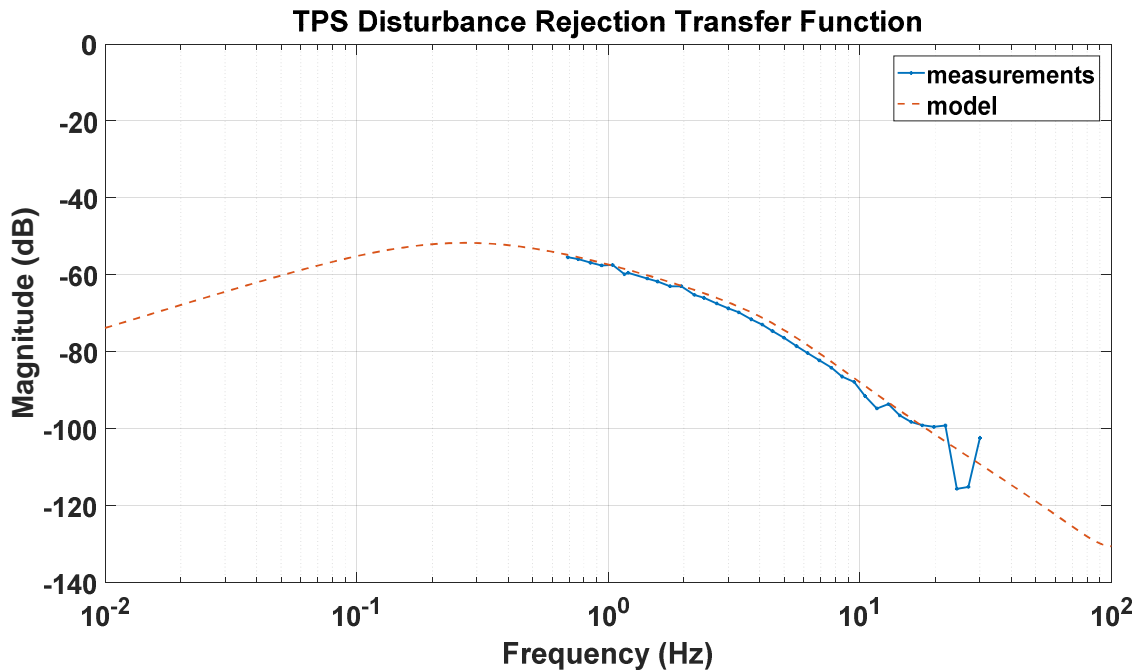


Figure 9. Measured Input Disturbance Transfer Function

Ground-Testing Solar Tracking Errors

After the BLDC control loops were properly tuned using the frequency response measurement approach previously discussed, steady-state solar tracking tests were performed using the test apparatus shown in Figure 7 that included ISS base motion simulated by a rotational stage and a fixed solar simulator.

Figure 10 shows the steady-state solar tracking errors (self-induced jitter) for the azimuth axis during ground testing as measured by the High-rate Fine Sun Sensor (HFSS). The HFSS errors are shown in magenta/red, and an independent angular measurement was provided by a ring laser gyro (RLG) shown in blue that tracks the HFSS errors throughout the dataset. The measured HFSS error is 6 arcseconds 1σ over this dataset, and the RLG error is slightly less at 4 arcseconds 1σ because it is only measuring the mechanical motion and not the optical noise from the solar stimulus. This dataset was of high importance during the test program because it demonstrated that the BLDC actuators were capable of providing very low self-induced jitter compared to the 60 arcseconds 1σ requirement and compared to the stepper motor results from Figure 8.

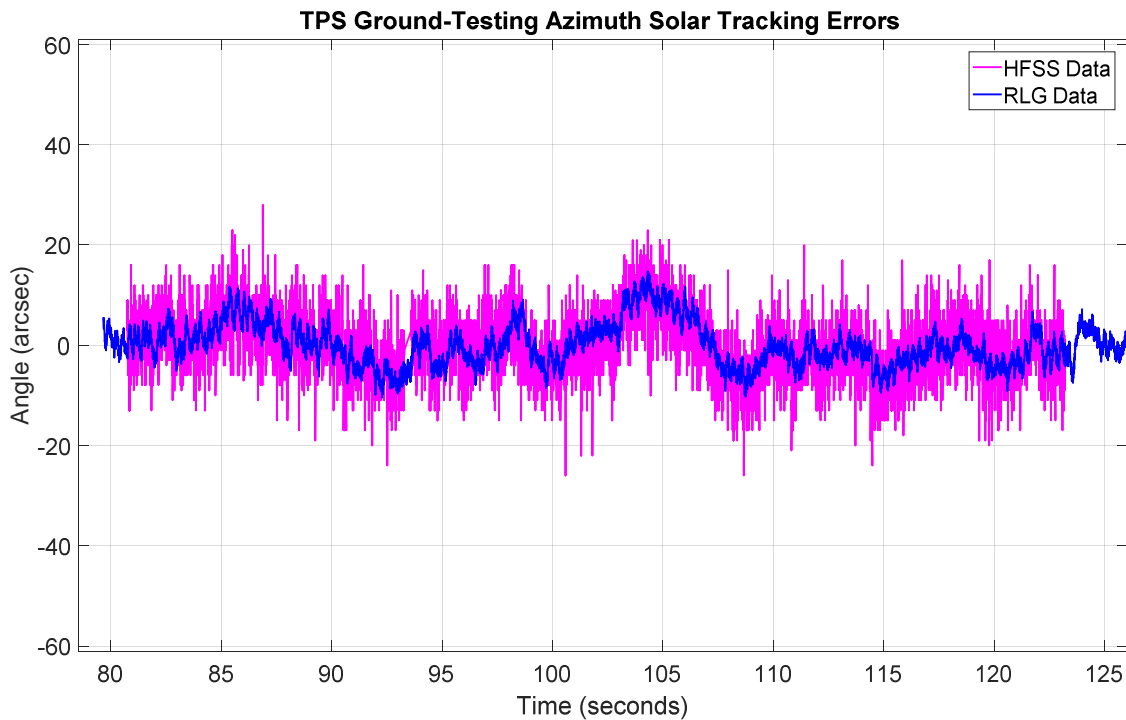


Figure 10. Solar Tracking Errors during Ground Testing

On-Orbit Solar Tracking Errors

As encouraging as the ground-testing results were, the true test of pointing performance was only possible with the TPS operating on-orbit. During the early-orbit commissioning program, all of the TPS functionality was exercised, which provided an opportune time to record high-rate 200-Hz measurements that are not available during nominal operations and are able to reveal high-frequency pointing characteristics.

Figure 11 shows the azimuth and elevation solar tracking errors as measured by the HFSS at the native control execution rate of 200 Hz. The measured pointing performance was slightly improved compared to the ground-test measurements with 4 arcseconds 1σ in the azimuth axis and 2 arcseconds 1σ in the elevation axis. Additional high-rate and low-rate pointing measurements from throughout the flight mission are all consistent with these results. This performance easily satisfies the jitter requirement of 60 arcseconds 1σ and is a dramatic improvement compared to the stepper actuator approach from the TSIS NPOESS-era in Figure 9. This significant improvement in pointing performance is a direct consequence of using direct-drive BLDC actuators instead of stepper-based actuators that will allow the TSIS scientific sensors to perform their critical measurements while pointed directly at the sun.

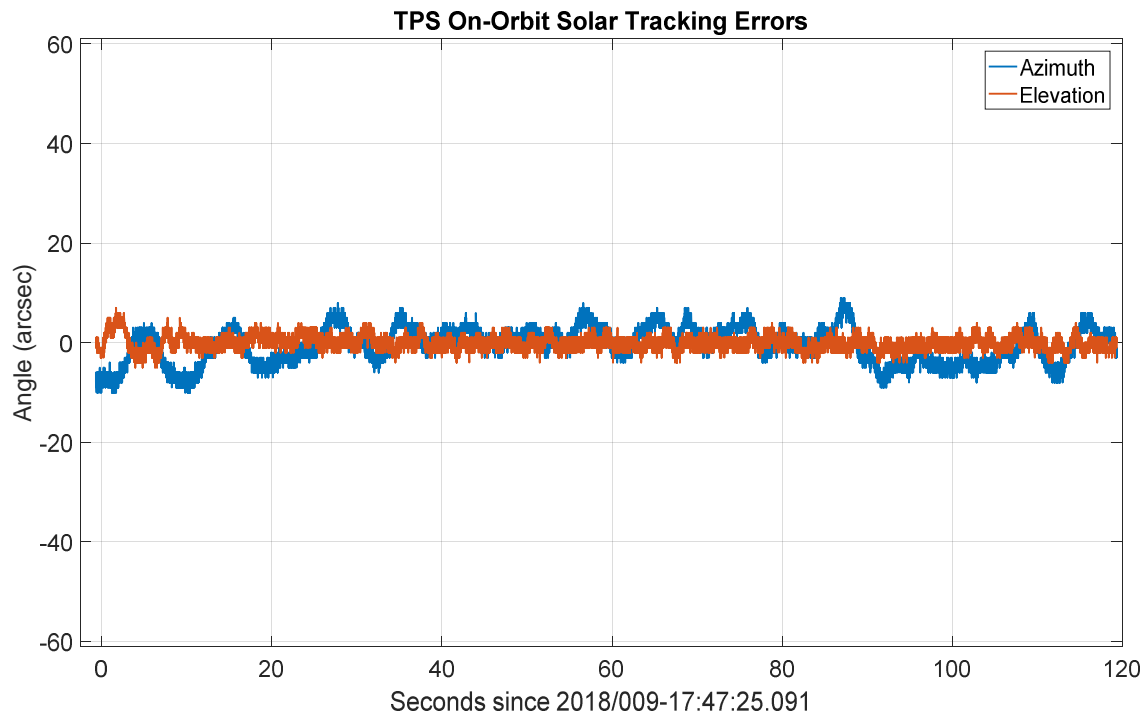


Figure 11. On-Orbit Solar Tracking Errors

Conclusion

Direct-drive BLDC actuators were selected and used for 2-axis solar pointing of the TSIS instrument payload on the ISS and have provided improved performance compared to stepper-based actuators due to a number of advantages. These advantages include continuous torque command authority, minimal self-induced jitter, increased active control bandwidth, and structural separation, all of which produce a dramatic increase in base disturbance attenuation and greatly reduced tracking errors.

As part of implementing the BLDC actuators for TSIS, many challenges were overcome and lessons were learned regarding control electronics complexity, the importance of controller tuning, sensitivity to center of gravity and bearing friction, how to account for unpowered free motion, the effect of structural coupling to closed-loop control, and the importance of end-to-end testing.

Pointing performance was greatly improved compared to stepper-based values as evidenced by the ground-test measurements of the disturbance transfer function that shows excellent broadband attenuation and of the solar tracking errors that show significantly lower self-induced jitter. The culmination of this effort are the on-orbit results that show solar tracking errors less than 4 arcseconds 1σ per axis, which provides ample margin compared to the requirement of 60 arcseconds 1σ .

References

1. LASP Website for TSIS: <http://lasp.colorado.edu/home/missions-projects/quick-facts-tsis/>
2. J. Budinoff, et al "Development of a Deployment and Latching Mechanism for a Pointing System on the Neutron Star Interior Composition Explorer (NICER) for Goddard Space Flight Center" *Proceedings of the 43rd Aerospace Mechanisms Symposium*, (May 2016), pp. 261-268
3. B. Oaida, D. Bayard, M. Abrahamson "On-orbit Measurement of ISS Vibrations during OPALS Extended Mission Operations" *IEEE Aerospace Conference* (2017)

Testing and Maturing a Mass Translating Mechanism for a Deep Space CubeSat

Alex Few*, Tiffany Lockett*, Richard Wilson**, David Boling** and Erik Loper*

Abstract

Near Earth Asteroid (NEA) Scout is a deep space satellite set to launch aboard NASA's Exploration Mission 1. The spacecraft fits within a CubeSat standard 6U (about 300 x 200 x 100 mm) and is designed to travel 1 AU over a 2.5-year mission to observe NEA VG 1991. The spacecraft will use an 86-m² solar sail to maneuver from lunar orbit to the NEA. One of the critical mechanisms aboard NEA Scout, the Active Mass Translator (AMT), has gone through rigorous design and test cycles since its conception in July of 2015. The AMT is a two-axis translation table required to balance the spacecraft's center of mass and solar sail center of pressure while also trimming disturbance torque created by off-nominal sail conditions. The AMT has very limited mass and volume requirements but is still required to deliver a large translation range—about 160 x 68 mm—at sub-mm accuracy and precision. The system is constrained to operate in complete exposure to space with limited power and data budgets for mechanical and thermal needs. The NEA Scout team developed and carried out a rigorous test suite for the prototype and engineering development unit (EDU). These tests uncovered numerous design failures and led to many failure investigations and iteration cycles. A paper was previously presented at the 43rd Aerospace Mechanisms Symposia entitled, 'Development of a High Performance, Low Profile Translation Table with Wire Feedthrough for a Deep Space CubeSat'. This paper will make note of specific lessons learned: manufacturing philosophy, testing ideologies for high-risk missions, thermal mitigation design for small, motor-driven mechanisms.

Introduction

The Near Earth Asteroid (NEA) Scout flight mission discovered the need for an active mechanism for controlling the location of center of pressure in relation to the center of mass during the early design phase of the mission, post preliminary design review. The Active Mass Translator (AMT) was then conceived and passed through Critical Design Review in July 2016 with minimum breadboard and bench top testing. The engineering team planned and prepared test procedures, facilities and a rigorous test schedule to meet the approaching flight hardware delivery date at the time. Due to resource constraints, the AMT design and development was handled by the same team producing the NEA Scout solar sail subsystem (Figure 1).

* NASA Marshall Space Flight Center, Huntsville, AL

** Jacobs Technologies, Huntsville, AL

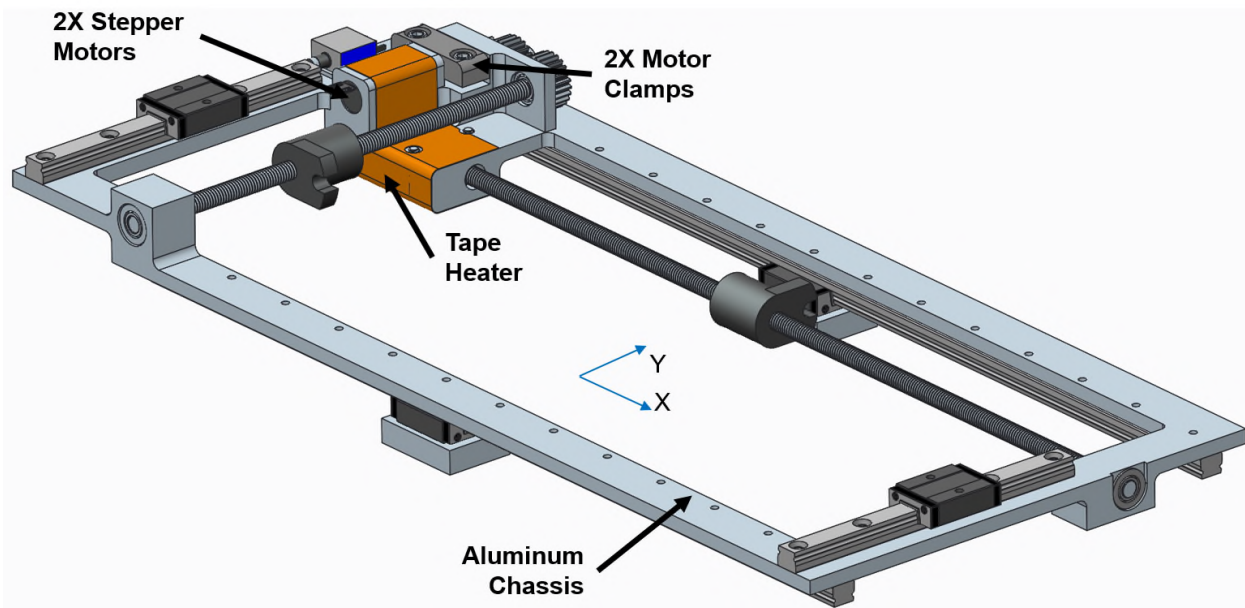


Figure 1. AMT design

The late addition to the flight mission introduced a schedule, cost, and volume constraint that maintained minimal margins for design development. The test approach for this high risk project was to perform as needed development tests with prototype units and environmental tests on a high fidelity design unit. The team utilized 3D printed ABS plastic prototypes, commercial parts and motors, and ambient environments to perform first order functional tests.

For the prototype units, the project accepted the risk of an outside vendor using CAD models to produce the mechanical parts. The cost and schedule approach was advantageous due to the low cost for each piece part and the quick turnaround for product delivery. The out-of-house manufacturing shop imported CAD models and produced hardware without needing a formal drawing. Navigating around the formal drawing release process reduced schedule by 6 weeks.

To reduce risk for the flight unit, the team adhered to the Marshall Space Flight Center flight hardware approved vendor list which did not include the manufacturing shop that produced the high-fidelity engineering units. This decision cost the project time with reintroducing the hardware to a new manufacturer. The flight hardware manufacturing company still operated with released drawings and configuration control. The drawings up to that point in the project were only issued drawings, requiring little oversight and signatures. The team had to build flight-quality release drawings and adhere to the quality control process.

Class D high-risk missions have the ability to tailor center-level mandates for development flight hardware build and manufacturing. The institutional understanding of that tailored approach was a technical and programmatic challenge. A major lesson learned was to clearly communicate and repeat constantly the project approach and risk posture for accepting lean manufacturing and acceptance processes. The knowledge lost between the development hardware manufacturer and the flight hardware manufacturer was not negligible. The team learned that using the same manufacturer for development and flight in the future would greatly reduce the quality assurance concerns upon flight hardware acceptance.

Repairing a Poor Thermal Design

After the engineering development unit (EDU) hardware was manufactured, accepted, and assembled on center, the bench top and environmental testing began. The team planned full functional tests, small lab vibration tests, thermal bake out, and a thermal vacuum test. The thermal vacuum test followed the same temperature profile as the solar sail subsystem and utilized NASA Marshall Space Flight Center environment test chambers. The on-site location was beneficial for off-nominal hour support.

The purpose of the thermal vacuum testing was to demonstrate the full functionality of the system in estimated limits of the cold and hot environments to be experienced on orbit. The engineering unit went through a thermal bake out for contamination control reasons at 80°C. The engineering unit was expected to see cold temperatures at -70°C and hot temperatures at 70°C. The unit would cycle through the hot and cold temperatures four times in vacuum with functional tests completed before test, during each cold and hot cycle, and after the test was completed.

The first thermal vacuum test had a successful functional test completed before the chamber door was closed. The ambient temperature was 23°C. Once the door was closed and before vacuum pump down, the AMT performed a limited functional test to ensure connection to the hardware was maintained. The test was completed successfully. After an 8-hour vacuum pump down, the AMT performed a limited functional test at ambient temperature with a pressure of 1.0E-5 Torr. After initial movement, the motors displayed abnormal behavior, then stalled. The test was halted.

After the TVAC failure, the NEA Scout design team met and constructed a detailed fault tree to determine as many failure causes as possible. This was crucial to ensure that no stone was left unturned, nor that the personal strengths and biases led to unconscious oversight of less obvious sources. The team produced 95% answer almost immediately: The stepper motors' internal coils had overheated and shorted. This was confirmed with impedance data and a day-of conversation with the vendor.

For the next few weeks, the team unearthed 3 root causes that led to this failure. First, the control board had provided 2.25x the motors' rated current. Second, the thermal design did not provide enough contact area to allow heat to escape the motors via conduction. Third, there was a clear misunderstanding of the motor's internal heat path and how residual heat could be dissipated.

Control Board Input Error

The first issue, the motor overcurrent, was remedied rather quickly. The board was reprogrammed to gradually accelerate the motors speed using a simple ramp. The overcurrent error had been hidden for two reasons. First, human error had the control board programmed to 2.25x nominal current. At low speeds, the ramping function is not critical, and a nominal current supply can accommodate for an instantaneous change from rest to operational speed, known as a step input. The vendor noted that these motors could handle a step input up to 1000 RPMs, but our motor was set to run at about 8000 RPMs.

At lower currents, the motor was stalled because there was not enough magnetic force to accelerate the motor from rest to the desired speed. The control board current output was increased until the motor operated, and the current output was not checked against the data sheet. This was the primary error.

Insufficient Thermal Conduction

Second, the small stepper motors predominant thermodynamic process is convection. Even at 2.25x power, the motors surface temperature barely fluctuates in atmosphere giving no tactile evidence that the motors were under thermal or mechanical stress. Once the motors entered vacuum, the overcurrent compounded by a poor thermal path led to motor failure in just seconds. Figure 2 shows the actual size of the motors and Figure 3 shows results from bench top tests comparing surface temperature rise versus time for multiple current inputs.



Figure 2. Size comparison of 6-mm stepper

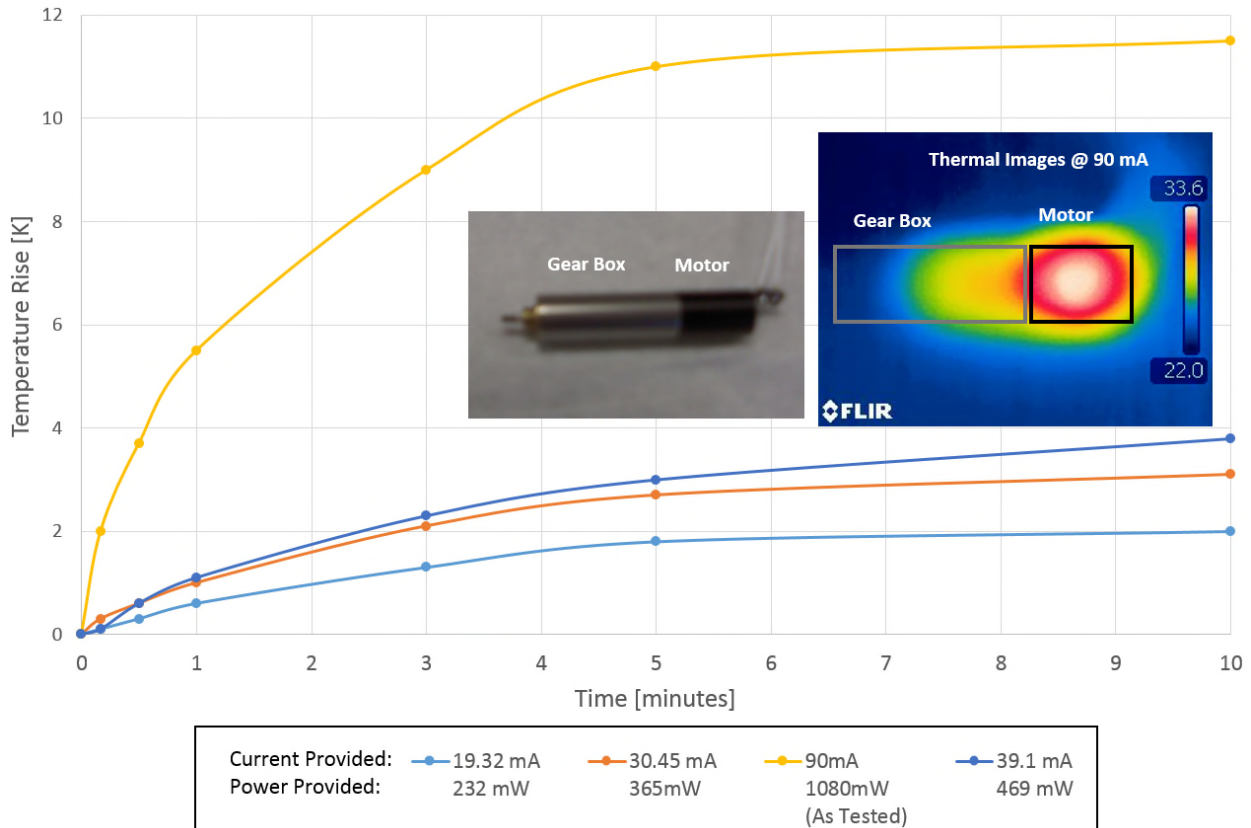


Figure 3. 6-mm stepper motor temperature rise vs. time with varying current inputs to determine sensitivity to conduction.

The motors did not have suitable mechanical joints to the structure to allow for effective thermal conduction. Early in the design phase, the motor vendor provided mechanical fastening information. Their suggestion—to clamp the motors on the gearbox end near the output shaft—was typical for most applications, but we soon learned that our vacuum environment required a very different design (Figure 4).

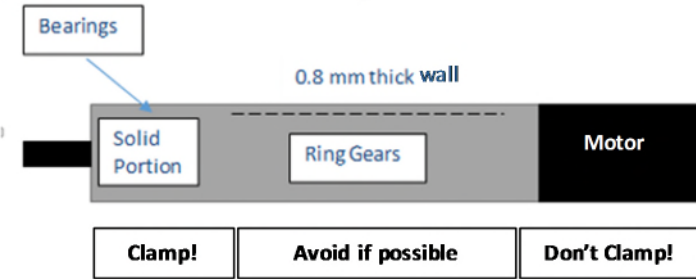


Figure 4. Simple motor diagram showing where clamps should be applied (near left-most areas, away from the motor).

The motors had been clamped near the end of the gearbox, a location opposite of the motor coils (Figure 5). Due to the construction of the motor, the gearbox and clamps were almost completely thermally isolated from the heat source due to little contact areas between internal ball bearings, planetary gears, and a magnetically powered rotor. Therefore, the design did not allow a conduction path between the coils and the AMT structure.



Figure 5. Application of clamping suggestion, CAD on left, EDU on right.

The FDM0620 motors, not including the gearbox, are the same size as a mechanical pencil eraser and weigh just 1 gram. With negligible surface area and thermal mass, the 0.5 W of power destroyed the motors in seconds. FLIR images, as seen in Figure 3, show the case temperatures elevating just a few degrees above ambient in atmosphere, even without any significant external conductive path. More accurate thermal models estimated temperature deltas in the 200°C range for vacuum if the conductive path went unchanged.

A new clamp design and thermal interface material was used to mitigate the issue. The new clamps covered almost all of the motor's cylindrical surface and a thin layer of conductive material added between the two clamp halves and the motor and gearbox casings (Figure 6). Three interface materials such as conductive greases, epoxies, and thermal springs were traded. Figure 7 shows the updated thermal analysis results without thermal interface materials, then compares the three interface material options. The three bars for each data set show the steady state coil temperature at 70°C, 20°C and -70°C.

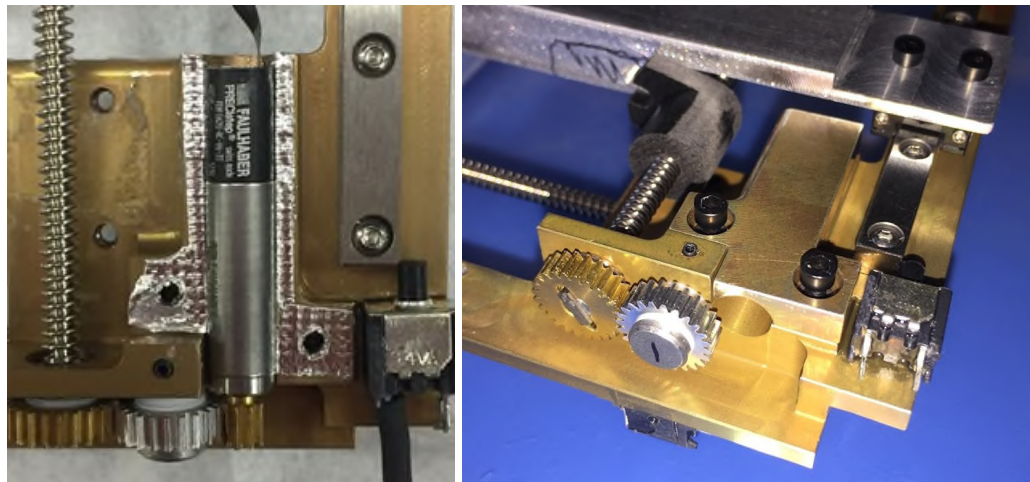


Figure 6. New clamp design: a motor test fit (L) and a motor-less clamp fit up (R).

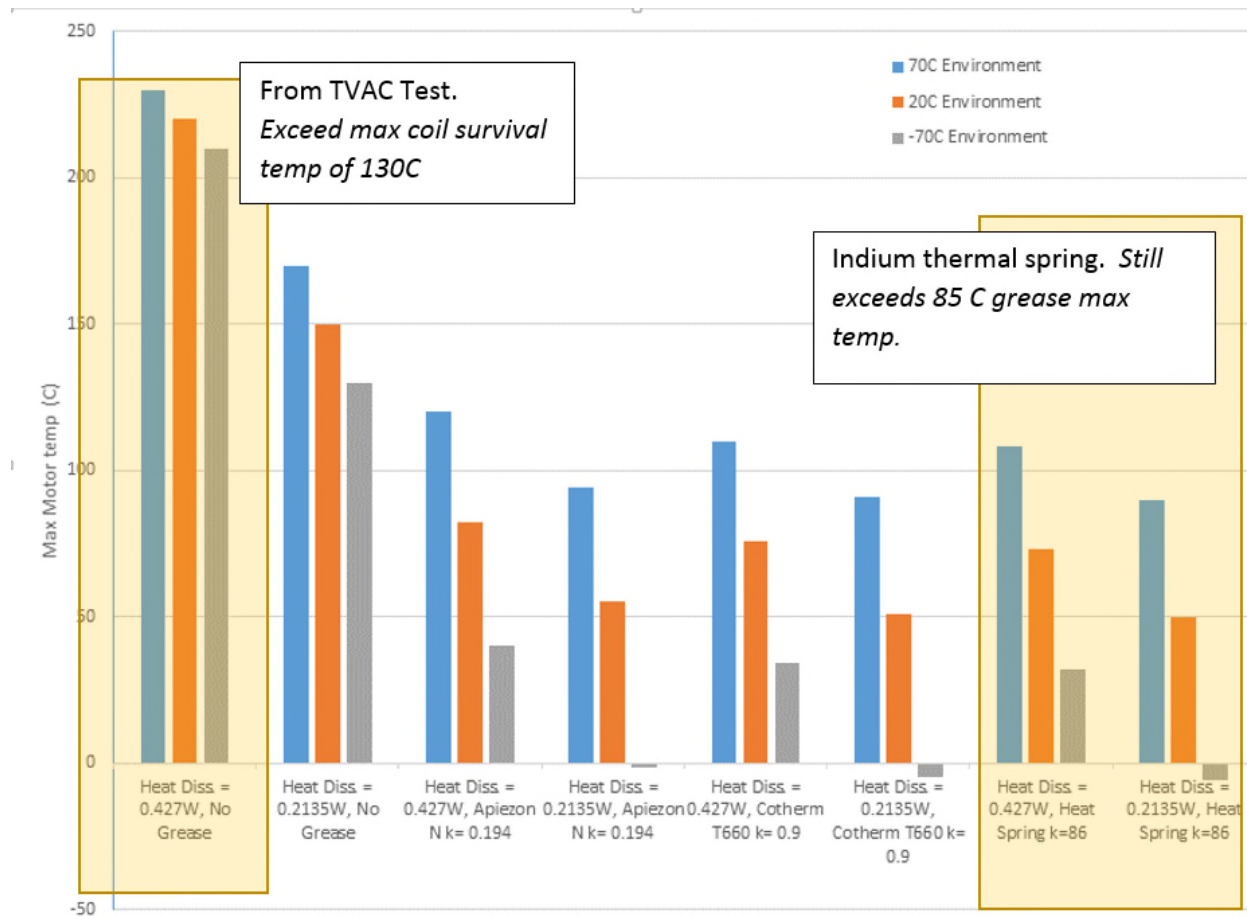


Figure 7. Thermal analysis data after updating internal conductive paths. Three conductive material were traded at varying temperatures and heat dissipation levels: Apiezon thermal grease, Cotherm T660, and Indium heat spring.

The 8 columns are divided into 4 pairs. Each pair describes the maximum temperature for each clamp interface material option. The first column is for when both AMT motors are powered, producing 427 mW of residual heat, and the second column describes one motor under power, producing 213 mW of residual heat.

Requirements to avoid offgassing, have a very high thermal conductivity, and simple disassembly directed the team towards the indium thermal spring. This material has high thermal conductive properties, is compressible (allowing for machining tolerances and clamping applications), and is common in space flight electronics. After taking a few weeks to redesign the AMT chassis to include the larger clamps and indium interface material, the team then set to properly understand the motor's internal conductive path (Figure 8).

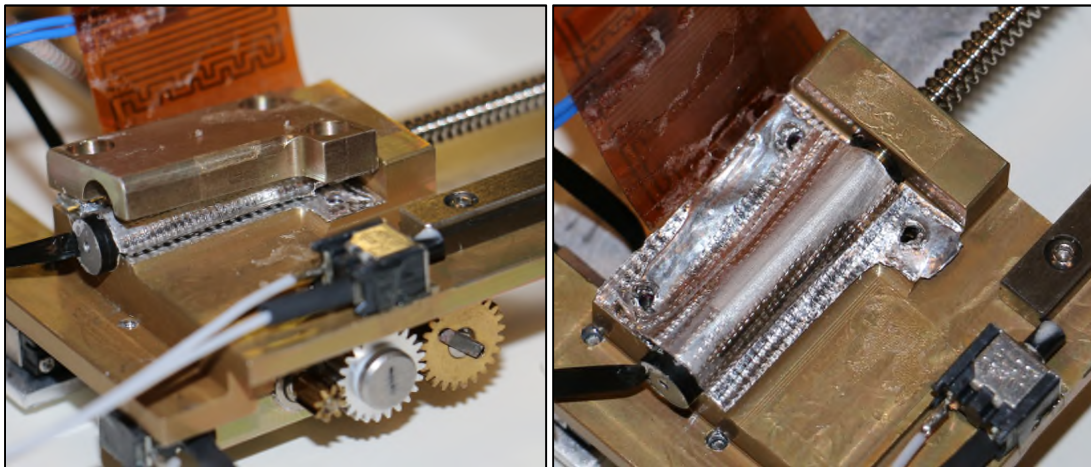


Figure 8. New clamp design showing compressed indium. Notice the textures. This perforated surface is characteristic of the uncompressed material. The indium sheet will flatten when compressed.

Misunderstood Motor Internal Design

The third issue uncovered during the failure investigation was the team's lack of knowledge of the motors internal design. Though it is common for vendors not to present *all* design data for a customer, we asked, and asked often. The vendor was responsive, uncommonly understanding and provided all data that was available.

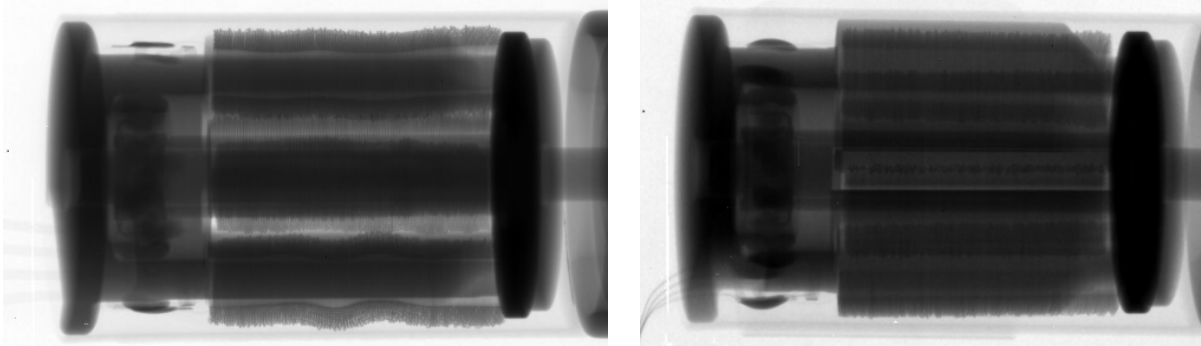


Figure 9. X-ray of failed motor (left) and new motor (right). Note the irregularities in the failed motor most likely created from temperature spikes.

In addition to consulting the vendor for internal design information, the team conducted non-destructive evaluation using X-ray (Figure 9). The team took X-rays of 4 failed vacuum test motors and 10 untested motors. The team compared the internal images to datasheets to determine that even our understanding of the heat path even after weeks of collaboration with the vendor was still inaccurate. It became clear that

the motors were not as readily suitable for vacuum as expected. The conductive paths were minuscule, even compared to the motors small stature. Heat was conducting through multiple small junctions before ever reaching the motor casing. This was proof that the coils were reaching incredible temperatures before the motor surface measured any change.

Thermal analyses were updated with the new conductive path information and produced results more consistent with the data from the first test. The analysis referenced in Figure 7 showed that coil temperatures rise about 100°C above their maximum survival temperature to nearly 230°C. During that time, the gearbox was seeing minimal thermal changes. The TVAC test thermocouple data confirmed that this updated analysis was more accurate. Figure 10 compares the thermal paths required under the old and new clamp designs.

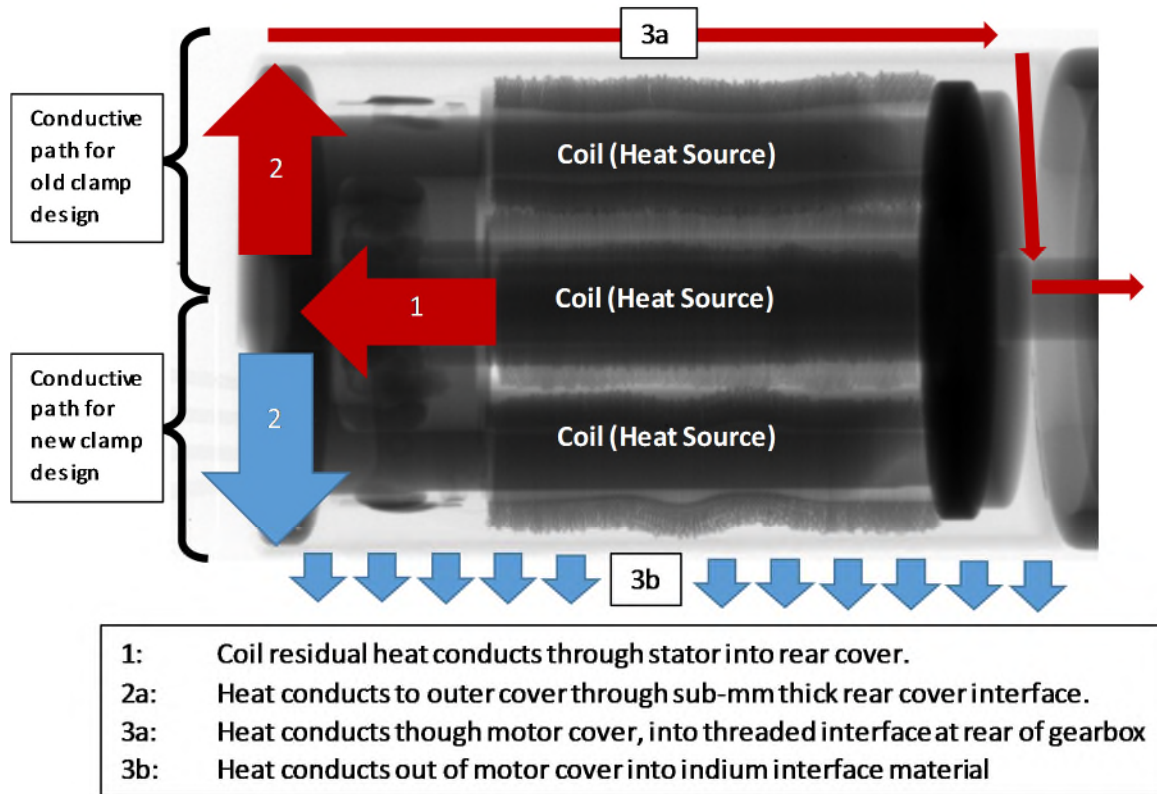


Figure 10. Thermal Path Explained: old clamp design vs. new clamp design.

Further complicating the issue, we had been relying on thermocouple data coming from the motor case and clamp to determine motor health. The thermal disconnect between the coils, case, and clamp voided our previous data and left us unsure how we could properly monitor motor health during a TVAC test. Thermocouple data from the motor surfaces had limited value due to poor internal conduction and the motors size did not allow internal monitoring with any test equipment. The team had no way to determine the motor's health with any available test equipment and any data received was of little value to determining the motor's coil status.

Method to Determine Motor Health

Eventually, the team realized that the motor coils were essentially a pair of resistance temperature detectors (RTDs). Any temperature change in the copper coils would correlate to a measurable impedance change and we could use this principal to determine the motor's internal temperature. The principal equation is shown in Eq. 1.

$$R(T) = R_0(1 + \alpha(T_c - T_0)) \quad (1)$$

Which could be applied as follows:

$R(T)$ = coil impedance at test environment temperature

R_0 = coil impedance at room temperature (120Ω)

α = coefficient of thermal resistance for coil material (copper = $0.0039 \Omega/\text{°C}$)

T_c = coil temperature at test environment temperature

T_0 = room temperature (20°C)

Giving the impedance-driven relationship for our experiment:

$$T_c = T_0 + \frac{\frac{R(T)}{R_0} - 1}{\alpha} = 20 + \frac{\frac{R(T)}{120} - 1}{0.0039} \quad (2)$$

This simple relationship between the coil temperature and impedance altered our test ideologies. The team now had a method of instantaneously measuring the coils temperatures at vacuum and could relate a max coil temperature to an ambient environment to determine operational ranges. The team conducted a new TVAC test aimed to determine the operation range for these motors in their new thermally-optimized design. The test ran each motor in vacuum for 15 minutes to achieve steady state. The motors were then powered off and the coil impedances were measure immediately after shutdown. The data was recorded and used to determine a max coil temperature at a given chamber ambient temperature.

The data was coarse, and even a few seconds of delay between shutdown and measurement would result in 10°C temperature drops (the coils are less than 1 gram each). The chamber was then heated up from -50°C by 5°C increments until the coils reached their maximum survival temperature. The data showed a striking trend, providing the test data needed to determine the thermal design was sufficient and the AMT operation range was well-founded. The chart in Figure 11 shows the temperature data collected from the AMT X and Y-axis motors, each having two coils, notated as "A" and "B". The four data sets were plotted against the chamber temperature and the tests concluded when the hottest coil measurement crossed the maximum coil survival temperature of 130°C .

Conclusion

After a lengthy design trade, a 6-mm stepper motor from Faulhaber (FDM0620) was selected for the EDU design. (If interested in more details from the design trade, please reference "Development of a High Performance, Low Profile Translation Table with Wire Feedthrough for a Deep Space CubeSat" from the 43rd Aerospace Mechanisms Symposium). These motors were the smallest available anywhere on the FY2015 market and were manufactured from a reputable vendor with flight heritage. Motors from this two-phase, PRECIstep® family had flown and were planning to fly on multiple NASA missions, including another 6U CubeSat manifested on SLS EM-1. Knowing this, it was assumed that the motors would operate in a vacuum environment once integrated into the AMT.

After a year of failure investigations and redesigns, the motors performed in vacuum within the operational temperature ranges determined by our thermal design during thermal vacuum tests. The lessons learned have been captured at the project level through engineering review board documentation. There is a minuscule market for flight-qualified stepper motors in mNm torque magnitudes. If small motors like these are required to meet mass, power, and volume budgets in vacuum, a thorough investigation and test plan should be implemented to validate their application.

The project could have saved considerable time and cost by budgeting a few thousand dollars to purchase a small vacuum chamber and test as often as needed, rather than invest months of labor and facility costs to purchase multiple high-fidelity tests. Small vacuum chambers with the data output required to thoroughly

test the motors in the correct thermal and vacuum environment are difficult to find on center without a cost and schedule burden.

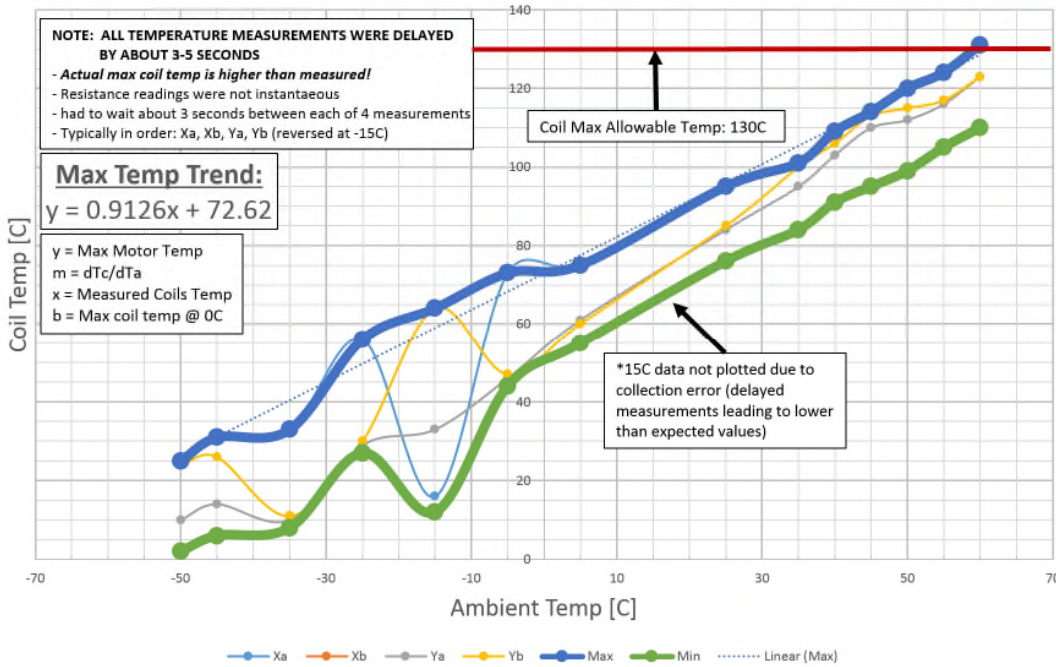


Figure 11. AMT motor coil temperature vs. vacuum chamber ambient temperature. Data collected using coil impedance measurements and temperatures calculated using Equation 1.

Development of the AMT flight unit was an excellent opportunity for the young NEA Scout team to learn about flight hardware testing. The team learned of the false sense of accomplishment bench top testing can provide. Blind dependence on vendor information proved to be a cost and schedule hit that fortunately the project was able to afford at the time. Do not take any analytical data from the family-oriented documentation provided by a vendor without application confirmation or performing inspections.

In summary, the project accepted the risk of utilizing a lien approach to hardware development to help save cost and schedule. The assumptions made early in the project were with the best information gathered at the time. Without the anomalies experienced during thermal vacuum testing

The project made the right decision with reserving a large portion of the project schedule to design and development. Leveraging rapid prototyping, out of house manufacturing shops, and communicative vendors allowed the project to be successful and absorb all of the lessons learned while still delivering flight hardware. Use of the lien development process allowed to team to get familiar with the hardware and confident in the design. This gave the project confidence in accepting the flight hardware mechanism design.

References

1. McNutt, L.; Johnson, L.; Clardy, D.; Castillo-Rogez, J.; Frick, A.; and L. Jones. "Near-Earth Asteroid Scout." AIAA Space 2014 Conference; 4-7 Aug. 2014; San Diego, CA; United States.
2. Few, A.; "Development of a High Performance, Low Profile Translation Table with Wire Feedthrough for a Deep Space CubeSat." 43rd Aerospace Mechanisms Symposia; 4-6 May 2016; Santa Clara, CA.; United States.

Solar Array Drive Assembly Qualification Lessons Learned

Jonathan Wood* and Timothy Pargett**

Abstract

Being handed the role of responsible engineer for qualification of an already completed design provides a unique challenge. Budget and schedule will not permit a complete review of every design detail or re-performing every analysis, so it is up to the knowledge and experience of the responsible engineer to anticipate which environments or design features pose the highest risk to a successful qualification. This paper presents two test failures that occurred during the Common Solar Array Drive Assembly (CSADA) qualification. Several potential issues were successfully averted, but this paper is focused on the design of the CSADA shock test apparatus and loss of step stability during hot thermal vacuum (TVAC) testing as both of these issues provide useful lessons learned or reinforce good design practice. Both issues were navigated successfully, resulting in a fully qualified design with several flight units successfully built and tested to date.

Introduction

Recently, Lockheed Martin developed a modernized version of the A2100 Bus with increased payload capacity, requiring higher power output from the solar arrays. This required a higher capacity Solar Array Drive Assembly. The new SADA, called the “Common” SADA or CSADA, had undergone a CDR in 2010 and was deemed ready for qualification testing.

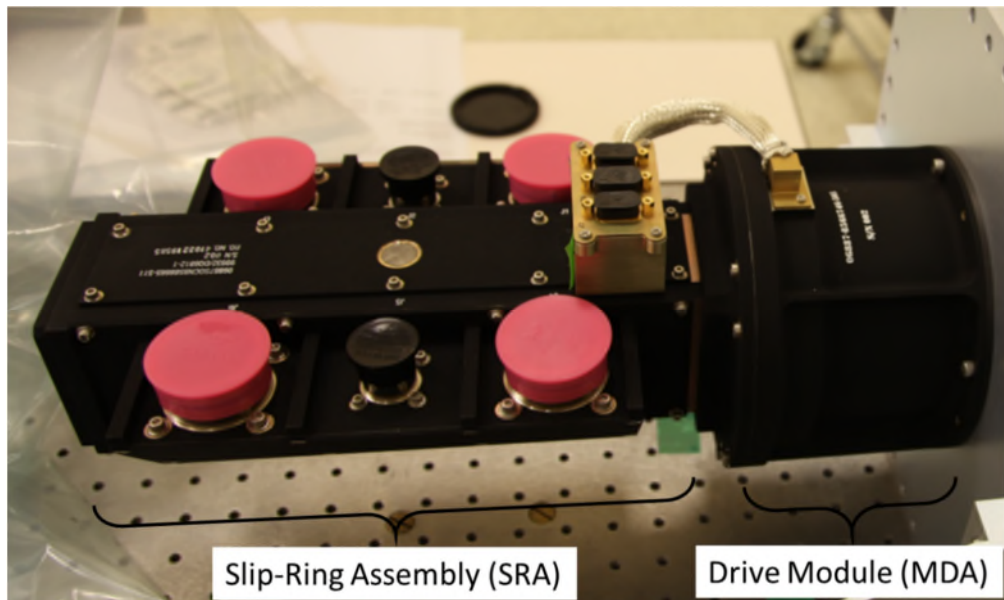


Figure 1. CSADA Assembly

* Lockheed Martin Space, Sunnyvale, CA

** Moog Space and Defense Group, Mountain View, CA

This document consists of general capabilities information that is not defined as controlled technical data under ITAR Part 120.10 or EAR Part 772.

Proceedings of the 44th Aerospace Mechanisms Symposium, NASA Glenn Research Center, May 16-18, 2018

CSADA Design Overview

The CSADA consists of two main sub-assemblies: the drive module and the slip ring assembly, as shown in Figure 1. The slip ring assembly has 118 circuits. Each circuit consists of a slip ring with redundant brushes. There are 96 power circuits (5.25-A capacity) and 22 signal circuits (1-A or 2-A capacity). The slip ring assembly is self-contained with its own bearings. The drive module consists of a 1.8-degree, 4-phase stepper motor, a 200:1 pancake-style harmonic drive, a potentiometer, and bearings. The drive module and slip ring housing are bolted together. An Oldham coupling mechanically links the two shafts.

At the time the author took responsibility for the CSADA qualification effort, manufacturability issues had been found in the drive module and a review of the design tolerances was performed. It was found that some critical CDR analyses had been inadequate, and a significant number of tolerance issues were found via a detailed critical clearance analysis. Additional review of the design led to the discovery of a potential failure of the potentiometer during vibration testing that was averted via design change. Concerns were raised about the inconsistent detent performance of the stepper motor design, but the budget and schedule were a big concern for the program, so the decision was made to proceed with risk in hopes of preserving schedule and cost rather than incur further delays by re-designing the motor. Mechanism engineering recommended deferring shock testing to the vehicle level to avoid the potential over-conservatism of traditional shock testing. Because shock was considered a risk, the program opted to perform shock testing during CSADA qualification, so that risk mitigation would occur sooner, but with a higher risk level, instead of mitigating the risk later at a lower risk level.

Shock Test Failure

Initially, shock testing was to be performed by an outside test house, however they were not able to tune their Mechanical Impulse Pyrotechnic Simulator (MIPS) table to an acceptable input shock level. Their MIPS table resulted in significant over-test over most of the frequency range. The large MIPS table in Lockheed Martin's Sunnyvale test facility was able to reduce the level of over-test, but not completely. Great effort was taken to eliminate the out-of-tolerance shock input, but it could not be completely eliminated. The Lockheed Martin Dynamics group was consulted and determined that risk was low moving forward since the out of tolerance (high) shock input was in the lower frequency range, which was believed to pose a lesser risk than a high input at higher frequencies. This was based on a review of the predicted modes for the slip ring, which did not predict significant brush motion at lower frequencies.

During the initial shock test, a short was found between adjacent slip ring circuits that was isolated to the unit itself, as illustrated in Figure 2. Removal of the slip ring inspection covers revealed that the short was caused by a brush having jumped over the raised barrier between the slip rings, making electrical contact with the adjacent ring.

In order to understand the failure mechanism, an old development unit was subjected to shock pulses with its cover removed, and high-speed video was taken. The high-speed video revealed that the pumping mode of the shaft was causing the “bouncing” motion of the brushes between the plastic barriers to resonate, and the impact of the brushes with the barriers was causing out of plane (lifting) motion on the brushes. The effective resonant frequency of the brushes was lower than predicted because the shaft displacement was large enough to impact the brushes. This created a non-linear resonance at a much lower frequency than the simple cantilevered brush motion expected for a linear analysis. The pumping mode of the shaft was lower in frequency (~200 Hz) and had a large displacement amplitude, which would not be excited to such an amplitude with a flight-like shock pulse consisting of a short duration and small displacement. It was also recognized that the “frequency” of the brushes bouncing between the barriers is a non-linear behavior, such that a reduced pumping amplitude of the shaft would increase the frequency of the brush motion. A higher frequency for the brush motions would reduce their shock susceptibility at the lower frequency range, assuming the contact with the barriers was reduced or eliminated.

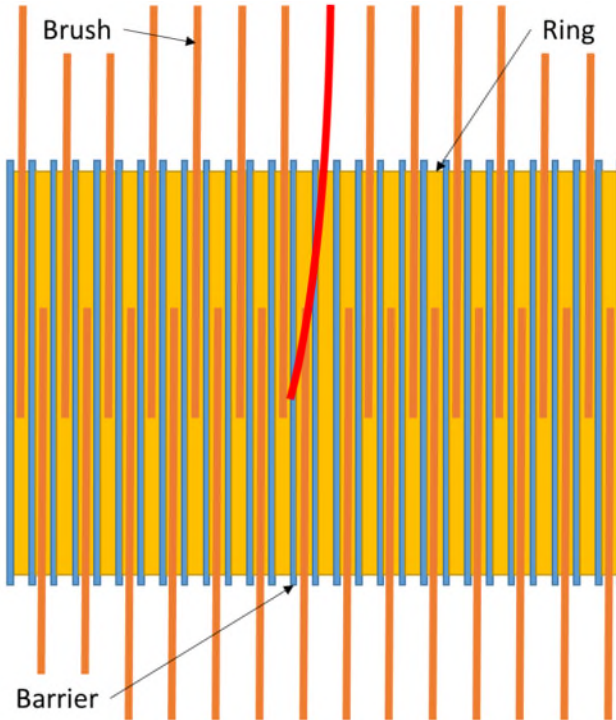


Figure 2. Jumped Slip Ring Brush

Based on the high-speed video results, the shock pulse duration was measured via the accelerometer time history data. The measured shock pulse duration was 15 ms, which is 3X longer than the worst-case on-orbit pulse duration of 5 ms. This is a limitation of MIPS table shock testing – typically, to meet the high frequency shock level, excessive energy has to be applied in the low frequencies, resulting in over-test in the lower frequency range, and a longer than desired shock pulse duration with larger displacements. Based on these observations, a more flight-like shock test setup was needed.

Revised Shock Test Setup

After the shock failure investigation demonstrated the sensitivity to over-testing the unit in the low frequency range, especially near 200 Hz, Moog was contacted to perform a mechanical impact shock test tailored to mitigate the low frequency over-test. Typically, shock level overages at lower frequencies are not a concern, but this was a critical parameter for the CSADA. Moog had developed shock test fixtures and techniques to provide this kind of pulse shaping capability previously and were able to adjust and tune an existing shock fixture to provide an acceptable shock dose to the test article using the Lockheed Martin-provided vibration test fixture.

The shock test method still relied on a mechanical impact to create the shock event, but several techniques were used to shape the frequency content of the shock environment to minimize the low-frequency energy while still achieving the required minimum levels across the full spectrum. The shock is created using a pneumatic gun and a shock test fixture. The pneumatic gun uses compressed air to propel a metal projectile that impacts the shock test fixture. The projectile and shock test fixture are specially designed and tuned to recreate a specific Shock Response Spectrum (SRS) upon impact. Once tuning of the fixture is complete, shock levels are controlled by the pressure in the air tank when the gun is fired; this results in highly repeatable shock levels from one shock event to the next. A simplified schematic representation of such a shock test is shown in Figure 3 and an example of a shock test setup with actual hardware in the Moog lab is shown in Figure 4.

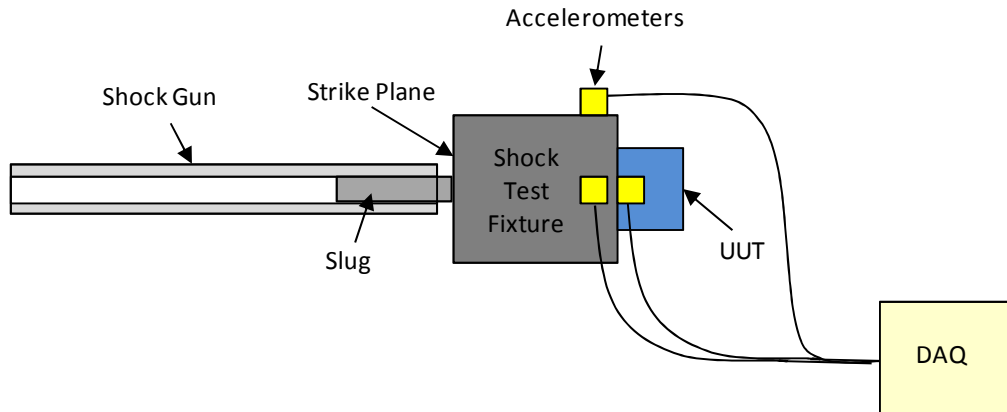


Figure 3. Schematic Representation of Shock Test

Moog used a metal-to-metal impact for imparting energy into the shock fixture. The key characteristics of the impact event are controlled by a combination of several variables. The size and shape of the metal bullet (See Figure 5), the design of the steel strike plate on the shock fixture, and the sacrificial target material placed between them during the impact are all used to shape the duration and frequency content of the impact. Moog has developed a set of bullets based around the four-inch (10-cm) diameter bore of their custom pneumatic gun that spans the range of input excitation typically required for pyroshock simulation. Similarly, a set of steel strike plates have been developed to be used in conjunction with these bullets. The combination of bullet and strike plate selection are the primary means used to adjust the excitation pulse width imparted to the shock fixture. This initial pulse then propagates through the shock fixture, exciting modes of that structure that further shape the resulting shock environment.

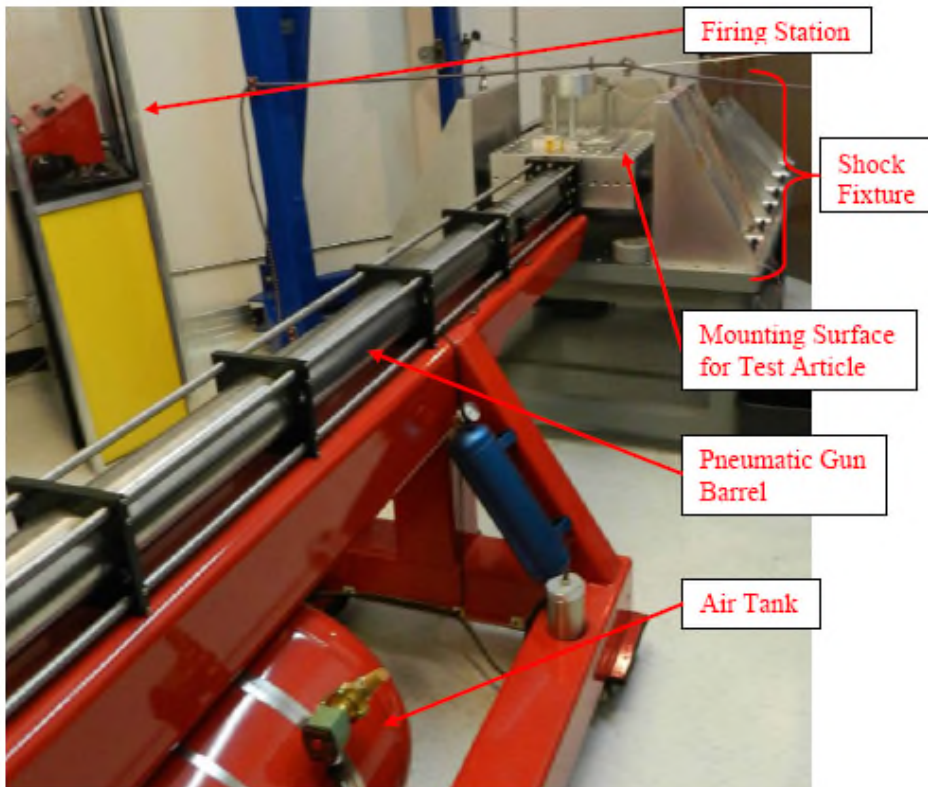


Figure 4. Example Shock Test Setup

The size of the test article required a shock fixture large enough that it would have numerous modes below the 10-kHz upper frequency bound for the test. The short impact duration by nature also excites these modes, resulting in amplification of the input shock at high frequencies. To address the adverse effects of numerous lightly damped resonances in the frequency band of interest, Moog designed viscoelastic damping into the shock fixture to control the amplification of these modes and to aid in tuning and controlling the shock spectrum. The addition of the viscoelastic damping in the design of the shock fixture helped mitigate high frequency over-tests due to fixture resonances. This fixture used is shown in Figure 7 and has a 0.6 x 0.6 meter (24 x 24 in) surface for integration to test articles with a grid pattern of fastener holes.



Figure 5. Various Shock Bullets

The final technique used for shaping the spectrum for this test was the use of a second fixture to absorb a significant portion of the momentum transmitted to the main shock fixture during the impact. Transferring this momentum from the primary shock fixture to the secondary fixture limits the net displacement of the primary shock fixture and consequently the low frequency shock levels that are otherwise an inherent part of many mechanical impact shock tests. This technique was developed at Moog starting in 2010 and was fine tuned over several years to develop a shock test process to provide controlled and repeatable tuning options with standard fixtures. The availability of standard shock fixtures enabled the CSADA re-test to be performed with a lesser schedule impact despite the unique demands on SRS shaping. The shock test setup used for the CSADA is shown in Figure 7.

Shock Test Results

At the start of the CSADA shock effort, the entire shock setup, including a mass simulator for the CSADA mounted to the Lockheed Martin-provided vibration fixture, was used to tune the shock environment to best match the required shock dose while limiting the low frequency portion of the SRS to a significantly lower dose than generated in the previous shock test. After suitable tuning results were achieved, an Engineering Development Unit (EDU) was installed into the test setup and two shocks were applied to it while high-speed video captured the resulting motion at the slip ring assembly. The review of this high-speed video data was used to verify that the shock environment no longer resulted in sufficient excitation of the slip ring, as evidenced by significantly reduced brush motion. After verifying the suitability of the shock environment with the EDU, the qualification unit was installed and tested.

The CSADA was subjected to three shock events in each of the axes tested (Y and Z). See Figure 6 for axis definition. The control accelerometer time histories for one of the 3 shocks in the Z axis is shown in Figure 8. From these time histories, the highly repeatable nature of the shock event can be seen. The pulse duration of approximately 5 milliseconds matches well with the type of duration expected in a flight shock event.

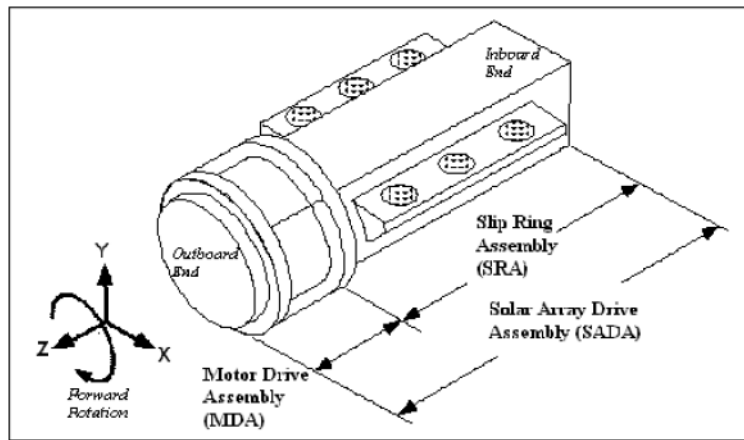


Figure 6. CSADA Axis Definition

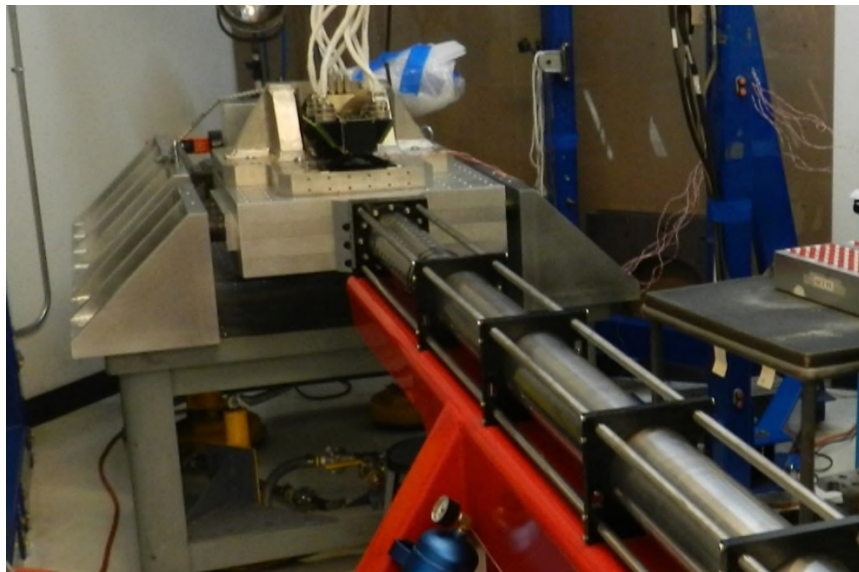


Figure 7. CSADA Shock Setup

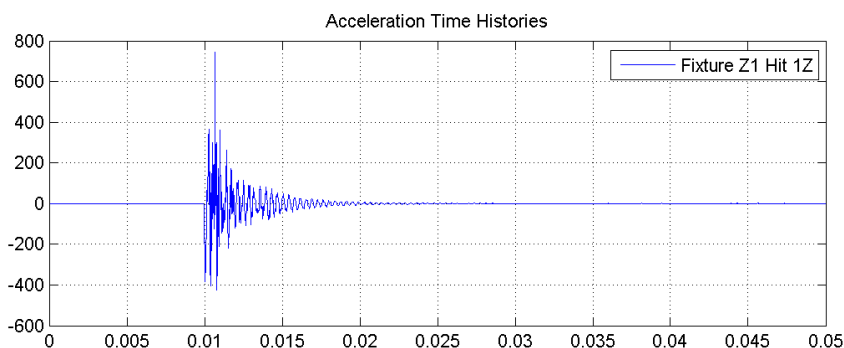


Figure 8. Example CSADA Z Direction Shock Time History

The shock response obtained from the original (failed) shock test is shown in Figure 9. Note the large degree of over-test in the low-to-mid frequency range. The control accelerometer shock response spectra for the Z direction shocks using the improved test setup are overlaid in Figure 10. The highly repeatable nature of the shock test method is even more apparent here where the shock dose as a function of frequency is shown to be nearly identical across all three shocks over the entire frequency band from 100 Hz to 10,000 Hz. The highly repeatable nature of the shock events allowed this test to be run very close to the nominal input level to further limit the shock dose to the CSADA without significant risk of an out-of-tolerance shock event. The Figure 10 SRS overlay also demonstrates the ability of this shock setup to achieve very low shock levels at low frequencies near 200 Hz where the slip ring assembly showed susceptibility to severe over test.

For the Y axis test, similar repeatability from one shock to the next, short pulse duration, and low shock levels at low frequencies were also achieved. The final shock testing of the CSADA resulted in a successful qualification of the unit and avoided a repeat of the slip ring assembly failure observed from the initial method of shock testing.

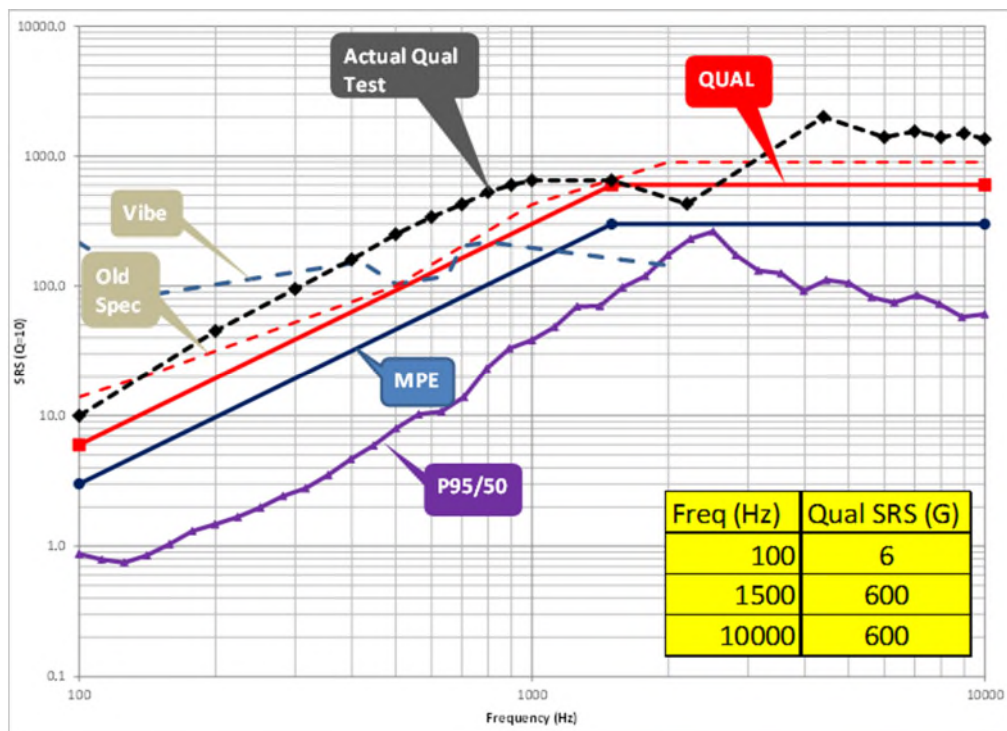


Figure 9. Original (Failed) Shock Test Data versus Input Level, MPE, P95/50, and Vibe Data

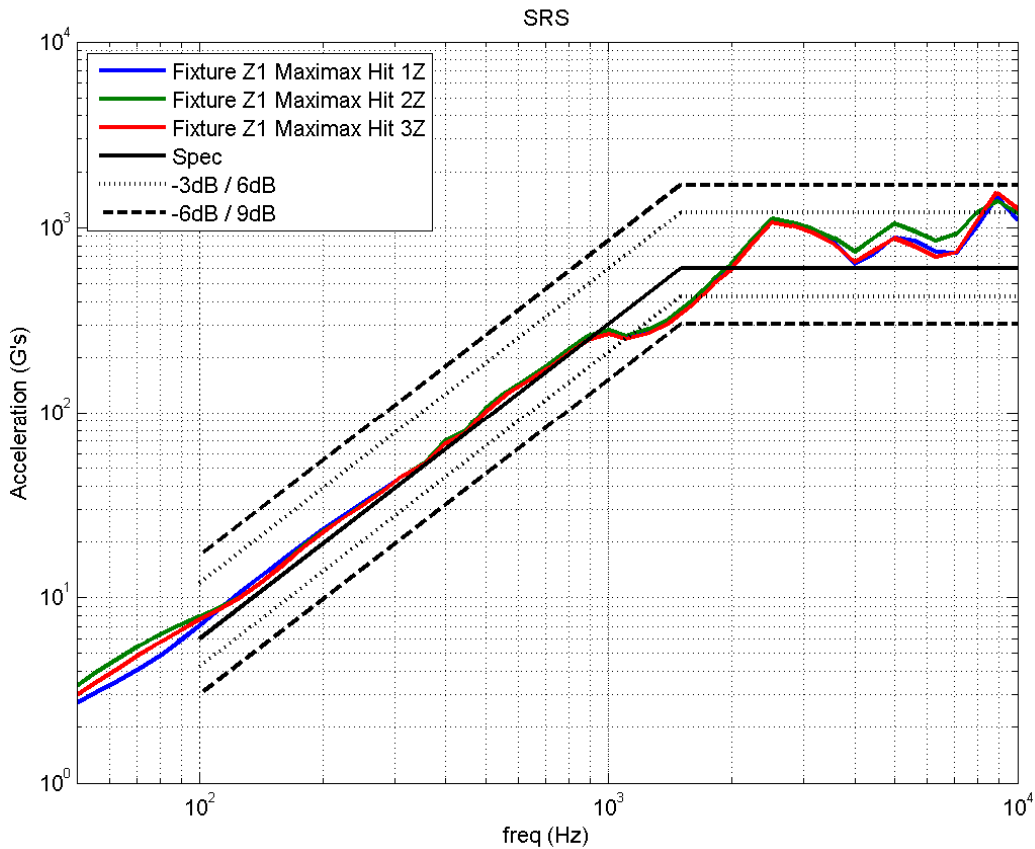


Figure 10. CSADA Z Direction SRS Overlay

Shock Test Guidelines

At the outset of any shock test effort, it is important to work through the physical implications of the shock test specification and what it means in terms of the type of event to be simulated. The shape of the shock spectrum, distribution of energy as a function of frequency, and the total pulse duration can provide vital information about the type of environment to be simulated. Significant low frequency energy and long duration pulse widths often correspond to events where thrust is being applied, such as the ignition shock pulse of a missile. Simulating these environments is a significantly different effort than a high frequency dominated pyrotechnic event like a spacecraft separation event. Where a significant change in velocity of the device is to be simulated, similar velocity change should be introduced in the test. Drop tests, etc. often work very well in these scenarios. Where little or no velocity is to result from the shock event, efforts should be taken to create a shock environment that minimizes the velocity change and net displacement in the test. Keeping in mind the type of real world event being simulated helps guide the test engineer through the process of setting up a good method of replicating the shock. The entire series of events to result in the simulation of the shock should then be reviewed to verify suitable capability and address challenges. The required force levels to achieve the shock must be within the excitation system's range. In the case of Moog's lab this equates to pressures at which the pneumatic gun can be fired with high repeatability.

The desired shape of the excitation pulse into the test fixture should be reviewed and initial assessments made about how to best approximate it. For Moog, this involves looking through the available combinations of bullets, strike plates, and sacrificial target materials. If an excitation shape is required that is significantly different from those available, the customer is engaged about needs for custom designs to be created prior to proceeding through test.

The effects of fixture modes should be assessed for how they can be used to help shape the shock environment and their effects mitigated when not beneficial to achieving the desired SRS. For certain environments, it is highly beneficial to introduce fixture modes at certain frequencies. Similarly having methods to introduce damping into fixture modes is often beneficial in controlling the amplification of the modes and keeping the SRS within specification at high frequencies. Moog often uses finite element analysis to estimate the effects of fixture modes and introduces modal damping through methods like viscoelastic constrained layer damping and particle damping.

Loss of Motor Stability during TVAC

During cycle 20 of 27 TVAC cycles, the CSADA motor stalled at the end of a hot dwell. The stall occurred when the motor was driven at its “normal” rate (1 rev per day on the output) at its maximum voltage (74 V). Troubleshooting determined that loss of step stability had caused the motor to stall. This was verified by driving the motor at 74 V and once stalled, changing the motor drive voltage to 25 V, which resulted in immediate rotation without any loss of steps. It was also shown that the CSADA would step stably with drive voltages up to 71 V, and it would quickly lose step stability when driven at 72 V or higher.

Loss of Step Stability:

The CSADA is driven by Lockheed Martin’s common 70-V stepper motor driver. This motor driver provides voltage excitation for approximately 60 ms each time a motor step is needed. At the normal rate, each 60-ms pulse occurs approximately every 2 seconds. The motor driver includes a diode network across each phase that allows motor current to flow if the Back-ElectroMotive Force (BEMF) voltage is below approximately -8 volts. This provides some additional damping to help the motor damp out after the short excitation pulse.

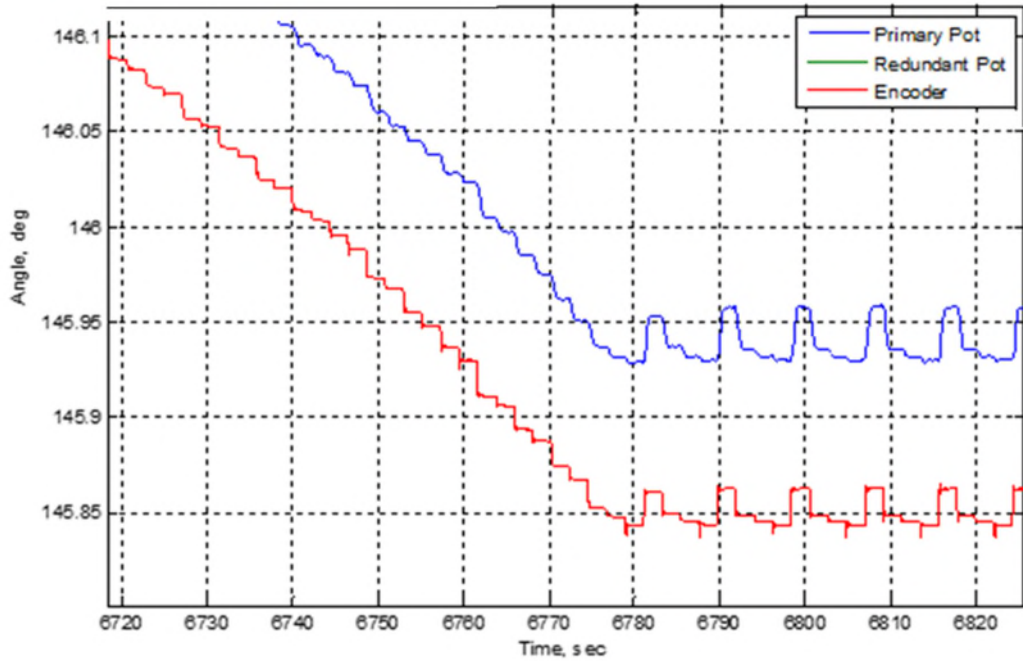


Figure 11. Telemetry Data Showing Loss of Step Stability

Stepper motor stability and dynamic stability analysis are well covered by references 1 & 2. It was determined that the primary contributors for the CSADA loss of step stability (an example of which is shown in Figure 11) were the extremely low and variable detent cogging torque and the relatively low motor BEMF constant. This issue was somewhat masked at ambient and cold by the high detent hysteresis torque

provided by the motor, which, combined with internal friction, provided sufficient damping for stable operation. After the unit was run-in during the initial TVAC cycles, the slight decrease in bearing and harmonic drive friction from run-in and the reduction in bearing and harmonic drive viscous drag at hot, combined with the slight reduction in motor detent hysteresis torque at hot, removed enough damping from the motor for it to become unstable when driven with an excitation voltage above 72 V.

Stability Model Issues

Clearly, based on the TVAC failure, the original step stability analysis was not sufficient. For the CSADA, a “heritage” stability model had been utilized, which up to this point had demonstrated a good track record. It is important to note that the heritage stability model was designed for 4-phase unipolar stepper motors driven at 70 V by the same motor driver. For conservatism, all combinations of the key parameters were analyzed at all combinations of minimum and maximum (see reference 1 for stability model methodology and background). The minimum bearing friction and damping values analyzed were zero, so a loss of stability was not expected. The model included the dynamic properties of the harmonic drive, output shaft, and solar array, being modeled as a multiple mass-spring torsional system. After the failure occurred, digging into the model revealed a serious flaw – the diode circuit in the motor driver was not modeled correctly. The diode circuit only allows current to flow when the BEMF voltage generated by any motor phase is less than -8 volts (as depicted in Figure 12). The model, as designed, allowed current to flow if the BEMF voltage generated by the motor was above +8V or below -8V, so the damping provided by the diode circuit in the stability model was double what would actually be provided.

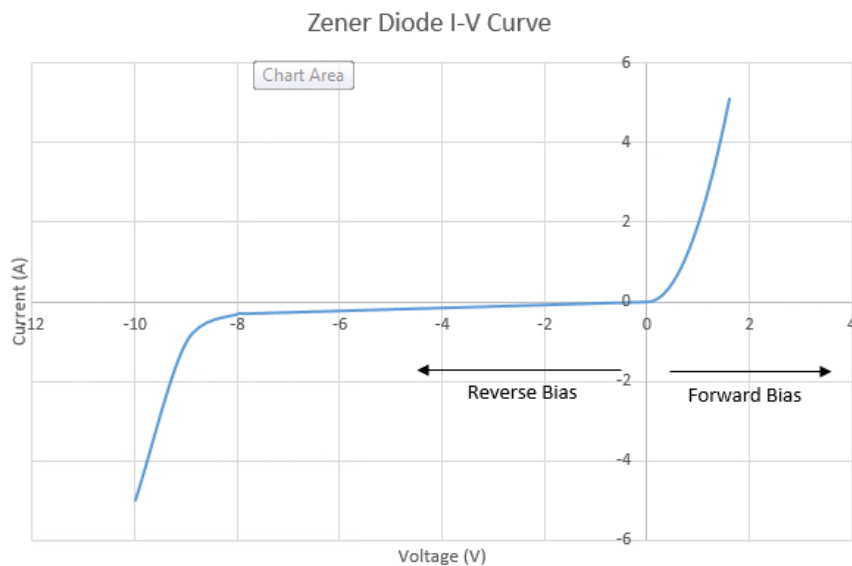


*Figure 12. Zener Diode I-V Curve Used to Aid in Stability Model Construction
Note: CSADA drive electronics include blocking diodes that prevent current from flowing in the forward bias direction.*

Once the stability model was corrected, it was validated by inputting the measured or estimated values for the qual unit that went unstable during TVAC, and comparing the predicted results to the TVAC failure (Figure 14). The corrected model was able to reproduce the failure, and even showed the same step pattern as the failure. Furthermore, the threshold voltage for stability with the corrected model was 70 volts, which is very close to the actual threshold voltage. Predicted BEMF plots were also compared to actual measured BEMF profiles (Figure 13), and the BEMF profiles matched well.

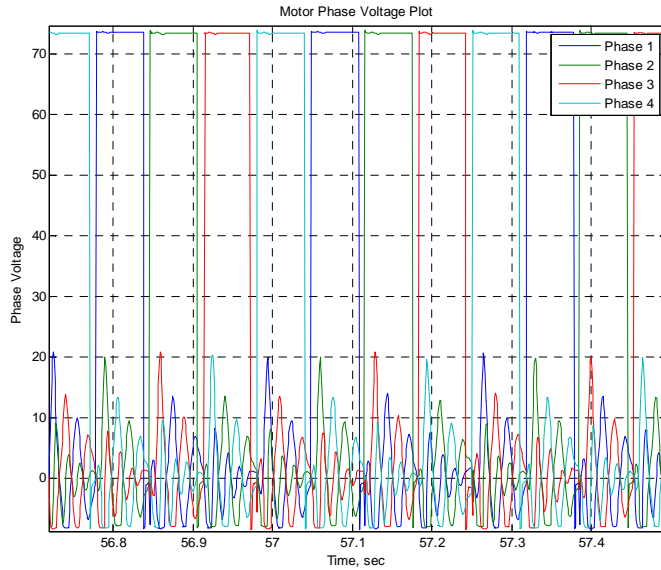


Figure 13. Stepper Motor Voltage Plot Showing Clipped BEMF Voltage at -8 Volts

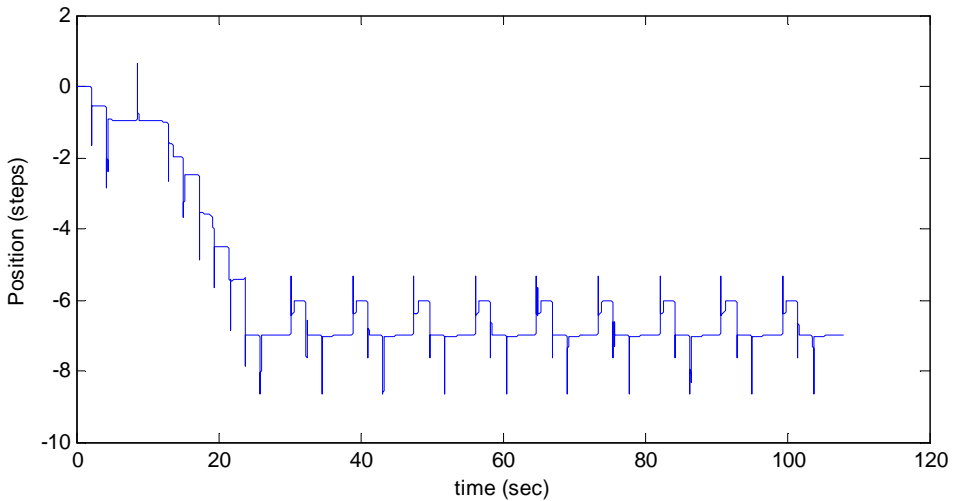


Figure 14. Corrected Stability Model, Showing the Same Behavior as Original TVAC Failure

Once the stability model was corrected, it was clear that the original motor design could not be salvaged. With the stability model corrected, it also became apparent that the motor suppliers request to reduce the required resistance, allowing more current to flow through each phase, would not address the stability problem since this approach would further reduce the motor BEMF constant. In contrast, the motor needed to have a higher BEMF constant in order to extract more damping from the motor drive electronics diodes, and a correspondingly higher motor resistance could be tolerated. At this point, the motor supplier's parallel development effort to improve detent consistency was not showing signs of positive progress, and the magnet wire size was already at the lower threshold allowed by internal Lockheed Martin design standards. Therefore, the effort with this motor supplier was terminated in favor of a new motor design that would provide a much higher BEMF constant, and was expected to provide more consistent detent properties.

New Motor Design

Based on the results from the corrected stability model, a new set of motor requirements was devised. Instead of increasing the maximum allowed current at the expense of the BEMF constant, a higher BEMF constant was specified, and higher resistance/lower current was allowed. This resulted in slightly higher powered torque with the advantage of higher BEMF voltage at lower rotor velocities, maximizing the damping provided by the drive electronics. This change was shown via the stability model to drastically improve motor stability. In addition to the increased BEMF constant, the detent cogging torque requirement was slightly increased with the allowable range significantly narrowed, and the hysteresis torque requirement was decreased substantially. These changes showed significant stability margin in the simulation, i.e. the motor performance characteristics had to be lowered substantially to cause a loss of stability, and predicted torque margin was very high. In order to meet these requirements, a completely different motor stator design was devised, with a different tooth count and winding layout. This configuration had fewer teeth and allowed larger coils so that the required BEMF constant could be met without excessively fine magnet wire. With the new design completed, a different motor supplier was selected to build the frameless rotor and stator. Prototype testing of the new motor design showed better than expected performance, further improving predicted stability margin.

Stability Verification

Since the stability model did not catch the loss of stability observed with the original motor, a stability demonstration program was desired to ensure that the new motor design was not at the “ragged edge” from a stability standpoint. Since it was observed that the stability of the original motor was very sensitive to pulse-width variation, a “pulse-width margin” test was conceived. In this test, the motor pulse-width was varied to find the minimum and/or maximum pulse-width that results in stable stepping. This threshold pulse-width can then be compared to the flight pulse-width range to compare stability margin.

To close on the motor failure investigation, the CSADA, with the original motor was first subjected to the pulse-width margin test. A thermal chamber was used to test the CSADA in the same thermal conditions as the original TVAC failure. The loss of stability did repeat, and stability margin was measured at ambient and cold. Next, the prototype of the new motor design was installed in the CSADA qual unit and the stability test was repeated again. This resulted in stability at hot (Figure 15), ambient, and cold, at the maximum and minimum input voltage. Stability margin was significantly higher than with the original motor. The new motor prototype was then left in the CSADA qual unit for the duration of the life test, and stability margin was measured during the periodic and final functional tests performed as part of the life test. Stability margin remained high over the entirety of the life test.

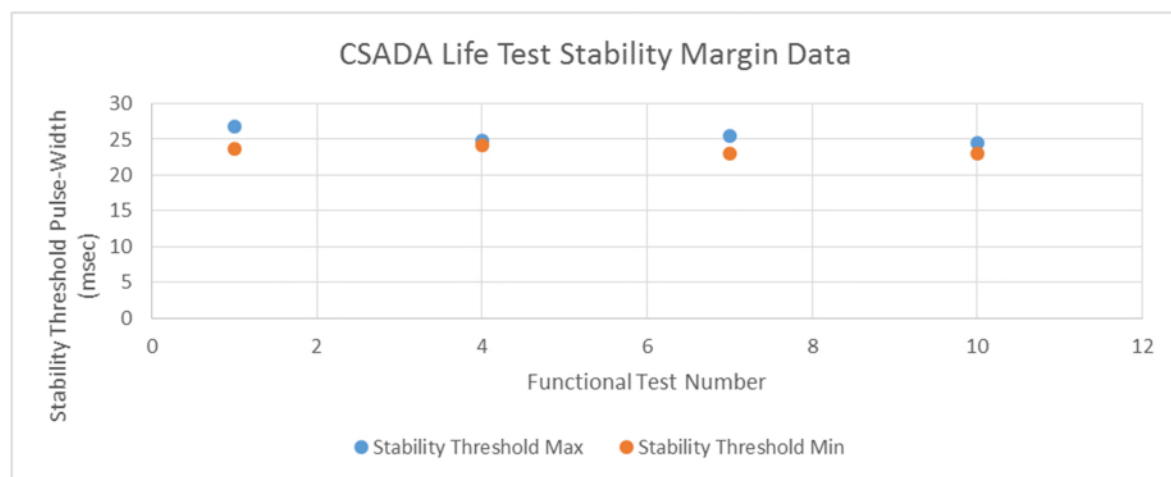


Figure 15. Trending of Stability Threshold Pulse-Width Over Life Test at Hot

In parallel, a qualification unit motor was built and subjected to motor-level qualification testing. The qualification motor passed all qualification tests and performed as expected. Finally, to fully close out the CSADA qualification program, the first production CSADA with the new motor design was subjected to proto-qualification. The proto-qualification CSADA met all test requirements, and the remaining three flight CSADAs built to date successfully completed unit acceptance testing.

Conclusions & Recommendations

Conclusion

The issues encountered during CSADA qualification testing are good examples of the challenge of taking on responsibility for a qualification program just before the start of qualification testing. Unfortunately, taking on such tasks is unavoidable, and there is often not sufficient budget or schedule to fully scrub every detail of the design, analyses, test plan, and derivation of test requirements. In the case of the CSADA, the most serious design issues identified were addressed before start of qualification, but a decision was made to proceed with some level of risk, a decision that was made based on a flawed stability model. The available in-house test equipment (MIPS table) has limited tuning capability, so although great effort was taken to minimize the level of over-test, this was not sufficient to eliminate the risk of a shock test failure. Therefore, an obvious recommendation is to ensure the qualification shock test method for slip ring is validated using engineering hardware early in the development, and utilize a shock input method that more closely matches the flight shock environment, as detailed in this paper.

In the case of the stepper motor issue, the poor detent characteristics were flagged as a risk to the program. With the heritage stability model showing stable operation, the decision was made with the program to press forward, and the motor ended up losing stability during TVAC testing. It is common in this industry to have an expert analyst performing analysis in support of design engineering, but ultimately, the responsible engineer, being most familiar with the configuration of the hardware, should go through analysis models in detail before the analysis is closed. In this case, the responsible engineer audited the stability model after the motor lost stability, and the model was found to be inadequate. The model issue could have been found much sooner in the flow by validating the model against BEMF voltage plots taken during baseline functional testing. Comparing predicted to actual BEMF plots would have unearthed the modelling issue sooner.

Recommendations

The issues discussed in this paper may be lessons learned to some, and to others they may simply reinforce good system and test design practice. The following recommendations are made based on the issues encountered during CSADA qualification.

- When performing shock tests on slip rings, care should be taken to avoid an excessive shock pulse duration, excessive displacement, and over-exposure in the lower frequency range.
- If shock testing cannot be deferred to the vehicle level, use an EDU or prototype to validate the shock test, paying particular attention to shock pulse duration and displacement.
- Design and implement a good shock test setup:
 - Ensure the method used provides a flight-like shock pulse duration and can be shaped to closely match the flight shock environment. Different shock scenarios will require different test setups.
 - Review the entire series of events to result in the simulation of the shock to verify suitable capability and address challenges.
 - The required force levels to achieve the shock must be within the excitation system's range.
 - Review desired shape of the excitation pulse into the test fixture and make initial assessments about how to best approximate it.
 - Assess the effects of fixture modes for how they can be used to help shape the shock environment and their effects mitigated when not beneficial to achieving the desired SRS. For certain environments, it is highly beneficial to introduce fixture modes at certain frequencies. Similarly, having methods to introduce damping into fixture modes is often beneficial in

controlling the amplification of the modes and keeping the SRS within specification at high frequencies. Fixture modes can be estimated using finite element analysis

- Ensure that dynamic models used for motor verification have high accuracy in the electrical portion of the model – do not rely on past models or electronics engineering to provide a good model. Go through every detail and understand every component modeled, and perform checks against prototype data, such as BEMF plots to verify realistic behavior of model.
- Voltage versus current plots for most electrical components can be easily found on the internet – Simulation of the electrical component should match the expected voltage versus current behavior before adding it into the stability model.
- Make sure a high enough number of steps is modeled, since the torsion windup of the harmonic drive or other factors can allow a motor to step stably for 25 or even 50 steps before losing stability. This is more of an issue when the motor does not have enough torque margin.
- Validate and calibrate the stability model early in the hardware development effort.
- Even if the model used has a good track record, and only the values for the various parameters are being updated, model calibration should be performed once prototype data is available.
- Motor-level prototype test data can allow for earlier validation of the electronic portion of the model, provided the motor is driven by flight-like drive electronics. If this data is available, the stability model can be chopped down to just the drive electronics and motor rotor, and compared to the motor-level test data.
- Driving the motor with flight-like drive electronics should be performed as early in the development process as possible. All motor level testing should include flight-like drive electronics.
- Motor hysteresis will decrease as temperature increases due to recoverable decrease in magnet strength. Motor designs should not rely on motor hysteresis (or friction!) to maintain stability at hot.
- Loss of motor hysteresis at hot can be estimated based on data from the magnet supplier. Since detent is usually measured at ambient only, use this data to “knock down” the minimum hysteresis torque value input to the stability model.
- Checking the motor operating point on the magnet B-H curve is recommended as operation at hot can lead to permanent demagnetization if the minimum permeance coefficient is too low. Demagnetization during operation at hot can also reduce detent torque and cause a loss of step stability.
- Poor detent characteristics are a red flag for a poorly designed motor. In the world of motor design, there are usually many options for stator tooth count in a given step size and phase count, even though the rotor pole count cannot be adjusted.
- Design the motor to take advantage of the drive electronics architecture – The drive electronics for the CSADA, although unusual and seemingly not conducive to stability, provide a significant amount of extra damping when needed if the motor design is properly optimized.

References

1. Kackley, Russel & McCully, Sean. "Stepper Motor Instabilities in an Aerospace Application." *Proceedings of the 26th Aerospace Mechanisms Symposium* (1992), 173-187.
2. Marks, D.B. "Integrating motion simulation with design for space stepper motor applications." *Proceedings of the 6th European Space Mechanisms & Tribology Symposium*, (1995), pp. 413-418.

Determining Root Causes of Mysterious Hardware Failures using High Resolution CT Scanning

Michael R. Johnson*

Abstract

During testing of actuators for flight programs, failures have occurred that required closure with an understanding of the root cause of the failure. Some actuators intended for a Mars mission called InSight exhibited intermittent changes of the winding resistance of the motors during temperature changes was extremely baffling. It was critical to determine the cause of the intermittent characteristic because the actuators were residual flight hardware from a previous program and the company that provided the motors was no longer in business. Using an X-Ray Computed-Tomography (CT) method that produces a three-dimensional computer model of the item, the exact source of the intermittent failure was determined and completely understood – at dimensions of less than 20 microns. In another case, after the completion of an actuator's life-test-to-failure, inspection was required to determine the source of the failure. The size of the actuator (10-mm diameter) required destructive means to get to the interior of the actuator for inspection, risking the loss of the source of the failure. Using CT imaging, the source of the failure was determined.

Introduction

Computed Tomography X-Ray inspection is a process that uses hundreds to thousands of X-ray images to assemble a finely detailed three-dimensional computer model of the object under inspection. By taking each image from a different location and angle around the perimeter of the object, a three-dimensional volumetric model can be created from the individual scans. This model can then be viewed, rotated, sectioned, and magnified in the same way as a computer design model of the object. By rotating, sectioning, and magnifying the scanned model, details of the actual assembled components within the assembly can be detected and measured. These measurements and views allow the illumination of anomalies within the assembly that may otherwise be undetectable.

Two anomaly investigations are discussed that demonstrate the power of the X-Ray Computed Tomography inspection method. One case allowed the detection of failure points that were not visible even though the hardware could be safely disassembled and inspected directly. The second case allowed the determination of the failure cause with a hardware assembly that could not be disassembled without destructive means. The destructive disassembly caused significant concern that the root cause would be lost in the process of disassembly. The use of the Computed Tomography method allowed the determination of the failure source and in-situ measurements of the effects of the failure could be made to fully demonstrate the extent of the failure cause.

The two cases described are:

1. Winding failures of brushed motors for the Instrument Deployment Arm on the Insight Project
2. Brushless Actuator Life Test failure of a 10-mm-diameter device for the Mars 2020 project

* Jet Propulsion Laboratory, California Institute of Technology, Pasadena, California

Insight Instrument Deployment Arm (IDA) Motor Winding Anomaly

Instrument Deployment Arm (IDA) Hardware Description

The IDA for the InSight Project is utilized to place instruments onto the Mars surface after landing of the spacecraft. A rendering of the lander on the surface of Mars is shown in Figure 1. The IDA is identified in the picture and has four axes of motion that utilize the motors under investigation.

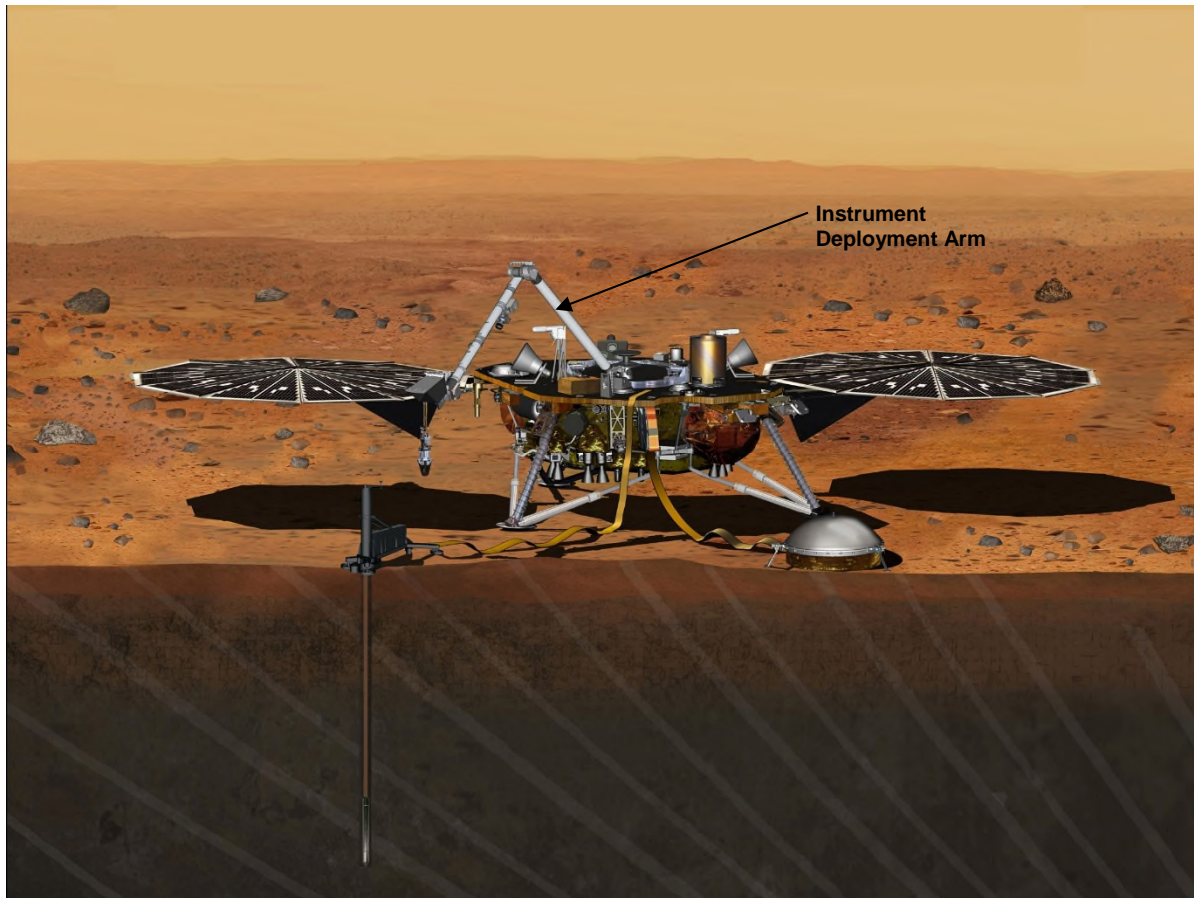


Figure 1. InSight Lander Shown on the Surface of Mars

The IDA is exposed directly to the environment of Mars and experiences large changes in temperature from day to night. This thermal cycling can have deleterious effects on assemblies composed of materials with different coefficients of thermal expansion. To demonstrate compliance to the motor's thermal cycle requirements, a thermal cycle test was performed on three units. To establish design margin, the number of test thermal cycles is much larger than the quantity of cycles during the mission. This type of thermal cycle testing is considered a qualification test and the hardware is not flight worthy after going through the testing. For brushed motor assemblies, the adhesively bonded windings on the rotor and the winding terminations to the commutator are the primary thermal cycle sensitive items. There are also the bonds between the magnets and the housing and other ancillary areas that are also stressed during the thermal cycle testing. One of the three test motors, serial number 041 is shown in Figures 2, 3, and 4.



Figure 2. Motor Serial Number 041
Motor Diameter is 30 mm

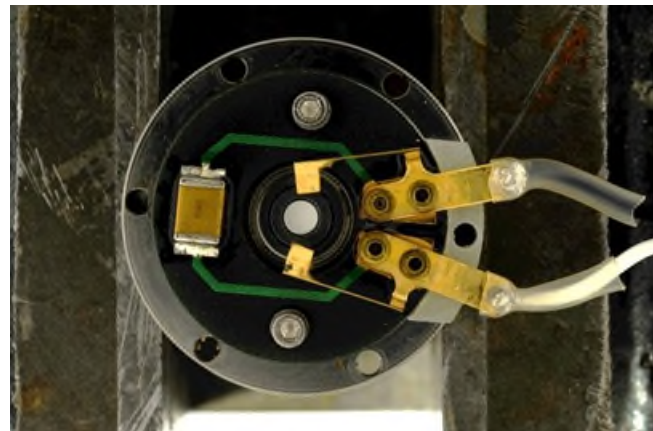


Figure 3. Brush Assembly

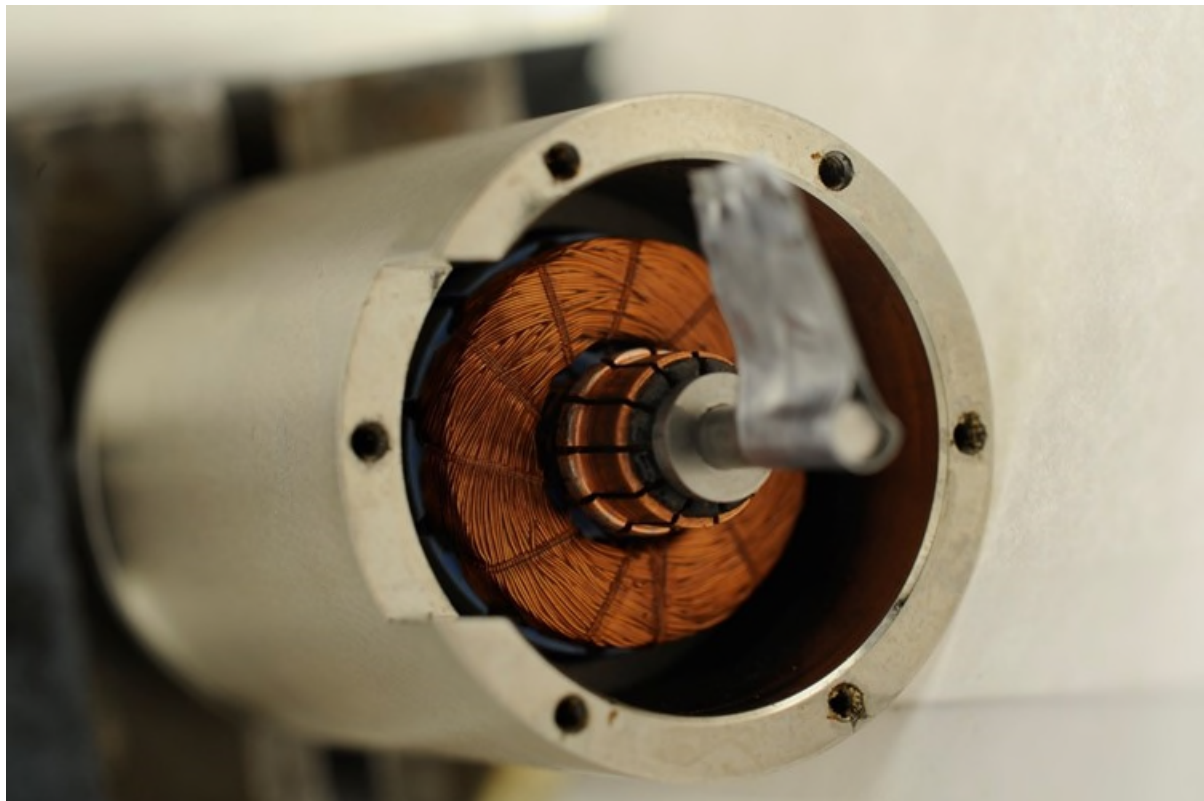


Figure 4. View of the Shaft End with the Commutator and Winding Terminations Shown

Thermal Cycle Test Setup

Three motors were selected for thermal cycle testing and placed in the thermal chamber. The motors are not rotated during the thermal cycle testing to enable accurate measurements of the winding resistance. The instrumentation was connected to read the winding resistance of the motors as shown in Figure 5 while the temperature was cycled from hot to cold. The temperature of various locations on the motor assemblies and voltage drop across the windings (resistance) was recorded continuously during the test. The resistance of the windings varies directly with the temperature of the test article. The expected appearance of the recorded data for the windings would show the resistance of the windings rising and falling smoothly with the temperature of motor as shown in Figure 6.

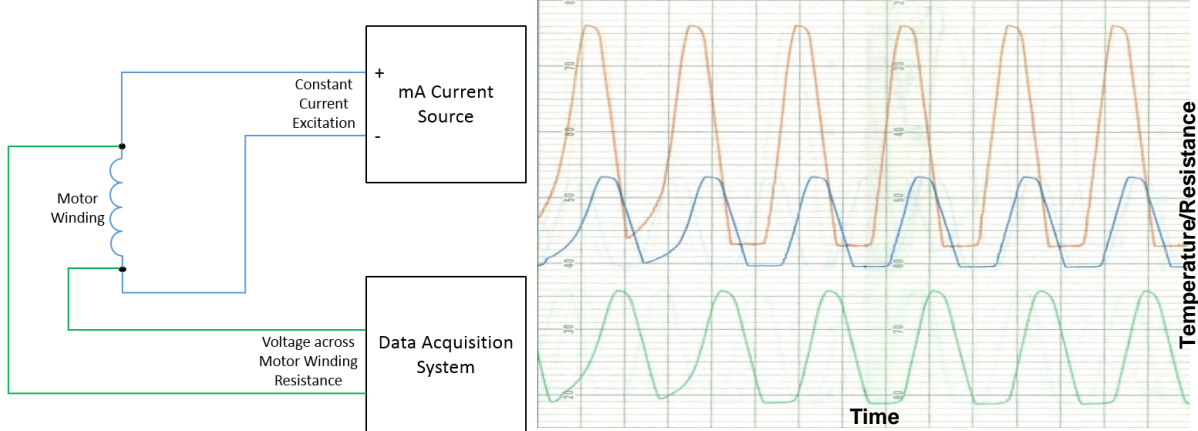


Figure 5. Test Instrumentation

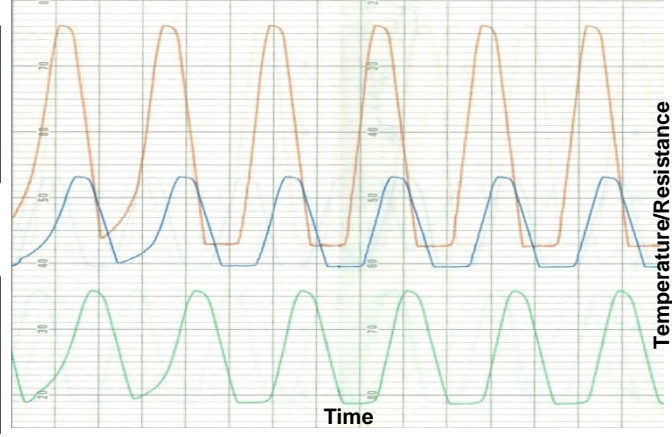


Figure 6. Typical Shape of Winding Resistance versus Time Showing Smooth Variation with Temperature Cycles

The Anomaly Appears

The resistance recorded for one of the three motors looked mostly as expected for the first few thermal cycles of the testing. Some measurement noise was present in the data traces. Two of the motors, however, did not produce the results expected. The traces instead appeared as in Figure 7. The blue curve is the temperature and the grey, orange, and yellow curves are the motor winding resistances.

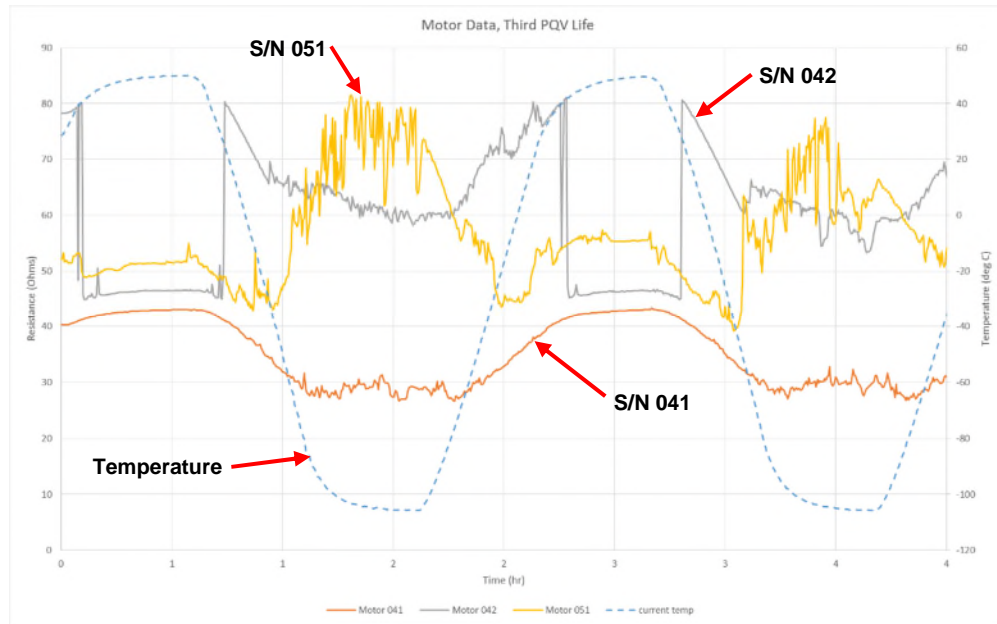


Figure 7. Motor Resistance and Temperature versus Time Plot for Cycle #3

The orange curve is motor serial number 041, the grey curve is motor serial number 042, and the yellow curve is motor serial number 051. The winding resistance of all of the motors shows electrical noise during the region of low temperature dwells. The orange motor data performed as expected. The noise within the data was unexpected and a little troubling, but the most significant feature of the grey and yellow curves is the sudden change in apparent resistance of the windings during the transitions to and from the cold temperatures. During the cold transition, the winding resistance should smoothly lower and at no time should it indicate an increase or sudden jump up in resistance. After 38 temperature cycles, serial number

041 adopted the same signature as the other two motors, with a sudden increase of winding resistance as the temperature was lowered through the cold portion of the cycle (see Figure 8).

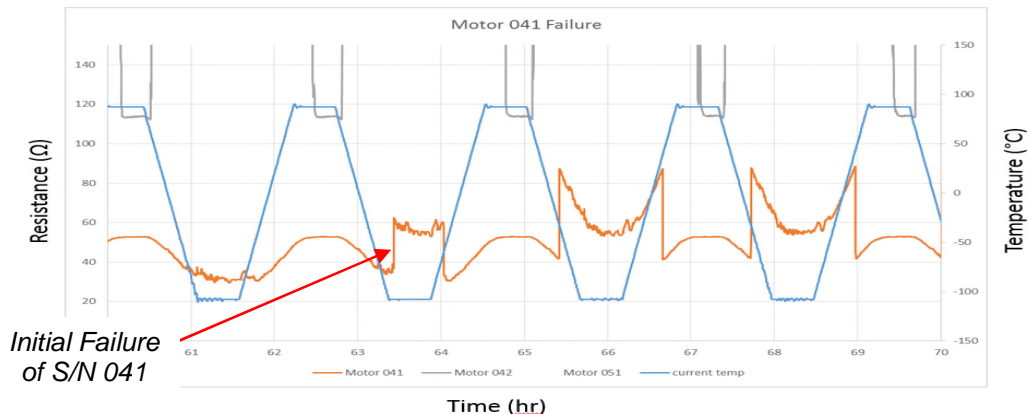


Figure 8. Failure of Serial Number 041 at Temperature Cycle #38

To determine the source of the strange increases in resistance, the motor was disassembled and inspected at high magnification. The motor windings are bonded together and to the rotor core laminations with an epoxy. During visual inspection under high magnification, some indications of cracks in the epoxy were detected. The images do not indicate if the cracks are the source of the winding resistance anomalies, but they are certainly potential locations for trouble. Some of the images taken are shown in Figures 9 and 10. The cracks indicated in the images were not present in the motor winding epoxy prior to the thermal cycle testing.

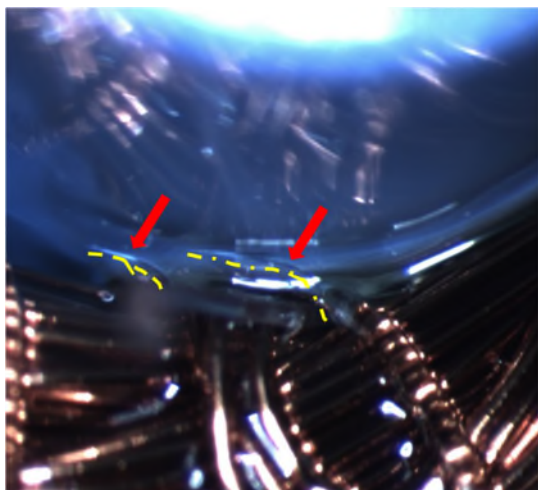


Figure 9. Winding/Rotor Epoxy Cracks Indicated by Lines and Arrows



Figure 10. Winding/Rotor Epoxy - Crack in Epoxy Shown in Red Oval

None of the inspection methods had indicated the actual source of the resistance changes. Some locations were implicated by the presence of cracks in the epoxy coating, but none of them showed any signs of a feature that would cause an increase in resistance as the temperature is reduced during the cold temperature portion of the thermal cycles. The solder joints at the commutator were inspected as well and, while some of the joints had workmanship issues, none of the connections showed any type of failure that would support the test data. The brush block/commutator/shaft assembly was X-Ray inspected while installed in the motor and the brush springs (cantilever arms) showed a proper preload on the brushes as indicated by the deflection of the spring arm (see Figure 11).

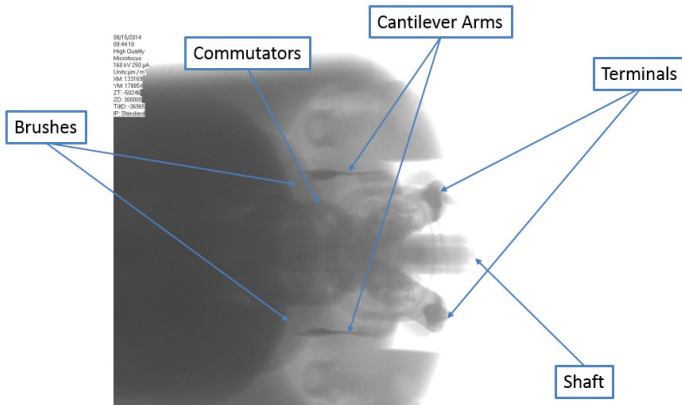


Figure 11. X-Ray Image of the Brush/Commutator Assembly

shows the rotor assembly with the individual winding wires clearly visible. Figure 13 is a cross-section of the rotor with one slot on the rotor exposed and the wires within the slot visible in fine detail. Figure 13 is a view of the brush assembly end of the shaft with the brushes and cantilever arms clearly visible.

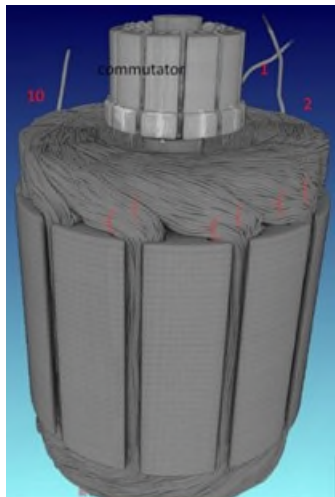


Figure 12. Rotor Assembly

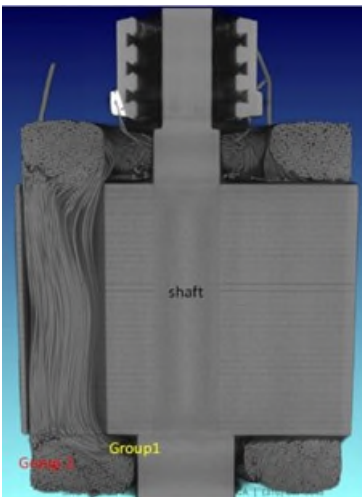


Figure 13. Section of Rotor Showing Wires in the Slot

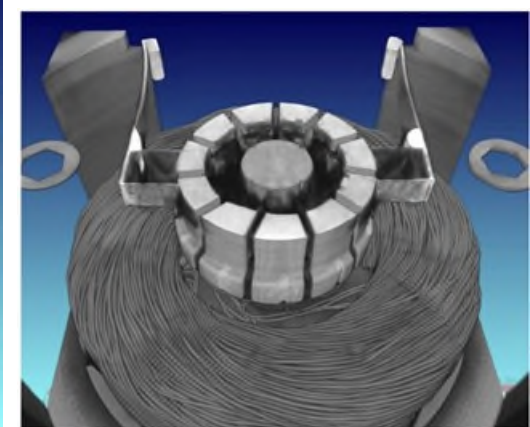


Figure 14. Brushes, Commutator, and Cantilever Arms

The CT Scan inspection method provides high resolution three-dimensional computer models that can be interrogated in locations within the assembly that are otherwise not possible to inspect. Since no disassembly is required, the in-situ state of all components can be viewed. Additionally, any failure condition that may be disturbed by disassembly can be captured without risk of losing the failure evidence in the process of removing intervening material.

Close inspection of the CT Scan model revealed the source of the winding failures to be coincident with the crack sites of the epoxy located on the opposite end of the rotor from the commutator assembly and winding wire terminations. Figure 15 shows a close-up view of the end of the rotor where the wires exit the slots and there is indication of damage to the winding wires, identified by the red arrows. Focusing on the areas of apparent damage, the culprit is finally found to be broken winding wires at the exact locations of the epoxy cracks. The wire can be seen to have necked down prior to failing, indicating a tensile failure.

The next inspection method used was a Computed Tomography X-Ray Three-Dimensional inspection technique, or "CT Scan". The motor assembly was placed on a plate in the CT Scanner machine that rotates about a vertical centerline. The motor is incrementally rotated a small amount and for each image slice that is taken. Several thousand image slices are taken, each from a different position and angle, around the motor. The multiple slices are then assembled into the three-dimensional computer model represented in the figures that follow.

Overall CT Scan views of the rotor assembly are shown in Figures 12, 13, and 14. Figure 12

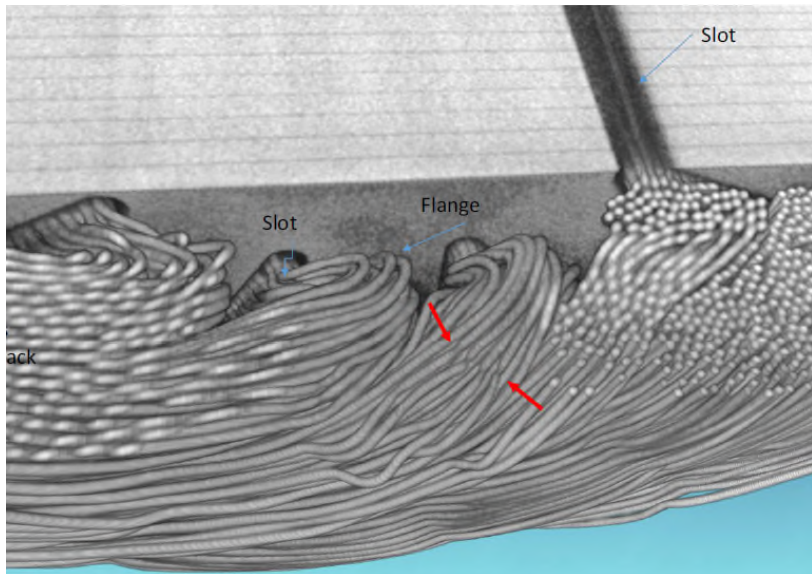


Figure 15. Magnified View of the CT Scan Model Showing the End Turns and the Slots in the Rotor Laminations

Further investigation of other epoxy crack locations revealed several failed wires and many stretched wires with necked down cross-sections. The necking would account for resistance changes in the first few cycles after the epoxy crack propagated to the location of the wires. The sudden increases of winding resistance in the test data were the result of several broken regions moving back together as the temperature was raised. While the winding resistance might have appeared nominal at a higher temperature, the winding wire damage points would certainly not have supported a high enough load current to produce the required torque output from the motor in the IDA application.

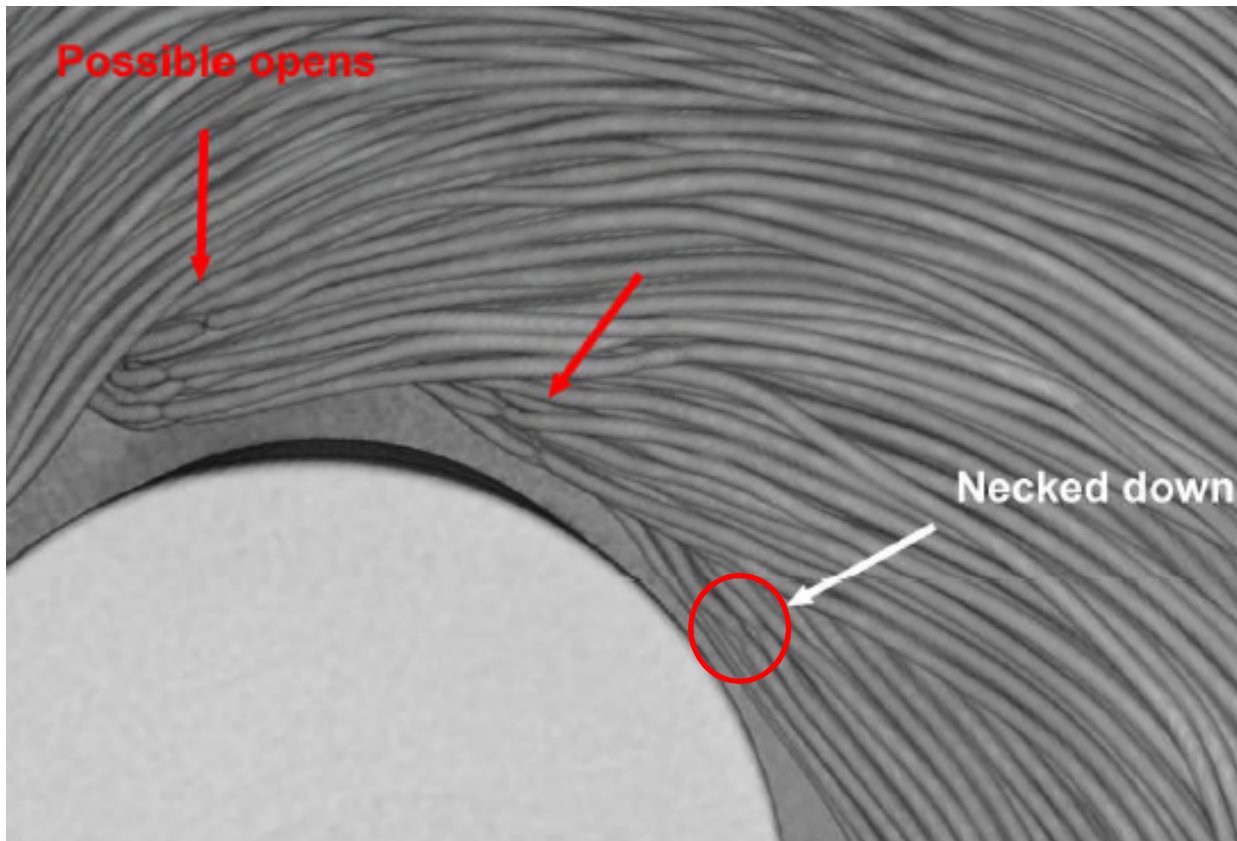


Figure 16. View Showing Several Locations of Failed Wires. The Necking Down of the Breaks Indicates Tensile Failures. The Wire Breaks Follow the Cracks in the Epoxy Coating. The wire diameter in the image is 80 microns.

10-mm Motor/Gearbox Life-Test-to-Failure Determination of Failure Source

10-mm Motor/Gearbox Application Hardware Description

The 10-mm motor and gearbox assembly is comprised of a three-phase brushless dc motor attached to a 16:1 reduction ratio planetary gearbox. The motor has ball bearings on the rotor and the gearbox planet gears use plane bearings. The gearbox is lubricated with Bray grease, type 601. There are two preloaded ball bearings on the output of the gearbox to provide a moment carrying capacity for offset loads on the output shaft. The face width of the planet gears is approximately one millimeter and the ring gear is made from bronze.

The 10-mm actuator drives the filter wheel of the Mast cameras on the Curiosity rover operating on the surface of Mars. The actuator has a pinion gear attached to the output shaft and is mounted into a housing that contains the larger filter wheel for the camera. The pinion gear on the actuator output drives the filter wheel directly with a gear mesh on the outside diameter of the filter wheel disc. The motor is operated as a stepper motor in this application, so no rotor position sensors are mounted within the motor housing. There is a magnetic detent wheel attached to the back of the rotor to provide the necessary magnetic detent for proper stepper motor function. The filter wheel assembly is shown in Figure 17. Magnets on the filter wheel itself are sensed with hall sensors in the housing to confirm filter position during operation of the mechanism.

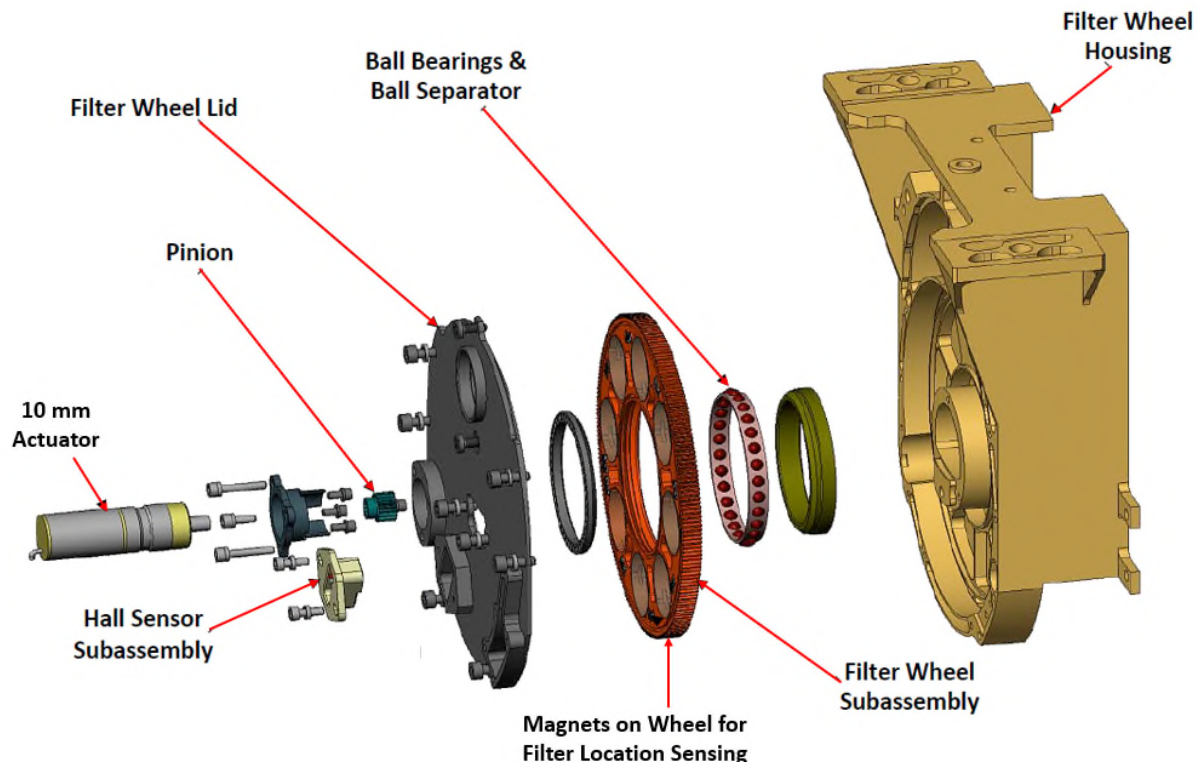


Figure 17. Filter Wheel Assembly Application of the 10-mm Actuator

Life Test Setup

Two Filter Wheel Assemblies were used on the Curiosity Rover mission. Two Filter Wheel Assemblies are also being put in the new camera build for the Mars 2020 mission. Since the Mars 2020 mission is a longer duration than the Curiosity mission, the life test that was performed on the Filter Wheel mechanism for the Curiosity mission was not adequate for the newer mission requirements. The life test Filter Wheel Assembly from the Curiosity hardware build was resurrected and placed into a life test to understand if any fundamental limitations of the hardware design existed that might affect its use for the Mars 2020 mission.

The test configuration placed the Filter Wheel assembly on a test bench with the actuator in the horizontal position. This was done to minimize the possible effect of the presence of a gravity vector. In the application on Mars, the actuators are in the horizontal position as well. The actuator was operated using a motor driver that provided a pulse width modulated motor coil drive current. The pulse width modulation was to set a current level for the motor that was less than the maximum possible winding current at the applied drive voltage. The current limit is used for the flight unit drive and allows limiting of the output torque of the motor. The setup of the test equipment for the life test is diagrammed in Figure 18. The Stepper Motor Driver operates the motor and the actuator rotates the Filter Wheel Assembly. The magnets on the filter wheel provide indications of filter position back to the comparator while the wheel is turning. The number of steps between filters is a known value. The comparator checks the number of steps it took to move between filters to the known number of steps between filters. If the step count does not match the predicted value within a couple of steps, the comparator declares missed steps.

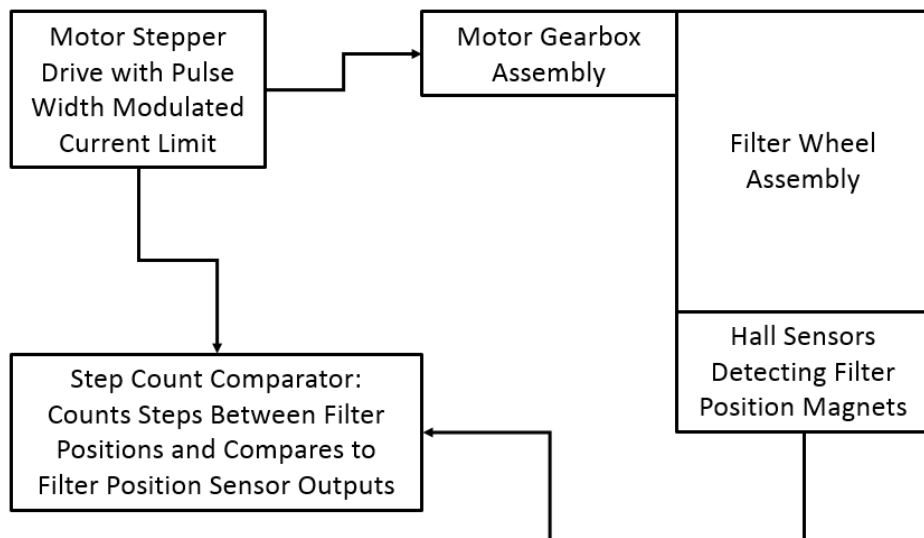


Figure 18. Block Diagram of the Filter Wheel Assembly Life Test Setup

For the life testing, the motor current limit was determined by reducing the limit until the operating motor started missing steps. This is the threshold limit for the operation of the stepper motor at the applied torque load. The life test was started with the motor driver current limit set to a value of 20% of the maximum drive capability, which was a little above the drive at which the motor missed steps. The motor was operated continuously and the number of steps between filter positions were checked until the motor skipped steps. The motor drive current limit was then raised to 45% of the maximum, which was the value needed to reliably rotate the actuator without missing steps at the higher torque load. The test was continued until the motor started missing steps again. The third time the motor drive output was raised to 100% of the output capability. The test was continued until the motor started skipping steps once more. Since the maximum drive capability was reached, the test was terminated at that time. The total number of output revolutions demonstrated was over 14 times the required life for the Mars 2020 mission, indicating a high level of robustness of the Filter Wheel Assembly design for the application.

Determination of the Cause of the Failure to Rotate

The final operation to perform after the completion of the life testing phase was to determine the cause of the Filter Wheel Assembly's failure to rotate reliably. The first step in this process was to remove the actuator from the filter Wheel Assembly and operate the actuator alone. The actuator would still not rotate reliably separated from the Filter Wheel Assembly. This indicated that the actuator was the source of the failure to rotate reliably for the entire mechanism. The actuator was placed into a Fein focus real-time X-ray machine and inspected for possible causes of the failure. Figures 19 and 20 show images from the x-ray machine.

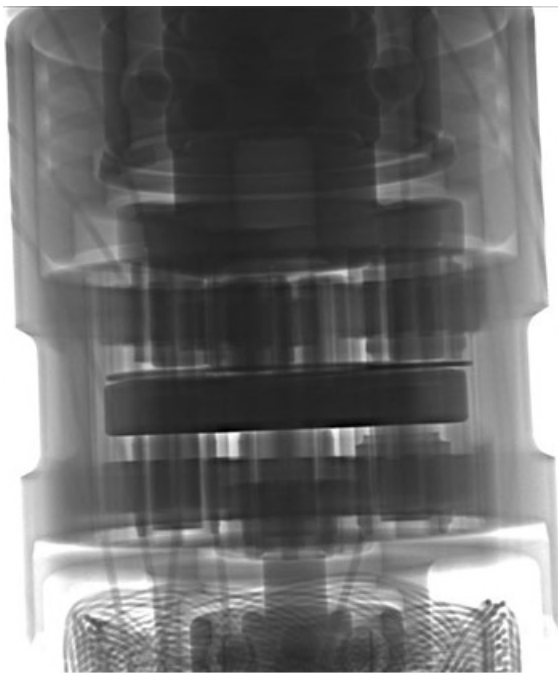


Figure 19. X-Ray Image Showing the Gearbox Section of the Actuator. Output Ball Bearings are at the Top of the Image and the Front Motor Bearing is at the Bottom

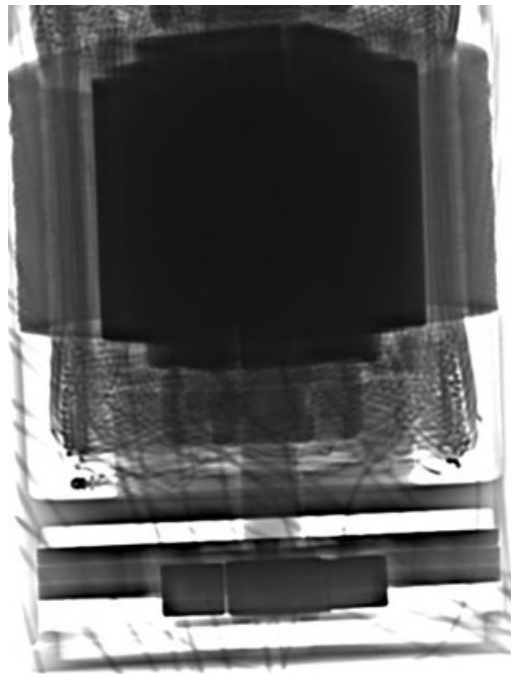


Figure 20. X-Ray Image Showing the Detent Magnet Section of the Motor Assembly. Magnets are on the Rotor and the Teeth are on the Stator

From the x-ray images there is no apparent problem within the actuator at all. The gearbox looks to be in good shape, the bearings at the gearbox output show no indication of extreme wear or debris, the motor bearings do not show any sign of wear or debris, and the motor windings show no indication of being damaged. The failure mechanism needed to be consistent with a wear phenomenon since the test required a slowly increasing drive current to keep the mechanism operating properly. This would indicate an increasing load torque as opposed to a sudden change. The only item detected with the x-ray images was the offset of the detent wheel from the detent stator. This appeared to be a manufacturing defect since it would not explain a slowly increasing load torque.

The Culprit is Exposed!

The next possible inspection method involved opening up the gearbox and motor to directly inspect the components for wear and debris. The problem with this method is that the 10-mm actuator is not built to be disassembled. The component items are bonded together and machining would be required to separate the parts. There was a significant concern that a machining process may dislodge the source of the drag torque and the failure would be permanently lost. To eliminate this concern, the CT Scanning method was employed. The volume of the actuator is small and the resolution of the machine is a fixed value for the scan volume. If the volume size is made smaller, the image dimensional resolution is increased. The actuator was CT Scanned and the model was queried to determine the source of the drag torque. The gearbox was the suspected guilty party, so it was inspected in detail first.

Figure 21 shows the overall view of the motor and gearbox assembly for the 10-mm actuator. The CT Scan detailed computer model allows the cross-sectioning of the image so internal components can be inspected. In this actuator, the planetary gear faces are one millimeter wide. The bright portions of the image are the permanent magnets due to their high density. Figures 22 and 23 show the planetary gear stages in a cross-section of the computer model at each stage location. No debris is visible and no wear of the gear tooth

form is evident from the image. The gear teeth and tooth form look as if there is no wear at all. The input to the first stage of the planetary gears had been through 258 million revolutions at this point.

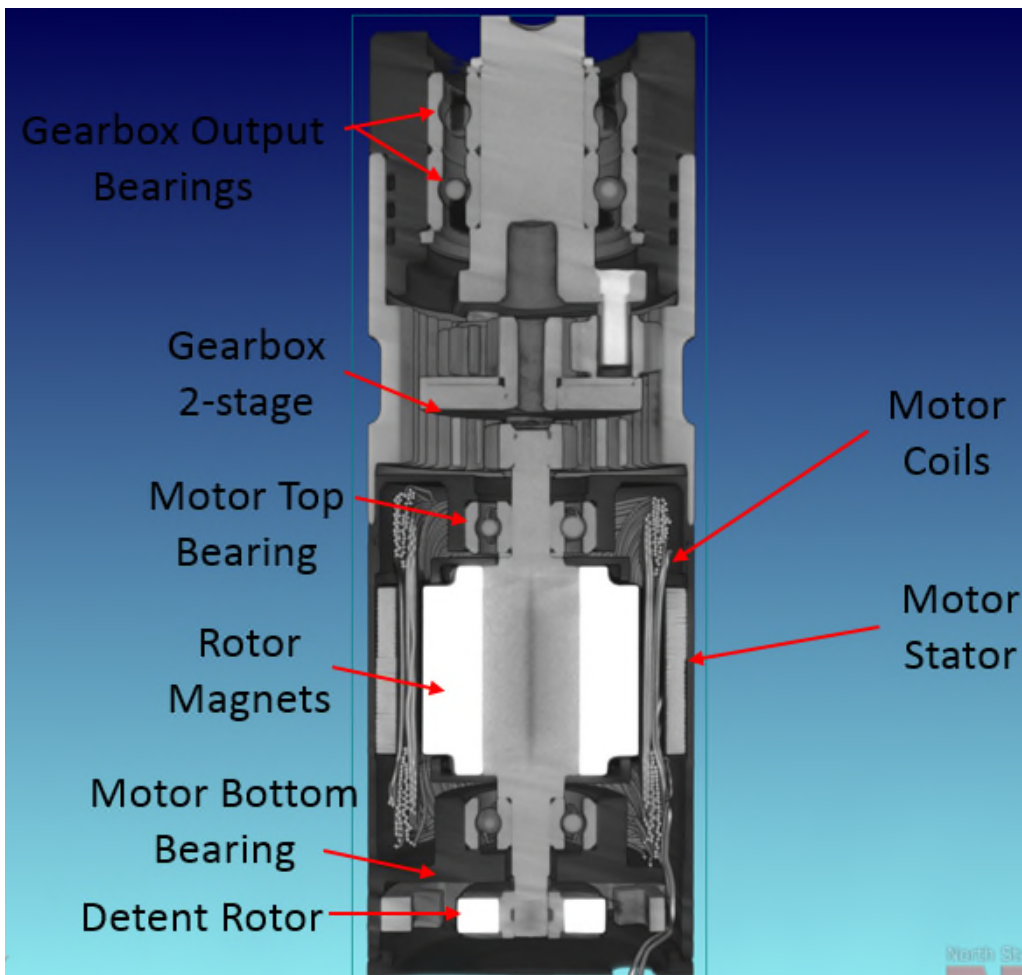


Figure 21. Overall Image Cross-Section of the 10-mm Actuator Assembly

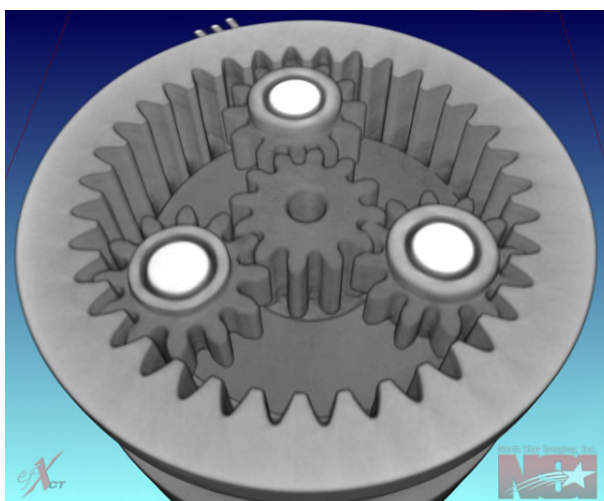


Figure 22. Second Planetary Gear Stage

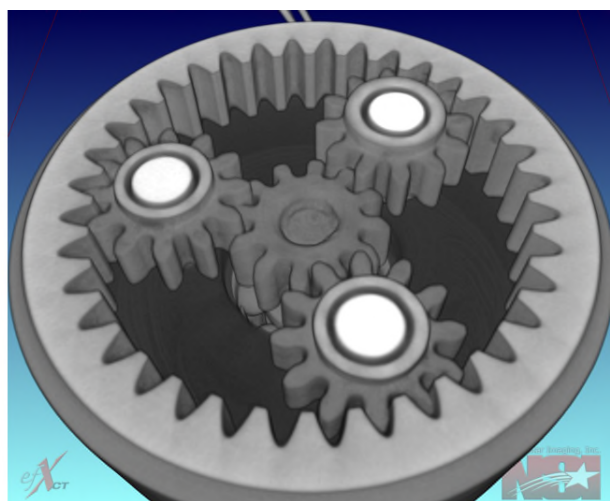


Figure 23. First Planetary Gear Stage with the Motor Pinion at the Center

The view of the first stage of the planetary gears seemed to show an offset of the pinion gear toward the motor. This necessitated an inspection of the front motor bearing. Looking at a section of the model from the side in Figure 24 shows that the motor bearing appears to have shifted downward in the image and the motor pinion gear has done the same. Scrutinizing the bearing assembly itself shows no unusual wear or debris. All other elements of the motor assembly in this region seem fine.

The offset of the rotor was a mystery and required further investigations. Looking at an isometric view of the section of the motor through the shaft at the front motor bearing did not expose anything unusual. Figure 25 shows the view with the front motor bearing fully intact with no significant wear or debris.

Moving down to the rotor detent assembly, the detent magnets are positioned properly within the inside diameter of the detent stator and no anomalous behavior appears at this location. Figure 26 shows this region of the motor assembly with no visible indication of a torque drag anomaly.

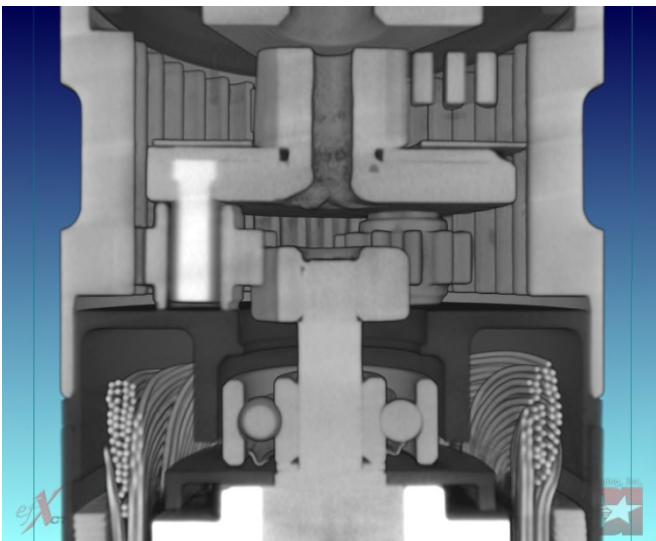


Figure 24. Side View of the First Planetary Gear Stage with the Motor Pinion at the Center. The Bearing is Displaced Downward in the Image

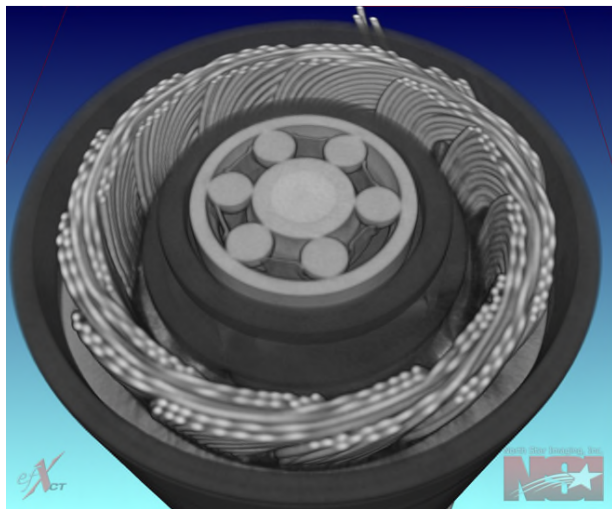


Figure 25. Front Motor Bearing Closest to the Gearbox Input

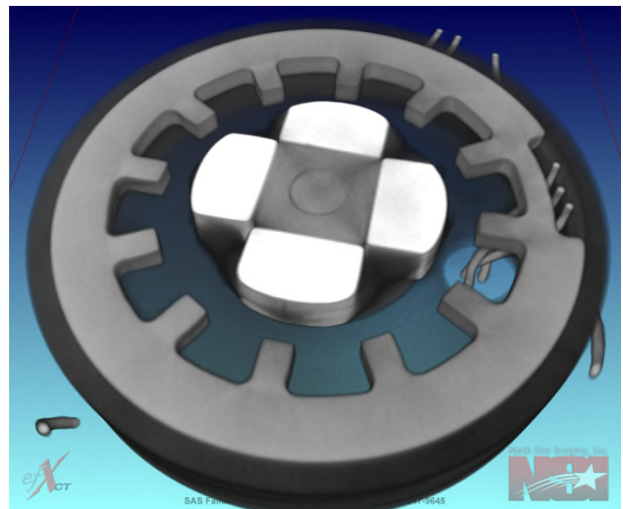


Figure 26. Detent Rotor and Stator

Inspecting the CT Scan model further finally showed a source of the drag. The rear motor bearing is shown in Figure 27 and the ball separator is missing. The balls have moved within the bearing assembly to a position where they have jammed and the bearing will not rotate. While the jammed bearing appeared to be the guilty party, it could not explain an increasing torque load over time. The problem with the bearing jam being the source of the drag is the jam does not allow the bearing to rotate. This should have stopped the actuator suddenly and not in the manner of a slowly increasing drag torque.

Closer inspection provided the needed clues to the solution. The shaft in the bore of the bearing in Figure 27 appears to be smaller than the bore. Figures 28 and 29 show a side-by-side comparison of the end of the motor with an as-built beginning of life motor on the left and the failed life test motor on the right.

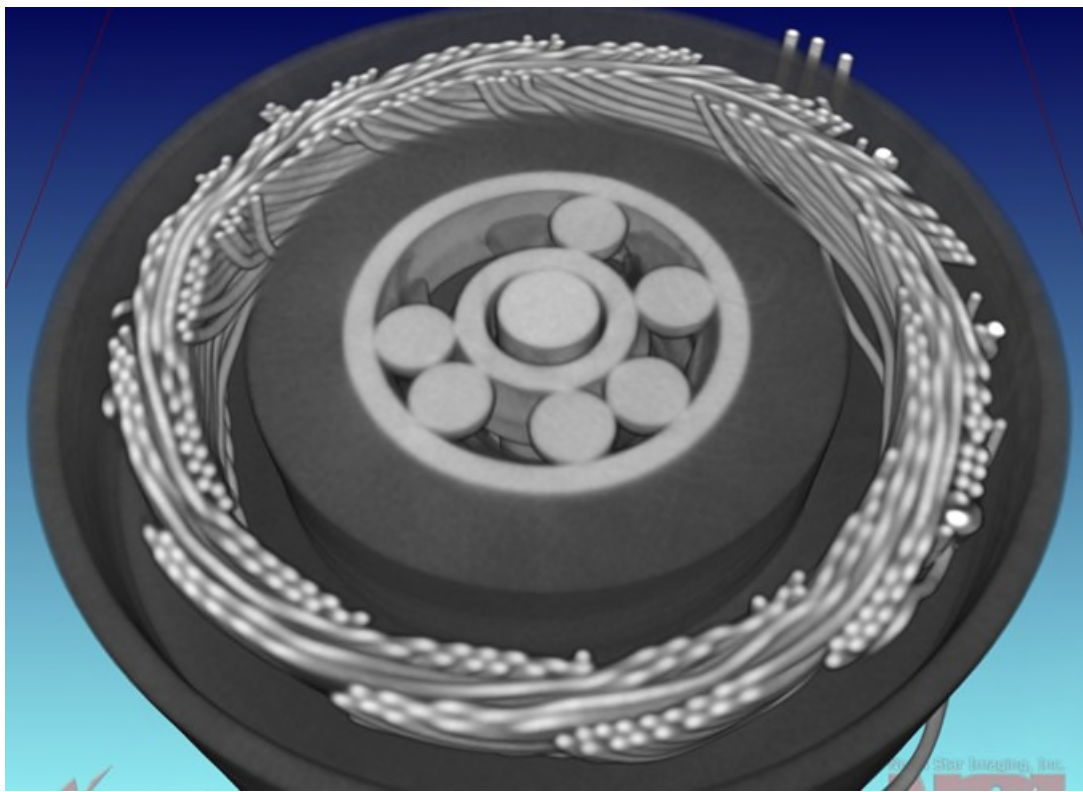


Figure 27. View of the Rear Motor Bearing Showing the Balls Have Displaced Around the Circumference of the Bearing Races to a Jamming Position. This Makes the Bearing Unable to Rotate at All.

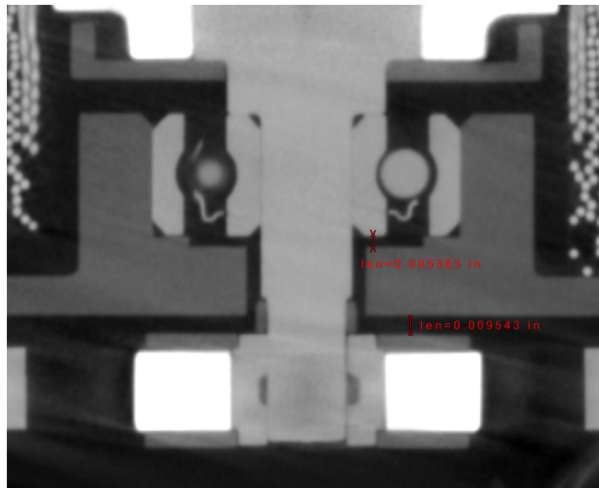


Figure 28. Healthy Motor at the Beginning of Life Showing Bearing Placement and Shaft Fit. The measurements in the images are in inches ($0.0095 \text{ in} = 241 \text{ microns}$)

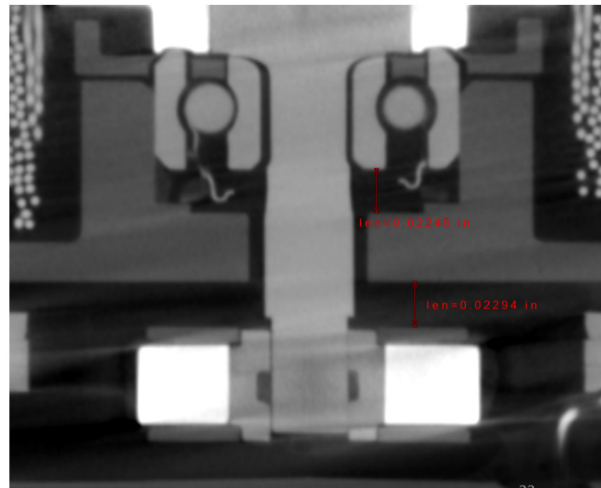


Figure 29. Life Test Motor Showing Shaft Wear and the Bearing Having Moved Toward the Rotor. The Ball Retainer is Seen Located Under the Bearing Assembly. ($0.0229 \text{ in} = 582 \text{ microns}$)

Figure 30 shows a close-up of the rear ball bearing and where it is dragging on the rotor (from Figure 29). The bearing has cut through the magnet end cap (aluminum) and started cutting into the magnet material. The rotor diameter has also worn significantly smaller than the bearing bore. The root cause of the failure was the bearing seizing and stopping rotation. This was followed by the rotor shaft rotating in the bore of the bearing inner race. Since a stepper motor does not provide current feedback that is related to load torque, the jamming of the ball bearing was not detected. This event was missed because the motor rotor was assembled with a small clearance to the ball bearing bore and that allowed the rotor to rotate within the bore of the bearing. This motion started the wearing of the rear section until too many components were dragging on each other.

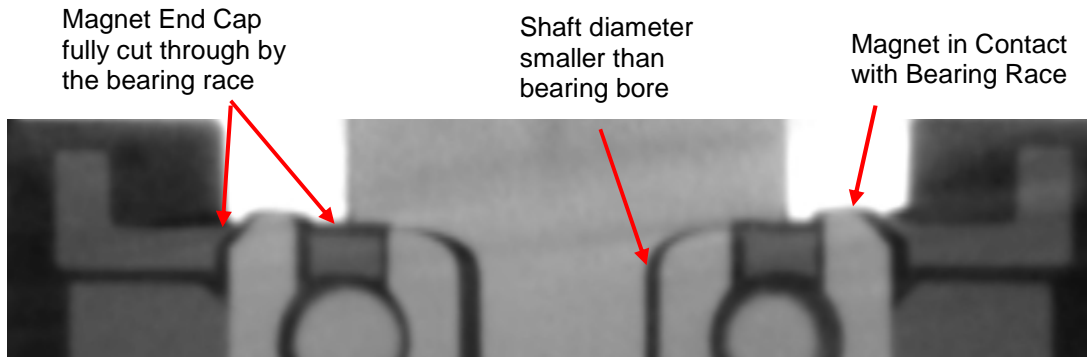


Figure 30. Close-up of the Motor Rear Bearing Showing the Wear of the Components of the Rotor

An interesting point is the components all have a thrust load on them that draws them toward the rotor. This thrust load is from the magnet flux at the end of the magnets. This is often not a significant player in the performance of a motor, but the thrust load is enough to draw the component into the rotor such that, if there is sliding contact, significant wear can occur.

Conclusions and Lessons Learned

The CT Scan inspection method is extremely powerful in diagnosing failures in mechanical assemblies where access to the suspect regions of the hardware is very difficult or impossible. It is also great to use where the accessing of the internals has the risk of losing the failure. Since the most important tenet of troubleshooting is to NEVER LOSE THE FAILURE, the CT Scanning method is a fantastic resource.

Additionally, thermal cycling of motor windings for extreme cases is paramount to having confidence in mission success. Continuous monitoring during the temperature cycling of the item being tested is critical since the failure may not be present at room temperature, as was the case with the InSight IDA motors.

Lastly, making the rotor free to rotate within the motor bearing bores, if possible, provides a robust and graceful degradation path for actuator motors. This is especially important at the lowest torque location within the mechanism – the motor rotor.

Acknowledgements

This work was performed at the Jet Propulsion Laboratory, California Institute of Technology, under a contract with the National Aeronautics and Space Administration. Reference herein to any specific commercial product, process, or service by trade name, trademark, manufacturer, or otherwise does not constitute or imply its endorsement by the United States Government or the Jet Propulsion Laboratory, Pasadena, California. Copyright 2018 California Institute of Technology. All rights reserved. Government sponsorship acknowledged.

The author wishes to acknowledge the great contributions provided by Raytheon SAS Failure Analysis Lab in El Segundo, California for expertise operating the North Star Imaging machine and the InSight failure analysis team and associated review boards in uncovering the root cause of the winding anomalies. On the 10-mm Actuator failure analysis effort, Malin Space Science Systems performed the life test and provided invaluable information and access to the Filter Wheel Assembly actuator at the conclusion of the life test. Malin Space Science Systems facility is located in San Diego, California.

Testing and Development of the NEA Scout Solar Sail Deployer Mechanism

Alex Few*, Tiffany Lockett*, Richard Wilson** and David Boling**

Abstract

The Near Earth Asteroid (NEA) [1] Scout is a deep space CubeSat designed to use an 86-m² solar sail to navigate to a near earth asteroid called VG 1991. The solar sail deployment mechanism aboard NEA Scout has gone through numerous design cycles and ground tests since its conception in 2014. An engineering development unit (EDU) was constructed in the spring of 2016 and since then the NEA Scout team has completed numerous ground deployments aiming to mature the deployment system and the ground test methods used to validate that system. Testing a large, non-rigid gossamer system in 1G environments has presented its difficulties to numerous solar sailing programs before, but NEA Scout's size, sail configuration, and budget has led the team to develop new deployment techniques and uncover new practices while improving their test methods. The program has planned and completed 5 separate full-scale sail deployments to date, with a flight sail deployment test scheduled for FY18. The paper entitled "Design and Development of NEA Scout Solar Sail Deployer Mechanism" [2] was presented at the 43rd Aerospace Mechanisms Symposia. Since then, the system has matured and completed ascent vent, random vibration, boom deployment, and sail deployment tests. This paper will discuss the lessons learned and advancements made while working on solar sail deployment testing and mechanical redesign cycles.

Introduction

In May of 2016, the Near Earth Asteroid (NEA) Scout engineering development unit (EDU) solar sail was prepared for a suite of environmental tests culminating in a full-scale deployment at NASA Marshall Space Flight Center's (MSFC) flat floor facility. The full-scale deployment premiered a fully machined EDU, flight-like motors, and a developing control system. Numerous half scale deployments and mechanical development efforts were completed in preparation for the full-scale test.

The solar sail development team developed a test suite that would begin with an ascent vent test to simulate the rapid depressurization during ascent on NASA's Space Launch System. This test was performed to indicate the viability of the sail folding pattern and verify that the vent paths were performing nominally. The folding pattern and vent paths proved to be acceptable and no sail damage was noted due to trapped air. After ascent vent the team prepared for a random vibration test. This test was intended to vibrate the system in all 3 axes with intermittent, boom-only deployment tests after each axis of vibration. The team encountered their first major lesson learned through an undersized stepper motor, which disabled the ability to perform intermittent tests. The team proceeded with the random vibration test with the undersized stepper motor. Post-test, an investigation into the undersized motor commenced. Causes identified included limited design space, improper scaling of half-scale loads to full-scale designs, and poor assumptions regarding the system's internal friction. The redesign effort required a major system reconfiguration.

After the redesign activities, boom-only deployments and retractions tests were completed. With the new configuration and properly sized stepper motor, the boom-only deployments demonstrated the capability and robustness of the system during nominal operations and risk mitigation activities, such as boom blooming characterization. The team learned several lessons that will be highlighted later in the paper. Examples are retraction rates to remove blooming, boom buckling recovery, and deployment shape dynamics.

* NASA Marshall Space Flight Center, Huntsville, AL

** Jacobs Engineering, Huntsville, AL

Once the team was comfortable with the boom deployments, the EDU sails were deployed. Two sails were produced for EDU activities: a Mylar sail and a colorless polymer-1 (CP1) sail. Both sails were 86 m² in size, and the CP1 version was built as flight-like as possible. During the deployments, the team updated procedures with boom support information, electrical inputs, sail attachment methods, and mechanical fixtures. These tests proved to be the most eye-opening tests to date.

Stepper Motor Deployment Failure and Motor Sizing Lessons Learned

Prior to the solar sail deployer (SSD) random vibe test, the engineering team conducted a boom-only deployment and learned that the existing stepper motor was undersized. This became a large setback that led to a drastic SSD mechanical redesign, lengthy coordination with the motor vendors, and a long list of failure causes. It was clear that the undersized motor was performing properly with suitable electrical inputs, but it was unclear why the booms would not deploy.

After investigating, the team determined that the torque requirement was vastly underestimated and a larger motor was needed. The design team then set about to redesign the deployer to house a larger stepper motor. Unfortunately, the SSD had no volume to spare. The motor volume was specifically tailored the previous motor with no margin. After weeks of redesigning 4 of the 5 primary structural components, the larger motor—just 4-mm taller than the undersized motor—was accommodated.

The rest of the team conducted a failure analysis in parallel with the redesign effort. After a month of discussion and investigation, a list of possible causes was created and the team commenced to find the root cause or causes. The team investigated the control board settings, the test setup and the deployer. Luckily, the SSD's redesign activities required complete deconstruction allowing the designer to inspect the assembly alignments and each part for wear, deformation, and/or any other visible damage. Wear and more severe damage was discovered and documented. Analysis comparing the CAD models, mechanical drawings, additively manufactured plastic prototype, and as-built EDU uncovered 6 contributing errors. The causes are listed in the order they were discovered with the final cause, number six, identified as the root cause.

1. The motor was undersized and lacked volume margin to allow for a larger version.
2. The prototype control board was overpowering the motors, producing more torque than expected.
3. The system was unknowingly susceptible to mechanical interference and wear.
4. Internal friction was grossly underestimated.
5. The boom spooling operation was prone to large irregularities and damaged other components.
6. The team drew too many comparisons between the plastic prototype and EDU.

Each item above will be discussed and presented as a lesson learned.

Undersized Motor Volume Allocation

The mechanical design team determined years before the EDU tests that stepper motors would power the SSD. There were few motors to choose from in a desirable form factor—about 15 mm in diameter or less—and steppers would produce the most torque per unit volume. Significant prototype testing with 3D printed components, friction estimation and torque calculations were made to select the first motor: a Faulhaber AM1524 with a 91:1 planetary gearbox (Figure 1). After selecting the motor, the designer matured the SSD design without allocating any significant clearances between the motor and other structural components. The motor was boxed in.

Just as it is common practice to design mechanical interfaces with extra material in the event larger fasteners are needed, the design team learned that this cautious practice applies to motor volume allocation as well. A new motor just 4-mm taller than its predecessor required a large redesign effort including major changes to 80% of the SSD structural components. All of the redesign efforts and cost could have been avoided if the motor volume allocation had just 10% of height margin.

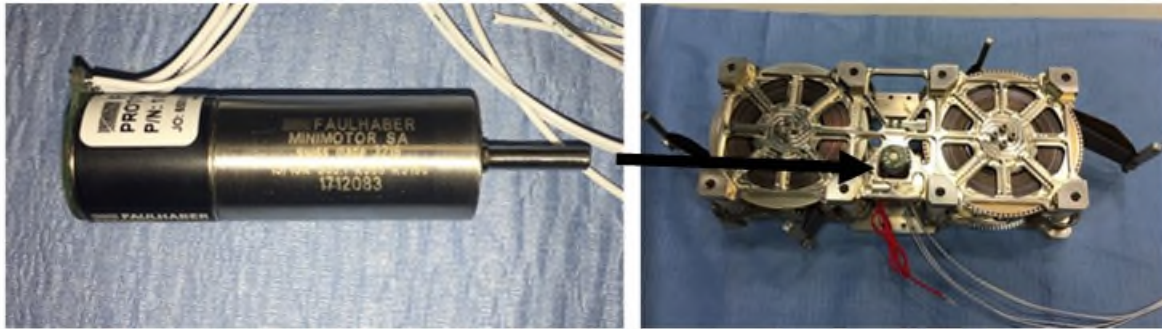


Figure 1. Faulhaber stepper motor and respective location on the NEA Scout SSD

Incorrect Electrical Inputs

During consultation with the motor vendor, the team learned that the SSD's electrical inputs needed investigation. The prototype control board had a single step input, commanding the running speed without ramping. This requires more current to instantaneously accelerate the motor to operational speeds. The overcurrent provided a "false positive": overpowering the motors produced more torque than the datasheets and designs allowed. The overcurrent lasted for the 15-minute deployment duration and showed no evidence of failure through about 50+ prototype tests. However, it did give a false sense of confidence that the smaller motors could produce the required torques due to the gross overcurrent. To correct the overcurrent input, the board designer reconfigured the algorithms to include a gradual ramp rate which reduced the heat output. It should be noted that this input change saved a potential failure at the next thermal vacuum test (This error nearly crippled the development of another NEA Scout subsystem, the Active Mass Translator and is discussed at length in "Testing and Maturing a Mass Translating Mechanism for a Deep Space CubeSat"). Had the board not been reprogrammed, the motor may have passed ground testing, hiding the issue until later in the program development.

Mechanical Interference and Wear

There were clear signs of interference and wear on most of the rotating components within the deployer. As the SSD was deconstructed, each part was inspected and any wear and debris was photographed. It was clear that the as-designed gaps had closed either during assembly or operation. Some of these gaps were 0.25 mm or less and resided between stiff structural plates and thin, rotating flanges (Figure 2, 3).

The flanges deformed during spooling and/or deployment and contacted their neighboring structural components. This produced gouges, aluminum dust and removed the chemical conversion coating from the contacting surfaces. Images of the damage are shown in Figures 4 and 5.

The interferences had three main causes. First, CAD models were made to the desired values and the associated clearances respected a "perfect" construction. Areas showing reasonable clearances in the models did not represent potential over or undersized components. Had the models been sized to their least desirable extremes, the areas susceptible to interference would have been more obvious. Furthermore, the tolerance analysis did not include a minimum clearance requirement on the rotating features, so even if the parts were made to specification, any deformation would have caused damage. Sadly, there was also no quality inspection on the EDU components so we are not sure that the EDU components even met the drawing requirements.

Second, the rotating flanges were too thin to resist loads from the boom coils and deformed. We did not understand the spring energy in the booms and that the thin flanges would be in the spring energy's load path. The flanges and gears were not stiff enough to resist and deflected through the as-designed gaps into the structural components.

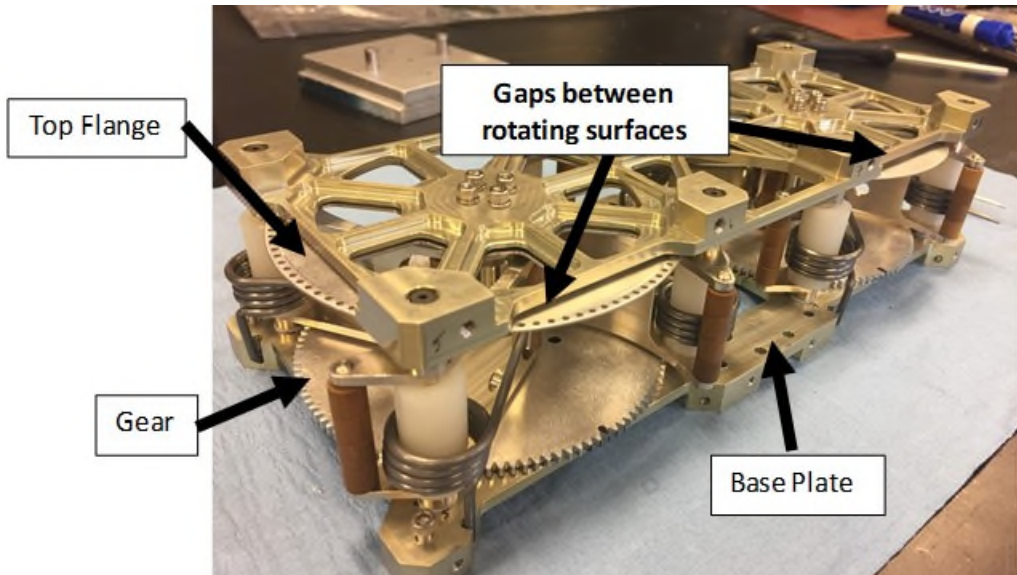


Figure 2. Boom-less assembly and as-expected gaps

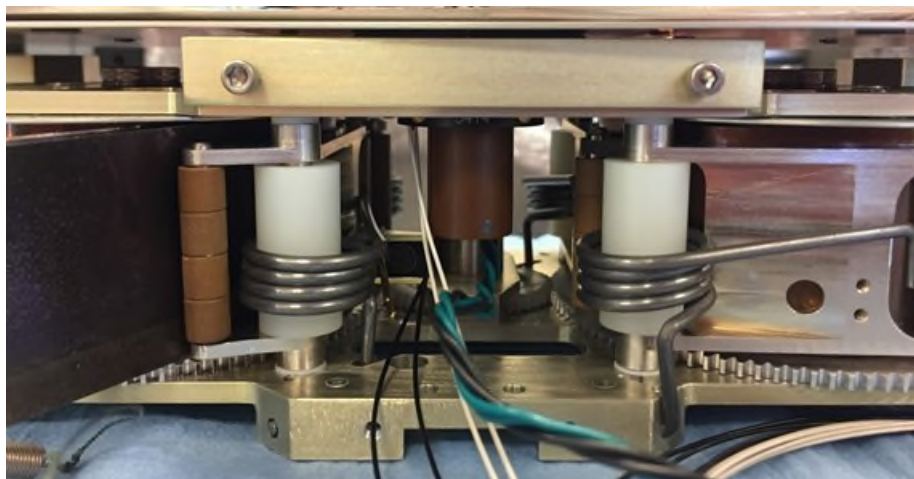


Figure 3. As-built gaps. Note the near line-to-line contact between the gear and base plates



Figure 4. Visible wear on top flange caused by boom coil irregularities. Note that the gold conversion coat has been removed.

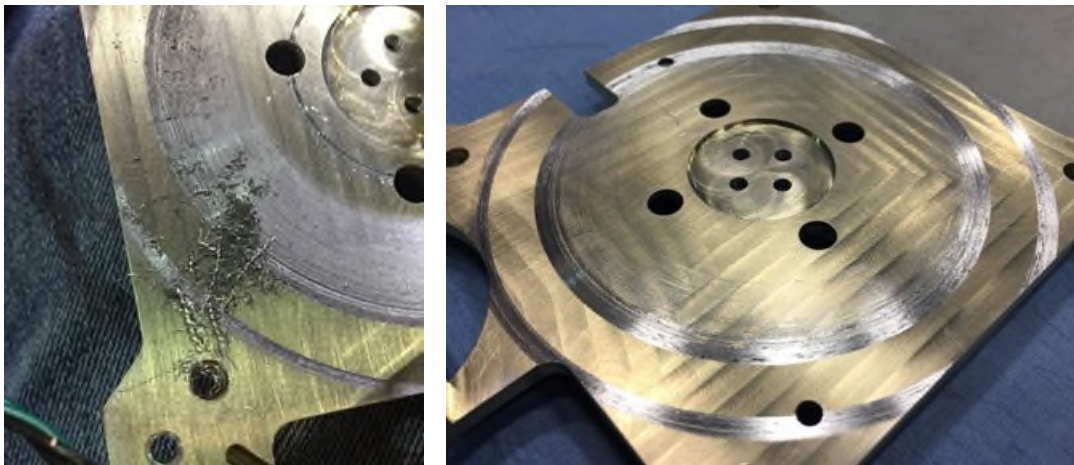


Figure 5. Gouging and wear on base plate caused by gear interference and coil irregularities

The final contributor was poor material selection. All wearing surfaces were aluminum to aluminum, producing a high friction coefficient (approximately 1.0) and covered surface areas around 50 cm^2 . The flanges were not structural and could have easily been changed to plastic or a polytetrafluoroethylene (PTFE) embedded material, reducing friction by a factor of 2 at least. Though the interference was an off-nominal case, lower friction materials would have reduced the torque requirement in the event of physical contact between these components.

The interferences were removed by making larger gaps between the rotating components. The flange damage was repaired and the base plate was redesigned to accommodate the new motor design. The gear's height was reduced by about 0.2 mm and 0.2-mm shims were added between the top flange and top plate. These changes nearly tripled the gap widths, allowing for spooling irregularities and reduced the wear observed at the next deployment tests.

Much of the mechanical interference and wear investigation uncovered other problems that were addressed in the SSD's redesign and test development. These causes were related to the internal friction assumptions, boom spooling irregularities, and 3D prototype comparisons.

Poor Understanding of Friction

The SSD is designed to slowly release the spring energies of four tightly wound 7.2-meter stainless steel booms. The spring forces naturally produce friction during boom deployment and retraction. The booms are rolling over numerous thermoplastic bushings, sliding along two thin aluminum surfaces and rubbing between their concentric coils as they "bloom" [2]. These loads are relatively straightforward to calculate individually, but as a system, there was no accurate way to represent behavior other than with prototype testing. The half scale plastic model provided some torque estimations and allowed the team to optimize contact surface designs, but the measured torques were not properly scaled to represent a full-scale system. This will be expounded upon in the "Inaccurate Correlation" section.

The three friction sources noted above—rolling, sliding, and blooming—are great contributors to the torque load, but there were many more that had to be considered during the redesign (Figure 6). First was the motor transmission inefficiencies. The vendor datasheets noted that the 91:1 motor operated at about 70% efficient, meaning only about 70% of the motor shaft output was transmitted to the gearbox shaft [3]. This means the speed was knocked down by a factor of 91, but the torque only increased by a factor of 63. This was a small oversight in reading a datasheet with huge ramifications. Furthermore, friction in the rulon bushings and between gear teeth was ignored and given that there was no quality inspection on the individual parts, these could have been either non contributors or primary causes of our system failure.

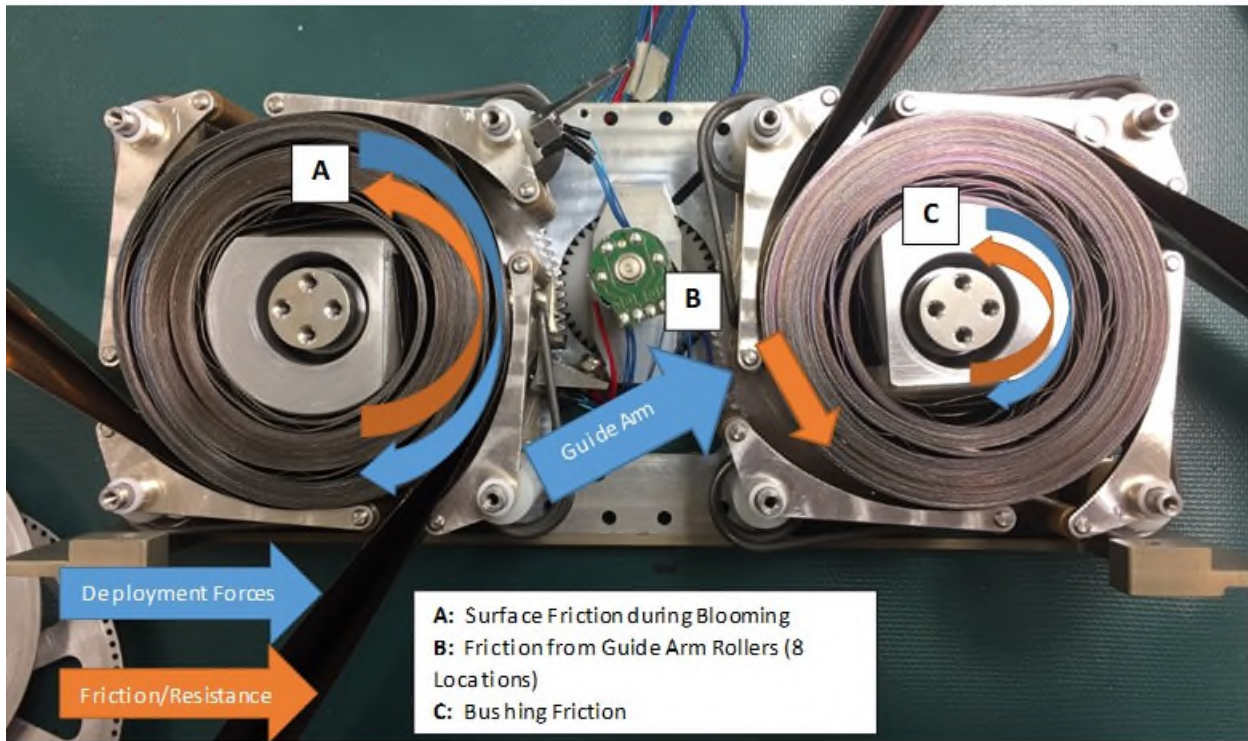


Figure 6. Three sources of friction in the deployer system

Lastly, there was significant external friction that had yet to be considered. As the booms deploy, small sliding feet were attached every couple of meters to prevent contact with the floor and boom flanges. These friction forces react back into the deployer and act as resistance loads against the motor torque. We had never considered this and even if the motor could have initiated deployment, there was a good chance that the ground testing would fail due to the test-induced loads as the booms deployed across a surface. The slider and test design impacts will be covered in the “Sail Deployment Development and Testing” section.

Boom Spooling Irregularities

One of the primary focuses during the deconstruction activities were the spooled boom configurations and their impacts on surrounding components. The coiled booms were expected to be 35-mm tall, but as they were deployed and retracted over time, small irregularities produced an inconsistent spool height. Within the concentric coils, the spool height may rise or fall by 0.3 mm. This inconsistency pressed against the spool flanges and gears, causing the deformation and wear shown in Figures 4, 5, and 7. The lack of alignment features for the boom spooling operation damaged surrounding components on retraction and deployment.

This design flaw was remedied during spooling operations. The retraction speed was reduced to about half the deployment speed and required two people to closely monitor the booms’ entrance angles and clearances between the upper flanges and lower gears. There was not enough structure or volume to include passive alignment features, and the hands-on solution proved to be acceptable. After properly spooling the booms, flange and gear damage was greatly reduced and deployment torque requirements were noticeably different.

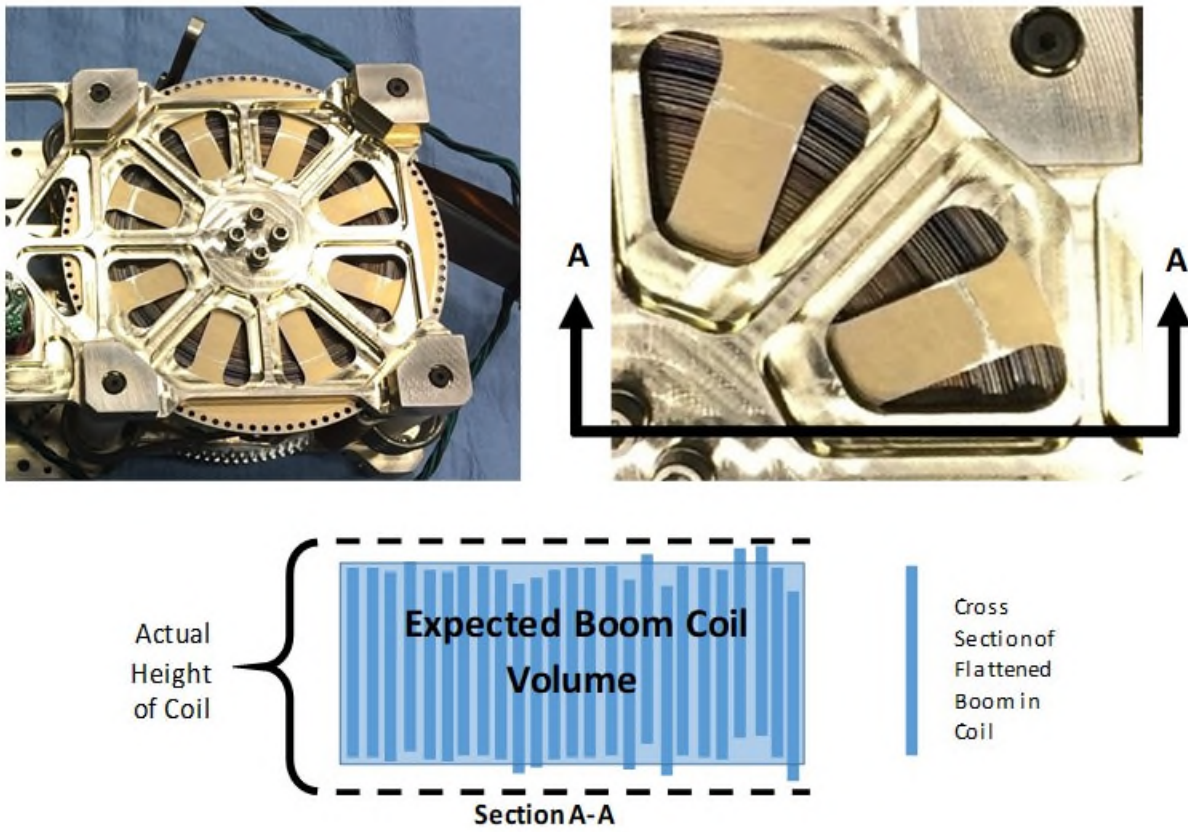


Figure 7. Visible Wear after a few boom-only deployments due to boom irregularities and depiction of spool cross section

Inaccurate Correlation between Prototype and EDU

The team's false confidence supplied by a full-scale 3D printed prototype is determined to be the failure's root cause. The prototype testing was critical to the development pace for the SSD, but where it did provide wonderful design inputs, it also gave a deceiving sense of familiarity to a different EDU system. The $\frac{1}{2}$ scale prototype was made of 3D printed ABS. Though the plastic parts may have resembled the aluminum parts on the EDU, the mechanical properties were incomparable. The similarities and differences can be observed in Figure 8. Furthermore, the booms' lengths on the prototype were 4 meters as compared to the 7.2 meters on the EDU.

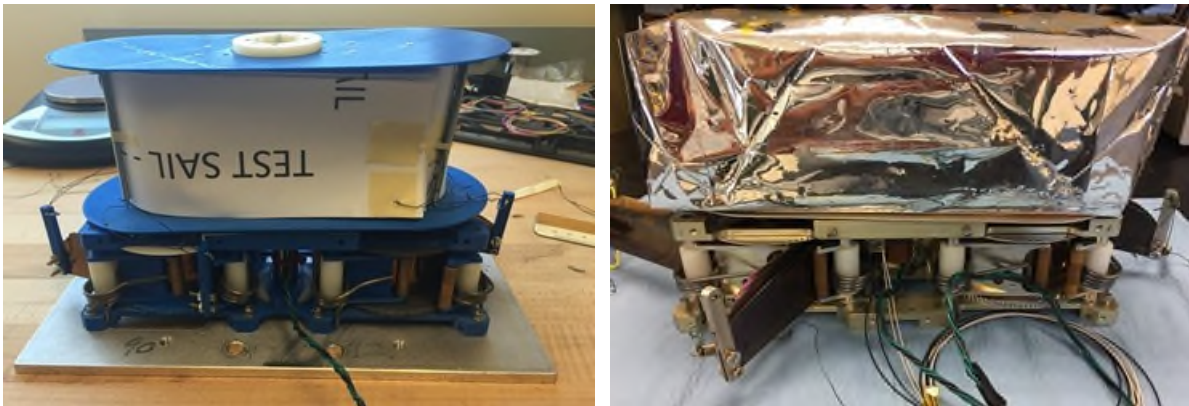


Figure 8. Prototype and EDU SSD

The boom lengths were used as improper metrics when relating the prototype and EDU. If the booms are examined as a spring, the deployed lengths relate to the square of the stored energy in the spool. Therefore, the coiled EDU booms, being about 1.8 times longer than the prototype booms contained about 3.24 times more energy. The plastic-to-plastic friction was an estimated 2x less than the EDU's aluminum-to-aluminum friction forces. To exacerbate this condition, the plastic would also deform more easily than the aluminum EDU. Therefore, the differing friction and stiffness properties discredited any linear correlation between the prototype and EDU based upon boom lengths. This correlation error played a significant role in leading to the 5 causes described above.

When the motor was sized, the designer assumed a linear relationship between the prototype and the EDU torque requirements. The controller board for the prototype was also used to baseline the EDU controller board, hiding some of the control input errors. The plastic material would also hide mechanical interference as it deformed in the presence of significant load. The friction between plastic parts was more advantageous than aluminum. Lastly, the boom spool irregularities were hidden because the booms were shorter and less likely to spool improperly.

Summary

All in all, the design team was inexperienced with prototyping mechanical systems with plastics and allowed a prototype to hinder a much-needed critique. The designers should have taken the time to create either a complete system dynamics analysis or a few simple subcomponent models to determine more realistic friction estimates. Do not base any dynamic or loads-related mechanical performance on a printed prototype. Volumetric data, part fit up, and interface development can and should benefit from a 3D printed model, but “form” similarities do not indicate “function” similarities.

Sail Deployment Development and Testing

As a risk mitigation strategy, the team planned several deployment tests during the project's design and development phases. The goal of ground deployment tests was to demonstrate the functionality of the deployment system. The ground tests did have two inherent flaws that were difficult to overcome – gravity and friction. Demonstrating the SSD's functionality in a 1G environment was taken into consideration while developing the test plan. The team started with half-scale, 3D prototype units and transitioned to a flight-like unit for full-scale testing. The team planned to perform two full-scale engineering development unit tests and two flight-scale tests. By the conclusion of the engineering development unit test phase, the team had completed five full-scale development tests. The development tests did not focus on simulating the space environment conditions during deployment and all deployment tests were conducted in an ambient environment. The team communicated to the project management the potential for false positives and negatives produced during the tests due to the 1G environment.

The first set of deployment tests were completed with the half-scale prototype using 4-meter booms and a 40-m² Mylar sail. The smaller sail took less time to refold and spool, allowing for quicker turnaround between tests and kept the focus of the tests on troubleshooting the deployer system. The deployment tests were conducted in the Flight Robotics Laboratory at Marshall Space Flight Center. The test location was a major factor in the success of demonstrating the systems capabilities. Due to resource constraints, the team was unable to design and build a support structure to offset the effects of gravity. Therefore, the approach to the deployment test was simple – deploy the system on a large, flat, clean, and low friction surface with minimal human intervention and ground support equipment.

The facility chosen, also known as the “Flat Floor”, allowed air bearings to float across the surface of the epoxy floor with negligible friction. Without friction loads, the air bearings were intended to simulate two lateral degrees of freedom in the floor's plane and a rotational degree of freedom normal to the floor. The team attached the deployer body and each boom tip to an air bearing and a compressed air supply (Figure 9). The “frictionless system” was supposed to help study the SSD's natural deployment motion, angular rates and angular accelerations. This information would have been beneficial for the guidance and control team's deployment modes and models, but the forces created by the air supply hoses dominated

deployment dynamics and produced inconclusive results. The air bearings were never used again on account of their high inertias and hose-induced loads.

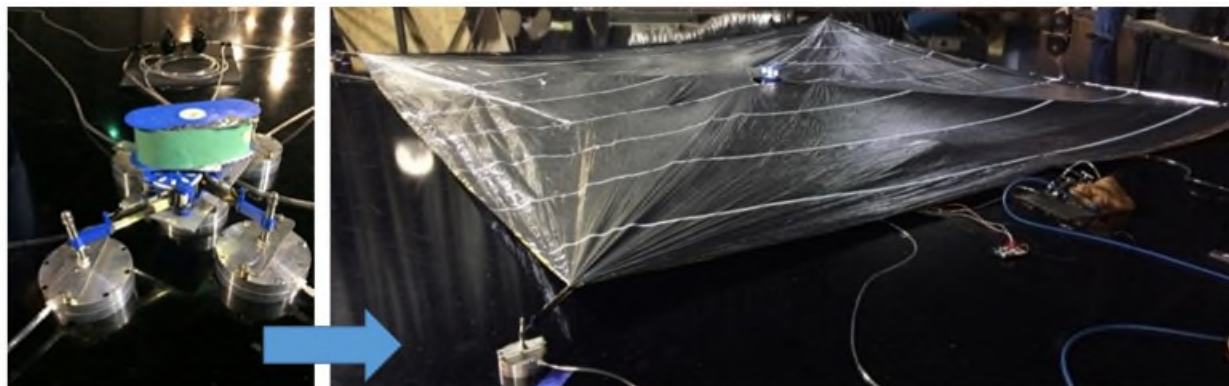


Figure 9. First sail deployment test: half-scale 3D-printed prototype.

After abandoning the air bearing system, the half-scale sails were deployed using low friction furniture sliders as boom supports. Though this method was cruder in nature, the results were more symmetric and predictable, helping baseline progress during the prototype phases. Despite the less flight-like test system, the prototype deployer helped determine intermittent sail shapes, reflective areas, and deployment failure modes. After about 10 boom-only and 3 half-scale sail deployments, the prototype was set aside as the team began focusing on EDU testing.

After the SSD redesign work, the NEA Scout team re-entered test activities and completed its final EDU deployment test in the fall of 2017. Full-scale SSD testing was a logistical and technical challenge for the team. The deployed sail is 9.3 x 9.2 m, 2.5-microns thick and incredibly fragile (Figure 10). The sheer size and sensitivity of the material limited the team to available facilities for large-scale testing. Even after looking to other NASA centers for possible deployment tests, the team determined the Flat Floor to be the most suitable facility based on its area, ease of access, and low cost.

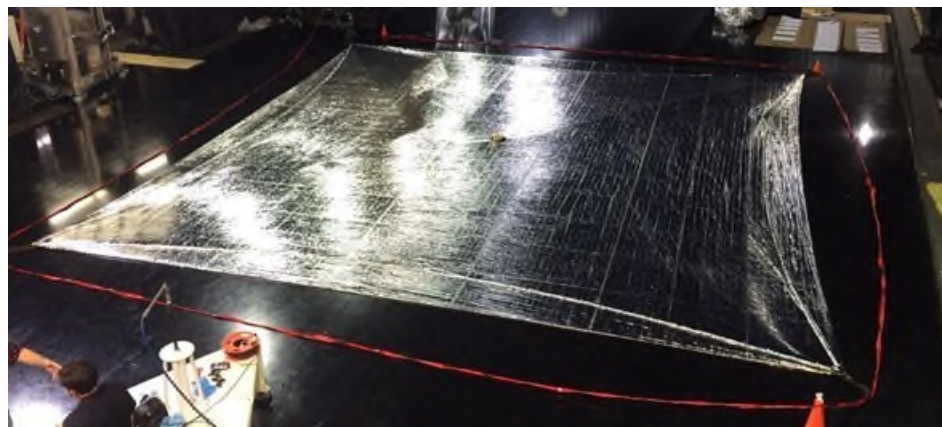


Figure 10. Full-scale EDU deployment

Throughout the full-scale deployment test suite, the team studied and applied lessons learned from more than a dozen off-nominal deployment cases, characterized the booms and sail in a 1G environment and produced a detailed deployment procedure. Sliding friction forces were reduced by 50%, a simple and effective method to gravity offload the boom tips developed. Furthermore, the team characterized boom and sail-related failure modes and operational methods to avoid them. These careful experiments developed a new test scheme that would remove some of the complicating factors present in deploying

flexible gossamer structures in 1G and allowed the booms and sail to behave in manners more similar to the zero-G flight environments.

Sail Development Test Lessons Learned

The first lesson learned relates to the air bearings. The air bearings were a large mass at the end of each boom (Figure 9). Even after allowing 3 degrees of freedom, the bearing masses dominated the boom tips' natural paths. The air hoses connected to each air bearing also introduced significant friction forces into the system. Though the air bearings were frictionless, their air supply hoses had to drag along the floor and the hoses bending resistance completely overwhelmed the booms' restoring forces. This problem only worsened as the booms increased in length until the booms eventually buckled. For large sail systems, large masses at the boom tips will dominate deployment dynamics and lessen the booms' abilities to self-correct. Avoid large masses and force inputs near boom tips during deployment testing.

The second deployment test was conducted on a basketball court. The team explored using the basketball court out of necessity of needing available floor space. The air bearings could not be used on the hardwood surface, requiring the team to get creative in the test approach. The wax finish on the floor coupled with the introduction of felt sliders proved to be a successful combination. The team introduced a felt slider design that would support the booms at multiple locations only grams of extra mass added to each boom. This removed the concern of ground support equipment mass overwhelming the dynamics of the test.

The next lesson learned came during the first successful SSD prototype deployment on a basketball court. This test showed a sail and boom shape progression that seemed more indicative of a flight deployment. Initially, the team assumed the sail would deploy in a uniform, rectangular manner. However, testing showed that the sail would form in a "bow-tie" shape during deployment (Figure 11 A-B). At half scale, the booms were able to compensate and correct at the end of deployment (Figure 11 C-E).

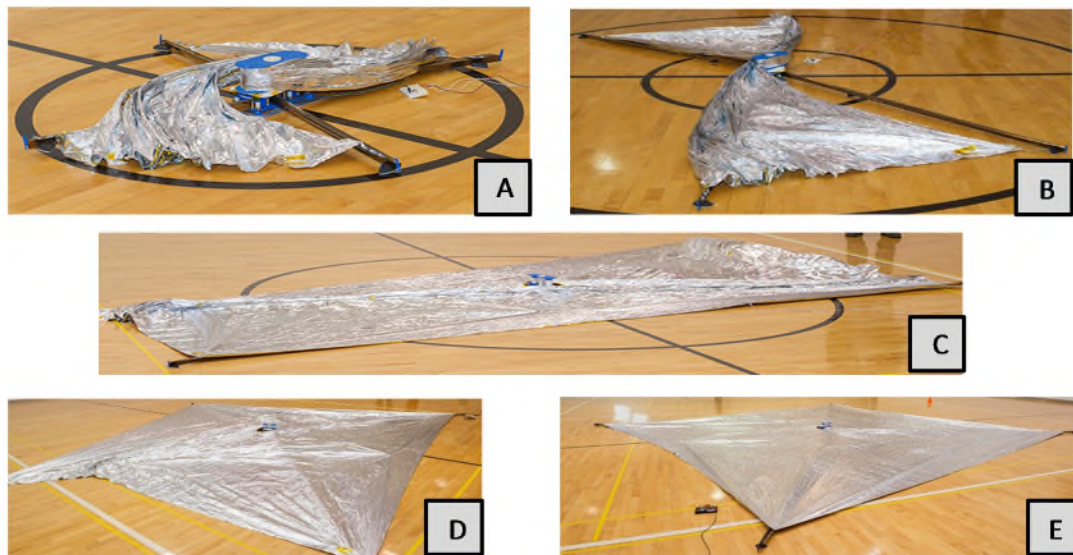


Figure 11. Sail shapes during nominal deployment.

With the success of the half-scale deployment tests, the full-scale tests followed the same procedure of integrating felt sliders on the booms at predetermined points. Originally the team thought the only human intervention needed was to monitor when to initiate and conclude the test. Additionally, the team was confident the boom's self-correcting behavior observed in the half-scale test would repeat in the full-scale test.

The third lesson learned through the deployment tests was boom buckling. During half-scale tests, when the sail was fully removed from the central spool, the tension along the perimeter of the sail assisted the

booms in assuming the final shape at the end of the deployment (Figure 11 C-E). The team noted that increasing the boom length from 4 to 7.2 meters for the full-scale test uncovered potential issues with boom buckling due to the shape dynamics during deployment.

The first area of focus while investigating boom buckling was the friction between the felt sliders and the test surface. The full-scale tests were conducted at the flat floor facility. The felt sliders were placed along the length of the boom at predetermined locations, shown in Figure 12. The sliders were assumed to put a negligible force back into the system, which the booms could overcome. This was found to be untrue. Even the small applied force of the sliders on the epoxy floor restricted the booms to follow their natural path out of the deployer. The epoxy flat floor has a higher coefficient of friction than the waxed hardwood floor. These forces had larger effects on the SSD and the boom root as the boom lengthened. The longer booms had significantly more lateral loads to correct as the booms lengthened and the sail area increased (Figure 13).

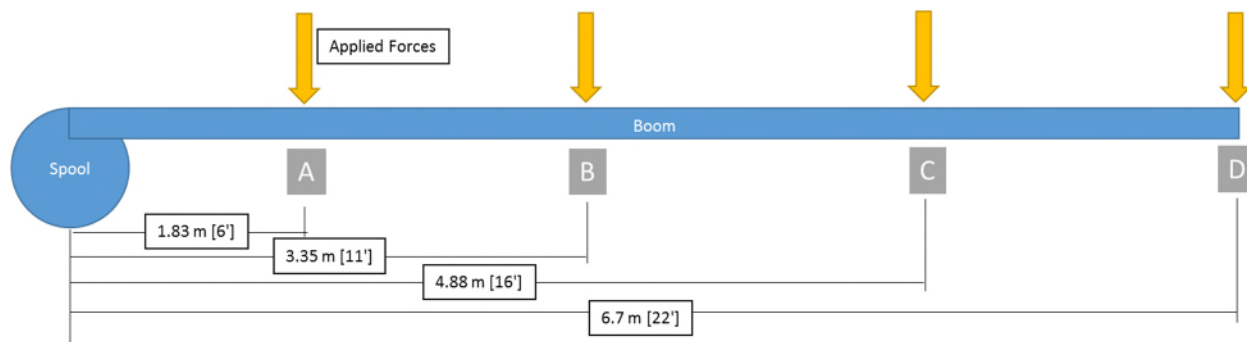


Figure 12. Boom slider locations for ground testing.

Another contributor to the boom buckling was the location of the sail material at initial deployment. The 1G environment pushes the sail material towards the floor, and as the sail deployed, friction and static electricity pulled the boom tips towards the centers of the sail areas. If the material was on the wrong side of the boom, the material would pull the boom in the wrong direction, thus starting a buckle like in Figure 13. In the zero-G environment, this behavior would not be observed. To mitigate this during test, the team decided that human intervention would be necessary if the sail material dragged over the booms and would be placed in the proper quadrant before resuming testing.



Figure 13. Boom buckling in full-scale deployment test

The final contributor to boom buckling is the boom mass. On orbit, the booms would not need to compete with gravity to support their own weight or deployment friction forces created by boom supports, sail friction, or static electricity. However, during ground testing, friction and electro-static forces between the sail and floor tended to cause boom buckling. As the sail deploys, the friction and static forces increase as the

deployed sail area increases and the boom root's restoring moment and stiffness lose any ability to correct. Figure 14 shows that the friction forces furthest from the boom roots dominate boom deployment dynamics.

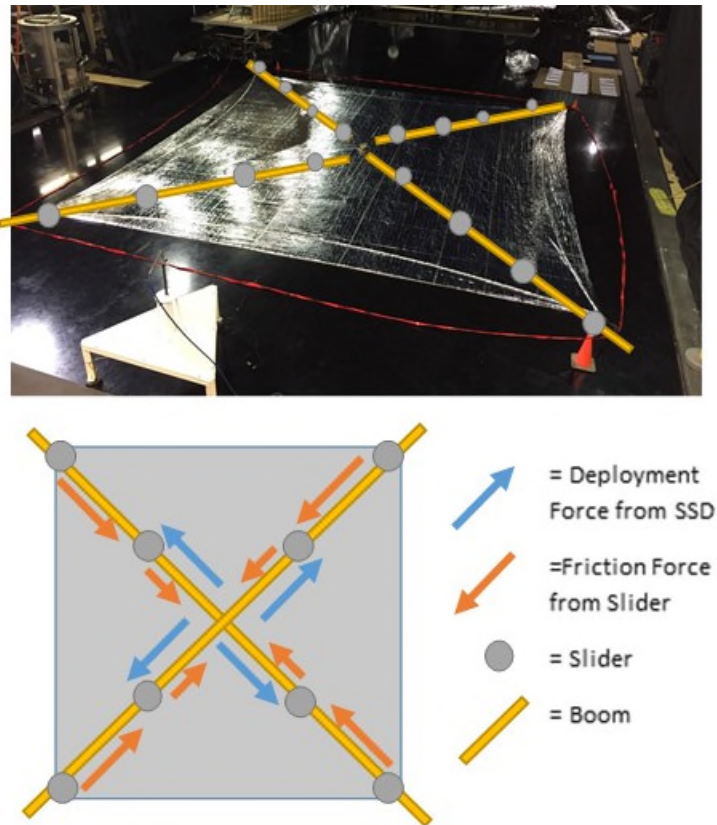


Figure 14. Deployed sail and deployment force diagram.

After observing this characteristic in many boom-only deployments, the team determined that any effort to gravity offload the boom tips would remove 1G deployment characteristics and produce a more flight-like test. Many offload options were traded, but tying balloons to the boom tips proved to be the simplest solution (Figure 15). By removing some weight and friction forces from the regions furthest from the boom root, the booms followed a more flight-like deployment path (similar to what was observed at the half-scale tests). Furthermore, boom tips were more realistically affected by the sail edge tensioning created at the final stages of deployment (Figure 11 D-E). The gravity offload and friction reduction methods gave the team far more insight in the boom behavior on orbit.

During the ground tests, when buckling was initially observed, the team manually removed the buckling from the system. As a risk mitigation activity, the team investigated whether or not the system could remove a boom buckle autonomously. The new SSD motors could produce enough torque to retract the booms on ground and on orbit. Knowing this, the team tested to see if strategic retraction operations during deployment could remove buckles formed during off-nominal cases. The team learned that retraction steps at 75% and 95% deployed would remove buckles while also reducing blooming in the boom spools. Though this was a convenient operational change, the SSD has no method to determine the presence of a buckle, nor that the buckles, if present, are removed.



Figure 15. Boom tip gravity offloading.

Conclusion

Future solar sailing missions are already calling for sails 3 to 15 times larger than the NEA Scout SSD. As solar sails continue to increase in area, projects need to designate a considerable amount of effort into developing a scaled test plan that can feasibly verify system-level requirements on the ground. The effects of gravity and friction in the test set up can greatly influence the success of the deployment tests. Large, thin film membrane structures are more susceptible to the effects of gravity and do not behave in a manner that is easy to predict in flight.

Scaled testing in this project proved to be valuable and educational path for this system design. For future cubesat missions with large deployable, thin-film structures, the team recommends allowing schedule and resources for scaled testing. Facilities to test sails greater than 100 m² will be difficult to find. Future projects should reserve time to consider the efficacy of performing full-scale tests and determining the risk posture of accepted scaled tests. Scaled testing with 3D prototype materials, motor sizing calculations, and sail dynamics during testing were the main areas of lessons learned for the solar sail subsystem.

In summary, the mechanism encountered design challenges that stretched the team's knowledge and limited resources. The resiliency of the team and novel approaches kept the project aligned with the class-D mission classification while keeping the overall success of the project in mind. The team hopes this paper will provide valuable information for future solar sail mechanism designers.

References

1. McNutt, L.; Johnson, L.; Clardy, D.; Castillo-Rogez, J.; Frick, A.; and L. Jones. "Near-Earth Asteroid Scout." AIAA Space 2014 Conference; 4-7 Aug. 2014; San Diego, CA; United States.
2. Sobey, A; Lockett, T. "Design and Development of NEA Scout Solar Sail Deployer Mechanism." 43rd Aerospace Mechanisms Symposia; 4-6 May 2016; San Jose, CA; United States.
3. Dr. Fritz Faulhaber GMBH and Co. "Planetary Gearheads, Series 15/10". www.micromo.com/media/pdfs/15-10_FMM.pdf

Mechanism Design & Flight Build of Furled High Strain Composite Antenna for CubeSats

Bruce Davis*, Ryan VanHalle*, Kevin Cox* and Will Francis*

Abstract

In August of 2016, Roccor was tasked to develop a CubeSat antenna mechanism that deploys four 20 x 5 inch (51 x 13 cm) radial petals from a small, 2U stowed volume. It was determined that High Strain Composites (HSC) coupled with a copper-beryllium alloy enabled a simplistic furled solution utilizing few mechanical parts. A two-stage mechanized deployment scheme was developed to first expose the wrapped petals to the outside of the spacecraft via a hinged joint and then separately trigger a dynamic unfurling of the petals with a tether. This paper describes the initial trade study and detailed design of this deployment mechanism as well as the lessons learned during the flight qualification. In May of 2017, Roccor delivered two, low-cost flight qualified units to the customer after a design, prototype, build and test campaign lasting a total of nine months. The hardware is slated to fly in late 2018.

Introduction

The emergence of the small satellite platform and subsequent ease of access to space has created high demand for advanced, yet compact spacecraft systems serving a range of science, commercial and defense applications. Furthermore, the industry-wide embracement of the CubeSat standard, establishing both spacecraft form factor and consistent launch requirements, has established investment in off-the-shelf spacecraft components and high quantity production within the field [1,2]. Across the community, one of the largest hurdles to developing a successful CubeSat system is the challenge in miniaturizing the technology to function within the desired form factor. This is especially challenging when designing deployable structures such as large antennas or solar arrays, where common physical components such as fastened interfaces, articulated joints and actuators are not efficient in the miniaturized form factor. Furthermore, structural performance does not often scale linearly in size causing the need to embrace different architectures at smaller scales to enable a desired deployed stiffness and precision. One such technology receiving increased attention within the CubeSat community are High Strain Composites [3,4] (HSC) or materials that deform from one shape to another during deployment. A commonly known high strain device is a slit-tube, or a deployable “tape-measure” boom that allows the cross section to be flattened and rolled into a coil reaching a high packaging efficiency [5,6]. Although the metallic slit-tube device has extensive flight heritage, a controlled deployment requires complex mechanisms to control the strain energy of the wrapped coil. When fabricating a slit-tube boom with a HSC material, the ability to tune the composite laminate to control the strain energy of the furled structure offers a new level of simplicity while enabling adequate control to deploy and retract the device. The use of HSCs offer an improved level of mechanism simplicity over architectures utilizing traditional moving mechanisms such as rotational joints, springs, dampers and latches.

In August of 2016, Roccor LLC was approached by an advanced CubeSat payload provider to design a mechanical system that would house and deploy a series of co-planer RF elements on orbit. This customer required a rapid system development ranging from early requirements definition to the delivery of multiple flight units over the course of a nine-month period. To add to the challenge, this effort was bounded by a relatively small budget, driving the need for mechanism simplicity. These desired elements consisted of four petals, each measuring roughly 20 in x 5 in (51 cm x 13 cm) in length and height respectively that would be aligned radially about a central hub. These petals would also need to be folded into a 2U CubeSat

* Roccor, Longmont, CO

Proceedings of the 44th Aerospace Mechanisms Symposium, NASA Glenn Research Center, May 16-18, 2018

form factor. The geometry of this antenna system is shown in Figure 1 with the four petals shown in the deployed state. Here the co-planer petals are shown in green, and the desired stowage volume of 10x10x20 cm is shown in purple. The remaining 6U CubeSat volume is identified with a semi-transparent box.

Structurally, the deployed petals needed to maintain a stiffness requirement above 0.5 Hz, a lateral precision of ± 4 in (± 10 cm) at the petal distal edge and a twist precision of 1 in (2.5 cm) measured with respect to the top/bottom of the outer ends. It was found that the simplest approach was to wrap the four petals around a central hub and utilize strain energy to deploy upon the release of a circumferential restraining band. The petals, consisting primarily of a copper to enable RF performance, were reinforced with high strain composite lamina to control the stowed strain energy and deployment dynamics. The added lamina also protected the metallic RF element while stowed, assist the deployment and finally to improve the deployed structural performance. In a recent publication [7], the end-to-end development process of the petal design is discussed at length; this includes the architectural trades, laminate fabrication, early challenges such as delamination and creep effects, and finally the integration efforts of this system into the spacecraft deployment mechanism. This current paper focuses on the mechanism specific design aspects of this system that secured, exposed and triggered the petal radial deployment within the CubeSat form factor. Challenges in design as well as lessons learned during initial fabrication and flight qualification are detailed at length as well as the challenges of integrating high strain composite deployables.

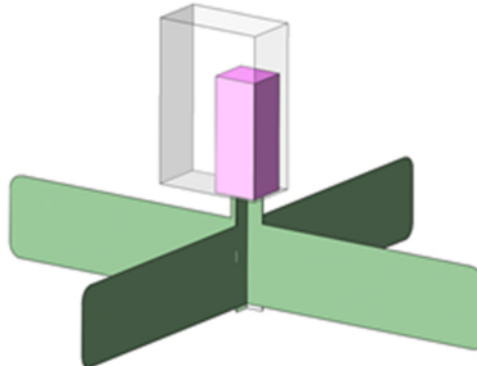


Figure 1. Basic geometry of deployed CubeSat antenna

Architectural Trade & Mechanical Design

The challenge of deploying a series of large, furled flat panels within a small CubeSat form factor was broken down into several targeted areas for the Roccor team to work through. The first consisted of designing a laminate that could withstand the high strains while stowed, ensure sufficient energy for a robust deployment and finally provide adequate stiffness and precision once exposed. Important considerations such as defining the furled geometry of the petals were a central focus, especially in the transition region between the furled panels and the central petal supporting structure. The second category focused on the mechanics for how to stow, package and protect the furled petals within the CubeSat volume during launch, and upon activation, release the petals in the space environment. This area had the added complexity of physically moving the stowed petals from the cocooned volume to the outside of the spacecraft prior to petal unfurling. In addition, the deployment synchronization and analysis of the petal unfurling were prime focus areas within this group. The final category consisted of the electrical considerations such as the incorporation of the actuation device, integration of the RF electronics, wire harness management and finally, providing sensory feedback indicating a successful deployment.

Petal Laminate Design

The first step in the design of the petal, was to define the key geometric constraints imparted by the CubeSat envelope and central hub structure. This latter component, supplied by the payload provider, consisted of two interlocking plates forming a cross, with each of the petals bonded to the exposed outboard surfaces.

This rigid structure had a diameter of 2.6 in (6.6 cm) and contained finely tuned RF elements and electronic components, requiring delicate care. This geometry is shown as the light green components in Figure 2. The RF petals extended beyond the interlocking plates and were geometrically required to sustain a ~0.25-in (6.4-mm) bend radius as they transitioned from the central hub structure to the larger, wrapped geometry required of the 2U CubeSat form factor. This immediate region, defined as the transition area, contained the highest strain within the system design. Finally, the petal length and spacecraft envelope of ~3.1-in (7.9-cm) square required each petal to be wrapped just over two full rotations around the central supporting structure with a maximum petal thickness of 0.020 in (0.5 mm). Further considerations were imparted to maximize volume such as a non-circular wrapping geometry and the clocking of the central hub with respect to the space envelope to maximize the transition area bend diameter as seen in Figure 2.

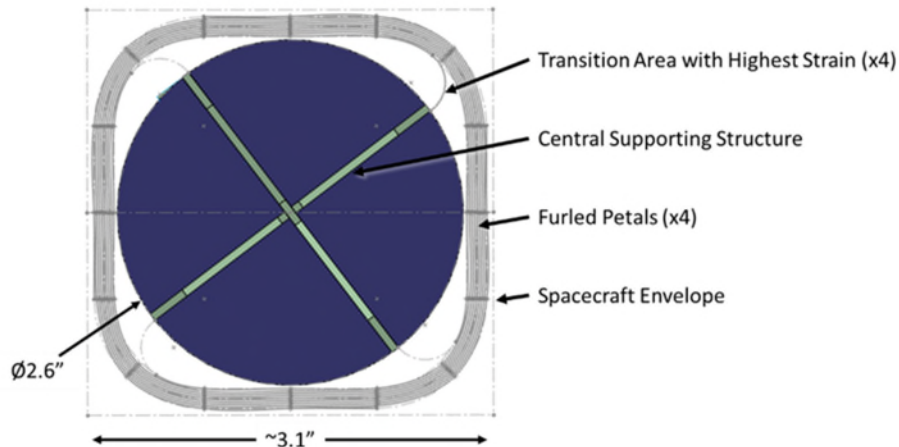


Figure 2. Basic geometry of deployed CubeSat antenna

The initial petal laminate design consisted of a homogenous approach where the central RF conducting element was sandwiched with reinforcing lamina across the entire petal length. Here the RF element was baselined to be Copper Beryllium (CuBe) due to its excellent electrical conductive performance and ability to withstand high strains. Several lamina materials were considered, however, E-glass was set as the baseline due to the material's high strain capability, availability and low cost. Upon early modeling and coupon fabrication, it was quickly determined that a variation of laminate designs across the length of the petal was required to optimize performance. For example, it was found that reinforcing the outer 1/3rd of the petal geometry did not increase deployed stiffness as the added mass of the lamina at the distal end overpowered the benefits of the improved localized stiffness resulting in an overall lower frequency. It was also found that this added distal mass reduced the 1g buckling resistance, a property that made ground testing more difficult. The finalized petal architecture of the petals is shown in Figure 3 with the R0-R3 regions representing different levels of high strain composite reinforcement. The R3 region is exposed CuBe while the R2 and R1 regions have one and two layers of glass reinforcement respectively. The R0 region is in the transition area, per Figure 2, experiences the highest strain during packaging and hence maintains only a single layer of reinforcement. This reduces the overall deployment energy and effects of creep. The length of each region, L_A, L_B and L_C were optimized to increase the petal's deployed frequency and 1g buckling resistance. The images on the bottom of Figure 3 show an early prototype of the petal design in the deployed and furled states.

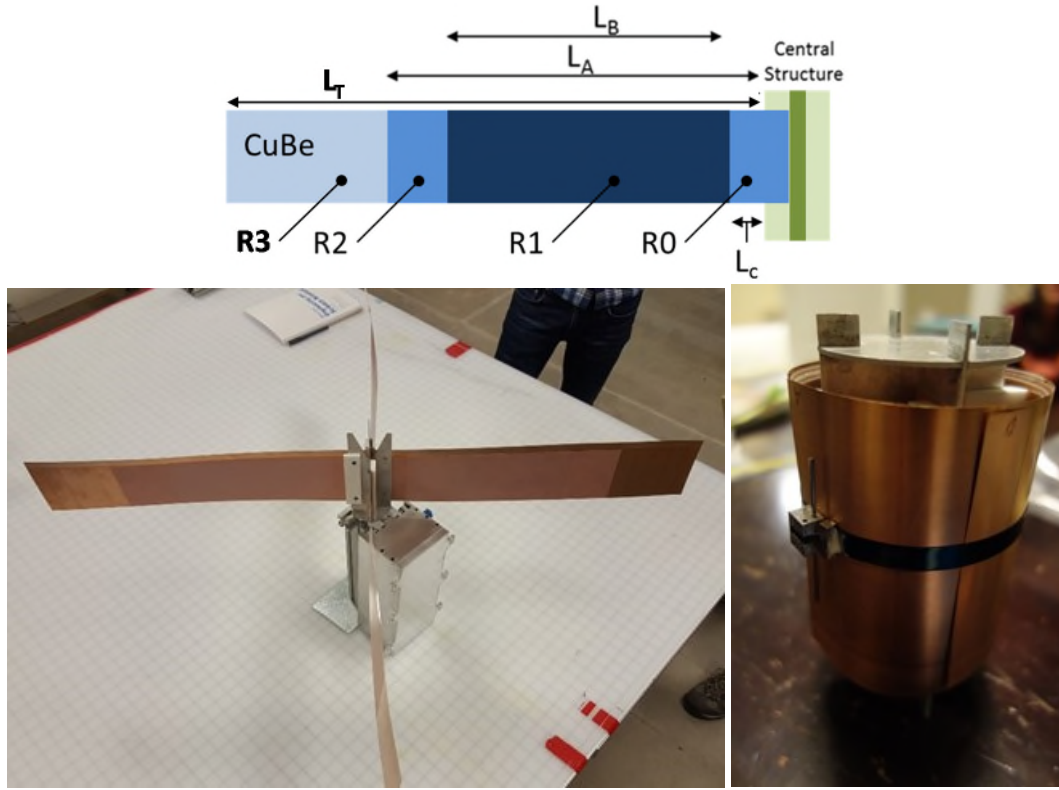


Figure 3. Schematic of petal geometry (top), photo of structural prototype deployed (bottom left) and stowed on the rigid hub (bottom right)

Mechanical Exposure and Deployment of Wrapped Wings

The initial mechanical deployment concepts consisted of a single-phase process whereas the unfurling and translation out of the enclosed envelope happened simultaneously. This approach however was deemed high risk due to uncertainties of blooming / binding of the petals during initial release. In addition, risk reduction testing of this highly coupled and dynamic deployment would require detailed analysis and a complex offloading setup. As such, a two-phase deployment was baselined where the wrapped assembly would initially move out of the stowed volume as a rigid body and then as a separate function, unfurl the wings. It was determined that the best way to restrain the wrapped system was with a single circumferential band applied at the mid-plane of the system. Upon exposure of the wrapped petal assembly outside of the spacecraft, the band could be released with a pin allowing for a dynamic unfurling of the four wings. Alternative approaches such as utilizing radial pins or a breakable wire that would penetrate through the wings, to provide continuous or sequential wing deployments, were deemed as technically feasible however not within the schedule or budget of this program.

To expose the wrapped petal assembly, several architectures were traded with the two strongest candidates focusing on 1) a linear sliding deployment and 2) a pivoting architecture, shown in Figure 4 & Figure 5 respectively. The linear translation approach utilized a sliding mechanism to shoot the wrapped petal assembly out in an axial fashion. This system was restrained with two release doors and triggered by a single hold down release mechanism. Once the petals were cleared from the cavity, the restraint band would be released and captured by a single tether. This architecture had several advantages such as the co-alignment with the spacecraft envelope, ease of the wiring harness management and similar design to mechanisms associated with p-pod deployment canisters. The challenges however were identified such as the complexity of multiple sliding interfaces, limited space at the region near the door where release device was housed and the opportunity of binding along the winged surfaces with particular concern focused on the restraint strap. The pivoting architecture consisted of a single door that preloaded the wrapped petal

assembly within the canister. Upon release of the door via pin puller, the petal assembly would pivot out, via torsional springs, a full 180 degrees in the opposite direction with respect to the door and hard stop outside of the spacecraft. Half-way through this rotation, the restraint band would be triggered and captured via tethers. Unique to this architecture is the load path and intentional contact of the wrapped petals and the spacecraft envelope. This allowed the petals to be further compressed and preloaded when stowed, forming a more direct and benign load path to the structure. This architecture was ultimately selected due to the simplistic nature of the rotational mechanism, the clean preload between the furled wings / stored envelope and lower concerns of petal binding.

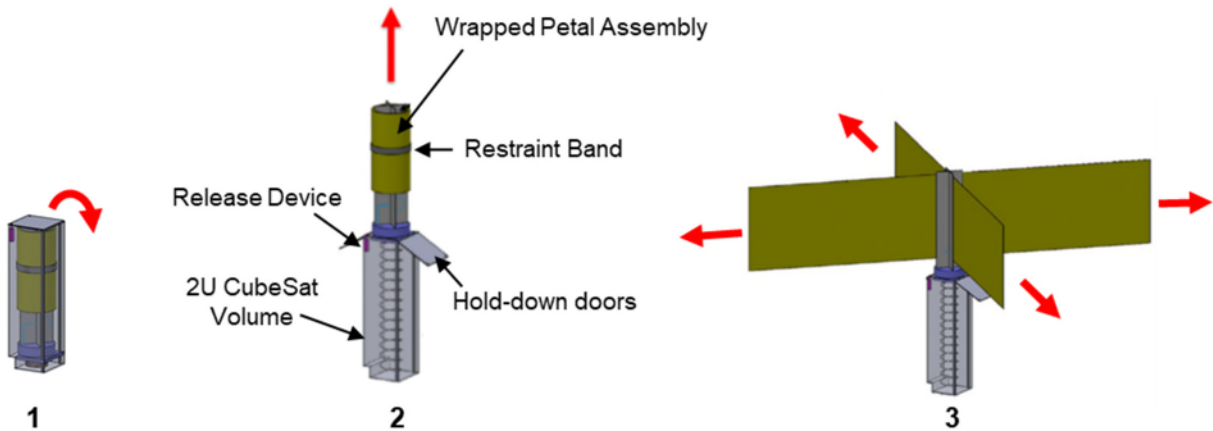


Figure 4. Translational architecture showing: 1- the stowed system, 2- post translation of the wrapped petal assembly outside of the storage volume, and 3- post petal unfurling

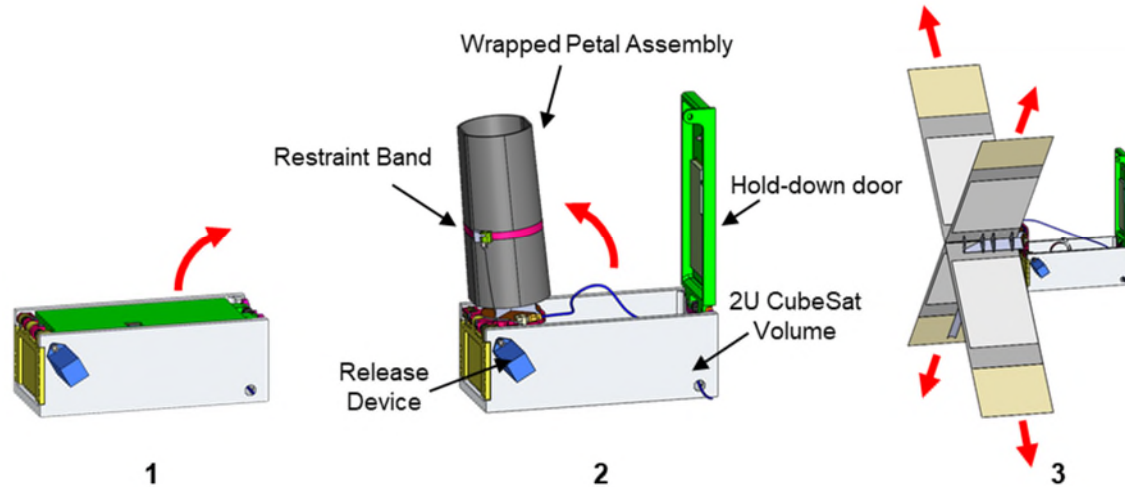


Figure 5. Pivot architecture showing: 1- the stowed system, 2- the door fully opened and rotation of the wrapped petal assembly, part way through the 180-degree motion and 3- post petal unfurling

HDRM, Electrical and RF Considerations

The system deployment was initiated by a 067-011 Pin Puller provided by GlenAir of Glendale, California. This hold down release mechanism (HDRM) restrained the door during launch and upon command, enabled free motion of the door and subsequent wing assembly. The door and wing were preloaded with torsional springs sized to enable swift motion to ensure unobstructed rotation of the wing assembly. While the release of the wing assembly preload provides a strong kick-off, the motion of these two components

are dominated by springs along the hinge axes. Hard stops on both the lid and wrapped wing assembly were placed to prevent bounce-back and potential re-contact during deployment.

The GlenAir Pin Puller operates via a fuse-wire system whereas an electrical current causes a preloaded wire to fuse, enabling a pre-loaded mechanical bolt to translate under considerable force. For this effort, the GlenAir team fabricated and qualified a custom size, delivering a series of flight mechanisms within three months of the request shown in Figure 6.

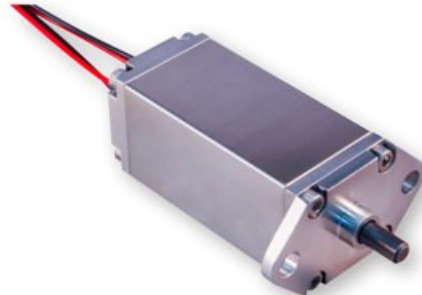


Figure 6. GlenAir 067-011 pin puller hold down release mechanism

The wing assembly required a rigid coaxial cable that would need to dynamically deploy with the system. To resolve this, the cable was laid along the base of the canister with a series of bends incorporated. During the full rotation of the wing assembly, the bends would allow for the cable to flex and twist with modest parasitic force. The clean nature of the canister walls eliminated potential snag hazards of the cable.

Detailed Flight Mechanism Design

An early prototype was fabricated in November of 2017 for design feedback and risk mitigation. The focus of this effort centered on verifying the stowed petal assembly shape and ensuring clearance during rotation. It was found that the wrapped, square-like shape shown in Figure 2 was hard to achieve and instead the petals, upon an application of preload from the system, formed an oblong shape with a defined and consistent elastic response. This result was built into the design of the flight system. Other details pertaining to the strap, tethers, incorporation of foam and wire harnessing are described in further detail below.

Strap and Tether Design

The stowed petals are held into a cylindrical shape with a circumferential restraint strap, this is shown in Figure 7 and as the pink component in Figure 8. The strap has clasp features bonded on either end which is temporarily held together with a removable release pin. This pin is connected to a tether that removes the pin from the clasp as the system deploys allowing the antenna elements to unfurl.

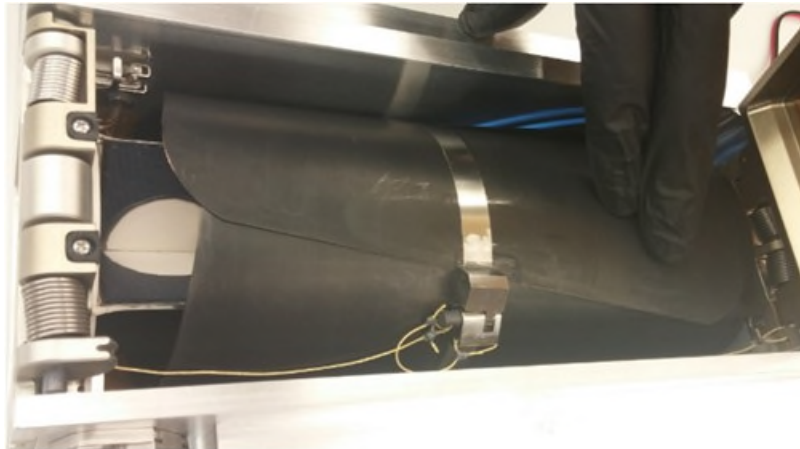


Figure 7. Strap assembly shown in the stowed configuration

The restraint pin pull tether works in tandem with two other tethers designed to restrict the location of the deployed strap assembly and to capture the hardware post deployment to prevent interference with the hardware and orbital debris. The sequence of system deployment can be seen in Figure 8. Phase 1 shows the system in the stowed configuration with everything constrained and preloaded by the door (green). Once the release is initiated, the door begins to open which allows the stowed hub assembly to begin exiting the stowed volume. Phase 2 shows how the door opens faster than the hub assembly to prevent contact. Both items are driven by torsion springs which are sized to provide adequate torque and sequence the deployment. The detail view of phase 2 shows the release tether (left side of image in turquoise) attached to the release pin. During this phase the tether is still loose. This view also shows the band tether (right side of image in turquoise) in a slack state.

Phase 3 shows the release tether becoming tight which is accomplished by the cam shaped feature near the root pivot of the hub assembly (bright yellow). As the hub assembly deploys the distance between the release tether and base increase, thus providing a pulling motion on the release pin. Once the hub assembly rotates a few degrees beyond the position shown in Figure 3 the release pin will be removed. It is important to note that the system was carefully sequenced such that the petals on the stowed hub would not begin to deploy until there was no chance of contact with the spacecraft. The springs are also sized so that the pin will be removed in the absence of kinetic energy.

Phase 4 shows the restraint band assembly completely removed from the stowed hub assembly which will allow the petals to begin unfurling. This image also shows how the band tether will restrict the location of the deployed strap assembly. This is critical for the system so that there is no interference in the deployed state. Also notice the release pin is still attached to the strap assembly with a third tether. The length of the three tethers is critical for consistent performance and to prevent tangling. Tether length was set at final assembly by hand deploying the hub assembly in order to guarantee successful performance.

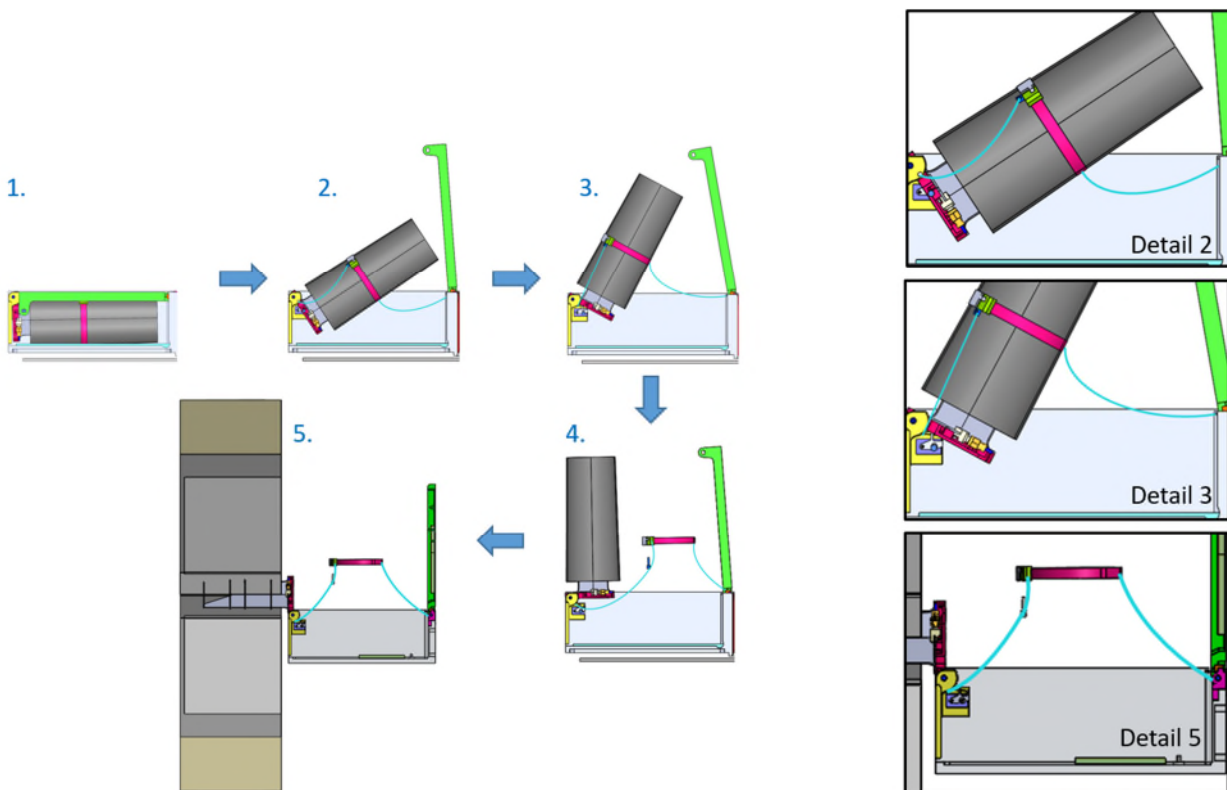


Figure 8. Deployment sequence with tether details

Strap Presence in the Door Window

A key requirement of the design involved verifying that each payload stow process was consistent and would remain in the proper configuration throughout testing and launch. A major concern was the placement of the restraint strap with respect to the hub assembly and placement in the stow volume. As described above if the restraint strap assembly were to shift it could impact the timing of the tethers, increasing risk of binding and/or premature petal unfurling. This risk was mitigated by designing a window into the door which trapped the clasp and release portion of the strap assembly. This entrapment prevents the release pin from shifting and being unintentionally removed from the clasps via direct interference with the door as shown in Figure 9. Once the deployment sequence is initiated, the door swings open first allowing the rest of the system to deploy unimpeded.

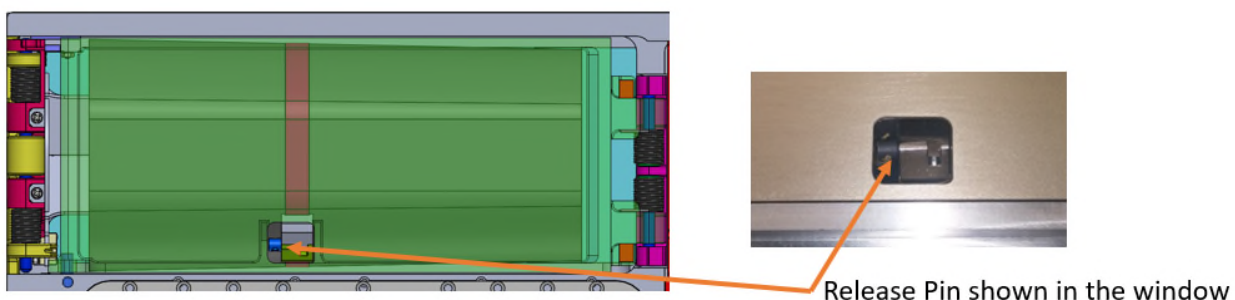


Figure 9. Release pin shown in door window

Incorporation of Foam

Polyimide foam was placed on the bottom surface of the chassis and inside the door to control the amount of deflection on the stowed antenna, thus generating preload to stabilize the assembly for launch. This style foam was chosen for its low outgassing and damping properties. The foam is also available in various thicknesses which allowed the fine tuning of preload on the antenna by simply scaling the thickness. Preload was measured and fine-tuned in the testing phase of the program.



Figure 10. Encapsulated polyimide foam on the system door

The foam must be preconditioned in order to function in a reliable manner. To do this Roccor essentially used a large rolling pin to flatten the foam into a consistent thickness. During this process it was noticed that the foam lost roughly 50% of its original height. Once in this state the amount of preload generated remained consistent throughout testing.

The foam was positioned in the deployer and held in place using pressure sensitive adhesive. Due to the likelihood for the foam to generate particulate, it was covered with a polyimide film and seamed around the perimeter, this essentially encapsulated the foam. One small area of the seam was left unsealed to allow venting of the cavity. This layer of foam and polyimide also had the secondary benefit of providing abrasion protection on the antenna elements by preventing direct contact with the aluminum surfaces inside of the deployer.

Wiring Harness Guidance

In order to electrically connect the deployed hub to the spacecraft, careful electrical harness routing was required. Due to the 180-degree rotation of the hub and baseplate, significant slack was allowed in the harness, and epoxy staking locations were limited. The only option for staking was a single location near the top of the antenna. The smooth walls of interior volume prevented any snagging that would prevent deployment. Careful routing also aided in providing deployment force as opposed to developing a parasitic torque.

Flight Development and Lessons Learned

In Q2 of 2017, two systems were fabricated and flight qualified. Due to the fast nature of this 9-month program, many of the design features discussed above were tailored during flight build to ensure the system functioned as expected. This included the exact sizing of tether lengths, implemented foam thickness to control stowed preload, and the final geometric coax cable routing scheme. While numerous minor unexpected issues presented themselves during the testing phase of the program, two were considered significant with the possibility of preventing or degrading successful deployment on orbit. Both of these were addressed with minor modifications to the design and are presented below.

Strap Performance

The first significant find during testing was the release pin jamming in the clevises and not being extracted during deployment. This prevented the restraint band from releasing causing a failed deployment. It was found that this issue was caused by a wedging effect created by the tether pull force on the strap. Figure 11 shows the ideal location of the strap represented by the green line and the as tested location in red.

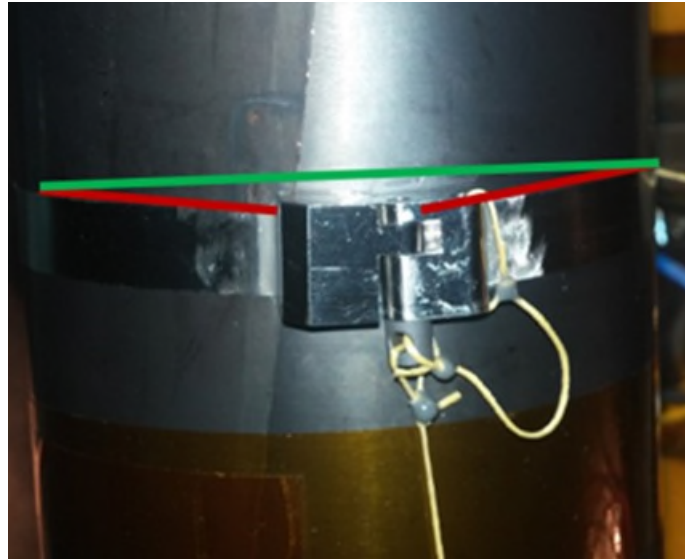


Figure 11. Wedging in the Release Strap Assembly

Upon further design review it was found that the geometry of the machined clasps with the tang offset from center caused wedging when the assembly was under tension. Future designs will incorporate a centered tang which will balance the tensile forces. Figure 12 shows the component names and geometry of the strap assembly to better explain the situation.

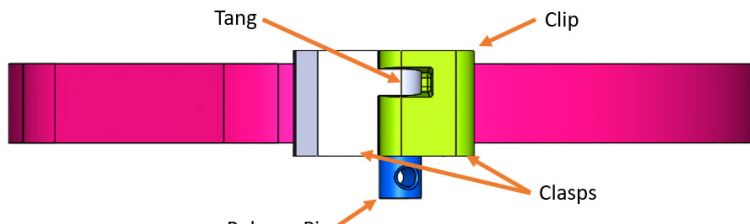


Figure 12. Release strap assembly details

Redesigning the parts was not an option due to schedule, so other modifications were implemented. First the sharp edges of the tang were chamfered to prevent them from digging into the pin. This decreased the amount of pull force needed to extract the pin. Figure 13 shows the chamfer added to the upper surface of the hole, this was also completed on the lower surface.

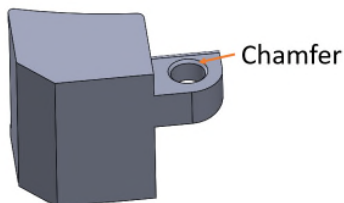


Figure 13. Tang chamfer

In order to combat the strap assembly taking on the wedge shape in the first place, epoxy was applied beneath the clasps to prevent a downward translation of the assembly. While the original design called for this feature, the location of those epoxy beads did not prevent the restraint band wedging near the clevis. The epoxy bead was therefore moved to provide better support by interfacing directly with one side of the clip while not interfering with the release pin. This epoxy bead also improved the tendency of the strap assembly to slide as a removal force was applied to the release pin. Figure 14 also shows how a second epoxy bead is placed 180 degrees from the first but on the top of the strap. This prevents the rear portion of the strap from sliding upwards which also causes a wedging at the clasps.

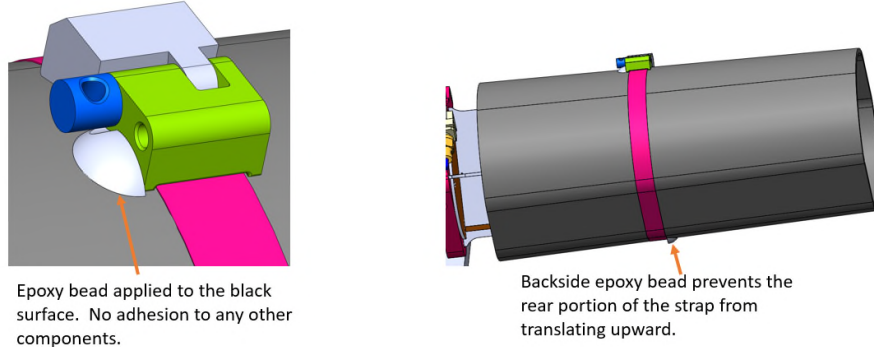


Figure 14. Epoxy bead placement

These updates prevented the strap assembly from translating with respect to the hub which allowed for consistent pull forces from the release pin.

Door bounce

The second significant find was the bouncing of the door during deployment. This was not noticed as an issue until a cold thermal deployment test. The door opens quickly and in the original design, a Viton bumper provided damping as the door hit a hard stop at ~90 degrees. At the cold temperature, the Viton did not damp all return motion and during testing, re-contact with the hub assembly was identified. While this did not prevent full deployment, it did have the potential to damage the sensitive RF element edges of the HSC petals, especially since the re-contact location was adjacent to the extrusions of the 'window' feature on the door. It was determined that a better bumper material was needed that would dissipate all energy and prevent door bounce back. Figure 15 shows the contact zone and the motion of the components at the time of contact.

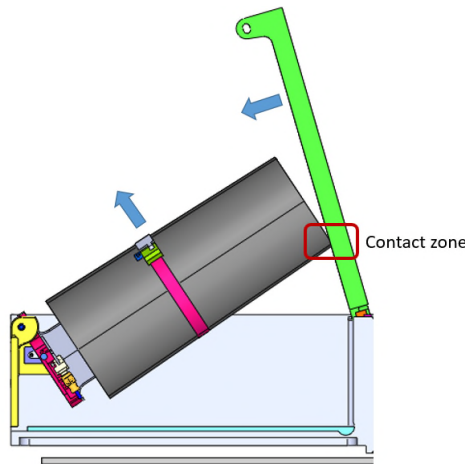


Figure 15. Door bounce back illustration

The Viton bumpers were replaced with copper mesh to better absorb the energy generated during deployment. These bumpers were a single use item that dissipated energy by crushing when contacted by

the door. Careful setup was required to ensure that the bumpers would enable full motion of the door eliminating the chance of the bumpers preventing the door from blocking / re-contacting the wrapped petal assembly during deployment. This was done by installing the copper mesh in place and then opening the door to pre-crush the bumpers to the minimum opening angle of the door. Figure 16 shows a pair of crushed bumpers on the left and a pair of partially pre-crushed bumpers on the right. In the left image the layer of copper sheet can be seen with copper mesh below it. The entire stack was encapsulated with Kapton tape. Many tests were conducted to determine the ideal cross section area, height and buildup of these to dissipate the proper amount of energy.

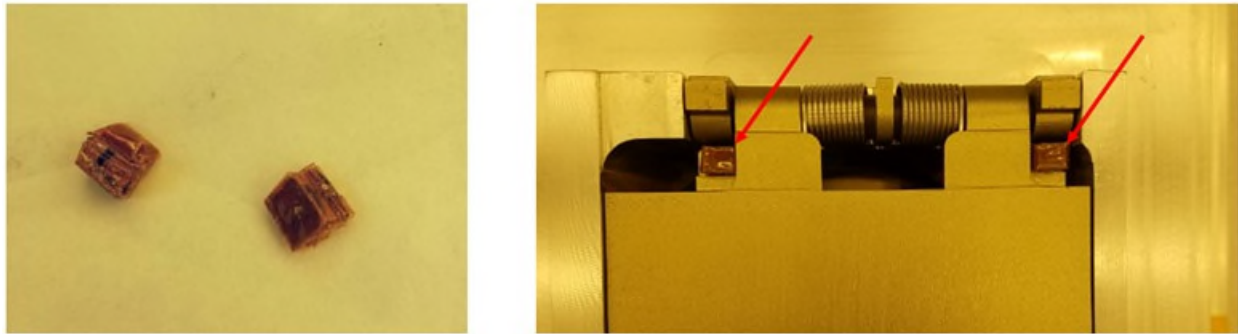


Figure 16. Copper mesh bumpers

Flight Assembly and Other Considerations

The two flight units were fabricated in March of 2017 and successfully passed qualification testing including vibration and stow / deploy cycles at the extreme operational temperatures. The system was found to be robust after multiple stow and deployment cycles however the high strain composite laminate did show signs of wear-and-tear (abrasion marks, roughening of edges, etc.) after successive deployment cycles. This was mainly due to the difficulty in handling / supporting the petals during the deployment testing and the inter-petal rubbing during the stowage process. As such, the flight units were subjected to a limited number of full unfurling tests as part of the acceptance testing checkout. It was also found that immediately after deployment, creep effects from the high strain composite prevented the wings from deploying in fully straight manner. As per the discussion defined in a separate publication [7], this deflection gradually reduced in severity after deployment due to stress relaxation within the laminate. The Roccor team performed a series of long-duration tests on the laminate architecture and determined that the petals would deploy within the required precision parameters.

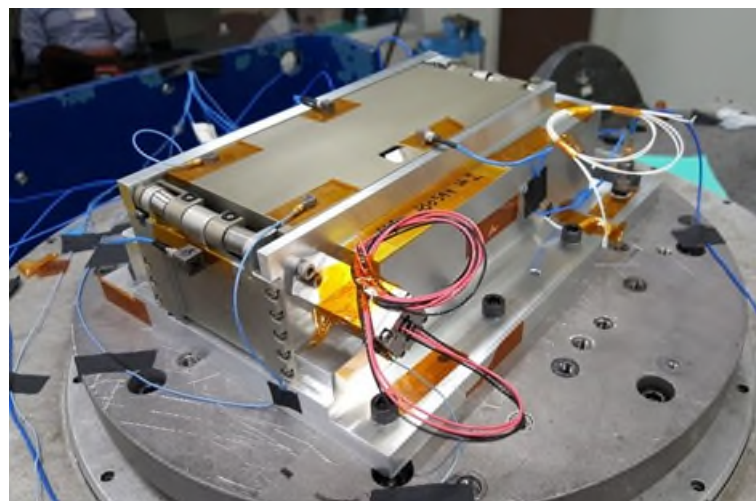


Figure 17. Stowed system during flight qualification vibration testing

Conclusion

In August of 2016, Roccor was approached to develop a CubeSat deployable antenna that would deploy four large radial petals while housed in a small, 2U volume. It was found that High Strain Composites coupled with a copper-beryllium alloy enabled a simplistic furled solution to stow the system with few mechanical parts. A two-stage mechanized deployment scheme was selected to first expose the wrapped petals to the outside of the spacecraft via a hinged joint and then separately trigger a dynamic unfurling of the petals with a tether. This scheme was selected over other two-stage approaches due to the low risk of binding, ease of securing the wrapped wings via external preload and overall mechanism simplicity. The design was triggered by a single commercial GlenAir pin puller and utilized torsional springs to allow rotation. The petals were unfurled via a restraint strap that was triggered and afterwards captured by a series of three tethers. During the flight build, details such as the tether lengths, foam thickness and coaxial wire routing were fine-tuned to ensure the system performed as expected. While there were numerous lessons learned and small tweaks implemented during the flight build, qualification testing revealed two significant issues that required action. The first was a modification to the restraint band clevis and addition of guides to prevent binding during release. The second involved improving the energy absorption to prevent bounce-back of the door and subsequent re-contact with the wrapped petal assembly of the door during deployment. In May of 2017, Roccor delivered two, low-cost flight-qualified units to the customer after a design, prototype, build and test campaign lasting a total of nine months. The hardware is slated to fly in late 2018.

References

1. Doncaster, B., et. al., "SpaceWorks' 2017 Nano/Microsatellite Market Forecast", *Proceedings of the AIAA/USU Conference on Small Satellites*, Swiftly Session 2, SSC17, 2017
2. Adamowski, J., "SmallSat Market Forecast to Exceed \$30 Billion in Coming Decade", Space News, 9th, August 2017, Online
3. Murphey, T. et. al., "High Strain Composites," *Proceedings of the 2nd AIAA Spacecraft Structures Conference, 2015 AIAA SciTech Conference, Session on Composite Materials for Spacecraft Structures*, AIAA 2015-0942, Kissimmee, FL.
4. Wikipedia page on "High Strain Composite Structure", authored primarily by B. Davis 2014, https://en.wikipedia.org/wiki/High_strain_composite_structure
5. Storable Tubular Extensional Member Device, US Patent #3434674
6. Annon, "Tubular Spacecraft Booms (Extendible, Reel Stored)," tech. Prep. SP-8065, NASA, Feb 1971
7. Cox, K., et. al., "Flight Build of a Furled High Strain Composite Antenna for CubeSats," *Proceedings of the 5th AIAA Spacecraft Structures Conference, 2018 AIAA SciTech Conference, Session on Composite Materials for Spacecraft Structures*, AIAA 2018-1678, Kissimmee, FL.

Failure of the Ball-Lock Mechanism on the NanoRacks CubeSat Deployer

Michael Lewis^{*} and Conor Brown^{**}

Abstract

The NanoRacks CubeSat Deployer (NRCSD) is a system that is used to deploy small-form-factor satellites off of the International Space Station. Deployment occurs by commanding the activation of each of eight deployers that comprise the system. On early iterations of the NRCSD, commanding initiated the release of a ball-lock mechanism, which in turn released the doors and allowed deployment of the satellites. Multiple failures were experienced on the Orb-1 and Orb-2 NRCSD missions. Failures on the Orb-1 mission were attributed to an electronics/avionics issue and were overcome without loss of mission. Failures on the Orb-2 mission were of a different nature; two deployers never deployed, even after multiple command attempts. Two deployers had an inadvertent deployment after previously being commanded.

Post-mission analysis included a Fault Tree Analysis of the NRCSD system as well as all individual components and mechanisms, including the ball-lock mechanism that is used to release the doors and deploy the satellites. The mechanisms were assessed by NASA's Mechanical Systems Working Group, NASA's Payload Safety Review Panel, JAXA engineering, and NanoRacks engineering. The conclusions of the Fault Tree Analysis and assessment showed that the cause of failure was excessive loading of the ball-lock mechanism; screws that were intended to preload the system were excessively torqued, which caused the ball-lock mechanism to seize. An operational procedure was implemented to remove the preload screws on-orbit. Once the screws were removed, all subsequent activations of the ball-lock mechanism were successful.

Introduction

The NanoRacks CubeSat Deployer (NRCSD) is a mechanism that is used to deploy small-form-factor satellites off of the International Space Station (ISS). The system consists of individual deployers that are bolted together in groups of four to form a 'quad pack'. A mission can consist of up to two quad packs (eight total deployers) mounted to the Multi-Purpose External Platform (MPEP), which is in turn mounted to the Japanese Experiment Module (JEM) airlock slide table (Figure 1). The Launch Command Multiplexer (LCM) and all associated cabling is also mounted to the MPEP, and the entire assembly is covered by Multi-Layer Insulation blanketing. The MPEP is transferred outside of the ISS by the JEM airlock, and then grappled by the JEM Remote Manipulator System (RMS); the JEM RMS then maneuvers the MPEP and NRCSD into the deploy position. Commanding is done from the ground, coordinated by the Payload Operations Integration Center at Marshall Space Flight Center and the Flight Operations Team at NanoRacks, and is executed by Japanese flight controllers at the JAXA agency's facility in Tsukuba, Japan.

The NRCSD was developed in response to a high customer demand for satellite deployment. The ISS has had the capability to deploy CubeSats since 2012, when the Japanese Small Satellite Orbital Deployer (JSSOD) was first used. The first deployments, which included a satellite flown by NanoRacks, served as a pathfinder and revealed the commercial demand for ISS satellite deployment. The JSSOD, which is still in operation to date, has been a reliable deployment mechanism, but is restricted by the limited capacity of 6U of satellites (by comparison the NRCSD has a capacity of 48U).

* NanoRacks, LLC, Webster, TX

Proceedings of the 44th Aerospace Mechanisms Symposium, NASA Glenn Research Center, May 16-18, 2018

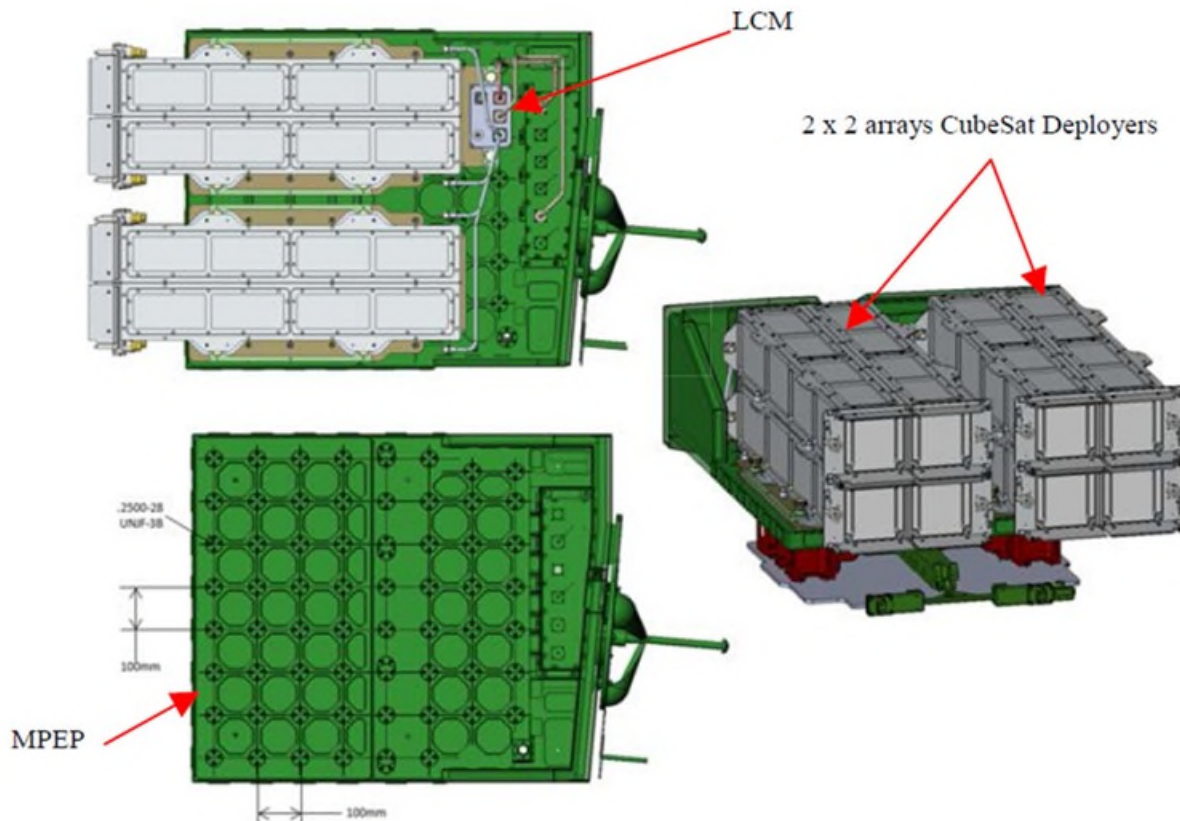


Figure 1. The NanoRacks CubeSat Deployers; Two ‘Quad Packs’ mounted to the MPEP (JAXA, 2013)

The NRCSD deployer has three major components: the baseplate assembly, the rails, and the door with release mechanism. The baseplate assembly is located at the back of each deployer and consists of an enclosing back plate, a spring that provides deployment velocity, and a pusher plate that interacts with the satellite. The spring is a linear coil spring that is fabricated with a custom spring rate; the spring rate is designed to deploy the satellites at 1.5 ± 0.5 meters per second in order to be compliant with the ISS jettison policy. Additionally, the baseplate assembly has a ‘jack screw’, which is a screw that is installed through the baseplate and against the pusher plate. It prevents the pusher plate from retracting as well as preloading the system stack. The preload is required so that the satellite system is determinate and does not move independently of the deployer during launch and ascent.

The rails are considered a mechanism and consist of features that are integrated into the NRCSD structure. They are precision-machined flat features and serve as the interaction points to the enclosed satellites. There are a total of eight rails that extend into the center volume of the deployer and serve to define the payload volume. The satellites are in direct contact with the rails and slide along them as they are deployed.

The doors of the NRCSD are a ‘barn door’ design, consisting of two overlapping doors. This was done instead of a single door so that the deployed configuration would remain inside the required volume of the JEM Airlock upon return inside the ISS. Each door has a hinge on the exterior side, with the centers overlapping. All doors and hinges, rails, and pusher plate mechanisms have remained the same in function throughout iterations of the NRCSD and have been evaluated by NASA’s Mechanical Systems Working Group. They have been determined to meet the requirements of MA2-00-057 and use the Design for Minimum Risk designation as hazard control for the ISS program (Robertson, 2016). Note that this evaluation was performed on later iterations of the NRCSD, and is now only applicable to the current design in use.

The release of the doors, and thus the deployment of the satellites, is performed by the ball-lock mechanism. The ball-lock is located between the two doors on one side of the door frame assembly (as to not interfere with the satellite deployment). All ball-lock components are contained inside a housing, which is fastened to the door frame assembly. When in the stowed (doors closed) position, the ball-lock functions by extending and holding precision ball bearings into receptacles in each of the doors. Release is performed by the retraction of the central plunger via pin puller, which allows the ball bearings to slide down a ramp geometry and retract into the housing. Retraction of the ball bearings from the receptacles allows the doors to swing freely and release the satellites.

On-Orbit Anomaly

The Orb-1 missions of the NRCSD experienced a deployment anomaly on-orbit that was diagnosed, troubleshooted, and overcome in real-time, resulting in the successful deployment of all satellites. The anomaly, which was determined to be electronic, was due to the cold temperature of the NRCSD system at time of deployment. Basically, the electronics did not function in the cold temperature extreme, and deployment was planned just as the ISS was coming out of eclipse. The problem was mitigated by turning on the Launch Command Multiplexer (LCM1) for a number of hours prior to deployment, which allowed the internal components to come to operating temperature and function correctly. The LCM was returned to Earth for diagnosis, and a newly-designed LCM (LCM2) was flown for the Orb-2 mission.

On Thursday, September 14, 2014 (GMT 247), the last round of commands was sent to the Orb-2 mission of the NRCSD. Four (4) deployers had deployed nominally, two (2) had not deployed. Two (2) had deployed hours after they had been commanded. A series of real-time safety meetings were held to determine a path forward. Of notable concern was the fact that two deployers had released at an undetermined time after being commanded, and that the two remaining un-deployed deployers had also been previously commanded. This was a concern because the NRCSD needed to be returned to the JEM airlock and brought inside; many options were considered, but ultimately a number of decisions were made. First, a translation path was determined that minimized the amount of safety-critical hardware in the line of deployment (should the deployment inadvertently occur during translation). Next, the safety-critical hardware components were analyzed for structural safety should they be impacted by a deployed satellite. Measures were taken to protect the ISS components that were identified as being at risk (specifically, the observation window in the JEM airlock was protected). Finally, a procedure was implemented for the protection of the astronauts once the NRCSD was returned inside the ISS pressurized volume. The plan was executed, and the NRCSD was returned and placed in a safe configuration without incident.

Anomaly Investigation

Aspects of the anomaly investigation occurred immediately upon discovery of the failure to deploy. Crew photography revealed that the first deployer that had inadvertently deployed after command had a slightly retracted ball-lock plunger (Figure 2). This exact signature was observed in one of the three remaining deployers that had failed to deploy. Scrutiny was applied to the electronics/avionics systems – this system as well as the associated cabling was photographed and observed during disassembly and analyzed on the ground. Finally, a Fault Tree Analysis was started and ground investigations began in earnest.

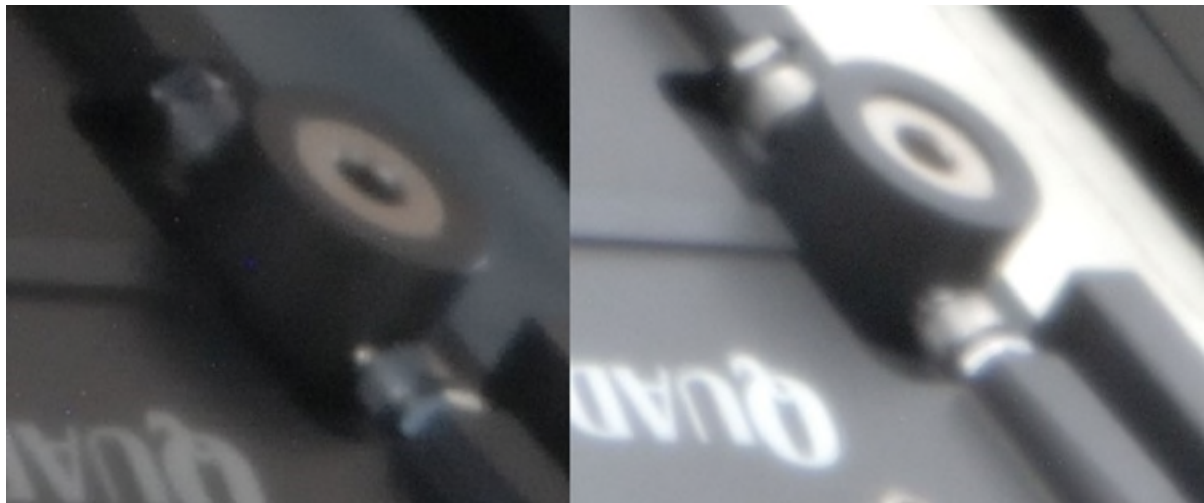


Figure 2. The Ball-Lock Mechanism Prior to Commanding (left) and After Commanding (right). A slight retraction of the central plunger can be seen.

Concurrently an effort began to develop and fly a secondary latching system that was designed to prevent inadvertent deployment in the case that commanding did not result in immediate satellite release. The system was designed and handed over to NASA in 38 days and proved successful for its first mission. Launched on the SpaceX-5 Crew Resupply Vehicle and installed on-orbit to the remaining NRCSD deployers, the next Orb-2 NRCSD mission that occurred included the secondary latch system and operated without incident. Later implementations of this mechanism by the manufacturer were not as successful, leading to another, unrelated deployment anomaly. Current iterations of the NRCSD do not have a secondary latch system.

Ground testing focused on the isolation of the variables that had been identified as possible failure causes. During a series of deployment tests, the jack screw was torqued beyond specification and the signature observed on-orbit was observed. The behavior proved to be repeatable, and the results were presented to NASA and the Mechanical Systems Working Group. With this discovery, the analysis of the system began and a mitigation plan was developed.

Assessment and Analysis

The baseplate assembly has threaded inserts that allow for screws to be inserted – these ‘jack screws’ pass through the external baseplate and touch the pusher plate. A total of four jack screws (Figure 3) were used in the baseplate assemblies during the Orb-2 missions. The purpose is to apply a clamping force on the system, namely the pusher plate-satellite-door system, and ensure that the stack-up is statically determinate. The deployment spring in its compressed state exerts approximately 22.2 N (5 lbf) on the pusher plate. Because of the satellite masses (typically 3-5 kg, 6.6-11 lb) and the launch vibration environment, the jack screws were implemented as a design feature to prevent system gapping. Nominally the jack screws are installed through the baseplate until they are touching the pusher plate, then torqued to 0.11 N·m (1 in-lb). A review of the Records of Assembly revealed that the installation torque had not been recorded. Additionally, the manufacturer had not performed a risk assessment analysis identifying this as a possible failure mode.

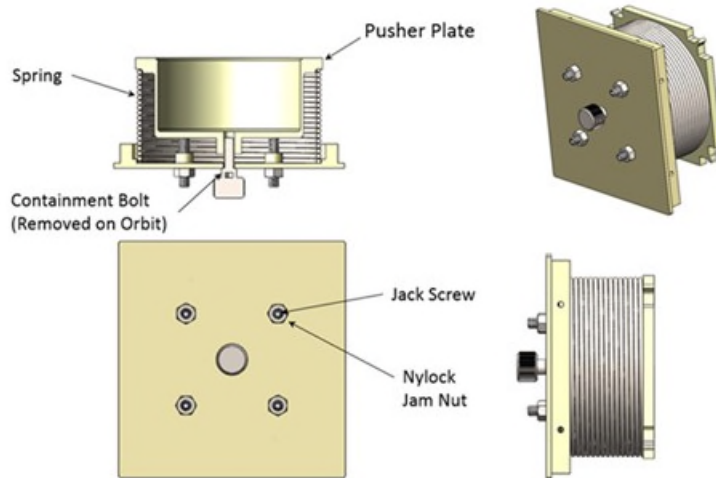


Figure 3. NRCSD Baseplate Assembly (Orb-2 Mission)

An individual NRCSD deployer was analyzed using a simple Free Body Diagram. The load path was identified from the baseplate assembly, through the satellites, into the door frame assembly, and eventually into the ball-lock mechanism. The satellites were analyzed separately and all shown to be adequate for the axial loads that they were possibly subject to. The analysis illustrated in Figure 4 identifies the system as extremely sensitive to jack screw installation torque. One important thing to note is that the pin puller that is used to retract the plunger is rated to 44.5 N (10 lbf) of retraction force. Additionally, all analysis cases include the force of the linear spring in the compressed state, which exerts a force of 22.5 N (5 lbf) on the system.

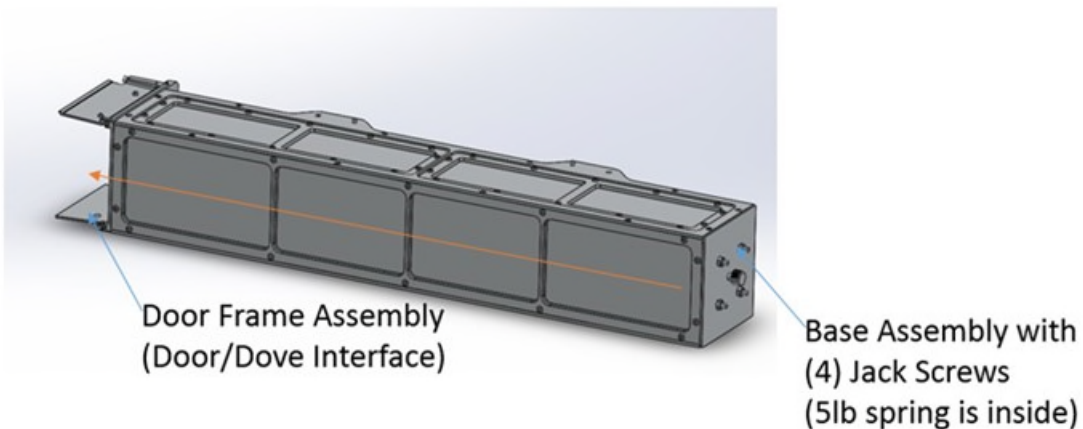


Figure 4. Load Path Direction of the NRCSD

The satellites are loaded into an individual NRCSD. Once loaded, with the doors closed and the baseplate assembly installed, a preload is applied to the back of the system via the jack screws. As shown above, the system transfers the jack screw loading through the satellites and into the doors. The satellites interact with the door as identified in Figure 5 and transfer the loading through the steel ball bearings into the retractable plunger. The free body diagram of the ball-lock system shows the force that is transferred to the plunger. Note that it is assumed that the loading is symmetric – each door is loaded equally and thus the force on each side of the plunger is equal.

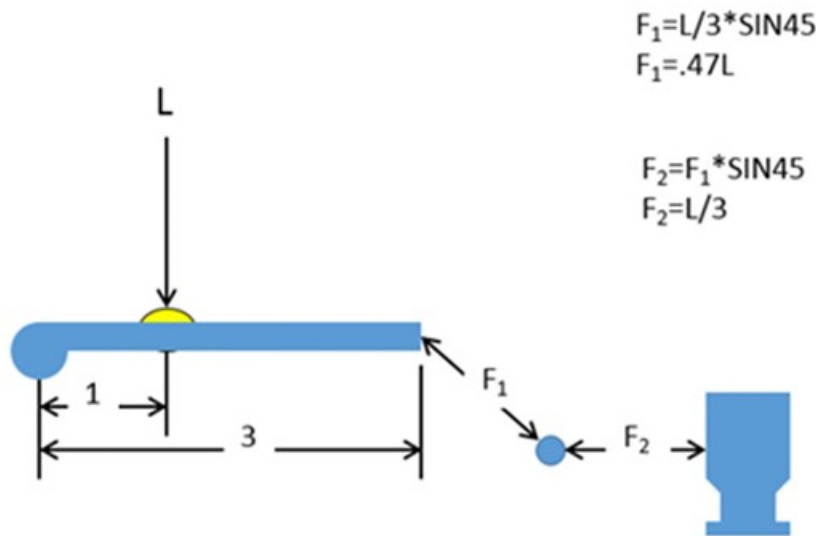


Figure 5. Free Body Diagram of the Ball-Lock Mechanism

The hinge screws, contact points, and doors were evaluated for structural adequacy, and all components had appropriate margin, even for extreme loading cases. Contributions to the system by the torque spring on the front door hinges were not considered because of the very low spring constant (0.027 N-m/rad) and corresponding low force (<<4 N). Additionally, the spherical contact surfaces were evaluated for Hertzian stress and were determined to not experience deformation under load; this was later confirmed by post-flight metrology. A coefficient of static friction was applied based on the material properties of the plunger and steel ball finishes, and no deformation was considered.

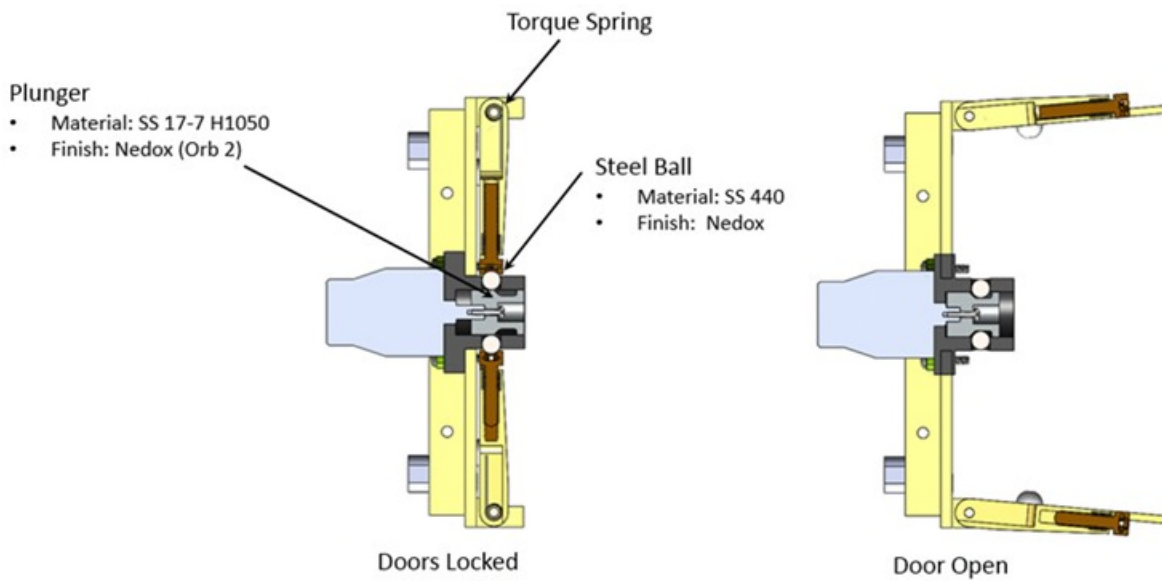


Figure 6. Cross-Section of the NRCSD Ball-Lock Mechanism

At approximately 44.5 N (10 lbf) of static friction, the pin puller does not have enough force to retract the ball-lock plunger. As can be seen in Table 1, this occurs at around 0.45 N-m (4 in-lb) of installation torque. Using linear interpolation, this value occurs at 0.42 N-m (3.69 in-lb).

Table 1. Installation Torques vs. Static Friction Force on the Ball-Lock Plunger

T- Applied Torque (inch-pounds)	Total Force at the Door (pounds)	Total Force at each Door (pounds)	Resultant Force on Plunger	Static Friction Force ($\mu=0.1$)
1	85	42.5	14.2	2.8
2	165	82.5	27.5	5.5
3	245	122.5	40.8	8.2
4	325	162.5	54.2	10.8
5	405	202.5	67.5	13.5
6	485	242.5	80.8	16.2
7	565	282.5	94.2	18.8
8	645	322.5	107.5	21.5
9	725	362.5	120.8	24.2
10	805	402.5	134.2	26.8

$$F_{\text{static}} = \mu * N$$



Conclusion

Due to jack screw torque variability, it is reasonable that Orb-2 NRCSDs that experienced anomalies were installed with a jack screw installation torques greater than or equal to 0.42 N-m (3.69 in-lb). This would lead to ball-lock mechanism binding. The installation procedure, which did not record the installation torque, which was uncontrolled in some cases, further indicates this as a cause.

The anomaly signature was repeatable in ground tests. If installation torques were higher than 0.68 N-m (6 in-lb), the entire system would seize and no deployment would occur. If the installation torque was between 0.45 and 0.68 N-m (4-6 in-lb), the signature observed on-orbit was recreated. In these cases, delayed deployment was observed in approximately 50% of cases, which is also consistent with the behaviors observed on-orbit.

Implementation of New Processes

A number of new processes were implemented based on the conclusions of the anomaly investigation. A notable early solution to the safety risk of delayed deployment, the secondary latch, actually led to additional anomalies. The primary solution was the removal of the jack screws on-orbit. Additional NRCSDs were onboard the ISS during the time of the anomalies and investigation; the jack screws were removed by astronauts onboard, and the mission was continued. All deployments were successful, and this operational procedure was implemented for all subsequent NRCSD missions.

Ground procedures were also modified to include the recording of the jack screw installation torque. The design of the baseplate was modified to include only a single screw, which provided a much more predictable control of installation torque. Tests were performed to measure the effect of installation torque variation, which validated the previous analytical models.

The anomaly, the secondary latch issues, and other factors led to the decision to perform a complete redesign of the NRCSD door and release mechanism. The new design was performed by NanoRacks engineering (previous design had been done by the manufacturer). The new design included the removal of the ball-lock mechanism and an overall reduction in part count. A tolerance assessment was performed as part of the design process, the results of which were presented to the Mechanical Systems Working

Group. Additionally, the Aerospace Corporation was hired as a third-party reviewer to ensure design functionality. The new door was first implemented within a year of the on-orbit anomalies and has had a 100% success rate.

References

1. JAXA. (2013). *JEMRMS Multi-Purpose Experiment Platform/Payload Standard Interface Control Document*. Japan Aerospace Exploration Agency.
2. Robertson, B. (2016). *Design for Minimum Risk (DFMR) of the NanoRacks CubeSat Deployer - Internal (NRCSD-I)*. Houston, TX: NASA.

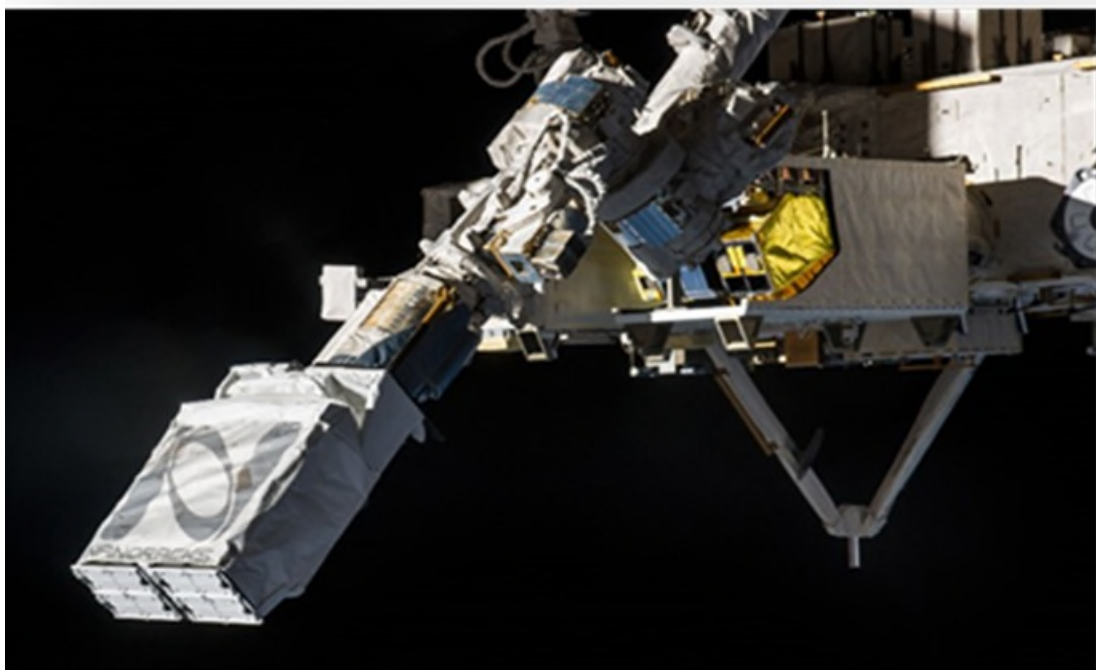


Figure 7. The NRCSD on the MPEP, grappled by the JEM RMS



Figure 8. The MPEP on the Slide Table (Left) and the NRCSD (Right)

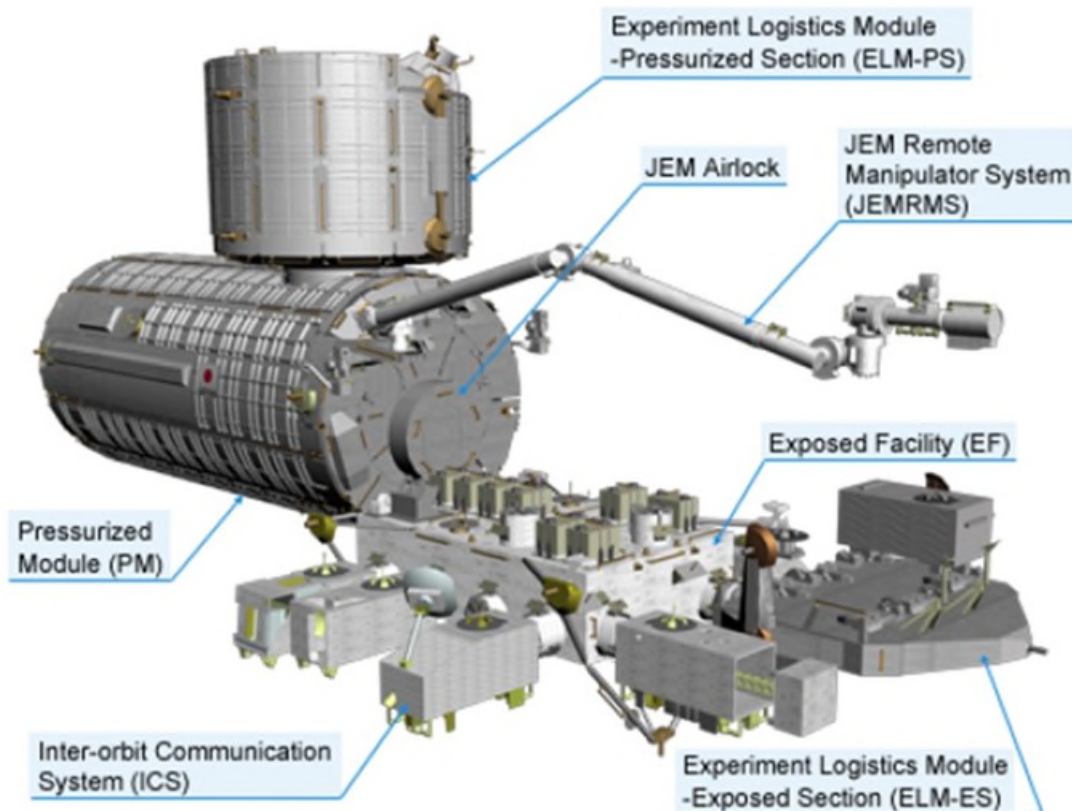


Figure 9. The JEM and Facilities

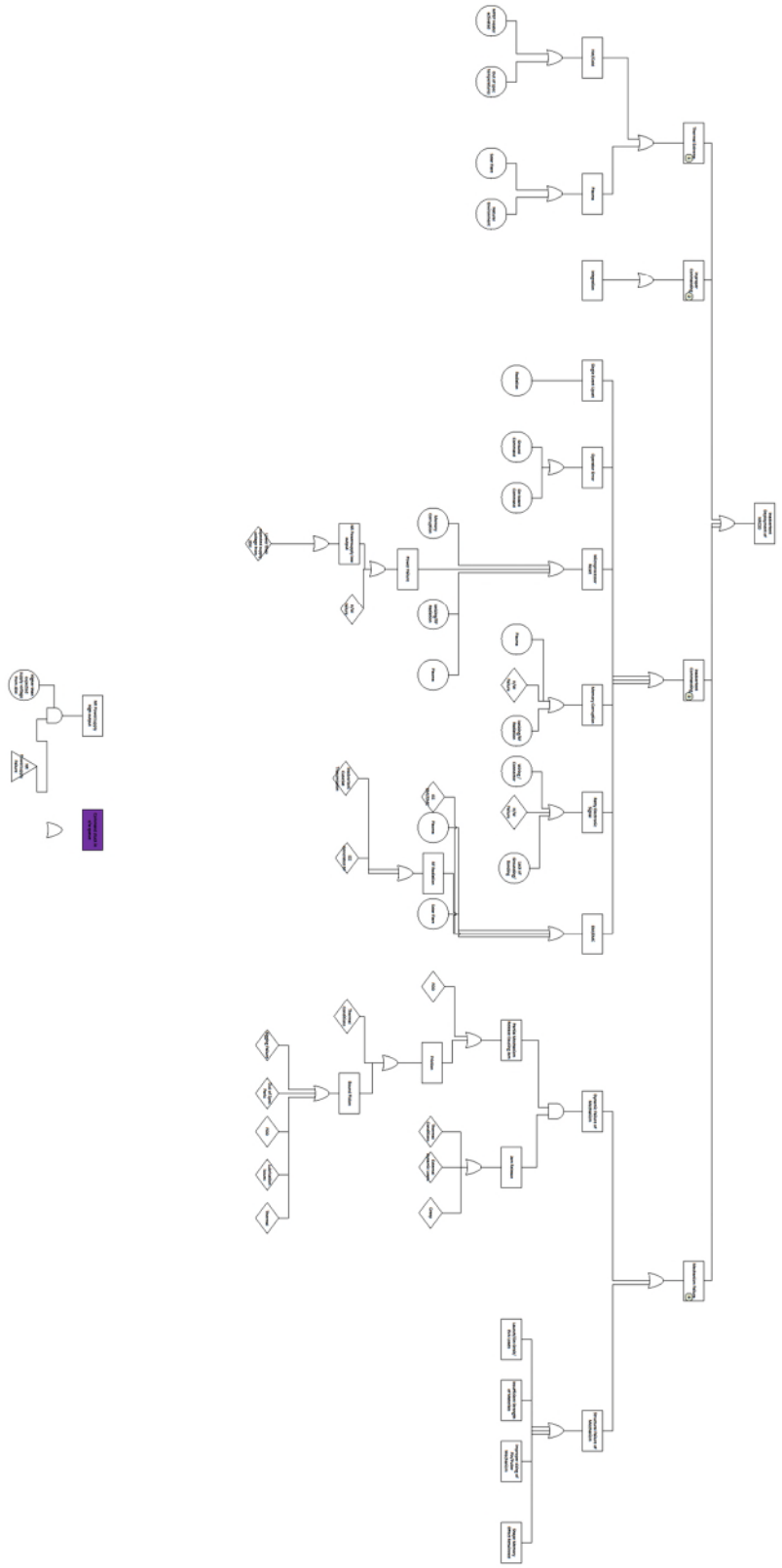


Figure 10. Fault Tree Analysis of the Orb-2 Mission Anomaly

Lessons Learned from a Deployment Mechanism for a Ka-band Deployable Antenna for CubeSats

Jonathan Sauder*, Nacer Chahat*, Richard Hodges*, Eva Peral^{*} Yahya Rahmat-Samii^{**}
and Mark Thomson[†]

Abstract

The Ka-band parabolic deployable antenna (KaPDA) is a 0.5-meter-diameter antenna that fits in a tiny, CubeSat compatible 10 cm by 10 cm by 16 cm volume. The design evolved from a rough concept in an R&D proposal to a fully flight-qualified design, scheduled for launch in May of 2018, in a timeframe of just 4 years. This paper focuses on key lessons learned on maintaining precision through structural depth, the use of fixtures, additive manufacturing for fabrication, the design of robust, deterministic mechanisms, and the dangers of friction and press fits.

Introduction

CubeSats have undergone an exciting evolution over the past decade. From being considered an academic exercise, they have grown to the point of obtaining real science data and are providing commercially viable business opportunities [1]. As the technology has increased in capability, so have the needs in the areas of power, propulsion, and communications. One critical need in the area of communications is high gain antennas, and specifically deployable antennas given the CubeSat's small size. Deployable antennas would enable communication at much higher data rates and radar instruments in small packages. Operating at a high frequency, like Ka-band, further increases the amount of data that can be transmitted. However, a deployable Ka-band parabolic antenna makes for a very challenging mechanism design problem. While there have been individual aspects of the mechanical design published in a series of AIAA conference papers [2], [3], and details on the radio-frequency design in a series of journal articles [4], [5], this paper focuses on key mechanism lessons learned from the KaPDA development.

The seed inspiring this concept started with the Aneas parabolic deployable antenna (APDA) folding rib parabolic mesh antenna used on the University of Southern California's Information Sciences Institute (USC/ISI) Aneas spacecraft [6]. The Aneas was launched in 2012, and the folding rib geometry illustrated a robust deployment sequence that has been used on larger antennas, like some of Harris's Unfurlable Antennas [7]. However, the APDA was designed to operate at S-band, whereas Ka-band brings an entirely new set of requirements. Therefore, while a similar general architecture was used, the RF design and each the mechanisms were completely re-engineered.

Requirements for KaPDA and Design Overview

Requirements

The goal of KaPDA was to create a new capability for CubeSats, to enable high-speed data rates from deep space. Data rates in a communications link budget depends on a number of things, including power of the transmitter, receiver sensitivity, ground antenna configuration, frequency of operation, and satellite antenna configuration. The goal for this task was to improve data rates through the satellite antenna, specifically to achieve a gain of 42 dBi. The three ways of accomplishing this are to 1) have a high frequency antenna 2) operate with high efficiency and 3) a large diameter.

* Jet Propulsion Laboratory, California Institute of Technology, Pasadena, CA

** University of California Los Angeles, Los Angeles, CA

† Northrop Grumman Astro Aerospace, Carpenteria, CA

The antenna was chosen to be optimized for Ka-band, specifically the frequency range from 32 to 35 GHz, as this is a frequency used by the Deep Space Network for communications and is also a frequency for precipitations radars. To ensure high efficiency at this frequency, the antenna had to deploy to a surface accuracy of 0.4-mm RMS or greater. A trade study on antenna diameters revealed a 0.5-meter antenna would be large enough to offer a major advancement in capabilities. Combining these three aspects into one antenna would multiply data rates by 100 times what the APDA antenna would have achieved.

Because this system was targeted for a CubeSat, it had several key dimensional constraints. CubeSats are modular satellites, built on around a 1-unit (U) system. One "U" is 10 cm by 10 cm by 10 cm. CubeSats have been launched in sizes of 1U, 1.5U, 2U, 3U, 6U, and 12U. (6U systems are approximately 10 cm by 20 cm by 30 cm, whereas 12U systems are 20 cm by 20 cm by 30 cm). To accommodate the CubeSat unit system, the antenna had to stow in a 10 cm by 10 cm cross-sectional square, with a goal of keeping the height as short as possible, at approximately 15 cm. This would allow the antenna to consume only half of a 3U spacecraft or a quarter of a 6U spacecraft.

Key Subsystems and Components

An overview of the key subsystems and components is beneficial before discussing the development of the KaPDA antenna. The subsystems are illustrated in Figure 1. The canister and hub make up the primary *deployment actuation* sub-system. The canister encircles the antenna when stowed. Near the bottom of the canister is the hub, to which the ribs and the horn mount. The ribs are divided into two parts, the *root ribs*, which attach to the hub and are the closest to the center of the antenna, and the *tip ribs*, which are the outermost ribs when the antenna is deployed. The tip ribs are attached to the root ribs via the *mid-rib hinge*. The *horn* is primarily an RF component, but the exterior walls serve to guide and position the *sub-reflector* and position the ribs when stowed.

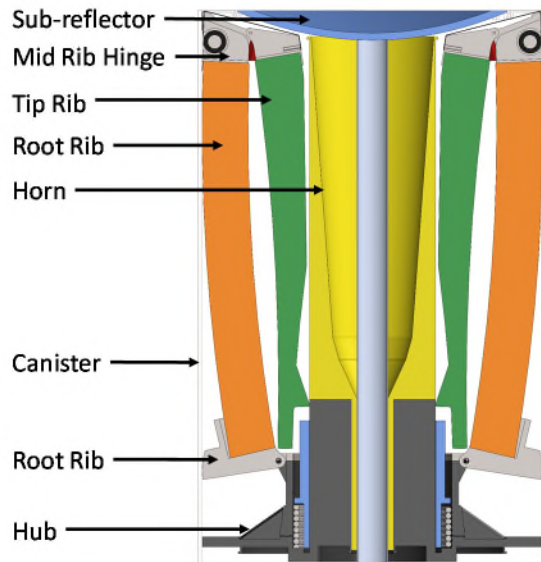


Figure 1. Key KaPDA Components

Overview of the KaPDA Development Sequence

To deploy, the hub is first driven upwards. (Figure 2, A-B). As the hub nears the top of the canister, the root ribs begin to bloom, opening (B-C). When the tip ribs reach the point where they become free of the horn interference, they are free to actuate at the mid-rib hinge (Image C). The hub continues to travel upwards until the root ribs fully deploy (image D). After the ribs are mostly deployed, the sub-reflector is allowed to telescope along the horn, and reach its final fully deployed location (C to D).

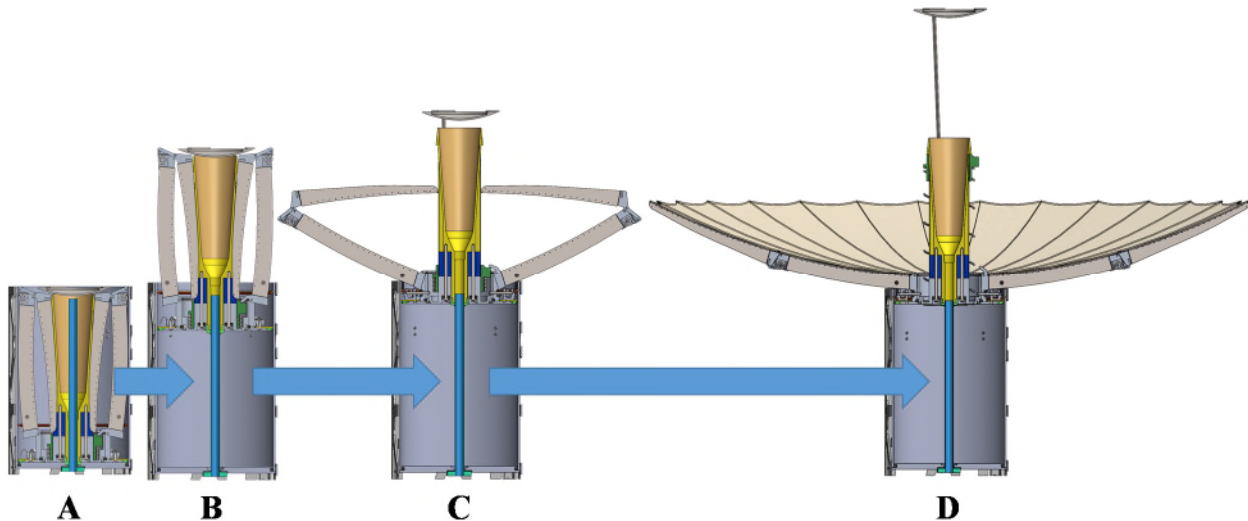


Figure 2. KaPDA Deployment Sequence

Early Development of KaPDA

Characterization of the Aneas Antenna

The development of KaPDA began by researching the Aneas antenna. The team first met with the Aneas team at USC/ISI to capture lessons learned, and was able to borrow the antenna from USC/ISI for metrology. A theodolite measured the accuracy of the deployed shape of APDA and found that the surface error was an average of 2.4-mm RMS. While this is perfectly adequate for an S-band antenna, requirements for a Ka-band antenna are tighter, at 0.4-mm RMS maximum error. APDA was designed with thin ribs, which helps to reduce storage space, but also impacted the surface accuracy possible. Torsion springs actuated the hinges and setscrews adjusted the position. These were key elements requiring redesign to improve accuracy.

A second issue when going from an S-band design to a Ka-band design is the mesh. At S-band, 10 openings per inch (OPI) mesh is adequate, which also requires a low amount of tension to achieve its shape. The 40 OPI Ka-band mesh requires a much greater tension of 17.5 N/m. This means the antenna must be designed to achieve greater values of preload upon deployment; approximately 250 N. The APDA deployment architecture only achieved a fraction of this, and therefore the deployment approach needed to be completely redesigned.

The third and most significant issue is the RF design. The Aeneas antenna used a splash plate feed connected to a co-ax cable. At Ka-band this would create far too much loss, removing any gains achieved through surface accuracy. As a result, an entirely new RF design was required for the antenna to operate at Ka-band with minimal loss.

RF Design Effort

The first approach to create a system that would operate at Ka-band was to develop the RF design. While the idea of using a parabolic dish to reflect RF energy remains the same as APDA, the rest of the system had to be completely redesigned, to the point which the KaPDA RF design and the Aeneas RF design share no heritage. In order to achieve high frequency communications with low loss, the RF energy must be kept in the electro-magnetic wave form all the way through exiting the antenna. Three subsystems were used to achieve this: the secondary reflector, horn and waveguide. The secondary reflector collects the RF energy from the parabolic dish, and reflects it into the horn. It also has a critical feature where it corrects for the geometric errors in the mesh which occur because of the finite number of ribs. The horn concentrates RF

energy and transitions it from the sub-reflector to the waveguide. The waveguide transports RF energy out of the antenna in electro-magnetic wave form.

Multiple types of secondary reflectors were considered including Gregorian, Displaced Axis, Cassegrain, and “Hat” style feeds. One of the key challenges was finding a feed that did not have to be placed far from the vertex of the parabolic reflector. If the feed was located far away from the parabola, it would be difficult to stow it in the short 15-cm height. While the “hat” style feed provided the most RF gain, they also had to be deployed the furthest. The Cassegrain secondary reflector, while not providing the best gain performance, would actually fit within the stowed volume as its geometry allowed the secondary reflector to be deployed below the focal point. Therefore, the Cassegrain secondary reflector was selected.

As already noted the horn takes the RF energy from the sub-reflector and concentrates it into the waveguide. While the horn is a very technical complex piece of RF design (discussed at length in [4]), from a mechanical perspective, it is a highly toleranced conical shape.

The waveguide presented a greater mechanical challenge. The waveguide must be connected to the fixed base of the antenna and also to the horn, which starts near the base of the canister, but then deploys to the top of the canister. While “flexible” waveguides exist, they are actually mostly rigid and would not work. Therefore, the only solution was to allow the horn to telescope around a fixed waveguide. This was a new RF innovation demanding tight mechanical tolerances. It was also risky, as a number of RF engineers did not think it would work. However, early prototyping of the concept with non-deploying hardware proved the concept would work from an RF point of view.

Detailed Mechanical Design of KaPDA

Design of the Ribs

The design of the ribs is crucial for defining the antenna’s parabolic shape, and therefore was the first place to start. The prior RF analysis indicated that 30 ribs were required to avoid significant losses, due to the “flat facets” which occur in between the ribs. To fit a 0.5-meter antenna in a 15-cm-tall canister, the ribs had to be folded in half when stowed. Therefore, each rib would have 2 hinges. While designs were also investigated to fold the ribs three times, it was determined this would result in an overly complex deployment sequence.

The next step was to determine how to enable the ribs to achieve a surface accuracy of 0.4-mm RMS. This was first accomplished by making the ribs deep, increasing the area moment of inertia, so they would be stiff against the tension of the mesh. To maximize the amount of depth where it is most needed (where bending moments are the highest), the rib was deepest at the base. It can be observed that the tip rib steadily gets less deep the further it is from the center of the antenna as less moment is applied to it. This design provides an approximately equal distribution of bending stress across the entire length and results in less material where it is not required.

The second key features to achieve accurate deployment were the hinges. The depth of the ribs was carried into the hinges to minimize the effect manufacturing tolerances could have on the hinges. The hinges had a hard stop located 12.7 mm on the opposite side of the hinge pin, compared to the approximately 3 mm which the Aeneas antenna had between its hinge pin and the position setting set-screw. This one architectural change increased the deployment accuracy of the hinges by at least 4 times. Further, using flat hard stops instead of setscrews prevented the position from changing with each deployment as set screws can move. The tips of the setscrews would dig into the aluminum hinge on deployment, whereas a flat hard stop prevents the deformation with better distribution of the load.

Rib Fabrication Process

As the hinges did not use setscrews, this also meant that the hinges were not adjustable. Therefore, it was very important that the ribs and hinges were placed relative to each other with a high degree of accuracy. While this could be achieved with extremely tight manufacturing tolerances, this was deemed too

expensive, especially on a quantity of 30 ribs. A better solution was found by using a bonding fixture to precisely set the position for the root and tip rib, and then insert and bond the hinges in place. This fixture also ensured all the ribs were identical to each other.

Design of the Antenna Deployment

A number of concepts were initially brainstormed for deploying the antenna, which included using springs, cable and pulley systems, springs combined with cable and pulley systems, and gas-powered piston systems. A major aid to developing the concept was creating a CAD drawing showing an outline of the canister and folded ribs, and printing it out to scale. Deployment mechanisms could then be sketched on this paper, as shown in Figure 3.

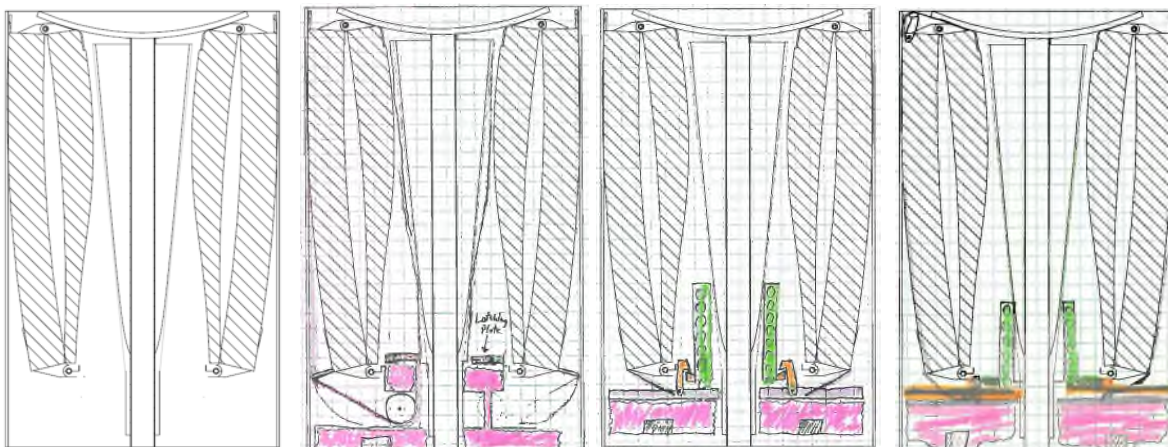


Figure 3. Original CAD template (left) and sketches made at scale on the template (center to right)

One of the major issues when working in CAD software is an unrealistic understanding of scale. By printing out drawings of the constraints, and sketching deployment systems to scale, it was quickly realized that any type of cable and pulley system fitting in the volume would require very small components. In addition, it would be hard to route cables in the small volume while also preventing tangling.

Springs alone were not a realistic system either because of the preload required to tension the mesh. While the total preload needed was calculated to be 250 N at the end of deployment, this would result in a force of at least 500 N when the spring was stowed prior to deployment. This means there would be a lot of excess energy in the spring which would go into accelerating the antenna, resulting in a dynamic impact. Therefore, the most reasonable system appeared to be a gas driven canister as the primary mode of actuating the deployment. As the entire system is stowed in a canister, it was convenient to also use the hub as a piston. Pumping gas between the piston and the base would cause it to expand in the cylinder, pushing the antenna out and deploying it. If the gas could be properly metered, the antenna would be allowed to slowly deploy, and then pressure could be increased only at the end when the additional preload was required. Given the 10-cm-diameter piston, operating in the vacuum of space, only 32 kPa (about 1/3rd of atmospheric pressure) would be required to achieve the 250-N load. Further, no miniature parts were required by such a pressurized system. To ensure the antenna would stay in the deployed state after the gas-powered deployment, the fully deployed antenna would be latched in place.

When considering the deployment system, beyond pushing the antenna out of the canister, the antenna ribs also required deployment from their initial state. While originally multiple cable systems for rib actuation were explored, and even tested, these were dropped for the same reasons they were not used for actuating the antenna out of the canister; lack of space. It was determined the best approach was to have the root ribs catch on the edge of the canister, leveraging them out to deploy. This ensured the root ribs, which react a majority of the moment, could have a high preload when deployed. Each rib has two springs attached to either side of it. These springs are all attached to one ring, which ensures all 30 ribs are synced together.

When the antenna reaches the top of the canister, the ring hits an internal stop in the canister, which prevents it from moving while the hub continues to travel up. This causes the root ribs to deploy as they are pulled by the springs attached to the ring. The springs also add compliance to the system accommodating for any small deviations in deployment of the root ribs.

The tip ribs are each deployed by a constant force spring in the mid-rib hinge. The tip rib spring actuates once the root ribs have deployed far enough such that the tip ribs are clear of the horn.

Use of Additive Manufacturing

When fabricating the spring ring, which coordinates all 30 springs to the ribs, it was found additive manufacturing was the most cost-effective approach and gave the best result for building this part. The spring ring consists of multiple small holes through which extension spring hooks attach. Traditional manufacturing would have been challenging as the spring holes would be at an angle, and thus hard to drill with a small diameter drill bit. Further, the holes would have sharp edges, which would catch on the hooks of the extension springs. However, by additively manufacturing this part, a full annular hole was created in the spring ring, perfectly fitting the geometry of the extension spring (Figure 4). This made it function better than a traditionally fabricated part.

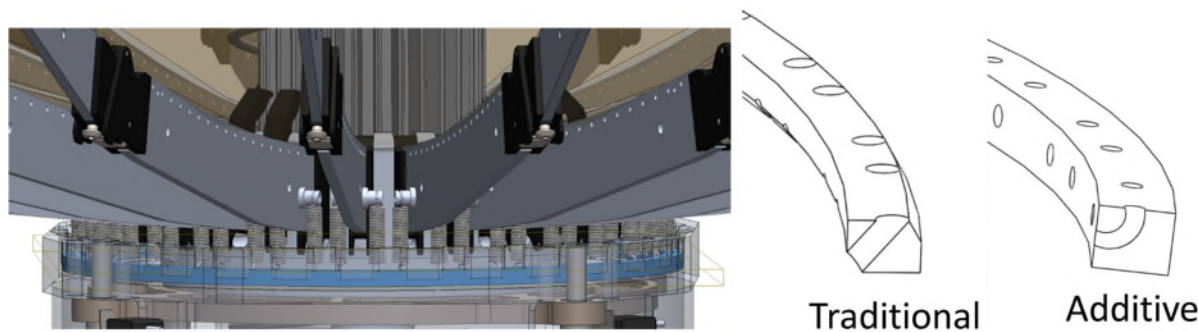


Figure 4. An Additively Manufactured Spring Ring Allows for Unique Features

The component was printed of 304 stainless steel, and as additive manufacturing has been known to have variable material properties, a stress analysis was performed and found the part had a factor of safety of greater than 10. Therefore, material property variance was deemed to be low risk enough to not require testing of the additively manufactured parts. Perhaps the most exciting part about additively manufacturing this component was that it was cheaper than machining the part traditionally. As material volume is the key cost in additive manufacturing, and complexity is not a driver, this part required minimal material and could thus be built inexpensively. This also provided a good example of using additive manufacturing for its strengths in creating complex features which would be hard to machine otherwise. While additive manufacturing is not the best option for many parts, for this one component, it had significant advantages.

Construction and Testing of the KaPDA Antenna

Three versions of the KaPDA antenna were constructed in series. First a prototype, then an engineering model, and finally a flight unit was constructed.

Prototype

The first prototype of KaPDA was constructed to primarily verify the accuracy with which the antenna could be built and test the gas-powered deployment system. The prototype was a full fidelity prototype, which used flight like materials.

To construct the antenna, first the 30 ribs and hinges were assembled. The ribs were then attached to the hub. Mesh was stretched and tensioned over a parabolic mold, and then the hub with ribs were set on top

of the mesh. The mesh was attached to the ribs through a series of holes in the ribs, with nearly 2,000 hand stitches attaching the two. The antenna then came off the mold in the fully deployed state.

The antenna was first RF tested to check the as-built tolerances prior to deployment, and found to achieve 42.5 dBi of gain, outperforming the gain requirement of 42 dBi. This indicated the RF design had adequate margin and the antenna was built to better than required tolerances.

After the RF test, the antenna was stowed by carefully folding the ribs and sliding the hub down into the canister. Then pressurized gas was inserted through the base plate, actuating the deployment, which appeared to be successful as illustrated in Figure 5.

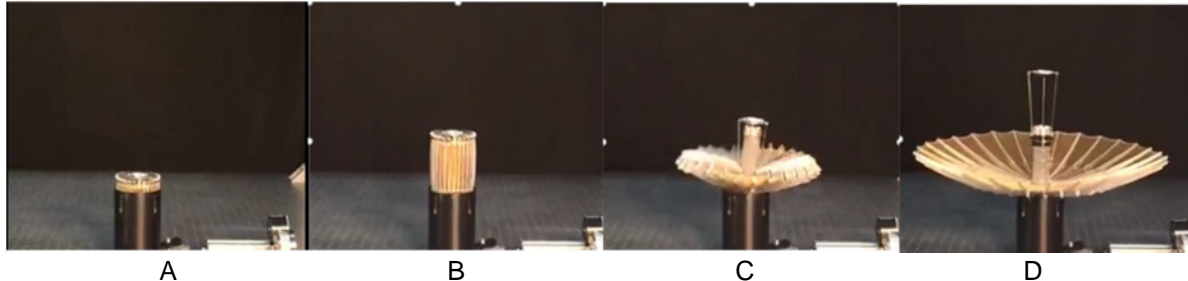


Figure 5. Antenna Deployment Via Gas Power

After deployment, the antenna was taken to the range for RF testing. When mounting the antenna horizontally, it was noted some of the ribs were folding closed. Further investigation showed that the inflation powered deployment had never latched the antenna. While the antenna was able to be manually latched in place, and the RF test could be finished, in orbit this would have been a requirement critical failure as the ribs would not be in the right location to achieve high gain. RF testing also revealed after being manually latched in place, the antenna only achieved 42.0 dBi of gain, just meeting the requirement.

Further investigation of the deployment video revealed that the spring ring and hub tilted to one side near the top of the deployment (Figure 5C). This angle prevented the ribs from properly latching in place. Because gas was just pushing on the antenna during deployment, nothing was constraining the antenna to ensure it deployed straight and vertical. The piston consisted of a thin plate attached to the hub, and therefore was free to rotate like a coin spinning its way down a pipe of similar diameter. While height could have been added to the plate, there was not enough room to add as much length as the cylinder diameter, which would mean the L/D for a sliding contact would be less than one, putting the design at risk for jamming.

While this was the first indicator that a gas-powered deployment would not be suitable for this space deployable, several other complications arose. First, when looking for a gas system to operate in orbit, the only commercially available parts that would fit in the system were small cold gas generators. Unfortunately, these release pressure relatively quickly, and would result in an explosive deployment. Secondly, even if the deployment could be controlled by a gas-powered system, there was the added complication of a canister of gas sitting in space. If it began to leak, even a small jet of gas would behave like a propulsion system, and could potentially cause the spacecraft to lose control. Finally, residual pressure and launch locks to resist residual pressure added further complications to the design. Because of this series of issues, it was determined an alternate approach for the primary deployment system had to be found.

Development of the Engineering Model

The engineering model began with a design process investigating alternatives to provide the main deployment of the antenna out of the canister. After going back to the drawing board, a motor-powered deployment with lead screws was investigated. This deployment approach was initially rejected during the early trades because the most intuitive place to locate a lead screw was in the middle of the antenna, conflicting with the waveguide. However, through further brainstorming, realization dawned: the antenna fit

into a canister, but a CubeSat is a square. As such, there were four corners not being utilized. Four lead screws could be located in the corners, driven by a motor (Figure 6). The main challenge: synchronization of all four lead screws to ensure a steady deployment.

To synchronize, each lead screw was attached to a “planet” gear. Each “planet” gear interfaced with the “sun” gear in the center of the antenna which kept all four lead screws in sync. While this is not a traditional planetary gearbox, it is easiest to reference the design in these terms. Because of the waveguide in the center of the antenna, the sun gear was mounted to a large diameter thin section bearing. A pinion attached to the motor would drive one of the planet gears, in turn driving the sun gear, and then the other three planet gears. While initially there was discussion of using two motors for redundancy in the system, if one of two motors failed, extra torque would be required to back drive the non-functioning motor. Therefore, the antenna was maintained with a single motor.

The lead screws attached to a brass threaded feature on the hub which would drive the antenna up and down. A further advantage of the motorized system was realized when investigating adding launch locks to the design. The lead screws could also be used to hold the hub down, in addition to deploying it. Therefore, one system provided the launch lock and deployment capabilities.

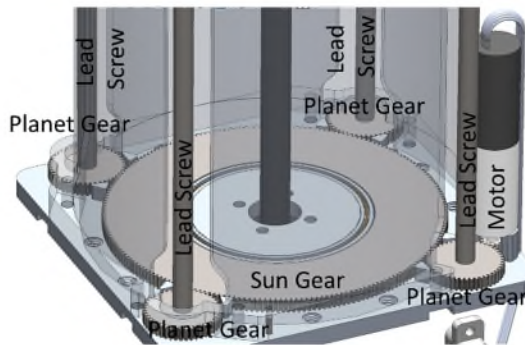


Figure 6. Motorized Deployment System Components

The prototype antenna was retrofitted with the motorized system. The same mesh, horn, and secondary reflector were used. This meant only the canister, base, and some components on the hub needed to be replaced, along with the additional motorized drive system. This retrofitted designed was referred to as the engineering model.

Engineering Model Testing

The antenna was then deployed with the motorized deployment system, where all systems behaved nominally. The antenna was taken to the RF range for testing after deployment to check the deployed shape. It was found the motorized system could apply more preload to the system in the deployed state, which resulted in a better surface accuracy, and thus a gain of 42.7 dBi, once again exceeding requirements.

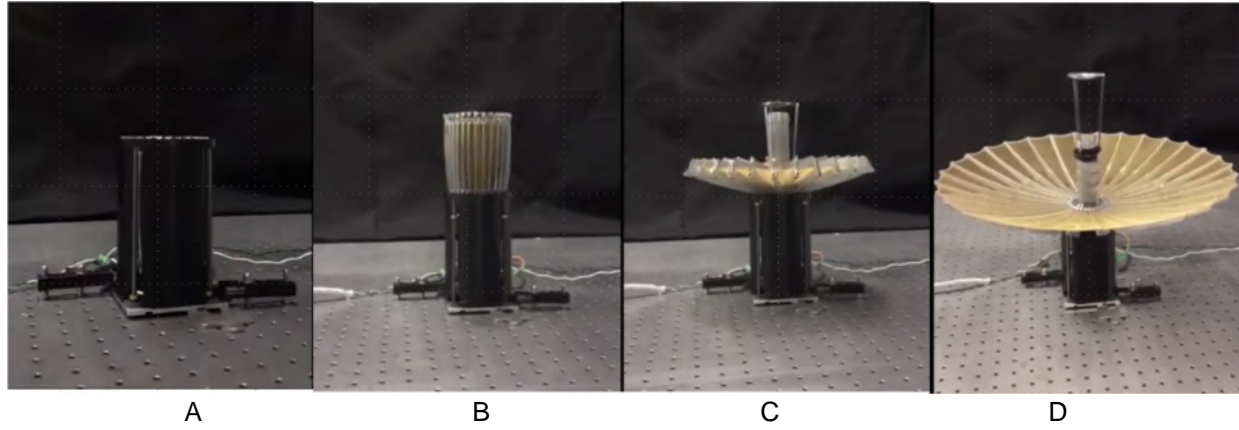


Figure 7. Antenna Deployment with Motorized System

After the deployment system demonstrated successfully, the next key challenge was to prove the design through vibration testing. The antenna was vibed at 14.1 GRMS in three axis, which is the General Environmental Verification Spectrum qualification level, as no launch had been determined at that point. After the vibration in the first axis, the antenna was deployed to ensure everything worked as planned. However, the deployment revealed a problem with the design. The mid-rib hinges, actuated by the constant force spring did not deploy. This resulted in the deployed antenna stopping in position illustrated in Figure 7C. While it was known the mid-rib hinges had a low torque margin, prior deployments had never failed to deploy the antenna. The root cause was found to be a combination of friction and gravity from a number of test runs with an extra hinge. When the antenna was stowed, the constant force spring is unrolled and pulled across the root portion of the mid-hinge. The friction on the spring prevents it from fully relaxing, resulting in tension. But vibration shifted the spring into lowest energy state, resulting in friction that was originally providing additional tension, now resisting the deployment. In addition, in the configuration the antenna was deployed, the mid rib hinges had to deploy against gravity. The combination of gravity and additional friction resulted in a negative torque margin.

After the failed deployment, kick-off springs were added under the constant force springs to ensure the antenna deployed. Vibration test proceeded in the remaining two axes, and afterward the antenna deployed successfully. Once, again, the antenna was taken to the RF range for testing, and found to achieve a gain of 42.7 dBi.

One final note on the engineering model antenna: during a subsequent deployment, after the RF test, one of the kick off springs became jammed in a closed rib which prevented the antenna from fully deploying. Thus, a more permanent solution was required.

Flight Model

After the completion of vibration testing on the engineering model, construction of the flight model began for the RainCube Spacecraft, a 6U CubeSat. RainCube is a precipitation radar and will be the first active instrument in the CubeSat form factor. Some redesign efforts were required, the first and foremost being changing the rib mid-hinge geometry to allow the constant force spring to generate more torque. Other changes included features to better hold the ribs in the stowed position, switches for deployment verification, and vacuum-compatible grease in all components. During construction of the flight model, the torque margin was checked on the mid-rib hinges, and found to be more than adequate when compared to the engineering model design.

After construction of the flight model, it was first deployed and then tested on the RF range, once again achieving a gain of 42.6 dBi. Next it was stowed and then deployed in thermal vacuum (TVAC) at a temperature of 65°C. In general, antennas are not fully deployed in thermal vacuum due to size, but because KaPDA was intended for a CubeSat, it was easy to find a chamber which could accommodate a

full deployment of the antenna. While initially the deployment went as planned, the antenna suddenly stalled about 2/3^{rds} through the deployment. After trouble shooting, it was found the motor controller, which had a poorly design thermal path to the chassis, was overheating. The motor controller had a thermal limit of 85°C, but without adequate heat conduction, the heat generated by running the antenna caused it to overheat at just 65°C. Deploying the antenna at 55°C eliminated this problem. While the initial thermal range from deployment was 10°C to 50°C, the range was decreased to 10 to 40°C.

After TVAC testing, the antenna was taken to the RF range for further testing, and no changes were observed to antenna gain. However, another problem occurred when stowing the antenna. When driving the antenna down, an odd noise was coming from the sun and planet gears. Investigation revealed the sun gear was running at a slight angle. It appeared that during thermal vacuum tests, because the gear was a 300 series, or austenitic stainless steel, and the bearing was a 400 series, or matriistic stainless steel, the coefficient of thermal expansion was different enough to cause the press fit to become loose. As the antenna was deployed with the loose press-fit at the high temperature, the sun gear worked its way off the thin section bearing. Further detailed analysis revealed, depending on the tolerances of manufacturing, when going cold the sun gear would likely crush the thin section bearing. The end solution was to increase the diameter for the hole in the sun gear, and then bond the sun gear to the bearing, providing compliance at the thermal interface. Further, a 0.4-mm bond line with EA9360 epoxy helped to athermalize the joint, resulting in less stress on the gear and bearing.

After re-installing the sun gear bearing, the antenna was installed on the RADAR instrument assembly. The RADAR instrument then went through a 6.1 G_{RMS} workmanship vibe, which was the minimum required as actual launch loads for RainCube are expected to be much lower, closer to 2 G_{RMS} (given it is being stowed with soft cargo to the International Space Station). After vibe, the antenna went through a second thermal vacuum test, this time where it was deployed at 0°C. The antenna behaved exactly as expected through both tests.

However, about 3 months prior to installation of the antenna on the spacecraft, it was realized the spacecraft (built by a vendor, Tyvak) would be supplying 12 V to the antenna, where previously the antenna operated at 5.5 V during testing. This change warranted investigation, and revealed the antenna would be performing fundamentally differently than before, and could generate a higher stall torque than observed in the prior test. As such, a current limiting feature was programmed in the motor controller to ensure the performance on orbit was similar to the performance in the number of environmental and deployment tests on the ground.

The KaPDA antenna and RainCube instrument has been integrated into the RainCube spacecraft at Tyvak, the spacecraft bus vendor. Assembly and EMI/EMC testing have been completed.

Current Status

The RainCube spacecraft assembly is about to undergo environmental testing for a 3rd time at the spacecraft level, although this testing is much more benign than the level to which the Instrument Assembly with the antenna was qualified. After environmental testing, the antenna will be deployed one last time to verify operation before it is stowed. RainCube is scheduled to launch in May 2018 from Kennedy Space Center and fly as soft cargo to the International Space Station. Once there, it will be deployed from the station via the NanoRacks CubeSat deployer. After approximately one month of bus checkout tests, the antenna will be deployed for a final time, in low earth orbit. The mission and antenna are designed to operate for approximately 1.5 years, before it reenters Earth's atmosphere and disintegrates.

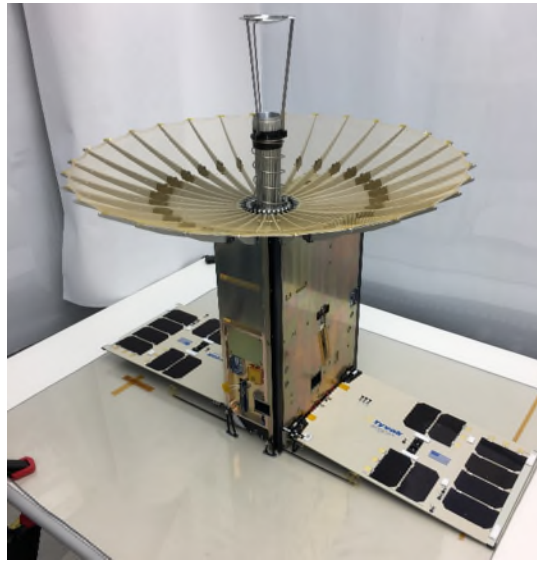


Figure 8. Flight KaPDA Installed with the Tyvak Spacecraft

Conclusions / Lessons Learned

KaPDA has provided a number of great lessons learned with regards to mechanism design, given it combines motors, gear trains, lead screws, springs, and at one point pneumatics. There are a number of separate actuating features, each of which have generated key lessons learned, detailed below.

Add as much Depth in a Deployable as Possible

It is common knowledge increasing the area moment of inertia improves cross section performance. While this seems like a minor change, it was a key instrumental factor in achieving the surface accuracy and deployed stiffness. While it is often challenging to add deep sections to a deployable because of stowed size constraints, the KaPDA design achieved additional depth by placing it where the bending moment was the highest and reducing it where the bending moment was lower. The additional depth also made the hinges less sensitive to manufacturing tolerances by allowing hard stops to be placed far away from the hinge pins.

Use Fixtures to Prevent Tolerance Stack up Issues

A key design decision in the assembly process was to use fixtures to assemble components, and bond them in place thereby achieving very accurate and consistent ribs. This effectively removed the effects of tolerance stack-up from assembly, such that the fixture was the key driver in achieving the appropriate geometry. This allowed both versions of the antenna to be extremely precise and provide high RF performance.

When to use Additive Manufacturing

Additive manufacturing was found to have advantages for building small, complex components. This allowed lower cost approaches than traditional machining for a part that had better function. However, most parts used in the antenna were still best implemented through traditional machining, and additive should not be considered a replacement for traditional methods. Rather, it becomes an alternate method in the designer's toolbox.

Use Deployment Methods Provide Control Authority

The original deployment method, using a gas powered pneumatic approach provided almost no control authority, other than deciding when to start the deployment. Moving to a motorized system allowed specific

control of the motor rate, and the encoder could even be used to monitor the deployment status. Therefore, a deterministic deployment was much preferred.

Friction on Sliding Components

Be very wary of any effects friction may have, as was learned in the constant force springs in the mid-rib hinges. When deploying, ensure all components have relaxed to their lowest strain energy state prior to deploying, to ensure there are no surprises later in the program.

Press fits

Beware of press fits. Even if the type of material is the same (i.e. stainless steel), ensure the microstructure and details of the alloys are understood, especially when it comes to CTE effects. We were able to use a thicker bond line to compensate for the dimension changes.

General Lessons Learned

While lessons learned above were quite specific, there were also two key general lessons learned. First, ensure understanding of all the variations of performance of a system, especially when dealing with a complex system like an electrical system. This was learned when working with the motor controller. Second, while we do our best to understand our mechanisms through environmental testing, one really is not done learning the ins and outs of a mechanism until the mechanism is fully qualified, or likely even operational in orbit. While we are not in orbit yet, given what we continue to learn about this mechanism design, we expect to continue to glean lessons learned throughout orbit.

Conclusions

Despite the challenges, lessons learned (many of which may be obvious to the experienced designer), it is truly exciting to have KaPDA functioning as expected, and slated to launch in the next several months. It will be even more exciting to see what KaPDA does for small satellites, as it is a new capability which will dramatically increase satellite gain, whether it be radar instruments, or high data rate communications. The design has also been licensed to a company for commercialization, so beyond just changing capabilities for future NASA missions, KaPDA may very well be a ground-breaking technology for a much broader array of missions.

Acknowledgements

This research was carried out at the Jet Propulsion Laboratory, California Institute of Technology, under a contract with the National Aeronautics and Space Administration. This work was funded by JPL internal R&D and the RainCube Mission through the NASA ESTO INVEST program. The authors would like to thank the many individuals who assisted in the course of the project on design, fabrication, and advice including: Taryn Bailey, Brian Hirsch, Pedro Moreira, Jeff Harrell, Michael Johnson, Mark Balzer, Kim Aaron, Mehran Mobrem, Gus Forsberg, Don Lewis, Gerry Gaughen, Richard Rebele, Miguel Ramsey, Building 103 Techs, Hugo Rodriguez, Rodolfo Herrera, Robert Demerjian, Michelle Easter, Gary Wang, Josh Ravich, Ryan Sorensen, Natalie Lockwood-Barajas, and especially Brian Merrill of Spectrum Marine and Model Services (SMMS), who ensured all the parts came together in a near perfect assembly. A number of interns also helped with the antenna development over the years including Leah Ginsberg, David Hunter, Ted Steiner, and Savannah Velasco.

References

- [1] N. A. of S. Medicine Engineering, and, D. on E. and P. Sciences, S. S. Board, and C. on A. S. G. with CubeSats, *Achieving Science with CubeSats: Thinking Inside the Box*. National Academies Press, 2016.
- [2] J. Sauder, N. Chahat, M. Thomson, R. Hodges, E. Peral, and Y. Rahmat-Samii, "Ultra-Compact Ka-Band Parabolic Deployable Antenna for RADAR and Interplanetary CubeSats," *AIAAUSU Conf. Small Satell.*, Aug. 2015.

- [3] J. F. Sauder, N. Chahat, R. Hodges, E. Peral, Y. Rahmat-Samii, and M. Thomson, "Designing, Building, and Testing a Mesh Ka-band Parabolic Deployable Antenna (KaPDA) for CubeSats," in *54th AIAA Aerospace Sciences Meeting*, American Institute of Aeronautics and Astronautics.
- [4] N. Chahat, R. E. Hodges, J. Sauder, M. Thomson, E. Peral, and Y. Rahmat-Samii, "CubeSat Deployable Ka-Band Mesh Reflector Antenna Development for Earth Science Missions," *IEEE Trans. Antennas Propag.*, vol. 64, no. 6, pp. 2083–2093, Jun. 2016.
- [5] N. Chahat, J. Sauder, M. Thomson, R. Hodges, and Y. Rahmat-Samii, "CubeSat deployable Ka-band reflector antenna for Deep Space missions," in *2015 IEEE International Symposium on Antennas and Propagation USNC/URSI National Radio Science Meeting*, 2015, pp. 2185–2186.
- [6] M. Aherne, T. Barrett, L. Hoag, E. Teegarden, and R. Ramadas, "Aeneas -- Colony I Meets Three-Axis Pointing," *AIAAUSU Conf. Small Satell.*, Aug. 2011.
- [7] "UNFURLABLE SPACE REFLECTOR SOLUTIONS." Harris Corporation, 15-Feb-2016.

Design and Development of CubeSat Solar Array Deployment Mechanisms Using Shape Memory Alloys

Allen Guzik* and Othmane Benafan*

Abstract

The Advanced eLectrical Bus (ALBus) project is a technology demonstration mission of a 3U CubeSat with an advanced, digitally controlled electrical power system capability and the novel use of Shape Memory Alloy (SMA) technology for reliable solar array (SA) deployable mechanisms. The ALBus CubeSat deploys four SAs in addition to the body-mounted arrays on each side of the CubeSat. A goal of the mission is to utilize the SMAs being developed at the NASA Glenn Research Center to deploy these SAs. The use of SMAs allows for the ability to test and reset the flight deployment mechanism prior to flight, which reduces the risk of in orbit deployment failures common to CubeSats. As a result, an SMA-driven Retention and Release (R&R) mechanism and an SMA-driven hinge were designed, developed, and integrated for flight. This paper summarizes the development of these mechanisms, types and functionalities of the SMAs used, as well as the lessons learned throughout the process.

Introduction

CubeSats are a high-risk, usually secondary payload, mission. They conform to the CubeSat Design Specification [1] and come in standard "U" sizes. A 1U CubeSat is a spacecraft with dimensions of 10 cm^3 . The Advanced eLectrical Bus (ALBus) spacecraft is a 3U size CubeSat roughly measuring 10 cm^2 by 30 cm long. The main mission goal of ALBus is to act as a technology demonstrator with an advanced, digitally controlled electrical power system capable of distributing 100 W of power. Typically, CubeSats operate in the 5 to 20 W power range. A higher power distribution capability opens more opportunities for CubeSat mission payloads, experiments, and functions, including propulsion and advanced communication. ALBus is not capable of generating 100 W continuously, so it uses SAs to store electrical power in batteries until enough power has been stored to test distributing 100 W of electrical power. To reduce the amount of time to charge the batteries, additional deployable SAs were added to the design. This drove the second mission goal, which is to leverage the SMAs being developed at Glenn as a way to deploy the SAs.

Flying and operating CubeSats have been a risky endeavor with a 40% failure rate of university class CubeSats [2]. Of those failures, less than 10% can be attributed to the mechanisms, however, 33% fail for unknown reasons [3]. A way to improve on this failure rate is to increase the reliability of the deployment mechanisms. Common deployment methods consist of nichrome burn wires to burn through a strap or tether [4]. This can fail by the burn wire shorting out prior to burning through the release strap or the strap getting tangled upon deployment. Another technique comprises of breakable links made of plastic retaining bars that are heated and burned [5]. While the latter is advantageous in securing the hardware from vibration damages, both methods employ consumables and do not allow direct testing of the actual flight hardware since parts are destroyed during the deployment and new hardware is needed to reconfigure the spacecraft into the stowed configuration. The deployment mechanisms designed for the ALBus are an attempt to eliminate all deployment consumables (or even human factors like winding strap wire) to allow a reliable and resettable means to deploy structures on a CubeSat. In this work, SMAs are used to deploy SAs and allow them to be functioned and tested on the ground with the same hardware that will be used during the flight mission.

* NASA Glenn Research Center, Cleveland OH

SMAs have been used in various applications in the past, including in space. CubeSats are a great way to verify and increase the capabilities of state-of-the-art SMA technology. SMAs have many advantages that can be utilized by CubeSats. In addition to being lightweight with a small footprint, SMAs are not pyrotechnics, produce low shock, do not create debris, and can be designed to be resettable. As part of the ALBus CubeSat technology development, two SMA forms were used. First, novel thermally activated SMAs with higher transition temperatures (compared to commercially available counterparts) were used for the R&R mechanism. Second, novel mechanically-activated SMAs (superelastic alloys) were used as deployment springs to specifically deploy ALBus' SAs and transmit the electrical power from the arrays. Reference [6] discusses more details of SMA functional behavior and types.

This paper will discuss the design and development process of the ALBus CubeSat deployable SA R&R and hinge deployment mechanisms. This includes the mechanisms' final design and capabilities, details on the SMAs, requirements of the design, design evolution and reasons for the design changes, analysis methods used, and the final flight hardware assembly and testing activities.

Design Requirements

The design requirements for the mechanisms are divided up into three categories: CubeSat standards, requirements specific to the ALBus mission and design, and mechanism specific requirements. The CubeSat specific requirements come from the CubeSat design specification [1] and the CubeSat deployer interface control document [7]. These requirements provide several sizing constraints such as keep-in zones for exterior dimensions, mass, and center of gravity. Other constraints include restrictions on creating space debris and use of pyrotechnics. These specifications also provide guidance on design environments. For example, they require using the launch random vibration environment in GSFC-STD-7000A if environments from the launch service provider are unavailable or if the launch provider is unknown while designing the CubeSat.

The ALBus mission's needs, goals, and configuration drove several of the SA deployment mechanism's performance and design requirements. The ALBus design is configured to use four deployable SA panels with seven of the ultra-triple-junction type solar cells installed on a FR-4 Printed Circuit Board (PCB) substrate. These deployable SAs run the length of the 340-mm-long CubeSat and are to be deployed along one of the short 100-mm sides of the CubeSat. This deployment configuration was chosen since the ALBus does not have an attitude control and determination system. It is designed to utilize gravity gradient masses installed on the ends of the deployable SAs to eventually point the CubeSat radiator down toward Earth. The final deployment angle was determined to be 135° from the stowed configuration for optimal power generation. However, a power analysis has shown that a 90° deployment angle is sufficient to recharge the batteries with acceptable power generation degradation.

The underlying goal for the ALBus mission is to design improved and reliable SA deployment mechanisms to reduce mission failures. This drove the design goals for the mechanism to be resettable in order to test and retest the actual flight hardware prior to launch. Reliability also drove the design goal to release all four SAs with one mechanism to minimize failure points. The ALBus mission chose to use new SMAs being developed at the NASA Glenn Research Center over traditional deployment methods. Finally, as the mechanism designs matured the desire to pass the electrical power from the solar cells on the deployable arrays through the SMAs was added in an effort to save the mass of a wiring harness.

The final mechanism's design converged on a two-stage SMA actively driven pin-puller type mechanism used to retain the arrays during ascent and release them in orbit (R&R mechanism). Once released, a passively driven SMA hinge mechanism, one for each of the four arrays, deploys each array to the desired deployment angle. To complete the designs, several specialized requirements were added specific to the R&R and hinge to ensure the desired functionality. NASA's mechanism design and development requirements specification, NASA-STD-5017 revision A [8], was used as a design guide and drove several of the performance requirements on the force and torque margin, mechanism design, and material

selection. Table 1 provides a summary and more detail on some of the key requirements that drove and constrained the mechanism's design.

Table 1. Mechanisms Key Driving Requirements Summary

Category	Requirement Text
CubeSat	No space debris shall be created at any point in the mission.
CubeSat	Pyrotechnics shall not be permitted.
CubeSat	The 3U CubeSat shall be 100.0 ± 0.1 mm wide. (X and Y dimensions) and be 340.5 ± 0.3 mm tall. (Z dimensions)
CubeSat	The only CubeSat structure that can contact the deployer are 8.5 mm wide rails and nothing can cross them.
CubeSat	Components shall not exceed 10 mm normal to the surface of the 100 mm cube sides.
ALBus	ALBus mechanisms are to be designed to increase reliability; e.g. releasing all four deployable SAs simultaneously.
ALBus	The ALBus mechanisms are to be designed using SMAs.
ALBus	The ALBus mechanisms shall be resettable so the flight hardware can be tested prior to flight and without disassembly of the CubeSat.
ALBus	The ALBus mechanisms shall be designed to structurally retain the deployable SAs during all mission phases prior to being commanded to release.
R&R	Upon command receipt, and only when desired, the R&R shall release the deployable SAs.
R&R	The R&R shall be designed to accept and operate by electrical power provided by the ALBus electrical power system which is 6 volt limited and 3.0 amps maximum.
Hinge	Upon command and only when desired, the hinge shall deploy the deployable SAs to the deployed state and prevent any detrimental damage to the deployable SAs, any other CubeSat structure, or to mission operations.
Hinge	The hinge shall allow the deployable SAs to deploy to 90° - 135° from the stowed configuration.
Hinge	The hinge shall be designed to structurally support the deployable SAs during all mission phases.
Hinge	The hinge shall allow two separate paths to conduct power from the deployable SAs to the spacecraft.
Mechanism	The ALBus mechanisms are to use NASA-STD-5017 rev A as a guide to design the mechanisms.

Final Design

Figure 1 shows the overall architecture of the ALBus CubeSat which illustrates the mechanisms' location.

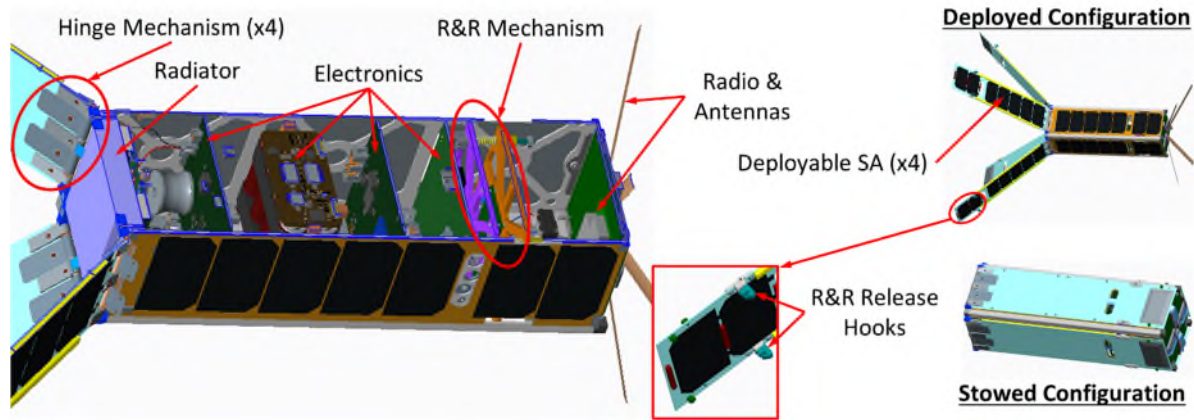


Figure 1. ALBus CubeSat Architecture

Design Summary of the R&R

The R&R final design consists of a two-stage activated mechanism. The first stage is a pin-puller device driven by an SMA linear actuator. The second stage is a hook and pin design that is released by a compression spring loaded plate riding on plain bearings. The operation and design of the mechanism is discussed in the following paragraphs. Figure 2 and Figure 3 illustrate details of the R&R component parts

that go along with the description. Table 2 summarizes the functional performance capability specifications and requirements. These specifications are driven to have positive margins per design guidance from NASA-STD-5017 [8].

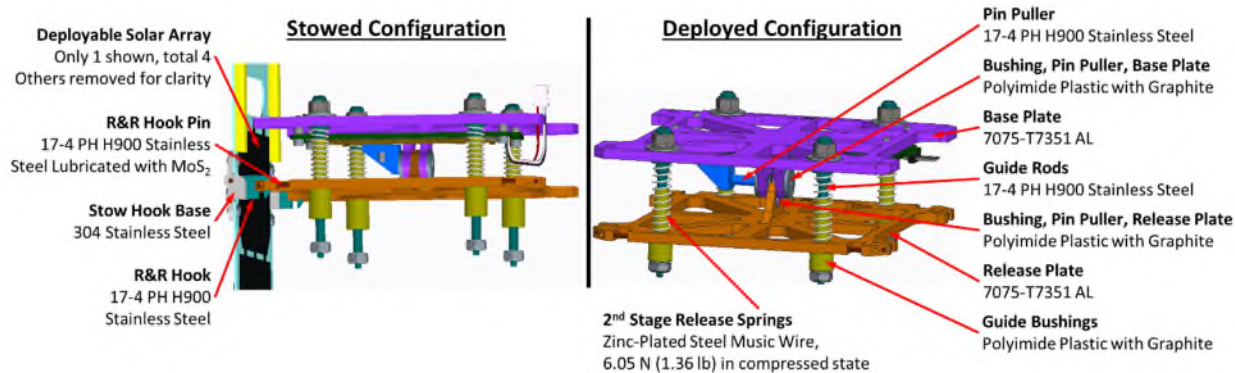


Figure 2. R&R Component Parts and Design

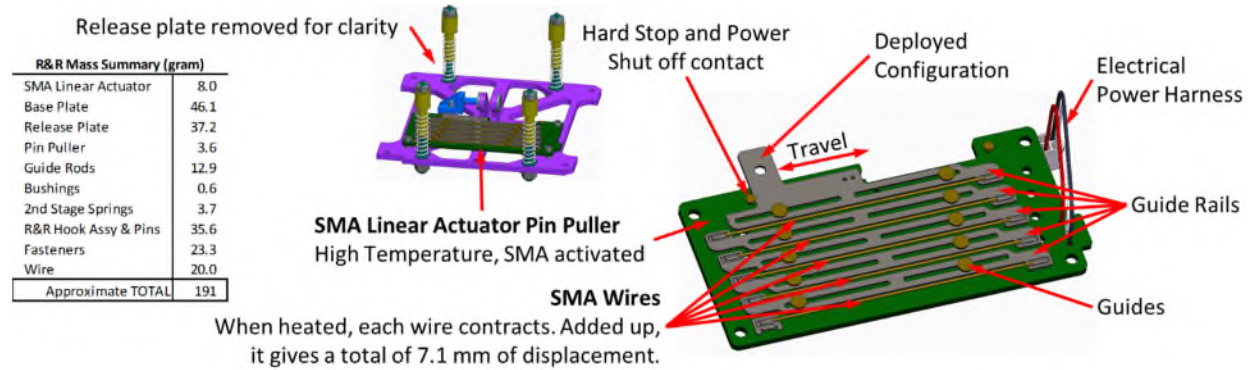


Figure 3. R&R Mass Estimate and SMA Linear Actuator Details

ALBus's initial temperature requirements for a safe SA deployment were set to be $>100^{\circ}\text{C}$, which exceeded any commercial alloy capability. Therefore, the linear actuator consists of an alloy with an atomic composition of Ni_{19.5}Ti_{50.5}Pd₂₅Pt₅ resulting in high transition temperatures above 100°C , work output exceeding 15 J/cm³ [9], and capability to process into small diameter wire. Thus, rods were drawn into a 0.508 mm diameter wire which was trained, cut into segments, and then installed on a custom linear actuator produced by MIGA Motor Company [10]. A total of five SMA wires are connected to guide rails. Once heated past the transition temperature using direct current (joule heating), each SMA wire contracts to pull its associated guide rail. The summation of the five SMA wires yield a cumulative displacement of 7.1 mm travel to pull the pin and release the second stage.

The pin-puller consists of a 17-4 PH H900 stainless steel pin put in a double-shear configuration between three bushings. The bushings are made of a polyimide plastic that has impregnated graphite.

Once the pin-puller releases the release plate, four compression springs move the plate, unlatching all four deployable SAs. The compression springs were installed concentrically over linear guide bushings. These bushings are made of the same polyimide plastic as the pin puller bushings. The guide bushings ride on guide rods that are made of 17-4 PH H900 stainless steel. The release plate unlatches the arrays using a hook and pin latch. There are two latches per SA panel for a total of eight hooks. Both the hooks and pins are made of 17-4 PH H900 stainless steel. A thin film of a MoS₂ lubricant is applied on the hooks and pin to mitigate any binding concerns from friction, although the joint is lightly loaded and lubrication is probably not needed.

Design Summary of the Hinge

The final design of the hinge consists of two aluminum hinge knuckles that pivot over a hinge pin, two superelastic SMAs, and a latch to keep the SA in the deployed state. The operation and design of the mechanism is discussed in this section. Figure 4 and Figure 5 illustrate details of the hinge component parts that accompany the description. Table 2 summarizes the functional performance capability specifications and requirements. These specifications are driven to have positive margins per design guidance from NASA-STD-5017 [8].

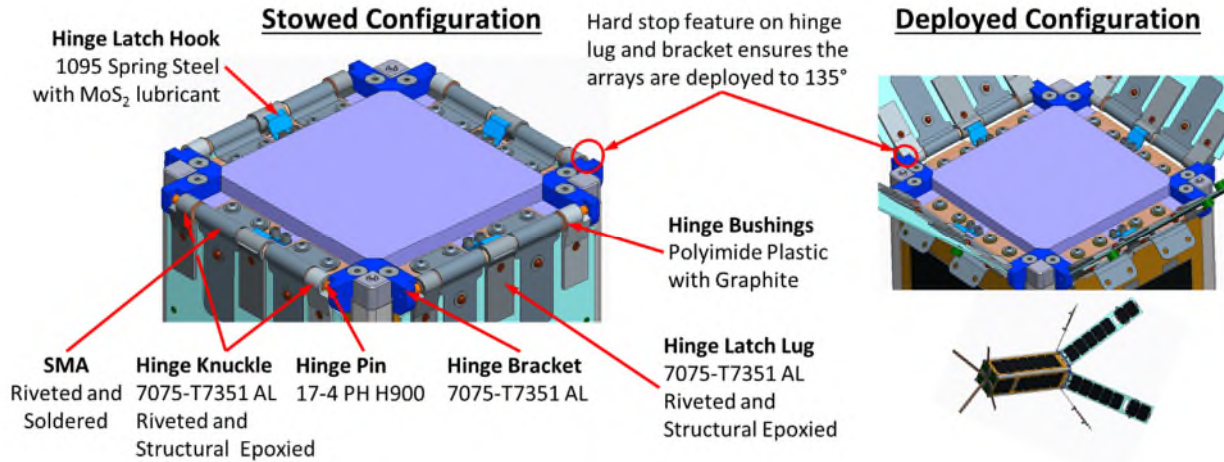


Figure 4. Hinge Component Parts and Design

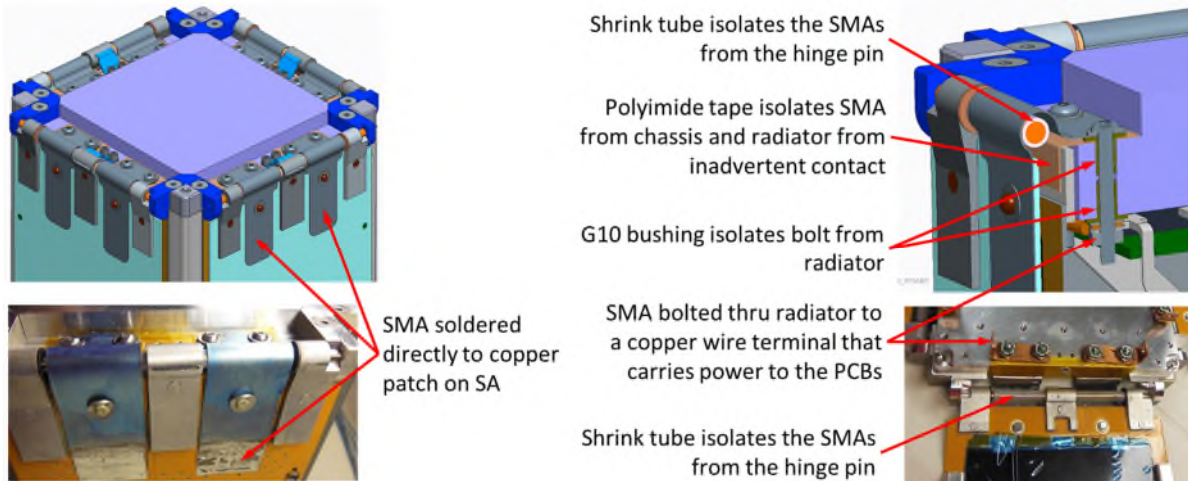


Figure 5. Hinge Component Electrical Interfaces and Design Details

After the R&R releases the SAs, they are free to rotate and each array is driven open by two preloaded superelastic SMAs per array. In this design, a Ni-rich $\text{Ni}_{50.7}\text{Ti}_{49.3}$ (atomic %) superelastic alloy was selected to serve a dual purpose of (*i*) a spring load to open the arrays and (*ii*) a current carrying conductor to transmit power from the SAs. The superelastic material was rolled into a 0.2-mm-thick sheet with a transition temperature (i.e., martensite start temperature) below 0°C. At room temperature, the sheets exhibited a superelastic plateau between 200 and 300 MPa, depending on the heat treatment used. This superelastic plateau denotes the effective start of the materials' stress-induced transformation from the stiffer phase known as austenite to the more compliant phase known as martensite. The superelastic sheets were machined into a flat-shape profile and then shape set to a specific U shape with a custom jig. After several

iterations, shape-setting parameters were selected to be 550°C for 2 minutes followed by water quenching, which yielded the best form in terms of stiffness and reversibility after deformation.

Table 2. R&R and Hinge Mechanism Performance/Functional Specifications and Requirements

Specification Description	Value	Requirement (with margin)
R&R Pin-Puller, Pull Force	13.34 N	≥ 12.19 N
R&R Pin-Puller Stroke Length	7.1 mm	≥ 6.14 mm
R&R 2 nd Stage Compression Spring, Spring Rate	0.701 N/mm	0.235 – 0.736 N/mm
R&R 2 nd Stage Compression Spring, Stowed Force	6.05 N	2.03 – 6.35 N
R&R 2 nd Stage Travel Distance	7.62 mm	≥ 5.87 mm
R&R Operating Power Rating	6 volt limited, 3.0 amps	6 volt limited, 3.0 amps max
R&R SMA Transition Temperature	150 to 160°C	> +50°C*
R&R Temperature Operation Range	-51 to +61°C	-40 to +50°C
R&R and Hinge Maximum Random Vibe Exposure**	14.1 gRMS, 3 minutes, 3 axes	10.0 gRMS, 1 minute, 3 axes
Hinge SMA Stowed Spring Torque (1 spring)	0.190 N•m	0.140 – 0.282 N•m
Hinge SMA Transition Temperature***	-20°C	> -40°C
Hinge Temperature Operating Range***	-20 to +61°C	-40 to +50°C
Other R&R Features	High temperature SMA, resettable, one mechanism releases all four SAs	
Other Hinge Features	Utilizes SMAs in a new application to advance the technology and SMAs transmit power from the SAs.	

* Initial R&R SMA transition temperatures were set above 100°C

** The development unit was exposed to 14.1 gRMS; the flight unit was only exposed to 10.0 gRMS

*** The hinge SMA transition temperature is known to not meet the low-temperature requirement and starts to soften around -20°C. This is handled through operational controls. When the CubeSat is in sunlight, the SMA springs will heat up beyond the transition temperature and the SAs will deploy.

From an operation standpoint, the U-shaped form is rotated by an amount of ~270° while in the stowed configuration and by ~135° while in the deployed configuration. When stowed, the material with the chosen thickness and form is designed to exist in the end of the superelastic plateau (i.e., martensitic phase) to provide enough force but no material damage. In the deployed state, the material partially unloads and exists in a multiphase region to continue providing some load in order to keep the arrays open, since the load-free state is the U shape.

In addition to the SMA springs, the hinge design consists of two lugs with bushings made out of the same polyimide plastic with graphite as used in the R&R. The lugs and bushings rotate around a precision ground, 17-4 PH H900 stainless steel hinge pin, constrained by aluminum hinge brackets on either end of the pin.

Upon deploying the arrays, a hard stop on the hinge brackets was designed to prevent the array from going beyond the required deployment angle, since the superelastic springs continue to apply a force. Once in the deployed state, a latch engages to act as a failsafe to keep the arrays in the deployed state should an unknown or unexpected environment cause the springs to become too cold and temporarily lose their spring stiffness. The design of the latch is a pin and detent type design. It converged on using a piece of spring steel lightly preloaded on a bare aluminum cylindrical surface. When the array rotates open, the latch falls into a slot locking the array in the deployed configuration. The latch to cylindrical surface has a thin film of a MoS₂ lubricant applied to ensure low friction and smooth deployment.

The hinge design also transfers the electrical power from the SAs to the power management system. This is done by conducting electricity through the superelastic springs. To ensure a good electrical path and strong structural stiffness accommodations, the superelastic springs were riveted and directly soldered to the SA panel and then attached to the radiator with screws. On the radiator end, the fasteners used to attach the superelastic springs also conduct the electricity to a copper lug. Wiring harnesses were soldered

directly to the copper lug, which takes the electrical power to the power management system. Isolating the various electrical paths from one another involved adding a shrink tube to the hinge pin, polyimide tape to various surfaces on the radiator and chassis (in case the superelastic springs inadvertently contact those surfaces), and G10 fiberglass laminate composite bushings around the fasteners used to attach the springs to the radiator.

Design Evolution, Development Issues, and Solutions

The following section discusses the design evolution, development issues, and solutions of each mechanism, starting with the R&R and followed by the hinge.

The mechanism's development started with proof of concepts tests. These involved building several early low-level hardware models to test out the design ideas and options. The R&R was subjected to several three-dimensional (3D) printed designs, which aided in choosing the design features to use and to discover issues with the concepts. The hinge also used 3D printed hardware to prove out the concepts. In particular, several of the latch concepts were tested quickly using 3D printed hardware. This proved to be advantageous since conventionally machined designs can be more expensive and time consuming.

When the designs were finally matured, an engineering design unit (EDU) of each mechanism was fabricated and tested to prove out the designs for flight. The EDU was built to be as flight-like as possible. The test program was conducted in the summer of 2016 and included subcomponent testing such as measuring performance parameters of the hinge SMA springs, R&R linear actuator pull force, and other data used to correlate to analysis. The subcomponents were then combined into a system and subjected to environmental testing. This included a random vibration test to 14.1 gRMS for 3 minutes in three axes and in extreme cold and hot environments with margin. The EDU functioned successfully before and after the vibration test and in the extreme thermal environments. This testing program was very successful. It proved out the designs and discovered issues that were corrected in the final build. Though the EDU and flight builds differed slightly, the EDU essentially acted as a qualification unit. After the EDU test campaign, a critical design review was held to present the final design that incorporated all of the changes discovered in the EDU tests.

R&R: Early Concepts

The final R&R in the ALBus design was the product of several iterations. Three main concepts were initially investigated. The first was a piston design using antagonistic SMA springs where one pulled and the other pushed to release the SAs when activated. This design never made it past the conceptual phase as it was determined the unrestrained condition of the SMA spring in one of the directions would mostly likely be detrimental under launch vibrations and possibly cause a premature deployment. The second concept involved a collet design and used an SMA to free up the collet fingers. A plastic 3D printed prototype was created and the design was moving toward development of a fully functional engineering unit. While this concept was very promising, the mass budget and forecasted development time stopped this concept from continuing. The mass of the entire CubeSat needs to be kept at or under 4 kg. A critical thermal issue demanded the addition of a radiator for the primary mission objective, which reduced the available mass for the R&R. At this point in the development of the mission, there was not enough time to redesign and reduce the mass. This led the design toward the third and final concept described in this paper.

The final R&R design was based on prior SMA work developed at Glenn and is an SMA linear actuator device that can be quickly procured and modified. Leveraging the second-stage loaded spring concept of the collet design and this SMA linear actuator, the SMA driven pin-puller design was created for the ALBus CubeSat. The moving pin frees up a secondary release plate used to constrain the deployable SAs through two hooks on each deployable array.

R&R: Development Issues and Solutions

The design of the R&R started by using the linear actuator in its originally designed configuration given our budgetary and time constraints. However, it became apparent that the linear actuator needed some modifications to meet our mission's application.

One of the most critical changes was the SMA material. Initial requirements listed a thermal environment that may have exceeded the activation temperature of commercially available SMAs. This would cause a premature activation and release of the SAs, which could cause the CubeSat to jam inside the deployer. Fortunately, an SMA wire with a higher phase transition temperature had already been developed by Glenn. This wire was incorporated into the design and alleviated the thermal concerns. However, this wire had never been tested or used in other flight applications and therefore, the ALBus mission was the first opportunity to use it.

Another change to the existing SMA linear actuator was the location of the pin-puller attachment point (output stage). The existing actuator caused the pin-puller to be off-center from the four guide rails. This was due to packaging the actuator in order to physically fit inside the CubeSat chassis. To install the linear actuator so the pin-puller would be centered, it would have to be offset so much that it would protrude outside of the walls of the chassis. The off-center pin-puller was clearly not ideal, however, that configuration was attempted nonetheless to identify potential issues and solutions. A plastic 3D-printed prototype was created and the concept worked. A metal prototype followed and was also shown to work, however, it was prone to occasional binding from the off-center pin-puller. Since the R&R is a mission-critical mechanism, this anomaly was unacceptable. The linear actuator was then modified to move the pin-puller attachment point to allow the actuator to be mounted in the R&R and align the pin-puller on center. This substantially reduced the observed binding, but did not remove it completely.

The R&R was still prone to binding occasionally when the release plate tilted. This led to the next change, which added guide bushings made out of a polyimide plastic. Prior to the bushings being added to the design, the thin 3.17-mm-thick aluminum release plate only had holes drilled in it so it could travel on steel guide rods. NASA-STD-5017 [8] provides guidance and recommends a length ratio of 2:1 for plain bearings that are used in this guide rod type configuration. For the ALBus, this is a physical impossibility as the bushing and resulting guide rails would become too long and take too much space inside the CubeSat. If this ratio cannot be met, as it is in this case, the specification recommends taking into account several potential binding-causing issues. It also suggests to perform an analysis based on report work by J.R. Schroeder [11]. This analysis was performed and a compromise between overall length of the guide rails and bushings to the physical packaging limitations of the CubeSat was made. As a result, the bushings were made as long as possible toward the base plate and extended toward the releasing direction. This change significantly reduced the observed binding, but did not prevent all of the binding occurrences.

The final change made to remove binding, also learned from the EDU, was to free up the guide rods. When the guide rods were fully installed by tightening the installation nut, the R&R was still prone to binding. When the nuts were loosened to allow the rails some freedom to move, the mechanisms released smoothly and consistently. Therefore, the final design allowed the guide rod to float. This was designed into the flight mechanism such that the guide rod diameter to the through hole in the base plate has a diametral clearance gap of 0.229 to 0.381 mm (0.009 to 0.015 in). When the installation nut was installed, it was preloaded onto a collar of the guide rod that extended past the base plate. As a result, the nut did not lock out the guide rod to the base plate, allowing each of the guide rods to float a small amount. All of these design modifications allowed the mechanism to consistently function during the development tests.

Hinge: Early Concepts

There was one previous concept for the hinge. This design consisted of solar cells on both sides of the SA, which complicated the assembly and design. This concept used one large blade-like hinge knuckle with smaller hinge brackets. However, three superelastic springs were needed to provide the power from both sides of the SA. The concept had solar cells installed onto PCBs that sandwiched the hinge and SMA springs. The difficulty with this design was getting the electrical power from the solar cells to the SMAs and

isolating those electrical paths from each other. A non-electrical conducting coating needed to be applied because this was a metallic blade hinge. Eventually, the requirement to have solar cells on both sides of the SA was deemed unnecessary and removed. This allowed the design to evolve into the final concept with reduced complexity.

Hinge: Development Issues and Solutions

From this initial concept, the hinge design still had several design, interface, and assembly issues to overcome. The design evolved to reduce the effects and risk of friction-causing issues. One was changing the large hinge knuckle in favor of two smaller knuckles at the corners in order to limit the contact area of the knuckle on the pin. The other change was to add a bushing made out of a polyimide plastic with impregnated graphite between the hinge knuckle and pin interface. This provides a low-friction interface on the rotating parts' surfaces without the need for grease or liquid lubricants.

Transmitting the electrical power through the SMAs and isolating them from each other required many design solutions. The SMA needed to be isolated over the steel hinge pin, chassis, and through the radiator. Isolating the hinge pin from the SMAs was solved by adding a polyimide tape layer covered by a heat shrink sleeve. The SMA was isolated from the radiator using G10 composite bushings, which isolated the terminal bolts from the metal radiator. These isolation solutions work in the stowed configuration. However, when deployed, the SMA bends and folds into a different shape that can contact the radiator and chassis in other areas, causing an electrical short. This was solved by adding the polyimide tape to the radiator and chassis in areas where the SMAs may make contact.

Designing the SMA to provide enough torque to open the array and transmit the electrical power required many considerations. The final shape of the SMA was driven by the required torque and the available room for installation onto the SA. The torque drove the width of the SMAs, however, that width was wider than the available footprint to install the SMAs to the PCB and keep them isolated. This was solved by maximizing the width of the SMA where it attaches to the radiator and over the hinge pin where the torque is generated. Then, the SMA's width narrows down at the installation location on the PCB. Some issues arose during mechanical tests. The SMAs were soldered to the PCB copper substrate and the torque generated by the SMA to open the array was enough to delaminate the copper layer from the rest of the PCB. This issue was solved by adding a rivet close to the edge of the PCB. However, installing the rivet caused the SMA and PCB to crack. This issue was solved by adding a washer to both sides of the rivet to spread out the load when driven. Lastly, the design decision on how to install the SMA to meet the SMAs' torque requirement was made. The initial SMA location was inboard under the hinge pins. This did not work because it prevented the array from fully deploying. The final configuration chosen was to install the SMAs outboard of the pin.

The hinge latch is provided as a backup to keep the SAs in the deployed configuration if the SMAs fail. The latch evolved from several different concepts, but was kept as a simple hook and detent latch. Overall, the latch worked well, although there were some special considerations performed during assembly for proper functionality. Initially, the latch had some issues staying latched. The hook would jump out of the detent when the array hit the hard stops and then rebound. Several mitigation methods were used to prevent this. Proper installation of the hook is key to ensure that it is preloaded with enough force. This is done by installing the hook in the deployed configuration. The latch design is a steel on aluminum surface. The loading is light enough that a thin film of a MoS₂ lubricant applied to the contacting rotating surfaces is enough to mitigate the friction concerns. However, the lubricant has to be limited to a thin film and cannot go onto the latching surfaces in the detent or the mating surface on the hook. If it does, the hook can slip out of the detent.

Analysis of Mechanisms

The analysis of these mechanisms was divided into three main areas: structural strength, mechanism tolerances (critical primarily to the thermal environments), and dynamic and kinematic analysis. The structural strength of the parts was primarily driven by the random vibration environment during ascent.

Loads from this environment were generated from a finite element random vibration model using Finite Element Modeling And Postprocessing (FEMAP) as the pre and post processor and MSC NASA Structural Analysis (NASTRAN) as the solver. These loads were applied to the various parts as appropriate to show positive margins using factors of safety of 2.0 on ultimate and 1.5 on yield strength. Overall, the stresses were low enough from the random vibration environment such that fatigue analysis was not necessary.

In both the R&R and hinge mechanisms, the thermal environment needed to be considered. Due to the coefficient of thermal expansion mismatches between parts, the mechanism may bind at the temperature extremes if enough dimensional tolerance is not accounted for in the design. The extreme hot and cold environment of 61°C to -51°C was evaluated on all of the moving parts. The analysis was also done by assuming the worst case tolerance stack that would result in the tightest fit at the installation temperature of 22°C. The analysis results showed the critical case is the cold environment and a gap of 7.6 µm (0.0003 in) between the hinge pin and the hinge bracket.

The critical analyses for these mechanisms, kinematic and dynamic analysis, were performed to ensure the mechanisms would have enough torque and force to release the arrays and deploy them at the appropriate angle. NASA-STD-5017 [8] was used as a guide to perform the analysis and calculate the margins.

The kinematics and dynamics of rotating the arrays to the deployed state via the preloaded SMAs formed the main analysis for the hinge mechanism. This analysis considered both design criteria of (i) sufficient torque to open the SA and (ii) minor impact force as to not damage the solar cells when the array deployed to the open configuration and contacted the hard stops. This was done by hand sketching free-body diagrams and developing the equations of motion. The free-body diagram listed the driving forces (the torque supplied by the SMA) and the resistive forces and torques (friction from the bushings to the hinge pin, friction from the latch hook, and the inertia of the SA that is needed to be deployed). The friction from the latch hook was difficult to quantify since it is a unique design and required building and testing hardware. Early attempts to approximate it did not align well with the test data. The bushing friction was easier to approximate since it is a cylinder on a pin and the manufacturer's suggested friction coefficients were used for estimating friction. The normal force on the bushings was conservative because it used the weight of the array from 1g of acceleration even though the deployment occurs in orbit. The inertia resistive torque was approximated by using the equation of motion, the known final deployment angle of 135°, and assuming a reasonable deployment time of 1.0 second (based on test observations). The equation of motion is a 1 degree of freedom rotation and derived using Eqs. 1-3. The torque supplied from the SMA was also difficult to approximate due to the hinge mechanism's unique springs. This also required building and testing the hardware. These values were then entered into the torque margin calculation from NASA-STD-5017 [8] with appropriate factors for whether it was an analysis or test value.

$$\text{Angular acceleration} \quad \alpha = \frac{T}{I} \quad (1)$$

$$\text{Angular velocity} \quad \omega = \omega_0 + \alpha t \quad (2)$$

$$\text{Angular displacement} \quad \theta = \omega_0 t + \frac{1}{2} \alpha t^2 \rightarrow \frac{1}{2} \frac{T}{I} t^2 \quad (3)$$

where: T = SA inertia resistive torque, I = SA mass moment of inertia, ω_0 = initial angular velocity is 0, t = time

The R&R required analysis of the mechanisms to ensure the two-stage concept would release the SAs. Starting with the first stage, the linear actuator, two aspects of the design were considered. These were the pin-puller activation force and the stroke margin. For the activation force, the linear actuator needed to pull the pin to disengage the release plate. To do this, the SMA linear actuator needed to overcome the pinching friction force that came from the 2nd stage compression springs. An analytical estimate was originally done based on the friction coefficient and geometry, however this proved to be inaccurate. Once the hardware

was built, the force to move the pin was measured directly. This measured force to move the pin and the available pull force from the SMA linear actuator, along with the appropriate safety factors, were used to calculate the force margin using NASA-STD-5017 [8] and ensure that it was positive. The other analysis evaluated the stroke margin of the linear actuator to ensure that it would move enough to clear the middle lug in the release plate and therefore release it. This was calculated using the geometry of the design, the total available stroke of the linear actuator of 7.1 mm, and assuming 10% extra for a positive margin as suggested by NASA-STD-5017 [8].

The 2nd stage mechanism's analysis evaluated the force margin of the compression springs, stroke margin of the release plate, and bearing analysis for linear-guided bearings. The force margin of the compression springs was calculated by adding up the resistive and friction forces and ensuring that the springs would overcome these forces, along with the appropriate safety factors. The resistive forces are from the eight deployable array hooks, friction between the guide pins, and other parasitic drag forces such as manufacturing misalignments, which were approximated. Additionally, to show the 2nd stage was failsafe, the margin for a one spring out case was calculated. For the stroke margin analysis, the release plate needs to clear the eight hooks used to hold the SAs in the stowed position. This analysis was done using the geometry of the hooks and ensuring that the release plate could move enough with at least 10% more distance than required. Finally, NASA-STD-5017 [8], gave guidance on how to analyze the four guide rails and plain bushings used in this mechanism to ensure that it would not bind and the stick-slip phenomena would not occur. The general rule of thumb is to assume a 2:1 ratio of allowable moment arm length to bearing length, which would cause the mechanism to become unrealistically long to fit in the CubeSat, so the bearing length was reduced. To ensure the design would not bind, an analysis was conducted using guidance from J.R. Schroeder [11], which essentially is a statics analysis of the design.

To aid in verifying that the mechanisms would deploy the SAs in orbit, an Automated Dynamic Analysis of Mechanical Systems (ADAMS) kinematic model was generated. The goal of the ADAMS model was to validate the design by showing all four SAs would deploy without adverse effects on the dynamics of the free-flying CubeSat. Moreover, the analysis was also used to evaluate some off-nominal pre-deployment rotations to see if there is a state when the arrays would not deploy or cause adverse effects on the dynamics of the free-flying CubeSat. This analysis also provided a way to support a test-like-you-fly exception, which is the inability to test the full deployment of all four SAs at the same time. The SMA hinge springs are designed to open the arrays in the freefall environment in orbit and the SMAs cannot open the arrays against Earth's gravity. Therefore, the fully assembled CubeSat's SAs are deployment tested with the array's gravity offloaded on its side, which results in only being able to test two SAs at one time. The ADAMS model was created to deploy all four arrays at the same time to learn about the full system's response and dynamics from a deployment in orbit. Additionally, the model was used to analyze other extreme initial conditions since it is unknown what state the CubeSat will be in before the deployment occurs. It could be tumbling and rotating, which would be impossible to test. Other off-nominal deployments were investigated, such as learning what would happen to the dynamics of the CubeSat if the arrays impact at different times or if one of the arrays became hung up then suddenly released. The ADAMS model was critical in observing the dynamics of a deployment from these various initial conditions.

The ADAMS analysis can retrieve other important data that can be difficult to generate from a ground test or analyze by hand such as deployment impact and latching forces. This information would aid in the structural design of subcomponents. An attempt was made to correlate impact load test data to the ADAMS model. However, the test data was significantly smaller than the ADAMS values. A very involved analysis and testing program is required to get the values to correlate better. This was deemed impractical and not necessary for this CubeSat project. However, it is important to be aware of the effort needed to capture these data for large projects.

The ADAMS model that was generated focused on the hinge mechanism and not the R&R since it can function completely on its own and against Earth's gravity. The model was useful early on in the development of the mechanism to give an idea of the required torque needed to deploy the arrays. However, many unknowns exist with analysis methods alone and it is pivotal to also build hardware to correlate to the

analysis model. The process for building the ADAMS model was the crawl, walk, run approach. A single-array model was generated first, which was correlated to single-array proof of concept tests. Data from those tests were used to adjust the ADAMS model so the observed test dynamics correlate to the model. This proved to be a very iterative process while the design matured. The key data that was correlated was the time from first motion to full deployment and the settling time for the deployed array to dampen out and stop moving. A complete model with four SAs was generated from the single-array model.

The analysis of the four-array model verified that the dynamics of the deployment in the microgravity environment should be successful and not detrimental to the dynamics of the CubeSat from either the nominal case, off-nominal cases, or any of the various initial conditions also analyzed. The various initial conditions analyzed included a no-rotating and free-floating case, moderate rotations (5, 20, 5 deg/s), high rotations (19, 80, 19 deg/s in the pitch, roll, and yaw directions respectively), and a hung-up array that impacted at a later time. These cases were sufficient for this CubeSat project, but for a more critical project, a full Monte Carlo analysis should be performed to capture more cases that may exist. An interesting result from the analysis was for the case when the CubeSat was tumbling or rotating; the deployment will somewhat reduce the rate of rotations while stabilizing the spacecraft.

Flight Assembly and Test

Building and testing the flight hardware started in February 2017. A number of unexpected issues arose during the assembly, which emphasized the need for schedule margin to work through those issues. Several of the hardware components required rework upon receipt from manufacturing. The R&R failed during subcomponent testing, primarily due to incorrectly-sizing the linear actuator and not fully understanding the friction forces in the pin-puller. This resulted in redesigning the R&R's 2nd stage compression springs and reducing their spring rate and stowed compression force. During the hinge assembly, one of the SMA springs fractured and had to be replaced. Then, during a critical time of final CubeSat integration with only a month left before the project was scheduled to be completed, multiple SMA hinge springs fractured and failed prematurely as seen in Figure 6. All of these issues did not occur during the EDU assembly and test.



Figure 6. SMA Hinge Spring Failed Flight Attachment

The failure of the SMA hinge springs during the final moment of integration proved to be a major issue and adversely impacted the schedule. From the failure investigation, it was determined that the failure occurred due to fatigue and over constraining the SMAs at the attachment point on the deployable SA panel. The EDU was cycled several times and this failure never occurred, making this failure even more unexpected. Further comparing the EDU and flight hardware, the issue was determined to be the SMA's attachment method to the panels. In the EDU version, there was a gradual bending slope in the SMA sheet where it attached to the deployable panel. In the flight version, a washer under a rivet head was added to prevent the process of driving the rivet from potentially cracking the SMA sheet, and the SMA was soldered more firmly past the rivet head toward the hinge pin. It was intended to solder the EDU hinges following the same procedure used in flight hardware. However, the EDU never adhered to the deployable panel near the rivet, and testing was conducted in that manner. This was corrected in the failed flight version by having a trained technician perform the soldering procedure, which was thought to have made the attachment better. The result actually caused the SMA to bend and crease at a very sharp corner when in the deployed

configuration as seen in Figure 6, which should be the lowest stress state. This was verified by attempting to perform 15 wear-in cycles on the flight design, which resulted in more SMA spring failures in early cycles.

The SMA hinge springs needed to be disassembled, redesigned, and replaced. The corrective action consisted of moving the solder attachment to cover the bottom half of the SMA hinge spring only and away from the rivet. The SMA was redesigned to remove a narrowed-down region that was no longer needed since the solder is only being applied at the very bottom edge. This increase in area was estimated to reduce the stress on the part by more than 20%. Finally, the washer under the rivet, which was still needed to prevent the rivet from potentially cracking the SMA, was bent upward to allow the SMA to have a smoother curve onto the PCB. These changes can be seen in Figure 7. New SMAs were then fabricated with the same processes that were conducted on the original batch such as torque testing each new spring. The new design was then installed onto the EDU and underwent a 4-times cycle life test (130 cycles) to gain confidence that the changes would correct the issue, which it passed. The redesign was then reinstalled on the flight hardware and underwent a 15 cycle wear-in test to ensure good workmanship and no other issues. Figure 7 shows the new SMA spring design and attachment method.

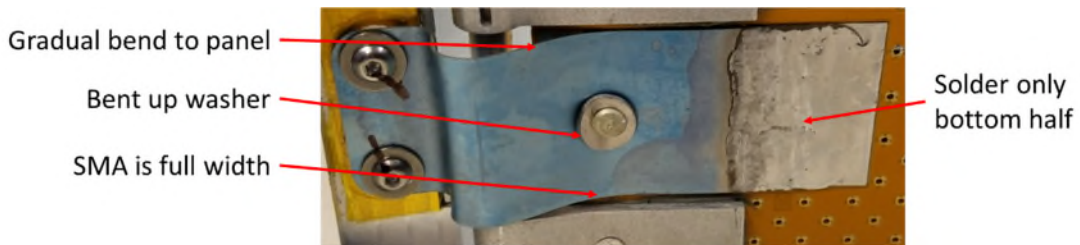


Figure 7. SMA Hinge Spring Flight Design Change, Attachment Corrective Action, and Repair

Once assembled, similar to the EDU testing, the flight subcomponents underwent functional and performance testing to ensure they were functioning correctly. Then, the units were integrated into the flight CubeSat assembly and underwent environmental testing. This included a random vibration test to 10 gRMS for 1 minute in three axes and a thermal/vacuum bake out. The CubeSat was functional before and after the vibration test and after the thermal/vacuum test. It was then stored for shipment to the launch service provider with a target launch date of April 2018. Images of the flight hardware are provided in Figure 8.

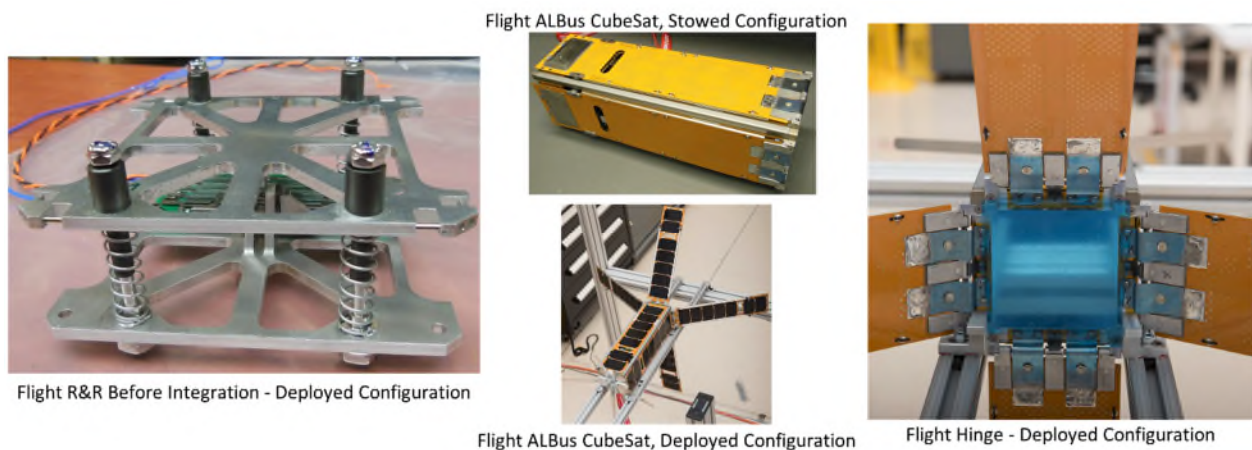


Figure 8. ALBus CubeSat R&R and Hinge Mechanisms Flight Hardware

Conclusion and Lessons Learned

The ALBus CubeSat mechanisms are an attempt to advance CubeSat technology by reducing mechanism risk from deployments of SAs. They also advance SMA technology by demonstrating the use of custom, unique, and high-temperature SMAs in the space environment. The project illustrates the potential of SMAs in CubeSat applications where space and weight are limited. This work is also a simplified example of the steps needed to develop a new design or technology from concept to final product and all of the common development challenges that occur along the way. Lessons learned include:

- Friction forces are difficult to quantify without validation from hardware tests.
- Sizing analyses such as loads, mechanisms, and kinematics should be done early on along with the design concepts even if firm inputs are not available. Do not focus only on the CAD design aspects.
- Building an EDU or 3D printing hardware to test is key in any new development to quickly uncover assembly issues and evaluate actual functional performance. Do not only rely on analysis only.
- Even though it can be easy to create dynamic and kinematic models for mechanisms, it may be very difficult to get meaningful correlations with the actual test data.
- SMA applications should be evaluated from a system level. For example, although the hinge mechanism uses simple SMA sheets, the integration process which involved bolting, riveting and soldering proved to be very difficult.

Acknowledgment

This CubeSat project was internally funded at NASA GRC (K.J. Oriti, project manager). The authors thank Y.H. Hau, C. Redding, and L.H. Yoon for design help. The authors thank P.B. Abel, C. DellaCorte, T.J. Halsmer, T.L. Kapucinski, D.R. Ludwiczak, R.J. Pawlik, and T.J. Ubienski for technical help. Othmane Benafan thanks J. Brown from Dynalloy and M. Gummin from Miga Motor Co. for SMA actuator help.

References

1. CubeSat Design Specification, Revision 13, California Polytechnic State University (February 2014).
2. Swartwout, Michael and Jayne, Clay. "University-Class Spacecraft by the Numbers: Success, Failure, Debris. (But Mostly Success.)" 30th Annual AIAA/USU Conference on Small Satellites (August 2016).
3. Langer, Martin and Bouwmeester, Jasper. "Reliability of CubeSats – Statistical Data, Developers' Beliefs and the Way Forward." 30th Annual AIAA/USU Conference on Small Satellites (August 2016).
4. Adam Thurn, Steve Huynh, Steve Koss, Paul Oppenheimer, Sam Butcher, Jordan Schlater, and Peter Hagan. "A Nichrome Burn Wire Release Mechanism for CubeSats." Proceedings of the 41st Aerospace Mechanisms Symposium, Jet Propulsion Laboratory, (May 2012).
5. Kepko, Larry et al. "Dellingr: NASA Goddard Flight Center's First 6U Spacecraft." 31st Annual AIAA/USU Conference on Small Satellites, Logan, UT, (Aug. 2017).
6. Benafan, Othmane. "Deformation and Phase Transformation Processes in Polycrystalline NiTi and NiTiHf High Temperature Shape Memory Alloys." NASA/TM-2012-217741, (2012).
7. Poly Picosatellite Orbital Deployer Mk III Interface Control Document, California Polytechnic State University (August 2007).
8. Design and Development Requirements for Mechanisms, Revision A, National Aeronautics and Space Administration (July 2015).
9. Bigelow, Glen, et al. "Development and Characterization of Improved NiTiPd High-Temperature Shape-Memory Alloys By Solid-solution Strengthening and Thermomechanical Processing." Proceedings of the International Conference on Shape Memory and Superelastic Technologies, Pacific Grove, California, (May 2006).
10. Miga Motor Company. "Miniature High Force, Long Stroke Linear Shape Memory Alloy Actuators." SBIR Phase-II Final report, (December 31, 2009).
11. Schroeder, Jonathan R. "Demystifying the 2:1 Ratio and the Stick-Slip Phenomenon: A Technical Whitepaper Explaining the Theory Behind the Binding Ratio and How It Relates to Stick-Slip." PBC Linear, (May 2010).

Lessons Learned in the Flight Qualification of the S-NPP and NOAA-20 Solar Array Mechanisms

Daniel Helfrich * and Adam Sexton **

Abstract

Deployable solar arrays are the energy source used on almost all Earth orbiting spacecraft and their release and deployment are mission-critical; rigorously testing them on the ground is both essential and quite difficult. The 8-meter-long deployable arrays flown on two sequential NASA weather satellites were each comprised of three rigid panels over 2.5 meters wide and almost 2 meters tall. These large panels were deployed by hinges comprised of stacked constant-force springs and eddy current dampers and were restrained through launch by a set of four releasable hold-downs using shape memory alloy release devices. The ground qualification testing of such unwieldy deployable solar arrays, whose design was optimized for orbital operations, proved to be quite challenging and provides numerous lessons learned. A paperwork review and follow-up inspection after hardware storage determined that there were negative torque margins and missing lubricant; this paper will explain how these unexpected issues were overcome. This paper will also provide details on how the hinge subassemblies, the fully-assembled array, and mechanical ground support equipment were subsequently improved and qualified for a follow-on flight with considerably less difficulty. These two solar arrays built by Ball Aerospace Corp. for the Suomi National Polar Partnership (S-NPP) satellite and the Joint Polar Satellite System (JPSS-1) satellite (now NOAA-20) were both successfully deployed on-orbit and are performing well.

Introduction

One of the first key events on larger spacecraft is the mission-critical deployment of the solar array, providing electrical power to sustain the mission for its duration. Prior Ball Aerospace satellites used smaller solar arrays that could stow around the body of the satellite structure. Embarking on a new design effort required the design and qualification of new solar array mechanisms, composite panels to support solar cells (substrates), and the ground test equipment. During the S-NPP lifecycle, the new mechanisms encountered design and test issues which included excessively stacked constant-torque springs, incorrectly processed parts, variable resistive torque profile through the range of motion of the hinge, unplanned resistive torques, inadequate harness characterization, inability to complete subsystem-level vibration testing, and issues with subsystem-level deployments. Design flaws identified from the S-NPP program were addressed during the JPSS-1 program and provided for much smoother delivery of mechanisms to the subsystem assembly, however lingering issues with the gravity-negation deployment system design and usage in different configurations provided some new challenges to overcome.

Sources of Driving Mechanisms Requirements

The solar array for S-NPP was required to be compliant with MIL-A-83577B, “Moving Mechanical Assemblies for Space Launch Vehicles (MMA),” and with GSFC-STD-7000, the “GEVS” standard, an acronym for Goddard Environmental Verification Standard. Both of these require margins on the driving torques to assure robust mechanism performance. GEVS mandates the use of factors of safety on the sources of drag torque in completing the analysis. When JPSS-1 began, the standard known as the “Gold Rules,” GSFC-STD-1000, was also implemented, driving the project towards more rigorous solar array

* NASA Goddard Space Flight Center, Greenbelt, MD

** Ball Aerospace Corporation, Boulder, CO

testing. Because of the extreme difficulty of implementing full solar array tests in compliance with the Gold Rules, most large solar array testing has to be scaled back via a waiver—true of these two arrays as well.

S-NPP Solar Array Development

Figure 1 depicts the S-NPP and JPSS-1 satellites with their highly similar solar arrays deployed, showing their zenith-facing and Earth-facing sides, respectively. Three solar panels are tied together by two inter-panel hinge (IPH) lines consisting of a passive and powered hinge and a main deployment hinge (MDH) at the interface between the inner panel and the rotational drive assembly (RDA), which rotates the entire array 360 degrees, to track the sun throughout each orbit. Each of the powered hinge lines are driven open one way by a constant-torque spring and rate controlled with eddy current dampers.

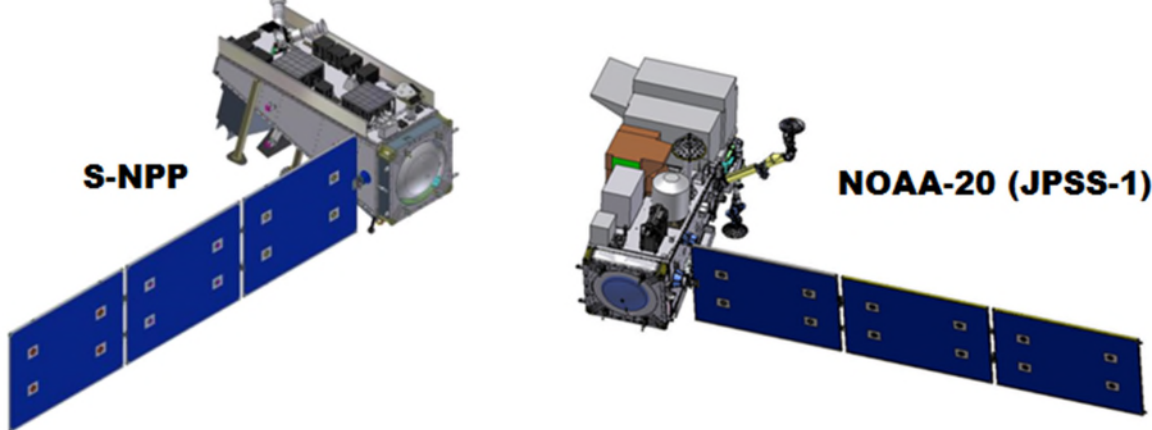


Figure 1. S-NPP and JPSS-1 Satellites (fully deployed)

Hinge Torque Margin Troubles

The solar array for S-NPP was designed to be compliant with the MMA requirements in the beginning of the program showing large torque ratios, but as the program reached the testing phase and the use of the GEVS torque margin analysis was followed, torque margins dropped. There were multiple issues that eventually drove torque margins negative which are explained below. Early in the design phase, the torque margins were required to be greater than zero using phased factors of safety applied to the sum of known torques (ΣT_K) and unknown torques (ΣT_U) according to the following formula:

$$\text{Torque Margin} = \left[\frac{\text{Torque Available}}{((FS_K \cdot \Sigma T_K) + FS_U \cdot \Sigma T_U)} \right] - 1 \text{ must be } > 0.0$$

Table 1. GEVS Factors of Safety through program life

Program Phase	Known Torque Factor of Safety (FS _K)	Variable Torque Factor of Safety (FS _V)
Preliminary Design Review	2.00	4.0
Critical Design Review	1.5	3.0
Acceptance/Qualification Test	1.25	3.0

Typical known resistive torque are things like inertia, or magnetic coulomb friction and unknown resistive torques are things like friction within the mechanism or the resistive torque of a harness.

Shown in column 2 of Table 2, the initial revision of the torque margin analysis, in 2003, was determined using analytical values for resistive torques and used the Critical Design Review (CDR) factors of safety from Table 1. (Take note that IPH1 is the hinge line closest to the spacecraft body.) Revision A of the analysis was an update based on initial testing of the hinges and the supporting harness as well as

measured values for damper resistive torques. The harness resistive torque changed from an anticipated value of 0.06 N-m (0.5 in-lb) to a measured value of 0.36 N-m (3.2 in-lb) for the IPH, and the MDH harness resistive torque changed from an anticipated value of 0.23 N-m (2 in-lb) to a measured value of 0.17 N-m (1.5 in-lb). Revision B resulted from a NASA project request to analyze the margin using a mix of factors of safety. Revision C of the analysis addressed a reduction in the available torque of the system (which was reduced) and another (and final) change in the factors of safety: the IPH and the MDH margins were both determined using Acceptance/Qualification values from Table 3. Available torque was measured in testing in 2004 and 2005 with a torque wrench which did not provide an accurate torque versus angle measurement, and minimum and maximum available torques were not available either.

Table 2. Changes in Margins during S-NPP

Hinge Type	Rev -	Rev A	Rev B	Rev C	Pre Spacecraft Integration	Pre-Ship Torque Margin	Pre-Ship Torque Ratio
IPH1	0.695	0.791	0.361	0.279	0.067	-0.016	1.58
IPH2	0.695	0.791	0.361	0.279	0.067	0.06	1.94
MDH	0.306	0.780	0.439	0.780	0.09	-0.22	1.48
IPH Torque – known N-m (in-lb)	0.73 (6.50)	0.65 (5.76)	0.65 (5.76)	0.65 (5.76)	0.73 (6.42)	4.98 (IPH 1) 5.55 (IPH 2)	
IPH Torque – variable N-m (in-lb)	0.61 (5.41)	1.28 (11.32)	1.28 (11.32)	1.28 (11.32)	1.20 (10.65)	15.25 (IPH 1) 10.50 (IPH 2)	
IPH available torque N-m (in-lb)	4.97 (44)	6.33 (56)	6.33 (56)	4.52 (40)	3.73 (33)	31.9 (IPH 1) 31.1 (IPH 2)	
MDH Torque – known N-m (in-lb)	1.39 (12.33)	1.28 (11.37)	1.28 (11.37)	1.28 (11.37)	0.89 (7.87)	7.85	
MDH Torque – variable N-m (in-lb)	0.86 (7.62)	1.48 (13.1)	1.48 (13.1)	1.48 (13.1)	1.88 (16.6)	33.1	
MDH Available torque (in-lb)	6.10 (54)	8.70 (77)	8.70 (77)	8.70 (77)	5.54 (49)	60.5	
FS known	1.5	1.5	1.25	1.5	1.5	1.5	
FS unknown	3.0	3.0/2.0	3.0	2.0	2.0	2.0	

Table 3. Updated Factor of Safety Values

Program Phase	Known Torque Factor of Safety (FS_K)	Variable Torque Factor of Safety (FS_V)
Preliminary Design Review	2.00	4.0
Critical Design Review	1.5	3.0
Acceptance/Qualification Test	1.5	2.0

In 2009, after hardware storage, concerns were raised about the variability of output torques in the hinges and it was determined that better characterization of the hinge lines was required. IPH testing was carried out to measure the output torque across the full range of motion in both directions and the available torque dropped from previously measured values thanks to better measurement technique. It also found that the resistive torque from the pawl was variable due to the cam shape of the hinge. The MDH was also re-characterized and again the minimum torque measured during the range of motion resulted in a significant drop in the torque margin at spacecraft pre-integration.

To remain consistent with prior NASA Goddard practice, torque resistances were updated using the more conservative “Zero-Neutral” approach for characterization of the harnesses, wherein the net resistance is the sum of the worst case deploying torque at beginning of rotation plus the worst-case stowing torque at the end of rotation. The use of non-flight harness in tests also arose as an issue because of the natural variability of wire geometry within their respective harnesses. Without photographic or other proof that the original test harnesses were essentially the same, re-testing of freshly built flight-like harnesses was mandated. This testing measured the actual harness route of the RDA and compared it to the test harness that was built. The results of this testing showed that the test harness matched the behavior of the flight harness. The “Zero-Neutral” approach changed the resistive torque of this harness from a resistive torque value of 0.17 N-m (1.5 in-lb) used from the harness testing done in 2004 to 2.26 N-m (20 in-lb). The IPH1 hinge line harness resistance values were changed from 0.23 N-m (2.0 in-lb) to 0.76 N-m (6.7 in-lb), and the IPH2 hinge line values were updated to 0.37 N-m (3.3 in-lb). The changes in these harness values and applying the required factors of safety drove the torque margins to negative values reported in Table 2.

During the 2009 investigation on the characterization of the torque output of the hinges it was found that the constant-torque springs were developing an unintended gap, shown in the right side of Figure 2. The gap indicates excessive frictional loss in the spring stack. A wet lubricant, Braycote 601VB, was applied to the both the roller and the spring stack to reduce friction and torque resistance. Additionally, the roller shaft that should have been dry lubricated was found to be unprocessed, so a grease plate mixture of Braycote 601 VB and 30% molybdenum disulfide was applied to it. Despite the team’s best efforts, margins were still negative, and it was too late to redesign, requiring the generation and processing of a waiver. In the waiver, since the torque ratio was higher than 1.0, indicating there was driving torque above the minimum, the negative margins were deemed acceptable based on the extensive and recent testing. This waiver was presented to NASA in mid-August 2011 and the array was successfully integrated 2 days after the waiver was approved, during final pre-shipment preparations.

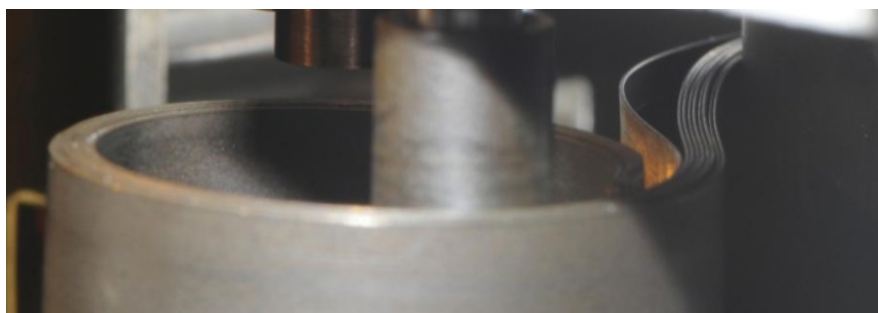


Figure 2. Gapping in the Leaf Spring of the Main Deployment Hinge

Testing the Solar Array

The testing flow for the components and assemblies in the S-NPP solar array was rigorous, starting at component-level testing for mechanisms, release mechanisms, panel substrates and the solar cells prior to and after attachment to the substrate. After these elements were assembled, the entire subassembly went through pre-environmental testing, environmental testing, and then post-environmental testing. Pre-environmental testing included deployment testing, electrical testing, and Large Area Pulsed Solar Simulator (LAPSS) testing. Environmental testing consisted of vibration testing and thermal vacuum testing after which the pre-environmental testing sequence was repeated.

Figure 3 shows the S-NPP solar array when it was tested at the system level while attached to the satellite and the arrangement of the gravity-negation ground support equipment (GSE)—also used for array testing when not attached to the satellite. For hardware safety and GSE simplicity, all of the full deployment tests of the S-NPP solar array were conducted on a separate test stand with the array removed from the RDA. This subsystem-level deployment testing was a challenge throughout the S-NPP life cycle. The deployment

GSE consisted of a number of thick honeycomb panels that were attached to each other to provide a surface that the solar array could be deployed on through the use of air bearings. This configuration presented a number of challenges as at each panel joint there often arose a discontinuity that resulted in the air bearing “dropping out” so that the solar array deployment would stop. A number of fixes were attempted to close out this gap and prevent the array from stopping during deployment. The final solution used a continuous, smooth, and flexible roofing material that was laid out over the top of the deployment fixture. This roofing material was a 1.52-mm (0.060-in) thick polyolefin membrane and the resulting smooth table surface is shown in Figure 4.

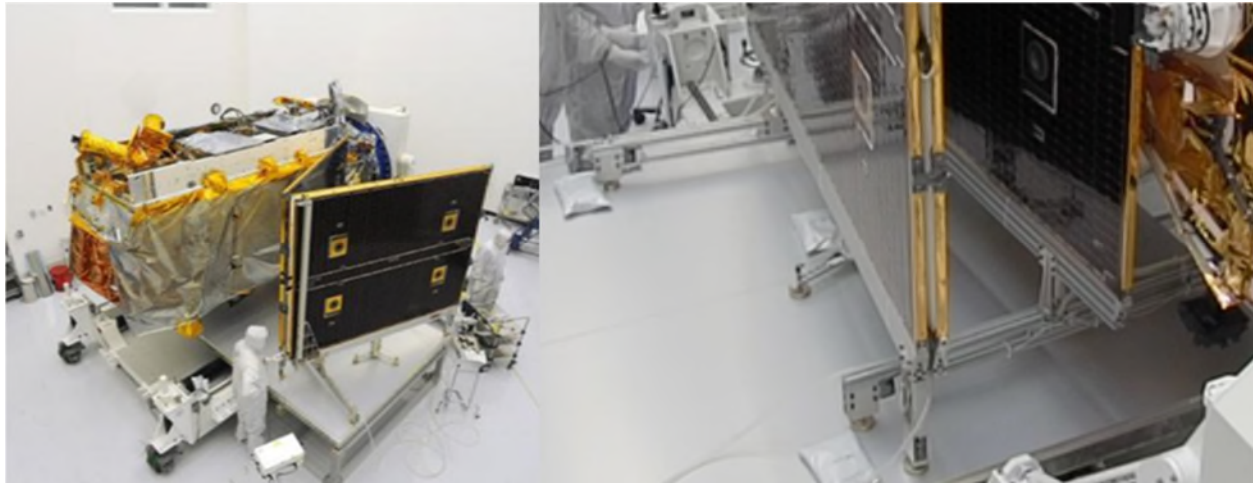


Figure 3. First Motion “Pop and Catch” Testing (Overview and GSE Closeup)



Figure 4. Subsystem Deployment Testing with Polyolefin Membrane Topping the Raised Deployment Floor

JPSS-1 Solar Array Development

Ball Aerospace was awarded JPSS-1 as a follow on to S-NPP in September 2010. The intention for JPSS-1 was for it to be a nearly exact copy, or “clone” of S-NPP. However, one of the differences that directly impacted the solar array design and accommodation was the inclusion of two TDRSS antennas, one nadir pointing and the other zenith pointing. Figure 5 shows where the nadir pointing ground antenna was mounted, where it needed to be stowed between the bus and the solar array. This forced the solar array to be translated 10 cm (4 in) farther from the bus panel than before. This accommodation was made by incorporating standoff brackets under the four RRS (Retention and Release Subsystem) brackets and under the RDA. JPSS-1 took advantage of new cell technology and transitioned to a new type, the “XTJ,” which increased current so that additional wires were required to cross each inner panel hinge line and the main deployment hinge line. Also, on JPSS-1, the Gold Rules were tailored in the mission specific requirements and flowed down to engineering through an Environmental Design and Testing Specification.

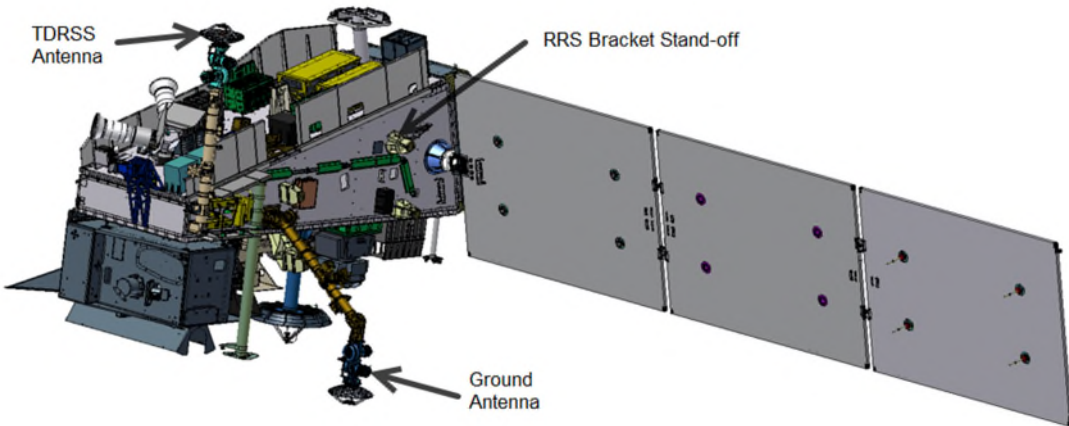


Figure 5. JPSS-1 Observatory (Deployed Configuration)

Hinge Design Updates

The issues raised during the S-NPP torque margin investigation were addressed with design updates for JPSS-1. One significant update addressed a “rule of thumb” of the constant-torque spring vendor to limit the number of springs in a stack to 3. The width and thickness of the springs were made larger to increase their torque and reduce the number needed to meet torque margin requirements. The hinges went through a test program, discussed below, that characterized the drag torques that had to be overcome and satisfy the torque margin requirements. JPSS-1 had an increase of 32 wires crossing the MDH hinge line and 7 additional wires crossing each IPH hinge line. The number of springs was determined based on the drag torque measurements. Then these springs were installed on the hinge and tested over the full range of motion.

Referring to Figure 6, the output drum was increased in diameter and arc length to accommodate the larger constant-torque spring. Two additional fasteners were added for load carrying capability and the ability to add a piece of Mechanical Ground Support Equipment (MGSE) that would make manual rotation of the hinge easier and to allow instrumented torque measurements. The change in the spring design required more spacing between the output drum and take up roller. The take up roller diameter was increased to reduce its deflection. An additional Vespel washer was placed between the end of the roller sleeve and the washer on the end to minimize friction between the roller sleeve and the CRES washer. The MDH axles were changed from the S-NPP design by eliminating cotter pins from the central area of the MDH where the RDA harness routes to the connector bracket on the inner panel. This minimized the extent of sharp edges exposed to the harness. The pawl, not shown, was modified to have a spherical surface that would engage the bottom of the cam surface at the end of range of motion and would provide a point contact during lockout.

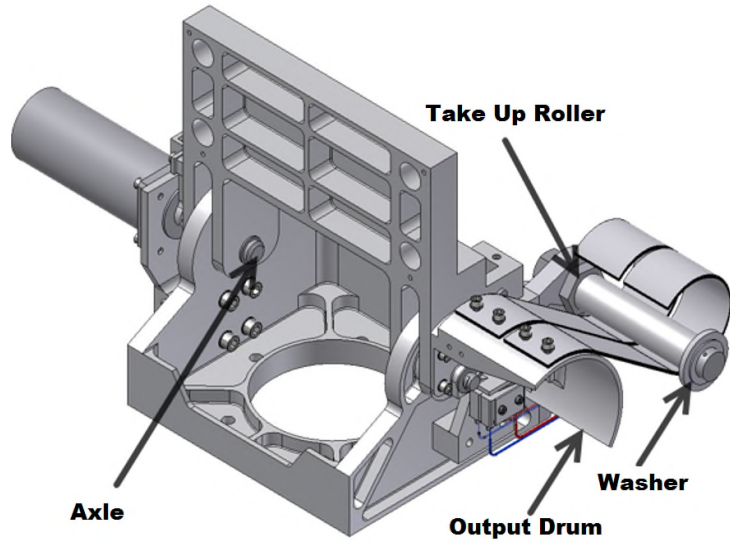


Figure 6. MDH in Deployed Orientation

This IPH hinge design shown in Figure 7 also went through similar evolutions as the MDH. The output drum was increased in size to accommodate the larger constant-torque spring. As with the MDH the take up roller was increased in diameter to minimize the deflection and accommodate the stronger spring sized for JPSS-1. The biggest change for the IPH design was the change in the design of the cam profile. The right side of Figure 7 shows the change from S-NPP, in blue, to JPSS-1 shown in yellow.

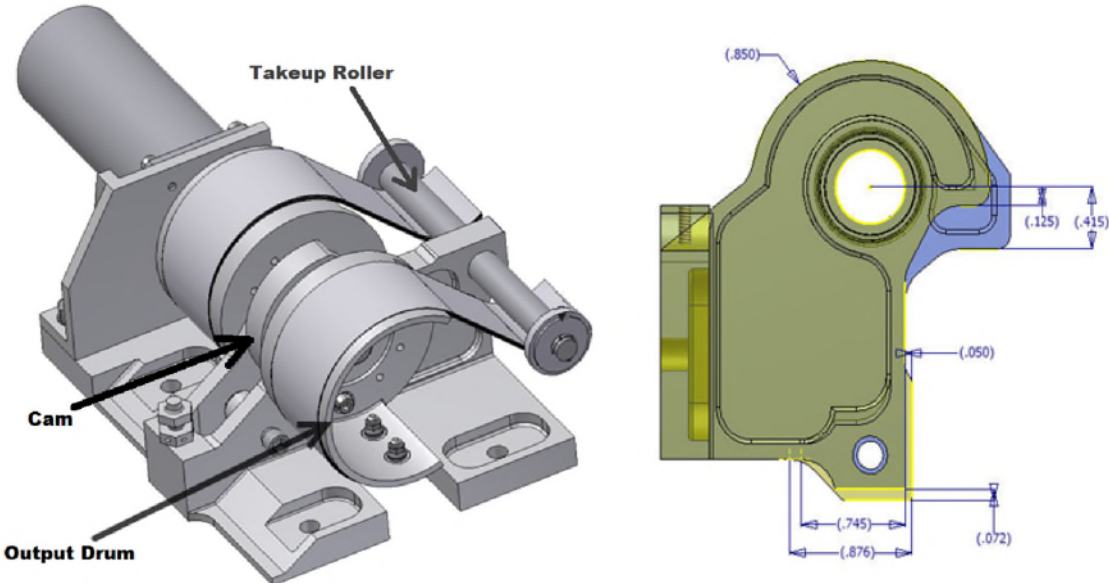


Figure 7. Powered IPH Shown in Stowed Position and Cam Profile Change (JPSS-1 changes in gold; dimensions in inches)

Figure 8 shows how the S-NPP cam profile produced a varying drag due to changes in the compression of the pawl spring across the range of motion. The modification to the cam profile for JPSS-1 achieved a constant resistive torque value, making it consistent with the non-varying profile for the MDH.

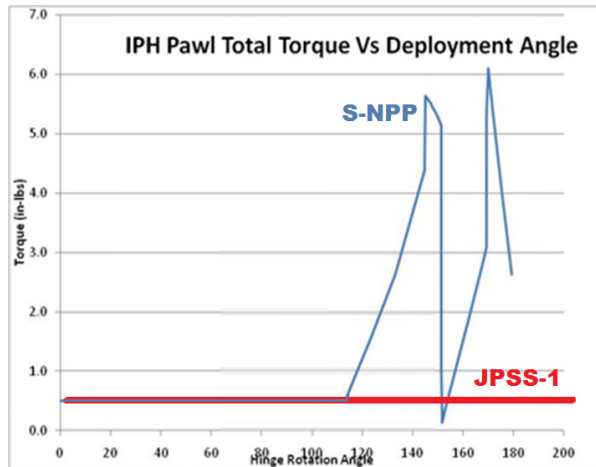


Figure 8. S-NPP Variation in Pawl Drag Torque Over Range of Motion

Hinge Testing

The JPSS-1 MDH and IPH hinge designs were both characterized for sources of drag torque in a much more consistent and repeatable method than S-NPP. Figure 9 shows the test set up used to characterize the MDH hinge. This apparatus consists of a drive motor in-line with a torque sensor and the unit under test. This test drove the hinge in both directions and had the pawls riding on the surface in both directions, but the apparatus did not go through the full range of motion to prevent the pawls from locking out. Figure 9 also shows an example data plot for the MDH hinge resistive torque test. In comparison, S-NPP characterized drag torque manually, with a torque wrench which was not as repeatable nor as controllable over the range of travel.

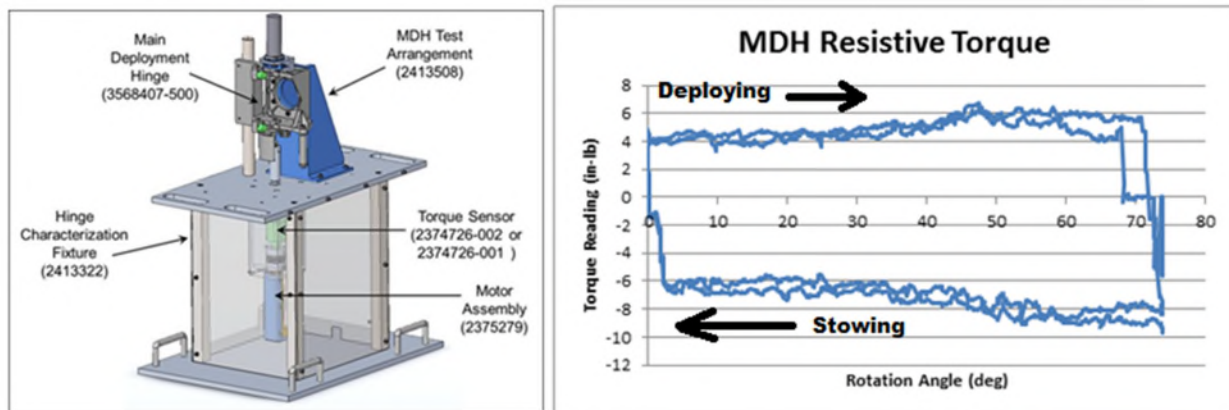


Figure 9. MDH Drag Torque Testing Apparatus and Results

In parallel, the harness resistive torque was characterized using a similar apparatus, shown in Figure 10. This apparatus allowed the harness to be articulated over the full 90 degrees in both the deploying and stowing direction to allow the peak resistive torque to be measured. Measurements are made at ambient, hot, and cold extremes. First the apparatus itself was cycled over the thermal environment and driven across the range of motion to characterize the effects of the apparatus and then testing was repeated after the harness was installed.

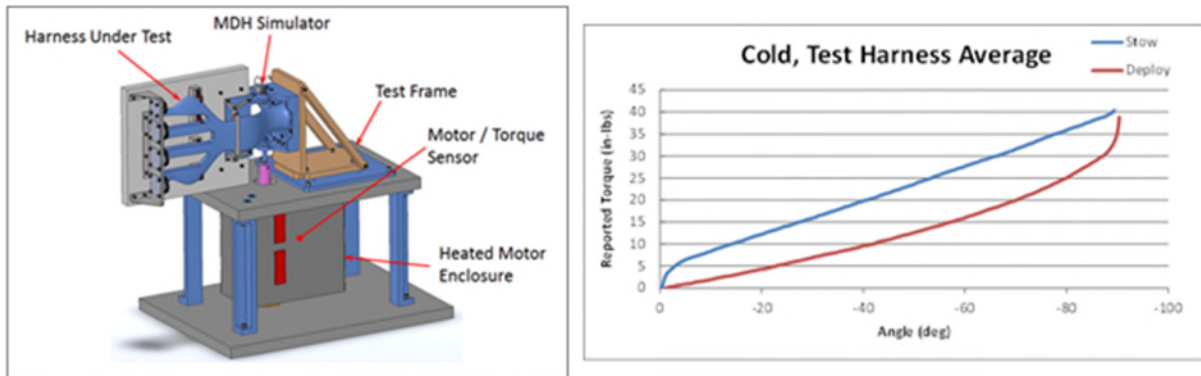


Figure 10 Harness Testing Apparatus and Results

A typical data plot on the right side of Figure 10 shows the reduced data, accounting for the parasitic effects of the apparatus and the resulting resistive torque of the harness over the range of motion. These results allowed engineering to determine the number springs that were required to meet the torque margin requirements. Once the springs were installed onto the mechanism, it was again attached to the apparatus used to characterize the drag torque of the hinge to measure the motion of the hinge and to directly measure the output torque of the hinge and validate the torque margin analysis.

Figure 11 shows a typical data plot and the slope of the data shows how the constant-torque spring has some variation over the range of motion that the hinge rotates through. The friction in the system due to the applied load of the springs is the difference between the curves divided by two, and the output torque of the spring is the average value of the curves. The minimum output torque is considered the available torque to the system for determining the torque margin and the minimum value was found to always be at the end of travel.

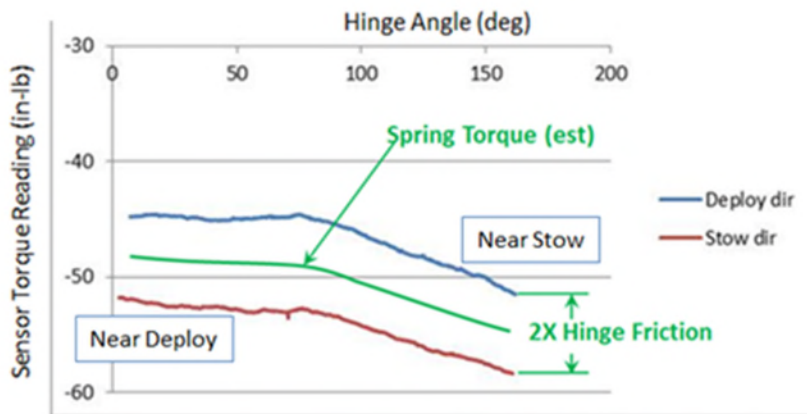


Figure 11. Typical Torque Data

A similar approach was used to characterize the inter-panel hinges and to determine the number of springs necessary to meet torque margin requirements. Running the hinges through this level of characterization was a significant improvement over the approach taken during the S-NPP effort and provided a high level of confidence in how well the hinges would perform at the solar array subsystem level.

Solar Array Subassembly Testing

To be acceptable for delivery to observatory integration, the solar array subsystem had to pass a suite of tests in the sequence shown in Figure 12 (which includes procedure numbers for reference only).

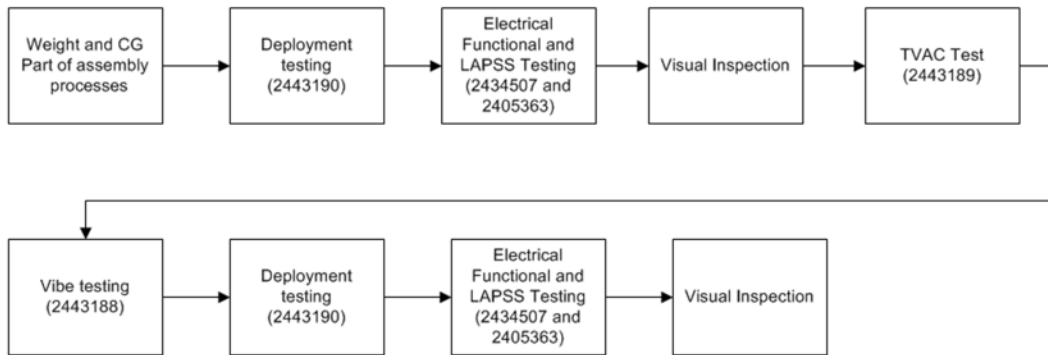


Figure 12. JPSS-1 Test Flow

Manual deployments were agreed upon at this level of testing since powered deployments were performed at the observatory level pre/post vibration/acoustics testing. Those powered deployments demonstrated the end-to-end capability of the system to power the release mechanism (TiNi actuator) and break the retention bolt.

Deployment testing was a challenge on S-NPP and formally recognized as a risk during the JPSS-1 program. There were no plans to change the approach in deployments from how S-NPP had done them; it was agreed that there were practical limitations with the air bearing gravity-negation system.

Due to test fixture limitations, during the S-NPP subsystem testing, it was not possible to reach the correct test levels during vibration testing; this testing had to be deferred to the observatory level. For JPSS-1, a thorough review of the MGSE led to the decision to create a handling fixture that the array could stay integrated to for deployment, vibration, and thermal testing. This new fixture allowed for easier handling and transportation of the entire array and is shown in Figure 13.

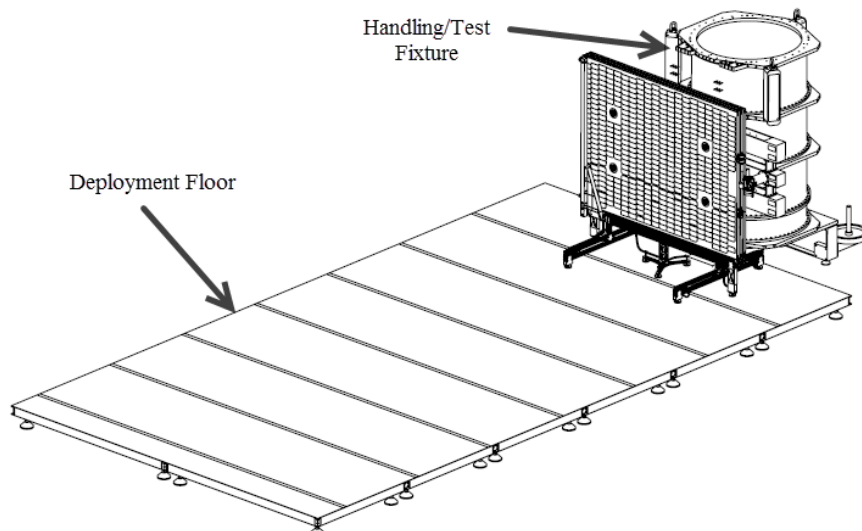


Figure 13. Solar Array Assembly Manual Deployment Test – Stowed Position

The setup for the alignment of the hinge axis is shown in Figure 14. The deployment floor was aligned to gravity and it was possible to align the main deployment hinge axis to the deployment floor. This was done by placing two laser tracker nests onto the panel and rotating it 90 degrees. The resulting arc measurements allowed the hinge axis orientation to be determined. It was not possible to account for the orientation of the inter-panel hinges to the deployment floor.

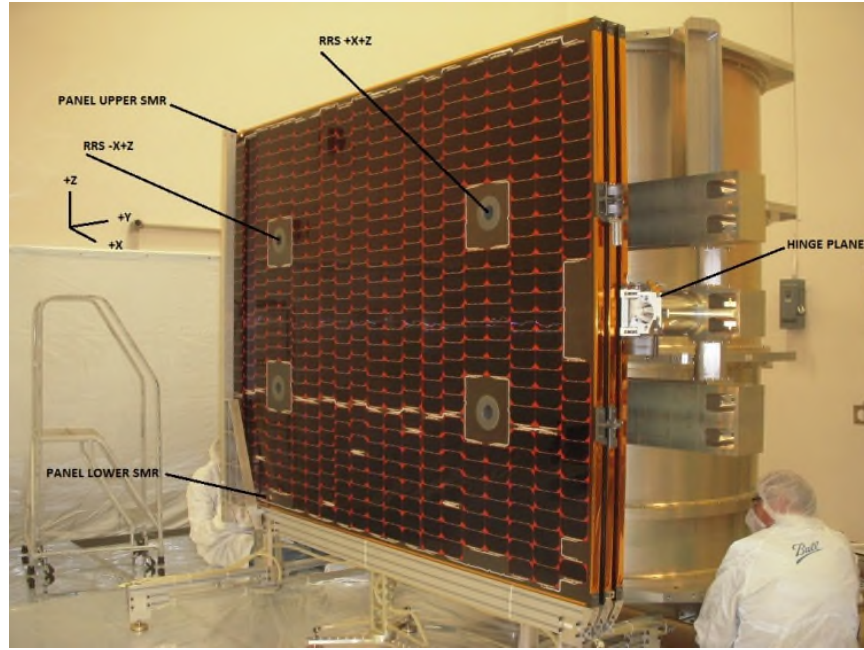


Figure 14. Setup for Alignment of MDH Hinge Axis

During preparation for JPSS-1 deployments, a problem that arose was that the S-NPP polyolefin membrane was wavy and would not lay flat. This was not acceptable and the material was discarded in favor of an approach that NASA had developed successfully during the GPM program. That approach consisted of two layers, a layer of Poron™ foam against the deployment floor and a layer of Melinix on top of that. Ball worked with NASA to understand the implementation of this system and it was successfully installed onto the deployment floor. Prior to the first manual deployment run-for-the-record some engineering tests were performed to gain confidence that the deployment would be successful. This was needed as the air bearing offload system was not instrumented to show the amount of load that each air bearing was carrying. The engineering deployments allowed evaluation of the air bearings to determine if they were adjusted correctly and operated over the full range of motion. One thing that was observed was that if an air bearing was overloaded it would “plow” through the Poron™ support and it was easy to note which bearings were not adjusted correctly.

The air bearing support was supplied with air through a single hose to each panel and can be seen in Figure 15. It became apparent that the manual handling of these hoses could potentially impact how the array deployed and care had to be taken in how the hoses were managed. If they were twisted the wrong way, then a retarding torque could be applied at the hinge line and impact deployment time or the sequence in which the panels locked out. The first manual deployment took 4 minutes and 30 seconds to complete without requiring intervention.

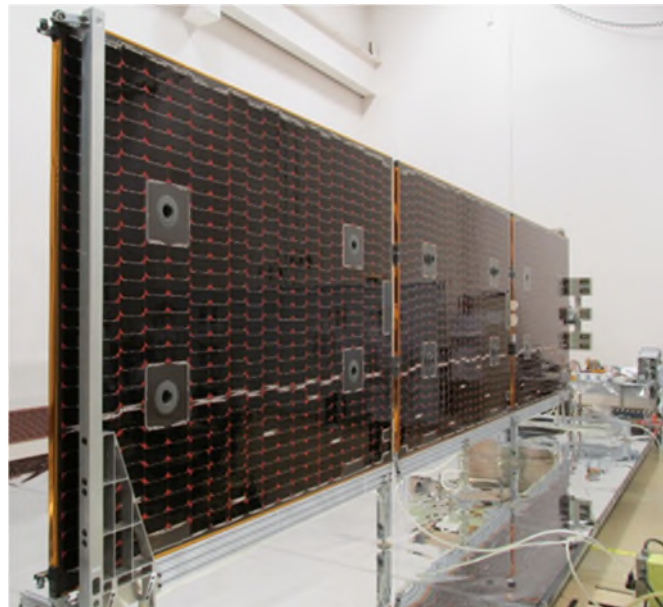


Figure 15. Deployed Array on Air Bearing Support Equipment

After the deployment was completed, each hinge line was inspect to verify that the pawls were engaging with the cams correctly. It can be seen in the left-side ovals in Figure 16 that the lower pawl of the MDH engages into the cam further than the upper pawl. This is a result of minor variations in the deployment floor height and the fact that the air bearings cannot be controlled to equally off-load the panel.

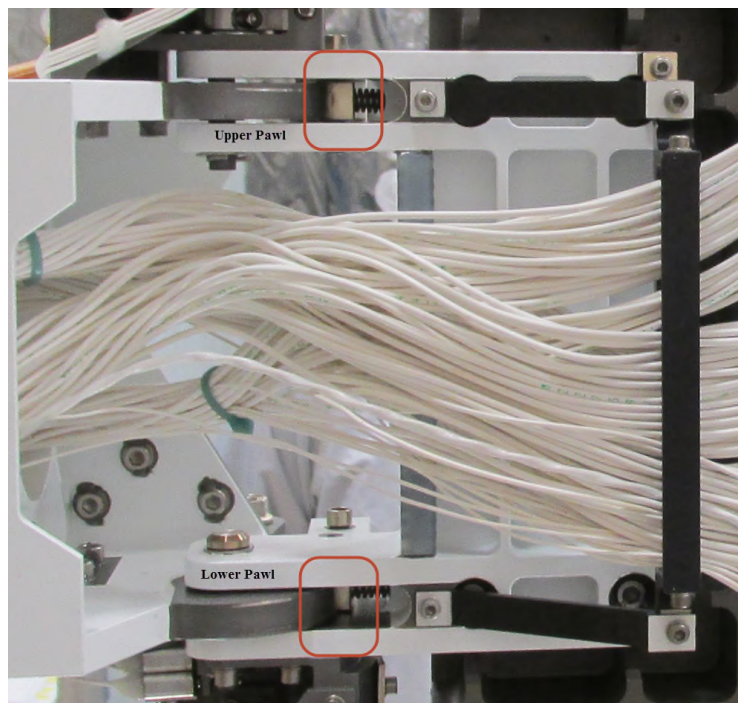


Figure 16. MDH Pawl Engagement Issue

Once the array was in the deployed position it was possible to perform electrical and Large Area Pulsed Solar Simulator (LAPSS) testing. Once the panels were secured in a flight stowed configuration to the MGSE the entire barrel assembly that the array was attached to was transported to perform environmental

testing. Thermal vacuum testing was performed on the entire array for four cycles, to make up for the four cycles missed at the observatory level when the wing is removed from the spacecraft for thermal balance. This test is limited in the ranges to which the array subsystem can be exercised. It was not possible to cycle to the hot operational temperature of the array as it would exceed the transition temperature of the shape memory alloy in the TiNi actuators and the limits of the wet lubrication in the eddy current dampers.

The solar array test set up was vibration tested with a solar array mass simulator prior to integration of the flight solar array to the MGSE to validate the modes of the MGSE prior to flight vibration testing. The array was exposed to sine sweep and sine burst to qualify all of the hardware for quasi-static loading and the low-frequency sine transient or sustained sine environments that were anticipated during launch. The test setup is shown in Figure 17. Random vibe was also performed as risk reduction; the array was to be qualified at observatory acoustic testing.

After environmental testing the array was transported back to the deployment floor and configured for manual deployment. With minimal adjustment done to the array and no verification of hinge line orientation the array was deployed and took 9 minutes and 30 seconds to complete. Each panel successfully locked out and completed its range of motion but this significant difference in time could have been an indication of damage to the hardware due to environmental testing. After adjusting the MGSE to orient the handling fixture in a similar manner as the pre-environmental tests, it deployed in 5 minutes. This was much more in line with the previous test and, after completing electrical and LAPSS testing, the array was delivered for observatory integration. Once mounted to the satellite bus, the array passed all of its electrical tests.



Figure 17. Solar Array Subsystem Vibration Testing

Satellite-Level Testing

At the Observatory level, the array was to see more vibration testing, after which first motion testing was required to demonstrate it was going to operate properly after launch. Then, while JPSS-1 was in TVAC testing, the solar array was removed and mounted back to the MGSE and a final full deployment test was completed. This testing was complicated by the fact that dampers were removed after the array was in the partially deployed condition, after a first motion release, also known as a “pop and catch,” so that the array could be safely stowed to the bus for removal. It was decided to start the deployment test where the pop

and catch test had ended to test the dampers thru their full range of motion without adjusting where on the gear train it had stopped. After the array had been attached to the air bearing hardware, the array was deployed. This deployment took longer than anticipated, 10 minutes and 27 seconds, without manual intervention. Without adjusting the test set up, the array was stowed and allowed to deploy from its stowed position again, and that took 8 minutes and 10 seconds, without manual intervention. Since this was still out of family with the subsystem results, an investigation was started to understand the difference. It was determined that since the air bearings were used and adjusted for the observatory-level test, and then utilized untouched for the subsystem-level test, they were now improperly adjusted for the subsystem testing. After adjusting the air bearing set up, by manually walking out the array with eddy current dampers removed, the deployment was repeated and completed in 4 minutes and 16 seconds, which matched the results from subsystem-level testing. With this success, all that remained before shipment and launch was to remount the array and complete a final pop and catch.

Summary and Lessons Learned

The design and development of the S-NPP array resulted in many lessons learned during the first implementation of this style of array by Ball Aerospace, in the following areas:

- Number of leaf springs used within each drive stack to limit inter-spring friction.
- Inspection of parts and verification of part processing.
- Cam profile of hinge surfaces to provide constant resistive torque.
- Inadequate resistive torque characterization.
- Inadequate output torque characterization.
- Agreed upon requirements for resistive torque characterization.
- Design of vibe fixtures to achieve required test spectrum.
- Deployment fixturing design and verification.

The JPSS-1 solar array design updates—changing the profile of IPH cam, updates to the constant-torque spring and the spring mounting, and removing potential harness hang-ups—and the follow-on tests were very successful, but some issues along the way made it necessary to repeat tests. Among these were:

- Deployment floor material changes from polyolefin membrane to Poron™ and Melinix.
- Repeatability of MGSE alignment.
- Maintaining configurations of air bearing MGSE between different test set up usage.
- Difficulty repeating air bearing alignments and determining proper offloading.

The issues associated with the air bearings and determining whether the offloading is being accomplished correctly has driven the undertaking of a new research and development effort to address these troubles found during S-NPP and JPSS-1.

Acknowledgements

The authors wish to acknowledge Mr. Joseph Pellicciotti for his crucial support with the S-NPP solar array flight qualification, and for the portions of his presentations which made it into this paper. The authors especially want to thank the engineers, technicians and support personnel of Ball Aerospace who turned the designs into hardware that made these two missions possible.

Spacecraft Common Deployable Boom Hinge Deploy and Latching Mechanisms

Paul Lytal* and Marcel Renson**

Abstract

JPL is developing deployable radio frequency (RF) reflector booms for spaceflight usage on two different Earth orbiter projects scheduled to launch in the early 2020's. The static alignment and thermal stability requirements for these RF reflector booms are challenging. A common mechanism design has been developed for the deployment and latching of boom hinges that avoids significant parasitic loads on the alignment critical structures after completion of mechanism function. The mechanism design includes a high-aspect-ratio torsion spring with viscous damper for hinge closure as well as an actuator-driven flexured hook and roller latch for joint preloading. This paper describes noteworthy mechanism design details, test results, challenges, and lessons learned during the development effort.

Introduction

The RF reflector boom deployment sequence is shown in Figure 1 for each project. On a given boom, only one hinge is deployed and then latched at a time. After completion of hinge closure and latching for all boom hinges, the passive RF reflector deploys.

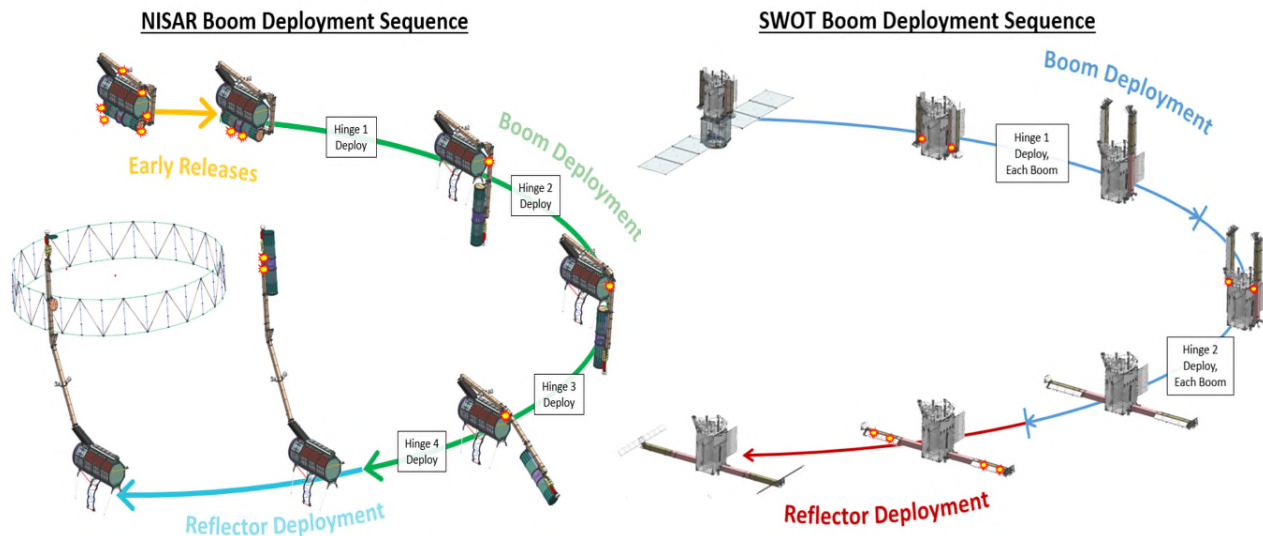


Figure 1. RF Reflector Boom Deployment Sequences

The boom hinge deploy and latching mechanism design includes a spring/damper mechanism for hinge closure and an actuator-driven latching mechanism for hinge joint preloading (Figure 2). The spring/damper mechanism automatically proceeds with hinge closure immediately following mast launch restraint separation. Hinge latching does not commence until successful confirmation of hinge closure to within the latching capture range from redundant hinge closure sensors.

* Jet Propulsion Laboratory, California Institute of Technology, Pasadena, CA

** D.E.B. Manufacturing Inc., Lakewood, NJ

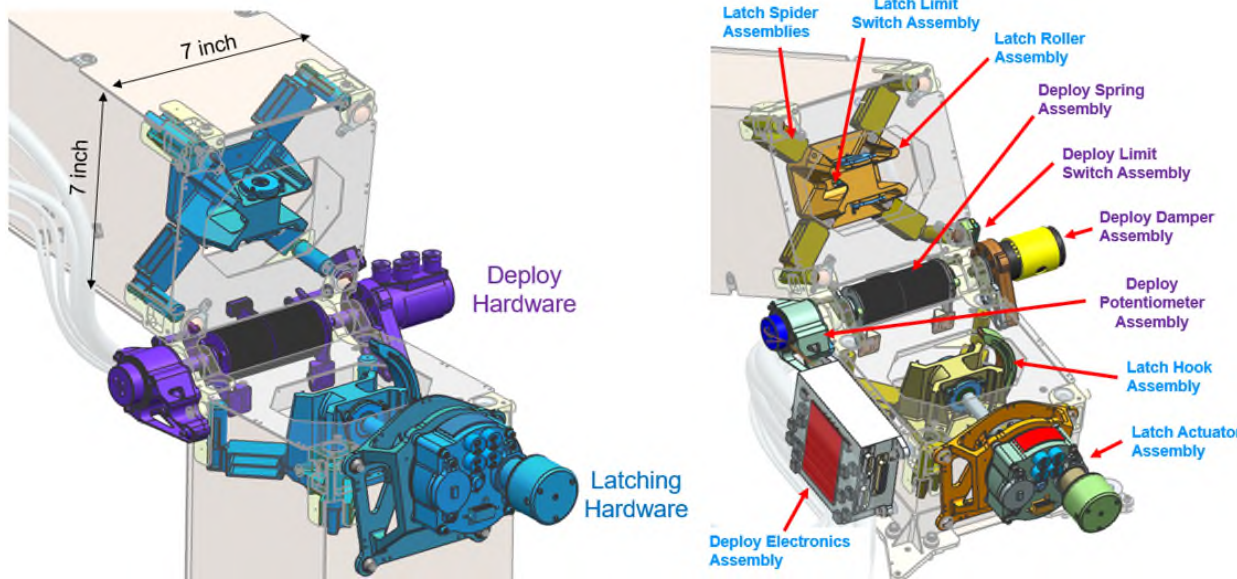


Figure 2. Hinge Deploy & Latching Mechanisms (NISAR Hinge Shown)

Project Background

This common boom hinge deploy and latching mechanism design is being developed for two different Earth-orbiter projects: the Surface Water Ocean Topography (SWOT) Project and the NASA-ISRO Synthetic Aperture Radar (NISAR) Project. The SWOT Project is an international collaborative effort between NASA and the French Government Space Agency. The earth science objectives of the SWOT Project include high-definition temporal and spatial mapping of all fresh and salt water bodies around the globe for a minimum 42-month time period. NISAR is an international collaborative effort between NASA and the India Space Research Organization (ISRO). The earth science objectives of the NISAR Project include land and ice mass observation to improve natural disaster prediction, deforestation modeling, and polar ice cap reduction modeling, amongst other objectives. Precision alignment and stability of the RF reflectors to the RF feeds is crucial to mission success of each project.

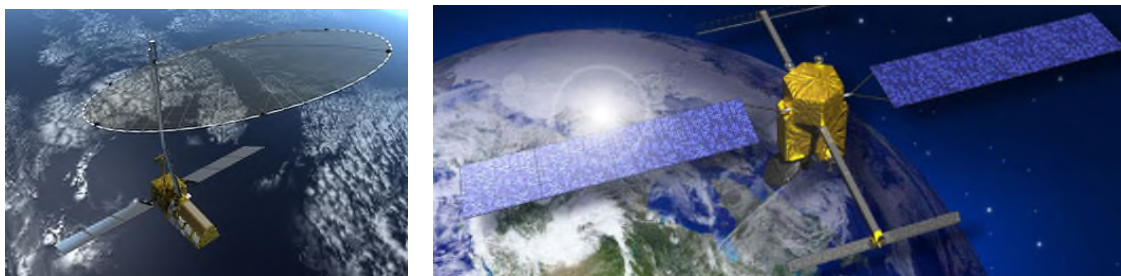


Figure 3. NISAR (Left) and SWOT (Right) Earth Observation Spacecraft

Common Boom Deploy & Latching Mechanism Development

The SWOT and NISAR Projects elected to pursue a common deployable boom design to the maximum extent practical to reduce overall development cost and schedule. While detailed mast geometry necessarily differs due to mission architecture and configuration differences, the basic design and construction of the booms is common between the two projects.

The deploy and latching mechanisms are highly similar between the two projects, only differing as required by the structure that the mechanisms mount to and differences in flight environments. Noteworthy differences between the two projects are highlighted in the sections that follow as relevant to the mechanisms described in this document.

Driving Design Considerations

In addition to typical spaceflight mechanism design constraints (limited mass and volume, launch environments, on-orbit environments, ground testing considerations), the avoidance of significant and variable loading from mechanisms hardware onto the alignment critical structure was a primary design driver. The approach taken was to mechanically disconnect all possible mechanisms hardware from the mast after completion of mechanism function as shown in Figure 4. In addition, the mechanical attachment of all mechanisms hardware to the mast uses flexures or non-preloaded pin/slot interfaces. Specific implementation of the mechanism mechanical decoupling is shown in Figure 4.

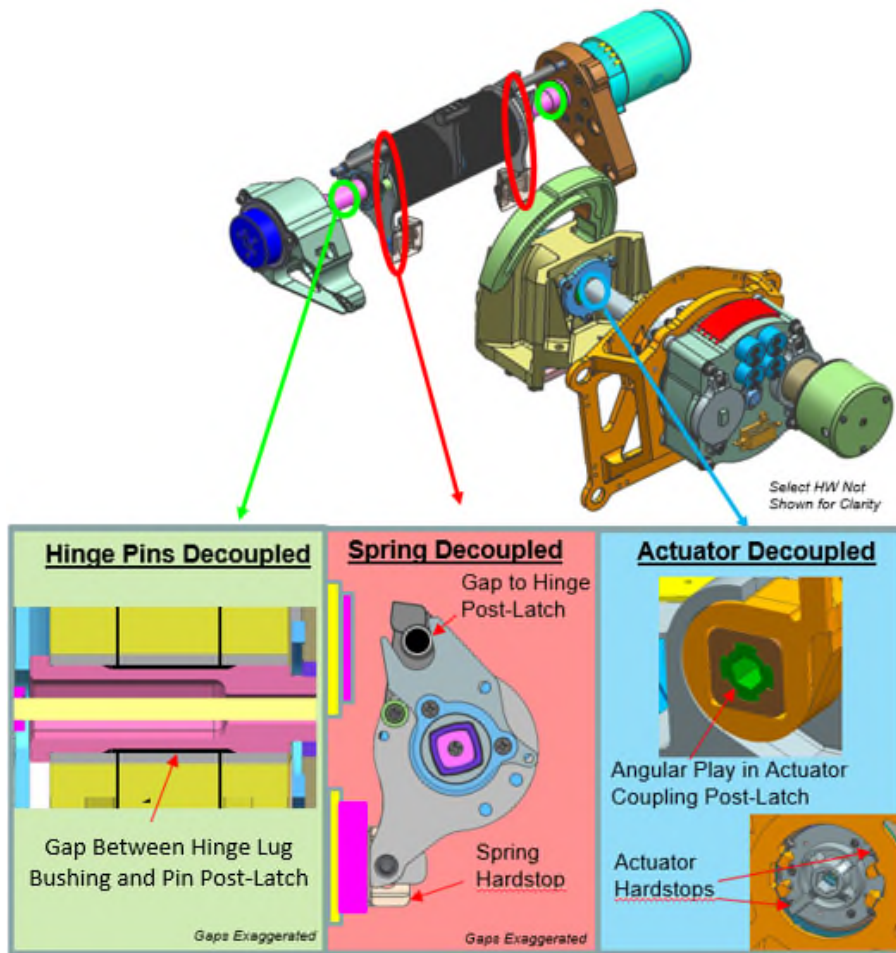


Figure 4. Mechanism Mechanical Disconnection from Alignment Critical Mast Structure

Another critical design driver for deploy and latching mechanisms hardware was conductive thermal isolation of mechanisms hardware from the mast structure. This enables the control of mechanism hardware to tighter temperature ranges than the parent structure as necessary. Isolation was accomplished using small contact areas and low thermal conductivity Ultem 2300 isolators. An example of this methodology is shown in Figure 5.

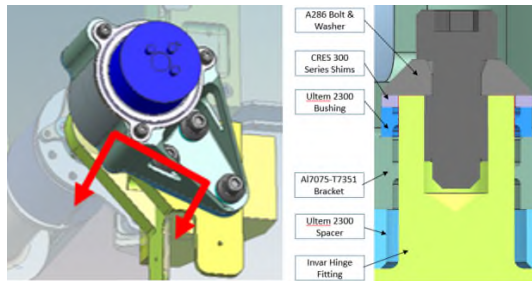


Figure 5. Example of SWOT and NISAR Mechanism Thermal Isolation Design

Hinge Deployment Mechanism

The hinge deployment mechanism is designed to close boom hinges from the launch position through the deployed/closed hinge configuration. A separate analogous hinge deployment mechanism is used at each hinge. The hinge deployment mechanism was designed to overcome worst-case torque opposing deployment associated with hinge-crossing wire harness, coulomb friction sources, and ball bearing rolling friction losses over the full range of thermal environments that could take place in flight. Challenges encountered during prototype hinge testing (Figure 6) in worst case thermal environments are described in the sections that follow.

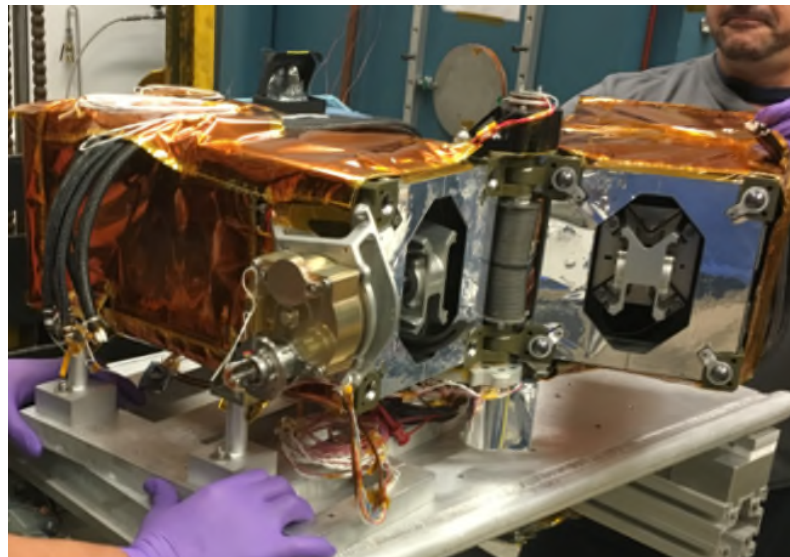


Figure 6. NISAR Prototype Thermal Test Hinge

A spring/damper mechanism was developed to perform hinge closure. Several different options were considered for the boom hinge closure mechanism. A serpentine wire rope spooler mechanism (as used on the SMAP Project RF boom) was considered but rejected primarily due to the inability to test mechanisms in a flight-like manner prior to full mast assembly. Various actuator-driven linkages were considered and discarded due to higher estimated mass than the spring/damper mechanism option. Direct actuator driven hinge closure was considered as well, but was also deemed more massive and a higher risk development than the spring/damper option.

The following sections provide information regarding unique design and testing challenges with the spring/damper mechanism as well as the deployable hinge crossing harness.

Spring Design Overview

A pair of torsion springs is used at each hinge, each capable of independently transmitting torque to deploy the hinge for robustness. Each spring is supported by an aluminum outer mandrel which in turn rotates on glass-filled Teflon bushings on an inner mandrel (Figure 7).

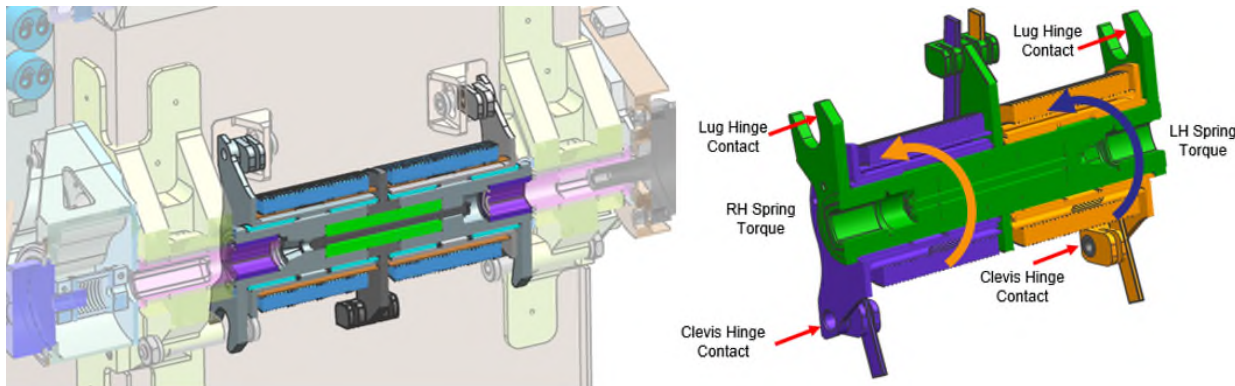


Figure 7. Spring Location in Hinge (Left) and Independent Spring Mandrels (Right)

A custom 17-7 CH900 torsion spring solution was deemed necessary given the limited volume and high output torque needed for the Hinge Deployment mechanism, particularly for the smaller volume available in the NISAR hinge configuration (116-mm [4.567-in] length and 43-mm [1.693-in] diameter for spring assembly). Elgiloy was briefly considered and dismissed due to long lead time as well as spring vendor cautionary guidance that Elgiloy spring development programs frequently encounter challenges, often with little to no improvement in measured strength performance over 17-7 CH900. The project elected to stick with the 17-7 CH900 material which the spring vendor had the most experience working with.

A high-aspect-ratio rectangular cross section (3.8 to 1) is being used for the spring to increase the spring wire moment of inertia per unit spring body length. This resulted in lower bending stress and higher spring constant than a round wire spring with the same wire width and number of spring turns.

There are six types of hinges for the SWOT and NISAR booms with different stow angles. It is worth noting that the relaxed spring arm angle of the springs for each hinge were selected to ensure maximum torque across the range of motion of the hinge without violating NASA-STD-5017A advisory that Mission Critical Springs maintain positive margins above a 1.5 factor of safety to yield at the maximum deflection (fully stowed) configuration [1].

Spring Arm Twist

In early testing with spring arms contacting round pins with no other support, undesirable arm longitudinal twisting was observed at spring windup angles greater than 180 degrees, resulting in significant reduction in spring stiffness and higher-than-intended stress in the spring arms. Destructive characterization testing at room temperature demonstrated the onset of yielding at approximately 445 degrees as opposed to approximately 730 degrees predicted by analysis with no spring arm twist. Guide vanes were added to the spring mandrel design to minimize this arm twist phenomenon. Follow-on destructive spring testing with the guide vanes demonstrated onset of yielding at approximately 740 degrees, which more closely matches analytical predictions (Figure 8).

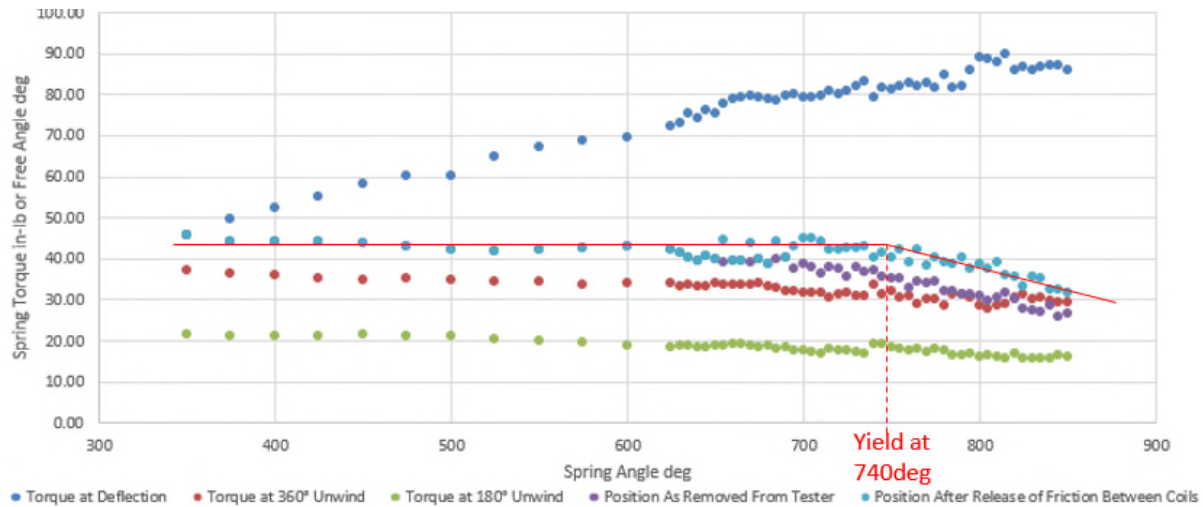


Figure 8. Destructive Spring Characterization Test Results, Spring Arms Supported

Spring Assembly Thermal Testing

Developmental testing was conducted to evaluate the impact of spring wet lubrication on spring performance across temperature. Torsion springs were grease plated with a thin film of Braycote 601EF and tested in the same configuration as identical clean, unlubricated springs. Test results indicated that lubricated spring performance was nearly identical to unlubricated spring performance at and above room temperature. Unlubricated spring torque performance was significantly better than lubricated spring performance in the worst case cold environment (-100°C) as shown in Figure 9. The average improvement in spring output torque was up to 1.7 N·m [15 in·lbf] at maximum spring deflection in usage. This is expected to be the result of wet lubricant thickening at cold temperature. The flight torsion springs were unlubricated for both projects.

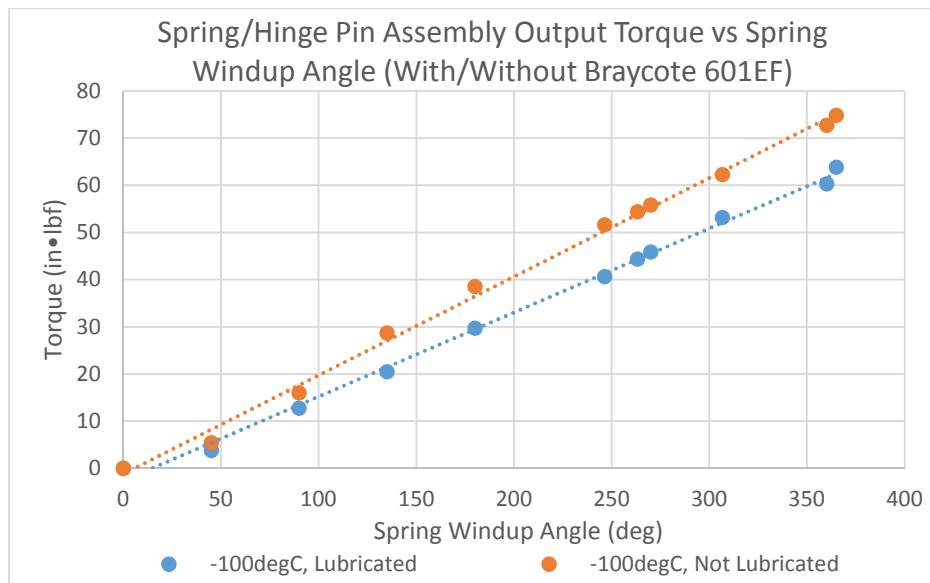


Figure 9. Prototype Spring Assembly Thermal Test, Lubricated versus Not Lubricated

Prototype spring assembly testing (consisting of a spring, mandrel, hinge pin, and bushings) was also conducted at the hot and cold extremes of the expected flight operational temperature range. Test results

demonstrate negligible change in spring/hinge pin assembly performance from 20°C to -100°C as shown in Figure 10. This is consistent with design expectations, as no wet lubricants are used in the spring assembly design and adequate clearance has been incorporated between all materials with dissimilar coefficients of thermal expansion internal to the mechanism. Furthermore, the flexural modulus of 17-7 CH900 springs changes negligibly from 20°C to -100°C. Similar results were observed between room temperature and the maximum flight design temperature for both projects (+105°C).

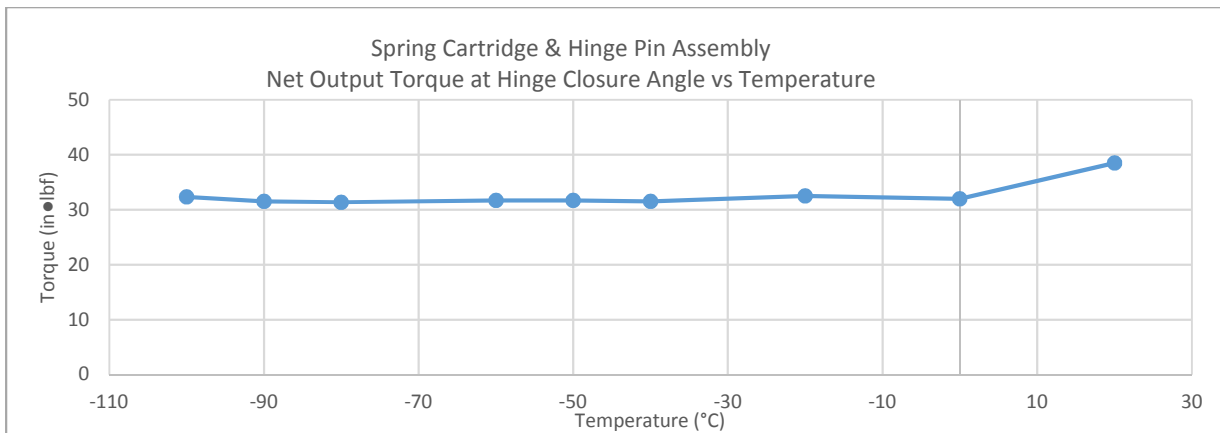


Figure 10. SWOT Mid-Hinge Spring Assembly Output Torque at Hinge Closure at Various Temperatures

Rotary Viscous Damper Design Overview

Rotary viscous dampers have been used in dozens of spaceflight missions. Significant challenges have been encountered in the development and qualification of these dampers and several noteworthy breakthroughs in the design and assembly process, including vacuum fluid degassing and fill methods as well as gasket sealing designs, have been established as standard practice to ensure acceptably consistent performance and reliable operation in flight [2].

Building upon the state of the art for rotary viscous dampers, JPL partnered with D.E.B. Manufacturing Inc. to qualify an improved spring/piston rotary viscous damper design. The rotary viscous damper design used in this program is a variant of the heritage D.E.B. Manufacturing Inc. 1025 model damper. New design features include the following items:

1. Higher strength steel single wing vane shaft
2. Updated custom ball bearing shields to reduce unintended leak paths from the damping chamber to the expansion chamber through the ball bearings
3. Reduced taper angle on the valve adjustment surface for precision damping rate setting
4. An additional fastener holding the case and abutment together for added strength
5. A new compression spring and gasketed piston arrangement to replace the heritage elastomeric diaphragm used to pressurize the damping fluid expansion chamber as shown in Figure 11. Note this basic functionality of the spring/piston arrangement is similar to that of the spring/piston damper temperature compensator used on Mariner, Viking, Galileo, NSCAT and other missions [3].

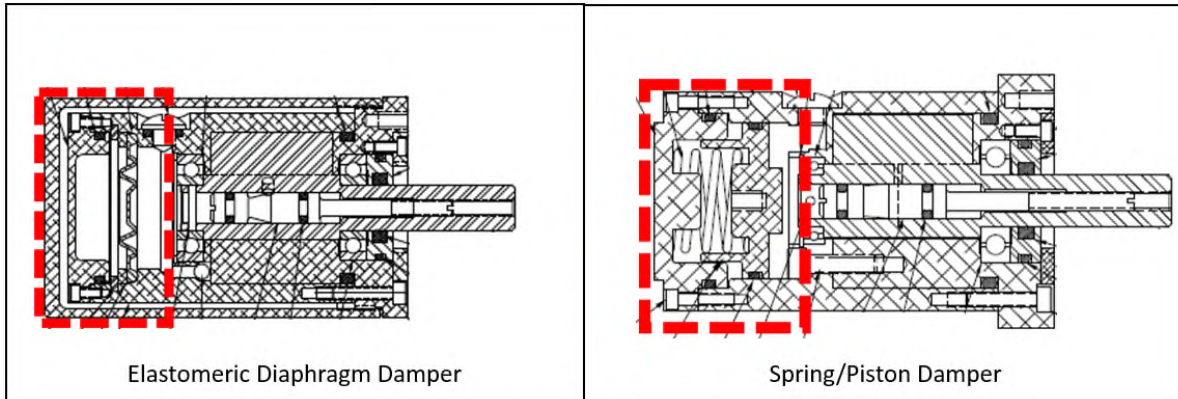


Figure 11. Heritage (Left) and New (Right) Viscous Dampers (Image Credit D.E.B. Manufacturing Inc.)

Initial prototype test results for this new D.E.B. Manufacturing Inc. damper design suggest several noteworthy performance advantages over heritage 1025 model dampers: reduced internal backlash, improved damping rate consistency, lower fluid recovery time, and greater structural robustness to transient impulse torque application (such as from deployable separation kickoff events). The sections that follow provide data supporting each of these observed advantages.

Empirical Data-Based Damper Analytical Model

As-tested damper performance for viscous dampers in this program did not conform well to ideal damper performance theory. This result is consistent with previous viscous damper characterization test program observations [3].

The ideal viscous damper is a rate-dependent torque device that conforms to the following simple equation:

$$T_{Damper} = c \cdot \dot{\theta} + T_{Coulomb} \quad (1)$$

where 'c' is the damping rate constant, ' $\dot{\theta}$ ' is the angular velocity of the damper shaft, and ' $T_{Coulomb}$ ' is rate-independent friction torque loss of the damper. Damper testing demonstrates that the damping rate for any given device is not constant, varying significantly with both temperature and with applied torque. Data from prototype damper thermal testing was used to generate functions for damping rate versus applied torque at qualification temperature limits as well as the nominal expected flight deployment temperature. These curve-fit functions are shown in Figure 12.

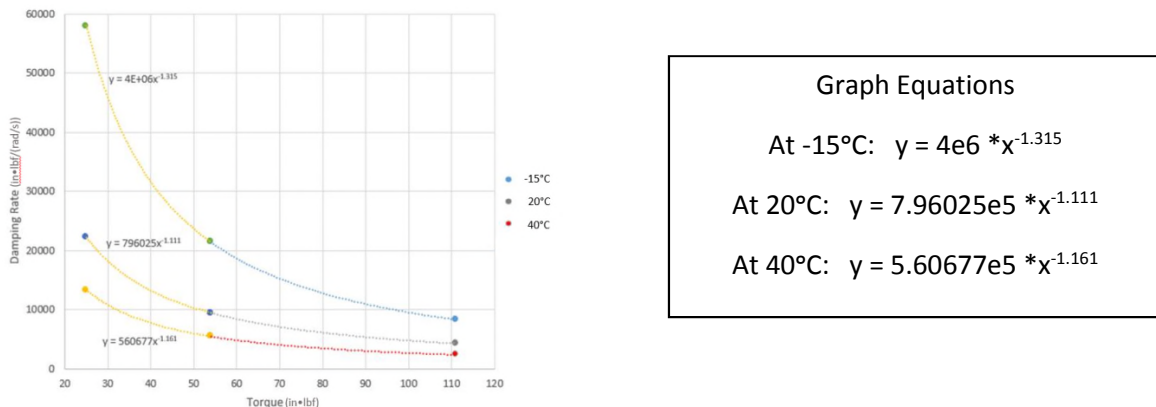


Figure 12. Measured Damping Rate vs Applied Torque at Different Temperatures

As shown in Figure 12, at a given applied torque, the damping rate varies by a factor of approximately four to five between qualification cold and qualification hot temperature extremes listed in Figure 12 for the low torque range shown. In order to comply with project deployment duration requirement limits in all allowable flight thermal environments, in spite of this significant damping rate variability with temperature, thermostatically-controlled film heaters have been added to the design baseline for all dampers on both the SWOT and NISAR spacecraft to actively control damper temperature.

Damper deployment simulations were conducted using this test-informed analytical model in order to calculate peak damper reaction loads and to generate preliminary deployment duration estimates for worst case flight environments and deployment configurations.

Damper Variable Torque and Temperature Testing

In order to reduce the risk of boom hinge deploy duration requirements non-compliances surfacing in the damper qualification program, prototype damper thermal testing was conducted with the highest and lowest net torque profiles applied to the damper throughout deployment at qualification temperature limits. Linearly decreasing torque was applied to the damper throughout the test using a chain-on-pulley configuration in which the chain piles on the floor, mimicking the near-linear reduction in torque available from flight deployment torsion springs. A linearly-decreasing maximum torque profile that bounds the worst-case flight torque profile was applied in the qualification hot temperature environment over the minimum hinge deploy angle to generate the shortest deployment duration result. Similarly, a linearly-decreasing minimum torque profile that bounds the worst case low flight torque profile was applied in the qualification cold temperature environment over the maximum hinge deploy angle to generate the longest deployment duration result. See test results in Figure 13.



Figure 13. Worst-Case Long (Left) and Worst-Case Short (Right) Deploy Duration Test Data

When these test results are compared to elastomeric diaphragm test results from past projects, the spring/piston damper exhibited more consistent damping rate performance under constant external torque application, as shown in Figure 14. The suspected explanation is that the spring recovers to achieve constant damping chamber pressure more quickly than the elastomeric diaphragm. Note there was a 9% difference in constant applied torque between the two plots in Figure 14. While the lower applied torque in the spring/piston damper test may have influenced the damping rate consistency result, this is not expected to be a significant factor.

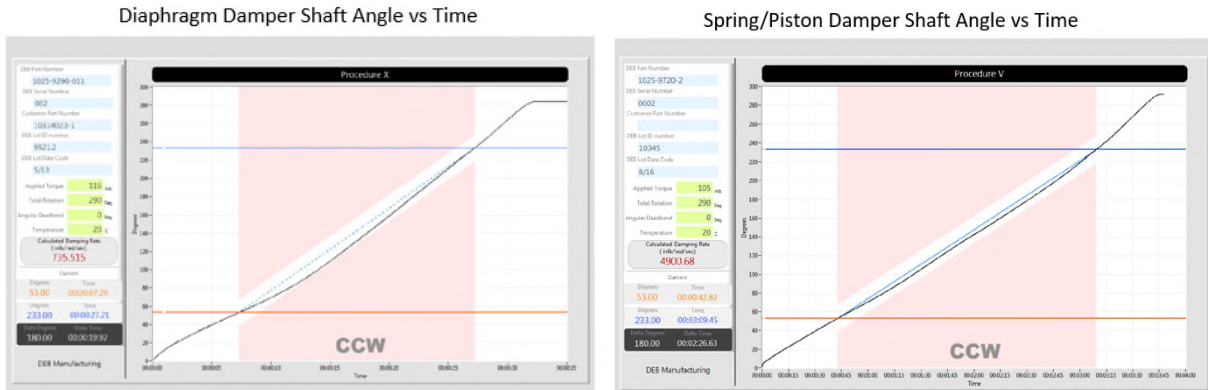


Figure 14. Comparison of Damping Performance with Constant Applied Torque

Damper Impulse Torque Testing

At the time of SWOT and NISAR deployable boom launch restraint release, significant separation forces act on the boom from explicit kickoff springs as well as thermal-strain induced structural forces. These large forces are applied at the separation interfaces, which are a significant distance from the hinge lines. The result is high torque in excess of 678 N•m (6000 in•lbf) applied about the hinge line. The damper is intentionally isolated from this torque with rotational backlash in the torque transmission hardware and by pre-setting the damper shaft rotation angle to the “backseat” of this backlash prior to launch.

A damper kickoff simulation test was implemented to represent this critical load case as shown in Figure 15. The maximum achievable kickoff torque for the test setup was implemented at approximately 775 N•m (6858 in•lbf), applied over the full stroke angle of the mast separation kickoff spring plungers. This peak torque was applied to rotational inertia simulators that bounded the relevant inertia of the flight hinges. Flight-like damper torque transmission backlash was represented in the test. Damper temperature was controlled to the extremes of the qualification temperature range, and damper torque response was measured (see Figure 15). Average damping rate over this brief duration was calculated and used to generate functions for damping rate versus applied torque in the high torque regime (see Analytical Modeling section).

The plot in Figure 16 shows significant initial damper backlash from the heritage elastomeric diaphragm damper design with significantly lower nominal damping rate of 101.7 N•m/(rad/s) (900 in•lbf/(rad/s)) versus 565 N•m/(rad/s) (5000 in•lbf/(rad/s)) with the current design. No damper backlash has been observed in prototype testing of the spring/piston damper.

With high enough torque applied, D.E.B. Manufacturing Inc. reported they have permanently deformed the elastomeric diaphragm in test dampers, resulting in cavitation issues and in some cases external gas entrainment into the expansion chamber and damping chamber (see Figure 17). Prototype high-torque impulse testing of the spring/piston damper has demonstrated the robustness of this design against catastrophic damage due to short duration high torque events, as can be generated by kickoff springs and strain energy in flight deployable separations. The elastomeric diaphragm can also permanently deform from hot and cold temperature deployments and thermal vacuum cycling. The spring/piston damper also reduces the list of non-metallic, permeable materials within the damper to only gaskets and O-rings, reducing the potential for unintended fluid seepage through the diaphragm (also reported by D.E.B Manufacturing Inc. in testing).

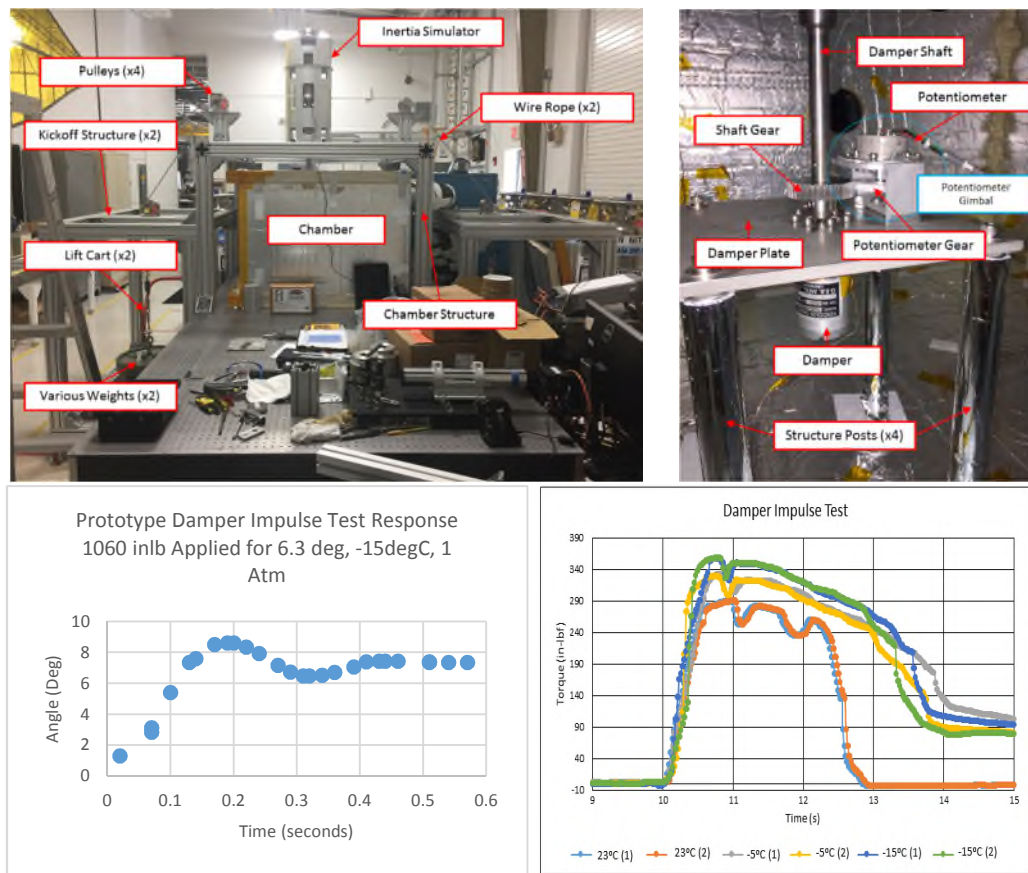


Figure 15. Prototype Damper Impulse Torque Test

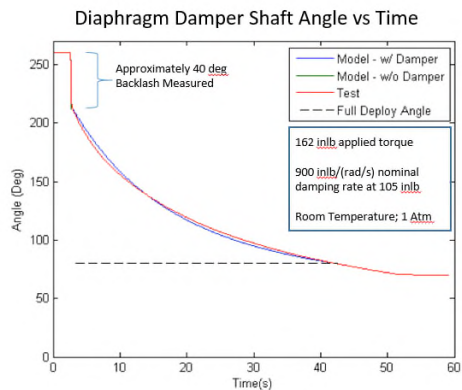


Figure 16. SMAP Project Damper Test Data Showing Typical Diaphragm Viscous Damper Backlash



Figure 17. New Diaphragm (Left) and Inelastically Deformed Test Diaphragm (Right)

Due to intermittent issues with cavitation and prolonged recovery time in developmental testing for the Soil Moisture Active Passive (SMAP) Project with the elastomeric diaphragm damper, the SMAP Project instituted a two hour wait for damping fluid recovery prior to subsequent damper usage. Prototype testing with the spring/piston damper has demonstrated that 30 minutes is adequate recovery time (note: less time may be acceptable but has not been tested). The slow process of the elastomeric diaphragm recovering its original shape is the suspected root cause of the prolonged recovery time for the elastomeric diaphragm damper. It is important to note the elastomeric diaphragm may never recover to its original shape and can be permanently deformed resulting in cavitation issues and in some cases external gas entrainment into the expansion chamber and damping chamber.

Damper Vibe Testing

In the SWOT and NISAR deployable reflector boom mechanism, the damper shaft must be mechanically isolated from the high kickoff torque of the boom. These high torques are applied to the boom over a maximum angle of 0.8 degree. In the ground stowing process, the damper shaft is positioned in the “backseat” of the 4-degree minimum backlash. It is critical that the shaft not rotate within this backlash in the launch vibe environment. To demonstrate that the damper shaft does not move in a bounding vibratory environment simulating launch vibe, a random vibration test was conducted with the damper mounted on its flight-like mounting bracket. Tests were conducted in 3 orthogonal axes as shown in Figure 18. The initial damper shaft clocking was marked on the housing. It was confirmed that the shaft did not rotate from the initial clocking after each 2.5-minute test. Test levels are shown in Figure 18.

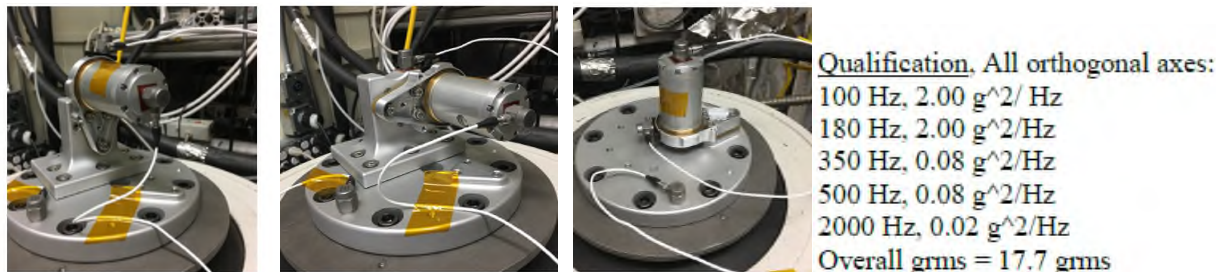


Figure 18. Damper Vibration Test (X-, Y-, & Z-Axes from Left to Right)

Hinge Latching Mechanism

The hinge latching mechanism preloads precision alignment features on each hinge half to each other after hinge closure. There is a separate latching mechanism located at each hinge. Each latching mechanism consists of an actuator with torque transmission hardware, and a flexured hook/roller assembly (see Figure 19). Noteworthy design, analysis, and test information for each of these are described in the sections that follow.

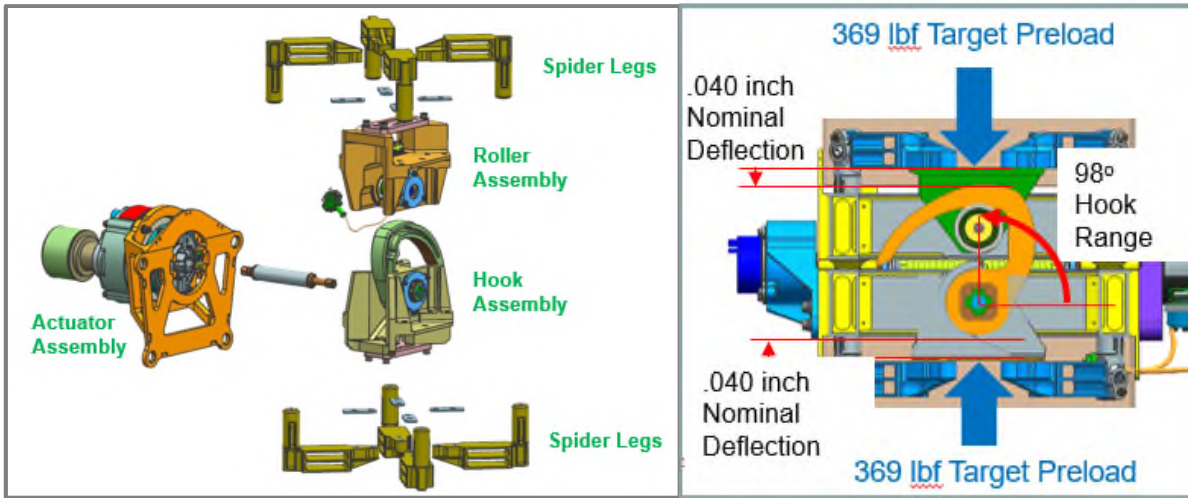


Figure 19. Hinge Latching Hardware Overview

Latching Actuator Thermal Testing

The harmonic gear set used in the actuator is not capable of transmitting more than 22.6 N•m (200 in•lbf) of torque without structural damage. Stall torque was adjusted to just below this threshold in the worst case hot (highest output torque) environment for actuator operation. A significant reduction in actuator output torque of about 43% was observed in prototype testing from this maximum at the worst-case hot environment (75°C) to the worst-case cold environment (-30°C) due to Braycote 601 lubricant thickening and reduction in motor winding resistance at cold temperature as shown in Figure 20. This reduced output torque performance in the worst case cold environment drives the minimum latching mechanism torque margin.

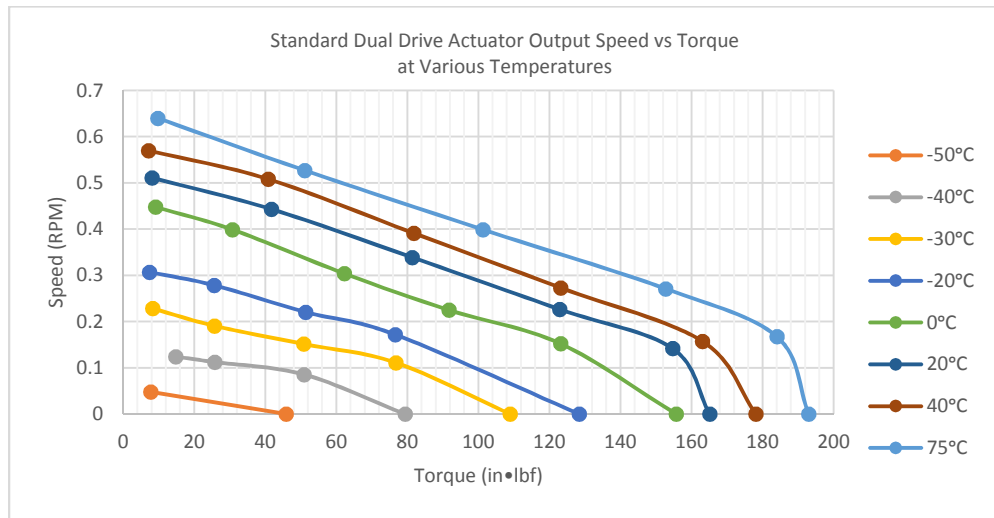


Figure 20. Actuator Speed versus Torque Performance at Various Temperatures

Dynamometer testing of a prototype actuator demonstrated a slight improvement in actuator output torque performance in the worst case cold condition by adding a few drops of Brayco 815Z to the Braycote 601 grease on the internal motor ball bearings when compared to the same bearings with only Braycote 601 added (see Figure 21). This lubrication approach is being used for both the SWOT and NISAR Projects.

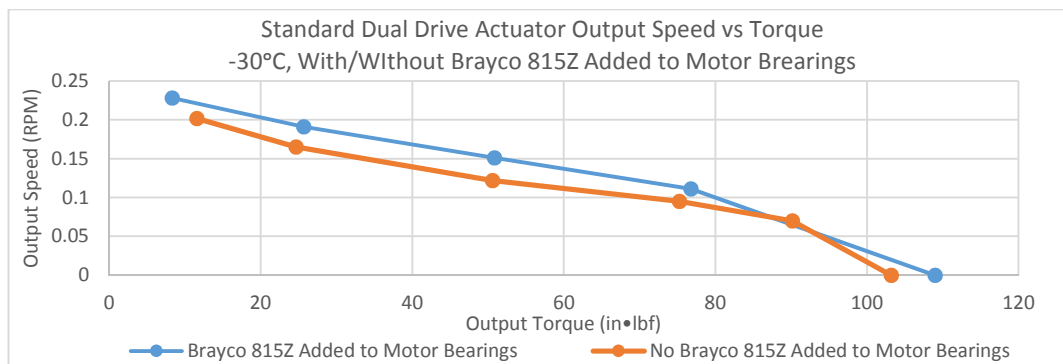


Figure 21. Actuator Performance with and without Brayco 815Z added to Braycote 601 on Motor Bearings

Flexured Hook and Roller Assembly

The flexured hook and roller assembly is designed to achieve the target joint preload of 1641 N (369 lbf) while requiring the minimum peak torque to latch within available volume constraints. A modified parabolic hook ramp profile was designed to maintain nearly constant torque load during the latching process, minimizing peak torque required to approximately 5.65 N•m (50 in•lbf) and thereby maximizing mechanism minimum torque margin.

The significant deflection of the flexures in the assembly of approximately 2.03 mm (0.080 in) under preload ensures that there is not significant change in preload due to mismatch in the coefficients of thermal expansion between latch component materials and alignment critical structure materials. A three-blade one-axis flexure was designed to achieve the required stiffness and stroke in the limited volume available.

Conclusions

The following key mechanism conclusions have been drawn based on the NISAR and SWOT RF Boom Hinge deploy and latch mechanism developmental testing and analysis results referenced in this document:

1. Mechanical decoupling of mechanism hardware from alignment critical structures is a robust and effective approach to avoid mechanism-induced thermal distortions.
2. High-aspect-ratio rectangular wire torsion spring arms must be adequately supported to prevent undesirable twist along the wire axis when used at significant angles of deflection.
3. The new spring/piston viscous damper design described in this document provides performance benefits over heritage elastomeric diaphragm dampers.
4. The addition of Brayco 815Z to Braycote 601 lubricant provides measurable improvement in cold temperature ball bearing performance.

References

1. NASA-STD-5017A, "Design and Development Requirements for Mechanisms", 2015-7-31, 62.
2. Stewart, Alphonso, Charles Powers, and Ron Lyons. "Improvements for Rotary Viscous Dampers Used in Spacecraft Deployment Mechanisms." Proceedings of the 32nd Aerospace Mechanism Symposium, 115-124.
3. Harper, Jack. "Viscous Rotary Vane Actuator/Damper." Proceedings of the 10th Aerospace Mechanisms Symposium, 198-207.

Acknowledgement

The research described above was carried out at the Jet Propulsion Laboratory, California Institute of Technology and at D.E.B. Manufacturing, Inc. under a contract with the National Aeronautics and Space Administration. © 2018. All rights reserved.

Precision High-Strain Composite Hinges for Deployable Space Telescopes

Mark Silver* and Michael Echter*

Abstract

Future large space-based telescopes will require precision mechanisms for deployment or alignment after they reach orbit. This research effort seeks to develop deployable primary-mirror telescope technologies that leverage recent advances in mirror phasing, actuation and deployable structure technologies. One way to obtain a precise deployed position of the optical components is with structures incorporating precision High-Strain Composite (HSC) hinges. This paper focuses on characterizing the deployment precision of individual HSC hinges and of a support frame utilizing multiple HSC hinges. Measurements of certain individual HSC hinges demonstrate position precision as low as 0.6 μm and angular precision as low as 6 μrad . A deployable frame concept produced axial precision of 0.2 μm , piston precision of 2.3 μm and angular precision of 6.3 μrad . A few modifications to the frame test setup are proposed that may improve the piston precision results.

Introduction

The size of space-based telescopes with monolithic primary mirrors is limited by allowable launch vehicle sizes. In order to have larger primary mirrors for a given launch vehicle size, some sort of on-orbit deployment or assembly is required. One example of a deployable primary mirror is the James Webb Space Telescope (JWST) primary mirror.¹ The JWST primary mirror is an assembly of mirror segments. Two wings with multiple mirror segments fold back when stowed to allow it to fit within the launch shroud. Besides JWST, many deployed or assembled primary mirror concepts for space-based telescopes have been considered for some time.²⁻⁹

The key performance requirement for deployed or assembled primary mirrors is positional accuracy. The deployment precision is how close the deployed shape of the structure matches the original shape of the structure before folding. Many factors can lead to positional errors in telescope structures, including assembly error, deployment precision, and shape change due to environmental loads. The level of positional accuracy needed is telescope-, wavelength- and mission-dependent but is generally about one-tenth to one-twentieth of the wavelength of interest and may vary in different degrees-of-freedom. The degrees-of-freedom used to describe deployment precision for the structures used in this paper are defined in Figure 1. In this figure, two displacement degrees-of-freedom are defined, Axial and Piston, and two rotational degrees-of-freedom are defined, Roll and Pitch.

* MIT Lincoln Laboratory, Lexington, MA

DISTRIBUTION STATEMENT A. Approved for public release. Distribution is unlimited.

This material is based upon work supported by the Assistant Secretary of Defense for Research and Engineering under Air Force Contract No. FA8721-05-C-0002 and/or FA8702-15-D-0001. Any opinions, findings, conclusions or recommendations expressed in this material are those of the author(s) and do not necessarily reflect the views of the Assistant Secretary of Defense for Research and Engineering.

Proceedings of the 44th Aerospace Mechanisms Symposium, NASA Glenn Research Center, May 16-18, 2018

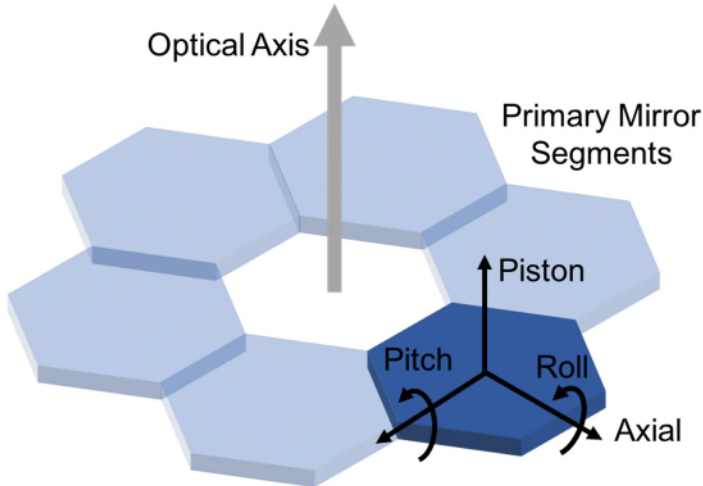


Figure 1. Deployment precision degrees of freedom

Deployment precision measurements of the JWST Development Optical Telescope Assembly (DOTA) demonstrated that the structure has 20 μm of piston precision error, 30 μm of axial precision error and 44 μrad of pitch precision error.¹⁰ JWST has been designed with a complex metrology system and 7 degrees-of-freedom of actuation for each primary mirror segment so that the deployment position error of the optical components only needs to be a few millimeters. Placing the precision alignment burden on the metrology system and shape correcting actuators leads to a more complicated and heavy telescope system than would be necessary with a higher precision structural deployment. Other precision deployable mechanisms and frame concepts have been developed and tested for deployment precision. A summary of previous deployment precision measurements for optical deployable hinges and structures is shown in Table 1. As can be seen from these data, while micron-level deployment precision has been measured, only one measurement of angular precision has been reported in the literature. To better understand the performance of optical precision deployable structures in all of these degrees-of-freedom and help mature the technology for future missions, more development is needed.

Table 1. Previous optical deployable structure deployment precision measurements

Test Article	Piston (μm)	Axial (μm)	Roll (μrad)	Pitch (μrad)
JWST DOTA ¹⁰	20	30	-	44
IFH Specimen 2 ¹²	0.85	0.31	-	-
EDSM ¹¹	2.97	2.97	-	-
Lidar Prototype ¹¹	8.59	0.81	-	-

MIT Lincoln Laboratory (MITLL) is currently working on technologies to simplify deployable space telescopes including precision deployable structures, precision actuation and image based metrology techniques. In this paper, we present recent technology developments in the area of precision deployable structures. First, deployment precision measurements for a newly developed hinge mechanism using thin, flexible composite materials are presented. Second, the design of a prototype deployable frame using this new hinge mechanism is presented along with deployment precision testing results for this deployable frame.

High-Strain Composite Hinges

High-Strain Composite (HSC) materials are thin, flexible composite laminates that can undergo strains much larger than metals with very little plastic deformation. This enables new ways of rolling or folding large structures without the use of traditional revolute joints. Furthermore, HSC-based mechanisms can serve as

a deployment drive actuator, deployment latch and a load-bearing structural member when deployed. This combination of attributes could potentially provide significant mass, complexity and cost savings for spacecraft deployable structures.

The HSC field has grown significantly since the early 2000s and is well defined in the seminal paper by Murphrey et al.¹³ One recent flight success involving HSC materials was the Air Force Research Laboratory Roll-Out Solar Array that flew on the International Space Station in 2017.¹⁴ The use of HSC materials for precision hinges was originally shown in the literature by Domber et al.¹² As indicated in Table 1, their work found submicron-level axial and transverse deployment precision for one HSC hinge design and higher precision error for two other hinges made from different composite layups. Since their work, many new HSC materials have been developed and high precision position sensors have become available enabling the measurement of more degrees-of-freedom. These new developments motivated the current work. In this paper, deployment precision performance in four degrees-of-freedom is presented for hinges of two different geometries and six different composite layups.

To make HSC hinges, two opposing tape sections are bonded together at the ends using end fittings. The hinges can be folding by locally buckling the tapes to flatten them at their midspan, then bending the tapes in the flattened region to fold the hinge. An HSC hinge is shown deployed and stowed in Figure 2.

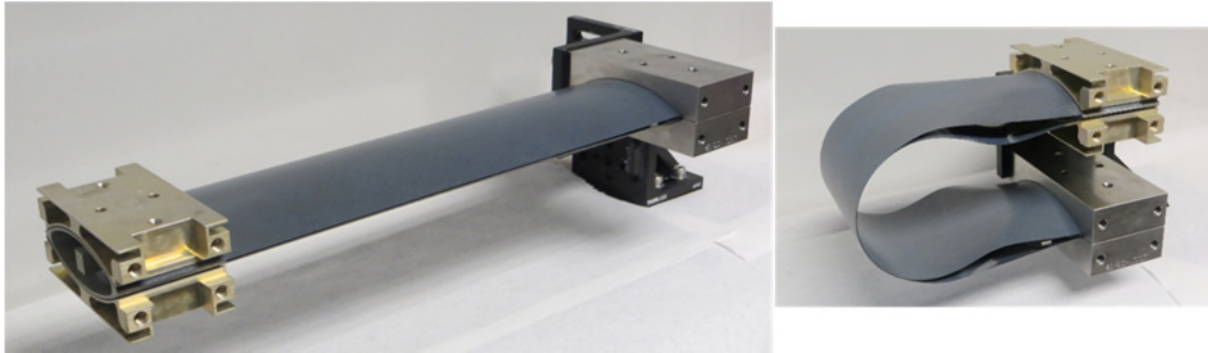


Figure 2. Hinge deployed (left) and stowed (right)

With no specific system in mind for the present study, the two HSC hinge geometries chosen for testing were selected based upon their applicability to small satellite deployable structures, available composite tooling, and available oven sizes. For CubeSat-scale small satellites, the maximum usable width along one side of the spacecraft is 8.5 cm. Using this limit as the flattened width of the tapes, only two available cylindrical composite mandrels were available to make hinges that could fold without damage: 15.2-cm (6-inch) and 10.2-cm (4-inch)-diameter mandrels. The free-edge length of 30 cm was chosen based on finite element analysis to avoid damage inducing strain concentrations near the end fittings when folded and so that the final hinge bonding can be done in an available oven.

The materials chosen for testing were based on materials available at the Air Force Research Laboratory (AFRL) Space Vehicles Directorate and the layups chosen were based on AFRL staff recommendations and previous publications.^{15, 16} The materials and layups chosen for this work are listed in Table 2. At least two tapes of each layup and diameter were made at the AFRL and provided to MITLL. At MITLL, the tapes were then trimmed to size and two tapes were bonded to end brackets to make hinge specimens. The bracket pieces for the fixed end were made from Invar to minimize thermally induced shape change. The bracket pieces for the free end were made from aluminum and significantly light weighted to minimize gravity-loading effects at the tip. The total mass of the light weighted bracket assembly is 173 grams. The base and tip bracket assemblies were bonded to the tapes in one operation using Hysol EA 9394 epoxy with 180- μ m glass beads to enforce a minimum bondline thickness. The tip and base bracket assemblies included alignment features to interface with tooling during the bonding process to set the distance and

parallelism between the tip and base. This ensured that a consistent tape free edge length was achieved for all of the test specimens

Table 2. Test specimen materials and layups

Specimen	Mandrel Diameter	Material	Angles (deg)	Total Ply Count
4-1	10.2 cm	IM7/PMT-F7 PW (a), IM10/PMT-F7 UD (b)	45(a)/0(b)/45(a)	3
4-2		IM7/PMT-F7 PW (a), IM10/PMT-F7 UD (b)	45(a)/0(b)/0(b)/45(a)	4
4-3		IM10/PMT-F7 PW	45/45	2
4-4		IM10/PMT-F7 PW	45/0/45	3
4-5		AstroQuartz (a), IM10/PMT-F7 UD (b)	45(a)/0(b)/45(a)	3
4-6		AstroQuartz (a), IM10/PMT-F7 UD (b)	45(a)/0(b)/0(b)/45(a)	3
6-1	15.2 cm	IM7/PMT-F7 PW (a), IM10/PMT-F7 UD (b)	45(a)/0(b)/45(a)	3
6-2		IM7/PMT-F7 PW (a), IM10/PMT-F7 UD (b)	45(a)/0(b)/0(b)/45(a)	4
6-3		IM10/PMT-F7 PW	45/45	2
6-4		IM10/PMT-F7 PW	45/0/45	3
6-5		AstroQuartz (a), IM10/PMT-F7 UD (b)	45(a)/0(b)/45(a)	3
6-6		AstroQuartz (a), IM10/PMT-F7 UD (b)	45(a)/0(b)/0(b)/45(a)	3

HSC Hinge Deployment Precision Testing

When HSC hinges are folded, they are under higher strain than they were in the deployed state. Under stress, the fibers in the composite can shift slightly within the matrix. In the folded position, the hinge is under stress and the fiber shifting results in a relaxation of the stress. This phenomenon is known as stress relaxation. When unfolded, over time the fibers shift back some amount to a new minimum stress state in a process known as creep recovery. In this new minimum stress state, the hinge has slightly shifted. The shape change is the deployed position error. When this fold and deploy process is repeated, the standard deviation of the test-to-test shape change is referred to as the deployment precision of the hinge in this paper.

The creep recovery behavior of the hinge specimens is related to the specimens' material properties, magnitude of applied strain, duration of applied strain and temperature. The current tests were designed to focus on the effect of stow duration and strain level on creep recovery for a set of composite layups. The applied strain level is a function of the stowed fold angle, the specimen geometry and the specimen material. Therefore, the only metrics varied in the test were stow duration, specimen material and specimen geometry. The folded hinges were strained by folding to a set angle and clamped in place, as shown in Figure 3.



Figure 3. Hinge in deployment precision measurement fixture deployed (left) and stowed (right)

Because these tests would need sub-micrometer level precision over long durations of creep recovery, position sensors with less than tens of nanometers scale errors were necessary. Temperature changes, humidity changes and vibrations in the testing environment can significantly affect measurements at this scale. Therefore, special attention was given to controlling and/or measuring the temperature change, humidity change and vibration of the specimens during testing.

Test Environment

In order to minimize temperature and humidity variation during the creep recovery, the tests were performed in a passively stabilized thermal chamber. With the doors sealed, the temperature variation within the chamber over 24 hours was generally less than 0.1 degree Celsius. The chamber also provided passive stabilization of humidity, but because the room housing the chamber was not humidity controlled the baseline humidity level did change throughout the tests. Measurements show that over a 24-hour period the humidity did not change by more than ± 1 percent. The tests were performed on a 91.4 cm x 122 cm, 90-kg optics breadboard that was isolated with respect to the surrounding floor with four Barry Controls SLM-1A passive, inflatable, air-spring isolators. The isolators did not remove all disturbances from the surrounding room, but it did decrease the resulting response levels at the test apparatus. However, because the creep recovery after each deployment was at least 15 hours and data were sampled at 1 Hz, everything but extremely low-frequency vibration in the specimen could be averaged out of the data.

The hinge deployment precision testing was performed on an Invar reference plate, as shown in Figure 4, so that the sensors at the tip of the specimen would not move significantly with respect to the base mounting point of the specimen during the tests. For the temperature variation seen in the sealed test chamber, the thermal expansion of the reference plate over 24 hours should be less than 50 nm. The Invar reference plate was mounted to the optics bench with one fixed and two flexured mounts. The flexured mounts minimize the load that is applied to the reference plate due to the thermal expansion differential between the Invar reference plate and the steel optics bench.

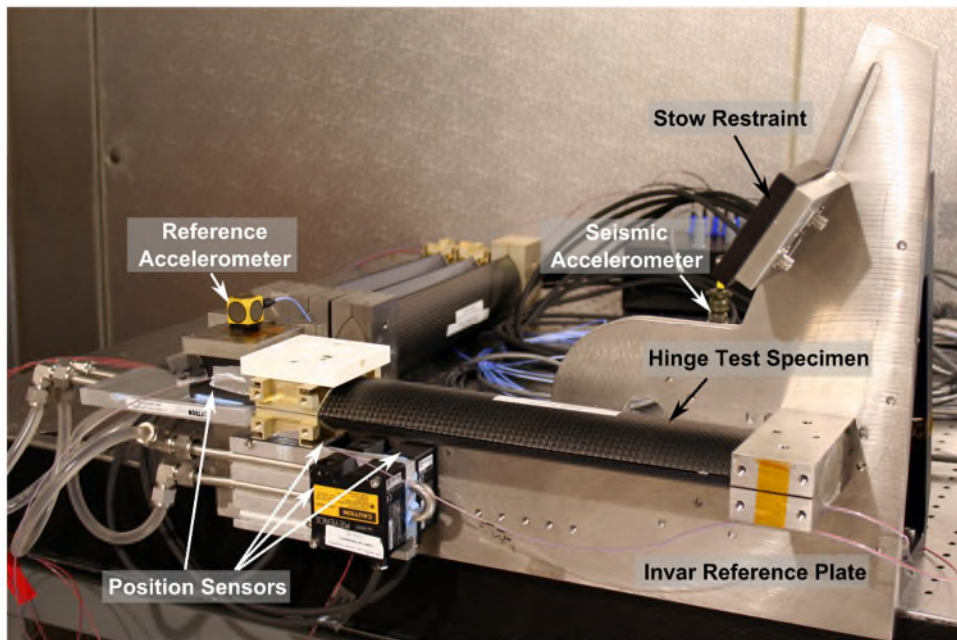


Figure 4. Hinge deployment precision test layout

The Invar reference plate also includes an adjustable stow restraint, shown in Figure 4. This provides a fixed point to stow the specimen in a repeatable manner. In order to ensure stowed position repeatability, the stow restraint contains one-half of a ThorLabs KB3X3 kinematic mounting base. At the mirror end of

the specimen, a 3D printed plastic version of the mating piece for the KB3X3 is attached for alignment when stowed. A 3D printed version was used to minimize the mass at the tip of the specimen while still enforcing good stow alignment.

Figure 4 also shows the location of some of the sensors used in the experiments. In the figure, the four laser position sensors used to measure creep recovery are shown mounted to cold plates. In order to achieve the temperature stability needed in the test chamber, the laser positions sensors needed to be actively cooled. They were cooled using a Polyscience FF-12930-38 benchtop chiller set at 20.5 degrees Celsius. Without this chiller, the temperature in the chamber would slowly increase over time due to the heat released from the laser position sensors.

Test Instrumentation

Accurate and precise position measurements are critical for the deployment precision testing. Because of the relatively small position range of interest, it was determined that only non-contact sensors could be used. Sensors that contact the tests specimen would apply a small, unknown amount of load to the specimen and most likely affect the precision measurements. After a survey of available precision, non-contact position sensors, laser displacement sensors were determined to be the best fit for this application. These sensors can provide very accurate measurements from larger stand-off distances than capacitive sensors, which was important for this application since we did not know how far from the nominal position the specimens would be initially after deployment. The sensors chosen were Keyence LK-H027 1D laser triangulation sensors. The specifications for this sensor are shown in Table 3. Based on these specifications and the 0.1-degree Celsius worst-case temperature variation during a test, the RMS error for a 10- μm measurement would be 63 nm. The Keyence LK-H027 were connected to a LK-G5001V controller unit. The controller sampled data from the sensors at 1 kHz in the diffuse reflection mode. The sensor measurements were then output from the unit as a moving mean of 4096 points. Four Keyence LK-H027 sensors were used during this experiment, as indicated in Figure 4. Three sensors were used to obtain the piston, roll and pitch of the mirror-mounting end of the specimen. The fourth sensor was used to measure axial displacement.

Table 3. Keyence LK-H027 position sensor specifications

Specification Name	Specification Value
Laser output	655 nm at 0.95 mW
Spot size	25 μm by 1400 μm
Nominal stand-off	20 mm
Range	± 3 mm
Linearity error	± 1.2 μm
Precision error	20 nm
Temperature error	0.6 $\mu\text{m}/\text{C}$

The level of precision desired from the specimens is on the same order of magnitude of what might be seen due to thermal expansion of many common materials in an unconditioned environment. Testing within the thermal chamber achieves a maximum variation of 0.1 degree Celsius over 24 hours. In order to monitor the temperatures of the test specimen, test apparatus and the test chamber, a number of temperature measurements were made during each test. A custom temperature measurement system was acquired from GEC Instruments to perform and acquire these measurements. The system is comprised of two 0.002-degree Celsius precision thermistors and five 0.02-degree Celsius precision thermocouples. One thermistor probe is located in the center of the optical breadboard and the second is located near the specimen root end of the Invar reference plate. The five thermocouples are distributed around the Invar reference plate and test specimen as shown in Figure 9. The specific location of each temperature sensors is described in Table 3. This spatial distribution of temperature measurements provides a better understanding of the temperatures at either end of the test specimen and at the sensor locations. The latter is important because of the temperature sensitivity of the laser sensors as shown in Table 2. The maximum temperature

fluctuations during a test were used to estimate the temperature related position sensor error in the test data analysis.

It is well known that composite materials expand and contract in response to humidity due to moisture absorption in the fiber and the matrix materials.¹⁸ This phenomenon is known as moisture expansion. Therefore, changes in humidity may affect the deployment precision of the specimens in these tests. As mentioned previously, the humidity is passively stabilized within the test chamber to ± 1 percent over 24 hours. While the level of moisture expansion for the specimens is not known, the humidity is measured to within 1 percent using an Omega HX92Bv0 humidity sensor so that any correlation between position change and humidity change could be identified during post processing.

During the initial testing, the vibration environment was monitored at normal structural frequency levels with two accelerometers during many of the early deployment precision tests, but no significant vibration levels were observed. Therefore, acceleration measurements were not continued beyond the first few specimen tests in order to decrease the data storage requirements for these long duration tests.

The position, acceleration and humidity measurements were all acquired using National Instruments LabView software. The Keyence LK-H027 sensors were connected to a Keyence LK-G5001V controller with a LK-HA100 controller expansion unit. Data was acquired digitally from the controller via an Ethernet connection using Keyence supplied LabView libraries at a rate of 1 Hz. The humidity measurement was acquired from the Omega HX92Bv0 using a National Instruments USB-6009 unit and sampled at 1 Hz. The data from each test was stored in a binary file which is then stored for later post-processing in MATLAB.

With all of the environmental and position measurements defined, the response of the overall test apparatus to temperature and humidity changes could be characterized. To do this, an Invar reference specimen that was a form and fit replacement for the hinge specimens was fabricated then installed and measured in the test apparatus. More details about these measurements are described in Silver et al.¹⁷ The results showed that the changes in the position measurement of the test apparatus to the range of temperature and humidity changes expected during the tests were approximately 50 nm or less.

Test Procedure

The test flow for a single specimen is shown in Figure 5. It begins with the specimen setup in the test fixture. However, before a specimen is setup in the test fixture, it is folded and unfolded at least ten times to force the majority of micro-cracking that may happen when the specimen is folded to occur before the testing begins. After the specimen is installed, the test chamber is closed out and data is recorded for at least 48 hours. The test chamber door is left closed at all times during the testing except when the specimen needs to be stowed or deployed. The measurement at the end of that initial settling period is considered the initial position that serves as the zero reference for all subsequent stow and deploy cycles. As indicated in Figure 5, a total of 10 creep recovery measurements were made for each specimen made up of three different stow durations, six tests with 360 minutes (6 hours), two tests with 36 minutes (0.6 hour), and two tests with 3600 minutes (60 hours) of stow time. The creep response after each stow cycle was measured for at least 15 hours. Including all of the stow time, recovery and any down time between tests, the full test sequence for a single specimen takes approximately 17 days.

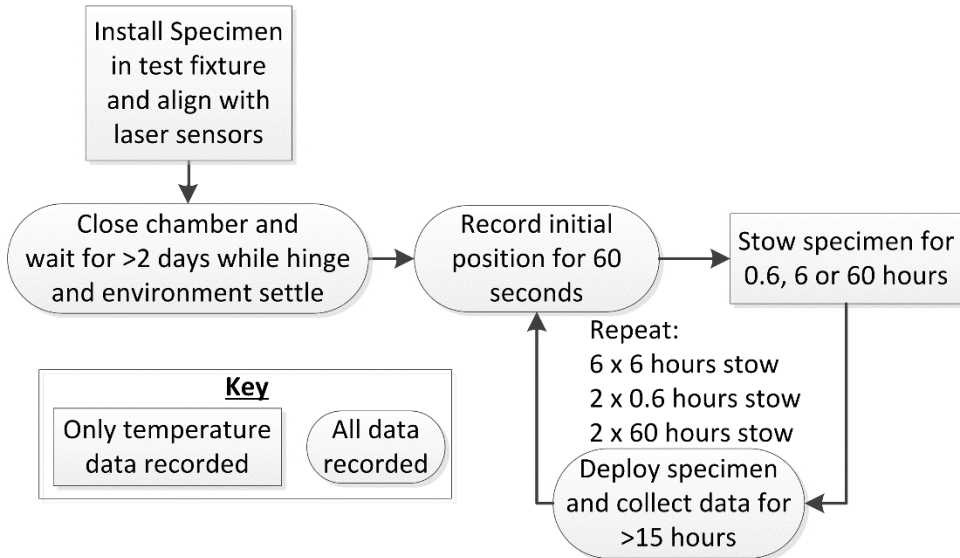


Figure 5. Test procedure flow chart

HSC Hinge Deployment Precision Results

An example of the post-processed results for all ten stow/deploy cycles for Specimen 4-6 is shown in Figure 6. In this figure, the periods with no data are either stow periods or down time after a deploy collection is complete and before the next stow. The blue points in the position plots are recovery periods, red points are the final positions before the next stow. The results for each specimen is summarized by comparing the absolute and consecutive change in the red final position data. For the tenth deployment, the final 60 seconds of recovery period data is used as the final recovered position for that cycle. A comparison of the absolute and consecutive change for the results shown in Figure 6 is provided in Figure 7. The results shown in Figure 7 highlight the fact that although the recovered position may drift over all ten stow and deploy cycles, the test-to-test change remains relatively small. This is the real performance metric needed for the planned application since the hinges will be folded up for launch then unfold a single time in orbit.

Two other characteristics were common in most of the specimen measurements. The first is the relatively large amplitude of the noise in the pitch data when compared to the other axes, which is evident in Figure 6. This is due to the small level of pitch error measured and the small baseline between the sensor positions for this measurement, which amplifies the measurement noise in this result. The second is the large position change that occurred after the first stow. While it is not as evident in the Specimen 4-6 data shown above, it is evident in many of the other specimens. This may be indicative of a one-time setting of the majority of the non-recoverable stress relaxation in the folded hinge. Therefore, in calculating the deployment precision data for the specimens only the consecutive position error for tests 2-10 are used.

The final deployment precision data for all test specimens is shown in Table 4. Results from Specimen 4-2 are not included because it failed due to creep rupture during the third stow period. Results from Specimen 6-3 are not included because it was not tested based on the poor results for this material demonstrated in Specimen 4-3. The hinge testing showed that two of the six composite layups demonstrated piston precision within 0.53 μm , pitch and roll precision within 5.9 μrad and axial precision within 0.36 μm . This level of piston and axial deployment precision with a passive hinge is similar to the best measurements presented by Domber et al after thermal bias was removed. Initial analysis of the current data to remove thermal bias show marginal improvement in deployment precision. These results will be included in future publications.

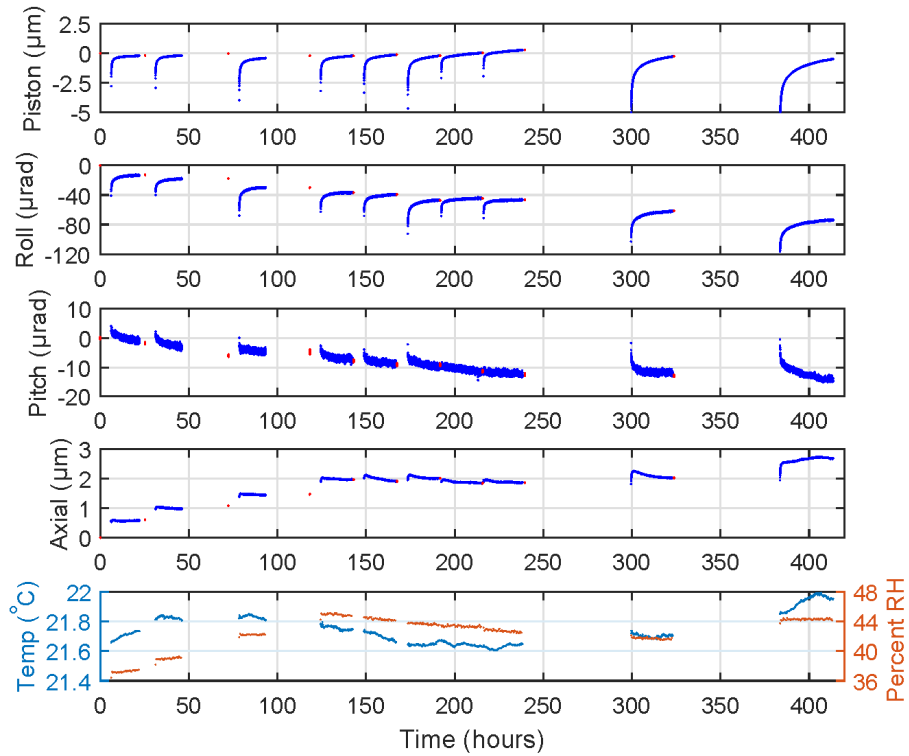


Figure 6. Creep recovery data for specimen 4-6 versus calendar time (blue lines are recovery, red circles are final position before next stow)

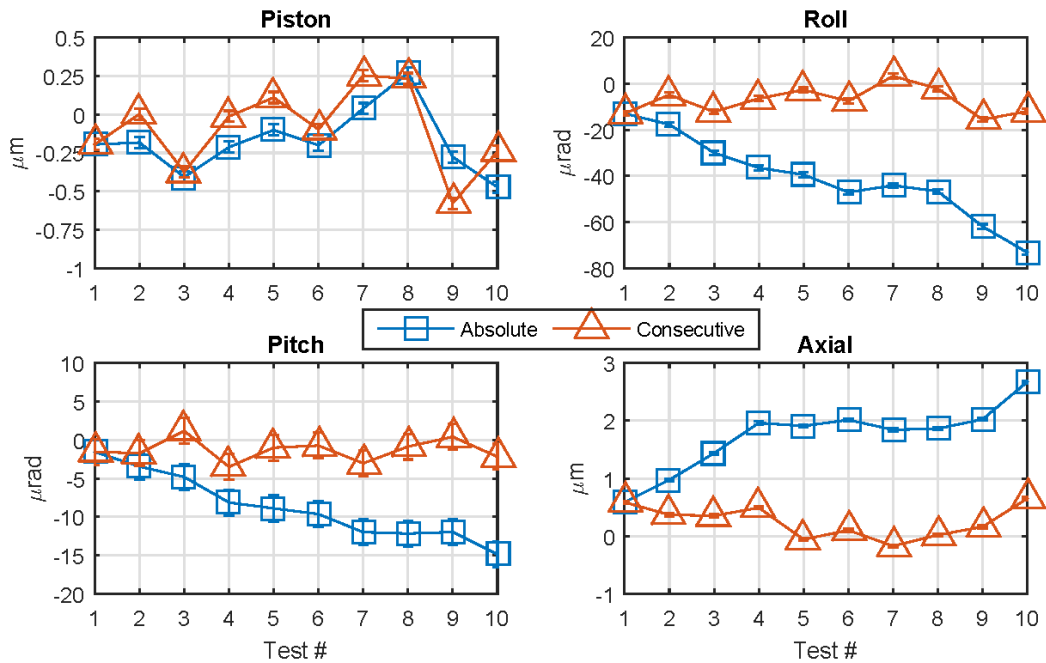


Figure 7. Absolute and consecutive relative position error for Specimen 4-6 for each test along with RSS measurement error

Table 4. Hinge deployment precision results

Measurement	RSS Error	4-1	4-3	4-4	4-5	4-6	6-1	6-2	6-4	6-5	6-6
Piston (μm)	0.04	1.26	19.91	1.32	0.53	0.27	1.38	0.80	1.58	0.38	0.39
Roll (μrad)	1.01	6.48	50.39	3.47	3.05	5.83	7.04	2.05	5.86	5.16	3.76
Pitch (μrad)	1.67	5.94	18.69	5.3	4.34	1.49	5.73	2.25	12.89	4.43	2.36
Axial (μm)	0.02	0.17	0.64	0.36	0.26	0.27	0.31	0.14	0.51	0.09	0.25

HSC Frame

After sub-micron deployment precision of HSC hinges had been demonstrated, the question remained as to whether sub-micron deployment precision could be achieved in a complex structure assembled from multiple HSC hinges. Although frames using HSC tapes have been developed before^{13,19}, HSC hinge based frames with sub-micron level deployment precision have not been demonstrated in the literature. To investigate the potential precision of a deployable frame, a deployable frame test article was designed that uses HSC hinges at each hinge point. A diagram of the frame and test apparatus is shown in Figure 8. The deployable frame is made up of low Coefficient of Thermal Expansion (CTE) carbon fiber tubes connected to HSC hinges. The hinges used in the frame are smaller than those presented previously in this paper. The hinges have a 12.7-cm free-edge length and are made from tapes with 5.04-cm-diameter curvature and 2.54-cm flat width. The material used in these hinges are made with the -6 layup defined in Table 2. The hinges are made with aluminum end fittings and are bonded to the low CTE tubes with Hysol EA 9394 epoxy. At these bond joints, the composite tapes and the low CTE tubes overlap by approximately 12 mm, so there is no portion of the frame expanse that does not contain composite materials. This is important because if a portion of the frame expanse was aluminum it would have much higher thermal expansion. The frame is bonded to the metrology frame through Invar joints. The mounting frame is fixed to the optical bench in the test chamber using thermal expansion flexures so that shape change in the optical bench is not transferred to the metrology frame. The final frame test article and metrology frame are shown in the stowed and deployed configurations in Figure 9.

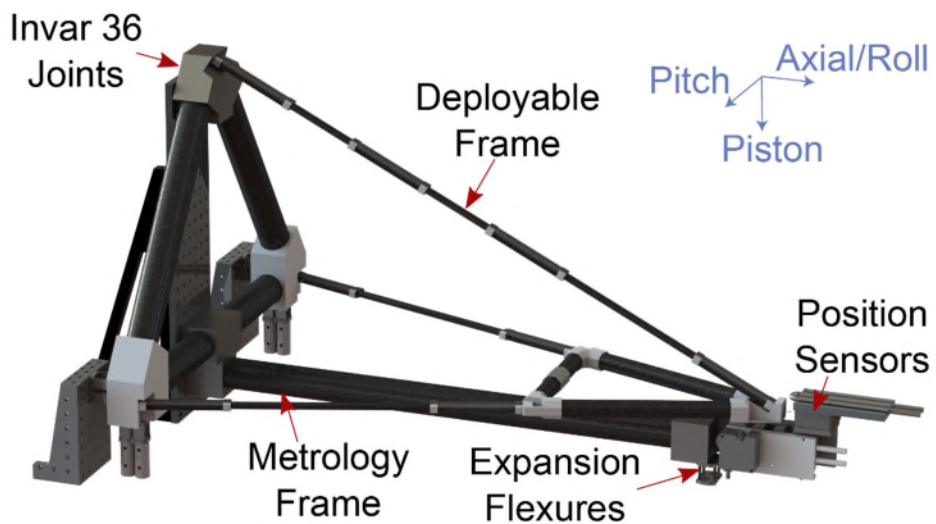


Figure 8. HSC frame deployment precision test setup



Figure 9. HSC frame in test chamber deployed (left) and stowed (right)

The frame deployment precision testing used the same sensors, test chamber and test sequence as described previously for the hinge. The initial round of deployment precision testing was performed in the orientation shown in Figure 9, with gravity pulling the tip of the frame down in the positive piston direction. The frame was held in a fixture when stowed, also shown in Figure 9, with the goal of having a repeatable stowed position for each test.

HSC Frame Deployment Precision Results

The deployment precision data obtained for the frame is shown in Figure 10. Based on these results the piston deployment precision is $2.3 \mu\text{m}$, the pitch and roll precision is less than $6.3 \mu\text{rad}$ and axial precision is $0.24 \mu\text{m}$. Two potential sources of unintended experimental error can be seen in the data from Figure 10. First, the piston creep-recovery data showed continuous drift over time that can most likely be attributed to gravity. Because the test-to-test deployment precision was determined from the final position before the next stow in the test sequence and the duration of recovery was varied from 15 hours to 180 hours, gravity shift over time potentially increased the deployment precision error during these tests. Second, a significant bias in piston position can be seen after stow 7, which is the creep recovery period between approximately 240 hours and 340 hours in Figure 10. A relatively large bias in piston position like this was not present in any of the hinge data. One potential source of the bias may be a variation in the stowed shape in the eighth stow. When the frame is folded, it is fairly compliant and has many possible stable configurations. It could be that the stowed frame was in a slightly different stowed configuration during this stow periods which led to a different stress-relaxation state than other stows. If this test is removed from the data, the deployment precision error decreases from $2.3 \mu\text{m}$ to $1.7 \mu\text{m}$. In order to address these potential unintended error sources, a new round of testing is being performed with the frame oriented vertically, as shown in Figure 9. The results from these tests will be in a future publication.

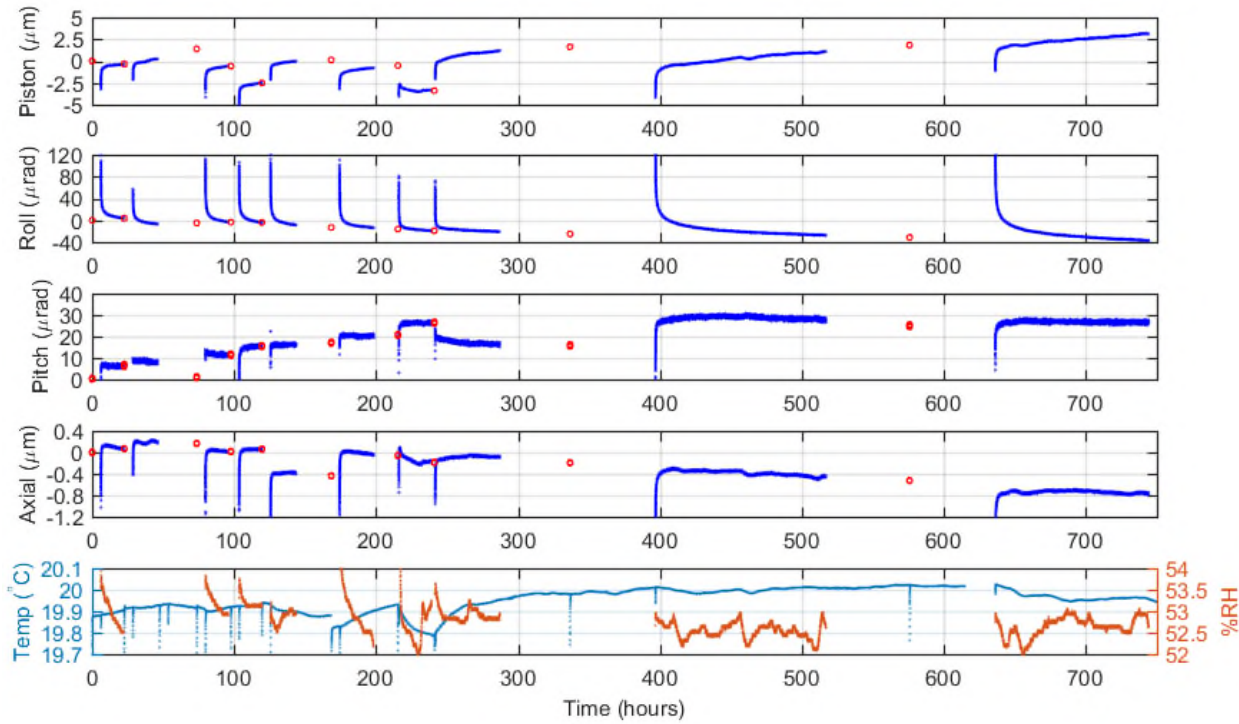


Figure 10. HSC frame creep recovery data versus calendar time (blue lines are recovery, red circles are final position before next stow)

Conclusions

This work has demonstrated the level of deployment precision achievable for several HSC hinges and a frame built from multiple HSC hinges. The deployment precision for the best performing hinges, the frame and several other precision deployable structures from the literature are presented in Table 5. As can be seen from this table, the current HSC hinge and frame measurements show a significant improvement over the JWST DOTA and other non-HSC deployable structures and are the first to include both roll and pitch precision. The level of precision demonstrated by the structures in this paper are still not sufficient for final alignment for visible-wavelength optical systems. Nonetheless, metrology and position actuation to correct for sub-micrometer position error can be much simpler than what is needed for less precise systems, such as JWST. To support the development of future HSC precision deployable telescopes, MITLL is currently developing actuation and metrology methods that take advantage of the precision enabled by HSC hinges.

Table 5. Previous optical deployable structure deployment precision measurements

Test Article	Piston (μm)	Axial (μm)	Roll (μrad)	Pitch (μrad)
JWST DOTA ¹⁰	20	30	-	44
IFH Specimen 2 ¹²	0.85	0.31	-	-
EDSM ¹¹	2.97	2.97	-	-
Lidar Prototype ¹¹	8.59	0.81	-	-
MITLL HSC Hinge 6-6	0.39	0.25	3.76	2.36
MITLL HSC Frame	2.27	0.24	4.01	6.28

References

1. Lightsey, P. A., Atkinson, C., Clampin, M., and Feinberg, L. D., "James Webb Space Telescope: large deployable cryogenic telescope in space," *Optical Engineering*, Vol. 51, No. 1, 2012.
2. Hedgepeth, J. M., "Support structures for large infrared telescopes," *NASA Contract Report 3800*, 1984.
3. Hedgepeth, J. M., "Structures for remotely deployable precision antennas," *NASA Contract Report 181747*, 1989.
4. Mikulas Jr, M. M., Collins, T. J., and Hedgepeth, J. M., "Preliminary design approach for large high precision segmented reflectors," *NASA-TM-102605*, 1990.
5. Rogers, C., Stutzman, W., Campbell, T., and Hedgepeth, J., "Technology Assessment and Development of Large Deployable Antennas," *Journal of Aerospace Engineering*, Vol. 6, No. 1, 1993, pp. 34-54.
6. Warren, P. A., Peterson, L. D., and Hinkle, J. D., "Submicron mechanical stability of a prototype deployable space telescope support structure," *Journal of spacecraft and rockets*, Vol. 36, No. 5, 1999, pp. 765-771.
7. Lake, M. S., Peterson, L. D., Mikulas, M. M., Hinkle, J. D., Hardaway, L. R., and Heald, J., "Structural concepts and mechanics issues for ultra-large optical systems," *1999 Ultra Lightweight Space Optics Workshop*, 1999.
8. Oegerle, W. R., Feinberg, L. D., Purves, L. R., Hyde, T. T., Thronson, H. A., Townsend, J. A., Postman, M., Bolcar, M. R., Budino, J. G., Dean, B. H., Clampin, M. C., Ebbets, D. C., Gong, Q., Gull, T. R., Howard, J. M., Jones, A. L., Lyon, R. G., Pasquale, B. A., Perrygo, C., Smith, J. S., Thompson, P. L., and Woodgate, B. E., "ATLAST-9.2m: a large-aperture deployable space telescope," Vol. 7731, 2010.
9. Feinberg, L. D., Budinoff, J., MacEwen, H., Matthews, G., and Postman, M., "Modular assembled space telescope," *Optical Engineering*, Vol. 52, No. 9, 2013.
10. Reynolds, P., Atkinson, C., and Gliman, L., "Design and Development of the Primary and Secondary Mirror Deployment Systems for the Cryogenic JWST," *37th Aerospace Mechanisms Symposium*, 2004.
11. Heald, J. C., and Peterson, L. D., "Deployment Repeatability of a Space Telescope Reflector Petal," *Journal of Spacecraft and Rockets*, Vol. 39, No. 5, 2002, pp. 771–779.
12. Domber, J. L., Hinkle, J. D., Peterson, L. D., and Warren, P. A., "Dimensional Repeatability of an Elastically Folded Composite Hinge for Deployed Spacecraft Optics," *Journal of Spacecraft and Rockets*, Vol. 39, No. 5, 2002, pp. 646-652, doi:10.2514/2.3877.
13. Murphey, T. W., Francis, W., Davis, B., and Mejia-Ariza, J. M., "High strain composites," *2nd AIAA Spacecraft Structures Conference*, 2015.
14. https://www.nasa.gov/mission_pages/station/research/experiments/2139.html#publications
15. Pollard, Eric L., and Thomas W. Murphey. "Development of deployable elastic composite shape memory alloy reinforced (DECSMAR) structures." *47th AIAA Structures, Structural Dynamics, and Materials Conference*. 2006.
16. Peterson, Michael. *High Shear Strain Characterization of Plain Weave Fiber Reinforced Lamina*. Master's Thesis, University of New Mexico, 2015.
17. Silver, Mark J., Michael A. Echter, Bryan M. Reid, and Jeremy A. Banik. "Precision High-Strain Composite Hinges for the Deployable In-Space Coherent Imaging Telescope." In *3rd AIAA Spacecraft Structures Conference*. 2016.
18. Wolff, Ernest G. *Introduction to the dimensional stability of composite materials*. DEStech Publications, Inc, 2004.
19. Black, Jonathan T., Jeffrey A. Whetzel, Brett J. DeBlonk, and Jack J. Massarello. "Deployment repeatability testing of composite tape springs for space optics applications." In *Proceedings of the 47th AIAA/ASME/ASCE/AHS/ASC Structures, Structural Dynamics, and Material Conference*, pp. 1-4. 2006.

The Synchronization Mechanism for Solar Array with a Three-Stage Deployment

Zehong Yan*, Hongjun Shang*†, Guowei Zhao**†, Qiaolong Yang*, Jingya Ma* and Jianjun Wang*

Abstract

Cable-and-pulley system (also called Closed Cable Loop, CCL) is a common type of synchronization mechanism to coordinate the motion of a multiple panel solar array. Typically, in applications the transmission ratio of a cable-and-pulley system is constant during the deployment. For other applications, the synchronization characteristic can be changed by varying the configuration of the pulley. The solar array of GF-3, a satellite operating on dawn-dust orbit, required a particular kind of two-stage deployment: during the first stage the four-panel stack rotates 90° around the root hinge; during the second half the root hinge rotates from 90° to 180° and each panel hinge rotates from 0° to 180° synchronously. The unique feature of the GF-3 solar array synchronization mechanism is that the root pulley consists of two half pulleys: a fixed pulley and a swing pulley. The design of such a root pulley changes the ratio between the root hinge and panel hinge. Although the deployment of the solar array contains three stages actually, the trajectory approximately meets the requirement. The detailed working principles and considerations of the synchronization mechanism are provided. The synchronization mechanism has been proven both in ground test and flight.

Introduction

GF-3 is a satellite operating on dawn-dust orbit, equipped with two deployable solar array wings^[1]. There is a particular layout of the solar array, characterized by the axis of rotation of the solar array drive mechanism parallel (rather than the more common normal) to the mounting surface of the solar array on the satellite. The root hinge must deploy 180 degrees, but more importantly, the trajectories of all panels have to be confined to a limited area that requires a two-stage deployment movement of the panels as shown in Figure 1.

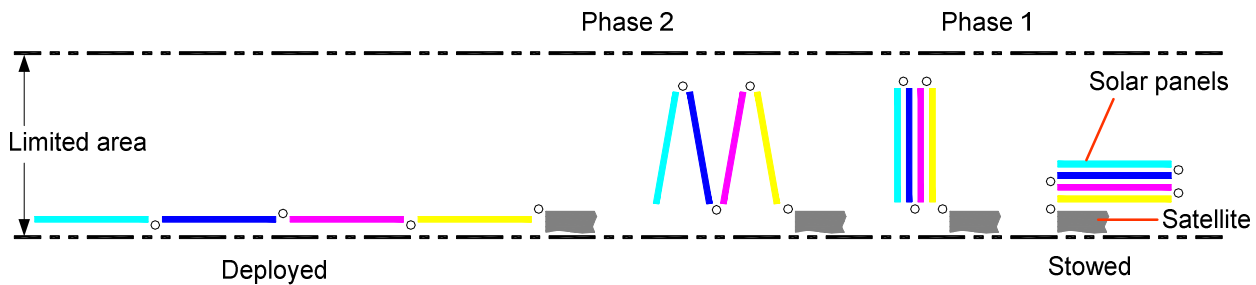


Figure 1. The two-stage deployment

There are several ways to achieve the trajectory, such as adding a special latch at 90°stroke of the root hinge. However, varying the synchronization characteristic is a better choice for this application due to the key advantages, such as simplicity, reliability, light weight, and more importantly, continuous controllable deployment and ability to reverse at any position. On the basis of the traditional cable-pulley system, the trajectory can be changed by varying the roll-on and roll-off rules of the root cables, and the key is how to

* Beijing Institute of Spacecraft System Engineering, Beijing, China

** Beihang University, Beijing, China

† denotes corresponding authors

derive the profile of the root pulley. Yannick Baudasse presented a new synchronization concept of solar array deployment used in Cosmo SkyMed [2]. The root pulley is changed into two parts: an unwinder arm and a winding with special contour. At the first 90° of deployment, root cables neither roll on nor roll off and just overpass the axis of rotation. After 90°, the arm begins to swing and the cable which it is attached to rolls off. Then, another root cable begins to wind on the winding, which means roll on. So, there is a nonlinear synchronization ratio between root hinge and panel hinge. Frans Doejaaren presented another solution used in Sentinel 1 [3]. The root pulley consists of two coupled pulleys that are offset when installed and use different radii. This adapted design changes the roll on and roll off characteristics of the cables such that the wing deploys approximately as required. The above two methods are simple enough, but resulted in the actual trajectory with more than acceptable deviation from the ideal one.

In the development of the GF-3 solar array, we found a synchronization method that could reduce the deviation remarkably. The method is an improvement on Yannick's design. The improved deployment of the solar array contains three stages. During the first stage, the four-panel stack rotates about 70° driven by the root hinge. During the second stage, the root hinge rotates from 70° to 110°, and each panel hinge rotates from 0° to 40° following a changing ratio (from null to 2:1) with respect to the root hinge. During the third stage, the root hinge rotates from 110° to 180°, and each panel hinge rotates from 40° to 180° following a 2:1 ratio. Although the synchronization ratio during the second stage is nonlinear, the process is transient. Therefore, the actual trajectory is much closer to the ideal trajectory.

The unique feature of the GF-3 solar array synchronization mechanism is that the root pulley consists of two half pulleys with same radii: a fixed pulley and a swing pulley, which is shown in Figure 2. In the folded state, the center of the swinging pulley is away from the center of the fixed pulley. During the first deployment stage, the root cables show the same performance as Yannick's. During the second stage, the swinging pulley gradually approaches the fixed pulley. The cable attached to swinging pulley rolls off. At the same time, the other root cable rolls on the fixed pulley. At the end of the second stage, the center of the swinging pulley coincides completely with the center of the fixed pulley to form a complete root pulley. During the third stage, the synchronization characteristic is identical to the traditional cable-pulley system.

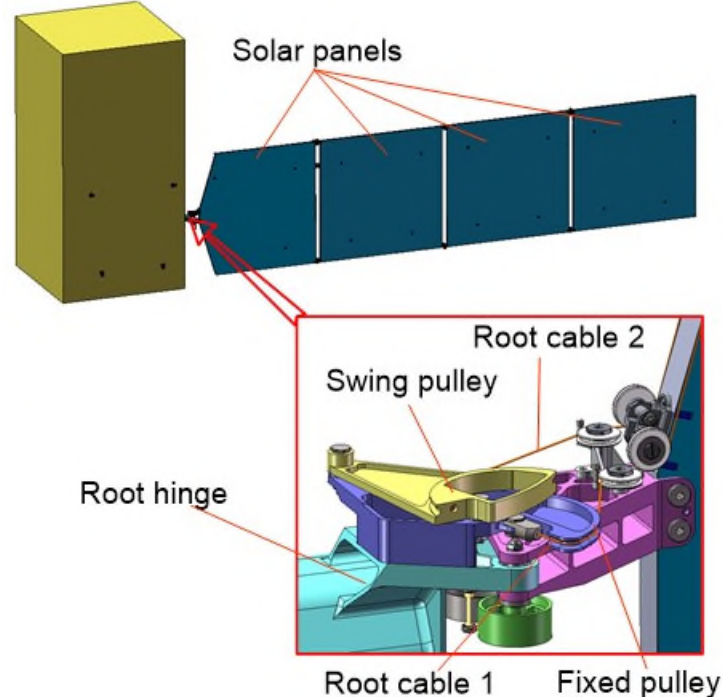


Figure 2. The root pulley of GF-3 solar array

Description of Synchronization Method

Overview

According to the requirement for solar array deployment, the angular velocity ratio between the panel hinge and root hinge is 0:1 during the first stage, and 2:1 during the second stage. In a cable-and-pulley system, only with zero radii of root pulley could the ratio be 0:1, which means that the cables should be placed across the axis of the root hinge. Nevertheless, due to the ratio 2:1, the radii of root pulley should be twice than the panel pulley in phase 2. That is to say, there is a “snap action” of the root pulley between phase 1 and phase 2, which is the main design challenge of synchronization mechanism.

It is hard to achieve that the radii of the root pulley rises suddenly from 0 to twice of the panel pulley. Meanwhile, the angular velocity of the panel hinge will increase immediately from 0 to twice of the root hinge even if the radii of root pulley can be changed successfully. This would cause a shock that is detrimental to deployment. The more important aspect of the requirement is that the trajectories of the mass centers of all panels have to be confined to a limited area. Therefore, it is a significant design challenge to add a transition between phase 1 and phase 2. The ratio needs to change smoothly from 0:1 to 2:1 with no jerk, and the trajectories must meet the requirement.

In a cable-and-pulley system, the rotation of the hinges is coordinated by the cables rolling on and rolling off the pulleys. If the cable rolls on the pulley during rotation, it must roll off on the other side due to the constant length of cable. If there is a reference point located on an intermediate position of the cable, the distance between the point and pulley decreases when rolling on, and increases when rolling off. Therefore, the mechanism that can alter the distance will perform the same function as the pulley. In GF-3, the root pulley is substituted by two half pulleys: a fixed pulley and a swing pulley, with the result that the ratio can change smoothly from 0:1 to 2:1.

Fixed Pulley and Cable

The schematic of the fixed pulley and cable during the deployment is shown in Figure 3. The fixed position of the cable passes through the spin axis of the root hinge. In phase 1, the cable rotates around the spin axis, but the distance between the reference point and fixed pulley is constant during the deployment. Therefore, the cable need not roll off the panel pulley on the other side. In phase 2, the cable rolls on the fixed pulley gradually during the rotation, and the distance between the reference point and pulley decreases at the same time. At the end of phase 2, the cable makes tangential contact with the circular contour of fixed pulley. The ratio between panel hinge and root hinge becomes 2:1 for the radii of the fixed pulley is twice of the panel pulley. In phase 3, the cable rolls on the fixed pulley continually, and the process is consistent with a traditional cable-pulley system.

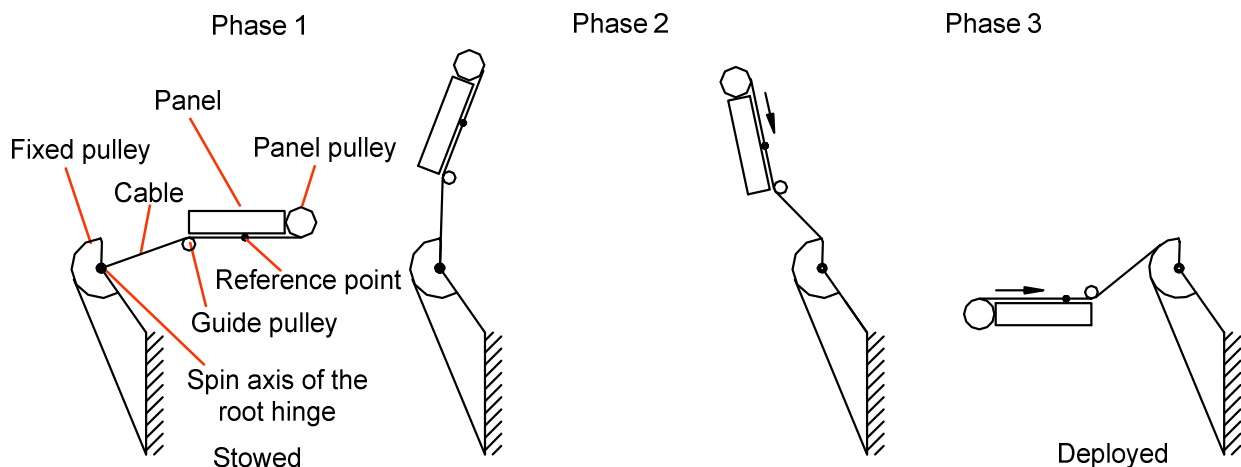


Figure 3. The schematic of fixed pulley and cable

Swing Pulley and Cable

The schematic of the swing pulley and cable during the deployment is shown in Figure 4. The cable winds on the swing pulley at the stowed configuration. In phase 1, the swing pulley tends to rest on the right stop by the tension of cable. The cable rotates around the axis of root hinge, where it contacts with the swing pulley. The distance between the reference point and swing pulley is constant during the deployment. At the end of phase 1, the extended line of cable between guide pulley and swing pulley just crosses the axis of the swing pulley. In phase 2, the swing pulley rotates counterclockwise and is apart from the right stop by the tension of cable. The distance between the reference point and swing pulley increases at the same time. At the end of phase 2, the swing pulley rests on the left stop, and the cable just makes tangential contact with the circular contour of swing pulley. The center of swing pulley's circular contour overlaps the axis of the root hinge at the same time. In phase 3, the cable rolls off the swing pulley continually, and the process is in accordance with a traditional cable-pulley system.

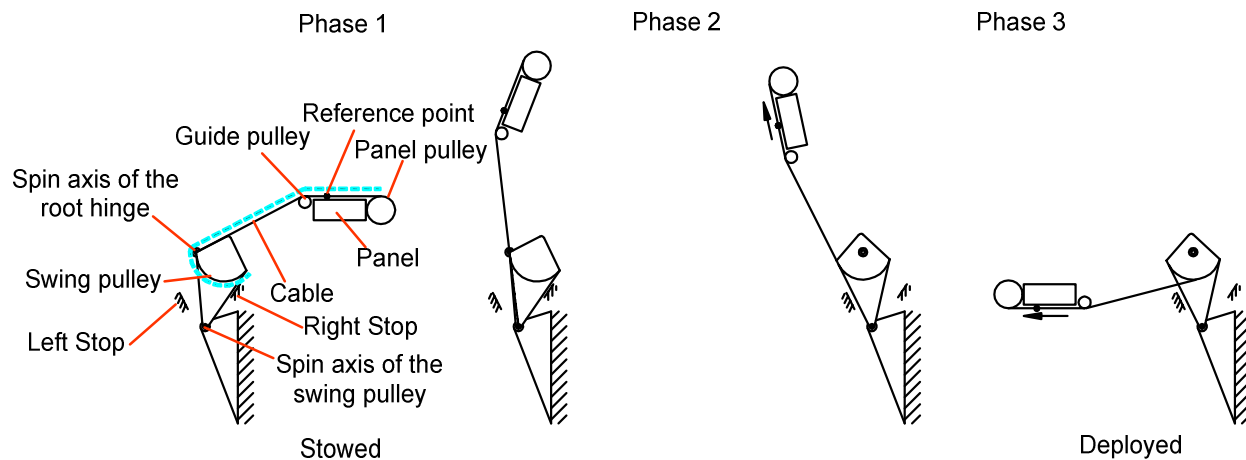


Figure 4. The schematic of swing pulley and cable

Deployment of Solar Array

Both the cable-fixed-pulley system and cable-swing-pulley system have a three-stage synchro process, which is the underlying premise for the deployment function. Furthermore, although they are installed separately, they must be kept consistent during deployment. The deployment of the solar array with two panels coordinated by such a cable-pulley system is shown in Figure 5. It illustrates an approximate synchronization principle. In phase 1, the outer panel keeps stacked with the inner panel because both cable 1 and cable 2 cross the axis of root hinge during deployment. In phase 2, the reference point 1 moves away from the panel pulley along with the cable 1 rolling on the fixed pulley gradually. Meanwhile, the reference point 2 approaches the panel pulley due to the swing pulley rotating off center of the axis of root hinge. The outer panel deploys against the inner panel. At the end of phase 2, the center of the swinging pulley coincides completely to the center of the fixed pulley to form a complete root pulley, and both of the cables make tangential contact with the root pulley. In phase 3, all panels deployed synchronically.

Phase 2 is the key process of the deployment. There are several problems that must be solved including:

- When should it start and finish?
- In such a cable-pulley system, the length of the cables rolling on the fixed pulley and rolling off the swing pulley must match with each other well. However, there is an obvious structural difference between the fixed pulley and swing pulley. How can they adapt to each other?

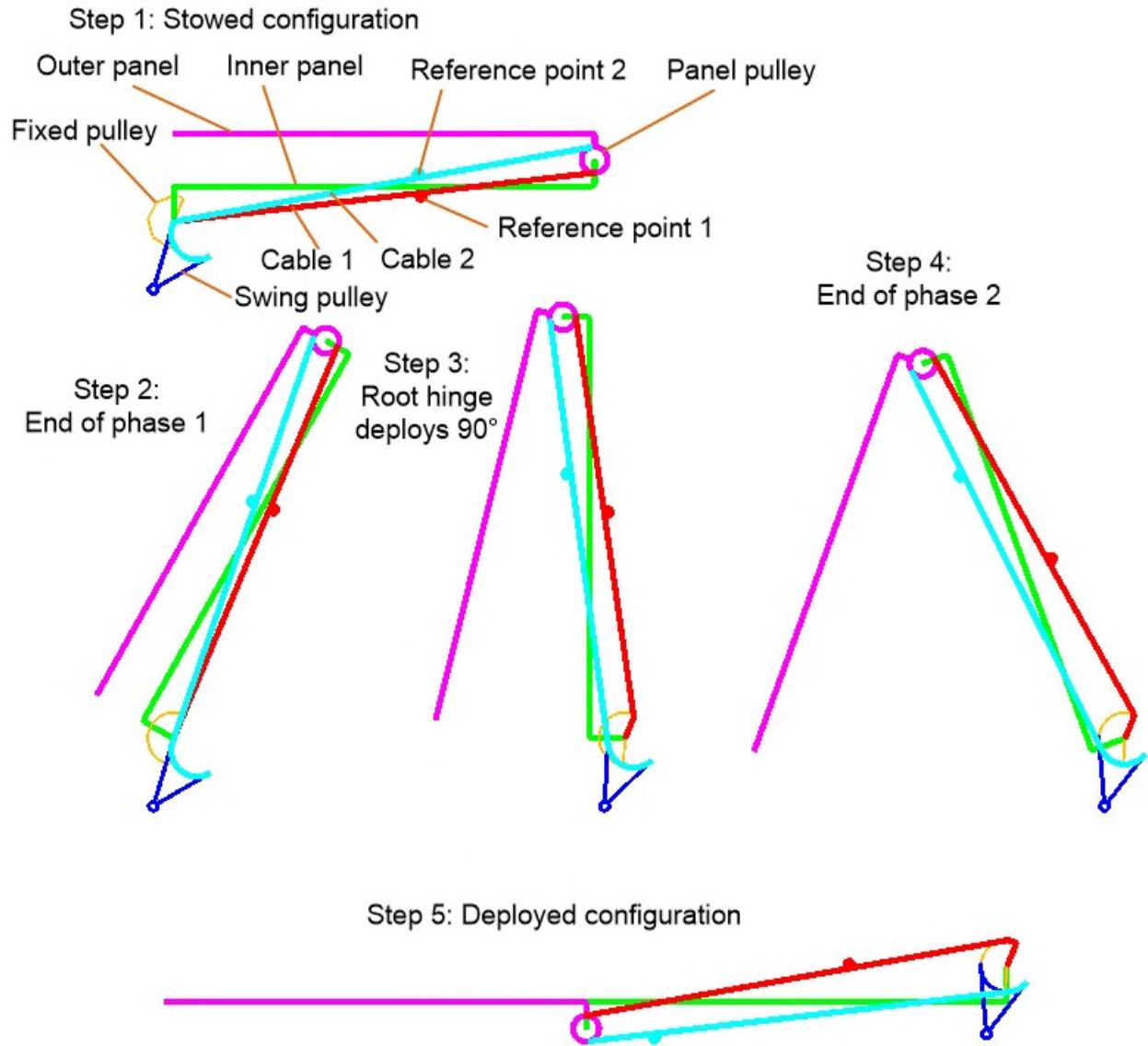


Figure 5. Deployment of solar array

Design and Analysis

Mathematical Model

Although the synchronization mechanism is not significantly bulkier than the standard one, the motion is much more complex. The baseline concept must be optimized by the mathematical model. The length of the cables is the only connection between the fixed pulley and swing pulley. Therefore, the mathematical models of the fixed pulley and swing pulley should be established respectively.

The mathematical model of the fixed pulley in phase 2 is shown in Figure 6. The displacement of the reference point on the cable is equal to the length variation of the cable between the guide pulley and the center of fixed pulley where the cable is fixed. The length variation is an important parameter that is derived from the following set of equations.

$$\Delta L_f = (\widehat{A'B'} + B'C + OC) - (\widehat{AB} + OB) \quad (1)$$

Where ΔL_f – the length variation of the cable
 A, A' – the tangency point between the cable and guide pulley
 B, B' – the other tangency point between the cable and guide pulley
 C – the point where the cable contacts with fixed pulley
 O – the center of the fixed pulley and also the axis of root hinge
 OC – equal to the radii of the fixed pulley

The model can be simplified if the radii of guide pulley is ignored. Equation 1 can be simplified to:

$$\Delta L_f = A'C + OC - OA = A'C + OC - OA' = \sqrt{OC^2 + OA^2 - 2 \cdot OC \cdot OA \cdot \cos \theta} + OC - OA \quad (2)$$

Where θ – the angle of root hinge rotation

Equation 2 defines phase 2. Particularly, at the end of phase 2:

$$OA = \frac{OC}{\cos \theta} \quad (3)$$

If root hinge rotated an angle α in phase 1, then ΔL_f and θ must meet the constraint:

$$2(\pi - \alpha - \theta) = \pi - \frac{2\Delta L_f}{OC} \quad (4)$$

In Equation 4, $(\pi - \alpha - \theta)$ is the angle of root hinge rotation in phase 3, while $\pi - \frac{2\Delta L_f}{OC}$ is the angle of the panel hinge rotating in phase 3

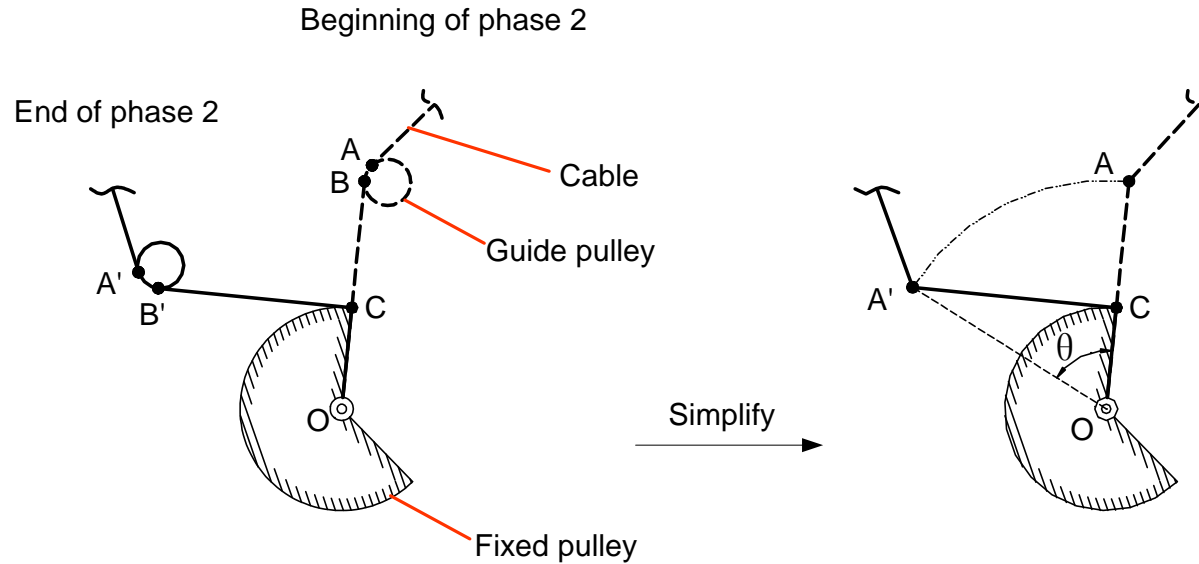


Figure 6. Mathematical model of the fixed pulley

The mathematical model of the swing pulley can be created similarly, which is shown in Figure 7. The relationship of the parameters can be described by Equation 5.

$$\Delta L_s = (\widehat{A_1B_1} + B_1C_1) - (\widehat{A'_1B'_1} + B'_1C'_1) \quad (5)$$

Where ΔL_s – the length variation of the cable
 A₁, A'₁ – the tangency point between the cable and guide pulley
 B₁, B'₁ – the other tangency point between the cable and guide pulley
 C₁, C'₁ – the point where the cable contacts with the swing pulley

O_1 – the axis of the root hinge

The model can be simplified with the radii of guide pulley ignored. Equation 5 can be simplified to:

$$\begin{aligned}\Delta L_s &= A_1 C_1 - A'_1 C'_1 = A'_1 O_1 + O_1 P_1 - A'_1 P_1 \\ &= O_1 A_1 + O_1 P_1 - \sqrt{O_1 A_1^2 + O_1 P_1^2 - 2 \cdot O_1 A_1 \cdot O_1 P_1 \cdot \cos(\pi - \theta)}\end{aligned}\quad (6)$$

Where θ – the angle of root hinge rotation
 P_1 – the axis of the swing pulley

Equation 6 defines phase 2. Particularly, at the end of phase 2:

$$\theta = \sin^{-1} \frac{OC}{O_1 A_1} + \sin^{-1} \frac{OC}{O_1 P_1} \quad (7)$$

Where OC – equal to the radii of the fixed pulley or swing pulley

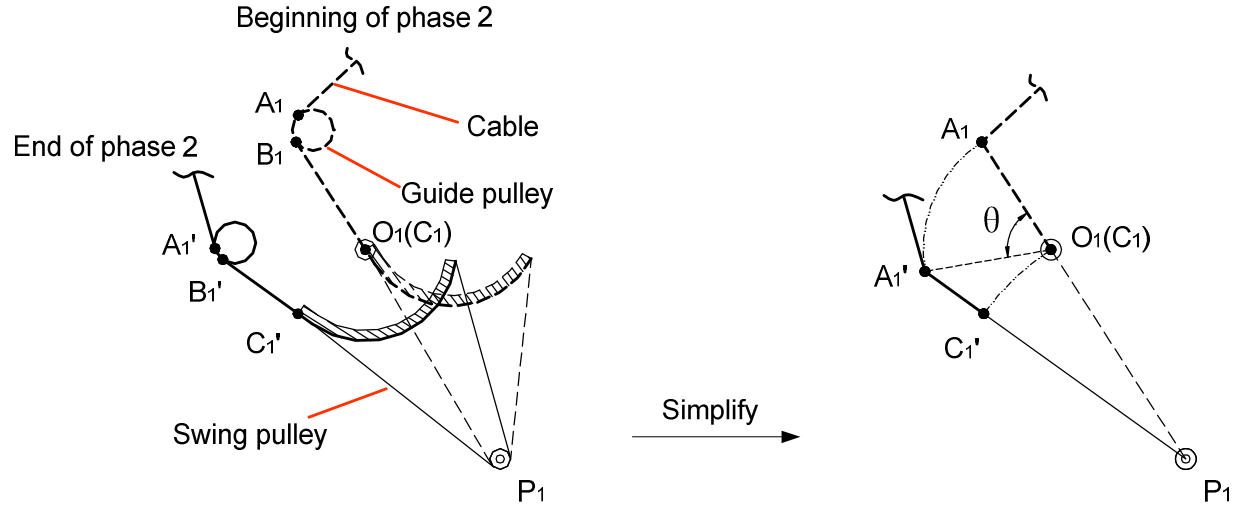


Figure 7. Mathematical model of the swing pulley

Examining Equations 2 and 6, we draw the conclusion that either the cable rolling on the fixed pulley or rolling off the swing pulley uses the characteristic of a triangle in geometry ($\Delta A'CO$ in Figure 6 and $\Delta A'_1 O_1 P_1$ in Figure 7), though there is an obvious structural difference between them.

In order to make the fixed pulley and swing pulley work consistently during phase 2, ΔL_s must be equal to ΔL_f at any moment. Unfortunately, the radii of guide pulley cannot be ignored due to its effect on ΔL_f and ΔL_s . The equations should be more complicated in engineering application, and it is too difficult to find an analytic solution. It is a simple and effective way to perform a numerical analysis.

Result of Design

In the development of the synchronization mechanism, the dimensioning parameters were determined by the result of numerical analysis. The length variation tolerance between rolling on cable and rolling off cable ($\Delta L_f - \Delta L_s$) is shown in Figure 8. The minimum was -0.47 mm during the deployment while the maximum was +0.65 mm. The tolerance was small enough to be accepted because the total length of each cable was more than 2000 mm.

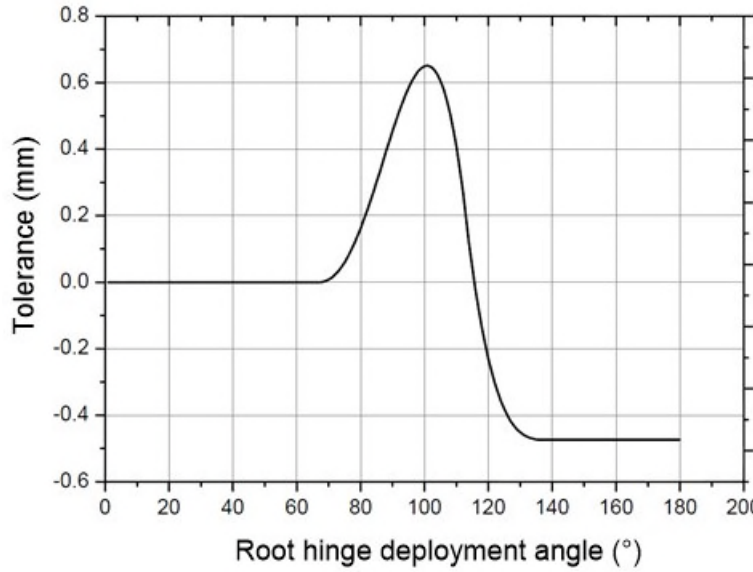


Figure 8. The length variation tolerance

The synchronization characteristic is shown in Figure 9. The nominal characteristic was fully compatible with the ideal one before 70° and after 110° of root hinge rotation. There was a transient and smooth transition in nominal characteristic between 70° and 110° of root hinge rotation.

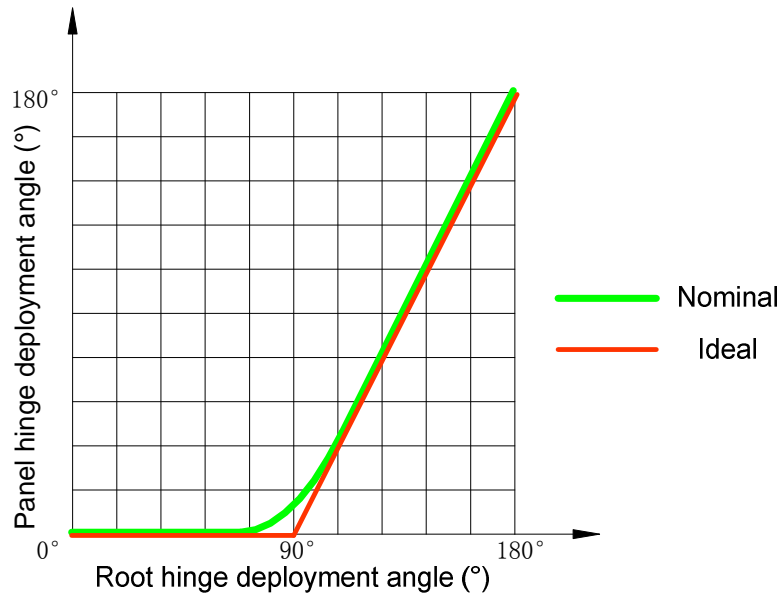


Figure 9. The synchronization characteristic

Figure 10 shows the configuration of the fixed pulley and swing pulley that are installed on the root hinge at the deployed state. The deployment of root hinge can be divided into three stages that shown in Figure 11. It illustrates the state of the pulleys and cables during the deployment.

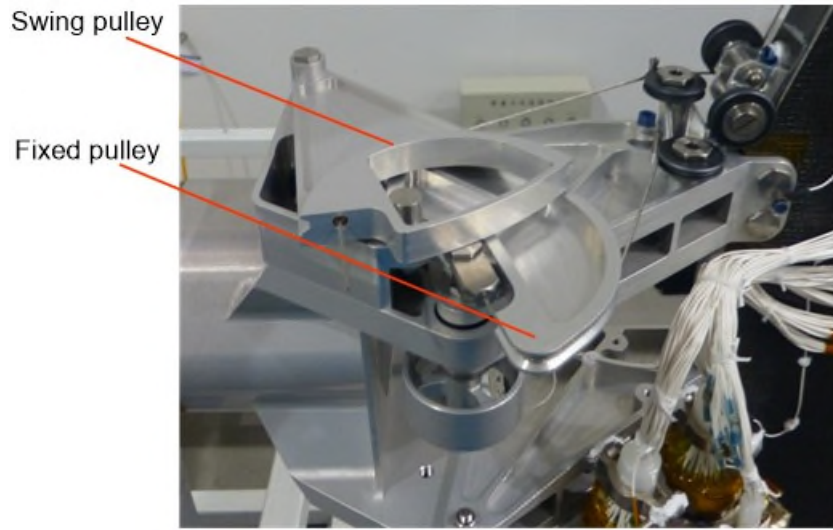


Figure 10. Deployed configuration of root hinge

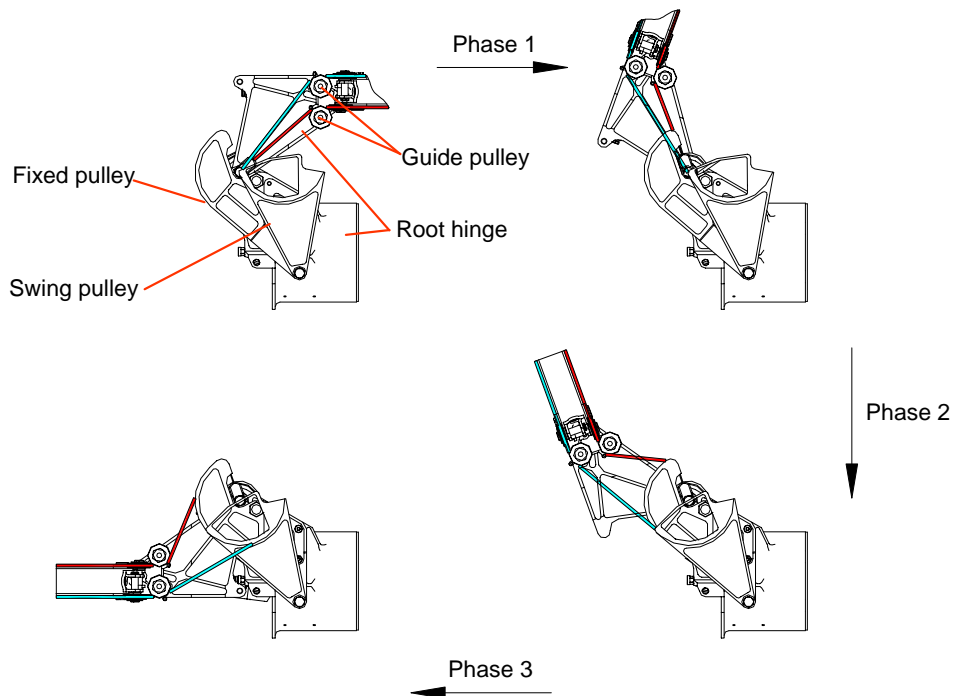


Figure 11. The three-stage deployment of root hinge

Deployment Test

The performance of the synchronization mechanism was verified in ground test using both an engineering model and flight model. The solar array was off-loaded by an air pad for testing (see Figure 12). The trajectories of the air pads were controlled by the synchronization mechanism, and it had to be confined to the area of the table, which corresponded to the requirements.

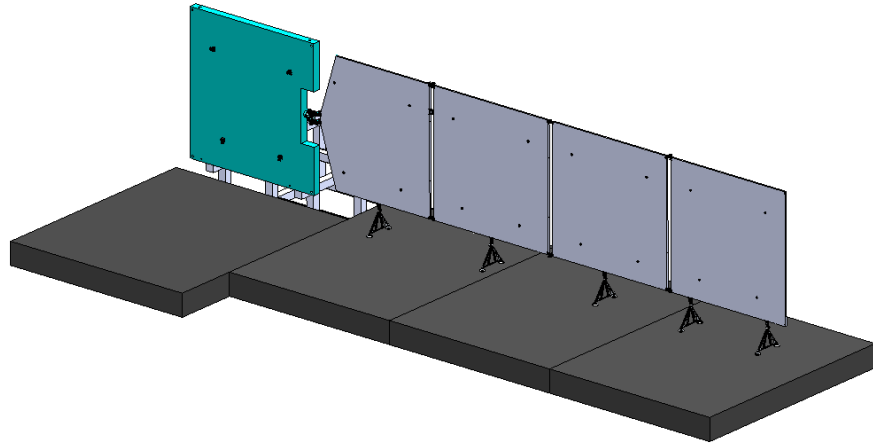


Figure 12. Using air pad for ground testing

The process of deployment using the flight model is shown in Figure 13. The realized synchronization characteristic was similar to the nominal characteristic, and the main difference between the two was that each panel hinge deployed a small angle in phase 1 of testing because of the flexibility of the cables. Nevertheless, the more important consideration was that the trajectories of the panels met the requirements excellently, as the angle was too small to affect trajectories significantly.

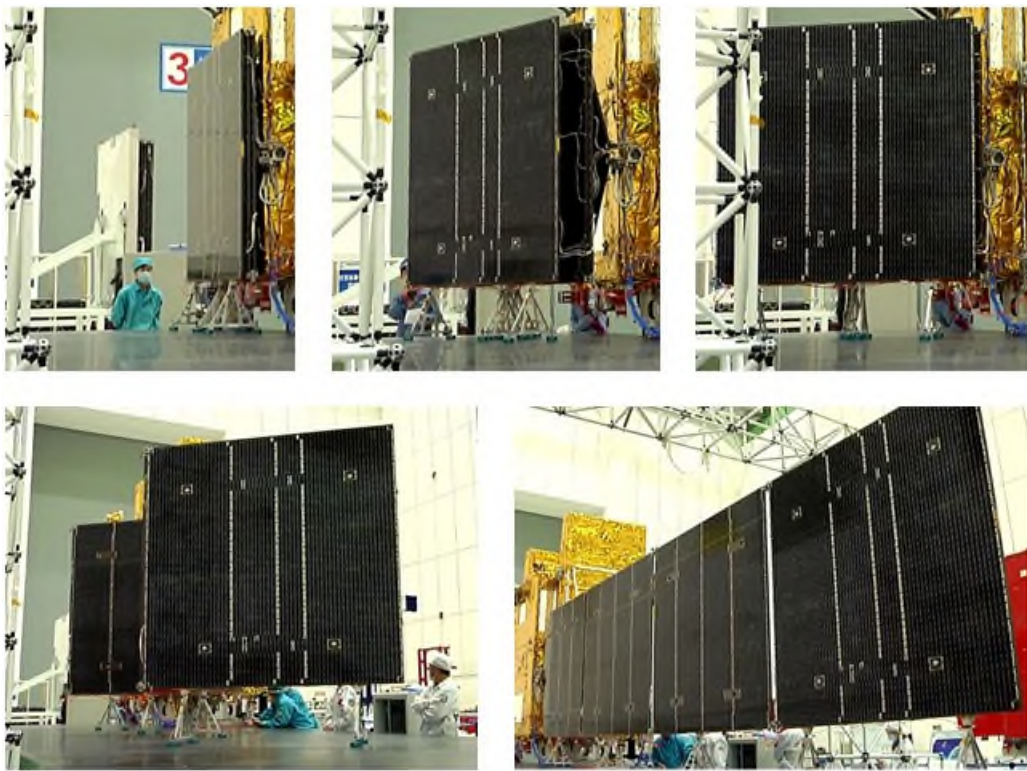


Figure 13. The deployment of the flight model

There were several tests in the development, and the performance of the synchronization mechanism was stable. Furthermore, the GF-3 was launched in August 2016, and the solar array deployed successfully on orbit. The synchronization mechanism demonstrated excellent performance during flight.

Conclusion

The synchronization mechanism of the solar array in this paper performs a three-stage deployment in order to meet the requirement to confine the trajectories of all panels to a limited area. The main design challenge of the synchronization mechanism is to change the ratio smoothly from 0:1 to 2:1 by adding a transient transition. The root pulley is divided to two parts called the fixed pulley and swing pulley in order to achieve the function. Although there is an obvious structural difference between the fixed pulley and swing pulley, they both use the characteristic of a triangle in the mathematical model to change the length of the cable rolling-on or rolling-off that performs a non-linear ratio. The coordination between fixed pulley and swing pulley is complex, and the dimensioning parameters are determined by the result of numerical analysis. The primary advantage of the method is that the trajectories of the panels meet the requirements excellently. The performance of the synchronization mechanism has proven to be effective and stable by ground test and flight usage. The synchronization mechanism is not significantly bulkier than the standard one, and it can be adapted to other multiple elements deployment that have a similar requirement.

References

1. Zhang Qingjun. System Design and Key Technologies of the GF-3 Satellite[J]. *Acta Geodaetica et Cartographica Sinica*. 2017, 46(3): 269-277 (in Chinese).
2. Yannick Baudasse, Laurent D'Abrijeon, Nicolas Pingault. "A New Synchronization Concept for Solar Array Deployments." *Proceedings of the 11th European Space Mechanisms and Tribology Symposium*, (2005), 219-224.
3. Frans Doejaaren, Marcel Ellenbroek. "The Damper Spring Unit of the Sentinel 1 Solar Array." *Proceedings of the 41st Aerospace Mechanisms Symposium*, (May 2012), 97-110.

Mechanisms and New Space

Bill Purdy*

Abstract

The objective of this paper is to provide the mechanisms community an understanding of “New Space” applications, giving insight on how to specify, design, produce, and test mechanisms for this emerging paradigm. An in-depth study of how New Space does and does not change the landscape for space mechanisms will be provided. The paper will study these questions generically to provide understand of the adaptation needed but does not intend to specify a recipe for success. The spectrum of applications and programs is very diverse, so the paper will focus on key thought processes, potentially applicable techniques, and the questions to consider for New Space mechanisms. The desired outcome of this paper is to help smart mechanism engineers create wise and unique solutions for specific New Space mechanisms.

Introduction

New Space changes a programmatic paradigm but cannot change physics, nor the space environment, nor the realities of a riding a rocket to space. The most impactful elements of this programmatic change are a very strong emphasis on low cost, usage of volume manufacturing and much tighter schedules than is the norm for current programs. This paper is written from the perspective of learning to thrive in this new paradigm. The author has spent a 30-year career primarily working research and development satellites and their mechanisms within the American space program but has recently refocused his career on the world of New Space. The paper will share the author’s growing understanding of the New Space paradigm and its impact on the mechanisms life cycle.

What is New Space?

We must understand the motivations and expectations of New Space enterprises to successfully provide mechanisms for their programs.

New Space Description

The trade magazine *New Space Global* defines New Space well. “New Space is a global industry of private companies and entrepreneurs who primarily target commercial customers, are backed by risk capital seeking a return, and seek to profit from innovative products or services developed in or for space.”

New Space will be examined in comparison to the most conventional approach to space, referred to in this paper as ‘Big Space.’ Big Space is defined for the purposes of this paper as large, very high reliability programs, including major NASA and ESA programs, DoD programs, and long-life Geostationary communication satellites.

The strongest motivation of New Space is simply to use space to make money, which drives a very different approach to satellite design and production than the Big Space motivation of extremely high reliability of each satellite. Low-cost production of satellites is a cornerstone of financial success for New Space enterprises. Programs using the New Space paradigm are endeavoring to build space hardware at a small fraction of the conventional cost by challenging the standard practices of big aerospace programs.

* Purdy Engineering, Poolesville, MD

New Space has emerged in recent years as a sizable business from its roots in the small satellite and CubeSat communities. More than 1000 electro-optical satellites are proposed and more than 10,000 communications satellites are proposed by various companies. Proposals are easy, but it takes a lot of money to become real. Commercial funding for New Space (Figure 2) has grown to an average level of \$3 Billion annually from 2015 through 2017. Three of the largest New Space ventures in current production are the SpaceX Falcon rockets, the Planet constellation of imaging satellites and the OneWeb constellation of internet communication satellites (Figure 1). The production programs and funding levels confirm this new paradigm is serious business. Multiple projections show this expenditure level growing in the coming years.

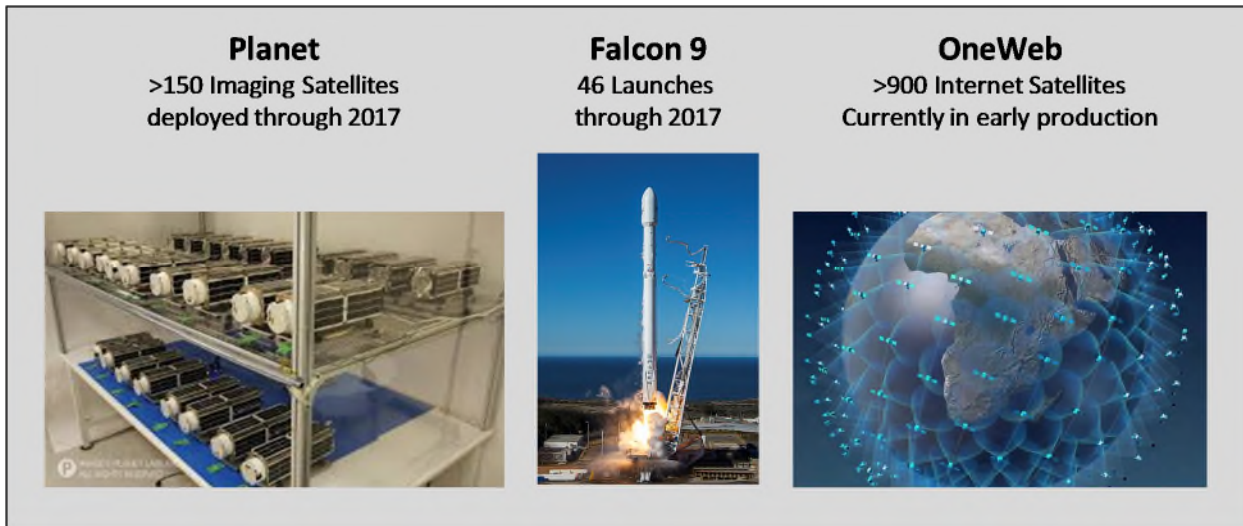


Figure 1. Major New Space Constellations Presently in Production

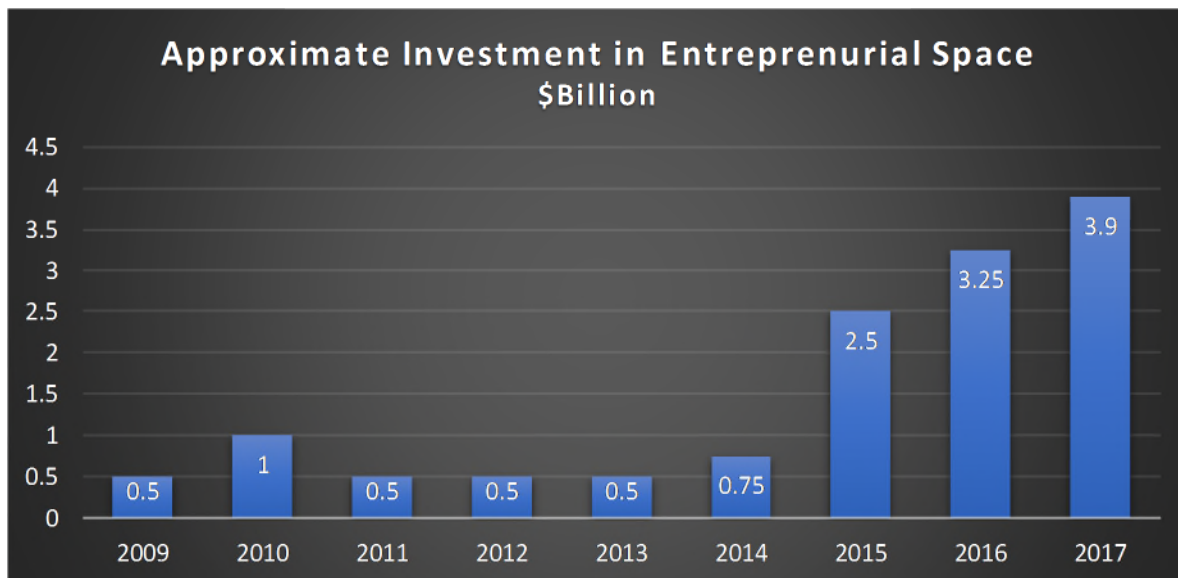


Figure 2. New Space Investment by Year Shows a dramatic increase from 2015 through 2017

New Space Missions

New Space missions can be loosely grouped into five categories. A brief overview of each is intended to provide the reader insight into the driving business cases.

- Internet from space: Satellite constellations of hundreds to thousands in Low Earth Orbit (LEO) are being pursued to provide internet connectivity with high bandwidth and low latency.
- Earth Observation: The purpose is to sell knowledge insights extracted from Earth observations. Constellations of satellites in the tens to hundreds already exist and more are being pursued providing optical imagery, radar imagery, signals monitoring and weather observations to feed new knowledge products.
- Internet of Things (IoT) communication: Satellite constellations of tens to hundreds already exist and more are being pursued to provide low bandwidth connectivity specifically for the IoT.
- Low Cost Launch: SpaceX has been the first to achieve this goal while several other companies are very close to selling low cost launch opportunities.
- Science and Technology demonstrations, typically on CubeSats, are presently being performed with high frequency.

Will New Space Become as Big as Projected?

Cynics will say New Space is just a revisit of the mid 90's when big constellations were successfully built at low cost but were business failures and New Space is doomed to repeat the past. Optimists and advocates will say New Space is the next big thing. The outcome is still uncertain, we will only begin to find out in the year 2020+ time frame as the new constellations materialize or do not materialize and as business plans succeed or fail. In the meantime, there is considerable enthusiasm and money being spent providing many smart and creative entrepreneurs and engineers the opportunity to make it work.

Comparison of New Space and Big Space

It is important to compare and contrast New Space and Big Space; we must understand what changes and what does not change. Table 1 provides a generalized look at this comparison, acknowledging that every space program is unique and there is a wide spectrum between the extremes of each paradigm.

Table 1. General Comparison of New Space and Big Space

#	New Space	Big Space
1	Commercially driven	Customer driven
2	Government is either uninvolved or hands-off	Government sponsored and managed, except commercial GEO communication satellites
3	Profit equation: <ul style="list-style-type: none">• High value products derived from space• Using low-cost satellites and launch	Profit equation: <ul style="list-style-type: none">• Meet customer requirements at all cost• Cost plus Fixed Fee• Except Geo Communications
4	\$100 million satellite is considered very expensive	\$100 million satellite is considered very cheap
5	3-year satellite development is considered slow	3-year satellite development is considered fast
6	Moderate capability satellites in high volume	High capability satellites in low volume
7	Reliability of business plan	Reliability of satellites
8	Space Environment	Space Environment
9	Rockets are a rough environment	Rockets are a rough environment
10	Streamlined processes	Very thorough processes
11	Ignore, adapt or use established standards	Mandated use of established standards
12	Why not change?	Why change?

Items 1-3 are the commercial drivers which combine to force New Space satellites to be manufactured at low cost. Items 4 and 5 illustrate the dramatic difference in cost and schedule mindset. However, items 8 and 9, the realities of space and the path from earth to space, are two of the fundamental technical drivers and these don't change. New Space is attempting to leverage the philosophy and practices of items 6, 7, 10 and 11 to drive down cost dramatically. It is well known that producing in larger volume (item 6) will drive down cost, but this in and of itself will not drive costs aggressively enough to meet New Space goals.

By focusing reliability on the success of the business plans, item 7 and using a large quantity of satellites, the occasional random failure of a satellite can be tolerated which leads New Space to an acceptance of risk at the individual satellite level. New Space certainly wants and demands reliable satellites but at a different risk posture. A poorly designed satellite, or unreliable satellite component will lead to frequent satellites failures and will not be acceptable. A well-designed satellite which experiences only a couple failures of individual satellites in a large constellation due to occasional manufacturing glitches is typically an accepted risk. This New Space reliability posture will flow down to mechanism builders as a somewhat increased acceptance of manufacturing / quality assurance risk in exchange for low cost but will not flow down as increased acceptance of poor designs.

The Big Space approach to process described in items 10 and 11 have developed through the decades and do an excellent job of capturing all the best practices to produce super high reliability satellites, however they also drive costs unacceptably for New Space. Thus, New Space programs make choices about which practices to use, which to adapt and which to ignore. Similarly, many New Space programs carry a mentality of 'Why Not?' when addressing the question of 'can we eliminate a certain practice or use a certain unconventional design?' Thus, New Space will consider designs and practices which would be considered unacceptable by Big Space. However, these choices are not always made correctly so this paper will carefully examine these choices and their implications to help the reader make the choices wisely.

Key Point: New Space is using streamlined practices and volume production to reduce cost and schedule

Key Point: There is no change in the space and launch environments for New Space

Can the aggressive cost targets be met?

Many other industries produce reliable items in volume at low cost so there is no reason the space industry cannot. Space will always be a demanding environment requiring sophisticated and rugged designs. Satellite repair for all intents and purposes is not practical and this forces a higher reliability threshold than that for industries in which repair is a tolerable option. It is the author's opinion that significant costs will be driven out of satellite production as the space industry learns how best to streamline the processes of Big Space and creatively leverages the huge advantages of volume production. There will be winners and losers in the transition to New Space, and the author suggests that the winners will be those who wisely make tough decisions and move fast.

Mechanisms Considerations for New Space

*The New Space mechanism challenge is:
Continue to design and build great mechanisms – but at a much lower cost than Big Space.*

This would be an unfair challenge except for the change in two variables: (i) New Space will be able to build mechanisms in volume and (ii) New Space will entertain options to reduce process and documentation.

The New Space approach will be explored by progressing through the life cycle of a mechanism from concept through flight. A discussion of opportunities to meet the low-cost demands of New Space with good reliability and acceptable performance will be provided. Differences between New Space and Big Space will be brought out in the discussion

Mechanisms Considerations for New Space: Requirements and Design Phase

Requirements

Perhaps the concept of working to minimized requirements is the biggest cost saving of the entire New Space endeavor. New Space programs attempt to pare their technical requirements down to the minimum necessary to satisfy a business case. Additionally, they are paring their mission assurance requirements down to the minimum necessary to produce the reliability necessary to support the business case. The amazingly low cost of cubesats and smallsats relative to Big Space is possibly a direct result of this approach to minimizing requirements.

Selection of appropriate requirements is extremely important to any engineering effort, and mechanisms for New Space is no different. The downward cost pressure and tight schedules of New Space greatly amplifies the importance of minimizing requirements. In contrast, the author has observed requirements development in the world of Big Space stemming from a pervasive mindset of choosing requirements equal to the best that can possibly be done. While this gives engineers fascinating challenges and has produced satellites with amazing capability, this mindset is incompatible with low cost.

Customer and supplier both need to realize that they both will benefit from the easiest acceptable level of requirements. The customer will get the product they need at the low cost they also need. The supplier will have the best chance of success as their task becomes less challenging. A true win – win.

To provide a good low-cost mechanism questions such as the following should be considered jointly by customer and supplier:

- Is this level of performance absolutely necessary?
- Is this required feature / capability absolutely necessary?
- Is this quality / mission assurance requirement going to be cost effective?

A mechanism provider should first assess for themselves, and then enlighten their requirement source about cost savings considerations using questions such as:

- Are you aware that this specific requirement is a significant cost driver for the mechanism?
- We have found that a given quality process has been largely unnecessary and recommend its elimination, can you concur?
- A given quality process is redundant since it is checking for issues that will be uncovered by this other process which we have found to be cost effective, will this be acceptable to you?

A person setting requirements should be asking the mechanism provider questions such as:

- What can I change in my specification to make your cost lower?
- Do you think I am asking for more than I really need?

The eight questions above can be used to identify and eliminate many unnecessary requirements. Time and money must be spent to meet an unnecessary requirement – but only if the requirement has not been eliminated. Elimination of waste is a valuable cost and risk reduction tool and an unnecessary requirement is a prime example of waste that we should be striving to eliminate. There is nothing unique to New Space in this effort to aim for good and minimized requirements. The difference is the critical relationship of minimized requirements to the driving objectives of low cost and fast schedules. Remember the adage ‘Be careful what you ask for, you just might get it.’

Key Point: Reducing and eliminating unnecessary requirements is one of the best ways to reduce cost and schedule for New Space programs and should be a joint effort between provider and customer.

Concept Design

The book Design for Manufacturability, by David M. Anderson (Ref. 3) puts forth that 60% of the total lifecycle cost is decided simply by the concept architecture (Figure 3). This makes a lot of sense simply by thinking about the costs of complexity that can be eliminated by a great concept. Not only does a great concept drive down costs, it drives down schedule and risk simply because there are less opportunities for problems to arise.

When one looks at this chart another way, a new design is the only method to achieve a cost reduction for an existing product to below 80% of the present cost, since reductions greater than 20% are not available by manufacturing improvements alone. Cost reductions to below 60% call for an innovative new concept.

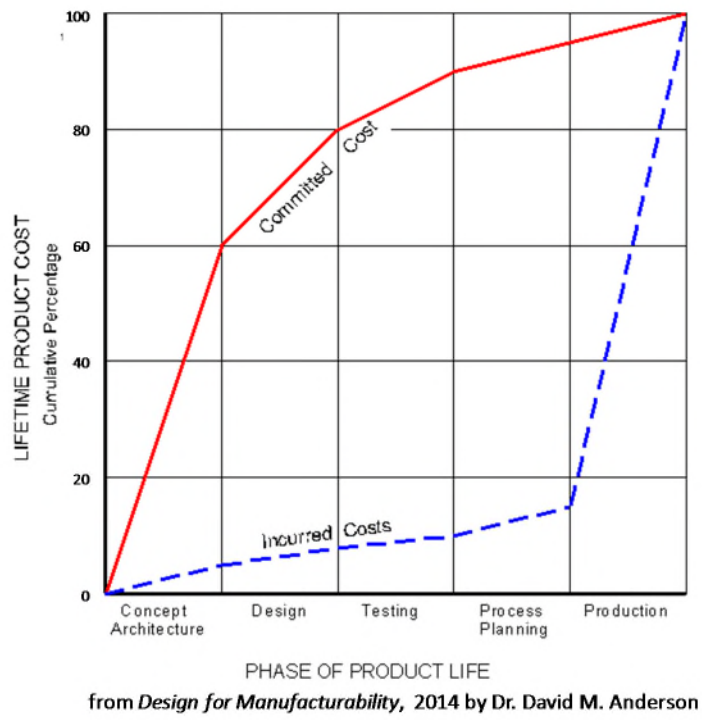


Figure 3. Costs Committed and Costs Incurred vs. Life Cycle. This figure shows the majority of total life cycle costs are committed by the completion of the concept architecture plus design phases even though these costs are not realized until the production phase. Plot courtesy of Dr. David Anderson

Many lessons from the referenced text and from the world of production emphasize a rapid cycle of conceive, test, iterate, and repeat as one of the best methods to evolve to a great concept. The speed at which this rapid design iteration can now be accomplished is greatly improved by leveraging additive manufacturing for rapid prototyping. It is also taught that extra time spent in the search for a great concept can ultimately save a program time when the benefits of the great concept are realized in development and production schedules.

One concept often seen in New Space is usage of mass-produced industrial components for flight even though they were not designed for space applications. With proper testing many industrial items can be

found to work for space applications either as-is or with minor modification. The use of industrial components, in our case, mechanisms, provides a great cost savings opportunity – but only if the mechanism is properly qualified for the application and the environment and the supplier's approach to quality is found acceptable. In contrast, the use of industrial components with industrial quality practices is virtually inconceivable in Big Space.

When considering a mechanism conceptual design, it is important to keep in mind that the goal is lowest overall system cost. For example, if a low-cost mechanism requires high-cost drive electronics then it may not provide the lowest overall cost to the satellite system.

Key Point: Concept design, including requirements definition, is the biggest driver of cost and schedule in a production program.

Detail Design

There is an entire engineering discipline of design-for-manufacturing which is beyond the scope of this paper. Some highlights providing the most potential benefit for mechanisms will, however, be discussed.

The Design for Manufacturability text points out that 80% of the total lifecycle cost is dictated by the combination of the concept architecture plus the detail design. Once an unnecessary feature has been designed in, there is no amount of manufacturing brilliance that can make it cost less than to never have had to manufacture it in the first place. Thus, the detail design phase is of crucial importance for the success of any mechanism, which, for New Space, includes performance, cost and schedule.

Low production cost must be an important design consideration from day one. This low cost emphasis requires a very different mindset than what is common in Big Space. Production cost can and should be traded against the typical design goals of performance and mass. The design considerations of low cost must include the full life cycle costs; parts manufacturing, assembly, testability, electrical interface costs, spacecraft interface and integration costs.

A powerful cost savings in design is simply a minimization of parts count. Every part in an assembly invokes all the following tasks at a minimum: design effort, a drawing, analysis, manufacturing, a vendor to manage, an opportunity for manufacturing problems, inspection, storage, and assembly.

Discussions with manufacturers during the part design process can prove extremely valuable as the manufacturers can provide unique feedback on features which either drive manufacturing costs into the part or, conversely, save manufacturing difficulties. Design engineers are often unaware of subtle design selections which accidentally drive manufacturing difficulty and cost.

A significant cost savings can be found by clever designs that leverage modern manufacturing methods to combine multiple parts into one. When multiple parts are combined, assembly costs and risks are eliminated, and the savings associated with reduced parts count are realized. The question becomes '*are the lifecycle costs of this single complex part, in fact, cheaper than an assembly of several simpler parts?*'

Designers must look at tolerancing as a source of cost savings because poor tolerancing will result in cost increases. Manufacturing costs rise exponentially with tighter tolerances. For example, studies have shown a 3.5X manufacturing cost increase simply by changing a tolerance from 0.005 inch (0.12 mm) to 0.001 inch (0.025 mm). Cost growth rates are even larger as one tolerance become even tighter. However, if tolerances are too loose then improper mechanism performance will sometimes result producing costly test failures. A good designer will carefully choose the loosest acceptable tolerances while carefully performing worst case tolerance analyses to avoid mechanism faults if tolerances are too loose.

Key Point: Detail design is the second biggest driver of cost and schedule in a production program.

Development Process

Development of New Space mechanisms varies from development for Big Space in two key ways; (i) New Space will have tighter timelines and more schedule pressure and (ii) The development phase needs to drive cost out of the design concept as well as validate and improve the design.

Most engineers will agree that multiple iterations continue to improve designs. This is very important considering the premise that 80% of the lifecycle cost is dictated by the concept and design. The leverage of design improvements in the concept phase is huge. Iteration early and often can be very cost effective even if early models are quite crude. A crude breadboard level prototype in-hand can often show a creative engineer design options not yet conceived or problems to be designed out.

A hardware-rich development period is a very powerful method of working within tighter timelines and enabling cost reduction. A hardware-rich development means that multiple prototypes of each design are built rather than just a single unit. The author has found this to be extremely valuable and cost effective in practice. The cost of the multiple prototypes is more than recovered in the flexibility it provides. Plus, it typically does not cost much more to make multiple prototypes than a single unit. For example, the hardware-rich approach of building four engineering models instead of one allows the following allocations and parallel efforts:

- Unit 1 - Test for functionality and performance
- Unit 2 - Test for environments
- Unit 3 – Test interfaces with electronics or with prototype spacecraft
- Unit 4 – Held in reserve for use in response to unforeseen occurrences or troubleshooting

Another aspect of a hardware-rich development can be the parallel production of multiple design options. In some cases, a trade between two or more options can be best made after being informed by prototype hardware evaluation. For example, one could prototype Design A offering lower cost with higher performance risks and Design B with better performance and higher production costs. This way the development program can hold schedule if the low-cost option fails to meet performance, but, does not give up the chance to hit a low cost, adequate performance mechanism home run.

Key Point: Fast paced, iterative, hardware-rich development is a powerful tool for improving the concept and detail design quickly.

In a development effort for a mechanism intended to enter volume production, working out all the bugs is of high importance before entering production. Minor design errors will be extremely costly if they are found during volume manufacturing. Imagine the pain of finding a design flaw that can cause intermittent failures after already having shipped 100 units to customers. Similarly, minor inconsistencies in manufacturing will make a mess of production schedules in volume production. For volume production, manufacturing and design are effectively indistinguishable, the design of the manufacturing process is part of the design of the mechanism. Thus, both manufacturing and design must be perfected in the development phase is one is to have smooth, cost effective volume production.

Mechanisms Considerations for New Space: Manufacturing Phase

There is a tremendous knowledge base available on volume production, both for volume production in general and specifically for space. The author has found significant value from the following references:

- Reference 1, a paper in the 29th Aerospace Mechanisms Symposium about the high-volume production of release mechanisms for the first Iridium program by Daryl Maus provides a powerful look an early usage of volume production for space.

- Reference 2, a paper in the 2017 European Space Mechanisms and Tribology Symposium about volume production of pointing mechanisms in volume production for several space programs by Jean-Nicholas Lajoie, provides good insight into current volume production for space.
- Reference 3 the book Design for Manufacturability: How to Use Concurrent Engineering to Rapidly Develop Low-Cost, High-Quality Products for Lean Production by Dr. David Anderson shows methods to develop manufacturable products with the lowest cost in the least time and provided the author good insight into cost savings in general.
- Reference 4. The book Toyota Production System by Taiichi Ohno is considered one of the fundamental texts of lean manufacturing.
- Reference 7, The Goal: A Process of Ongoing Improvement, serves as a good introduction to the value of and methodologies for streamlining manufacturing told as a story.
- Personal observations of a certain burrito restaurant showed the author lean manufacturing in action.

The field of lean manufacturing provides many techniques for us to leverage to reduce the effort and costs of all aspects of the mechanism build and test cycle. These principles are best suited for volume production but several of the principles are valuable for build quantities of a few units. The engineering in the field of lean manufacturing is well developed and is well outside the scope of this paper. This paper will illustrate a few key principles that will provide extremely valuable to inspire readers to learn more.

One of the key philosophies that has provided the author immediate benefit is a ‘relentless search for waste.’ Continually questioning any production, test or for that matter any design element with the question of ‘Is this necessary?’ will tend to expose a wide variety of improvements by simplification.

A second key philosophy of value to the author has been a strong mindset in constantly thinking about the manufacturing cycle while designing. Questions such as (i) ‘How will this be built?’, (ii) ‘How will this be tested?’ (iii) ‘Can this be simplified?’ (iv) ‘Is there a way to change the design to allow more efficient manufacturing?’ should be continually asked of oneself.

Part Manufacturing

Many New Space mechanisms will now be manufactured in quantities of hundreds if not thousands per year. There are considerable advantages to volume production in and of itself, but more so with a search for ways to best utilize its advantages.

There is nothing unique about volume manufacturing of parts for space relative to industry. This is good news because there is tremendous existing knowledge and capability for us to leverage. A trip to a manufacturing show was enlightening for the author and is highly recommended to readers. Tremendous manufacturing capability exists to manufacture parts and assemblies in volume at low cost. The key for those of us who've spent a career building in low volume is to find and utilize this existing volume manufacturing capability base.

The emerging field of additive manufacturing (AM) is receiving a lot of excitement these days and can certainly be valuable for mechanisms. However, it is not a panacea, nor is it one-size-fits-all. The author has found four key points to understand about additive manufacturing:

1. AM is not as simple as sending the CAD file to the printer. The part to be printed must be designed to work within the parameters of the additive manufacturing technology chosen.
2. Additive manufacturing is very valuable for use in accelerating the prototyping phase. This can greatly enhance the critical concept development process. Even if the production parts will not be made by AM, AM can often be used to produce prototype parts faster than any other method.
3. AM enables the creation of shapes not possible by any other method. A classic example is embedding curved internal passages in an otherwise solid part. Creative designers can utilize this capability to improve or simplify their designs.
4. AM can be leveraged to make a single part which otherwise would have required many individual parts. It should be noted that 5-axis CNC machining can also offer this advantage.

Inspection and Quality Assurance

Considerable schedule and cost efficiency is available from modern computerized inspection equipment. When one thinks about the time involved to inspect a single part and then multiplies that time by a thousand parts it is easy to see the large cost savings available from quick and accurate automated inspection. Camera based inspection systems and automated Coordinate Measurement Machines (CMM) are available with associated software to streamline the inspection process. Simple parts can be inspected in a couple minutes and complex parts in a half hour with very little operator effort. This quick inspection also results in a published inspection report against required tolerances.

There are multiple vendors offering camera based systems producing inspection accuracy on the order of 0.002 inch / 0.05 mm. These systems are available at a modest cost. The automated photographic inspection process is:

1. An operator puts a part on a stand.
2. A pair of cameras on a motion control platform move around the part accumulating stereo photos.
3. The part is flipped over and then more photos are accumulated.
4. The photos are then processed in image analysis software to produce a point cloud. The point cloud is then mapped onto the dimensioned CAD file and an inspection report is produced. The inspection report will include pass-fail assessment against every required dimension and will show margin against tolerances.
5. The whole process typically takes a couple minutes per part and all the operator must do is put the part on a table, flip it over, then remove it.

Automated CMM inspection provides much greater accuracy than the camera systems and is available at a higher investment cost. An automated CMM works comparably to a manual CMM except the CMM axes are motor driven and follow a programmed measurement path. Here an operator needs to put the part into a jig setting the part datums for inspection. The CMM then drives through its inspection path. Ultimately this process produces an automated inspection report comparable to that described above, but at better accuracy than the camera process. A complex part with many features to inspect at both high and low precision might take about 30 minutes for a full inspection.

Key Point: Modern automated inspection methods can provide accurate inspection very quickly while minimizing the documentation burden.

Big Space programs invoke considerable costs with extensive quality assurance requirements. Every deliverable document costs time and money. Every requirement flowed to subtler vendors adds to the cost of each part. New Space programs are re-evaluating how much of this existing quality assurance process is necessary. The right answer is neither (i) none of it nor (ii) all of it.

It is far less expensive to stop problems before mechanism test than to troubleshoot and resolve mechanism failures and anomalies. New Space programs have the philosophy to drive costs out of process control and quality assurance by re-evaluating what is truly necessary. However, New Space programs cannot afford failures any more than Big Space programs. So, the mechanisms programs for New Space can and must carefully address which process controls ultimately save more cost than they add, and conversely, which processes add more cost than they save. This decision process will be driven by judgments unique to each provider and program. It is crucial to perform this re-evaluation of quality assurance process controls, but this paper will not attempt to address the relative merits of each.

Key Point: Done right, significant portions of conventional mission assurance can be simplified to reduce cost and schedule with minimal increase in risk.

Assembly

Efficiency in assembly is always valuable and becomes crucial for keeping costs low in volume manufacturing. An example from the restaurant industry illustrates key principles clearly. Most readers have the opportunity to view very good lean manufacturing in action at a popular chain of burrito

restaurants. These restaurants manufacture custom burritos in an assembly line with remarkable efficiency. The author observed one of these outlets finding the following truly impressive statistics:

- It took only one minute twelve seconds from “Hi may I take your order” to “thank you for paying” for the author to receive a burrito custom ordered with nine individually selected ingredients.
- 28 burritos were made in a 10 minute period – 2.8 burritos per minute.
- There were 8 workers involved in burrito production, including the cashier.
- This works out to just 2.8 man-minutes labor per assembled burrito.

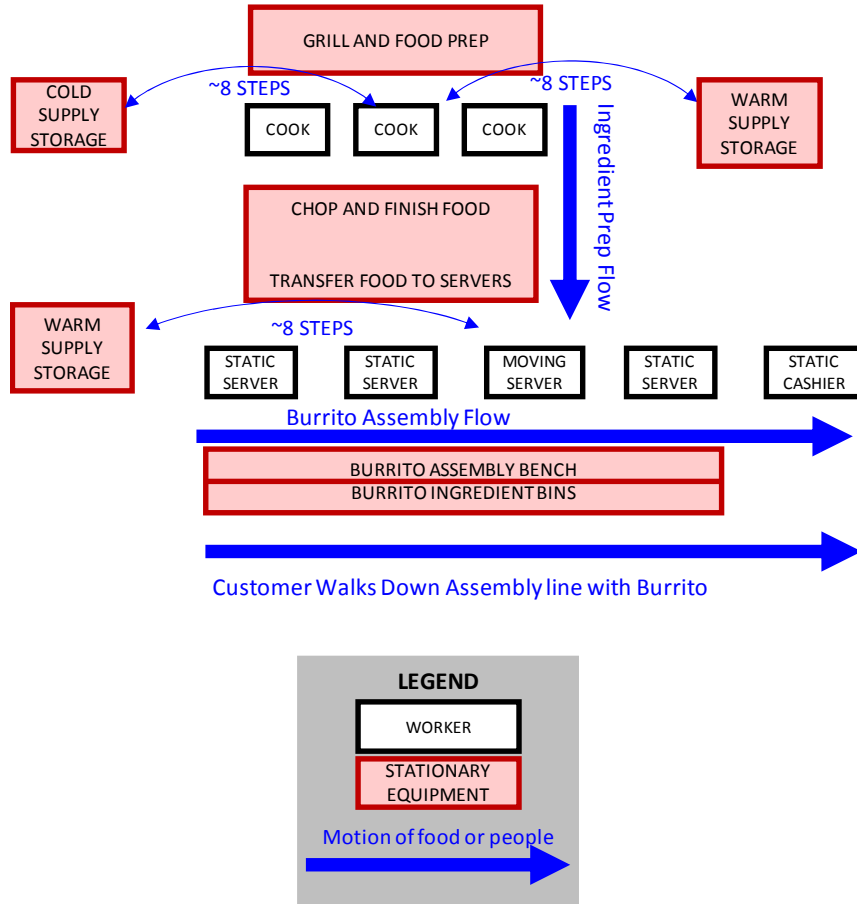


Figure 3. Efficient Burrito Assembly Diagram serves as an example for efficient mechanism assembly

One will see many principles of lean manufacturing of which two will be described. The basic burrito production line and key features is shown in Figure 3.

- Principle one – eliminate waste. The burrito manufacturing employees spend very little time walking from their work station. The principle is that walking around is waste and to be minimized. Four of the eight employees, identified as ‘static’ in the figure *Figure 3* never took more than three steps from their work station. Four of the employees had tasks to replenish supplies and their walk was typically only eight steps from work station to supply location.
- Principle two – excess inventory is waste. In any assembly line, if worker A gets ahead of worker B and keeps piling up inventory, there is waste in building the inventory pile, waste in the floor space for the inventory and waste in pulling material off the inventory pile. At the restaurant, the burrito ingredient supplies for the servers are only replenished when they fall below half full. The servers communicate to the cooks when it is time for the cooks to make more supplies. The communication is timed so that the server’s supplies will be replenished at some point between

half full and empty. There is no inventory piling up between the cooks (worker A) and the servers (worker B), yet the servers never run out of ingredients.

Just imaging if a nine-part mechanism could be assembled with only 2.8 man-minutes of labor. While this may be extreme for the space mechanism field it is illustrative of the incredible power of efficient design of an assembly process.

Key Point: The principles of lean manufacturing are very applicable to volume production of mechanisms.

Key Point: A relentless search for waste will prove valuable in any aspect of any mechanism program.

There are some opportunities to improve mechanism assembly with automation. Most engineers immediately think of the rapidly growing field of robotics. Robotics have been found effective for pick and place type tasks. In some cases, pick and place machines common in electronic card manufacturing can be designed to support mechanism assembly tasks. Robots are not a panacea but can provide good value in the right applications. The best applications for robotics seem to be repetitive tasks and those tasks that could be performed 24 hours a day without supervision.

One can look for labor intensive tasks which can be automated, one example being parts washing. Systems that automate multi-stage cleaning processes are available and will save cost given sufficient manufacturing volume. The conclusion is that there are many automation tools and processes available from industry to investigate leveraging to reduce assembly costs.

Mechanisms Considerations for New Space: Integration and Test Phase

Test. Big Space programs generally start test planning from a perspective of ‘what can be tested?’. New Space programs generally start test planning from a perspective of ‘what absolutely must be tested?’. The nature of mechanisms is that test is often the only true method of validating performance and reliability. Reducing the amount of testing goes against the author’s comfort zone, yet it can and must be done for volume production of space mechanisms as it is done successfully in other manufacturing fields.

Most mechanisms engineers would agree that the nature of mechanisms is that testing is crucial to proving performance and reliability. Verification by analysis and inspection of mechanisms without a test has historically proven inadequate. This is a particular challenge for mechanism production where testing is very expensive, and we are looking to drive cost out of the program. There is no easy answer – extensive testing is great for proving reliability. Limited testing is great for cost reduction but exposes the risk of the severe pain of an on-orbit failure.

Each testing program is unique, so the following is a discussion of options for the reader to consider for their unique mechanism effort. Each mechanism team must make their own tough choices regarding the balance of testing versus cost.

Development testing: The goal of development testing is to expose all flaws in a design so that they will be removed prior to going into production because design flaws found while in a production run are extremely damaging. Extensive development testing is key to eliminating flaws and benefits considerably from the hardware rich approach described above. When time is short, one can also find value by finishing development testing in parallel with early production. While it is ideal to finish development before starting production, continuing development can serve useful to expose a remaining flaw while still early in production instead of building the flaw into a large quantity of delivered mechanisms. Life testing of development units is a prime example of the value in finishing development in parallel with early production since it takes so much time to complete.

Environmental Testing: Launch environments are driven by the choice of launch vehicle. Satellites built for New Space typically want to be compatible with many different launch vehicles for maximum access to space and for flexibility to adapt to launch delays. In addition, new launch vehicles coming on the market will not yet have well characterized launch environments. This scenario results in considerable uncertainty in the vibration, acoustics and loads environment to test against. Testing against an envelope of all launch vehicles is conservative but can result in a significant overtest. Some programs elect to use the generalized environments from the NASA GEVS (General Environmental Verification Standard) or comparable specifications to address this uncertainty. Using generic environments such as these certainly carries some risk that specific environments from specific launch vehicles will exceed the tested limit. There is no easy answer to address environments uncertainty, so the answer becomes a judgment call balancing the risk of undertest versus the risk of false failures from overtest.

Qualification Testing: Formal qualification testing of one or more mechanisms never intended to fly prior to completion of the flight articles was prevalent in the early days of the space program. In recent times, most programs have moved to protoqual (or protoflight) testing in a quest to save the time and money associated with testing units that will never fly.

As New Space moves into volume production, qualification testing becomes a much more viable and valuable option. The premise of qualification testing is to test flight equivalent units to demonstrate high margins. For example, vibration testing would be to levels twice as high for three times the flight duration. Testing to these high margin levels is not smart for units intended to fly but is a great tool for showing the robustness of a design. A plan to build hundreds or thousands of mechanisms draws two large benefits from qualification testing; (i) high margin testing exposes flaws prior to the commitment to major production and (ii) provides confidence that streamlined acceptance testing will be adequate to assure reliability.

Acceptance Testing: There are significant costs of mechanism testing which provides an opportunity for considerable savings during a flight production run if the risks of reduced testing are well managed. Given that a mechanism has been through a formal qualification program, the objective of the acceptance test program becomes a verification that each flight unit performs the same as the qualification units. Once tests demonstrate that an individual unit has performance in-family with the qualification units, it follows that the individual units are ready for flight. Paring a mechanisms acceptance test down to only those tests necessary to prove manufacturing and performance consistent with qualification is key to realizing the cost savings.

Sampling Tests: Consideration should be given to pulling one or more units off a production line on a regular basis for more extensive testing to verify that inconsistencies have not crept into the production process. This approach is quite common in non-space industries. This sampling testing could be a subset of the qualification test to perform more extensive and insightful testing to ensure that small flaws are not hiding from the simplified acceptance test. The periodic nature of the sampling tests acts to reduce exposure to the misery of finding a problem after a very large quantity of mechanisms have already been delivered. The sampling tests can be a powerful complement to an acceptance approach with very limited testing on each unit.

Automation of Testing: As we move into testing of larger quantities of mechanisms there are many test automation systems on the market which we can use to reduce the hand labor typically associated with mechanisms test. Electrical pinout verification is made much easier with automated harness testers. These automated testers make harness testing as simple as plugging the harness into the tester which uses a computer driven electronic tester to very rapidly perform all the resistance, continuity, dielectric and HiPot type measurements needed. Motor testing can be performed by all-in-one motor test stands in which the motor is mechanically and electrically connected to a test stand including both a dynamometer and harness tester. One can easily see how these automated testers can change a series of tests that might take hours per unit into a couple automated tests that takes only minutes per unit and produce a finished electronic test report. Reference 2 presents an approach for thermal testing of many gimbal

drives concurrently on a single fixture. This is an example of creatively driving testing costs out of a volume production mechanism.

Key Point: Modern automated testing methods can provide accurate testing very quickly while minimizing the documentation burden.

Test architecture Design: The author proposes that a mechanism engineer consider the following questions in designing a low-cost test program:

- What type of performance test provides great insight into mechanism performance yet is easy to perform?
- What combination of qualification, acceptance and sampling tests will be best?
- Do I need to test each individual mechanism for:
 - Vibration?
 - Thermal?
 - Vacuum?
- How can I automate the tests performed on each unit?
- How can I automate the test reporting and deliverable documentation?
- What testing will provide me confidence that problems have not crept into the production line?
- How much does this test really cost? And what is its true value?
- Can I create a single test that provides confidence in multiple aspects of performance?

Key Point: A wide variety of opportunities for streamlining during acceptance testing of volume produced mechanisms are available but need tailoring for the unique aspects of each mechanism production program.

Spacecraft Integration and Test

New Space programs are looking to simplify the satellite level integration and test process for recurring production. The testing for qualification satellites and early prototype satellites will tend to be extensive, much like Big Space programs. Once a new satellite design and its production processes have been qualified, however, the integration and test emphasis shifts towards confirming that each satellite has been built and performs the same as those units qualified. The biggest difference is that New Space will consider satellite level environmental testing as a choice to be made rather than something that simply must be done.

Mechanisms for New Space satellites may receive requirements to be compatible with streamlined satellite assembly processes. For example, satellite builders may ask for certain features to enable automated handling, and, will certainly desire mechanisms interfaces that make for fast and easy installation.

Flight Operations

There should be no fundamental differences in the flight operations of mechanisms between Big Space and New Space. In both cases mechanism operations are typically performed with very little intervention by human operators. New Space constellations will desire even more automation of satellite operations, so they will certainly not want any mechanisms that require complex operations with intensive human intervention. Any space program will benefit from an analysis of flight operations to either (i) simplify mechanism requirements or (ii) expose mechanism requirements which had inadvertently been missed.

Conclusions

1. The New Space effort is presently very active with significant continuing commercial funding.
2. Done right, the New Space objective of satellites produced in volume at low cost is achievable although it adds some risk of individual satellite failures.
3. New Space requires mechanisms very similar to Big Space but at greatly reduced cost and schedule.
4. New Space programs will tend to be accepting of simplifications in mechanism performance and mission assurance requirements in support of cost and schedule targets.
5. Design excellence is a far more powerful cost saver than manufacturing engineering.
6. No amount of manufacturing brilliance can make a poor design cheaper than a great and simple design.
7. The move into volume production of mechanisms needs to leverage the tremendous knowledge base for lean manufacturing.
8. Readily available equipment for the automation of inspection and testing offers significant advantages over more labor intensive manual efforts presently common in mechanism production.

***There is no reason the space mechanisms community
cannot produce reliable products at low cost,
many other industries do.***

References

1. Maus, Daryl and Monick, Doug. "Changing Paradigms: Manufacturing vs. Fabricating a High Volume Hold Down and Release Mechanism." *Proceedings of the 29th Aerospace Mechanisms Symposium*, 1995, pp. 94-108.
2. Lajoie, J., Horth, R., Lemelin-Auger, B., Gregorio, P., "Development, Qualification and Manufacturing of Antenna Pointing Mechanism Rotary Actuators." *Proceedings of the European Space Mechanisms and Tribology Symposium*, (September 2017).
3. Design for Manufacturability: How to Use Concurrent Engineering to Rapidly Develop Low-Cost, High-Quality Products for Lean Production; by David M. Anderson (2014, Productivity Press, 486 pages).
4. Toyota Production System; Beyond Large-Scale Production; by David M. Anderson (2014, Productivity Press, 486 pages).
5. <https://www.newspaceglobal.com/>, Definition of New Space
6. <https://www.spaceangels.com/post/space-investment-quarterly>, "Space Investment quarterly", 4th quarter 2017
7. The Goal: A Process of Ongoing Improvement; by Eliyahu M. Goldratt, Jeff Cox, and David Whitford, (4th Edition, 2014, The North River Press Publishing Corporation)
8. GSFC-STD-7000A, General Environmental Verification Standard (GEVS) for GSFC Flight Programs and Projects, 4/22/2013

Development of the Multi-Purpose Transportation System for the Space Launch System Core Stage Flight Article

Sarah Sandridge*, Hue Lien**, Ronald Hunt**, Ayana Reese** and Christopher Doktor**

Abstract

NASA's Multi-Purpose Transportation System (MPTS) is designed to transport the Space Launch System (SLS) vehicle segments by waterway and roadway. It is tasked with transporting the vehicle from where it is manufactured to its intermediate test location and final launch destination. Its design incorporates mechanisms that release degrees of freedom to prevent excessive loading during transit and ensure a successful delivery of the vehicle to its intended destination. In addition to the Core Stage (CS) flight article, the system will also move three Structural Test Articles (STAs), the Dynamic Demonstration Unit, and a simulated CS Pathfinder (weight, center of gravity, outer mold line dimensions, and overall length) over road terrain at four NASA centers and on the Pegasus barge. The MPTS independently supports the article at both ends while operating as a combined unit through automated monitoring of its released degree of freedom and corrective responses. This allows the system to constrain its payload in a statically determinate manner while traversing highly variable terrain. Multi-body simulation of the transportation route is useful to predict free-body motion within its range of mobility. The MPTS has completed its design and analysis developmental cycles. This paper describes the design challenges encountered in developing this system of large-scale structure, which incorporates complex mechanisms. The unique techniques and methodologies developed for analytical assessment of the hardware are also discussed.

Introduction

In large launch vehicle programs, the design challenges presented during launch are apparent. However, many efforts leading up to launch are not so obvious. Included in those many efforts is the development of Ground Support Equipment (GSE), i.e., equipment that interfaces directly to the flight hardware after it leaves the production line. The MPTS supports the delivery of the NASA's latest launch vehicle, SLS. This hardware interfaces directly with the flight vehicle after it has been built, and is therefore classified as GSE.

Historically, different GSE designs have transported flight hardware. Developers customized the designs to meet the particular needs of each program. Every launch vehicle has depended on this equipment to transport it between various locations without inadvertently damaging it. NASA's past launch programs, including Apollo and Shuttle as shown in Figures 1 and 2, used customized equipment to transport flight hardware between NASA facilities.

* NASA Marshall Space Flight Center, AL

** Jacobs Space Exploration Group, Huntsville, AL



Figure 1. The Saturn V second stage moves over roads at KSC, using GSE hardware (Reference 1).

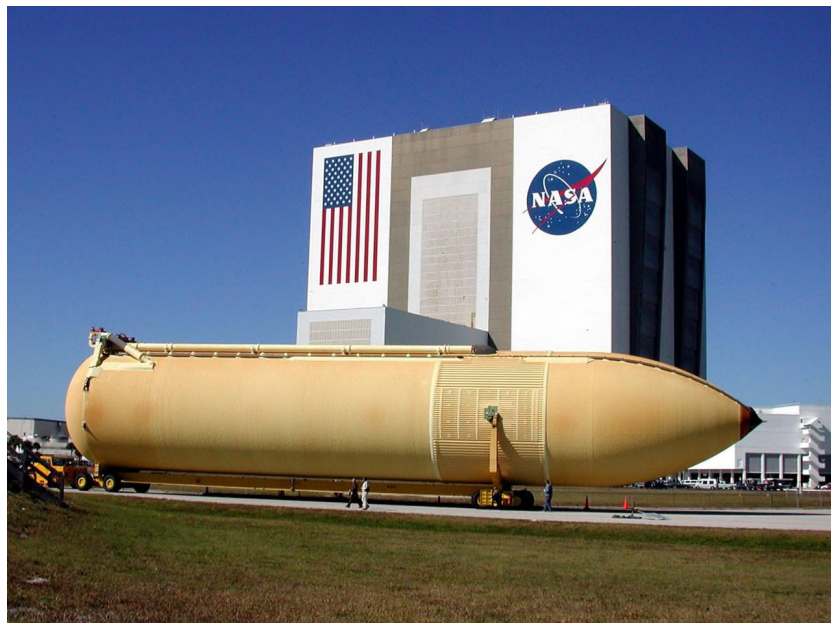


Figure 2. The Shuttle ET moves over the road at KSC (Reference 2).

However, the MPTS designed for SLS is different; its design is to accommodate multiple size articles. Figure 3 shows the initial concept of the MPTS where the intent is to support multiple hardware along with the possibility to be used in future programs.

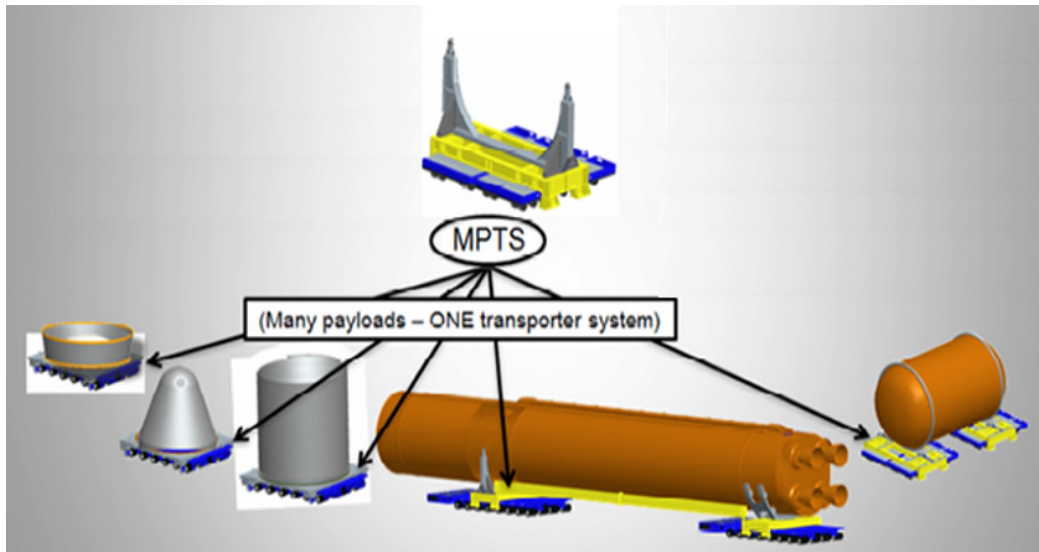


Figure 3. The CS flight hardware is among the payloads that the MPTS will transport (Reference 3).

Current planned uses for the MPTS include the shipment of the SLS CS – NASA's largest and heaviest rocket – as well as Pathfinder – a simplified simulation of the CS that is similar in mass and length – Dynamic Demonstration Unit, and three different STAs – each with their own distinctive mass and length. The various payloads will also need to be transported to different locations, as shown in Figure 4. The MPTS will take the three different STAs from Michoud Assembly Facility (MAF) in New Orleans, LA to Marshall Space Flight Center (MSFC) in Huntsville, AL while the CS and Pathfinder will be shipped to Kennedy Space Center (KSC) on Merritt Island, Florida via Stennis Space Center (SSC) in Hancock County, MS.



Figure 4. GSE is used for transportation at and to multiple centers, including KSC, MAF, MSFC, and SSC (Reference 4).

The MPTS design has encountered some unique challenges. Primarily, with its use to support various size payloads, a modular design was needed. Previous hardware, along with initial concepts, used a strongback,

a structure connecting the front and back to form a single rigid unit. While including a strongback can simplify design, it quickly became impractical for the MPTS design. Some reasons to eliminate a strongback includes weight and maneuverability. Due to constraints of existing infrastructure such as roads and floor loading, the design weight of the MPTS had to stay below certain limits, and the size necessary to produce a rigid strongback structure to redirect loads away from the flight article were determined to exceed these limits. Following Hurricane Katrina, a levee was added along the transport route to address flooding. Surmounting this levee with something as long as the CS would have been difficult to accomplish with a strongback structure, and the operation to accommodate the different lengths would be taxing.

The elimination of the strongback left the front and back end of the article free to operate independently. To prevent an excessive load from occurring at payload interfaces, released degrees of freedom (DOF) are included at strategic locations. This also serves to improve the predictability of loads at the interfaces. Figure 5 shows released DOF at a high level.

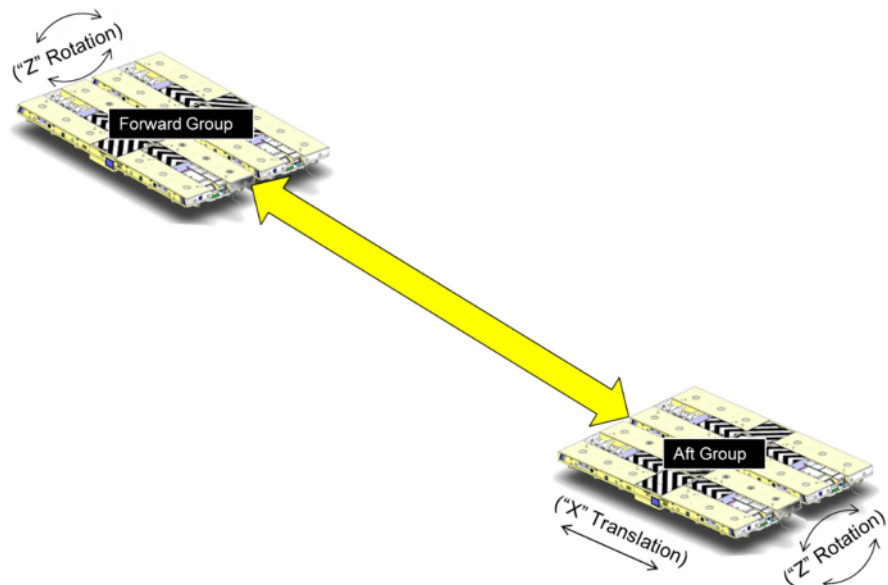


Figure 5. The MPTS includes released DOF, to prevent excessive loads at payload interfaces.

In place of the strongback, a laser alignment guide on the transporter maintains the separation distance. A monitoring system tracks relative motion of multiple released degrees of freedom. The combination of the released degrees of freedom and monitoring system provides the means for the article to traverse compound road contours, as illustrated in Figure 6. A remote-controlled drive system will shut down if set travel limits are violated.



Figure 6. The MPTS articulating over the contour of the road.

Design and Analysis Challenges

Designing the heaviest and largest rocket to date is not an easy task. Designing a transportation unit for that rocket comes with its own challenges. With the increased size, the need for larger and stronger hardware also increased. This shifts the selections of hardware, such as bearings for released degrees of freedom or bolts in fastened joints, from commonly produced parts, to specially-sized items that are difficult to procure.

Figure 7 shows an example of some catalog-available vendor hardware. The catalog lists a range of sizes for a particular part. The larger load-rated items are in less demand, and therefore require longer lead time. The increased size makes handling difficult, and special consideration is needed for even simple touch tasks. The size also makes logistics a challenge; passing through doors that were adequately sized for smaller articles designed in the past becomes a tight-fit operation. A balance between managing loads and maintaining an optimum size was ultimately achieved.

HR-1000CT UN Threads												
Frame Size No.	HR-1000CT Stock No.	Working Load Limit (lbs.)*	Torque (ft-lb)	Dimensions (in.)								Mass Each (lb)
				Bolt Size A ‡	Eff. Thread Projection Length B	C	D	Radius E	Diameter F	G	H	
2	6608103	1900	28	1/2 - 13 x 2.25	0.70	6.32	1.96	1.25	0.75	4.20	2.50	3
2	6608112	1900	28	1/2 - 13 x 2.75	1.20	6.32	1.96	1.25	0.75	4.20	2.50	3
2	6608121	3000	60	5/8 - 11 x 2.25	0.70	6.32	1.96	1.25	0.75	4.20	2.50	3
3	6608130	4800	100	3/4 - 10 x 3.00	0.85	8.59	2.96	1.63	1.00	6.25	3.25	11
3	6608139	6200	160	7/8 - 9 x 3.00	0.85	8.59	2.96	1.63	1.00	6.25	3.25	11
3	6608148	8300	230	1 - 8 x 3.50	1.35	8.59	2.96	1.63	1.00	6.25	3.25	11
4	6608149	12500	470	1-1/4 - 7 x 5.00	2.10	11.31	3.71	2.00	1.44	8.13	4.00	24
4	6607669	20000	800	1-1/2 - 6 x 5.50	2.60	11.31	3.71	2.00	1.44	8.13	4.00	27
4	6607727	20000	800	1-1/2 - 8 x 5.50	2.60	11.31	3.71	2.00	1.44	8.13	4.00	27
5	6607670	28000	1100	2 - 4.5 x 7.50	3.20	15.15	4.00	2.69	1.75	11.64	5.00	69
6	6607671	45000	2100	2 1/2 - 4 x 9.50	3.73	19.93	5.75	3.00	2.75	14.47	5.62	157

Figure 7. The Crosby Group catalog of Cold-Tuff Heavy Lift Swivel Hoist rings (Reference 5).

Following the egress from the facilities building, the next challenge is to travel on the road. Consider, for a moment, the one-time transport operation of the shuttle Endeavour through the streets of Los Angeles from the airport to the science center. Careful planning was performed in evaluating its travel route. Obstacles were assessed and removed as needed along the travel path; adjustments were needed to avoid impacts. Figure 8 shows a snapshot from a video of the shuttle as it travels from the airport to the science center.



Figure 8. Snapshot footage of shuttle Endeavor during its transport through Los Angeles (Reference 6).

A similar evaluation was performed in the design of the MPTS. Because this transport operation is meant to be repeated for different articles, consideration of the terrain and any obstructions along its path must be made. Factors include road grade, turns, signposts, overgrown flora, culverts, and bridges. Careful consideration of the travel path was taken to ensure the MPTS, while transporting its cargo, is capable of traversing the terrain without additional effort to modify the terrain or travel path.

This consideration led MPTS development to the challenge of evaluating the released degree of freedom our transportation system provides. Numerous computer model simulations and dynamic analyses were performed to ensure the range of motion provided by the system is adequate to support the path it needs to travel. The simulations involved creating a 3D model of Saturn Boulevard at the Michoud Assembly Facility in New Orleans, LA. The model was generated from data collected in a road survey, which includes the grade created by the levee that was added after Hurricane Katrina. Traversing this levee would require the unit to ascend and descend a steep grade, while making a turn and negotiating a bank in the road. This all occurs while each end is individually managing the sectional contours of the road beneath it. The evaluation was conducted using MSC Adams to ensure there is sufficient range to prevent the movements from bottoming out and to avoid unintentional loading of the article being transported. This simulation includes a flexible finite element model of our GSE hardware and the various payloads it supports, which is connected by joint mechanisms. The flexible body also includes contact definition between mating surfaces and accounts for dimensional tolerances that could develop in production. The maximum design range of motion also required consideration. Excessive motion would result in a larger-than-necessary structure that would create ingress/egress problems of wheel loading, and weight concerns on the road, and over bridges and culverts. The maximum range of motion also necessitates evaluation from a loading standpoint in order to ensure the shifting load does not overload a section of the hardware or article. With the MPTS designed to support multiple sized articles, the evaluation was conducted on each unit to ensure all the articles would be safely transported by a single MPTS design.

Most importantly, the objective is to ensure the design does not impart loads that could potentially damage the flight hardware during transport. The challenge stems from requiring the MPTS to be designed to the standard factors of safety for ground equipment, but a lower factor of safety is used in the design of the launch vehicle as a means of lowering the weight. Added to the complexity is how the loads are applied to the vehicle. The design of flight hardware typically considers the launch loads as the driving load case. However, the vehicle is typically transported horizontally. The loads induced by the MPTS are imparted in a different orientation during the transportation loads as compared to the launch environment.

The vehicle design seeks to minimize the need for local reinforcements. Early discussion with the flight vehicle engineer allowed us to determine the interface definition between the article and the MPTS. This is to ensure suitable locations are provided on the flight hardware capable of supporting the transport load without the need to add weight for localized reinforcements. The collaborative effort includes the identification of interface locations along with the number and size of the contact area. Attachment brackets are designed to connect to these interfaces. This minimizes the weight on the flight article, but also adds the challenge of designing brackets that are light enough to handle, or are situated in a manner allowing the use of support equipment. On-site installation also makes alignment and tolerance control difficult, particularly when attempting to align multiple parts as shown in Figure 9. With various articles requiring transport, the MPTS is designed to accommodate the different tolerances associated with aligning the multiple attachment locations.

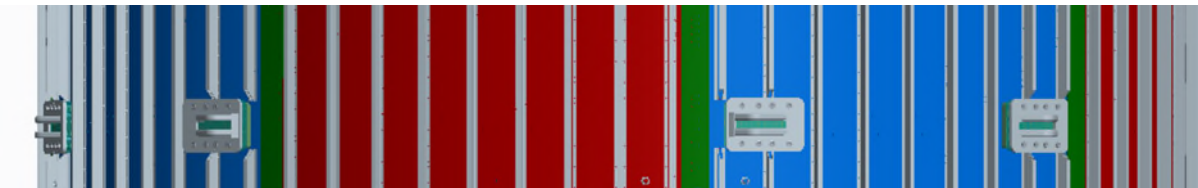


Figure 9. Illustrative depiction of multiple interface locations.

Lessons Learned

Additive Manufacturing

Additive manufacturing processes, commonly referred to as 3D printing, were used to generate tangible models of the MPTS. This offered a unique and straightforward approach to replicate plastic models of individual components of the SLS transportation system. A picture of a model generated in the preliminary phase of MPTS development is shown in Figure 10.



Figure 10. Preliminary conceptual additive manufacturing model.

Creating models generated through additive manufacturing was an expedient way to understand and demonstrate the interdependency of MPTS mechanisms. Released degrees of freedom at various locations of the MPTS affect both local and global movement of the combined payload and transportation system. The relative motion of the system was able to be simulated real time with a scaled down version of ground support equipment. The model shown in Figure 11 demonstrates MPTS relative motion.



Figure 11. MPTS Additive Manufacturing Model (Top View)

In addition to predicting system response, during the early development cycle, additive manufacturing models served as advantageous visual aids to assist with communication of concepts. Handheld models provide a foundation for quickly grasping concepts with increased levels of engagement during collaborative sessions.

Dynamics Simulations

Multi-body simulation of the transportation route has proven to be a useful tool to ensure the mechanisms will remain within the specified travel ranges, and to identify the locations on each route that are likely to be most challenging. General analysis tools for multi-body dynamics were already available, but a process for turning road survey data into boundary conditions needed to be developed from scratch. The MPTS inherently relies upon contact and various types of nonlinearities that cannot be linearized away. Adding control systems for dozens of wheel modules, with many contact definitions between a road surface and the tires, would make a miles-long roadway simulation strain solvability and still require a lot of guesswork. As an alternative, the as-built survey data was used to create splines for the center, and each side of the road. The splines incorporate features such as cross-fall, crown, and grade. A simplified mechanism of links and joints spans between the splines in order to be pulled along the path without binding. The resultant pitch, yaw, roll, and elevation for each location is imposed on a dynamic model of the MPTS mechanisms. Thereafter, the model is able to illustrate points on the surveyed road, the system will have the least available range-of-motion margin, and operators can respond to this information appropriately.

Since the MPTS mechanism model is built using both dynamically-reduced finite element models and realistic joints, it is also possible to capture the effects of structural flexibility, friction, and gapping. Through simulation, it was discovered that tolerances on a number of mechanisms needed to be kept extremely tight for the system to operate properly. A degree of freedom that is designed to be released at a particular location requires it to be released there, and nowhere else. Simulating the effects of tolerances revealed a loose fit of certain interfaces would result in redundant joints and indeterminate states for the system. This simulation resulted in a changed design, resulting in tight or adjustable interfaces at critical locations.

Friction Testing

In the first complete, end-to-end test of the integrated system, it was discovered that the friction at a critical joint was higher than anticipated. Moreover, this friction was high enough to impede proper operation. Initially, there was no plan in place to quantify or monitor this friction, but the Test Load Facility, designed to statically load the structure, proved flexible enough to perform this task. This led to the development of a means to test friction levels for critical functions (mechanism joints) which are essential to how the system operates. This testing should also be included for periodic maintenance during the design life of the system.

Another lesson associated with the friction test was the need to fully understand a vendor product, even something considered intuitively simple like a friction liner. A specific liner was selected in the design, based on the specification provided by the vendor. This liner was expected to have a coefficient of friction range that was crucial in one of our released degrees of freedom, and be capable of supporting the maximum calculated load during our transport operation.

During testing, it was discovered the friction load was higher than expected, and the friction coefficient of the liner was not as anticipated. Further research indicated the liner material is a specially designed product where the friction coefficient decreases with increasing load as shown in Figure 12, which is counter-intuitive with classic textbook problems.

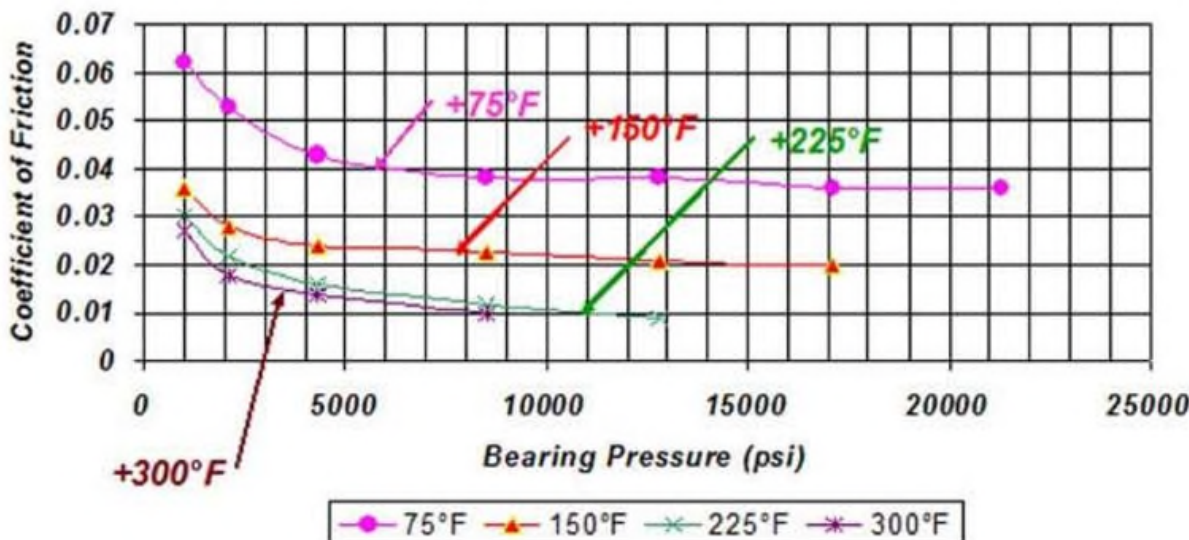


Figure 12. Vendor-reported coefficient of friction in relation to bearing pressure loads (Reference 7).

The coefficient of friction documented by the vendor is based on this condition. An evaluation of our design indicated our bearing pressure on the liner was below what was needed to achieve the desired friction. Our worst case loading conditions, which includes higher level wind loads in combination with the worst case operating, was considered in the selection. However, under normal operating conditions, the bearing pressure is significantly less and resulted in a negative impact to our anticipated friction loads.

Advertised properties provided by vendors should be investigated early in the design development process. Meanwhile, hardware strength evaluations should be conducted using enveloping values with additional margin until the stated properties can be verified. With the understanding of the vendor's required condition, the MPTS was able to be modified, and the friction load was verified to be within acceptable range after the changes were made.

Managing Interfaces and Parallel Development Efforts

To streamline the overall process, MPTS and payload development schedules included overlap. That is, the GSE design began before the payload designs were finalized. This reduced risk for the overall program because it allowed each side of the interface to take the other into account. If the GSE were developed after the payload design was completed, the payload design runs the risk of not having an interface with adequate strength to be transported, necessitating costly redesign effort. While concurrent development is desirable, two key challenges arose: how to address mismatched Factors of Safety (FOS) requirements and how to manage design changes in the payload.

GSE is typically required to meet higher FOS than the payload, and this was the case for the MPTS and its payloads. Early in the design phase, questions arose regarding how to enable each side of the interface to meet its requirements. *GSE loads can and do drive flight hardware design*, albeit at a local level in most cases.

Mismatches were addressed in the following manner: for interfaces where the payload added an interface solely to provide an attachment for the GSE, the interface was designed to allow the GSE to meet its required factors of safety. These interfaces were determined by the payload in order to minimize the impact to the payload. For interfaces where the interface was also used for flight, a less desirable situation, the interface design still attempted to allow the GSE to meet its required factors of safety. However, in these situations, there was often less flexibility to accommodate the GSE, and waivers to the GSE requirements often came into discussion. In situations where reduced FOS were considered, proof load planning became

a point of discussion because FOS below the proof load level would mean the GSE could yield during proof testing.

In all cases, the goal was to allow GSE to meet its FOS requirements, as this is ultimately a benefit to the overall program in that it reduces risk of damage to valuable hardware during transportation.

One challenge of two designs working concurrently is that changes to one side of the interface impacts the other interface. As payload designs evolved and the needs of the interfaces became better understood, the MPTS design frequently had to adapt. For some component designs of the MPTS, this required up to three significant redesigns and an unplanned development effort. As a result, design reviews and drawing releases were regularly adjusted. While program schedule fortunately allowed for these redesigns, planning them upfront would clarify expectations for affected teams.

Summary and Conclusion

Throughout the development of the MPTS, various methods and tools were used. This included developing 3-D printed models, performing multi-body simulations, and conducting tests. These methods aided in the production of a highly complicated system capable of adapting to the multiple articles it was tasked to support. 3-D printed models provided a means to understand and demonstrate complicated mechanisms inherent in the design. Performing multi-body simulations allowed a means of verifying the released degrees of freedom and the limited range of motion they provide. The use of models and simulated analysis offered a cost-effective means to identify critical locations, features, and tolerances. Testing has also proven to be essential to ensure the MPTS functions appropriately. This aided in assessing specific issues that would have otherwise been overlooked on paper, or with smaller scale modeling. Early communication is key to successfully delivering hardware in a timely manner. All the work performed in developing the MPTS was done in conjunction with the design of the flight hardware. This was accomplished by identifying the interface locations on the vehicle and understanding the MPTS requirements to safely deliver the spaceflight hardware to test locations and the launch platform.

References

1. NASA. "KSC-70P-19." *Apollo 14 Multimedia*, scan by J.L. Pickering, 22 Jan. 1970, <https://www.hq.nasa.gov/alsj/a14/images14.html#KSC70P19>.
2. NASA. "KSC00padig095." *NASA Image and Video Library*, 21 Nov. 2000, <https://images.nasa.gov/details-KSC00padig095.html>.
3. Wheelift. "nasa2." *NASA Uses Wheelift Transporters for Spacecraft Assembly and Transport*, accessed 31 Jan. 2018, <http://www.wheelift.com/case-studies/case-study-detail/nasa-uses-wheelift-transporters-for-spacecraft-assembly-and-transport>.
4. Bergin, Chris. "Z71." *SPMT: Providing transport to SLS core stages*, NASA Space Flight.com, 10 Dec. 2013, <https://www.nasaspacelift.com/2013/12/spmt-transport-sls-core-stages>.
5. "Crosby® HR-1000CT COLD-TUFF® UNC Heavy Lift Swivel Hoist Rings." *Crosby Catalog*. Crosby, 2017. <https://www.thecrosbygroup.com/catalog/rigging-accessories/crosby-hr-1000ct-cold-tuff-unc-heavy-lift-swivel-hoist-rings/>, 31 Jan. 2018.
6. "Timelapse video: Space shuttle Endeavor's crosstown journey through L.A." Los Angeles Times, <http://www.latimes.com/local/73406669-132.html>, 31 Jan 2018.
7. "Karon Design Guide." KAMAN Specialty Bearings & Engineered Products, <https://www.kaman.com/sites/default/files/KaronDesignGuide.pdf>, 31 Jan. 2018.

NASA Docking System Block 1: NASA's New Direct Electric Docking System Supporting ISS and Future Human Space Exploration

Justin McFatter*, Karl Keiser** and Timothy Rupp[†]

Abstract

The NASA Docking System (NDS) Block 1, shown in Figure 1, is a key component of NASA's vision for space exploration. It is designed to provide capability for visiting vehicles to dock to the International Space Station's recently-installed International Docking Adapter ports. It is the first docking system to be developed by NASA since the Apollo-Soyuz Test Project of the 1970's. The NDS Block 1 includes provisions for capture, structural attachment, power/data transfer, and undocking. It uses a direct-drive electromechanical Stewart Platform capture system architecture, along with an innovative automated control scheme to achieve an unprecedented level of performance and simplicity. Its design implements the new International Docking System Standard, which will be a key enabler of diverse and flexible exploration missions. NDS qualification was completed in 2017 to support a planned first flight in 2018 on the Boeing CST-100 Starliner.

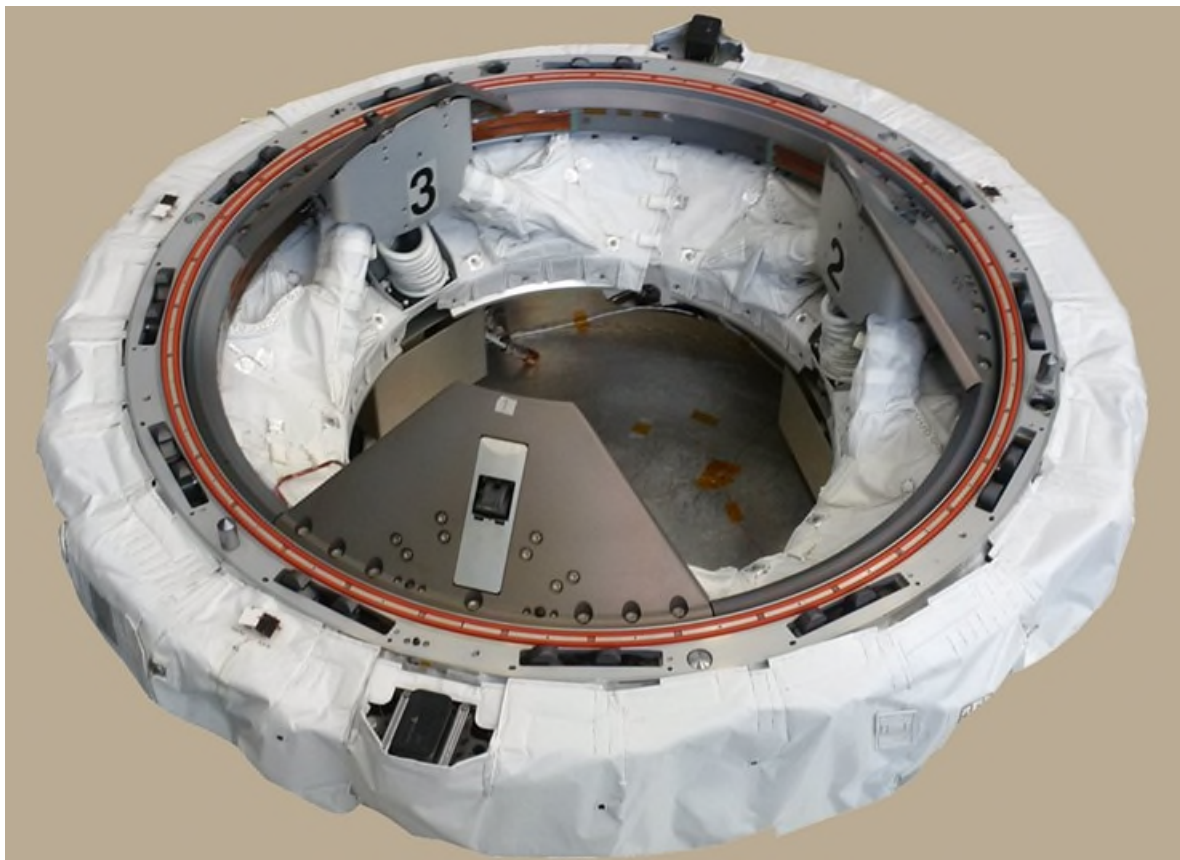


Figure 1. NASA Docking System Block 1

* The Boeing Company, Houston, TX

** The Boeing Company, Huntsville, AL

[†] NASA Johnson Space Center, Houston, TX

Introduction

The technical fascination with spacecraft rendezvous and docking is unmistakable. The attraction of watching complex vehicles carrying humans approach, align, collide, attach, park, and structurally anchor is timeless. For as long as travelers have set off on perilous voyages, onlookers have been mesmerized by their departure, return or arrival in a foreign port. The vocabulary of spacecraft docking harkens back to the days of wind-driven ships. Docking, berthing, ports and other mating system terminology are vestiges of our maritime traditions. The special allure of spacecraft docking is evident in popular culture. Most space travel motion pictures inevitably include a detailed technical scene depicting how the spacecraft docks or undocks, complete with the whoosh of a hatch opening and the clunk of the final structural connection to symbolize the consequence and finality of arrival and departure.

NASA's newest docking system evolved from systems developed during the Apollo-Soyuz Test Project. This paper will trace the considerations that drove that evolution to the current design. It will provide an overview of the NDS architecture, components, and operation, and will recount a few of the key technical challenges and lessons learned during system development and qualification. System performance as demonstrated by dynamic testing is also summarized.

Historical Context

NASA makes a distinction between docking and berthing operations. Docking is defined as the process of connecting two spacecraft without external assistance. Continuing with the maritime analogy, docking represents the combination of a port and a ship for which the captain in a boat is able to navigate, make land and tie up to a boat dock without external aid. Berthing, on the other hand, is analogous to the large ship scenario where a harbor master or pilot boat is required to aid moving the boat into the boat dock. Wigbert Fehse defines docking and berthing in *Automated Rendezvous and Docking of Spacecraft* as follows [1]:

In the case of *docking*, the guidance, navigation and control system of the chaser controls the vehicle state parameters required for entry into the docking interfaces of the target vehicle and for capture.

In the case of *berthing*, the guidance, navigation and control system of the chaser delivers the vehicle at nominally zero relative velocities and angular rates to a meeting point, where a manipulator, located either on the target or chaser vehicle, grapples it, transfers it to the final position and inserts it into the interfaces of the relevant target berthing port.

In the current International Space Station (ISS) berthing operations, the pilot boat is replaced by the Space Station robotic arm. Visiting vehicles or other external hardware are plucked from a station keeping position or removed from a cargo bay, and placed onto an attachment mechanism on the ISS. Berthing allows for a lighter and less complex attachment mechanism than docking, but requires an external robotic manipulator to be present at all berth and unberth events. The safe handoff of the payload from the robotic arm to the berthing mechanism presents technical challenges as well.

In docking, the attachment mechanism includes its own robotic manipulator, known as the Soft Capture System (SCS), for maneuvering the vehicles after soft capture into final position for hard mate. The SCS has a capture envelope large enough to accommodate the inaccuracies of the Guidance, Navigation and Control (GN&C) system. It attenuates the relative motion of the two vehicles, and then slowly brings them together with enough accuracy to engage the shear features of the interfacing tunnels.

The development of ISS created several different mechanisms for berthing, most notably the Common Berthing Mechanism. Common Berthing Mechanisms are used to connect the pressurized elements of the Space Station and allow crew to move between elements. Several other berthing mechanisms are used around the Space Station to attach the unpressurized truss elements. Despite its array of berthing mechanisms, NASA lacked a man-rated pressurized docking system design before the development of NDS. The last US-built docking system, shown in Figure 2, flew in support of the Apollo Soyuz mission.

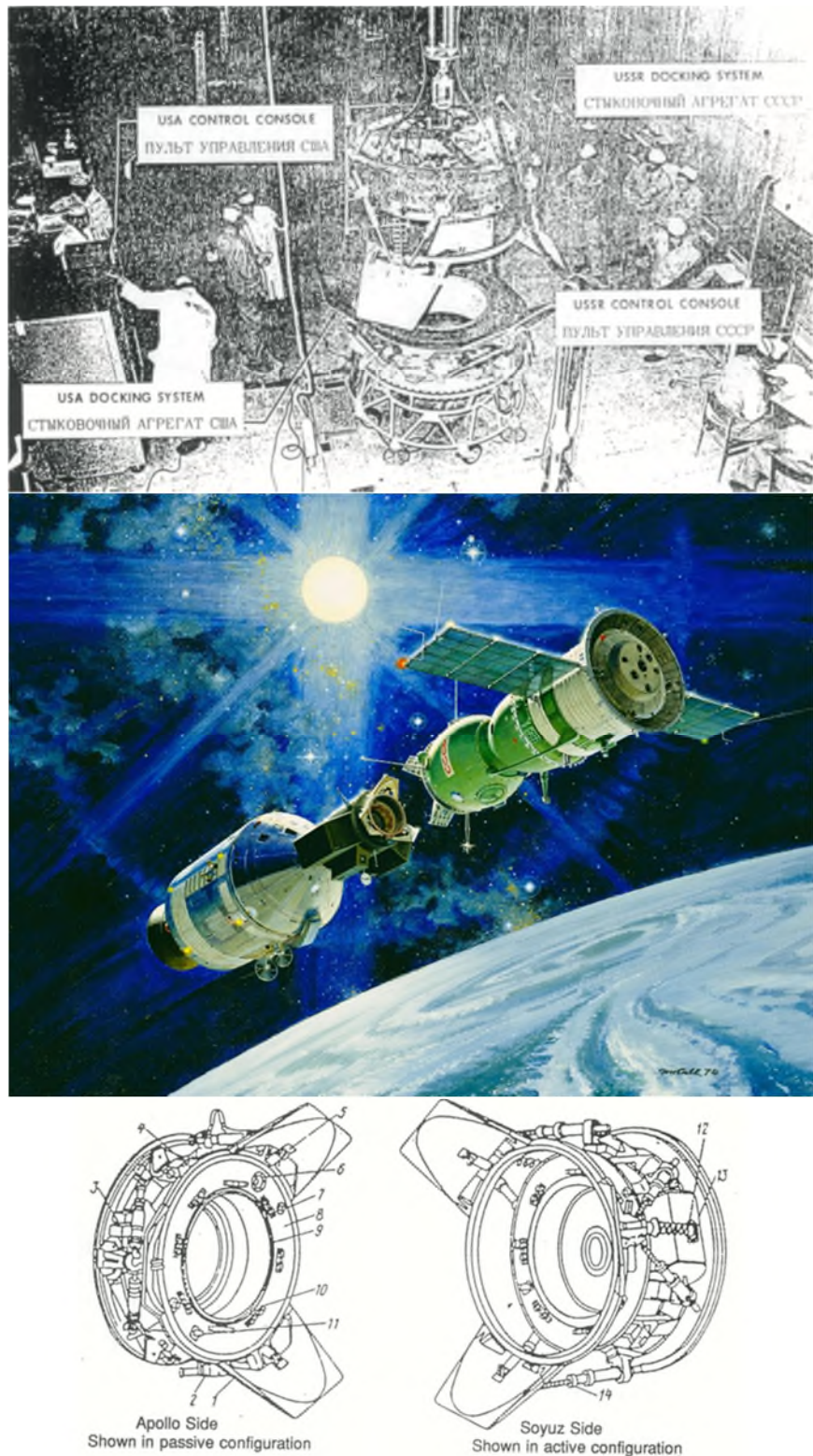


Figure 2. Images of NASA's last US-built human-rated docking system - circa 1975

All of the docking that occurred during the Space Shuttle and Space Station era has used hardware procured from Russia. The systems were developed by Russian (then Soviet) contractor RSC-Energia and had been used previously in the Russian MIR space station complex. The Space Shuttle docking system was known as the Androgynous Peripheral Attachment System (APAS), which is shown in Figure 3. APAS was a variant of the Apollo Soyuz design with the petal direction reversed. The interface requirements of the new International Docking System Standard trace much of their heritage to the APAS in terms of hard capture and soft capture hardware geometry. The soft capture design of the APAS capture system was largely mechanical. The three bi-pods were all mechanically connected via a triple differential. In simple terms, pushing down on one petal pushed the other two up. This was a significant advantage in terms of capture success but the mechanical transmissions were extremely complicated. The system needed a large contingent of electromechanical hardware including; motors, brakes, slip clutches, fixers, eddy current damper and 9 control boxes.



Figure 3. NASA image of the Space Shuttle with Russian APAS docking mechanism

In the early 1970s, NASA commissioned the Space Division of North American Rockwell to conduct trade studies on docking technologies in support of the Apollo Soyuz Test Mission [2]. The contract produced detailed analysis and sub-scale mechanisms to evaluate most of the major technology areas of docking. Many of the technical parameters identified in this study remain in today's docking system. The study selected a cable retracted hydraulic actuator for the US soft capture system design. It also built and modeled the Russian mechanical soft capture system and postulated the viability of two other architectures.

The other architectures were direct servo electric (shown in Figure 4) and cold gas pneumatic-hydraulic soft capture systems. The cold gas system was undesirable due to a low cycle associated with the gas consumables. Reduced weight and lower friction were identified as key improvements of a direct servo system. The development time, weight, power consumption and reliability of the electronics needed to control an electric platform of the early 1970s prevented this architecture from being selected. Today's electronics and the NDS controls approach have overcome these problems, allowing the NDS to implement a direct electrically controlled soft capture system.

There are several unique characteristics of this system. The design employs a control approach originally envisioned in 2003 by Boeing in support of the Orbital Space Plane Program [3]. The NDS soft capture system externally appears very similar to APAS, but the control and effector architecture is completely different. Unlike the APAS ball screws, the NDS linear actuators are mechanically independent of one another, each being driven by a dedicated motor. Because of this lack of mechanical coupling, the coordination required to accomplish capture and alignment must be provided by the controller. In most ground-based Stewart Platform applications, the coordination involves calculating the position and

orientation of the motion platform using the measured lengths of the six actuators. The lengths of the actuators can then be adjusted to accomplish the desired motion of the platform. In these ground-based systems, the calculation of the platform position and orientation, known as the forward kinematic solution, must be performed numerically using a processor-based computer due to the lack of a closed form solution. During the early phases of NDS development, the cost and schedule impact of developing a processor-based controller certified for the space environment were identified as a major program risk for architectures that required it. This risk was one of the key discriminators that led to the selection of a SCS architecture that does not require the forward kinematic solution.

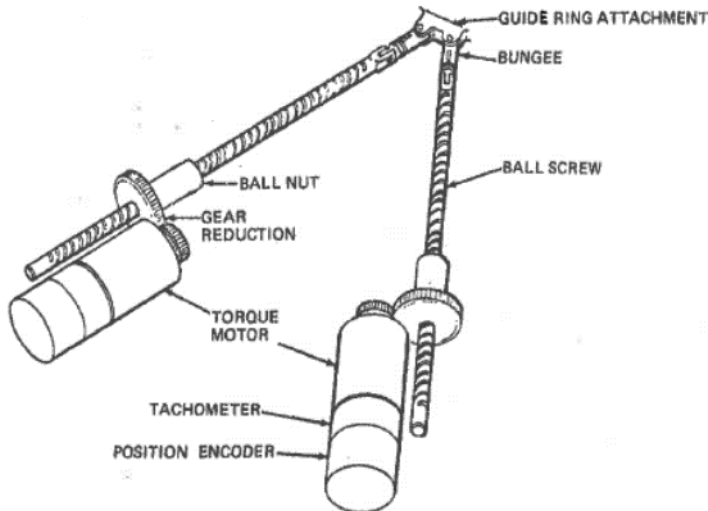


Figure 4. Torque Motor Servo System from Apollo Soyuz study

The arrangement of the NDS linear actuators is such that the soft capture ring is coaxially aligned with the tunnel whenever the six actuator lengths are the same. The NDS control architecture makes use of this fact to simplify the commanding of the actuators during capture and ring alignment. During capture, the controller calculates the average length of the six actuators at every instant of time and uses it as a point of reference for commanding current to the motors. This logic gives the soft capture ring a central tendency as it complies to accommodate vehicle misalignments. The simple coordination algorithms used in the SCS allow for an implementation that does not require a processor-based controller. During soft capture operations, the NDS relies solely on position and current feedback to control the six linear actuators as they bring the vehicles together and engage the structural mating features of the two tunnels. Major components of the NDS are shown in Figure 5.

Operational Sequence

The docking event is an automated sequence punctuated by several discrete events. During the approach, the SCS is extended to the “ready to capture” position, where it awaits initial contact between the two spacecraft. The GN&C system of the chaser vehicle ensures that initial contact occurs within the capture envelope of the docking system. From initial contact onward, the chaser vehicle is in free drift and relies on the docking system to capture and maneuver the vehicles to hard mate. This approach distinguishes NDS from previous docking mechanisms, which all relied on the host vehicle thrusters to push the soft capture features together after contact to achieve capture. The design of the NDS SCS has eliminated this need. Qualification testing of the SCS in the summer of 2016 demonstrated 100% capture success for a robust set of initial contact conditions, without the use of post-contact thrust.

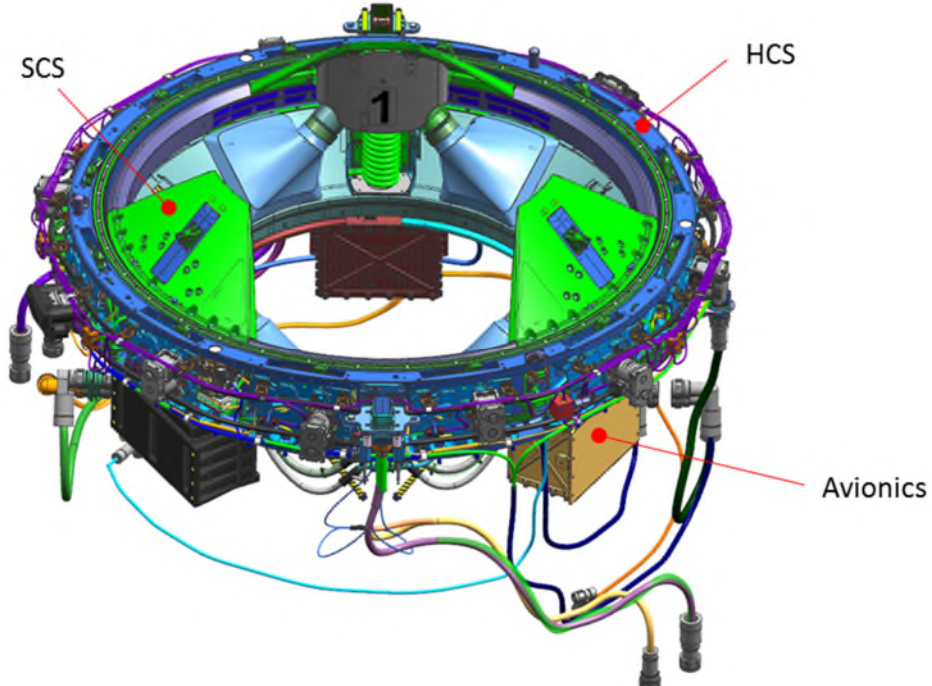


Figure 5. NASA Docking System Schematic

At contact, the forces between the coarse alignment guides cause the NDS linear actuators to be displaced from the ready to capture position. This event signals the controller to initiate a maneuver known as the Lunge. During Lunge, the soft capture system extends in a compliant manner to accommodate vehicle misalignments and engage the soft capture latches, one of which is mounted in each of the three guide petals on the soft capture ring. Each latch engages an opposing striker plate mounted behind the passive side soft capture ring. The interface between the capture latch and the striker is shown in Figure 6.

Once the capture latches are engaged, sensors mounted in the soft capture ring indicate that capture is achieved, signaling the system to begin attenuating the relative motion of the two vehicles. At this point, the two soft capture rings are loosely held together by the capture latches such that the incoming vehicle cannot escape. Once the time allocated for attenuation expires, the controller begins adjusting the lengths of the actuators to equalize them, thereby aligning the two mating tunnels. With alignment complete, the linear actuators retract, closing the gap between the two tunnels and engaging their shear features.

Once the two structural tunnels are in close proximity, a set of twelve structural hooks are driven, which engage corresponding compliant passive hooks on the opposing tunnel. The structural hooks close the remaining gap between the tunnels, compressing an elastomeric seal and creating an airtight structural interface. With the hard part finished, motorized umbilical connectors can then be driven, allowing for power and data transfer between the docked spacecraft. The major hard capture interface components are shown in Figure 7.

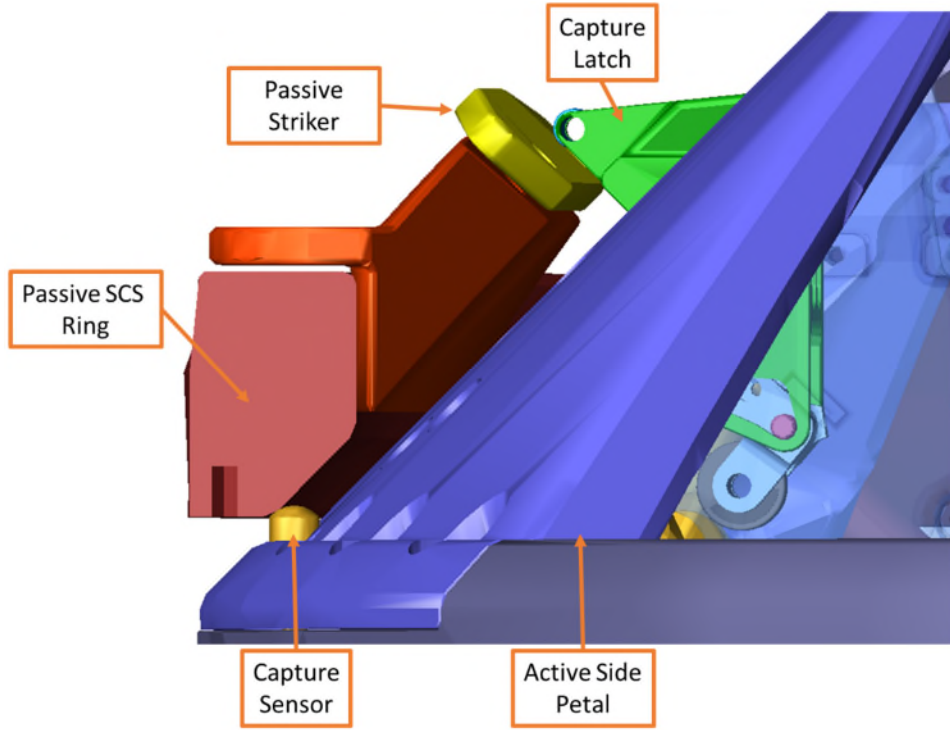


Figure 6. Soft Capture Latch Interface

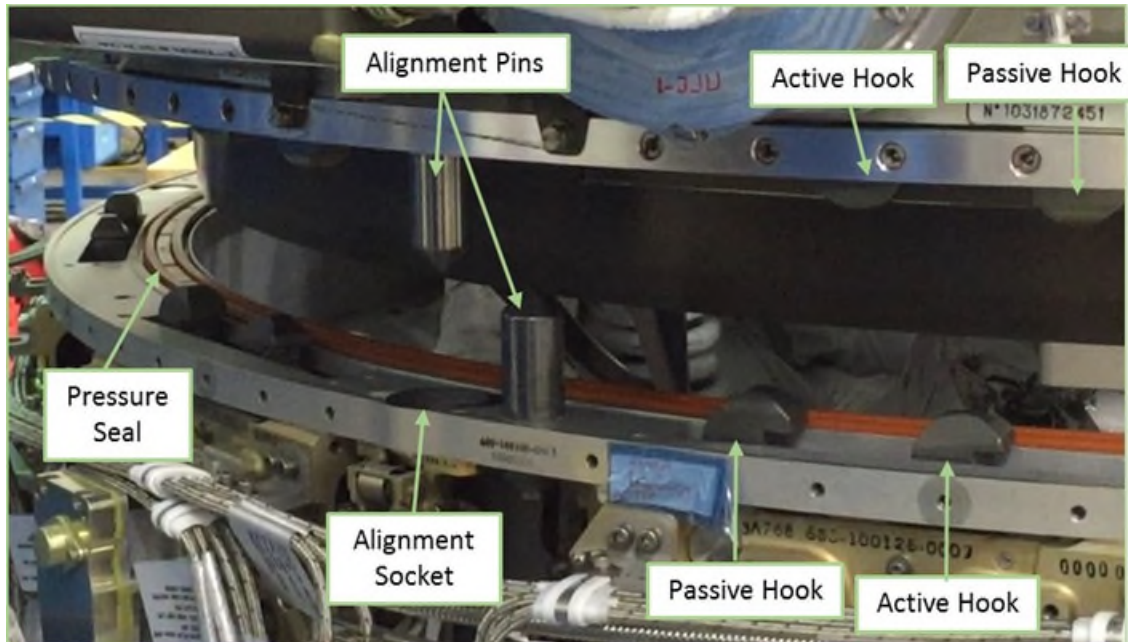


Figure 7. Hard Capture Interface

Technical Challenges

The thermal environment in Low Earth Orbit presented one of the key technical challenges to the docking system design. The temperature of hardware in space varies from extreme heat when in direct sunlight to extreme cold when facing deep space. Even with the protection afforded by insulating blankets, the linear actuators must perform over a wide temperature range. In order to perform the delicate capture operation, the actuators must control their force output accurately. The NDS is able to accomplish this feat without the use of load sensing because of its highly efficient ball screws. As a result, the current feedback from the motors is able to provide a reliable indication of actuator force output.

The risk of collision between the chaser vehicle and the Space Station was another key technical challenge faced by the NDS designers. Because of the direct electric design of the soft capture system, a power loss or avionics failure during docking results in loss of ability to control vehicle relative motion. The high efficiency ball screw actuators present little resistance when unpowered, and therefore introduce the risk that the chaser vehicle could drift into the Space Station after a failure, with catastrophic consequences. To mitigate this risk, a redundant string of avionics was included in the NDS design, which can be activated in a time-critical failure scenario during docking. The redundant string is able to slow the vehicle's motion enough to give it time to open the capture latches and perform a controlled abort, after which the docking can be reattempted. To protect against the unlikely event that both avionics strings fail during docking, a secondary capture latch release, independent of both avionics strings, was also included in the design. The secondary release uses a non-explosive separation mechanism that, while irreversible, is fast enough to separate the soft capture interface and allow the incoming vehicle to escape without collisions and return home safely.

System Performance

The Six Degree of Freedom (6DoF) test system at Johnson Space Center provides a sophisticated hardware-in-the-loop simulation of the docking event. As shown in Figure 8, the target vehicle side is represented by a qualification-fidelity test article of the Space Station's docking adapter, mounted to a motion table. The motion table is driven by a computer simulation of the relative motion of the two spacecraft in zero gravity. Although the active docking system test article is mounted to fixed structure in the test, the simulated motion of both vehicles is incorporated into the table's motion. The 6DoF facility is able to introduce misalignments and off-axis rates to simulate the inaccuracies of the spacecraft GN&C systems.

In order to characterize the NDS capture performance in a statistically representative manner, the test cases were randomly distributed within limits that envelope the expected GN&C performance of the target and chaser vehicles. The initial contact condition limits are shown in *Table 1*. The simulated chaser vehicle masses were selected to bound the lightest and heaviest cargo and crew vehicles planned to dock to the Space Station (10 t and 18 t). At the outset of the NDS design, it was established that missed captures are acceptable in up to 1% of misalignment cases, provided that the system is capable of safely recovering for a second docking attempt. Despite this allowance, the NDS successfully captured all misalignment cases during the 6DoF test, while remaining within load and vehicle relative motion limits. For practical reasons, the 6DoF test was performed in the ambient air environment. As a result, the final verification of capture performance comes from an analysis that incorporates the temperature-dependent component data into a test-correlated computer simulation.



Figure 8. NDS 6DoF Docking Test

Table 1. NDSB1 Initial Contact Condition Limits

Initial Conditions	Limiting Value
Closing (axial) rate	3 to 6 cm/s
Lateral (radial) rate	up to 4 cm/s
Angular rate	up to 0.2 deg/s about closing axis up to 0.2 deg/s about any lateral axis
Lateral (radial) misalignment	up to 11 cm
Angular misalignment	up to 5 deg about closing axis up to 5 deg about any lateral axis

A test case used to validate the docking simulation was the case of an 18 t host vehicle docking to the ISS Node 2 Forward docking port with an approach velocity of 4.5 cm/s and a Yaw misalignment of -5 deg about the nadir axis. At initial contact the NDS is tilted towards Petal 1, located in the starboard direction of the chaser vehicle, as shown in Figure 9. Initial contact occurs between the capture latch on Petal 1 and the corresponding striker on the passive. Contact is detected when the SCS ring at the base of the petal contacts the passive SCS ring. Struts 1 and 2, which are attached to Petal 1, are then driven backwards during Lunge due to the contact at the SCS ring. During this time, the Lunge control law causes the other four SCS struts to extend and engage the latches on Petals 2 and 3. The time history of strut lengths is shown in Figure 10.

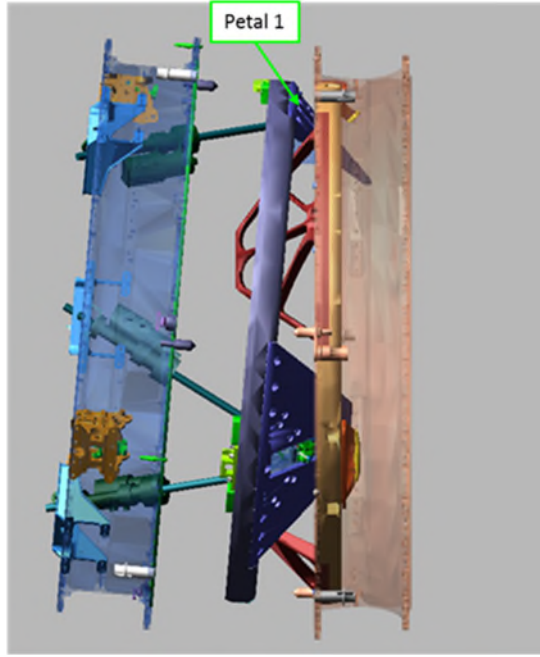


Figure 9. Initial Contact at -5 deg Yaw

After the capture sensors are activated, the SCS transitions into Attenuate, where the actuators counter the momentum of the chaser vehicle while limiting force output via current limiting. After the initial high load event in Attenuate, the motion of the chaser is essentially arrested, with only small motion remaining within the space between capture latches and the strikers. The measured and predicted motor currents for the -5 deg Yaw case are shown in Figure 11.

For the test program as a whole, the results showed good agreement with analytical predictions. The docking simulation parameters were adjusted based on test results to match the performance observed in the single-axis extreme misalignment cases. After completion of the model correlation activity, the results of the randomly distributed contact cases were compared to the model. The results of this comparison, shown in Figure 12, indicate good agreement between test results and predicted system performance.

To demonstrate safety and robustness, the system was tested with a number of simulated failure conditions including missed captures, single string avionics failures, and failure of a single capture latch. In all cases, the system was able to recover safely either by bouncing off without collision or by safely terminating the docking attempt. To round out the test program, the flexibility of the system for other mission scenarios was demonstrated by adjusting the control law gains to optimize for lighter vehicles. With this alternate configuration, the system successfully docked a 15 t chaser vehicle to a 5 t payload with single-axis misalignments of 5 deg and 11 cm. The ability to support light vehicles is key to exploration missions that may involve docking a crew capsule to a Mars or Lunar surface lander or other small payload.

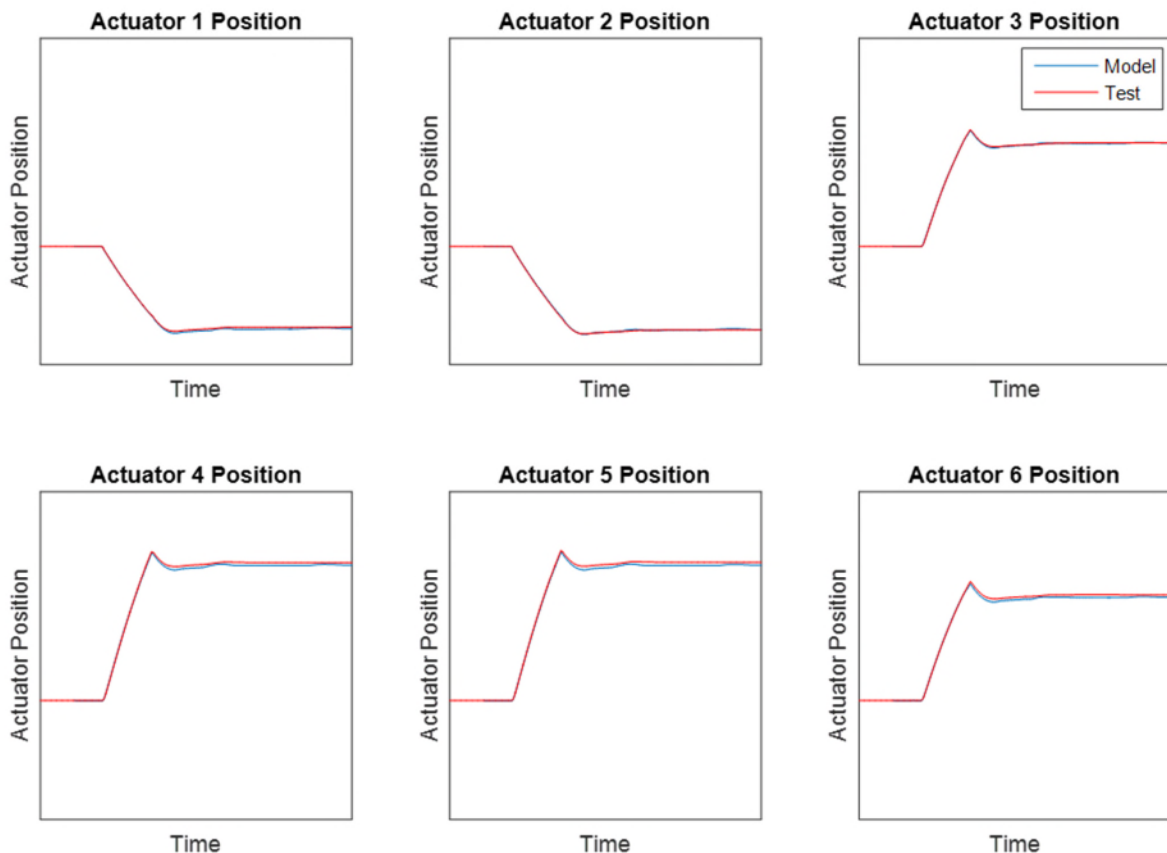


Figure 10. Linear Actuator lengths for 18 t Host Vehicle, -5 deg Yaw, 4.5 cm/s approach velocity

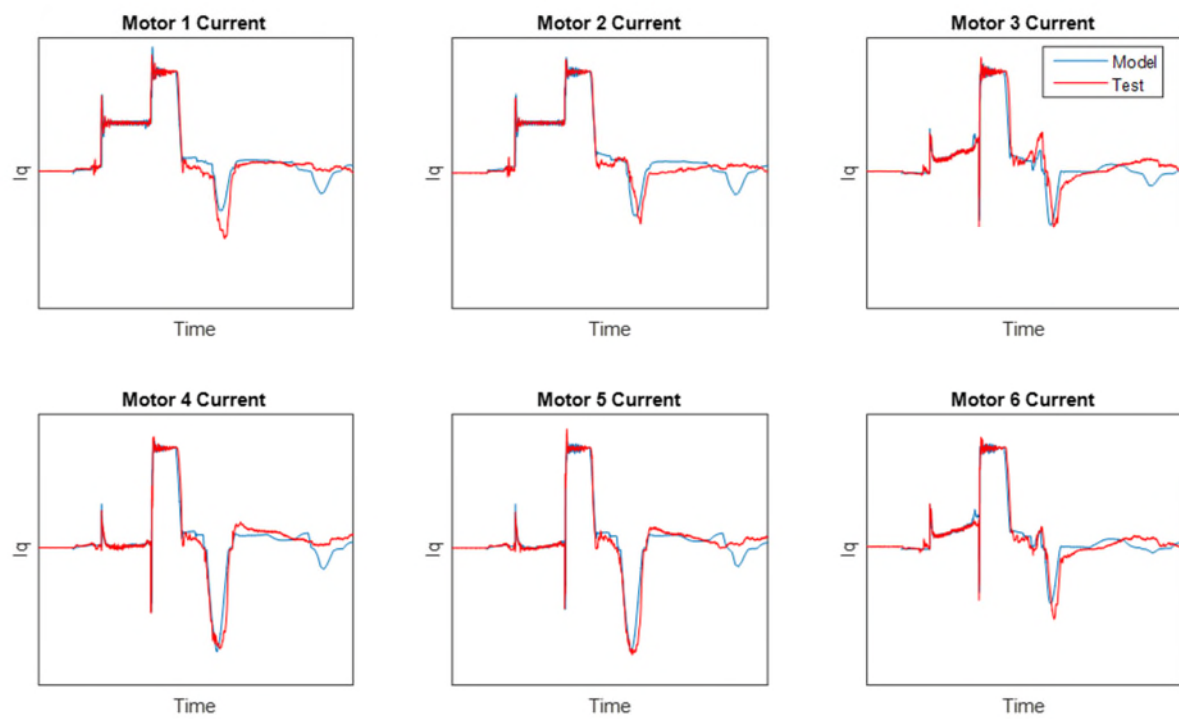


Figure 11. Linear Actuator Currents for 18 t Host Vehicle, 5 deg Yaw, 4.5 cm/s approach velocity

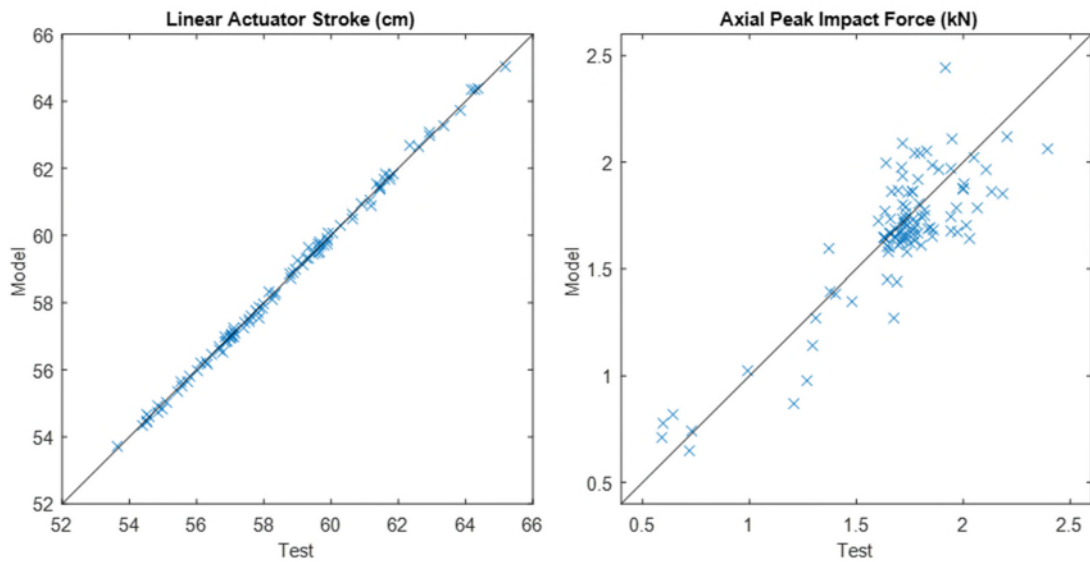


Figure 12. 6DoF Test Results

Lessons Learned during 6DoF Testing

Successful engagement of the soft capture latches is indicated by the activation of a set of capture sensors embedded in the active soft capture ring at the base of the coarse alignment petals. Each capture sensor is activated by a simple spring-plunger mechanism that is depressed by contact with the opposing soft capture ring. The arrangement of these sensors is shown in Figure 13.

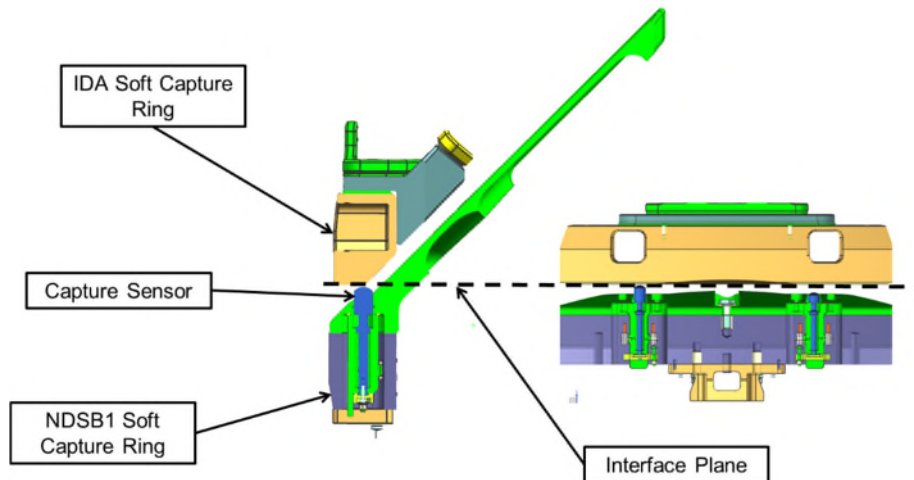


Figure 13. Soft Capture Sensors

Both the button and shaft of the capture sensor are coated with a polytetrafluoroethylene (PTFE) impregnated hard anodize. During development-level 6DoF testing in 2014, capture sensors began seizing intermittently after approximately 400 docking cycles. This condition prevented the capture latches from successfully engaging the strikers on the passive test article. The seizing was caused by damage to the anodize coating on the button and shaft wear surfaces of the capture sensor, due to repeated impact against the passive soft capture ring. Figure 14 shows the condition of the capture sensor plunger and housing at

the end of the development test program. In order to improve the durability of the capture sensor flight design, a grease lubricant was added to the wear surfaces of the capture sensor, with a plan to maintain the lubricant between flights. When qualification 6DoF testing of the modified design was completed in 2016, the unit completed 216 docking cycles with one re-lubrication midway through the test matrix. The lubricated sensors showed no visible signs of wear on the anodize coating or opposing ring contact area, indicating that the grease lubricant was effective at mitigating damage to these surfaces.



Figure 14. Capture sensor and opposing ring wear pattern during development testing

A key design decision that was validated during 6DoF testing was actuator optimization. The selection of actuator type and careful design of actuator components were important in optimizing the responsiveness of the soft capture system. Because system requirements allowed enough time for the docking vehicles to be slowly maneuvered into position, relatively little force output was needed from the linear actuators. As a result, the need for aggressive gearing was avoided.

Due to the fidelity compromises in the engineering development unit (EDU) used for the first round of 6DoF testing, the linear actuators were less optimized than the flight design. The capture sensors on the passive Space Station side of the docking interface (similar to those on the active side) were also omitted. The second round of 6DoF testing used a high-fidelity qualification test article for both the active and passive halves of the docking system. In the qualification 6DoF test, the linear actuator's design fidelity was increased, and the passive side capture sensors were included. The optimized actuator design reduced the impact energy between the soft capture rings at the instant of capture, while the addition of the passive-side capture sensors helped further cushion the impact. The net effect of these changes is evident in the axial docking loads measured by the 6DoF facility load cells that were mounted underneath the passive test article. Figure 15 compares the axial docking loads for the EDU and Qualification 6DoF tests for the case of an 18 t chaser vehicle docking to the ISS forward docking adapter, with a 5 deg Roll offset between the two mechanisms at the instant of contact, and a 4.5 cm/sec approach velocity. The results indicate a significant reduction in peak axial force at the moment of capture.

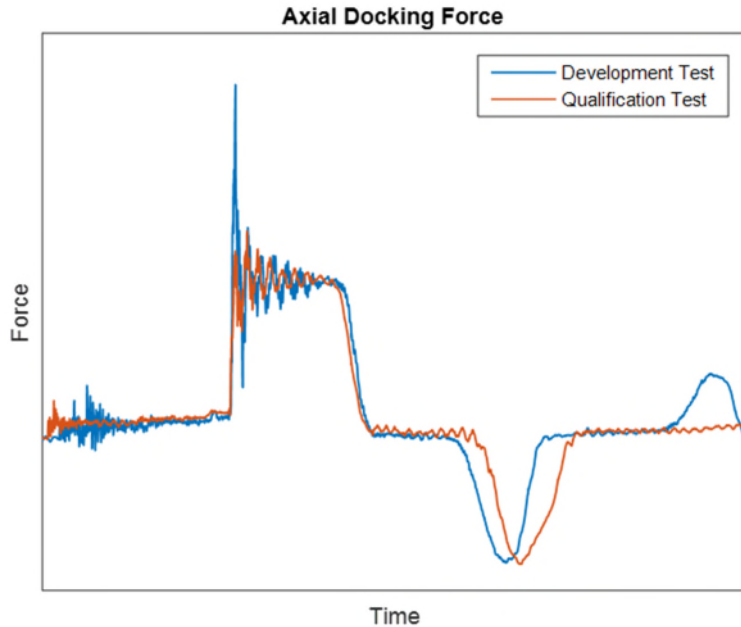


Figure 15. Axial docking force from 6DoF testing of an 18 t chaser vehicle with ISS with a 5 deg Roll misalignment

The results of the 6DoF testing validated the SCS design approach. The use of optimized linear actuators allows the SCS to control its motion and limit interface loads without the need for force feedback. As demonstrated by component-level thermal testing of the linear actuators, this capability extends over the expected range of on-orbit thermal environments. Furthermore, the design is extensible to a variety of target and chaser vehicle mass properties through adjustment of control law parameters.

Conclusion

The NDS is NASA's first docking system since the Apollo-Soyuz Test Project of the 1970's, and the first implementation of the new International Docking System Standard. Its direct electrical architecture leverages modern technology to greatly reduce mechanical complexity compared to the heritage APAS design used for the space shuttle. Its innovative controls approach eliminates the need for post contact thrusting to effect capture, reducing operational complexity for vehicle providers, flight controllers and crew. Its flexible architecture allows for controller settings to be adjusted either on the ground or in flight in order to capture target vehicles ranging from small 5 t landers to the 450 t International Space Station. Importantly, it also provides a robust capability to recover safely from a wide variety of failure scenarios. As a key enabler of modular mission architectures, NDS will be critical to making NASA's vision for space exploration a reality.

References

1. Fehse, W. *Automated Rendezvous and Docking of Spacecraft*. Cambridge University Press. 2008. p. 3
2. Report SD 72-CS-0048-3, Apollo/Salyut Test Mission Study Report, June 1972, Space Division North American Rockwell
3. Motaghedi, P. and Ghofranian, S. "Feasibility of the SIMAC for the NASA Docking System." *AIAA Space and Astronautics Forum and Exposition (SPACE 2014)*; 14 Jul 2014.

Capture Latch Assembly for the NASA Docking System

Brandon N. Dick*, Nathan Mauch* and Timothy Rupp**

Abstract

This paper will present a summary of the Design, Development, and Qualification of the Capture Latch Assembly (CLA) for the NASA Docking System (NDS) Block 1 (NDSB1). The CLA is an integral part of the Soft Capture System (SCS) of the NDSB1, serving the purpose of connecting the mating SCS Rings of two docking vehicles. The paper will present an overview of the function of the CLA and its basic concept of operations, including a summary of the major components of the CLA. The development, qualification, and production of the CLA will then be described. Particular focus will be provided on two major issues that occurred during production and qualification of the CLA. The first issue was failures of the CLA Motor (CLM) during acceptance testing. The failures of the CLM were ultimately determined to be due to design defects and manufacturing errors in the motor commutation sensor assembly. The second issue was failure of the secondary release mechanism, or Contingency Capture Latch Release (CCLR) mechanism during development and qualification testing. The CCLR failures were found to be a result of excess free play in the release mechanism, resulting in wear leading to galling inside the release mechanism. An overview of each failure will be provided, along with a summary of the failure investigation and recovery process. Finally, Lessons Learned from each of the major issues and the overall development of the Capture Latch will be presented.

Introduction

The Capture Latch is an indeterminate mechanism in the NDSB1 tasked with providing the initial connection (soft capture) between space vehicles during a docking procedure. The Capture Latch maintains the connection between space vehicles during initial contact, vehicle alignment, and vehicle hard capture. Once hard capture is completed the capture latches are released and the NDS SCS is stowed. Each NDS has three latches, one on each petal of the NDS as shown in Figure 1.

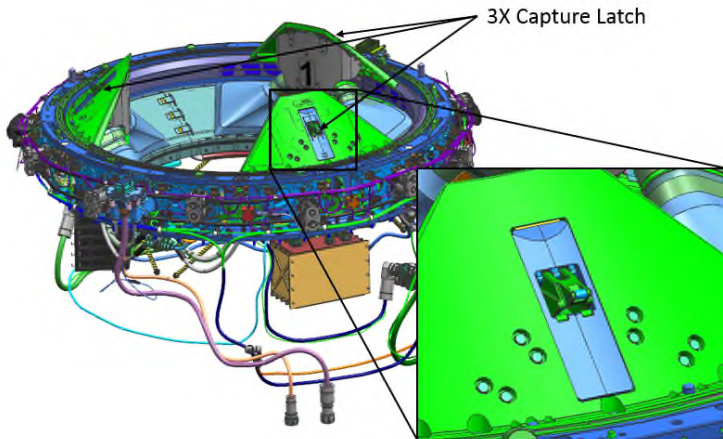


Figure 1. NDS with 3 Capture Latches

* The Boeing Company, Huntsville, Alabama

** NASA Johnson Space Center, Houston, Texas

The CLA is a derivative design of the latch on the docking system used in the Apollo–Soyuz Test Project (ASTP) [1]. The ASTP latch design was further refined for follow-on docking systems including the APAS-95 docking system used in the Space Shuttle [2]. There were several critical upgrades in this design revision that were previously absent. They include the ability to release under significantly larger loads, meeting requirements set forth in NASA-STD-5017 (design for minimum risk), and an automated secondary release.

Design Requirements

The primary CLA requirements were derived from system performance characteristics and needs. The primary requirement was to be able to release under a specified tensile load quickly enough to ensure two vehicles could detach during a failed docking attempt without collision between spacecraft or damage to the NDS.

The secondary release requirements were derived for conditions under which the capture latch experienced a failure in the primary drive train and had to be released very quickly. The pre-capture force of the mechanism had to be limited to reduce the amount of forward vehicle velocity needed to push the latches out of the way and complete a capture. The latch is designed for a relatively short mission life of 214 days on-orbit with up to 4 dockings per mission.

Design Overview

Figure 2 shows the main components for the capture latch mechanism. They are:

1. Motor: Provides the nominal actuation for the mechanism. The motor is a dual wound brushless motor with redundant Hall-Effect Device (HED) position sensors. Each string of the motor is driven by a separate controller.
2. Latch Pawl: Latching feature that reacts load from Passive Striker to attain capture between mating docking systems. Can be positioned to latch (Ready to Capture) or release (Ready to Release) using the motor.
3. Transmission/Linkage System (internal, not shown): Transmits torque from the motor to the Latch Pawl and retains the pawl in desired position.
4. Secondary Release Mechanism: Provides for secondary release in the event of a nominal drive system failure. The mechanism contains a Non-Explosive Actuator (NEA) that is activated with a simple on/off power supply. The mechanism also contains a compressed spring that provides the force necessary to extend the Secondary Release Mechanism and drive the latch into the released mode.
5. Passive latch striker plate: This is a simplified representation of the stationary latch interface hardware on the passive docking system.

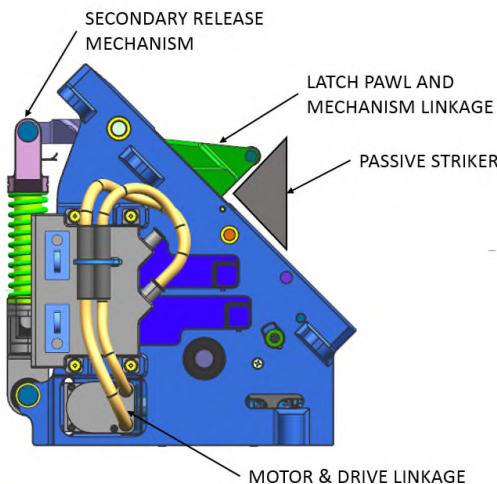


Figure 2. Latch Nomenclature

The capture latch mechanism has three main configurations or modes, as shown in Figure 3 and Figure 4: Ready to Capture, Ready to Release, and secondary release. The Ready to Capture position (Figure 3.1) is the nominal mode that allows for the latch to capture and hold the passive striker on the opposing docking system. The ready for release (Figure 3.4) and secondary release (Figure 4) modes allow for the release of the striker plate. The Ready to Release mode is the nominal release position achieved via the motor drive system. This is the primary release mode utilized while the latch is operating nominally. The secondary release mechanism allows for the release of the passive striker plate in the event the latch drive system is rendered inoperable (whether due to motor failure, jamming, binding, seizing, etc.). The secondary release mechanism is operated via a Non-Explosive Actuator (NEA) that releases a spring-operated push rod. Once the secondary release mechanism is fired the system is in an unrecoverable released state and the latch can no longer perform docking.

A full nominal capture and release operation is shown in Figure 3. The operational steps are as follows:

- Step 1: Latch is set to the ready to capture mode.
- Step 2: During docking the incoming passive latch depresses the latch pawl.
- Step 3: The latch pawl passively snaps over the striker plate.
- Step 4: To release the motor and drivetrain reposition internal latch linkages to a Ready To Release configuration.
- Step 5: The latch pawl is then pushed and rotated out of the way by the passive latch striker plate.
- Step 6: The motor and drivetrain reconfigure the internal latch linkages into the Ready To Capture mode. The latch is ready for another nominal docking operation.

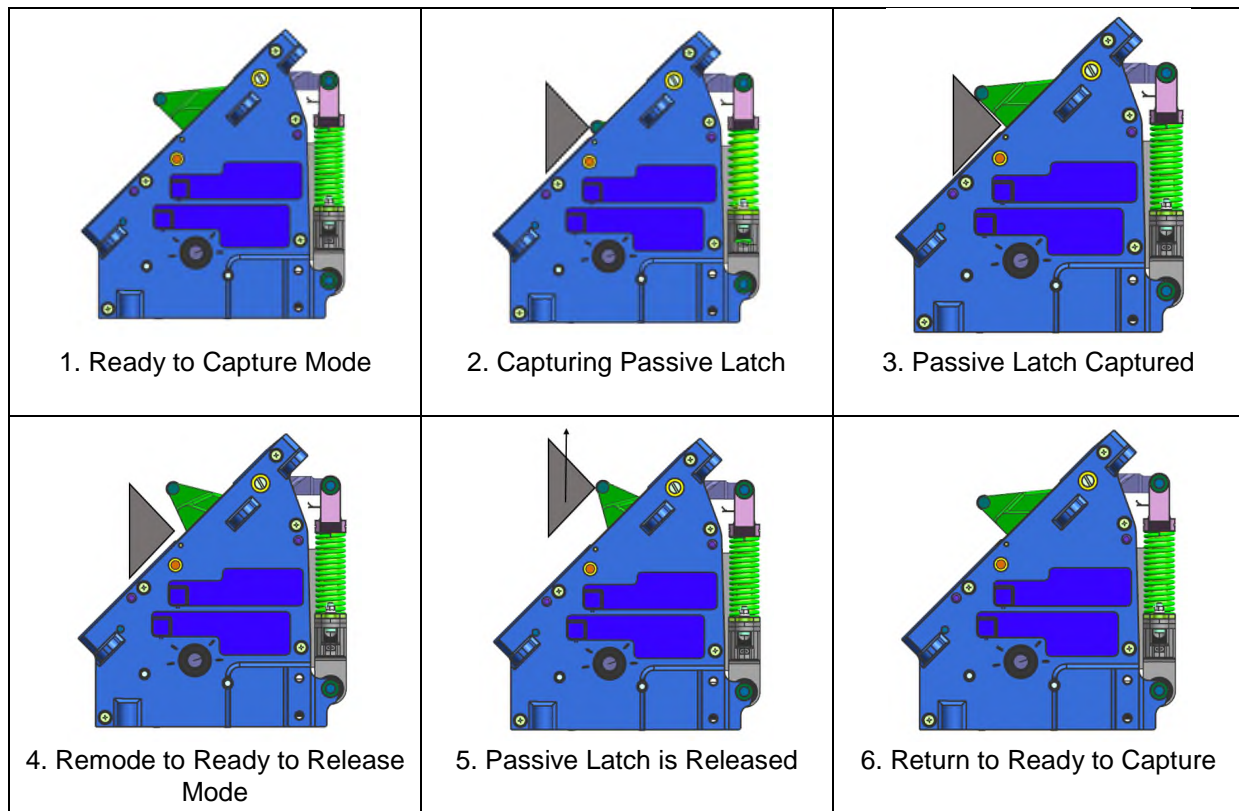


Figure 3. Nominal Capture and Release Sequence

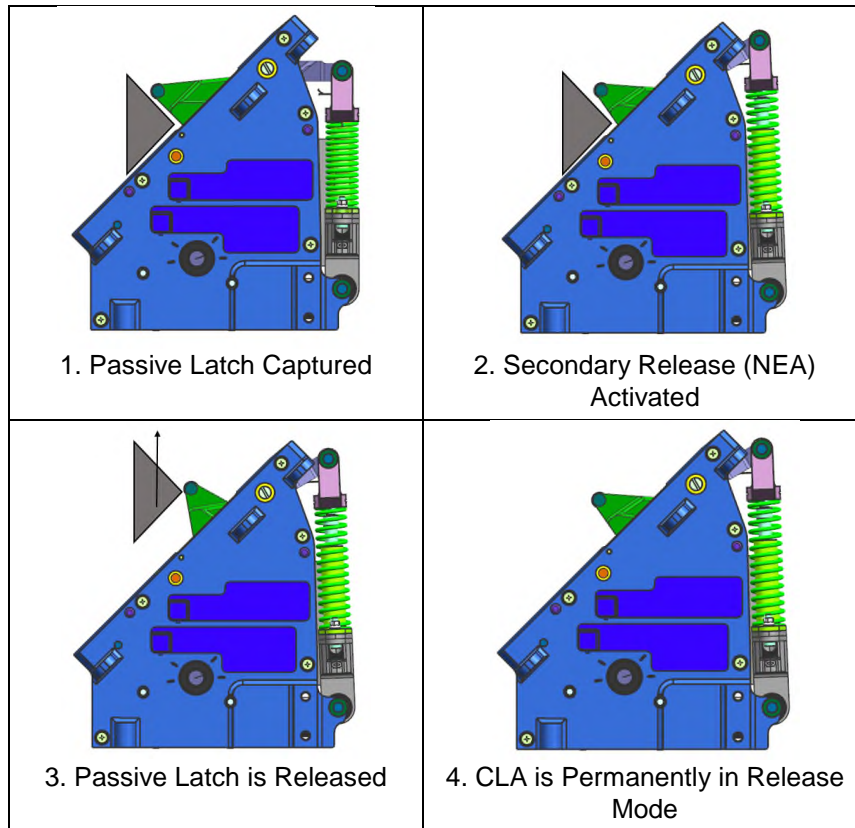


Figure 4. Secondary Release Sequence

A secondary release operation is shown in Figure 4. The operational steps are as follows:

- Step 1: Latch is in the ready to capture mode and has captured the passive latch.
- Step 2: After a failure of the primary drive system, the secondary release mechanism is activated, and the NEA releases energy stored in the compression spring causing the secondary release mechanism to extend.
- Step 3: The latch pawl is then pushed and rotated out of the way by the passive latch striker plate.
- Step 4: The capture latch is now permanently in the secondary release mode.

Summary of Development/Qualification/Acceptance Testing

Development Testing

The purpose of the Capture Latch Development Test was to reduce technical risk associated with the assembly and test of the flight design configuration by conducting testing early in the project. The development unit was built to the same design configuration as the flight Capture Latch. Some variations from the flight design were permitted to facilitate a quick test. First, the NEA in the Secondary Release Mechanism was a development article and the spherical bearing at the base of the NEA was not swaged in place. Second, the Capture Latch Motor and Controller were also development articles. Lastly, the cover for the controller was a 3D-printed metal casing, instead of the flight machined part.

The development test consists of the following tests: 1. Run-In, 2. Functional, 3. Random Vibration (qualification levels/durations), 4. Thermal Vacuum (TVAC), 5. Primary Release, 6. Secondary (NEA) Release, and 7. Static (Ultimate) Load. Run-In testing consists of five functional cycles, where the Capture Latch is cycled between Ready to Capture and Ready to Release modes. Functional testing starts with the Capture Latch in Ready to Capture mode. A test fixture is used to simulate docking and verify that the latch engages a passive latch striker. The latch is then commanded to Ready to Release mode and the test

fixture is used to simulate undocking. Functional testing was completed using both the A and B string motor/controller. During vibration testing, the capture latch was mounted on a fixture on a vibration table and subjected to the Qualification vibration spectrum in each of the three axes (X, Y, and Z). Between each axis and after the final axis, the Latch was functionally tested. During TVAC testing, the unit is placed in a thermal vacuum chamber and functionally tested at both the hot and cold vacuum conditions. The Primary Release test demonstrates that the capture latch can release while loaded up to the maximum expect load for undocking at both ambient and vacuum conditions.

The Secondary (NEA) release test demonstrates that the secondary release mechanism can release the latch when subjected to the maximum expected load during a contingency release. This test was conducted only at ambient conditions. Finally, the Static (Ultimate) load test demonstrates that the Capture Latch remains contained after being subjected to the ultimate design load.

All development tests were completed successfully except the Secondary Release test, which failed. This test will be discussed later.

Qualification Testing

Qualification testing was the same as development testing, with the following exceptions. Thermal Cycle testing was included, with 24 cycles to the same temperature extremes as the development test. Three thermal vacuum cycles were conducted. Finally, a Life Cycle test was performed.

All tests were completed successfully, with two exceptions. (1) During the Thermal Vacuum test, one channel of the motor failed as described in the next section of this paper. However, since one string of the motor was still operational, the test was allowed to continue with the remaining string. (2) The Secondary Release Mechanism failed to release the latch during the Secondary Release Test. This test failure is also discussed in subsequent sections of this paper.

Acceptance Testing

The Acceptance Test consists of the following tests: 1. Run-In, 2. Functional, 3. Random Vibration (acceptance levels/durations), 4. Thermal Vacuum (TVAC), and 5. Primary Release. In general, the levels and durations of exposure are lower during Acceptance Testing, as compared to qualification testing. NEA functionality cannot be checked since the NEA is a single use item.

The Acceptance Test was successful in screening a number of minor defects in some of the capture latches. Minor defects detected included limit switch rigging issues, worm gear alignment problems, and motor-to-controller splicing deficiencies. The test also uncovered a major defect in the motor assemblies, which will be discussed later.

Motor Failures During Acceptance Testing

Description of Failures

Failures occurred in four separate motors during Capture Latch Assembly Acceptance Test at Boeing and at the supplier of the motor/controller. A timeline of events is shown in Table 1. The initial failure (Failure 1) occurred during Acceptance Test of the Capture Latch motor at the supplier. During the ninth hot cycle of the Thermal Cycle test, the motor ceased operating on the A string. The second failure (Failure 2) occurred during Thermal Cycle testing of the Capture Latch Assembly at Boeing. During the eighth hot cycle of the thermal cycle test, the motor failed to operate on the B string. The third and fourth failures (Failure 3 and Failure 4) occurred during Hot Thermal Vacuum testing of the Capture Latch Assembly at Boeing. During this test, high current spikes were observed, and the units operated intermittently on both the A and B strings.

Table 1. Motor Failure Timeline of Events

August 2015	Failure 1 – Motor Acceptance Test Thermal Cycling
November 2015	Initial investigation of Failure 1 completed
December 2015	Start of Capture Latch Acceptance Test
February 2016	Failure 2 – Capture Latch Acceptance Test Thermal Cycling
March 2016	Failure 3 & 4 – Capture Latch Acceptance Test Thermal Vacuum
July 2016	Failure Investigation and Redesign complete
October 2016	Restart Capture Latch Acceptance Test

Failure Investigation Summary

After the occurrence of Failure 1, the supplier performed a failure analysis. The supplier confirmed the B string of the motor functioned properly even though the A string had failed, indicating the failure was not related to mechanical binding inside the motor assembly. Further, they were able to validate the failure was isolated to the motor, not the test equipment or the motor controller. Fault isolation testing showed that on the A string of the motor, one of three HEDs on each string was non-operational. Pre-teardown imaging of the motor was determined to be possible but impractical due to the difficulty of imaging through the metal casing of the motor. Additionally, the motor could not be disassembled without damage due to the permanent manner in which the casing was assembled. Therefore, it was determined that the only practical troubleshooting step remaining was a destructive teardown of the motor, to be followed by X-Ray imaging and physical inspection of the affected HED subassembly. These steps were performed, but no clear cause of the failure was identified.

Out-of-place solder was observed adjacent to the failed HED; however, it could not be determined whether this solder was the cause of the failure or if it had flowed there during the teardown, which involved heating up the motor to loosen epoxy on the casing. A review of the soldering processes for the HED was performed and a defect in the process was identified. A full fault tree was developed for the issue, but no additional likely causes were identified at the time. The soldering process issue was determined to be the most likely cause of the failure.

Failure 2 occurred approximately four months after Failure 1. After the failure occurred, an investigation along with troubleshooting testing began. The test setup was exonerated as the cause of the failure following a thorough inspection and checkout of the equipment. A full timeline outlining the history of the failed unit was developed, starting with assembly and test of the motor/controller at the supplier and continuing up through the failure. The timeline showed that unit had performed nominally through all assembly and test activities, until TVAC testing. Erratic behavior in the CLA began to emerge during the TVAC test. During operation of the Capture Latch Motor, there are three parameters monitored, current and voltage applied to the active string and voltage on the inactive string. Voltage on the active string is controlled by the test equipment and remains relatively constant. Current provides an indication of motor performance, although the current measurement is taken between the test equipment and motor controller and not between the motor and motor controller.

Because the controller affects the current demand through its own usage and current limiting, it does not provide direct insight into the motor performance. But large variations in current are indicative of motor behavior. The third parameter measured during Capture Latch Motor operation is voltage on the inactive string, which provides an indication of the speed of the motor. Since the motor has dual windings, the inactive string generates current during operation. Like the current reading, this is also filtered through the controller, so the reading at the test equipment is not a direct measurement. However, large variations are indicative of changes in motor speed. In Failure 2, the motor current exhibited significant current dropouts on the B string during the hot test.

These dropouts did not cause the motor to slow down significantly as evidenced by the fact that the inactive (A-String) voltage remained relatively constant, and the transition time was nominal. Because the unit transitioned normally, the spikes in current were not flagged by the test team for evaluation.

After this initial indication of an issue, the latch proceeded through the remainder of the TVAC test as well as the first 5 cycles of the Thermal Cycle test without issue. During the sixth hot thermal cycle, the latch again exhibited current spikes. This occurrence was much more severe, with more spikes resulting in a slower transition time for both the A and B strings. Although this was abnormal performance, it was within the threshold established for compliance and was not flagged by the test team.

During the subsequent cold operation, the unit failed to meet the transition time requirement. Review of the data showed no current spikes, but the inactive string voltage was abnormally low, indicating a slow motor speed. At this point troubleshooting of the failure began, which included inspections for debris (none identified) and operation of the motor at temperature with data recorded at a higher sampling rate. The motor operated inconsistently, where some operations were nominal whereas other operations had current spikes. The motor/controller supplier reviewed this data and concluded that this current signature was consistent with either a failed HED, a failed HED circuit in the controller, or a break in the wiring for the HEDs between the two.

At this time, it was determined that the motor and controller should be returned to the supplier for further investigation. Prior to shipment, the wires between the motor and controller were inspected to confirm no wires were damaged or cut.

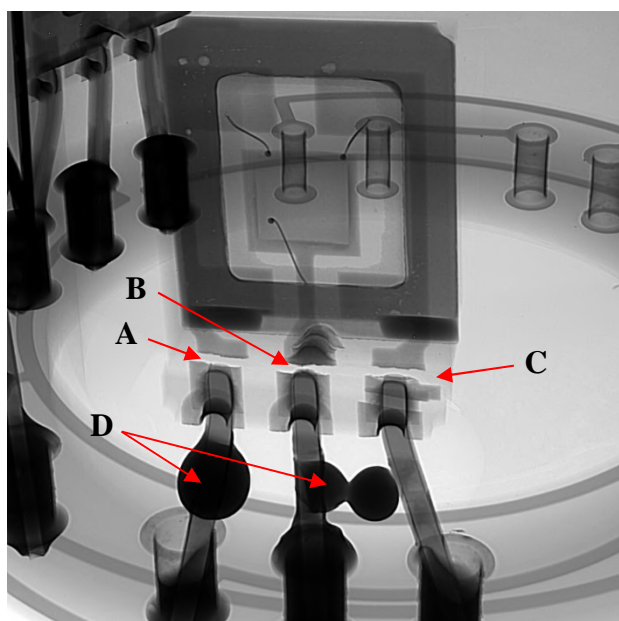


Figure 5. HED X-Ray Showing Cracked Lead

imaging was performed on the HEDs, which ultimately revealed the cause of the failure, cracks in the HED and HED lead wires, as shown in Figure 5 (items A, B, and C) and Figure 6 (item A). The imaging also revealed the presence of large voids in the potting compound used to fix the HEDs in place, as shown in Figure 5 (item D) and Figure 6 (item B).

Root Cause

Once the fault had been isolated to the HED leads, a root cause analysis was performed to determine why the cracks in the leads had occurred with two contributing factors identified. First, it was noted that the HED leads were splayed apart during assembly to align with holes in the printed circuit board, as shown in

Upon receipt of the motor/controller, the supplier replicated the failure observed during the acceptance test. The motor and controller were separated and tested individually to isolate the failure. This individual testing showed the motor as the source of the failure and that a teardown and inspection of the motor would be required to determine the cause of the failure. However, based on the experience of Failure 1, where the teardown process was too destructive, additional NDI (Non Destructive Inspections) were performed prior to teardown. Using Time Domain Reflectometry inspection techniques, a break in the wiring in the vicinity of the HED was identified, either in the HED itself, the solder joint at the circuit board, or immediately adjacent to the solder joint. Initial X-Ray imaging through the casing of the motor failed to provide meaningful images. Therefore, a careful disassembly of the motor was performed, with additional care taken to avoid heat related damage that occurred during the disassembly of the motor in Failure 1. High-resolution imaging and X-Ray

Figure 5. The reason the leads were splayed apart during assembly was that an existing circuit board, designed for HED's with different lead spacing, was used for the Capture Latch motor to minimize development costs. While NASA processes do allow for forming of leads in situations like this, a minimum distance must be maintained between bends in the leads and any joints. In this application, the minimum distance was not maintained for the solder joint at the body of the HED, resulting in stress concentrations at the solder joint and ultimately crack formation over time.

The second contributing factor and root cause was thermal induced stresses in the HED and its lead wires caused by voids in the potting material. These voids allowed for large thermal gradients between the exposed and unexposed portions of the HED, leading to large component stresses and crack formation. The voids were a byproduct of the process for applying and curing the potting material which did not sufficiently eliminate entrained air bubbles prior to curing. The voids were caused by weaknesses in the degas process, and by difficulties containing the potting material prior to curing in the small surrounding volume. Additionally, it was found that differences in the Coefficient of Thermal Expansion (CTE) of the potting material and adjacent materials contributed to the high stresses in the HED.

Corrective Action

There were a number of corrective actions performed to resolve this issue. First, the primary root cause was addressed by changing the potting material to a new type that was easier to remove entrained air bubbles and with a CTE that was more compatible with the encapsulated materials. The degas process was improved to ensure bubbles were removed from the potting material and the HED was also encased in RTV silicone to cushion it during thermal expansion. Additional measures were also taken to ensure that if a motor with large voids was produced in spite of the improved processes, it would be flagged and removed from use. To that end, inspections of the potting material were implemented so motors with large voids are rejected. Additionally, the motor testing process was revised (both at the supplier and at Boeing) to include oscilloscope-based current monitoring to confirm all HED operate nominally. Furthermore, a secondary corrective action changed the circuit board design to allow for installation of the HEDs without lead forming.

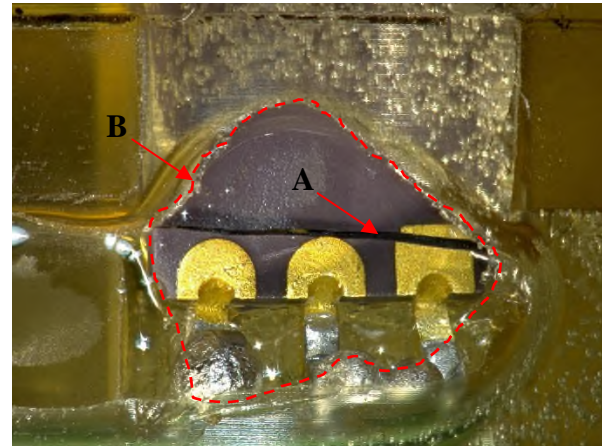


Figure 6. HED Image Showing Body Crack

Results

The redesigned motor was subjected to qualification testing and no issues with the HEDs were identified. Additionally, all twelve flight motors successfully completed all Acceptance Testing, at the component, subsystem, and system levels, without any issues.

Secondary Release Mechanism Failures During Qualification Testing

Description of Development Test Failure

The initial failure of the CCLR occurred during testing of the development Capture Latch. Prior to the failure the CLA had been subject to a suite of tests for the Capture Latch, including functional tests, random vibration, thermal cycling, and thermal vacuum. The secondary release test was the next to last test, to be followed only by an ultimate load test.

The CCLR failure was the first significant issue that occurred during the CLA development test although one off-nominal condition was noted earlier in test which later proved to be a missed indication of the eventual failure. During the random vibration test, the spherical bearing located on the NEA pushed its way out of the NEA housing. After investigating, it was determined that the issue was caused by the development

configuration of the NEA. The spherical bearing in the development NEA was only press fit and not swaged in place. Swaging was skipped to allow quicker delivery of the NEAs, but skipping this critical process allowed the bearing slide out of the housing during the test. Even without the swage, the press fit bearing should not have moved without being subjected to extremely high side loads, which was overlooked in the test article assessment. As a result, the bearing was pressed back into place and development testing resumed.

The secondary release qualification test is conducted at the worst case cold temperature in a vacuum and performed with a large load applied to the Latch pawl, which simulate the worst-case condition for operation of the mechanism on-orbit. For the development test, however, it was determined that the test would be conducted at ambient conditions. During the test, the mechanism is not directly observable and instead it is monitored using sensors. A position sensor mounted on the load attached to the Capture Latch pawl provides confirmation that the Latch has released and current monitoring on the NEA activation circuit confirms the proper application of current/voltage to the NEA.

After the NEA was activated, the mechanism failed to release which would have been evident by the sound of the dropping counterweight and data from the position sensor.

Development Test Failure Investigation Summary

The test setup was inspected to be sure the correct electrical signal was passed to the NEA and shown to be correct. A continuity measurement on the NEA electrical leads indicated an open circuit, consistent with an activated NEA. The hardware was inspected but no signs of debris or other jamming was evident indicating a potential jam inside the secondary release mechanism. The hardware would need to be unloaded and removed from the fixture prior to further investigation, but prior to removal, after approximately 24 hours, the mechanism inadvertently released. The release occurred while the wires leading to the NEA were being inspected for damage or breaks.

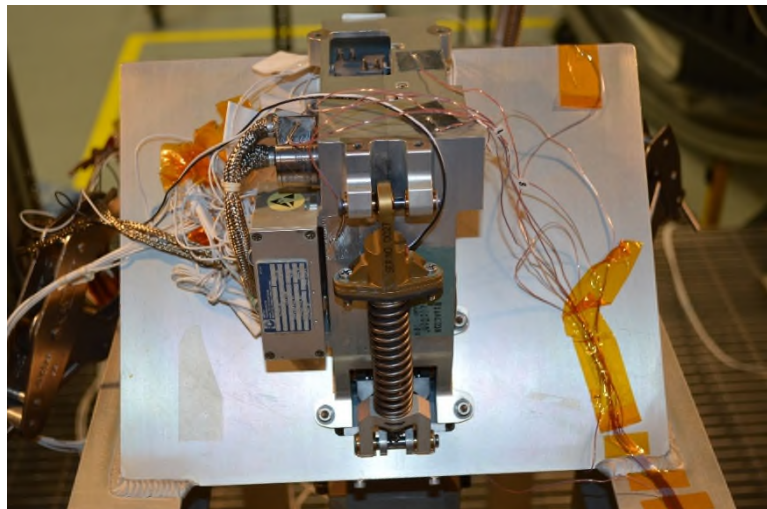


Figure 7. Qualification Capture Latch in CCLR Test Setup

After the NEA released, the unit was again inspected for any debris or other explanation for the delayed release. The capture latch was then removed from the fixture for additional investigation. The secondary release mechanism of the capture latch and the NEA were disassembled and inspected for debris or evidence of jamming. All inspections were performed using visual inspections only aided with simple magnification. No explanation for the jamming was discerned. The portions of the secondary release mechanism that reside in the capture latch housing were also inspected (without disassembly). That portion of the mechanism was free moving and showed no evidence of jamming.

Troubleshooting was performed using shop aids to simulate the secondary release mechanism to validate that the latch functioned properly. Ultimately, a new NEA was installed in the Capture Latch and activated in a test resulting in the mechanism functioning nominally. No satisfactory explanation for the failure was identified during the investigation. After review with the NDS Program, the failure was deemed an unexplained anomaly. Three potential causes for the failure were identified: 1. NEA damaged during environmental testing resulting in failure to release, 2. NEA failed to release due to manufacturing error caused by use of development processes for assembly, and 3. NEA failed to release due to

binding/jamming/seizing within the NEA release mechanism. Because the NEA is a simple, reliable mechanism that has been used successfully in many other applications – including numerous space applications, an internal design flaw leading to this failure was considered unlikely. The most probable cause was considered a defect in manufacturing due to the test article being a development unit.

Description of Qualification Test Failure

The second CCLR failure occurred during qualification testing of the capture latch assembly. Similar to the development test, the qualification secondary release test occurred toward the end of the qualification program, to be followed only by the ultimate load test. However, for the qualification testing, the mechanism was tested under the thermal vacuum (cold) conditions. Like the development test, the unit had already been subjected to all other environmental tests, including random vibration. Additionally, the test load was lowered based on updated structural analysis of the worst case undocking conditions. The test setup for the qualification test was identical to flight except that a camera was added inside the thermal vacuum chamber to allow direct viewing of the NEA, and an oscilloscope was used to obtain high speed current data for the performance of the NEA. The test setup is shown in Figure 7.

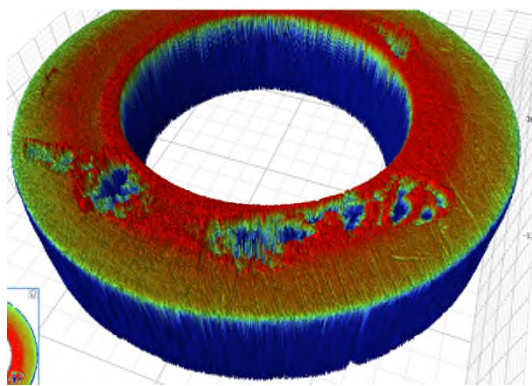


Figure 9. Load Washer Profile

During the secondary release test when current was applied, there was no evidence the release mechanism moved. Additionally, the position sensor and the camera showed no discernable movement. It was then decided that an inspection, including both visual and x-ray of the test hardware must be performed, so the chamber was returned to ambient conditions, which took approximately 24 hours. During the visual inspection, no signs of debris or jamming were observed. However, during the setup for the x-ray imaging, the load released prior to any direct imaging being performed.

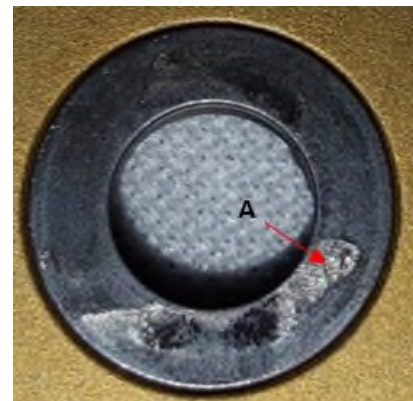


Figure 8. NEA Load Washer

Qualification Test Failure Investigation Summary

After the test failure and then inadvertent release, a Failure Investigation Team was convened to investigate and resolve the test failure. The initial goals of the team were to review the development test failure, collect all data relating to the qualification failure, development of a fault tree, and establishing a troubleshooting plan. After reviewing all data and developing the fault tree, the team determined that the first investigation step should be the teardown and inspection of the secondary release mechanism. The most significant finding of the teardown was the identification of wear marks potentially consistent with galling found on the load washer inside the NEA. The load washer is part of the NEA Cover and has the surface that reacts the load from tension applied to the NEA shaft. Figure 8 shows the load washer and Figure 11 item B shows the approximate position of the load washer in the mechanism. The apparent galling is evident in the silver area on the otherwise black surface of the load washer, as noted as item A in Figure 8.

Corresponding wear marks were also observed on the spool half that was located against this surface. Both parts were examined using a laser profilometer, light microscopy, and a scanning electron microscope to determine whether galling of the wear surfaces had occurred. As shown in Figure 9, the profilometry analysis showed that material on the load washer was displaced and removed. The light microscopy measurement confirmed the presence of fretting and galling, as shown in Figure 10. From these results, the investigation team concluded that the most likely cause of the failure to release was galling of the load washer to the spool inside the NEA. The team's next task was to determine the cause of the galling.

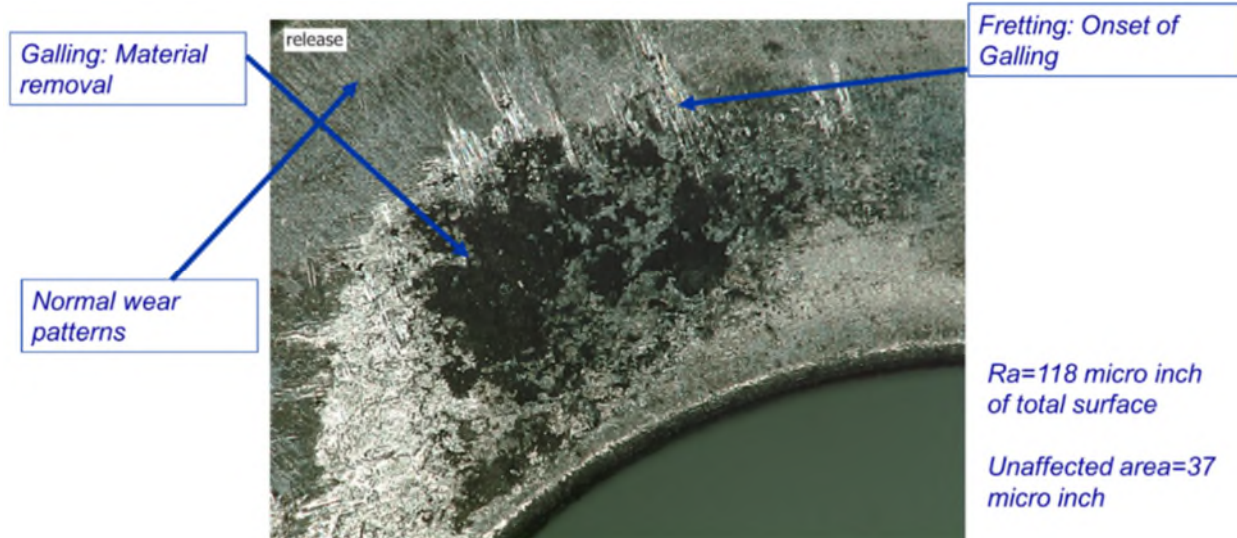


Figure 10. Load Washer Light Microscopy

The investigation into the galling covered many aspects of the design and test for the NEA and Capture Latch, but immediately focused on random vibration testing as the most likely source. It was proposed that free play in the secondary release mechanism along the pin axis could have permitted the secondary release mechanism to move excessively during vibration testing, causing the spool to move relative to the load washer. With enough motion, this could remove all the dry film lubrication coating, and allow galling between the two surfaces. The design of the mechanism included free play along the pin axis to facilitate assembly under worst case tolerance conditions. Additionally, the NEA was not preloaded. To test this theory, the Development Capture Latch was reassembled to be subjected to a repeat of the random vibration test and secondary release test. During the testing, high-speed video was used to capture the dynamics of the secondary release mechanism movement.

This test was informative, showing that the motion of the mechanism was extremely violent, subjecting it to nearly continuous shock loads as the mechanism shifted between the hard stops on either side of the free play. This motion was especially evident during testing in the axis parallel to the pins. Following the completion of the vibration testing, the unit was subjected to a Secondary Release Test, which it passed. The NEA was disassembled, and similar wear was observed. Although the failure could not be duplicated, the excessive wear was duplicated, and the test was considered successful.

Based on these results it was determined that the mechanism should be redesigned to remove free play. The design improvement was implemented by installing flat washers and Belleville washers on the pins to remove all gaps, with a slight preload, as shown in Figure 11. Additionally, the NEA was given a small preload. The development capture latch was rebuilt with the redesigned configuration and subject to the same set of tests. The redesigned configuration showed no signs of the galling/excess wear. The Qualification Capture Latch was then rebuilt per the new configuration and subjected to random vibration testing and a secondary release test. The unit passed and was shown to have no excessive wear during a post-test inspection.

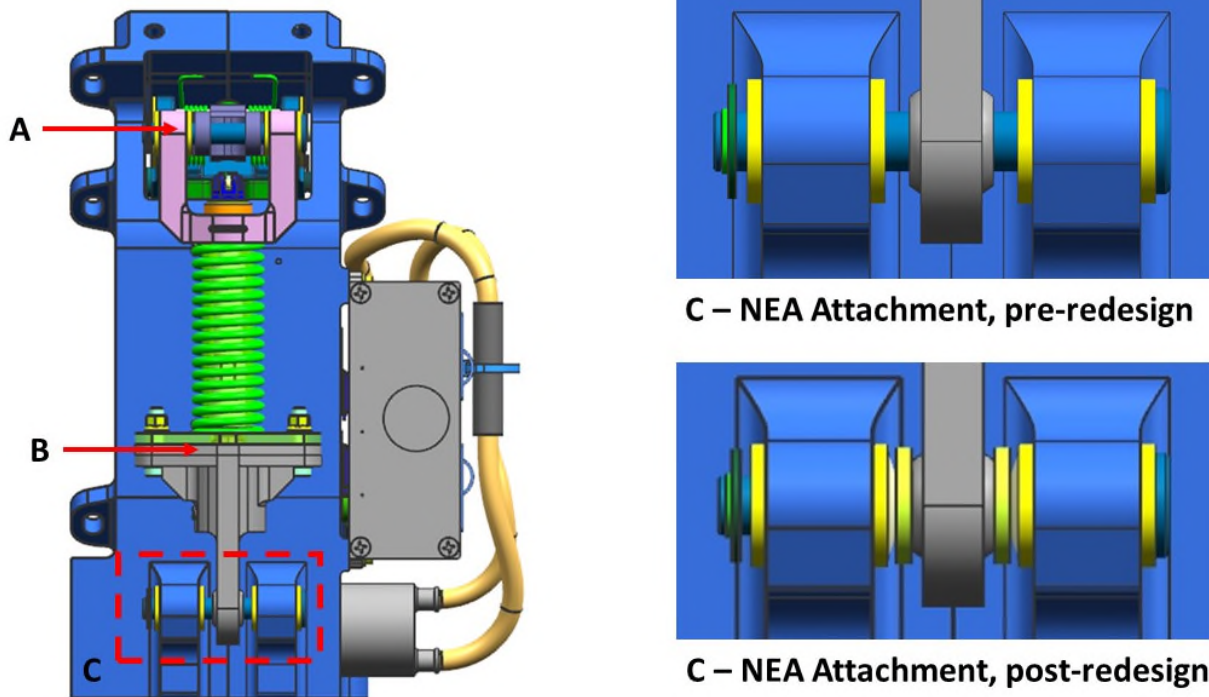


Figure 11. CCLR Detail

Lessons Learned

Avoid Loosely Constrained Parts

Loosely constrained parts can be damaged when subjected to vibration or dynamic loading events. Avoid loosely constrained parts whenever possible.

Thermal Stresses In Potted Parts

Thermally induced stress in potted parts due to differences in CTE between the potting material and the supported parts can be significant.

Fully Address Failures During Development Testing

Not fully addressing or investigating failures during development testing can allow design defects to propagate into the flight design and production.

Watch the Test Whenever Possible

The Test Engineers/Technicians may not see the same things that a designer would. When the design engineers observed the vibration test for the first time, it was very clear that the motion induced by the test was unacceptable. If they had observed the development random vibration test, the issue may have been addressed much sooner in the design.

Use Caution with Commercial Off The Shelf (COTS) Parts

Using COTS parts in a design results in a less rigorous verification of the part performance and suitability for use in the desired application. When using COTS parts, or tailored COTS parts, the designer is responsible for ensuring that all critical interfaces between the COTS part and the assembly are compatible.

Conclusions

After overcoming the difficulties discussed in this paper, the Capture Latch Assemblies for the NDSB1 were successfully designed, qualified, and manufactured/tested. A total of twelve flight assemblies – representing four NDSB1 units – have been completed. A number of lessons were learned during this process which will be applied to future CLA production and development as part of the next version of the NDS – the NDS Block 2, which will be used with the Orion and Deep Space Gateway programs.

References

1. Swan, W, "The Apollo –Soyuz Test Project Docking System," *10th Aerospace Mechanism Symposium*, NASA TM 33-777, Pasadena, CA., 1976, pp. 29, 36.
2. Cook, J., Aksamentov, V., Hoffman, T., & Bruner, W. "ISS Interface Mechanisms and their Heritage", AIAA Space 2011, pp. 24.
3. Dick, B., Oesch, C., and Rupp, T., "Linear Actuator System for the NASA Docking System," 17th European Space Mechanisms and Tribology Symposium.

High Speed Bearing Wear Rate Measurements for Spacecraft Active Thermal Control Fluid Pumps with a Novel Pin on Disk Apparatus

Robert J. Bruckner * and Richard A. Manco II **

Abstract

A novel pin on disc tribometer was designed and constructed to generate a high-speed, wear coefficient database for hydrodynamic bearings that are typically used in canned motors found in the active thermal control circuits of robotic and inhabited spacecraft. The primary motivation for this work was the premature failure of the active external thermal control pump on the International Space Station in 2010. During the failure investigation of this incident, the root cause was postulated to be high-speed wear of the bearings. Although a detailed forensic analysis gave credibility to this theory, the lack of wear coefficient data at relevant conditions prevented validation of this finding. The database generated from the new Extreme Environment Tribometer (EET) enabled a closure calculation within 5% of the observed wear from inspections of the failed hardware. Testing in anhydrous ammonia and surrogate fluid was performed to provide a means for simplified testing in the future and to populate a preliminary database for the design of future active thermal control systems on spacecraft. The EET and test techniques developed for the measurement of high-speed wear coefficients are available to future system designers.

Introduction

Active thermal control systems on spacecraft, both robotic and inhabited, most commonly rely upon a high-speed canned motor pump to circulate the heat transfer fluid between heat exchangers and radiators. Three notable NASA examples of spacecraft with such pumps are the Parker Solar Probe, the Orion Crew Module, and the International Space Station [1-10]. A graphical representation of a canned motor pump is shown in Figure 1 [11,12]. The working fluid in Figure 1 is colored light blue and highlights the most unique feature of the pump. This feature includes the use of the primary working fluid as the hydrodynamic bearing lubricant and the heat transfer medium to remove eddy current losses from the rotating group. The primary reason for the use of canned motor pumps in spacecraft is the elimination of high-speed shaft seals, which are the most likely cause of failures in traditional pump designs. The canned motor pump has become ubiquitous not only in spacecraft active thermal management but also in ground-based applications where high reliability and an intolerance to working fluid contamination are key design constraints. While these pumps are elegant in their dual use of working fluid, this feature brings with it two key complications. First, the entire motor (rotor and stator) must be internally shrouded from the working fluid to protect electromagnetic components from the primary working fluid. Secondly, the characteristics of an excellent heat transfer fluid are in stark contrast to the optimum rheology required of lubricants for hydrodynamic bearings. A third complication arises from the use of these pumps in micro-gravity applications, such that the primary force on the bearings is not determined by gravity and the weight of the rotor. In ground-based applications this preferential load direction is used to identify the critical bearing locations and to incorporate health monitoring instrumentation to determine incipient failure of the bearings due to high wear.

* NASA Glenn Research Center, Cleveland, Ohio

** HX5 Sierra at NASA Glenn Research Center, Cleveland, Ohio

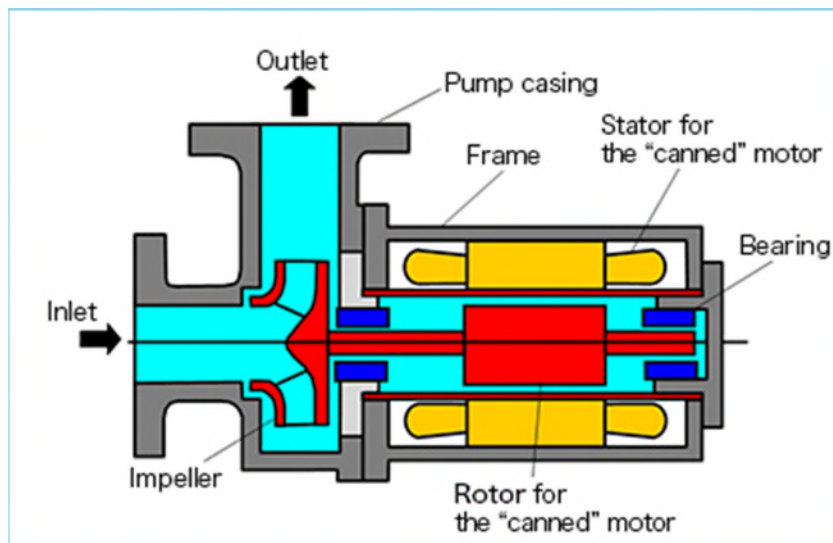


Figure 1. A typical high-speed canned motor pump.

These complicating factors aligned in an unfortunate way on the International Space Station in 2010 and led to the premature failure of one of two active thermal control pumps used to maintain heat balance within the habitable volume. A failure investigation on this pump indicated that extreme wear of the bearings was the root cause due to operation beyond the hydrodynamic load capacity of the bearing. A complete description of this failure and early operational recovery efforts has been documented in [13].

This failure triggered an extensive study of the wear rates for this bearing material in relevant environments. An experimental approach was taken for this investigation due to the high rubbing speed and flooded, liquid condition at which this wear occurs. A new experimental apparatus was designed, constructed and operated to generate a database of relevant wear rate coefficients suitable for predicting wear life of high-speed canned motor pumps in operating microgravity conditions. The apparatus, known as the Extreme Environment Tribometer (EET), includes an operating temperature range of -68°C to 65°C (-90° to 150°F), pressure range from 6.9 to 2585 kPa (1 to 375 psia), and rubbing speeds up to 25 mps (81 fps). It was designed to operate in 100% anhydrous ammonia and therefore will also accommodate both the new class of designer heat transfer fluids with anti-corrosion additives as well as the traditional heat transfer fluids such as propylene glycol and water.

Wear in Hydrodynamic Bearings

Hydrodynamic bearings, such as those commonly used in canned motor pumps, experience wear at both high-speed and low-speed operation. Low-speed wear is primarily experienced during startup and shutdown of the rotating system. Figure 2 has been reproduced from [13] to demonstrate this phenomenon. At low rotational speeds the shaft contacts the static bearing until the mixed lubrication regime is reached. As speed is increased further, beyond the mixed lubrication region, the bearings operate in a non-contacting or hydrodynamic mode. In this mode, no wear occurs and the surfaces are separated by a thin layer of lubricant, or working fluid in the case of a canned motor pump. In the low-speed phase of operation, solid surface contact occurs and a wear condition may exist. Typically, the static bearing material is selected to tolerate this wear while the shaft in the bearing location is prepared with a hard coating having a very low surface roughness. This low-speed wear condition is a well understood phenomenon and wear coefficient data of various bearing and shaft coating combinations is readily available. Even if the data is not readily available, wear coefficient data at low speeds can be obtained from a test program conducted on a large number of commercially available pin-on-disc or block-on-ring tribometers. In fact, in the early phases of the work described herein, low-speed wear coefficient data was generated to gain an understanding of the wear couple at hand.

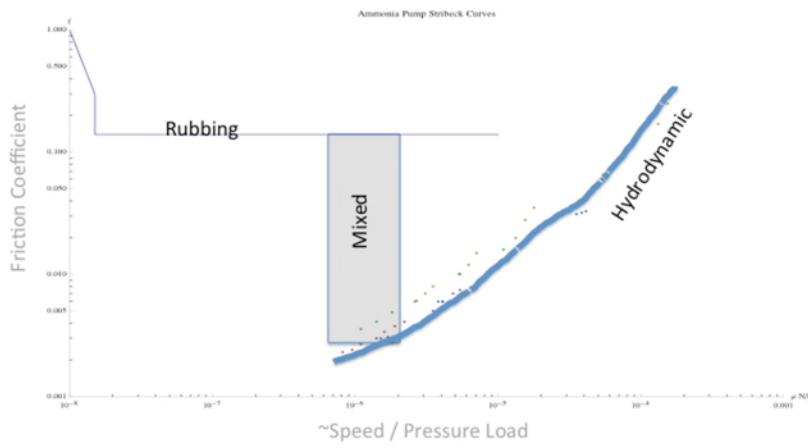


Figure 2. The Stribeck Curve for the Hydrodynamic Bearing.

High-speed wear on hydrodynamic bearings is a unique phenomenon and can only occur when the load capacity of a bearing is exceeded at high speed. This situation occurred on the cooling pumps of the International Space Station (ISS) in 2010 and triggered the premature shutdown of one of the pumps. Although in this situation the weight of the rotor was not present due to operation in a microgravity environment, secondary forces aligned to overcome the non-contacting load capacity of the bearing leading to severe and unexpected wear. The phenomenon of high-speed wear has not been studied in the application to hydrodynamic bearings, and this phenomenon is unique to niche applications such as microgravity operation. Wear mechanisms and material wear coefficients in this region require a test-based approach to quantify the functional life of a bearing which experiences these conditions.

The Extreme Environment Tribometer (EET)

Design

A survey of commercial and custom designed research tribometers was conducted in order to identify a test rig that could meet the needs of the current test program [14-20]. No such apparatus was identified, which triggered a new tribometer design effort. The EET was designed with the following characteristics, which were required to conduct high-fidelity wear coefficient measurements in conditions that matched those in the ISS cooling pump bearings:

- Pin-on-disc configuration with modular running gear and test chamber capable of block-on-ring or hydrodynamic testing.
- Capable of high rubbing speeds that spanned the front and rear journal bearing design space.
- Flooded liquid operation at the rubbing contact points with liquids that are unfriendly to many materials, specifically anhydrous liquid ammonia.
- Vacuum and elevated pressure capabilities to enable test operation with liquids that are not thermodynamically stable at standard temperature and pressure (STP).
- Constant temperature operation during test operations.

The final design of the EET is shown in Figures 3 and 4. The design consists of a pressure vessel that houses a vertical, rotating shaft supported on dry, unlubricated rolling element bearings. The use of unlubricated bearings was paramount to the successful creation of the wear coefficient database, since contamination of the test fluid, anhydrous ammonia in this case, by the oils or greases in the rolling element bearings would invalidate the data applicability to the ISS wear conditions. Additionally, the high pH of the

anhydrous ammonia would likely degrade conventional lubricants, cage materials, and steels. Ball bearings that were made with ceramic zirconia races, zirconia balls, and a polytetrafluoroethylene (PTFE) cage were used in this application. A key EET running gear design feature was the elimination of inner race radial interference fits. A purely axial preload was used to maintain shaft bearing interface alignment and eliminate potential slip through the use of an axial spring pack. This configuration enabled the ceramic to be placed in compression during all phases of assembly and operation and eliminated the ceramic bearing tensile stresses at the inner race failure mode.

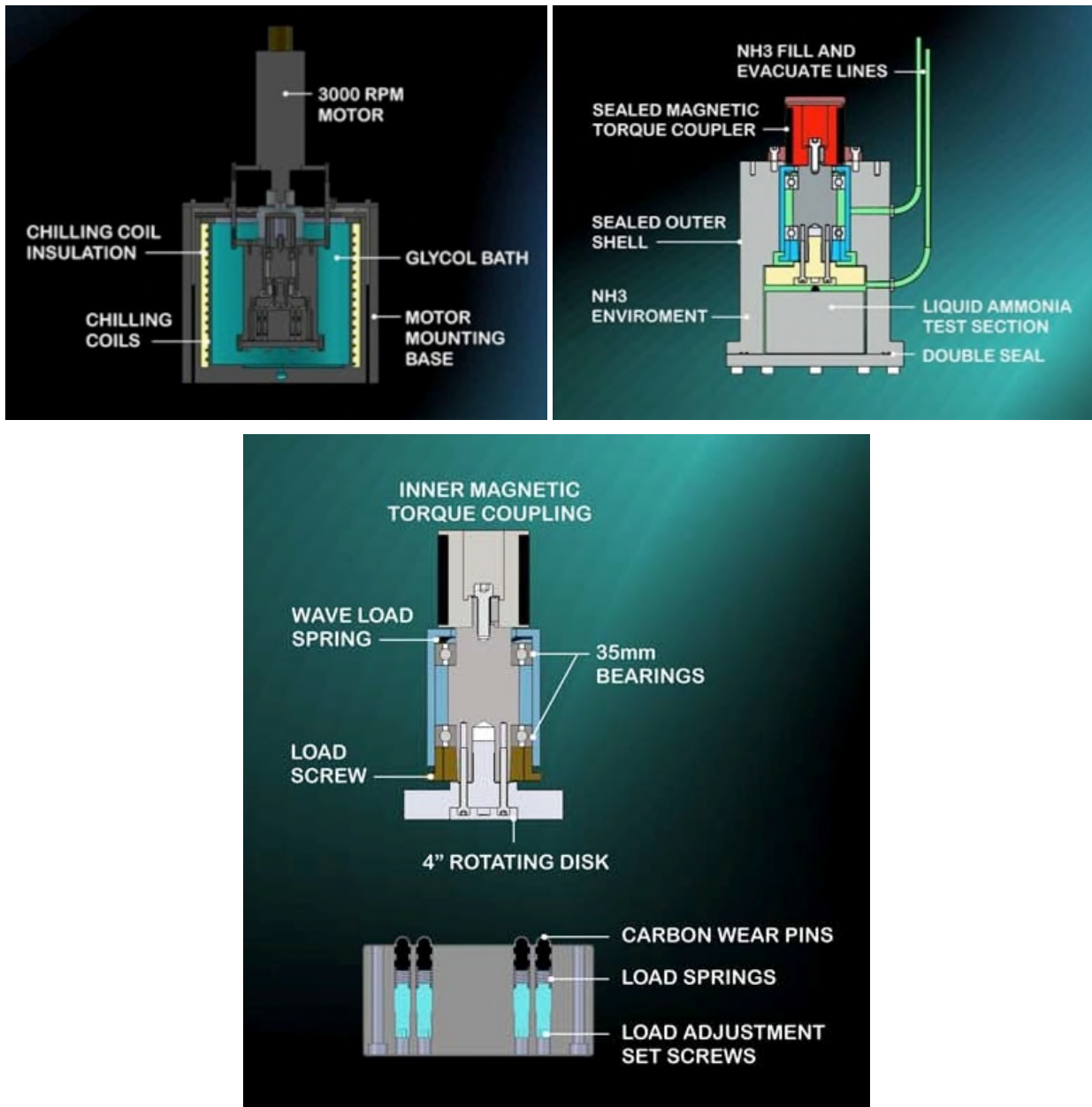


Figure 3. EET Design



Figure 4. EET and Test Specimens

Mounted to the rotating shaft bottom was the disc. The disc was 100 mm in diameter, and each disc was manufactured with a hard chrome coating polished to a 0.1- μm surface finish, the same specification as is typical in rotor bearing surfaces.

Below the rotating disc was the test chamber, which consisted of a four-pin load block. Each pin ran on its own wear track, which enabled four data points at unique speeds to be obtained with each test operation. Contact load between the carbon pins and the rotating disc was maintained by a spring pack and a load screw arrangement whose features were machined into the load block.

The entire pin-on-disc arrangement was enclosed in a pressure vessel to enable safe operation in a thermodynamically controlled environment. A motor was mounted on the pressure vessel top, and torque was transferred to the shaft through a magnetic coupling. Three types of materials were used for the magnetic coupling dome to manage operational risk with eddy current heating of the pressure vessel. Design calculations and operational experience provided the following constraints:

- Stainless steel dome: use to 300 rpm.
- Titanium dome: use to 900 rpm.
- Glass-filled polyetheretherketone (PEEK) dome: use to 3500 rpm.

To maintain a constant temperature during test operations and to enable tribometer precooling or preheating to simplify liquid filling operations, a thermal bath was constructed in which the sealed tribometer could be submerged. This thermal chamber was designed to meet a -75°C to +125°C temperature range.

Operation

The procedure for operation of the EET was as follows:

Test Specimen Preparation

- Perform pretest photomicroscopy and profilometry of the chrome-coated disc and four carbon pins to document pretest configuration.
- Install runner onto the shaft and verify axial runout is less than 12.6 μm.
- Verify motor operation, magnetic coupling alignment, and set speed point in motor controller.
- Install carbon pins in PTFE sabot and set spring preload.
- Measure and record pretest spring preload for each pin.
- Install load block into pressure.
- Install bottom seal and flange.
- Environmental Control
- Prepare the constant temperature bath with appropriate heaters, chillers, and heat transfer fluids.
- Immerse the tribometer in the temperature-controlled bath.
- Monitor internal temperature of the EET through purge gas exit temperature.
- At the desired temperature, fill the EET with a predetermined volume of test fluid.
- Monitor the tribometer and fill vessel mass, and the EET pressure and temperature.
- After pressure, temperature, and fluid levels have stabilized, initiate test.

Test Operation

- During startup, monitor motor speed to ensure proper operation.
- Continuously record motor speed and power draw at a minimum of 10 Hz.
- Verify motor speed with external strobe every 10 minutes.
- Monitor pressure, temperature, and speed for stability and trends.

- Terminate the test at the first onset of unexpected or unexplained variability in test conditions.
- Terminate test at the desired sliding distance (time).
- Collect post-test data.
- Drain test liquid from test chamber and collect in specimen jar and any debris.
- Purge test chamber with nitrogen and bring to room temperature while monitoring pressure temperature and gas exit conditions.
- When safe conditions exist within the tribometer, remove the lower flange and seal.
- Remove the load block.
- Measure and record the post-test normal force on each carbon pin.
- Perform photomicroscopy, profilometry, debris analysis, and additional diagnostics as the test conditions or results dictate.

Wear Coefficient Data

Low-Speed Wear Data

In order to build an early database of wear coefficients while the EET was under fabrication and to gain experience with the material couple, a series of low-speed wear tests were performed on commercial pin on disc tribometers in both dry and flooded contact conditions. A photograph of typical test hardware is shown in Figure 5 and results are captured in Table 1. Test results indicated a wear coefficient on the order of 10^{-7} ($\text{mm}^3/\text{N m}$) with strong sensitivity to contact area (i.e., pressure). The wear coefficient is defined as cubic millimeters of worn material normalized by normal force (N) and sliding distance (m). The friction coefficient of the wear couple was measured in these tests to be in the range of 0.14 to 0.22 in room temperature air. Testing in flooded liquid conditions revealed a reduction of friction coefficient to the range of 0.07 to 0.11 while the wear coefficient remained within the same order of magnitude.



Figure 5. Test Specimens for low speed wear testing

EET Validation – Dry

Preliminary EET testing was conducted at STP conditions to establish operating procedures and confirm traceability to low-speed testing. Once the traceability and operating procedures were established, the EET was operated at high speeds to expand the wear coefficient database. A summary of pertinent wear coefficient data for both low- and high-speed EET operation in air is included in Table 2. High-speed wear coefficients measured in air at ambient conditions were equivalent to those measured on the commercial tribometers. This provided confidence in the EET design and operation.

Surrogate Fluid Wear Coefficient

The wear coefficient database was expanded to include flooded liquid conditions at high speeds. Initially, water was used in the high-speed flooded liquid tests. These initial tests uncovered a nontrivial issue in the test operation. Hydrodynamic lift was being generated between the carbon pin to chrome runner interface. This lift was the result of several factors, including low axial runout in the rotating disk, low surface roughness on the chrome, low surface roughness on the worn carbon bearing material, high absolute viscosity of the water at room temperature, and relatively high speeds. During the testing initial phase, wear was observed during the initial (i.e., high contact pressure) phase of pin wear. It was postulated that even at relatively high contact pressures the pin-disc interface could develop sufficient hydrodynamic lift to prevent further wear. To overcome this limitation for high-speed flooded operation, several modified test techniques were developed without success to disrupt the hydrodynamic film. The only reliable technique for eliminating hydrodynamic lift in these tests was reduction of the absolute fluid viscosity through elevated temperature.

Once an acceptable test technique was developed, surrogate fluid testing was conducted. Water, 4 percent ammonia in water, and 28 percent ammonia in water solutions were tested at temperatures below their boiling points. The evolution of wear coefficient with reduced contact pressure was tracked during this test campaign. A summary of the test data is included in Table 2.

Anhydrous Ammonia Measured Wear Coefficients

The final phase of testing on the EET encompassed the exact conditions found in the failed ISS pump from 2010, high contact speeds in flooded anhydrous ammonia. Data is presented in Table 3 along with data for a 28% ammonia in water mixture and bone-dry, gaseous nitrogen at -45°C.

The wear coefficient database enables calculations to be performed to evaluate the failure progression theory for the ISS active thermal control pump. By combining the available on-orbit operations data from the failed pump with the new wear coefficient database, the closure calculation was within 5% of the observed wear found during the failure investigation. This compares to calculations based on estimates of wear coefficients that ranged from -98% to over 5 times the observed wear volume.

Cold, Dry Material Performance

One final set of tests was conducted after the anhydrous ammonia data were obtained. The objective of this test was to evaluate the effect of low temperature on the wear rates because the EET was operated at approximately -45°C during the anhydrous ammonia tests to keep the internal pressure low and minimize the risk of a thermal runaway and boil-off situation. The final cold test was conducted in a dry gaseous nitrogen environment at -45°C. The measured wear coefficients were three orders of magnitude higher than those measured in the flooded anhydrous ammonia tests. Three potential causes for these high wear coefficients were postulated. The resin binding the graphitic carbon could go through a secondary glass transition temperature, causing embrittlement. The differential thermal expansion between resin and carbon may cause stress cracking and induce a weaker composite material. The surface layer of the carbon in rubbing contact may be highly sensitive to humidity and trace hydrogen.

The first theory was investigated with differential calorimetry. Specimens were sent to a polymers lab to search for an embrittlement temperature between room temperature and –100°C. None were found.

The second theory of differential thermal expansion causing microcrack formation at the resin-carbon bond was investigated using two methods. First, high-power microscopy was used to search for cracks, but none were observed. The second technique was to continue testing the specimens in ambient conditions. At ambient conditions, the measured wear coefficients returned to normal levels, which indicated that a reversible phenomenon was occurring, thus eliminating the microcracking theory.

The third cause of the high wear rate coefficients was investigated by testing in dry nitrogen gas at ambient temperatures. Under these conditions, the high wear rates were repeated, which gave credibility to the sensitivity of this material to humidity and trace hydrogen to achieve low wear rates.

Discussion

A new pin on disc apparatus was designed and fabricated to provide high-speed wear coefficient data for hydrodynamic bearings in canned motors. These motors and bearing arrangements are commonly used in actively pump thermal control circuits for manned and robotic spacecraft. The dramatic increase in desired life of these pumps has led to the need to understand the high-speed wear phenomenon of the bearings. Test data in surrogate fluids has reveal important trends in the wear coefficients. Surrogate fluids are significant because they may ease the burden of testing and provide a level of similarity between different coolants used in various spacecraft. The significant trends include:

- Twenty-eight percent ammonia hydrate solution is a suitable surrogate fluid for 100 percent anhydrous ammonia for the material wear couple present in the PCVP bearings.
- Four percent ammonia hydrate solution behaves similarly to pure water for the material wear couple present in the PCVP bearings.
- Wear rates measured in water are two orders of magnitude higher than wear rates measured in anhydrous ammonia.
- Wear rates measured in dry nitrogen gas were two orders of magnitude higher than those measured in air at ambient temperature, pressure, and humidity.
- At rubbing speeds greater than 4 m/s, the wear rate decreased with increasing speed for flooded ammonia conditions.
- Based on testing, the high-speed wear coefficient of the ISS pump bearings to be in the range of 1.4 to 8.3E-09 ($\text{mm}^3/(\text{N m})$).

Additionally, certain best practices were determined to be useful for future, long duration canned motor bearing designs.

- Document the bearing groove orientations with respect to key motor housing features if bearing pads are used.
- Preclude the secondary flow paths from generating rotor-bearing asymmetric loading.
- Maintain a symmetric journal bearing design to the greatest extent possible.

The EET and the test technique developed to measure high-speed wear coefficients is available to future spaceflight programs that may utilize actively pumped thermal control circuits. Furthermore, the database generated from the initial EET test program was able to validate the failure mode of the 2010 ISS thermal control pump failure to within 5% of the observed material loss, which was measured during the failure

investigation. This significant improvement in the closure calculations have provided increased confidence in the wear progression and the recovery procedures for the ISS thermal control system.

References

1. Birur, G. C., Bhandari, P., Gram, M. B., and Durkee, J., "Integrated Pump Assembly – An Active Cooling System for Mars Pathfinder Thermal Control," Society of Automotive Engineers, 26th International Conference on Environmental Sciences, Monterey, CA, 1996.
2. Lockwood, M. K., Ercol, C. J., Cho, W. L., Hartman, D., and Adamson, G., "An Active Cooling System for the Solar Probe Power System," AIAA, International Conference on Environmental Systems, AIAA-2010-6294, 2010.
3. Swanson, T. D. and Birur, G. C., "NASA Thermal Control Technologies for Robotic Spacecraft," National Aeronautics and Space Administration, N20030031332, 2003.
4. Westheimer, D. T. and Tuan, G. C., "Active Thermal Control System Considerations for the Next Generation of Human Rated Space Vehicles," AIAA AeroSpace Sciences Meeting, AIAA-2005-342, 2005.
5. Paris, A. D., Bhandari, P., and Birur, G. C., "High Temperature Mechanically Pumped Fluid Loop for Space Applications – Working Fluid Selection," SAE International, 04ICES-282, 2004.
6. Shen, F., Drolen, B., Prabhu, J., Harper, L., Eichinger, E., and Hgyuen, C., "Long Life Mechanical Fluid Pump for Space Applications," AIAA AeroSpace Sciences Meeting, AIAA-2005-273, 2005.
7. Baldauf, R. W., Kawecki, T., Purdy, W., and Hoang, T. T., "Development of a Bearingless Ammonia Pump for Spacecraft Thermal Control," NRL Review, 2008.
8. Shen, F., Drolen, B., Prabhu, J., Harper, L., Eichinger, E., Nguyen, C., "Long Life Mechanical Fluid Pump for Space Applications," 43rd AIAA Aerospace Sciences Meeting, AIAA-2005-273, January 10-13, 2005
9. Lockwood, M. K., Ercol, C. J., Cho, W. L., Hartman, D., and Adamson, G., "An Active Cooling System for the Solar Probe Power System," AIAA 40th International Conference on Environmental Systems, AIAA-2010-6294, 2010.
10. Paris, A. D., Bhandari, P., and Birur, G. C., "High Temperature Mechanically Pumped Fluid Loop for Space Applications – Working Fluid Selection," SAE International, 04ICES-282, 2004.
11. Bloch, P. E., "Understanding Canned Motor Pumps," Maintenance Technology, September 1, 2008.
12. Foscz, J. L., "Canned Motor Pumps," *Plant Engineering*, June 3, 1993.
13. Bruckner, R.J., Manco R. A., "ISS Ammonia Pump Failure, Recovery, and Lesson Learned – A Hydrodynamic Bearing Perspective", Proceedings of the 42nd Aerospace Mechanisms Symposium, NASA Goddard Space Flight Center, May 14-16, 2014.
14. Jeon, H. G., Lee and Y. Z., "The Evaluation of Wear Life Based on Accelerated Test through Analysis of Correlation between Wear Rate and Lubricant Film Parameter," *Tribology Transactions*, February 19, 2013.
15. ASTM International, "Standard Test Method for Wear Testing with a Pin-on-Disk Apparatus," G99-05, reapproved 2010.
16. Gomes, J. R., Silva, O. M., Silva, C. M., Pardini, L. C., and Silva, R. F., "The Effect of Sliding Speed and Temperature on the Tribological Behavior of Carbon-carbon Composites," *Wear*, Elsevier, Vol. 249, pp. 240–245, 2001.
17. Lancaster, J. K., "Dry Bearings: A Survey of Materials and Factors Affecting their Performance," *Tribology*, December 1973.

18. Midgley, J. W. and Teer, D. G., "An Investigation of the Mechanism of the Friction and Wear of Carbon," *Transactions of the American Society of Mechanical Engineers (ASME)*, December 1963.
19. Sliney, H. E. and Jacobson, T. P., "Some Effects of Composition on the Friction and Wear of Graphite Fiber Reinforced Polyimide Liners in Plain Spherical Bearings," *NASA Technical paper 1229*, 1997.
20. Demas, N. G. and Polycarpou, A. A., "Ultra High Pressure Tribometer for Testing CO₂ Refrigerant at Chamber Pressures up to 2,000 psi to Simulate Compressor Conditions," *Tribology Transactions*, Vol. 49, pp. 291–296, 2006.

Table 1. Wear Coefficient Data from Low-Speed Tribometer

Fluid	Load (N)	Linear Speed	Wear Coefficient (mm ³ /N·m)	Sample Temperature	Contact Pressure (MPa)
4%NH ₃ Hydrate	10	100 mm/s	4.97865E-07	25.5 to 27°C	2.601
4%NH ₃ Hydrate	10	200 mm/s	2.41698E-07	25.5 to 27°C	3.581
4%NH ₃ Hydrate	10	200 mm/s	2.95354E-07	25.5 to 27°C	1.798
dry, air	10	300 mm/s	6.38000E-07	25.5 to 27°C	12.109
dry, air	10	300 mm/s	1.29384E-07	25.5 to 27°C	8.416
dry, air	10	900 mm/s	1.83617E-07	25.5 to 27°C	6.466
dry, air	10	900 mm/s	1.92718E-07	25.5 to 27°C	7.101
propylene glycol	5	300 mm/s	0.23949E-07	25.5 to 27°C	8.043
dry, air	2	900 mm/s	1.57290E-07	25.5 to 27°C	1.378
dry, air	1	900 mm/s	1.33452E-07	25.5 to 27°C	0.842
4%NH ₃ Hydrate	10	100 mm/s	3.23704E-07	25.5 to 27°C	2.011
4%NH ₃ Hydrate	10	600 mm/s	0.329972E-07	25.5 to 27°C	7.082
4%NH ₃ Hydrate	10	400 mm/s	0.803432E-07	25.5 to 27°C	4.744
dry, air	10	600 mm/s	3.54035E-07	25.5 to 27°C	2.244
dry, air	10	400 mm/s	1.67000E-07	25.5 to 27°C	3.393

Table 2. Wear Coefficient Data Using 4 Percent Ammonium Hydrate Surrogate Fluid

	Plan A			Plan B			Plan C			Plan D			
Test Date	Motor Speed (rpm)	Sliding Speed (m/s)	Wear Coefficient (mm ³ /N·m)	Motor Speed (rpm)	Sliding Speed (m/s)	Wear Coefficient (mm ³ /N·m)	Motor Speed (rpm)	Sliding Speed (m/s)	Wear Coefficient (mm ³ /N·m)	Motor Speed (rpm)	Sliding Speed (m/s)	Wear Coefficient (mm ³ /N·m)	Temperature, °C
10-Mar	901.9	4.1982	2.57E-07	901.9	2.9987	6.32E-07	901.9	2.9389	1.18E-06	901.9	3.5984	8.19E-07	52-59
17-Mar	902.6	4.2014	1.74E-07	902.6	2.9987	6.37E-07	902.6	2.9389	1.16E-06	902.6	3.5984	8.30E-07	52-59
18-Mar	600	2.7929	1.60E-07	600	1.9949	4.48E-07	600	1.5959	5.27E-07	600	2.3939	3.95E-07	52-59
20-Mar	300.6	1.3992	1.76E-07	300.6	0.9995	2.74E-07	300.6	0.7996	3.02E-07	300.6	1.1993	2.93E-07	52-59
25-Mar	303.1	1.4109	2.29E-07	303.1	1.0078	2.53E-08	303.1	0.8062	1.11E-07	303.1	1.2093	1.18E-07	52-59
27-Mar	901.8	4.1977	7.09E-08	901.8	2.9984	9.70E-08	901.8	2.2987	2.78E-07	901.8	3.5980	2.05E-07	52-59
31-Mar	302.9	1.4099	1.87E-07	302.9	1.0071	4.05E-07	302.9	0.8057	5.60E-07	302.9	1.2085	3.95E-07	95-98
1-Apr	301.2	1.4020	5.19E-08	301.2	1.0014	1.51E-07	301.2	0.8012	1.74E-07	301.2	1.2017	1.79E-07	95-98
7-Apr	302.7	1.4090	7.18E-08	302.7	1.0064	5.83E-08	302.7	0.8051	1.09E-07	302.7	1.2077	7.67E-08	95-98
9-Apr	600.5	2.7952	5.98E-08	600.5	1.9966	4.94E-08	600.5	1.5973	4.97E-08	600.5	2.3959	5.63E-08	ambient
10-Apr	605.3	2.8175	8.11E-08	605.3	2.0125	1.12E-07	605.3	1.6100	1.25E-07	605.3	2.4150	9.20E-08	95-98
13-Apr	903.7	4.2065	4.98E-08	903.7	3.0047	5.63E-08	903.7	2.4037	6.55E-08	903.7	3.6056	1.35E-07	95-98
14-Apr	903.7	4.2065	4.20E-08	903.7	3.0047	2.94E-08	903.7	2.4037	6.98E-08	903.7	3.6056	1.34E-07	95-98
15-Apr	1200.1	5.5862	3.11E-08	1200.1	3.9902	1.50E-07	1200.1	3.1921	1.83E-07	1200.1	4.7882	1.35E-07	95-98
16-Apr	1200.1	5.5862	2.02E-08	1200.1	3.9902	6.77E-08	1200.1	3.1921	3.85E-08	1200.1	4.7882	1.32E-08	95-98
17-Apr	1510.1	7.0292	2.68E-08	1510.1	5.0209	4.55E-08	1510.1	4.0167	1.18E-07	1510.1	6.0250	8.10E-08	95-98
		7.0292	2.59E-08		5.0209	4.41E-08		4.0167	1.14E-07		6.0250	8.28E-08	ambient

Table 3. Wear Coefficient Data for 28 Percent Ammonia, 100 Percent Ammonia, and Dry Nitrogen Environments

Fluid	Linear Speed (m/s)	Test Pressure (psig)	Test Temperature (°C)	Contact Pressure (MPa)	Wear Coefficient (mm ³ /N-m)
28% NH ₃	1.07	6.0-7.5	45	32	9.00E-09
28% NH ₃	1.33	6.0-7.5	45	29	8.00E-09
28% NH ₃	1.60	6.0-7.5	45	9.8	8.50E-09
28% NH ₃	1.87	6.0-7.5	45	20	6.50E-09
100% NH ₃	3.30	15	-43	31	6.20E-09
100% NH ₃	4.16	15	-43	29	8.30E-09
100% NH ₃	4.98	15	-43	20	5.40E-09
100% NH ₃	5.80	15	-43	21	8.30E-09
100% NH ₃	4.85	20	-43	22	6.90E-09
100% NH ₃	4.85	20	-43	23	3.10E-09
100% NH ₃	6.06	20	-43	34	2.33E-09
100% NH ₃	6.06	20	-43	28	1.69E-09
100% NH ₃	7.27	20	-43	34	1.99E-09
100% NH ₃	7.27	20	-43	22	2.47E-09
100% NH ₃	8.48	20	-43	35	1.48E-09
100% NH ₃	8.48	20	-43	26	1.38E-09
N ₂ , bone dry	4.85	20	-45	21	7.15E-05
N ₂ , bone dry	6.06	20	-45	21	4.99E-05
N ₂ , bone dry	7.28	20	-45	21	3.85E-05
N ₂ , bone dry	8.50	20	-45	21	2.19E-05

Accelerated Testing of Tribological Components - Uncertainties and Solutions

Simon Lewis*, Mike Buttery*, Oliver Poyntz-Wright*, Anthony Kent* and Achilleas Vortsellas*

Abstract

A fundamental requirement of any spacecraft mechanism development is to demonstrate the integrity of the selected lubricant system by means of an appropriate life test. As mechanism lifetimes are often long, and development times compressed some form of accelerated test procedure may be required for programmatic reasons though the strict tribological validity of such tests both for fluid-lubricants and for mechanisms employing solid lubricants or self-lubricating bearing is often a point of concern.

This paper discusses the current state of knowledge and limitations regarding accelerated testing, including the influences on lifetime, torque and material wear of the accelerated conditions. The uncertainties of presently available acceleration techniques and limitations of available data and methods are highlighted together with some potential future solutions.

Introduction

The challenges of successful accelerated life testing of spacecraft mechanisms and lubricants have been a recurring consideration for many years (for example [1], [2]). A simple review of the main classes of spacecraft mechanisms, their typical operating speeds and typical un-factored lifetimes is shown in Figure 1 and highlights the desirability of accelerated testing for missions where operational lifetimes (measured in terms of cycles or revs) are “long” but development times may be rather short. However accelerated tests may also be considered even for mechanisms with more modest life requirements for example where confidence pre-tests are needed (prior to qualification), for mechanisms which have a dwell (stationary period) or duty cycle with long stationary periods (e.g. refocus or calibration mechanisms), where a fixed launch date exists (e.g. “missions of opportunity” for comets/planetary exploration), where programmatic concerns dominate or where a compressed development cycle is being taken (e.g. low-cost missions).

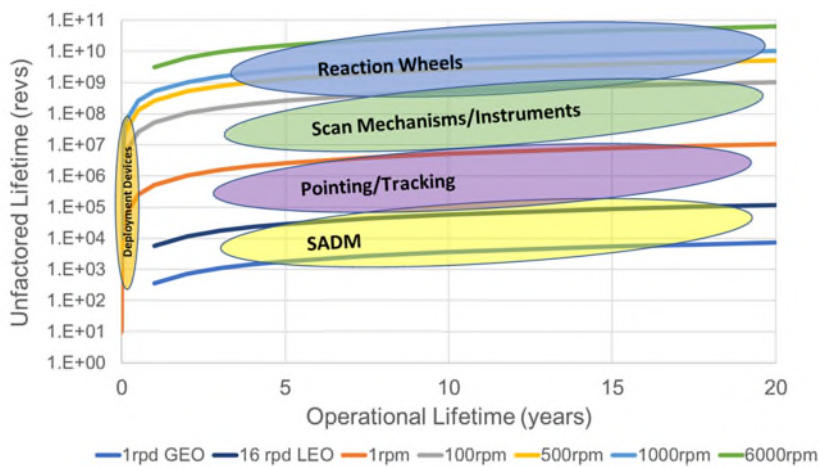


Figure 1. Typical unfactored lifetime requirements in revolutions for different mechanisms

* ESTL (European Space Tribology Laboratory), ESR Technology Ltd., Warrington, U.K.

Proceedings of the 44th Aerospace Mechanisms Symposium, NASA Glenn Research Center, May 16-18, 2018

In 1995 Murray et al [3] highlighted the range of mechanisms for which accelerated testing would be desirable, the technical challenges in developing a valid accelerated test methodology, and a technology roadmap which might lead to greater understanding of the issues. In 1997 ESTL reviewed the topic and in proposing a methodology for a more tribologically rigorous accelerated test for oil or grease lubricated mechanisms [4] also highlighted some of the main challenges and uncertainties which could lead to a misleading test conclusion or invalid test.

More than 20 years on, the authors have experienced many accelerated tests of different types, and this paper seeks to highlight, both by review and presentation of new material, areas where additional understanding has been developed and some remaining technical needs in order to further reduce the risk that an accelerated test method may be adopted which could lead to an invalid or misleading test result – and in the worst case an undertest of life or performance.

Uncertainties of the Usual Approach to Accelerated Test - Fluid Lubricants

Accelerated testing of fluid-lubricated mechanisms is based on the notion that if the same lubrication regime can be maintained between the critical loaded contacts (e.g. ball and raceway) in the test as found in the application at nominal speed then the test will be tribologically valid.

In classical EHL, the lubrication regime is usually determined based on a Stribeck curve approach using an analysis as typically presented by Hamrock and Dowson [4]. Using this approach, a specific film thickness, λ (the ratio of minimum lubricating film thickness to composite surface roughness of the counterfaces) is calculated for the nominal (λ_n) and accelerated conditions (λ_a), the assumption being made that if accelerated test conditions can be established in which $\lambda_a \geq \lambda_n$ the lubrication regimes will be similar and therefore the risk of wear/rate of degradation of the lubricant or other tribological failures might be expected to be similar. By this approach a valid test can in principle be achieved if the increased speed of an accelerated test is compensated, by reduced viscosity achieved by increasing temperature, such that the same specific film thickness and lubrication regime might be obtained in the accelerated test as in the application at nominal operating conditions.

Whilst attractive in its simplicity it was pointed out in [5] that this approach can be inappropriate and flawed for many reasons. Since that time publications by many authors have contributed to the up-to-date status of these concerns for each phenomenon which is reviewed below.

Non-Newtonian Lubricant Behavior

Though the above approach assumes Newtonian lubricants, in fact for many lubricants, including widely used space oils (and their derived greases) there ceases to be a well-defined relationship between shear stress and velocity gradient (or in fact the fluid partially solidifies) at some stress/shear condition. For example, high pressure rheological experiments on the oils 815Z and 2001A [6,7] suggest reversible solidification changes at relatively modest pressures and room temperature as shown in Table 1 (and at lower pressures if temperature is reduced). These figures suggest that at a relatively modest mean Hertzian contact stress $>\sim 700$ MPa (~ 1 GPa peak) visco-elastic solidification (rather than the straightforward increase in viscosity with pressure represented by the pressure-viscosity coefficient in the Barus equation) might start to become a factor for these lubricants causing deviations from the expected friction and film thickness behaviors.

Table 1. Onset of Visco-elastic and Elastic-plastic Solid Behavior in Space Oils

Oil	Pressure for Onset of Visco-elastic Solid Behavior	Pressure for Onset of Elastic-plastic Solid Behavior
815Z [6,7]	$>\sim 1.1$ GPa	>1.6 GPa
2001A [6,7]	$>\sim 0.95$ GPa	$>\sim 1.5$ GPa

Whilst such changes are temporary (as the fluid passes through the ball/raceway contact for example) permanent viscosity loss has been reported [8] at mean contact stress $> \sim 2$ GPa (~ 3 GPa peak) for 815Z/Z25. Though a high contact stress for most space mechanism applications, this phenomenon should nevertheless be borne in mind.

Rheological changes as discussed are cited by some authors, notably Vergne, Bair et al (9,10) as the dominant reason for the common failure to correlate experimental and calculated specific film thickness. Indeed, the implication of their work is that the kind of “Quantitative EHL assessment” needed in order to define and demonstrate valid accelerated testing can only be achieved by a fully detailed assessment of the lubricant rheology. To our knowledge such an assessment is not yet available for the most common space lubricants, and the situation for greases seems still more complex – requiring both the rheological properties of the base oil, its flows and thickener behaviors to be well understood.

Batch Variability and Degradation Effects

For fluid lubricants, intra-batch property variations, usually assumed small, are not well understood or quantified in the open literature. Perhaps more significant, but also not well understood at component level, are the effects of degradation/deterioration due to the nature of the fluid lubricant (for example grease bleed (oil separation); evaporation of volatile constituents (e.g. additives which typically have a vapor pressure an order of magnitude higher than the base oil); oxidation or tribo-degradation (viscosity loss or even auto-catalysis)).

Lubricant Availability

The actual quantity of lubricant available at a given contact (e.g. ball/raceway) is dependent on various loss routes which deplete the local supply, primarily migration due to 1g orientation, surface energy driven creep and evaporation. Of these, only the latter is considered calculable, losses due to evaporation being typically estimated using a Langmuir equation approach. However, in general a lubricant may have components of different molecular weights and a range of volatilities. This could render an analysis using the Langmuir equation and published vapor pressure data too simplistic, the true situation being that the rate of mass loss, even for nominally single component fluids without additives is dependent on the thermal history of the lubricant. Indeed, there is evidence [11] that the Langmuir equation may predict higher loss rates than found in practice by approximately an order of magnitude at typical operating temperatures as shown in Figure 2 suggesting a high uncertainty on the quantity of oil to be initially added or remaining within a mechanism at the end of life.

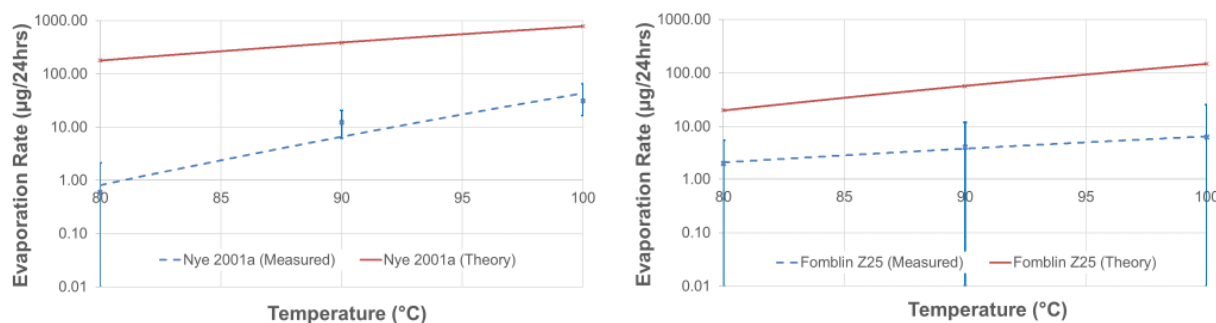


Figure 2. Comparison of experimentally measured evaporative loss rates for Nye 2001A (left) and Fomblin Z25 (right) with the predictions of Langmuir theory [11]

For cotton phenolic cages, which are usually vacuum impregnated over a period of hours to saturate the cotton fabric with the lubricant oil prior to use, there is evidence [12] that even “fully impregnated” cages may absorb a significant mass and a disproportionately high percentage of bearing free oil during subsequent storage as the phenolic matrix itself absorbs oil. The infiltration of oil into the phenolic matrix is a very low rate process, taking months, but as shown in Figure 3 the total mass absorbed can be relatively high and assuming this were to be absorbed entirely from the free oil quantity typically added to a bearing,

upon assembly would be a high proportion (rapidly reaching 100%) suggesting that this phenomenon is perhaps an overlooked lubricant loss route which could cause the onset of a bearing with very minimal remaining free oil at the ball/raceway contacts (essentially starved/almost dry).

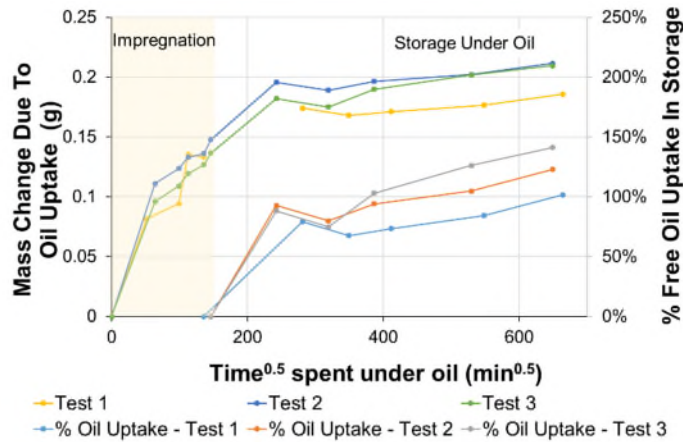


Figure 3. Oil mass uptake by cage and potential impact on proportion of free oil
(Basis: 28 μl free oil available, storage period up to 9 months)

Environment

Lubricant flow (including wake effects) and lubricating film thickness behaviors are clearly highly dependent on environmental and local temperatures. Tribometer level tests in both sliding (e.g. Pin-on-Disc tribometer (PoD)) and rolling/pivoting contacts (e.g. Spiral Orbit Tribometer (SOT)) demonstrate that the tribo-life of common space lubricants is environmentally sensitive. SOT tests demonstrate that the assumption of parity of environmental effects between air or nitrogen and vacuum would result in a factor 5-10 over-estimate of the in vacuum lifetime achievable. Whilst the factor may be different in a specific real application, this demonstrates clearly that the potential error from the erroneous assumption of parity can be large.

For example, the lifetimes of the PFPE grease, Braycote 601EF, as measured in the SOT (in terms of normalized lifetime in orbits per rev) and in pure sliding pin-on-disc (PoD) testing (absolute life in revs) in various environments [13] is shown in Figure 4. This data, is reinforced by more recent work for PFPE and MAC oils [14] clearly shows that environment has a considerable impact on both measures of lifetime, implying that life test should be executed in vacuum to avoid under-test.

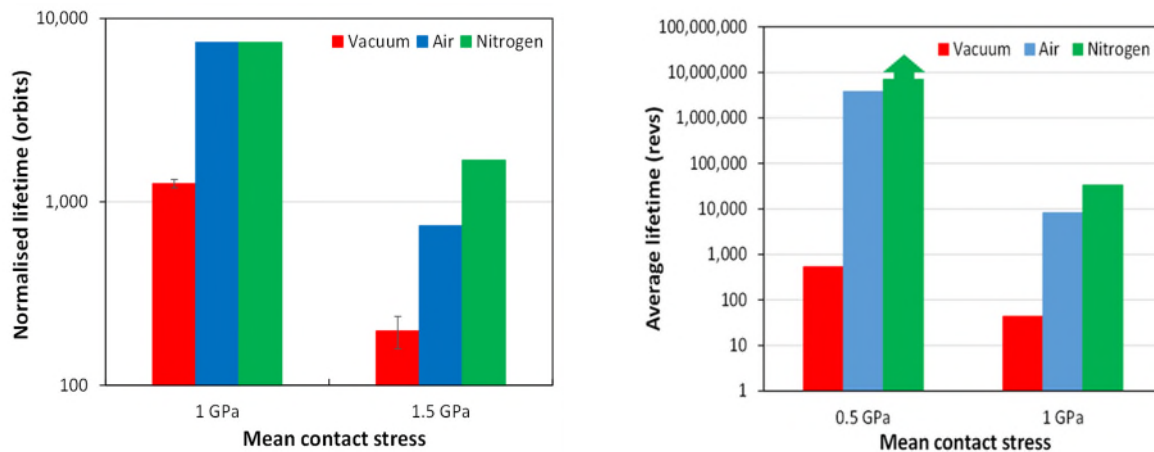


Figure 4. Lifetime of Braycote 601EF in various environments as assessed on SOT (left) and PoD (right) [13]

Incorrect Assessment of Lubricant Regime

Even in the absence of lubricant rheological effects such as solidification or shear thinning there are other challenges in the correct assessment of lubricant regime. The λ -ratio is usually assumed fixed and based on the specified or measured un-deformed ball/raceway surfaces prior to run-in/asperity modification or wear. In reality however, this will likely be incorrectly assessed. A higher λ may be applicable under bearing preload due to contact asperity flattening and λ -ratio may even be variable throughout test, increasing as surfaces run-in or decreasing due to thermally-driven contact angle changes or wear. It may only be possible to assess the impact of the test on the bearing surfaces by sophisticated pre- and post-test profilometry and analysis.

Changes During Operation

For ball bearings, the cage is rarely fully benign and its stability fundamentally impacts both torque performance and wear. For a valid accelerated test, the cage behavior needs to match that of the application at nominal operating conditions. However, changes to ball/cage and cage/land friction and cage geometry (e.g. due to wear) may have a considerable impact on subsequent cage stability or wear. Meaning that at the beginning of bearing life a cage could be stable, but develop instability due to oil absorption or changes in the surface friction or geometry of pockets or lands.

Non-Calculable Performances

Finally, there is a range of “non-calculable”, even non-predictable performances, meaning behaviors that are not predictable by analysis, but apparently real and commonly observed phenomena. In this context we might list:

- Evidence for the regimes of starved/parched lubrication – where viscous losses are low, films theoretically of implausibly low thickness, but wear also low [15].
- Differences between fully-flooded and starved films in grease. When fully flooded greases tend to have a thickness higher than predicted based on oil properties alone (by a factor ~ 2), whereas when starved (and indeed there is evidence that greases may “self-starve”) the film thickness resulting is ~ 50-70% of that of the base oil under the same speed, load and thermal conditions. (see [16] for example). Indeed, as greases age, both types of behavior may be observable.

Given the above, it was highlighted [5] that in some cases it may not be possible at the start of an accelerated test involving a fluid lubricant to be certain that the test would ultimately be valid, even if the target life was achieved. In the intervening years the proposed “tribologically valid” approach has been little used and given the new knowledge exemplified above now seems to require update since new knowledge renders this kind of accelerated test likely less, rather than more, representative.

Perhaps due to the above uncertainties, accelerated tests of fluid lubricated mechanisms are not common, and it seems that, where used, either the speed and the acceleration factor adopted remain relatively low, or there is an implicit acceptance and engineering judgement that the above effects may be second order or neglectable in the overall performance. Such judgements are not normally supported by experimental data and so the tests themselves remain, in the absence of appropriate experimental data on the fluid lubricant behaviors, to some greater or lesser extent, flawed.

Uncertainties Surrounding Accelerated Test – Solid Lubricants and Self-Lubricating Bearings

It is often assumed that, in contrast to the quite complex situation with oils and greases, the accelerated test of solid lubricated or self-lubricating bearings is much more likely to be valid.

Solid lubricated bearings usually rely on shear of anisotropic lamellar solids (e.g. MoS₂) or low shear strength Face Centered Cubic (FCC) metals (e.g. lead, silver, gold). This “primary lubricant” is supplemented often by a cage material which undergoes the double-transfer mechanism to transfer cage material via the surface of the balls to the raceway, a “secondary lubricant” phenomenon which may

become increasingly important later in the bearing lifetime. Since they have no lubricant pre-applied to balls or races, self-lubricating bearings are entirely dependent on this kind of in-situ lubricant double-transfer from the beginning of life

The most common material for MoS₂-lubricated or self-lubricating bearings is PGM-HT (a PTFE glass-fiber, MoS₂ composite) though other transferring polymers and metals may be used also for specific applications or with alternative primary lubricants.

Primary Solid Lubricant – MoS₂

Where the primary solid lubricant is sputtered MoS₂ there is a considerable body of work which documents in general terms the expected performance at tribometer level (for example summarized in [17]) and while life data at component level in absolute terms may be scarce and variable due to different definitions of end-of-life or end-of-test, normalized lifetime plots show the trend to be expected.

In pure sliding, whereas there seems no relationship between the friction coefficient of any individual MoS₂ sample and the lifetime obtained, there is a strong relationship between sliding life and mean contact stress, P_m, in which life is stated [17] to be proportional to P_m^{-3.8}, a value also shown in the best-fit line for coatings on a range of substrate materials of different hardness [18] as shown in Figure 5. A similar relationship exists for data from rolling contact experiments using a SOT in which the life of MoS₂ applied to a 52100 steel ball running against a 52100 disc is found proportional to P_m^{-3.2}.

A limited number of tests have also been carried out on spur gears [19], and whilst the initial test campaign used low precision, relatively low hardness and non-hunting ratio gears, some tentative relationship of gear lifetime versus mean contract stress from MoS₂-lubricated gears has begun to emerge.

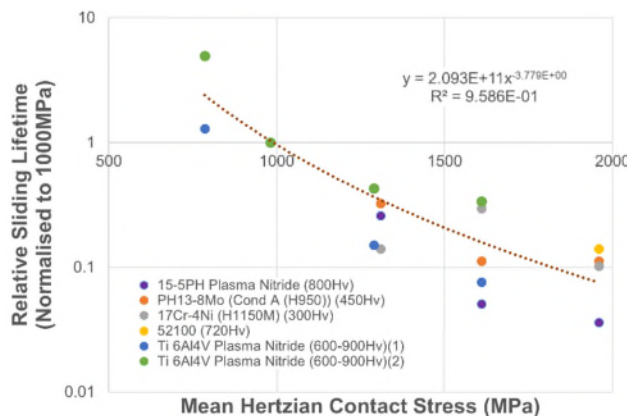


Figure 5. Normalized in vacuum lifetimes of sputtered MoS₂ in PoD test on various substrates [18]

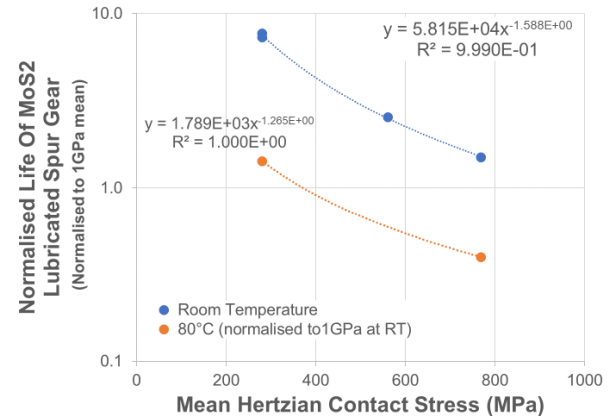


Figure 6. Normalized in vacuum lifetime of sputtered MoS₂ lubricated spur gears [19]

Whilst the spread of results in Figure 5 is due to different material combinations, if any regression curve approach is to be used to estimate life (for example Figure 6 for gear life), or as a basis of accelerated test justification, then the spread of results needs to be minimized. In general, this spread could come from two potential sources, the natural variability of the test (whether tribometer or gear test), or some supposed variability in the sputtered MoS₂ material itself. However, recent work suggests the spread of lifetime obtained from sputtered MoS₂ is broadly similar to that of PFPE or MAC lubricants (when compared in like-for-like test such as the SOT). The typical standard deviation on life of a batch of MoS₂ tested in the SOT is ~15%, a figure which compares well with the variability found in the same test for PFPE and MAC lubricants [20] (measured at 1.5 GPa mean stress and room temperature).

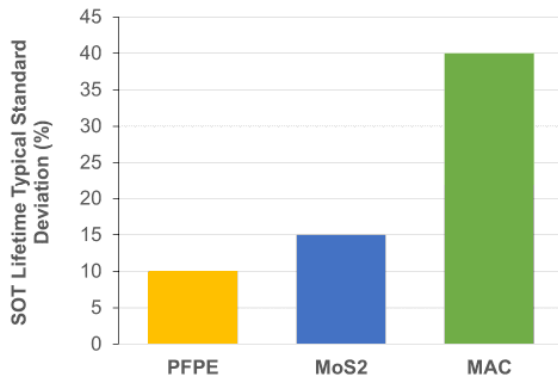


Figure 7. Comparison standard deviation of in-vacuum lifetime of 3 lubricants tested in SOT

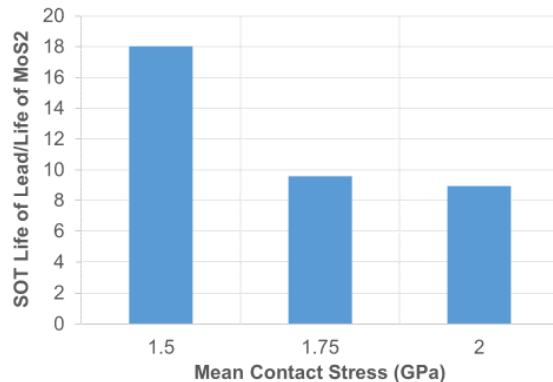


Figure 8. Relative lifetime of sputtered lead as compared to sputtered MoS₂ in vacuum (~1 μm) as function of contact stress

Primary Solid Lubricant – Lead

Since its high ductility permits transfer and re-transfer to different surfaces, like that of other low shear strength metals, the lifetime of lead in rolling contact tribometer tests (and in components) is very long. As it seems to persist as a very thin layer (deposited at around 1-μm thickness but functional even when the remaining film is only ~100 Å) [21]. In the SOT for example (with Pb applied to 52100 steel balls only running against 440C plates) Pb achieves in vacuum lifetimes at least an order of magnitude greater than MoS₂ and appears relatively insensitive to contact stress, however its corresponding friction coefficient is somewhat higher than that of MoS₂ in the same tests.

Primary Solid Lubricant - Summary

In general, primary solid lubricants, whether metallic or lamellar such as MoS₂ can be relatively well characterized by tribometer tests in vacuum, nitrogen and air. For example, in tribometers at least, the relationship between contact stress and life for MoS₂ seems well established, and the dependencies of life on temperature and substrate hardness have also been studied [22, 17]. Nevertheless, the relationship between life and sliding speed, though often stated to be low, is not well documented (although at very low speeds similar to slip velocities in low speed bearings a known friction/speed dependency exists).

Secondary Lubricant – PGM-HT

Regarding the secondary lubricant there are typically two principle accelerated test concerns, firstly that the material itself may display unexpected wear behaviors as a function of speed, stress or local temperature, and secondly that the cage may become unstable at speed, again causing different wear behavior in the accelerated test to the nominal speed application and thus invalidating an accelerated test.

ESTL carried out a program of PoD and SOT test work aimed at improving understanding of the behavior of PGM-HT material. As originally supplied, the material was found to be dimensionally unstable at elevated temperature, a problem subsequently overcome by introduction of a thermal conditioning pre-treatment [23]. In characterizing the tribological behavior of the thermally conditioned material ESTL carried out a number of PoD tests in vacuum [24] which showed that whilst in general higher friction tests correlated to higher wear rate, a wide range of frictional behaviors and wear rates could be expected (Figure 9). Interestingly also the legacy material RT Duroid 5813 (“Duroid”) seemed to have approximately a 4 times higher wear rate than found for the PGM-HT.

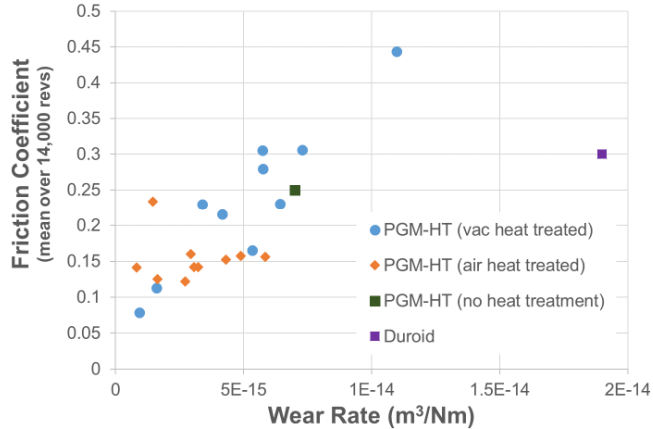


Figure 9. In vacuum PoD friction vs wear rate of PGM-HT and Duroid v Steel [24]
(Mean Hertzian stress 10 -16.2 MPa ,52100 steel disc, $R_a < \sim 0.1 \mu\text{m}$, sliding speed 0.01-0.1 m/s)

As a first experiment the SOT was used to characterize the initial formation of a transfer film by the double transfer method described above [25]. In this work a single ball loaded between plates was initially unlubricated but developed a transfer film of the PTFE/glass-fiber/MoS₂ due to its once per revolution impact with the guide plate and in subsequent rolling this material was also transferred from the ball to the flat plates (this was considered as analogous to a cage/land or cage/ball collisions within a ball bearing). Tests were run for only 50,000 ball orbits as a trial, but nevertheless the results added somewhat to understanding.

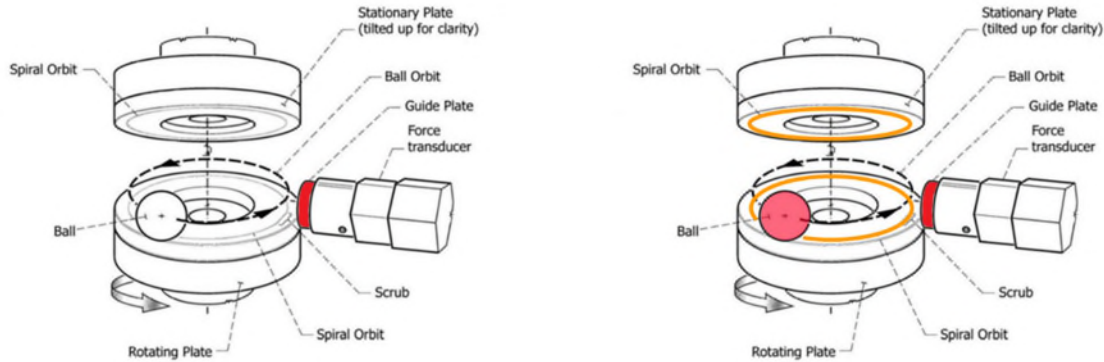


Figure 10. Schematic SOT with polymeric guide plate at start of test (left) and after material transfer from guide via ball surfaces to upper and lower plates (right).

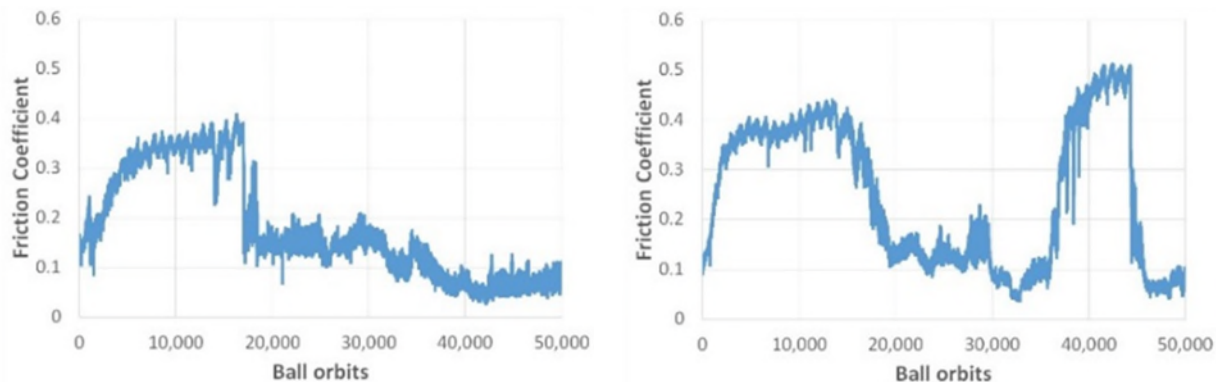


Figure 11. SOT Friction of PGM-HT (left) and Duroid (right)
(In vacuum, mean contact stress 600 MPa) [25]

Tests were carried out in vacuum, moist air and dry nitrogen on three materials: RT Duroid 5813 (legacy material), PGM-HT (current widely used cage material), and C29 [26] a potential future cage material (containing PTFE, carbon nano-fibers and MoS₂). Standard test conditions were 600 MPa mean contact stress (increased to 1000 MPa for high load tests), 50-rpm rotational speed (increased to 100 rpm for high speed tests), 21°C (increased to 50°C for high temperature tests).

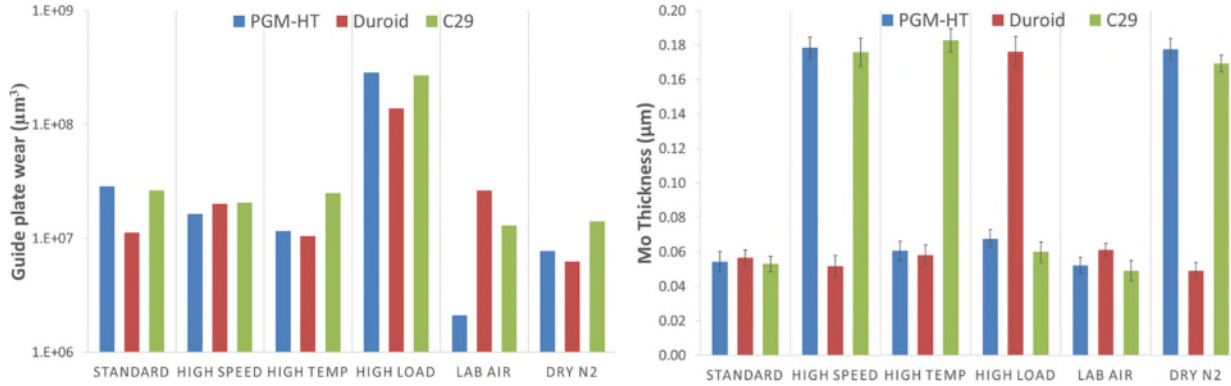


Figure 12. SOT guide plate wear (left) and XRF-measured residual Mo thickness (right) for PGM-HT, Duroid and C29 materials

Results, presented in [27], showed similar characteristics for all materials with variable friction, apparent rapid transitions from a low friction ($\mu\sim 0.05-0.15$) value to a higher value ($\mu\sim 0.4$ or higher). Subsequent measurements of Mo thickness (made by X-ray fluorescence spectrometry (XRF)) showed a two-valued population perhaps also suggesting rapid transitions from one state to another. Subsequent profilometry showed the transfer film to be very thin and discontinuous (with thickness of order 1-3 μm in the “best” cases and some small amount of metallic wear ($\sim 1 \mu\text{m}$) in the “worst case”.

Given that transfer film formation was shown to be relatively rapid, but also that the film was observed to be quasi-stable with evidence of a high rate of variability of thickness and frictional behavior with time, the equilibrium wear rate of the material in sliding was also investigated. The main concerns were that accelerated test might lead to quite different wear regime, and perhaps difference in transferred material characteristics, especially when thermal effects are also considered. PoD tests were carried out in vacuum under load and speed conditions considered appropriate for the simulation of cage/ball and cage/land contacts for low-speed, nominal (~160 rpm) and accelerated bearing test conditions.

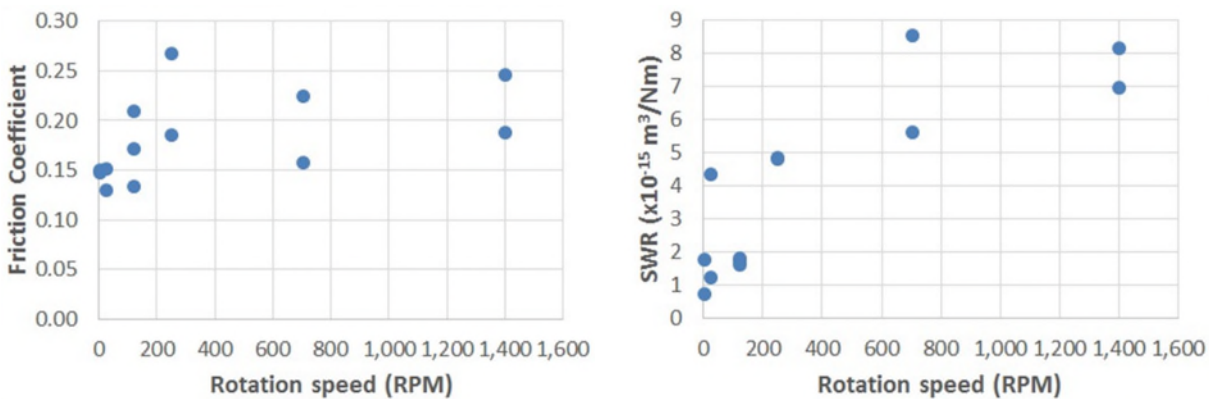


Figure 13. PoD Friction and Specific Wear Rate for PGM-HT v steel in vacuum as function of rotational speed (4 N, ~17 MPa mean)

As can be seen, for pin-on-disc tests there is quite a wide spread of friction and wear behavior and although mean friction seems approximately constant with speed, there may be some small increase in equilibrium wear rate with speed (but also a relatively high variability between tests).

When considering the impact of temperature (at temperatures typical of an accelerated test 21°C and 50°C), again the changes in tribological behavior were modest.

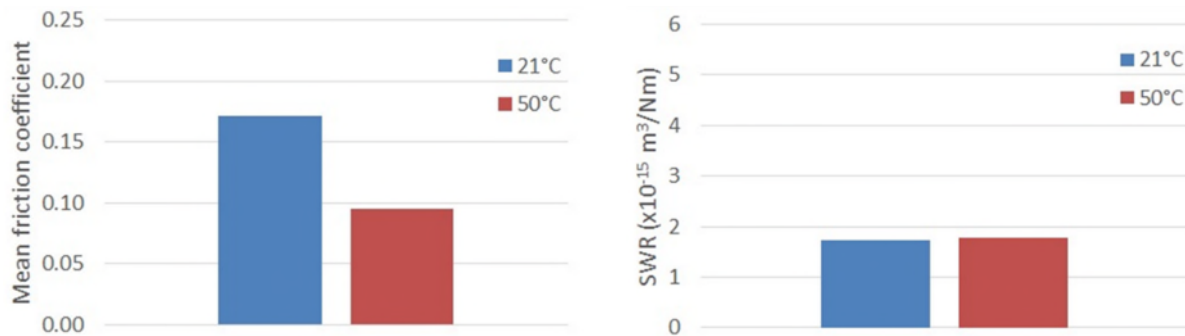


Figure 14. Effect of temperature on in vacuum friction coefficient and specific wear rate of PGM-HT v steel

When considering the impact of load, though there is clearly also some spread, results show that while the mean friction is not greatly impacted by increased load, the wear rate does increase with increased load, a result which substantiates the practice of accelerating test by increasing both load and speed when using this material.

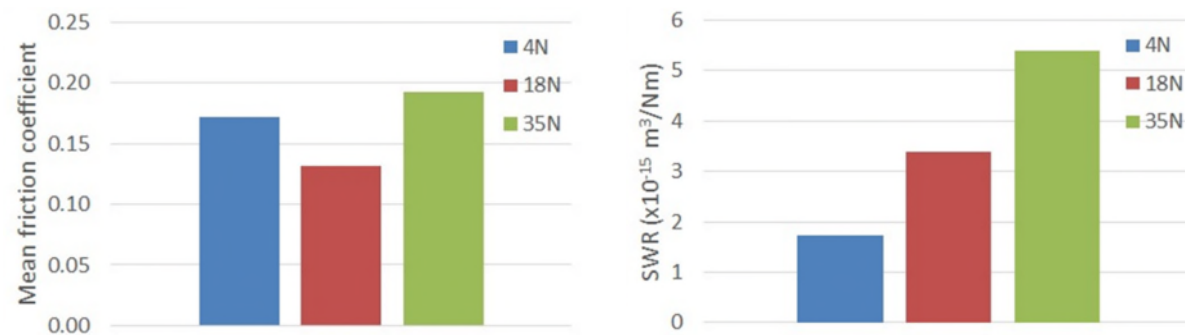


Figure 15. Effect of load on in vacuum friction and specific wear rate of PGM-HT v steel

Whilst it is acknowledged that small changes in friction can impact cage stability, the above data suggests that provided the bearing cage remains stable throughout test then acceleration of a test by increasing speed, load or both could be appropriate. This is because in general the friction and wear behaviors for PGM-HT have a quite wide spread and the effects of speed on wear, even over a quite wide speed range are approximately “within the noise” for this material.

The detection of cage instability then becomes a key enabler for the accelerated test envisaged. A recent test at ESTL [28] highlighted that a cage can be stable, quasi-stable or unstable at various times depending on complex factors (friction coefficients, instantaneous geometry, mass distribution, speed etc). Whilst validation of cage numerical models requires a detailed understanding of these phenomena, it may be argued that the success of an accelerated test needs only to demonstrate the absence of instability in the accelerated test if none is found at nominal speed operation.

The onset of cage instability will be detectable in the frequency domain (by the presence of the cage whirl frequency and other easily detectable frequency domain changes) or in the time domain by assessing the dependency of torque on speed (if unstable the mean torque may show a dependency on rotational speed squared since torque becomes more directly related to cage energy rather than load-dependent (Coulombic) ball/raceway friction (essentially fixed independent of speed).

In principle therefore, the validation of an accelerated test of a solid or self-lubricating bearing seems achievable, on the basis of tribometer tests of primary and secondary lubricant behavior and the monitoring of cage stability throughout the test. However more proof, in the form of a substantial number of bearing tests of the validity of this kind of approach would be needed and the existing evidence for this is now explored.

For MoS₂ Lubricated Bearings

ESTL's Space Tribology Handbook [17] summarizes data for MoS₂ bearing lifetime from [29]. Whilst strictly relating to the legacy PTFE/Glass-fiber MoS₂ material RT Duroid 5813 (rather than PGM-HT), in this program the end-of-life of the MoS₂ film was defined by the onset of a mean torque equivalent to a friction coefficient of 0.3 between ball and raceway. This data, shown in Figure 16, therefore relates to the MoS₂ "film lifetime" within the bearing and not specifically to the cage material performance.

For Self-lubricating Bearings

Data taken from [30] has been used as survey of the lifetime of self-lubricating bearings using PTFE/glass-fiber/MoS₂ cages. It should be noted that the data from this survey contains both tests which completed end-of-life (according to some undefined criterion) and those for which the end of test may have been due to completion of the test target revolutions (with or without failure). Furthermore, this data relates to a range of different bearing sizes and types as well as to the legacy Duroid material and to the currently used PGM-HT.

If these two populations are combined, a power-law trend-line seems to provide an appropriate fit to the data. The fit could likely be improved if the data were expressed in terms of ball passes (rather than revolutions), nevertheless, this seems a reasonable "first approximation" guide to lifetime to be expected.

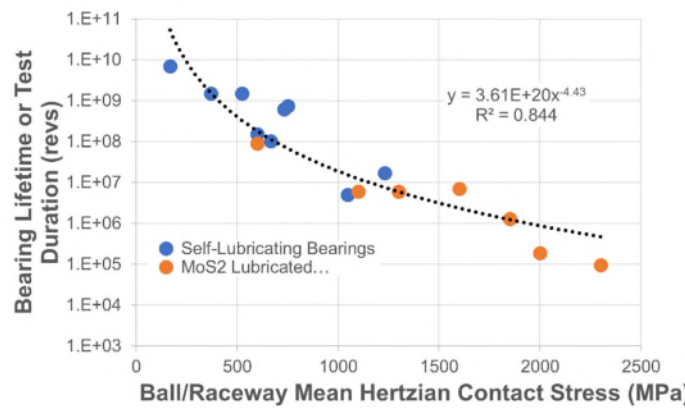


Figure 16. In-vacuum bearing life or test duration v ball/raceway Hertzian contact stress for MoS₂ films and self-lubricating bearings

In summary, even if the behavior of the lubricant is known at tribometer level, the extrapolation of such test results to bearing level is difficult due to differences in the definition of end-of-life torque for different applications. A moderately well-defined relationship exists between bearing life and contact stress as shown above. This kind of relationship has been used in the past to substantiate highly accelerated tests based on increasing speed AND load for low cost and mission of opportunity applications. The observation that products developed from an original mission of opportunity qualification carried out under accelerated load

and speed testing have demonstrably met and exceeded life requirements in flight, with outlier units completing lifetime >3 billion revs [31] suggests the approach may not only have been pragmatic for a schedule requiring full development of spacecraft from contract to flight in ~27 months, but entirely appropriate.

In summary we could state that whilst at component level the relationship between contact stress and life is beginning to become clearer, to reduce the spread of results (in the above curve experimental results may be a factor 10 higher or lower than predicted by the curve) more controlled tests are needed.

New Analysis and Measurement Techniques

Given the number of complexities and considerations applicable to the accelerated testing of fluid and solid lubricated bearings, it is desirable to classify these considerations as likely to be of first or second order significance such that in test definition first order effects would be accurately addressed, whereas compromises could perhaps be made concerning full representativity for second order effects without invalidating the whole test. In this respect, the use of quite sophisticated test techniques at component level might inform mechanism/instrument level accelerated tests (in which inevitably the quality of data which can be obtained may be relatively low).

In order to develop further the understanding of fluid, solid or self-lubricating lubricated bearings an enhanced Advanced Bearing Test Rig (ABTR) facility has been developed (which traces its conceptual heritage to the work of Ward [32]. This new bearing test rig enables simultaneous direct measurement of lubricant film thickness, torque, preload, inner/outer ring electrical resistance and local temperature. The bearing system used is compliantly preloaded (allowing compliance to be a test variable) and the lubricant film thickness is determined by measurement of shaft motion from an on-axis high sensitivity capacitance displacement transducer.

Measurements derived from this kind of setup include:

- Lubricating film thickness or torque evolution vs. speed or test duration (in time or frequency domain)
- Improved bearing level understanding of solid-lubricated bearing performance – e.g. PVD film life, onset of transfer-film dominated behavior, effect of run-in, speed or environment on subsequent lubricant film behavior
- Effect of preload compliance on lubricant performance
- Cage stability (presence of cage whirl frequency in the FFT of torque)

First data, presented below, relates to a Type 7004 bearing with preload 48 N (~820/707 MPa peak Hertz stress at inner and outer raceway contacts), compliantly preloaded using a spring (compliance 1.7E-4 m/N). All testing is in vacuum (<1E-5 mbar). In Figure 17 we show the mean torque and film thickness evolution for a bearing lubricated only by transfer film formation from its PGM-HT cage (i.e. a self-lubricating bearing without MoS₂ applied to balls or races initially). From this it can be seen that after an initially high peak, some millions of revolutions are required for the torque and film thickness to become quasi-stable. If we follow the evolution of this behavior further into the operational life of the bearing, we see that there are periods of high and low torque which seem to be accompanied by increased PGM-HT film thickness. Statistically the two parameters film thickness and torque are closely and positively correlated with a coefficient of 0.83. The peak film thickness reached during run-in is around 2.5 µm (which correlates to the 1-3 µm transfer films found in the SOT trials above), however the mean film thickness seems to be around 0.5 µm when the bearing is stationary. It is also notable that the mean torque observed is a little higher than calculated, even assuming a friction coefficient, $\mu=0.4$. This may be due to the relatively low preload used (hence perhaps not all balls are fully loaded as assumed in the bearing model), or to local changes in ball/raceway conformity due to the presence of the transfer film.

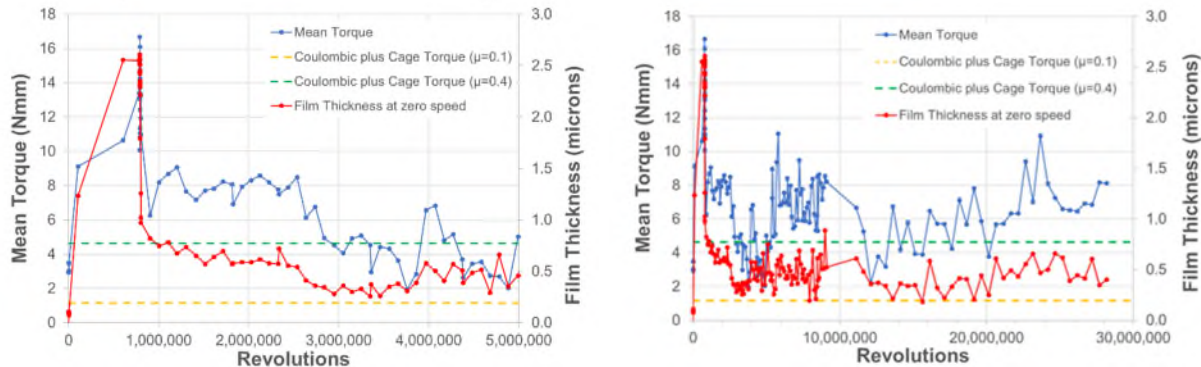


Figure 17. Type 7004 Bearing mean torque and PGM-HT film thickness vs. revolutions in vacuum

In future work, the facility will be used to characterize not only self-lubricating bearings, but also solid and fluid lubricated bearings using oils and greases. For appropriately characterized fluid lubricants, it is hoped that the lubricating film thickness measured will be correlated to predictions. For solid and self-lubricating bearings, it is hoped that the speed effects on cage wear and transfer film formation (including perhaps its viscoelasticity), will be understood so as to substantiate or not the accelerated test approach with increased speed and/or load.

Discussion

Accelerated testing of oil or grease lubricated bearings by increasing speed alone or speed and temperature remains risky (high probability of a misleading result). In addition to the main uncertainties regarding the rheological behavior of the fluid (especially at the high pressures within the contacts) and its flow, especially where grease is used, the local quantity of lubricant available seems difficult to predict. The conventional Langmuir theory seems to be predict higher evaporation rates for space oils than are measured in practice, yet fully saturated cages seem capable of absorbing a high proportion of the free oils within a bearing within their phenolic matrix. These competing factors and others mentioned above result in relatively high uncertainty concerning the lubrication regime in any space bearing either under nominal or accelerated test conditions. However, a series of carefully controlled tests in which the film thickness is monitored throughout test using the ABTR could improve understanding and even remove some of the more significant test uncertainties.

For solid and self-lubricating bearings, since the friction and wear behavior of both lubricant, transfer film and cage material are relatively well known and correlated to contact stress, then the possibility of accelerated test by speed, load or both seems feasible and indeed this method has already been used with some success. Nevertheless, the data newly available from the ABTR will allow the substantiation of claims concerning the validity of accelerated test methods and a ranking of the concerns listed above as of primary or secondary significance. This facility will also provide information of dynamic and static film thickness and may prove or dis-prove the assertions that behavior is substantially speed independent.

Conclusions

Despite considerable developments in understanding and characterization of fluid lubricants in recent years, accelerated test of fluid lubricated bearings remains highly likely to produce misleading results for the reasons discussed.

Life tests not carried out under an appropriately representative environment must be avoided as they will inevitably result in a tribological under-test. For example, results from Braycote 601EF suggest that tribolifetime of the grease performance is 1-3 orders of magnitude slower in air or nitrogen than in vacuum and similar results are documented for oils (and of course for solid lubricants).

Accelerated tests of solid or self-lubricating bearings are already supported by considerable tribometer data as summarized here. However, at bearing level, life data is much more scarce and there is a much larger spread of results. Better controlled and instrumented tests, such as those proposed for the ABTR are needed in order to reduce the spread so that existing regressions may be refined into still more credible and useful life estimation tools.

Acknowledgements

Much of the work presented was made possible by the financial support of the European Space Agency through its ESTEC technical center, whose leading role in directing and furthering the understanding of space tribological issues is gratefully acknowledged.

References

1. Meeks, C.R., Christy, R.I., Cunningham, A.C., "Accelerated Vacuum testing of Long Life Ball Bearings and Slip Rings", *Proc. 5th Aerospace Mechanisms Symposium*, NASA-SP-282, (1970)
2. Ward, W.E and Benzing, R.J., "Approaches to the accelerated life-testing of lubricants for space", *Proc. 1st European Space Tribology Symposium*, ESA-SP111 (1975)
3. Murray, S.F., Heshmat, H. & Fusaro, R., "Accelerated Testing of Space Mechanisms" *MTI Report 95TR29 for NASA* (April 1995)
4. Hamrock, B. J. and Dowson, D., "Ball Bearing Lubrication", New York, Wiley (1981)
5. Lewis, S.D. "Accelerated Testing of Liquid Lubricated Spacecraft Mechanisms", *Proc. 7th European Space Mechanisms and Tribology Symposium (ESMATS)*, Noordwijk, ESA – SP113 (1997)
6. Mia, S., Komiya, H., Hayashi, S., Morita, S., Ohno, N., Obara, S., "Viscosity Loss in PFPE Lubricant for Space Applications under EHL Conditions", *Tribology Online* 2, 54–58 (1997).
7. Ohno, N., Mia, S., Morita, S., Obara, S., "Friction and Wear Characteristics of Advanced Space Lubricants.", *Tribology Transactions* 53, 249–255 (2010).
8. Nakamura, Y., Yukawa, T., Kubo, S., Matsui, M., "Rheological Evaluations of Solidified Lubricating Greases and Their Base Oils under Very High Pressure", *Tribology Online* 8, 303–307 (2013).
9. Vergne, P., Bair, S., "Classical EHL Versus Quantitative EHL: A Perspective Part I—Real Viscosity-Pressure Dependence and the Viscosity-Pressure Coefficient for Predicting Film Thickness", *Tribology Letters* 54,1–12 (2014)
10. Bair, S., Martinie, L., Vergne, P., "Classical EHL Versus Quantitative EHL: A Perspective Part II—Super-Arrhenius Piezoviscosity, an Essential Component of Elastohydrodynamic Friction Missing from Classical EHL", *Tribology Letters* 63, (2016).
11. Stanley, S., Hampson, M., "An Experimental Assessment of the Evaporation Lives of Space Oils", *ESA-ESTL-TM-0162 01-* (2018)
12. Kent, A., "Long Term Storage and Cage Impregnation", *ESA-ESTL-TM-0181 01-* (2018)
13. Kent, A., "Life of Space Greases in Air" *ESA-ESTL-TM-0190 01-* (2016)
14. Buttery, M., "Further SOT Studies of Fluid Lubrication - Phase 1", *ESA-ESTL-TM-0158 01-* (2018)
15. Kingsbury, E., "Parched Elastohydrodynamic Lubrication" *ASME J. Tribology* 107(2), 229-232 (1985).
16. Cousseau, T., Graca, B., Campos, A., Seabra, J., "Grease Aging Effects on Film Formation Under Fully Flooded and Starved Lubrication", *Lubricants* 3,197-221 (2015).
17. ESTL Space Tribology Handbook, 5th Edition v2 (2013)
18. Wardzinski, B., "Life vs Contact stress for Dry Lubricated Gear Steels", *ESA-ESTL-TM-0101 01-* (2014)
19. Vortselas, A., "Preliminary Evaluation of Solid, Fluid and Hybrid Lubricated Gears", *ESA-ESTL-TM-0202 01-* (2018 in prep.)
20. Buttery, M., "An Evaluation of Liquid, Solid, and Grease Lubricants for Space Mechanisms Using a Spiral Orbit Tribometer", *Proc. 40th Aerospace Mechanisms Symposium*, NASA Kennedy Space Center. NASA/CP-2010-216272 (2010)
21. Buttery, M., "Spiral Orbit Tribometer Assessment of Space Lubricants", *ESA-ESTL-TM-066 01-* (2010)
22. Buttery, M., Kent, A., Forster, D., Vortselas, A., "Hybrid Lubrication of PFPE Fluids and Sputtered MoS₂", *Proc. 44th Aerospace Mechanisms Symposium*, NASA Glenn Research Center (2018).

23. Buttery, M., Wardzinski, B., Houton, K., Modern Self-Lubricating Composites For Space Applications: PGM-HT & Sintimid 15M" *Proc. 14th European Space Mechanisms & Tribology Symposium (ESMATS)*, Constance, Germany, 87, (2011)
24. Buttery, M., Cropper, M., Roberts, E.W., "Thermally Conditioned PGM-HT", ESA-ESTL-TM-0069 01- (2011).
25. Buttery, M., "Fundamentals of Transfer Film Lubrication", ESA-ESTL-TM-0206 01- (2018)
26. Merstallinger,A., Simon, Z., Nuss, G., Paul, C.E., Palladino, M., Buttery, M., "New Self Lubricating Polymer Matrix Composites for Journal and Ball Bearing Applications in Space (SLPMC2)", *Proc. 17th European Space Mechanisms and Tribology Symposium (ESMATS)*, Hatfield, U.K. (2017)
27. Buttery, M., Kent, A. "Validity of Accelerated Testing for Self-Lubricating Materials", ESA-ESTL-TM-0197 01- (2018)
28. Vortselas, A., "Cage Stability Study Using High-Speed Video", ESA-ESTL-TM-0227 01- (2018)
29. Cunningham, J., Swales, G., "Assessment Of The Influence Of Contact Stress On The In-Vacuo Torque Performance & Lifetime Of MoS₂-Lubricated Bearings Fitted With Duroid Cages" ESTL/TM/208 (2001).
30. Lewis, S.D., Anderson, M.J. & Haslehurst, A., "Recent Developments In Performance And Life Testing Of Self-lubricating Bearings For Long-Life Applications", *Proc. 12th European Space Mechanisms and Tribology Symposium (ESMATS)*, Liverpool, UK, (ESA SP-653) (2007).
31. Wade, A., "In-orbit Health Monitoring of PGM-HT Lubricated Reaction Wheels", *ESA Workshop on Mechanisms Testing and Health Monitoring* (2017)
32. Ward, P., Leveille, A., Frantz, P., "Measuring the EHD Film Thickness in a Rotating Ball Bearing", *Proc. 39th Aerospace Mechanisms Symposium*, 107, (2008)

Developmental Bearing and Bushing Testing for Mars Gearboxes

David Suffern^{*} and Jonathan Parker^{*}

Abstract

As a part of NASA Jet Propulsion Laboratory's (JPL) upcoming Mars 2020 mission, Sierra Nevada Corporation (SNC) will be providing a number of new gearbox designs to fulfill various functions in the rover's robotic arms. At the time of the design reviews, SNC was unable to reference published or heritage design data that encompassed the Mars 2020 mission requirements regarding bearing lubricant life and bushing wear. As a result of this lack of information and the accelerated schedule, component-level and gearbox-level developmental testing was performed during the program's procurement phase to substantiate design choices in advance of qualification-level testing of deliverable flight gearboxes. These tests successfully demonstrated that the necessary mission life could be achieved. This paper aims to highlight the benefit of these developmental tests and provide new data in an area previously unpublished for bearing lubricant life [1][2][3] with mean Hertzian contact stresses up to 2.18 GPa (316 ksi). Additionally, the bushing wear test results are included, indicating that the required Mars cold operating temperatures were particularly stressing.

Introduction

SNC was tasked with providing eight different custom planetary gearbox designs to drive mechanisms on the new Mars 2020 rover. Gearbox size and volumetric constraints required high torque-density designs that required pushing the envelope in terms of component stresses in the bearings and bronze alloy bushings supporting the planet gears. The life requirements for several of these gearboxes exceeded requirements for hardware previously delivered by SNC on the Mars Science Laboratory mission, the Lightweight gearbox design study [4], and other published data for Perfluoropolyether (PFPE) bearing lubricant life [1][2][3]. General industrial design standards for bushings were considered uncertain for these applications due to the use of vacuum-rated lubricants and a non-terrestrial operating environment [5].

Summary of Successful Developmental Test Exposures:

- Operating Temperature Range: -70°C to +70°C
- Ball Bearing Max Mean Hertzian Stresses:
 - 2.179 GPa (316 ksi) up to 389,501 stress cycles
 - 1.682 GPa (244 ksi) up to 2,621,338 stress cycles
 - 1.517 GPa (220 ksi) up to 29,077,592 stress cycles
- Operating Pressures for Bronze Bushing:
 - 8.487 MPa (1,231 psi) for 1.78 km (5,895 ft) at speeds of 40.1 mm/s (7.89 ft/min)
 - 2.766 MPa (401 psi) for 22.97 km (75,358 ft) at speeds of 17-31 mm/s (3.35-6.10 ft/min)
 - 1.866 MPa (274 psi) for 34.17 km (112,122 ft) at speeds of 17-31 mm/s (3.35-6.10 ft/min)
 - 0.625 MPa (91 psi) for 51.20 km (167,981 ft) at speeds of 17-31 mm/s (3.35-6.10 ft/min)

SNC worked with JPL to define developmental tests for reducing programmatic risk ahead of qualification level testing since there was a lack of widely available data to provide confidence that these operating parameters had a high probability of success. The scope of this developmental testing was strictly focused on demonstrating the capability of these components for the Mars 2020 mission parameters including temperature profile, operating speeds, and frequency of direction changes. As such, these

* Sierra Nevada Corporation, Durham, NC

results do not guarantee success for alternate mission parameters, nor do they summarize the limits of these components; rather, they provide a handful of data points for which successful operation has been demonstrated.

Planet Support Load Within a Planetary Gearbox

Planetary gearboxes are a power-dense option for translating high-speed, low-torque motor shaft outputs into more useable lower-speed, higher-torque outputs. The planet gears that operate within these gearboxes must be supported by and rotate upon carrier posts. Friction losses at the interface between the planet gears and carrier posts are typically minimized through the use of bushings or rolling element bearings. Rolling element bearings are generally selected in the faster moving, more lightly loaded initial stages of a planetary gearbox. By contrast, bushings may be effectively used in the latter planetary gearbox stages, where their additional drag is counterbalanced by their ability to withstand higher loads with less volume. A well-designed bushing can successfully operate at higher radial loads than a rolling-element bearing of the same proportions. Bushings have also proven to be far more tolerant of slight imperfections or contamination than plain steel bearings. Figure 1 shows the typical construction of a planetary gearbox.

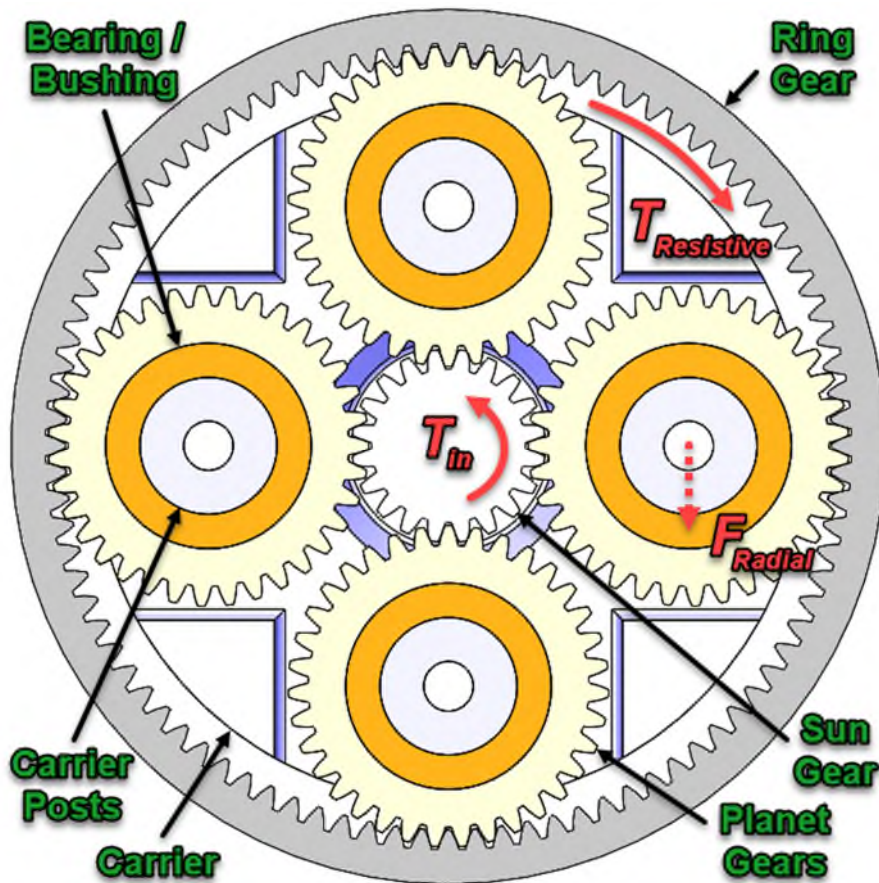


Figure 1. Generic Planetary Gearbox Components and Planet Support Load

Figure 1 also shows the radial load, F_{Radial} , to which the bushing or bearing is subjected as a result of the torque transmission through the gearbox. This radial load is generated as torque and is transferred from the torque input, T_{in} , to the resistive load at the output, $T_{Resistive}$. The severity of this radial load is related in terms of pressure for a bushing and Hertzian contact stress for a rolling element bearing. It is these

bushing pressures, bearing stresses, and the associated effects on the lubricant which this developmental testing was designed to evaluate.

The bushing pressures and distances are calculated from the bushing inner diameter and assume that the outer diameter does not rotate relative to the planet gear. Ball bearing Hertzian stresses were calculated with COBRA AHS™ software, using radial play and raceway curvatures provided by the bearing vendor for each serialized bearing.

Component-Level Testing

Because high stresses in ball bearings and bushings presented one of the largest gearbox program risks, component level life tests were expediently developed in order to demonstrate that the final design could meet the 2X life requirement set forth by NASA JPL.

Materials and Lubrication

All materials and lubrication were based on the designed flight configuration at the time of the Detailed Design Reviews. For test expediency, commercially available 440C bearings of the same basic bearing size as the flight configuration were procured to undergo component-level testing. These bearings contained stainless steel crown retainers equivalent to the flight configuration. They were delivered with serialized inspection data for radial play and inner/outer raceway curvature that allowed loads to be tailored to achieve the required max mean Hertzian stresses. The bearings were lubricated with grease plate and a 5-10% free volume fill of 50/50 slurry containing Braycote Micronic 600 EF grease and Brayco 815Z oil. This lubrication fill was selected on the basis of prior published research [6]. Braycote Micronic 600 EF grease was selected over the very similar 601 EF grease because the use of stainless steel components lessened the need for the corrosion inhibiting additives found in 601 EF.

SAE 841 bronze alloy bushings (now procured to material specification CT-1000-K26) were also readily available. This bushing material, in combination with hardened 440C posts, was shown to be most effective in the NASA Phase II SBIR Lightweight Gearbox Technology Program [4]. For lubrication, the bushings were impregnated with Brayco Micronic 815Z oil and the surrounding parts were grease plated with Braycote 600 EF grease.

Component-Level Bushing Testing

The test rig shown in Figure 2 was available from the Lightweight Gearbox program and repurposed to allow for expedient component-level testing on bushings and bearings. This test setup involved a stationary gear blank to hold the outer diameter of the bushing under test with a rotating shaft interfacing with its bore. The radial load was applied with a Radial Load bar, having its fulcrum on the far side of the component under test, and a mass was hung on the near side to generate the radial loads experienced within a planetary gearbox. Finally, the rotating shaft was driven by a motor through a rotary torque sensor via an opening in the thermal chamber wall.

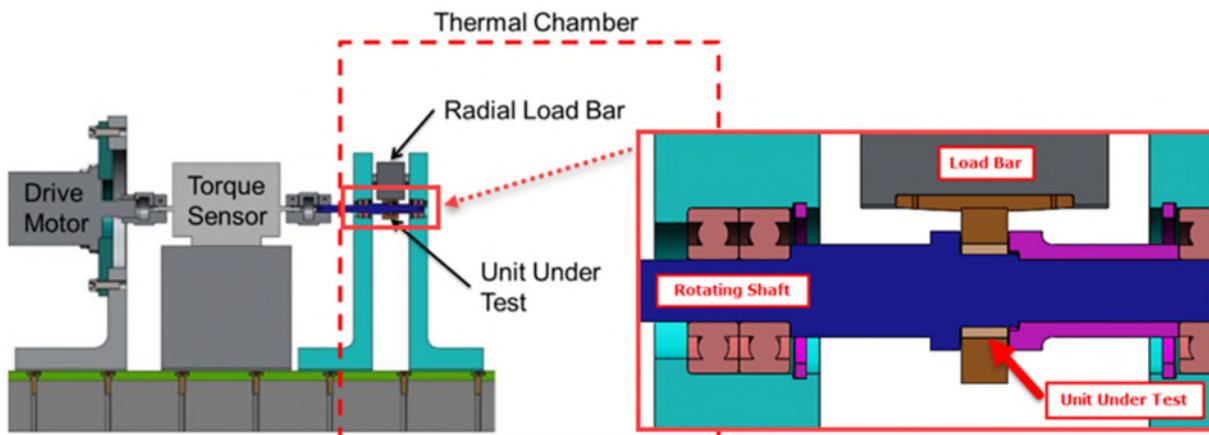


Figure 2. Component Test Fixture

At this point in the program, design reviews were complete and procurement was underway. Table 1 shows the two enveloping design points to which a single bushing would need to successfully operate in order to satisfy the cumulative 2X life requirement. Figure 3 shows the cumulative required operating pressures and durations for each of the five gearbox designs utilizing bushings, along with the enveloping component test points. Some of these design points later changed due to revisions JPL made to the design specifications, further supporting the need for this initial developmental testing.

The test temperature was the final, crucial variable which needed to be defined for this developmental test. The required operational temperature range was -70°C to $+70^{\circ}\text{C}$. For simplicity and conservatism, the team decided to run the entire test at the worst-case temperature. Elevated temperatures were assumed in design reviews to be worst-case because of PFPE's propensity to chemically break down in high stress environments. Hot environments lower the viscosity of PFPE lubricants, resulting in thinner lubricant film thicknesses for the otherwise same speed and load conditions. When sufficiently thin, the lubricant regime will be near or in boundary contact, which accelerates the breakdown of the lubricant due to the high stresses occurring at the molecular level, shearing apart molecules. Broken down, the lubricant can no longer effectively protect the bushing from more rapid wear.

Table 1. Initial Bushing Operational Requirements

Load Case	Load	Duration	Speed
High Load / Short Duration	8.49 MPa (1,231 psi)	1.78 km (5,895 ft)	39.6-77.2 mm/s (7.8-15.2 ft/min)
Low Load / Long Duration	2.59 MPa (376 psi)	122 km (400,170 ft)	127-249 mm/s (25-49 ft/min)

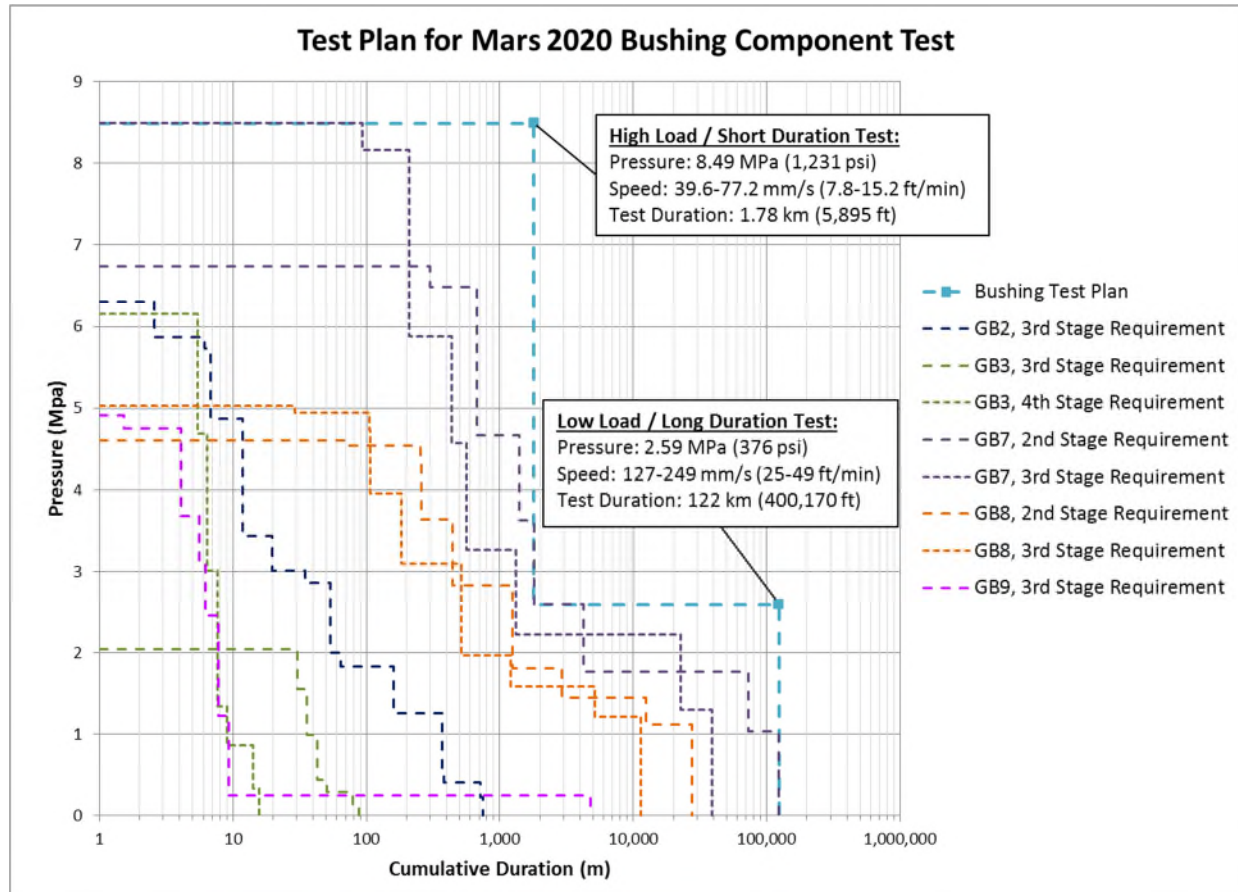


Figure 3. Initial Gearbox Bushing Pressure v. Duration Requirements and Test Plan

To confirm the assumption that the hot operational temperature limit was the more stressing environment, two bushings were tested: Bushing A at the hot extreme (+65°C to +70°C) and Bushing B at the cold extreme (-65°C to -70°C). The two bushings were exposed to the identical loads and life of the High Load/Short Duration load case of Table 1: 8.487 MPa (1,231 psi) load at a speed of 40.1 mm/s (7.89 ft/min) for a total duration of 1.78 km (5,895 ft). Direction was alternated every five minutes as a rough replication of the change in direction to which the gearboxes would be subjected. After this exposure, the bushings were removed from the test fixture and visually evaluated.

Unexpectedly, the wear on Bushing B from the cold test was more severe than on Bushing A from the hot test, as shown in Figure 4. This was likely due to lubricant starvation from sub-optimum oil replenishment at the wear interface due to such cold operating temperatures. The pour point of Braycote 815Z oil is -72°C. Operation between -65°C and -70°C, so close to the -72°C pour point, likely reduced the oil's ability to flow within the pores of the impregnated sintered bushing, hampering its ability to protect the bushing from more rapid wear.

Hot Bushing:



Cold Bushing:

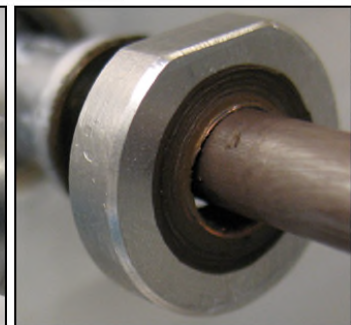


Figure 4. Initial Wear on Bushings: 8.487 MPa @ 40.1 mm/s for 1.78 km

Since the cold environment proved more stressing on the bushings in this flight lubrication scheme, the program updated its life test temperature requirements to bias them colder than originally planned. A new requirement was added to operate at least 25% of the life at an expected mission nominal temperature of -55°C. These cycles were in addition to the existing requirements to operate at least 25% at cold (-70°C) and 25% at hot (+70°C); with the remainder of cycles anywhere between hot and cold temperatures. Also, the life requirements of the dominating gearbox designs (GB7 and GB8) were iterated in JPL's specifications after the initial tests on Bushings A and B. The peak load was reduced from 8.487 MPa (1231 psi) to 8.173 MPa (1185 psi), but the required Low Load duration was increased from 122 km (400,170 ft) to 301 km (987,101 ft), as can be seen in Figure 5.

The remainder of the component-level bushing test was planned to be completed using Bushing A, but biased cold. Having already completed the required operation at hot, this bushing would be exposed to 25% of the updated High Load/Short Duration load case at cold, and then exposed to 100% of the Low Load/Long Duration cycles at a continuous -55°C, as indicated by Test #2 and Test #3 in Figure 5.

The operational profile was also updated for the following tests, incorporating a five-minute pause for every 20 minutes of operation (two cycles of five minutes clockwise, five minutes counter clockwise). This was in acknowledgement that the gearmotors would not be run continuously on Mars, and that the periodic pause may allow for some beneficial oil reflow from the bushing without dramatically increasing the length of the developmental test. Finally, as the Low Load point would correspond to a lower gearbox torque transmission and higher operating speed, the operating speed at 2.45 MPa (356 psi) was increased to 192 mm/s (37.7 ft/min).

Unfortunately, this Low Load testing in the fixture with Bushing A resulted in a premature bushing failure after only 25.58 km (83,914 ft) at 2.45 MPa (356 psi) shown in Figure 5. Furthermore, after the torque cell data was reviewed, it was determined that the bushing began operating in a degraded condition after 19.20 km (62,977 ft). See Figure 6 for the failed condition. While this failure occurred short of the duration required to envelope the life of all design configurations, it was sufficient to satisfy the life requirements of the GB2, GB3, and GB9 designs.

It was believed that the test setup led in part to the premature bushing failure. Clearances in the fixture could allow the radial load bar to apply a slight axial load into the bushing and cause edge loading. Concerns regarding the fixture and the negative test result led to the desire for additional testing that better represented a flight-like configuration within the context of a planetary gearbox. However, as flight-like gearboxes of the GB7 and GB8 configurations would not be available to utilize in testing for several months, the results of this initial test led to a decision to begin a parallel procurement of components that would allow the GB7 2nd Stage and GB8 2nd Stage planet supports to be ball bearings instead of bushings. Without bushings in these locations, the enveloping required life of bushings at low load would be significantly reduced. Additionally, the possibility of ball bearings in these locations would drive the requirements of component-level bearing testing.

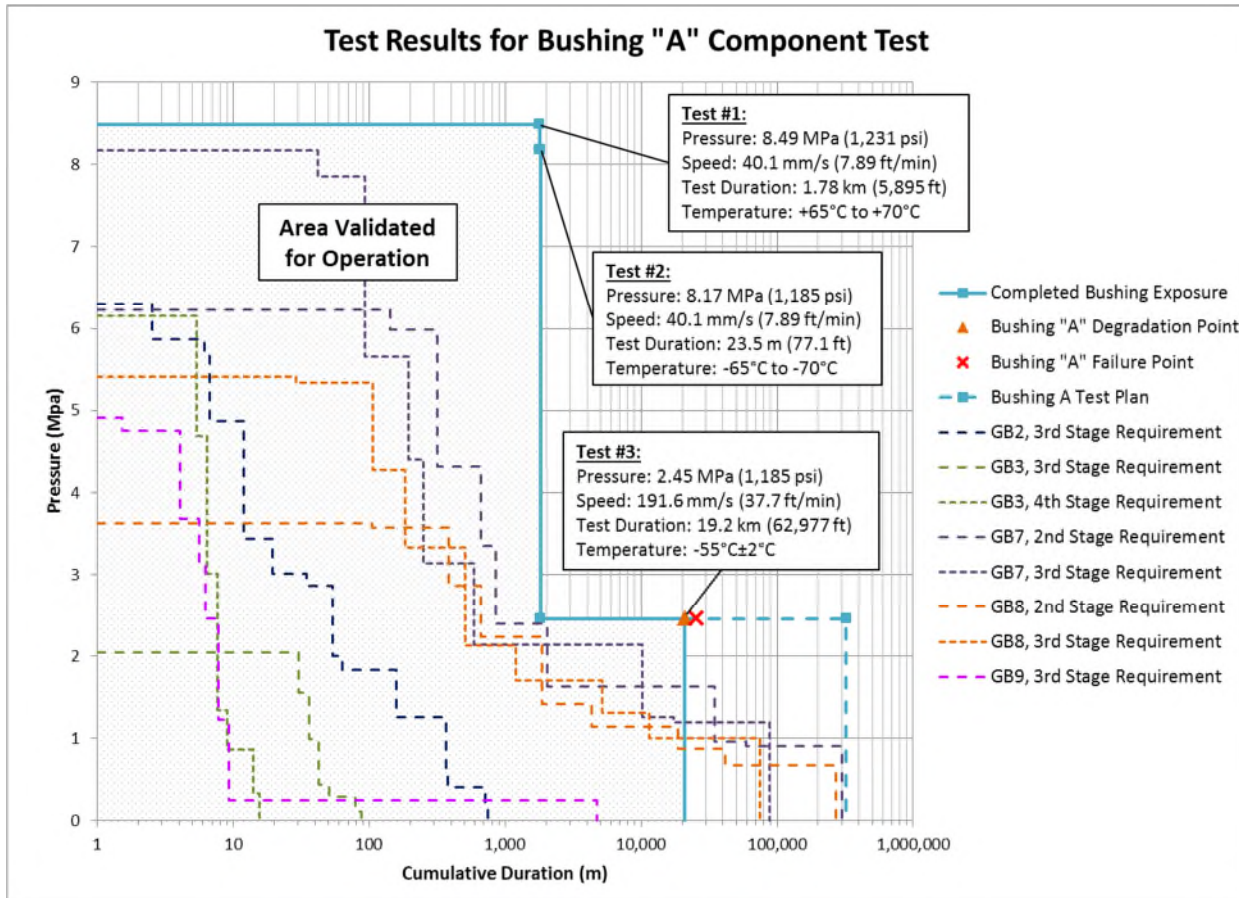


Figure 5. Revised Gearbox Bushing Pressure v. Duration Requirements and Test Results

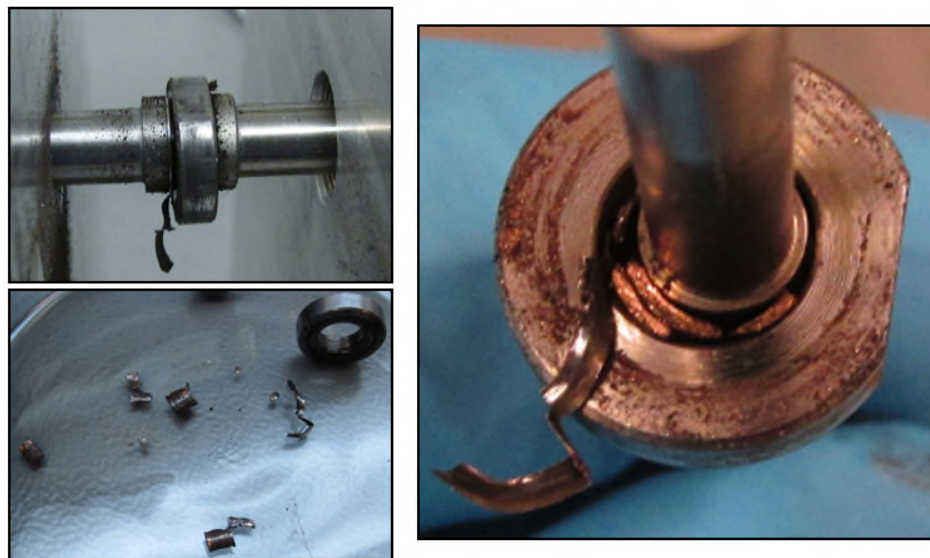


Figure 6. Component-Level Test Bushing Failure: 2.45 MPa @ 191.6 mm/s for 25.58 km at -55°C

Component-Level Bearing Testing

A representative radial ball bearing was tested in the fixture shown in Figure 2, understanding that it would be more tolerant of fixture shortcomings. The bearing was tested at loads, speeds, and durations representative of and encompassing all Mars 2020 gearbox designs, including the newly-planned 2nd Stage applications in the GB7 and GB8 gearboxes.

Ball bearing testing was completed successfully. The max mean Hertzian contact stress, number of stress cycles, and inner race speed of the tested bearing are shown in Figure 7. Although the speed was uniform at each stress level, the lambda factor varied with temperature. The final condition of the bearing grease is shown in Figure 8. The bearing completed approximately 32 million stress cycles at stresses exceeding 1.31 GPa (190 ksi), including 29 million over 1.517 GPa (220 ksi) and nearly 390,000 at 2.179 GPa (316 ksi). Historically available PFPE curves are also shown in Figure 7 for reference:

- The Cumulative Degradation Factor (CDF) curves (“CDF = 2” and “CDF = 8”) indicate greater concern for long life usage of PFPE lubricants without directly cautioning against high stresses at a lower number of stress cycles [3]. The CDF is calculated as the product of max mean stress times the number of stress cycles and is typically expressed in units of 10^{12} psi-cycles (e.g. CDF = 2 is shorthand for 2×10^{12} psi-cycles).
- Conversely, curves from other test data (“Upper Limit Line” and “Lower Limit Line”), based on NASA CP-3062 [1], indicate a greater concern for high stresses which accelerate the polymerization and breakdown of PFPE lubricants, but suggest very long life is possible at low stresses.

Stress cycles are the number of times a ball passes across a given spot on the raceway. The conversion from bearing revolutions to stress cycles is a function of bearing geometry as shown in Eq. 1:

$$\# \text{ Stress Cycles} = \# \text{ Revs} \times N \left[1 - \left(\frac{1}{(d+D)/(d-D)+1} \right) \right] \quad (1)$$

Where N is the number of balls, d is the pitch diameter, and D is the diameter of the balls.

It is worth noting that the bearing under test was exposed to all of these stress cycles while running continuously in a thermal chamber cycled to achieve a distribution of 25% hot (+65°C to +70°C), 25% cold (-65°C to -70°C) and the remainder between -65°C and +65°C. Each thermal cycle was approximately 400 minutes with the average test temperature of approximately 0°C. The thermal chamber ramp time made it impractical to include the additional temperature plateau for 25% of cycles at the nominal temperature, -55°C.

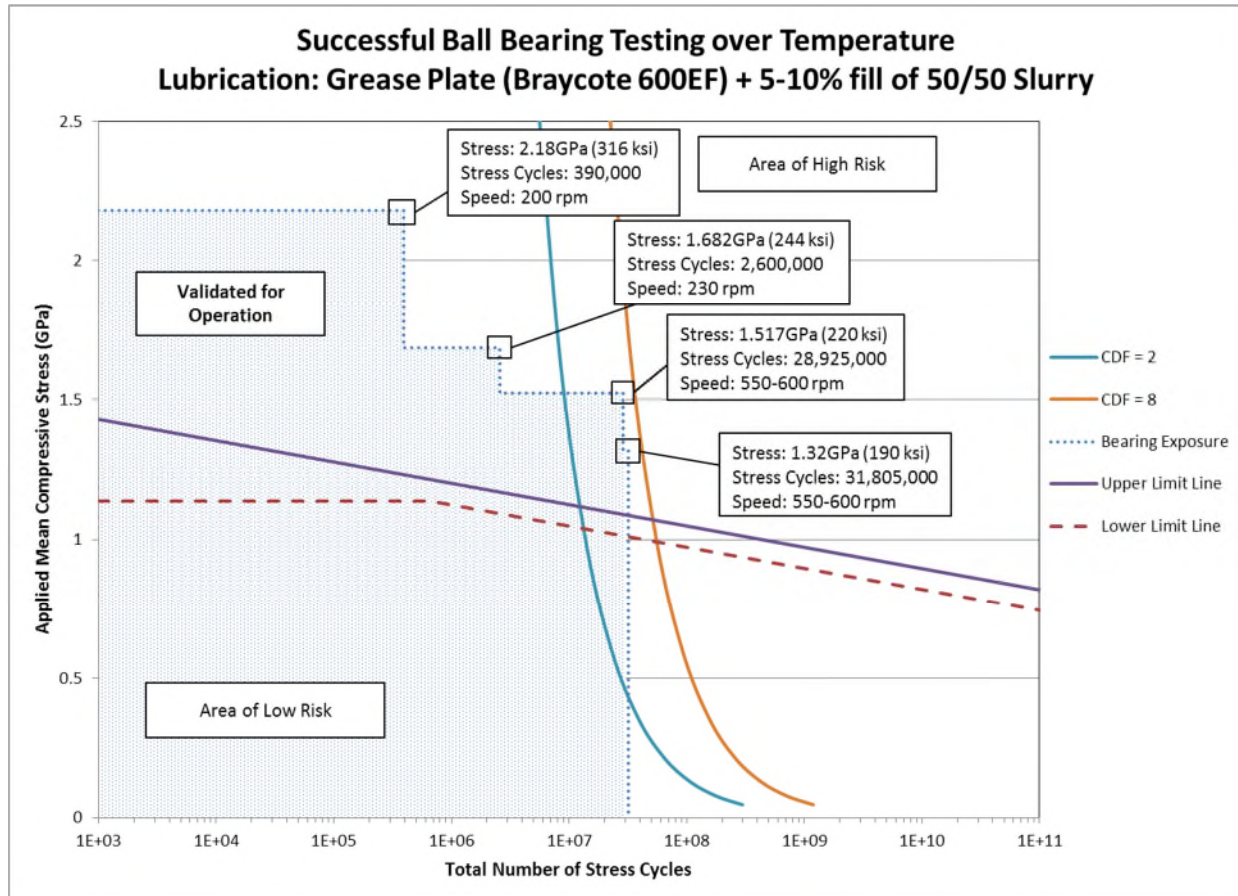


Figure 7. Successful Component-Level Bearing Exposure

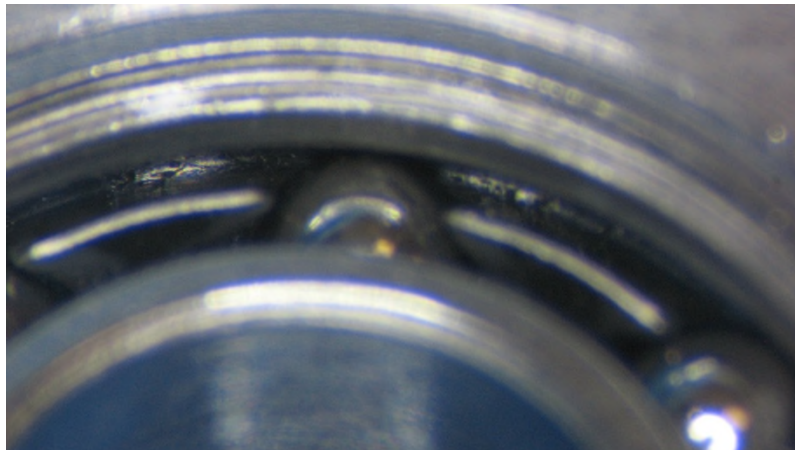


Figure 8. Condition of Grease at Conclusion of Component-Level Bearing Test

Flight-Like Gearbox Testing

Concerns regarding the potential influence of fixture design on the results of the component-level bushing test and the receipt of the flight-like hardware allowed the team to assemble a three-stage planetary gearbox which could be used to execute the life test requirements on flight hardware. In the interim between the component-level bushing tests and this gearbox-level test, JPL changed the life requirements of the dominating gearbox designs (GB7 and GB8), nearly halving them.

In conjunction with using a flight-like gearbox, this test had the added benefit of testing four bushings simultaneously (Reference Figure 1) in addition to the other life-limited gearbox components: gears, ball bearings, and associated lubricant. Concern regarding increased bushing wear seen at cold temperatures was thought to be due to lubricant starvation related to poor mobility of highly viscous oil in the porous bushing. This led to a decision to lubricate two of the four bushings with Brayco 814 oil, a discontinued Castrol product with a pour point and cold temperature viscosity significantly lower than Brayco 815Z oil: 2,121 cSt [7] versus 10,855 cSt [8] at -54°C. One remaining bottle of Brayco 814 oil was obtained through distribution. Loads were applied to bushings through the gear mesh inside the planetary gearbox in the form of resistive torque by a particle brake. Loads on each planet bushing were calculated based on ANSI/AGMA Standard 6123-B06 [9] Mesh Load factors. This document provides a mesh load factor of 1.25 for four planets with one floating member, meaning the highest loaded planet may carry 31.25% of the total stage torque.

The first gearbox available for testing was the GB2 design, but the flight-like gearbox bushing wear test was designed to encompass the load cases from all of the Mars 2020 applications including GB7 and GB8 as follows:

- Initial run-in at ambient conditions to distribute the lubricant.
- Back to back 1X life tests of the “ground test” cycles (total of 2X) with a temperature distribution of 25% ambient ($23^{\circ}\text{C} \pm 5^{\circ}\text{C}$), 25% hot ($+65^{\circ}\text{C}$ to $+70^{\circ}\text{C}$), 25% cold (-65°C to -70°C), and 25% ambient ($23^{\circ}\text{C} \pm 5^{\circ}\text{C}$).
- Back-to-back 1X life tests of the “mission life” cycles (total of 2X) were conducted at a sustained -55°C . It is worth noting that the temperature chamber was held at -55°C during the entire mission life test, even during periods of non-operation. This was considered important for preventing the lubricant from reflowing better at room temperature, potentially providing a false-positive test result.
- All operation, except initial run-in, distributed clockwise and counter clockwise cycles evenly at five-minute intervals. Run-in consisted of 30 minutes operation clockwise followed by 30 minutes operation counter clockwise.

In contrast to the component-level bushing test which failed prematurely, the flight-like gearbox test successfully completed the test protocol. This satisfied the life and loads required for all the Mars 2020 gearbox designs and provided the necessary confidence to proceed with the designed gearbox configurations. The as-tested loads and durations are summarized in Table 2 and illustrated in Figure 9, with the component-level bushing wear test loads and durations shown for reference.

Table 2. As-Tested Flight-Like Gearbox Bushing Exposure

Test Step	Bushing Pressure (MPa)	Total Duration (m)	Bushing Speed (mm/s)
Run-In	0.625	61	17.04
	1.258	3,301	
	2.499	157	
	2.954	1,555	
	3.583	16	
	5.155	52	
	5.332	42	
	7.858	100	
2X Ground Test Cycles	0.625	6,788	30.97
	1.375	74	
	2.766	5,533	
	1.886	444	
	0.625	6,728	
	1.375	74	
	2.766	15,670	
	1.886	10,605	

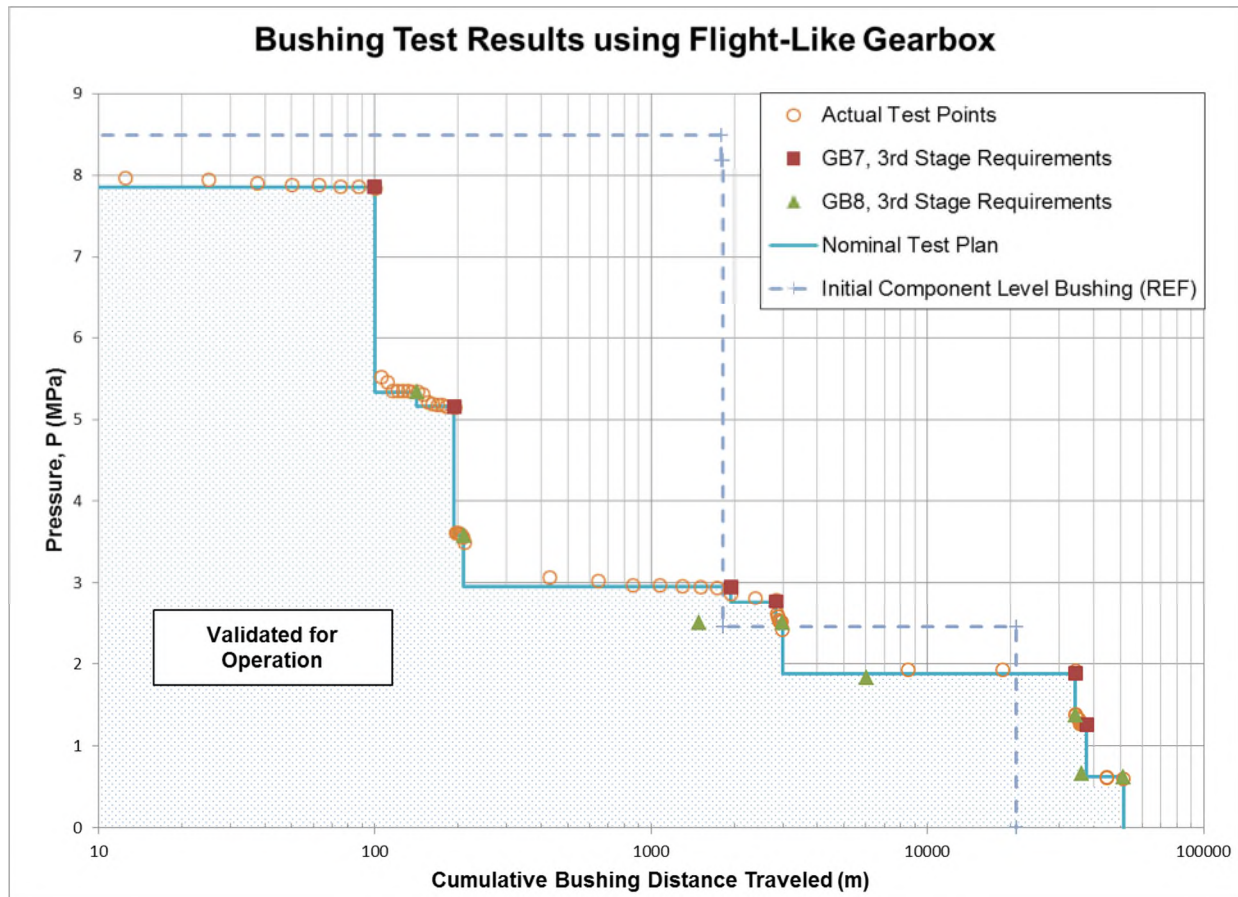


Figure 9. Bushing Wear Exposures

© 2018 Sierra Nevada Corporation

Disassembly and inspection of the bronze alloy bushings and 440C posts at the conclusion of testing are shown in Figure 10. The results of surface roughness measurements along the axial length of the bushing outer diameters are shown in Figure 11. A visual comparison and these roughness measurements indicate the Brayco 814 oil provided superior wear protection to the bushings for this predominately cold operational test. The 814 oiled bushings displayed a surface condition more similar to the virgin bushing pulled from stock for comparison. The improvement seen from the Brayco 814 oil is most likely due to the lower viscosity of 814 at cold temperature versus the 815Z oil allowing improved lubricant flow and replenishment.

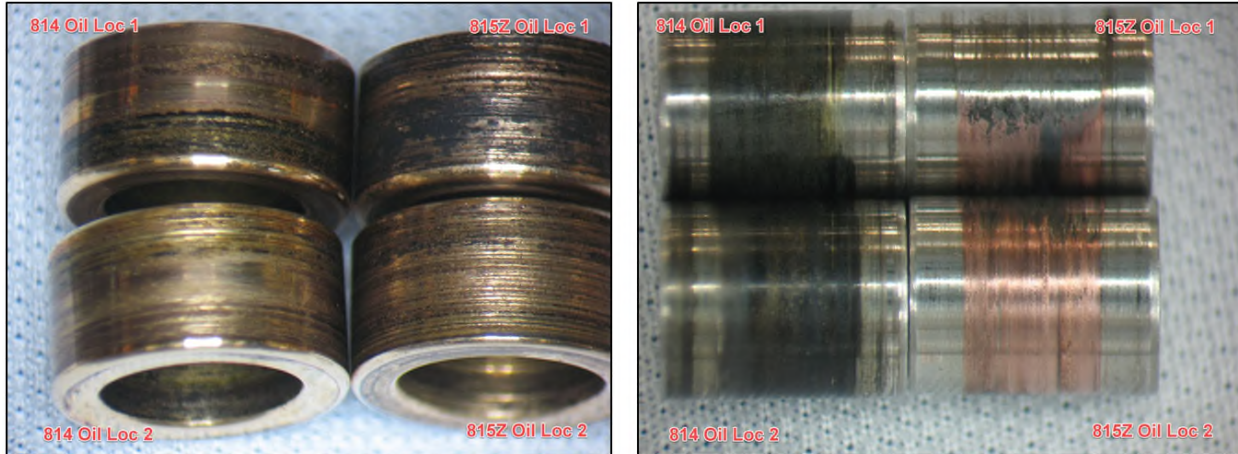


Figure 10. Bushings (Left) and Posts (Right) at the Conclusion of Wear Testing

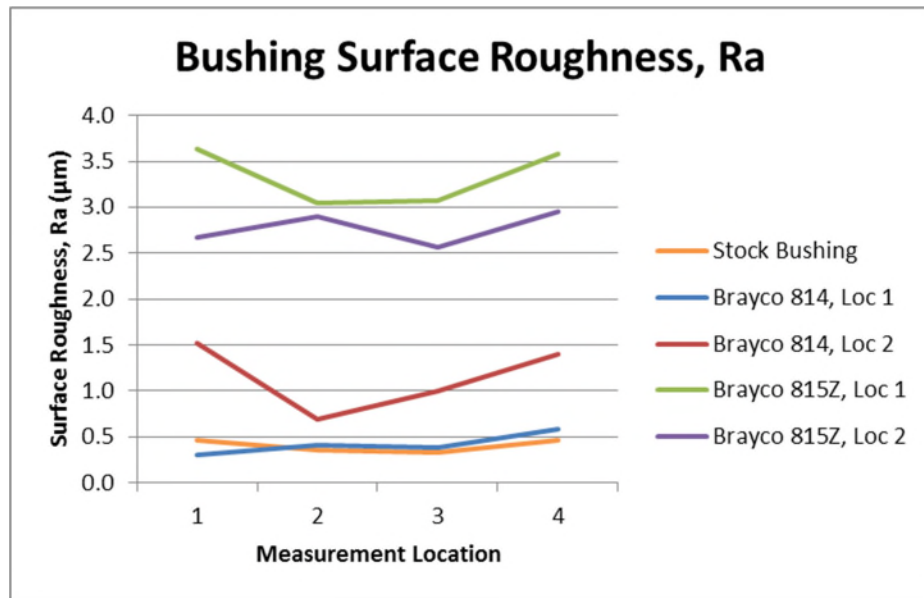


Figure 11. Bushing OD Surface Roughness Measurements

Conclusions

Developmental testing to inform design decisions and provide confidence in qualification life was successfully completed. These developmental tests were not intended to address all possible operational variables, but were specifically targeted to the mission parameters of these Mars 2020 gearbox designs.

Several other observations, conclusions, and areas for future work were recorded as a result of this developmental testing:

- If necessary and financially feasible, a parallel path of procurement different design options while awaiting developmental test results can preserve accelerated program schedules by allowing final design decisions to be informed by those test results.
- PFPE-family lubricants may have successful use for short durations at higher Hertzian contact stresses than previously published. Testing of mission-specific operational characteristics is recommended.
- The extremely cold operating temperatures for Mars mechanisms are particularly challenging for wet lubrication schemes since operation at temperatures near the lubricant pour point may result in poor lubricant mobility, leading to starvation and insufficient protection of wear surfaces, especially for porous bushings.
- While bushings lubricated with either oil completed testing successfully in the flight-like gearbox, bushings lubricated with Brayco 814 oil exhibited less wear than those lubricated with Brayco 815Z oil in SNC's development testing, likely due the lower viscosity of Brayco 814 oil at cold temperatures.
- Every effort should be made to scrutinize test fixtures and test components in the most flight-representative configuration possible to prevent false failures, as was believed to have occurred in the component-level bushing test.

Acknowledgements

This work was funded by JPL under Subcontract 1541135. The authors wish to express appreciation to the Motion Control Subsystem (MCS) team at JPL for their collaboration in the preparation and review of these developmental tests.

References

1. Conley, P.L. and Bohner, J.J., "Experience with Synthetic Fluorinated Fluid Lubricants", *Proc. 24th Aerospace Mech. Symp.*, NASA CP-3062, Kennedy Space Center, FL (1990)
2. Mobley, J.D. et al., "Extended Life Testing of Duplex Ball Bearings", *Proc. 43rd Aerospace Mech. Symp.*, NASA CP-2016-219090, Santa Clara, CA (2016)
3. Lo, C.J., et al., "Use of Cumulative Degradation Factor Prediction and Life Test Result of the Thruster Gimbal Assembly Actuator for the Dawn Flight Project", NASA CR-2009-215681
4. Mobley, J.D., "Trade Studies for a High Torque Density Planetary Gearbox", *Proc. 41st Aerospace Mech. Symp.*, NASA CP-2012-217653, Pasadena, CA (2012)
5. *Materials Standards for PM Self-Lubricating Bearings*. Metal Powder Industries Federation, 2010. MPIF Standard 35
6. Herman, J. and Davis, K., "Evaluation of Perfluoropolyether Lubricant Lifetime in the High Stress and High Stress-Cycle Regime for Mars Applications", *Proc. 39th Aerospace Mech. Symp.*, NASA CP-2008-215252, Huntsville, AL (2008)
7. Castrol. Brayco Micronic 814 Product Datasheet, Castrol, 2009, <https://thelubricantoracle.castrol.com/product/brayco-micronic-814/alternatives/industrial/en-JP>
8. Castrol. Brayco Micronic 815 Z Product Datasheet, Castrol, 2009, thelubricantoracle.castrol.com/product/brayco-micronic-815-z/industrial/en-JP
9. *Design Manual for Enclosed Epicyclic Gear Drives*. American Gear Manufacturers Association, 2006. ANSI/AGMA 6123-B06

Experimental Method for Determining Ball Bearing Lubricant Quantity Factor

Yoshimi R. Takeuchi*, Peter P. Frantz* and Tim P. Woodard*

Abstract

Ball bearing temperature prediction methods for spacecraft applications require, in part, a knowledge of the lubricant contribution to bearing drag torque. This can be estimated using a model derived by Palmgren and Snare. When implemented in bearing analysis software, the viscous drag torque model depends on a variable known as the Lubricant Quantity Factor (LQF). This value is critical to understanding spacecraft ball bearing temperatures for cases where motion is involved. In this paper, we describe the results of experiments that were conducted on a bearing test fixture that is capable of measuring bearing thermal parameters including heat generation of an operating bearing. The heat generation and speed measurements are used to determine bearing drag torque, which is then used to determine LQF. We show that the LQF depends on operating conditions, and that this variability should be considered when calculating bearing drag and operational temperature.

Introduction

There are two main bearing parameters that contribute to the final bearing temperatures in a spacecraft bearing: bearing thermal conductance and heat generation. Bearing thermal conductance has been written about in the past by this research group [1]. Heat generation caused by energy lost to bearing drag is used in this paper to deduce changes in viscous component of drag torque.

Heat generation can be calculated as the product of torque and speed. Speed is often easily experimentally measured. Torque can be estimated using a computational bearing analysis program, discriminating between the two main contributors to total energy loss: mechanical and lubricant torque. The mechanical contribution is due to the resistance to motion from the Coulombic friction forces at the rolling and sliding interfaces between the ball, races, and cage. By contrast, the lubricant is due to resistance from the viscous friction caused by the ball “plowing through” the lubricant. The mechanical torque is often better known, because the parameters needed for its calculation are easily obtainable. These include the bearing geometry, materials properties, and loading configuration.

Some of the same properties are necessary to calculate the viscous drag torque due to the lubricant. However, one required value that is not easily determined in the design phase is the lubricant quantity factor (LQF). In bearing models of viscous drag, the LQF is a multiplication factor that scales the torque output of a bearing due to the energy lost to plowing through the lubricant. It is a dimensionless parameter that is intended to be directly related to the quantity of oil in the ball, race, and cage interfaces that contributes to the viscous drag of the system. Only a small fraction of the lubricant in a typical bearing contributes to these losses at the critical interfaces in the ball path. The rest of the lubricant is held in reserve elsewhere in the bearing, where it does not interfere with motion. Since the fraction of oil in the ball path is not easily measured or controlled, the LQF cannot be deduced a-priori.

To find an explicit value for the LQF, one typically must conduct an actual bearing test, measure the total bearing drag, subtract from this the mechanical drag, and solve for the LQF. Torque data is collected after run-in conditions have been met, upon which the bulk quantity of bearing lubricant is often assumed to be fixed throughout the range of operating conditions that are expected for the mission requirements. When calculated this way, all of the drag torque that is not caused by the nominal mechanical drag is ascribed to the lubricant, and the calculated LQF value depends linearly on this residual torque.

* The Aerospace Corporation, El Segundo, CA

Proceedings of the 44th Aerospace Mechanisms Symposium, NASA Glenn Space Flight Center, May 16-18, 2018

Unfortunately, there may be other contributions to bearing drag that are not accounted in the model (such as ball speed variations or cage instabilities). Unless they are recognized and quantified, these additional sources of torque will be captured in the LQF, and may be misinterpreted as a value due to the presence of additional lubricant. Due to these unpredictable contributors, the LQF is often considered to be a "catch-all" adjustment factor that includes both the lubricant and other unknown or un-modeled quantities.

Our purpose with the present report is to establish an experimental and analytical method for using heat generation to determine LQF values, which then can be used in further analysis of bearing performance. In a future report, we will probe more deeply into the relationship between LQF and the actual quantity of lubricant in the critical rolling and sliding interfaces. This paper will explain the experimental and analytical method behind quantifying LQF, and the resulting data collected for two different ball bearing types: 1) An all-52100 steel angular contact 305-size ball bearing, and 2) A Silicon Nitride – 52100 steel hybrid angular contact 305-size ball bearing

Experimental Method of Determining Lubricant Quantity Factor

The LQF was determined experimentally by measuring heat generation and temperatures of an isolated bearing in a vacuum environment, where the inner race was moving at a constant 6000 rpm speed while the outer race was held stationary. Both the test rig's thermal and mechanical boundary conditions were monitored and set for a given test. A series of boundary conditions were varied to create a test matrix and resulting bearing temperature and heat generation values were measured. The bearing and test conditions were then modeled and LQF was correlated to the test data using computational bearing analysis software. The influence of temperature and axial loads were then determined and compared for the two different bearing types. The next sections will describe the experiment, the test method and models required to characterize LQF for the two bearings tested.

Test Rig Overview

The test rig, originally designed to measure bearing thermal conductance [1], provided control of thermal and mechanical loads while monitoring the heat generated by a single test bearing. All tests were conducted in a vacuum environment.

Figure 1 is a photograph and schematic of the test stand, which is housed in a vacuum bell jar. The hardware shown was used for measuring heat generation of the 305-size bearings tested. The thermal system consists of a heat source and sink. Lamps generate a heat source that applies a thermal load on the rotating shaft. Heat travels up the shaft, through the test bearing and transfers through the disk-shaped Outer Heat Meter into a chiller-controlled heat sink on the perimeter of the Outer Heat Meter.

The mechanical controls include an applied axial load and a known and constant rotational speed. An axial load is applied using the Axial Load Device which applies a controlled and constant measured load to the outer rim of the Outer Heat Meter. The load transfers to the test bearing that is supported at the inner race by the shaft. In this way, a controlled axial load is applied and held constant throughout the test. The speed of the bearing is controlled by a vacuum motor that applies a constant and known rotational speed of the shaft and bearing inner race while the outer race is held stationary. The test is contained in a vacuum environment at pressures in the order of magnitude of 1×10^{-6} Torr.

Testing Method

The control thermal and mechanical boundary condition variables include a known heat sink chiller temperature, a known axial load, rotational shaft speed, and a heat lamp voltage output. While we can regulate the voltage to the heat source, the amount of heat input into the shaft is not controlled, although it is measured at steady state conditions so it is a known value. Thus, the test matrix includes the following:

1. Apply a range of axial loads
2. Apply a range of thermal sink chiller temperatures
3. Apply a range of voltage to the heat lamps
4. All test data is collected at a constant shaft rotational speed of 6000 rpm

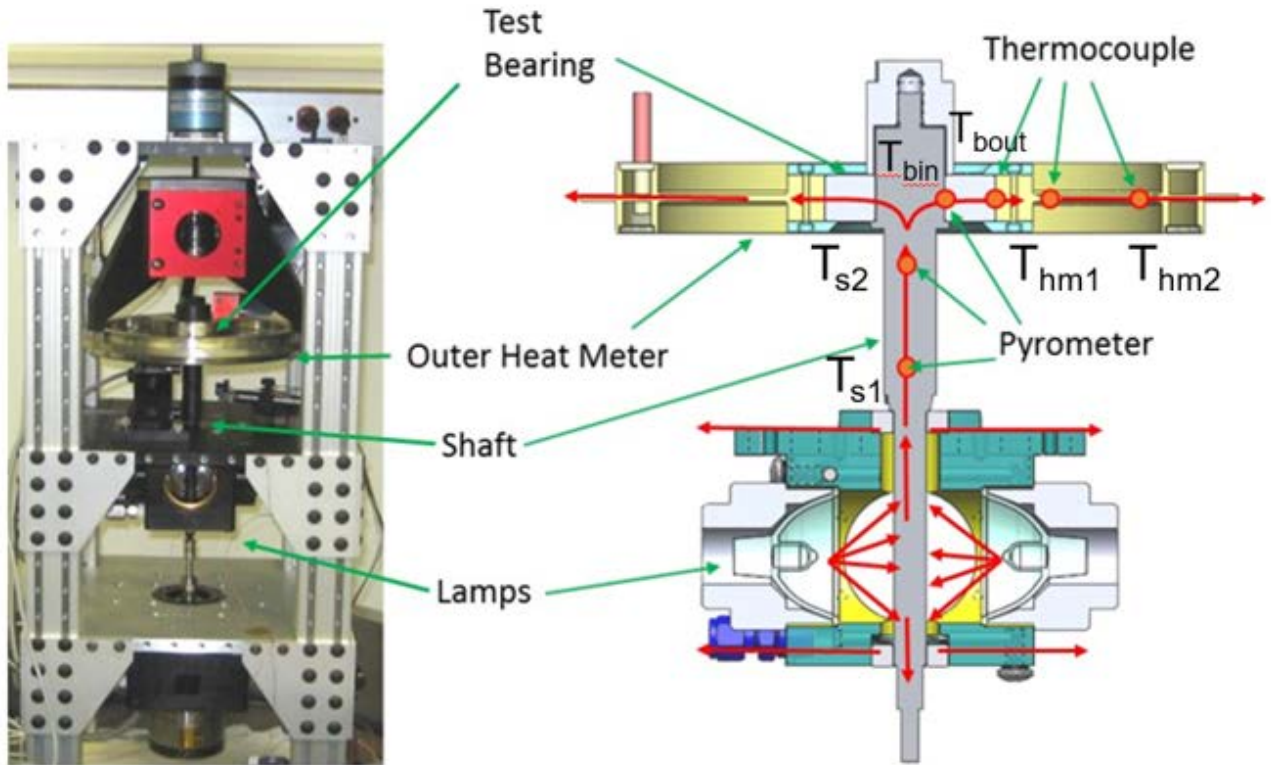


Figure 1. Bearing Test Fixture's Thermal Sub-System

Since the bearing temperatures are not controlled, a test matrix is needed to allow the results to be processed by interpolation. If, for instance, LQF is desired for a given temperature, it can be determined by selecting data points near the desired temperature and using linear interpolation.

Non-contact pyrometers are used to measure temperatures of rotational components, while thermocouples measure temperatures of stationary components. Sensors include two pyrometer measurements on the shaft, determining the heat entering the bearing, and two thermocouple measurements on the Outer Heat Meter that determine the heat exiting the bearing. The difference between the heat leaving and entering the test bearing determines the heat generated by the bearing. The inner race temperature is measured with a pyrometer and the outer race with a thermocouple (Figure 1).

To calculate heat entering the shaft, Q_{in} , we have:

$$Q_{in} = \frac{\pi d^2 k_s}{4L_s} (T_{s1} - T_{s2}) \quad (1)$$

where

- Q_{in} Heat entering the bearing from the shaft [W]
- d Diameter of the shaft [m]
- k_s Conductivity of the shaft [W/m·°C]
- L_s Pyrometer measurement separation distance [m]
- T_{s1} Temperature of the shaft at pyrometer location 1 [°C]
- T_{s2} Temperature of the shaft at pyrometer location 2 [°C]

To calculate the heat leaving the test bearing, we have:

$$Q_{out} = \frac{2\pi h k_{hm}}{\ln(\frac{r_2}{r_1})} \cdot (T_{hm1} - T_{hm2}) \quad (2)$$

where

Q_{out}	Heat exiting the bearing and entering the heat sink [W]
h	Thickness of the Outer Heat Meter [m]
k_{hm}	Conductivity of the Outer Heat Meter [W/m-°C]
r_1	Location of thermocouple close to bearing [m]
r_2	Location of thermocouple furthest from bearing [m]
T_{hm1}	Temperature of the shaft at thermocouple location close to bearing [°C]
T_{hm2}	Temperature of the shaft at thermocouple location furthest from bearing [°C]

Thus, the calculation of the heat generated by the bearing, Q_{int} , is as follows:

$$Q_{int} = Q_{out} - Q_{in} \quad (3)$$

From test measurements, we know the following quantities:

1. Test rig thermal boundary conditions
 - a. Q_{in} – heat entering into the bearing from the shaft
 - b. T_{sink} – temperature sink along the outer rim of the Outer Heat Meter
2. Bearing thermal variables
 - a. Q_{int} – Heat generated by the test bearing
 - b. T_{bin} – Bearing inner race temperature
 - c. T_{bout} – Bearing outer race temperature

The next section will explain how to determine the LQF based on test data and a detailed bearing-level mechanical model.

Modeling Method

The total bearing heat generation, Q_{int} , may be related to the total bearing drag torque, t , based on the model described here.

$$Q_{int} = 2\pi \cdot t \cdot \frac{rpm}{60} \quad (4)$$

The total torque, t , is the sum of the mechanical components, t_m , of torque and the viscous shear torque, t_{vs} , (lubricant torque). The total mechanical torque, is due to the motion and mechanics of contact between the ball, race and cage, while the viscous shear torque is due to the ball “plowing” through the lubricant.

$$t = t_m + t_{vs} \quad (5)$$

Mechanical Torque Modeling

The total mechanical torque has three components:

1. Ball spin friction torque [2-3] – a function of friction between ball and raceway, bearing geometries, mechanical loads, and bearing speed
2. Interfacial slip friction torque [4-6] – a function of friction between ball and raceway, bearing geometries, mechanical loads
3. Material hysteresis torque [7] – a function of mean contact stress, bearing geometries, and mechanical loads

Viscous Torque Modeling

Calculation of the viscous torque is based on a model by Palmgren and Snare [8]

$$t_{vs} = 1.42 \cdot 10^{-5} \cdot LQF \cdot E^3 \cdot (rpm \cdot v)^{2/3} \quad (6)$$

where E is the bearing pitch diameter and ν is the lubricant viscosity in centistokes.

A recent review of the literature revealed that there are new models of viscous drag that take into account significant progress in the understanding of EHD film formation that occurred during the late 1970's [9]. A review of these models is underway, but beyond the scope of this paper.

All the values required for calculation of the torques and heat generation are known from bearing geometries, materials properties, operational conditions, and temperature measurements, except for the LQF. Thus, we use Equations 1 through 3 to determine Q_{int} , and 4 through 6 to solve for LQF. Using this method, we conducted a series of parametric studies to explore the impact of various factors on LQF. The effect of operational conditions such as average temperature, temperature gradient, and axial load, for instance, was separated using a test matrix. The method of separating variables using this test matrix will be explained next.

A test matrix is created of LQF for various thermal and mechanical conditions. Separation of each variable's influence can be ascertained by maintaining one operational condition constant while changing the other. For instance, axial load is held constant through a series of tests, where either the heat input (heat lamp voltage) or heat sink temperatures (Outer Heat Meter chiller setting) settings are changed. Measurements are made at steady state conditions. Once a matrix of thermal boundary conditions are tested at a given axial load, the load itself is changed and measurements are taken for a matrix of thermal boundary conditions for the new mechanical state. Since the precise bearing temperature is not controlled, we use linear interpolation to ascertain the value of LQF for a precise temperature. All tests are taken for a bearing with an inner race rotating at a constant 6000 rpm.

All the LQF values are normalized by dividing the value by the maximum measured value of LQF (designated as LQFn) measured for a 305-sized all-steel bearing.

$$\text{normalized LQF} = \text{LQF}/\text{LQFn} \quad (7)$$

Test Bearing Specifications

Two different angular contact bearings were used in the experiments shown below. The primary difference between the two bearings was the material composition of the balls, which were 52100 steel in the first set of experiments, and Silicon Nitride in the second. Pennzane 2001 oil was used in all test data collected. This is a fully synthetic multiple-alkylated cyclopentane (MAC), formulated with a phosphate wear inhibiting additive and anti-oxidants. Both bearings were manufactured by Barden. Specifications of both bearings are provided in Table 1.

Table 1. Test Bearing Specifications

<i>Description</i>	<i>305 size all-steel</i>	<i>305 size hybrid</i>
Bore size	25 mm	25 mm
Outer diameter	62 mm	62 mm
Width	17 mm	17 mm
Number of balls	10	10
Ball size	11.91 mm (15/32 inch)	11.91 mm (15/32 inch)
Contact angle	15 degree	15 degree
Ball material	52100 steel	52100 steel
Race material	52100 steel	Silicon Nitride
ABEC rating	7	7
Manufacturer	Barden	Barden
Lubricant	Formulated MAC	Formulated MAC

In preparation for these experiments, bearings were flushed with heptane and relubricated by depositing 130 mg of Pennzane 2001 with a syringe. Portions of the oil charge were applied to each ball, the raceways, and the phenolic retainer. The bearing was then rotated to distribute the oil.

Each bearing was run-in in vacuum at room temperature at 6000 rpm. In each case, the measured value of heat generation decreased erratically until stabilizing after approximately 3 hours. Stability of heat generation, conductance, and temperature were all used to establish that the lubricant had been run-in. After this run-in period, the bearings were weighed to determine the quantity of oil remaining in the bearing. These values are reported in Table 2. The remainder of the oil was believed to be thrown from the bearings during run-in, and no longer able to contribute to ongoing lubrication of the critical interfaces. Similar tests of other bearings in this test configuration have been done to determine the quantity of oil that is lost after continued operation at 6000 rpm. These have shown that after completing the initial run-in, no additional oil (within the gravimetric measurement uncertainty of approximately 10 mg) is lost from the bearing due to prolonged operation at 6000 rpm. This observation was not detectably affected by variations in the thermal conditions of the tests. Therefore, we deduce that changes in the viscous drag reported below are due to changes in distribution of oil within the bearing, and not due to changes in the total quantity of oil in the bearing.

Table 2. Lubricant Pre and Post Run-In Weights

Bearing type	Dry bearing weight (g)	Initial oil weight (mg)	Post run-in oil weight (mg)	Post run-in oil/bearing %
Steel	228.54	130	100	0.0438%
Hybrid	188.05	130	90	0.0479%

Results from the All-Steel Bearing

This section shows the results of tests done on the 305-size all-steel angular contact ball bearing. In this series of tests, the applied axial load ranged from 89 to 222 N (20 to 50 lb). The exact bearing temperature was not controlled to a specific predetermined temperature, but rather was varied and recorded while testing under a wide set of heat sinks and heat lamp output. This resulted in a range of average temperatures from approximately 12 to 35°C, and a temperature differential that ranged from approximately 8 to 16°C. The LQF observations throughout this range of test conditions will be presented in the next sections.

Effect of Average Temperature on LQF

Figures 2 represent the normalized LQF as a function of average temperature (T_{ave}) for a 305-size all-steel bearing, where each graph displays a different axial load. In these graphs, each curve represents a particular fixed temperature differential value (DT). The trends show that LQF generally increases in direct proportion with the average temperature. The rate of increase is least at 89 N (20 lb) preload, but nearly equivalent through the range from 133 to 222 N (30 to 50 lb). As the preload is increased, there appears to be a bias offset that increases with the DT, but there is no detectable change in the slope throughout the range of DT.

In Figure 3, the DT=12°C data from each preload were grouped together to show the relative effect of preload on the temperature sensitivity. This plot shows the relative insensitivity to preload in the 133 to 222 N (30 to 50 lb) range, with the moderately less effect of T_{ave} in the 89 N (20-lb) case.

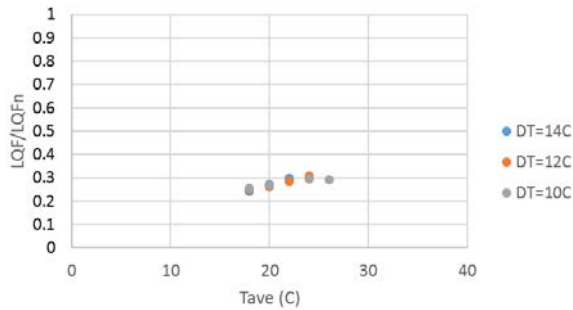


Figure 2a. Applied load of 89 N (20 lb)

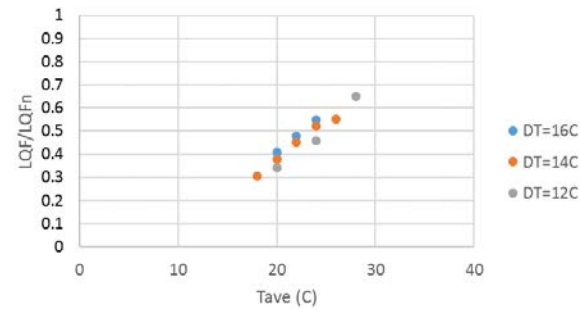


Figure 2b. Applied load of 133 N (30 lb)

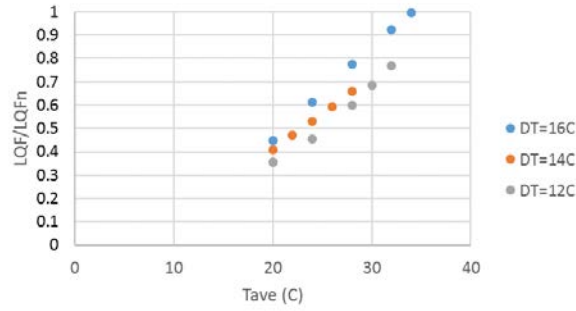


Figure 2c. Applied load of 178 N (40 lb)

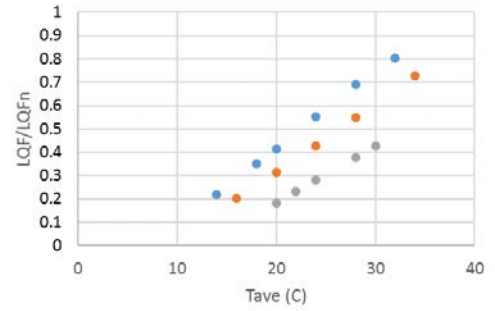


Figure 2d. Applied load of 222 N (50 lb)

Figure 2. Normalized LQF vs. average temperature (T_{ave}) for variable applied loads and constant temperature gradient (DT) for 305-size all-Steel Bearing

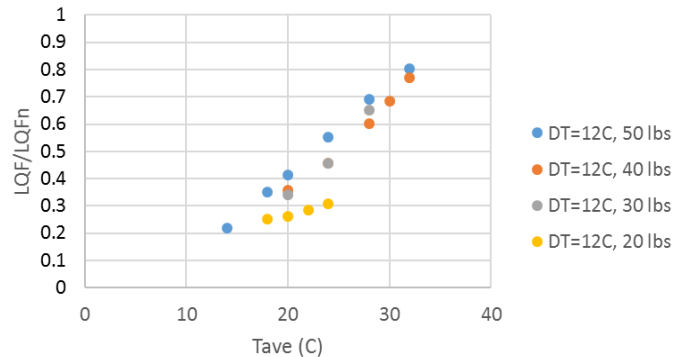


Figure 3. Normalized LQF vs. average temperature for variable applied loads and constant temperature gradient of 12°C for 305-size all-Steel Bearing

Effect of Temperature Gradient on LQF

Figures 4 were generated from the same data set as those shown in the previous section. However, in this section, the normalized LQF is plotted against temperature gradient (DT) for the all steel 305-size bearing. Each graph in this series represents a different axial load. Each individual curve represents a particular fixed average temperature. The trends show that there is an increase in LQF with increased temperature gradient, but the slope is strongly influenced by axial loads. This implies that there is a coupled relation between temperature gradient and axial loads.

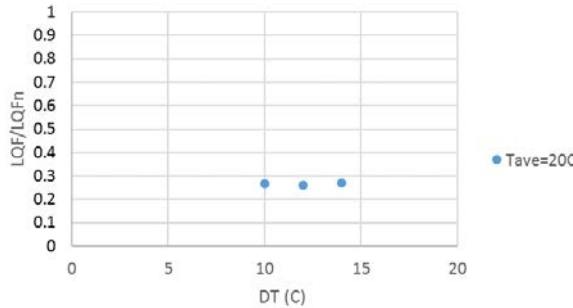


Figure 4a. Applied load of 89 N (20 lb)

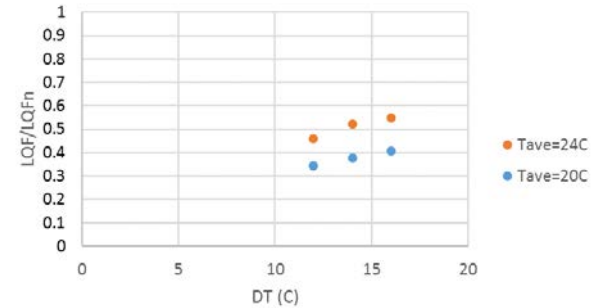


Figure 4b. Applied load of 133 N (30 lb)

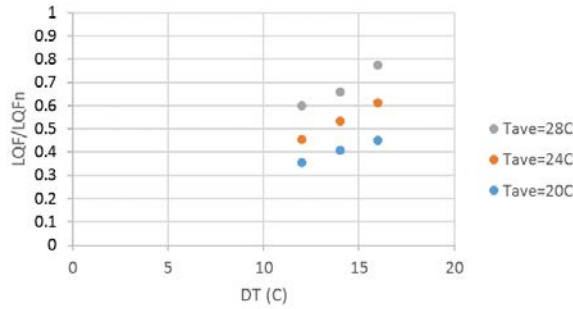


Figure 4c. Applied load of 178 N (40 lb)

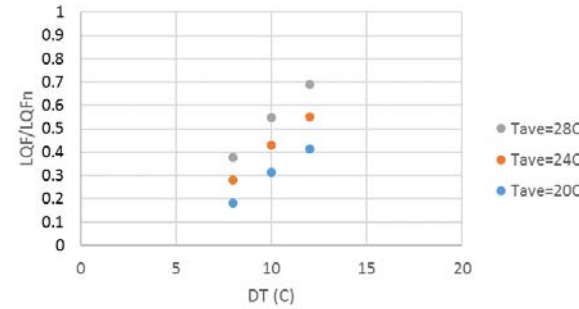


Figure 4d. Applied load of 222 N (50 lb)

Figure 4. Normalized LQF vs. temperature gradient for variable applied loads and constant average temperature for 305-size all-Steel Bearing

Figure 5 shows the coupled relation between temperature gradient and axial load on LQF in a more condensed way. Here, the normalized LQF is plotted as a function of temperature gradient for a constant average temperature of 20°C for each of the applied loads. The data indicates that there is an approximately linear relation between temperature gradient and LQF. But the slope of this relation is non-linearly dependent on the axial load.

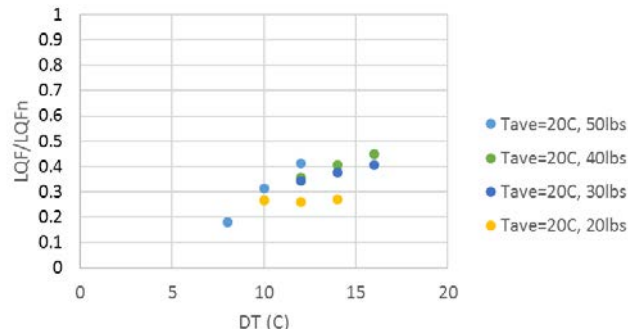


Figure 5. Normalized LQF vs. temperature gradient for variable applied loads and constant average temperature of 20°C for 305-size all-Steel Bearing

Effect of Axial Load on LQF

In Figure 6, the data are plotted to show the dependence of axial load for the all-steel 305-size bearing. All of the data in this plot were collected with a temperature gradient of 12°C. Each curve on this plot represents a unique constant average temperature. The results show that the LQF generally increases with axial load. And although the LQF is generally higher with greater T_{ave} , the rate of increase with preload is not sensitively dependent on T_{ave} .

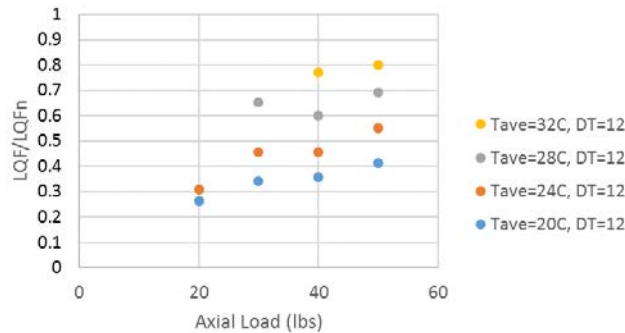


Figure 6. Normalized LQF vs. axial load for a range of average temperature but constant temperature gradient of 12°C for 305-size all-Steel Bearing

Results from the Silicon Nitride Hybrid Bearing

A matrix of test data was also collected for an ABEC 7 305-size hybrid ball bearing with silicon nitride balls. In this series of tests, the applied axial load ranged from 89 to 222 N (20 to 50 lb). The exact bearing temperature was not controlled to a specific predetermined temperature, but rather was varied and recorded while testing under a wide set of heat sinks and heat lamp output. This resulted in a range of average temperatures from approximately 15 to 30°C, and a temperature differential that ranged from approximately 10 to 16°C. The LQF observations throughout this range of test conditions will be presented in the next sections.

Effect of Average Temperature on LQF

Figure 7 represents the normalized LQF as a function of average temperature for a 305-size hybrid bearing, where each graph represents a different axial load. In these graphs, each curve represents a particular fixed temperature differential value (DT). The trends show that there is an increase in LQF as average temperature rises in an approximately linear fashion. However, in some fixed load values, the slopes of curves at different DT values are not parallel. This indicates that the sensitivity of LQF to T_{ave} is dependent on the temperature differential across the bearing. Figure 7a suggests that at low preload, a smaller DT results in a slightly higher sensitivity to T_{ave} , while Figure 7c suggests that at higher preload, a smaller DT results in a slightly lower sensitivity to T_{ave} .

To separate the impact of thermal gradient, Figure 8 shows the normalized LQF as a function of average temperature for a constant temperature gradient of 12 °C for each of the axial loads tested. The results show that each curve appear somewhat parallel under these conditions, indicating for the same gradient, the LQF is sensitive to average temperature to the same degree, except for the 222 N (50 lb) load case. This contrasts with the steel bearing, where each curve was parallel except for the lowest load of 89 N (20 lb).

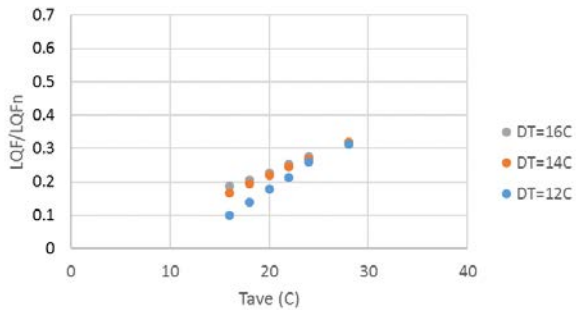


Figure 7a. Applied load of 89 N (20 lb)

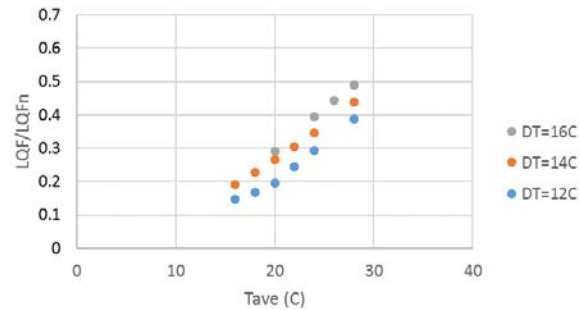


Figure 7b. Applied load of 133 N (30 lb)

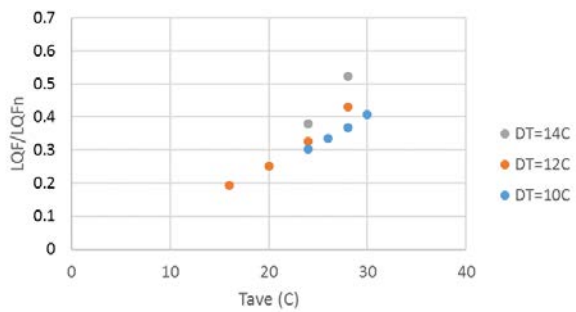


Figure 7c. Applied load of 178 N (40 lb)

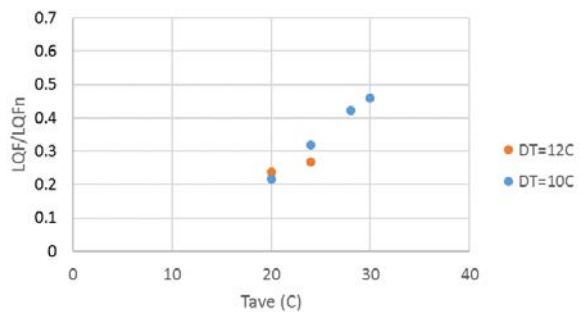


Figure 7d. Applied load of 222 N (50 lb)

Figure 7. Normalized LQF vs. average temperature for variable applied loads and constant temperature gradient for 305-size Hybrid Bearing

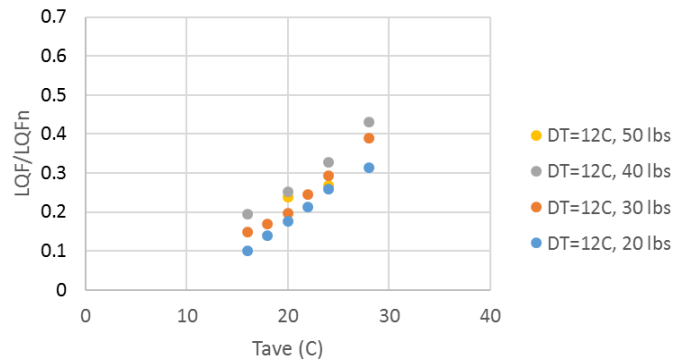


Figure 8. Normalized LQF vs. average temperature for variable applied loads but constant temperature gradient of 12°C for 305-size Hybrid Bearing

Effect of Temperature Gradient on LQF

Figures 9 represents the normalized LQF as a function of temperature gradient for a 305-size hybrid bearing, where each graph represents a different axial load. In the plots, each curve represents a fixed average temperature. The trends show that there is generally an increase in LQF with increased temperature gradient, but the slope is influenced by axial loads. Although it is only one data point, in the case of the largest 222 N (50 lb) load, the LQF actually decreased with increasing DT for an average temperature of 24°C. Again, the LQF trends suggest a complex interdependence between average temperature, temperature gradient, and axial loads.

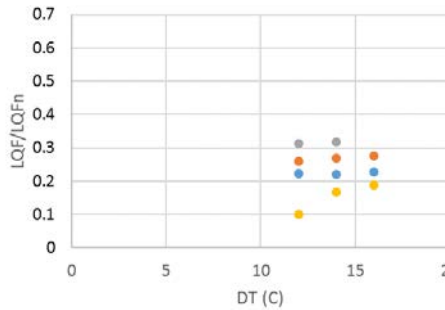


Figure 9a. Applied load of 89 N (20 lb)

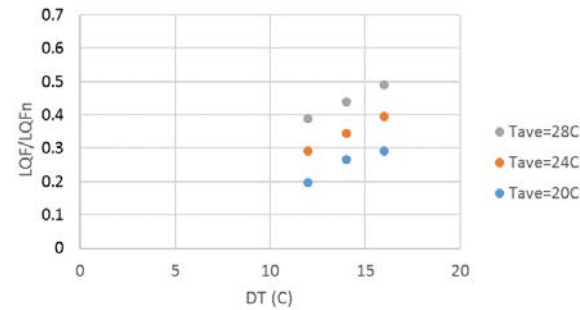


Figure 9b. Applied load of 133 N (30 lb)

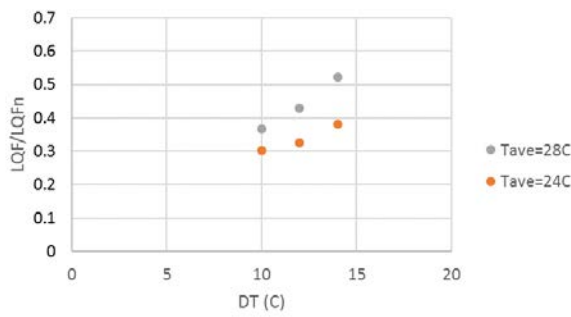


Figure 9c. Applied load of 178 N (40 lb)

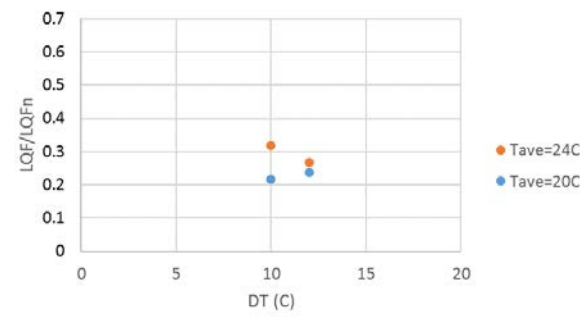


Figure 9d. Applied load of 222 N (50 lb)

Figure 9. Normalized LQF vs. temperature gradient for variable applied loads and constant average temperature for 305-size Hybrid Bearing

Figure 10 shows the coupled relation between temperature gradient and axial load on LQF in a more condensed way. This graphs the LQF as a function of temperature gradient for a constant average temperature of 24°C for each of the applied loads. The curves show that the slope of this relation between LQF and temperature gradient is non-linearly a function of axial load.

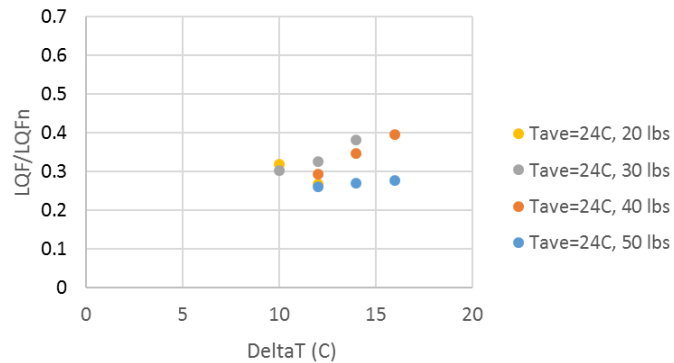


Figure 10. Normalized LQF vs. temperature gradient for variable applied loads and constant average temperature of 20°C for 305-size Hybrid Bearing

Effect of Axial Load on LQF

Figure 11 represents the normalized LQF as a function of axial loads for a 305-size hybrid bearing. Each curve represents a constant average temperature, and all data were collected with a temperature gradient of 12°C. The results show that the LQF generally increases in direct proportion with the axial load, and the magnitude of the LQF increases with the average temperature. These trends are consistent with the

all steel bearing. However, one data point at 222 N (50 lb) suggests a deviation from this trend as the load is increased.

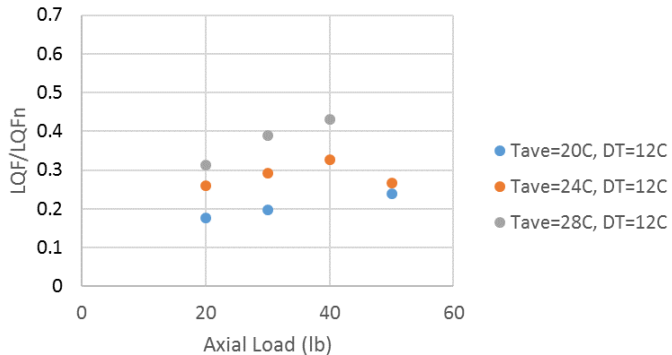


Figure 11. LQF vs. axial load for a range of average temperature but constant temperature gradient of 12°C for 305-size all-Steel Bearing

Discussion

The results show that LQF generally increases with T_{ave} , DT, and preload. However, we do not directly conclude from this that the quantity of lubricant in the rolling and sliding interfaces is also increasing with each variable. Instead, it is likely that the full complexity of bearing drag is not fully realized in the model described above, and that there are other factors that might influence the calculated values of LQF. For this reason, we assert that the measured values of LQF are to be used cautiously for purposes of thermal modeling, and to demonstrate the degree to which LQF may fluctuate with changes in test conditions. It may also be used as a guide to deeper analysis of bearing function as it depends on the interplay between temperature, mechanics, and oil quantity. In the discussion below, we explore some possible causes and implications of the observed behavior.

Dependence of LQF on T_{ave}

For both test bearings, the data show that the normalized LQF increases in direct proportion with the average temperature of the test bearing (Figures 2, 3, 7, and 8). We surmise that this is primarily due to an increase in the actual quantity of lubricant in the rolling and sliding interfaces. This may be partly due to reduced viscosity of the oil, resulting in improved oil mobility. Lower viscosity may also augment the influence of dynamic centripetal forces driving oil on the surface of the balls towards the rolling contact at the expense of static surface forces that drive the oil towards spreading more uniformly on the surfaces. When the environment is warmer, there may also be some reduction in the significance of localized heating at the ball path, which creates a thermocapillary differential to drive oil away from the contact.

A similar dependence on temperature has been observed with aging gyroscopes on satellites [10]. With this application, the magnitude of the dependence of viscous bearing drag on temperature is used to estimate oil quantity. When gyroscopes become starved of oil, the sensitivity of viscous drag to brief temperature fluctuations becomes diminished. However, during periods of elevated time-average temperature, a robust viscous response has been observed to recover. During these periods of recovery, bearing noise due to retainer instability is often quieted. This has been interpreted as a reversible increase in the oil quantity, caused by increased bearing temperature.

LQF comparisons between the hybrid and all-steel bearing generally indicate that the hybrid bearing has a lower LQF than the equivalent all-steel bearing under similar conditions. One example is shown in Figure 12. This indicates that under similar thermal and mechanical conditions, the hybrid bearing will have lower viscous torque. While there seemed to be some degree of variances between the all-steel and hybrid

bearings, the data are in the same order of magnitude of each other, for the same size bearing. However, since the all-steel bearing tends to have a higher LQF than the hybrid bearing, this indicates that the torque output of an all-steel bearing will be slightly higher than the hybrid if all other conditions are equal.

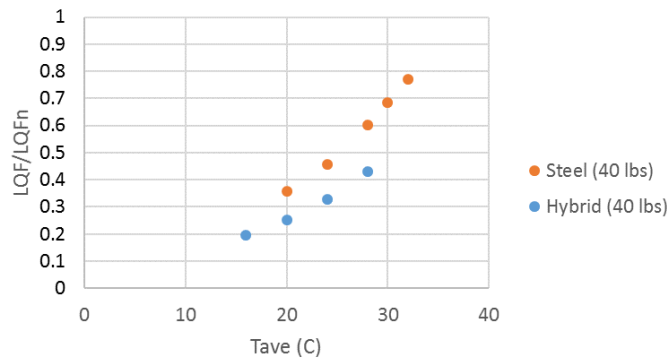


Figure 12. Normalized LQF vs. average temperature for 178 N (40 lb) load and constant temperature gradient of 12°C for 305-size all-Steel and Hybrid Bearing

Dependence of LQF on DT

For both test bearings, the data generally show that LQF increases in direct proportion with the temperature differential (DT) across the bearing (Figures 4,5,9, and 10). We surmise that this is not due to an increase in the actual quantity of oil, but more likely due to imperfections in the model since it fails to account for the circumstances created by the large differential across the bearing. For example, the model may underestimate the actual viscosity, and correct for this by overestimating the quantity. The viscosity used in the calculations of LQF shown here was chosen to be the viscosity at the temperature midway between the outer and inner race temperatures. However, because the dependence of viscosity on temperature is not linear, the actual average viscosity will be lower than the viscosity at average temperature. The deviation (from the average viscosity) of the low temperature outer race contact will be larger than the deviation of the warmer inner race contact, resulting in an underestimate of the viscosity if the average viscosity is used in the model. To account for a given amount of measured torque, an underestimate of the viscosity would result in an overestimate of the LQF (Equation 6). This error will increase with increasing DT, resulting in a gradual increase in LQF with DT. Since the actual temperature of the oil at each interface (inner and outer raceway) is not known, the magnitude of this error could not be calculated to determine if it can account for the entire effect observed here.

We note, however, that the magnitude of the temperature differentials studied here is larger than one would likely encounter in a typical application. This large DT was imposed to aid in the measurement of thermal conductance. Therefore, the results are important for the purposes of thermal analysis of test articles but are not expected to have significant impact on typical applications.

Dependence of LQF on Load

Figures 6 and 11 show a moderate dependence of LQF on load for both the all-steel and hybrid bearings. The LQF generally increases in direct proportion to the load, although deviation from this trend was observed at the highest load with the hybrid bearing. The cause of this dependence has not been determined. As the load is increased, the dimensions of the conformal contact between the balls and races will change. This change in the contact geometry could possibly result in an increase of the volume of oil in the contact meniscus due to having a larger interfacial surface area in close proximity. This would hypothetically be an actual increase in the lubricant quantity.

The load dependence may also be partly due to changes in the width of the Hertzian contact ellipse. Since our model for viscous drag torque (Equation 6) is independent of load, it does not account for any increased viscous drag due to expansion of the contact ellipse. The Palmgren-Snare model [8] neglects any such

effects. However, there is a linear dependence on contact width in a newer model of viscous drag [10]. If there are actual changes in viscous drag due to the changing contact geometry, they would be captured in the LQF and possibly misinterpreted as an increase in oil quantity. While it is possible that this would account for the observed increase in LQF in Figures 6 and 11, a thorough evaluation of viscous models is beyond the scope of this work. Data from this study will be used in the future to test other models.

Conclusion

The distribution of oil in an operating angular contact bearing will depend on a number of competing forces. These include mechanical forces, such as centripetal accelerations and contact pressures, and surface forces, such as the capillary action at the ball/race interface and the surface tension gradient in a region of varying temperature. As a result, the quantity of lubricant in the rolling contact will depend on operational and environmental conditions. And with it, many other bearing performance characteristics (for example, thermal conductance and oil film thickness) will also depend on condition. This complex dependence is not often taken into account when modeling dynamic bearing behavior, where the LQF is often taken as a fixed value. The results of this series of tests shows the significance of this effect and provides first-order estimates of the degree of sensitivity to some important variables.

This report covered the LQF test data based on two bearing types tests: 305-size hybrid and 305-size steel bearings. Results showed that LQF was significantly impacted by average temperature (Figures 2, 3, 7, and 8), temperature gradient (Figures 4, 5, 9, and 10) and axial loads (Figures 6 and 11). We surmise that these effects may be due to changes in the viscosity of the oil, affecting the volume of oil in the ball/race meniscus, or they may be due to changes in the thermal gradient in the vicinity of the contact, affecting the flow of oil to the meniscus. While it is likely that the dependence on average bearing temperature is caused by an actual change in the quantity of oil at the ball/race contact, the dependence on DT across the bearings is more likely due to inadequacies in the drag torque model. The cause of the dependence on load remains undetermined, but there are potential causes that are due to changes in actual oil volume and others due to errors in the drag torque model. Regardless of the cause, these dependencies should be considered when applying the conventional drag model shown in Equation 6.

There are some differences in trends between the hybrid and all steel bearing. In the hybrid bearing, all load conditions show a sensitivity of LQF to average temperature, but the degree of sensitivity is dependent on both temperature gradient and axial loads. The constant thermal gradient curves are NOT parallel in the case of the hybrid bearings. This indicates that there is an interdependency between LQF and average temperature, temperature gradient, and axial loads. The cause of differences between steel and hybrid are the subject of future work.

Acknowledgements

The authors would like to acknowledge the management, Dr. Michael R. Hilton and Dr. Michael C. Lee for their help on this project. This work would not be possible without their continued support.

References

1. Y. R. Takeuchi, P. P. Frantz, and M. R. Hilton, "Observations of Spacecraft Bearing Lubricant Redistribution Based on Thermal Conductance Measurements", Proceedings of the 42nd Aerospace Mechanisms Symposium, NASA GSFC, May, 2014.
2. H. Poritsky, C. W. Hewlett, and R. E. Coleman, "Sliding Friction of Ball Bearings of the Pivot Type", *Journal of Applied Mechanics*, December 1947.
3. G. S. Reichenback, "The Importance of Spinning Friction in Thrust Carrying Ball Bearings", *ASME 59-LUB-6*.
4. R. C. Drutowski, "The Role of Micro-Slip for Freely Rolling Bodies", ASME-ASLE International Lubrication Conference, 1964.
5. H. L. Heathcote, "The Ball Bearing: In the Making, Under Test and on Service", *Proc. Instn. Of Automobile Engineers*, Vol. 15, page 569, 1921.
6. A. Palmgren, "Sliding Friction in Ball Bearings", *Engineering*, Vol. 107, pages 289, 1919.
7. J. A. Greenwood, H. Minshall, and D. Tabor, "Hysteresis Losses in Rolling and Sliding Friction", *Proc. Royal Society*, pages 480-507, July 1960.
8. A. Palmgren and B. Snare, "Influence of Load and Motion on the Lubrication and Wear of Rolling Elements", Inst. Of Mech. Eng., London, 1957.
9. N. Biboulet and L. Houpert, "Hydrodynamic Force and Moment in Pure Rolling Lubricated Contacts", *Proc. IMechE Vol. 224 Part J: J. Engineering Tribology*, March 2010.
10. P. Frantz, "Diagnostic Methods for High Cycle Precision Mechanisms", 2015 ASTM International Rolling Element Bearings Conference, Anaheim, CA, April 29, 2015.

